MDPI

Electromaterials for Environment & Energy

Volume II

Edited by

Marc Cretin, Sophie Tingry and Zhenghua Tang

Printed Edition of the Topic Published in

Electrochem, Materials, Membranes, Nanomaterials and Catalysts

www.mdpi.com/topics

Electromaterials for Environment & Energy: Volume II

Electromaterials for Environment & Energy: Volume II

Editors

Marc Cretin
Sophie Tingry
Zhenghua Tang

MDPI • Basel • Beijing • Wuhan • Barcelona • Belgrade • Manchester • Tokyo • Cluj • Tianjin

Editors

Marc Cretin
Institut Européen des Membranes (IEMM, ENSCM UM CNRS UMR5635)
France

Sophie Tingry
Institut Européen des Membranes (IEMM, ENSCM UM CNRS UMR5635)
France

Zhenghua Tang
South China University of Technology
China

Editorial Office
MDPI
St. Alban-Anlage 66
4052 Basel, Switzerland

This is a reprint of articles from the Topic published online in the open access journals *Nanomaterials* (ISSN 2079-4991), *Materials* (ISSN 1996-1944), *Membranes* (ISSN 2077-0375), *Catalysts* (ISSN 2073-4344), and *Electrochem* (ISSN 2673-3293) (available at: https://www.mdpi.com/topics/materials_energy).

For citation purposes, cite each article independently as indicated on the article page online and as indicated below:

LastName, A.A.; LastName, B.B.; LastName, C.C. Article Title. *Journal Name* **Year**, *Volume Number*, Page Range.

Volume 2
ISBN 978-3-0365-6910-9 (Hbk)
ISBN 978-3-0365-6911-6 (PDF)

Volume 1-2
ISBN 978-3-0365-6499-9 (Hbk)
ISBN 978-3-0365-6500-2 (PDF)

Contents

About the Editors

Marc Cretin

Marc Cretin has been a Professor at the Faculty of Sciences, Montpellier University since 2012. His research interests focus on electrochemistry and material for applications in wastewater treatment and energy. In particular, he works on the development of electrochemical advanced oxidation processes (EAOP) and reactive electrochemical membranes (REM). He has published over 130 peer-reviewed papers in well-recognized scientific journals.

Sophie Tingry

Sophie Tingry is a CNRS Research Director at the European Membrane Institute in Montpellier. Her field of interest concerns the development of electrochemical systems for energy conversion and particularly the reactions at the interfaces of innovative electrocatalytic materials for energy production and storage.

Zhenghua Tang

Dr. Zhenghua Tang is currently is an Associate Professor at the School of Environment and Energy at South China University of Technology, China. He obtained his BS degree at Lanzhou University in 2005, and a PhD. degree at Georgia State University in 2012. After two years of postdoctoral training at the University of Miami, he started his faculty position at SCUT since 2014. His research focuses on the controllable synthesis and electrocatalytic applications of atomically precise metal nanoclusters and single-atom-based nanomaterials. He has published over 80 peer-reviewed papers in J. Am. Chem. Soc., Angew. Chem., Chem. Sci. and other well-recognized scientific journals.

Preface to "Electromaterials for Environment & Energy: Volume II"

In a developing world, the demands for energy and water and the damage to our environment are constantly increasing. Electrochemistry could be a great tool to solve these problems, with an impact that could minimize or at least control damage in our environment, since the main driver of the reaction is the electron that can be produced in a sustainable manner.

In electrochemical approach to energy conversion and production, drinking water production and wastewater treatment, the materials and interfaces are key elements that greatly affect a system's performance.

The objective of this topic is to propose a set of publications gathering the current research trends in the fields of energy, water and environmental pollution treatment, with a focus on the control of materials and interfaces, in view of process optimization.

Marc Cretin, Sophie Tingry, and Zhenghua Tang
Editors

nanomaterials

MDPI

Article

N-Doped Graphene as an Efficient Metal-Free Electrocatalyst for Indirect Nitrate Reduction Reaction

Jujiao Zhao [1], Bo Shang [2] and Jun Zhai [1,*]

[1] College of Environment and Ecology & MOE Key Laboratory of the Three Gorges Reservoir Region's Eco-Environment, Chongqing University, Chongqing 400045, China; zhaojujiao@cqu.edu.cn
[2] School of Chemistry and Chemical Engineering & Chongqing Key Laboratory of Theoretical and Computational Chemistry, Chongqing University, Chongqing 401331, China; bshang@cqu.edu.cn
* Correspondence: zhaijun@cqu.edu.cn

Abstract: N-doped graphene samples with different N species contents were prepared by a two-step synthesis method and evaluated as electrocatalysts for the nitrate reduction reaction (NORR) for the first time. In an acidic solution with a saturated calomel electrode as reference, the pyridinic-N dominant sample (NGR2) had an onset of 0.932 V and a half-wave potential of 0.833 V, showing the superior activity towards the NORR compared to the pyrrolic-N dominant N-doped graphene (onset potential: 0.850 V, half-wave potential: 0.732 V) and the pure graphene (onset potential: 0.698 V, half-wave potential: 0.506 V). N doping could significantly boost the NORR performance of N-doped graphene, especially the contribution of pyridinic-N. Density functional theory calculation revealed the pyridinic-N facilitated the desorption of NO, which was kinetically involved in the process of the NORR. The findings of this work would be valuable for the development of metal-free NORR electrocatalysts.

Keywords: nitrate reduction reaction; N-doped graphene; pyridinic-N

Citation: Zhao, J.; Shang, B.; Zhai, J. N-Doped Graphene as an Efficient Metal-Free Electrocatalyst for Indirect Nitrate Reduction Reaction. *Nanomaterials* **2021**, *11*, 2418. https://doi.org/10.3390/nano11092418

Academic Editors: Jin Suk Chung and Marc Cretin

Received: 16 August 2021
Accepted: 9 September 2021
Published: 17 September 2021

1. Introduction

The global nitrogen cycle has been disrupted by human activities and industries, resulting in an increased nitrate concentration in the hydrosphere [1,2]. Since a high nitrate level in the drinking water has been proven to be one of the inducements of methemoglobinemia and gastrointestinal cancer, it is important to limit the concentration of nitrate in groundwater and other water bodies [3–5]. Reducing the nitrate emission from industry effluents is an effective way to limit nitrate pollution since nitric acid is widely used in several industries, such as the nuclear industry and the explosives industry [6,7]. The wastewater from these industries could be strongly acidic with a high concentration of nitrate, which is hardly treated by traditional biological treatments [7]. An efficient method of removing nitrate from acidic solutions is highly needed.

The electrochemical reduction of nitrate has attracted huge interest thanks to its controllable process and relatively low costs [8]. However, the sluggish kinetics of the nitrate reduction reaction (NORR) leads to an extreme demand for robust electrocatalysts [9–11]. Generally, noble metals, such as Pt [12–17], Rh [18,19], Au [20], and Pd [21–23] based catalysts, present excellent electrochemical activity for the NORR, but the scarcity and high cost hinder their practical applications. To develop cheaper alternatives, most efforts have been devoted into metal-based electrodes, such as Cu [24–28], Sn [29–31], Co [32], Fe [33], and Cu-based bimetallic metals (Cu-Zn, Cu-Ni, Cu-Mn, etc.) [34–36]. However, the possible release of metal ions during operation also limits their usefulness for practical applications, especially under acidic conditions. Despite many efforts devoted to developing electrocatalysts for the NORR, few of these studies involved the NORR under strongly acidic conditions [8]. By comparison, cheap and earth-abundant metal-free electrocatalysts with high activity and good stability in acidic conditions are highly desired.

Carbon nanomaterial is widely used as electrocatalysts due to their chemical stability and good conductivity [37–42]. Graphene, the typical carbon nanomaterial with two-dimensional structure, has been demonstrated to facilitate the electrochemical reduction of nitrate into nitrite [43], which is regarded as the rate-determining step in the entire process of nitrate reduction [44–47]. The NORR on graphene is effective in acidic solution through the indirect process with NO as the key intermediate. According to the literature, the indirect NORR on graphene even presented better performance than that on Pt [43]. However, there are still scarce reports on the NORR with graphene-based catalysts. It is still highly desirable to develop carbon-based metal-free electrocatalysts with higher NORR performance than pristine graphene.

N doping can significantly enhance the electrochemical activity of graphene for oxygen reduction [48], oxygen evolution [49], hydrogen evolution [50], and CO_2 electroreduction [51], due to the change of charge densities. The improved charge densities of surrounding C atoms may facilitate the electron-transfer reaction, which also suggests an improved activity for the NORR. However, to the best of our knowledge, no related study has been reported. Furthermore, since the effects of N species (pyridinic-N, pyrrolic-N, and graphitic-N) on the electrochemical activity are substantially different [52,53], it would be meaningful to reveal their contribution to the NORR, which will guide the design of superior metal-free electrocatalysts for the NORR in the future.

Herein, we synthesized N-doped graphene containing different N species and evaluated their NORR activity. For the first time, an N-doped carbon material was adopted as the NORR electrocatalyst and the contribution of active N species was investigated. We demonstrated that pyridinic-N played the dominant role in the enhanced NORR activity and density functional theory (DFT) calculations were further conducted to reveal the mechanism.

2. Materials and Methods

2.1. Materials

All solid chemicals and 20% commercial Pt/C were purchased from Aladin Ltd. (Shanghai, China). HNO_3, HCl, H_2O_2, and H_2SO_4 were obtained from Chongqing Chuandong Co., Ltd. (Chongqing, China). Dupont Nafion PFSA Polymer Dispersion D-520 was obtained from Dupont.

2.2. Preparation of N-Doped Graphene

Firstly, graphene oxide (GO) was prepared by a modified Hummer's method [52]. Then, GO was reduced by hydrothermal method to produce graphene. Urea or melamine was chosen as precursor to provide N atoms during the hydrothermal reaction. In a typical process, 35 mg of GO and 1050 mg of urea were mixed with 35 mL of de-ionized (DI) water and transferred into a Teflon-lined stainless-steel autoclave. After heating at 180 °C for 12 h and then cooling down to room temperature, the as-prepared sample was washed by DI water and dried overnight to obtain the N-doped graphene named as NGR1. NGR2 was produced by a similar hydrothermal process but with 35 mg of GO and 800 mg of melamine as precursors. Pure reduced GO (GR) was also prepared by a similar hydrothermal process without the addition of N-containing precursors.

2.3. Characterizations

Scanning electron microscopy (SEM, Hitachi S-4800) and transmission electron microscopy (TEM, FEI-Tecnai G2 20) were used to characterize the morphology of catalysts. Energy dispersive X-ray spectrometer (EDS) elemental mapping was recorded on an Iridium Ultra Premium EDS System (A550I, IXRF, USA). X-ray diffraction (XRD) patterns were carried out on a Shimadzu LabX XRD-6000 to investigate the crystal structure. X-ray photoelectron spectra (XPS) were obtained with an ESCALAB 250Xi spectrometer using a nonmonochromatized A1 Kα X-ray source (1486.6 eV) for elemental composition analyses, together with a Renishaw Micro-Raman system 2000 with He-Ne laser excitation for

Raman spectroscopy. N_2 adsorption–desorption isotherms were obtained at 77 K with a Quadrasorb 2MP instrument.

2.4. Electrochemical Performance for the NORR

Electrochemical measurements were performed on a CHI660E electrochemical workstation in a three-electrode cell. The saturated calomel electrode (SCE) and Pt wire were chosen as reference electrode and counter electrode, respectively. All the potentials mentioned in this work are versus SCE. For the electrode preparation, the prepared catalyst powders were mixed with a Nafion solution and loaded on glassy carbon with a mass loading of 0.2 mg cm^{-2} for all the samples. Linear sweep voltammetry was carried out in a 5 M HNO_3 solution with a scan rate of 10 mV s^{-1}. Chronoamperometry was conducted in a 5 M H_2SO_4 solution at 0.8 V in the absence and presence of 2 mM HNO_3. The nitrate removal experiment was conducted in a two-chamber reactor divided by a Nafion 117 membrane. The working electrode was prepared with a carbon cloth as the substrate with an area of 4 cm^2. The volume of the solution was 20 mL. The concentrations of nitrate and nitrite were determined by the standard colorimetric method according to the Chinese Environment Standards using a UV-2450 spectrophotometer (Text S2).

2.5. DFT Calculation Details

The Vienna Ab initio Package (VASP) [54,55] was employed to perform all the DFT calculations within the generalized gradient approximation (GGA) using the PBE formulation (details were described in Text S1) [56]. Three graphene models corresponding to the undoped graphene with defects (model 1), graphene with pyridinic-N (model 2), and graphene with pyrrolic-N (model 3) were constructed. The adsorption energy (E_{ads}) of NO was defined as:

$$E_{ads} = E_{NO/surf} - E_{surf} - E_{NO\,(g)} \quad (1)$$

where $E_{NO/surf}$, E_{surf}, and $E_{NO\,(g)}$ are the energy of NO adsorbed on the surface, the energy of clean surface, and the energy of isolated NO molecules in a cubic periodic box with a side length of 20.00 Å and a 1 × 1 × 1 Monkhorst–Pack k-point grid for Brillouin zone sampling, respectively.

3. Results and Discussions

3.1. Characterizations of Samples

To accurately investigate the effects of different N species on the NORR performance, NGR1 and NGR2 with similar elemental contents (Table S1) were prepared under similar hydrothermal conditions by controlling the N-containing precursors. Figure 1a,b shows the morphology of NGR1 and NGR2. Both samples exhibited the typical two-dimensional structure of graphene with massive wrinkles. No residues could be found on the graphene surface, indicating the samples consisted of only graphene without any undecomposed precursors. TEM (Figure 1c,d) was also employed to reveal the microstructure of the samples, which further indicated NGR1 and NGR2 possessed a voile-like topography. From the EDS images (Figures S1 and S2), the color plots representing the N atoms were dispersed uniformly throughout the selected sample area, indicating the successful doping of N into the graphene.

X-ray diffraction (XRD) patterns of NGR1, NGR2, and GR (Figure 2a) exhibited similar broad peaks centered at 20°~30° corresponding to the carbon (002) facet. The absence of peak relating to graphene oxide at 10° in all three patterns indicated that the graphene was successfully prepared by reducing the graphene oxide through hydrothermal method. The Brunauer–Emmett–Teller (BET) surface areas of NGR1 and NGR2 were revealed by N_2 adsorption–desorption isotherms, as shown in Figure 2b. NGR1 and NGR2 had surface areas of 232 and 208 m^2 g^{-1}, respectively. It is known that the BET surface area significantly affects electrochemical activity. The difference in BET surface areas between NGR1 and NGR2 was less than 10%, which is helpful to rule out the influence of the BET surface area on the NORR activity.

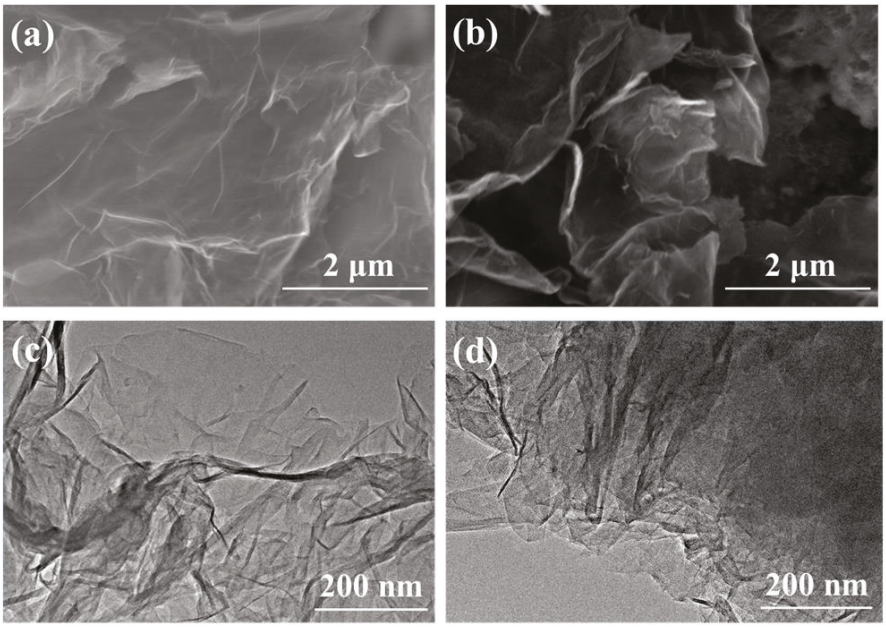

Figure 1. (**a**,**b**) SEM and (**c**,**d**) TEM images of NGR1 and NGR2.

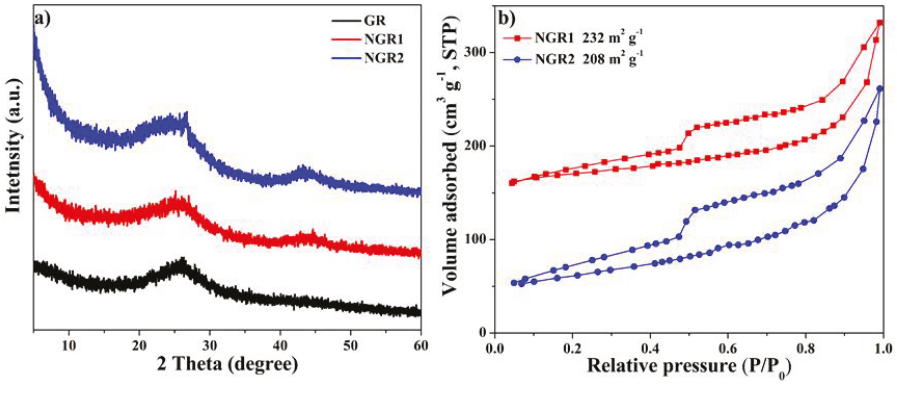

Figure 2. (**a**) XRD patterns of NGR1, NGR2, and GR, and (**b**) N_2 adsorption–desorption curves of NGR1 and NGR2.

XPS was employed to reveal the elemental composition of samples. As shown in Figure 3a, compared to the GR without adding N-containing precursor in synthetic process, the full survey XPS spectra of NGR1 and NGR2 presented obvious peaks corresponding to C 1s, O 1s and N 1s, further indicating the successful N doping in samples. Table S1 indicates that the N contents of NGR1 and NGR2 were 5.35% and 5.19%, respectively. The high-resolution N 1s spectra of both NGR1 and NGR2 (Figure 3b,c) could be deconvoluted into three peaks located at 398.1 eV (pyridinic-N), 399.5 eV (pyrrolic-N) and 401.1 eV (graphitic-N), respectively [52]. However, it is worth noting that pyrrolic-N was the dominant N species in NGR1 and its content reached 50.9% of total N. In comparison, NGR2 had a higher content of pyridinic-N (40.48% of total N) over pyrrolic-N. In addition, the graphitic-N contents of NGR1 and NGR2 were similar. This difference could be attributed to the different structures of N precursors for synthesizing the samples (urea for NGR1 and

melamine for NGR2). Based on these analyses, the different N-species-dominated NGR was synthesized.

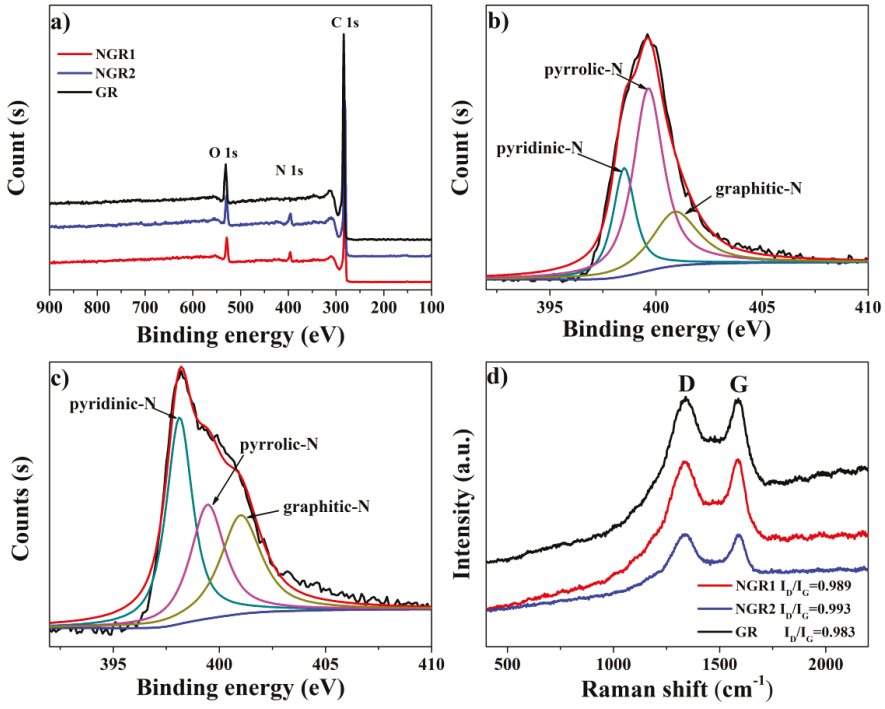

Figure 3. (**a**) Full survey XPS spectra of NGR1, NGR2, and GR. High-resolution N 1s spectra of NGR1 (**b**) and NGR2 (**c**), respectively; (**d**) Raman spectra of GR, NGR1, and NGR2.

Since it was reported that graphene defects could be the active sites for the NORR, it was important to clarify the degree of structural defect of the samples before evaluating the effect of N doping [43]. Raman spectroscopy was employed here and the spectra of all samples presented two prominent peaks. The peak located at 1350 cm^{-1} corresponded to the D band, which was caused by the disorder in graphitic structure of carbon materials, and the G band peak, located at 1580 cm^{-1}, arose from the sp^2 hybridized graphitic carbon atoms. Generally, the D/G peak intensity ratio (I_D/I_G) was highly correlated with the quantity of structural defects, which may reveal the degree of structural defect. As shown in Figure 3d, the I_D/I_G values for NGR1, NGR2, and GR were 0.989, 0.993, and 0.983, respectively, indicating the three samples had a similar degree of structural defect. Therefore, the effect of N species, i.e., pyrrolic-N and pyridinic-N, on the electrochemical performance could be accessible.

3.2. Electrochemical Measurements of N-Doped Samples

Linear sweep voltammetries (LSVs) were measured in a 5 M HNO_3 solution with a scan rate of 10 mV s^{-1} to investigate the NORR activity of the samples. Each sample was tested in a fresh solution to exclude the possible by-products produced during the survey. As shown in Figure 4a, the glassy carbon electrode without any electrocatalyst showed negligible current response, which indicated that glassy carbon electrode, the substrate for all samples, had a poor catalytic activity for the NORR. After loading with GR, it presented an onset potential of 0.698 V (in this work, the onset potential was defined as the potential to deliver a current density of 1 mA cm^{-2}) and a half-wave potential of 0.506 V, indicating that GR was electrochemical active towards the NORR. However, the activity of GR was

still lower than that of commercial 20 wt % Pt/C (Pt/C) since Pt/C had a higher onset potential (0.83 V) and half-wave potential (0.642 V). When NGR1 was adopted, the onset potential and the half-wave potential positively shifted to 0.85 V and 0.732 V, respectively, which were 20 mV and 90 mV more positive, respectively, than that of Pt/C, demonstrating the higher activity of NGR1 compared to Pt/C. Since NGR1 and GR had the same degree of structural defect revealed by Raman measurements, the significantly enhanced activity of NGR1 could be attributed to the N doping.

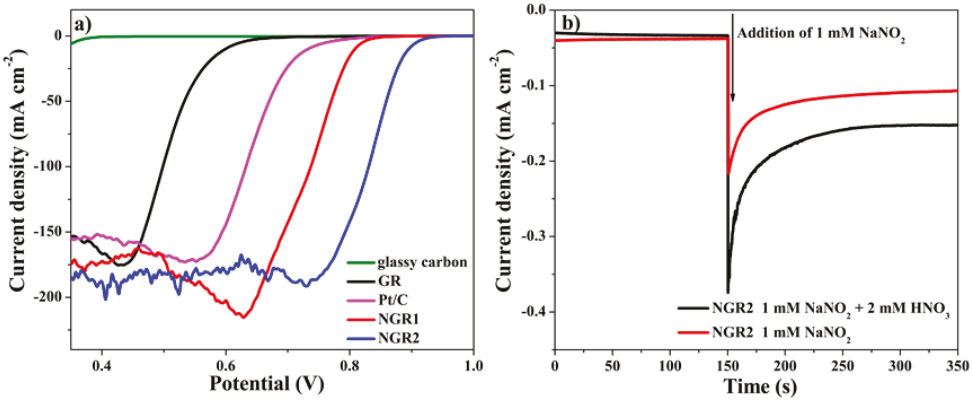

Figure 4. (**a**) Linear sweep voltammetries of glass carbon, GR, Pt/C, NGR1, and NGR2 in 5 M HNO_3 solution with a scan rate of 10 mV s^{-1}. (**b**) Chronoamperometric response of NGR2 in 5 M H_2SO_4 at 0.8 V in the absence (red line) and presence (black line) of 2 mM HNO_3. A total of 1 mM $NaNO_2$ was dropped into the solution at 150 s.

To further investigate the effect of different N species on the NORR performance, the activity of pyridinic-N-dominated NGR2 was also tested. The onset potential of NGR2 further increased to 0.932 V, which was 83 mV more positive than that of NGR1. Additionally, the half-wave potential of NGR2 was 101 mV more positive than that of NGR1. Although the catalytic activity of pyridinic- or pyrrolic-N sites alone could not be distinguished based on our experimental results, the boosted electrochemical performance of NGR2 compared to NGR1 implied that pyridinic-N played an important role in the enhanced NORR activity of N-doped graphene since the major difference between NGR1 and NGR2 was the contents of pyridinic-N and pyrrolic-N.

3.3. Investigation into the Mechanism of Electrochemical NORR on N-Doped Graphene

The mechanism of the NORR on N-doped graphene was further discussed. Kamiya et al. [43] reported that the autocatalytic mechanism (Equations (2)–(5)) on pure graphene was similar to that on Pt [45] and that graphene defects could facilitate the adsorption of NO^+ to enhance the activity, since the C atoms located at defects had different density states. The N doping could change the charge densities of surrounding C atoms due to the larger electronegativity of N (3.04) compared to C (2.55), therefore we speculated that the mechanism for the NORR on N-doped graphene might be the same.

$$2\,NO^+ + 2e^- \rightarrow 2\,NO \quad (2)$$

$$2\,NO + HNO_3 + H_2O \leftrightharpoons 3\,HNO_2 \quad (3)$$

$$2\,HNO_2 + 2\,H^+ \leftrightharpoons 2\,NO^+ + 2\,H_2O \quad (4)$$

$$HNO_3 + 2\,H^+ + 2\,e^- \rightarrow HNO_2 + H_2O \text{ (overall reaction)} \quad (5)$$

According to this mechanism, the nitrite was not only the product, but also a key intermediate, since the nitrite could be reduced into NO^+, as shown in Equation (4). To demonstrate the critical role of nitrite for the reduction of nitrate in the autocatalytic

reaction, a chronoamperometric measurement was employed here with NGR2 in a 5 M H_2SO_4 solution in the absence or presence of 2 mM nitrate at 0.8 V, which was more positive than the onset potential of GR. As shown in Figure 4b, the NGR2 in the presence of 2 mM nitrate presented no current response towards the NORR compared to NGR2 in the absence of 2 mM nitrate. After adding 1 mM $NaNO_2$, NGR2 with $NaNO_2$ presented a reduction current corresponding to the electrochemical reduction of nitrite. Remarkably, NGR2 with both 2 mM nitrate and 1 mM $NaNO_2$ exhibited a larger current than that of NGR2 with only 1 mM $NaNO_2$. The larger current could be ascribed to the sum of the reduction currents of nitrite and nitrate, indicating that the nitrate could be reduced in the presence of nitrite. The results demonstrated that nitrite was the important reactive intermediate in the NORR.

The nitrate removal experiment with NGR2 as the working electrode was conducted in the presence and absence of nitrite to identify the electrochemical reduction of nitrate, as well as provide more evidence supporting the importance of nitrite in this process. A two-chamber reactor was employed to exclude the influence of the counter electrode. The initial concentration of nitrate was 10 mM and the electrolyte was 5 M H_2SO_4. As shown in Figure S3a, only 4.4% of nitrate was removed within 180 min at the potential of 0.6 V without the addition of nitrite. In the presence of 10 mM nitrite at the onset, 30.4% of nitrate was removed within 180 min, further demonstrating the important role of nitrite in the indirect NORR on NGR2. It could be noticed that the removal kinetics decreased after 90 min. The concentration of nitrite was also detected, as shown in Figure S3b. The decreased kinetics could be attributed to the decreased concentration of nitrite, which is also reduced by the electrode under this condition.

To further reveal the effect of N doping on the NORR activity, DFT calculations were performed. The enhanced adsorption of NO^+ onto the edge of graphene rather than the basal plane of graphene has been reported by Kamiya et al. [43]. Due to the positive charge of NO^+, the adsorption of NO^+ on the edge of graphene was extremely strong. It is well known that N doping results in the presence of defects on the graphene. Thus, it was reasonable to speculate that Equation (2) was not the rate-determining step. Based on the proposed mechanism, another important process was related to the desorption of NO according to Equation (3). NO was expected to be desorbed from the active sites so that it could react with HNO_3 to produce HNO_2 and the active sites were therefore regenerated for the next reactive cycle. By taking these into consideration, the adsorption energies of NO (E_{ads}) on different types of graphene were calculated and are shown in Figure 5. Since it was reported that the C atom on the edge of graphene was the active site for the NORR [43] and the C atom near the N atom was influenced by the N doping mostly [57,58], the C atom near the N atom was treated as the active site and the desorption of NO was calculated. E_{ads} for undoped graphene with defects was −5.89 eV meanwhile the E_{ads} for graphene with pyridinic-N was only −0.12 eV. The more positive E_{ads} of NO on graphene with pyridinic-N than those of NO on undoped graphene with defects, indicated that NO would drop from the graphene with pyridinic-N more easily. These results demonstrate that the pyridinic-N doping facilitated the desorption of NO as well as the regeneration of active sites. The adsorption of NO on the graphene with pyrrolic-N was also calculated but the result after optimization was unreasonable, implying that the C atom near pyrrolic-N atom was not the active site. Considering pyridinic-N existed in both of NGR1 and NGR2 but with 1.8 times higher content in NGR2, the excellent NORR performance of NGR2 compared to NGR1 implied a positive correlation between the content of pyridinic-N and the NORR activity. Thus, both the experimental results and DFT calculations indicated that pyridinic-N played the most important role in the NORR and that the facilitated desorption of NO might be a possible origin of the enhanced NORR performance of N-doped graphene.

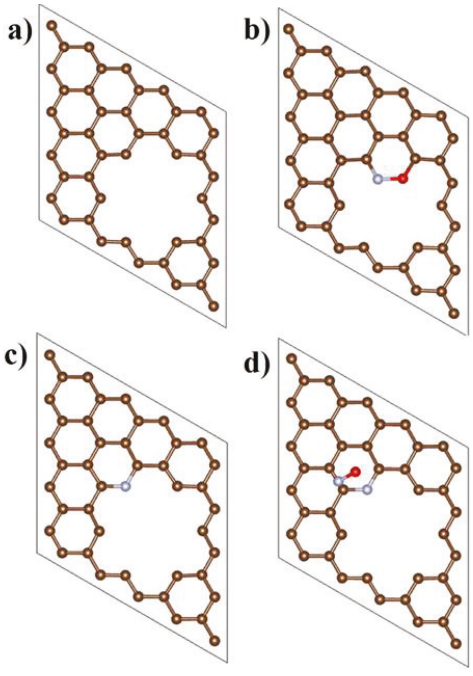

Figure 5. Top view of the modeling of (**a**) the undoped graphene and (**c**) graphene with pyridinic-N with defects; Adsorption of NO on (**b**) undoped graphene and (**d**) on graphene with pyridinic-N after optimization.

4. Conclusions

In summary, we prepared N-doped graphene and evaluated its electrochemical performance towards the NORR in an acidic solution. To the best of our knowledge, it was the first time that N doping carbon materials were adopted as NORR electrocatalysts. The N doping could significantly improve the electrocatalytic activity of graphene for the NORR, which was better than the activity of commercial Pt/C. Furthermore, our results indicated that Pyridinic-N played an important role in the NORR by facilitating the desorption of NO from reaction sites as shown by density functional theory calculations. The findings of this work shed lights on the new application of N doping carbon-based materials and would be valuable for the design of metal-free electrocatalyst for the NORR.

Supplementary Materials: The following are available online at https://www.mdpi.com/article/10.3390/nano11092418/s1, Figure S1: (a) SEM and (b–d) EDS mapping of C, O, and N in NGR1, respectively, Figure S2: (a) SEM and (b-d) EDS mapping of C, O, and N in NGR2, respectively, Figure S3: (a) Electrochemical reduction of NO_3^- on NGR2 at 0.6 V for 3 h, with and without initial 10 mM NO_2^-, with a 5 M H_2SO_4 electrolyte; (b) the amount of NO_2^- on NGR2 at 0.6 V for 3 h with the initial 10 mM NO_2^- and 10 mM NO_3^-, Table S1: Summary of chemical composition analysis from XPS and Raman results and electrochemical properties of samples, Text S1: Computational details of the DFT calculations, Text S2: Detection of nitrate and nitrite.

Author Contributions: Conceptualization, J.Z. (Jujiao Zhao) and J.Z. (Jun Zhai); methodology, J.Z. (Jujiao Zhao); software, B.S.; investigation, J.Z. (Jujiao Zhao); resources, B.S.; writing—original draft preparation, J.Z. (Jujiao Zhao); writing—review and editing, B.S. and J.Z. (Jun Zhai); visualization, J.Z. (Jujiao Zhao); supervision, J.Z. (Jun Zhai); funding acquisition, J.Z. (Jujiao Zhao). All authors have read and agreed to the published version of the manuscript.

Funding: This work was supported by National Natural Science Foundation of China (grant number 22006005) and Natural Science Foundation of Chongqing, China (grant number cstc2020jcyj-bshX0121).

Conflicts of Interest: The authors declare no conflict of interest. The funders had no role in the design of the study; in the collection, analyses, or interpretation of data; in the writing of the manuscript, or in the decision to publish the results.

References

1. Carpenter, S.R.; Caraco, N.F.; Correll, D.L.; Howarth, R.W.; Sharpley, A.N.; Smith, V.H. Nonpoint pollution of surface waters with phosphorus and nitrogen. *Ecol. Appl.* **1998**, *8*, 559–568. [CrossRef]
2. Birdja, Y.Y.; Yang, J.; Koper, M.T.M. Electrocatalytic Reduction of Nitrate on Tin-modified Palladium Electrodes. *Electrochim. Acta* **2014**, *140*, 518–524. [CrossRef]
3. Wang, H.; Turner, J.A. Photoelectrochemical reduction of nitrates at the illuminated p-GaInP2 photoelectrode. *Energy Environ. Sci.* **2013**, *6*, 1802–1805. [CrossRef]
4. Su, J.F.; Ruzybayev, I.; Shah, I.; Huang, C.P. The electrochemical reduction of nitrate over micro-architectured metal electrodes with stainless steel scaffold. *Appl. Catal. B Environ.* **2016**, *180*, 199–209. [CrossRef]
5. Manzo-Robledo, A.; Lévy-Clément, C.; Alonso-Vante, N. The interplay between hydrogen evolution reaction and nitrate reduction on boron-doped diamond in aqueous solution: The effect of alkali cations. *Electrochim. Acta* **2014**, *117*, 420–425. [CrossRef]
6. Dima, G.E.; de Vooys, A.C.A.; Koper, M.T.M. Electrocatalytic reduction of nitrate at low concentration on coinage and transition-metal electrodes in acid solutions. *J. Electroanal. Chem.* **2003**, *554*, 15–23. [CrossRef]
7. Mishra, S.; Lawrence, F.; Mallika, C.; Pandey, N.K.; Srinivasan, R.; Mudali, U.K.; Natarajan, R. Kinetics of reduction of nitric acid by electrochemical method and validation of cell design for plant application. *Electrochim. Acta* **2015**, *160*, 219–226. [CrossRef]
8. Wang, Y.; Wang, C.; Li, M.; Yu, Y.; Zhang, B. Nitrate electroreduction: Mechanism insight, in situ characterization, performance evaluation, and challenges. *Chem. Soc. Rev.* **2021**, *50*, 6720–6733. [CrossRef]
9. Li, M.; Feng, C.; Zhang, Z.; Yang, S.; Sugiura, N. Treatment of nitrate contaminated water using an electrochemical method. *Bioresour. Technol.* **2010**, *101*, 6553–6557. [CrossRef]
10. Souza-Garcia, J.; Ticianelli, E.A.; Climent, V.; Feliu, J.M. Nitrate reduction on Pt single crystals with Pd multilayer. *Electrochim. Acta* **2009**, *54*, 2094–2101. [CrossRef]
11. Chen, Y.; Zhu, H.; Rasmussen, M.; Scherson, D. Rational Design of Electrocatalytic Interfaces: The Multielectron Reduction of Nitrate in Aqueous Electrolytes. *J. Phys. Chem. Lett.* **2010**, *1*, 1907–1911. [CrossRef]
12. Yang, J.; Calle-Vallejo, F.; Duca, M.; Koper, M.T.M. Electrocatalytic Reduction of Nitrate on a Pt Electrode Modified by p-Block Metal Adatoms in Acid Solution. *ChemCatChem* **2013**, *5*, 1773–1783. [CrossRef]
13. Wang, Q.; Zhao, X.; Zhang, J.; Zhang, X. Investigation of nitrate reduction on polycrystalline Pt nanoparticles with controlled crystal plane. *J. Electroanal. Chem.* **2015**, *755*, 210–214. [CrossRef]
14. Hasnat, M.A.; Ahamad, N.; Uddin, S.M.N.; Mohamed, N. Silver modified platinum surface/H+ conducting Nafion membrane for cathodic reduction of nitrate ions. *Appl. Surf. Sci.* **2012**, *258*, 3309–3314. [CrossRef]
15. Figueiredo, M.C.; Souza-Garcia, J.; Climent, V.; Feliu, J.M. Nitrate reduction on Pt(111) surfaces modified by Bi adatoms. *Electrochem. Commun.* **2009**, *11*, 1760–1763. [CrossRef]
16. Figueiredo, M.C.; Solla-Gullón, J.; Vidal-Iglesias, F.J.; Climent, V.; Feliu, J.M. Nitrate reduction at Pt(100) single crystals and preferentially oriented nanoparticles in neutral media. *Catal. Today* **2013**, *202*, 2–11. [CrossRef]
17. Chen, T.; Li, H.; Ma, H.; Koper, M.T.M. Surface Modification of Pt(100) for Electrocatalytic Nitrate Reduction to Dinitrogen in Alkaline Solution. *Langmuir* **2015**, *31*, 3277–3281. [CrossRef]
18. Yang, J.; Sebastian, P.; Duca, M.; Hoogenboom, T.; Koper, M.T.M. pH dependence of the electroreduction of nitrate on Rh and Pt polycrystalline electrodes. *Chem. Commun.* **2014**, *50*, 2148–2151. [CrossRef]
19. da Cunha, M.C.P.M.; de Souza, J.P.I.; Nart, F.C. Reaction Pathways for Reduction of Nitrate Ions on Platinum, Rhodium, and Platinum−Rhodium Alloy Electrodes. *Langmuir* **2000**, *16*, 771–777. [CrossRef]
20. Calle-Vallejo, F.; Huang, M.; Henry, J.B.; Koper, M.T.M.; Bandarenka, A.S. Theoretical design and experimental implementation of Ag/Au electrodes for the electrochemical reduction of nitrate. *Phys. Chem. Chem. Phys.* **2013**, *15*, 3196–3202. [CrossRef] [PubMed]
21. Souza-Garcia, J.; Ticianelli, E.A.; Climent, V.; Feliu, J.M. Mechanistic changes observed in heavy water for nitrate reduction reaction on palladium-modified Pt(hkl) electrodes. *Chem. Sci.* **2012**, *3*, 3063–3070. [CrossRef]
22. Guy, K.A.; Xu, H.; Yang, J.C.; Werth, C.J.; Shapley, J.R. Catalytic Nitrate and Nitrite Reduction with Pd−Cu/PVP Colloids in Water: Composition, Structure, and Reactivity Correlations. *J. Phys. Chem. C* **2009**, *113*, 8177–8185. [CrossRef]
23. Anastasopoulos, A.; Hannah, L.; Hayden, B.E. High throughput optimisation of PdCu alloy electrocatalysts for the reduction of nitrate ions. *J. Catal.* **2013**, *305*, 27–35. [CrossRef]
24. Li, M.; Feng, C.; Zhang, Z.; Shen, Z.; Sugiura, N. Electrochemical reduction of nitrate using various anodes and a Cu/Zn cathode. *Electrochem. Commun.* **2009**, *11*, 1853–1856. [CrossRef]
25. Hamam, A.; Oukil, D.; Dib, A.; Hammache, H.; Makhloufi, L.; Saidani, B. Polypyrrole coated cellulosic substrate modified by copper oxide as electrode for nitrate electroreduction. *Surf. Rev. Lett.* **2015**, *22*, 1550065. [CrossRef]
26. Çirmi, D.; Aydın, R.; Köleli, F. The electrochemical reduction of nitrate ion on polypyrrole coated copper electrode. *J. Electroanal. Chem.* **2015**, *736*, 101–106. [CrossRef]
27. Bae, S.-E.; Stewart, K.L.; Gewirth, A.A. Nitrate Adsorption and Reduction on Cu(100) in Acidic Solution. *J. Am. Chem. Soc.* **2007**, *129*, 10171–10180. [CrossRef]

28. Bae, S.-E.; Gewirth, A.A. Differential reactivity of Cu(111) and Cu(100) during nitrate reduction in acid electrolyte. *Faraday Discuss.* **2009**, *140*, 113–123. [CrossRef] [PubMed]
29. Wang, Y.; Qu, J.; Wu, R.; Lei, P. The electrocatalytic reduction of nitrate in water on Pd/Sn-modified activated carbon fiber electrode. *Water Res.* **2006**, *40*, 1224–1232. [CrossRef]
30. Siriwatcharapiboon, W.; Kwon, Y.; Yang, J.; Chantry, R.L.; Li, Z.; Horswell, S.L.; Koper, M.T.M. Promotion Effects of Sn on the Electrocatalytic Reduction of Nitrate at Rh Nanoparticles. *ChemElectroChem* **2014**, *1*, 172–179. [CrossRef]
31. Katsounaros, I.; Dortsiou, M.; Polatides, C.; Preston, S.; Kypraios, T.; Kyriacou, G. Reaction pathways in the electrochemical reduction of nitrate on tin. *Electrochim. Acta* **2012**, *71*, 270–276. [CrossRef]
32. Shen, J.; Birdja, Y.Y.; Koper, M.T.M. Electrocatalytic Nitrate Reduction by a Cobalt Protoporphyrin Immobilized on a Pyrolytic Graphite Electrode. *Langmuir* **2015**, *31*, 8495–8501. [CrossRef] [PubMed]
33. Kim, H.-K.; Jeong, J.-Y.; Cho, H.-N.; Park, J.-Y. Kinetics of nitrate reduction with the packed bed iron bipolar electrode. *Sep. Purif. Technol.* **2015**, *152*, 140–147. [CrossRef]
34. Zhang, H.; Ni, Y.; Zhong, Y.; Wu, H.; Zhai, M. Fast electrodeposition, influencing factors and catalytic properties of dendritic Cu–M (M = Ni, Fe, Co) microstructures. *RSC Adv.* **2015**, *5*, 96639–96648. [CrossRef]
35. Mattarozzi, L.; Cattarin, S.; Comisso, N.; Gambirasi, A.; Guerriero, P.; Musiani, M.; Vázquez-Gómez, L.; Verlato, E. Hydrogen evolution assisted electrodeposition of porous Cu-Ni alloy electrodes and their use for nitrate reduction in alkali. *Electrochim. Acta* **2014**, *140*, 337–344. [CrossRef]
36. Imar, S.; Maccato, C.; Dickinson, C.; Laffir, F.; Vagin, M.; McCormac, T. Enhancement of Nitrite and Nitrate Electrocatalytic Reduction through the Employment of Self-Assembled Layers of Nickel- and Copper-Substituted Crown-Type Heteropolyanions. *Langmuir* **2015**, *31*, 2584–2592. [CrossRef] [PubMed]
37. Ahsan, M.A.; Santiago, A.R.P.; Rodriguez, A.; Maturano-Rojas, V.; Alvarado-Tenorio, B.; Bernal, R.; Noveron, J.C. Biomass-derived ultrathin carbon-shell coated iron nanoparticles as high-performance tri-functional HER, ORR and Fenton-like catalysts. *J. Clean. Prod.* **2020**, *275*, 124141. [CrossRef]
38. Ahsan, M.A.; Santiago, A.R.P.; Sanad, M.F.; Weller, J.M.; Fernandez-Delgado, O.; Barrera, L.A.; Maturano-Rojas, V.; Alvarado-Tenorio, B.; Chan, C.K.; Noveron, J.C. Tissue paper-derived porous carbon encapsulated transition metal nanoparticles as advanced non-precious catalysts: Carbon-shell influence on the electrocatalytic behaviour. *J. Colloid Interface Sci.* **2021**, *581*, 905–918. [CrossRef]
39. Sanad, M.F.; Santiago, A.R.P.; Tolba, S.A.; Ahsan, M.A.; Fernandez-Delgado, O.; Adly, M.S.; Hashem, E.M.; Abodouh, M.M.; El-Shall, M.S.; Sreenivasan, S.T.; et al. Co-Cu Bimetallic Metal Organic Framework Catalyst Outperforms the Pt/C Benchmark for Oxygen Reduction. *J. Am. Chem. Soc.* **2021**, *143*, 4064–4073. [CrossRef] [PubMed]
40. Santiago, A.R.P.; Sanad, M.F.; Moreno-Vicente, A.; Ahsan, M.A.; Ceron, M.R.; Yao, Y.R.; Sreenivasan, S.T.; Rodriguez-Fortea, A.; Poblet, J.M.; Echegoyen, L. A New Class of Molecular Electrocatalysts for Hydrogen Evolution: Catalytic Activity of $M_3N@C_{2n}$ ($2n$ = 68, 78, and 80) Fullerenes. *J. Am. Chem. Soc.* **2021**, *143*, 6037–6042. [CrossRef] [PubMed]
41. Santiago, A.R.P.; He, T.; Eraso, O.; Ahsan, M.A.; Nair, A.N.; Chava, V.S.N.; Zheng, T.; Pilla, S.; Fernandez-Delgado, O.; Du, A.; et al. Tailoring the Interfacial Interactions of van der Waals 1T-MoS_2/C_{60} Heterostructures for High-Performance Hydrogen Evolution Reaction Electrocatalysis. *J. Am. Chem. Soc.* **2020**, *142*, 17923–17927. [CrossRef]
42. Ahsan, M.A.; Santiago, A.R.P.; Hong, Y.; Zhang, N.; Cano, M.; Rodriguez-Castellon, E.; Echegoyen, L.; Sreenivasan, S.T.; Noveron, J.C. Tuning of Trifunctional NiCu Bimetallic Nanoparticles Confined in a Porous Carbon Network with Surface Composition and Local Structural Distortions for the Electrocatalytic Oxygen Reduction, Oxygen and Hydrogen Evolution Reactions. *J. Am. Chem. Soc.* **2020**, *142*, 14688–14701. [CrossRef]
43. Kamiya, K.; Hashimoto, K.; Nakanishi, S. Graphene Defects as Active Catalytic Sites that are Superior to Platinum Catalysts in Electrochemical Nitrate Reduction. *ChemElectroChem* **2014**, *1*, 858–862. [CrossRef]
44. Sander, E.M.; Virdis, B.; Freguia, S. Dissimilatory nitrate reduction to ammonium as an electron sink during cathodic denitrification. *RSC Adv.* **2015**, *5*, 86572–86577. [CrossRef]
45. Rosca, V.; Duca, M.; de Groot, M.T.; Koper, M.T.M. Nitrogen Cycle Electrocatalysis. *Chem. Rev.* **2009**, *109*, 2209–2244. [CrossRef] [PubMed]
46. Lange, R.; Maisonhaute, E.; Robin, R.; Vivier, V. On the kinetics of the nitrate reduction in concentrated nitric acid. *Electrochem. Commun.* **2013**, *29*, 25–28. [CrossRef]
47. Han, S.-B.; Song, Y.-J.; Lee, Y.-W.; Ko, A.R.; Oh, J.-K.; Park, K.-W. High-performance hydrogen fuel cell using nitrate reduction reaction on a non-precious catalyst. *Chem. Commun.* **2011**, *47*, 3496–3498. [CrossRef]
48. Gong, K.; Du, F.; Xia, Z.; Durstock, M.; Dai, L. Nitrogen-Doped Carbon Nanotube Arrays with High Electrocatalytic Activity for Oxygen Reduction. *Science* **2009**, *323*, 760–764. [CrossRef]
49. Zhang, J.; Zhao, Z.; Xia, Z.; Dai, L. A metal-free bifunctional electrocatalyst for oxygen reduction and oxygen evolution reactions. *Nat. Nanotechnol.* **2015**, *10*, 444–452. [CrossRef]
50. Jiao, Y.; Zheng, Y.; Davey, K.; Qiao, S.-Z. Activity origin and catalyst design principles for electrocatalytic hydrogen evolution on heteroatom-doped graphene. *Nat. Energy* **2016**, *1*, 16130. [CrossRef]
51. Wu, J.; Liu, M.; Sharma, P.P.; Yadav, R.M.; Ma, L.; Yang, Y.; Zou, X.; Zhou, X.-D.; Vajtai, R.; Yakobson, B.I.; et al. Incorporation of Nitrogen Defects for Efficient Reduction of CO_2 via Two-Electron Pathway on Three-Dimensional Graphene Foam. *Nano Lett.* **2016**, *16*, 466–470. [CrossRef] [PubMed]

52. Zhong, H.-X.; Wang, J.; Zhang, Y.-W.; Xu, W.-L.; Xing, W.; Xu, D.; Zhang, Y.-F.; Zhang, X.-B. ZIF-8 Derived Graphene-Based Nitrogen-Doped Porous Carbon Sheets as Highly Efficient and Durable Oxygen Reduction Electrocatalysts. *Angew. Chem. Int. Ed.* **2014**, *53*, 14235–14239. [CrossRef]
53. Wang, D.-W.; Su, D. Heterogeneous nanocarbon materials for oxygen reduction reaction. *Energy Environ. Sci.* **2014**, *7*, 576–591. [CrossRef]
54. Kresse, G.; Furthmüller, J. Efficiency of ab-initio total energy calculations for metals and semiconductors using a plane-wave basis set. *Comput. Mater. Sci.* **1996**, *6*, 15–50. [CrossRef]
55. Kresse, G.; Furthmüller, J. Efficient iterative schemes for ab initio total-energy calculations using a plane-wave basis set. *Phys. Rev. B* **1996**, *54*, 11169–11186. [CrossRef] [PubMed]
56. Perdew, J.P.; Burke, K.; Ernzerhof, M. Generalized Gradient Approximation Made Simple. *Phys. Rev. Lett.* **1996**, *77*, 3865–3868. [CrossRef]
57. Sharma, P.P.; Wu, J.J.; Yadav, R.M.; Liu, M.J.; Wright, C.J.; Tiwary, C.S.; Yakobson, B.I.; Lou, J.; Ajayan, P.M.; Zhou, X.D. Nitrogen-Doped Carbon Nanotube Arrays for High-Efficiency Electrochemical Reduction of CO_2: On the Understanding of Defects, Defect Density, and Selectivity. *Angew. Chem.-Int. Edit.* **2015**, *54*, 13701–13705. [CrossRef]
58. Wu, J.J.; Yadav, R.M.; Liu, M.J.; Sharma, P.P.; Tiwary, C.S.; Ma, L.L.; Zou, X.L.; Zhou, X.D.; Yakobson, B.I.; Lou, J.; et al. Achieving Highly Efficient, Selective, and Stable CO_2 Reduction on Nitrogen-Doped Carbon Nanotubes. *ACS Nano* **2015**, *9*, 5364–5371. [CrossRef] [PubMed]

nanomaterials

MDPI

Article

Effect of Copper Doping on Electronic Structure and Optical Absorption of $Cd_{33}Se_{33}$ Quantum Dots

Fengai Zhao [1], Shuanglin Hu [1,*], Canhui Xu [1], Haiyan Xiao [2], Xiaosong Zhou [1], Xiaotao Zu [2] and Shuming Peng [1,*]

[1] Institute of Nuclear Physics and Chemistry, China Academy of Engineering Physics, Mianyang 621900, China; fengaizh0506@163.com (F.Z.); xuch1209@caep.cn (C.X.); zlxs77@126.com (X.Z.)
[2] School of Physics, University of Electronic Science and Technology of China, Chengdu 610054, China; hyxiao@uestc.edu.cn (H.X.); xtzu@uestc.edu.cn (X.Z.)
* Correspondence: hushuanglin@caep.cn (S.H.); pengshuming@caep.cn (S.P.); Tel.: +86-28-2496710 (S.H.); +86-28-2496715 (S.P.)

Abstract: The photophysical properties of Cu-doped CdSe quantum dots (QDs) can be affected by the oxidation state of Cu impurity, but disagreement still exists on the Cu oxidation state (+1 or +2) in these QDs, which is debated and poorly understood for many years. In this work, by using density functional theory (DFT)-based calculations with the Heyd–Scuseria–Ernzerhof (HSE) screened hybrid functional, we clearly demonstrate that the incorporation of Cu dopants into the surface of the magic sized $Cd_{33}Se_{33}$ QD leads to non-magnetic Cu 3d orbitals distribution and Cu^{+1} oxidation state, while doping Cu atoms in the core region of QDs can lead to both Cu^{+1} and Cu^{+2} oxidation states, depending on the local environment of Cu atoms in the QDs. In addition, it is found that the optical absorption of the Cu-doped $Cd_{33}Se_{33}$ QD in the visible region is mainly affected by Cu concentration, while the absorption in the infrared regime is closely related to the oxidation state of Cu. The present results enable us to use the doping of Cu impurity in CdSe QDs to achieve special photophysical properties for their applications in high-efficiency photovoltaic devices. The methods used here to resolve the electronic and optical properties of Cu-doped CdSe QDs can be extended to other II-VI semiconductor QDs incorporating transition-metal ions with variable valence.

Keywords: DFT; CdSe quantum dots; oxidation state of Cu; doping; optical absorption

Citation: Zhao, F.; Hu, S.; Xu, C.; Xiao, H.; Zhou, X.; Zu, X.; Peng, S. Effect of Copper Doping on Electronic Structure and Optical Absorption of $Cd_{33}Se_{33}$ Quantum Dots. *Nanomaterials* **2021**, *11*, 2531. https://doi.org/10.3390/nano11102531

Academic Editor: Marc Cretin

Received: 6 September 2021
Accepted: 23 September 2021
Published: 28 September 2021

1. Introduction

Doping of semiconductor nanocrystals (NCs) or quantum dots (QDs) with transition-metal ions has attracted significant interest in the applications of lasers [1,2], biolabeling [3–6], light-emitting diodes [7–9], and optoelectronics devices [10–14]. In particular, the transition-metal ions that can introduce permanent, electrically, or optically active charges are desired dopants [2,15,16]. The active charge can be permanently introduced into the NC host lattice by incorporating a transition-metal ion having a variable valence [17,18]. By such doping, new energy levels could be introduced into the bandgap of the host NCs, which can exchange charges with the valence band or the conduction band, thereby significantly influence their electronic and optical properties. Copper exhibits variable valences (+1 and +2) and has become a promising doping element in II-VI semiconductor NCs to modify the electronic and optical properties for their desirable applications [2,17,19–21].

Several studies have been devoted to the incorporation of Cu impurity in II-VI semiconductor NCs (e.g., CdSe, CdS, and ZnSe) to introduce copper-related intragap emission property [18,22–25]. However, some questions still exist on the origin of dopant emission in these Cu-doped NCs. In materials such as CdSe NCs, a model system for studying the electronic and photophysical properties of doped II-VI semiconductor NCs [15,26–30], there is still disagreement on the oxidation state of Cu ion whether it presents a +1 or +2 valence state. Meulenberg et al. used soft X-ray absorption near-edge spectroscopy (XANES), X-ray photoelectron spectroscopy (XPS), and photoluminescence (PL) to examine

the electronic and chemical structures of Cu ions dispersed in CdSe QDs and concluded that Cu ions had a +1 oxidation state [29]. The same +1 oxidation state for Cu in CdSe NCs was also assumed in Refs. [21,31]. However, Viswanatha et al. reported that Cu impurities in ZnSe/CdSe core–shell NCs exhibited a +2 oxidation state and served as a permanent source of optically active holes [17]. Brovelli et al. claimed that although the photoluminescence from their ZnSe/CdSe core–shell QDs was mainly attributed to Cu^{2+} ions, the possibility that some QDs might contain Cu^{+} ions could not be excluded [18]. To date, it is still unclear whether the oxidation state of Cu depends on its spatial distribution in CdSe QDs. This is mainly due to the difficulty of incorporating a well-controlled number of dopants at precise positions in small QDs. Therefore, it is important to understand the effects of the dopant environment on the photophysical properties of small-sized QDs. The second question is the location of Cu 3d orbitals within the forbidden band of II-VI NCs. Several research groups have reported that Cu 3d states were just above the valence band [24,32,33], while others claimed that Cu 3d orbitals were close to the conduction band [34]. The different positions of Cu 3d energy levels within the forbidden band will lead to very different recombination mechanisms of Cu impurity emission [32,35]. Thus far, it is unknown how the position of Cu 3d states varies with the dopant location in QDs either. Therefore, it is critical to investigate how the location of dopants in QDs influences the local atomic structure of QDs and thus modifies the state of Cu 3d orbitals as well as the optical properties of QDs.

To explore how the location of Cu dopants (at the surface or in the core region) affects the oxidation state of Cu ions and the position of Cu 3d orbitals in the energy levels of the Cu-doped semiconductor nanocrystals, we conduct a systematic density functional theory (DFT)-based study of the structural, energetic, electronic, and optical properties on the Cu-containing CdSe QDs. The Heyd–Scuseria–Ernzerhof (HSE) screened Coulomb hybrid functional was used in our DFT calculations, which is well known to predict the correct bandgaps of a wide range of materials successfully [36–38]. Wurtzite-based $Cd_{33}Se_{33}$ nanocluster with a core–cage structure was used as the host NC in this work, which has been experimentally demonstrated to be extremely stable and used as a model system for the II-VI semiconductor nanocrystals [30]. Previous extensive theoretical studies have been conducted focusing on its special atomic arrangement [39–42]. Therefore, the $Cd_{33}Se_{33}$ is a suitable host nanocrystal for the incorporation of copper impurity. Here, up to three Cu atoms are doped to substitute Cd atoms at different locations of a $Cd_{33}Se_{33}$ QD. Details of the dopant locations are described in the Methodologies Section. The corresponding structural distortions, energetics, electronic properties, and optical absorption spectra were investigated, respectively. The present work provides a theoretical perspective on how to control Cu dopants in CdSe NCs to achieve desired optoelectronic properties for their applications in high-efficiency photovoltaic devices.

2. Methodologies

All calculations were carried out based on the density functional theory (DFT) implemented in the Vienna ab initio simulation package (VASP) [43]. The ion–electron interactions were treated by the projector augmented-wave (PAW) approach [44,45]. The exchange-correction effects were described by the screened hybrid functional of HSE with a mixed approach combining Hartree–Fock (HF) and Perdew–Burke–Ernzerhof (PBE) [44]. Here, an HF:GGA mixing ratio of 0.33 and a range-separation parameter of 0.15 $Å^{-1}$ were used, which successfully predicted the lattice parameters and bandgap for bulk wurtzite CdSe. The HSE setup was used for all the CdSe QDs in this work. A $1 \times 1 \times 1$ Monkhorst-Pack mesh in the Brillouin zone was set for all CdSe QDs. Plane-wave cutoff energy of 350 eV was used, which resulted in good convergence of the total energy. To prevent spurious interactions between a QD and its periodic images, a vacuum spacing of at least 16 Å between the QD and its replicas was used in the simulation cells.

The $Cd_{33}Se_{33}$ was constructed on the basis of bulk wurtzite (WZ) lattice with a Cd–Se bond distance of 2.688 Å. Similar construction methods for modeling CdSe quantum

dots have been widely used in previous publications [39–42]. In the unrelaxed $Cd_{33}Se_{33}$ (Figure 1), the wurtzite core was formed by stacking two Cd_3Se_3 rings (so the core is Cd_6Se_6), which were enclosed by the Cd-terminated and Se-terminated surface facets, respectively. The definition of Cd or Se termination followed that in Ref [41]. The non-core atoms were treated as surface atoms. It should be noted that the core and surface of a nanocrystal can be distinguished in experiments [39,46]. In the core region, a Cu dopant binds to four adjacent Se atoms before relaxation, which is the same as in a bulk CdSe. On the surface, a Cu dopant has two to four nearest Se atoms before relaxation. In the case of the core doping, Cu dopants can be close to the Cd or Se termination or both. Therefore, the incorporation of Cu atoms into the core region is divided into three cases: a Cu dopant substituting a Cd atom near the Cd-terminated facet is defined as type I substitution in the core region (marked as "C_I"); a Cu dopant replacing a Cd atom near the Se-terminated facet is defined as the type II substitution in the core region (denoted as "C_{II}"); a Cu dopant near the Cd-terminated and the other near the Se-terminated is defined as type III substitution in the core region (marked as "C_{III}"). As for the surface substitution (S), all Cd sites on the surface were tested for Cu doping, and the lowest energy site was selected for further study.

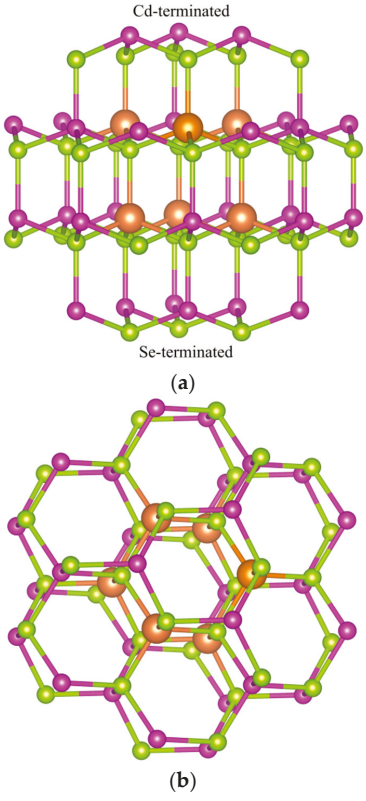

Figure 1. Geometrical structures of the unrelaxed $Cd_{33}Se_{33}$ quantum dots: (**a**) side view of the $Cd_{33}Se_{33}$ with the Se-terminated (bottom) and Cd-terminated (top) facets; (**b**) top view of $Cd_{33}Se_{33}$. The candidate doping sites (Cd sites) for a Cu impurity are labeled by small purple spheres for surface sites and large orange spheres for core sites, respectively; the Se atoms are represented by green spheres.

3. Results and Discussion

3.1. Geometry Distortions of Cu-Doped $Cd_{33}Se_{33}$ Quantum Dots

After relaxation, the wurtzite core structure is retained in both pristine and Cu-doped $Cd_{33}Se_{33}$ QDs, although the surface structure has some degree of reconstruction. The average Se-Cd bond length in the relaxed pristine QD is determined to be 2.667 Å located between 2.678 Å in the core region and 2.657 Å in the surface region, which agree well with the value of 2.685 Å in other DFT calculations [39]. These values are slightly smaller than the Cd-Se bond length of 2.688 Å in bulk wurtzite CdSe, suggesting the lattice contraction effect in the nanocrystal. To further analyze the local environment for Cu atoms in $Cd_{33}Se_{33}$ QDs, the <Cu-Se> bond distance and <Se-Cu-Se> bond angles are summarized in Table 1 and graphically presented in Figure 2. For comparison, the <Cd-Se> bond distances and <Se-Cd-Se> bond angles in the pristine $Cd_{33}Se_{33}$ are also presented. It is found that the value of d<Cd-Se> in the pristine $Cd_{33}Se_{33}$ is larger than those of d<Cu-Se> in Cu-doped QDs, meaning that Cu doping results in shorter distances between a substituting site (Cd-site) and its neighboring Se atoms. This phenomenon may be attributed to the larger ionic radius of Cd than that of Cu [47]. The optimized Cu-Se bonds on the surface of the QD are about 6–8% shorter than those in the core, as indicated in Table 1 and Figure 2a. The 6–8% deviation is greater than the 0.8% difference between the core and surface region in Cd-Se bonds, indicating that the surface Cu induces a significant surface reconstruction. For the bond angle (∠), the ∠Se-Cu-Se between a Cu atom and its adjacent Se atoms in Cu-doped $Cd_{33}Se_{33}$ QDs are calculated in Table 1. The Se-Cd-Se bond angles in the core and surface regions for pristine $Cd_{33}Se_{33}$ (denoted as $Cd_{33}Se_{33}$ (C) and $Cd_{33}Se_{33}$ (S), respectively) are also presented, where Cd atom is the one replaced by Cu. The Se-Cu-Se bond angle in Cu-doped $Cd_{33}Se_{3}3$ (C) QDs ranging from 109.85° to 120.0° is generally larger than the original Se-Cd-Se bond angle of 109.04° in pristine $Cd_{33}Se_{33}$ QD, indicating the inward relaxation of Cu atoms in the core region. The phenomenon is similar to the case of Ag in CdSe QDs [48]. The <Se-Cd-Se> bond angle is calculated to be around 109.5° (sp^3-like bond feature), and the coordination of substituted atoms (Cd atoms) in the core region of $Cd_{33}Se_{33}$ QDs is four. When a Cu atom incorporates into the core region, the coordination of substituted atoms became four-coordinated upon relaxation since <Se-Cu-Se> bond angles are around 120° (sp^2 bond character). As for two Cu atoms incorporated in the core region, the distribution of <Se-Cu-Se> bond angles is similar to the case of <Se-Cd-Se> bond angles in $Cd_{33}Se_{33}$ (C), suggesting that the coordination of substituted atoms does not change after Cu atoms incorporation. However, in the surface-doped QDs, Cu dopants are finally bonded to two Se atoms after relaxation with the <Se-Cu-Se> bond angles ranging from 168.5° to 177.83° as shown in Table 1, which are different from <Se-Cu-Se> bond angles of 119.78° in surface-doped $Cd_{33}Se_{33}$ QDs. These differences in Cu-Se bonds (or <Se-Cu-Se> bond angles) of the surface and core region before and after Cu incorporation indicate that Cu doping in the QDs induces significant structural reconstruction.

Table 1. The Cu-Se bond length (d<Cu-Se>) and Se-Cu-Se bond angle (∠Se-Cu-Se) between a Cu atom and its adjacent Se atoms in Cu-doped $Cd_{33}Se_{33}$ QDs. The Cd-Se bond length (d<Cd-Se>) in the core region (denoted as "C"), and Se-Cd-Se bond angle (∠Se-Cd-Se) in the surface region (denoted as "S") for pristine $Cd_{33}Se_{33}$ are also presented as references, where Cd atom is the one replaced by Cu. The C_I, C_{II}, and C_{III} are defined in Methodologies.

	d<Cd-Se> (Å)	d<Cu-Se> (Å)	∠Se-Cd-Se (°)	∠Se-Cu-Se (°)
$Cd_{33}Se_{33}$ (C)	2.678		109.04	
$Cd_{33}Se_{33}$ (S)	2.657		119.78	
$CuCd_{32}Se_{33}$ (S)		2.262		177.83
$Cu_2Cd_{31}Se_{33}$ (S)		2.269		171.93
$Cu_3Cd_{30}Se_{33}$ (S)		2.272		168.50
$CuCd_{32}Se_{33}$ (C_I)		2.414		120.0
$CuCd_{32}Se_{33}$ (C_{II})		2.385		119.8
$Cu_2Cd_{31}Se_{33}$ (C_I)		2.442		113.28
$Cu_2Cd_{31}Se_{33}S$ (C_I)		2.477		109.39
$Cu_2Cd_{31}Se_{33}$ (C_{II})		2.522		109.85
$Cu_2Cd_{31}Se_{33}S$(C_{II})		2.486		104.85
$Cu_2Cd_{31}Se_{33}$ (C_{III})		2.451		112.51

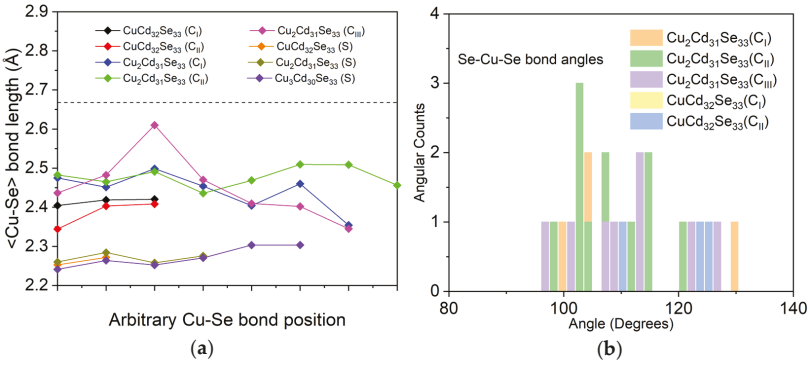

Figure 2. (**a**) The Cu-Se bond length in Cu-doped $Cd_{33}Se_{33}$ quantum dots, together with the Cd-Se bond length in pristine $Cd_{33}Se_{33}$ as indicated by the dashed line; (**b**) the bond-angle distributions of Se-Cu-Se when Cu atoms are doped in the core region of $Cd_{33}Se_{33}$.

3.2. Stability of Cu-Doped $Cd_{33}Se_{33}$ QDs

To investigate the stability of Cu dopants in $Cd_{33}Se_{33}$ QDs, the binding energy (E_b) per Cu atom is calculated by using the following Equation [49]:

$$E_b = \left[\left(E_{undoped} + nE_{Cu}\right) - \left(E_{doped} + nE_{Cd}\right)\right]/n$$

Here, $E_{undoped}$ and E_{doped} are the total energies of the $Cd_{33}Se_{33}$ and Cu-doped $Cd_{33}Se_{33}$ QDs, respectively; E_{Cd} and E_{Cu} are the total energies per atom in bulk Cd and Cu, respectively; n is the number of Cu dopants. The binding energy per Cu atom and total dopant binding energy are presented in Table 2. Similar to [22], here, a positive binding energy means that Cu is energetically favorable to replace Cd; meanwhile, a larger binding energy means that the Cu dopant has a stronger tendency to bind with the CdSe QDs. As shown in Table 2, the Cu binding energy decreases with the increasing number of Cu atoms for both surface- and core-doped $Cd_{33}Se_{33}$, meaning that the stability of the system decreases as Cu content increases. When three Cu atoms are introduced in $Cd_{33}Se_{33}$, the binding energy becomes negative. This result suggests that the number of doped Cu atoms in $Cd_{33}Se_{33}$ should be less than three per QD to maintain the system stability. In terms of Cu dopants at different locations of $Cd_{33}Se_{33}$, incorporation of one Cu atom at the surface ($CuCd_{32}Se_{33}$ (S)) generally results in a larger binding energy than that in the core region ($CuCd_{32}Se_{33}$ (C_I) and $CuCd_{32}Se_{33}$ (C_{II})), suggesting that a Cu dopant prefers to segregate to the surface. For doping two Cu atoms, $Cu_2Cd_{31}Se_{33}$ (C_{III}) has a larger binding energy than the surface-doped $Cu_2Cd_{31}Se_{33}$ (S), while $Cu_2Cd_{31}Se_{33}$ (C_I) and $Cu_2Cd_{31}Se_{33}$ (C_{II}) exhibit smaller binding energies, compared to $Cu_2Cd_{31}Se_{33}$ (S). As discussed in the next section, these differences originate from the different oxidation states of Cu dopants in $Cd_{33}Se_{33}$ QDs. The results also demonstrate that the location and concentration of Cu atoms play important roles in system stability.

3.3. Oxidation State for Cu Dopants in $Cd_{33}Se_{33}$ Quantum Dots

Generally, Cu^+ has a fully filled $3d^{10}$ electron shell and exhibits non-magnetic properties, whereas Cu^{2+} has one unpaired electron in their $3d^9$ shell and thus behaves paramagnetically [17,18]. In our calculations, when Cu dopants are incorporated on the surface, the spin-up and spin-down states are symmetric for the Cu 3d orbitals (Figure 3a), indicative of a non-magnetic character. Therefore, Cu dopants in surface-doped $Cd_{33}Se_{33}$ present the +1 oxidation state. When one or two Cd sites in the QD core are replaced by Cu, the Cu 3d orbitals show distinct electronic features for different substitution locations, as presented in Figure 3b–f. In the case of doping a Cu atom in the core regardless near the Cd-terminated or Se-terminated surface ($CuCd_{32}Se_{33}$ (C_I) or $CuCd_{32}Se_{33}$ (C_{II})), as shown

in Figure 3b–c), the density of states (DOS) of the Cu 3d states shows similar symmetric characters as those of surface-doped one ($CuCd_{32}Se_{33}$(S)), indicating that the +1 oxidation state of Cu is presented in these systems. The Cu 3d orbitals in $Cu_2Cd_{31}Se_{33}$ (C_{III}) (where one Cu dopant is close to the Cd termination and the other is near the Se termination) also show non-magnetic DOS distributions and thus the Cu^+ electronic character, as shown in Figure 3f. However, when both Cu dopants are near the Cd termination ($Cu_2Cd_{31}Se_{33}$ (C_I)) or Se termination ($Cu_2Cd_31Se_{33}$ (C_{II}), the spin-up and spin-down states are asymmetric, as shown in Figure 3d–e. Such electronic characters indicate that the systems contain some magnetism, which further indicates the oxidation state of Cu is Cu^{2+}. It should be noted that the Cu impurity energy levels in both $Cu_2Cd_{31}Se_{33}$ (C_I) and $Cu_2Cd_{31}Se_{33}$ (C_{II}) reside about 0.43 eV and 0.46 eV above from the valence band maximum (which is very close to the Fermi level), respectively. These impurity levels correspond to the lower half of the forbidden gap (i.e., $E_{g/2}$ = 0.93 eV and 1.12 eV, where Eg is bandgap) indicative of p-type dopants, which is evidence for the +2 oxidation state of Cu [18]. In addition, the behavior of Cu^{2+} orbitals in our calculations is similar to the experimental observation of Cu^{2+} level in Cu-doped ZnSe NCs in which it was in the bandgap about 0.3–0.4 eV above the top of the valence band [50]. To further analyze the oxidation state of Cu in the QD, Bader charge calculations are performed for all Cu-doped $Cd_{33}Se_{33}$. A positive value of a Bader charge means the loss of electrons; otherwise, it means the gain of electrons. As shown in Table 3, the charge state of Cu ions in $Cu_2Cd_{31}Se_{33}$ (C_I) and $Cu_2Cd_{31}Se_{33}$ (C_{II}) is about 0.084–0.129 |e| more positive than that for Cu ions in $CuCd_{32}Se_{33}$ (S), $CuCd_{32}Se_{33}$ (C_I), $CuCd_{32}Se_{33}$ (C_{II}), and $Cu_2Cd_{31}Se_{33}$ (C_{III}), suggesting that Cu ions lose more electrons in $Cu_2Cd_{31}Se_{33}$ (C_I) and $Cu_2Cd_{31}Se_{33}$ (C_{II}) than in other cases. This is consistent with that the oxidation state of Cu^{2+} in $Cu_2Cd_{31}Se_{33}$ (C_I) and $Cu_2Cd_{31}Se_{33}$ (C_{II}) is larger than the oxidation state of Cu^{1+} in other CdSe QDs.

Table 2. The total binding energy of Cu atoms and the binding energy per Cu atom for Cu in $Cd_{33}Se_{33}$. The location where Cd atoms are substituted by Cu is indicated in the parenthesis. The S, C_I, C_{II}, and C_{III} are defined in Methodologies.

	Total Binding Energy (eV)	Binding Energy/Cu Atom (eV)
$CuCd_{32}Se_{33}$ (S)	1.824	1.824
$CuCd_{32}Se_{33}$ (C_I)	1.726	1.726
$CuCd_{32}Se_{33}$ (C_{II})	1.466	1.466
$Cu_2Cd_{31}Se_{33}$ (S)	0.538	0.269
$Cu_2Cd_{31}Se_{33}$ (C_I)	0.267	0.134
$Cu_2Cd_{31}Se_{33}$ (C_{II})	0.497	0.248
$Cu_2Cd_{31}Se_{33}$ (C_{III})	0.797	0.398
$Cu_3Cd_{30}Se_{33}$ (S)	−0.397	−0.466

Table 3. Average Bader charge (|e|) for each ion in Cu-doped $Cd_{33}Se_{33}$ QDs. The S,C_I,C_{II} and C_{III} are defined in Methodologies.

	Cu	Cd	Se
$CuCd_{32}Se_{33}$ (S)	0.204	0.647	−0.634
$CuCd_{32}Se_{33}$ (C_I)	0.288	0.671	−0.660
$CuCd_{32}Se_{33}$ (C_{II})	0.261	0.671	−0.659
$Cu_2Cd_{31}Se_{33}$ (S)	0.266	0.673	−0.648
$Cu_2Cd_{31}Se_{33}$ (C_I)	0.345	0.674	−0.654
$Cu_2Cd_{31}Se_{33}$ (C_{II})	0.390	0.670	−0.653
$Cu_2Cd_{31}Se_{33}$ (C_{III})	0.287	0.670	−0.647
$Cu_3Cd_{30}Se_{33}$ (S)	0.260	0.667	−0.630

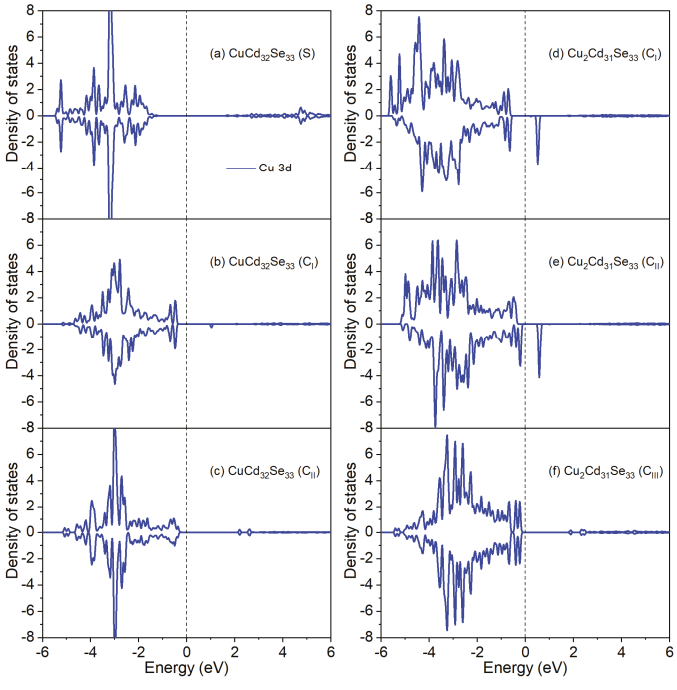

Figure 3. Orbital projected density of state (DOS) for Cu 3d in (**a**) $CuCd_{32}Se_{33}$ (S); (**b**) $CuCd_{32}Se_{33}$ (C_I); (**c**) $CuCd_{32}Se_{33}$ (C_{II}); (**d**) $Cu_2Cd_{31}Se_{33}$(C_I); (**e**) $Cu_2Cd_{31}Se_{33}$(C_{II}); (**f**) $Cu_2Cd_{31}Se_{33}$(C_{III}). Here, only the case of $CuCd_{32}Se_{33}$ (S) is presented since the spin-up and spin-down states of the Cu 3d orbitals are symmetric for all the surface-doped Cu:$Cd_{33}Se_{33}$. The Fermi level is located at 0 eV.

Combined with the calculated binding energy in Section 3.2, it seems that the system with Cu^+ ions ($CuCd_{32}Se_{33}$ (S), $CuCd_{32}Se_{33}$ (C_I), $CuCd_{32}Se_{33}$ (C_{II}), $Cu_2Cd_{31}Se_{33}$ (C_{III}), and $Cu_2Cd_{31}Se_{33}$ (S)) is more stable than that with Cu^{2+} impurity ions ($Cu_2Cd_{31}Se_{33}$ (C_{II})) because the former has larger binding energies than the later (Table 2). Our results are consistent with previous studies in which the oxidation state of Cu (+1) is more stable than Cu (+2) in some ZnS and CdS hosts [32,51].

3.4. Electronic Properties for Cu-Doped $Cd_{33}Se_{33}$ Quantum Dots

To explore how Cu impurity influences the electronic structure of $Cd_{33}Se_{33}$, the density of states with and without Cu dopants are presented in Figure 4 for surface doping and Figure 5 for core doping, respectively. For the pristine $Cd_{33}Se_{33}$ (Figure 4a), previously we have demonstrated [48] that the mid-gap states primarily consist of Se 4p orbitals locating above the valence band (VB); the conduction band is mainly composed of Cd 5s and Se 4p states. With one Cu dopant incorporated into the surface (Figure 4b), the mid-gap states, which mainly consist of Se 4p states from two-coordinated surface Se atoms, are located on the top of the valence band. The Cu 3d orbitals in the VB are located about 1.35 eV below the Fermi level so that they do not contribute to the mid-gap states. In the forbidden band, a new Se 4p impurity state above Fermi level emerges. With the increasing Cu dopants on the surface (Figure 4c), the mid-gap states above the VB disappear and Cu 3d orbitals shift toward the top of the valence band. The impurity levels still exist in the forbidden gap but shift toward the conduction band minimum.

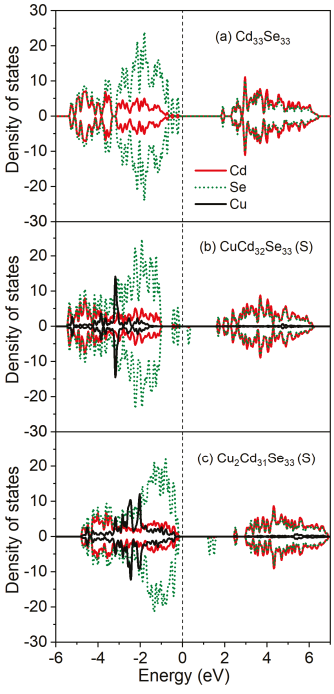

Figure 4. Projected density of states (DOS) for each type of ion when Cu atoms are doped at the surface of $Cd_{33}Se_{33}$: (**a**) pristine $Cd_{33}Se_{33}$; (**b**) $CuCd_{32}Se_{33}$ (S); (**c**) $Cu_2Cd_{31}Se_{33}$(S). The Fermi level is located at 0 eV.

The incorporation of Cu dopants into the core region (Figure 5) results in very different electronic structures from those on the surface, but these doped NCs still maintain the insulating character. Such an insulating character for core-doped Cu:$Cd_{33}Se_{33}$ is in drastic contrast to the metallic-like character for core-doped Ag:$Cd_{33}Se_{33}$ in which some electrons are located at the Fermi level of the system [48]. In $CuCd_{32}Se_{33}$ (C_I) shown in Figure 5b, the mid-gap states consisting of mainly Se 4p orbitals and slightly Cu 3d orbitals are just located above the valence band. Hybridization of Cu 3d orbitals with Se 4p states appears above the VB and both of them contribute to the mid-gap states. Similar hybridization electronic states above the VB have been also observed when a Cu impurity replaces a central Cd atom in zinc-blende-based CdSe NCs (note our NCs are based on the Wurtzite structure), although they consist of Cu 3d orbitals primarily [52]. The energy levels of dopant d orbitals are deeper than the anion p states in VB showing the "inverted" bonding character in $CuCd_{32}Se_{33}$ (C_I). This is different from the "normal" bonding feature (in which the dopant d orbitals are located at shallower energy levels than the anion p states in VB) for a Cu impurity locating on the center of a zinc blende (ZB) based CdSe nanocrystal [52]. When two Cu dopants are incorporated into the core region near the Cd-terminated ($Cu_2Cd_{31}Se_{33}$ (C_I)) shown in Figure 5d, the mid-gap states are still above the VB but without the contribution from Cu 3d orbitals. However, as the Cu dopants are close to the Se-terminated ($CuCd_{32}Se_{33}$ (C_{II}) and $Cu_2Cd_{31}Se_{33}$ (C_{II})), the mid-gap states disappear, as can be seen in Figure 5c,e. More interestingly, when Cu dopants are near both Se-terminated and Cd-terminated in $Cu_2Cd_{31}Se_{33}$ (C_{III}), the mid-gap states with the hybridization of Cu 3d and Se 4p orbitals appear above the VB (Figure 5f). As for the conduction band of core-doped Cu:$Cd_{33}Se_{33}$ QDs, an impurity level consisting of Se 4p states locates within the forbidden band in $CuCd_{32}Se_{33}$ (C_I) (Figure 5b) and $CuCd_{32}Se_{33}$ (C_{II}) (Figure 5c). With the increasing Cu dopants, an additional impurity level composed

of Cu 3d orbitals appears within the forbidden band for $Cu_2Cd_{31}Se_{33}$ (C_I) (Figure 5d) and $Cu_2Cd_{31}Se_{33}$ (C_{II}) (Figure 5e). This is consistent with the electronic character of Cu^{2+} as described in Section 3.4. However, in the case of $Cu_2Cd_{31}Se_{33}$ (C_{III}) (Figure 5f), there are no impurity levels. The above electronic structure analysis demonstrates that the energy levels and shapes of the valence and conduction bands can be modified by changing Cu concentrations and locations in CdSe QDs, which will, in turn, affect the optical absorption properties of these QDs as discussed in the next section.

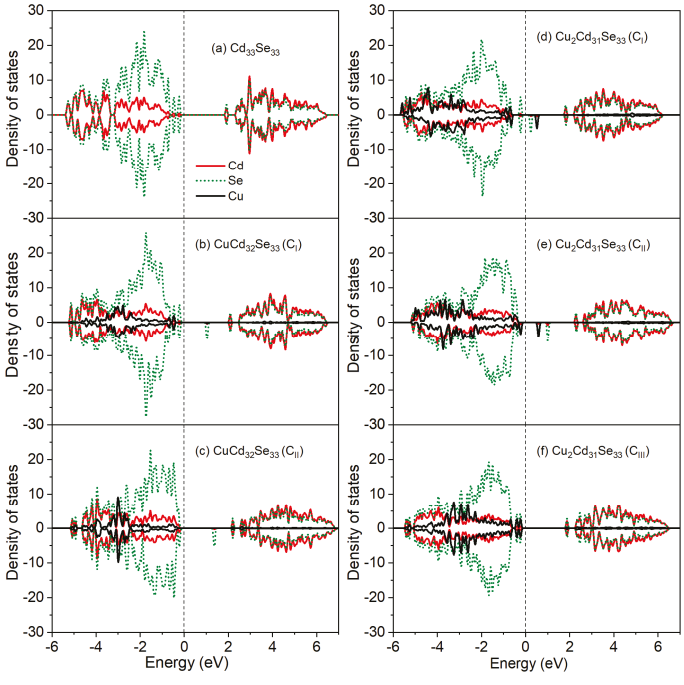

Figure 5. Projected density of states (DOS) for each type of ion when Cu atoms are doped in core region of $Cd_{33}Se_{33}$: (**a**) pristine $Cd_{33}Se_{33}$; (**b**) $CuCd_{32}Se_{33}$ (C_I); (**c**) $CuCd_{32}Se_{33}$ (C_{II}); (**d**) $Cu_2Cd_{31}Se_{33}$(C_I); (**e**) $Cu_2Cd_{31}Se_{33}$(C_{II}); (**f**) $Cu_2Cd_{31}Se_{33}$(C_{III}). The Fermi level is located at 0 eV.

3.5. Optical Absorption Spectra for Cu-Doped $Cd_{33}Se_{33}$ Quantum Dots

To explore how the copper incorporation affects the optical properties of $Cd_{33}Se_{33}$ QDs, the optical absorption spectra of $Cd_{33}Se_{33}$ with and without Cu dopants are calculated within the independent-particle approximation, which is known to provide a qualitative agreement of dielectric response functions between theory and experiment while neglecting self-energy, excitonic and local-field effects in the optical response [53,54]. For the $Cd_{33}Se_{33}$ QD, the calculated lowest absorption peak is in good agreement with the experiments [30,55]. Clearly, doping of Cu in the $Cd_{33}Se_{33}$ leads to different absorption spectra from the pristine one, as can been seen in Figure 6. In the visible region (the main figure of Figure 6), just one Cu dopant induces high-intensity absorption peaks in the range of 408–502 nm for $CuCd_{32}Se_{33}$ (S), 380–428 nm for $CuCd_{32}Se_{33}$ (C_I), and 445–574 nm for $CuCd_{32}Se_{33}$ (C_{II}). In experiments, the enhancement of absorption spectra in the wavelength range between 390 and 600 nm was also observed in Cu-doped CdSe NCs [19,22,31]. When two or three Cu atoms are doped, absorption peaks are relatively weaker within the same wavelength range. These results indicate that the optical intensity of Cu-doped $Cd_{33}Se_{33}$ in the visible region strongly correlates with Cu dopant content. A similar dopant–concentration-dependent trend in optical

absorption was also observed in Ag-doped CdSe QDs [48]. These new absorption features result predominantly from the electronic transition from Se 4p orbitals in the valence band to Se 4p and Cd 5s states in the conduction band (as shown in Figures 4 and 5).

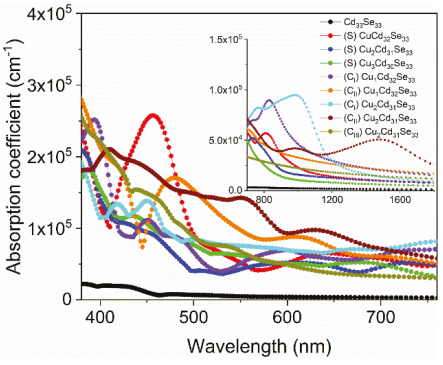

Figure 6. Absorption coefficients as a function of wavelength for $Cd_{33}Se_{33}$ QDs without and with Cu doping in the visible region in the main figure. The inset shows the absorption coefficients of these QDs in the infrared region.

In the infrared regime (displayed in the inset of Figure 6), the $Cu_2Cd_{31}Se_{33}$ (C_I) exhibits a stronger absorption peak than other CdSe QDs between 815 and 1161 nm; The $Cu_2Cd_{31}Se_{33}$ (C_{II}) has a unique absorption peak from 1148 to 1777 nm. These absorption features are induced mainly by electronic excitations from Se 4p orbitals on the top of VB to Cu 3d orbitals in the forbidden gap (as indicated in Figure 5). As analyzed in Section 3.4, Cu dopants show the +2 oxidation state in $Cu_2Cd_{31}Se_{33}$ (C_I) and $Cu_2Cd_{31}Se_{33}$ (C_{II}) while exhibiting the +1 oxidation state in other QDs. The result indicates that incorporation of Cu^{2+} in $Cd_{33}Se_{33}$ QDs can cause stronger optical absorption in the infrared regime than Cu^{+}. This can be explained by the fact that the 3d states of Cu^{2+} reside above the Fermi level and are near the valence band edge (Figure 5d,e). Such an electronic structure can lead to a small sub-bandgap electronic transition from VB to impurity levels and thus enhance optical absorption in the long-wavelength range.

Our results suggest that the incorporation of Cu can dramatically enhance the optical absorption of $Cd_{33}Se_{33}$ QD within the visible regime and extend the absorption edges into the infrared regime. Furthermore, the optical absorption of Cu-doped $Cd_{33}Se_{33}$ in the visible regime is affected mainly by Cu dopant concentration, while the absorption in the infrared regime is closely related to the oxidation state of Cu.

4. Conclusions

In this work, a systematic density functional theory (DFT) modeling using the Heyd–Scuseria–Ernzerhof (HSE) screened Coulomb hybrid functional was conducted to explore how the location and concentration of Cu dopants influence the structural, energetic, electronic, and optical properties of a magic-sized $Cd_{33}Se_{33}$ QD. It was found that the oxidation state of Cu dopants is closely related to their substitution location and concentration. Doping of Cu at the surface of $Cd_{33}Se_{33}$ QD leads to the Cu^{+} 3d orbitals distributions. Similar distributions of Cu^{+} 3d states were also observed for Cu in the core region such as $CuCd_{32}Se_{33}$ (C_I) (Cu atom near the Cd-terminated), $CuCd_{32}Se_{33}$ (C_{II}) (Cu atom near the Se-terminated), and $Cu_2Cd_{31}Se_{33}$ (C_{III}) (one Cu atom near the Cd-terminated and the other near the Se-terminated). However, doping of both copper atoms at internal Cd-sites near Cd-terminated or Se-terminated leads to the Cu^{2+} electronic character. Further binding energy calculations showed that in general, the Cu dopants with a +1 oxidation state are energetically more stable than those with a +2 oxidation state in $Cd_{33}Se_{33}$. It was also found that the optical absorption coefficient of Cu-doped $Cd_{33}Se_{33}$ in the infrared regime

is closely related to the oxidation state of Cu rather than Cu concentration. On the other hand, doping of only one Cu atom introduces stronger absorption peaks than the doping of two Cu atoms in the range of 380–574 nm, indicating that the absorption coefficient is sensitive to Cu concentration in the visible regime. This work demonstrates that the dopant location and concentration can have significant effects on the electronic structure of Cu 3d states. Therefore, the proper control of the dopant concentration and position is critical for improving the efficiency and performance of CdSe QD-based optoelectronic devices.

Author Contributions: Conceptualization, F.Z. and S.P.; methodology, F.Z. and S.H.; validation, F.Z. and C.X.; investigation, H.X., X.Z. (Xiaosong Zhou), X.Z. (Xiaotao Zu); writing—original draft preparation, F.Z.; writing—review and editing, S.H., C.X., H.X., X.Z. (Xiaosong Zhou) and X.Z. (Xiaotao Zu); supervision, S.P. All authors have read and agreed to the published version of the manuscript.

Funding: This work is partially supported by a funded project by the China Postdoctoral Science Foundation (2021TQ0312), the National Key Research and Development Program of China (2017YFE0301600, 2016YFB0201203), and the President Foundation of CAEP (YZJJLX2018003).

Institutional Review Board Statement: Not applicable.

Informed Consent Statement: Not applicable.

Data Availability Statement: The data presented in this study are available on request from the corresponding author. The data are not publicly available due to ethical.

Acknowledgments: The calculations were performed at the National Supercomputing Center at Wuxi and Shanghai Supercomputer Center.

Conflicts of Interest: The authors declare no conflict of interest.

References

1. Klimov, V.I.; Ivanov, S.A.; Nanda, J.; Achermann, M.; Bezel, I.; McGuire, J.A.; Piryatinski, A. Single-Exciton Optical Gain in Semiconductor Nanocrystals. *Nature* **2007**, *447*, 441–446. [CrossRef] [PubMed]
2. Mocatta, D.; Cohen, G.; Schattner, J.; Millo, O.; Rabani, E.; Banin, U. Heavily Doped Semiconductor Nanocrystal Quantum Dots. *Science* **2011**, *332*, 77–81. [CrossRef] [PubMed]
3. Mattoussi, H.; Mauro, J.M.; Goldman, E.R.; Anderson, G.P.; Sundar, V.C.; Mikulec, F.V.; Bawendi, M.G. Self-Assembly of CdSe−ZnS Quantum Dot Bioconjugates Using an Engineered Recombinant Protein. *J. Am. Chem. Soc.* **2000**, *122*, 12142–12150. [CrossRef]
4. Mattoussi, H.; Mauro, J.; Goldman, E.; Green, T.; Anderson, G.; Sundar, V.; Bawendi, M. Bioconjugation of Highly Luminescent Colloidal CdSe-ZnS Quantum Dots with an Engineered Two-Domain Recombinant Protein. *Phys. Status Solidi B* **2001**, *224*, 277–283. [CrossRef]
5. Santra, S.; Yang, H.; Holloway, P.H.; Stanley, J.T.; Mericle, R.A. Synthesis of Water-Dispersible Fluorescent, Radio-Opaque, and Paramagnetic CdS:Mn/ZnS Quantum Dots: A Multifunctional Probe for Bioimaging. *J. Am. Chem. Soc.* **2005**, *127*, 1656–1657. [CrossRef]
6. Pradhan, N.; Battaglia, D.M.; Liu, Y.; Peng, X. Efficient, Stable, Small, and Water-Soluble Doped ZnSe Nanocrystal Emitters as Non-Cadmium Biomedical Labels. *Nano Lett.* **2007**, *7*, 312–317. [CrossRef]
7. Wood, V.; Halpert, J.E.; Panzer, M.J.; Bawendi, M.G.; Bulović, V. Alternating Current Driven Electroluminescence from ZnSe/ZnS:Mn/ZnS Nanocrystals. *Nano Lett.* **2009**, *9*, 2367–2371. [CrossRef] [PubMed]
8. Janβen, N.; Whitaker, K.M.; Gamelin, D.R.; Bratschitsch, R. Ultrafast Spin Dynamics in Colloidal ZnO Quantum Dots. *Nano Lett.* **2008**, *8*, 1991–1994. [CrossRef]
9. Yang, H.; Holloway, P.H.; Ratna, B.B. Photoluminescent and Electroluminescent Properties of Mn-Doped ZnS Nanocrystals. *J. Appl. Phys.* **2003**, *93*, 586–592. [CrossRef]
10. Warkentin, M.; Bridges, F.; Carter, S.A.; Anderson, M. Electroluminescence Materials ZnS:Cu,Cl and ZnS:Cu,Mn,Cl Studied by EXAFS Spectroscopy. *Phys. Rev. B* **2007**, *75*, 075301. [CrossRef]
11. Smith, B.A.; Zhang, J.Z.; Joly, A.; Liu, J. Luminescence Decay Kinetics of Mn^{2+}-Doped ZnS Nanoclusters Grown in Reverse Micelles. *Phys. Rev. B* **2000**, *62*, 2021–2028. [CrossRef]
12. Lu, W.; Gao, P.; Jian, W.B.; Wang, Z.L.; Fang, J. Perfect Orientation Ordered In-Situ One-Dimensional Self-Assembly of Mn-Doped PbSe Nanocrystals. *J. Am. Chem. Soc.* **2004**, *126*, 14816–14821. [CrossRef]
13. Norberg, N.S.; Parks, G.L.; Salley, G.M.; Gamelin, D.R. Giant Excitonic Zeeman Splittings in Colloidal Co^{2+}-Doped ZnSe Quantum Dots. *J. Am. Chem. Soc.* **2006**, *128*, 13195–13203. [CrossRef] [PubMed]
14. Fainblat, R.; Barrows, C.J.; Gamelin, D.R. Single Magnetic Impurities in Colloidal Quantum Dots and Magic-Size Clusters. *Chem. Mater.* **2017**, *29*, 8023–8036. [CrossRef]

15. Sahu, A.; Kang, M.S.; Kompch, A.; Notthoff, C.; Wills, A.W.; Deng, D.; Winterer, M.; Frisbie, C.D.; Norris, D.J. Electronic Impurity Doping in CdSe Nanocrystals. *Nano Lett.* **2012**, *12*, 2587–2594. [CrossRef]
16. Chen, D.; Viswanatha, R.; Ong, G.L.; Xie, R.; Balasubramaninan, M.; Peng, X. Temperature Dependence of "Elementary Processes" in Doping Semiconductor Nanocrystals. *J. Am. Chem. Soc.* **2009**, *131*, 9333–9339. [CrossRef]
17. Viswanatha, R.; Brovelli, S.; Pandey, A.; Crooker, S.A.; Klimov, V.I. Copper-Doped Inverted Core/Shell Nanocrystals with "Permanent" Optically Active Holes. *Nano Lett.* **2011**, *11*, 4753–4758. [CrossRef] [PubMed]
18. Brovelli, S.; Galland, C.; Viswanatha, R.; Klimov, V.I. Tuning Radiative Recombination in Cu-Doped Nanocrystals via Electrochemical Control of Surface Trapping. *Nano Lett.* **2012**, *12*, 4372–4379. [CrossRef]
19. Dutta, A.; Bera, R.; Ghosh, A.; Patra, A. Ultrafast Carrier Dynamics of Photo-Induced Cu-Doped CdSe Nanocrystals. *J. Phys. Chem. C* **2018**, *122*, 16992–17000. [CrossRef]
20. Ning, J.; Liu, J.; Levi-Kalisman, Y.; Frenkel, A.I.; Banin, U. Controlling Anisotropic Growth of Colloidal ZnSe Nanostructures. *J. Am. Chem. Soc.* **2018**, *140*, 14627–14637. [CrossRef] [PubMed]
21. Yang, L.; Knowles, K.E.; Gopalan, A.; Hughes, K.E.; James, M.C.; Gamelin, D.R. One-Pot Synthesis of Monodisperse Colloidal Copper-Doped CdSe Nanocrystals Mediated by Ligand–Copper Interactions. *Chem. Mater.* **2016**, *28*, 7375–7384. [CrossRef]
22. Alperson, B.; Rubinstein, I.; Hodes, G. Identification of Surface States on Individual CdSe Quantum Dots by Room-Temperature Conductance Spectroscopy. *Phys. Rev. B* **2001**, *63*, 081303. [CrossRef]
23. Jana, S.; Srivastava, B.B.; Acharya, S.; Santra, P.K.; Jana, N.R.; Sarma, D.D.; Pradhan, N. Prevention of Photooxidation in Blue–Green Emitting Cu Doped ZnSe Nanocrystals. *Chem. Commun.* **2010**, *46*, 2853. [CrossRef] [PubMed]
24. Mandal, P.; Talwar, S.S.; Major, S.S.; Srinivasa, R.S. Orange-Red Luminescence from Cu Doped CdS Nanophosphor Prepared Using Mixed Langmuir–Blodgett Multilayers. *J. Chem. Phys.* **2008**, *128*, 114703. [CrossRef] [PubMed]
25. Pradhan, N.; Goorskey, D.; Thessing, J.; Peng, X. An Alternative of CdSe Nanocrystal Emitters: Pure and Tunable Impurity Emissions in ZnSe Nanocrystals. *J. Am. Chem. Soc.* **2005**, *127*, 17586–17587. [CrossRef]
26. Xie, F.; Xie, R.; Wang, Q. Synthesis and Characterization of $CuIn(S_xSe_{1-x})_2$ Nanocrystals. *Adv. Sci. Lett.* **2011**, *4*, 3624–3628. [CrossRef]
27. Buonsanti, R.; Milliron, D.J. Chemistry of Doped Colloidal Nanocrystals. *Chem. Mater.* **2013**, *25*, 1305–1317. [CrossRef]
28. Luo, H.; Tuinenga, C.; Guidez, E.B.; Lewis, C.; Shipman, J.; Roy, S.; Aikens, C.M.; Chikan, V. Synthesis and Characterization of Gallium-Doped CdSe Quantum Dots. *J. Phys. Chem. C* **2015**, *119*, 10749–10757. [CrossRef]
29. Meulenberg, R.W.; van Buuren, T.; Hanif, K.M.; Willey, T.M.; Strouse, G.F.; Terminello, L.J. Structure and Composition of Cu-Doped CdSe Nanocrystals Using Soft X-Ray Absorption Spectroscopy. *Nano Lett.* **2004**, *4*, 2277–2285. [CrossRef]
30. Kasuya, A.; Sivamohan, R.; Barnakov, Y.A.; Dmitruk, I.M.; Nirasawa, T.; Romanyuk, V.R.; Kumar, V.; Mamykin, S.V.; Tohji, K.; Jeyadevan, B.; et al. Ultra-Stable Nanoparticles of CdSe Revealed from Mass Spectrometry. *Nat. Mater.* **2004**, *3*, 99–102. [CrossRef]
31. Whitham, P.J.; Knowles, K.E.; Reid, P.J.; Gamelin, D.R. Photoluminescence Blinking and Reversible Electron Trapping in Copper-Doped CdSe Nanocrystals. *Nano Lett.* **2015**, *15*, 4045–4051. [CrossRef]
32. Corrado, C.; Jiang, Y.; Oba, F.; Kozina, M.; Bridges, F.; Zhang, J.Z. Synthesis, Structural, and Optical Properties of Stable ZnS:Cu,Cl Nanocrystals. *J. Phys. Chem. A* **2009**, *113*, 3830–3839. [CrossRef] [PubMed]
33. Srivastava, B.B.; Jana, S.; Pradhan, N. Doping Cu in Semiconductor Nanocrystals: Some Old and Some New Physical Insights. *J. Am. Chem. Soc.* **2011**, *133*, 1007–1015. [CrossRef] [PubMed]
34. Isarov, A.V.; Chrysochoos, J. Optical and Photochemical Properties of Nonstoichiometric Cadmium Sulfide Nanoparticles: Surface Modification with Copper(II) Ions. *Langmuir* **1997**, *13*, 3142–3149. [CrossRef]
35. Lilhare, D.; Sinha, T.; Khare, A. Influence of Cu Doping on Optical Properties of (Cd–Zn)S Nanocrystalline Thin Films: A Review. *J. Mater. Sci. Mater. Electron.* **2018**, *29*, 688–713. [CrossRef]
36. Harb, M.; Masih, D.; Takanabe, K. Screened Coulomb Hybrid DFT Investigation of Band Gap and Optical Absorption Predictions of $CuVO_3$, $CuNbO_3$ and $Cu_5Ta_{11}O_{30}$ Materials. *Phys. Chem. Chem. Phys.* **2014**, *16*, 18198–18204. [CrossRef]
37. Deák, P.; Aradi, B.; Frauenheim, T.; Janzén, E.; Gali, A. Accurate Defect Levels Obtained from the HSE06 Range-Separated Hybrid Functional. *Phys. Rev. B* **2010**, *81*, 153203. [CrossRef]
38. Heyd, J.; Scuseria, G.E.; Ernzerhof, M. Hybrid Functionals Based on a Screened Coulomb Potential. *J. Chem. Phys.* **2003**, *118*, 8207–8215. [CrossRef]
39. Kilina, S.; Ivanov, S.; Tretiak, S. Effect of Surface Ligands on Optical and Electronic Spectra of Semiconductor Nanoclusters. *J. Am. Chem. Soc.* **2009**, *131*, 7717–7726. [CrossRef]
40. Kuznetsov, A.E.; Beratan, D.N. Structural and Electronic Properties of Bare and Capped $Cd_{33}Se_{33}$ and $Cd_{33}Te_{33}$ Quantum Dots. *J. Phys. Chem. C* **2014**, *118*, 7094–7109. [CrossRef]
41. Puzder, A.; Williamson, A.J.; Zaitseva, N.; Galli, G.; Manna, L.; Alivisatos, A.P. The Effect of Organic Ligand Binding on the Growth of CdSe Nanoparticles Probed by Ab Initio Calculations. *Nano Lett.* **2004**, *4*, 2361–2365. [CrossRef]
42. Puzder, A.; Williamson, A.J.; Gygi, F.; Galli, G. Self-Healing of CdSe Nanocrystals: First-Principles Calculations. *Phys. Rev. Lett.* **2004**, *92*, 217401. [CrossRef] [PubMed]
43. Hafner, J. ChemInform Abstract: Ab-Initio Simulations of Materials Using VASP: Density-Functional Theory and Beyond. *J. Comput. Chem.* **2008**, *29*, 2044–2078. [CrossRef] [PubMed]
44. Perdew, J.P.; Burke, K.; Ernzerhof, M. Generalized Gradient Approximation Made Simple. *Phys. Rev. Lett.* **1996**, *77*, 3865–3868. [CrossRef]

45. Perdew, J.P.; Burke, K.; Wang, Y. Generalized Gradient Approximation for the Exchange-Correlation Hole of a Many-Electron System. *Phys. Rev. B* **1996**, *54*, 16533–16539. [CrossRef]
46. Winkler, U.; Eich, D.; Chen, Z.H.; Fink, R.; Kulkarni, S.K.; Umbach, E. Detailed Investigation of CdS Nanoparticle Surfaces by High-Resolution Photoelectron Spectroscopy. *Chem. Phys. Lett.* **1999**, *306*, 95–102. [CrossRef]
47. Shannon, R.D. Revised Effective Ionic Radii and Systematic Studies of Interatomic Distances in Halides and Chalcogenides. *Acta Cryst. A* **1976**, *32*, 751–767. [CrossRef]
48. Zhao, F.A.; Xiao, H.Y.; Bai, X.M.; Zu, X.T. Effects of Ag Doping on the Electronic and Optical Properties of CdSe Quantum Dots. *Phys. Chem. Chem. Phys.* **2019**, *21*, 16108–16119. [CrossRef] [PubMed]
49. Suyver, J.F.; van der Beek, T.; Wuister, S.F.; Kelly, J.J.; Meijerink, A. Luminescence of Nanocrystalline ZnSe:Cu. *Appl. Phys. Lett.* **2001**, *79*, 4222–4224. [CrossRef]
50. Ganesan, P.; Lakshmipathi, S. Influence of Dopants Cu, Ga, In, Hg on the Electronic Structure of Cd_nS_n (n = 6, 15) Clusters–a DFT Study. *RSC Adv.* **2016**, *6*, 93056–93067. [CrossRef]
51. Liu, J.; Zhao, Y.; Liu, J.; Wang, S.; Cheng, Y.; Ji, M.; Zhou, Y.; Xu, M.; Hao, W.; Zhang, J. From Cu2S Nanocrystals to Cu Doped CdS Nanocrystals through Cation Exchange: Controlled Synthesis, Optical Properties and Their p-Type Conductivity Research. *Sci. China Mater.* **2015**, *58*, 693–703. [CrossRef]
52. Nelson, H.D.; Hinterding, S.O.M.; Fainblat, R.; Creutz, S.E.; Li, X.; Gamelin, D.R. Mid-Gap States and Normal vs Inverted Bonding in Luminescent Cu^+- and Ag^+-Doped CdSe Nanocrystals. *J. Am. Chem. Soc.* **2017**, *139*, 6411–6421. [CrossRef] [PubMed]
53. Gajdoš, M.; Hummer, K.; Kresse, G.; Furthmüller, J.; Bechstedt, F.J.P.R.B. Linear optical properties in the projector-augmented wave methodology. *Phys. Rev. B* **2006**, *73*, 045112. [CrossRef]
54. Schmidt, W.G. Calculation of reflectance anisotropy for semiconductor surface exploration. *Phys. Status Sol. B* **2005**, *242*, 2751–2764. [CrossRef]
55. Kudera, S.; Zanella, M.; Giannini, C.; Rizzo, A.; Li, Y.; Gigli, G.; Cingolani, R.; Ciccarella, G.; Spahl, W.; Parak, W.J.; et al. Sequential Growth of Magic-Size CdSe Nanocrystals. *Adv. Mater.* **2007**, *19*, 548–552. [CrossRef]

nanomaterials

MDPI

Article

Organic Dye-Derived N, S Co-Doped Porous Carbon Hosts for Effective Lithium Polysulfide Confinement in Lithium–Sulfur Batteries

Eunji Kim [1], Albert S. Lee [2], Taewoong Lee [1], Hyeok Jun Seo [1], Seongwook Chae [1], Kihyun Kim [3,*], Jun-Woo Park [4,*], Seung Geol Lee [1,*] and Jin Hong Lee [1,*]

[1] School of Chemical Engineering, Pusan National University, Busan 46421, Korea; eunjikim@pusan.ac.kr (E.K.); wmfrlwk12@pusan.ac.kr (T.L.); seohj@pusan.ac.kr (H.J.S.); swchae0708@pusan.ac.kr (S.C.)
[2] Materials Architecturing Research Center, Korea Institute of Science and Technology, Seoul 02792, Korea; aslee@kist.re.kr
[3] Department of Materials Engineering and Convergence Technology, Gyeongsang National University, Jinju 52828, Korea
[4] Next Generation Battery Research Center, Korea Electrotechnology Research Institute (KERI), Changwon 51543, Korea
* Correspondence: kihyun@gnu.ac.kr (K.K.); parkjw@keri.re.kr (J.-W.P.); seunggeol.lee@pusan.ac.kr (S.G.L.); jinhong.lee@pusan.ac.kr (J.H.L.)

Abstract: Lithium–sulfur batteries are considered as attractive candidates for next-generation energy storage systems originating from their high theoretical capacity and energy density. However, the severe shuttling of behavior caused by the dissolution of lithium polysulfide intermediates during cycling remains a challenge for practical applications. Herein, porous carbon materials co-doped with nitrogen and sulfur atoms were prepared through a facile hydrothermal reaction of graphene oxide and methylene blue to obtain a suitable host structure for regulating the lithium polysulfide shuttling behavior. Experimental results demonstrated that the abundant heteroatom-containing moieties in the carbon frameworks not only generated favorable active sites for capturing lithium polysulfide but also enhanced redox reaction kinetics of lithium polysulfide intermediates. Consequently, the corresponding sulfur composite electrodes exhibited excellent rate performance and cycling stability along with high Columbic efficiency. This work highlights the approach for the preparation of nitrogen and sulfur co-doped carbon materials derived from organic dye compounds for high performance energy storage systems.

Keywords: lithium sulfur batteries; organic dye; graphene; heteroatom doping

Citation: Kim, E.; Lee, A.S.; Lee, T.; Seo, H.J.; Chae, S.; Kim, K.; Park, J.-W.; Lee, S.G.; Lee, J.H. Organic Dye-Derived N, S Co-Doped Porous Carbon Hosts for Effective Lithium Polysulfide Confinement in Lithium–Sulfur Batteries. *Nanomaterials* **2021**, *11*, 2954. https://doi.org/10.3390/nano11112954

Academic Editors: Marc Cretin, Sophie Tingry and Zhenghua Tang

Received: 15 October 2021
Accepted: 2 November 2021
Published: 4 November 2021

1. Introduction

With the noticeably increasing demands for energy storage systems and electric vehicles, lithium–sulfur (Li-S) batteries have been widely investigated as promising next-generation battery systems due to their overwhelming electrochemical performances, such as high theoretical specific capacity (1675 mAh/g) and energy density (2800 Wh/L) [1,2]. Furthermore, sulfur has the additional advantages of natural abundance and cost-effective as well as environmentally friendly resources [3]. Despite these advantages over the conventional lithium-ion batteries, the practical application of the rechargeable Li-S batteries is still hindered by many problems, in particular the limited utilization of sulfur active materials and poor cycling performance [4]. During the repeated charge–discharge processes, the lithium polysulfide species (Li_2Sx, $4 \leq x \leq 8$) formed from the cathode are progressively solvated in the organic electrolyte and diffuse between the anode and the cathode, resulting in parasitic reactions [5]. This phenomenon is referred to as a shuttling behavior, which causes loss of an active material and fast capacity fading. In addition, Li-S batteries suffer from the inherent poor electrical conductivity of sulfur and the discharge products of Li_2S/Li_2S_2, leading to sluggish reaction kinetics [6]. In addition, the

large volume expansion of ~80% upon full lithiation leads to the formation of an unstable electrode/electrolyte interface layer [7].

To solve these issues of the Li-S batteries, various strategies of incorporating sulfur species in a carbonaceous host material derived from micro/mesoporous carbons [8], carbon nanotubes (CNTs) [9], graphene [10], and carbon nanofiber [11] have been investigated. The physical/chemical confinement of sulfur in these host materials not only mitigates the shuttling behavior by preventing the dissolution of lithium polysulfide but also promotes redox reaction kinetics with the help of conductive pathways provided by the carbon framework. Moreover, the porous carbonaceous materials with large specific surface area accommodate a large amount of sulfur and offer a lot of active sites for electrochemical reactions, which leads to improved lithium storage behavior [12,13]. However, non-polar carbon materials exhibit only weak physical adsorption to the polar lithium polysulfides, resulting in an unsatisfactory suppression of lithium polysulfide shuttling behavior during long-term cycling [14].

Therefore, it is essential to introduce a reasonable design of carbon-based materials with polar moieties to provide strong chemical interactions with the lithium polysulfide. To date, tremendous efforts have been devoted to develop advanced carbon composite materials based on many different types of polymers [15], metal oxides [16,17], and metal-organic frameworks [18]. While these approaches have been demonstrated to be effective for the chemisorption of lithium polysulfides, the limited conductivity of these materials is still not sufficient to achieve good rate capability. As such, modifications of the carbon materials with heteroatoms, such as boron, oxygen, sulfur, nitrogen, and phosphorus, have been explored [19–21]. Of these heteroatoms, nitrogen and sulfur atoms have proved to effectively increase the adsorption capability of carbon materials via strong chemical interactions, with the π-conjugated structures ensuring an efficient electron transport to promote redox reaction kinetics [22].

In this study, microporous nitrogen and sulfur co-doped reduced graphene oxides (rGO) regulating the lithium polysulfide shuttling behavior were prepared as a host material for Li-S cathode through facile hydrothermal and freeze-drying treatments. A cationic dye, methylene blue (MB) was chosen as a precursor for heteroatom doping, because the heterocyclic aromatic structure with positively charged nitrogen or sulfur moiety of the MB could allow for favorable interactions with GO aqueous suspensions, giving rise to well-developed porous graphene structures with ample nitrogen- and sulfur-containing moieties. The sulfur cathodes were able to deliver higher specific capacity and better cycling performance during cycling when compared with those of rGO cathodes. Spectroscopic analysis and electrochemical performance evaluation coupled with redox reaction kinetics investigations revealed that the heteroatom-containing moieties in the carbon frameworks were able to provide facilitated charge transport and alleviate lithium polysulfide shuttling behavior, leading to the enhanced Li-S battery performances.

2. Materials and Methods

2.1. Preparation of Nitrogen and Sulfur Co-Doped Carbon via Hydrothermal Method

To prepare the nitrogen and sulfur co-doped carbon materials, different amounts of methylene blue (MB, Sigma-Aldrich, St. Louis, MO, USA) were dissolved in graphene oxide (GO) aqueous dispersion (5 mg/mL) and vigorously sonicated for 30 min. MBGOx represent the precursor mass ratio of MB:GO = x:100. The mixed solution was transferred into a Teflon-lined autoclave and heated 180 °C for 24 h, followed by cooling to room temperature. The hydrogel mixture was repeatedly washed with deionized water and freeze-dried under a vacuum. For comparison, the rGO sample was also prepared via the same process without the addition of MB.

2.2. Material Characterizations

Zeta potential (Zetasizer, Malvern Panalytical, Malvern, UK) measurement was performed to identify surface charges. Scanning electron microscope (SEM, SUPRA25, Zeiss,

Oberkochen, Germany) was used to analyze the morphology of the MBGOs and rGO materials. The elemental distribution of MBGO20 were observed using a transmission electron microscope (TEM, TALOS F200X, FEI, Hillsboro, OR, USA) equipped with an energy dispersive X-ray spectroscopy (EDS). X-ray diffraction (XRD, Xpert 3, Malvern Panalytical, Malvern, UK) and Raman spectroscopy (RAMANtouch, Nanophoton, Minato, Japan) were performed to carbon crystallographic properties. The X-ray photoelectron spectroscopy (XPS, AXIS SUPRA, Kratos Analytical Ltd., Manchester, UK) was carried out to the surface chemical binding state.

2.3. Electrochemical Measurements

The sulfur/MBGO composites were prepared by heating a mixture of sulfur and MBGO20 with a mass ratio of 3:1 at 155 °C for 12 h in a stainless-steel vessel (Figure S1). The sulfur cathode was prepared by stirring the slurry mixture of 70 wt% of sulfur/MBGO20 composites, 10 wt% of the polyvinylidene fluoride (PVDF) binder and 10 wt% of Super-P in N-methyl-2-pyrrolidone (NMP) solvent. The slurry was coated on an aluminum current collector, and then dried at 80 °C for 24 h under a vacuum. Similarly, a cathode with the rGO sample was prepared using the same procedure. The loading of sulfur mass was about 1.0 mg/cm^2. The as-prepared cathode, lithium metal anode and polypropylene separator were assembled into a CR2032 coin cell with an electrolyte of 1.0 M lithium bis(trifluoromethane)sulfonamide lithium (LiTFSI) and 0.1 M lithium nitrite ($LiNO_3$) additive in a mixture of 1,3-dioxolane (DOL) and 1,2-dimethoxyethane (DME) (1:1 by volume). The electrochemical performances were conducted using an automatic charge–discharge instrument (WBCS3000, WonATech Co., Seoul, Korea) in a voltage window of 1.8–2.8 V. Cyclic voltammetry (CV) and electrochemical impedance spectroscopy (EIS) measurements were performed with Biologic BCS-805 and Biologic SP-150 workstation, respectively. EIS tests were carried on the frequency ranges from 1.00 MHz to 0.01 Hz with a disturbance amplitude of 10 mV.

3. Results and Discussion

As schematically illustrated in Figure 1a, porous N, S co-doped rGO host materials regulating the lithium polysulfide shuttling behavior were prepared via a simple hydrothermal method using methylene blue (MB) as a precursor for doping of heteroatoms onto the graphene layers. The MB is a heterocyclic aromatic organic dye that contains a delocalized charge distribution in aqueous solution; only weak positive charge characteristic was detected from the zeta potential measurement. (Figure 1b). We speculated that negatively charged oxygen-containing functional groups on the surface of GO sheets could induce a complexation of GO and MB through electrostatic interactions, with π-π bond providing additional interactions for the interfacial assembly. To investigate the interaction of MB and GO, different amounts of MB aqueous solutions were added to a GO suspension and left for several hours. We found that these mixtures spontaneously assembled with increasing the content of MB. For the MBGO20, small aggregates were observed as presented by optical microscopy. (Figure 1c) Remarkably, after increasing the content of methylene blue of up to 40%, MBGO40, relatively larger and more aggregates were obviously visible at the bottom of the vial, which could be a consequence of complete covering of the charge of the GO sheets, leading to the formation of highly aggregated precipitates out of the solutions. Thus, we considered that the addition of excessive amount of MB would be a negative influence on achieving a homogeneity and porous structure of host materials during the hydrothermal reaction.

The morphologies of the MBGO were investigated by scanning electron microscopy (SEM) with the images displayed in Figure 1d,e. After thermal expansion by the hydrothermal reaction, the rGO nanosheet formed a three-dimensional network with slight folds and crumpled edges (Figure S2), while maintaining the well-defined porous structure. Similarly, the MBGO samples revealed the layered and porous network structures, but

the nanosheets were progressively stacked to form a compact structure with dense and continuous surface morphologies upon increasing the content of MB.

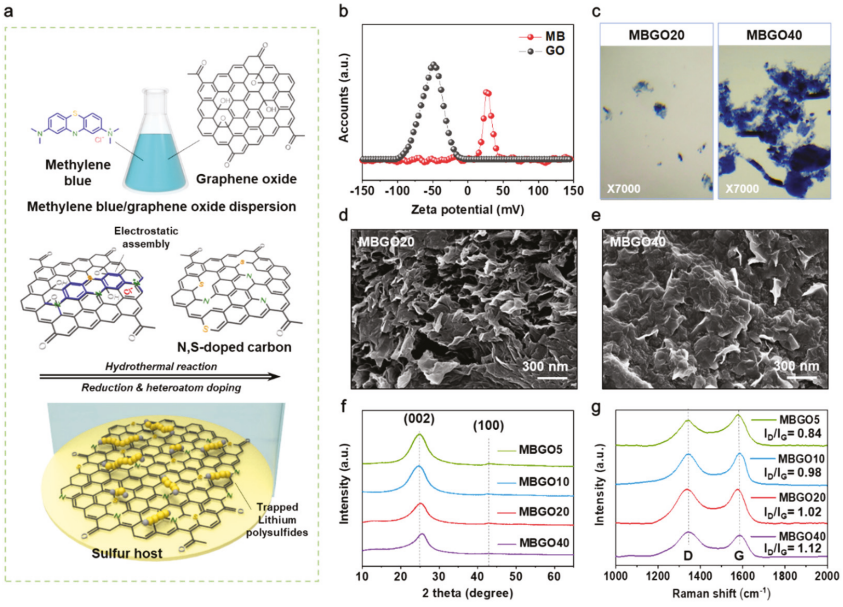

Figure 1. (**a**) Schematic of the preparation process of N, S–doped carbon as a sulfur host. (**b**) Zeta potential of graphene oxide and methylene blue. (**c**) Optical microscopy observations of the bottom of vial for MBGO20 and MBGO40 solutions. SEM image of (**d**) MBGO20 and (**e**) MBGO40. (**f**) XRD patterns and (**g**) Raman spectra of MBGOs with different MB contents.

The X-ray diffraction (XRD) analysis was performed to better understand the microstructure of the MBGOs. As shown in Figure 1f, the MBGOs exhibited two broad peaks around 24° and 43°, corresponding to the (002) and (100) reflections of planes in the disordered carbon materials, indicative of the partially restacked rGO [23]. We observed that the (002) peak position shifted toward the higher angle of 2θ with increasing the content of methylene blue compared to the pristine rGO (Figure S3), suggesting that the introduction of methylene blue decreases the interlayer distance of the MBGOs [24]; this is generally coupled with the deoxidization of oxygen functional group due to the heteroatom (e.g., B, N, and S) doping in the graphitic layer. The structural disorder tendency of MBGOs was also investigated by Raman spectroscopy. As shown in Figure 1g, the MBGOs exhibited two distinctive peaks at 1320 cm^{-1} and 1590 cm^{-1} related to the D (defects and disorder in the graphitic layer) and G band (sp^2 hybridized carbon atoms) respectively, indicating a presence of disordered graphitic layers [25]. The corresponding intensity ratio of the D and G bands (I_D/I_G) gradually increased with the rise of methylene blue content, which could be ascribed to the incorporation of heteroatoms into the carbon framework [24].

Figure 2a displays the STEM images and corresponding energy-dispersive X-ray spectroscopy (EDS) mapping images of the MBGO20. Uniform distribution of carbon, nitrogen, and sulfur elements over the entire carbon structure was observed, again demonstrating that the nitrogen and sulfur atoms were successfully incorporated in the carbon matrix through the hydrothermal treatment.

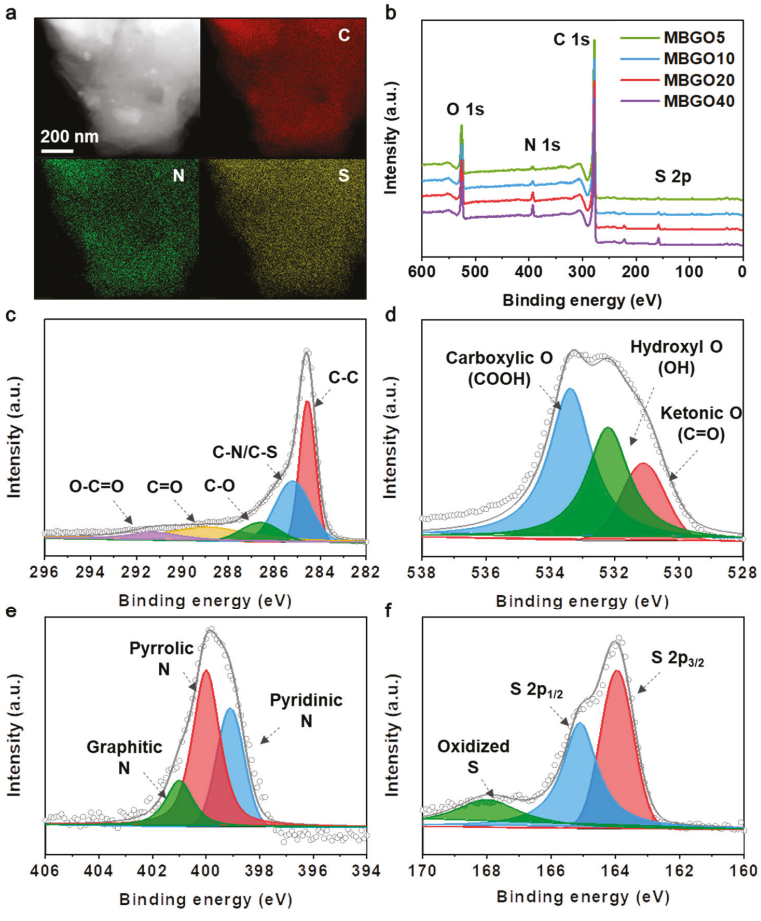

Figure 2. (**a**) STEM image and corresponding elemental mapping images of C, N and S for MBGO20. (**b**) XPS survey spectra with different MB contents. The high-resolution XPS spectra of (**c**) C 1s, (**d**) O 1s, (**e**) N 1s and (**f**) S 2p of the MBGO20.

The XPS analysis was performed further to investigate the surface element composition and chemical state of MBGOs depending on the contents of methylene blue. As shown in Figure 2b, the XPS survey spectrum exhibited the presence of carbon, nitrogen, sulfur, and oxygen species. The amount of nitrogen and sulfur atoms increased continuously with the increasing the amount of methylene blue, accompanied by decreasing the content of oxygen element as listed in Table S1. The high-resolution C 1s, O 1s, N 1s, and S 2p spectrum of MBGO20 are displayed in Figure 2c–f, respectively. The C 1s spectrum (Figure 2c) exhibited the characteristic peaks located at 284.5 and 285.2 eV, which could be indexed to the C–C groups constituting the carbon structure and the C–N/C–S groups formed by heteroatoms doping, respectively. In addition, small peaks for C–O, C=O, and O–C=O originated from oxygen functional groups were observed at 286.6 eV, 289.0 eV, and 291.3 eV [26]. The O 1s spectrum could be deconvoluted into C=O, –OH, and COOH three peaks centered at 531.1, 533.4, and 533.4 eV, respectively (Figure 2d) [27]. The binding state of nitrogen and sulfur containing moieties was also investigated. As shown in Figure 2e, the N 1s spectrum was fitted by three typical peaks, including pyridinic N (N–6, 399.1 eV), pyrrolic N (N–5, 400.1 eV), and graphitic N (N–Q, 401.0 eV) [28]. The S 2p spectrum

exhibited three sub-peaks located at 163.9, 165.2, and 167.9 eV, corresponding to the S $2p_{3/2}$, S $2p_{1/2}$, and oxidized S, respectively [29]. Previous studies have proved that the incorporation of nitrogen and sulfur containing moieties into the carbon materials could not only offer favorable physical and/or chemical trapping sites to alleviate the lithium polysulfide shuttling behavior, but also expedite the redox reaction kinetics of sulfur species, resulting in the high electrochemical performances [22,30]. Although the heteroatom content of the MBGO40 was estimated to be slightly lower than that of the MBGO20, we considered that the highly stacked MBGO40 hybrid structure that would hamper ion transport during cycling and decrease the contact sites between the heteroatoms and the lithium polysulfide when employed as sulfur hosts for Li–S batteries.

As such, the electrochemical performance was evaluated for the Li–S cells fabricated with MBGO20 cathode. The cyclic voltammetry (CV) was initially carried out to identify redox reaction behavior of the MBGO20 cathode at a current rate of 0.1 mV/s. For comparison, the CV curve for the cell with pristine rGO cathode is also provided. As shown in Figure 3a, during the cathodic scan, two peaks were observed at around 2.1 and 2.3 V, indicating the reduction of sulfur (S_8) to long-chain lithium polysulfide (Li_2S_x) and the reduction of long-chain lithium polysulfide (Li_2S_X) to insoluble lithium polysulfide (Li_2S_2/Li_2S), respectively. In the anodic scan, the oxidation peaks at around 2.4 V and 2.5 V correspond to the conversion of Li_2S_2/Li_2S into long-chain Li_2S_X and eventually to S_8 [31]. Obviously, the cell with MBGO20 cathodes showed significantly higher and sharper redox peaks along with larger area than those of the rGO cathode, suggesting that the MBGO20 cathode was able to improve redox reaction kinetics and capacitive behavior.

The rate capability of the cells with MBGO20 and rGO cathode was measured at different current rates from C/10 to 1 C. As shown in Figure 3b, MBGO20 cathode showed higher specific capacities at all current rates when compared to the rGO cathode, and the difference in specific capacity was noticeable with increasing current rates. Furthermore, when returned to the current rate of C/10, the specific capacity of MBGO20 cathode recovered reasonable specific capacities, indicating high electrochemical reversibility. The galvanostatic charge–discharge profiles of MBGO20 and rGO cathode at various current rates are compared, where the two well-defined charge and discharge plateaus were observed at a mild condition of 1/10 C, which was in good agreement with the CV results. As presented in Figure 3c,d, we observed that there is a difference between the charge capacity and the discharge capacity, especially in the first cycle. This result indicates the low Coulombic efficiency during the initial cycling, which could be attributed to the formation of a solid electrolyte interphase (SEI) layer. [5] Additionally, we were not able to suppress completely the parasitic reactions derived from the diffusion of lithium polysulfide dissolved in electrolytes [32]. Nonetheless, the MBGO20 cathode showed much improved electrochemical performances and Coulombic efficiency compared to the rGO cathode possibly due to well-developed porous graphene structures with ample nitrogen- and sulfur-containing moieties, which suggests that the MBGO20 cathode was able to mitigate the parasitic reactions to the electrode. In addition, the voltage differences between the charge–discharge curves of the rGO cathode were found to be larger than those of the MBGO20 cathode, and the differences were more prominent with increasing current rates, with the discharge plateaus gradually disappearing. By comparison, the MBGO20 cathode showed a relatively stable charge–discharge behavior with lower polarization, which further indicates the enhanced reaction kinetics.

Figure 3e displays the cycling performance and CE of the cells with MBGO20 and rGO cathodes at a current rate of 0.2C. As expected, the MBGO20 cathode was able to deliver improved cycling performance compared to the rGO cathode. The rGO cathode exhibited a limited capacity retention of about 21%, while the MB20 cathode showed a double capacity retention. In addition, CE of the MBGO20 cathodes was observed to be close 99% during cycles, confirming excellent cycling stability. We considered that the introduction of heteroatom into the carbon framework not only gives rise to fast redox reaction kinetics but also mitigates the shuttling behavior of lithium polysulfide derived from a polar interaction

during cycling, which in turn improves utilization of active materials and thus provide the higher electrochemical performances.

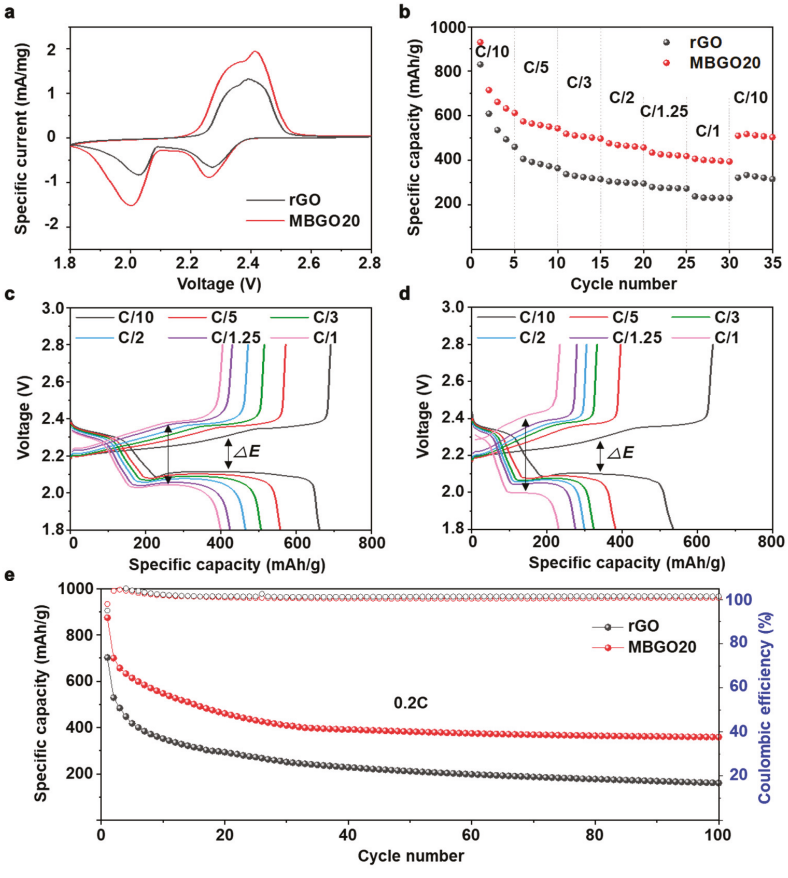

Figure 3. (**a**) CV curve of MBGO20 and rGO cells at 0.1 mV/s in the voltage window of 1.8 to 2.8 V. (**b**) Rate capability and galvanostatic charge–discharge profiles of (**c**) MBGO20 and (**d**) rGO cells at various current rates. (**e**) Cycling performance and Coulombic efficiency at 0.2 C.

To better understand the redox reaction kinetics, electrochemical impedance spectra (EIS) measurements were conducted after cycling, and the relevant equivalent circuit model is shown in Figure S4. As displayed in Figure 4a, both Nyquist plots exhibited two semicircles at high- to medium-frequency ranges, an oblique line at low frequency. The first semicircle is a combination of bulk resistance of the electrolyte (R_0) and insulating surface layer (R_{surf}), and the second semicircle relates to charge-transfer resistance (R_{ct}). In addition, the oblique line corresponds to the Warburg impedance (W_s) associated with the diffusion of lithium ions in the electrode [33]. It can be noticed that the MBGO20 cathodes showed smaller R_{surf} and R_{ct} values, which demonstrates the suppressed formation of insulating Li_2S_2/Li_2S layer and excellent lithium polysulfide conversion kinetics. Additionally, we speculated that the lone pair electrons in nitrogen and sulfur would form conjugation structures which improve the electrical conductivity of the MBGO20, leading to the reduced charge transfer resistance and fast redox reaction kinetics, as reported previously [34].

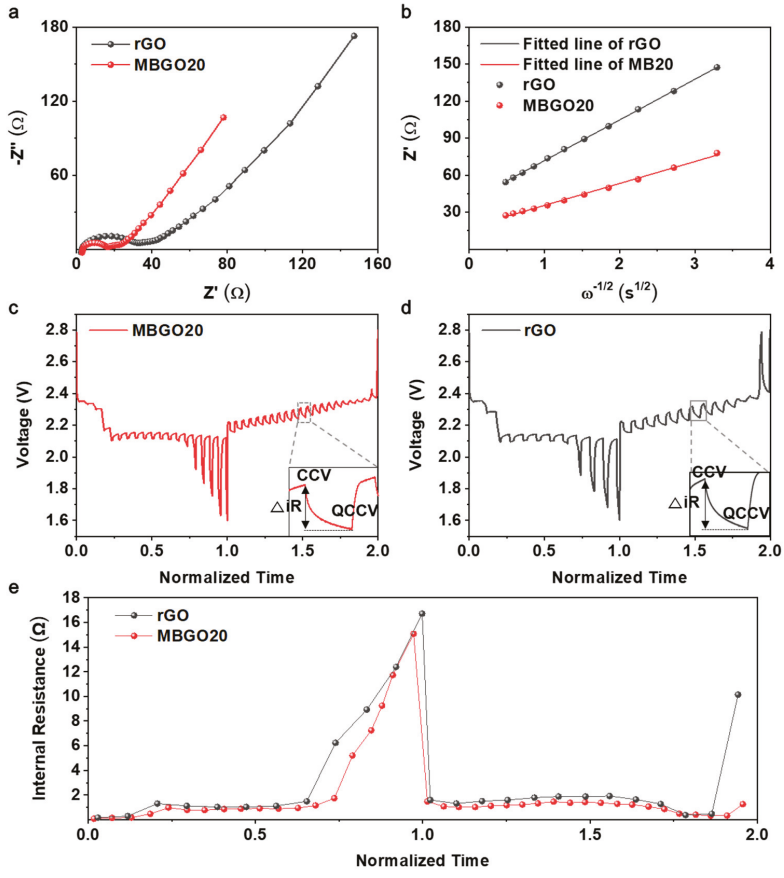

Figure 4. (**a**) Nyquist plots of MBGO20 and rGO cathodes. (**b**) Relationship between Z′ and $\omega^{-1/2}$ in the low-frequency region. GITT curves of (**c**) MBGO20 and (**d**) rGO cathode at 0.02 C. (**e**) Internal resistance based on GITT.

The diffusion coefficient of lithium ions ($D_{Li}{}^{+}$) in the low-frequency region was calculated further by the following Equation (1) [35,36]:

$$D_{Li}{}^{+} = R^2T^2/2A^2n^4F^4C^2\sigma^2 \quad (1)$$

where R, T, A, n, F, and C are gas constant, absolute temperature, cathode surface area, electrons number per molecule in redox reaction, Faraday constant and lithium ion concentration in electrolyte, respectively. σ is Warburg coefficient, calculated according to the following Equation (2):

$$Z' = R_0 + R_{ct} + \sigma\omega^{-1/2} \quad (2)$$

where ω represents the angular frequency. The linear relationship between Z' and $\omega^{-1/2}$ is shown in Figure 4b, and the Warburg coefficient of the MBGO20 cathode found to be smaller than that of the rGO cathode, demonstrating the improved redox reaction kinetics and Li^+ diffusion for the MBGO20 cathode. The $D_{Li}{}^{+}$ values of MBGO20 and rGO cathodes were calculated to be 5.5×10^{-12} cm^2/s and 1.6×10^{-12} cm^2/s, respectively.

Subsequently, the galvanostatic intermittent titration technique (GITT) was performed at 0.02 C in order to further investigate the effect of MBGO on the lithium polysulfide conversion kinetics. As presented in voltage fluctuations (Figure 4c,d), during charge and

discharge processes, the MBGO20 cathode exhibited lower cell polarizations that are clearly evident in the magnified pulse compared with the rGO cathode, which is in accordance with the charge transfer behavior. For stricter comparison, the internal resistances of MBGO20 and rGO cathodes during cell operation were calculated using the following Equation (3) [37,38]:

$$\Delta R_{\text{internal}}(\Omega) = |\Delta V_{\text{QOCV-CCV}}| / I_{\text{applied}} \quad (3)$$

where ΔV represents the voltage difference between the closed-circuit voltages (OCV) and the quasi-open-circuit voltage (QOCV), and I_{applied} represents the applied current. $\Delta R_{\text{internal}}$ is defined as the internal resistance of cell related to lithium polysulfide conversion during charge and discharge. As shown in Figure 4e, the internal resistance values for the MBGO20 cathode observed to be the lower during both charge and discharge processes compared with rGO cathode, which demonstrates a significant improvement in the redox kinetics for lithium polysulfide through rapid electron and lithium-ion transport.

After 100 cycles, the surface morphology of the lithium metal anode was observed to monitor the change in lithium polysulfide shuttling behavior using scanning electron microscopy (SEM). As presented in Figure 5a, the lithium metal anode surface of the rGO cathode showed a lot of irregular dendritic particles and holes along with rough passivation layers, which resulted from the continuous lithium polysulfide shuttling behavior and decomposition of the electrolyte. In comparison, the lithium metal anode of MBGO20 cathode was observed to be smoother and flatter surface as displayed in Figure 5b. These results suggest that the MBGO20 cathode was able to effectively alleviate the dendrite growth on the surface of lithium anode and lithium polysulfide shuttling behavior.

We performed the lithium polysulfide confinement experiment under ambient conditions. For the test, a Li_2S_6 solution of red-brown color was prepared by mixing a 1:5 molar ratio of Li_2S and sulfur in DOL/DME solution (1:1, v/v). After adding the MBGO20 powder into the Li_2S_6 solution, the solution showed color fading. This result indicates that the MBGO20 was able to trap the lithium polysulfide through strong chemical and physical interactions. In order to further investigate the suppressed lithium polysulfide shuttling behavior for the MBGO20 cathode, XPS analysis was performed after 100 cycles. As shown in Figure 5c,d, the peaks related to Li^+TFSI^- electrolyte salt at 170–166 eV detected for both two cathodes in the S 2p spectra. However, the MBGO20 cathode clearly exhibited a series of distinct peaks corresponding to polysulfide (S_n^{2-}, 165–164 eV) and Li_2S/Li_2S_2 (164–160 eV), which indicated that a high degree of lithium polysulfide was anchored in the MBGO20 cathode [39]. We considered that the differences in lithium polysulfide shuttling behavior were closely related to the introduction of heteroatoms in the carbon materials. Possibly the electronegative nitrogen and sulfur containing moieties in the MBGO20 were able to offer efficient chemical interactions for the lithium polysulfide, with a lot of structural defects generated after heteroatoms doping providing an increase in physical adsorption sites for the lithium polysulfide. The XPS spectra of Li 1s and N 1s of MBGO20 cathode further demonstrated the alleviated lithium polysulfide shuttling behavior. As shown the Figure 5e, the Li 1s spectrum was deconvoluted into two peaks at 55.6 eV and 56.5 eV, which relates to the Li–S bond derived from lithium polysulfide and the Li–N bond from the interaction between the lithium polysulfide and nitrogen atom moieties [40]. In addition, the N 1s spectrum was divided into three peaks of pyridinic N (398.53 eV), pyrrolic N (399.42 eV), and graphitic N (400.82 eV) as presented in Figure 5f. Compared with the N 1s XPS spectra of Figure 2e, we observed a peak shift towards higher binding energy values for pyridinic N (+0.57 eV), pyrrolic N (+0.58), and graphitic N (+0.18 eV), due to the favorable polar interactions [41,42]. Therefore, the MBGO20 with active nitrogen and sulfur containing moieties was able to achieve the mitigated lithium polysulfide behavior, leading to the improved reactivation and reutilization of active materials, which in turn contributes to the enhanced electrochemical performances.

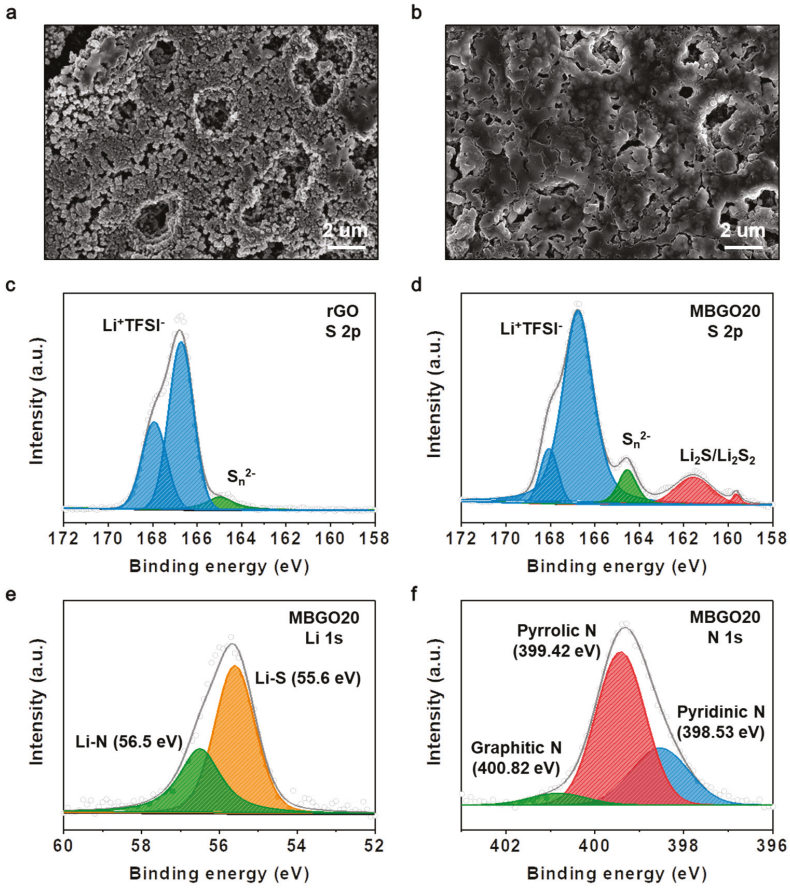

Figure 5. SEM images of the lithium metal anode surface of (**a**) rGO and (**b**) MBGO20 cathode after 100 cycles. High–resolution XPS spectra of (**c**) S 2p of rGO cathode and (**d**) S 2p, (**e**) Li 1s and (**f**) N 1s of MBGO20 cathode after cycling.

4. Conclusions

In summary, we rationally prepared a series of heteroatom-doped porous rGO to utilize as host materials for the sulfur cathode. A simple hydrothermal process of the methylene blue and graphene oxide simultaneously enabled the reduction of graphene oxide and the incorporation of N and S atoms into the carbon framework. The electronegative N, S–containing moieties of MBGOs were able to alleviate the polysulfide shuttling behavior through the combining effect of physical and chemical adsorptions, with promoting the redox reaction kinetics of lithium polysulfide intermediates. Thus, electrochemical investigation revealed that the sulfur cathode based on MBGO20 displayed the improved rate capability and cycling stability along with high along with high Columbic efficiency when compared to those with the rGO based cathode. This work provides an effective and facile method for the preparation of organic dye-derived carbon host materials for high performance Li–S batteries.

Supplementary Materials: The following are available online at https://www.mdpi.com/article/10.3390/nano11112954/s1, Figure S1: TGA thermograms of carbon composite and elemental sulfur, Figure S2: SEM images of (a) rGO, (b) MBGO5 and (c) MBGO10, Figure S3: XRD pattern of rGO sample, Figure S4: Equivalent circuit model of after cycling, Figure S5: Digital photo image of the

confined lithium polysulfides within MBGO20, Table S1: Elemental ratios of MBGOs with different methylene blue contents.

Author Contributions: E.K. conceived the research idea. E.K., K.K., J.-W.P., S.G.L., A.S.L. and J.H.L. wrote the main manuscript. T.L., H.J.S., E.K. and S.C. performed the experiments. All authors reviewed the manuscript. All authors have read and agreed to the published version of the manuscript.

Funding: This research was supported by the National Research Foundation of Korea (NRF) funded by the MSIT (Grant Numbers. NRF-2019R1G1A1100122 and NRF-2021R1A4A1022198). This work was supported by BK21 FOUR Program by Pusan National University Research Grant, 2020. In addition, this research was supported by Korea Electrotechnology Research Institute (KERI) (No.21A01016).

Institutional Review Board Statement: Not applicable.

Informed Consent Statement: Not applicable.

Data Availability Statement: The data presented in this study are available on request from the corresponding author.

Conflicts of Interest: The authors declare no conflict of interest.

References

1. Zeng, Z.; Li, W.; Wang, Q.; Liu, X. Programmed design of a lithium–sulfur battery cathode by integrating functional units. *Adv. Sci.* **2019**, *6*, 1900711. [CrossRef]
2. Yin, Y.X.; Xin, S.; Guo, Y.G.; Wan, L.J. Lithium–sulfur batteries: Electrochemistry, materials, and prospects. *Angew. Chem. Inter. Ed.* **2013**, *52*, 13186–13200. [CrossRef]
3. Eftekhari, A.; Kim, D.-W. Cathode materials for lithium–sulfur batteries: A practical perspective. *J. Mater. Chem. A* **2017**, *5*, 17734–17776. [CrossRef]
4. Song, M.-K.; Cairns, E.J.; Zhang, Y. Lithium/sulfur batteries with high specific energy: Old challenges and new opportunities. *Nanoscale* **2013**, *5*, 2186–2204. [CrossRef]
5. Son, Y.; Lee, J.S.; Son, Y.; Jang, J.H.; Cho, J. Recent advances in lithium sulfide cathode materials and their use in lithium sulfur batteries. *Adv. Energy Mater.* **2015**, *5*, 1500110. [CrossRef]
6. Rehman, S.; Khan, K.; Zhao, Y.; Hou, Y. Nanostructured cathode materials for lithium–sulfur batteries: Progress, challenges and perspectives. *J. Mater. Chem. A* **2017**, *5*, 3014–3038. [CrossRef]
7. Kim, H.; Lee, J.; Ahn, H.; Kim, O.; Park, M.J. Synthesis of three-dimensionally interconnected sulfur-rich polymers for cathode materials of high-rate lithium–sulfur batteries. *Nat. Commun.* **2015**, *6*, 7278. [CrossRef] [PubMed]
8. Li, G.; Sun, J.; Hou, W.; Jiang, S.; Huang, Y.; Geng, J. Three-dimensional porous carbon composites containing high sulfur nanoparticle content for high-performance lithium–sulfur batteries. *Nat. Commun.* **2016**, *7*, 10601. [CrossRef]
9. Guo, J.; Xu, Y.; Wang, C. Sulfur-impregnated disordered carbon nanotubes cathode for lithium–sulfur batteries. *Nano Lett.* **2011**, *11*, 4288–4294. [CrossRef] [PubMed]
10. Yang, X.; Zhang, L.; Zhang, F.; Huang, Y.; Chen, Y. Sulfur-infiltrated graphene-based layered porous carbon cathodes for high-performance lithium–sulfur batteries. *ACS Nano* **2014**, *8*, 5208–5215. [CrossRef] [PubMed]
11. Zhu, P.; Zhu, J.; Yan, C.; Dirican, M.; Zang, J.; Jia, H.; Li, Y.; Kiyak, Y.; Tan, H.; Zhang, X. In situ polymerization of nanostructured conductive polymer on 3D sulfur/carbon nanofiber composite network as cathode for high-performance lithium–sulfur batteries. *Adv. Mater. Interfaces* **2018**, *5*, 1701598. [CrossRef]
12. Li, Z.; Yuan, L.; Yi, Z.; Sun, Y.; Liu, Y.; Jiang, Y.; Shen, Y.; Xin, Y.; Zhang, Z.; Huang, Y. Insight into the electrode mechanism in lithium–sulfur batteries with ordered microporous carbon confined sulfur as the cathode. *Adv. Energy Mater.* **2014**, *4*, 1301473. [CrossRef]
13. Wang, X.; Zhang, S.; Zhang, H.; Gao, S.; Han, S.; Xu, Q.; Xu, J.; Lu, W.; Wu, X.; Chen, L. 3D porous spherical sulfur/carbon cathode materials with in situ vapor-phase polymerized polypyrrole coating layer for high-performance lithium–sulfur batteries. *ACS Sustain. Chem. Eng.* **2019**, *7*, 17491–17499. [CrossRef]
14. Peng, H.J.; Hou, T.Z.; Zhang, Q.; Huang, J.Q.; Cheng, X.B.; Guo, M.Q.; Yuan, Z.; He, L.Y.; Wei, F. Strongly coupled interfaces between a heterogeneous carbon host and a sulfur-containing guest for highly stable lithium–sulfur batteries: Mechanistic insight into capacity degradation. *Adv. Mater. Interfaces* **2014**, *1*, 1400227. [CrossRef]
15. Li, G.C.; Li, G.R.; Ye, S.H.; Gao, X.P. A polyaniline-coated sulfur/carbon composite with an enhanced high-rate capability as a cathode material for lithium/sulfur batteries. *Adv. Energy Mater.* **2012**, *2*, 1238–1245. [CrossRef]
16. Sun, Q.; Xi, B.; Li, J.Y.; Mao, H.; Ma, X.; Liang, J.; Feng, J.; Xiong, S. Nitrogen-Doped Graphene-Supported Mixed Transition-Metal Oxide Porous Particles to Confine Polysulfides for Lithium–Sulfur Batteries. *Adv. Energy Mater.* **2018**, *8*, 1800595. [CrossRef]
17. Sun, Z.; Zhang, J.; Yin, L.; Hu, G.; Fang, R.; Cheng, H.-M.; Li, F. Conductive porous vanadium nitride/graphene composite as chemical anchor of polysulfides for lithium–sulfur batteries. *Nat. commun.* **2017**, *8*, 14627. [CrossRef]

18. Razaq, R.; Sun, D.; Xin, Y.; Li, Q.; Huang, T.; Zhang, Z.; Huang, Y. Nanoparticle Assembled Mesoporous MoO_2 Microrods Derived from Metal Organic Framework and Wrapped with Graphene as the Sulfur Host for Long-Life Lithium–Sulfur Batteries. *Adv. Mater. Interfaces* **2019**, *6*, 1801636. [CrossRef]
19. Hou, T.Z.; Chen, X.; Peng, H.J.; Huang, J.Q.; Li, B.Q.; Zhang, Q.; Li, B. Design principles for heteroatom-doped nanocarbon to achieve strong anchoring of polysulfides for lithium–sulfur batteries. *Small* **2016**, *12*, 3283–3291. [CrossRef] [PubMed]
20. Zhou, G.; Zhao, Y.; Manthiram, A. Dual-confined flexible sulfur cathodes encapsulated in nitrogen-doped double-shelled hollow carbon spheres and wrapped with graphene for Li–S batteries. *Adv. Energy Mater.* **2015**, *5*, 1402263. [CrossRef]
21. Song, J.; Gordin, M.L.; Xu, T.; Chen, S.; Yu, Z.; Sohn, H.; Lu, J.; Ren, Y.; Duan, Y.; Wang, D. Strong lithium polysulfide chemisorption on electroactive sites of nitrogen-doped carbon composites for high-performance lithium–sulfur battery cathodes. *Angew. Chem. Inter. Ed.* **2015**, *127*, 4399–4403. [CrossRef]
22. Pang, Q.; Tang, J.; Huang, H.; Liang, X.; Hart, C.; Tam, K.C.; Nazar, L.F. A nitrogen and sulfur dual-doped carbon derived from polyrhodanine@ cellulose for advanced lithium–sulfur batteries. *Adv. Mater.* **2015**, *27*, 6021–6028. [CrossRef]
23. Chen, M.; Zhao, S.; Jiang, S.; Huang, C.; Wang, X.; Yang, Z.; Xiang, K.; Zhang, Y. Suppressing the polysulfide shuttle effect by heteroatom-doping for high-performance lithium–sulfur batteries. *ACS Sustain. Chem. Eng.* **2018**, *6*, 7545–7557. [CrossRef]
24. Ngidi, N.P.; Ollengo, M.A.; Nyamori, V.O. Effect of doping temperatures and nitrogen precursors on the physicochemical, optical, and electrical conductivity properties of nitrogen-doped reduced graphene oxide. *Materials* **2019**, *12*, 3376. [CrossRef] [PubMed]
25. Ma, Z.; Dou, S.; Shen, A.; Tao, L.; Dai, L.; Wang, S. Sulfur-Doped Graphene Derived from Cycled Lithium–Sulfur Batteries as a Metal-Free Electrocatalyst for the Oxygen Reduction Reaction. *Angew. Chem. Inter. Ed.* **2015**, *54*, 1888–1892. [CrossRef] [PubMed]
26. Sun, J.; Liu, Y.; Du, H.; He, S.; Liu, L.; Fu, Z.; Xie, L.; Ai, W.; Huang, W. Molecularly designed N, S co-doped carbon nanowalls decorated on graphene as a highly efficient sulfur reservoir for Li–S batteries: A supramolecular strategy. *J. Mater. Chem. A* **2020**, *8*, 5449–5457. [CrossRef]
27. Zhou, X.; Tian, J.; Wu, Q.; Hu, J.; Li, C. N/O dual-doped hollow carbon microspheres constructed by holey nanosheet shells as large-grain cathode host for high loading Li-S batteries. *Energy Storage Mater.* **2020**, *24*, 644–654. [CrossRef]
28. Qiu, Y.; Li, W.; Zhao, W.; Li, G.; Hou, Y.; Liu, M.; Zhou, L.; Ye, F.; Li, H.; Wei, Z. High-rate, ultralong cycle-life lithium/sulfur batteries enabled by nitrogen-doped graphene. *Nano Lett.* **2014**, *14*, 4821–4827. [CrossRef] [PubMed]
29. Zhu, J.; Tu, W.; Pan, H.; Zhang, H.; Liu, B.; Cheng, Y.; Deng, Z.; Zhang, H. Self-templating synthesis of hollow Co_3O_4 nanoparticles embedded in N, S-dual-doped reduced graphene oxide for lithium ion batteries. *ACS Nano* **2020**, *14*, 5780–5787. [CrossRef] [PubMed]
30. Ai, W.; Zhou, W.; Du, Z.; Chen, Y.; Sun, Z.; Wu, C.; Zou, C.; Li, C.; Huang, W.; Yu, T. Nitrogen and phosphorus codoped hierarchically porous carbon as an efficient sulfur host for Li-S batteries. *Energy Storage Mater.* **2017**, *6*, 112–118. [CrossRef]
31. Yao, W.; Zheng, W.; Xu, J.; Tian, C.; Han, K.; Sun, W.; Xiao, S. ZnS-SnS@ NC Heterostructure as robust lithiophilicity and sulfiphilicity mediator toward high-rate and long-life lithium–sulfur batteries. *ACS Nano* **2021**, *15*, 7114–7130. [CrossRef] [PubMed]
32. Kasnatscheew, J.; Evertz, M.; Streipert, B.; Wagner, R.; Klöpsch, R.; Vortmann, B.; Hahn, H.; Nowak, S.; Amereller, M.; Gentschev, A.-C. The truth about the 1st cycle Coulombic efficiency of $LiNi_{1/3}Co_{1/3}Mn_{1/3}O_2$ (NCM) cathodes. *Phys. Chem. Chem. Phys.* **2016**, *18*, 3956–3965. [CrossRef] [PubMed]
33. Lee, J.H.; Kang, J.; Kim, S.-W.; Halim, W.; Frey, M.W.; Joo, Y.L. Effective suppression of the polysulfide shuttle effect in lithium–sulfur batteries by implementing rGO–PEDOT: PSS-coated separators via air-controlled electrospray. *ACS Omega* **2018**, *3*, 16465–16471. [CrossRef] [PubMed]
34. Niu, S.; Lv, W.; Zhou, G.; He, Y.; Li, B.; Yang, Q.-H.; Kang, F. N and S co-doped porous carbon spheres prepared using l-cysteine as a dual functional agent for high-performance lithium–sulfur batteries. *Chem. Commun.* **2015**, *51*, 17720–17723. [CrossRef]
35. Lu, L.; Pei, F.; Abeln, T.; Pei, Y. Tailoring three-dimensional interconnected nanoporous graphene micro/nano-foams for lithium–sulfur batteries. *Carbon* **2020**, *157*, 437–447. [CrossRef]
36. Chen, S.; Ming, Y.; Tan, B.; Chen, S. Carbon-free sulfur-based composite cathode for advanced Lithium–Sulfur batteries: A case study of hierarchical structured $CoMn_2O_4$ hollow microspheres as sulfur immobilizer. *Electrochim. Acta* **2020**, *329*, 135128. [CrossRef]
37. Li, M.; Zhou, X.; Ma, X.; Chen, L.; Zhang, D.; Xu, S.; Duan, D.; Chen, C.; Yuan, Q.; Liu, S. Development of sulfonated-carbon nanotubes/graphene three-dimensional conductive spongy framework with ion-selective effect as cathode in high-performance lithium–sulfur batteries. *Chem. Eng. J.* **2021**, *409*, 128164. [CrossRef]
38. Zhang, F.; Li, Z.; Cao, T.; Qin, K.; Xu, Q.; Liu, H.; Xia, Y. Multishelled Ni_2P microspheres as multifunctional sulfur host 3D-printed cathode materials ensuring high areal capacity of lithium–sulfur datteries. *ACS Sustain. Chem. Eng.* **2021**, *9*, 6097–6106. [CrossRef]
39. Wang, X.; Gao, T.; Han, F.; Ma, Z.; Zhang, Z.; Li, J.; Wang, C. Stabilizing high sulfur loading Li–S batteries by chemisorption of polysulfide on three-dimensional current collector. *Nano Energy* **2016**, *30*, 700–708. [CrossRef]
40. Su, D.; Cortie, M.; Wang, G. Fabrication of N-doped graphene–carbon nanotube hybrids from Prussian blue for lithium–sulfur batteries. *Adv. Energy Mater.* **2017**, *7*, 1602014. [CrossRef]
41. Bao, W.; Liu, L.; Wang, C.; Choi, S.; Wang, D.; Wang, G. Facile synthesis of crumpled nitrogen-doped mxene nanosheets as a new sulfur host for lithium–sulfur batteries. *Adv. Energy Mater.* **2018**, *8*, 1702485. [CrossRef]
42. Kim, E.; Kim, J.; Lee, T.; Kang, H.; Yu, S.; Park, J.W.; Lee, S.G.; Li, O.L.; Lee, J.H. Plasma-engineered organic dyes as efficient polysulfide-mediating layers for high performance lithium–sulfur batteries. *Chem. Eng. J.* **2021**, *430*, 132679. [CrossRef]

nanomaterials

MDPI

Review

Recent Development in Vanadium Pentoxide and Carbon Hybrid Active Materials for Energy Storage Devices

Andrew Kim [1], Golap Kalita [2], Jong Hak Kim [3,*] and Rajkumar Patel [4,*]

[1] Department of Chemical Engineering, The Cooper Union for the Advancement of Science and Art, New York, NY 10003, USA; kim70@cooper.edu
[2] Department of Physical Science and Engineering, Nagoya Institute of Technology, Gokiso-Cho, Showa-ku, Nagoya 466-8555, Japan; golapkalita@gmail.com
[3] Department of Chemical and Biomolecular Engineering, Yonsei University, 50, Yonsei-ro, Seodaemun-gu, Seoul 03722, Korea
[4] Energy & Environmental Science and Engineering (EESE), Integrated Science and Engineering Division (ISED), Underwood International College, Yonsei University, 85 Songdogwahak-ro, Yeonsugu, Incheon 21983, Korea
* Correspondence: jonghak@yonsei.ac.kr (J.H.K.); rajkumar@yonsei.ac.kr (R.P.)

Abstract: With the increasing energy demand for portable electronics, electric vehicles, and green energy storage solutions, the development of high-performance supercapacitors has been at the forefront of energy storage and conversion research. In the past decade, many scientific publications have been dedicated to designing hybrid electrode materials composed of vanadium pentoxide (V_2O_5) and carbon nanomaterials to bridge the gap in energy and power of traditional batteries and capacitors. V_2O_5 is a promising electrode material owing to its natural abundance, nontoxicity, and high capacitive potential. However, bulk V_2O_5 is limited by poor conductivity, low porosity, and dissolution during charge/discharge cycles. To overcome the limitations of V_2O_5, many researchers have incorporated common carbon nanostructures such as reduced graphene oxides, carbon nanotubes, carbon nanofibers, and other carbon moieties into V_2O_5. The carbon components facilitate electron mobility and act as porous templates for V_2O_5 nucleation with an enhanced surface area as well as interconnected surface morphology and structural stability. This review discusses the development of various V_2O_5/carbon hybrid materials, focusing on the effects of different synthesis methods, V_2O_5/carbon compositions, and physical treatment strategies on the structure and electrochemical performance of the composite material as promising supercapacitor electrodes.

Keywords: electrochemical energy storage; supercapacitor; vanadium pentoxide; carbon nanocomposite

Citation: Kim, A.; Kalita, G.; Kim, J.H.; Patel, R. Recent Development in Vanadium Pentoxide and Carbon Hybrid Active Materials for Energy Storage Devices. *Nanomaterials* **2021**, *11*, 3213. https://doi.org/10.3390/nano11123213

Academic Editors: Marc Cretin, Sophie Tingry and Zhenghua Tang

Received: 4 November 2021
Accepted: 24 November 2021
Published: 26 November 2021

1. Introduction

The demand for improved energy storage devices has increased due to the rapid development of portable electronics, electric vehicles, and green energy storage devices [1]. Supercapacitors are promising replacements for traditional energy storage devices such as batteries and capacitors with high energy and power densities, respectively, because supercapacitors can be fabricated using readily accessible materials with outstanding cyclability and can provide a balance of both high power and energy densities (Figure 1) [2–5]. The two main classifications of supercapacitors are electric double-layer capacitors (EDLCs) and pseudocapacitors (faradic supercapacitors) [6,7]. EDLCs produce a charge separation at the boundary between the electrode and electrolyte to store energy [8]. In contrast, pseudocapacitors rely on fast faradic reactions at the electrode surface to store energy [9]. Depending on the electrode material, supercapacitors primarily exhibit electric double-layer (EDL) or pseudocapacitive characteristics or a combination of both.

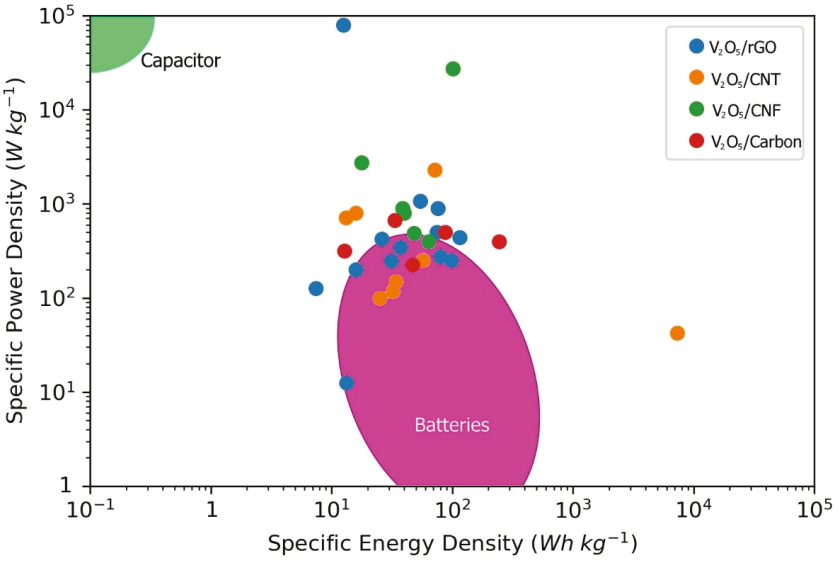

Figure 1. Ragone plot showing the energy and power density ranges of common electrochemical energy storage devices such as capacitors, supercapacitors, and batteries.

Transition metal oxide/carbon hybrid materials have recently attracted considerable attention as composites with easily controllable pseudocapacitive and EDL characteristics. Transition metal oxides such as vanadium pentoxide (V_2O_5) are pseudocapacitive, yielding supercapacitors with high specific capacitances (C_{sp}) and energy densities [10]. However, V_2O_5 is limited by poor conductivity, low power density, and minimal cyclic stability [11]. In contrast, carbon nanostructures, such as reduced graphene oxide (rGO), carbon nanotubes (CNTs), and carbon nanofibers (CNFs), show dominant EDL characteristics, resulting in highly stable and power-dense supercapacitors. However, carbon-based materials suffer from low specific capacitances and energy densities [12]. Transition metal oxide/carbon composite materials supplement the high energy potential of transition metal oxides with the high power potential and stability of carbon nanostructures [13–15]. These composite materials will be essential to meet the demand for fast-charging portable electronics, long-lasting electric vehicles, and environmentally friendly energy storage devices.

V_2O_5 has attracted significant attention as a transition metal oxide with multiple oxidation states (II–V), enabling a high maximum theoretical capacitance of 2120 F g^{-1} [16]. With a wide effective potential window, V_2O_5 can provide a high theoretical energy density [17]. Additionally, owing to its natural abundance and low toxicity, V_2O_5 is a low-cost material that is ideal for mass production [18,19]. The crystal structure of V_2O_5 allows electrolyte ions such as Li^+ to reversibly intercalate/de-intercalate, thereby improving the faradic reactivity with the electrolyte [20,21]. However, bulk V_2O_5 is limited by poor electrical conductivity, slow reaction kinetics, and vanadium dissolution [22,23]. To improve the properties of bulk V_2O_5, the bulk crystal nanostructure has been converted into nanorods [24], nanotubes [25], nanosheets [26], nanobelts [27], and other porous nanostructures [28]. These nanostructures allow better reaction kinetics with shorter diffusion pathways than those observed in the bulk crystal structure, and they improve cyclability with less strain on the crystal structure during ion intercalation/de-intercalation. However, these V_2O_5 materials still have drawbacks, such as low electrical conductivity [29,30].

Recent developments in improving V_2O_5 supercapacitor materials involve the addition of carbon nanomaterials, such as graphene [31], rGO [32], CNTs [33], and activated carbon (AC) [34], to improve the conductivity and structural stability of V_2O_5. Carbon materials are ideal sources of EDL capacitance for efficient supercapacitors, owing to high

porosities, conductivities, and natural abundances [35,36]. Highly porous carbon materials have large surface areas, resulting in more active sites on the electrode material [37]. Increased porosity allows fast ion intercalation/de-intercalation with short ion diffusion pathways [38]. The large surface area improves the interfacial contact between the electroactive material and the current collector, resulting in more efficient electron transfer. Moreover, the carbon content improves the overall conductivity of the electrode, increasing the specific capacitance and decreasing the energy losses during charge/discharge [39].

Despite the recent developments in V_2O_5/carbon composites, many review articles on supercapacitor electrode materials only briefly discuss V_2O_5 materials as part of a broader review of transition metal oxide [40–45] or carbon-based supercapacitors [46–48]. V_2O_5/carbon hybrid materials are promising materials that have been the focus of recent research, so it is essential to organize the most up-to-date information on factors affecting the performances of V_2O_5/carbon composite electrodes. This review describes the physical and electrochemical characteristics of different V_2O_5/carbon nanostructures, including V_2O_5/rGO, V_2O_5/CNTs, V_2O_5/CNFs, and other V_2O_5/carbon hybrid materials. This review focuses on the effects of different synthesis methods, carbon to V_2O_5 ratios, and physical treatment procedures on the structures and performances of V_2O and carbon hybrid nanomaterials.

2. V_2O_5/rGO

rGOs have been extensively investigated as additive materials for V_2O_5 composites because of their large surface areas, high conductivities, and good stabilities [49]. Similar to pristine graphene (sometimes reported in the literature as graphene), rGO is a monolayer of sp^2 hybridized carbon atoms arranged in a hexagonal lattice [50,51]. However, unlike pure graphene, rGO contains varying degrees of defects caused by functional groups such as hydroxyl and carbonyl groups remaining after the reduction of highly functionalized graphene oxide (GO) [52]. Various factors involved in the fabrication of a V_2O_5/rGO (VrG) electrode affect its electrochemical performance by altering the morphology and crystalline structure of the hybrid material. VrG composites are versatile materials that often possess a lamellar structure with high porosity and surface area. The effects of different synthesis pathways, V_2O_5/carbon compositions, and physical treatment conditions were closely examined for their impact on the nanostructures and the resulting capacitive performances of the VrG electrodes. The morphology and electrochemical performances of V_2O_5/rGO electrodes for supercapacitor applications reported in the literature are summarized in Table 1.

2.1. Effects of Synthesis Method

Many synthesis strategies for the fabrication of VrG composites include a hydro/solvothermal method. Typically, a mixture of V_2O_5 precursors such as vanadium oxytriisopropoxide (VTIP), rGO precursors such as GO, and water or other solvents are heated at high temperatures and pressures for extended periods in a Teflon-lined stainless steel autoclave [53]. The hydro/solvothermal procedure is frequently used because it is facile and allows the formation of diverse V_2O_5 morphologies on the 2D rGO substrate. Pandey et al. synthesized V_2O_5 nanospheres anchored to thin rGO sheets via a hydrothermal synthesis route. A uniform dispersion of VTIP, GO, isopropyl alcohol, and DI water was heated at 180 °C in an autoclave for 18 h, yielding a mesoporous VrG composite material [54]. The resulting material had a layered structure with large V_2O_5 nanospheres intercalated into the rGO layers. The vanadium crystals had an organized orthorhombic crystal structure that promoted deep ion adsorption. The lamellar structure of rGO increased the surface area for additional surface redox reactions and porosity for abundant electrolyte ion intercalation/de-intercalation. In a symmetric, two-electrode configuration with the VrG working electrodes, the composite exhibited a large maximum C_{sp} of 448 F g^{-1} at a current density of 0.75 A g^{-1} that decreased slightly to 296 F g^{-1} at a significantly higher current density of 15.5 A g^{-1}. The excellent rate capability was due to the low charge

transfer resistance (0.6 Ω), which was enabled by the strong bonds formed between the intercalated V_2O_5 nanospheres and conductive rGO sheets.

Table 1. V_2O_5 morphology and electrochemical performances of V_2O_5/reduced graphene oxide composite electrodes for supercapacitor applications.

Morphology	Maximum C_{sp} (F g^{-1})	Cycling C_{sp} Retention (%)	Cycle Number	Energy Density (Wh kg^{-1})	Power Density (W kg^{-1})
Nanowires	579	79	5000	-	-
Nanowires	710	95	20,000	98.6	250
Nanosheets	635	94 *	3000 *	75.9	900
Nanostrips	309	95.2	10,000	475	-
Amorphous	178.5	85	8000	13.3	12.5
Nanoflowers	1235	92	5000	116	440
Nanoribbons	-	720	500	16	200
Nanorods	37.2	90 *	1000 *	54.2	1075.9
Amorphous	484	83	1000	7.4	127
Amorphous	226	92	5000	12.5	79,900
Nanobelts	128.8	82	5000	-	-
Nanobelts	310.1	90.2 *	5000 *	31.3	249.7
Nanofibers	218	87 *	700 *	37.2	345
Nanowires	272	80	1000	26.22	425
Nanorods	537	84	1000	74.58	500
Nanospheres	386	-	-	80.4	275

* Cycling performance was determined using a two-electrode configuration.

The hydro/solvothermal synthesis route can also yield V_2O_5 nanowires. Ahirrao et al. followed a similar hydrothermal process with ammonium metavanadate (NH_4VO_3) to yield a similar lamellar rGO structure with intercalated V_2O_5 nanowires [55]. First, NH_4VO_3 was calcinated into V_2O_5, and the V_2O_5 powder was then sonicated with GO in DI water and heated at 180 °C for two days in an autoclave. The hydrothermal processes yielded thin nanowires with lengths ranging from 100 nm to several micrometers anchored to the rGO layers. The nanowire morphology increased the surface area of V_2O_5 for more active sites and decreased the ion diffusion pathways. The VrG composite was drop-cast onto carbon paper to yield a supercapacitor electrode. The VrG electrode exhibited a maximum C_{sp} of 1002 F g^{-1} at a current density of 1 A g^{-1}. Because of its low charge transfer resistance (0.53 Ω), the composite exhibited good rate capability, as indicated by the high C_{sp} of 828 F g^{-1} at a high current density of 3 A g^{-1}. Similarly, Geng et al. synthesized thin V_2O_5 nanowires anchored to curly rGO sheets using a hydrothermal process [56]. As the hydro/solvothermal process often yields a VrG composite powder, it is combined with a conducting filler and polymer binder and coated onto a current collector for use as an electrode. The VrG material was combined with Super P carbon (conducting filler), polyvinylidene fluoride (PVDF) (polymer binder), and N-methyl-2-pyrrolidone (NMP) (solvent) in an 8:1:1 ratio. The resulting slurry was coated onto Ni foam, vacuum dried, and compressed into a thin sheet. Unlike a 2D metal foil current collector, Ni foam provided a 3D macroporous network for large volumes of electrolyte diffusion. Anchoring the VrG material to the porous foam increased the surface area for more active redox sites. The electrochemical performance of the VrG hybrid material was tested in a three-electrode configuration with a VrG working electrode, Pt counter electrode, and Ag/AgCl reference electrode in 1 M KCl electrolyte. The Ni foam-based VrG electrode exhibited a high C_{sp} of 579 F g^{-1} at a current density of 1 A g^{-1}. Despite the lower conductivity than that of Cu, the relatively high conductivity and larger pore size of Ni foam enabled good rate capability, as indicated by a large C_{sp} of 534 F g^{-1} at a high current density of 4 A g^{-1}. Because of its rigid and porous structure, the VrG material was less susceptible to mechanical strain arising from electrolyte intercalation/de-intercalation, resulting in a high C_{sp} retention of 79% after 5000 cycles at a current density of 4 A g^{-1}. Sun et al. found that the duration of the hydro/solvothermal reaction affected the growth of V_2O_5 nanowires on rGO sheets [57].

V_2O_5 was modified with the N-doped rGO (N-rGO) aerogel via solvothermal synthesis in an autoclave at 160 °C for different durations. The composite was then freeze-dried to yield a marshmallow-shaped, free-standing VrG electrode. Tiny hair-like V_2O_5 nanowires were vertically anchored on the surfaces of the amorphous N-rGO sheets (Figure 2).

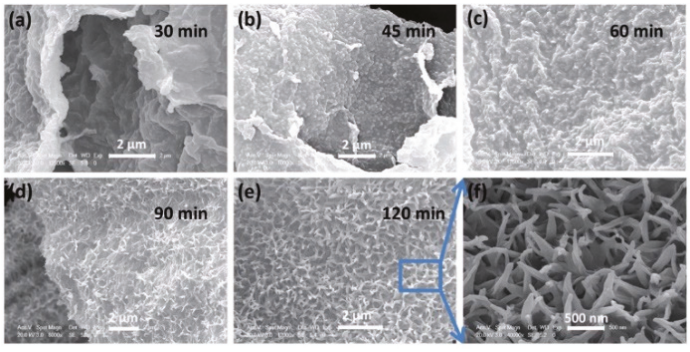

Figure 2. SEM images of N-doped rGO anchored to vertically aligned V_2O_5 nanowires after solvothermal synthesis for (**a**) 30, (**b**) 45, (**c**) 60, (**d**) 90, and (**e**) 120 min. (**f**) Magnified SEM image of the N-doped VrG after solvothermal reaction for 120 min. Reprinted with permission from Ref. [57]. Copyright 2018 Royal Society of Chemistry.

A short reaction time of 30 min between V_2O_5 and rGO resulted in a smooth rGO surface without many V_2O_5 nanowire growths (Figure 2a). After 45 to 60 min, larger V_2O_5 nanowires were obtained (Figure 2b,c), suggesting additional V_2O_5 nucleation and growth. Prolonged reactions for 90 to 120 min resulted in long, vertical V_2O_5 crystal growths uniformly spread on the rGO surface (Figure 2d,e). A magnified view of the V_2O_5 coated surface (Figure 2f) showed the porosity of vertically grown V_2O_5 nanowires. The mesoporous network of N-rGO sheets combined with the nanowire extrusions resulted in a large BET surface area of 416 $m^2\ g^{-1}$, which allowed fast ion diffusion and increased the number of active sites for surface reactions. The porous VrG electrode exhibited an excellent C_{sp} of 710 F g^{-1} at a current density of 0.5 A g^{-1}. The nitrogen defects in the rGO frame lowered the charge transfer resistance of the electrode from 1.54 to 1.11 Ω, resulting in improved rate capability, indicated by a high C_{sp} of 360 F g^{-1} at a large current density of 10 A g^{-1}. As the nitrogen groups in rGO were more reactive than carbon, N-rGO contained more V_2O_5 nucleation sites than bare rGO, resulting in denser distributions of V_2O_5 nanowires throughout the N-rGO-based composite. The V_2O_5/N-rGO material exhibited excellent cyclic stability with 95% C_{sp} retention after 20,000 cycles at a high current density of 10 A g^{-1}.

In addition to nanospheres and nanowires, the hydrothermal process can yield more sheet-like V_2O_5 morphologies anchored to rGO. Nagaraju et al. synthesized a VrG composite with V_2O_5 and rGO nanosheets via a hydrothermal method to obtain a lamellar composite structure [58]. V_2O_5 had a pure orthorhombic crystal structure that allowed good ion diffusion. The layered structure of the V_2O_5 and rGO nanosheets resulted in a large surface area of 36.2 $m^2\ g^{-1}$, which was four times larger than that of bulk V_2O_5. The VrG material exhibited both EDL and pseudocapacitive characteristics because of the even composition of V_2O_5 and rGO. The porosity and crystallinity enhanced the pseudocapacitive capability to a maximum C_{sp} of 635 F g^{-1} at a current density of 1 A g^{-1}. Even at a high current density of 30 A g^{-1}, the composite exhibited a large 240 F g^{-1} C_{sp}, highlighting the layered composite's potential for high-energy and high-power applications. An asymmetric supercapacitor with the VrG electrode exhibited an energy density of 75.9 Wh kg^{-1} with a power density of 900 W kg^{-1}. Sahu et al. used a hydrothermal method to synthesize V_2O_5 nanostrips anchored to rGO nanoribbon [59]. The V_2O_5 nanostrips shrank during the hydrothermal reaction with rGO as the rGO template inhibited large V_2O_5 growth. The

retention of small V_2O_5 crystals doubled the surface area to 15.6 m^2 g^{-1}, thereby increasing the efficiencies of surface redox reactions. The composite material had high mesoporosity, facilitating the fast diffusion of electrolytes through the ion channels. Thus, the C_{sp} of the composite (309 F g^{-1}) was approximately five times greater than that of bulk V_2O_5 nanostrips. The VrG material had a low equivalent series resistance and charge transfer resistance of 4.6 and 1.2 Ω, respectively, which provided good rate capability, indicated by the relatively high 114 F g^{-1} C_{sp} at a high scan rate of 100 mV s^{-1}. A solid-state electrode comprising the VrG composite exhibited a high conductivity of 1.4×10^{-2} S m^{-1}, which minimized the energy loss as heat. A symmetric VrG electrode supercapacitor had an energy density of 42.09 Wh kg^{-1} at a power density of 475 W kg^{-1}, which decreased to 13.44 Wh kg^{-1} at a power density of 8400 W kg^{-1}.

The facile hydrothermal method can also alter the large sheet-like structure of rGO. Zhang et al. employed a hydrothermal and freeze-drying procedure to fabricate a VrG hydrogel with thin rGO strips instead of large sheets [60]. The outer appearance of the hydrogel constituted a marshmallow-like macrostructure. The rGO strips were laced together to form a macroporous 3D structure. The V_2O_5 nanobelts were uniformly intercalated in the web-like rGO architecture. The VrG electrode with 64 wt% V_2O_5 exhibited a large C_{sp} of 320 F g^{-1} at a current density of 1.0 A g^{-1}. In a symmetric supercapacitor setup, VrG retained 70% of its initial C_{sp} after 1000 cycles at a current density of 1 A g^{-1}.

An alternative to the versatile hydrothermal process is the sol-gel method, which is a low-cost synthesis strategy that involves the formation of a V_2O_5 sol that is converted into a gel via hydrolysis and condensation reactions. The resulting porous V_2O_5 xerogel can be used as a free-standing, binderless material used directly as a supercapacitor electrode [61]. Yilmaz et al. utilized the sol-gel synthesis route to fabricate free-standing VrG electrodes [62]. The V_2O_5 gel was first synthesized via a hydrothermal process involving V_2O_5 powder and H_2O_2. The V_2O_5 gel, GO, and thiourea (cross-linking agent) were reacted for two weeks in a cylindrical glass vial. The resulting VrG aerogel was washed with ethanol, freeze-dried, and annealed at 300 °C in air. The highly porous composite had a large BET surface area of 83.4 g m^2 because of the lamellar rGO sheet structure with V_2O_5 nanoribbons anchored to the rGO surface. The addition of thiourea increased the chemical grafting between rGO and V_2O_5 by functioning as a redox couple, temporarily reducing V^{5+} to V^{4+} to initiate the polymerization between rGO and V_2O_5. The reduced V^{4+} was subsequently oxidized to V^{5+} during the final annealing step, yielding a hydrated orthorhombic V_2O_5 crystal structure. The symmetric supercapacitor with the thiourea-doped VrG electrodes exhibited a C_{sp} of 484.9 F g^{-1} at a current density of 0.6 A g^{-1}, which was twice that of a thiourea-less VrG. Using thiourea during the synthesis also resulted in sulfur and nitrogen functionalization of rGO. The functional groups decreased the equivalent series resistance to 1.6 Ω, resulting in good rate capability with a high C_{sp} of ~300 F g^{-1} at a high current density of 10 A g^{-1}. The mesoporous structure allowed high ion adsorption and decreased the mechanical strain during rapid ion intercalation/de-intercalation, resulting in a high C_{sp} retention of 80% after 10,000 cycles at a high current density of 5 A g^{-1}. A symmetric capacitor with the VrG xerogel electrodes possessed an energy density of 43.0 Wh kg^{-1} at a power density of 480 W kg^{-1}, which decreased to 24.2 Wh kg^{-1} at a power density of 9300 W kg^{-1}. Kiruthiga et al. also used the sol-gel method to synthesize V_2O_5 nanorods anchored to rGO sheets [63]. A V_2O_5 sol was prepared by reacting ammonium metavanadate with citric acid, and the sol was heated to form a gel that was subsequently heated at 450 °C in air to produce V_2O_5 powder. V_2O_5 was subsequently intercalated into the rGO sheets via sonication in DI water. The VrG composite exhibited a C_{sp} of 224 F g^{-1} at a current density of 0.01 A g^{-1} with a high C_{sp} retention of 85% after 1000 cycles at a current density of 0.06 A g^{-1}. An asymmetric Na-ion supercapacitor with a VrG anode and an AC cathode exhibited a maximum C_{sp} of 62 F g^{-1} at a current density of 0.01 A g^{-1} with 74% C_{sp} retention after 1000 cycles at a current density of 0.06 A g^{-1}. The supercapacitor produced a maximum energy density of 65 Wh kg^{-1} at a power density of 72 W kg^{-1} and a current density of 0.03 A g^{-1}.

Another method of synthesizing a VrG composite involves the filtration of an rGO and V_2O_5 suspension through a membrane. Unlike the hydrothermal method, the filtration process produces a stable and binderless thin-film electrode material. Wang et al. synthesized a VrG composite via the filtration of a solution of poly(3,4-ethylenedioxythiophene) (PEDOT), a conducting polymer, V_2O_5, and rGO through a cellulose acetate membrane [64]. The resulting binderless VrG thin film was then roll pressed onto various substrates such as ITO glass and Al to yield a substrate/PEDOT/VrG electrode. During synthesis, the V_2O_5 crystals were recrystallized into thin nanobelts coated evenly with PEDOT without the intercalation of the 3,4-ethylenedioxythiophene (EDOT) monomer into the V_2O_5 lattice. PEDOT acted as a bridge between V_2O_5 and rGO through π–π conjugation, such that V_2O_5 did not interact directly with rGO. These strong bonds allowed the composite material to form a stable film structure that was easily transferred to and compressed onto different substrates without a binder between the substrate and composite material. Figure 3a shows the procedure for transferring the thin-film hybrid material. A facile electrode fabrication procedure was applied to various substrates such as ITO, plastic, and glass. The VrG material exhibited smooth surface adhesion and good optical transparency for all tested substrates (Figure 3b,c). A large thin-film electrode with a diameter of 170 mm was easily fabricated (Figure 3d) and placed in an array (Figure 3e), demonstrating the viability of this fabrication strategy for scale-up. When placed on an Ag/PET current collector, the PEDOT/VrG electrode yielded an areal capacitance of 22.4 mF cm^{-2} at a current density of 0.7 A m^{-2}. A lack of binder between the substrate and PEDOT/VrG enabled direct contact between the conductive Ag substrate and composite material, increasing the overall electrochemical performance. The PEDOT coating on V_2O_5 reduced the dissolution of V_2O_5, resulting in a high capacitance retention of 98% after 150,000 cycles. Moreover, the outer rGO layer trapped the vanadium ions within the composite structure for maximum vanadium retention. A symmetric supercapacitor yielded a high C_{sp} retention of 92.4% after 50,000 cycles with a maximum energy density of 1800 Wh m^{-2} at a power density of 110,000 W m^{-2}. Similarly, Liu et al. synthesized a stable V_2O_5/rGO composite electrode via vacuum filtration through a cellulose acetate membrane [65]. A thin VrG film was fabricated by first preparing a lytropic liquid crystal suspension of rGO and V_2O_5 in DI water. The lamellar phase suspension was filtered through the cellulose membrane, yielding a VrG thin film that could withstand a maximum pressure of 120 MPa. With a 67 wt% V_2O_5, the thin film possessed a maximum C_{sp} of 205 F g^{-1} at a current density of 1 A g^{-1}. The electrode exhibited excellent rate capability by retaining more than 50% of its initial C_{sp} at a high current density of 50 A g^{-1}. The electrode retained 94% of its C_{sp} after 3000 cycles at a current density of 10 A g^{-1}. An added advantage of thin-film VrG materials is their high flexibility. Foo et al. utilized vacuum filtration through a nitrocellulose filter to synthesize a flexible VrG composite [66]. The VrG was peeled from the filter, heated in an autoclave with hydrazine monohydrate, dried, and acid-treated to yield a flexible, binderless VrG electrode. The hydrazine exfoliated the VrG into layers with an average spacing of 30 μm. Small amorphous V_2O_5 crystals were embedded on the surface of planar rGO layers. The thin-film material possessed a large Young's modulus of 1.7 GPa and tensile strength of 6.1 MPa and could be repeatedly bent and unbent around a test tube with no sign of permanent deformation. The flexible electrode material exhibited a C_{sp} of 178.5 F g^{-1} at a current density of 0.05 A g^{-1}. The hybrid thin film had a moderate rate capability due to a low equivalent series resistance of 3.36 Ω, resulting in a C_{sp} of 129.7 F g^{-1} at twice the current density. An asymmetric supercapacitor with a flexible VrG anode had maximum energy densities of 13.3 Wh kg^{-1} (unbent) and 13.6 Wh kg^{-1} (bent) at a power density of 12.5 W kg^{-1}.

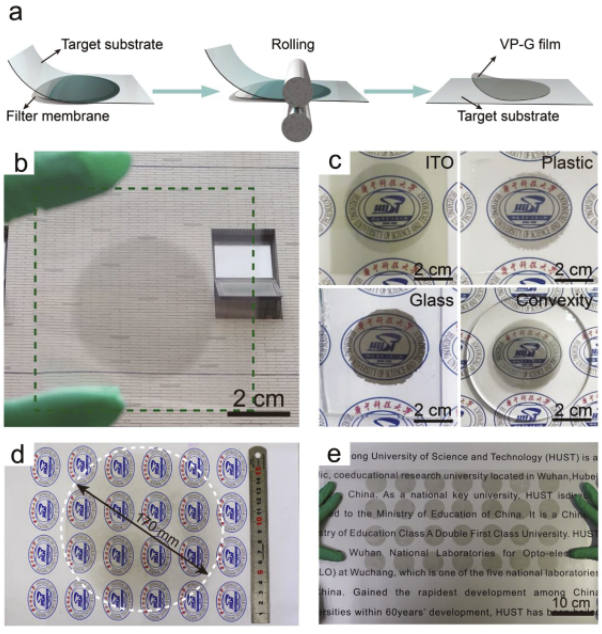

Figure 3. (**a**) Illustration of the transfer of the VrG film onto a substrate via a rolling process. Digital photographs of (**b**) transparent VrG films with a thickness of 22 nm, (**c**) transparent VrG on ITO, plastic, and glass with good convexity, and (**d**) a large VrG disc pressed on a substrate. (**e**) Digital photograph of a 7 × 4 array of the large-scale VrG films. Reprinted with permission from Ref. [64]. Copyright 2020 Elsevier.

Chemical deposition is a facile strategy for synthesizing a VrG composite directly on a conductive substrate. Different deposition techniques allow the composite material to bind to a well-structured, porous 3D network for structural stability and maximum porosity without the need for insulative additives or binders. Van Hoa et al. utilized chemical vapor deposition (CVD) to fabricate a free-standing graphene/V_2O_5 composite with a Ni foam template [67]. First, graphene was deposited on a Ni foam template using CVD, yielding a porous macrostructure with smooth graphene plates. Subsequently, V_2O_5 was deposited on the graphene/Ni foam substrate via a solvothermal method in an oxalic acid solution. The Ni foam was covered with uneven graphene plates after the initial CVD, increasing the surface area of the template. Small V_2O_5 nanoflowers were uniformly packed on the graphene surface. The flower-like nanostructures were intricately connected ultrathin V_2O_5 nanosheets with a highly orthorhombic crystal phase. The nanoflower extrusions on the porous graphene/Ni foam template further increased the BET surface area to 49.4 m^2 g^{-1} for increased redox reactions. As V_2O_5 was synthesized directly on the graphene/Ni foam template, there was no binder material to reduce the number of active sites. The electrode exhibited one of the highest reported C_{sp} values of 1235 F g^{-1} at a current density of 2 A g^{-1}. The direct contact between graphene and Ni foam resulted in high conductivity throughout the electrode material, resulting in a slight decrease in C_{sp} to 800 F g^{-1}, even at a large current density of 20 A g^{-1}. The large capacitance was due to the high specific surface area provided by the porous template and gaps between the petal-like V_2O_5. The composite electrode retained 92% of its C_{sp} after 5000 cycles at a high current density of 4 A g^{-1}, indicating good reversibility because of stable chemical bonding and enhanced conductivity. The energy density was 116 Wh kg^{-1} at a power density of 440 W kg^{-1}, which decreased to ~330 Wh kg^{-1} at a power density of ~3500 W kg^{-1}. Wang et al. employed a similar synthesis strategy to fabricate a Ni foam-based V_2O_5/rGO electrode [68]. HCl

and $FeCl_3$ were used to etch the Ni foam before graphene CVD to ensure strong, more homogeneously spread bonding. V_2O_5 was then synthesized directly on the rGO/Ni foam substrate via a solvothermal method in an ethanol solution, resulting in long V_2O_5 nanoribbons that were several micrometers in length. V_2O_5 was not completely oxidized and possessed a monoclinic crystal phase, while rGO showed a dominant graphitic crystal phase. The areal capacitance of the free-standing electrode was 822 mF cm^{-2} at a current density of 1 mA cm^{-2}. An asymmetric supercapacitor composed of a VG cathode had an energy density of 16 Wh kg^{-1} at a power density of 200 W kg^{-1}. Using chemical bath deposition (CBD) instead of CVD, Korkmaz et al. synthesized a binder-free, thin-film VrG [69]. Glass (G), poly(methyl methacrylate) (PMMA) (P), fluorine-doped tin oxide (FTO) glass (F), and indium tin oxide (ITO) glass (I) substrates were added to a solution of GO, $NaVO_3$, galactic acid, and methanol, and reacted for 24 h at ambient temperature. The coated substrate materials were removed via chemical blanket removal. The texture of the film surface differed for each substrate, showing spherical structures of different sizes for VrG-G, a smooth and homogeneous structure for VrG-P, a dense and grainy structure for VrG-F, and dispersed agglomerations for VrG-I. The crystallinity also changed depending on the substrate with amorphous, orthorhombic crystal growth observed in VrG-G and VrG-P, but well-oriented orthorhombic crystal growth in VrG-F and VrG-I. The thickness of the VrG film was also different, with values of 1025, 988, 689, and 393 nm for VrG-G, VrG-P, VrG-F, and VrG-I, respectively. Despite containing a thin V_2O_5 layer for limited pseudocapacitance potential, VrG-F exhibited the largest C_{sp} of 949.6 F g^{-1} owing to its organized crystalline structure.

Different synthesis strategies such as hydro/solvothermal, sol-gel, filtration, and chemical deposition methods are available for the preparation of VrG composites with varying V_2O_5 and rGO morphologies. The hydrothermal method is frequently used as a facile and versatile means of embedding V_2O_5 nanospheres, nanowires, nanorods, and nanosheets onto lamellar rGO sheets. The product is typically a VrG powder that must be combined with a conductive filler and binder for use as an electrode. The sol-gel method is an alternate process that yields a porous gel instead of a powder that can be directly applied as a supercapacitor electrode. The filtration method yields a thin-film, binderless electrode that can be physically transferred to different substrates such as ITO and plastic. Chemical deposition techniques such as CVD and CBD also allow the direct growth of V_2O_5 on porous and conductive substrates such as Ni foam and ITO for improved conductivity and stability.

2.2. Effects of Composition

Altering the ratio of rGO and V_2O_5 can improve the overall electrochemical performance by balancing the conductivity of rGO and the pseudocapacitance of V_2O_5. Li et al. emphasized the importance of carefully tuning the carbon content for improved electrochemical performance [70]. Different amounts of rGO were added during hydrothermal synthesis to yield VrG electrodes with 15, 22, and 26 wt% rGO. Even a relatively small difference of 4 wt% in the carbon content between VrG-22 and VrG-26 resulted in a significant increase in conductivity, with VrG-26 retaining 46% of its charge capacity (compared to 26% capacity retention of VrG-22) when the scan rate was increased from 1 to 20 mV s^{-1}. As the orthorhombic V_2O_5 nanorods were wrapped by and intercalated between the crumpled rGO sheets, an increase in the rGO content resulted in few nanorod agglomerations and high conductivity, resulting in improved rate capability. An asymmetric capacitor with a VrG-26 anode and AC cathode exhibited a C_{sp} of 37.2 F g^{-1} at a current density of 0.5 A g^{-1}. The integrated, layered structure of rGO reduced the permanent dissolution of V_2O_5, leading to 90% C_{sp} retention after 1000 cycles at a current density of 2 A g^{-1}. The maximum energy density exhibited was 54.3 Wh kg^{-1} at a power density of 136.4 W kg^{-1}. Saravanakumar et al. physically mixed different ratios of already prepared rGO and V_2O_5 in disodium citrate and aged the solution for three days to yield a VrG composite [71]. All VrG compositions had an orthorhombic V_2O_5 crystal structure and produced a complex

V_2O_5 network on the 2D rGO surface. However, among these, VrG-5 (5 wt% rGO) and VrG-15 (15 wt% rGO) resulted in more agglomeration of V_2O_5, whereas VrG-10 (10 wt% rGO) had a more homogeneous spread of the V_2O_5 crystals. V_2O_5 agglomeration limited surface ion adsorption as the electrolyte could not intercalate deep into the bulk V_2O_5 crystal structure. Thus, well-spread VrG-10 exhibited the highest C_{sp} of 519 F g^{-1} at a scan rate of 2 mV s^{-1}, which was significantly greater than the 326 F g^{-1} C_{sp} for pristine V_2O_5. An increase in rGO content improved the electron mobility to balance the high pseudocapacitive charge capacity of V_2O_5. VrG-15 performed worse than bare V_2O_5 with a C_{sp} of 210 F g^{-1} because of the lower V_2O_5 content and V_2O_5 agglomeration on rGO, which limited electron mobility and ion intercalation/de-intercalation. An increase in the rGO content enhanced the rate capability of the VrG electrodes, with VrG-5 showing only 47% C_{sp} retention compared to 68% retained by VrG-15 when the current density was increased from 0.5 to 10 A g^{-1}. Increasing the rGO content decreased the internal resistance, as indicated by 0.4 Ω resistance in VrG-10 compared to 1.73 Ω for pristine V_2O_5. The physical support provided by the rGO sheets further reduced the damage caused by repeated intercalation/de-intercalation, resulting in an 83% C_{sp} retention after 1000 cycles for VrG-10. An appropriate rGO composition is required to decrease V_2O_5 agglomeration for maximum pseudocapacitive efficiency and improve the conductive pathways for higher rate capability.

Although a high carbon content is desirable, a high V_2O_5 composition is required for energy-dense supercapacitor electrodes. Ramadoss et al. examined the effect of varying rGO to V_2O_5 ratio by controlling the initial ratio of GO and V_2O_5 during microwave synthesis [72]. All three VrG variations, V_1rG_2 (1:2 V_2O_5 to GO), V_1rG_1 (1:1 V_2O_5 to GO), and V_2rG_1 (2:1 V_2O_5 to GO), possessed a pure orthorhombic crystal phase with uniform nanorods of 150–200 nm lengths. The VrG electrodes exhibited mixed pseudocapacitive and EDL contributions to the overall capacitance. An increase in the V_2O_5 content increased the C_{sp} of the VrG electrode, as indicated by the higher C_{sp} of 250 F g^{-1} for V_2rG_1 than 103 F g^{-1} for V_1rG_2 at a scan rate of 5 mV s^{-1}. As V_2O_5 contributed toward most of the capacitance via faradic reactions, increasing the proportion of V_2O_5 increased the total capacitance. A symmetric supercapacitor with V_2rG_1 electrodes had an energy density of 12.5 Wh kg^{-1} at a power density of 79,900 W kg^{-1}, which decreased to 8.4 Wh kg^{-1} at 10 times the power density. Lee et al. also concluded that high V_2O_5 content increased the total capacitance [73]. VrG material was synthesized via a low-temperature hydrothermal process with different ratios of V_2O_5 powder and GO. V_3rG_1 (3:1 V_2O_5 to GO), V_1rG_1 (1:1 V_2O_5 to GO), and V_1rG_3 (1:3 V_2O_5 to GO) all yielded orthorhombic crystalline V_2O_5 nanobelts with uniform size. V_2O_5-rich V_3rG_1 outperformed the other two variations with a C_{sp} of 288 F g^{-1} at a scan rate of 10 mV s^{-1}, doubling the C_{sp} of V_1rG_3. Although an increase in the rGO content theoretically increased the conductivity, the low-temperature hydrothermal reduction led to only a partial reduction of GO to rGO, which limited the conversion to highly conductive rGO [73]. A large capacitance requires significant pseudocapacitive contributions, supporting the need for a V_2O_5-rich composite material. Many active sites were available for surface redox reactions because of the high surface area of the V_2O_5 nanobelts anchored to the rGO layers. However, excessive V_2O_5 content could lead to agglomeration that decreases the performance of the VrG composite. Fu et al. found a balance between the rGO and V_2O_5 contents by synthesizing VrG electrodes with different weight percentages of V_2O_5 [74]. The fabricated VrG composite synthesized via microwave synthesis method resulted in a uniform distribution of amorphous V_2O_5 nanoparticles on lamellar rGO sheets. Flaky rGO prevented the agglomeration of V_2O_5, which is a common problem that decreases the surface ion adsorption capability of the V_2O_5 nanostructure. More V_2O_5 crystals were formed on the rGO surface without agglomeration at a high initial V_2O_5 loading up to 34.1 wt%. VrG-34 (34.1 wt% V_2O_5) exhibited excellent electrochemical performance with a C_{sp} of 673.2 F g^{-1} at a current density of 1 A g^{-1}. The high rGO content resulted in high rate capability, as indicated by a large C_{sp} of 474.6 F g^{-1} at a high current density of 10 A g^{-1}. A high V_2O_5 composition decreased the ion adsorption and number

of interlayer rGO bridges, which are essential for fast electron transport. With an increase in current density, the high capacitance shifted from the redox dependence of V_2O_5 to the capacitive dependence provided by rGO. The porous and stable architecture of the composite allowed good cycling with a 96.8% C_{sp} retention after 10,000 cycles at a current density of 1 A g^{-1}. A symmetric supercapacitor exhibited good performance with an energy density of 46.8 Wh kg^{-1} at a power density of 499.4 W kg^{-1}. A high V_2O_5 content is necessary for high energy density through faradic energy storage; but ultimately, a balance between V_2O_5 and rGO is essential for maximizing the electrochemical performance.

A variation in the ratio of rGO to V_2O_5 also alters the porosity and surface area of the final VrG composite. Typically, a greater amount of rGO results in a larger surface area owing to its high surface area. Yao et al. found that decreasing V_2O_5 content increased the porosity of the composite [75]. A mixture of V_2O_5 powder with varying initial loading, H_2O_2, and GO sols was heated at 200 °C for 5 h to yield a VrG composite. The resulting VrG aerogel comprised V_2O_5 nanobelts with a pure orthorhombic crystal phase uniformly intercalated between the layers of rGO. VrG with 80.5 wt% V_2O_5 exhibited a small BET surface area of 20.5 m^2 g^{-1}, whereas VrG with 15.6 wt% V_2O_5 exhibited a large BET surface area of 103.4 m^2 g^{-1}. As rGO had a greater surface area than V_2O_5, the addition of higher amounts of rGO increased the overall surface area of the VrG material. Moreover, V_2O_5 tended to agglomerate at high concentrations. A decrease in the total V_2O_5 content resulted in a more homogeneous distribution of V_2O_5 throughout the rGO surface to provide more active sites. VrG-62 (61.6 wt% V_2O_5) outperformed other VrG electrodes owing to a good balance of EDLC and pseudocapacitance while maintaining a high pore volume of 0.008 cm^3 g^{-1}. The VrG-62 electrode exhibited a maximum C_{sp} of 310.1 F g^{-1} at a current density of 1 A g^{-1}. The VrG composite had good rate capability, as indicated by a high C_{sp} of 195.2 F g^{-1} at a large current density of 10 A g^{-1}. Choudhury et al. also reported that a lower V_2O_5 content of a V_2O_5/graphene (VG) composite increased the specific surface area [76]. The VG material was synthesized via an in situ chemical reaction between V_2O_5 powder and exfoliated graphene with H_2O_2. V_4G_1 (4:1 V_2O_5 to graphene) and V_2G_1 (2:1 V_2O_5 to graphene) exhibited a layered structure with V_2O_5 nanofibers anchored between the layers of rough graphene. The BET surface area of V_2G_1 was 142 m^2 g^{-1}, which decreased to 117 m^2 g^{-1} for V_4G_1. A low amount of V_2O_5 produced a composite with a high surface area, resulting in more active redox sites and greater intercalation/de-intercalation. Accordingly, V_2G_1 exhibited a higher C_{sp} of 218 F g^{-1} compared to 112 F g^{-1} for V_4G_1 at a current density of 1 A g^{-1}. A symmetric supercapacitor of V_2G_1 yielded an energy density of 22 Wh kg^{-1} at a power density of 3594 W kg^{-1}.

However, a balance between V_2O_5 and rGO could increase the surface area to greater than that of pure rGO. Deng et al. found that a VrG composite yielded higher porosity than that of pure rGO because of the increased interlayer spacing of the rGO sheets caused by V_2O_5 intercalation [77]. A VrG monolith was synthesized via a hydrothermal method, resulting in a lamellar rGO structure with V_2O_5 nanowires embedded between the thin rGO sheets (22 wt% rGO). The resulting BET surface area of the VrG monolith was 172.9 m^2 g^{-1}, which was ~100 m^2 g^{-1} larger than that of a pure rGO monolith and approximately five times larger than that of pure V_2O_5. The VrG monolith was also compressed into a thin film electrode. The C_{sp} of VrG monolith and thin-film were 385 and 272 F g^{-1}, respectively, at a current density of 0.25 A g^{-1}. The VrG material exhibited enhanced ion diffusion rates owing to increased porosity, resulting in good rate capability, as indicated by a high C_{sp} of 224 F g^{-1} at a current density of 10 A g^{-1}. The energy density of the asymmetric supercapacitor with the VrG electrode was 26.22 Wh kg^{-1} at a power density of 425 W kg^{-1}, which decreased to 7 Wh kg^{-1} at a power density of 8500 W kg^{-1}. Ndiaye found that an increase in the graphene foam (GF) content only increased the porosity to a certain extent [78]. A V_2O_5/GF composite was synthesized with varying initial GF loading. The BET surface area increased from 4.9 m^2 g^{-1} for pristine V_2O_5 nanosheets to 5.1 m^2 g^{-1} when 50 mg of GF was added. Because GF has a high specific surface area of 208.8 m^2 g^{-1}, the initial integration of GF increased the overall surface area. The low

GF content also prevented the homogeneous integration of the V_2O_5 nanosheets with GF. An increase in the GF loading to 150 mg (VrG-150) resulted in a maximum surface area of 9.5 m^2 g^{-1}. However, further increase in the GF loading to 200 mg resulted in the reduction of surface area to 6.2 m^2 g^{-1}. A high GF content caused GF and V_2O_5 to form separate agglomerations instead of a homogeneous composite. Consequently, the porous and homogeneous VrG-150 outperformed the other electrodes, with a specific capacity of 73 mAh g^{-1} at a current density of 1 A g^{-1}. An asymmetric capacitor assembled using a VrG-150 positive electrode and carbonized Fe-adsorbed polyaniline (C-FE-PANI) negative electrode yielded a specific capacity of 41 mAh g^{-1} at a current density of 1 A g^{-1}. The energy density was 39 W h kg^{-1} at a power density of 947 W kg^{-1}.

Determining the optimal ratio between rGO and V_2O_5 is essential for synthesizing a high-performance electrode material with a balance between the EDL and pseudocapacitive characteristics. An appropriate rGO content improves the conductivity and electrode cyclability, whereas a sufficient V_2O_5 content is necessary for high specific capacitance. The addition of rGO to bulk V_2O_5 increases the surface area of the composite material, and the intercalation of V_2O_5 into rGO layers can also increase the porosity of the composite material. However, a balance between the two components is necessary to prevent agglomeration.

2.3. Effects of Physical Treatment

Annealing newly fabricated VrG composites can alter oxidation states of vanadium oxides and improve their crystallinity, resulting in enhanced electrochemical performance. Control of the temperature during the heat treatment can increase the oxidation of V_2O_5 and the formation of a homogeneous composite. Following a hydrothermal synthesis procedure, Li et al. synthesized V_xO_y nanoflowers anchored to rGO sheets [79]. Annealing of the resulting composite caused the nanoflowers to morph into V_2O_5 nanorods with varying lengths and diameters depending on the annealing temperature. Moreover, an increase in the annealing temperature converted amorphous vanadium oxides into orthorhombic V_2O_5 crystals through the oxidation of V^{4+} to V^{5+}. VrG annealed at 350 °C under nitrogen atmosphere exhibited the maximum C_{sp} of 537 F g^{-1} at a current density of 1 A g^{-1} due to short ion diffusion pathways in the organized V_2O_5 crystal lattice. Because the nanorods were uniformly anchored to the mesoporous rGO surface, the high conductivity and porosity afforded by the rGO resulted in a good rate capability, indicated by the 60% C_{sp} retention at a high current density of 20 A g^{-1}. Improved cyclic performance of the VrG material was also observed, with 84% C_{sp} retention after 1000 cycles at a current density of 1 A g^{-1}. The VrG electrode exhibited a high energy density of 74.58 Wh kg^{-1} at a power density of 500 W kg^{-1}, which decreased slightly to 29.33 Wh kg^{-1} at a power density of 10,000 W kg^{-1}. In a similar study, Liu et al. fabricated a VrG composite via a hydrothermal method using an NH_4VO_3 precursor followed by annealing at different temperatures in air [80]. Without annealing, V_2O_5 nanospheres of inconsistent sizes and incomplete formation were observed, whereas VrG annealed at a high temperature of 350 °C (VrG-350) exhibited a degraded rGO support without distinct V_2O_5 nanospheres. However, VrG annealed at 300 °C (VrG-300) had uniformly sized V_2O_5 nanospheres homogeneously embedded on the surface of the rGO. VrG-300 exhibited greater GO reduction and an increase in V_2O_5 composition from 12 to 30 wt%, owing to greater V^{4+} oxidation to V^{5+}. With fewer defects in the carbon lattice and a higher V_2O_5 content, VrG-300 exhibited the largest C_{sp} of 386 F g^{-1} at a current density of 0.5 A g^{-1}. An asymmetric supercapacitor with the VrG-300 electrode had a maximum energy density of 80.4 Wh kg^{-1} at a power density of 275 W kg^{-1}, which decreased to 32 Wh kg^{-1} at a power density of 1374 W kg^{-1}. Thangappan et al. electro-spun a mixture of vanadium acetylacetonate, GO, polyvinyl pyrrolidone, dimethylformamide (DMF), and ethanol, and subsequently annealed the composite at 350 or 550 °C in air [81]. Non-annealed VrG and VrG annealed at 350 °C resulted in a web of uniformly thin and straight nanowires. VrG annealed at 550 °C resulted in a twisted and aggregated structure with arched webs that were half the diameter of the

non-annealed VrG due to the decomposition of the organic binder material. Annealing at 550 °C completely reduced GO, resulting in a more conductive composite fiber. However, high temperature disintegrated the carbon material, resulting in a low carbon content of 0.3 wt%. Non-annealed and low-temperature annealed VrG had amorphous crystal structures, whereas the VrG annealed at 550 °C possessed an orthorhombic crystal structure, as indicated by the formation of large V_2O_5 crystals. The stable crystals and mesoporous, web-like structure of VrG annealed at 550 °C allowed a large amount of ion diffusion into the electrode for high energy storage. The C_{sp} was 453.8 F g^{-1} at a scan rate of 10 mV s^{-1} because of the slow ion intercalation at low scan rates. The C_{sp} decreased to 111.01 F g^{-1} at a scan rate of 100 mV s^{-1}. Therefore, the control of the annealing temperature is essential for both the reduction of GO to rGO and improving the crystallinity of V_2O_5.

Despite the previously mentioned benefits of heat treatment, the annealing of VrG electrodes may decrease the electrical performance. Lee et al. analyzed the discrepancy in the electrochemical performance of a non-annealed V_2O_5 composite in comparison with an annealed composite, where an rGO thin film was fabricated from GO using CO_2 laser reduction, and V_2O_5 was deposited on the film via atomic layer deposition [82]. The CO_2 laser changed the porosity of the compact GO by increasing the interstitial gap between the rGO sheets while creating pores that penetrated multiple rGO sheets. The spacing between the rGO sheets increased with V_2O_5 infiltration. The V_2O_5 deposition left the rGO template intact, and further annealing the composite in an argon atmosphere did not significantly change the surface morphology of the electrode. However, annealing converted the amorphous V_2O_5 crystal structure into a more crystalline V_2O_5 with varying oxidation states of vanadium oxide. The amorphous crystal characteristics of V_2O_5 before annealing allowed deeper ion diffusion through the distorted lattices, resulting in a greater faradic character. In contrast, the annealed VrG exhibited higher crystallinity and greater EDL contribution. Considering the lamellar structure of the rGO sheets, the diffusion-based faradic capacitance of the non-annealed VrG resulted in a higher C_{sp} of 189 F g^{-1} at a current density of 1 A g^{-1}. The charge transfer resistance was also lower for the non-annealed VrG. Initial cycling increased the C_{sp} to 108% for the non-annealed VrG material owing to electro-activation caused by the initial intercalation of electrolyte ions. However, this did not occur for annealed VrG because of the more rigid crystallized structure of the annealed VrG (Figure 4).

In addition to heat treatment, the morphology and crystallinity of a VrG composite can be altered by laser irradiation. Lazauskas et al. first synthesized a V_2O_5/GO nanoribbon composite using a melt-quenching process and further applied laser treatment to reduce GO to rGO [83]. A 405-nm laser was used to irradiate specific regions of the V_2O_5/GO composite, resulting in a VrG composite with surface protrusions. The laser treatment resulted in pillar-like V_2O_5 protrusions that uniformly extruded from the rGO base. These protrusions increased the surface area by four times to 17.27 m^2 g^{-1}. An increase in the laser power output from 1.69 to 2.03 W cm^{-2} to 2.37 W cm^{-2} resulted in more protrusions. However, further increase in power to 2.71 W cm^{-2} led to larger V_2O_5 agglomerations, thereby decreasing the surface area of the composite material. The laser treatment also decreased the amount of intercalated H_2O molecules in the V_2O_5 crystal lattice while further reducing GO to rGO. The laser treatment resulted in a VrG composite with a more organized V_2O_5 crystal structure and high conductivity of 6.8 S m^{-1}.

Physical treatment of V_2O_5 with heat or laser can alter the crystallinity of V_2O_5, oxidize V^{4+} to V^{5+} and reduce GO to rGO. Highly crystalline V_2O_5 is more conductive than amorphous V_2O_5, allowing for greater rate capability, but it is less efficient for ion diffusion than the latter. The reduction of GO to rGO improves the conductivity of the carbon backbone in the VrG composite. Physical treatment can also be used to control the formation of agglomerations, and excessive heat exposure can destroy the carbon content of the hybrid material.

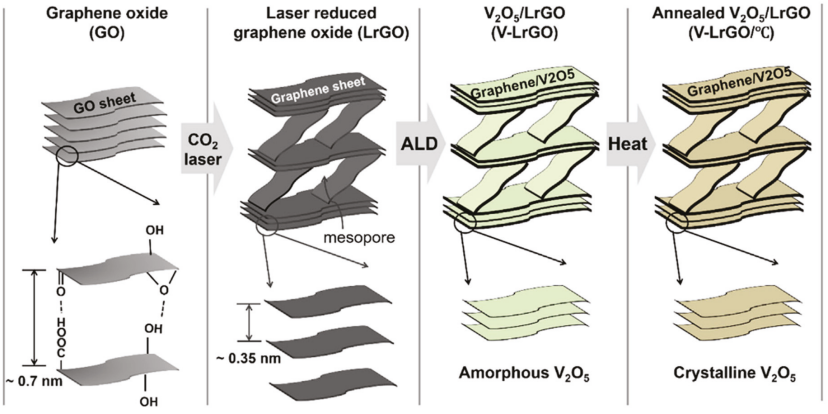

Figure 4. Schematic illustration for the fabrication process of the multilayered graphene (i.e., LrGO) and amorphous or crystalline V_2O_5 coated LrGO. Firstly, the prepared GO was reduced by a home engraver equipped with a CO_2 laser. Then, the LrGO was coated with amorphous V_2O_5 by a low-temperature ALD process, followed by annealing at high temperatures. Reprinted with permission from Ref. [82]. Copyright 2020 Elsevier.

3. V_2O_5/CNT

CNTs have received considerable attention owing to their high conductivities, large surface areas, mechanical stability, and unique 1D tubular structures [84,85]. The ability of CNTs to be functionalized allows precise control of their properties to meet the needs of specific supercapacitor applications [86]. Single-walled CNTs (SWCNTs) and multi-walled CNTs (MWCNTs) have been utilized in conjunction with vanadium oxides to yield high-performance hybrid materials for supercapacitor applications [87]. Herein, the effects of different synthesis pathways, V_2O_5/CNT compositions, and physical treatments on the morphology and electrochemical performances of V_2O_5/CNT (VCNT) composite materials are discussed. The morphology and electrochemical performances of V_2O_5/CNT electrodes for supercapacitor applications reported in the literature are summarized in Table 2.

Table 2. V_2O_5 morphology and electrochemical performances of V_2O_5/carbon nanotube composite electrodes for supercapacitor applications.

Morphology	Maximum C_{sp} (F g^{-1})	Cycling C_{sp} Retention (%)	Cycle Number	Energy Density (Wh kg^{-1})	Power Density (W kg^{-1})
Nanostars	1016	64 *	5000 *	13.24	710
Nanospheres	125	-	400	25	100
Nanobelts	685	99.7	10,000	34.3	150
Amorphous	410	86	600	57	250
Nanoflakes	629	93	4000	72	2300
Nanosheets	207.7	75 *	10,000 *	7300	42.6
Nanospheres	284	76 *	5000 *	32.3	118
Nanosheets	357.5	99.5	1000	-	-
CNT Coating	510	96	5000	16	800

* Cycling performance was determined using a two-electrode configuration.

3.1. Effects of Synthesis Method

A common procedure for fabricating VCNT composites is the hydro/solvothermal method. Jiang et al. grew V_2O_5 crystals on a GF/CNT substrate by employing a hydrothermal process [88]. Subsequently, PEDOT coating was deposited via a chronoamperometry technique, yielding a VCNT/GF/PEDOT composite (Figure 5).

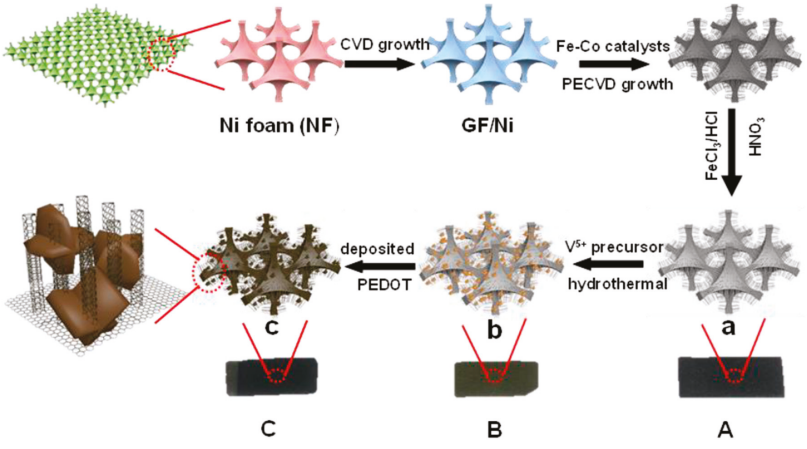

Figure 5. Schematic of the synthesis of (**A**) CNT/GF, (**B**) VCNT/GF, (**C**) VCNT/GF/PEDOT. Reprinted with permission from Ref. [88]. Copyright 2017 Royal Society of Chemistry.

Orthorhombic crystal phase V_2O_5 nanostars were intercalated into the interstitial space between the vertically aligned CNTs. The addition of the PEDOT coating reduced the V_2O_5 dissolution during synthesis and increased the size of the V_2O_5 nanostars by ~15%. The high surface area of the enlarged V_2O_5 nanostars increased the pseudocapacitive surface reactions. The composite electrode was tested in a three-electrode configuration with a Pt counter electrode and an Ag/AgCl reference electrode in 5 M $LiNO_3$ electrolyte, yielding a high C_{sp} of 1016 F g^{-1} at a current density of 1 A g^{-1}. The direct growth of V_2O_5 on the vertically aligned CNTs enabled good surface contact for efficient electrical conduction. The porous Ni foam/CNT frame also provided structural stability to the overall electrode. The result indicated good rate capability with an excellent C_{sp} of 484 F g^{-1} at a high current density of 20 A g^{-1} and high coulombic efficiency of 97.8%. The asymmetric supercapacitor with a VCNT electrode exhibited a maximum energy density of 13.24 Wh kg^{-1} at a power density of 710 W kg^{-1}, which decreased to 10.34 Wh kg^{-1} at a power density of 2659 W kg^{-1}. The energy density decreased slightly at high power owing to the absence of an insulating binder material and the high conductivity provided by the Ni/CNT frame. Wang et al. synthesized a VCNT composite by adding CNTs to the V_2O_5 nanosheets that were synthesized via a hydrothermal reaction between bulk V_2O_5 and H_2O [89]. CNTs were subsequently added to a solution of V_2O_5 nanosheets and aged for two days. This fabrication method resulted in a lamellar nanostructure with V_2O_5 layers intercalated with CNTs, corresponding to 13.7 wt% of the total composition. The CNTs increased the interstitial spacing between the V_2O_5 nanosheets, preventing V_2O_5 agglomeration and increasing the porosity, yielding a large specific surface area of 102.05 m^2 g^{-1}. The C_{sp} of the VCNTs was 553.33 F g^{-1} at a current density of 5 mA cm^{-2}. The increased interlayer spacing between the V_2O_5 planes allowed greater ion intercalation/deintercalation, which promoted faradic redox reactions. Furthermore, the CNTs increased the overall conductivity of the device, resulting in a low series resistance of 0.95 Ω and a charge transfer resistance of 0.6 Ω for enhanced rate capability. Owing to the structural stability provided by the CNTs, the charge/discharge stability increased, as indicated by a high C_{sp} retention of 83% after 1000 cycles at a current density of 10 mA cm^{-2}.

Deposition techniques have also been used to grow vertically aligned CNTs and V_2O_5 composites directly on conductive substrates such as Ni, yielding a binderless electrode material. Jampani et al. used CVD to synthesize an array of vertically aligned CNTs on flat Ni disks that formed a forest-like microstructure. Atmospheric pressure CVD was used to deposit Ti-doped V_2O_5 on the CNTs [90]. The resulting composite had an amorphous

crystal phase with V_2O_5 globules anchored to the vertically aligned CNT forest; a C_{sp} of 313 F g^{-1} was observed at a scan rate of 2 mV s^{-1}. The amorphous crystal structure of the Ti-doped V_2O_5 decreased the V_2O_5 dissolution during charge/discharge, resulting in nearly perfect C_{sp} retention even after 400 cycles at a high scan rate of 100 mV s^{-1}. The areal capacitance was 350 mF cm^{-2} at a scan rate of 2 mV s^{-1}, which decreased to 20 mF cm^{-2} at a scan rate of 200 mV s^{-1}. The decent rate capability was due to the low resistance of the binderless composite at 0.0182 Ω cm^{2}, which was two orders of magnitude more conductive than pristine V_2O_5. The electrodes had a maximum energy density of 25 Wh kg^{-1} at a power density of 100 W kg^{-1}, which decreased to 11 Wh kg^{-1} at a power density of 4500 W kg^{-1}. Shakir et al. used spray coating to prepare a layered V_2O_5/MWCNT (VMWCNT) composite electrode on a Ni/Cu/Ni/Au electroplated substrate [91]. A polyester fiber fabric was first plated with Ni/Cu/Ni/Au layers sequentially via electroless plating. The MWCNT/V_2O_5 core/shell nanotubes were synthesized via a bottom-up assembly method using pre-functionalized MWCNTs and NH_4VO_3. A layer of graphene was then deposited on the conductive fabric. Subsequently, a mixture of V_2O_5-coated MWCNTs was spray-coated on the top graphene layer. Alternating graphene and VMWCNT layers were applied repeatedly to yield a binderless VMWCNT/graphene composite electrode. The electrode comprised a thick orthorhombic V_2O_5 shell coating the MWCNTs. The C_{sp} of the VMWCNT/graphene electrode with 3-nm-thick V_2O_5 layers had an excellent C_{sp} of 2590 F g^{-1} at a scan rate of 1 mV s^{-1}. Increasing the V_2O_5 coating thickness to 20 nm decreased the C_{sp} to 510 F g^{-1} because of inefficient ion penetration into the inner layers of the VMWCNTs. The 3-nm-thick VMWCNT/graphene electrode retained 96% of its initial C_{sp} after 5000 cycles at a scan rate of 20 mV s^{-1} because of the effective conductive MWCNT bridge linking electron transport from V_2O_5 to graphene. The energy density was 96 Wh kg^{-1} at a power density of 800 W kg^{-1}, which decreased to 28 Wh kg^{-1} at a power density of 9000 W kg^{-1}.

One major advantage of CNTs is their easy functionalization to yield high-performance VCNT electrodes through various synthesis methods. Modifying CNTs with specific functional groups such as hydroxyl or carboxyl groups can improve the conductivity of the CNTs and promote the nucleation of V_2O_5 crystals. Hu et al. used a one-step hydrothermal method to synthesize a vanadium oxide composite with functionalized CNTs [92]. The CNTs were functionalized with hydroxyl and carbonyl groups using concentrated sulfuric and nitric acids, which acted as the activation centers for coordinate bond formation with VO. Vanadium oxide nanoribbons were formed at the nucleation sites via a hydrothermal reaction and were bonded to the CNTs via hydroxyl functional groups. By adding GO to a mixture of V_2O_5 and CNTs, Hu et al. fabricated a V_3O_7/CNT/rGO composite (rGO-VCNT) comprised of rGO sheets uniformly coated with large V_3O_7 nanobelts and thin CNTs. The rGO-VCNT composite with 40 wt% rGO exhibited a maximum C_{sp} of 685 F g^{-1} at a current density of 0.5 A g^{-1}, which decreased to ~375 F g^{-1} at a high current density of 10 A g^{-1}. The high porosity of rGO and improved conductivity because of well-distributed CNTs resulted in an excellent rate capability. With a primarily carbon-based composition and strong bonds between V_2O_5 and CNTs, the rGO-VCNT (40 wt% rGO) electrode retained 99.7% of its initial C_{sp} after 10,000 cycles at a high scan rate of 100 mV s^{-1}. The maximum energy density of the symmetric supercapacitor was 34.3 Wh kg^{-1} at a power density of 150 W kg^{-1}, which decreased to 18.8 Wh kg^{-1} at a power density of 3000 W kg^{-1}. Mtz-Enriquez et al. reported an improved discharge time of a VCNT electrode by functionalizing the CNTs to promote V_2O_5 defects [93]. The CNTs were first deposited on a flexible graphene electrode and activated with strong acids. A V_2O_5 slurry was then applied to the CNT-coated graphene electrode and hot-pressed at 0.1 ton for physical binding. The resulting composite was comprised of rectangular V_2O_5 orthorhombic nanoribbons intercalated into a fibrous CNT structure. Oxygen vacancies formed in the V_2O_5 crystal structure due to the reduction of V^{5+} to V^{4+}, which acted as redox centers for delayed current discharge. The functionalization of CNTs with carboxylic groups also created oxygen vacancies in the carbon lattice, promoting the formation of additional V_2O_5 defects.

The CNTs also provided a secondary layer for ion storage and a large surface area for V_2O_5 contact, resulting in a high capacity and rate capability. The asymmetric supercapacitor with a graphene/VCNT anode had an energy density of 369.6 Wh kg^{-1}.

MWCNTs can also be functionalized to achieve an increase in conductivity and homogeneous V_2O_5 formation. Saravanakumar et al. functionalized MWCNTs with hydroxyl, carboxyl, and keto-carbonyl groups using concentrated H_2SO_4 and HNO_3 [94]. A mixture of functionalized MWCNTs and V_2O_5 crystals was aged for three days at room temperature to yield a V_2O_5/MWCNT (VMWCNT) composite. The orthorhombic V_2O_5 crystals formed the cores surrounded by MWCNTs, resulting in a highly porous network. Even with a relatively low carbon content of 8.73 wt%, the surface area was large (14.4 m^2 g^{-1}) because of the mesoporous web-like architecture of the MWCNTs. The VMWCNT electrode exhibited a maximum C_{sp} of 410 F g^{-1} at a current density of 0.5 A g^{-1}, which decreased to 280 F g^{-1} at a current density of 10 A g^{-1}. The high rate capability was because of the porous structure that allowed the fast intercalation/de-intercalation of ions and high conductivity of the functionalized CNT web. The functionalized CNTs improved the cyclability of the VMWCNT electrode, as indicated by 86% C_{sp} retention after 600 cycles at a high current density of 10 A g^{-1}. The symmetric supercapacitor with functionalized VMWCNT electrodes exhibited an energy density of 8.9 Wh kg^{-1} at a power density of 121 W kg^{-1}. Pandit et al. functionalized MWCNTs with carboxyl groups using H_2O_2 [95]. A stainless-steel current collector was first dip coated with the MWCNTs, and the resulting MWCNT/stainless-steel electrode was dip coated with a solution of $VOSO_4$ and NaOH. After repeated dipping and drying, the resulting VMWCNT/stainless-steel electrode had a layered structure of orthorhombic V_2O_5 flakes intercalated in a web of long MWCNTs. A C_{sp} of 629 F g^{-1} was observed at a current density of 2 A g^{-1}, which decreased to ~320 F g^{-1} at a current density of 8 A g^{-1}. The C_{sp} of the composite electrode was high because the porous structure formed by the web-like MWCNTs allowed large volumes of counterion intercalation/de-intercalation deep in the V_2O_5 crystals. The VMWCNT electrode retained 93% of its C_{sp} after 4000 cycles at a high scan rate of 100 mV s^{-1}, showing good reversibility and stability. A symmetric supercapacitor with VMWCNT electrodes yielded an energy density of 72 Wh kg^{-1} at a power density of 2300 W kg^{-1} that decreased to 18.66 Wh kg^{-1} at a power density of 8400 W kg^{-1} and current density of 4 A g^{-1}.

Different synthesis strategies, including hydro/solvothermal and deposition methods, can result in VCNT composites with different nanostructures. The hydrothermal method is a facile technique that involves the nucleation of V_2O_5 crystals from vanadium precursors on CNTs at high temperatures. Deposition techniques such as CVD allow the direct layering of V_2O_5 on CNTs with a controllable thickness. Functionalizing the CNTs with hydroxyl and carbonyl groups before synthesis with V_2O_5 can improve the overall conductivity, porosity, and stability of the hybrid material.

3.2. Effects of Composition

The ratio of V_2O_5 to CNTs affects the electrochemical performance of VCNT electrodes via changes in their morphologies, conductivities, porosities, and pseudocapacitive potentials. Guo et al. reported increases in the conductivity and rate capability with high CNT content [96]. The $V_2O_5 \cdot nH_2O$ aerogel and CNTs were dispersed in DI water, vacuum filtered with a cellulose membrane, and dried at 60 °C. The film was comprised of densely packed V_2O_5 nanosheets with homogeneously intercalated CNTs between the V_2O_5 layers, preventing V_2O_5 self-stacking. An increase in the CNT content increased the thickness of the VCNT film by increasing the interstitial space between the V_2O_5 sheets. The increased thickness prevented deep ion infiltration into the inner V_2O_5 layers near the center of the electrode. However, an increase in the CNT content increased the conductivity of the overall electrode by introducing more interlayer CNT connections, as indicated by the low square resistance of 128 Ω sq^{-1} for VCNT-10 (10 wt% CNT). VCNT-10 exhibited the highest C_{sp} of 207.7 F g^{-1} (521 F cm^{-3}) at a current density of 0.5 A g^{-1}. An increase in the CNT content increased the rate capability, with VCNT-15 (15 wt% CNT) exhibiting the

highest C_{sp} retention of 49.5% compared to the 42% retention of the VCNT-10 electrode at a high current density of 20 A g^{-1}. The flexible symmetric supercapacitor exhibited good performance in both bent and unbent states with a high energy density of 7300 Wh kg^{-1} at a power density of 42.6 W kg^{-1}. Yilmaz et al. reported similar improvements with fewer V_2O_5 nanosheets intercalated with CNT [97]. V_2O_5 gel was rigorously mixed in solutions with different amounts of CNTs, yielding free-standing electrodes consisting of V_2O_5 nanosheets with an orthorhombic crystal structure. The CNTs were homogeneously intercalated between the V_2O_5 nanosheets. An increase in the V_2O_5 content decreased the porosity of the V_2O_5 nanosheets, decreasing the overall surface area of the VCNT composite. The composite gel was printed on a 1 cm × 1 cm ITO glass plate and dried before use as an electrode. V_1CNT_2 (1:2 ratio of V_2O_5 to CNT) yielded the highest C_{sp} of 116 F g^{-1} at a current density of 0.1 A g^{-1}. An increase in the V_2O_5 loading to 1:1 ratio (V_1CNT_1) resulted in a lower C_{sp} value of 32 F g^{-1} at a current density of 0.1 A g^{-1} because of a decrease in the number of active sites on V_2O_5 nanosheets. Further addition of V_2O_5 decreased the C_{sp} due to V_2O_5 agglomeration, which decreased surface ion adsorption. Because of the highly conductive CNT linkages, the carbon-dominant V_1CNT_2 electrode exhibited a good cycling capability, with 91.2% capacitance retention after 5000 cycles at a current density of 5 A g^{-1}. A symmetric supercapacitor with V_1CNT_2 electrode yielded a volumetric energy density of 0.67 mWh cm^{-3} at a power density of 0.27 W cm^{-3}. Wu et al. fabricated a thin-film electrode with varying V_2O_5 content using a sol-gel method [98]. V_2O_5 nanobelts, CNTs, ethanol, terpilneol, and ethyl cellulose were mixed at 80 °C to yield a gel that was then doctor bladed onto a ceramic plate and annealed at 350 °C in air. The thin film was peeled off the ceramic to yield a free-standing VCNT thin film. The V_2O_5 nanobelts were highly uniform with an orthorhombic crystal phase, resulting in uniformly thick (20–100 nm) and long (>100 nm) nanobelts. A conductive current collector was added by compressing the thin-film electrode between Ti foils at 4000 psi. The VCNT-75 (75 wt% V_2O_5 composition) thin-film exhibited the highest C_{sp} of 216 F g^{-1} at a scan rate of 5 mV s^{-1}, which was five times greater than that of the bare CNTs. VCNT-75 also exhibited the highest volumetric capacitance of 540 F cm^{-3} at a scan rate of 5 mV s^{-1}, which decreased by 79% at a scan rate of 100 mV s^{-1}. The poor rate capability was due to an inefficient electron transfer caused by the low carbon composition. VCNT-61 (60.5 wt% V_2O_5) exhibited the best balance between maximum capacitance and electrode stability with a C_{sp} of 192 F g^{-1} at a scan rate of 5 mV s^{-1} and a 64% C_{sp} retention at a scan rate of 100 mV s^{-1}. Moreover, the higher CNT content increased the electron conduction, resulting in 79.8% C_{sp} retention after 5000 cycles at a scan rate of 50 mV s^{-1}. A symmetric supercapacitor with VCNT-61 electrodes yielded a maximum volumetric energy density of 41 Wh L^{-1} at a volumetric power density of ~400 W L^{-1}, which decreased to 29.1 Wh L^{-1} at a volumetric power density of 6500 W L^{-1}. A balance between conductive CNTs and energy-dense V_2O_5 is necessary for achieving the maximum electrochemical performance.

The CNT to V_2O_5 ratio changes the extent of the EDL and pseudocapacitive characteristics of the hybrid material. Perera et al. found that altering the V_2O_5 to CNT ratio can also affect the physical properties of the composite thin film [99]. A free-standing VCNT electrode was fabricated by filtering a suspension of CNTs and V_2O_5 through nylon filter paper. The VCNT-covered filter papers were dried, yielding a highly flexible thin-film supercapacitor electrode. The hybrid material was comprised of long V_2O_5 nanowires that formed a web-like structure. Short and curly CNTs were uniformly intercalated into the V_2O_5 web. Increasing V_2O_5 content decreased the porosity of the composite while increasing the CNT content increased the brittleness of the thin-film electrode. A 1:1 ratio of V_2O_5 and CNTs (V_1CNT_1) exhibited the greatest structural integrity and optimal electrochemical performance with a C_{sp} of 57.3 F g^{-1} at a current density of 0.5 A g^{-1}. The V_1CNT_1 electrode exhibited good rate capability with a C_{sp} of 42.9 F g^{-1} at a current density of 10 A g^{-1}. A coin-cell type supercapacitor with a V_1CNT_1 anode exhibited an energy density of 46.3 Wh kg^{-1} at a power density of 5260 W kg^{-1}. In comparison, the VCNTs with a 1:5 ratio of V_2O_5 to CNTs had a lower energy density of 6 Wh kg^{-1} because of the decreased

pseudocapacitive energy storage capacity. A good balance of V_2O_5 content for maximum pseudocapacitive capacity and increased CNT content for improved porosity is essential for optimized VCNT electrode performance. Such flexible, high-performance electrodes allow the development of more powerful portable and bendable technologies. Sathiya et al. reported different contributions of intercalative and capacitive charge capacities by varying the V_2O_5 content [100]. VTIP was dispersed in a suspension of pre-functionalized CNTs and stirred for one day to allow slow hydrolysis. The resulting VCNT composite gel was aged for a week, washed with acetone, dried at room temperature, and further dried at 200 °C. Long CNTs were uniformly coated with a layer of V_2O_5 crystals, resulting in a web-like structure of long V_2O_5/CNT core/shell nanotubes. Pristine CNTs relied purely on nonfaradic mechanisms for charge storage, whereas pure V_2O_5 mainly used faradic ion intercalation for charge storage. An increase in the V_2O_5 content from 0 to 25 wt% increased both faradic and nonfaradic contributions owing to the synergistic effect between the CNTs and V_2O_5. However, further increase in the V_2O_5 content decreased the faradic contribution due to increased V_2O_5 coating thickness. With a V_2O_5 loading of 25 wt%, 67% of the total stored charge was from pseudocapacitive redox reactions and surface ion adsorption. The maximum specific capacity was 850 mAh g^{-1}, which was more than twice the capacity of purely pseudocapacitive pristine V_2O_5.

Because essential factors, including conductivity, porosity, and the charge storage method, are dependent on the ratio of V_2O_5 to CNT, it is important to optimize each type of VCNT composite. In general, a higher CNT content increases the EDL contribution, conductivity, and rate capability. In contrast, a large V_2O_5 content results in a higher faradic contribution, energy storage potential, and flexibility.

3.3. Effects of Physical Treatment

Heat treatment is often used as the final step in VCNT synthesis because annealing the composite material improves the crystallinity and morphology of the composite. Sun et al. found an increased conversion of amorphous vanadium oxide to V_2O_5 after heat treatment [101]. Vertically aligned CNTs were deposited on a Si substrate via CVD and reacted with vanadium(III) acetylacetonate. Upon annealing at 350 °C in air, V_2O_5 microspheres were uniformly grown on the CNT surface. Annealing the composite converted the vanadium precursor to V_2O_5 and improved the crystallinity of the vanadium oxide precursor. Even after high-temperature annealing, the composite contained mixed valence states of vanadium oxide, which enhanced the ion diffusion. The C_{sp} of the VCNT composite was 284 F g^{-1} at a current density of 2 A g^{-1}, which decreased by ~50% at a high current density of 15 A g^{-1}. The direct growth of V_2O_5 on the CNTs improved the surface contact, thereby decreasing the charge transfer resistance to 1.2 Ω and resulting in good rate performance. Moreover, interstitial spacing between the vertically aligned CNTs provided a spacious environment that decreased the internal strain during charge/discharge, resulting in a high C_{sp} retention of 89.3% after 2500 cycles at a high current density of 10 A g^{-1}. An asymmetric supercapacitor with the VCNT electrode had an energy density of 32.3 Wh kg^{-1} at a power density of 118 W kg^{-1}. Similarly, Wang et al. reported increased V_2O_5 formation after calcination [102]. A solution of NH_4VO_3, CNTs, super AC (SAC), and DI water was reacted in an autoclave at 180 °C for one day and subsequently calcinated in a muffle furnace at 250 °C for 6 h in air. The resulting VCNT material had orthorhombic V_2O_5 sheets interspaced with thick CNTs and SAC bundles. The addition of CNTs increased the BET surface area from 14 to 19 m^2 g^{-1}, and the addition of both CNTs and SAC further increased the surface area to 78 m^2 g^{-1} because of the increased mesopore volume. The VCNT electrode without SAC outperformed pristine V_2O_5 with a C_{sp} of 231.8 F g^{-1} at a high current density of 10 A g^{-1}. A high C_{sp} was observed even at a high current density because of the improved conductivity provided by the intercalated CNTs and short ion diffusion pathways to the crystalline V_2O_5 sheets. Moreover, the VCNT electrode with SAC yielded a maximum C_{sp} of 357.5 F g^{-1} because of the increased surface area that provided more activation sites. Shakir et al. synthesized a VMWCNT material through a

heat-induced reaction and further annealed the composite at 350 °C for 2 h under ambient conditions [103]. The resulting VMWCNT thin film had layers of highly orthorhombic V_2O_5 crystals surrounded by long and curly MWCNTs. VMWCNTs that were 3 nm thick exhibited the highest C_{sp} of 510 F g^{-1} at a scan rate of 1 mV s^{-1} because the thickness maximized the surface area-to-volume ratio of V_2O_5. The C_{sp} of the composite was significantly higher than that of bare MWCNTs at 80 F g^{-1} because of the pseudocapacitive reactions enabled by the V_2O_5 crystals. The VMWCNT electrode exhibited good stability with 96% of its initial C_{sp} retained after 5000 cycles at a high scan rate of 20 mV s^{-1} because of the improved conductivity of the MWCNTs and structural stability of the web-like nanostructure. The energy density of the electrode was 16 Wh kg^{-1} at a power density of 800 W kg^{-1}. Physical treatment is a key component of VCNT synthesis because it promotes the conversion of amorphous vanadium oxides to a more crystalline V_2O_5.

4. V_2O_5/CNFs

CNFs have attracted significant attention as a substrate material for V_2O_5 growth because of their ease of synthesis, pore size controllability, and high conductivity [104]. Moreover, their stable 3D structures allow them to be used as free-standing electrodes for decreased internal resistance, high porosity, and flexible electrode applications [105]. V_2O_5/CNF (VCNF) composites often comprise either a CNF/V_2O_5 core/shell structure, V_2O_5 crystal growth on long CNFs, or V_2O_5 crystals intercalated in the CNF pores. The effects of the synthesis method, V_2O_5 content, and physical treatment on the electrochemical performances of the VCNF composite electrodes are reviewed. The morphology and electrochemical performances of V_2O_5/CNF electrodes for supercapacitor applications reported in the literature are summarized in Table 3.

4.1. Effects of Synthesis Method

Electrodeposition is a common technique used to form a V_2O_5 coating on long carbon fibers, resulting in a CNF/V_2O_5 core/shell structure. Song et al. used electrodeposition to coat the nanofibers of exfoliated carbon cloth (CC) with V_2O_5 [106]. The architecture of the fibrous structure was preserved, and two additional layers, an exfoliated carbon middle layer and a V_2O_5 outer layer, were added to the preexisting nanofibers. Due to a lack of heat or catalyst during electrodeposition, only half of the initial V_2O_5 precursor was oxidized, resulting in amorphous, mixed-valence V_2O_5. The areal capacitance of the device was 106 F cm^{-2} at a current density of 2 mA cm^{-2}, which decreased by 24% at a current density of 20 mA cm^{-2}. The good rate capability was attributed to the conductive carbon skeleton and improved electron mobility through the V-O-C bonds in the exfoliated carbon middle layer. Unlike most electrodes that degrade with repeated cycling, a 40% increase in the C_{sp} of the exfoliated VCNF electrode was observed after 10,000 cycles at a current density of 60 mA cm^{-2} because of the activation of the material via ion intercalation/de-intercalation. Repeated cycling introduced more intercalated water molecules, which expanded the interlayer distance for additional active sites. Water also shuttled the electrolyte ions during intercalation/de-intercalation. A similar V^{4+} to V^{5+} ratio decreased the dissolution of the V_2O_5 crystals during charge/discharge for improved stability.

Table 3. V_2O_5 morphology and electrochemical performances of V_2O_5/carbon nanofiber composite electrodes for supercapacitor applications.

Morphology	Maximum C_{sp} (F g^{-1})	Cycling C_{sp} Retention (%)	Cycle Number	Energy Density (Wh kg^{-1})	Power Density (W kg^{-1})
Nanorods	535.3	91.1	5000	38.7	900
CNF Coating	-	-	-	101	27,370
Nanosheets	-	89.3	10,000	40.2	800
CNF Coating	227	89	2000	63.6	400
CNF Coating	-	94 *	10,000 *	17.7	2728
Nanospheres	475.5	89.7 *	6000 *	-	-
Nanohairs	460.8	92 *	10,000 *	48.32	490

* Cycling performance was determined using a two-electrode configuration.

Crystallization can be used to coat CNFs with V_2O_5. Zhou et al. synthesized a high-performance V_2O_5/polyindole/ACC (VPIAC) composite electrode via crystallization [107]. Activated carbon cloth (ACC) was synthesized via CC activation with HNO_3, H_2SO_4, and $KMnO_4$, followed by heat-induced reduction in N_2/H_2 (95%/5%) atmosphere at 1000 °C. Sodium metavanadate was dripped onto the ACC and crystallized at 400 °C. Subsequently, a solution of H_2O_2, indole, and DI water was dripped onto V_2O_5/ACC to promote V^{4+} oxidation to V^{5+}. The resulting composite exhibited a bamboo-like structure with V_2O_5 and polyindole anchored to the surface of the long nanofibers. The electrochemical performance of the composite electrode was determined using a three-electrode configuration with a Pt counter electrode, Ag/AgCl reference electrode, and 5 M $LiNO_3$ electrolyte. The VPIAC hybrid material exhibited a high C_{sp} of 535.3 F g^{-1} at a current density of 1 A g^{-1} because of the increased conductivity of the polyindole. The VPIAC electrode had a low series resistance and charge transfer resistance of 1.1 and 7.6 Ω, respectively. The hybrid material exhibited excellent 91.1% C_{sp} retention after 5000 cycles at a high current density of 10 A g^{-1} because the polyindole decreased the dissolution of V_2O_5 during charge/discharge and increased adhesion between the CNFs and V_2O_5. The energy density of an asymmetric supercapacitor with the VPIAC electrode was 38.7 Wh kg^{-1} at a power density of 900 W kg^{-1}, which decreased to 32.6 Wh kg^{-1} at a power density of 18,000 W kg^{-1}.

The sol-dipping method can also allow the uniform coating of CNFs with a V_2O_5 shell. Azadian et al. employed a sol-dipping method involving the repeated dipping and drying of polyacrylonitrile-based carbon paper into a V_2O_5 sol [108]. The dip–dry process was performed multiple times to promote the growth of a thick layer of V_2O_5 crystals on the carbon paper nanofibers. The V_2O_5 grown on the CNFs exhibited a high C_{sp} of 800 F g^{-1}. Because of the porous architecture of the carbon fibers, the intercalation/de-intercalation was highly reversible, yielding a high Coulombic efficiency of 92%. The energy density of the electrode was 101 Wh kg^{-1} at a power density of 27 370 W kg^{-1}.

In addition to the formation of a CNF/V_2O_5 core/shell nanostructure, small V_2O_5 nanoparticles can be intercalated within the porous CNFs. Zhou et al. fabricated a CC-based electrode with V_2O_5 nanosheets embedded within the CNF webs [109]. CC/graphene foam/$CoMoS_4$ was mixed with a V_2O_5 supernatant for 12 h. The $CoMoS_4$ bound to CC/graphene resulted in the uniform coating of thin $CoMoS_4$ nanowires on the smooth CNFs, and the nanowires hosted the V_2O_5 nanosheets. The cyclic voltammetry (CV) curves of the hybrid material exhibited a distinct peak, indicating a large pseudocapacitive contribution. The CV curves retained their shape upon increasing scan rates from 5 to 50 mV s^{-1}, indicating good rate capability owing to the conductive carbon matrix (Figure 6a). The composite behaved more like a battery instead of a capacitor, based on the large IR drop shown in the galvanostatic charge–discharge (GCD) plot in Figure 6b. The specific capacity of the electrode was 158.6 mAh g^{-1} at a current density of 1 A g^{-1} (Figure 6c).

Vanadium promoted faradic redox reactions, which increased the charge storage potential of the electrode. The addition of graphene to the carbon fibers enhanced the charge transfer from V_2O_5 to the current collector and functioned as a buffer to prevent physical deformation during intercalation/de-intercalation. Thus, the hybrid material was highly cyclable with a >90% C_{sp} retention after 5000 cycles (Figure 6d). An asymmetric supercapacitor with a V_2O_5/$CoMoS_4$/CC/graphene positive electrode exhibited an energy density of 40.2 Wh kg^{-1} at a power density of 800 W kg^{-1}.

Unlike other synthesis strategies for growing V_2O_5 on a carbon nanofiber substrate, the electrospinning technique can directly produce VCNF composite materials [110]. The placement of a solution of a carbonaceous material such as polyacrylonitrile (PAN) and V_2O_5 in an electrospinning apparatus resulted in a flexible nanofiber composite material with controllable porosity and composition [111]. Kim et al. electrospun VCNF fibers using a dispersion of PAN and different amounts of V_2O_5 in a DMF solution [112]. The resulting nanofibers were heat treated at 800 °C under a nitrogen atmosphere for further oxidation and stabilization. The resulting nanofiber structure was primarily composed of

carbon with small, amorphous V_2O_5 agglomerations anchored on the CNF surface. The size of the agglomerations increased from 20 to 80 nm with an increase in the V_2O_5 content. Increasing the V_2O_5 content also increased the surface area of the electrode by introducing more pores into the nanofiber structure. The BET surface area of VCNF-20 (20 wt% V_2O_5) was 595.21 $m^2\ g^{-1}$ compared to 510.45 $m^2\ g^{-1}$ for VCNF-5 (5 wt% V_2O_5). In a symmetric electrode setup, the VCNF-20 electrode exhibited a C_{sp} of 150.0 F g^{-1} at a current density of 1 mA cm^{-2}, which was three times greater than that of the bare CNF because of the faradic contributions from the V_2O_5 crystals.

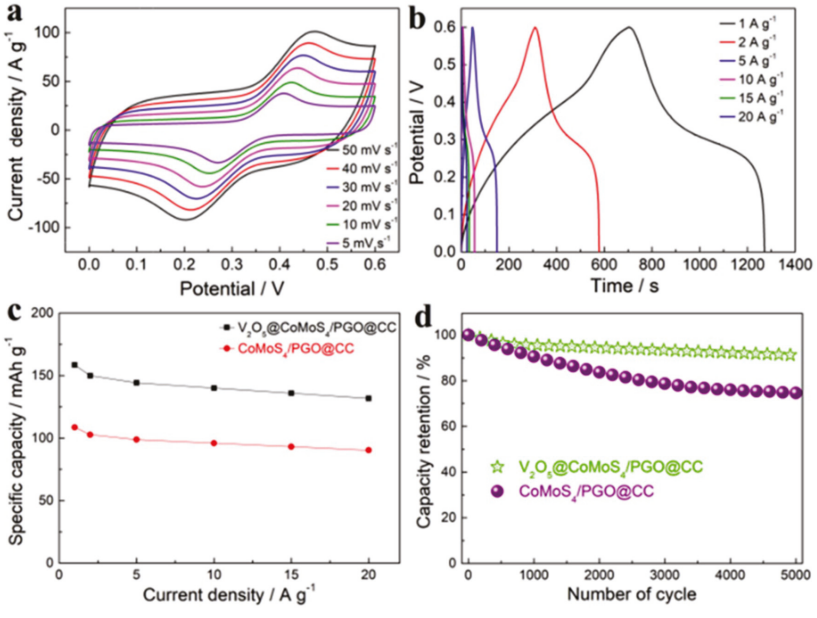

Figure 6. (**a**) CV and (**b**) GCD curves of V_2O_5/$CoMoS_4$/CC/graphene at different scan rates and current densities, respectively. (**c**) C_{sp} values of V_2O_5/$CoMoS_4$/CC/graphene and $CoMoS_4$/CC/graphene at different current densities and (**d**) cycling performances of V_2O_5/$CoMoS_4$/CC/graphene and $CoMoS_4$/CC/graphene. Reprinted with permission from Ref. [109]. Copyright 2020 Elsevier.

Various synthesis methods are available for the fabrication of VCNF hybrid materials. Strategies that involve the coating of nanofibers on a CC substrate, such as electrodeposition, sol dipping, and crystallization, utilize the porous architecture and high conductivity of CNFs for improved electrochemical performance. Alternatively, V_2O_5 nanocrystals can be intercalated into the CNFs for similar benefits. Electrospinning can be used to synthesize a VCNF material without any dependence on the CNF substrate. Instead, V_2O_5 and the carbon precursor can be electrospun into a fibrous product, allowing easily controllable composition and porosity.

4.2. Effects of Composition

The ratio between CNF and V_2O_5 plays a vital role in determining the electrochemical properties of a VCNF composite by altering its conductivity, porosity, and morphology. Kim et al. electrospun a solution with varying V_2O_5 loading and PA [113]. The mixture was subsequently heat treated and steamed under a nitrogen atmosphere at 800 °C for 1 h for carbon activation. The activated VCNF material had a fibrous structure with V_2O_5 agglomerations of 15 to 60 nm in diameter. The size of the agglomerations increased with increasing V_2O_5 loading owing to a change in the viscosity and conductivity of the

electrospun solution. The activation of the nanofibers increased the diameter from 108 to 200 nm. A lower V_2O_5 content increased the surface area of the composite with a maximum BET surface area of 1113.5 m^2 g^{-1} for activated VCNF-5 (5 wt% V_2O_5) because more carbon was accessible for activation by the steam. Activated VCNF-5 had the greatest C_{sp} (73.85 F g^{-1}) at a current density of 1 mA cm^{-2}, which decreased slightly to 58.02 F g^{-1} at a large current density of 20 mA cm^{-1} because of its low charge transfer resistance of 1.20 Ω. The symmetric supercapacitor with activated VCNF-5 electrodes had an energy density of 68.84 Wh kg^{-1} at a power density of 20,000 W kg^{-1}.

The composition of V_2O_5 and CNF can be altered by changing the duration of V_2O_5 exposure to the CNF substrate. Choudhury et al. submerged CNF paper in a solution of V_2O_5 and H_2O_2 for five and seven days [114]. The resulting free-standing paper electrode was dried at 100 °C for one day in an oven. Increased exposure to V_2O_5 resulted in more V_2O_5 crystallization on the CNFs. VCNF-5 (five days) had a V_2O_5 layer thickness of ~8 nm, whereas VCNF-7 (seven days) had a thickness of ~17 nm. Although both VCNF variants were limited by the incomplete oxidation of V_2O_5, VCNF-5 exhibited higher crystallinity and decreased water intercalation because of the shorter exposure to the V_2O_5 solution. VCNF-5 also had a larger BET surface area of 573.65 m^2 g^{-1} compared to the surface area of 442.16 m^2 g^{-1} for VCNF-7 because each nanofiber in VCNF-5 was thinner, resulting in larger pore sizes. VCNF-5 exhibited larger EDL characteristics than VCNF-7 because VCNF-5 had a higher amount of accessible carbon content. VCNF-5 yielded a C_{sp} of 227 F g^{-1} at a current density of 1 A g^{-1}. The C_{sp} decreased slightly to 154 F g^{-1} at a current density of 10 A g^{-1} because of its low 5.49 Ω charge transfer resistance. The VCNF-5 electrode had a maximum energy density of 63.6 Wh kg^{-1} at a power density of ~400 W kg^{-1}, which decreased to 18.8 Wh kg^{-1} at a power density of 4555 W kg^{-1}. Velayutham et al. examined the importance of electrodeposition duration on the composition of binderless VCNF electrodes [115]. Rope-like V_2O_5 with a pure orthorhombic crystal phase was evenly deposited onto the carbon fibers, resulting in V_2O_5 surface extrusions. The wrinkled surface from the V_2O_5 crystal growths resulted in a greater surface area for faradic redox reactions. Increasing the deposition time beyond 40 min resulted in a smoother surface because of the increased V_2O_5 growth, leading to a smaller surface area. VCNF-40 (40 min deposition) exhibited the highest areal capacitance of 394 mF cm^{-2} at a current density of 1 mA cm^{-2}. A 40 min deposition time had a large V_2O_5 composition for higher energy storage potential while creating a rough CNF coating for more surface redox reactions. At higher scan rates, VCNF-30 performed better than VCNF-40 with an areal capacitance of 143 mF cm^{-2} at a current density of 15 mA cm^{-2} because the higher carbon composition improved the electron mobility. An asymmetric supercapacitor with a VCNF-30 positive electrode yielded an energy density of 17.7 Wh kg^{-1} at a power density of 2728 W kg^{-1}.

The composition of VCNF composites can be altered by controlling the initial loading of V_2O_5 during synthesis or exposing a CNF substrate to V_2O_5 for different durations of time. Optimizing the composition of the VCNF material is essential for maximizing the faradic energy storage potential while maintaining high porosity and conductivity for the hybrid material.

4.3. Effects of Physical Treatment

The heat treatment of the VCNF composites improves their stability and increases V_2O_5 oxidation for better electrochemical performance. Chen et al. formed arrays of thin V_2O_5 nanosheets on a CC template via a hydrothermal synthesis route and subsequently annealed the composite at different temperatures in an H_2/argon atmosphere [116]. An increase in the annealing temperatures created more defects in the V_2O_5 crystal structure, and the non-uniform crystal structure resulted in high ion diffusion and fast redox reactions. The VCNF material contained amorphous V_2O_5 nanosheets with more metallic than semiconductor characteristics due to the oxygen defects. Figure 7 summarizes the effects of annealing on the formation of defects for enhanced electrochemical performance. The VCNF annealed at the highest temperature of 500 °C yielded the highest areal capacitance

of 554 mF cm^{-2} at a current density of 0.63 A g^{-1}. An asymmetric supercapacitor with the VCNF electrode exhibited an energy density of 161.8 μWh cm^{-2} at a power density of 500 μW cm^{-2}. You et al. found that annealing a VCNF composite at different temperatures affected the formation of V_2O_5 agglomeration [117]. A VCNF composite was synthesized via a hydrothermal process and subsequently annealed at 500 °C in a nitrogen atmosphere for different durations. V_2O_5 had a partial orthorhombic crystal structure owing to the incomplete oxidation of V_2O_5 during the hydrothermal process. Long annealing durations increased the size of the V_2O_5 agglomeration on the CNF surface. VCNF-24 (24 h annealing) contained a uniform distribution of V_2O_5 nanospheres coating the CNFs. However, an increase in the annealing time to 48 h resulted in large agglomerations of V_2O_5, decreasing the number of V_2O_5 active sites for surface redox reactions. With a homogeneous distribution of V_2O_5 crystals on the CNFs, VCNT-24 outperformed the other electrodes. VCNT-24 yielded a high C_{sp} of 475.5 F g^{-1} at a current density of 1 A g^{-1}, more than three times that of pristine V_2O_5. With many V_2O_5 nanospheres, most of the capacitance was attributed to ion diffusion instead of surface capacitance. A flexible asymmetric supercapacitor with a VCNT-24 positive electrode exhibited a volumetric energy density of 0.928 mWh cm^{-3} at a power density of 17.5 mW cm^{-3}.

Annealing the composite material also allowed the formation of doped VCNF composites. Guo et al. doped a VCNF composite with additional carbon to form carbon/V_2O_5 core/shell nanowires on a CNF substrate [118]. First, the VCNF electrode was fabricated via a hydrothermal technique. The VCNF was then dipped in a glucose solution and heat-treated at 500 °C under a nitrogen atmosphere, resulting in C-doped VCNF. The overall nanofibrous macrostructure of CC was preserved after heat treatment. The long CNFs were uniformly coated with thin strands of long V_2O_5 nanowires. The annealed glucose coated the thin V_2O_5 strands with an outer layer of carbon. The C-doped VCNF electrode exhibited an areal capacitance of 128.5 mF cm^{-2} at a scan rate of 10 mV s^{-1}, which decreased by 60% at a scan rate of 400 mV s^{-1}. The good rate capability was because of the additional carbon coating that increased the conductivity. The areal capacitance was 164.2 F cm^{-2} at a current density of 0.5 A cm^{-2}, with major contributions from both faradic and EDL characteristics. The charge transfer resistance (3.8 Ω) was low because of the conductive contact between the CNFs on the CC and the outer carbon layer on the V_2O_5 nanowires. The carbon coating also reduced vanadium dissolution, resulting in high cyclic stability, as indicated by a high 94.4% C_{sp} retention after 10,000 cycles at a high scan rate of 100 mV s^{-1}, which was significantly higher than that of pure V_2O_5 (13.3%). Sun et al. doped CNFs with nitrogen by first preparing a solution of CNF, pyrrole monomer, and ammonium persulfate and subsequently heating the mixture to 900 °C under argon atmosphere for 2 h, yielding an N-doped CNF (N-CNF) composite [119]. A V_2O_5 sol was added dropwise into the N-CNF material to yield a sol-gel that was subsequently cured for two days in an oven at 50 °C. The resulting aerogel was freeze dried and annealed at 350 °C in air, yielding a free-standing N-VCNF electrode. The N-CNFs were coated with a 20-nm-thick layer of V_2O_5. The V_2O_5 layer constituted a pure orthorhombic crystal phase, suggesting the complete oxidation of V^{4+} to V^{5+} due to the annealing procedure. The addition of the V_2O_5 layer to the N-CNFs decreased the BET surface area to 334.2 m^2 g^{-1}. The C_{sp} of N-VCNF was 595.1 F g^{-1} at a current density of 0.5 A g^{-1}, which was almost twice that of the non-doped VCNF. The nitrogen substitutions in the CNF lattice functioned as nucleation sites for additional V_2O_5 crystal growth, allowing a more uniform formation of the core/shell microstructure. The homogeneous V_2O_5 coating decreased the charge transfer resistance to 1.04 Ω. The N-VCNF electrode exhibited good reversibility with almost no change in C_{sp} after 10,000 cycles at a current density of 0.5 A g^{-1} and only a 3% decrease after 12,000 cycles because of the stable core/shell nanostructure. The symmetrical supercapacitor with N-VCNF electrodes had a maximum energy density of 82.65 Wh kg^{-1} at a power density of 250 W kg^{-1} which decreased to 26.83 Wh kg^{-1} at a power density of 5000 W kg^{-1}.

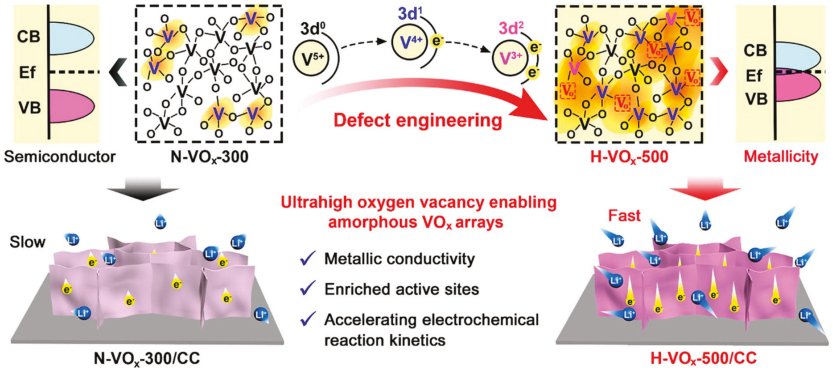

Figure 7. Schematic of the regulation of the V 3d band edge with high electrical conductivity by defect engineering and electrochemical advantages of the as-formed metallic amorphous VO_x nanosheet arrays. Reprinted with permission from Ref. [116]. Copyright 2021 Elsevier.

In addition to the heat treatment, other physical treatments can alter the morphology of the VCNF electrodes. Parmar et al. further modified the V_2O_5 crystals grown on carbon fiber surfaces using lasers to dehydrate amorphous V_2O_5 crystals [120]. A VCNF material with intercalated water molecules was synthesized via electrodeposition. Pristine V_2O_5 had an interstitial spacing of ~4.4 Å with an alternating VO_5–VO_5 pyramid structure, whereas hydrated V_2O_5 had a spacing that was two to three times greater than that of the atomic pyramids facing the same direction. De-intercalating water from the crystal structure of V_2O_5 decreased the interlayer gap to ~4 Å, reverting the atomic structure to the alternating pyramid form. Panigrahi et al. grew hair-like V_2O_5 crystals on AC felt but restrained one side of the AC felt to a glass slide [121]. Thus, V_2O_5 formation occurred only on the exposed side, allowing better electrical contact on the uncoated side. The acid-activated carbon felt acted as a porous template, resulting in a large BET surface area of 76.434 $m^2\ g^{-1}$ for better ion diffusion. The porous architecture of the hair-like V_2O_5 resulted in a greater pseudocapacitive contributions than EDL contributions, resulting in a high C_{sp} of 460.8 F g^{-1} at a current density of 2 A g^{-1}. The highly interconnected CNF structure increased the rate capability such that C_{sp} only decreased to 81.25% at 10 times the current density. The good electron mobility of the hybrid material was further supported by a low series resistance of 2.7 Ω and charge transfer resistance of 1.1 Ω. A symmetric supercapacitor with the VCNF electrode exhibited an energy density of 48.32 Wh kg^{-1} at a power density of 490 W kg^{-1}.

5. Other V_2O_5/Carbon Composites

Many studies have been conducted on other V_2O_5/carbon (VC) composites based on carbon moieties such as carbon quantum dots (CQDs) or bio-based carbon materials. As a stable, green, and conductive material, carbon can be added as supplementary materials to enhance the pseudocapacitive performance of V_2O_5 for supercapacitor applications [122]. These VC hybrid materials can be synthesized with carbon obtained from both inorganic and organic sources for diverse composite nanostructures. Herein, the effects of the synthesis process, V_2O_5/carbon composition, and physical treatment on the electrochemical performances of other carbon-based V_2O_5 composites are discussed. The morphology and electrochemical performances of other V_2O_5/carbon composite electrodes for supercapacitor applications reported in the literature are summarized in Table 4.

Table 4. V_2O_5 morphology and electrochemical performances of other V_2O_5/carbon composite electrodes for supercapacitor applications.

Morphology	Maximum C_{sp} (F g^{-1})	Cycling C_{sp} Retention (%)	Cycle Number	Energy Density (Wh kg^{-1})	Power Density (W kg^{-1})
Amorphous	120	89	10,000	-	-
Nanorods	300	87 *	5000 *	-	-
Nanoflowers	417	92.3	2250	47	224
Nanoflowers	-	88 *	25,000 *	33.4	670
Nanobelts	281	87	2000	-	-
Nanorods	313	81	4000	-	-
Amorphous	157.7	93 *	10,000 *	87.6	497
Nanosheets	487	84	2000	12.8	317
Nanobelts	406	13.8	100	245.7	396
Nanobelts	260	92	5000	-	-

* Cycling performance was determined using a two-electrode configuration.

5.1. Effects of Synthesis Method

The final nanostructure of the VC composite material depends significantly on the initial carbon precursor. Daubert et al. compared the morphologies of the VC electrodes synthesized using either microporous Supra 50 or mesoporous G60 carbon powders [123]. Both carbon powders were activated with concentrated acid and pasted on Ni foil with an acetylene black filler and PVDF binder. V_2O_5 was subsequently coated on the carbon-coated Ni foam using atomic layer deposition (ALD). The resulting hybrid material had a layer of amorphous V_2O_5 crystals covering the carbon surface. Additional V_2O_5 deposition cycles resulted in increasingly uneven V_2O_5 coatings. For mesoporous G60, the maximum C_{sp} was 540 F g^{-1} with 25 ALD cycles and 120 F g^{-1} for 75 ALD cycles. The high capacitance was due to the even V_2O_5 surface coating, thereby providing a large surface area for more ion adsorption. Because the micropores of Supra 50 matched the size of the atomic layer deposition precursor, the deposition process could not effectively coat Supra 50. Moreover, the coating process blocked the formation of micropores and decreased the number of active sites for faradic redox reactions. Thus, carefully selecting the carbon precursor is essential in maximizing the VC hybrid material's electrochemical performance.

Bio-based carbon sources have also been utilized for the synthesis of VC materials. Glucose is a promising carbon precursor for VC materials because it can act as an oxidizing agent at high temperatures and function as a conductive carbon additive [124]. Narayanan employed a facile hydrothermal synthesis method using V_2O_5 powder and glucose as precursors to yield VC [125]. The VC material was composed of V_2O_5 nanorods with glucose-derived carbon quantum dots (CQDs) uniformly scattered on the nanorod surface. Incomplete oxidation of V^{4+} to V^{5+} was observed due to partial reduction by glucose; however, the V_2O_5 rods still exhibited an orthorhombic crystal structure. The electrochemical performance of the VC material was tested using a three-electrode configuration with a CQD counter electrode and an Ag/AgCl reference electrode in 3 M KCl electrolyte. The C_{sp} of VC was 300 F g^{-1} at a current density of 0.5 A g^{-1}, which decreased slightly to 250 F g^{-1} at a current density of 2 A g^{-1}. The intercalated CQDs improved the conductivity of the device, as indicated by a low charge transfer resistance of 14.5 Ω. Moreover, the layered crystal structure of the V_2O_5 nanorods allowed better electron mobility via the attached CQDs. An asymmetric cell with a VC working electrode yielded a C_{sp} of 119 F g^{-1} at a current density of 1 A g^{-1}. The energy density was 60 Wh kg^{-1} at a current density of 1 A g^{-1}. The maximum power density was 4200 W kg^{-1} at a current density of 5 A g^{-1}. Balasubramanian et al. used dextran, a naturally occurring polysaccharide, as the carbon precursor [126]. Dextran was slowly added to a solution of V_2O_5 and H_2O_2 and stirred for 4 h to allow precipitation. The precipitate was subsequently annealed at 400 °C for 2 h to yield a VC hybrid material. The composite exhibited a flower-like macrostructure with urchin-like protrusions. The soft dextran decomposed and covered V_2O_5 in a sharp

urchin-like structure after annealing. The amorphous carbon layer increased the conductivity of VC and reduced V_2O_5 dissolution during charge/discharge. The flower-like architecture increased the surface area of the composite, resulting in more active sites for ion intercalation/de-intercalation, increasing the C_{sp} value to a maximum of 417 F g^{-1} at a current density of 0.5 A g^{-1}. The energy density of the VC composite was 47 Wh kg^{-1} at a power density of 224 W kg^{-1}.

The carbon sources used for VC synthesis can also be derived from once-living organisms. Ngom et al. fabricated VC electrodes from different strains of hibiscus flower: light red (LR), dark red (DR), and white (W) [127]. The flowers were dried in sunlight and crushed into powder. The powder was dissolved in DI water and filtered to remove the large organic residue. The V_2O_5 powder was added to the solution with H_2O_2 and subsequently heated in an autoclave for one day at 180 °C. The hibiscus-derived graphitic flakes were used as the template for V_2O_5 growth, resulting in the nucleation of flower-like V_2O_5 nanosheets. H_2O_2 promoted the exfoliation of the carbon flakes, resulting in a more porous structure that allowed better ion diffusion. DR-VC exhibited the largest orthorhombic crystal size, with the largest specific surface area of 3.3 m^2 g^{-1}. Due to the increased surface area and organized crystal structure, DR-VC exhibited the highest specific capacity of 99.1 mAh g^{-1}. An asymmetric supercapacitor with DR-VC and AC electrodes yielded an energy density of 33.4 Wh kg^{-1} at a power density of 670 W kg^{-1}. Mei et al. pyrolyzed bacterial cellulose to yield carbonized bacterial cellulose (CBC), which was reacted with V_2O_5 powder via a hydrothermal method [128]. The resulting composite comprised web-like carbon strands coated with thick V_2O_5 nanobelts with a width of ~70 nm and length of ~600 nm. The amorphous carbon strands formed a highly conductive web that prevented V_2O_5 aggregation. The orthorhombic crystal phase V_2O_5 supported the faradic redox reactions, and both EDL and pseudocapacitive characteristics contributed to charge storage. The C_{sp} was 198 F g^{-1} at a scan rate of 10 mV s^{-1}, which decreased to ~75 F g^{-1} at a scan rate of 200 mV s^{-1}. The CBC/V_2O_5 composite had a maximum C_{sp} of 281 F g^{-1} at a current density of 0.25 A g^{-1}, which decreased to 65 F g^{-1} at a current density of 5 A g^{-1}. The high C_{sp} at a lower current density was due to the increased pseudocapacitive contribution from V_2O_5. The CBC/V_2O_5 electrode exhibited a high cyclic stability with 97% C_{sp} retention after 1000 cycles and 87% of its initial C_{sp} after 2000 cycles at a high scan rate of 100 mV s^{-1} because of the highly conductive carbon network. The V_2O_5/CBC electrode was highly reversible because the carbon webs stabilized the V_2O_5 nanobelts.

The initial carbon precursor is vital for determining the final morphology of the VC composite. A carbon source with large pores provides a large surface area for V_2O_5 nucleation and more active sites for faradic redox reactions. Bio-derived carbon materials from various sources such as glucose, plants, and bacteria have organized carbon structures that can be carbonized and combined with V_2O_5 to improve conductivity and structural stability.

5.2. Effects of Composition

The ratio of the carbon component to V_2O_5 affects the synergetic balance between conductivity and charge capacity and can also alter the morphology of the resulting composite. Fleischmann et al. varied the ratio of V_2O_5 to carbon onion precursors for hydrothermal synthesis [129]. Figure 8 shows the SEM micrographs of V_2C_7 (2:7 V_2O_5 to carbon onion), V_3C_6 (3:6 V_2O_5 to carbon onion), and V_4C_5 (4:5 V_2O_5 to carbon onion). Fleischmann et al. also physically combined the carbon onions and V_2O_5 crystals after synthesizing each of these individually (C_5V_4-COMP).

Quasi-spherical V_2O_5 nanoflowers were grown at the nucleation sites on the carbon onions. Thus, an increase in the initial carbon content also increased the V_2O_5 growth. An increase in the carbon onion content resulted in a larger surface area for additional surface reactions. V_2C_7 (Figure 8A) was more spread out with smaller agglomerations than V_3C_6 (Figure 8B). Increasing V_2O_5 content to V_4C_5 (Figure 8C) produced larger V_2O_5 agglomerations, as indicated by the dark coloring. Physical mixing of carbon onions and

V_2O_5 resulted in large agglomerations of vanadium oxide and carbon onions (Figure 8D), which prevented the synergy between the two materials. The various VC composites were analyzed using a two-electrode configuration with a PTFE-bound AC counter electrode and a VC working electrode with $LiClO_4$ in acetonitrile electrolyte. V_3C_6 outperformed the other three composites because of well-integrated conductive carbon with a large surface area and sizable V_2O_5 growth. Zhang et al. reported an increase in conductivity with an increase in the carbon content [130]. V_2O_5 was combined with mesoporous carbon hollow spheres (MCHSs) in different ratios to form a suspension that was rigorously stirred and subsequently freeze dried to yield a macroporous VC composite. The hybrid material comprised a web-like V_2O_5 maze with sporadic MCHS nanospheres anchored to the webs. Increasing the weight percentage of MCHSs from 33% (VC-33) to 67% (VC-67) increased the number of spherical carbon agglomerations. VC-33 had sparse carbon nanospheres, whereas VC-67 formed grape-like bundles on the V_2O_5 webs. VC-50 (50 wt% MCHS) contained a uniform spread of graphitic carbon nanospheres on the V_2O_5 web. A low carbon content reduced agglomerations that allowed ion adsorption into V_2O_5. However, an increase in the carbon content increased the conductivity of the material. Thus, VC-50 with a uniform distribution of carbon nanospheres exhibited the highest C_{sp} of 313 F g^{-1} at a current density of 0.25 A g^{-1}. The macroporous web structure decreased the stress due to repeated ion insertion/de-insertion, resulting in an increase in cyclability from 43% for bare V_2O_5 to 81% for VC-50 after 4000 cycles at a current density of 5 A g^{-1}.

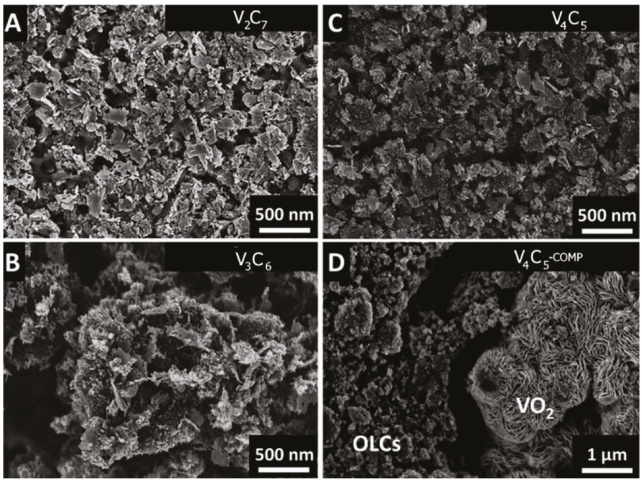

Figure 8. SEM micrographs of (**A**) V_2C_7, (**B**) V_3C_6, (**C**) V_4C_5, and (**D**) V_4C_5-COMP. Reprinted with permission from Ref. [129]. Copyright 2017 Royal Society of Chemistry.

Control of the carbon to V_2O_5 ratio can also change the porosity of the VC material, thereby altering the ion diffusion capability and number of active sites for faradic redox reactions. Zhu et al. determined the effects of V_2O_5 loading on the porosity and performance of a VC electrode [131]. The VC composite was synthesized using a liquid-phase impregnation technique, yielding a hierarchically porous VC material. The VC material had a macroporous carbon frame with V_2O_5 intercalated through the pores. At a low 17.6 wt% of V_2O_5 (VC-18), the pores in the carbon were small and tightly packed, resulting in a BET surface area of 622 m^2 g^{-1}. At a high V_2O_5 loading of 52 wt% (VC-52), the sheets were covered with large micropores with tiny gaps between the layers, resulting in a smaller BET surface area of 487 m^2 g^{-1}. The VC material with a 38.7 wt% V_2O_5 (VC-39) had the greatest BET surface area of 645 m^2 g^{-1} because of its larger pores. Thus, VC-39 yielded the highest C_{sp} of 492.1 F g^{-1} at a scan rate of 5 mV s^{-1} because of the numerous active

sites provided by the micropores and ease of ion diffusion through the high volume of macropores. The C_{sp} value decreased slightly to ~400 F g^{-1} at a scan rate of 100 mV s^{-1}, indicating good rate capability because the amorphous carbon dispersion enabled good electron mobility with low series and charge transfer resistances of 0.54 and 1.05 Ω, respectively. A symmetric supercapacitor assembled with VC-39 had an energy density of 87.6 Wh kg^{-1} at a power density of 497 W kg^{-1} that decreased to 20.4 Wh kg^{-1} at a power density of 3272 W kg^{-1}. Saravanakumar et al. controlled the ratio of N-doped mesoporous carbon (N-MPC) nanospheres to V_2O_5 to obtain a superior supercapacitor electrode with maximum porosity [132]. The VC material comprised V_2O_5 flakes anchored onto the spherical N-MPC. These V_2O_5 covered carbon spheres formed agglomerations with other VC nanospheres. The hydrothermal method oxidized V_2O_5 to form pure orthorhombic crystals, while reducing the carbon into a graphitic crystal phase. A low N-MPC loading of 10% (VC-10) resulted in many uncoated carbon spheres due to V_2O_5 agglomeration. This decreased the accessibility to V_2O_5 for surface ion intercalation. At 5 wt% N-MPC, the carbon nanospheres were homogeneously covered to maximize the pseudocapacitive capacity of V_2O_5 with an optimal surface area of 8.77 m^2 g^{-1}. The addition of 15 wt% N-MPC resulted in nanospheres that were completely coated by V_2O_5, decreasing the accessibility to N-MPC for a suboptimal surface area of 10.35 m^2 g^{-1}. At 10 wt% N-MPC, the carbon nanospheres were effectively covered to maximize the pseudocapacitive capacity of V_2O_5 with an optimal surface area of 8.77 m^2 g^{-1}. VC-10 exhibited the highest C_{sp} of 487 F g^{-1} at a current density of 0.5 A g^{-1}, which was 34% higher than that of bare V_2O_5. The increase in capacitance was caused by a significant increase in surface area from 5.64 to 8.77 m^2 g^{-1} and increased conductivity because of N-MPC. An asymmetric supercapacitor with the VC-10 electrode had an energy density of 12.8 Wh kg^1 at a power density of 317 W kg^{-1}. Kudo et al. added varying amounts of acetylene black to a V_2O_5 sol to create a suspension with acetone surfactant [133]. The Ni foam was subsequently submerged in the suspension and heated at 120 °C for 5 h. The resulting VC was comprised of spherical carbon cores with an uneven V_2O_5 outer layer coating. These nanospheres formed bumpy agglomerations, yielding a BET surface area of 30 m^2 g^{-1}. With a large carbon content (30 wt% acetylene black), the VC exhibited good rate capability, maintaining a charge capacity of 340 mAh g^{-1} at a high current density of 54 A g^{-1}. The VC electrode maintained 100% of its capacity even after 2000 cycles at a charge rate of 20 C because the porosity of the VC material allowed unobstructed Li ion insertion/de-insertion. The maximum energy density was 80 Wh kg^{-1} at a power density of 26,000 W kg^{-1} with an average working voltage of 2 V, which rapidly deteriorated with repeated cycles. The average energy density was 15–20 Wh kg^{-1}. Peng et al. followed a similar synthesis route using Ketjen black powder and a V_2O_5 sol [134]. Ni foam was used as a template for VC coating. The VC material comprised V_2O_5 nanosheets covered with carbon nanospheres uniformly distributed on the hydrated V_2O_5 surface. An increase in the initial Ketjen black loading increased the final surface area of VC, with a maximum BET surface area of 264.72 m^2 g^{-1} for VC_1 (1 g Ketjen black loading). $VC_{0.5}$ (0.5 g Ketjen black loading) exhibited the highest C_{sp} of 1634 F g^{-1} at a current density of 5 mA cm^{-2} because of effective synergy between carbon for fast electron mobility and V_2O_5 nanosheets for high pseudocapacitance. A symmetric supercapacitor with the $VC_{0.5}$ electrodes had an energy density of 56.83 Wh kg^{-1} at a power density of 303 W kg^{-1}, which decreased slightly to 30.86 Wh kg^{-1} at a power density of 2433 W kg^{-1}. Despite not having a lower surface area and containing less conductive carbon content than VC_1, $VC_{0.5}$ retained a good rate capability while sustaining a high energy storage capacity.

5.3. Effects of Physical Treatment

Heat treatment of a VC composite can alter the morphology of the hybrid material [135]. Kim et al. synthesized VC by heating a mixture of vanadium trichloride, terephthalic acid, and DI water in an autoclave at 200 °C for four days. Subsequently, the VC powder was calcinated at 400 °C for 6 h in an argon atmosphere [136]. Prior to calcination, the VC exhibited a rectangular structure with large crystals that were 1–4 μm in length.

The heat-treated VC had a highly orthorhombic crystal structure with thinner nanorods that were 0.5–3 μm in length. A 4–6-nm-thick layer of graphitic carbon coated the V_2O_5 nanorods. The annealed VC exhibited an initial discharge rate of 286 mAh g^{-1} at 0.1 C, which was close to the theoretical limit of 294 mAh g^{-1}. Zhang et al. also analyzed the effects of annealing temperature and duration on the morphology of the VC material [137]. The VC composite was synthesized via a hydrothermal method and was further heat treated in a muffle furnace at varying temperatures of 300 to 500 °C for different durations in air. The hydrothermal synthesis yielded smooth prism-like monoclinic V_2O_5 protrusions with amorphous carbon nanospheres embedded between the V_2O_5 crystals. Calcination under air resulted in porous V_2O_5 nanoparticles with uneven surfaces due to combustion reactions with air. At a low calcination temperature of 300 °C, many carbon nanospheres remained scattered within the V_2O_5 nanorods, whereas no nanospheres were present in the VC that was heat treated at 500 °C. The presence of carbon nanospheres indicated the incomplete oxidation of V_2O_5, resulting in a lower C_{sp} of 151 F g^{-1} at a current density of 1 A g^{-1} for VC-300 compared to 367 F g^{-1} for VC-500. An increase in the calcination duration up to 8 h increased the C_{sp} of the VC composite because V_2O_5 had more time to nucleate. However, further increasing the calcination time to 12 h decreased the C_{sp} because the agglomeration of V_2O_5 resulted in limited surface ion diffusion.

Heat treatment can also promote the oxidation of V^{4+} to V^{5+} for a more crystalline V_2O_5. Zeiger et al. fabricated vanadium carbide/carbide core/shell composites (VC-C) by reacting vanadium carbide with $NiCl_2$ in a graphite crucible at 700 °C in chlorine gas followed by calcination at 450 °C in synthetic air to promote further oxidation of V^{4+} [138]. The resulting VC-C nanostructure was composed of a V_2O_5 core and carbide-derived carbon shell. Increasing the calcination temperature to 600 °C increased V_2O_5 oxidation but burned off most of the carbon shell. VC-C-90 (90% theoretically converted) exhibited the highest specific capacity of 415 mAh g^{-1} at a current density of 0.01 A g^{-1} with almost 100% coulombic efficiency. The partial conversion of the V_2O_5 core from vanadium carbide provided a large storage capacity, while the outer carbon shell increased the conductivity of the composite. A decrease in the annealing temperature to decrease the carbide shell burnoff while effectively oxidizing the vanadium carbide core was essential for maximum yield. An asymmetric supercapacitor setup with the VC-C-90 negative electrode yielded an energy density of 90 Wh kg^{-1} for charging and 50 Wh kg^{-1} for discharging at a power density of 166 W kg^{-1}. The energy density decreased to 27 Wh kg^{-1} at a high-power density of 6700 W kg^{-1}, retaining 80% of its energy density after 10,000 cycles at a current density of 1 A g^{-1}. Narayanan et al. annealed glucose-based VC at temperatures of 250–400 °C in air [139]. The composite contained thin V_2O_5 nanorods with CQDs anchored to the nanorods; the V_2O_5 nanorods also had a thin carbon coating. Increasing the annealing temperature decreased the thickness of the V_2O_5 nanorods and promoted V_2O_5 oxidation using oxygen from the atmosphere, resulting in more orthorhombic V_2O_5 crystals. VC annealed at 250 °C (VC250) exhibited the highest C_{sp} of 260 F g^{-1} at a current density of 1 A g^{-1}. The layered V_2O_5 crystal structure improved electron propagation, and the high surface area of the VC material increased the surface adsorption. VC250 also exhibited the lowest charge transfer resistance of 11.4 Ω. The VC250 electrode exhibited high cycling capability, retaining 92% of its C_{sp} after 5000 cycles at a current density of 5 A g^{-1} because the carbon coating decreased vanadium dissolution. The imperfections in the V_2O_5 lattice caused by V^{4+} enhanced the Li-ion intercalation capability and decreased V_2O_5 dissolution.

The heat treatment of VC composites can change the morphology of the composite and promote the oxidation of vanadium oxide to V_2O_5. Thus, controlling the annealing temperature and duration allows the formation of partially oxidized VC materials for increased stability and surface ion intercalation. However, excessive annealing temperatures and durations disintegrate the carbon content, resulting in a low conductivity. Therefore, it is essential to optimize both the annealing temperature and duration.

6. Conclusions

The synthesis of various metal oxide and carbon composites as supercapacitor electrode materials has attracted significant attention because of the increasing demand for high energy and power-dense energy storage devices used in portable electronics and electric vehicles. The development of stable vanadium oxide-based electrode materials has been extensively investigated due to the high energy storage potential and natural abundance of vanadium oxide. Common carbon nanostructures such as rGO, CNTs, CNFs, and CQDs have been combined with V_2O_5 to yield high-performance supercapacitor electrode materials.

V_2O_5/rGO composites can be synthesized using many methods, including hydro/solvothermal, sol-gel, filtration, and chemical deposition methods. These strategies often yield a lamellar rGO nanostructure with V_2O_5 intercalated between the nanosheets. V_2O_5/CNT hybrid materials are frequently synthesized as vertically aligned nanotubes infiltrated by V_2O_5 crystals or long nanotubes with V_2O_5 growth using various synthesis methods. The CNTs have the advantage of facile functionalization with hydroxyl or carboxyl groups to increase V_2O_5 nucleation and conductivity. The V_2O_5/CNF composites offer the unique advantage of having a highly stable 3D macrostructure that can be used as a template for the fabrication of free-standing and binderless electrodes. Using electrodeposition, crystallization, sol-dipping, or electrospinning methods, a fibrous structure with a CNF/V_2O_5 core/shell nanostructure or V_2O_5 crystals intercalated into web-like CNFs can be synthesized. Other V_2O_5/carbon materials such as CQD-based and amorphous carbon-flake-based composites can be easily synthesized via facile strategies such as the hydro/solvothermal method. Carbon precursors can be sourced from both artificially synthesized and bio-based carbonaceous materials.

In most cases, an increase in the V_2O_5 content in the V_2O_5/carbon hybrid materials increases the total energy storage potential because of faradic redox reactions. However, a high V_2O_5 content results in agglomerations that hinder surface ion adsorption. An increase in the carbon content leads to increased EDL contributions and conductivity for improved rate capability and cyclic stability. However, the low energy storage potential of carbon nanomaterials limits high carbon content for energy-dense electrode materials. An optimal balance of V_2O_5 and carbon can increase the surface area and porosity beyond that of solely the carbon material alone, enabling more activation sites for greater ion intercalation/deintercalation. The synergy between V_2O_5 and carbon can also inhibit vanadium ion dissolution, resulting in a more stable charge/discharge. Physical treatment via annealing, calcination, and laser treatment can promote vanadium oxide oxidation to V_2O_5, altering the crystallinity of the hybrid material for improved electrochemical performance.

This review discusses the effects of different synthesis methods, V_2O_5/carbon compositions, and physical treatment strategies on the morphology and electrochemical performances of V_2O_5/carbon composites. This review is expected to serve as a catalyst for further research for the development of an ideal supercapacitor electrode material with high power and energy properties. Furthermore, light, solid-state supercapacitors based on V_2O_5/carbon nanomaterials have potential applications for portable, stretchable and wearable electronics. Continued research efforts in this area could make great contribution to developing supercapacitor technologies.

Author Contributions: Conceptualization, A.K., J.H.K. and R.P.; methodology, A.K., R.P.; writing—original draft preparation, A.K.; writing—review and editing, A.K., G.K., J.H.K. and R.P. All authors have read and agreed to the published version of the manuscript.

Funding: This work was supported by the National Research Foundation (NRF) of South Korea, funded by the Ministry of Science and ICT, Republic of Korea (NRF-2017R1D1A1B06028030 and NRF-2018M3A7B4071535).

Data Availability Statement: Not applicable.

Conflicts of Interest: The authors declare no conflict of interest.

References

1. Najib, S.; Erdem, E. Current progress achieved in novel materials for supercapacitor electrodes: Mini review. *Nanoscale Adv.* **2019**, *1*, 2817–2827. [CrossRef]
2. Zhang, S.; Pan, N. Supercapacitors Performance Evaluation. *Adv. Energy Mater.* **2015**, *5*, 1401401. [CrossRef]
3. Simon, P.; Gogotsi, Y.; Dunn, B. Where do batteries end and supercapacitors begin? *Science* **2014**, *343*, 1210–1211. [CrossRef]
4. Lin, T.; Chen, I.W.; Liu, F.; Yang, C.; Bi, H.; Xu, F.; Huang, F. Nitrogen-doped mesoporous carbon of extraordinary capacitance for electrochemical energy storage. *Science* **2015**, *350*, 1508–1513. [CrossRef]
5. Vlad, A.; Singh, N.; Rolland, J.; Melinte, S.; Ajayan, P.M.; Gohy, J.F. Hybrid supercapacitor-battery materials for fast electrochemical charge storage. *Sci. Rep.* **2014**, *4*, 4315. [CrossRef]
6. Suganya, B.; Maruthamuthu, S.; Chandrasekaran, J.; Saravanakumar, B.; Vijayakumar, E.; Marnadu, R.; Al-Enizi, A.M.; Ubaidullah, M. Design of zinc vanadate ($Zn_3V_2O_8$)/nitrogen doped multiwall carbon nanotubes (N-MWCNT) towards supercapacitor electrode applications. *J. Electroanal. Chem.* **2021**, *881*, 114936. [CrossRef]
7. Patel, R.; Inamdar, A.I.; Hou, B.; Cha, S.N.; Ansari, A.T.; Gunjakar, J.L.; Im, H.; Kim, H. Solvothermal synthesis of high-performance Ni-Co layered double hydroxide nanofoam electrode for electrochemical energy storage. *Curr. Appl. Phys.* **2017**, *17*, 501–506. [CrossRef]
8. Zhu, J.; Chen, S.; Zhou, H.; Wang, X. Fabrication of a low defect density graphene-nickel hydroxide nanosheet hybrid with enhanced electrochemical performance. *Nano Res.* **2012**, *5*, 11–19. [CrossRef]
9. Nandi, D.; Mohan, V.B.; Bhowmick, A.K.; Bhattacharyya, D. Metal/metal oxide decorated graphene synthesis and application as supercapacitor: A review. *J. Mater. Sci.* **2020**, *55*, 6375–6400. [CrossRef]
10. Mathis, T.S.; Kurra, N.; Wang, X.; Pinto, D.; Simon, P.; Gogotsi, Y. Energy Storage Data Reporting in Perspective—Guidelines for Interpreting the Performance of Electrochemical Energy Storage Systems. *Adv. Energy Mater.* **2019**, *9*, 1902007. [CrossRef]
11. Iro, Z.S.; Subramani, C.; Dash, S.S. Electrochemical science: A brief review on electrode materials for supercapacitor. *Int. J. Electrochem. Sci.* **2016**, *11*, 10628–10643. [CrossRef]
12. Majumdar, D.; Mandal, M.; Bhattacharya, S.K. V_2O_5 and its Carbon-Based Nanocomposites for Supercapacitor Applications. *ChemElectroChem* **2019**, *6*, 1623–1648. [CrossRef]
13. Borenstein, A.; Hanna, O.; Attias, R.; Luski, S.; Brousse, T.; Aurbach, D. Carbon-based composite materials for supercapacitor electrodes: A review. *J. Mater. Chem. A* **2017**, *5*, 12653–12672. [CrossRef]
14. Ho, M.Y.; Khiew, P.S.; Isa, D.; Tan, T.K.; Chiu, W.S.; Chia, C.H. A review of metal oxide composite electrode materials for electrochemical capacitors. *Nano* **2014**, *9*, 1430002. [CrossRef]
15. Zhu, J.; Cao, L.; Wu, Y.; Gong, Y.; Liu, Z.; Hoster, H.E.; Zhang, Y.; Zhang, S.; Yang, S.; Yan, Q.; et al. Building 3D structures of vanadium pentoxide nanosheets and application as electrodes in supercapacitors. *Nano Lett.* **2013**, *13*, 5408–5413. [CrossRef] [PubMed]
16. Qian, A.; Pang, Y.; Wang, G.; Hao, Y.; Liu, Y.; Shi, H.; Chung, C.H.; Du, Z.; Cheng, F. Pseudocapacitive Charge Storage in MXene-$V_2O_5$for Asymmetric Flexible Energy Storage Devices. *ACS Appl. Mater. Interfaces* **2020**, *12*, 54791–54797. [CrossRef] [PubMed]
17. Zhi, M.; Xiang, C.; Li, J.; Li, M.; Wu, N. Nanostructured carbon-metal oxide composite electrodes for supercapacitors: A review. *Nanoscale* **2013**, *5*, 72–88. [CrossRef] [PubMed]
18. Qu, Q.; Zhu, Y.; Gao, X.; Wu, Y. Core-Shell Structure of Polypyrrole Grown on V_2O_5 Nanoribbon as High Performance Anode Material for Supercapacitors. *Adv. Energy Mater.* **2012**, *2*, 950–955. [CrossRef]
19. Augustyn, V.; Simon, P.; Dunn, B. Pseudocapacitive oxide materials for high-rate electrochemical energy storage. *Energy Environ. Sci.* **2014**, *7*, 1597–1614. [CrossRef]
20. Chalker, C.J.; An, H.; Zavala, J.; Parija, A.; Banerjee, S.; Lutkenhaus, J.L.; Batteas, J.D. Fabrication and Electrochemical Performance of Structured Mesoscale Open Shell V_2O_5 Networks. *Langmuir* **2017**, *33*, 5975–5981. [CrossRef]
21. Gerbaldi, C.; Destro, M.; Nair, J.R.; Ferrari, S.; Quinzeni, I.; Quartarone, E. High-rate V_2O_5-based Li-ion thin film polymer cell with outstanding long-term cyclability. *Nano Energy* **2013**, *2*, 1279–1286. [CrossRef]
22. Mjejri, I.; Manceriu, L.M.; Gaudon, M.; Rougier, A.; Sediri, F. Nano-vanadium pentoxide films for electrochromic displays. *Solid State Ionics* **2016**, *292*, 8–14. [CrossRef]
23. Liu, Y.; Jia, C.; Wan, Z.; Weng, X.; Xie, J.; Deng, L. Electrochemical and electrochromic properties of novel nanoporous NiO/V_2O_5 hybrid film. *Sol. Energy Mater. Sol. Cells* **2015**, *132*, 467–475. [CrossRef]
24. Karade, S.S.; Lalwani, S.; Eum, J.H.; Kim, H. Coin cell fabricated symmetric supercapacitor device of two-steps synthesized V_2O_5 Nanorods. *J. Electroanal. Chem.* **2020**, *864*, 114080. [CrossRef]
25. Zhang, H.; Han, X.; Gan, R.; Guo, Z.; Ni, Y.; Zhang, L. A facile biotemplate-assisted synthesis of mesoporous V_2O_5 microtubules for high performance asymmetric supercapacitors. *Appl. Surf. Sci.* **2020**, *511*, 145527. [CrossRef]
26. Li, H.; Tian, H.; Chang, T.H.; Zhang, J.; Koh, S.N.; Wang, X.; Wang, C.H.; Chen, P.Y. High-Purity V_2O_5 Nanosheets Synthesized from Gasification Waste: Flexible Energy Storage Devices and Environmental Assessment. *ACS Sustain. Chem. Eng.* **2019**, *7*, 12474–12484. [CrossRef]
27. Zhang, S.; Chen, S.; Luo, Y.; Yan, B.; Gu, Y.; Yang, F.; Cao, Y. Large-scale preparation of solution-processable one-dimensional V_2O_5 nanobelts with ultrahigh aspect ratio for bifunctional multicolor electrochromic and supercapacitor applications. *J. Alloys Compd.* **2020**, *842*, 155882. [CrossRef]

28. Lee, H.; Kumbhar, V.S.; Lee, J.; Choi, Y.; Lee, K. Highly reversible crystal transformation of anodized porous V_2O_5 nanostructures for wide potential window high-performance supercapacitors. *Electrochim. Acta* **2020**, *334*, 135618. [CrossRef]
29. Uma Shankar, V.; Govindarajan, D.; Christuraj, P.; Salethraj, M.J.; Johanson, F.J.; Raja, M.D. Enhanced the electrochemical properties of Ni doped V_2O_5 as a electrode material for supercapacitor applications. In *Materials Today: Proceedings*; Elsevier BV: Amsterdam, The Netherlands, 2020.
30. Hsiao, Y.S.; Chang-Jian, C.W.; Syu, W.L.; Yen, S.C.; Huang, J.H.; Weng, H.C.; Lu, C.Z.; Hsu, S.C. Enhanced electrochromic performance of carbon-coated V_2O_5 derived from a metal–organic framework. *Appl. Surf. Sci.* **2021**, *542*, 148498. [CrossRef]
31. Ke, Q.; Wang, J. Graphene-based materials for supercapacitor electrodes–A review. *J. Mater.* **2016**, *2*, 37–54. [CrossRef]
32. Thalji, M.R.; Ali, G.A.M.; Lee, S.P.; Chong, K.F. Solvothermal Synthesis of Reduced Graphene Oxide as Electrode Material for Supercapacitor Application. *Chem. Adv. Mater.* **2019**, *4*, 17–26.
33. Yang, Z.; Tian, J.; Yin, Z.; Cui, C.; Qian, W.; Wei, F. Carbon nanotube- and graphene-based nanomaterials and applications in high-voltage supercapacitor: A review. *Carbon* **2019**, *141*, 467–480. [CrossRef]
34. Faraji, S.; Ani, F.N. The development supercapacitor from activated carbon by electroless plating–A review. *Renew. Sustain. Energy Rev.* **2015**, *42*, 823–834. [CrossRef]
35. Cottineau, T.; Toupin, M.; Delahaye, T.; Brousse, T.; Bélanger, D. Nanostructured transition metal oxides for aqueous hybrid electrochemical supercapacitors. *Appl. Phys. A Mater. Sci. Process.* **2006**, *82*, 599–606. [CrossRef]
36. Patel, R.; Park, J.T.; Patel, M.; Dash, J.K.; Gowd, E.B.; Karpoormath, R.; Mishra, A.; Kwak, J.; Kim, J.H. Transition-metal-based layered double hydroxides tailored for energy conversion and storage. *J. Mater. Chem. A* **2017**, *6*, 12–29. [CrossRef]
37. Noked, M.; Avraham, E.; Bohadana, Y.; Soffer, A.; Aurbach, D. Development of anion stereoselective, activated carbon molecular sieve electrodes prepared by chemical vapor deposition. *J. Phys. Chem. C* **2009**, *113*, 7316–7321. [CrossRef]
38. Xu, Y.; Lin, Z.; Zhong, X.; Huang, X.; Weiss, N.O.; Huang, Y.; Duan, X. Holey graphene frameworks for highly efficient capacitive energy storage. *Nat. Commun.* **2014**, *5*, 4554. [CrossRef]
39. Cheng, J.; Gu, G.; Guan, Q.; Razal, J.M.; Wang, Z.; Li, X.; Wang, B. Synthesis of a porous sheet-like V_2O_5-CNT nanocomposite using an ice-templating "bricks-and-mortar" assembly approach as a high-capacity, long cyclelife cathode material for lithium-ion batteries. *J. Mater. Chem. A* **2016**, *4*, 2729–2737. [CrossRef]
40. Mohd Abdah, M.A.A.; Azman, N.H.N.; Kulandaivalu, S.; Sulaiman, Y. Review of the use of transition-metal-oxide and conducting polymer-based fibres for high-performance supercapacitors. *Mater. Des.* **2020**, *186*, 108199. [CrossRef]
41. González, A.; Goikolea, E.; Barrena, J.A.; Mysyk, R. Review on supercapacitors: Technologies and materials. *Renew. Sustain. Energy Rev.* **2016**, *58*, 1189–1206. [CrossRef]
42. Delbari, S.A.; Ghadimi, L.S.; Hadi, R.; Farhoudian, S.; Nedaei, M.; Babapoor, A.; Sabahi Namini, A.; Van Le, Q.; Shokouhimehr, M.; Shahedi Asl, M.; et al. Transition metal oxide-based electrode materials for flexible supercapacitors: A review. *J. Alloys Compd.* **2021**, *857*, 158281. [CrossRef]
43. Kumar, K.S.; Choudhary, N.; Jung, Y.; Thomas, J. Recent Advances in Two-Dimensional Nanomaterials for Supercapacitor Electrode Applications. *ACS Energy Lett.* **2018**, *3*, 482–495. [CrossRef]
44. Raghavendra, K.V.G.; Vinoth, R.; Zeb, K.; Muralee Gopi, C.V.V.; Sambasivam, S.; Kummara, M.R.; Obaidat, I.M.; Kim, H.J. An intuitive review of supercapacitors with recent progress and novel device applications. *J. Energy Storage* **2020**, *31*, 101652. [CrossRef]
45. Lokhande, V.C.; Lokhande, A.C.; Lokhande, C.D.; Kim, J.H.; Ji, T. Supercapacitive composite metal oxide electrodes formed with carbon, metal oxides and conducting polymers. *J. Alloys Compd.* **2016**, *682*, 381–403. [CrossRef]
46. Dubey, R.; Guruviah, V. Review of carbon-based electrode materials for supercapacitor energy storage. *Ionics* **2019**, *25*, 1419–1445. [CrossRef]
47. Fisher, R.A.; Watt, M.R.; Jud Ready, W. Functionalized Carbon Nanotube Supercapacitor Electrodes: A Review on Pseudocapacitive Materials. *ECS J. Solid State Sci. Technol.* **2013**, *2*, M3170–M3177. [CrossRef]
48. Bose, S.; Kuila, T.; Mishra, A.K.; Rajasekar, R.; Kim, N.H.; Lee, J.H. Carbon-based nanostructured materials and their composites as supercapacitor electrodes. *J. Mater. Chem.* **2012**, *22*, 767–784. [CrossRef]
49. Perera, S.D.; Liyanage, A.D.; Nijem, N.; Ferraris, J.P.; Chabal, Y.J.; Balkus, K.J. Vanadium oxide nanowire-Graphene binder free nanocomposite paper electrodes for supercapacitors: A facile green approach. *J. Power Sources* **2013**, *230*, 130–137. [CrossRef]
50. Ding, B.; Guo, D.; Wang, Y.; Wu, X.; Fan, Z. Functionalized graphene nanosheets decorated on carbon nanotubes networks for high performance supercapacitors. *J. Power Sources* **2018**, *398*, 113–119. [CrossRef]
51. Ding, B.; Wu, X. Transition metal oxides anchored on graphene/carbon nanotubes conductive network as both the negative and positive electrodes for asymmetric supercapacitor. *J. Alloys Compd.* **2020**, *842*, 155838. [CrossRef]
52. Chem, J.M.; Tarcan, R.; Todor-boer, O.; Petrovai, I.; Leordean, C. Reduced graphene oxide today. *J. Mater. Chem. C* **2019**, *8*, 1198–1224.
53. Patil, S.J.; Chodankar, N.R.; Han, Y.K.; Lee, D.W. Carbon alternative pseudocapacitive V_2O_5 nanobricks and δ-MnO_2 nanoflakes@α-MnO_2 nanowires hetero-phase for high-energy pseudocapacitor. *J. Power Sources* **2020**, *453*, 227766. [CrossRef]
54. Pandey, G.P.; Liu, T.; Brown, E.; Yang, Y.; Li, Y.; Sun, X.S.; Fang, Y.; Li, J. Mesoporous Hybrids of Reduced Graphene Oxide and Vanadium Pentoxide for Enhanced Performance in Lithium-Ion Batteries and Electrochemical Capacitors. *ACS Appl. Mater. Interfaces* **2016**, *8*, 9200–9210. [CrossRef] [PubMed]

55. Ahirrao, D.J.; Mohanapriya, K.; Jha, N. V_2O_5 nanowires-graphene composite as an outstanding electrode material for high electrochemical performance and long-cycle-life supercapacitor. *Mater. Res. Bull.* **2018**, *108*, 73–82. [CrossRef]
56. Geng, Z.D.; Wang, Y.-P. Synthesis of $V_2O_5{\cdot}1.6H_2O$/graphene composite and its application in supercapacitors. *J. Solid State Electrochem.* **2015**, *19*, 3131–3138. [CrossRef]
57. Sun, W.; Gao, G.; Du, Y.; Zhang, K.; Wu, G. A facile strategy for fabricating hierarchical nanocomposites of V_2O_5 nanowire arrays on a three-dimensional N-doped graphene aerogel with a synergistic effect for supercapacitors. *J. Mater. Chem. A* **2018**, *6*, 9938–9947. [CrossRef]
58. Nagaraju, D.H.; Wang, Q.; Beaujuge, P.; Alshareef, H.N. Two-dimensional heterostructures of V_2O_5 and reduced graphene oxide as electrodes for high energy density asymmetric supercapacitors. *J. Mater. Chem. A* **2014**, *2*, 17146–17152. [CrossRef]
59. Sahu, V.; Goel, S.; Kumar Tomar, A.; Singh, G.; Sharma, R.K. Graphene Nanoribbons @ Vanadium Oxide Nanostrips for Supercapacitive Energy Storage. *Electrochim. Acta* **2017**, *230*, 255–264. [CrossRef]
60. Zhang, H.; Xie, A.; Wang, C.; Wang, H.; Shen, Y.; Tian, X. Bifunctional reduced graphene oxide/V_2O_5 composite hydrogel: Fabrication, high performance as electromagnetic wave absorbent and supercapacitor. *ChemPhysChem* **2014**, *15*, 366–373. [CrossRef]
61. Tabatabai Yazdi, S.; Mousavi, M.; Khorrami, G.H. Effect of Co-doping in V_2O_5 nanoparticles synthesized via a gelatin-based sol-gel method. *Mater. Today Commun.* **2021**, *26*, 101955. [CrossRef]
62. Yilmaz, G.; Lu, X.; Ho, G.W. Cross-linker mediated formation of sulfur-functionalized V_2O_5/graphene aerogels and their enhanced pseudocapacitive performance. *Nanoscale* **2017**, *9*, 802–811. [CrossRef] [PubMed]
63. Kiruthiga, R.; Nithya, C.; Karvembu, R.; Venkata Rami Reddy, B. Reduced Graphene Oxide Embedded V_2O_5 Nanorods and Porous Honey Carbon as High Performance Electrodes for Hybrid Sodium-ion Supercapacitors. *Electrochim. Acta* **2017**, *256*, 221–231.
64. Wang, L.; Shu, T.; Guo, S.; Lu, Y.; Li, M.; Nzabahimana, J.; Hu, X. Fabricating strongly coupled V_2O_5@PEDOT nanobelts/graphene hybrid films with high areal capacitance and facile transferability for transparent solid-state supercapacitors. *Energy Storage Mater.* **2020**, *27*, 150–158. [CrossRef]
65. Liu, H.; Tang, Y.; Wang, C.; Xu, Z.; Yang, C.; Huang, T.; Zhang, F.; Wu, D.; Feng, X. A Lyotropic Liquid-Crystal-Based Assembly Avenue toward Highly Oriented Vanadium Pentoxide/Graphene Films for Flexible Energy Storage. *Adv. Funct. Mater.* **2017**, *27*, 1606269. [CrossRef]
66. Foo, C.Y.; Sumboja, A.; Tan, D.J.H.; Wang, J.; Lee, P.S. Flexible and highly scalable V_2O_5-rGO electrodes in an organic electrolyte for supercapacitor devices. *Adv. Energy Mater.* **2014**, *4*, 1400236. [CrossRef]
67. Van Hoa, N.; Quyen, T.T.H.; Nghia, N.H.; Van Hieu, N.; Shim, J.J. In situ growth of flower-like V_2O_5 arrays on graphene@nickel foam as high-performance electrode for supercapacitors. *J. Alloys Compd.* **2017**, *702*, 693–699. [CrossRef]
68. Wang, A.Y.; Chaudhary, M.; Lin, T.W. Enhancing the stability and capacitance of vanadium oxide nanoribbons/3D-graphene binder-free electrode by using $VOSO_4$ as redox-active electrolyte. *Chem. Eng. J.* **2019**, *355*, 830–839. [CrossRef]
69. Korkmaz, S.; Tezel, F.M.; Kariper, A. Synthesis and Characterization of GO/V_2O_5 Thin Film Supercapacitor. *Synth. Met.* **2018**, *242*, 37–48. [CrossRef]
70. Li, G.; Wang, X.; Hassan, F.M.; Li, M.; Batmaz, R.; Xiao, X.; Yu, A. Vanadium Pentoxide Nanorods Anchored to and Wrapped with Graphene Nanosheets for High-Power Asymmetric Supercapacitors. *ChemElectroChem* **2015**, *2*, 1264–1269. [CrossRef]
71. Saravanakumar, B.; Purushothaman, K.K.; Muralidharan, G. Fabrication of two-dimensional reduced graphene oxide supported V_2O_5 networks and their application in supercapacitors. *Mater. Chem. Phys.* **2016**, *170*, 266–275. [CrossRef]
72. Ramadoss, A.; Saravanakumar, B.; Kim, S.J. Vanadium Pentoxide/Reduced Graphene Oxide Composite as an Efficient Electrode Material for High-Performance Supercapacitors and Self-Powered Systems. *Energy Technol.* **2015**, *3*, 913–924. [CrossRef]
73. Lee, M.; Balasingam, S.K.; Jeong, H.Y.; Hong, W.G.; Lee, H.B.R.; Kim, B.H.; Jun, Y. One-step hydrothermal synthesis of Graphene decorated V_2O_5 nanobelts for enhanced electrochemical energy storage. *Sci. Rep.* **2015**, *5*, srep08151. [CrossRef] [PubMed]
74. Fu, M.; Zhuang, Q.; Zhu, Z.; Zhang, Z.; Chen, W.; Liu, Q.; Yu, H. Facile synthesis of V_2O_5/graphene composites as advanced electrode materials in supercapacitors. *J. Alloys Compd.* **2021**, *862*, 158006. [CrossRef]
75. Yao, L.; Zhang, C.; Hu, N.; Zhang, L.; Zhou, Z.; Zhang, Y. Three-dimensional skeleton networks of reduced graphene oxide nanosheets/vanadium pentoxide nanobelts hybrid for high-performance supercapacitors. *Electrochim. Acta* **2019**, *295*, 14–21. [CrossRef]
76. Choudhury, A.; Bonso, J.S.; Wunch, M.; Yang, K.S.; Ferraris, J.P.; Yang, D.J. In-situ synthesis of vanadium pentoxide nanofibre/exfoliated graphene nanohybrid and its supercapacitor applications. *J. Power Sources* **2015**, *287*, 283–290. [CrossRef]
77. Deng, L.; Gao, Y.; Ma, Z.; Fan, G. Free-standing graphene/vanadium oxide composite as binder-free electrode for asymmetrical supercapacitor. *J. Colloid Interface Sci.* **2017**, *505*, 556–565. [CrossRef]
78. Ndiaye, N.M.; Ngom, B.D.; Sylla, N.F.; Masikhwa, T.M.; Madito, M.J.; Momodu, D.; Ntsoane, T.; Manyala, N. Three dimensional vanadium pentoxide/graphene foam composite as positive electrode for high performance asymmetric electrochemical supercapacitor. *J. Colloid Interface Sci.* **2018**, *532*, 395–406. [CrossRef]
79. Li, M.; Sun, G.; Yin, P.; Ruan, C.; Ai, K. Controlling the formation of rodlike V_2O_5 nanocrystals on reduced graphene oxide for high-performance supercapacitors. *ACS Appl. Mater. Interfaces* **2013**, *5*, 11462–11470. [CrossRef]
80. Liu, Z.; Zhang, H.; Yang, Q.; Chen, Y. Graphene/V_2O_5 hybrid electrode for an asymmetric supercapacitor with high energy density in an organic electrolyte. *Electrochim. Acta* **2018**, *287*, 149–157. [CrossRef]

81. Thangappan, R.; Kalaiselvam, S.; Elayaperumal, A.; Jayavel, R. Synthesis of graphene oxide/vanadium pentoxide composite nanofibers by electrospinning for supercapacitor applications. *Solid State Ionics* **2014**, *268*, 321–325. [CrossRef]
82. Lee, S.M.; Park, Y.J.; Van Lam, D.; Kim, J.H.; Lee, K. Effects of annealing on electrochemical performance in graphene/V_2O_5 supercapacitor. *Appl. Surf. Sci.* **2020**, *512*, 145626. [CrossRef]
83. Lazauskas, A.; Marcinauskas, L.; Andrulevicius, M. Modification of Graphene Oxide/$V_2O_5{\cdot}nH_2O$ Nanocomposite Films via Direct Laser Irradiation. *ACS Appl. Mater. Interfaces* **2020**, *12*, 18877–18884. [CrossRef] [PubMed]
84. Zhu, S.; Ni, J.; Li, Y. Carbon nanotube-based electrodes for flexible supercapacitors. *Nano Res.* **2020**, *13*, 1825–1841. [CrossRef]
85. Kumar, S.; Saeed, G.; Zhu, L.; Hui, K.N.; Kim, N.H.; Lee, J.H. 0D to 3D carbon-based networks combined with pseudocapacitive electrode material for high energy density supercapacitor: A review. *Chem. Eng. J.* **2021**, *403*, 126352. [CrossRef]
86. Lin, Z.; Yan, X.; Lang, J.; Wang, R.; Kong, L. Bin Adjusting electrode initial potential to obtain high-performance asymmetric supercapacitor based on porous vanadium pentoxide nanotubes and activated carbon nanorods. *J. Power Sources* **2015**, *279*, 358–364. [CrossRef]
87. Wallar, C.J.; Poon, R.; Zhitomirsky, I. High Areal Capacitance of V_2O_3–Carbon Nanotube Electrodes. *J. Electrochem. Soc.* **2017**, *164*, A3620–A3627. [CrossRef]
88. Jiang, H.; Cai, X.; Qian, Y.; Zhang, C.; Zhou, L.; Liu, W.; Li, B.; Lai, L.; Huang, W. V_2O_5 embedded in vertically aligned carbon nanotube arrays as free-standing electrodes for flexible supercapacitors. *J. Mater. Chem. A* **2017**, *5*, 23727–23736. [CrossRef]
89. Wang, X.; Zuo, C.; Jia, L.; Liu, Q.; Guo, X.; Jing, X.; Wang, J. Synthesis of sandwich-like vanadium pentoxide/carbon nanotubes composites for high performance supercapacitor electrodes. *J. Alloys Compd.* **2017**, *708*, 134–140. [CrossRef]
90. Jampani, P.H.; Velikokhatnyi, O.; Kadakia, K.; Hong, D.H.; Damle, S.S.; Poston, J.A.; Manivannan, A.; Kumta, P.N. High energy density titanium doped-vanadium oxide-vertically aligned CNT composite electrodes for supercapacitor applications. *J. Mater. Chem. A* **2015**, *3*, 8413–8432. [CrossRef]
91. Shakir, I.; Ali, Z.; Bae, J.; Park, J.; Kang, D.J. Layer by layer assembly of ultrathin V_2O_5 anchored MWCNTs and graphene on textile fabrics for fabrication of high energy density flexible supercapacitor electrodes. *Nanoscale* **2014**, *6*, 4125–4130. [CrossRef]
92. Hu, T.; Liu, Y.; Zhang, Y.; Chen, M.; Zheng, J.; Tang, J.; Meng, C. 3D hierarchical porous $V_3O_7{\cdot}H_2O$ nanobelts/CNT/reduced graphene oxide integrated composite with synergistic effect for supercapacitors with high capacitance and long cycling life. *J. Colloid Interface Sci.* **2018**, *531*, 382–393. [CrossRef]
93. Mtz-enriquez, A.I.; Gomez-solis, C.; Oliva, A.I.; Zakhidov, A.; Martinez, P.M.; Garcia, C.R.; Herrera-ramirez, A.; Oliva, J. Enhancing the voltage and discharge times of graphene supercapacitors depositing a CNT/V_2O_5 layer on their electrodes. *Mater. Chem. Phys.* **2020**, *244*, 122698. [CrossRef]
94. Saravanakumar, B.; Purushothaman, K.K.; Muralidharan, G. V_2O_5/functionalized MWCNT hybrid nanocomposite: The fabrication and its enhanced supercapacitive performance. *RSC Adv.* **2014**, *4*, 37437–37445. [CrossRef]
95. Pandit, B.; Dubal, D.P.; Gómez-Romero, P.; Kale, B.B.; Sankapal, B.R. V_2O_5 encapsulated MWCNTs in 2D surface architecture: Complete solid-state bendable highly stabilized energy efficient supercapacitor device. *Sci. Rep.* **2017**, *7*, srep43430. [CrossRef]
96. Guo, K.; Li, Y.; Li, C.; Yu, N.; Li, H. Compact self-standing layered film assembled by V_2O_5 nH_2O/CNTs 2D/1D composites for high volumetric capacitance flexible supercapacitors. *Sci. China Mater.* **2019**, *62*, 936–946. [CrossRef]
97. Yilmaz, G.; Guo, C.X.; Lu, X. High-Performance Solid-State Supercapacitors Based on V_2O_5/Carbon Nanotube Composites. *ChemElectroChem* **2016**, *3*, 158–164. [CrossRef]
98. Wu, J.; Gao, X.; Yu, H.; Ding, T.; Yan, Y.; Yao, B.; Yao, X.; Chen, D.; Liu, M.; Huang, L. A Scalable Free-Standing V_2O_5/CNT Film Electrode for Supercapacitors with a Wide Operation Voltage (1.6 V) in an Aqueous Electrolyte. *Adv. Funct. Mater.* **2016**, *26*, 6114–6120. [CrossRef]
99. Perera, S.D.; Patel, B.; Nijem, N.; Roodenko, K.; Seitz, O.; Ferraris, J.P.; Chabal, Y.J.; Balkus, K.J. Vanadium oxide nanowire-carbon nanotube binder-free flexible electrodes for supercapacitors. *Adv. Energy Mater.* **2011**, *1*, 936–945. [CrossRef]
100. Sathiya, M.; Prakash, A.S.; Ramesha, K.; Tarascon, J.M.; Shukla, A.K. V_2O_5-anchored carbon nanotubes for enhanced electrochemical energy storage. *J. Am. Chem. Soc.* **2011**, *133*, 16291–16299. [CrossRef] [PubMed]
101. Sun, G.; Ren, H.; Shi, Z.; Zhang, L.; Wang, Z.; Zhan, K.; Yan, Y.; Yang, J.; Zhao, B. V_2O_5/vertically-aligned carbon nanotubes as negative electrode for asymmetric supercapacitor in neutral aqueous electrolyte. *J. Colloid Interface Sci.* **2021**, *588*, 847–856. [CrossRef] [PubMed]
102. Wang, Q.; Zou, Y.; Xiang, C.; Chu, H.; Zhang, H.; Xu, F.; Sun, L.; Tang, C. High-performance supercapacitor based on V_2O_5/carbon nanotubes-super activated carbon ternary composite. *Ceram. Int.* **2016**, *42*, 12129–12135. [CrossRef]
103. Shakir, I.; Choi, J.H.; Shahid, M.; Shahid, S.A.; Rana, U.A.; Sarfraz, M.; Kang, D.J. Ultra-thin and uniform coating of vanadium oxide on multiwall carbon nanotubes through solution based approach for high-performance electrochemical supercapacitors. *Electrochim. Acta* **2013**, *111*, 400–404. [CrossRef]
104. Zhou, X.; Wang, Y.; Gong, C.; Liu, B.; Wei, G. Production, structural design, functional control, and broad applications of carbon nanofiber-based nanomaterials: A comprehensive review. *Chem. Eng. J.* **2020**, *402*, 126189. [CrossRef]
105. Adam, A.A.; Dennis, J.O.; Al-Hadeethi, Y.; Mkawi, E.M.; Abdulkadir, B.A.; Usman, F.; Hassan, Y.M.; Wadi, I.A.; Sani, M. State of the art and new directions on electrospun lignin/cellulose nanofibers for supercapacitor application: A systematic literature review. *Polymers* **2020**, *12*, 2884. [CrossRef] [PubMed]
106. Song, Y.; Liu, T.Y.; Yao, B.; Kou, T.Y.; Feng, D.Y.; Liu, X.X.; Li, Y. Amorphous Mixed-Valence Vanadium Oxide/Exfoliated Carbon Cloth Structure Shows a Record High Cycling Stability. *Small* **2017**, *13*, 1700067. [CrossRef]

107. Zhou, X.; Chen, Q.; Wang, A.; Xu, J.; Wu, S.; Shen, J. Bamboo-like Composites of V_2O_5/Polyindole and Activated Carbon Cloth as Electrodes for All-Solid-State Flexible Asymmetric Supercapacitors. *ACS Appl. Mater. Interfaces* **2016**, *8*, 3776–3783. [CrossRef]
108. Azadian, F.; Rastogi, A.C. V_2O_5 Film Embedded Carbon Fiber Paper Synthesized by Sol Process as Highly Pseudocapacitive Electrode for Energy Storage. *ECS Meet. Abstr.* **2020**, *97*, 25.
109. Zhou, X.; Gao, X.; Liu, M.; Wang, C.; Chu, F. Synthesis of 3D phosphorus doped graphene foam in carbon cloth to support V_2O_5/$CoMoS_4$ hybrid for flexible all-solid-state asymmetry supercapacitors. *J. Power Sources* **2020**, *453*, 227902. [CrossRef]
110. Xiao, Y.; Xu, Y.; Zhang, K.; Tang, X.; Huang, J.; Yuan, K.; Chen, Y. Coaxial electrospun free-standing and mechanical stable hierarchical porous carbon nanofiber membrane for flexible supercapacitors. *Carbon* **2020**, *160*, 80–87. [CrossRef]
111. Wang, H.; Niu, H.; Wang, H.; Wang, W.; Jin, X.; Wang, H.; Zhou, H.; Lin, T. Micro-meso porous structured carbon nanofibers with ultra-high surface area and large supercapacitor electrode capacitance. *J. Power Sources* **2021**, *482*, 228986. [CrossRef]
112. Kim, B.H.; Kim, C.H.; Yang, K.S.; Rahy, A.; Yang, D.J. Electrospun vanadium pentoxide/carbon nanofiber composites for supercapacitor electrodes. *Electrochim. Acta* **2012**, *83*, 335–340. [CrossRef]
113. Kim, B.H.; Yang, K.S.; Yang, D.J. Electrochemical behavior of activated carbon nanofiber-vanadium pentoxide composites for double-layer capacitors. *Electrochim. Acta* **2013**, *109*, 859–865. [CrossRef]
114. Choudhury, A.; Kim, J.; Yang, K.; Yang, D. Electrochimica Acta Facile synthesis of self-standing binder-free vanadium pentoxide-carbon nano fi ber composites for high-performance supercapacitors. *Electrochim. Acta* **2016**, *213*, 400–407. [CrossRef]
115. Velayutham, R.; Manikandan, R.; Raj, C.J.; Kale, A.M.; Kaya, C.; Palanisamy, K.; Kim, B.C. Electrodeposition of vanadium pentoxide on carbon fiber cloth as a binder-free electrode for high-performance asymmetric supercapacitor. *J. Alloys Compd.* **2021**, *863*, 158332. [CrossRef]
116. Chen, S.; Jiang, H.; Cheng, Q.; Wang, G.; Petr, S.; Li, C. Amorphous vanadium oxides with metallic character for asymmetric supercapacitors. *Chem. Eng. J.* **2021**, *403*, 126380. [CrossRef]
117. You, M.; Zhang, W.; Yan, X.; Jiang, H.; Miao, J.; Li, Y.; Zhou, W.; Zhu, Y.; Cheng, X. V_2O_5 nanosheets assembled on 3D carbon fiber felt as a free-standing electrode for flexible asymmetric supercapacitor with remarkable energy density. *Ceram. Int.* **2021**, *47*, 3337–3345. [CrossRef]
118. Guo, Y.; Li, J.; Chen, M.; Gao, G. Facile synthesis of vanadium pentoxide@carbon core-shell nanowires for high-performance supercapacitors. *J. Power Sources* **2015**, *273*, 804–809. [CrossRef]
119. Sun, W.; Gao, G.; Zhang, K.; Liu, Y.; Wu, G. Self-assembled 3D N-CNFs/V_2O_5 aerogels with core/shell nanostructures through vacancies control and seeds growth as an outstanding supercapacitor electrode material. *Carbon* **2018**, *132*, 667–677. [CrossRef]
120. Parmar, R.; Neto, D.D.F.; Matsubara, E.Y.; Gunnella, R.; Rosolen, J.M. Electrochemical synthesis and structural characterization of nanostructured $V_2O_5.nH_2O$ on CNTs coated/uncoated carbon felt composite. *Nano-Struct. Nano-Objects* **2020**, *24*, 100538. [CrossRef]
121. Panigrahi, K.; Howli, P.; Chattopadhyay, K.K. 3D network of V_2O_5 for flexible symmetric supercapacitor. *Electrochim. Acta* **2020**, *337*, 135701. [CrossRef]
122. Zhu, Z.; Xu, Z. The rational design of biomass-derived carbon materials towards next-generation energy storage: A review. *Renew. Sustain. Energy Rev.* **2020**, *134*, 110308. [CrossRef]
123. Daubert, J.S.; Lewis, N.P.; Gotsch, H.N.; Mundy, J.Z.; Monroe, D.N.; Dickey, E.C.; Losego, M.D.; Parsons, G.N. Effect of Meso- and Micro-Porosity in Carbon Electrodes on Atomic Layer Deposition of Pseudocapacitive V_2O_5 for High Performance Supercapacitors. *Chem. Mater.* **2015**, *27*, 6524–6534. [CrossRef]
124. Zhang, Y.; Zheng, J.; Wang, Q.; Zhang, S.; Hu, T.; Meng, C. One-step hydrothermal preparation of $(NH_4)2V_3O_8$/carbon composites and conversion to porous V_2O_5 nanoparticles as supercapacitor electrode with excellent pseudocapacitive capability. *Appl. Surf. Sci.* **2017**, *423*, 728–742. [CrossRef]
125. Narayanan, R. Single step hydrothermal synthesis of carbon nanodot decorated V_2O_5 nanobelts as hybrid conducting material for supercapacitor application. *J. Solid State Chem.* **2017**, *253*, 103–112. [CrossRef]
126. Sethuraman, B.; Kamatchi Kamaraj, P. Carbon Coated Flowery V_2O_5 Nanostructure as Novel Electrode Material for High Performance Supercapacitors. *Electrochim. Acta* **2015**, *186*, 285–291.
127. Ngom, B.D.; Ndiaye, N.M.; Sylla, N.F.; Mutuma, B.K.; Manyala, N. Sustainable development of vanadium pentoxide carbon composites derived from: Hibiscus sabdariffa family for application in supercapacitors. *Sustain. Energy Fuels* **2020**, *4*, 4814–4830. [CrossRef]
128. Mei, J.; Ma, Y.; Pei, C. V_2O_5 nanobelt-carbonized bacterial cellulose composite with enhanced electrochemical performance for aqueous supercapacitors. *J. Solid State Electrochem.* **2017**, *21*, 573–580. [CrossRef]
129. Fleischmann, S.; Zeiger, M.; Jäckel, N.; Krüner, B.; Lemkova, V.; Widmaier, M.; Presser, V. Tuning pseudocapacitive and battery-like lithium intercalation in vanadium dioxide/carbon onion hybrids for asymmetric supercapacitor anodes. *J. Mater. Chem. A* **2017**, *5*, 13039–13051. [CrossRef]
130. Zhang, G.; Ren, L.; Hu, D.; Zhang, S.; Gu, H. Fabrication of mesoporous carbon hollow spheres intercalated three-dimensional network structure V_2O_5 nanosheets with enhanced electrochemical performance. *J. Alloys Compd.* **2019**, *781*, 407–414. [CrossRef]
131. Zhu, C.; Hu, D.; Liu, Z. Interconnected three-dimensionally hierarchical heterostructures with homogeneously-dispersed V_2O_5 nanocrystals and carbon for high performance supercapacitor electrodes. *Electrochim. Acta* **2017**, *229*, 155–165. [CrossRef]
132. Saravanakumar, B.; Purushothaman, K.K.; Muralidharan, G. V_2O_5/nitrogen enriched mesoporous carbon spheres nanocomposite as supercapacitor electrode. *Microporous Mesoporous Mater.* **2018**, *258*, 83–94. [CrossRef]

133. Kudo, T.; Ikeda, Y.; Watanabe, T.; Hibino, M.; Miyayama, M.; Abe, H.; Kajita, K. Amorphous V_2O_5/carbon composites as electrochemical supercapacitor electrodes. *Solid State Ionics* **2002**, *152–153*, 833–841. [CrossRef]
134. Peng, T.; Wang, J.; Liu, Q.; Liu, J.; Wang, P. Mesoporous V_2O_5/Ketjin black nanocomposites for all-solid-state symmetric supercapacitors. *CrystEngComm* **2015**, *17*, 1673–1679. [CrossRef]
135. Xing, L.L.; Zhao, G.G.; Huang, K.J.; Wu, X. A yolk-shell V_2O_5 structure assembled from ultrathin nanosheets and coralline-shaped carbon as advanced electrodes for a high-performance asymmetric supercapacitor. *Dalt. Trans.* **2018**, *47*, 2256–2265. [CrossRef] [PubMed]
136. Kim, T.; Kim, H.; You, T.S.; Kim, J. Carbon-coated V_2O_5 nanoparticles derived from metal-organic frameworks as a cathode material for rechargeable lithium-ion batteries. *J. Alloys Compd.* **2017**, *727*, 522–530. [CrossRef]
137. Zhang, Y.; Zheng, J.; Wang, Q.; Hu, T.; Meng, C. Hydrothermal synthesis of vanadium dioxides/carbon composites and their transformation to surface-uneven V_2O_5 nanoparticles with high electrochemical properties. *RSC Adv.* **2016**, *6*, 93741–93752. [CrossRef]
138. Zeiger, M.; Ariyanto, T.; Krüner, B.; Peter, N.J.; Fleischmann, S.; Etzold, B.J.M.; Presser, V. Vanadium pentoxide/carbide-derived carbon core-shell hybrid particles for high performance electrochemical energy storage. *J. Mater. Chem. A* **2016**, *4*, 18899–18909. [CrossRef]
139. Narayanan, R.; Dewan, A.; Chakraborty, D. Complimentary effects of annealing temperature on optimal tuning of functionalized carbon-V_2O_5 hybrid nanobelts for targeted dual applications in electrochromic and supercapacitor devices. *RSC Adv.* **2018**, *8*, 8596–8606. [CrossRef]

nanomaterials

MDPI

Article

Li_2ZrO_3-Coated Monocrystalline $LiAl_{0.06}Mn_{1.94}O_4$ Particles as Cathode Materials for Lithium-Ion Batteries

Chunliu Li [1,2,†], Banglei Zhao [3,†], Junfeng Yang [1,4,*], Linchao Zhang [1,*], Qianfeng Fang [1,2] and Xianping Wang [1,*]

[1] Key Laboratory of Materials Physics, Institute of Solid State Physics, HFIPS, Chinese Academy of Sciences, Hefei 230031, China; lcliu@southmn.com (C.L.); qffang@issp.ac.cn (Q.F.)
[2] Science Island Branch, Graduate School of University of Science and Technology of China, Hefei 230026, China
[3] School of Management Science and Engineering, Anhui University of Finance and Economics, Bengbu 233030, China; zbl1234@mail.ustc.edu.cn
[4] Lu'an Branch, Anhui Institute of Innovation for Industrial Technology, Lu'an 237100, China
* Correspondence: jfyang@issp.ac.cn (J.Y.); lczhang@issp.ac.cn (L.Z.); xpwang@issp.ac.cn (X.W.)
† These authors contributed equally to this work.

Abstract: Li_2ZrO_3-coated and Al-doped micro-sized monocrystalline $LiMn_2O_4$ powder is synthesized through solid-state reaction, and the electrochemical performance is investigated as cathode materials for lithium-ion batteries. It is found that Li_2ZrO_3-coated $LiAl_{0.06}Mn_{1.94}O_4$ delivers a discharge capacity of 110.90 $mAhg^{-1}$ with 94% capacity retention after 200 cycles at room temperature and a discharge capacity of 104.4 $mAhg^{-1}$ with a capacity retention of 87.8% after 100 cycles at 55 °C. Moreover, Li_2ZrO_3-coated $LiAl_{0.06}Mn_{1.94}O_4$ could retain 87.5% of its initial capacity at 5C rate. This superior cycling and rate performance can be greatly contributed to the synergistic effect of Al-doping and Li_2ZrO_3-coating.

Keywords: lithium zirconium oxide; lithium manganese oxide; monocrystallite; cathode materials; lithium-ion batteries

Citation: Li, C.; Zhao, B.; Yang, J.; Zhang, L.; Fang, Q.; Wang, X. Li_2ZrO_3-Coated Monocrystalline $LiAl_{0.06}Mn_{1.94}O_4$ Particles as Cathode Materials for Lithium-Ion Batteries. *Nanomaterials* **2021**, *11*, 3223. https://doi.org/10.3390/nano11123223

Academic Editors: Sophie Tingry, Marc Cretin and Zhenghua Tang

Received: 21 October 2021
Accepted: 22 November 2021
Published: 27 November 2021

1. Introduction

Spinel $LiMn_2O_4$ (LMO) has been recognized as one of the promising cathode materials for the lithium-ion batteries due to the environmental compatibility, low cost, and high specific capacity [1–4]. However, the poor rate performance caused by the low Li^+ conductivity and the rapid capacity fading induced by the Jahn–Teller distortion have severely impeded its commercial applications [5–7].

Nanocrystallization has been proved to be an effective way to improve the electrochemical kinetics by decreasing the diffusion path of Li^+ and enlarging contact area between electrode and electrolyte [8,9]. Nevertheless, the enlarged specific surface area will inevitably increase the side reactions. Although the ion-doping technique could alter the electrochemical properties to some extent, the capacity decay still occurs due to the Mn ions dissolution, especially under high temperatures [10–13]. Alternatively, surface coating is often adopted to improve the cycling performance by inhibiting the side reactions between LMO and electrolyte [14,15]. Unfortunately, the coating strategy cannot improve the transport kinetics of Li^+. Therefore, the combination of ion-doping and coating should be considered to make full advantages.

Except for the side reactions, the nanocrystallization will lead to flawed crystallinity which is harmful for the Li^+ ion transport, however LMO has a unique three-dimensional tunnel structure in which the Li^+ could transfer through the 8a-16c-8a pathway [16]. Therefore, the monocrystal size should not be the determining factor to restrain the Li^+ transport. Moreover, the micron-sized monocrystalline LMO modified with ion-doping and surface coating may simultaneously decrease the contact area with electrolyte and improve the electrochemical performance.

In this work, we propose combined tactics to fabricate micro-sized monocrystalline $LiAl_{0.06}Mn_{1.94}O_4$ particles with Li_3BO_3 as sintering additive. The resultant Li_2ZrO_3-coated and Al-doped micro-sized monocrystalline $LiMn_2O_4$ powder was adopted as cathode materials for lithium-ion batteries, and their electrochemical performance was investigated in detail.

2. Materials and Methods

The Li_2ZrO_3-coated micro-sized monocrystalline $LiAl_{0.06}Mn_{1.94}O_4$ was prepared with solid-state sintering. First, Li_2CO_3 (Aldrich, St. Louis, MI, USA), Al_2O_3 (Aldrich) and Mn_3O_4 (EMD, Aldrich) were ball-milled with the molar ratio of Li:Al:Mn = 1.06:0.06:1.94. The excess Li_2CO_3 was used to compensate the lithium loss during heat treating. Then, the mixture was sintered at 450 °C for 5 h. After that, the pre-sintered mixture was ball-milled with Li_2CO_3, H_3BO_3, and ZrO_2. Then, the mixture was sintered at 780 °C for 18 h. Li_3BO_3 and Li_2ZrO_3 could be synthesized as the following Equations (1) and (2).

$$H_3BO_3 + Li_2CO_3 \rightarrow Li_3BO_3 \quad (1)$$

$$ZrO_2 + Li_2CO_3 \rightarrow Li_2ZrO_3 \quad (2)$$

The detailed ingredient of the micron-sized monocrystalline $LiAl_{0.06}Mn_{1.94}O_4$ was listed in Table 1. As a comparison, the $LiMn_2O_4$ samples without Al-doping, Li_3BO_3 additive or Li_2ZrO_3-coating were also prepared through the same sintering process.

Table 1. Specific component of the micron-sized monocrystalline $LiMn_2O_4$ samples (* No addition).

Samples	Composition		
	$LiMn_2O_4$	**Li_3BO_3**	**Li_2ZrO_3**
LMO	$LiMn_2O_4$	*	*
LMO-B	$LiMn_2O_4$	1 mol%	*
LAMO-B	Li $Al_{0.06}Mn_{1.94}O_4$	1 mol%	*
LAMO-B-Zr1	Li $Al_{0.06}Mn_{1.94}O_4$	1 mol%	1 mol%
LAMO-B-Zr2	Li $Al_{0.06}Mn_{1.94}O_4$	1 mol%	2 mol%
LAMO-B-Zr3	Li $Al_{0.06}Mn_{1.94}O_4$	1 mol%	3 mol%
LAMO-B-Zr4	Li $Al_{0.06}Mn_{1.94}O_4$	1 mol%	4 mol%

Structural characterization of the samples was analyzed by X-ray diffraction (XRD, Rigaku SmartLab diffractometer) with Cu Kα radiation in the 2θ range of 10–70°. The particle size, surface morphology, and elemental composition were observed by scanning electron microscopy (SEM, Hitachi S-3400N) equipped with an energy dispersive spectrometer (EDS, Oxford 7426). The microstructure was detected with transmission electron microscopy (TEM, FEI Tecnai G2 F20). The samples were smashed before the TEM analysis.

Synthesized $LiMn_2O_4$ particle was mixed with carbon black and polyvinylidene fluoride (PVDF) with the mass ratio of 90:5:5 in N-methyl pyrrolidinone (NMP). Then, the slurry was coated on the aluminum foil and vacuum-dried at 100 °C. The electrode laminate was roll-pressed and punched to be discs with a diameter of 14 mm. The loading density of active material is approximately 5–8 mg cm^{-2}. The electrolyte was 1 M $LiPF_6$ in dimethyl carbonate (DMC)/ethyl carbonate (EMC)/ethylene carbonate (EC) (1:1:1, *v*/*v*/*v*). The 2032-type coin cells using Li metal as anode were prepared in an argon-filled glove box and tested in the voltage range of 3.0–4.3 V at several rates (1C = 148 $mAhg^{-1}$) on a battery test system (Neware). The cells were charged/discharged at 0.2C for 3 times first and then cycled at 0.5C for 200 times at 25 °C. Meanwhile, same cells were charged/discharged at 0.2C for 3 times and at 0.5C for 100 times at 55 °C, successively. Moreover, to evaluate the

rate performance, the cells were also charged at 0.5C and discharged at 0.5C, 1C, 2C, 3C, and 5C, respectively.

The electrochemical impedance spectroscopy (EIS) of the cells was performed on electrochemical workstation (CHI600E) with the frequency range of 10^5 to 10^{-2} Hz. The EIS tests were performed after the 1st and 200th cycle, respectively.

3. Results and Discussion

3.1. Li_3BO_3 Additive Promote the Grain Growth

The XRD patterns of the samples are shown in Figure S1. All the diffraction peaks match well with $LiMn_2O_4$ (JCPDF 35-0782). It proves that the Al-doping Li_3BO_3 additive or the Li_2ZrO_3-coating has no effect on the spinel cubic structure with the spatial group Fd3m. While focusing on the effect of the Li_3BO_3 additive, it could be found that the full width at half maximum (FWHM) of the LMO-B is much broader than that of the LMO (Table S1). As shown in Figure 1a, the FWHM of the main peaks of LMO are 0.188 (111), 0.152 (311), 0.155 (222), 0.163 (400), 0.151 (331), and 0.176 (511), respectively. While the corresponding values for the LMO-B are 0.071, 0.061, 0.053, 0.064, 0.066, and 0.073, respectively. It is suggested that the grain size of the monocrystal $LiMn_2O_4$ has grown up with the help of the Li_3BO_3 additive. Meanwhile, the conclusion is verified by the morphological observation (Figure 1b,c). The grain size of the LMO is less than 2 μm, while that of the LMO-B sample is approximately 2–8 μm according to the particle size distribution analysis (Figure S2). Both the XRD and SEM results prove that the Li_3BO_3 additive could promote the grain growth of monocrystal $LiMn_2O_4$ effectively.

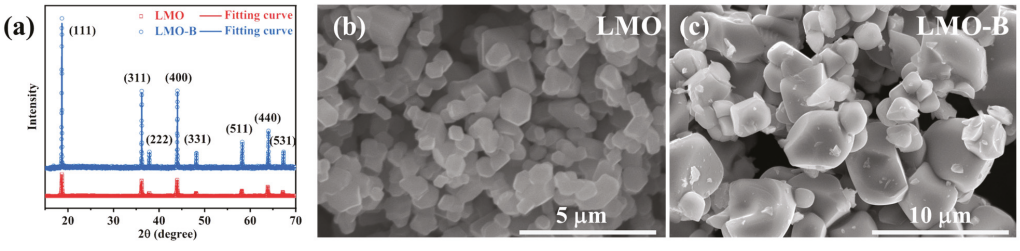

Figure 1. (**a**) XRD patterns of the LMO and LMO-B samples; the SEM images of the (**b**) LMO and (**c**) LMO-B.

3.2. Effect of the Al-Doping

With the Al-doping in $LiMn_2O_4$, the morphology of the LAMO-B (Figure 2a) has no significate change in comparison with the LMO-B sample (Figure 1c). While the systematic right shift of diffraction peaks could be observed, compared with the LMO-B sample, the main diffraction peaks of the LAMO-B sample shifted toward to the high angles as shown in Figure 2b. Meanwhile, the calculated lattice parameter of the LMO-B and LAMO-B is 8.2235 and 8.2090, respectively. It means that the Al atom with smaller radius has occupied the Mn site in the monocrystal $LiMn_2O_4$ lattice structure.

3.3. Li_2ZrO_3-Coating on the Monocrystal $LiMn_2O_4$

To analyze the influence of the Li_2ZrO_3-coating amount, the morphologies of the four samples with Al-doping and Li_2ZrO_3 coating were compared as shown in Figure 3. It is found that the micro-sized large grains are surrounded by smaller ones in all four samples and all the secondary particles show a diameter as large as ~10 mm. It proves that the Li_2ZrO_3 coating could not affect the size distribution.

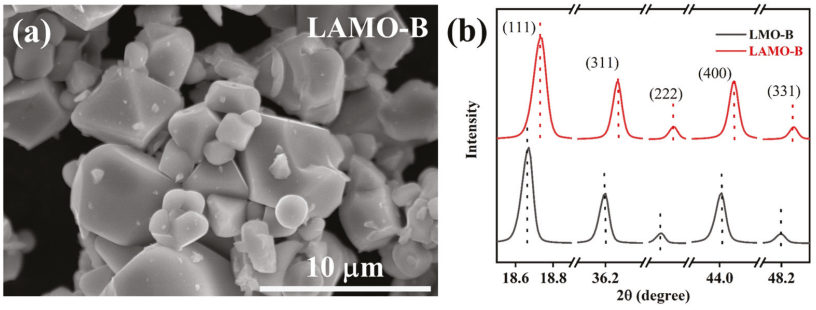

Figure 2. (**a**) Morphology of the LAMO-B sample. (**b**) The comparison of diffraction peaks of LMO-B and LAMO-B samples.

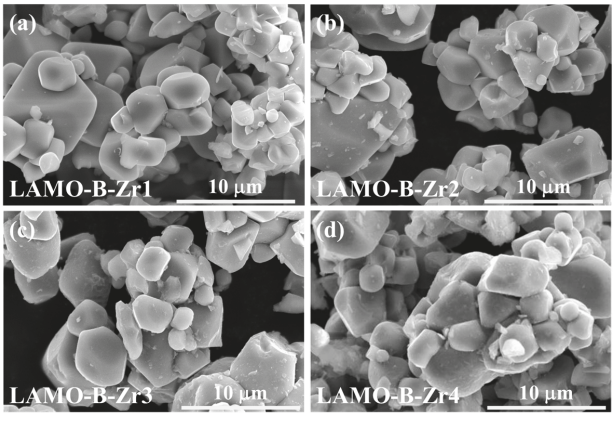

Figure 3. The SEM images of the (**a**) LAMO-B-Zr1; (**b**) LAMO-B-Zr2; (**c**) LAMO-B-Zr3 and (**d**) LAMO-B-Zr4 samples.

Meanwhile, it is found that the Al-doping and Li_2ZrO_3 coating distribute uniformly in the final samples. Taking the LAMO-B-Zr2 sample for example, the EDS mapping results exhibit uniform distribution of the Mn, Al, and Zr elements in the secondary particles as shown in Figure 4.

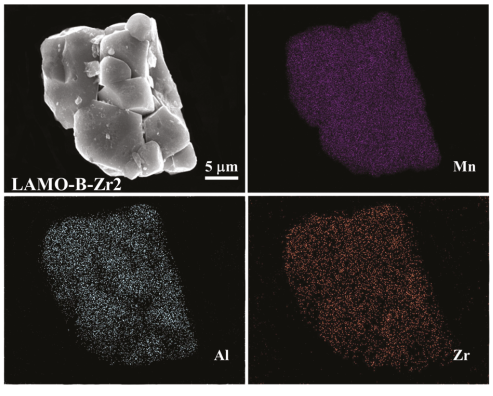

Figure 4. The EDS mapping of the LAMO-B-Zr2 sample.

To further observe the microstructure of the samples, TEM analysis and corresponding selected area electron diffraction (SAED) of the LMO-B are shown in Figure 5a. The diffraction spots can be indexed to (220), (111), (311), and (400) planes of cubic spinel $LiMn_2O_4$ (JCPDS 35-0782). Compared with the pristine surface of the LMO-B sample, a coating layer with a thickness of ~5.2 nm could be found in the LAMO-B-Zr2 sample (Figure 5b). Moreover, the coating layer should be brought from the Li_2ZrO_3 additive.

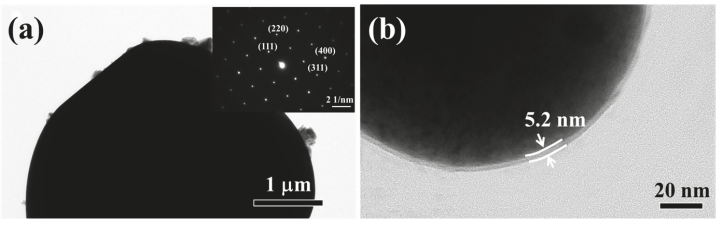

Figure 5. The TEM images and corresponding selected area electron diffraction (SAED) of the (**a**) LMO-B and (**b**) LAMO-B-Zr2.

3.4. Electrochemical Performances

The cycling and rating performance of the cells with the Al-doping and Li_2ZrO_3-coating samples was tested at the same conditions (Figure 6). The initial discharge capacity of the cells at 25 °C and 0.2C rate decreased steadily with the increscent Li_2ZrO_3-coating as shown in Figure 6a. It is reasonable, as the Li_2ZrO_3 provides no capacity contribution, the more coating, the less proportion of the active materials in the cell. Nevertheless, Li_2ZrO_3 aimed at reducing the side reactions serving as a protect layer. The effect of the Li_2ZrO_3-coating amount on the cycling performance at 25 °C and 55 °C is shown in Figure 6b,c, respectively. It was found that the capacity retention of the four samples is 93.0%, 93.9%, 90.2%, and 82.3% at 25 °C after 200 cycles with the increasing Li_2ZrO_3-coating amount. Moreover, at 55 °C, the corresponding capacity retention is 81.0%, 87.5%, 79.2%, and 79.5%, respectively. It is obvious that the LAMO-B-Zr2 could decrease the capacity loss and provide the optimal protection at both temperatures. Moreover, as shown in Figure 6d, the rate performance of LAMO-B-Zr2 is also better than the other three samples, especially at higher rates. Although the discharge capacity of LAMO-B-Zr2 at 0.5C is less than the LAMO-B-Zr1, the capacity at 1, 2, 3, and 5C rates is larger than the other three samples. It proves that the deficiency of Li_2ZrO_3 could not provide overall protection from the side reactions, while the excess of Li_2ZrO_3 would impede the migration of lithium ion. LAMO-B-Zr2 exhibited the best performance in a series of Al-doping and Li_2ZrO_3 coating samples.

To explore the influence of the Al-doping and the Li_2ZrO_3 coating, the electrochemical performance of the LMO-B, LAMO-B, and LAMO-B-Zr2 samples were characterized in parallel. Figure 7a presents the first charge–discharge curves obtained at 0.2C and 25 °C between 3.0 and 4.3 V (vs. Li/Li^+). There are two voltage plateaus near 4.0 V and 4.1 V, which indicates the two-stage processes of Li^+ ion insertion/extraction reactions for a typical characterization of a well-crystallized spinel $LiMn_2O_4$ [17,18]. The initial discharge specific capacities of the as-prepared samples show a decline trend with the Al-doping and the Li_2ZrO_3 coating. This result is comprehensible because the percentage of Mn^{3+} is partially occupied by the Al-doping or lowered by the Li_2ZrO_3 coating.

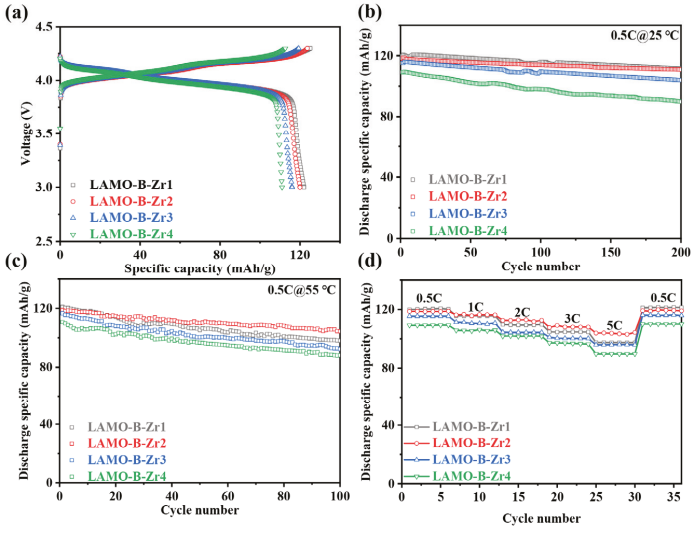

Figure 6. The electrochemical performance of the Li_2ZrO_3-coated LAMO-B-Zr cells. (**a**) The initial charge–discharge profiles at 0.2C and 25 °C; The cycling performance with 0.5C rate at (**b**) 25 °C and (**c**) 55 °C. (**d**) The rate performance at 0.5C, 1C, 2C, 3C and 5C, respectively.

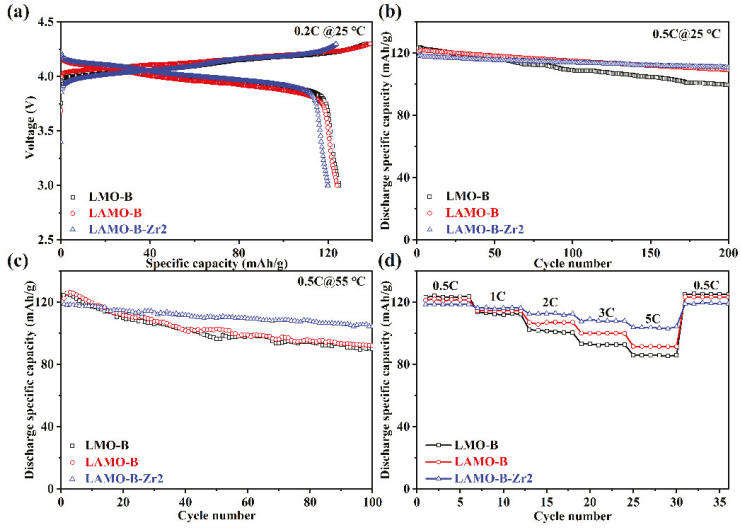

Figure 7. The electrochemical performance of the LMO-B, LAMO-B, and LAMO-B-Zr2 cells. (**a**) The initial charge-discharge profiles at 0.2 °C and 25 °C. The cycling stability with 0.5C rate at (**b**) 25 °C and (**c**) 55 °C. (**d**) The rate performance at 0.5C, 1C, 2C, 3C, and 5C, respectively.

However, according to the cycling stability at room temperature and 55 °C shown in Figure 7b,c, respectively, the capacity retention of the LAMO-B-Zr2 is much higher than that of the LMO-B and LAMO-B (Table 2). The possible reason may lie in that the Al-doping could stable the crystal structure during the cycling. Analogous results could be found in other literature reports [19,20]. On the other hand, with the help of the Li_2ZrO_3 coating, the capacity retention rate of the LAMO-B-Zr2 could go further to 93.9% after 200 cycles

at 25 °C and keep at 87.8% after 100 cycles at 55 °C. It turns out that the Li_2ZrO_3-coating could suppress the side-reactions effectively.

Table 2. The capacity retention ratios of LMO-B, LAMO-B, and LAMO-B-Zr2.

Samples	Capacity Retention Ratios	
	After 200 Cycles at 25 °C	After 100 Cycles at 55 °C
LMO-B	81.0%	72.2%
LAMO-B	90.0%	75.2%
LAMO-B-Zr2	93.9%	87.8%

Otherwise, the rate performance of the cells between 3.0 and 4.3 V (vs. Li/Li^+) is shown in Figure 7d. All the cells exhibit reduced discharge capacities as the increased C-rates. Although the capacity of LAMO-B-Zr2 at 0.5C is inferior to the other cells as the lowered proportion of active substances, the discharge capacities themselves or the capacity retention of the LAMO-B-Zr2 at 1C, 2C, 3C, and 5C rates are much higher than the other control samples. Moreover, the discharge capacity of LAMO-B-Zr2 could reach up to 103.41 $mAhg^{-1}$ at 5C.

The specific discharge capacity and the capacity retention of the LAMO-B-Zr2 sample at both room temperature and 55 °C are better than those of some reported $LiMn_2O_4$ single-crystalline and Al-doped $LiMn_2O_4$. The detailed comparisons of the electrochemical performance are listed in Table S2.

Furthermore, the EIS results of the LMO-B, LAMO-B, and LAMO-B-Zr2 cells after the 1st and 200th cycle is shown in Figure 8a,b, respectively. All the cells are discharged to 4.0 V before testing. All the Nyquist plots comprises two depressed semicircles in the high and middle frequency region and a straight line in the low frequency region. The intersection at the high frequency shows the Ohmic resistance (R_o), the diameter of the semicircle at the high frequency means the resistance (R_s) of solid electrolyte interface (SEI), and the diameter of the semicircle at low frequency suggests the resistance of the charge transfer (R_{ct}). The right intersection of the semicircle with the horizontal axis in the low frequency represent the total internal resistance ($R_t = R_o + R_s + R_{ct}$) [21,22]. The EIS plots were fitted with equivalent circuit shown in Figure 8a by Zview software. Moreover, the corresponding fitting results of the impedance are listed in Table 3. It is found that the Al-doping could decrease the impedance compared with the pristine LMO-B and the LAMO-B samples. It is suggested that the coating strategy is an efficient method of decreasing impedance.

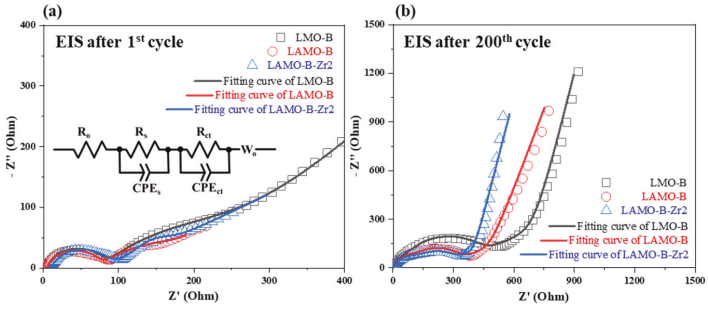

Figure 8. The Nyquist plots of the LMO-B, LAMO-B, and LAMO-B-Zr2 cells after the (**a**) 1st and (**b**) 200th cycle over the frequency range of 10^5 to 10^{-2} Hz. Inset figure is the equivalent circuit.

Table 3. The fitting results of the LMO-B, LAMO-B, and LAMO-B-Zr2 cells after the 1st and 200th cycle.

Sample	Rt (Ω) after 1st Cycle	Rt (Ω) after 200th Cycle
LMO-B	248.1	377.8
LAMO-B	235.8	293.1
LAMO-B-Zr2	101.1	270.8

4. Conclusions

The micron-sized monocrystalline $LiAl_{0.06}Mn_{1.94}O_4$ with a grain size of 2–8 μm was prepared in this work. With the synergistic modification of Al-doping and Li_2ZrO_3 coating, the cycling stability and rating performance have been significantly improved. Meanwhile, the optimal Li_2ZrO_3 coating amount was investigated. The LAMO-B-Zr2 with 2 mol% Li_2ZrO_3 addition possesses capacity retention of 93.9% after 200 cycles at room temperature and 87.8% after 100 cycles at 55 °C. This work provides appreciable point of view into the practical application of the LMO cathode in lithium-ion batteries.

Supplementary Materials: The following are available online at https://www.mdpi.com/article/10.3390/nano11123223/s1, Figure S1: The XRD patterns of the $LiMn_2O_4$ samples; Figure S2. The particle size distribution of the (**a**) LMO; (**b**) LMO-B; (**c**) LAMO-B-Zr1; (**d**) LA-MO-B-Zr2; (**e**) LAMO-B-Zr3; (**f**) LAMO-B-Zr4; Table S1: The full width at half maximum (FWHM) of the LMO and LMO-B samples; Table S2: Comparison of electrochemical performance of different $LiMn_2O_4$ electrode materials.

Author Contributions: Conceptualization, J.Y. and X.W.; methodology, C.L.; validation, J.Y.; formal analysis, L.Z.; investigation, C.L.; writing—original draft preparation, C.L.; writing—review and editing, L.Z. and B.Z.; supervision, X.W.; project administration, X.W.; funding acquisition, Q.F., J.Y. and L.Z. All authors have read and agreed to the published version of the manuscript.

Funding: This research was funded by the National Key Research and Development Program of China, grant number 2017YFA0402800, 2017YFE0300402, and 2017YFE0302400; National Natural Science Foundation of China, grant number 51502300; and Anhui Provincial Natural Science Foundation, grant number 1608085QE88.

Institutional Review Board Statement: Not applicable.

Informed Consent Statement: Not applicable.

Data Availability Statement: Data presented in this study are available on request from the corresponding authors.

Conflicts of Interest: The authors declare no conflict of interest. The funders had no role in the design of the study; in the collection, analyses, or interpretation of data; in the writing of the manuscript; or in the decision to publish the results.

References

1. Paulsen, J.M.; Thomas, C.L.; Dahn, J.R. Layered Li-Mn-Oxide with the O2 Structure: A Cathode Material for Li-Ion Cells Which Does Not Convert to Spinel. *J. Electrochem. Soc.* **1999**, *146*, 3560–3565. [CrossRef]
2. Potapenko, A.V.; Kirillov, S.A. Enhancing high-rate electrochemical properties of $LiMn_2O_4$ in a $LiMn_2O_4/LiNi_{0.5}Mn_{1.5}O_4$ core/shell composite. *Electrochim. Acta* **2017**, *258*, 9–16. [CrossRef]
3. Kim, J.-S.; Kim, K.; Cho, W.; Shin, W.H.; Kanno, R.; Choi, J.W. A Truncated Manganese Spinel Cathode for Excellent Power and Lifetime in Lithium-Ion Batteries. *Nano Lett.* **2012**, *12*, 6358–6365. [CrossRef]
4. Tarascon, J.M.; Armand, M. Issues and challenges facing rechargeable lithium batteries. *Nature* **2001**, *414*, 359–367. [CrossRef] [PubMed]
5. Armand, M.; Tarascon, J.M. Building better batteries. *Nature* **2008**, *451*, 652. [CrossRef] [PubMed]
6. Michalska, M.; Ziółkowska, D.A.; Jasiński, J.B.; Lee, P.H.; Ławniczak, P.; Andrzejewski, B.; Ostrowski, A.; Bednarski, W.; Wu, S.H.; Lin, J.Y. Improved electrochemical performance of $LiMn_2O_4$ cathode material by Ce doping. *Electrochim. Acta* **2018**, *276*, 37–46. [CrossRef]

7. Jiang, C.; Tang, Z.; Wang, S.; Zhang, Z. A truncated octahedral spinel $LiMn_2O_4$ as high-performance cathode material for ultrafast and long-life lithium-ion batteries. *J. Power Source* **2017**, *357*, 144–148. [CrossRef]
8. Zhu, X.; Wu, X.; Doan, T.N.L.; Tian, Y.; Zhao, H.; Chen, P. Binder-free flexible $LiMn_2O_4$/carbon nanotube network as high power cathode for rechargeable hybrid aqueous battery. *J. Power Source* **2016**, *326*, 498–504. [CrossRef]
9. Cao, J.; Guo, S.; Yan, R.; Zhang, C.; Guo, J.; Zheng, P. Carbon-coated single-crystalline $LiMn_2O_4$ nanowires synthesized by high-temperature solid-state reaction with high capacity for Li-ion battery. *J. Alloys Compd.* **2018**, *741*, 1–6. [CrossRef]
10. Yi, T.-F.; Xie, Y.; Wu, Q.; Liu, H.; Jiang, L.; Ye, M.; Zhu, R. High rate cycling performance of lanthanum-modified $Li_4Ti_5O_{12}$ anode materials for lithium-ion batteries. *J. Power Source* **2012**, *214*, 220–226. [CrossRef]
11. Chen, M.; Chen, P.; Yang, F.; Song, H.; Liao, S. Ni, Mo Co-doped Lithium Manganate with Significantly Enhanced Discharge Capacity and Cycling Stability. *Electrochim. Acta* **2016**, *206*, 356–365. [CrossRef]
12. Fu, Y.; Jiang, H.; Hu, Y.; Dai, Y.; Zhang, L.; Li, C. Synergistic Enhancement Effect of Al Doping and Highly Active Facets of $LiMn_2O_4$ Cathode Materials for Lithium-Ion Batteries. *Ind. Eng. Chem. Res.* **2015**, *54*, 3800–3805. [CrossRef]
13. Wang, J.; Zhang, Q.; Li, X.; Wang, Z.; Guo, H.; Xu, D.; Zhang, K. Sputtering graphite coating to improve the elevated-temperature cycling ability of the $LiMn_2O_4$ electrode. *Phys. Chem. Chem. Phys.* **2014**, *16*, 16021–16029. [CrossRef]
14. Tron, A.; Park, Y.D.; Mun, J. AlF_3-coated $LiMn_2O_4$ as cathode material for aqueous rechargeable lithium battery with improved cycling stability. *J. Power Source* **2016**, *325*, 360–364. [CrossRef]
15. Waller, G.H.; Brooke, P.D.; Rainwater, B.H.; Lai, S.Y.; Hu, R.; Ding, Y.; Alamgir, F.M.; Sandhage, K.H.; Liu, M.L. Structure and surface chemistry of Al_2O_3 coated $LiMn_2O_4$ nanostructured electrodes with improved lifetime. *J. Power Source* **2016**, *306*, 162–170. [CrossRef]
16. Wang, L.; Wu, B.; Mu, D.; Liu, X.; Peng, Y.; Xu, H.; Liu, Q.; Gai, L.; Wu, F. Compounds, Single-crystal $LiNi_{0.6}Co_{0.2}Mn_{0.2}O_2$ as high performance cathode materials for Li-ion batteries. *J. Alloys Compd.* **2016**, *674*, 360–367. [CrossRef]
17. Li, J.; Cameron, A.R.; Li, H.; Glazier, S.; Xiong, D.; Chatzidakis, M.; Allen, J.; Botton, G.; Dahn, J. Comparison of single crystal and polycrystalline $LiNi_{0.5}Mn_{0.3}Co_{0.2}O_2$ positive electrode materials for high voltage Li-ion cells. *J. Electrochem. Soc.* **2017**, *164*, A1534. [CrossRef]
18. Jiang, Q.; Liu, D.; Zhang, H.; Wang, S. Plasma-Assisted Sulfur Doping of $LiMn_2O_4$ for High-Performance Lithium-Ion Batteries. *J. Phys. Chem. C* **2015**, *119*, 28776–28782. [CrossRef]
19. Liu, J.; Li, G.; Yu, Y.; Bai, H.; Shao, M.; Guo, J.; Su, C.; Liu, X.; Bai, W. Synthesis and electrochemical performance evaluations of polyhedra spinel $LiAl_xMn_{2-x}O_4$ ($x \leq 0.20$) cathode materials prepared by a solution combustion technique. *J. Alloys Compd.* **2017**, *728*, 1315–1328. [CrossRef]
20. Taniguchi, I.; Song, D.; Wakihara, M. Electrochemical properties of $LiM_{1/6}Mn_{11/6}O_4$ (M = Mn, Co, Al and Ni) as cathode materials for Li-ion batteries prepared by ultrasonic spray pyrolysis method. *J. Power Source* **2002**, *109*, 333–339. [CrossRef]
21. Yang, C.; Yu, S.; Lin, C.; Lv, F.; Wu, S.; Yang, Y.; Wang, W.; Zhu, Z.-Z.; Li, J.; Wang, N.; et al. $Cr_{0.5}Nb_{24.5}O_{62}$ Nanowires with High Electronic Conductivity for High-Rate and Long-Life Lithium-Ion Storage. *ACS Nano* **2017**, *11*, 4217–4224. [CrossRef] [PubMed]
22. Tao, S.; Zhao, H.; Wu, C.; Xie, H.; Cui, P.; Xiang, T.; Chen, S.; Zhang, L.; Fang, Y.; Wang, Z.; et al. Enhanced electrochemical performance of MoO_3-coated $LiMn_2O_4$ cathode for rechargeable lithium-ion batteries. *J. Mater. Chem. A* **2017**, *199*, 203–208. [CrossRef]

nanomaterials

MDPI

Article

The Effect of Annealing Temperature on the Synthesis of Nickel Ferrite Films as High-Capacity Anode Materials for Lithium Ion Batteries

Mansoo Choi [1,*], Sung-Joo Shim [2], Yang-Il Jung [3], Hyun-Soo Kim [2] and Bum-Kyoung Seo [1]

[1] Decommissioning Technology Research Division, Korea Atomic Energy Research Institute, Daejeon 34057, Korea; bumja@kaeri.re.kr
[2] Battery Research Center, Korea Electrotechnology Research Institute, Changwon 51543, Korea; sjsim@keri.re.kr (S.-J.S.); hskim@keri.re.kr (H.-S.K.)
[3] LWR Fuel Technology Division, Korea Atomic Energy Research Institute, Daejeon 34057, Korea; yijung@kaeri.re.kr
* Correspondence: teracms@kaeri.re.kr

Abstract: Anode materials providing a high specific capacity with a high cycling performance are one of the key parameters for lithium ion batteries' (LIBs) applications. Herein, a high-capacity $NiFe_2O_4$(NFO) film anode is prepared by E-beam evaporation, and the effect of the heat treatment is studied on the microstructure and electrochemical properties of LIBs. The $NiFe_2O_4$ film annealed at 800 °C (NFO-800) showed a highly crystallized structure and different surface morphologies when compared to the electrode annealed at a lower temperature (NFO-600, NFO-700). In the electrochemical measurements, the high specific capacity (1804 mA g^{-1}) and capacity retention ratio (95%) after 100 cycles were also achieved by the NFO-800 electrode. The main reason for the good electrochemical performance of the NFO-800 electrode is a high structure integrity, which could improve the cycle stability with a high discharge capacity. The $NiFe_2O_4$ electrode with an annealing process could be further proposed as an alternative ferrite material.

Keywords: anode; thermal treatment; nickel ferrites; li-ion batteries

Citation: Choi, M.; Shim, S.-J.; Jung, Y.-I.; Kim, H.-S.; Seo, B.-K. The Effect of Annealing Temperature on the Synthesis of Nickel Ferrite Films as High-Capacity Anode Materials for Lithium Ion Batteries. *Nanomaterials* **2021**, *11*, 3238. https://doi.org/10.3390/nano11123238

Academic Editors: Marc Cretin, Sophie Tingry and Zhenghua Tang

Received: 28 October 2021
Accepted: 25 November 2021
Published: 29 November 2021

1. Introduction

Ever growing concerns of energy consumption are one of the important issues in modern society [1]. In order to meet an increasing energy demand, the Li-ion battery (LIB) has been considered as a potential candidate for electric vehicles and energy storage systems, which should have a high power and energy densities [2]. To have a high performance in an LIB, it is necessary to design optimized anode materials with a high capacity and long cycle stability. These requirements can be fulfilled with an anode electrode development with a higher specific capacity than commercial anode material such as graphite (372 mAh g^{-1}). The transition metal oxide that has a conversion reaction shows higher specific capacities when compared to intercalation compounds. For instance, ferrites with the general formula of an MFe_2O_4 (M = bivalent cation) spinel oxide, are considered promising anode materials because of their high specific capacities, natural abundance, and low cost. Among the ferrite materials, $NiFe_2O_4$ is an inverse spinel structure where Ni^{2+} and half of the Fe^{3+} cations occupy the octahedral sites and the remaining Fe^{3+} are on the tetrahedral site. Moreover, $NiFe_2O_4$ delivers its theoretical capacity of 915 mAh g^{-1}, which can electrochemically react with 8 mol of Li. Despite of advantages of $NiFe_2O_4$, the volume expansion of the electrode during the charge-discharge process resulted in a poor cycle performance [3]. As a result, this prevents them from being practical anode materials for LIBs (lithium ion batteries'). Several studies discussed anode materials with a higher specific capacity, rate capability, and cycle performance than graphite [3–6]. Various strategies have been proposed to overcome the above obstacles

related to the $NiFe_2O_4$ electrode by employing nanostructures such as nanosheet, nanowire, and nanoparticles [7–9]. The nanostructured electrode is favorable to an outstanding electrochemical performance owing to the short distance of Li ion diffusion and large surface area [9]. Another strategy has been that nanostructured carbon such as a carbon nanotube or graphene has been used as a support for the $NiFe_2O_4$ electrode [10,11]. The nanocarbon materials could not only improve the electronic conductivity but also be served as buffering media against the volumetric expansion of the electrode. It has been reported that the deposition method could be a favorable method to prepare a (Ti, Fe)-alloyed Si thin film anode with an accurate stoichiometric composition of materials [12]. Although $LiMn_2O_4$ (LMO) can be synthesized at room temperature in tetragonal and cubic forms, it can be synthesized at high temperatures, and the influence of the annealing temperature on the physical and electrochemical properties of the LMO thin film is investigated as an anode material [13–15].

In this study, the $NiFe_2O_4$ film as an anode electrode was prepared by a one-step synthesis using the E-beam evaporation equipment. The as-prepared $NiFe_2O_4$ film was followed by a heat treatment and directly used as an anode electrode for LIBs without further process such as adding conductive materials or binder, or conducting pressure roast processes. The effects of the heat temperature of the $NiFe_2O_4$ film were systematically investigated, and the structural and electrochemical properties will be discussed in details.

2. Materials and Methods

$NiFe_2O_4$ film was coated on stainless foil (SUS 304, thickness 25 μm) prepared by an electron beam evaporation system. Before the deposition process, the chamber was evacuated down to 3×10^{-6} Torr, and the surface of the stainless foil was etched by Ar ions for 5 min before deposition to remove any oxide layer. A $NiFe_2O_4$ pellet (purity 99.9%, from KOJUNDO chemical laboratory Co. LTD, Saitama, Janpan) was used as the target, and the deposition rate (0.5 Å/s) was monitored by a thickness sensor. For the investigation of the heating effect, the $NiFe_2O_4$ film was annealed at 600, 700, 800 °C, for 1 h in Ar atmosphere.

The morphology of the $NiFe_2O_4$ film surface were examined by field emission scanning electron microscopy, FESEM, (S-4800, Hitachi, Tokyo, Janpan), and a high resolution transmission electron microscope, HRTEM, (JEOL-2100F, JEOL, Tokyo, Japan) an elemental mapping analysis of the $NiFe_2O_4$ sample was also performed with energy dispersive spectroscopy. For the cross-sectional image, we prepared the sample by using focused ion beam-scanning electron microscopy (FID-SEM, HITACHI, Tokyo JAPAN) with Ga ion sputtering. To prevent a morphological change by the ion beam, the Pt coating was applied on the surface of the electrode. The thin film X-ray diffraction (X-pert PRO MRD, Philips, Washington, DC, USA, Cu Kα radiation (λ = 1.5406 Å)) was carried out 2θ from 10° and 90° at a scan rate of 0.01°. A Raman measurement (NTEGRA SPECTRA, NT-MDT, Tempe, AZ, USA) was conducted with an Ar laser excitation source emitting at a wavelength of 514 nm. The elemental composition and depth profile were characterized by the X-ray photoelectron spectroscopy system. The X-ray source was used with monochromatic Al Kα radiation (1486.6 eV), and the spectra was calibrated using C 1s (BE = 284.8 eV) of hydrocarbon.

The electrochemical performance of the NFO anode electrodes was evaluated using 2032 coin cells assembled in a dry room. The Li foil and polypropylene 2400 (Celgard, Charlotte, NC, USA) were used as a counter and reference, and as a separator, respectively. The electrolyte was 1.3 M LiPF6 in ethylene carbonate (EC) and diethyl carbonate (DEC) (3:7 in volume) (Soulbrain, Northville, MI, USA). Galvanostatic charge-discharge and the cyclic voltammetry (CV) tests were performed within a potential range of 0.005–3.0 V (vs. Li^+/Li) with an applied current density of 0.1 C (1 C = 915 mA g^{-1}) and at a scan rate of 0.5 mV s^{-1}, respectively. All the electrochemical measurements were carried out at room temperature using a battery test system (Battery Analyzer, Won-A tech, Daejeon, Korea). The mass loading of NFO on the stainless steel according to the density of NFO, and the average thickness of NFO from the cross-section SEM images, is about 0.3 mg and

500 nm. The cyclic voltammetry (CV) was recorded in the potential range of 0.005–3.0 V at a scan rate of 0.5 mV s^{-1}. All the electrochemical measurements were carried out at room temperature.

3. Results

The crystal structure of $NiFe_2O_4$ film according to the heat temperature was determined by X-ray diffraction (XRD, X-pert PRO MRD, Philips, Washington, DC, USA). Figure 1 shows the XRD patterns of the NFO-600, NFO-700, and NFO-800 electrodes. Obviously, the crystallinity of NFO film electrodes depend on the heat treatment temperature, and they are shown in Figure 1, where it can be seen that with an increase of the temperature from 600 to 800 °C the peaks become sharper, resulting in a higher crystallinity of the $NiFe_2O_4$ materials.

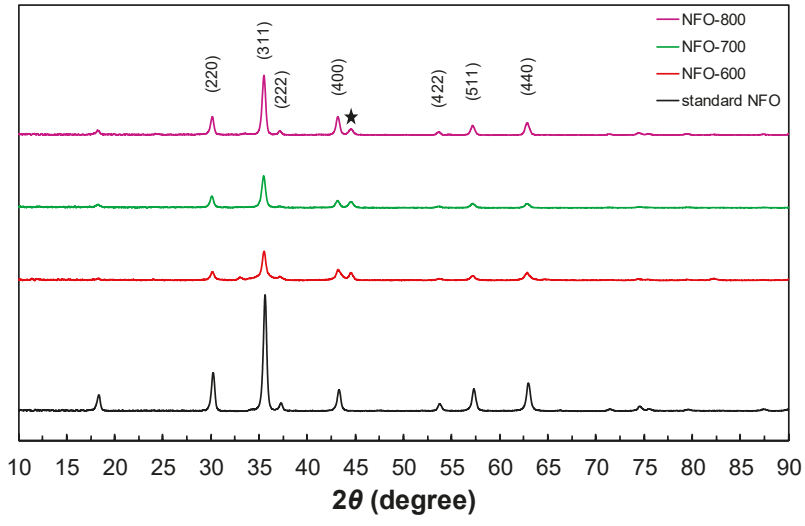

Figure 1. X-ray diffraction patterns of $NiFe_2O_4$ electrode annealed at different temperatures.

As shown in Figure 1, all samples have shown diffraction peaks at a similar 2θ degree when compared with the $NiFe_2O_4$ target peak, corresponding to the (220), (311), (222), (400), (511), and (440) crystal planes of the $NiFe_2O_4$ (JCPDS No. 54-0964) [16–18]. These diffraction peaks confirmed the presence of single-phase $NiFe_2O_4$ with a face-centered cubic and F*d3m* space group. The peak intensity becomes sharper when the annealing temperature is increased from 600 to 800 °C, resulting in a higher crystallinity for NFO-800 than NFO-600. The crystallite sizes of the NFO-600, NFO-700, and NFO-800 electrodes are calculated as 17, 19, and 22 nm, respectively, using Scherrer's equation. Peaks related to any other phase or impurities were not observed. The peak at 45° corresponds to the stainless foil (denoted by a star), which is similar to previous studies [19,20].

Figure 2a–c shows the surface morphologies of the NFO-600, NFO-700, and NFO-800 electrodes. As can be seen in Figure 2a,b, the $NiFe_2O_4$ film shows numerous streaks based on the mother substrate, without any cracking, and a few droplets are also observed. These particles are ascribed to the incomplete elimination of target splashing during deposition [17]. After the heat treatment at 800 °C, however, the surface morphology is very different from electrodes heated at a lower temperature. The roughness and porosity of the surface is observed, evidencing the effect of the annealing temperature. This observation of a roughened surface suggests that the film might be undergoing a change of orientation. It is reported that the heat treatment of stainless steel changes its chemical composition and the thickness of the passive film [21]. Thus, the surface morphologies

are dependent on the heat temperature. It is anticipated that the roughened surface of the $NiFe_2O_4$ electrode could lead to a low resistance interface of the electrode. Besides, the thickness of the electrode on glass was about 500 nm (Figure 2d), and the conformal $NiFe_2O_4$ film was clearly observed in the cross-sectional image to be without any splits.

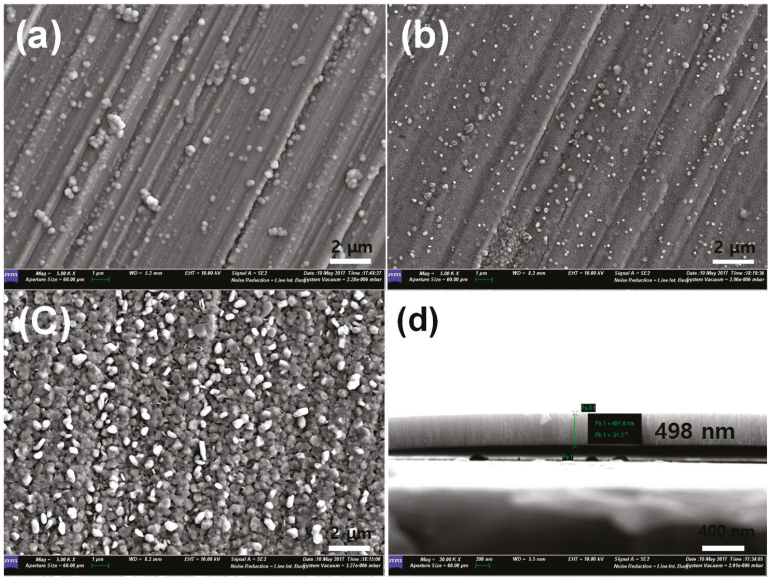

Figure 2. SEM images of $NiFe_2O_4$ electrode of (**a**) NFO-600, (**b**) NFO-700, and (**c**) NFO-800 °C. (**d**) Cross-sectional image of $NiFe_2O_4$ electrode on the glass.

Figure 3 shows the cross-sectional TEM image with energy dispersive X-ray spectrum (EDS) elemental maps of the NFO-800 electrode. The clearly defined $NiFe_2O_4$ electrode and SUS substrate were observed. The EDS elemental mapping analysis was also conducted in order to observe the elemental composition distribution at the $NiFe_2O_4$/interface between the oxide layers and stainless steel. As shown in Figure 3, Ni, Fe, and O were distributed in the outer layer, which indicated that Cr did not exist in the $NiFe_2O_4$ electrode. However, the Fe element was depleted in the interface between the oxide and substrate. In contrast to Fe, the Cr element becomes denser at the interface. This indicates that the Cr ions are diffused from the substrate to the outer oxide layer, which is composed of chromium and oxygen represented as chromium oxide. It is reported that the duplex oxide layer is formed at a high temperature with the inner and outer layer [22].

The outer layer is grown by the out-diffusion of metal ions from the substrate. Moreover, the stainless steel containing sufficient chromium established a protective chromium rich oxide layer as a Cr_2O_3 and Fe-Cr spinel structure during oxidation at a high temperature [23]. Consequently, the $NiFe_2O_4$ electrode was formed by $NiFe_2O_4$ (outer layer)/Cr_2O_3 (transition layer), Fe-Cr spinel, and stainless steel (substrate) from the outer to inner oxide layer. In a previous study, low density regions were observed at the interface between $NiFe_2O_4$ and the substrate due to the high density of this film and the different temperature expansion coefficients (10.3×10^{-6} K^{-1} of $NiFe_2O_4$ and 16×10^{-6} K^{-1} of stainless foil) [17]. In this study, however, the $NiFe_2O_4$ electrode annealed at a high temperature has been formed without any crack or low-density regions. We have assumed that the internal phase (Cr_2O_3 and Fe-Cr spinel) could be beneficial for achieving an enhanced electrochemical performance. Figure 4 shows the TEM cross-sectional image of the NFO-800 and associated selected area electron diffraction (SAED) patterns of the inner layer and outer layer of the $NiFe_2O_4$ electrode. As shown in Figure 4, the $NiFe_2O_4$ electrode was formed as a double-

layer structure, which is shown in Figure 3. The inner and outer layer of the $NiFe_2O_4$ electrode show spinel SAED patterns. The d-values calculated from the concentric rings of both layers match well with (220), (311), and (400), indicating the spinel-type structure of the $NiFe_2O_4$. The SAED patterns from the inner layer show a spot pattern, whereas the outer layer ($NiFe_2O_4$) indicates a ring pattern. This difference could be attributed to the amount of Cr in the spinel structure.

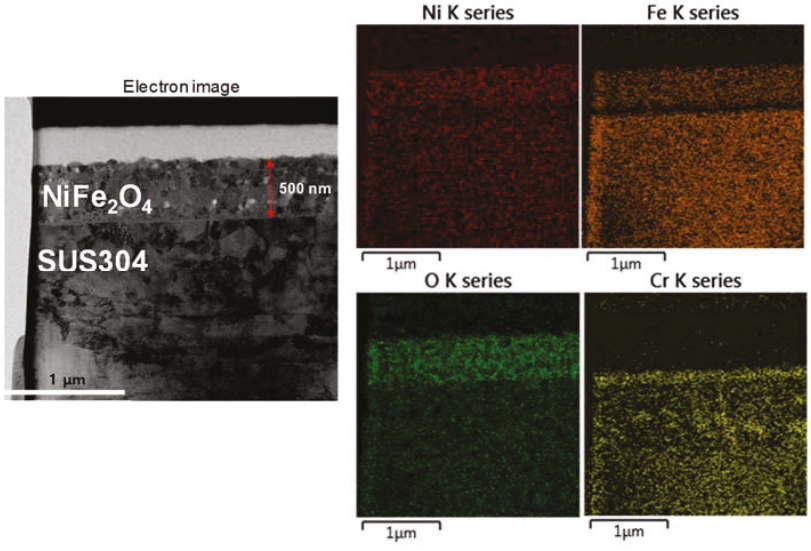

Figure 3. Cross-sectional and EDS mapping image of NFO-800 electrode.

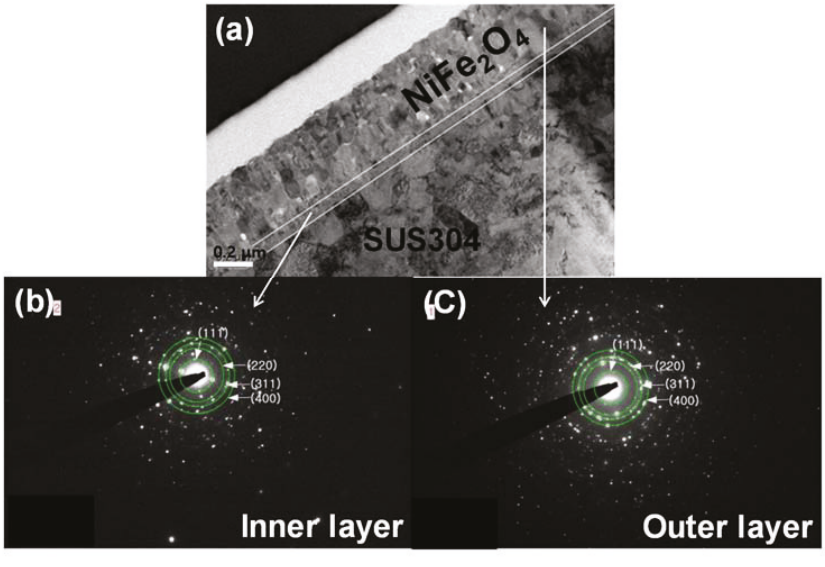

Figure 4. SAED pattern for the NFO-800 electrode. (**a**): cross-section; (**b**): Inner layer; (**c**): Outer layer.

Figure 5 shows the typical Raman spectra of the $NiFe_2O_4$ electrode annealed at 800 °C. As can be seen in Figure 5, the Raman spectra showed the inverse spinel structure of $NiFe_2O_4$, which is consistent with previous reports [24,25]. It is reported that the $NiFe_2O_4$ spinel structure group can be described with the space group of F*d3m* (No. 227), and the factor group theoretical calculations result in five Raman active bands, namely $A_{1g} + E_g + 3T_{2g}$ [25]. In this study, the Raman spectra have shown the crystallized $NiFe_2O_4$ electrode, which confirms the XRD result. Any peaks related to the $NiFe_2O_4$ were not observed on the SUS substrate.

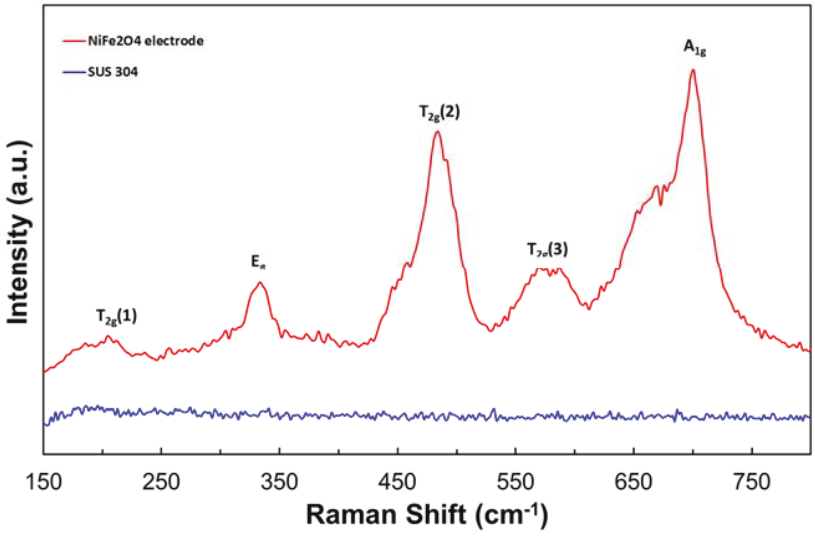

Figure 5. Raman spectra of NFO-800 and stainless steel.

The XPS depth profiling was carried out to observe the chemical concentration of iron, nickel, and chromium with Ar^+ ion beam sputtering. Figure 6 shows the XPS depth profiles of $NiFe_2O_4$ according to the annealing temperature. As shown in Figure 6, in the $NiFe_2O_4$ region, Ar^+ etching extending up to 4000 s was clearly observed, and the thickness of the $NiFe_2O_4$ electrode was similar before and after annealing except for the NFO-800 electrode. Before the heat treatment of $NiFe_2O_4$ electrodes, the chemical ratio of Fe:Ni was irregularly observed, but the composition ratio of Fe:Ni was consistently close to the theoretical composition of the $NiFe_2O_4$ electrode after the heat treatment. This indicates that the $NiFe_2O_4$ electrodes may be undergoing a change of orientation during annealing. The Cr element was much more increased at the interface layer between $NiFe_2O_4$ and the SUS substrate, which was consistent with the EDS mapping result. However, the Fe and Ni of the NFO-800 electrode showed different chemical compositions when compared with a lower annealing temperature. The Cr elements were outwardly diffused at 800 °C from substrate, which resulted in more migration of Fe and Ni from the $NiFe_2O_4$ electrode to the interface. From the results of the XPS depth profile, the stainless steel annealed at a high temperature established a protective chromium rich oxide (Cr_2O_3) and Fe-Cr spinel structure in the interface layer [23].

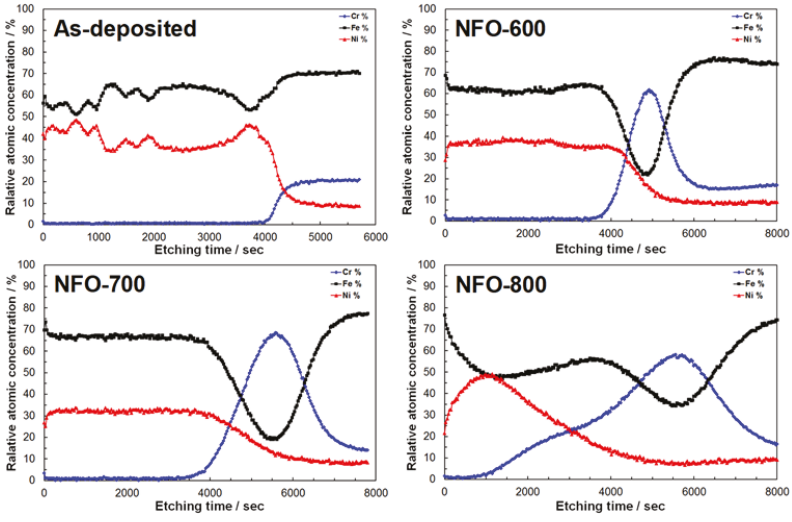

Figure 6. The "in depth" relative atomic concentrations of the $NiFe_2O_4$ electrode annealed at different temperatures from XPS-depth profiles.

Figure 7 shows the charge-discharge profiles of the $NiFe_2O_4$ electrode at 0.1 C in the range of 0.005–3.0 V, with all of the electrodes showing typical voltage profiles of the discharging (lithiation) and charging process (delithiation). In the first discharge process, a long-range plateau was observed around 0.75 V, which corresponded to the reduction of Fe^{3+}/Ni^{2+} during Li insertion. This constant region from 0.7 to 0.5 V showed a specific capacity of more than 1000 mAh g^{-1}. This indicates that Ni and Fe has been completely converted to metallic elements and the formation of Li_2O [26]. In the charge process, the quasi-plateau was also observed at 1.5 V, which resulted in the oxidation of transition metals [26]. A similar charge-discharge process has been observed in other transition metal oxides [27,28]. The second and third cycles almost remained the same profile, which revealed that the $NiFe_2O_4$ electrode became stable and had reversible reactions. The initial discharge capacities of the NFO-600, NFO-700, and NFO-800 electrodes were 1551, 1553, and 1804 mAh g^{-1}, and the columbic efficiencies of each sample were 76, 77, and 76%, respectively. The discharge capacity obviously showed the highest capacity at an annealing temperature of 800 °C. The discharge capacities of the $NiFe_2O_4$ electrodes exceed the theoretical capacity of $NiFe_2O_4$ (~915 mAh g^{-1}), which is attributed to the decomposition of the electrolyte when the potential is decreased at a low voltage [29]. However, the initial columbic efficiencies (CE) were relatively low. The reason for the low columbic efficiencies is the formation of a solid electrolyte interface film (SEI) film of the electrode and the decomposition of the electrolyte [30]. In the subsequent cycle, the CE was increased to 98%.

In order to investigate the reaction mechanism of $NiFe_2O_4$, the cycle voltammetry (CV) of NFO-800 was carried out at a scan rate of 0.1 mV s^{-1} in the potential range of 0.005–3.0 V and is depicted in Figure 8. In the first cathodic cycle, a large peak at 0.7 V is observed, which is attributed to the reduction reaction of Fe^{3+} and Ni^{2+} to Fe^0 and Ni^0, respectively. In the subsequent cycles, the reduction peaks were shifted to 0.8 and 1.1 V, indicating the irreversible reaction in the first cycle. For the reversible cycle, the anodic peak at 1.6 V was related to the oxidation of Fe and Ni to Fe^{3+} and Ni^{2+}, and it shifted to 1.9 V in the second cycle due to the change in the ionic environment [31]. The redox mechanism observed during the charge-discharge reaction may occur in the following steps:

$$NiFe_2O_4 + 8Li+ + 8e^- \leftrightarrow Ni + 2Fe + 4Li_2O$$

$$Ni + Li_2O \leftrightarrow NiO + 2Li+ + 2e^-$$

$$2Fe + 3Li_2O \leftrightarrow Fe_2O_3 + 6Li^+ + 6e^-$$

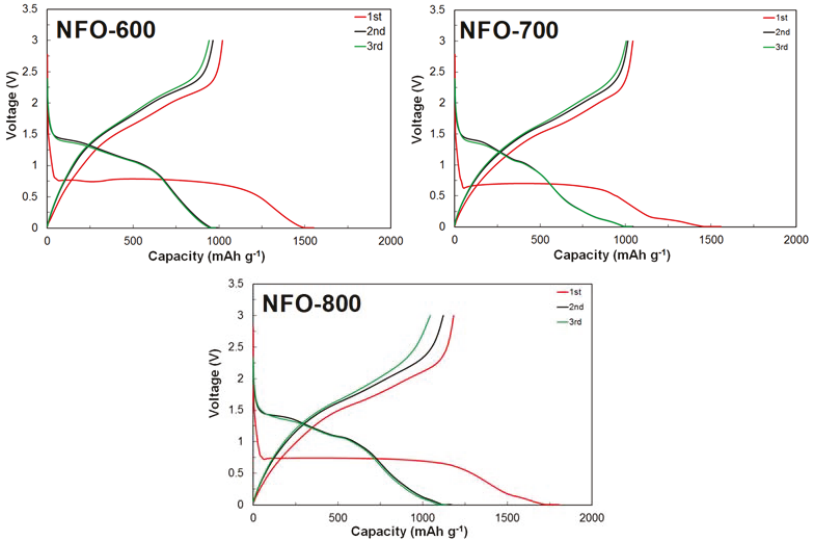

Figure 7. The initial charge-discharge profiles of the $NiFe_2O_4$ electrode annealed at different temperatures.

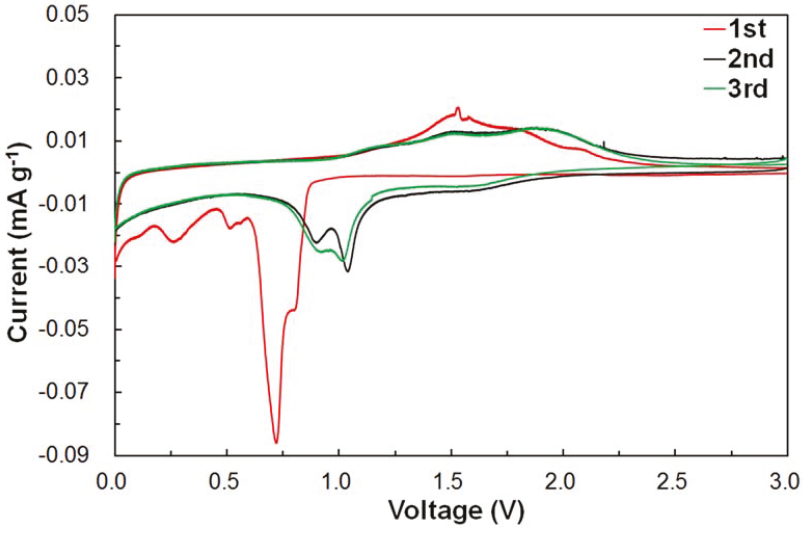

Figure 8. Cyclic voltammetry curves of the $NiFe_2O_4$ electrode annealed at 800 °C.

In addition, the subsequent cathodic and anodic CV cycles almost overlapped, indicating a stable cycle performance against the Li.

Figure 9 reveals the cycle performance of the $NiFe_2O_4$ electrode according to the annealing temperature at a current density of 91.5 mA g^{-1} for 100 cycles. As shown in Figure 9, the specific discharge capacities of the first cycle of annealed NFO-600, NFO-700, and NFO-800 electrodes were 1551, 1559, and 1804 mA g^{-1}, respectively. The CE of

the first cycle of three different electrodes was around 76.7, 77.6, and 77%, respectively, which was attributed to the formation of the SEI film. After the first cycle, the CE was retained to more than 99% until 100 cycles, indicating the superior cycle stability of the electrode. The discharge capacities of the NFO-600 and NFO-700 electrodes gradually decreased during 30 cycles and then stabilized at their capacity until 100 cycles. However, the NFO-800 electrodes showed less capacity degradation in the initial cycles and a much higher reversible capacity of 1086 mAh g^{-1} during the cycles. The capacity retention ratio of the NFO-600, NFO-700, and NFO-800 electrodes was 65, 72, and 95% after 100 cycles, respectively. This indicates that the annealing process of the $NiFe_2O_4$ electrodes at a high temperature provides a favorable lithium storage capacity and exceptional cycle stability. The reason for the high capacity retention ratio of NFO-800 was the good structural integrity during the cycling. Figure 10 shows the surface morphologies and cross-section images of the NFO-800 electrode before and after the cycle. Before cycling, the $NiFe_2O_4$ electrode surface was interconnected with distinct $NiFe_2O_4$ particles, indicating a relatively good electron pathway. However, the $NiFe_2O_4$ particles were densely embedded and showed a smooth surface without any cracks or individual particles. Thus, the optimization of the annealing temperature could lead to a high structural integrity of the $NiFe_2O_4$ electrode. The C-rate performance will be carried out when pursuing further research.

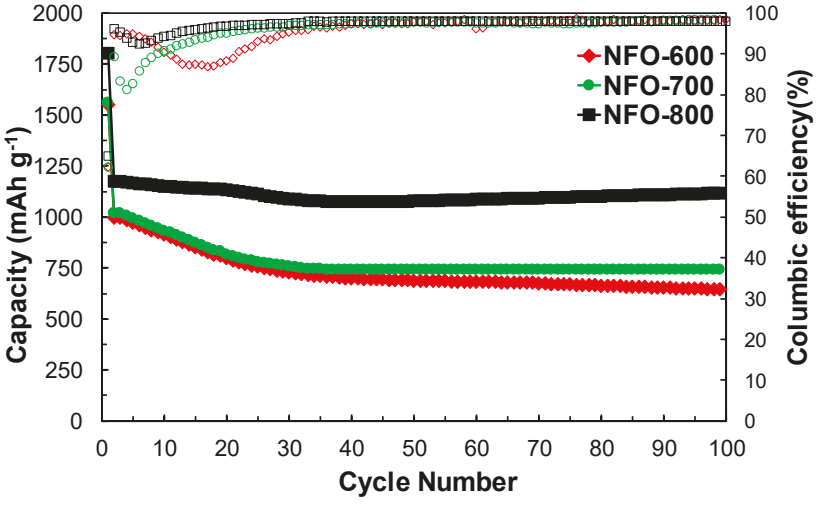

Figure 9. Cycle performance of the $NiFe_2O_4$ electrode annealed at different temperatures.

Based on the above results, the annealed $NiFe_2O_4$ electrodes not only improve the high crystal structure, but also show better electrochemical properties. The $NiFe_2O_4$ electrode with an interface layer between $NiFe_2O_4$ and the SUS substrate has given a higher discharge capacity than the theoretical $NiFe_2O_4$ anode materials. In particular, the NFO-800 electrodes have maintained their structural integrity, which improves the cycle stability with a high discharge capacity after 100 cycles. Moreover, this study reveals different physical and electrochemical properties of the $NiFe_2O_4$ electrode when compared to a conventional electrode that is based on a copper current collector. Finally, the $NiFe_2O_4$ electrode prepared by an e-beam evaporator followed by an annealing process should be an ideal electrode design with a strong adhesion onto the substrate when compared to other preparation methods.

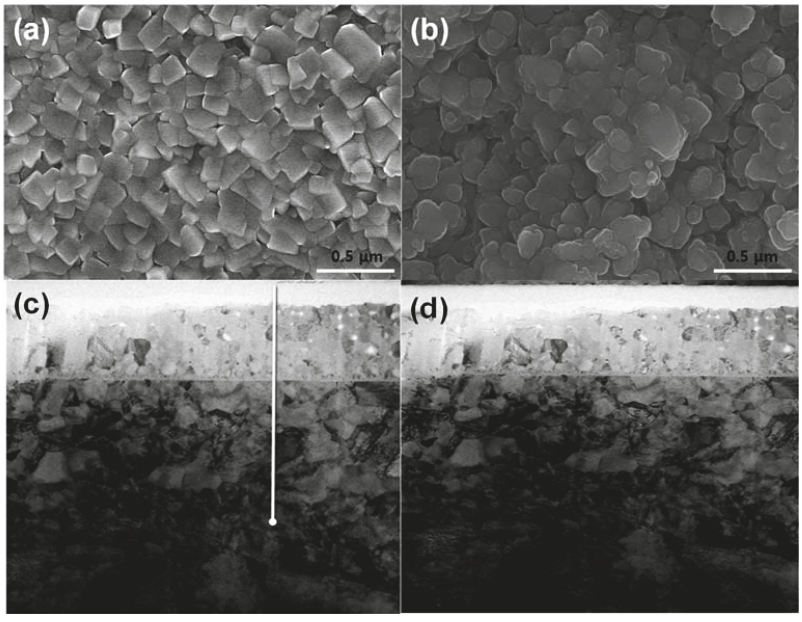

Figure 10. Surface morphologies of the NFO-800 electrode (**a**) before and (**b**) after cycles; (**c**) cross-section image; (**d**) cross-section image.

4. Conclusions

In summary, NFO thin film electrodes have been successfully prepared via deposition method, and the annealing effects on the structural and electrochemical properties of NFO electrodes were investigated in a Li-ion battery system. The XRD diffraction demonstrated the high crystallinity of $NiFe_2O_4$, and the interlayer of Cr_2O_3 was a beneficial feature that was ascribed to a higher specific capacity after the annealing process. The NFO-800 electrode that showed a charge capacity of about 1100 mAh g^{-1} was stable after 100 cycles at a current density of 91.5 mA g^{-1} (0.1C) and with a high capacity retention ratio of 95%. The $NiFe_2O_4$ electrodes also maintained their reversible capacity of 1100 mAh g^{-1} after 100 cycles. The unique properties of the $NiFe_2O_4$ electrode with the annealing process could be further proposed for alternative ferrite materials, which is applicable for anode electrodes for LIB.

Author Contributions: Conceptualization, M.C.; methodology, S.-J.S. and Y.-I.J.; formal analysis and investigation, M.C.; writing—original draft preparation, M.C.; writing—review and editing, B.-K.S.; supervision, M.C. and H.-S.K. All authors have read and agreed to the published version of the manuscript.

Funding: This work was funded by the National Research Foundation of Korea (NRF) grant funded by the Korea government (MSIT) (No.2020M2A8A5079107).

Institutional Review Board Statement: Not applicable.

Informed Consent Statement: Not applicable.

Data Availability Statement: The data presented in this study are available from the corresponding author upon request.

Acknowledgments: The authors acknowledge the National Research Foundation of Korea (NRF) grant funded by the Korean government (MSIT) for financially supporting this research.

Conflicts of Interest: The authors declare no conflict of interest.

References

1. Tang, H.; Zheng, M.B.; Hu, Q.; Chi, Y.; Xu, B.Y.; Zhang, S.T.; Xue, H.G.; Pang, H. Derivatives of coordination compounds for rechargeable batteries. *J. Mater. Chem. A* **2018**, *6*, 13999–14024. [CrossRef]
2. An, Y.L.; Fei, H.F.; Zeng, G.F.; Ci, L.J.; Xiong, S.L.; Feng, J.K.; Qian, Y.T. Green, scalable, and controllable fabrication of nanoporous silicon from commercial alloy precursors for high-energy lithium-ion batteries. *ACS Nano* **2018**, *12*, 4993–5002. [CrossRef]
3. Xu, Z.; Liu, W.; Kim, Y.; Cho, J. Nanostructured transition metal sulfides for lithium ion batteries: Progress and challenges. *Nano Today* **2014**, *9*, 604–630. [CrossRef]
4. Obrovac, M.N.; Chevrier, V.L. Alloy negative electrodes for Li-ion batteries. *Chem. Rev.* **2014**, *114*, 11444–11502. [CrossRef] [PubMed]
5. Yang, Y.H.; Liu, S.; Bian, X.F.; Feng, J.K.; An, Y.L.; Yuan, C. Morphology and porosity tunable synthesis of 3D nanoporous SiGe alloy as a high performance lithium ion battery anode. *ACS Nano* **2018**, *12*, 2900–2908. [CrossRef] [PubMed]
6. Zhang, W.J. A review of the electrochemical performance of alloy anodes for lithium-ion batteries. *J. Power Sources* **2011**, *196*, 13–24. [CrossRef]
7. Gao, G.X.; Wu, H.B.; Lou, X.W. Citrate-assisted growth of $NiCo_2O_4$ nanosheets on reduced graphene oxide for highly reversible lithium storage. *Adv. Energy Mater.* **2014**, *4*, 1400422. [CrossRef]
8. Hou, L.R.; Bao, R.Q.; Denis, D.K.; Sun, X.; Zhang, J.Y.; Zaman, F.U.; Yuan, C.Z. Synthesis of ultra-long $ZnFe_2O_4$@polypyrrole nanowires with enhanced electrochemical Li storage behaviors for lithium-ion batteries. *Electrochim. Acta* **2019**, *306*, 198–208. [CrossRef]
9. Mujahid, M.; Khan, R.U.; Mumtaz, M.; Mubasher, S.A.; Ullah, S. $NiFe_2O_4$ nanoparticles/MWCNTs nano hybrid as anode material for lithium-ion battery. *Ceram. Int.* **2019**, *45*, 8486–8493. [CrossRef]
10. Zhao, Y.; Li, J.; Ding, Y.; Guan, L.J. Enhancing the lithium storage performance of iron oxide composites through partial substitution with Ni^{2+} or Co^{2+}. *Mater. Chem.* **2011**, *21*, 19101–19105. [CrossRef]
11. Heidari, E.K.; Zhang, B.; Sohi, M.H.; Ataie, A.; Kim, J.K. Sandwich-structured graphene–$NiFe_2O_4$–carbon nanocomposite anodes with exceptional electrochemical performance for Li ion batteries. *J. Mater. Chem. A* **2014**, *2*, 8314–8322. [CrossRef]
12. Oh, M.; Kim, I.; Lee, H.-J.; Hyun, S.; Kang, C. The role of thermal annealing on the microstructures of (Ti, Fe)-alloyed Si thin film anodes for high-performance Li-ion batteries. *RSC Adv.* **2018**, *8*, 9168–9174. [CrossRef]
13. Maino, G.; D'haen, J.; Mattelaer, F.; Detavernier, C.; Hardy, A.; Van Bael, M.K. Effect of annealing atmosphere on $LiMn_2O_4$ for thin film Li-ion batteries from aqueous chemical solution deposition. *J. Mater. Chem. A* **2016**, *4*, 18457–18469. [CrossRef]
14. Abdollahifar, M.; Huang, S.S.; Lin, Y.H.; Sheu, H.S.; Lee, J.F.; Lu, M.L.; Wu, N.L. Tetragonal $LiMn_2O_4$ as dual-functional pseudo capacitor-battery electrode in aqueous Li-ion electrolytes. *J. Power Sources* **2019**, *412*, 545–551. [CrossRef]
15. Abdollahifar, M.; Lannelongue, P.; Liu, H.W.; Chen, H.; Liao, C.-H.; Sheu, H.-S.; Lee, J.-F.; Liao, Y.-F.; Wu, N.-L. Room-temperature synthesis of Li_2MnO_4 by electrochemical ion exchange in aqueous medium. *ACS Sustain. Chem. Eng.* **2021**, *9*, 13717–13725. [CrossRef]
16. Wang, J.N.; Yang, G.R.; Wang, L.; Yan, W. Synthesis of one-dimensional $NiFe_2O_4$ nanostructures: Tunable morphology and high-performance anode materials for Li ion batteries. *J. Mater. Chem. A* **2016**, *4*, 8620–8629. [CrossRef]
17. Fu, M.; Qiu, Z.Z.; Chen, W.; Lin, Y.M.; Xin, H.L.; Yang, B.; Fan, H.S.; Zhu, C.Z.; Xu, J. $NiFe_2O_4$ porous nanorods/graphene composites as high-performance anode materials for lithium-ion batteries. *Electrochim. Acta* **2017**, *248*, 292–298. [CrossRef]
18. Islam, M.; Ali, G.; Jeong, M.G.; Choi, W.; Chung, K.Y.; Jung, H.G. Study on the electrochemical reaction mechanism of $NiFe_2O_4$ as a high-performance anode for Li-ion batteries. *ACS Appl. Mater. Interfaces* **2017**, *9*, 14833–14843. [CrossRef] [PubMed]
19. Choi, M.; Lee, S.-H.; Jung, Y.-I.; Jung, J.-Y.; Park, J.-S.; Choi, W.-K.; Park, S.-Y.; Won, H.-J.; Moon, J.-K.; Choi, J.; et al. The high capacity and cycle stability of $NiFe_2O_4$ thin film prepared by E-beam evaporation method for lithium ion batteries. *J. Alloys Compd.* **2017**, *729*, 802–808. [CrossRef]
20. Choi, M.; Lee, S.-H.; Jung, Y.-I.; Choi, W.-K.; Moon, J.-K.; Choi, J.; Seo, B.-K.; Kim, S.-B. The preparation of Fe_3O_4 thin film and its electrochemical characterization for Li-ion battery. *Trans. Electr. Electron. Mater.* **2018**, *19*, 417–422. [CrossRef]
21. Guo, K.; Soeriyadi, A.H.; Feng, H.; Prevoteau, A.; Patil, S.A.; Gooding, J.J.; Rabaey, K. Heat-treated stainless steel felt as scalable anode material for bioelectrochemical systems. *Bioresour. Technol.* **2015**, *195*, 46–50. [CrossRef] [PubMed]
22. Robertson, J. The mechanism of high temperature aqueous corrosion of stainless steels. *Corros. Sci.* **1991**, *32*, 443–465. [CrossRef]
23. Behnamian, Y.; Mostafaei, A.; Kohandehghan, A.; Amirkhiz, B.S.; Serate, D.; Sun, Y.; Liu, S.; Aghaie, E.; Zeng, Y.; Chmielus, M.; et al. A comparative study on corrosion behavior of stainless steel and nickel-based superalloys in ultra-high temperature supercritical water at 800 °C. *Corros. Sci.* **2016**, *106*, 188–207. [CrossRef]
24. Kreisel, J.; Lucazeau, G.; Vincent, H. Raman spectra and vibrational analysis of $BaFe_{12}O_{19}$ hexagonal ferrite. *J. Solid State Chem.* **1998**, *137*, 127–137. [CrossRef]
25. Himcinschi, C.; Vrejoiu, I.; Salvan, G.; Fronk, M.; Talkenberger, A.; Zahn, D.R.T.; Rafaja, D.; Kortus, J. Optical and magneto-optical study of nickel and cobalt ferrite epitaxial thin films and submicron structures. *J. Appl. Phys.* **2013**, *113*, 084101–084108. [CrossRef]
26. Oh, H.D.; Lee, S.W.; Kim, S.O.; Lee, J.K. Facile synthesis of carbon layer-entangled Fe_2O_3 clusters as anode materials for improved Li-ion batteries. *J. Power Sources* **2013**, *244*, 575–580. [CrossRef]
27. Wang, Y.; Su, D.; Ung, A.; Ahn, J.-H.; Wang, G. Hollow $CoFe_2O_4$ nanospheres as high capacity anode material for lithium ion batteries. *Nanotechnology* **2012**, *23*, 055402. [CrossRef]

28. Liu, S.; Xie, J.; Fang, C.; Cao, G.; Zhu, T.; Zhao, X. Self-assembly of $CoFe_2O_4$/graphene sandwich by a controllable and general route: Towards a high-performance anode for Li-ion batteries. *J. Mater. Chem.* **2012**, *22*, 19738–19743. [CrossRef]
29. Laruelle, S.; Grugeon, S.; Poizot, P.; Dolle, M.; Dupont, L.; Tarascon, J.-M. On the Origin of the Extra Electrochemical Capacity Displayed by MO/Li Cells at Low Potential. *J. Electrochem. Soc.* **2002**, *149*, A627–A634. [CrossRef]
30. Zhou, G.; Wang, D.W.; Li, F.; Zhang, L.; Li, N.; Wu, Z.-S.; Wu, L.; Lu, G.Q.; Cheng, H.-M. Graphene-wrapped Fe_3O_4 anode material with improved reversible capacity and cyclic stability for Lithium ion batteries. *Chem. Mater.* **2010**, *18*, 5306–5313. [CrossRef]
31. Kumar, P.R.; Mitra, S. Nickel ferrite as a stable, high capacity and high rate anode for Li-ion battery applications. *RSC Adv.* **2013**, *3*, 25058–25064. [CrossRef]

nanomaterials

MDPI

Review

Hetero-Element-Doped Molybdenum Oxide Materials for Energy Storage Systems

Bo Hu [1,2], Shuofeng Jian [1], Ge Yin [1], Wenhao Feng [1], Yaowen Cao [1], Jiaxuan Bai [1], Yanan Lai [1], Huiyun Tan [1,*] and Yifan Dong [1,*]

[1] Engineering Research Center of Nano-Geomaterials of Ministry of Education, Faculty of Material Science and Chemistry, China University of Geosciences, Wuhan 430074, China; hubocug@cug.edu.cn (B.H.); jianshuofeng@163.com (S.J.); yinge3111818157@126.com (G.Y.); wenhaofeng5@gmail.com (W.F.); caoyaowen12@163.com (Y.C.); Phoenix9360@yeah.net (J.B.); nannan2002617@163.com (Y.L.)

[2] Faculty of Material Science and Chemistry, China University of Geosciences, Wuhan 430074, China

* Correspondence: thy98_cug@163.com (H.T.); dongyf@cug.edu.cn (Y.D.)

Abstract: In order to meet the growing demand for the electronics market, many new materials have been studied to replace traditional electrode materials for energy storage systems. Molybdenum oxide materials are electrode materials with higher theoretical capacity than graphene, which was originally used as anode electrodes for lithium-ion batteries. In subsequent studies, they have a wider application in the field of energy storage, such as being used as cathodes or anodes for other ion batteries (sodium-ion batteries, potassium-ion batteries, etc.), and electrode materials for supercapacitors. However, molybdenum oxide materials have serious volume expansion concerns and irreversible capacity dropping during the cycles. To solve these problems, doping with different elements has become a suitable option, being an effective method that can change the crystal structure of the materials and improve the performances. Therefore, there are many research studies on metal element doping or non-metal doping molybdenum oxides. This paper summarizes the recent research on the application of hetero-element-doped molybdenum oxides in the field of energy storage, and it also provides some brief analysis and insights.

Keywords: molybdenum oxides; hetero-element doping; energy storage materials

Citation: Hu, B.; Jian, S.; Yin, G.; Feng, W.; Cao, Y.; Bai, J.; Lai, Y.; Tan, H.; Dong, Y. Hetero-Element-Doped Molybdenum Oxide Materials for Energy Storage Systems. *Nanomaterials* **2021**, *11*, 3302. https://doi.org/10.3390/nano11123302

Academic Editor: Marc Cretin

Received: 20 October 2021
Accepted: 22 November 2021
Published: 6 December 2021

1. Introduction

The rapid growth of the population and industrial production have put great pressure on natural resources, and, with the depletion of fossil energy and the rapid development of electronic products, the demands for high energy density and power density energy storage equipment, such as ion batteries and supercapacitors, continues to grow [1–3]. Over the last few decades, lithium-ion batteries (LIBs) have become the favorite in the consumer electronics market due to their good energy density, long cycle life, and environmental friendliness. The abundant mineral materials in nature are used as the matrix for the research of electrode materials for lithium-ion batteries [4]. As we know, transition metal oxides are appropriate for the insertion/extraction of small ions, such as H^+ and Li^+, so they are candidates for a wide range of applications, including energy storage devices [5]. Among the transition metal oxides, molybdenum oxides have diverse crystal structures, oxidation states, and particular physicochemical properties, such as conductivity, mechanical and thermal stability, as well as cyclability [6]. In addition, they are wide band gap n-type semiconductors, which plays a vital role in technological applications [7]. At the same time, graphite materials have been successfully marketed as anodes for LIBs for decades, but the low theoretical specific capacity of 372 mA h g^{-1} has gradually failed to meet the growing demand for high energy density batteries [8,9]. Molybdenum oxide, particularly MoO_2, has received considerable attention due to its metallic conductivity and high theoretical capacity (838 mA h g^{-1}) [10]. Therefore, molybdenum oxides, as

cathode or anode materials, appear to be promising candidates for ion secondary batteries and supercapacitors.

There has been a great deal of research on pure molybdenum oxides using different methods, such as thermal decomposition [11], chemical vapor deposition [12], hydrothermal-solvothermal process [13–15], thermal evaporation, and nanocasting, to synthesize nanostructure molybdenum oxides to increase electrochemical performance. However, the interlamellar spacing of pure molybdenum oxides is limited, it is difficult to enhance their specific capacities, and they cannot hold big ions, such as Na^+, K^+, Zn^{2+}, and Mg^{2+}. Therefore, it is necessary to approach them from another perspective to improve the electrochemical performance of molybdenum oxide-based materials. Doping with different elements is an effective strategy, which can increase the distance between the layers in the crystal structure, change the layered crystal structure to a tunnel-type structure, or enhance conductivity.

Hetero-element doping molybdenum oxides can be divided into several varieties, namely alkali metal (Li, Na, or K) and alkaline earth metal (Mg or Ca) doping, transition metal (Zn, Ni, Mn, Ti, or Co) or their oxides doping, non-metal (C or N) doping, as well as non-metal-/metal-doped composites. Metal doping molybdenum oxides are attractive as hosts for ions, which can form multiple crystal structures or phases. The combination of dissimilar metal with molybdenum oxides is able to produce materials with new architectural and chemical characteristics; thus, a variety of systems could be explored [6]. In addition, some metal-doped molybdenum oxides have a pseudocapacitive property according to the literature [16,17]. Non-metal doping is a common way of material modification, while the frame structure composed of carbon or nitrogen can greatly increase the specific surface area of the materials and enhance conductivity. Because molybdenum has different oxidation states in the compounds, molybdenum oxides doped with different elements have a variety of chemical compositions and crystal phases, and there are bound to be many synthetic methods to obtain new materials. In this review, we primarily highlight and summarize the variety of hetero-element-doped molybdenum oxide materials and their synthetic methods, as well as their electrochemical performance as energy storage materials. Figure 1 summarizes some typical crystal structures and nanostructures of hetero-element-doped molybdenum oxide materials, as well as the schematic diagram of their application in energy storage systems; the details will be introduced later.

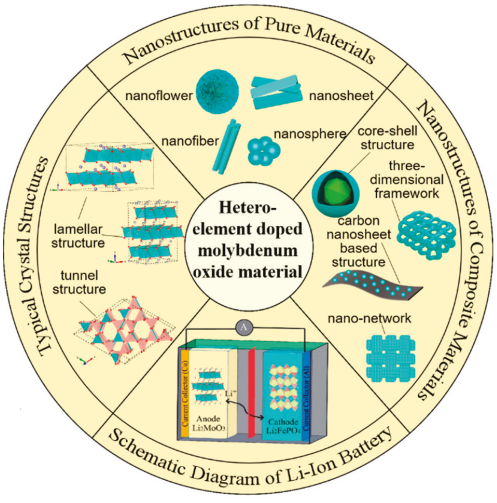

Figure 1. Summarization of some typical crystal structures and nanostructures of hetero-element-doped molybdenum oxide materials, as well as the schematic diagram of their application in energy storage systems.

2. Alkali Metal and Alkaline Earth Metal-Doped

2.1. Alkali Metal-Doped

Alkali metal-doped molybdenum oxides mainly include A_xMoO_2, A_xMoO_3, A_2MoO_4 (A = Li, Na, or K), $Li_4Mo_3O_8$, and $Li_2Mo_4O_{13}$ [18–24]. Most $LiMO_2$ (M = Co, Mn, Ni, Fe) is associated with rock-salt architectures and is an ordered or distorted form of NaCl. $AMoO_2$ (A = Li, Na or K) is isostructural to well-known $LiMO_2$ materials for LIBs, having the potential to be the lithium storage material. Per unit of MoO_2 can hold up to 0.85 Li at an average potential of 3 V [19,25]. Li_2MoO_3 has a novel, disordered α-$NaFeO_2$ structure (R-3m) with the molybdenum present as Mo_3O_{13} clusters (Figure 2b), firstly determined by James and Goodenough [26]. The Mo^{4+} in the Li_2MoO_3 compound can be oxidized to Mo^{6+} oxidation state when the Li_2MoO_3 is charged to 4.4 V (vs. Li^+/Li). Therefore, Li_2MoO_3 can carry out a two-electron electrochemical reaction per unit molecule, so it has a huge potential for energy storage (theoretical capacity is about 339 mA h g^{-1}) [27,28]. The crystal of Li_2MoO_4 (Figure 2a) shows a tunnel structure, consisting of a three-dimensional network of corner-linked, slightly distorted LiO_4 and MoO_4 tetrahedra along crystallographic c-axis [29,30]. As is well-known, materials with NASICON-type structure are also promising candidates for energy storage systems.

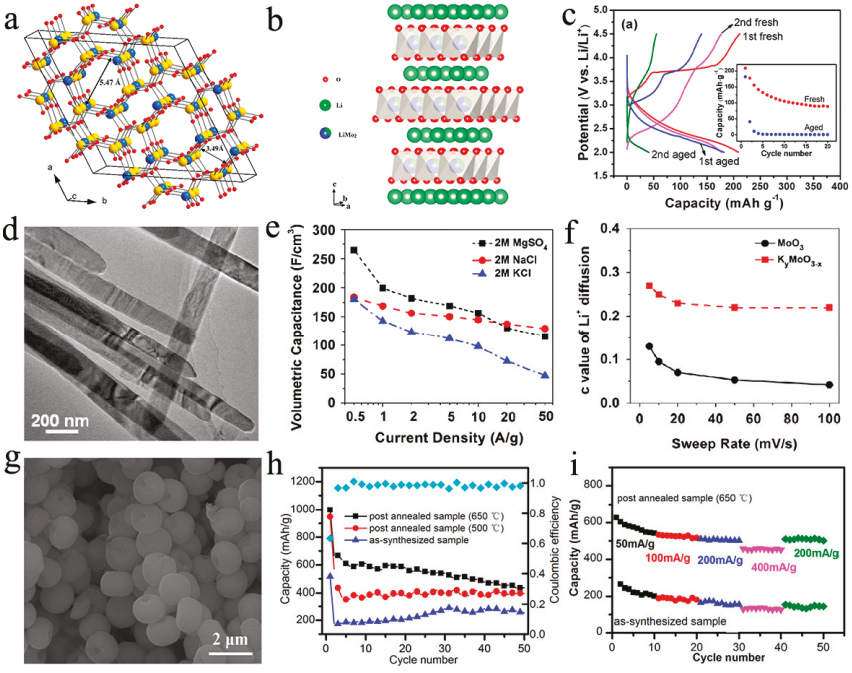

Figure 2. (**a**) Crystal structure of the rhombohedral modification of Li_2MoO_4. Blue and yellow spheres represent Mo and Li ions, respectively. Narrow and wide channels along the c-axis feature 4-member rings and 6-member rings, respectively. Reproduced with permission. [30] Copyright 2015, American Chemical Society. (**b**) Lattice structure of Li_2MoO_3. (**c**) Charge and discharge potential curves of the fresh and aged Li_2MoO_3; the inset is for their cycling performances. Reproduced with permission. [31] Copyright 2014, Elsevier B. V. (**d**) Low-resolution TEM image of K_yMoO_{3-x} nanobelts. (**e**) Volumetric capacitance and current density for K_yMoO_{3-x} in different electrolytes. (**f**) Numbers of Li^+ inserted in the tunneled MoO_3 and K_yMoO_{3-x} (c value of Li^+ diffusion). Reproduced with permission. [16] Copyright 2015, Elsevier B. V. (**g**) Morphological of as-synthesized $CaMoO_4$ microspheres by reaction time of 0.5 h. (**h**) Cycling performance of the $CaMoO_4$ microspheres before and after being heat-treated at different temperatures at current densities of 200 mA g^{-1}. (**i**) Rate performance of $CaMoO_4$ microspheres before and after calcination at 650 °C. Reproduced with permission. [32] Copyright 2018, Springer Nature.

Recently, many studies about alkali metal-doped molybdenum oxides have been reported. Ma et al. [31] investigated the structural and performance stability of Li_2MoO_3 in air. They found that Li_2MoO_3 can be oxidized/decomposed in air at room temperature. The oxidation of Mo^{4+} and the consumption of Li^+ led to the generation of Li^+ vacancies, Mo^{4+} migration, Li-Mo inversion, and the destruction of Mo_3O_{13} clusters in Li_2MoO_3. Therefore, as shown in Figure 2c, the aged material (storing the phase-pure Li_2MoO_3 in desiccators with a relative humidity of below 10% at room temperature for 120 days) delivered more attenuation of capacity after the initial cycle. Verma and coworkers [24] devised a novel procedure for the synthesis of $Li_2Mo_4O_{13}$ using a single-step conventional solid-state reaction. The rod-like (size range of 1–10 μm) material shows an initial reversible capacity of 1062 mA h g^{-1} at 0.1 C (up to theoretical capacity), and the capacity retention is 74% over 50 cycles with coulombic efficiency close to 98% during the subsequent cycles, proving that $Li_2Mo_4O_{13}$ electrodes exhibit high reversible capacity and great cycling performance. K^+ pre-intercalated hydrogenated MoO_3 (K_yMoO_{3-x}) material was reported by Xiao [16]. The MoO_3 nanobelts were synthesized using the hydrothermal method, hydrogenation was used to introduce oxygen vacancies into MoO_3 nanobelts (Figure 2d), and the resulting $MoO_{3-\delta}$ was further reacted with KBH_4. It was proved that several kinds of ions (Li^+, Na^+, K^+, and Mg^{2+}) with different ion dimensions can embed into the K_yMoO_{3-x}. In Figure 2e,f, the authors calculated volumetric capacitance at different current density for K_yMoO_{3-x} in three electrolytes, as well as the number of inserted Li^+ in K_yMoO_{3-x} and MoO_3. It is noted that Mg^{2+} has the greatest capacitance, while Na^+ has the best retaining capacitance, and, when the sweep frequency is augmented to 100 mV s^{-1}, the quantum of inserted Li^+ in K_yMoO_{3-x} remains almost invariant (from 0. 27 to 0.22), but only 0.042 Li^+ is embedded in MoO_3, demonstrating that K_yMoO_{3-x} has a wider interlayer distance and stronger conductivity compared to pure MoO_3. Zhu et al. [33] reported a novel layered sodium molybdenum oxide $Na_{0.3}MoO_2$ synthesized by solid-state reaction as an anode material for sodium-ion batteries (SIBs). The crystal and nanostructure of $Na_{0.3}MoO_2$ are both layered morphologies, and the long-term cycling performance shows an excellent capacity retention of 72.4% after 1000 cycles, and the coulombic efficiency is up to about 100%, except for the preliminary cycle.

In addition to single element doping, there are also some double elements-doped materials. In the existing research, potassium is doped in Li-rich molybdenum-based oxide or sodium molybdate. Yu et al. [34] prepared K-doped Li_2MoO_3 cathode material for the first time; the K-doped MoO_3 nanobelts were synthesized by hydrothermal method and used as templates and then annealed at high ambient temperatures. The larger K^+ could not be extracted from the interlayer during de-lithiation, staying in the Li slab to restrain the phase transformation, so the doped samples are more stable. The obtained $Li_{1.9}K_{0.1}MoO_3$ has a satisfying initial capacity (235 mA h g^{-1} at 0.05 C rate, 1C = 320 mA g^{-1}). Additionally, after a certain number of cycles, it maintains 56% of its initial capacity, which is much better than the undoped sample Li_2MoO_3 (38%). The enhanced electrochemical performance may be due to the change in the valence state of Mo^{4+} in the $Li_{1.9}K_{0.1}MoO_3$ crystal, making the sample hardly release oxygen even if it is charged to a potential of 4.4 V (vs. Li^+/Li). Serdtsev and coworkers [35] predicted the possible sodium-ion pathways and the energy barriers for sodium diffusion in the glaserite-type $A_{3-x}Na_{1+x}(MoO_4)_2$ (A = Cs, K) through the approximate bond valence sum approach. The double molybdate $K_3Na(MoO_4)_2$ has a monoclinic distorted superstructure (space group C2/c) with a quadruple unit cell, which corresponds to a much lower energy barrier for migration through the K site compared to the normal sodium site, while the ionic conductivity of sodium can be strengthened for pyrochlore doped with divalent or trivalent ions. At present, there are relatively few studies related to bimetallic elements-doped molybdenum oxide materials. However, according to the existing work, it can be seen that this strategy is expected to obtain electrode materials with a long cycle life and further improve the performance of single metal-element-doped molybdenum oxide materials.

2.2. Alkaline Earth Metal-Doped

Ca_xMoO_3, $CaMoO_4$, Mg_xMoO_3, and $MgMoO_4$ [36–39] are several common alkaline earth metal doping molybdenum oxides. $CaMoO_4$ adopts a tetragonal scheelite structure with the Mo in tetrahedral O-coordination [37]. The $CaMoO_4$ microspheres with nano-pits were synthesized through the facile hydrothermal method by You et al. [32]. The SEM of $CaMoO_4$ microspheres is shown in Figure 2g; the nano-pits distributed on the $CaMoO_4$ microspheres can alleviate the volume expansion problem and increase the specific surface area and wettability with the electrolyte, thus improving cycle stability and electrochemical performance. They discovered that the discharge capacity of $CaMoO_4$ tends to increase with increasing calcination temperature. In Figure 2h,i, for $CaMoO_4$, which is annealed at 650 °C, the leftover organic matter is fully carbonized and the best crystallinity is obtained after the high temperature treatment. When the post-annealed $CaMoO_4$ is used as anode for Li-ion battery, it has a higher reversible capacity (434 mA h g^{-1} at 200 mA g^{-1} after 50 cycles) than the theoretical capacity of graphite (372 mA h g^{-1}). The single crystals of $MgMoO_4$ displayed monoclinic symmetry and adopted the C2/m space group at normal temperature and pressure [40]. Haetge [41] reported the synthesis of templates for porous $MgMoO_4$ films with nanocrystalline walls. These materials were produced by solution phase co-assembly of chlorinated salt precursors with KLE-type poly(ethylene-co-butylene)-block-poly (ethylene oxide) di-block copolymers using the evaporation-induced self-assembly process. As the electrodes for the Li-ion battery, $MgMoO_4$ thin films deliver 162 mA h g^{-1} at C/1.5 (1C is defined as the intercalation of 1 Li^+ per formula unit in 1 h at 25 °C) after 100 cycles, and the capacity decreases only slightly between the 20th and 100th cycles. At the same time, the material employed in this work can be reversibly cycled at C/2 (175 mA h g^{-1}), 1 C (167 mA h g^{-1}), 2 C (147 mA h g^{-1}), 4 C (130 mA h g^{-1}), and 8 C (116 mA h g^{-1}) rates. It can be known that not all alkaline earth metal-doped molybdenum oxide materials can have a high capacity, although their cycling stability is relatively excellent. This may be related to the crystal structure of the material itself, which determines the material's ability to hold active ions. Of course, this is also reflected in other hetero-element-doped molybdenum oxide materials.

3. Transition Metal-Doped

Two main forms of transition metal-doped molybdenum oxides exist, namely $A_2Mo_3O_8$ and $AMoO_4$ (A = transition metal) [42–44]. $AMoO_4$ (A = transition metal), namely Mo-containing mixed oxides, are appropriate for ions to insertion, which can form multiple crystal structures or phases. The combination of dissimilar metal with molybdenum oxides is able to produce materials with new structures and chemical properties. The crystal structure of $NiMoO_4$ belongs to monoclinic crystal system (Figure 3a), and the rod-like $NiMoO_4$ produced through solution combustion synthesis was used for sodium batteries for the first time by Minakshi and coworkers [45], exhibiting a safe operation potential (~1.0 V vs. Na^+/Na). The rod crystalline phasing consists of tiny NiO grains (30 nm clusters of 10 nm grains) solidly fixed to the $NiMoO_4$ rods. The percentage of NiO rises with the quantity of oxidant, while the rods show cracks and fractures at the highest oxidant levels. These rods display a staggered morphology, allowing good surface pathways for ion exchange. Therefore, this hetero-structure material produces a high initial discharge capacity of 550 mA h g^{-1} at a current density of 0.05 A g^{-1}. In addition, it has good capacity retention of 82% after 50 cycles. Rod-shaped $MnMoO_4$ crystals with two-dimensional nanosheets have been satisfactorily produced by a new and facile wet chemical method with the help of polyvinylpyrrolidone by Liu's group [46]. Figure 3b shows the schematic diagram of the synthesis process. The rod-shaped $MnMoO_4$ is used as the work electrode for the supercapacitor and shows excellent long cycling and rate performance due to the two-dimensional nanosheets providing increased interfacial contact between the $MnMoO_4$ active material and the electrolyte, which facilitates the diffusion and charge transfer of the electrolyte. Figure 3c further illustrates the charge/discharge curves at the current density of 1 A g^{-1} for last 10 cycles (totally cycled for 1000 cycles), and

the coulombic efficiency remains nearly 100% for each cycle, with a completely reversible lithium storage process. Fei et al. [47] analyzed the electrochemical properties of α-$ZnMoO_4$ nanoparticles as anode material for Li-ion battery by a simple co-precipitation method and subsequently calcined for the first time. TEM shows the morphological property of α-$ZnMoO_4$ in Figure 3d, and the samples show a dispersed and uniform morphology with a diameter of 200–300 nm. As shown in Figure 3e, the as-prepared α-$ZnMoO_4$ exhibits excellent electrochemical performance, including a very stable capacity of 389 mA h g^{-1} at 50 mA g^{-1} with capacity loss of 0.2% per cycle for the 80th cycle. It also has excellent rate performance, and the capacity is basically restored when the current density returns to the initial value.

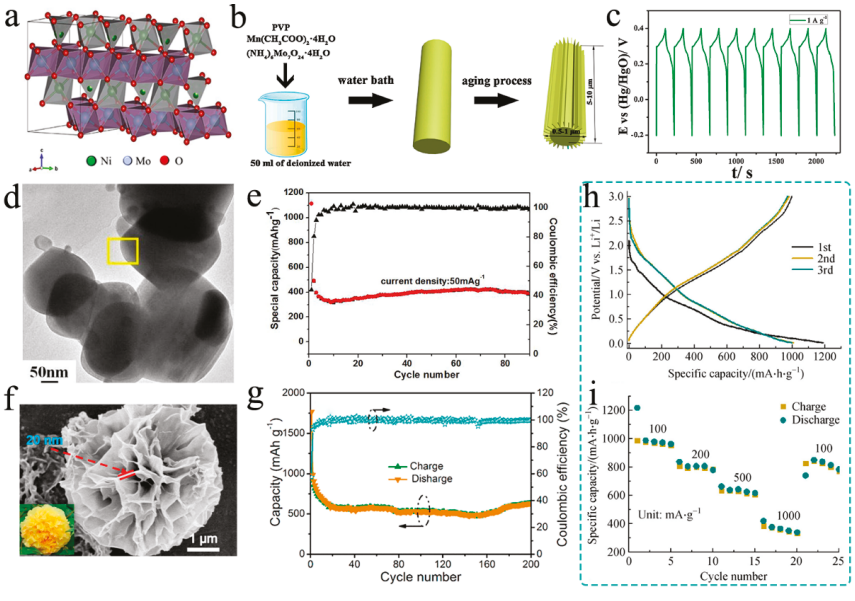

Figure 3. (**a**) Crystal structure of monoclinic $NiMoO_4$ illustrating the coordination relationship of NiO_6 and MoO_6 octahedra. Reproduced with permission. [45] Copyright 2018, Elsevier Ltd. (**b**) Schematic diagram illustrating the formation process of rod-like $MnMoO_4$ crystalline with two-dimensional nanoflakes. (**c**) GCD (galvanostatic charge–discharge) curves of the energy storage made from rod-like $MnMoO_4$ crystalline in last 10 cycles at 1A g^{-1}. Reproduced with permission. [46] Copyright 2017, Elsevier Ltd. (**d**) SEM image of α-$ZnMoO_4$. (**e**) Cycling performance of α-$ZnMoO_4$. Reproduced with permission. [47] Copyright 2017, Elsevier B. V. (**f**) SEM image of $Cu_3Mo_2O_9$. (**g**) Cycling performance and coulombic efficiency of $Cu_3Mo_2O_9$ at 0.1 A g^{-1}. Reproduced with permission. [48] Copyright 2017, Elsevier B. V. (**h**,**i**) Discharge–charge voltage profiles and rate performance of $Fe_2Mo_3O_8$ hollow spheres. Reproduced with permission. [49] Copyright 2020, Higher Education Press.

$LiHoMo_3O_8$ was prepared successfully through carbothermal reaction at 750 °C by Das et al. [50]. The Li-storage and recyclability have been examined, which delivered a high level of capacity (~470 mA h g^{-1} at 30 mA g^{-1} in rate performance) under ambient temperature. This work lays the foundation for the study and understanding of the lithium cycling mechanism of molybdenum cluster oxides and their potential applications in lithium storage devices. In the meantime, there have been many studies of isostructural Mo-cluster mixtures in which Ho is substituted by Y and possibly other heavy rare earth ions, or those in which the Li and Ho ions are substituted by two divalent metal ions, such as transition metals [42,51]. Thus, more research on the use of $A_2Mo_3O_8$ (A = transition metal) for energy storage has been reported [42,49,52,53]. Chowdari's group [42] reported the electrochemical performance and the Li-cycling mechanism of $Mn_2Mo_3O_8$ early. The

synthesized $Mn_2Mo_3O_8$ belongs to the P63mc space group and the Rietveld refined lattice parameters are: a = 5.795(2) Å and c = 10.254(2) Å. The first discharge capacity of $Mn_2Mo_3O_8$ is about 710 mA h g^{-1}, while it shows bad cycling performance. Recently, Zhang and coworkers [49] constructed novel self-assembled iron (II) molybdenum (IV) oxide hollow globules with a wall of 100 nm by a bubble-template-assisted hydrophile method of synthesis combined with simple calcination. The tight integration of miniature nanoparticles on the surface of the hollow globules not only offers more active sites for $Fe_2Mo_3O_8$ but also contributes to the stability of the hollow structure, thus enhancing the lithium storage performance. The discharge–charge voltage profiles and rate performance of $Fe_2Mo_3O_8$ hollow spheres are shown in Figure 3h,i; $Fe_2Mo_3O_8$ hollow spheres deliver the initial discharge and charge capacities of 1189 and 997 mA h g^{-1} at 100 mA g^{-1}, respectively, which are higher than the theoretical capacity of 813 mA h g^{-1} based on lithium storage mechanism of redox conversion. Additionally, in the rete performance, when the current rate decreases to 0.1 A g^{-1}, a high discharge capacity of 812 mA h g^{-1} can still be regained, suggesting the desirable tolerance of the $Fe_2Mo_3O_8$ electrode. Therefore, it is very important to improve the cycling stability and rate performance of the electrode materials by seeking suitable synthesis methods and modification methods.

In addition to these two types of transition metal-doped molybdenum oxides, $A_2Mo_3O_8$ and $AMoO_4$ (A = transition metal), $Cu_3Mo_2O_9$ used as anode for Li-ion battery was reported by Guo's group [48]. They developed a facile strategy to fabricate the 3D hierarchical $Cu_3Mo_2O_9$ flowers via simply calcining the $Cu_3(OH)_2(MoO_4)_2$ nano-cuboids, which can be accomplished easily by one-pot hydrothermal method. The final hierarchical flower-like $Cu_3Mo_2O_9$ was transferred from self-assembled rectangular parallelepiped single nanocrystal via calcination in air (SEM is shown in Figure 3f). They investigated the influence of temperature during the calcination, finding that the 3D hierarchical morphology of the $Cu_3Mo_2O_9$ annealed at 600 °C is different either from the one that is composited of irregular nanoparticles at 400 °C or from the one that is excessively aggregated at 700 °C, which is the best in these three materials. As shown in Figure 3g, after 200 cycles, the $Cu_3Mo_2O_9$ electrode was still capable of delivering a specific capacity of 632 mA h g^{-1} at 0.1 A g^{-1} with a large coulombic efficiency (~99%), demonstrating its remarkable cycling stability and reversibility. When designing experiments, we often need to set concentration gradients, temperature gradients, etc., to find the best reaction conditions. In fact, this is a very basic understanding for the synthesis of nanomaterials.

4. Non-Metal-Doped

Doping with non-metallic elements, such as carbon and nitrogen, is a typical method of electrode material modification. Carbon and nitrogen doping modification generally does not affect the crystal structure of molybdenum-based materials, but different synthesis methods, such as co-precipitation, hydrothermal technology, etc., can be used to obtain composite materials with different nanostructures. Although some molybdenum oxides possess metallic conductivity, it is necessary to improve on their electrical conductivity for better electrochemical performances. In addition, substantial volume expansion during repetitive cycling remains the key to limiting its practical deployment in lithium-ion batteries [54]. Crossbreeding with carbonaceous substrates, such as graphene, carbon nanotubes and meso/microporous carbon, carbon black, and carbon dots [55–61], is an efficient tactic to address these issues. The nanostructure of the composite material can increase the specific surface area of the material to a certain extent so that the material and the electrolyte can be more fully contacted. For doping methods, in situ synthesis, hydrothermal, calcination, etc., have been proven to be the simple and scalable approach [56,61,62]. Lu's group [60] investigated the carbon vacancy defects using density functional theory (DFT); C vacancy formation in a perfect graphene matrix was taken as a reference. When one C atom is replaced by N, the relative C vacancy formation energy becomes more negative, indicating that C atoms are gradually easier to detach, especially when replaced by bonding to N (−2.99 eV), and N doping can effectively induce C defect formation. This kind of

ability could improve the electron conductivity of electrodes and increase the active sites for ions storage. Therefore, besides doping carbon, additionally doping with nitrogen is also an effective strategy to modify materials.

In specific studies, Cao's group [63] presented a two-step hydrothermal-calcination method to produce MoO_2/N-doped graphene (MoO_2/N-GNS) hybrids, in which MoO_2 nanoparticles were homogeneously distributed on N-GNS sheets through Mo-N chemical bonds formed between MoO_2 and N-GNS (Figure 4a). Benefiting from the substrate of graphene and N-doping, the mixture has a large specific surface area (Figure 4b). As Figure 4c indicates, this material was used as an anode for Li-ion battery, delivering a high initial discharge capacity of 1517 mA h g^{-1}, and the MoO_2/N-GNS still offered a reversible capacity of up to 1139 mA h g^{-1} at 100 mA g^{-1} after 60 cycles. Three molybdenum oxide-carbon nanotube hybrid materials were investigated as the negative electrodes in an Li-ion capacitor (LICs) by Fleischmann and coworkers [64] for the first time. They compared the properties of materials with different crystal structures and morphologies obtained by annealing after deposition. The SEM of MoO_2-CNT (the best performance) is shown in Figure 4d, and flake crystals were observed in CNT networks with transverse dimensions up to 150 nm and thicknesses up to about 50 nm. Based on its excellent morphological characteristics, MoO_2-CNT negative electrodes exhibit a superior rate handling, delivering a higher maximum capacity of around 150 mA h g^{-1} compared with MoO_x-CNT and MoO_3-CNT when the current density decreased to 0.05 A g^{-1} (Figure 4e). Additionally, the calculated high power density refers to 70 Wh kg^{-1} at 83 W kg^{-1}. In fact, in molybdenum oxides, molybdenum dioxide itself has a pseudocapacitive property, so it is a matter of course that MoO_2-CNT has the best performance as the electrode for Li-ion capacitor in these three materials. This also lets us know that, sometimes, we can make assumptions about the test results based on whether the matrix material has certain properties.

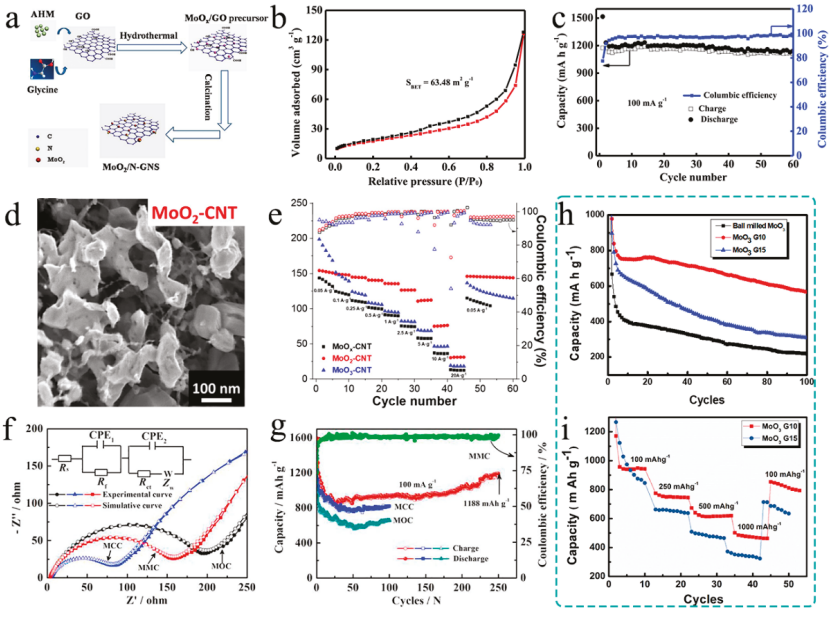

Figure 4. (**a**) Schematic illustration of the synthesis procedure of MoO_2/N-GNS hybrid. (**b**) N_2 adsorption–desorption isotherm. (**c**) Capacity vs. cycle number and the corresponding coulombic efficiency of MoO_2/N-GNS hybrid electrode. Reproduced with permission. [63] Copyright 2014, Elsevier B. V. (**d**) SEM of MoO_2-CNT after annealing at 500 °C in an argon atmosphere. (**e**) Specificde-lithiation capacity and coulombic efficiency derived from galvanostatic cycling at specific

currents between 0.05 and 20 A·g^{-1}. Reproduced with permission. [64] Copyright 2018, American Chemical Society. (**f**) The pore size distributions of MOC, MMC, and MCC samples. (**g**) The discharge–charge of MOC, MMC, and MCC samples at the current density of 100 mA g^{-1}. Reproduced with permission. [65] Copyright 2017, Elsevier B. V. (**h**) Galvanostatic tests of ball-milled MoO_3, MoO_3-10 wt % rGO, and MoO_3-15 wt % rGO. (**i**) Rate performance of MoO_3-10 wt % rGO and MoO_3-15 wt % rGO. Reproduced with permission. [66] Copyright 2019, Elsevier B.V.

For an in situ synthesis method, Chai's group [65] reported MoO_2-Mo_2C-C microspheres (MMC) synthesized via in situ carbonization as anode materials for lithium-ion batteries. Figure 4f shows the electrochemical impedance spectroscopy (EIS) of the materials. Obviously, carbon doping could reduce the charge transfer resistance, leading to a better electron conductivity, and ultimately enhance the diffusion of lithium ions to the MMC samples. Owing to the combination of the higher conductivity of Mo_2C, C and the appropriate content of Mo_2C, the MMC microspheres exhibit excellent cyclability and good stability. As shown in Figure 4g, for the MMC electrode, the initial discharge/charge specific capacities are nearly 1594/1171 mA h g^{-1} at 100 mA g^{-1}, respectively, with a relatively low coulombic efficiency of 73.5%. The loss capacity was accorded with the irreversible procedure, including the insertion of Li^+ into the MoO_2 lattice and the formation of solid electrolyte interface (SEI) film. However, this material visibly delivers an excellent discharge capacity of 1188 mA h g^{-1} after 250 cycles. Recently, Li et al. [67] produced extremely small and widely dispersed MoO_x nanoparticles anchored on N-doped three-dimensional delaminated porous carbon (3D-MoO_x@CN) based on an efficient in situ chelation and hard induction strategy. The MoO_x nanoparticles anchor on the surface of the 3D N-doped carbon with sizes between 1.5 and 3.5 nm. Therefore, the volume change during charge and discharge can be effectively mitigated, while the three-dimensional carbon skeleton can provide a conductive network, thus improving the lithium storage performance (delivering specific capacities of 742 mA h g^{-1} at current density of 100 mA g^{-1} and 431 mA h g^{-1} at 1000 mA g^{-1} after 1000 cycles, respectively).

Satyanarayana's group [66] used a facile high-energy ball-milling process followed by ultrasonication method to prepare MoO_3/rGO composites. Same as above, the composites exhibit better electrochemical performance than just nanostructured due to the increase in surface area and conductivity

Although the specific capacities of three samples drop gradually in the first five cycles, the MoO_3-10 wt % rGO sample still shows higher reversible capacity (568 mA h g^{-1} at a high current density of 500 mA g^{-1} even after 100 cycles) than commercially available graphite (Figure 4h) and good rate performance with specific capacity 502 mA h g^{-1} even at a higher current density of 1000 mA g^{-1}, and it retained the specific capacity of 853 mA h g^{-1} as the current density switched from 1000 mA g^{-1} to 100 mA g^{-1} (Figure 4i). It is conceivable that, in addition to the theoretical capacity of the material itself, enhancing the conductivity of the materials and constructing hetero-structure composite materials is very effective at improving the actual capacities and cycling stability of the electrode materials.

5. Metal and Non-Metal-Doped Composite

As previously mentioned, metal doping molybdenum oxide can change the crystal structures and phases of molybdenum oxides. If the formed metal doping molybdenum oxides have a layered crystal structure, the interlamellar spacing will increase to a certain extent. On the other hand, the crystal structure of some metal doping molybdenum oxides, such as Li_2MoO_4, is NASICON-type, which can also provide an ion storage property. Meanwhile, carbon or nitrogen doping plays a typical role in modifying materials by enhancing the electron conductivity and introducing some active sites to improve the electrochemical performance of electrode materials for ion batteries or supercapacitors. Therefore, combining the metal doping and non-metal doping has been an attractive method recently. Hu and coworkers [68] designed a carbon-coated and K-doped MoO_3 composite prepared by hydrothermal treatment followed by a high-temperature annealing to solve the problems

of low conductivity and irreversible structure change impediment. The pre-insertion of a layer of K^+ as a backbone not only provides stability to the lamellar structure but also prevents Li^+ from inserting the intralayer sites of the MoO_3 crystals [69,70]. Therefore, the reduced resistance of the modified material facilitates a performance improvement. The as-prepared $K_{0.046}MoO_3$@C composites can deliver the specific capacities of 258 and 118 mA h g^{-1} at the current densities of 30 and 3000 mA g^{-1} over the potential range of 1.5–4.0 V (vs. Li^+/Li), respectively, displaying an outstanding rate capability. When cycled at 1500 mA g^{-1}, it can retain 83.9% of the initial capacity after 500 cycles. Meanwhile, the calculated value of Li-diffusion coefficient for KMC-3 is 2.06 × 10^{-12} cm^2 s^{-1}, showing a good Li^+ diffusion efficiency.

Earlier, yolk–shell-structured microspheres composed of N-doped-carbon-coated $NiMoO_4$ hollow nanospheres (Y-$NiMoO_4$-H@C) synthesized via a spray pyrolysis process as anode for Li-ion battery was reported by Kang's group [71]. The TEM is shown in Figure 5a, and it is clear that there is the cavity in a single nanosphere. They compared the properties of hollow and dance structure of nanospheres and the samples whether in coated carbon or not. The Y-$NiMoO_4$-H@C microspheres have the largest BET surface area (55.7 m^2 g^{-1}) and show the lowest Rct value owing to the highly conductive N-doped carbon layers (Figure 5b). Obviously, yolk–shell-structured microspheres deliver great coulombic efficiency, cycling performance, and rate performance. The specific data of rate performance can be depicted in Figure 5c (final discharge capacities of 1267, 1221, 1120, 991, 907, 839, and 757 mA h g^{-1} at current densities of 0.5, 1, 2, 4, 6, 8, and 10 A g^{-1}, respectively), indicating that Y-$NiMoO_4$-H@C have fast charging and discharging processes at high current densities. Compared with the phase-pure β-$NiMoO_4$ yolk–shell sphere (719 mA h g^{-1} at 4 A g^{-1} in rate performance) [72], N-doping and carbon coating have greatly improved the capacity of $NiMoO_4$ by increasing the specific surface area and enhancing the electroconductivity.

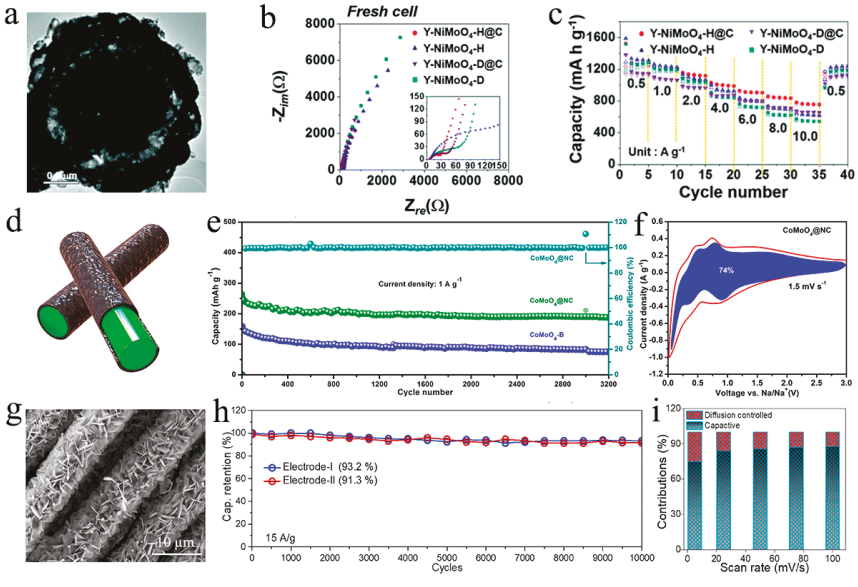

Figure 5. (**a**) TEM image of N-doped carbon coated hollow $NiMoO_4$ nanospheres. (**b**) Nyquist plots of Y-$NiMoO_4$-H@C, Y-$NiMoO_4$-H, Y-$NiMoO_4$-D, and Y-$NiMoO_4$-D@C of fresh cells. (**c**) Rate performances of Y-$NiMoO_4$-H@C. Reproduced with permission. [71] Copyright 2019, The Royal Society of Chemistry. (**d**) Schematic illustration of $CoMoO_4$@NC nanorods; the green part is rod-like $CoMoO_4$, and the coated part is N-doped carbon coatings. (**e**) Long-term cyclic performance at of

1 A g^{-1} $CoMoO_4$@NC and $CoMoO_4$-B. (**f**) The separation of the capacitive and diffusion currents of $CoMoO_4$@NC at a scan rate of 1.5 mV s^{-1}; the capacitive contribution to the total current is presented by the shaded region. Reproduced with permission. [73] Copyright 2020, Elsevier Inc. (**g**) SEM of $CoMoO_4$@CFC (hexagonal nanosheets $CoMoO_4$ are grown on the Carbon Fabric Cloth). (**h**) Cycling performance up to 10,000 cycles at current density of 15 A g^{-1} for two separate electrodes. (**i**) Capacitive and diffusive contribution at different scan rates. Reproduced with permission. [74] Copyright 2020, Elsevier Ltd. and Techna Group S.r.l.

Recently, Zhu's group [73] designed N-doped carbon-encapsulated $CoMoO_4$ ($CoMoO_4$ @NC) nanorods by a facile co-precipitation method to obtain a long-cycle-life anode material for sodium-ion battery. As shown in Figure 5d, the N-doped carbon shell acts as a cushion to adapt to gross volume changes during Na^+ insertion/extraction while enhancing the electronic conductivity and activating the surface sites of $CoMoO_4$. In fact, it shows a prolonged cycle life, especially at a high current density of 1 A g^{-1} (Figure 5e). Interestingly, the calculated capacitive current of $CoMoO_4$@NC shows that 74% of the total charge contributions are quantified as capacitive (Figure 5f). Analogously, Hussain and coworkers [74] reported a $CoMoO_4$/C composite by co-friendly hydrothermal method as a positive electrode for pseudocapacitors. Binder-free $CoMoO_4$ hexagonal nanosheets (SEM is shown in Figure 5g) were directly grown on the surface of conductive carbon fabric cloth ($CoMoO_4$@CFC), and the hexagonal-like 2D structure possesses mesoporous characteristics (BET = 68 m^2 g^{-1}) with abundant electroactive sites as the main body of charge storage. The electrochemical properties show that the material has excellent cycling stability as the capacitance retained up to 93.2% after up to 10,000 cycles, especially at a high current density of 15 A g^{-1} (Figure 5h). In addition, Figure 5i indicates the capacitive charge storage contributions at different scan rates and, accordingly, the $CoMoO_4$@CFC electrode was attributed to a high capacitive charge value of 75% at 2.5 mV s^{-1}. Using carbon-based materials as a coating layer or as a base frame material is an effective strategy for constructing new nanostructures of composite materials. At the same time, the materials with heterogeneous structure tend to have better cycling stability due to structural stability and almost having no volume expansion problem.

6. Summary and Outlook

In this review, we have attempted to chart the significant progress in hetero-element-doped molybdenum oxides for ion batteries and supercapacitors. The summarized series data and parameters of some hetero-element-doped molybdenum oxides are shown in Table 1. As can be seen from Table 1, the hetero-element-doped molybdenum oxide materials are mainly applied to the anode materials of lithium-ion batteries at present, and a small portion of them are used as the cathode materials in ion batteries and electrodes in supercapacitors. When they are applied to batteries, these materials generally have a voltage window of about 0~3.0 V. Among these hetero-element-doped molybdenum oxide materials, there is no way to make a specific comparison of different materials due to the inconsistency in the current densities and the number of cycles during the test, but the performances of these materials are much better than that of pure molybdenum oxide without doping. At the same time, the nanostructures of the materials also have a great influence on the performance. Therefore, in addition to the selection of doping elements, researchers also need to find a suitable synthesis method to obtain a nanostructure with a larger specific surface area and a small volume expansion effect.

Table 1. Summary of the properties and applications of some hetero-element-doped molybdenum oxide materials.

Active Component		Application Fields	Specific Capacity (mA h g^{-1})	Cycles	Current Density (mA g^{-1})	Voltage Window (V)	Refs.
Alkali metal	$Na_{1/3}MoO_2 \cdot H_2O$	Li/Na dual-ion battery (cathode)	650	500	50	0~3.0	[18]
	Li_2MoO_4@C	Li-ion battery (anode)	504	150	100	0.02~3.0	[75]
	$Li_2Mo_4O_{13}$	Li-ion battery (anode)	768	50	106	0.1~2.5	[24]
	Lithiated MoO_3 Nanobelts	Li-ion battery (cathode)	220	15	50	0.15~3.0	[76]
Non-metal	3D-MoO_x@CN-700	Li-ion battery (anode)	431	1000	1000	0.01~3.0	[66]
	MoO_3/NC	Li-ion battery (anode)	1250	60	410	0.01~3.0	[77]
	a-MM/NCc	Sodium-ion battery (anode)	1253	50	100	0.01~3.0	[78]
	MoOC/N-doped C	Li-ion battery (anode)	793	100	100	0.01~3.0	[79]
Transition metal or doped non-metal composites	$MnMoO_4$@C	Li-ion battery (anode)	1050	200	100	0~3.0	[54]
	$NiMoO_4$	Sodium-ion battery (anode)	245	100	50	0~3.0	[45]
	$Cu_3Mo_2O_9$	Li-ion battery (anode)	632	200	100	0.01~3.0	[53]
	$MnMoO_4/CoMoO_4$	Supercapacitor	187 (F g^{-1})	1000	1000	0.1~0.4	[80]
	$CoMoO_4$/AF-CNT	Sodium-ion battery (anode)	220	200	100	0.01~3.0	[81]
	$ZnMoO_4$/rGO	Li-ion battery (anode)	632	100	100	0.01~3.0	[82]

Doping with different elements can change the crystal structure of molybdenum oxides (enlarge the interlamellar spacing or completely convert them to tunnel-type), introduce more active sites to increase the diffusion rate of the ions in the solid phase, increase the conductivity of the material, as well as make the material structure not easy to collapse and expand. These developments have greatly enriched molybdenum oxide-based materials and pave the way for possible design ideas of commercial materials. In addition, the changes in the complex structure and composition evolution during the electrochemical reactions and ion storage mechanisms of some molybdenum oxide-based materials are clarified, although many details of the electrochemical mechanisms on molybdenum oxide-based materials remain controversial and unclear. Except for designing different doped compounds and microstructures of hetero-element-doped molybdenum oxides to improve the capacity and cyclability for energy storage systems, how to reduce irrepressible capacity is an issue that needs attention. In many studies, it has been found that the initial charge capacity is very high, and the subsequent capacity will have a large attenuation and then remain within a certain range, indicating that the coulombic efficiency of the first cycle is very low, especially in nanostructure materials. Doping with hetero-elements and confirming the synthetic process usually involves the design of nanostructures of electrode materials. It is worth noting that irreversible capacity loss is crucial to real full cells, compromising the energy density and even the effect of nanostructuring. Therefore, using the current advanced technology to find ways to improve the coulombic efficiency of the first cycle is worthy of attention. The development of hetero-element-doped molybdenum oxide materials still faces great challenges, but notable progress has been made in the past years. Significant progress has been made regarding the material synthesis, improving electrochemical performances, and understanding the charge transport mechanism used in the energy storage systems.

In order to obtain materials with better performance, in addition to continuing to try different synthesis methods to obtain single metal-element-doped molybdenum oxides

with different nanostructures, we could explore the synthesis of more bimetal-element-doped molybdenum oxide materials on the basis of the existing work [33,34], which will contribute to a significant expansion for molybdenum oxide-based materials. Based on the high capacity of different element-doped molybdenum oxide materials for lithium ions, most of the materials are now studied as anode materials for lithium-ion batteries. The active ions of other ion batteries, such as sodium-ion, potassium-ion, magnesium-ion, etc., have a larger radius than lithium-ion batteries. Therefore, hetero-element-doped molybdenum oxides may not meet the performance requirements as anodes for other ion batteries, but we could try to use them as cathode materials, which is a direction that has not been extensively studied. For non-metallic doping, there are a few cases that use materials that can be carbonized in nature as the substrate to obtain peculiar nanostructured composite materials. This is also a promising research idea; after all, nature is always worth learning from. There is no doubt that a basic understanding of the electrode structure, electrode/electrolyte interface, and charge storage mechanism, as well as a good study of the electron and ion transport in electrode/electrolytes through theoretical calculations, have important guiding significance for the development of molybdenum oxide-based materials.

Author Contributions: Investigation, B.H., S.J., G.Y., W.F., Y.C., J.B., Y.L., H.T.; writing—original draft preparation, B.H.; writing—review and editing, H.T.; visualization, S.J., G.Y., W.F., Y.C., J.B., Y.L., H.T.; supervision, Y.D.; funding acquisition, Y.D. All authors have read and agreed to the published version of the manuscript.

Funding: This work was supported by the National Key R&D Program of China (2017YFA0208000), the National Natural Science Foundation of China (22004112, 51902296).

Conflicts of Interest: The authors declare no conflict of interest.

References

1. Harper, G.; Sommerville, R.; Kendrick, E.; Driscoll, L.; Slater, P.; Stolkin, R.; Walton, A.; Christensen, P.; Heidrich, O.; Lambert, S.; et al. Recycling lithium-ion batteries from electric vehicles. *Nature* **2019**, *575*, 75–86. [CrossRef]
2. Nai, J.; Zhao, X.; Yuan, H.; Tao, X.; Guo, L. Amorphous carbon-based materials as platform for advanced high-performance anodes in lithium secondary batteries. *Nano Res.* **2021**, *14*, 2053–2066. [CrossRef]
3. Du, H.; Feng, S.; Luo, W.; Zhou, L.; Mai, L. Advanced Li-Se_xS_y battery system: Electrodes and electrolytes. *J. Mater. Sci. Technol.* **2020**, *55*, 1–15. [CrossRef]
4. Manthiram, A. An Outlook on Lithium Ion Battery Technology. *ACS Cent. Sci.* **2017**, *3*, 1063–1069. [CrossRef]
5. Kukushkin, V.Y. Thionyl chloride as comprehensive reagent in preparative inorganic and coordination chemistry. *Zhuarnal Neorg. Khimii* **1990**, *35*, 2236–2249.
6. Hu, X.; Zhang, W.; Liu, X.; Mei, Y.; Huang, Y. Nanostructured Mo-based electrode materials for electrochemical energy storage. *Chem. Soc. Rev.* **2015**, *44*, 2376–2404. [CrossRef]
7. Farsi, H.; Gobal, F.; Raissi, H.; Moghiminia, S. On the pseudocapacitive behavior of nanostructured molybdenum oxide. *J. Solid State Electr.* **2010**, *14*, 643–650. [CrossRef]
8. Zhu, J.; Li, P.; Chen, X.; Legut, D.; Fan, Y.; Zhang, R.; Lu, Y.; Cheng, X.; Zhang, Q. Rational design of graphitic-inorganic Bi-layer artificial SEI for stable lithium metal anode. *Energy Storage Mater.* **2019**, *16*, 426–433. [CrossRef]
9. Kim, H.; Kim, S.; Park, Y.; Gwon, H.; Seo, D.; Kim, Y.; Kang, K. SnO_2/graphene composite with high lithium storage capability for lithium rechargeable batteries. *Nano Res.* **2010**, *3*, 813–821. [CrossRef]
10. Zhou, L.; Wu, H.B.; Wang, Z.; Lou, X.W.D. Interconnected MoO_2 Nanocrystals with Carbon Nanocoating as High-Capacity Anode Materials for Lithium-ion Batteries. *ACS Appl. Mater. Inter.* **2011**, *3*, 4853–4857. [CrossRef] [PubMed]
11. Xuan, H.C.; Zhang, Y.Q.; Xu, Y.K.; Li, H.; Han, P.D.; Wang, D.H.; Du, Y.W. A facile route to large-scale synthesis MoO_2 and MoO_3 as electrode materials for high-performance supercapacitors. *Physic. Status Solidi* **2016**, *213*, 2468–2473. [CrossRef]
12. Vorobeva, N.S.; Lipatov, A.; Muratov, D.S.; Sinitskii, A. Chemical vapor deposition and characterization of two-dimensional molybdenum dioxide (MoO_2) nanoplatelets. *Nanotechnology* **2018**, *29*, 505707. [CrossRef]
13. Zhuang, R.; Yao, S.; Shen, X.; Li, T. Hydrothermal synthesis of mesoporous MoO_2 nanospheres as sulfur matrix for lithium sulfur battery. *J. Electroanal. Chem.* **2019**, *833*, 441–448. [CrossRef]
14. Mccrory, M.; Kumar, A.; Ram, M.K. Hydrothermal Synthesis of MoO_2 Nanoparticles Directly onto a Copper Substrate. *Mrs Adv.* **2016**, *1*, 1051–1054. [CrossRef]
15. Zhang, H.; Zeng, L.; Wu, X.; Lian, L.; Wei, M. Synthesis of MoO_2 nanosheets by an ionic liquid route and its electrochemical properties. *J. Alloy. Compd.* **2013**, *580*, 358–362. [CrossRef]

16. Xiao, X.; Zhang, C.J.; Lin, S.; Huang, L.; Hu, Z.; Cheng, Y.; Li, T.; Qiao, W.; Long, D.; Huang, Y.; et al. Intercalation of cations into partially reduced molybdenum oxide for high-rate pseudocapacitors. *Energy Storage Mater.* **2015**, *1*, 1–8. [CrossRef]
17. Tomar, A.K.; Marichi, R.B.; Singh, G.; Sharma, R.K. Enhanced electrochemical performance of anion-intercalated lanthanum molybdenum oxide pseudocapacitor electrode. *Electrochim. Acta* **2019**, *296*, 120–129. [CrossRef]
18. Li, X.; Wang, Z.; Duan, X.; Xu, L.; Yang, M.; Yuan, S.; Meng, C.; Wu, Q.; Wang, Q. A novel layered birnessite-type sodium molybdate as dual-ion electrodes for high capacity battery. *Electrochim. Acta* **2020**, *363*, 137229. [CrossRef]
19. Ben-Kamel, K.; Amdouni, N.; Groult, H.; Mauger, A.; Zaghib, K.; Julien, C.M. Structural and electrochemical properties of $LiMoO_2$. *J. Power Sources* **2012**, *202*, 314–321. [CrossRef]
20. Kobayashi, H.; Tabuchi, M.; Shikano, M.; Nishimura, Y.; Kageyama, H.; Ishida, T.; Nakamura, H.; Kurioka, Y.; Kanno, R. Synthesis and electrochemical properties of lithium molybdenum oxides. *J. Power Sources* **1999**, *81*, 524–529. [CrossRef]
21. Komaba, S. Molybdenum oxides synthesized by hydrothermal treatment of A_2MoO_4 (A=Li, Na, K) and electrochemical lithium intercalation into the oxides. *Solid State Ion.* **2002**, *152–153*, 319–326. [CrossRef]
22. Hibble, S.J.; Fawcett, I.D.; Hannon, A.C. The True Structure and Metal-Metal-Bonded Framework of $LiMo^{III}O_2$ Determined from Total Neutron Scattering. *Inorg. Chem.* **1997**, *36*, 1749–1753. [CrossRef]
23. Leroux, F.; Nazar, L.F. Uptake of lithium by layered molybdenum oxide and its tin exchanged derivatives: High volumetric capacity materials. *Solid State Ion.* **2000**, *133*, 37–50. [CrossRef]
24. Verma, R.; Park, C.; Kothandaraman, R.; Varadaraju, U.V. Ternary lithium molybdenum oxide, $Li_2Mo_4O_{13}$: A new potential anode material for high-performance rechargeable lithium-ion batteries. *Electrochim. Acta* **2017**, *258*, 1445–1452. [CrossRef]
25. Mikhailova, D.; Bramnik, N.N.; Bramnik, K.G.; Reichel, P.; Oswald, S.; Senyshyn, A.; Trots, D.M.; Ehrenberg, H. Layered Li_XMoO_2 Phases with Different Composition for Electrochemical Application: Structural Considerations. *Chem. Mater.* **2011**, *23*, 3429–3441. [CrossRef]
26. James, A.; Goodenough, J.B. Structure and bonding in Li_2MoO_3 and $Li_{2-X}MoO_3$ ($0 \leq x \leq 1.7$). *J. Solid State Chem.* **1988**, *76*, 87–96. [CrossRef]
27. Lee, J.; Urban, A.; Li, X.; Su, D.; Hautier, G.; Ceder, G. Unlocking the Potential of Cation-Disordered Oxides for Rechargeable Lithium Batteries. *Science* **2014**, *343*, 519–522. [CrossRef]
28. Ma, J.; Zhou, Y.; Gao, Y.; Yu, X.; Kong, Q.; Gu, L.; Wang, Z.; Yang, X.; Chen, L. Feasibility of Using Li_2MoO_3 in Constructing Li-Rich High Energy Density Cathode Materials. *Chem. Mater.* **2014**, *26*, 3256–3262. [CrossRef]
29. Liu, X.; Lyu, Y.; Zhang, Z.; Li, H.; Hu, Y.S.; Wang, Z.; Zhao, Y.; Kuang, Q.; Dong, Y.; Liang, Z.; et al. Nanotube Li_2MoO_4: A novel and high-capacity material as a lithium-ion battery anode. *Nanoscale* **2014**, *6*, 13660–13667. [CrossRef]
30. Mikhailova, D.; Voss, A.; Oswald, S.; Tsirlin, A.A.; Schmidt, M.; Senyshyn, A.; Eckert, J.; Ehrenberg, H. Lithium Insertion into Li_2MoO_4: Reversible Formation of Li_3MoO_4 with a Disordered Rock-Salt Structure. *Chem. Mater.* **2015**, *27*, 4485–4492. [CrossRef]
31. Ma, J.; Gao, Y.; Wang, Z.; Chen, L. Structural and electrochemical stability of Li-rich layer structured Li_2MoO_3 in air. *J. Power Sources* **2014**, *258*, 314–320. [CrossRef]
32. You, J.; Xin, L.; Yu, X.; Zhou, X.; Liu, Y. Synthesis of homogeneous $CaMoO_4$ microspheres with nanopits for high-capacity anode material in Li-ion battery. *Appl. Phys. A* **2018**, *124*, 1–8. [CrossRef]
33. Zhu, K.; Guo, S.; Yi, J.; Bai, S.; Wei, Y.; Chen, G.; Zhou, H. A new layered sodium molybdenum oxide anode for full intercalation-type sodium-ion batteries. *J. Mater. Chem. A* **2015**, *3*, 22012–22016. [CrossRef]
34. Yu, S.; Peng, C.; Li, Z.; Zhang, L.; Xiao, Q.; Lei, G.; Ding, Y. K-Doped Li-Rich Molybdenum-Based Oxide with Improved Electrochemical Properties for Lithium-Ion Batteries. *Arab. J. Sci. Eng.* **2017**, *42*, 4291–4298. [CrossRef]
35. Serdtsev, A.V.; Suetin, D.V.; Solodovnikov, S.F.; Gulyaeva, O.A.; Medvedeva, N.I. Electronic structure and sodium-ion diffusion in glaserite-type $A_{3-x}Na_{1+x}(MoO_4)_2$ (A = Cs, K) studied with first-principles calculations. *Solid State Ion.* **2020**, *357*, 115484. [CrossRef]
36. Arroyo-De, D.M.; Krich, C.; Nava-Avendano, J.; Palacin, M.R.; Barde, F. In quest of cathode materials for Ca ion batteries: The $CaMO_3$ perovskites (M = Mo, Cr, Mn, Fe, Co, and Ni). *Phys. Chem. Chem. Phys.* **2016**, *18*, 19966–19972. [CrossRef] [PubMed]
37. Sharma, N.; Shaju, K.M.; Subba Rao, G.V.; Chowdari, B.V.R.; Dong, Z.L.; White, T.J. Carbon-Coated Nanophase $CaMoO_4$ as Anode Material for Li Ion Batteries. *Chem. Mater.* **2004**, *16*, 504–512. [CrossRef]
38. Bullard, J. Structural evolution of the MoO_3(010) surface during lithium intercalation. *Solid State Ion.* **2003**, *160*, 335–349. [CrossRef]
39. Mikhailik, V.B.; Kraus, H.; Itoh, M.; Iri, D.; Uchida, M. Radiative decay of self-trapped excitons in $CaMoO_4$ and $MgMoO_4$ crystals. *J. Phys. Condens. Matter* **2005**, *17*, 7209–7218. [CrossRef]
40. Sleight, A.W.; Chamberland, B.L. Transition metal molybdates of the type $AMoO_4$. *Inorg. Chem.* **1968**, *7*, 1672–1675. [CrossRef]
41. Haetge, J.; Suchomski, C.; Brezesinski, T. Ordered Mesoporous β-$MgMoO_4$ Thin Films for Lithium-Ion Battery Applications. *Small* **2013**, *9*, 2541–2544. [CrossRef] [PubMed]
42. Das, B.; Reddy, M.V.; Krishnamoorthi, C.; Tripathy, S.; Mahendiran, R.; Rao, G.V.S.; Chowdari, B.V.R. Carbothermal synthesis, spectral and magnetic characterization and Li-cyclability of the Mo-cluster compounds, $LiYMo_3O_8$ and $Mn_2Mo_3O_8$. *Electrochim. Acta* **2009**, *54*, 3360–3373. [CrossRef]
43. Buhrmester, T.; Leyzerovich, N.N.; Bramnik, K.G.; Ehrenberg, H.; Fuess, H. Electrochemical intercalation of lithium in ternary metal molybdates $MMoO_4$ (M=Cu, Zn). *Mat. Res. Soc. Symp. Proc.* **2003**, *756*, 671–676. [CrossRef]

44. Kim, S.; Ogura, S.; Ikuta, H.; Uchimoto, Y.; Wakihara, M. Synthesis of $MnMoO_4$ as High Capacity Anode Material for Li Secondary Battery. *Chem. Lett.* **2001**, *30*, 760–761. [CrossRef]
45. Minakshi, M.; Barmi, M.; Mitchell, D.R.G.; Barlow, A.J.; Fichtner, M. Effect of oxidizer in the synthesis of NiO anchored nanostructure nickel molybdate for sodium-ion battery. *Mater. Today Energy* **2018**, *10*, 1–14. [CrossRef]
46. Cao, H.; Wu, N.; Liu, Y.; Wang, S.; Du, W.; Liu, J. Facile synthesis of rod-like manganese molybdate crystallines with two-dimentional nanoflakes for supercapacitor application. *Electrochim. Acta* **2017**, *225*, 605–613. [CrossRef]
47. Fei, J.; Sun, Q.; Li, J.; Cui, Y.; Huang, J.; Hui, W.; Hu, H. Synthesis and electrochemical performance of α-$ZnMoO_4$ nanoparticles as anode material for lithium ion batteries. *Mater. Lett.* **2017**, *198*, 4–7. [CrossRef]
48. Zhang, L.; He, W.; Liu, Y.; Ling, M.; Zheng, P.; Guo, S. 3D hierarchical flower of copper molybdate $Cu_3Mo_2O_9$: Synthesis, nanostructure and lithium storage properties. *J. Alloy. Compd.* **2017**, *723*, 512–519. [CrossRef]
49. Zhang, L.; Song, Y.; Wu, W.; Bradley, R.; Hu, Y.; Liu, Y.; Guo, S. $Fe_2Mo_3O_8$ nanoparticles self-assembling 3D mesoporous hollow spheres toward superior lithium storage properties. *Front. Chem. Sci. Eng.* **2021**, *15*, 156–163. [CrossRef]
50. Das, B.; Reddy, M.V.; Subba Rao, G.V.; Chowdari, B.V.R. Synthesis of Mo-cluster compound, $LiHoMo_3O_8$ by carbothermal reduction and its reactivity towards Li. *J. Solid State Electr.* **2008**, *12*, 953–959. [CrossRef]
51. McCarroll, W.H.; Katz, L.; Ward, R. Some Ternary Oxides of Tetravalent Molybdenum. *J. Am. Chem. Soc* **1957**, 5410. [CrossRef]
52. Sun, Y.; Hu, X.; Luo, W.; Huang, Y. Hierarchical self-assembly of $Mn_2Mo_3O_8$-graphene nanostructures and their enhanced lithium-storage properties. *J. Mater. Chem.* **2011**, *21*, 17229. [CrossRef]
53. Chu, Y.; Shi, X.; Wang, Y.; Fang, Z.; Deng, Y.; Liu, Z.; Dong, Q.; Hao, Z. High temperature solid-state synthesis of dopant-free $Fe_2Mo_3O_8$ for lithium-ion batteries. *Inorg. Chem. Commun.* **2019**, *107*, 107477. [CrossRef]
54. Guan, B.; Sun, W.; Wang, Y. Carbon-Coated $MnMoO_4$ Nanorod for High-Performance Lithium-Ion Batteries. *Electrochim. Acta* **2016**, *190*, 354–359. [CrossRef]
55. Raccichini, R.; Varzi, A.; Passerini, S.; Scrosati, B. The role of graphene for electrochemical energy storage. *Nat. Mater.* **2015**, *14*, 271–279. [CrossRef]
56. Wang, B.; Xin, H.; Li, X.; Cheng, J.; Yang, G.; Nie, F. Mesoporous CNT@TiO_2-C Nanocable with Extremely Durable High Rate Capability for Lithium-Ion Battery Anodes. *Sci. Rep.* **2015**, *4*, 3729. [CrossRef]
57. Lee, S.W.; Yabuuchi, N.; Gallant, B.M.; Chen, S.; Kim, B.; Hammond, P.T.; Shao-Horn, Y. High-power lithium batteries from functionalized carbon-nanotube electrodes. *Nat. Nanotechnol.* **2010**, *5*, 531–537. [CrossRef]
58. Fang, B.; Kim, J.H.; Kim, M.; Yu, J. Hierarchical Nanostructured Carbons with Meso–Macroporosity: Design, Characterization, and Applications. *Accounts Chem. Res.* **2013**, *46*, 1397–1406. [CrossRef]
59. Song, H.; Li, Y.; Shang, L.; Tang, Z.; Zhang, T.; Lu, S. Designed controllable nitrogen-doped carbon-dots-loaded MoP nanoparticles for boosting hydrogen evolution reaction in alkaline medium. *Nano Energy* **2020**, *72*, 104730. [CrossRef]
60. Wei, Z.; Liu, Y.; Peng, Z.; Song, H.; Liu, Z.; Liu, B.; Li, B.; Yang, B.; Lu, S. Cobalt-Ruthenium Nanoalloys Parceled in Porous Nitrogen-Doped Graphene as Highly Efficient Difunctional Catalysts for Hydrogen Evolution Reaction and Hydrolysis of Ammonia Borane. ACS Sustain. *Chem. Eng.* **2019**, *7*, 7014–7023. [CrossRef]
61. Zhang, Y.; Zhao, Z.; Chen, J.; Cheng, L.; Chang, J.; Sheng, W.; Hu, C.; Cao, S. C-doped hollow TiO_2 spheres: In situ synthesis, controlled shell thickness, and superior visible-light photocatalytic activity. *Appl. Catal. B Environ.* **2015**, *165*, 715–722. [CrossRef]
62. Pan, L.; Muhammad, T.; Ma, L.; Huang, Z.; Wang, S.; Wang, L.; Zou, J.; Zhang, X. MOF-derived C-doped ZnO prepared via a two-step calcination for efficient photocatalysis. *Appl. Catal. B Environ.* **2016**, *189*, 181–191. [CrossRef]
63. Wang, X.; Xiao, Y.; Wang, J.; Sun, L.; Cao, M. Facile fabrication of molybdenum dioxide/nitrogen-doped graphene hybrid as high performance anode material for lithium ion batteries. *J. Power Sources* **2015**, *274*, 142–148. [CrossRef]
64. Fleischmann, S.; Zeiger, M.; Quade, A.; Kruth, A.; Presser, V. Atomic Layer-Deposited Molybdenum Oxide/Carbon Nanotube Hybrid Electrodes: The Influence of Crystal Structure on Lithium-Ion Capacitor Performance. *ACS Appl. Mater. Inter.* **2018**, *10*, 18675–18684. [CrossRef]
65. Yang, X.; Li, Q.; Wang, H.; Feng, J.; Zhang, M.; Yuan, R.; Chai, Y. In-situ carbonization for template-free synthesis of MoO_2-Mo_2C-C microspheres as high-performance lithium battery anode. *Chem. Eng. J.* **2018**, *337*, 74–81. [CrossRef]
66. Naresh, N.; Jena, P.; Satyanarayana, N. Facile synthesis of MoO_3/rGO nanocomposite as anode materials for high performance lithium-ion battery applications. *J. Alloy. Compd.* **2019**, *810*, 151920. [CrossRef]
67. Li, Z.; Wang, C.; Chen, X.; Wang, X.; Li, X.; Yamauchi, Y.; Xu, X.; Wang, J.; Lin, C.; Luo, D.; et al. MoOx nanoparticles anchored on N-doped porous carbon as Li-ion battery electrode. *Chem. Eng. J.* **2020**, *381*, 122588. [CrossRef]
68. Hu, Z.; Zhang, X.; Peng, C.; Lei, G.; Li, Z. Pre-intercalation of potassium to improve the electrochemical performance of carbon-coated MoO_3 cathode materials for lithium batteries. *J. Alloy. Compd.* **2020**, *826*, 154055. [CrossRef]
69. Xia, Q.; Zhao, H.; Du, Z.; Zeng, Z.; Gao, C.; Zhang, Z.; Du, X.; Kulka, A.; Świerczek, K. Facile synthesis of MoO_3/carbon nanobelts as high-performance anode material for lithium ion batteries. *Electrochim. Acta* **2015**, *180*, 947–956. [CrossRef]
70. Noerochim, L.; Wang, J.; Wexler, D.; Chao, Z.; Liu, H. Rapid synthesis of free-standing MoO_3/Graphene films by the microwave hydrothermal method as cathode for bendable lithium batteries. *J. Power Sources* **2013**, *228*, 198–205. [CrossRef]
71. Park, G.D.; Hong, J.H.; Lee, J.; Kang, Y.C. Yolk–shell-structured microspheres composed of N-doped-carbon-coated $NiMoO_4$ hollow nanospheres as superior performance anode materials for lithium-ion batteries. *Nanoscale* **2019**, *11*, 631–638. [CrossRef]
72. Ahn, J.H.; Park, G.D.; Kang, Y.C.; Lee, J. Phase-pure β-$NiMoO_4$ yolk-shell spheres for high-performance anode materials in lithium-ion batteries. *Electrochim. Acta* **2015**, *174*, 102–110. [CrossRef]

73. Huang, X.; Zhang, W.; Zhou, C.; Yang, L.; Wang, H.; Gao, Q.; Zhu, M. N-doped carbon encapsulated $CoMoO_4$ nanorods as long-cycle life anode for sodium-ion batteries. *J. Colloid Interf. Sci.* **2020**, *576*, 176–185. [CrossRef]
74. Hussain, S.; Khan, A.J.; Arshad, M.; Javed, M.S.; Ahmad, A.; Shah, S.S.A.; Khan, M.R.; Akram, S.; Zulfiqar; Ali, S.; et al. Charge storage in binder-free 2D-hexagonal $CoMoO_4$ nanosheets as a redox active material for pseudocapacitors. *Ceram. Int.* **2021**, *47*, 8659–8667. [CrossRef]
75. Zhang, J.; Li, R.; Chen, Q.; Zhao, G.; Jia, J. Porous carbon-coated Li_2MoO_4 as high-performance anode materials for lithium-ion batteries. *Mater. Lett.* **2018**, *233*, 302–305. [CrossRef]
76. Mai, L.Q.; Hu, B.; Chen, W.; Qi, Y.Y.; Lao, C.S.; Yang, R.S.; Dai, Y.; Wang, Z.L. Lithiated MoO_3 Nanobelts with Greatly Improved Performance for Lithium Batteries. *Adv. Mater.* **2007**, *19*, 3712–3716. [CrossRef]
77. Qiu, J.; Yang, Z.; Li, Y. N-doped carbon encapsulated ultrathin MoO_3 nanosheets as superior anodes with high capacity and excellent rate capability for Li-ion batteries. *J. Mater. Chem. A* **2015**, *3*, 24245–24253. [CrossRef]
78. Zhu, K.; Wang, X.; Liu, J.; Li, S.; Wang, H.; Yang, L.; Liu, S.; Xie, T. Novel Amorphous MoS_2/MoO_3/Nitrogen-Doped Carbon Composite with Excellent Electrochemical Performance for Lithium Ion Batteries and Sodium Ion Batteries. ACS Sustain. *Chem. Eng.* **2017**, *5*, 8025–8034. [CrossRef]
79. Xiu, Z.; Kim, D.; Alfaruqi, M.H.; Song, J.; Kim, S.; Duong, P.T.; Mathew, V.; Baboo, J.P.; Kim, J. Ultrafine molybdenum oxycarbide nanoparticles embedded in N-doped carbon as a superior anode material for lithium-ion batteries. *J. Alloy. Compd.* **2017**, *696*, 143–149. [CrossRef]
80. Mai, L.Q.; Yang, F.; Zhao, Y.L.; Xu, X.; Xu, L.; Luo, Y.Z. Hierarchical $MnMoO_4/CoMoO_4$ heterostructured nanowires with enhanced supercapacitor performance. *Nature Commun.* **2011**, *2*, 1–5. [CrossRef]
81. Zhao, Y.; Xu, Z.; Fu, H.; Xiao, R.; Fu, M.; Yue, H.; Huang, J. Swallow-Nest Architectures with Cobalt Molybdate Particulates Fixed Constructed Carbon Nanotube Supports for Stable Sodium-Ion Battery Anode. *J. Electrochem. Soc.* **2020**, *167*, 80528. [CrossRef]
82. Xue, R.; Hong, W.; Pan, Z.; Jin, W.; Zhao, H.; Song, Y.; Zhou, J.; Liu, Y. Enhanced electrochemical performance of $ZnMoO_4$/reduced graphene oxide composites as anode materials for lithium-ion batteries. *Electrochim. Acta* **2016**, *222*, 838–844. [CrossRef]

nanomaterials

MDPI

Article

Efficient Recovery of Lithium Cobaltate from Spent Lithium-Ion Batteries for Oxygen Evolution Reaction

Ayesha Arif [1,†], Ming Xu [2,3,*], Jamshaid Rashid [1,3,4,*], Chaudry Sajed Saraj [5,†], Wei Li [5], Bilal Akram [6] and Binbin Hu [7]

[1] Department of Environmental Science, Faculty of Biological Sciences, Quaid-I-Azam University, Islamabad 45320, Pakistan; a_ayesha113@outlook.com
[2] BNU-HKUST Laboratory of Green Innovation, Advanced Institute of Natural Sciences, Beijing Normal University at Zhuhai, Zhuhai 519087, China
[3] College of Environment and Planning, Henan University, Kaifeng 475004, China
[4] Key Laboratory of Geospatial Technology for the Middle and Lower Yellow River Regions, Ministry of Education, Henan University, Kaifeng 475004, China
[5] GPL, State Key Laboratory of Applied Optics, Changchun Institute of Optics, Fine Mechanics and Physics, Chinese Academy of Sciences, Changchun 130033, China; sajedsaraj@ciomp.ac.cn (C.S.S.); weili1@ciomp.ac.cn (W.L.)
[6] Department of Chemistry, Tsinghua University, Beijing 100084, China; bilalakram626@gmail.com
[7] Key Laboratory for Special Functional Materials of Ministry of Education, National & Local Joint Engineering Research Centre for High-Efficiency Display and Lighting Technology, School of Materials and Engineering, Collaborative Innovation Centre of Nano Functional Materials and Applications, Henan University, Kaifeng 475004, China; hbb@henu.edu.cn
* Correspondence: mingxu@henu.edu.cn (M.X.); jamshaidrashid@gmail.com (J.R.)
† These authors contributed equally to this work.

Citation: Arif, A.; Xu, M.; Rashid, J.; Saraj, C.S.; Li, W.; Akram, B.; Hu, B. Efficient Recovery of Lithium Cobaltate from Spent Lithium-Ion Batteries for Oxygen Evolution Reaction. *Nanomaterials* **2021**, *11*, 3343. https://doi.org/10.3390/nano11123343

Academic Editors: Marc Cretin, Sophie Tingry and Zhenghua Tang

Received: 21 October 2021
Accepted: 29 November 2021
Published: 9 December 2021

Abstract: Owing to technological advancements and the ever-increasing population, the search for renewable energy resources has increased. One such attempt at finding effective renewable energy is recycling of lithium-ion batteries and using the recycled material as an electrocatalyst for the oxygen evolution reaction (OER) step in water splitting reactions. In electrocatalysis, the OER plays a crucial role and several electrocatalysts have been investigated to improve the efficiency of O_2 gas evolution. Present research involves the use of citric acid coupled with lemon peel extracts for efficient recovery of lithium cobaltate from waste lithium-ion batteries and subsequent use of the recovered cathode material for OER in water splitting. Optimum recovery was achieved at 90 °C within 3 h of treatment with 1.5 M citric acid and 1.5% extract volume. The consequent electrode materials were calcined at 600, 700 and 800 °C and compared to the untreated waste material calcined at 600 °C for OER activity. The treated material recovered and calcined at 600 °C was the best among all of the samples for OER activity. Its average particle size was estimated to be within the 20–100 nm range and required a low overpotential of 0.55 V vs. RHE for the current density to reach 10 mA/cm^2 with a Tafel value of 128 mV/dec.

Keywords: lemon peel extracts; lithium-ion batteries; oxygen evolution reaction; renewable energy; waste management

1. Introduction

With the advancements in technology and the growing population, continuously degrading the environment and increasing the demand of energy have become mankind's major concerns. The use of renewable sources for energy conversion has been deemed an inspiring solution to reduce the dependance on the unsustainable exploitation of fossil fuels, which is also a major cause of growing pollution in the environment. Some of the major renewable energy resources include fuel cells and metal air batteries. Oxygen evolution reactions (OER) are the fundamental reactions for the above-mentioned renewable

systems [1]. In OERs, the molecular oxygen is produced through a multistep four-electron oxidation reaction, thus considered kinetically sluggish [2]. Therefore, the need for an effective and efficient electrocatalyst comes forward to reduce the overpotential and to accelerate the reaction, thus increasing the energy conversion efficiency. Generally, precious metals and transition metals such as Pt, Ir, Co, Mn, and Ru, etc., are needed to promote OERs. Ru and Ir, to this day, are still considered as the most efficient electrocatalysts for OERs as they show a relatively low overpotential and a Tafel slope [3]. Another case is the use of transition metal oxides as OER electrocatalysts due to their multiple oxidation states, low-cost and good corrosion resistance [4]. NiO, for example, is receiving huge attention in the field of electrocatalysis. Many studies have reported the fabrication of higher oxidation states of Ni, which have proven to be very active for OERs. Fominykh and co-workers fabricated NiO NPs by solvothermal reactions, in which an Ni^{3+} state was formed on the surface and obtained excellent results [5]. The synergistic effect of transition metals has also been wildly studied. Lankouf and colleagues studied the impact of adding Mn to the cubic Co_3O_4 and obtained increased electrocatalytic activity with a current density of 10 mA cm^{-2} at a relatively low overpotential of 327 mV [6]. Another study demonstrated the use of ultra-thin Co nanosheets coupled with N-doped carbon plate, which possessed a high specific surface area of 446.49 m^2 g^{-1}, which resulted in its efficient performance with an overpotential of 278 mV at 10 mA cm^{-2} [7]. Zhang et. al., fabricated ZnO/Co_3O_4 core-shell nanorods on Ni foil, which exhibited excellent electrochemical performance for OERs, with an overpotential of 294 mV at 10 mA cm^{-2}, a Tafel slope of 49 mV dec^{-1}, and excellent stability [8]. However, the high costs and low reserves of these metals limits their usage at a commercial level. In this respect, scientists all over the world are making efforts to develop novel electrocatalysts to replace these metals completely or partially or at least lessen their costs. One of such attempts is the use of cathode material used in lithium-ion batteries (LIBs) for OERs. Lithium-ion batteries have been largely employed in various devices such as laptops, video cameras, mobile phones and other portable appliances [9], electric vehicles and photovoltaic cells [10], owing to their characteristics such as long-life cycle, light weight, high working voltage, no memory effect, high energy density, light weight, small size and low self-discharge rate [11]. The cathode of lithium-ion batteries is made up of lithium-transition metal oxides [12], which have been tested for the OER activities [13,14]. Chen and co-workers developed a simple method to convert the recycled $LiCoO_2$ into an electrocatalyst for OERs. They cycled the battery several times and discovered that after cycling for 500 cycles, the recycled $LiCoO_2$ can deliver a current density of 9.68 mA cm^{-2} at 1.65 V [15]. Lu and colleagues demonstrated a method for the electrochemical lithium tuning of catalytic materials in organic electrolytes to enhance the catalytic activity in an aqueous solution. By continuously extracting lithium ions out of $LiCoO_2$, the catalytic activity can be improved [16]. However, the same problem is noticeable in this case as well, i.e., short reservoirs. The components of lithium-ion batteries are considered "critical minerals" by the U.S. government due to their short reservoirs and fluctuating prices [17]. For a decade, a debate on the importance of recycling of Li-ion batteries has been ongoing. Cobalt is mined majorly in African countries such as Congo and Zambia, as well as other vital countries, including Australia, Brazil, Cuba, Canada, Russia, Madagascar, and China. The volatile pricing of cobalt due to supply demand contrast and ongoing global issues is wreaking havoc for both manufacturers and miners [18,19]. Although lithium reserves of 53.5 million tons worldwide may seem to last for a century, not all the resources are recoverable, and many require extremely high costs, such as Li recovery from brine and sea water etc. [20]. The recoverable resources of Li are limited to the Li-triangle (China, Chile, Argentina, and Bolivia). Due to its increasing demands, the price of lithium is also rising [21–23]. The hazards of waste LIBs are an additional factor to be considered while discussing the need to recycle theses batteries [23]. Previous studies employed methods such as pyrometallurgy, which involves the reduction of metals by heating of the waste LIBs at a very high temperature [24,25], or hydrometallurgical processes [26,27], for the recovery of cathode material from waste LIBs. However, all of

these methods have drawbacks. The hydrometallurgical process, for instance, can salvage and purify battery materials with a high yield; however, the unjustified consumption of alkalis and acids causes secondary pollution and the corrosion of equipment [28]. On the contrary, pyrometallurgy has the disadvantages of high temperature requirements (above 1300 °C), which results in high energy consumption, along with high pollution and low extraction efficiency of lithium. The present study reports, for the first time, the use of environmentally friendly lemon peel extract and citric acid for the recovery of Li and Co from spent LIBs due to their superior leaching performance, low toxic emissions, easy natural degradation, and potentially low price. Recycled $LiCoO_2$ was calcined at different temperatures, characterized by X-ray photoelectron spectroscopy (XPS), X-ray diffraction (XRD), scanning electron microscopy (SEM), and transmission electron microscopy (TEM), and subsequently tested and compared for OER performance.

2. Experimental Section

2.1. Materials and Instruments

The glassware utilized in the experimental procedure included beakers (1000 mL and 250 mL), measuring cylinders, spatulas, pipettes, Whattman filter paper, and crucibles. The glassware was made up of either Pyrex or borosilicate glass. Citric acid ($C_6H_8O_7$) was used as a leaching agent. Sodium carbonate (Na_2CO_3) and oxalic acid ($C_2H_2O_4$) were used as precipitating agents. All of the chemical reagents used were purchased from Sigma Aldrich (St. Louis, MO, USA). All solutions were prepared or diluted by deionized water. Spent lithium ion (mobile phone) batteries were collected from various colleagues. The lemon peel extract was prepared by using lemons bought from the local market. Peel extract was made by drying the lemon peel from the used lemons and then grinding the peel into powder. The powder was then heated at 100 °C for 1 h in deionized water. The solution was filtered and stored in a refrigerator for future use. To weigh the chemicals, a Shimadzu ATY244 microbalancer (Shimadzu, Kyoto, Japan) was used. An 8000 Adwa pH-meter (Adwa, Romania) was used for the measurement of the pH of the chemical and reaction mixtures. A muffle furnace was utilized for calcination during the preparation of lithium metal oxide. To note the changes in temperature, a thermometer was used. An Atomic Absorption Spectrophotometer (AAS), (AA-7000 by Shimadzu, Kyoto, Japan) and Flame Photometer (Model 360 Flame Photometer by Sherwood, Cambridge, UK) were used for quantitative analysis of the cobalt and lithium recovery by leaching.

2.2. Metal Recovery and Sample Preparation

The positive and negative terminals of batteries, if handled irresponsibly, will ignite. Hence, there is a need to discharge them first. For this purpose, the batteries in this experiment were discharged by being connected to a 100 ohm load and the batteries were steadily discharged to a safe voltage of 1.0 volts. Then, the batteries were manually dismantled. Next, the binder (PVDF) was removed to separate the cathode material from the Al foil (current collector) by dissolving the foil in DMSO. The obtained powder was dried in an oven for 1 h at 100 °C. Then, the resultant powder was heated at 600 °C in a furnace to get rid of the carbon and binder or any other organic matter present. The powder was then crushed and grounded manually. The leaching experiments were conducted in a 250 mL flask, placed on a hot plate to control the temperature. A thermometer was used to constantly check the temperature of the reaction mixture. A magnetic stirrer was used to stir the material uniformly. The flask was then covered with aluminum foil to avoid the unnecessary evaporation of the reaction mixture. A predetermined quantity of the cathode material (2 g) was accurately measured, and citric acid and peel extract in different concentrations were added to the flask. During the experiments, the stirring was kept constant to 300 rpm. The amount of lemon peel extract and the acid concentration were varied to obtain the optimal efficiency. Similarly, the temperature and time were varied to achieve the optimum conditions. The periodically collected samples were filtered using a syringe filter (0.2 μm). As a result, a black residue, and a filtrate of different shades of pink

were obtained. The filtrates were estimated for Co and Li ions using an atomic absorption spectrometer (AAS), and the leaching efficiency of lemon peel was measured using the following formula [29]:

$$y = \frac{Cw, t \times V}{mw} \times 100\%$$

where: y is the leaching efficiency in %, $C_{w,t}$ denotes the concentration (g/L) of metal W (Li and Co) at a given time, V is volume of the leachant (L), and m denotes the mass of metal in the cathode scrape (g), which was calculated by dissolving the cathode material (approximately 2 g) completely in aqua regia, and AAS was used to reveal the mass of Li and Co in the cathode scrape. A diagrammatic representation of the recovery process is provided in Figure 1.

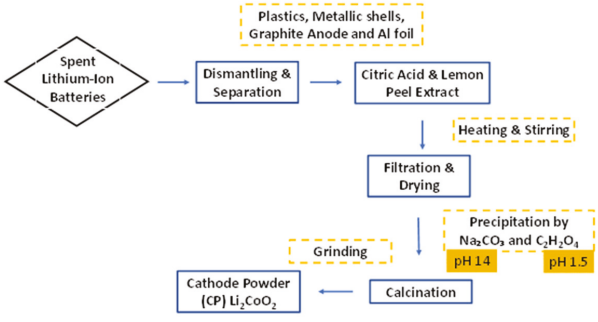

Figure 1. Schematic diagram for the leaching and recycling of an LIB cathode.

2.3. Reductive Leaching

Citric acid falls under the category of polyprotic acids, which can dissociate and give out more than two hydrogen ions in an aqueous solution [30]. As a result, the following reaction takes place when $LiMO_2$ is placed in the reaction mixture:

$$H_3Cit + LiMO_2 \rightarrow Li^+(aq) + H_2Cit^-(aq) + M^+(aq) + H^+ + O_2(g) \quad (1)$$

However, the transition metals in the layered structure are difficult to remove from the lattice. This situation can be improved by adding a reducing agent, as shown in previous studies. However, the addition of a reducing agent must not make the process economically and/or environmentally unfeasible. In the present study, lemon peel extract was used as a source of reducing agent (ascorbic acid), as it has more ascorbic acid (Vit C) than its juice [31,32]. Ascorbic acid has good reducing ability, as it can provide two electrons and can be oxidized two times to the stable dehydro-ascorbic acid ($C_6H_6O_6$) [33]. Furthermore, it is also able to provide hydrogen ions for the leaching process, hence efficiently speeding up the reaction efficiently [34]. After the leaching of metals (lithium and cobalt), the metals were removed and recovered by adding sodium carbonate (2 mol L^{-1}) and oxalic acid (1 mol L^{-1}) in their precipitate forms [35]. Precipitation reactions were carried out in a 250 mL flask on hot plate. A magnetic stirrer was used for the stirring of the reaction mixture, and Al foil was used to cover the flask to avoid evaporation of the reaction mixture. The recycled material (precipitates of lithium carbonate and cobalt oxalate) was then combined and calcined at different temperatures to harvest the active cathode material. The precursors (precipitates obtained by precipitation) were mixed at a ratio of 1.05/1 (Li/Co) heated at 600 °C (CP3), 700 °C (CP1) and 800 °C (CP2) in a muffle furnace.

2.4. Electrode Preparation

A BioLogic VMP3 multichannel workstation with a three-electrode system was utilized for electrochemical measurements, where a Pt wire, a catalyst-loaded carbon cloth electrode,

and a saturated calomel electrode (SCE) were used as a counter and working and reference electrodes, respectively. Aqueous solutions of 1M KOH were used as alkaline electrolytes for the electrochemical measurements. LSV curves were measured by sweeping voltage in the range of −0.2 to −1.6 V vs. the SCE electrode with the a scan rate of 10 $mV{\cdot}s^{-1}$. The expression $E_{RHE} = E_{SCE} + E^0_{SCE} + 0.0592pH$, where $E^0_{SCE} = 0.242$ V, was used to translate V vs. SCE to V vs. the reverse hydrogen electrode (RHE). Working electrodes were first pre-stabilized in the electrolyte solution using 30 scans of cyclic voltammetry at 20 $mV{\cdot}s^{-1}$ before performing linear sweep voltammetry measurements. Electrochemical impedance spectra (EIS) were recorded with the biasing of the working electrode at −1.4 V (HER) and 0.5 V (OER) (vs. SCE) and superimposing a small alternating voltage of 10 mV over the frequency range of 0.01 Hz to 1 MHz. The CV curves were further measured in the non-Faradaic region of potential from 1.091 to 1.191 V (vs. RHE) with different scan rates (from 10 to 120 $mV{\cdot}s^{-1}$) to estimate the double layer capacitance (Cdl).

2.5. Analytical Methods

The crystalline nature of the recovered material was characterized by X-ray diffraction (XRD, Bruker AXS-D8, Billerica, MA, USA), which was carried out using Cu-Kα (λ = 1.5406 nm) as a source of radiation and secondary monochromator in the range 2θ from 10 to 80°. The surface morphologies of the samples were explored by SEM (Hitachi S-4800, Tokyo, Japan at an operating voltage of 25 kV, as well as by JEOL-2100 TEM). For the verification of chemical or elemental composition of the materials Energy Dispersive X-ray Analysis (EDAX) were performed using the Omicron system (Al Kα 1486.7 eV X-ray source operated at 15 KeV). For a better insight of the OER activities X-ray Photoelectron spectroscopy was performed using the Omicron system (Al Kα 1486.7 eV X-ray source operated at 15 KeV) at constant analyzer energy (CAE) = 100 eV for survey scans and 20 eV for detailed scans. A binding energy of 284.8 eV of C1-s was used for calibration.

3. Results and Discussion

3.1. Metal Recovery

The proposed reaction for the reductive leaching process can be represented as follows [36]:

$$6H_3Cit + 2LiCoO_2 \rightarrow 2Li^+(aq) + 6H_2Cit^-(aq) + 2\,Co^{2+}(aq) + 6H^+ + 2O_2(g) \quad (2)$$

$$6H_2Cit^-(aq) + 2LiCoO_2 \rightarrow 2Li^+(aq) + 2Co^{2+} + 6H^+ + 6HCit^{-2}(aq) + 2O_2(g) \quad (3)$$

$$6HCit^{-2}(aq) + 2LiCoO_2 \rightarrow 2Li^+(aq) + 2Co^{2+} + H^+ + 6Cit^{-3}(aq) + 2O_2(g) \quad (4)$$

The efficiency of the method utilized for the recovery of crucial metals, i.e., Li and Co, from waste lithium-ion batteries was evaluated by repeating the experiments three times under same conditions, and their average was taken. The influencing parameters, such as temperature, time, acid concentration, and peel volume, were studied. During the experiments, stirring was kept constant at 300 rpm. The intermittently collected samples were filtered using a syringe filter (0.2 μm) and assessed for Co and Li ions using an AAS.

3.1.1. Temperature and Time

The impact of temperature and retention time was studied, as portrayed in Figure 2. It was observed that leaching of both lithium and cobalt gradually increased when the temperature raised from 70 °C, then to 80 °C and 90 °C (Figure 2a). The leaching efficiency was noted to be 39% for Co, 34% for Li, 52% for Co, 46% for Li, and 70% for Co, and 98% for Li at temperatures of 60 °C, 70 °C, and 80 °C, respectively. The maximum leaching efficiency was obtained at a 90 °C temperature when the mixture was heated for 3 h. At this stage, 90% of Co and 99% of Li was leached. This increase in leaching efficiency is attributed to the fact that a higher temperature can raise the speed of the molecular motion and increase the energy of a particle's collisions. No further tests were conducted with an increased temperature, since a marginal increase in leaching efficiency may prove to be

costly due to the significant increase in energy consumption by raising the temperature from 90 to 100 or 110 °C. A balanced temperature of 90 °C was considered as the optimal temperature for the remaining experiments. Figure 2b depicts 3 h to be the optimum time for the metals (lithium and cobalt) to reach maximum dissolution, indicating that the leaching equilibrium had been reached. Hence, 3 h was taken as the optimal leaching time.

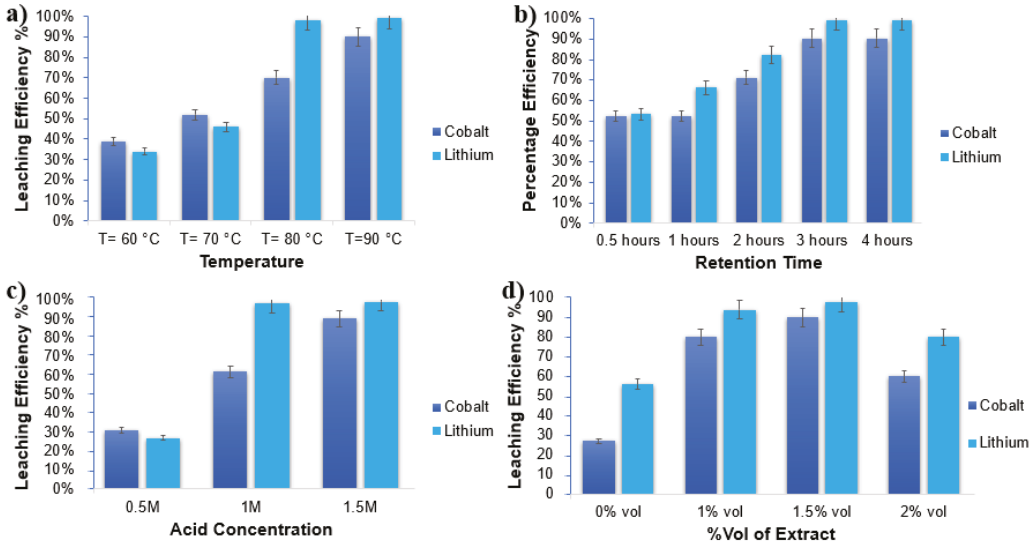

Figure 2. (**a**) Impact of temperature on leaching efficiency. (**b**) Impact of retention time on leaching efficiency. (**c**) Impact on the acid concentration of leaching efficiency. (**d**) Impact of extract vol% on leaching efficiency.

3.1.2. Acid Concentration and Extract Volume

The impact of the citric acid concentration was also investigated under an optimum condition of 1.5% by volume of extract, at a 90 °C temperature for 3 h of the experiment. As shown in Figure 2c, an insignificant increase in leaching efficiency was observed at an acid strength of 0.5 M, i.e., 31% and 27% for cobalt and lithium, respectively. However, with an increase in acid strength, the leaching efficiency improved significantly. At a 1.5 M acid concentration, 90% cobalt and 99% lithium were recovered. Experiments were also conducted with a varied amount of lemon peel extract to check the impact of the concentration of peel extract on the leaching efficiency of lithium and cobalt. Citric acid alone, as shown in the Figure 2d, had no significant leaching activity. Cobalt, showed leaching efficiency of only 27% in 3 h and 90 °C temperature. However, the maximum leaching efficiency was observed when the volume of the extract was increased. The maximum leaching efficiency of 98% and 90% for lithium and cobalt, respectively, was obtained with extract % volume of 1.5% at a 90 °C temperature and after 3 h of the experiment. However, a further increase in peel extract resulted in a decrease in the leaching efficiency for both lithium and cobalt. Lemon peel extract, as a reducing agent, was used, together with citric acid, as a complexing agent. The reducing agents in the lemon peel extract may have disturbed the lattice, leading to the leaching of Co II, as well as Li^+ ions, through complexation. Since citrate is a strong complexing agent, both Co and Li ions were anticipated as citrate complexes. As the dissolution proceeded, the initially black solution turned dark pink. All of the parameters provided results in accordance with many of the previous studies. For example, Nayaka [37] used ascorbic acid, along with citric acid, and achieved the maximum efficiency (100% in the case of Li and 80% in the case of Co) in 6 h. The present study reached the maximum efficiency within 3 h. The cause

may have been the presence of phenolics and saccharides in the lemon peel extract that aided in speeding up the reaction and helped along the reduction in Co in a lesser time. After 3 h of the reaction, there was no improvement in the leaching efficiency. Some studies, however, have shown some discrepancies. Small contrasts of the obtained results related to the metal (Li and Co) yield compared to those in the literature were also indicated. Chen and co-workers proposed a hydrometallurgical process and obtained leaching efficiencies as high as 95%, for Co and 99% for Li using 2 mol L^{-1} of citric acid, at 80 °C, a 90 min retention time, and 2 vol% H_2O_2 [38]. Similarly, Yu et al., in a similar study obtained 99% recovery rate under conditions, such as 1.0 M citric acid, and 8% H_2O_2 at 70 °C in 70 min [39]. The different experimental and preconditions resulted in slight differences in the results.

3.2. Material Characterization

Figure 3 shows the impact of the calcination temperature on the crystallographic structure of $LiCoO_2$. It can be clearly observed that samples CP4 (waste cathode material calcined at 600 °C) and CP2 (recovered material calcined at 800 °C) indeed constituted indeed of active cathode materials as matched with the literature [40–42], with a hexagonal α-$NaFeO_2$ layered structure with an R-3m symmetry (JPCDS card No. 50-0653). The waste cathode material however showed peaks of Co_3O_4 (JCPDS card No. 073-1701), identifying it as Co_3O_4 with a cubic structure [43]. The presence of Co_3O_4 in sample CP4 might be due to the solid reaction that occurs during the charge–discharge cycles [44]. When the calcination temperature was lowered a crystallographic structure was obtained i.e., sample CP1 (recovered material calcined at 700 °C) and CP3 (recovered material calcined at 600 °C) showed some peaks that matched the Fd3m-type space group (JPCDS card No. 74-1631) with the spinel setting for example, the disappearance of a 003 peak in both samples, the appearance of a 440 peak in CP1 and CP3 in place of original 110, and the appearance of a 222 peak in CP3 [41,45,46]. Sample CP3 also contained phases of Co_3O_4. The presence of Co_3O_4 in the sample CP3 might have resulted from the fact that that incomplete lithiation occurs at low temperatures, as shown in previous studies [46]. The organic impurities shown as the addition peaks near 15° (2θ) in CP3 and CP1 disappeared in CP2 when the temperature was raised to 800 °C.

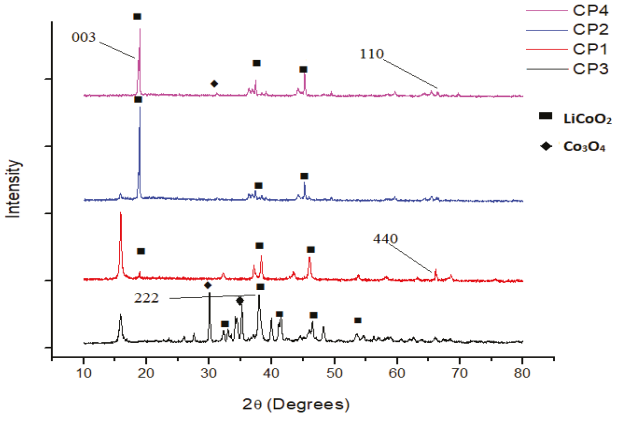

Figure 3. X-ray diffractogram of CP4 (waste material after calcination at 600 °C), CP2 (recovered material, calcined at 800 °C); CP1 (Recovered material, calcined at 700 °C), and recovered material, (calcined at 600 °C).

To estimate the chemical compositions of the synthesized powders, EDAX analysis was performed. The main elements as proven by the literature, included Li, Co, and O_2,

with the presence of other metals as well. The presence of Ni and Mn can be understood by the fact that they are present in the chemical composition of battery active materials, as proven by the literature. These metals not only aid in decreasing the price of the batteries, but also provide stability to the $LiCoO_2$ structure [47]. A small amount of Zn and Cu can be attributed to the inaccurate manual processing, for example contamination from the dismantling of the steel casing. Furthermore, it should be highlighted that the research material came from spent batteries collected from various sources, often kept in unfitting conditions that cause them to be spoiled, which can add little bits of contamination. Since EDAX is not able to detect elements with atomic numbers less than 3, Li was not detected by it. The presence of Li and the formation of $LiCoO_2$ was confirmed by XRD and XPS. The BET surface area, pore size and pore volume were also measured for the samples and the results are provided in Table 1. According to the BET results, sample CP1 had the highest surface area and pore size, while the used cathode material (CP4) had the minimum.

Table 1. BET surface area.

	BET Surface Area (m^2/g)	Pore Size (nm)	Pore Volume (cm^3/g)
CP1	16.3016	17.53716	0.071471
CP2	5.1648	10.98172	0.014216
CP3	4.8027	11.57406	0.013897
CP4	2.5255	6.68136	0.004218

The powder morphologies were observed by SEM as presented in Figure 4. The SEM micrographs of the $LiCoO_2$ catalysts revealed small crystallites of nanometric diameters. These particles were identified as $LiCoO_2$ crystals based on the energy dispersive X-ray diffra ction studies. The SEM results of all samples showed semi-disc to rod-like shapes. Differences in the morphologies of all of the samples were observed. CP4 (Figure 4d) (waste cathode material, calcined at 600 °C) and CP2 (sample after leaching calcined at 800 °C) (Figure 4b) showed similar morphologies, i.e., no agglomeration, and well-defined particles. The other two samples showed irregularities and agglomeration. CP1 (Figure 4a), in contrast to the rest of the samples, showed a rough surface and more agglomeration as the particles can be seen clustered together. These results are in accordance with the findings of Li and colleagues [48], where the smallest size is of the samples prepared at 600 °C. Since the size of the CP3 (Figure 4c) particles was smallest among all of the samples, it had most agglomeration as well, since smaller sized particles provided more surface tension [49]. Consequently, CP2 (800 °C) had the least agglomeration. Hence, it can be concluded that the leaching has impacted the size of the $LiCoO_2$ particles.

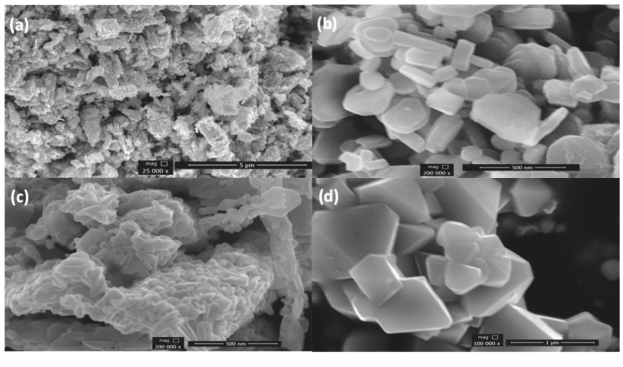

Figure 4. SEM results for the samples. (**a**) CP1 calcined at 700 °C after leaching, (**b**) CP2 calcined at 800 °C after leaching, (**c**) CP3 calcined at 600 °C after leaching, and (**d**) CP4 unprocessed waste cathode material calcined at 600 °C.

The TEM results shown in Figure 5 complement the SEM findings and reveal quite similar particle size distributions. The CP1 (Figure 5a–c) showed a small particle size (within the range of 50–100 nm) while CP2 (Figure 5d–f) showed larger particle sizes (up to 200 nm). Sample CP3 (Figure 5g–i) showed extremely small particles (up to 20 nm) in diameter.

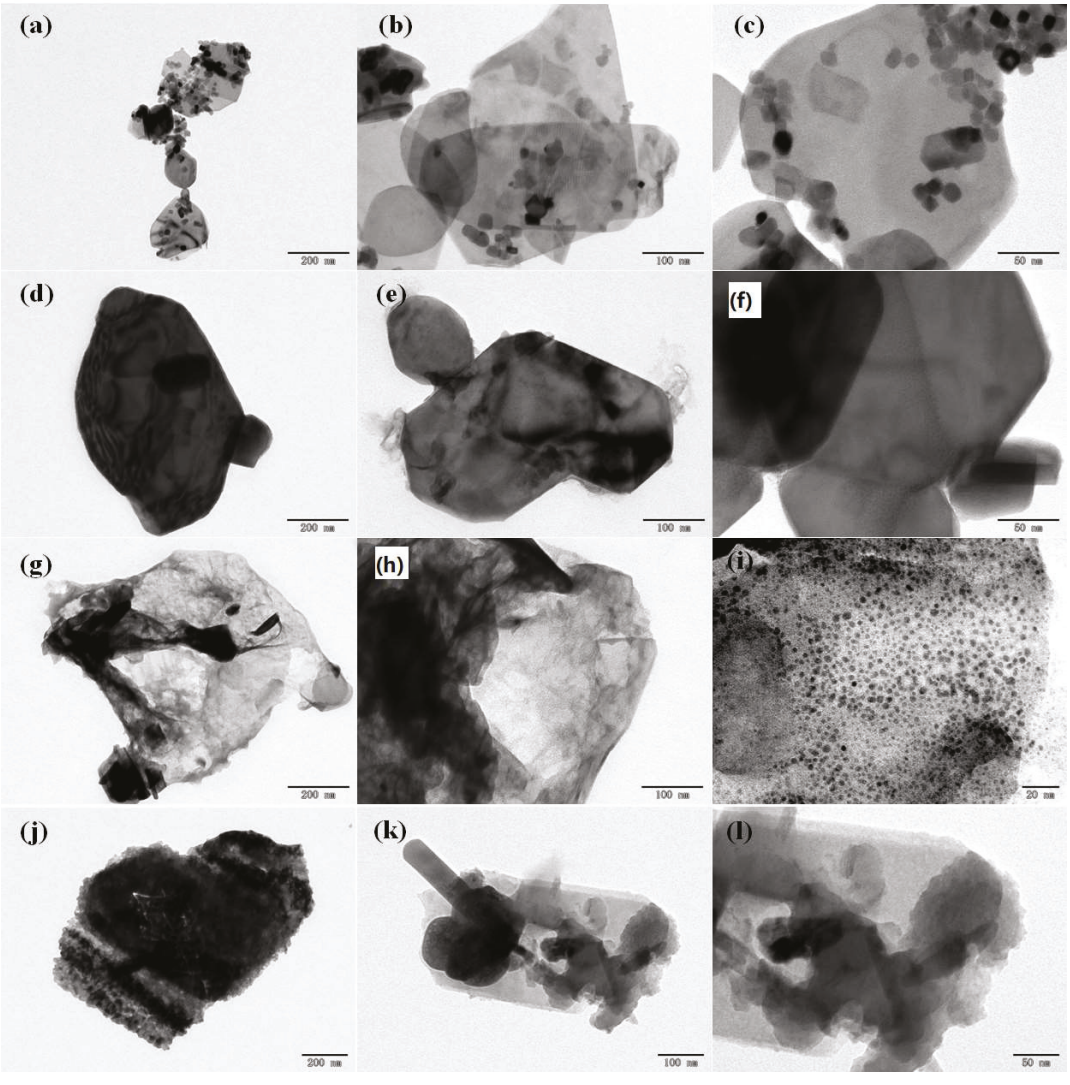

Figure 5. TEM results of all samples at different resolutions. (**a–c**) CP1 calcined at 700 °C after leaching; (**d–f**) CP2 calcined at 800 °C after leaching; (**g–i**) CP3 calcined at 600 °C after leaching; (**j–l**) CP4 unprocessed waste cathode material calcined at 600 °C.

3.3. Electrocatalytic Performance

The prepared material from the recovered waste cathode of lithium-ion batteries using citric acid coupled with lemon peel extracts and the original waste material after calcination at 600 °C were tested for the OERs reactions. The OER catalytic activity of $LiCoO_2$ (waste

cathode material, and cathode material prepared at 600, 700 and 800 °C) is shown in the Figure 6b). All of the samples showed low overpotential. However, only CP4 and CP3 exhibited a rapid acceleration in current at low overpotential. A low overpotential (0.55 V and 0.6 V vs. RHE, respectively) was required for the current density to reach 10 mA/cm^2. This finding contradicts with the findings of a study conducted on high temperature LIB cathode material by Pegoretti and colleagues, where high-temperature (800 °C) LIB cathode material showed an OER activity at a lower potential [50]. The difference in activity may lie in the presence of separate Co_3O_4 in samples CP4 and CP3 (as previously shown in the XRDs of both samples), i.e., delithiation. It has been previously proven that delithiated $LiCoO_2$ has more electrochemical active sites as compared to lithiated $LiCoO_2$ [16]. The Tafel slope and Rct values were obtained to evaluate the catalytic performance of a catalyst towards an OER. The Tafel slope (Figure 6c) of CP4 and CP3 showed small values of 104.7 mV/dec and 128.24 mV/dec compared to the rest of the samples under similar conditions. This slight difference indicates the similar reaction kinetics, and the smaller values of CP4 and CP3 indicates more favorable OER performance than the rest of the samples. The values of the CP4 and CP3 slopes indicates a favorable OER performance than the rest of the samples, as the smaller values are indicative of a higher electron conductivity and charge transfer process. To support the OER activity of the samples further, EIS (Nyquist real Z' vs. imaginative Z") was carried out on the samples. The EIS (Figure 6a) results manifested a semi-circle with a smaller diameter for CP3, which indicates the lower charge transfer resistance compared to other samples. CP4, despite its low onset potential, showed a comparatively high charge transfer resistance (R_{ct}). Figure 6a shows that the R_{ct} value for the CP1, CP2, CP3, and CP4 electrocatalysts are 17,802 Ω, 111.4 Ω, 24.99 Ω, and 401.54 Ω, respectively. The C_{dl} values (Figure 6f) extracted from the CV curves recorded in the non-Faradaic region (1.09 to 1.191 V) at different scan rates were estimated (Figure 6f) to explore the intrinsic activities of the samples. Sample CP3, displayed a significantly higher C_{dl} value (2.57 mF/cm^2) over CP1 (0.56 mF/cm^2) and CP2 (0.77 mF/cm^2), and CP4 (0.57 mF/cm^2). The larger C_{dl} indicated that CP3 had a significantly increased number of exposed active sites and a higher efficient mass and charge transport capability [51]. Furthermore, as demonstrated in Figure 6e, CP3 had a larger current density at the same scan rate compared to the rest of the samples. The long-term electrochemical stability of the sample CP3 was also tested at a static current of 10 mA cm^{-2}. CP4 proved to be unstable. The stability curve of CP3 (Figure 6d) showed an increase in the current density due to activation process and production of high oxidation intermediates and then became stable for 6500 s. Continuous gas evolution was observed during the stability measurement which dissipated rapidly into the electrolyte. The very small change in the potential during 6000 s indicates good durability of the CP3 OER electrocatalyst in the alkaline medium.

To dig deeper into the electrocatalytic performance of the catalyst, X-ray photoelectron spectroscopy (XPS) was employed on CP3, as it showed the best OER activity, to explore the surface composition and oxidation states of the electrocatalysts. The XPS results corroborated the findings of the XRD and EDAX analyses. As suggested by previous studies [52,53], the transition-metal-based materials exhibited excellent OER properties. The reason involves the existence of cations with mixed valence states. Furthermore, the weaker binding between cations leads to a flexible electronic configuration. This then leads to a higher conductivity and catalytic activities. Studies have revealed that, theoretically, the oxygen evolution reactions activities are vastly linked to the electronic structures of the metals, including their oxidation states. To illustrate the electronic configuration of our catalysts and their oxidation states, C 1 s peak at 284.8 eV was used as a reference for calibrating the binding energies. The binding energy values of all of the metals present in the sample showed that the Co in the sample was the real reason for the OER activity in this study. The XPS spectra of Co in sample CP3 (Figure 7a) showed main peaks at 780.0 eV (Co $2p_{3/2}$) and 795.1 eV (Co $2p_{1/2}$). After OER, in the high-resolution spectrum of Co 2p, detected only Co^{3+} was detected (two main peaks at 780.6 eV and 795.9 eV) (Figure 7d) [54]. While reviewing the above results, it can be inferred that the sample CP3 exhibited a higher

electrocatalytic performance (during OER) compared to the rest of the samples. The boosted activity might be due to the several reasons, such as the electron structure effect and surface properties etc. It has been established that the Co_3O_4 and $LiCoO_2$, are p-type semiconductors [14]. When a metal oxide electrode is inserted into an electrolyte, an electrical double layer or space charge layer is formed. For p-type semiconductors, the space charge layer is negligible [51]. So, as a catalyst material, a p-type semiconductor is more suitable. Secondly, the active sites in delithiated $LiCoO_2$ are much more than $LiCoO_2$ catalyst. With delithiation, the Co–O bond covalency increases which may lead to the development of holes in the hybridized Co 3d—O 2p orbitals, making the material more electrophilic aiding the adsorption of the hydroxyl group and hence enhancing the OER activity [16]. Furthermore, it is also known that electrochemical performance can be strongly influenced by the surface properties of the catalyst as the reactions usually occur on the surface of the catalyst. Figure 7a–f represents the XPS spectra of the CP3 sample after the OER stability test. As evident from the XPS, the sample CP3 was rich in Co^{3+} and O^{-2} species, both of which are electrophilic agents. In Figure 7e the binding energy value 531.9 eV associated with surface O_2 species could be ascribed to non-stoichiometric oxygen, reported as the active site in OER catalyst, which occupied a higher percentage of 52.3% (=(non-stoichiometric oxygen)/[(non-stoichiometric oxygen) + (hydroxyl oxygen)). In comparison, 532.8 eV (with a proportion of 47.6%) is associated with chemisorbed or dissociated oxygen or the presence of OH species on the surface. Figure 7e shows a small shift in the binding energy in the O 1s spectrum from 531.9 eV to 531.68 eV. The peak at around 531.68 eV could be associated with non-stoichiometric oxygen, which occupied a higher percentage (57.6% compared with the 52.3% pre-OER test), and only a 5% reduction in the intensity of the 532.8 eV peak was observed after the OER. The increasing percentage of non-stoichiometric oxygen may be assigned to the transition from Co_3O_4 to CoOOH. The analysis results suggested that Co_3O_4 on the surface was transformed to CoOOH, which is in fact the active species to OER in some literature works. Moreover, electrochemical stability is another important criterion for measuring electrocatalysts' performance; the stability of configured catalysts was investigated by chronopotentiometry (CP). A slight shift in the XPS results after the chronopotentiometry test proved the excellent stability of the CP3 sample for the OER catalyst [13].

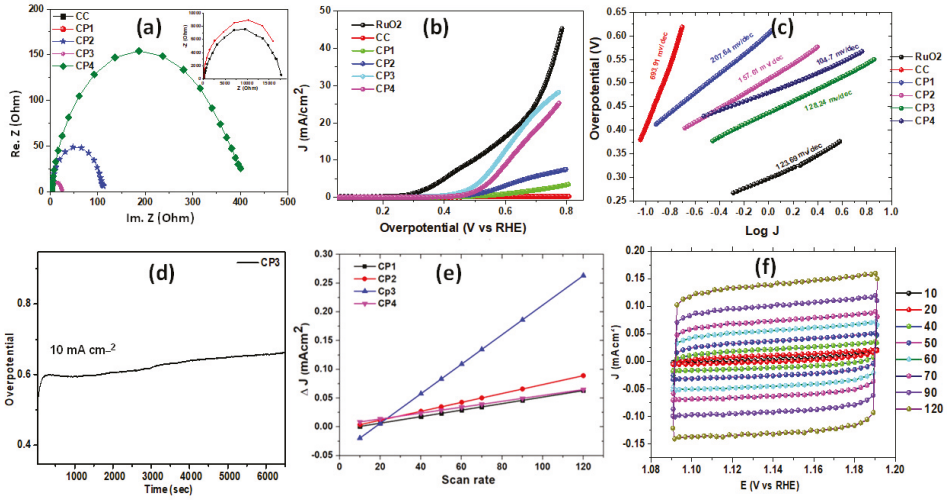

Figure 6. Oxygen evolution activities of the samples. (**a**) Nyquist plot; (**b**) polarization curve depicting the overpotential vs. current density of all samples; (**c**) Tafel plot; (**d**) stability curve of sample; CP3 (**e**) plot of the scan rate and current density; (**f**) CV curves for Cdl at different scan rates.

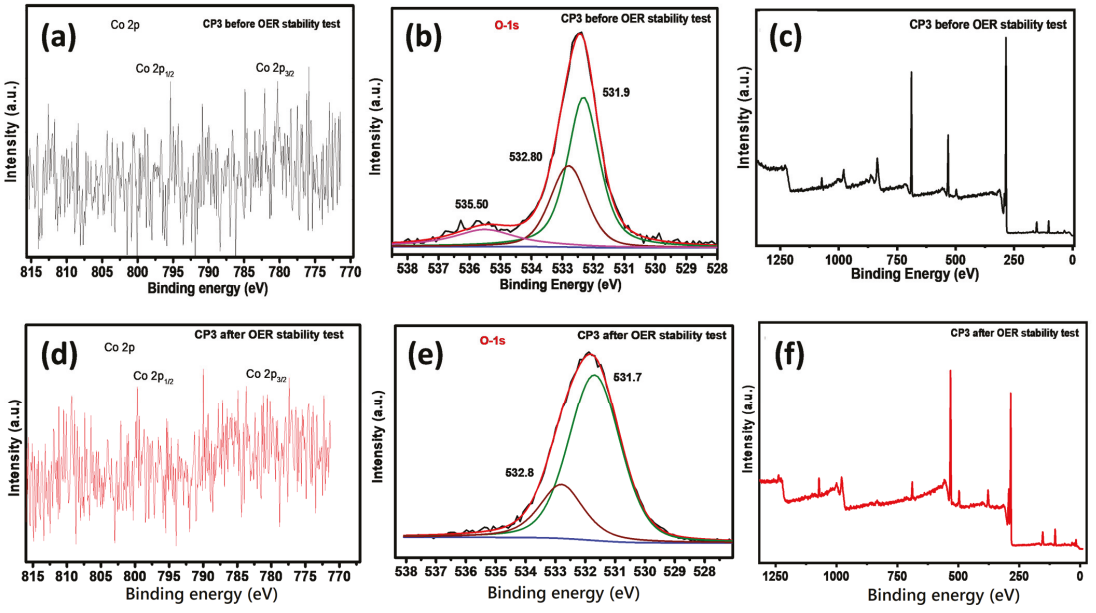

Figure 7. XPS spectra of Co 2p and O 1s in sample CP3; (**a**) XPS spectra representing the oxidation state of Co 2p before OER; (**b**) resolved XPS spectra representing the oxidation state of O 1s before OER; (**c**) Survey scan of CP3 before OER stability Test; (**d**) XPS spectra representing the oxidation state of Co 2p after OER; (**e**) resolved XPS representing oxidation state of the O 1s after OER; (**f**) survey scan of CP3 after OER stability test.

4. Conclusions

Lemon peel extract along with citric acid proved to be a good reducing and leaching agent for the recovery of metals from waste lithium-ion batteries. Furthermore, the economical and environmentally friendly nature of the method may aid further in solving problems related to pollution. The subsequent recovered material after calcination at different temperatures was tested for OER activity and it was established that the recovered material calcined at 600 °C was not only best amongst all of the samples but was also stable in terms of catalytic activity. Its average particle size was also within 20–100 nm range and the BET surface area was calculated to be 4.8027 m^2/g. A low potential of 0.55 V vs. RHE was required for the current density to reach 10 mA/cm^2 with a Tafel value of 128 mV/dec.

Author Contributions: Data curation, methodology, experimentation, writing–original draft preparation, A.A.; resources, supervision, writing–reviewing and editing, M.X.; conceptualization, supervision, resources, material characterization, manuscript revision and editing, J.R.; methodology, experimentation, C.S.S. and W.L.; characterization support, B.A.; Characterization support, B.H. All authors have read and agreed to the published version of the manuscript.

Funding: Material characterization was funded by Henan University through postdoctoral research funding. The APC was funded by Ming Xu.

Institutional Review Board Statement: Not applicable.

Informed Consent Statement: Not applicable.

Conflicts of Interest: The authors declare no conflict of interest.

References

1. Wang:, L.; Yin, F.; Yao, C. N-doped graphene as a bifunctional electrocatalyst for oxygen reduction and oxygen evolution reactions in an alkaline electrolyte. *Int. J. Hydrog. Energy* **2014**, *39*, 15913–15919. [CrossRef]

2. Gong, M.; Dai, H. A mini review of NiFe-based materials as highly active oxygen evolution reaction electrocatalysts. *Nano Res.* **2015**, *8*, 23–39. [CrossRef]
3. Bizzotto, F.; Quinson, J.; Zana, A.; Kirkensgaard, J.J.K.; Dworzak, A.; Oezaslan, M.; Arenz, M. Ir nanoparticles with ultrahigh dispersion as oxygen evolution reaction (OER) catalysts: Synthesis and activity benchmarking. *Catal. Sci. Technol.* **2019**, *9*, 6345–6356. [CrossRef]
4. Risch, M.; Stoerzinger, K.A.; Han, B.; Regier, T.Z.; Peak, D.; Sayed, S.Y.; Wei, C.; Xu, Z.; Shao-Horn, Y. Redox Processes of Manganese Oxide in Catalyzing Oxygen Evolution and Reduction: An in Situ Soft X-ray Absorption Spectroscopy Study. *J. Phys. Chem. C* **2017**, *121*, 17682–17692. [CrossRef]
5. Fominykh, K.; Chernev, P.; Zaharieva, I.; Sicklinger, J.; Stefanic, G.; Döblinger, M.; Müller, A.; Pokharel, A.; Böcklein, S.; Scheu, C.; et al. Iron-Doped Nickel Oxide Nanocrystals as Highly Efficient Electrocatalysts for Alkaline Water Splitting. *ACS Nano* **2015**, *9*, 5180–5188. [CrossRef]
6. Lankauf, K.; Cysewska, K.; Karczewski, J.; Mielewczyk-Gryń, A.; Górnicka, K.; Cempura, G.; Chend, M.; Jasińskia, P.; Molin, S. $Mn_xCo_{3-x}O_4$ spinel oxides as efficient oxygen evolution reaction catalysts in alkaline media. *Int. J. Hydrog. Energy* **2020**, *45*, 14867–14879. [CrossRef]
7. Wang, Y.; Li, M.; Zhou, Q.; Wang, Q.; Zhang, X.; Tang, Y.; Sun, D. Coupling Hierarchical Ultrathin Co Nanosheets with N-doped Carbon Plate as High-Efficiency Oxygen Evolution Electrocatalysts. *Front. Nanotechnol.* **2021**, *3*, 17. [CrossRef]
8. Zhang, L.; Li, H.; Yang, B.; Zhou, Y.; Zhang, Z.; Wang, Y. Photo-deposition of ZnO/Co_3O_4 core-shell nanorods with pn junction for efficient oxygen evolution reaction. *J. Solid State Electrochem.* **2019**, *23*, 3287–3297. [CrossRef]
9. Zhu, S.; He, W.Z.; Li, G.M.; Xu, Z.; Zhang, X.; Huang, J. Recovery of Co and Li from spent lithium-ion batteries by combination method of acid leaching and chemical precipitation. *Trans. Nonferrous Met. Soc. China* **2012**, *22*, 2274–2281. [CrossRef]
10. Lewis, C.; Li, Y.; Wang, L.; Li, J.; Stach, E.; Takeuchi, K.J.; Marschilok, A.C.; Takeuchi, E.S.; Wong, S.S. Correlating Titania Nanostructured Morphologies with Performance as Anode Materials for Lithium-Ion Batteries. *ACS Sustain. Chem. Eng.* **2016**, *4*, 6299–6312. [CrossRef]
11. Ordoñez, J.; Gago, E.J.; Girard, A. Processes and technologies for the recycling and recovery of spent lithium-ion batteries. *Renew. Sustain. Energy Rev.* **2016**, *60*, 195–205. [CrossRef]
12. Ferreira, D.A.; Prados, L.; Majuste, D.; Mansur, M. Hydrometallurgical separation of aluminium, cobalt, copper and lithium from spent Li-ion batteries. *J. Power Sources* **2009**, *187*, 238–246. [CrossRef]
13. Lee, S.W.; Carlton, C.; Risch, M.; Surendranath, Y.; Chen, S.; Furutsuki, S.; Yamada, A.; Nocera, D.G.; Shao-Horn, Y. The Nature of Lithium Battery Materials under Oxygen Evolution Reaction Conditions. *J. Am. Chem. Soc.* **2012**, *134*, 16959–16962. [CrossRef]
14. Garcia, E.M.; Freitas, V.; Lins, C.; Tarôco, H.A.; Matencio, T.; Domingues, R.Z.; dos Santos, J.A. The anode environmentally friendly for water electrolysis based in $LiCoO_2$ recycled from spent lithium-ion batteries. *Int. J. Hydrog. Energy* **2012**, *37*, 16795–16799. [CrossRef]
15. Chen, N.; Qi, J.; Du, X.; Wang, Y.; Zhang, W.; Wang, Y.; Lu, Y.; Wang, S. Recycled $LiCoO_2$ in spent lithium-ion battery as an oxygen evolution electrocatalyst. *RSC Adv.* **2016**, *6*, 103541–103545. [CrossRef]
16. Lu, Z.; Wang, H.; Kong, D.; Yan, K.; Hsu, P.; Zheng, G.; Yao, H.; Liang, Z.; Sun, X.; Cui, Y. Electrochemical tuning of layered lithium transition metal oxides for improvement of oxygen evolution reaction. *Nat. Commun.* **2014**, *5*, 4345. [CrossRef] [PubMed]
17. EPA. Environmental Protection Agency. Available online: https://www.epa.gov/recycle/used-lithium-ion-batteries (accessed on 12 November 2021).
18. U.S. Geological Survey. Mineral Commodity Summaries 2021. Available online: https://pubs.er.usgs.gov/publication/mcs2021 (accessed on 11 November 2021).
19. Statista Research Department. Cobalt Monthly Futures Price 2021. 4 October 2021. Available online: https://www.statista.com/statistics/1171975/global-monthly-price-of-cobalt/ (accessed on 10 November 2021).
20. Vargas., P. Lithium and the Foreseeable Future. Bachelor's Thesis, University of Arkansas, Fayetteville, AR, USA, 2018.
21. Lithium and Cobalt CBS September 2021—Lithium Price Surges, Cobalt Range-Bound. Available online: https://www.spglobal.com/marketintelligence/en/news-insights/blog/lithium-and-cobalt-cbs-september-2021-lithium-price-surges-cobalt-range-bound (accessed on 10 November 2021).
22. Eason, E. *World Lithium Supply*; Stanford University: Stanford, CA, USA, 2010.
23. Zheng, X.; Gao, W.; Zhang, X.; He, M.; Lin, X.; Cao, H.; Zhang, Y.; Sun, Z. Spent lithium-ion battery recycling–Reductive ammonia leaching of metals from cathode scrap by sodium sulphite. *Waste Manag.* **2017**, *60*, 680–688. [CrossRef] [PubMed]
24. Georgi-Maschler, T.; Friedrich, B.; Weyhe, R.; Heegn, H.; Rutz, M. Development of a recycling process for Li-ion batteries. *J. Power Sources* **2012**, *207*, 173–182. [CrossRef]
25. Hu, J.; Zhang, J.; Li, H.; Chen, Y.; Wang, C. A promising approach for the recovery of high value-added metals from spent lithium-ion batteries. *J. Power Sources* **2017**, *351*, 192–199. [CrossRef]
26. Takacova, Z.; Havlik, T.; Kukurugya, F.; Orac, D. Cobalt and lithium recovery from active mass of spent Li-ion batteries: Theoretical and experimental approach. *Hydrometallurgy* **2016**, *163*, 9–17. [CrossRef]
27. Pinna, E.G.; Ruiz, M.C.; Ojeda, M.W.; Rodriguez, M.H. Cathodes of spent Li-ion batteries: Dissolution with phosphoric acid and recovery of lithium and cobalt from leach liquors. *Hydrometallurgy* **2017**, *167*, 66–71. [CrossRef]
28. Yao, Y.; Zhu, M.; Zhao, Z.; Tong, B.; Fan, Y.; Hua, Z. Hydrometallurgical processes for recycling spent lithium-ion batteries: A critical review. *ACS Sustain. Chem. Eng.* **2018**, *6*, 13611–13627. [CrossRef]

29. Gao, W.; Song, J.; Cao, H.; Lin, X.; Zhang, X.; Zheng, X.; Zhang, Y.; Sun, Z. Selective recovery of valuable metals from spent lithium-ion batteries–process development and kinetics evaluation. *J. Clean. Prod.* **2018**, *178*, 833–845. [CrossRef]
30. Chen, X.; Fan, B.; Xu, L.; Zhou, T.; Kong, J. An atom-economic process for the recovery of high value-added metals from spent lithium-ion batteries. *J. Clean. Prod.* **2016**, *112*, 3562–3570. [CrossRef]
31. Eaks, I.L. Ascorbic Acid Content of Citrus During Growth and Development. *Bot. Gaz.* **1964**, *125*, 186–191. [CrossRef]
32. Sir Elkhatim, K.A.; Elagib, R.A.; Hassan, A.B. Content of phenolic compounds and vitamin C and antioxidant activity in wasted parts of Sudanese citrus fruits. *Food Sci. Nutr.* **2018**, *6*, 1214–1219. [CrossRef] [PubMed]
33. Li, L.; Lu, J.; Ren, Y.; Zhang, X.; Chen, R.; Wu, F.; Amine, K. Ascorbic-acid-assisted recovery of cobalt and lithium from spent Li-ion batteries. *J. Power Sources* **2012**, *218*, 21–27. [CrossRef]
34. Nayaka, G.P.; Zhang, Y.; Dong, P.; Wang, D.; Zhou, Z.; Duan, J.; Li, X.; Lin, Y.; Meng, Q.; Pai, K.V.; et al. An environmental friendly attempt to recycle the spent Li-ion battery cathode through organic acid leaching. *J. Environ. Chem. Eng.* **2019**, *7*, 102854. [CrossRef]
35. Li, J.; Zhao, R.; He, X.; Liu, H. Preparation of $LiCoO_2$ cathode materials from spent lithium–ion batteries. *Ionics* **2009**, *15*, 111–113. [CrossRef]
36. Li, L.; Ge, J.; Wu, F.; Chen, R.; Chen, S.; Wu, B. Recovery of cobalt and lithium from spent lithium ion batteries using organic citric acid as leachant. *J. Hazard. Mater.* **2010**, *176*, 288–293. [CrossRef]
37. Nayaka, G.P.; Manjanna, J.; Pai, K.V.; Vadavi, R.; Keny, S.J.; Tripathi, V.S. Recovery of valuable metal ions from the spent lithium-ion battery using aqueous mixture of mild organic acids as alternative to mineral acids. *Hydrometallurgy* **2015**, *151*, 73–77. [CrossRef]
38. Chen, X.; Zhou, T. Hydrometallurgical process for the recovery of metal values from spent lithium-ion batteries in citric acid media. *Waste Manag. Res.* **2014**, *32*, 1083–1093. [CrossRef] [PubMed]
39. Min, Y.; Zhang, Z.; Xue, F.; Yang, B. A more simple and efficient process for recovery of cobalt and lithium from spent lithium-ion batteries with citric acid. *Sep. Purif. Technol.* **2019**, *215*, 398–402.
40. Zhuravlev, V.; Shikhovtseva, A.; Ermakova, L.; Evshchik, E.; Sherstobitova, E.; Novikov, D.; Bushkova, O.V.; Dobrovolsky, Y.A. Solution combustion synthesis of lithium cobalt oxide–cathode material for lithium-ion batteries. *Int. J. Electrochem. Sci.* **2019**, *14*, 2965–2983. [CrossRef]
41. Xia, H.; Wan, Y.; Assenmacher, W.; Mader, W.; Yuan, G.; Lu, L. Facile synthesis of chain-like $LiCoO_2$ nanowire arrays as three-dimensional cathode for microbatteries. *NPG Asia Mater.* **2014**, *6*, e126. [CrossRef]
42. Qi, Z.; Koenig, G.M., Jr. High-performance $LiCoO_2$ sub-micrometer materials from scalable microparticle template processing. *ChemistrySelect* **2016**, *1*, 3992–3999. [CrossRef]
43. Manigandan, R.; Giribabu, K.; Suresh, R.; Vijayalakshmi, L.; Stephen, A.; Narayanan, V. Cobalt oxide nanoparticles: Characterization and its electrocatalytic activity towards nitrobenzene. *Chem. Sci. Trans.* **2013**, *2*, S47–S50.
44. Freitas, M.B.; Garcia, E.M. Electrochemical recycling of cobalt from cathodes of spent lithium-ion batteries. *J. Power Sources* **2007**, *171*, 953–959. [CrossRef]
45. Abdel-Ghany, A.E.; Eid, A.E.; Salman, A.A.; Sharaby, C.M.; Abdel-Hamied, S.K. Synthesis and Structural Characterization of Lithiated and Delithiated $LiCoO_2$ Using Different Chelating Agents. *Egypt. J. Chem.* **2010**, *53*, 417–434.
46. Soltanmohammad, S.; Asgari, S. Characterization of $LiCoO_2$. Nanopowders Produced by Sol-Gel Processing. *J. Nanomater.* **2010**, *2010*, 104012. [CrossRef]
47. Mossali, E.; Picone, N.; Gentilini, L.; Rodrìguez, O.; Pérez, J.M.; Colledani, M. Lithium-ion batteries towards circular economy: A literature review of opportunities and issues of recycling treatments. *J. Environ. Manag.* **2020**, *264*, 110500. [CrossRef]
48. Li, G.; Chuang, P. Identifying the forefront of electrocatalytic oxygen evolution reaction: Electronic double layer. *Appl. Catal. B Environ.* **2018**, *239*, 425–432. [CrossRef]
49. Habibi, A.; Jalaly, M.; Rahmanifard, R.; Ghorbanzadeh, M. The effect of calcination conditions on the crystal growth and battery performance of nanocrystalline Li (Ni 1/3 Co 1/3 Mn 1/3) O_2 as a cathode material for Li-ion batteries. *New J. Chem.* **2018**, *42*, 19026–19033. [CrossRef]
50. Pegoretti, V.C.B.; Dixini, P.V.M.; Magnago, L.; Rocha, A.K.S.; Lelis, M.F.F.; Freitas, M.B.J.G. High-temperature (HT) $LiCoO_2$ recycled from spent lithium ion batteries as catalyst for oxygen evolution reaction. *Mater. Res. Bull.* **2019**, *110*, 97–101. [CrossRef]
51. Liu, P. Recycling Waste Batteries: Recovery of Valuable Resources or Reutilization as Functional Materials. *ACS Sustain. Chem. Eng.* **2018**, *6*, 11176–11185. [CrossRef]
52. Park, K.R.; Jeon, J.E.; Ali, G.; Ko, Y.; Lee, J.; Han, H.; Mhin, S. Oxygen Evolution Reaction of Co-Mn-O Electrocatalyst Prepared by Solution Combustion Synthesis. *Catalysts* **2019**, *9*, 564. [CrossRef]
53. Shi, J.; Du, N.; Zheng, W.; Li, X.; Dai, Y.; He, G. Ultrathin Ni-Co double hydroxide nanosheets with conformal graphene coating for highly active oxygen evolution reaction and lithium ion battery anode materials. *Chem. Eng. J.* **2017**, *327*, 9–17. [CrossRef]
54. NIST X-ray Photoelectron Spectroscopy Database. 2012. Available online: https://srdata.nist.gov/xps/ (accessed on 20 June 2019).

nanomaterials

MDPI

Communication

Improved Light Harvesting of Fiber-Shaped Dye-Sensitized Solar Cells by Using a Bacteriophage Doping Method

Sung-Jun Koo [1,2,†], Jae Ho Kim [1,†], Yong-Ki Kim [3], Myunghun Shin [3], Jin Woo Choi [1], Jin-Woo Oh [2,4,*], Hyung Woo Lee [2,5,*] and Myungkwan Song [1,*]

[1] Department of Energy and Electronic Materials, Korea Institute of Materials Science (KIMS), Changwon 51508, Korea; sungun666@kims.re.kr (S.-J.K.); jho83@kims.re.kr (J.H.K.); jinwoo.choi@kims.re.kr (J.W.C.)
[2] Department of Nano Fusion Technology, Pusan National University, Busan 46241, Korea
[3] School of Electronics and Information Engineering, Korea Aerospace University, Goyang 10540, Korea; ygk3373@kau.kr (Y.-K.K.); mhshin@kau.ac.kr (M.S.)
[4] Bio-IT Fusion Technology Research Institute, Pusan National University, Busan 46241, Korea
[5] Department of Nanoenergy Engineering and Research Center of Energy Convergence Technology, Pusan Natuional University, Busan 46241, Korea
* Correspondence: ojw@pusan.ac.kr (J.-W.O.); LHW2010@pusan.ac.kr (H.W.L.); smk1017@kims.re.kr (M.S.)
† These authors contributed equally to this work.

Abstract: Fiber-shaped solar cells (FSCs) with flexibility, wearability, and wearability have emerged as a topic of intensive interest and development in recent years. Although the development of this material is still in its early stages, bacteriophage-metallic nanostructures, which exhibit prominent localized surface plasmon resonance (LSPR) properties, are one such material that has been utilized to further improve the power conversion efficiency (PCE) of solar cells. This study confirmed that fiber-shaped dye-sensitized solar cells (FDSSCs) enhanced by silver nanoparticles-embedded M13 bacteriophage (Ag@M13) can be developed as solar cell devices with better PCE than the solar cells without them. The PCE of FDSSCs was improved by adding the Ag@M13 into an iodine species (I^-/I_3^-) based electrolyte, which is used for redox couple reactions. The optimized Ag@M13 enhanced FDSSC showed a PCE of up to 5.80%, which was improved by 16.7% compared to that of the reference device with 4.97%.

Keywords: fiber-shaped solar cells; dye-sensitized solar cells; M13 bacteriophage; plasmon resonance

Citation: Koo, S.-J.; Kim, J.H.; Kim, Y.-K.; Shin, M.; Choi, J.W.; Oh, J.-W.; Lee, H.W.; Song, M. Improved Light Harvesting of Fiber-Shaped Dye-Sensitized Solar Cells by Using a Bacteriophage Doping Method. *Nanomaterials* **2021**, *11*, 3421. https://doi.org/10.3390/nano11123421

Academic Editors: Sophie Tingry, Marc Cretin and Zhenghua Tang

Received: 26 November 2021
Accepted: 14 December 2021
Published: 17 December 2021

1. Introduction

Harvesting solar energy has been regarded as one of the easiest solutions to collect the promising renewable energy resources for sustainable development. Among various flexible energy harvesting technologies, fiber-shaped dye-sensitized solar cells (FDSSCs), which represent a promising future energy source with flexible and wearable properties, are drawing the attention of many researchers because it is lightweight, inexpensive, simple to manufacture, and flexible [1–7]. The FDSSCs typically consist of three parts: a photoanode (PA), a counter electrode (CE), and a redox electrolyte. Under illumination, dyes act as photosensitizer, in which photons excite electrons at the highest occupied molecular orbital (HOMO) to the lowest unoccupied molecular orbital (LUMO). The excited electrons are injected into the conduction band of the PA and then diffused through the PA into the electrode to reach the CE through an external circuit. On one hand, iodide (I^-), a reductive species in the electrolyte, supplies electrons to the oxidized dye and becomes triiodide (I_3^-), which in turn gains electrons from the CE to complete the redox couple [8,9].

The electrolyte is one of the most important components of dye-sensitized solar cells (DSSCs) and has a significant impact on the high power conversion efficiency (PCE) in solar cells. The electrolyte in solar cell devices should have the following characteristics: (I) It should be able to regenerate the oxidized dye efficiently. (II) Should not corrode with

DSSC components. (III) Should rapidly diffuse charge carriers, improve conductivity, and enable effective contact between the working and counter electrodes. (IV) Absorption spectra of an electrolyte should not overlap with the absorption spectra of a dye [10,11]. Therefore, to satisfy the above functions, bacteriophage-metallic nanostructures, which exhibit prominent localized surface plasmon resonance (LSPR) properties, were integrated with the iodine species (I^-/I_3^-) based electrolyte that has been proven as a highly efficient electrolyte. The metallic nanoparticles (NPs) mainly increase the light-surface plasmon coupling, realizing a plasmonic enhancement effect in photoelectric devices [12]. Hence, incorporating bacteriophage-metallic nanostructures into on unit of solar cells is a promising alternative strategy that can improve the performance of photoelectric devices by inducing the LSPR properties, which is receiving great attention for light scattering, fluorescence, charge transfer, and local field enhancement [13–15].

Recently, among the bacteriophage-metallic nanostructures, an M13 bacteriophage has attracted particular attention due to its non-toxic, self-assembly, and specific binding properties. This bacterial virus, M13 bacteriophage, is 880 nm in length and 6.6 nm in diameter, consisting of a single-stranded DNA molecule enclosed by 2700 identical copies of the major coat protein pVIII and capped with five copies of four different minor coat proteins at the ends [16], as shown in Figure 1a. The M13 bacteriophage is easily applicable to wearable applications because it is stable in a wide range of pH [17,18] and temperatures and organic solvents [19,20] and is not injurious to humans or animals. In addition, since the functionalization such as easily attaching metal ions to the DNA surface, there is a possibility that it can be applied to various fields of electronic devices [21,22]. Previous study reported plasmon-enhanced light absorption, photocurrent density and PCE by incorporating metallic NPs into mesoporous TiO_2 (mp-TiO_2) and electrolyte interface [23,24]. However, these plasmonic DSSCs have the critical issues when metal NPs were incorporated into the liquid electrolyte such as the aggregation of NPs [25]. For photoelectric applications, M13 bacteriophage-metallic nanostructure conjugates can be an excellent platform because M13 is easily fictionalized with metallic NPs by using phage display technology [26].

Herein, the M13 bacteriophage, which has improved the LSPR properties by anchoring of metallic silver (Ag) NPs, was added to the electrolyte of the solar cell. The electrolyte improved with an Ag NPs-embedded M13 bacteriophage (Ag@M13) showed a high absorbance in a long wavelength region of 500 nm or more, confirming that the plasmonic Ag NPs were uniformly oriented and aligned in nanoscale M13 bacteriophages. Furthermore, the FDSSCs were fabricated using an enhanced electrolyte supplemented with Ag@M13, which was demonstrated to improve the PCE by plasmonic enhancement effect. The optimized Ag@M13 enhanced FDSSC boasts effective electron extraction, unidirectional electron transportation, and suppressed charge recombination processes, resulting in a PCE of up to 5.80%, which was improved by 16.7% compared to that of the reference device with 4.97%.

2. Materials and Methods

2.1. Materials

Titanium wire (ϕ 250 μm, 99.7%) was purchased from Sigma-Aldrich (Burlington, MA, U.S.). TiO_2 paste (18NR-T) and iodine species (I^-/I_3^-) based High Performance Electrolyte (HPE) were purchased from Greatcellsolar (Queanbeyan, Australia). Y123 dye (DN-F05Y) was purchased from Dyenamo (Stockholm, Sweden). Platinum wire (ϕ 125 μm, 99.9%) was manufactured by a Wooillmetal (Yongin, South Korea).

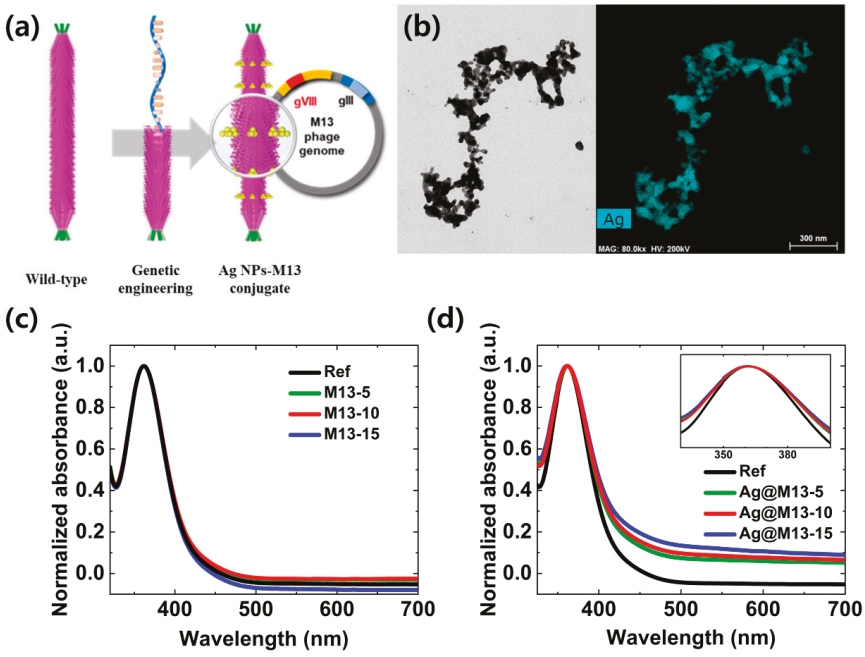

Figure 1. Morphological and optical characteristics of Ag@M13 bacteriophage: (**a**) schematic representation with structure on Ag@M13, (**b**) HR-TEM image (left) of morphology of Ag@M13 and EDS-STEM (right) to investigate its elemental mapping spectra, (**c**) normalized absorbance of as a function of M13 bacteriophage without Ag NPs, and (**d**) normalized absorbance of as a function of Ag@M13 bacteriophage. The inset is a high magnification of the main absorbance peak.

2.2. Optical Simulation of Ag-BP-DSSC

The light scattering effect by Ag particles for a DSSC is simulated in the following way. The elemental samples of an electrolyte layer (60 μm) sealed with two glass substrates and an active layer (30 μm) that consists of a porous TiO_2 (40% porosity) and dye mixture layer without the electrolyte were prepared on a glass substrate, and transmittance and reflectance of the samples were measured. Optical parameters (the effective refractive index, n-k values) of the DSSC active layer were extracted in consideration of TiO_2 porosity, which was the result of the iterative process continuing the comparison of the measured transmittance and reflectance spectra with the calculated spectra several times [27]. Using a finite-difference time-domain method (FDTD) with the obtained optical parameters of the DSSC, the absorbance spectra in the active layer and Ag particles for different concentrations of Ag particles were calculated.

2.3. Fabrication of the FDSSC

The FDSSCs fabricated here are based on previous experiments [28,29]. A Ti wire was cleaned by deionized water, acetone, and isopropanol alcohol (IPA) sequentially for 10 min under the sonication. A compact-TiO_2 (c-TiO_2) layer was formed by electric heating with a current of 1.6 A for 10 s in air, allowing the oxidation of Ti wire and oxygen in the air to generate the c-TiO_2 layer. The diluted TiO_2 solution (1 g commercial TiO_2 paste and 1 mL ethanol) was deposited by using the dip-coating technique with 10 mm s^{-1} for the withdraw rate and annealed at 120 °C for 3 m, and the cycle of dip-coating and annealing process was repeated five times to control the thickness of the mp-TiO_2 layer. The PA layer consisting of the Ti/c-TiO_2/mp-TiO_2 layer was then crystallized by electric heating of 2 A for 10 m at ambient atmosphere. The PA was immersed in the Y123 dye solution dissolved

in anhydrous ethanol (0.1 mM) for 4 h. The CE, Pt wire, was wound around the Y123 dye-sensitized PA so as not to damage the Y123 dye-sensitized PA and put into the Teflon tube. Then, after the electrolyte was injected, both ends of the tube were sealed.

2.4. Liquid Crystal (LC) Layering

Indium tin oxide (ITO) glass substrates with dimensions of 210 × 297 mm^2 and a sheet resistance of 10 Ω sq^{-1} were ultrasonically cleaned using a semiconductor cleaning process. Polyimide (PI SE-7492; Nissan Chemical, Tokyo, Japan) was uniformly spin-coated onto the ITO-coated glass substrates to form liquid-crystal (LC) alignment layers. The PI layers were prebaked at 80 °C for 10 min and then imidized at 230 °C for 1 h. The thickness of the PI layer as an insulating film was set to approximately 100 nm. The PI layer was rubbed using a unidirectional rubbing method with a rubbing strength of 300 mm. Twisted-nematic (TN) LC cells were fabricated with a cell gap of 4.2 μm. To inject positive nematic LCs (MJ001929; ne = 1.5859, no = 1.4872, and Δε = 8.2, Merck, Darmstadt, German) effectively, a seal pattern was formed to create a vacuum inside the TN LC cell, and a vacuum injection method was used to inject liquid crystals using the capillary phenomenon and pressure difference at room temperature.

2.5. Characterization

Field-emission scanning electron microscopy (FE-SEM) images were obtained using a JEOL JSM-6700F field-emission scanning electron microscope (Tokyo, Japan). The optical transmittance was identified via UV-Vis-NIR spectroscopy (Cary 5000, Agilent Technologies, Santa Clara, CA, U.S.). The photocurrent density–voltage (*J*–*V*) characteristics of the FDSSCs were obtained by an electrometer (Keithley 2400, Keithley, Cleveland, OH, U.S.) under air-mass (AM) 1.5 illumination (100 mW cm^{-2}) provided by a solar simulator (Oriel Sol3A Class AAA solar simulator, models 94043A, Newport, RI, U.S.). The calibrated light intensity was set to 1 sun using a standard silicon cell. The effective area of the device is defined as the project area transmitted by the mask, which is equal to the diameter of the photoanode multiplied by its length (1 cm). The external quantum efficiency (EQE) was measured using the incident photon-to-current conversion efficiency (IPCE) measurement system (QuantX 300, Oriel, Newport, RI, U.S.) with a 250 W quartz-tungsten-halogen lamp, an Oriel Cornerstone^{TM} 130 1/8 m monochromator operated in AC mode, an optical chopper, a lock-in amplifier, and a calibrated Si photodetector. The intensity of the sunlight for outdoor measurements was observed via a UV light meter (TM-208, Tenmars, Neihu, Taiwan). Electrochemical impedance spectroscopy (EIS) measurement was measured with an oscillation amplitude of 15 mV under dark conditions (Bio-Logic VMP-3, Seyssinet-Pariset, France) by using the open-circuit voltage and the frequency ranges from 1 Hz to 10 MHz. The experimental data were simulated using commercial Z-view software to estimate the values of each component of the corresponding equivalent circuits. The bending test was performed as a function of the number of bending cycles with a bending radius of 10 mm.

3. Results and Discussion

The metallic NPs, especially Ag NPs, are traditionally used to enhance the light-harvesting efficiency of optical devices due to their prominent LSPR properties. In addition, due to the unique charge selectivity of peptide receptors in M13 bacteriophage, the metallic NPs can be directly anchored onto the bacteriophage through charge-driven interactions without binder or surfactant [30]. Figure 1b shows high-resolution transmission electron microscopy (HR-TEM) (left) to investigate the morphology of Ag@M13 and an energy dispersive X-ray spectroscopy in scanning transmission electron microscopy (EDS-STEM) (right) to investigate its elemental mapping spectra. The nanoscale template of M13 bacteriophage nanostructures was well observed, which consists of nearly spherical NPs smaller than 20 nm in diameter. In addition, the elemental mapping spectra reveal the presence of the Ag NPs element onto an M13 bacteriophage nanostructure. From these

results, it is confirmed that the Ag NPs are embedded by maintaining the nanoscale distance well in the bacteriophage template. Hence, the gap-plasmon effect can be expected as the metallic NPs maintain a constant nanoscale distance between them [31,32]. In addition, the gap-plasmon effect can be expected to have an additional effect of amplifying the absorption spectra in a long-wavelength region (about 600 nm) along with the existing effect of amplifying the absorption spectra in a short-wavelength region (about 300 nm) [33].

The normalized UV-Vis optical absorption spectra of the iodine based electrolytes as a function of the concentration of bare M13 bacteriophage and Ag@M13 bacteriophage are presented in Figure 1c,d, respectively. The electrolytes in which bare M13 bacteriophage (or Ag@M13) are added at concentrations of 5, 10, and 15 μL are referred to as M13-5, M13-10, and M13-15 (or Ag@M13-5, Ag@M13-10, and Ag@M13-15), respectively. Reference electrolyte (Ref) and the electrolyte with M13 and Ag@M13 had one absorption band at 370 nm. The absorption spectra of bare M13 bacteriophage increased from M13-5 to M13-10 and then decreased at M13-15. It was confirmed that the bare M13 bacteriophages as a function of the concentration added to the electrolyte hardly change each absorption spectra. In contrast, in the electrolyte to which Ag@M13 was added, it was confirmed that the absorption spectra improved in the long-wavelength region as the concentration of Ag@M13 increased and the full width at half maximum (FWHM) of the absorption band was also widened, as shown in the inset of Figure 1d. The LSPR properties, which are affected by the size of the metallic NPs, are limited to less than about 500 nm when the size of NPs becomes too small [30,34]. This research shows that the normalized absorbance has increased from 400 nm to the long-wavelength region, which means that the Ag NPs were aligned in a uniform arrangement on nanoscale template of M13 bacteriophage having uniform intervals in nanoscales. Therefore, the plasmonic Ag NPs were uniformly oriented and aligned in nanoscale bacteriophage, which contributed to overcoming the limitation of LSPR in smaller NPs.

The Ag particles included in the DSSC not only increase the absorbance of the active layer by scattering the incident light, which increases the photocurrent of the device, but also absorb the light the Ag particles absorb the light, which cannot contribute to the output photocurrent and lowers the overall photocurrent. Figure 2a shows the plasmonic effects that Ag particles absorb and scatter the light. The Ag particle effects increase with the size as shown in Figure 2b. Here, it is assumed that the size of Ag particles can be randomly distributed between 10–100 nm. As shown in Figure 2c, when the density of Ag particles increases, the amount of the light absorption by the Ag particles increases. In Figure 2d, when the density of Ag particles is ~$1 \times 10^9/mm^3$, the absorption by the active layer can increase in the mid-range of visible light (500–700 nm), but above that concentration, the absorption decreases and even lowers compared to when the Ag is not present, due to the absorption by the Ag particles as shown in Figure 2c [35].

The photovoltaic performance of FDSSCs fabricated with or without improved by Ag@M13 was evaluated by investigating the current density–voltage (J–V) characteristic curves under AM 1.5 illumination, as shown in Figure 3a. In addition, their corresponding photovoltaic parameters are summarized in Table 1. Four parameters for identifying the characteristics of photovoltaic: open-circuit voltage (V_{OC}), short-circuit current density (J_{SC}), fill factor (FF), and PCE are important measures for analyzing the photovoltaic characteristics of FDSSCs. The conditions for FDSSCs in the form of (Ti wire/mp-TiO_2/Y123 dye/Ag@M13 enhanced electrolyte/Pt wire) are shown in Figure S1. The V_{OC} increased from 0.65 to 0.66 V depending on the presence or absence of Ag@M13, but the change is very small. The V_{OC}, which is the gap between the electrolyte and the Fermi level of the photoanode, showed insignificant changes even when Ag@M13 was added. This is interpreted as adding Ag@M13 into the electrolyte not affecting the energy level of the iodine based electrolyte. On one hand, the J_{SC} and the FF increased from the reference to Ag@M13-10 and then decreased at Ag@M13-15. Overall, the PCEs of FDSSCs enhanced by Ag@M13 enhanced electrolyte were higher than those of the bare electrolyte due to the increase in J_{SC} and FF. It is considered that the increase in J_{SC} means that Ag@M13 present

in the electrolyte has a high probability of penetrating into the dye-sensitized photoanode with the mesoporous structure, which may have caused higher PCE. Furthermore, the increased FF was attributed to the increased shunt resistance (R_{sh}), which represents the resistance to recombination, as well as the decreased series resistance (R_s), which represents the overall resistance of the photoanode. The R_s is ideal for minimizing the decrease in current flow through the solar cell devices as its value is lower. In addition, the R_{sh} is ideal for preventing the recombination of photoexcited electrons into the electrolyte and maximizing the current flow to the external load as its values is higher. Thus, it is inferred that Ag@M13-10 has the lowest R_s value and the highest R_{sh} value, which would have affected the higher values of the J_{SC} and the FF. Hence, the Ag@M13-10 based FDSSC demonstrated the highest PCE of 5.80% with J_{SC} of 12.16 mA cm^{-2}, V_{OC} of 0.66 V, and FF of 72.1%, whereas the bare electrolyte based FDSSC showed a PCE of 4.97% with J_{SC} of 10.71 mA cm^{-2}, V_{OC} of 0.65 V, and FF of 71.7%.

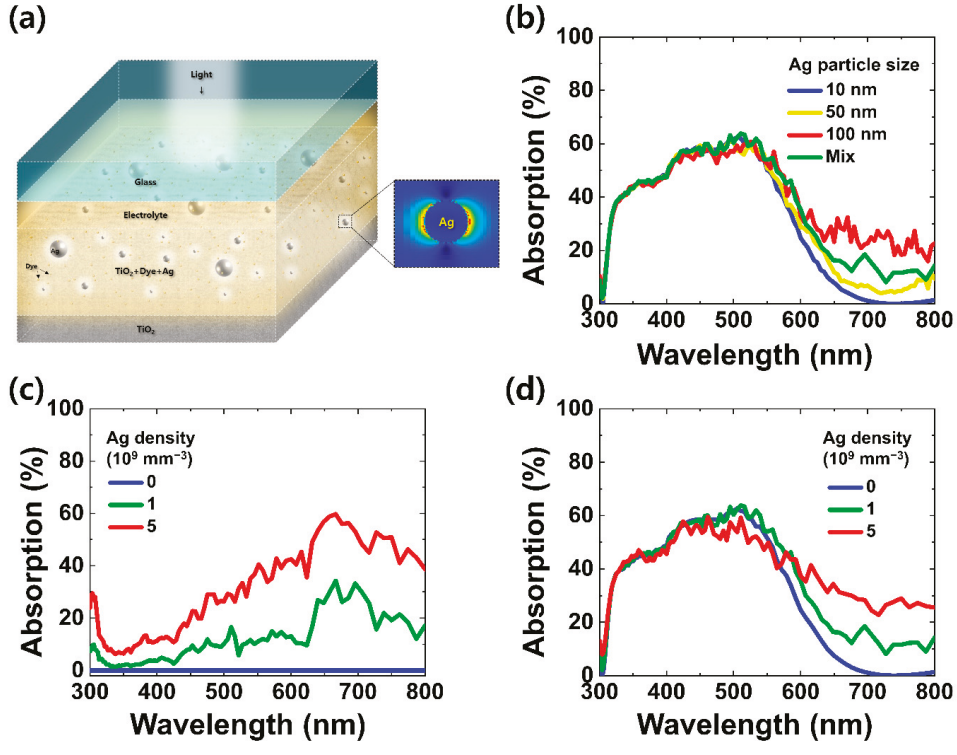

Figure 2. FDTD simulation of Ag-particle effects in the DSSC: (**a**) illustrated image of DSSC structure, (**b**) absorption spectra of active layer for the different Ag particle sizes, and absorption at (**c**) Ag particles and (**d**) at an active layer for the different Ag densities.

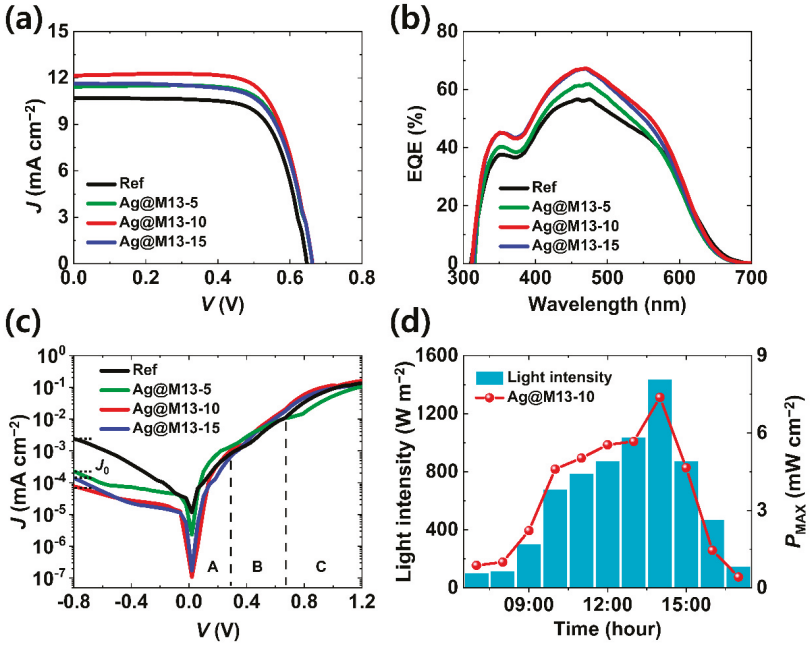

Figure 3. Photovoltaic properties of Ag@M13 enhanced FDSSCs: (**a**) comparison of *J*–*V* curves, (**b**) the IPCE spectra, (**c**) dark current profiles of FDSSCs as a function of Ag@M13, respectively, and (**d**) P_{max} values over time as an outdoor test.

Table 1. Photovoltaic properties of FDSSCs as a function of Ag@M13.

	V_{OC} (V)	J_{SC} (mA cm^{-2})	FF (%)	PCE (%)	R_s (Ω cm^2)	R_{sh} (Ω cm^2)
Ref	0.65	10.71	71.7	4.97	7.13	6.97×10^4
Ag@M13-5	0.66	11.44	71.8	5.47	5.36	8.90×10^4
Ag@M13-10	0.66	12.16	72.1	5.80	4.32	1.26×10^5
Ag@M13-15	0.66	11.61	69.9	5.39	5.29	9.43×10^4

The external quantum efficiency (EQE) spectra of the FDSSCs as a function of the concentration of Ag@M13 were investigated, and the results are shown in Figure 3b. In particular, the optimized Ag@M13-10 enhanced FDSSC showed a higher maximum EQE response than the other devices, which is consistent with the J_{SC} value in the *J*–*V* curve. The results shown *J*–*V* curves and EQDs above coherently demonstrate that there were more efficient charge extraction and less charge recombination in the Ag@M13 enhanced FDSSCs that the bare FDSSC. The improved performance by Ag@M13 enhanced electrolyte based FDSSCs benefited from the synergistic interaction between the plasmonic Ag NPs and M13 bacteriophages caused by the gap–plasmon effect amplified by the Ag NPs-embedded M13 bacteriophage nanostructures.

The dark *J*–*V* curves in Figure 3c show that the dark current curve slope varies as the voltage increases, which reflects different physical mechanisms. A, B, and C areas of the dark current have been reported to be associated with the shunt, recombination, and diffusion currents, respectively. In the A area, the dark current was mainly affected by the shunt current under a small applied bias voltage. It is shown that the R_{sh} value of Ag@M13-10 at the lowest slope in area A is very consistent with the R_{sh} value obtained from *J*–*V* curves in Figure 3a. As the bias voltage increases, the recombination current

gradually increases similar to the diffusion current in the dark *J–V* characteristics, as shown in area B. It can be seen that the slope of area B increases more gently than that of area C. Moreover, the current increase in the area C is caused by the diffusion-dominated current. Indeed, in an area C higher than the built-in potential of DSSCs (about 0.7 V), the effect on the recombination current is negligible, and the curve is dominated only by the diffusion current limited by the R_s of the device [36]. Therefore, the Ag@M13 enhanced FDSSCs indicates that the leakage current decreased and the charge extraction and transport efficiency improved due to the relatively increased R_{sh} and decreased recombination current. Furthermore, the dark current density (J_0) of the FDSSCs, which fabricated Ag@M13 as a function of concentration, was smaller than those of the bare electrolyte. This can be inferred as a phenomenon indicating that the dark current density was decreased due to the rapid transport of photoexcited electrons by the presence of Ag@M13 [37].

Power generation of wearable fiber electronic solar cells that depending on the daylight intensity should be considered for further development. Figure 3d shows the maximum power (P_{MAX}) values corresponding to the time-dependent change of sunlight in an outdoor environment to evaluate the characteristics of the wearable applications. The P_{MAX} values of the Ag@M13 enhanced FDSSCs were verified by the following equation: $P_{MAX} = I \times V \times FF$. The sunlight intensity increased from the initial 400 W m^{-2} at 9:00 a.m. to 1400 W m^{-2} at 2:00 p.m., when the sun's altitude reached its highest point. The light intensity gradually decreased to under 200 W m^{-2} at 5:00 p.m. As expected, the time-dependent change in daylight intensity and the corresponding P_{MAX} values of the solar cell devices showed the equivalent tendency.

EIS was performed under dark conditions at a bias voltage of 0.7 V in the frequency range of 0.1 Hz–1 MHz to accurately analyze the interfacial dynamics for the charge transfer behavior in Ag@M13 enhanced FDSSCs, as shown in the Nyquist plots in Figure 4a. The Nyquist plots simulated by the equivalent circuit diagram, as shown in Figure S2. The equivalent circuit, R_s + ($CPE_{ct1}//R_{ct1}$) + ($CPE_{ct2}//R_{ct2}$), consists of a series resistance (R_s) and two charge-transfer resistances. The R_{ct1} and R_{ct2}, which mean charge transfer resistance, are represented by the first smaller half-circle in the high-frequency region and the second larger half circle in the low-frequency region, respectively. These values are interpreted as interfacial resistance between CE/electrolyte and interfacial resistance between dye-sensitized PA/electrolyte, respectively. Moreover, the CPE_{ct1} and CPE_{ct2} represent the constant-phase elements for interfaces at CE/electrolyte and dye-sensitized PA/electrolyte, respectively [38]. The fitting values of R_s, which is related to the transfer resistance of the photoanode, were 7.49, 6.85, 4.57, and 5.16 Ω for the Ref, Ag@M13-5, Ag@M13-10, and Ag@M13-15 enhanced FDSSCs, respectively, as shown in the inset of Figure 4a and Table 2. This tendency was very consistent with the R_s values obtained from the aforementioned *J-V* characteristic curves, and it can be seen that the R_s value is the lowest in Ag@M13-10 enhanced FDSSC. The R_{ct1} values showed very slight difference from 24.30 Ω at the Ag@M13-10 enhanced FDSSC, the lowest value, to 26.99 Ω at the Ref-FDSSC, the highest value. This tendency is also shown in CPE_{ct1}. These results are interpreted that the Ag@M13 bacteriophages added to the electrolyte were not significantly correlated with CE. On the other hand, the R_{ct2} values representing the interfacial resistance between dye-sensitized PA/electrolyte were 129.0, 117.2, 53.1, and 75.8 Ω for the Ref, Ag@M13-5, Ag@M13-10, and Ag@M13-15 enhanced FDSSCs, respectively, showing clear difference. The lowest R_s, R_{ct1}, and R_{ct2} values observed for the Ag@M13-10 enhanced FDSSCs are most probably the consequence of the faster charge-transport process arising from the high probability that Ag@M13 penetrates into the dye-sensitized PA with the mesoporous structure, as mentioned above. Based on the improved charge transfer characteristics at the dye-sensitized PA/electrolyte interface, it can be confirmed that all the key parameters of the Ag@M13-10 enhanced FDSSCs could be enhanced, which resulted in high J_{SC} and PCE.

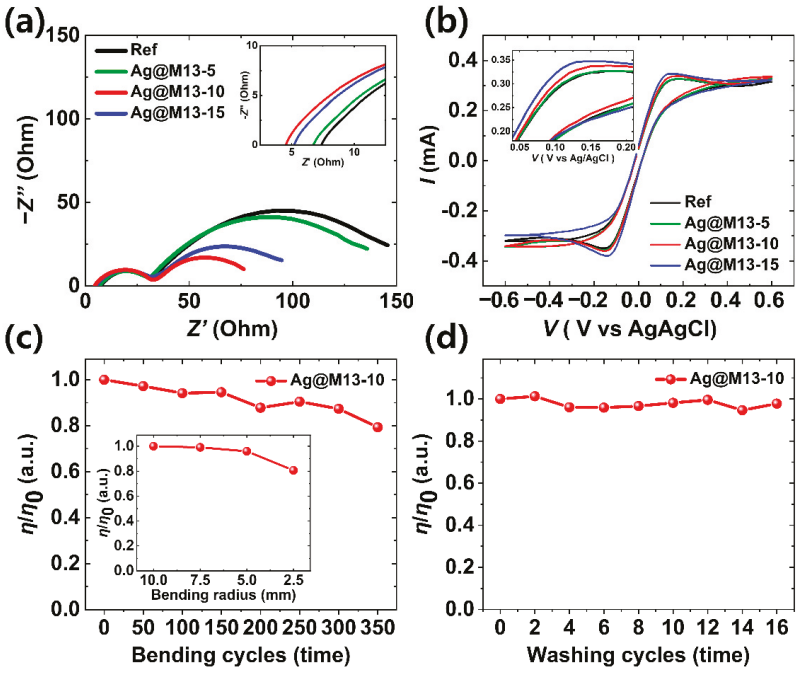

Figure 4. Electrochemical properties of the Ag@M13 enhanced FDSSCs: (**a**) Nyquist plots and onset point of Nyquist plots in the high-frequency region (inset), (**b**) CV characteristics. The three-electrode system, measured at a scan rate of 200 mV s^{-1}, contains an Ag/AgCl as a reference electrode, Pt wires as working and counter electrodes, respectively. Normalized η/η_0 of Ag@M13-10 enhanced FDSSCs as a function of (**c**) bending cycles and (**d**) washing cycles. The inset in Figure 4c is the normalized η/η_0 under extreme bending conditions, such as radii 2.5, 5.0, and 7.5 mm.

Table 2. EIS parameters of SS-FDSSCs as a function of Ag@M13.

	R_s (Ω)	R_{ct1} (Ω)	CPE_{ct1} (F)	R_{ct2} (Ω)	CPE_{ct2} (F)
Ref	7.49	26.99	4.68×10^{-5}	129.2	2.51×10^{-3}
Ag@M13-5	6.85	26.24	4.66×10^{-5}	117.2	2.75×10^{-3}
Ag@M13-10	4.57	24.30	3.01×10^{-5}	53.1	8.37×10^{-3}
Ag@M13-15	5.16	25.01	4.27×10^{-5}	75.8	5.74×10^{-3}

Catalytic activities and reaction kinetics of the Ag@M13 enhanced electrolyte were investigated by electrochemical characterization using cyclic voltammetry (CV) measurement, as shown in Figure 4b. The CV measurement of the enhanced electrolyte as a function of Ag@M13 was based on a three-electrode system consisting of two Pt wire electrodes as the working and counter electrode, respectively, and an Ag/AgCl as the reference electrode. The CV measurement was performed under the same conditions of applying the Pt wire as a working electrode and a counter electrode, and the analysis was focused on the catalytic properties of Ag@M13 injected into the electrolyte. The electrolyte used for CV was proceeded under the same condition as the electrolyte in the solar cell, and was used by adding 5, 10, and 15 μL of Ag@M13 to HPE. A pair of oxidation and reduction peaks

can be identified, which corresponds to cathodic and anodic peaks indicated by reduction (Equation (1)) and oxidation (Equation (2)) reactions of iodide/triiodide, respectively [39]:

$$I_3^- + 2e^- \leftrightarrow 3I^- \quad (1)$$

$$3I^- \leftrightarrow 2e^- + I_3^- \quad (2)$$

Although the distribution and morphological shape of the peaks are not significantly different under all conditions, the intensity of the peak increased as the concentration of Ag@M13 increased, as shown in the inset of Figure 4b. This suggests that the interaction between Ag@M13 added to the electrolyte and CE is not large, but it can be considered that the injection of Ag@M13 into the electrolyte contributed to the catalytic activity to some extent. Thus, Ag@M13 added to the electrolyte exhibits higher current density on both the oxidation and reduction characteristics, indicating efficient charge transfer due to improved catalytic activities.

Weaving ability, durability, and water resistance are very important parameters in wearable device applications. The Ag@M13-10 enhanced FDSSCs exhibited excellent mechanical durability, as shown in Figure 4c. It can be seen that the normalized η/η_0 of the Ag@M13-10 enhanced FDSSCs with a radius of about 10 mm showed a slight degradation in change to almost 80% even after 350 bending cycles. Even under extreme bending conditions such as radii 2.5, 5.0, and 7.5 mm, the normalized η/η_0 was maintained without significant reduction, as shown in the inset of Figures 4c and S3. Furthermore, the Ag@M13-10 enhanced FDSSCs exhibited excellent water resistance, as shown in Figure 4d. Repeated washing tests of Ag@M13-10 enhanced FDSSC were performed with an automatic cleaner, as shown in Figure S4. It was confirmed that the normalized η/η_0 of the Ag@M13-10 enhanced FDSSC hardly decreased even after repeating the 16 iterations of the washing tests. These results indicate that Ag@M13 enhanced FDSSCs have excellent characteristics as wearable electronic devices. On the other hand, the Ag@M13 enhanced FDSSCs were connected in series and parallel to drive a liquid-crystal (LC) device for smart windows such as indoor lighting, as shown in Figure S5. The voltage and current density generated by the series and parallel connections of the Ag@M13 enhanced FDSSCs were about 2.3 V and 1.8 μA under indoor lighting of 172.8 W m^{-2}, respectively, generating sufficient power for the operation of the LC device.

4. Conclusions

In conclusion, the Ag metallic NPs embedded M13 bacteriophages with the improved LSPR properties were supplemented to the electrolyte of the FDSSCs. It was confirmed that the Ag@M13 enhanced electrolyte showed high absorbance in a long wavelength region of 500 nm or more, and that the plasmonic Ag NPs were uniformly oriented and aligned in nanoscale M13 bacteriophages. The FDSSCs were fabricated using an Ag@M13 enhanced electrolyte, which was demonstrated to improve the PCE by plasmonic enhancement effect. The optimized Ag@M13 enhanced FDSSC boasts effective electron extraction, unidirectional electron transportation, and suppressed charge recombination processes, resulting in a PCE of up to 5.80%, which was improved by 16.7% compared to that of the reference device with 4.97%. In addition, the Ag@M13 enhanced FDSSCs maintained the PCE of >80% over 350 cycles of bending tests and >90% over 16 repetitions of washing tests.

Supplementary Materials: Supplementary materials are available in the online version of the article at https://www.mdpi.com/article/10.3390/nano11123421/s1. Figure S1, Schematic diagram of the fabrication process of the FDSSCs; Figure S2, The equivalent circuit for EIS; Figures S3 and S4, Further details of photographs on bending and washing tests; Figure S5, Application driving photograph using FDSSCs.

Author Contributions: Conceptualization of idea, synthesis, S.-J.K. and J.H.K.; overall manuscript writing and analysis of results, J.H.K. and J.W.C.; FDTD simulation, Y.-K.K., M.S. (Myunghun Shin);

TEM analysis, J.-W.O.; review and editing, H.W.L. and J.-W.O.; supervision, M.S. (Myungkwan Song). All authors have read and agreed to the published version of the manuscript.

Funding: This research was supported by the Fundamental Research Program (PNK 7350) of the Korea Institute of Materials Science (KIMS) and by a National Research Foundation (NRF) grant funded by the Korean government (MEST) (2019M3D1A1067389).

Data Availability Statement: Not applicable.

Conflicts of Interest: The authors declare no conflict of interests.

References

1. Sun, H.; Li, H.; You, X.; Yang, Z.; Deng, J.; Qiu, L.; Peng, H. Quasi-solid-state, coaxial, fiber-shaped dye-sensitized solar cells. *J. Mater. Chem. A* **2014**, *2*, 345–349. [CrossRef]
2. Song, W.; Wang, H.; Liu, G.; Peng, M.; Zou, D. Improving the photovoltaic performance and flexibility of fiber-shaped dye-sensitized solar cells with atomic layer deposition. *Nano Energy* **2016**, *19*, 1–7. [CrossRef]
3. Fu, X.; Sun, H.; Xie, S.; Zhang, J.; Pan, Z.; Liao, M.; Xu, L.; Li, Z.; Wang, B.; Sun, X.; et al. A fiber-shaped solar cell showing a record power conversion efficiency of 10%. *J. Mater. Chem. A* **2018**, *6*, 45–51. [CrossRef]
4. Liu, G.; Wang, M.; Wang, H.; Ardhi, R.E.A.; Yu, H.; Zou, D.; Lee, J.K. Hierarchically structured photoanode with enhanced charge collection and light harvesting abilities for fiber-shaped dye-sensitized solar cells. *Nano Energy* **2018**, *49*, 95–102. [CrossRef]
5. Zhang, J.; Wang, Z.; Li, X.; Yang, J.; Song, C.; Li, Y.; Cheng, J.; Guan, Q.; Wang, B. Flexible Platinum-Free Fiber-Shaped Dye Sensitized Solar Cell with 10.28% Efficiency. *ACS Appl. Energy Mater.* **2019**, *2*, 2870–2877. [CrossRef]
6. Utomo, D.S.; Kim, J.H.; Lee, D.; Park, J.; Kang, Y.-C.; Kim, Y.H.; Choi, J.W.; Song, M. Fractional structured molybdenum oxide catalyst as counter electrodes of all-solid-state fiber dye-sensitized solar cells. *J. Colloid Interface Sci.* **2021**, *584*, 520–527. [CrossRef] [PubMed]
7. Kim, J.H.; Utomo, D.S.; Lee, D.; Choi, J.W.; Song, M. Catalytic fower-shaped α-MoO_3 lamellar structure for solid-state fiber-dye-sensitized solar cells. *J. Power Sources* **2021**, *512*, 230496. [CrossRef]
8. Joshi, P.; Zhang, L.; Davoux, D.; Zhu, Z.; Galipeau, D.; Fong, H.; Qiao, Q. Composite of TiO_2 nanofibers and nanoparticles for dye-sensitized solar cells with significantly improved efficiency. *Energy Environ. Sci.* **2010**, *3*, 1507–1510. [CrossRef]
9. Elbohy, H.; Kim, M.R.; Dubey, A.; Reza, K.M.; Ma, D.; Zai, J.; Qian, X.; Qiao, Q. Incorporation of plasmonic Au nanostars into photoanodes for high efficiency dye-sensitized solar cells. *J. Mater. Chem. A* **2016**, *4*, 545–551. [CrossRef]
10. Sharma, K.; Sharma, V.; Sharma, S.S. Dye-Sensitized Solar Cells: Fundamentals and Current Status. *Nanoscale Res. Lett.* **2018**, *13*, 381. [CrossRef]
11. Gao, F.; Wang, W.; Shi, D.; Zhang, J.; Wang, M.; Jing, X.; Humphry-Baker, R.; Wang, P.; Zakeeruddin, S.M.; Grätzel, M. Enhance the Optical Absorptivity of Nanocrystalline TiO_2 Film with High Molar Extinction Coefficient Ruthenium Sensitizers for High Performance Dye-Sensitized Solar Cells. *J. Am. Chem. Soc.* **2008**, *130*, 10720–10728. [CrossRef] [PubMed]
12. Atwater, H.A.; Polman, A. Plasmonics for improved photovoltaic devices. *Nat. Mater.* **2010**, *9*, 205–213. [CrossRef]
13. Barnes, W.L.; Dereux, A.; Ebbesen, T.W. Surface plasmon subwavelength optics. *Nature* **2003**, *424*, 824–830. [CrossRef]
14. Schuller, J.A.; Barnard, E.S.; Cai, W.; Jun, Y.C.; White, J.S.; Brongersma, M.L. Plasmonics for extreme light concentration and manipulation. *Nat. Mater.* **2010**, *9*, 193–204. [CrossRef] [PubMed]
15. Green, M.A.; Pillai, S. Harnessing plasmonics for solar cells. *Nat. Photonics.* **2012**, *6*, 130–132. [CrossRef]
16. Butler, J.C.; Angelini, T.; Tang, J.X.; Wong, G.C.L. Ion Multivalence and Like-Charge Polyelectrolyte Attraction. *Phys. Rev. Lett.* **2003**, *91*, 028301. [CrossRef]
17. Petrenko, V.A.; Smith, G.P. Phages from landscape libraries as substitute antibodies. *Protein Eng.* **2000**, *13*, 589–592. [CrossRef]
18. Petrenko, V.A.; Vodyanoy, V.J. Phage display for detection of biological threat agents. *J. Microbiol. Methods.* **2003**, *53*, 253–262. [CrossRef]
19. Royston, E.; Lee, S.-Y.; Culver, J.N.; Harris, M.T. Characterization of silica-coated tobacco mosaic virus. *J. Colloid Interface Sci.* **2006**, *298*, 706–712. [CrossRef]
20. Bruckman, M.A.; Kaur, G.; Lee, L.A.; Xie, F.; Sepulveda, J.; Breitenkamp, R.; Zhang, X.; Joralemon, M.; Russell, T.P.; Emrick, T.; et al. Surface Modificaion of Tobacco Mosaic Virus with "Click" Chemistry. *ChemBioChem.* **2008**, *9*, 519–523. [CrossRef]
21. Scibilia, S.; Lentini, G.; Fazio, E.; Franco, D.; Neri, F.; Mezzasalma, A.M.; Guglielmino, S.P.P. Self-assembly of silver nanoparticles and bacteriophage. *Sens. Bio-Sens. Res.* **2016**, *7*, 146–152. [CrossRef]
22. Lentini, G.; Fazio, E.; Calabrese, F.; De Plano, L.M.; Puliafico, M.; Franco, D.; Nicolò, M.S.; Carnazza, S.; Trusso, S.; Allegra, A.; et al. Phage-AgNPs complex as SERS probe for U937 cell identification. *Biosens. Bioelectron.* **2015**, *74*, 398–405. [CrossRef] [PubMed]
23. Brown, M.D.; Parkinson, P.; Torres, T.; Miura, H.; Herz, L.M.; Snaith, H.J. Surface Energy Relay Between Consensitized Molecules in Solid-State Dye-Sensitized Solar Cells. *J. Phys. Chem. C* **2011**, *115*, 23204–23208. [CrossRef]
24. Choi, H.; Chen, W.T.; Kamat, P.V. Know Thy Nano Neighbor. Plasmonic versus Electron Charging Effects of Metal Nanoparticles in Dye-Sensitized Solar Cells. *ACS Nano* **2012**, *6*, 4418–4427. [CrossRef]
25. Isah, K.U.; Jolayemi, B.J.; Ahmadu, U.; Kimpa, M.I.; Alu, N. Plasmonic effect of silver nanoparticles intercalated into mesoporous betalain-sensitized-TiO^2 film electrodes on photovoltaic performance of dye-sensitized solar cells. *Mater. Renew. Sustain. Energy.* **2016**, *5*, 10. [CrossRef]

26. Franco, D.; De Plano, L.M.; Rizzo, M.G.; Scibilia, S.; Lentini, G.; Fazio, E.; Neri, F.; Guglielmino, S.P.P.; Mezzasalma, A.M. Bio-hybrid gold nanoparticles as SERS probe for rapid bacteria cell identification. *Spectroc. Acta Pt. A-Molec. Biomolec. Spectr.* **2020**, *224*, 117394. [CrossRef] [PubMed]
27. Kim, H.; Jo, J.; Lee, G.; Shin, M.; Lee, J.-C. Optical Modeling of Dye-Sensitized Solar Cells for Color Analysis. *J. Nanosic. Nanotechnol.* **2017**, *17*, 8425–8431. [CrossRef]
28. Kim, J.H.; Koo, S.-J.; Cho, H.; Choi, J.W.; Ryu, S.Y.; Kang, J.-W.; Jin, S.-H.; Ahn, C.; Song, M. 6.16% Efficiency of Solid-State Fiber Dye-Sensitized Solar Cells Based on LiTFSI Electrolytes with Novel TEMPOL Derivatives. *ACS Sustain. Chem. Eng.* **2020**, *8*, 15065–15071. [CrossRef]
29. Kim, J.H.; Hong, S.K.; Yoo, S.-J.; Woo, C.Y.; Choi, J.W.; Lee, D.; Kang, J.-W.; Lee, H.W.; Song, M. Pt-free, cost-effective and efficient counter electrode with carbon nanotube yarn for solid-state fiber dye-sensitized solar cells. *Dyes Pigment.* **2021**, *185*, 108855. [CrossRef]
30. Lee, H.B.; Kim, W.-G.; Lee, M.; Lee, J.-M.; He, S.; Kumar, N.; Devaraj, V.; Choi, E.J.; Jeon, I.; Song, M.; et al. Gap Plasmon of Virus-Templated Biohybrid Nanostructures Uplifting the Performance of Organic Optoelectronic Devices. *Adv. Optical Mater.* **2020**, *8*, 1902080. [CrossRef]
31. Zhang, Y.; Zhen, Y.-R.; Neumann, O.; Day, J.K.; Nordlander, P.; Halas, N.J. Coherent anti-Stokes Raman scattering with single-molecule sensitivity using a plasmonic Fano resonance. *Nat. Commun.* **2014**, *5*, 4424. [CrossRef]
32. Yi, C.; Dongare, P.D.; Su, M.-N.; Wang, W.; Chakraborty, D.; Wen, F.; Chang, W.-S.; Sader, J.E.; Nordlander, P.; Halas, N.J.; et al. Vibrational coupling in plasmonic molecules. *Proc. Natl. Acad. Sci. USA* **2017**, *114*, 11621–11626. [CrossRef]
33. Li, G.; Chang, W.-H.; Yang, Y. Low-bandgap conjugated polymers enabling solution-processable tandem solar cells. *Nat. Rev. Mater.* **2017**, *2*, 17043. [CrossRef]
34. Jang, Y.H.; Jang, Y.J.; Kochuveedu, S.T.; Byun, M.; Lin, Z.; Kim, D.H. Plasmonic dye-sensitized solar cells incorporated with Au-TiO_2 nanostructures with tailored configurations. *Nanoscale* **2014**, *6*, 1823–1832. [CrossRef]
35. Topič, M.; Čampa, A.; Filipič, M.; Berginc, M.; Krašovec, U.O.; Smole, F. Optical and electrical modelling and characterization of dye-sensitized solar cells. *Curr. Appl. Phys.* **2010**, *10*, S425–S430.
36. Liao, P.; Zhao, X.; Li, G.; Shen, Y.; Wang, M. A New Method for Fitting Current-Voltage Curves of Planar Heterojunction Perovskite Solar Cells. *Nano-Micro Lett.* **2018**, *10*, 5. [CrossRef] [PubMed]
37. Peng, H.; Sun, X.; Weng, W.; Fang, X. Energy Harvesting Based on Polymer. In *Polymer Materials for Energy and Electronic Applications*, 1st ed.; Academic Press: Cambridge, MA, USA, 2017; pp. 151–196.
38. Kim, J.H.; Yoo, S.-J.; Lee, D.; Choi, J.W.; Han, S.-C.; Ryu, T.I.; Lee, H.W.; Shin, M.; Song, M. Highly efficient and stable solid-state fiber dye-sensitized solar cells with Ag-decorated SiO_2 nanoparticles. *Nano Res.* **2021**, *14*, 2728–2734. [CrossRef]
39. Shukla, S.; Loc, N.H.; Boix, P.P.; Koh, T.M.; Prabhakar, R.R.; Mulmudi, H.K.; Zhang, J.; Chen, S.; Ng, C.F.; Huan, C.H.A.; et al. Iron Pyrite Thin Film Counter Electrodes for Dye-Sensitized Solar Cells: High Efficiency for Iodine and Cobalt Redox Electrolyte Cells. *ACS Nano* **2014**, *8*, 10597–10605. [CrossRef]

nanomaterials

MDPI

Article

Biomass-Derived Porous Carbon from Agar as an Anode Material for Lithium-Ion Batteries

Nurbolat Issatayev [1,2], Gulnur Kalimuldina [3,*], Arailym Nurpeissova [1] and Zhumabay Bakenov [1,2,*]

[1] National Laboratory Astana, Nazarbayev University, Kabanbay Batyr Ave. 53, Nur-Sultan 010000, Kazakhstan; nurbolat.issatayev@nu.edu.kz (N.I.); arailym.nurpeissova@nu.edu.kz (A.N.)
[2] Department of Chemical and Materials Engineering, School of Engineering and Digital Sciences, Nazarbayev University, Kabanbay Batyr Ave. 53, Nur-Sultan 010000, Kazakhstan
[3] Department of Mechanical and Aerospace Engineering, School of Engineering and Digital Sciences, Nazarbayev University, Kabanbay Batyr Ave. 53, Nur-Sultan 010000, Kazakhstan
* Correspondence: authors: gkalimuldina@nu.edu.kz (G.K.); zbakenov@nu.edu.kz (Z.B.); Tel.: +7-717-269-4578 (G.K.); +7-717-270-6530 (Z.B.)

Abstract: New porous activated carbons with a high surface area as an anode material for lithium-ion batteries (LIBs) were synthesized by a one-step, sustainable, and environmentally friendly method. Four chemical activators—H_2SO_4, H_3PO_4, KOH, and $ZnCl_2$—have been investigated as facilitators of the formation of the porous structure of activated carbon (AC) from an agar precursor. The study of the materials by Brunauer–Emmett–Teller (BET) and scanning electron microscopy (SEM) methods revealed its highly porous meso- and macro-structure. Among the used chemical activators, the AC prepared with the addition of KOH demonstrated the best electrochemical performance upon its reaction with lithium metal. The initial discharge capacity reached 931 mAh g^{-1} and a reversible capacity of 320 mAh g^{-1} was maintained over 100 cycles at 0.1 C. High rate cycling tests up to 10 C demonstrated stable cycling performance of the AC from agar.

Keywords: activated carbon; agar; anode; lithium-ion battery; chemical activators

Citation: Issatayev, N.; Kalimuldina, G.; Nurpeissova, A.; Bakenov, Z. Biomass-Derived Porous Carbon from Agar as an Anode Material for Lithium-Ion Batteries. *Nanomaterials* **2022**, *12*, 22. https://doi.org/10.3390/nano12010022

Academic Editors: Marc Cretin, Sophie Tingry and Zhenghua Tang

Received: 9 November 2021
Accepted: 17 December 2021
Published: 22 December 2021

1. Introduction

Lithium-ion batteries (LIBs) are conquering the worldwide market due to their high specific capacity, absence of memory effect, long service life, and stable operation [1–5]. LIBs are extensively used in portable electronics applications and are currently expanding into the field of plug-in hybrid and electric vehicles [6]. Thus, the requirements for LIBs are increasing not only in terms of specific energy of its components (cathode, anode) but also in their eco-friendliness owing to growing awareness of environmental issues. Therefore, the development of electrode materials that correspond to the stated requirements is in high demand.

Nowadays, in commercially available LIBs, graphite is mainly used as an anode material. Despite this fact, some critical shortcomings are associated with graphite—such as a low specific capacity, poor rate capability, and slow charge–discharge processes—limiting their applicability in the next generation technologies in electronics and electric transport. Furthermore, it is worth mentioning the high cost and negative environmental impact due to its synthesis from fossil carbon sources such as coal and petroleum coke [7]. Therefore, it is highly desirable to explore alternative negative electrode materials for Li-ions such as tin [8,9], transition metal oxides [10–13], silicon [14,15], and others. Although the alternative anodes can provide higher specific capacity, they suffer from substantial volume changes during insertion/extraction of Li-ions causing materials disintegration leading to huge irreversible capacity loss and poor cyclability. The challenges faced by non-carbon anode materials hinder their broad application in the next-generation LIBs. Hence, considerable research efforts continue on the development of carbonaceous materials for high-capacity anodes, especially for the porous carbon materials with the high surface area

were extensively researched due to their enhanced electrochemical performance in reaction with Li-ions [16]. This improvement has been associated with porous structure that forms shorter distances for Li-ions and electrons to travel, facilitating enhanced charge transfer, diffusion rate, and better kinetics [17].

Various types of biomass have been intensively researched as a promising renewable source to prepare porous and functional carbon materials. Their low cost, tunable physical/chemical properties, recyclability, abundant availability, and harmony with the environment are especially of high interest [18]. Two mechanisms of Li-ion storage in carbonaceous materials derived from biomass can be defined as the invertible lithiation/delithiation into/out of the expanded graphitic layers and the surface-induced capacitive behavior summoned by pores, regions of structural defects, and functional groups [19]. Pursuant to earlier research, biomass activated carbon nanostructures can be produced and generated from a variety of natural resources such as rice husk [20], wheat stalk [21], cellulose [22], green tea wastes [23], natural cotton [24], puffed corn [25], sucrose [26].

Physical activation [27], chemical activation [28], catalytic activation [29], and microwave activation [30] are commonly used methods for producing biomass-derived AC materials. Among them, chemical activation is extensively utilized to produce porous carbon due to its advantages over other activation methods—such as high yield, less surface damage, low activation temperature, and short reaction time. During the activation process, an activator is usually added to form a new porous structure to increase the specific surface area of the material. The most common chemical activators are Bronsted (H_2SO_4, H_3PO_4) [31], Lewis acids ($CuCl_2$ and $ZnCl_2$) [32], alkali metal hydroxides, and carbonates (NaOH, KOH, K_2CO_3, Na_2CO_3) [33–35].

In this work, we propose a facile method of preparation of AC material with a large surface area and a developed porous structure from agar. Agar biopolymer was used as a carbon precursor due to its low cost, high carbon content, and the lack of any traces of heavy metals. The pore formation and expanding effect of chemical activators as H_2SO_4, H_3PO_4, KOH, and $ZnCl_2$ on the AC morphology were compared and studied. The materials were examined as an anode for LIBs and demonstrated high capacity and excellent cycling and rate characteristics. To the best of our knowledge, this is the first application of agar activated carbon as anode for LIBs. Previous studies of activated carbon with agar precursor have been investigated for supercapacitors [36,37]. In addition, the activation of agar at the molecular level was performed according to the method described by Chen et al. [36], which requires a one-step calcination of the agar without high-temperature carbonation.

2. Materials and Methods

Agar, KOH, H_3PO_4, H_2SO_4, $ZnCl_2$, and HCl were purchased from Sigma-Aldrich (St. Louis, MO, Germany). All the reagents were analytical grade and used as received without further purifications.

2.1. Fabrication of the Activated Carbon

For preparing the porous activated carbon material, 0.25 g of each KOH, H_3PO_4, H_2SO_4, and $ZnCl_2$ was mixed with agar separately in 10 mL water (DI) at 95 °C. The mixture was stirred until homogeneous hydrogels were obtained. After cooling to room temperature, the mixture was further freeze-dried for 24 h. The sample was pyrolyzed at 800 °C (the heat treatment steps are shown schematically in Scheme 1) in a conventional furnace for 2 h in argon. Finally, after rinsing with 10% HCl and an ample amount of water, the activated carbon was dried at 70 °C in a vacuum oven for 24 h. The preparation route is illustrated in Figure 1. The final agar-derived activated by KOH, H_3PO_4, H_2SO_4, and $ZnCl_2$ carbons were denoted as KAAC, PAAC, SAAC, and ZAAC, respectively.

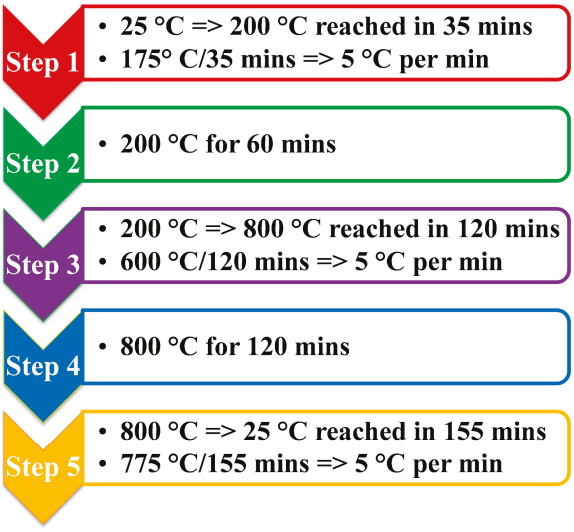

Scheme 1. Optimal temperature and time for preparation of AC from agar.

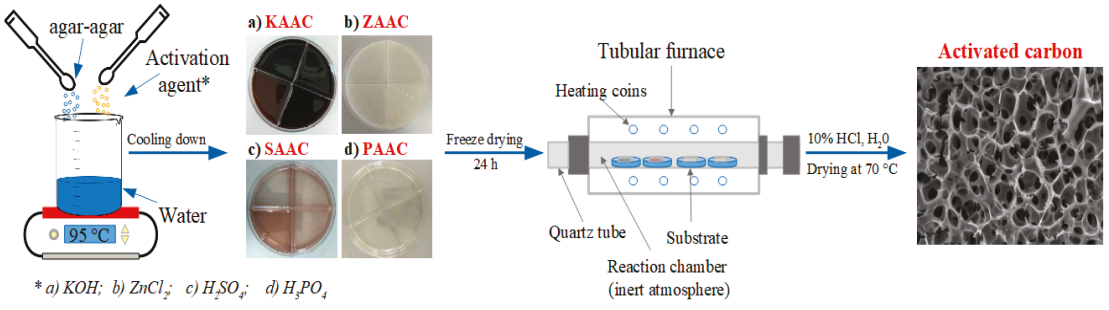

Figure 1. Preparation method of AC with four different activating agents: (**a**) KOH; (**b**) $ZnCl_2$; (**c**) H_2SO_4; (**d**) H_3PO_4.

2.2. Characterizations

The resulting AC powders were analyzed by Raman spectroscopy (Horiba LabRam Evolution) with a 633 nm excitation laser range from 200 to 2000 cm^{-1}. The functional groups of the ACs were examined using Nicolet iS10 Fourier Transform Infrared (FTIR) Spectrometer in the range of 400–4000 cm^{-1} and X-ray photoelectron spectrometer (XPS)-NEXSA (Thermo Scientific, Waltham, MA, USA). The morphology of the disordered carbons was observed by scanning electron microscope Crossbeam 540 (SEM, Zeiss, Germany) and transmission electron microscope JEOL JEM—1400 Plus (TEM, JEOL, Peabody, MA, USA). Thermogravimetric analysis (TGA) was carried out by Simultaneous Thermal Analyzer (STA, PerkinElmer, Waltham, MA, USA) 6000 at a heating rate of 10 °C min^{-1} from 30 to 800 °C in nitrogen (N_2). The surface area and pore size distribution of the powders were studied by N_2 adsorption on Autosorb iQ and ASiQwin gas sorption system (Quantachrome instruments; Boynton Beach, FL, USA).

2.3. Cell Preparation

The electrochemical activity of the carbon samples was examined using CR2032-type coin cells. The electrodes were prepared by mixing the obtained ACs, carbon black (Super-P), and polyvinylidene fluoride (PVDF) in the ratio of 8:1:1 in N-methyl-2-pyrrolidone

(NMP). The resulting mixture was then applied onto copper foil using the Doctor Blade technique and then dried overnight at 60 °C in a vacuum oven. The coated copper foil was cut into the disks with a diameter of 14 mm. The mass loadings of the active materials were approximately 1–1.5 mg cm^{-2}. The cells were assembled in an argon-filled glove box (MBRAUN, LABmaster Pro Glovebox, Germany, containing <0.1 ppm O_2 and <0.1 ppm H_2O) using lithium metal foil as the counter and reference electrode. A 1 M $LiPF_6$ in ethylene carbonate (EC) and dimethyl carbonate (DMC) (1:1, v/v) was used as an electrolyte solution and a polypropylene membrane (Celgard® 2400) as a separator. Each cell contains~150 µL of electrolyte. Galvanostatic cycling of the electrodes was investigated by a multichannel battery testing system (Arbin Inc. and Neware Battery tester, Neware Co., Shenzhen, China) between the cut-off potentials of 0.01 and 3.0 V vs. Li^+/Li at a current density of 0.1 and 1.0 C for 100 cycles. Cyclic voltammetry (CV) measurements were performed using a VMP3 potentiostat/galvanostat (Bio-Logic Science Instrument Co.) in a potential range of 0.01–3.0 V at a scan rate of 0.1 mV s^{-1}.

3. Results and Discussion

The TGA curves (Figure 2a) for all samples, including pure agar, consist of two distinct zones. At the first step, the weight loss of around 5–10% was registered at the temperatures around 50–130 °C which can be associated with water loss. Then there is an abrupt transition at about 210 °C, indicating that the decomposition process involves rapid weight loss. At the temperature of 800 °C, the weight loss reaches approximately 85.5%, 87.2%, 83.3%, 73.4%, and 60.2% for pure agar, SAAC, ZAAC, PAAC, and KAAC, respectively. Comparison of the obtained activated carbons illustrates that KOH activation results in a lower peak temperature, shorter pyrolysis duration, and thermal decomposition at a higher instantaneous rate. These results also imply that the activation of KOH and H_3PO_4 is faster and easier than the activation of H_2SO_4 and $ZnCl_2$.

The structural characteristics of obtained AC were investigated by Raman spectroscopy, as illustrated in Figure 2b. The patterns of all four samples showed two distinct peaks for the G band at about 1580 cm^{-1} assigned to carbon atoms with the sp^2 electronic configuration in the structure of the graphite sheet, and the D band at about 1340 cm^{-1}, which corresponds to the presence of a disordered and defective structure of carbon materials. The degree of disorder in carbon can be evaluated from the ratio of the integrated intensities of the D-band to the G-band (I_D/I_G), and higher values represent a greater number of imperfection in carbon atoms. The I_D/I_G ratios of KAAC, PAAC, SAAC, and ZAAC are 1.02, 0.99, 0.98, and 0.97, respectively. It can be seen that the ratio of $I_D/I_G > 1$ for the KOH sample, which emphasizes the largest number of defects and boundaries in the resulting sp^2-hybridized graphene sheet. A decrease in the ratio for the other three samples (<1) indicates a decrease in the number of voids or defects and, therefore, an upper degree of graphitization [38]. However, all four samples illustrate the high-intensity ratio, which indicates a high amorphous degree, edges, and other defects.

Furthermore, the structural characteristics of the materials were studied by FT-IR spectroscopy. As shown in Figure 2c, all obtained ACs retain some functional group of agar. From the FT-IR spectra, one can observe vibrational peaks at approximately 3650 cm^{-1} which illustrates the -OH (hydroxyl) group and at around 2905 cm^{-1} attributed to the $-CH_3O-$ (methoxyl) group. In addition, the presence of the peaks at about 933 cm^{-1} and 1075 cm^{-1} are related to the 3,6-anhydrogalactose bridges. However, some peaks of the obtained ACs are less intense. This can be explained by the cleavage of some functional groups during activation [39]. For example, in the process of activation with KOH, it was suggested that the cyclic ether bond of six-membered rings and hydroxyl groups with hydrogen bonds in agar undergoes a dehydration reaction with potassium hydroxide, which is clearly seen from a decrease in the intensity of broad absorption, the band at 3650 cm^{-1} and the peak at 1075 cm^{-1} [40,41]. Analysis of the XPS spectra on the ACs C1s confirmed the partial graphitization and the presence of oxygen functional groups on

the surface and is in good agreement with the results of Raman and FT-IR spectroscopy (Figure S1).

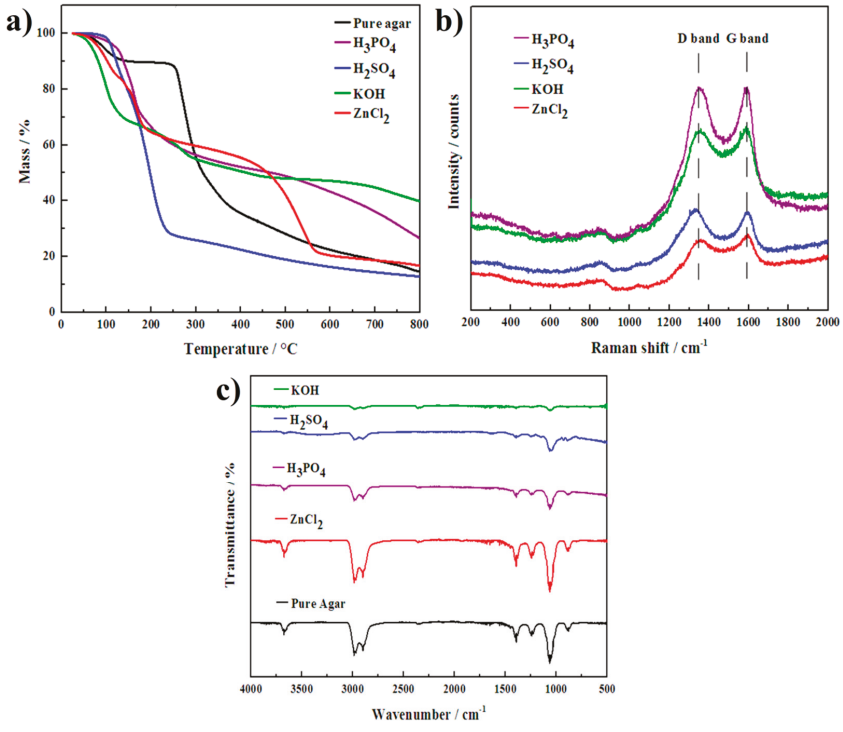

Figure 2. (**a**) TGA curves of pure agar and hydrogels with different activating agents; (**b**) Raman spectra of obtained carbons; (**c**) FT-IR spectra of pure agar and obtained carbons.

The morphological characteristics of ACs were studied using SEM as shown in Figure 3. All samples have a porous three-dimensional (3D) structure, which facilitates the better access of the electrolyte to the active material and accelerates the migration of electrons and ions when the materials are used in LIBs. KAAC and ZAAC have a similar 3D interconnected hierarchical structure with meso- and microporous morphology as illustrated in Figure 3a,b. Acid-ACs have similar 3D structures with mesopores (Figure 3c,d). However, the pore sizes of the resulting materials differ, which is discussed further below. Further TEM analysis was performed for the ACs. A disordered hierarchical porous structure can be observed that contains meso- and micro-pores (see Figure S2). The presence of abundant pores in the ACs from the agar can be identified by the large number of white spots between the disordered carbon layers [42].

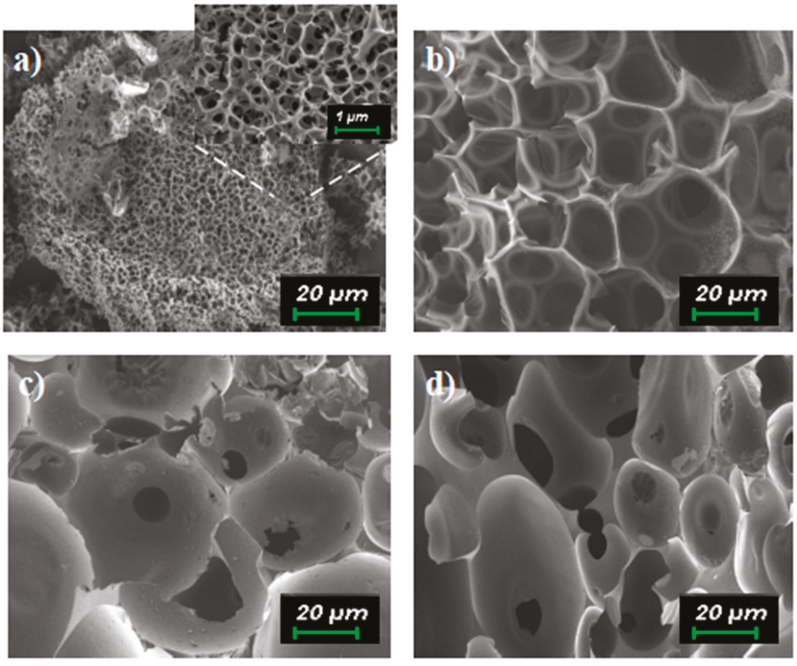

Figure 3. SEM images of ACs with four different activating agents: (**a**) KAAC; (**b**) ZAAC; (**c**) SAAC; (**d**) PAAC.

The detailed studies of the porous structure and surface of ACs were carried out by nitrogen adsorption measurements. As shown in Figure 4a, all samples demonstrate a type IV desorption isotherm. When relative pressure is above 0.8, the isotherm increases significantly due to capillary condensation. The desorption isotherm is situated over the adsorption isotherm, which means that the samples have a high amount of mesopores [43]. In Figure 4b, which shows pore size distribution diagrams, it can be seen that the pore size ranges from 12 to 60 nm. The specific surface areas for KAAC, ZAAC, PAAC, and SAAC were defined as 2417.5, 3309.0, 974.1, and 548.3 m^2 g^{-1}, while the average pore size was 15.2, 19.5, 19.2, and 19.0 nm, respectively. The results indicate that the acid activators and $ZnCl_2$ tend to form a mesoporous structure, while using a KOH activator results in meso- and macroporous structures.

The prepared ACs were tested as anode materials in LIBs. Figure 5a,b show the charge–discharge profiles of the electrodes at a charge–discharge rate of 0.1 C. At the initial cycle, KAAC, PAAC, SAAC, and ZAAC exhibited charge/discharge capacities of 360/836, 311/1018, 230/564, and 110/597 mAh g^{-1}, respectively. The Coulombic efficiencies were 42.9%, 30.5%, 40.8% and 18.4% for KAAC, PAAC, SAAC, and ZAAC, respectively. The low Coulombic efficiency in the 1st cycle is caused by the decomposition of the electrolyte, the formation of an SEI layer, and some irreversible capture of Li ions in a special position of the carbonaceous material, which may be associated with a surface reaction, for example, near residual H atoms [44]. At the 10th cycle, the charge-specific capacities for KAAC, PAAC, SAAC, and ZAAC were 290, 292, 169, and 123 mAh g^{-1}, while the discharge-specific capacities were 309, 337, 174, and 132 mAh g^{-1}, respectively. The Coulombic efficiency improved significantly in the 10th cycle and amounted to 95, 88, 97, and 96%, respectively. The increase in the Coulombic efficiency might be in the formation of a stabilized SEI film. The SEI layer acts as a passivation layer, the formation of which is advantageous for carbon anodes as it prevents the continuous electrolyte decomposition on the activated carbon electrode, and therefore the anode is in a stable state [7].

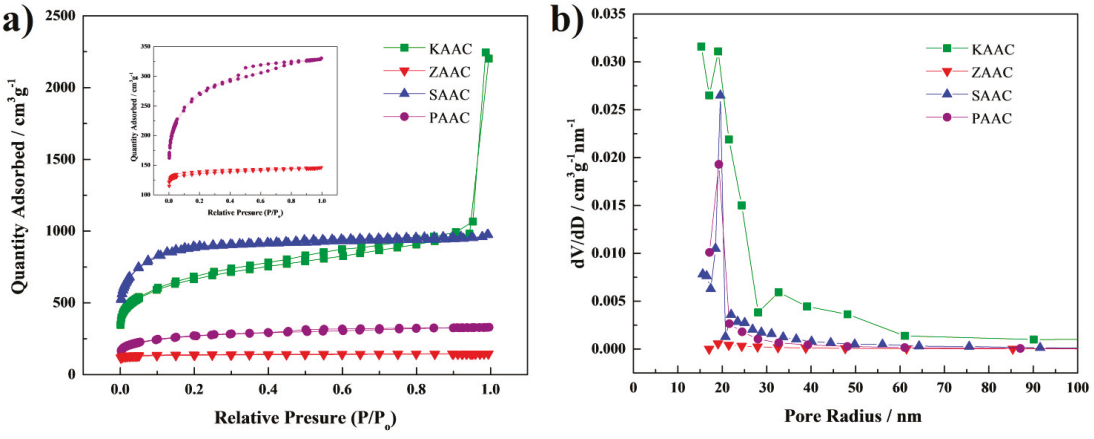

Figure 4. (**a**) Nitrogen adsorption–desorption isotherms and (**b**) pore sizes distribution.

The CV curves of the samples ranging from 0.01 to 2.8 V (versus Li/Li^+) at a scan rate of 0.1 mV s^{-1} are illustrated in Figure 5e,f. It is clearly seen that the 1st cycle differs from the second and fifth cycles. The area of the reduction peak of the 1st cycle is more significant than that of the second and fifth cycles. This difference is associated with the non-reversible intercalation of Li-ions into the ACs [45]. There are two peaks for KAAC at around 0.01–0.2 V and 0.45 V at the first cycle. The latter peak corresponds to the decomposition and generation of SEI on the surface of carbon that disappears in subsequent cycles owing to the stabilization of the SEI layer. The influence of the SEI layer is vital for the CV cycle and Coulombic efficiency [46]. Consequently, at the first cycle, the Coulomb efficiency was low as shown in Figure 5, but in further cycles, it stabilized. A peak around 0.01 V is related to the incorporation of Li-ions into the layered carbon, and a flat peak between 0.2 and 0.6 V is attributed to the extracting process of Li-ions from the electrode [47]. The CV curves of the second and fifth cycles have a partial overlap, which indicates the outstanding stability of the electrode material.

To investigate the cyclic stability of the prepared carbons, the cells were galvanostatically cycled at current densities of 0.1 C and 1 C for 100 cycles as shown in Figure 5c,d. The stable discharge capacity of KAAC was the highest reversible capacity at 0.1 and 1 C compared to PAAC, SAAC, and ZAAC. The specific capacity for KAAC, PAAC, SAAC, and ZAAC was 330, 239, 212, and 157 mAh g^{-1} at 0.1 A g^{-1} and 190, 150, 136, and 79 mAh g^{-1} at 1 C, respectively. The reversible capacity of KAAC is higher than recently reported ACs obtained from cherry pit activated with KOH and H_3PO_4 [48]. Comparison with other bio-derived activated carbons is illustrated in Table 1. Although upon the initial cycles the Coulombic efficiency of all samples was low, it increased upon further cycling and reached almost 100%. These results demonstrate the excellent cycling capability and reversibility of all samples. Such tendencies can be observed practically for bio-mass derived activated carbon used as anode materials [7,48,49].

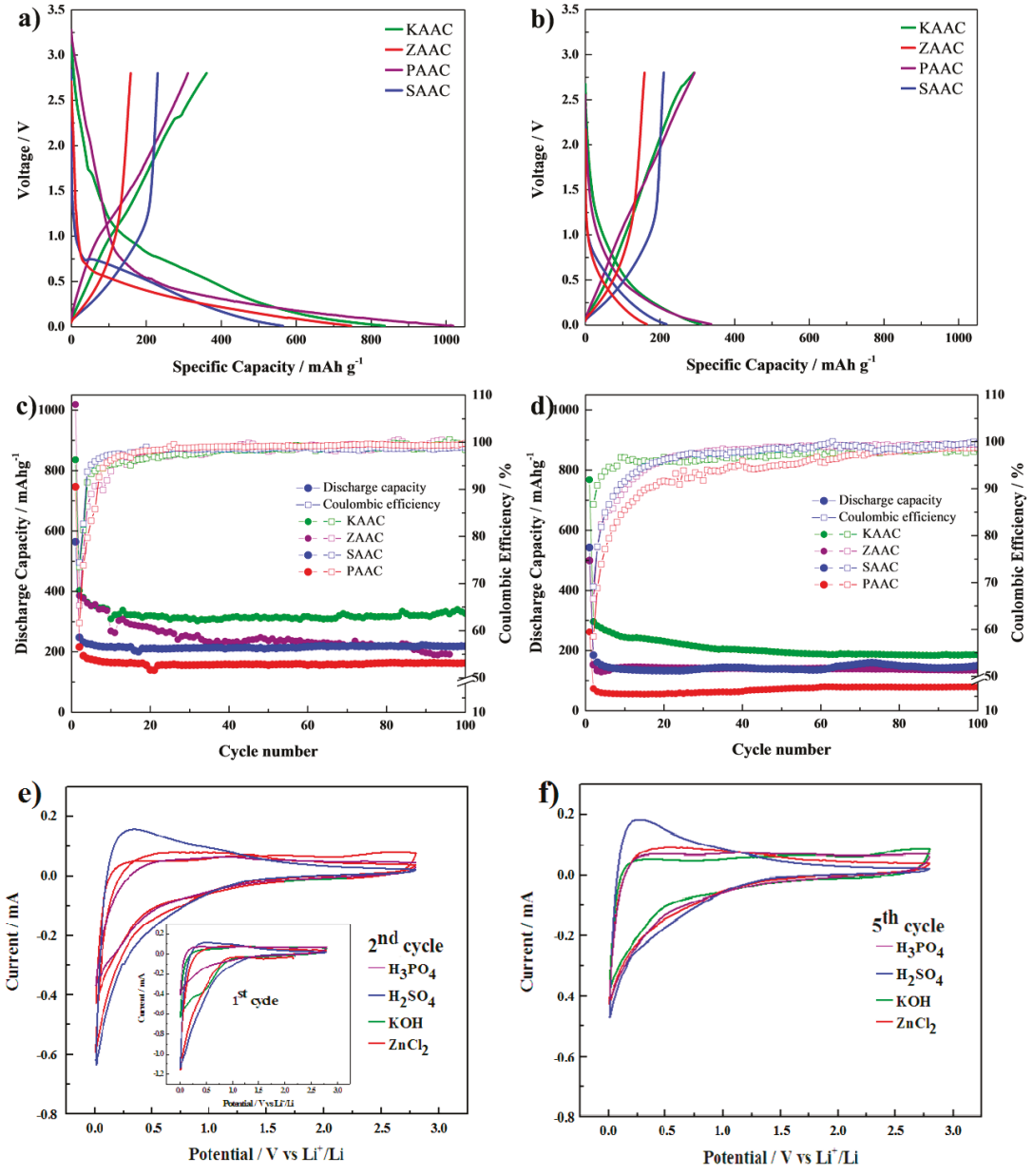

Figure 5. Cycling performances of AC electrodes (**a**) at 1st cycle at 0.1 C rate; (**b**) at 10th cycle at 0.1 C rate. Cycling performance with Coulombic efficiency (right *Y*-axis) of PAAC, SAAC, KAAC, and ZAAC cycled at (**c**) 0.1 C rate; (**d**) 1 C rate. CV profiles of PAAC, SAAC, KAAC, and ZAAC at a scan rate of 0.1 mV s^{-1}, from 0.01 to 2.8 V: (**e**) 2nd cycle and (**f**) 5th cycle.

Table 1. Comparison of the electrochemical characteristics of different bio-derived ACs used as anode materials for lithium-ion batteries (LIBs)

AC Precursor	Activating Agent	Measurement Conditions	Initial Capacity (mAh g^{-1})	Reversible Capacity (mAh g^{-1})	References
Agar	KOH	0.1 C	931	320 at 0.1 C after 100 cycles	This work
Sisal fiber	KOH	0.1 C	646	Capacity loss of 363 compared to initial capacity	[5]
Corn straw	$CaCl_2$	0.2 C	1534	546 at 0.2 after 100 cycles	[7]
Shaddock peel	KOH	50 mAg^{-1}	1284	673 at t 50 mAg^{-1} after 100 cycles	[19]
Wheat stalk	KOH	0.1 C	502	139.6 at 10 C after 3000 cycles	[21]
Green tea wastes	KOH	0.1 A/g	706	400 at 0.1 A/g after 100 cycles	[23]
Jute fiber	$ZnCl_2$	0.2 C	2117	742.7 at 0.2 C after 100 cycles	[32]
Pomelo peels	-	90 mAg^{-1}	756	452 at 90 mAg^{-1} after 200 cycles	[44]
Bamboo chopsticks	KOH	~0.37 C	~500	~360 at ~0.37 C after 100 cycles	[45]
Cherry pit	KOH	C/3	-	210 at C/3 after 200 cycles	[48]

To determine the structural stability of the activated carbon anodes, the electrodes were analyzed by SEM before and after 20 cycles. SEM images show that the electrodes before and after cycles have a rough surface with many pores, which indicates the stability of the electrodes (Figure S3). In order to further explain the reversible surface redox reaction at the porous anode, the CVs of the SAAC anode were performed at various scan rates (Figure S4a). The linkage between peak currents and scan rates, which is almost linear with a correlation of 0.999, was studied using redox peaks of roughly 0.64 V (Figure S4b). This result shows that the redox reaction is surface-limited rather than diffusion-limited [50]. As indicated earlier, porous carbon materials have a large surface area. As follows, the quantity of oxygen-containing functional groups and other functional groups on the surface of carbon corresponds to the surface area of the porous material. The beforementioned oxygen-containing functional groups participate in the redox reaction with lithium-ion, schematically described as: C=O + Li^+ + e^- => C-O-Li. Consequently, the pseudo-capacitive effect, prompted by surface reactions, has a significant effect on the advancement of electrochemical energy storage. Moreover, this effect might explain the high specific capacity and excellent performance of the activated porous carbon materials in lithium-ion batteries [51].

Furthermore, the rate performance of samples was investigated by charging and discharging the cells at various current densities between 0.1 and 10 C each for 5 cycles as illustrated in Figure 6. At a current density of 0.1 C, the specific discharge capacities of KAAC, PAAC, SAAC, and ZAAC were 359, 331, 232, and 161 mAh g^{-1}, respectively. Although the specific capacity of the samples reduced upon increasing the cycling current density to 0.5, 1, 2, 5, and 10 C, the cells could recover their original value when the current density was changed back to 0.1 C. The pore system and large S_{BET} of the samples are likely to facilitate the rapid transfer of Li-ions and enhance the rate characteristics.

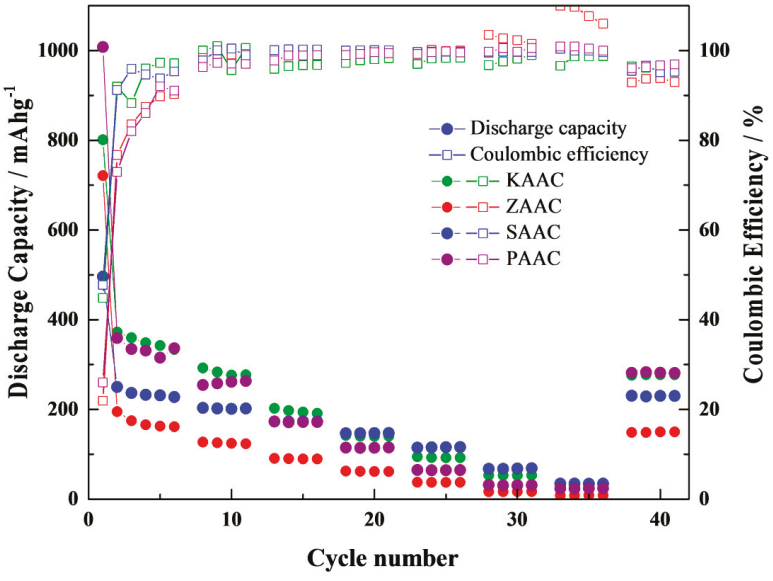

Figure 6. Rate capability of AC electrodes with $ZnCl_2$, H_2SO_4, KOH, and H_3PO_4 activators from 0.1 to 10 C.

4. Conclusions

In summary, we have successfully prepared low-cost and sustainable ACs using a renewable agar precursor activated by four different activators. Through investigating the effect of the activators on the morphology of AC, it was found that the AC anode obtained with KOH as an activating agent achieved the best electrochemical performance. The initial discharge capacity of AC with KOH reached 931 mAh g^{-1} and a reversible capacity of 326 mAh g^{-1} was delivered over 100 cycles at 0.1 C. The Coulombic efficiency remained above 96% after 10 cycles. Furthermore, all prepared samples exhibited excellent capacity retention and reversibility upon prolonged cycling and high rate capability. This research demonstrates a simple and effective method for preparation of mesoporous AC, and provides an effective synthesis route for a production of unique 3D templates that can be used to host various electrode materials.

Supplementary Materials: The following are available online at https://www.mdpi.com/article/10.3390/nano12010022/s1, Figure S1: XPS spectra of (a) KAAC; (b) ZAAC; (c) PAAC; (d) SAAC, Figure S2: TEM images of ACs with four different activating agents: (a) SAAC; (b) PAAC; (c) KAAC; (d) ZAAC, Figure S3: SEM images of pristine electrodes: (a) KAAC, (c) PAAC, (e) ZAAC, and (g) SAAC, and electrodes after 20 cycles: (b) KAAC, (d) PAAC, (f) ZAAC, and (h) SAAC, Figure S4: (a) CV curves of SAAC electrodes at various scan rates of 1.0 mV s^{-1}, 1.5 mV s^{-1}, and 2.0 mV s^{-1}; (b) Relationship between the redox peak current and scanning rates.

Author Contributions: Conceptualization, N.I., A.N. and G.K.; Methodology, N.I., A.N. and G.K.; Validation, G.K.; Investigation, all authors; Data curation, N.I. and A.N.; Writing—original draft preparation, N.I., A.N. and G.K.; Writing—review and editing, N.I. and G.K.; Funding acquisition, Z.B. All authors have read and agreed to the published version of the manuscript.

Funding: This research was funded by the research grants OPFE2021001 "New materials and devices for defense and aerospace applications" from the Ministry of Digital Development, Innovations and Aerospace Industry of the Republic of Kazakhstan and 091019CRP2114 "Three-Dimensional All Solid State Rechargeable Batteries", 240919FD3914 "Self-Charging Rechargeable Lithium-ion Battery" from Nazarbayev University, and AP08052143 "Development of wearable self-charging power unit" from the Ministry of Education and Science of the Republic of Kazakhstan.

Data Availability Statement: The data presented in this study are available on request from the corresponding author.

Conflicts of Interest: The authors declare no conflict of interest.

References

1. Kang, K.; Meng, Y.S.; Breger, J.; Grey, C.P.; Ceder, G. Electrodes with High Power and High Capacity for Rechargeable Lithium Batteries. *Science* **2006**, *311*, 977–980. [CrossRef]
2. Lecce, D.D.; Verrelli, R.; Hassoun, J. Lithium-ion batteries for sustainable energy storage: Recent advances towards new cell configurations. *Green Chem.* **2017**, *19*, 3442–3467. [CrossRef]
3. Hu, M.; Pang, X.; Zhou, Z. Recent progress in high-voltage lithium ion batteries. *J. Power Sources* **2013**, *237*, 229–242. [CrossRef]
4. Chen, W.; Zhou, Z.; Wang, R.; Wu, Z.; Liang, H.; Shao, L.; Shu, J.; Wang, Z. High performance Na-doped lithium zinc titanate as anode material for Li-ion batteries. *RSC Adv.* **2015**, *5*, 49890–49898. [CrossRef]
5. Yu, X.; Zhang, K.; Tian, N.; Qin, A.; Liao, L.; Du, R.; Wei, C. Biomass carbon derived from sisal fiber as anode material for lithium-ion batteries. *Mater. Lett.* **2015**, *142*, 193–196. [CrossRef]
6. Scrosati, B.; Hassoun, J.; Sun, Y.K. Lithium-ion batteries. A look into the future. *Energy Environ. Sci.* **2011**, *4*, 3287–3295. [CrossRef]
7. Yu, K.; Wang, J.; Wang, X.; Liang, J.; Liang, C. Sustainable application of biomass by-products: Corn straw-derived porous carbon nanospheres using as anode materials for lithium ion batteries. *Mater. Chem. Phys.* **2020**, *243*, 122644. [CrossRef]
8. Kamali, A.R.; Fray, D.J. Tin-based materials as advanced anode materials for lithium ion batteries: A review. *Rev. Adv. Mater. Sci.* **2011**, *27*, 14–24.
9. Nurpeissova, A.; Adi, A.; Aishova, A.; Mukanova, A.; Kim, S.S.; Bakenov, Z. Synergistic effect of 3D current collector structure and Ni inactive matrix on the electrochemical performances of Sn-based anodes for lithium-ion batteries. *Mater. Today Energy* **2020**, *16*, 100397. [CrossRef]
10. Poizot, P.; Laruelle, S.; Grugeon, S.; Dupont, L.; Tarascon, J. Nano-sized transition-metal oxides as negative-electrode materials for lithium-ion batteries. *Nature* **2000**, *407*, 496–499. [CrossRef]
11. Zhou, L.; Xu, H.; Zhang, H.; Yang, J.; Hartono, S.B.; Qian, K.; Zou, J.; Yu, C. Cheap and scalable synthesis of α-Fe2O3 multi-shelled hollow spheres as high-performance anode materials for lithium ion batteries. *Chem. Commun.* **2013**, *49*, 8695–8697. [CrossRef]
12. Zhao, Y.; Li, X.; Yan, B.; Xiong, D.; Li, D.; Lawes, S.; Sun, X.L. Recent Developments and Understanding of Novel Mixed Transition-Metal Oxides as Anodes in Lithium Ion Batteries. *Adv. Energy Mater.* **2016**, *6*, 1502175. [CrossRef]
13. Li, Q.; Zhu, S.; Lu, Y. 3D Porous Cu Current Collector/Li-Metal Composite Anode for Stable Lithium-Metal Batteries. *Adv. Funct. Mater.* **2017**, *27*, 1606422. [CrossRef]
14. Liu, S.; Hou, H.; Liu, X.; Hu, W.; Yan, C.; Duan, J.; Meng, R. High-performance hierarchical homologous scale-like CuCl/Cu foam anode for lithium ion battery. *Ceram. Int.* **2016**, *42*, 8310–8315. [CrossRef]
15. Nurpeissova, A.; Mukanova, A.; Kalimuldina, G.; Umirov, N. Onion-Structured Si Anode Constructed with Coating by Li4Ti5O12 and Cyclized-Polyacrylonitrile for Lithium-Ion Batteries. *Nanomaterials* **2020**, *10*, 1995. [CrossRef]
16. Hwang, S.Y.; Lee, H.R.; Lee, Y.K.; Lee, G.B.; Lee, S.; Kim, H.J.; Joh, H.I. Stable fast-charging electrodes derived from hierarchical porous carbon for lithium-ion batteries. *Int. J. Energy Res.* **2021**, *45*, 4718–4726. [CrossRef]
17. Gao, F.; Geng, C.; Xiao, N.; Qu, J.; Qiu, J. Hierarchical porous carbon sheets derived from biomass containing an activation agent and in-built template for lithium ion batteries. *Carbon* **2018**, *139*, 1085–1092. [CrossRef]
18. Titirici, M.M.; White, R.J.; Brun, N.; Budarin, V.L.; Su, D.S.; Monte, F.D.; Clark, J.H.; MacLachlan, M.J. Sustainable carbon materials. *Chem. Soc. Rev.* **2015**, *44*, 250–290. [CrossRef] [PubMed]
19. Li, R.; Huang, J.; Li, J.; Cao, L.; Zhong, X.; Yu, A.; Lu, G. Nitrogen-doped porous hard carbons derived from shaddock peel for high-capacity lithium-ion battery anodes. *J. Electroanal. Chem.* **2020**, *862*, 114044. [CrossRef]
20. Alam, M.M.; Hossain, M.A.; Hossain, M.D.; Johir, M.A.H.; Hossen, J.; Rahman, M.S.; Zhou, J.L.; Hasan, A.T.M.; Karmakar, A.K.; Ahmed, M.B. The potentiality of rice husk-derived activated carbon: From synthesis to application. *Processes* **2020**, *8*, 203. [CrossRef]
21. Zhou, X.; Chen, F.; Bai, T.; Long, B.; Liao, Q.; Ren, Y.; Yang, J. Interconnected highly graphitic carbon nanosheets derived from wheat stalk as high performance anode materials for lithium ion batteries. *Green Chem.* **2016**, *18*, 2078–2088. [CrossRef]
22. Sevilla, M.; Fuertes, A.B. Graphitic carbon nanostructures from cellulose. *Chem. Phys. Lett.* **2010**, *490*, 63–68. [CrossRef]
23. Sekar, S.; Lee, Y.; Kim, D.Y.; Lee, S. Substantial LIB anode performance of graphitic carbon nanoflakes derived from biomass green-tea waste. *Nanomaterials* **2019**, *9*, 871. [CrossRef]
24. Wang, H.; Yi, H.; Zhu, C.; Wang, X.; Fan, H.J. Functionalized highly porous graphitic carbon fibers for high-rate supercapacitive electrodes. *Nano Energy* **2015**, *13*, 658–669. [CrossRef]
25. Zhu, L.; Jiang, H.; Yang, Q.; Yao, S.; Shen, X.; Tu, F. An effective porous activated carbon derived from puffed corn employed as the separator coating in a lithium–sulfur battery. *Energy Technol.* **2019**, *7*, 1900752. [CrossRef]
26. Yang, J.; Zuo, S. Facile synthesis of graphitic mesoporous carbon materials from sucrose. *Diam. Relat. Mater.* **2019**, *95*, 1–4. [CrossRef]
27. Zaini, M.A.A.; Zhi, L.L.; Hui, T.S.; Amano, Y.; Machida, M. Effects of physical activation on pore textures and heavy metals removal of fiber-based activated carbons. *Mater. Today Proc.* **2020**, *39*, 917–921. [CrossRef]

28. Nahil, M.A.; Williams, P.T. Pore characteristics of activated carbons from the phosphoric acid chemical activation of cotton stalks. *Biomass Bioenergy* **2012**, *37*, 142–149. [CrossRef]
29. Wang, A.; Sun, K.; Xu, R.; Sun, Y.; Jiang, J. Cleanly synthesizing rotten potato-based activated carbon for supercapacitor by self-catalytic activation. *J. Clean. Prod.* **2021**, *283*, 125385. [CrossRef]
30. Ao, W.; Fu, J.; Mao, X.; Kang, Q.; Ran, C.; Liu, Y.; Zhang, H.; Gao, Z.; Li, J.; Liu, G.; et al. Microwave assisted preparation of activated carbon from biomass: A review. *Renew. Sustain. Energy Rev.* **2018**, *92*, 958–979. [CrossRef]
31. Kong, L.; Peng, H.J.; Huang, J.Q.; Zhang, Q. Review of nanostructured current collectors in lithium–sulfur batteries. *Nano Res.* **2017**, *10*, 4027–4054. [CrossRef]
32. Dou, Y.; Liu, X.; Wang, X.; Yu, K.; Liang, C. Jute fiber based micro-mesoporous carbon: A biomass derived anode material with high-performance for lithium-ion batteries. *Mater. Sci. Eng. B* **2021**, *265*, 115015. [CrossRef]
33. Sankar, S.; Saravanan, S.; Ahmed, A.T.A.; Inamdar, A.I.; Im, H.; Lee, S.; Kim, D.Y. Spherical activated-carbon nanoparticles derived from biomass green tea wastes for anode material of lithium-ion battery. *Mater. Lett.* **2019**, *240*, 189–192. [CrossRef]
34. Wang, J.; Kaskel, S. KOH activation of carbon-based materials for energy storage. *J. Mater. Chem.* **2012**, *22*, 23710–23725. [CrossRef]
35. Dai, Y.Q.; Li, G.C.; Li, X.H.; Guo, H.J.; Wang, Z.X.; Yan, G.C.; Wang, J.X. Ultrathin porous graphitic carbon nanosheets activated by alkali metal salts for high power density lithium-ion capacitors. *Rare Met.* **2020**, *39*, 1364–1373. [CrossRef]
36. Zhang, L.; Gu, H.; Sun, H.; Cao, F.; Chen, Y.; Chen, G.Z. Molecular level one-step activation of agar to activated carbon for high performance supercapacitors. *Carbon* **2018**, *132*, 573–579. [CrossRef]
37. Zhang, M.; Cheng, J.; Zhang, L.; Li, Y.; Chen, M.; Chen, Y.; Shen, Z. Activated carbon by one-step calcination of deoxygenated agar for high voltage lithium ion supercapacitor. *ACS Sustain. Chem. Eng.* **2020**, *8*, 3637–3643. [CrossRef]
38. Han, S.W.; Jung, D.W.; Jeong, J.H.; Oh, E.S. Effect of pyrolysis temperature on carbon obtained from green tea biomass for superior lithium ion battery anodes. *Chem. Eng. J.* **2014**, *254*, 597–604. [CrossRef]
39. Yang, Z.; Gleisner, R.; Mann, D.H.; Xu, J.; Jiang, J.; Zhu, J.Y. Lignin Based Activated Carbon Using H_3PO_4 Activation. *Polymers* **2020**, *12*, 2829. [CrossRef]
40. Laksaci, H.; Khelifi, A.; Trari, M.; Addoun, A. Synthesis and characterization of microporous activated carbon from coffee grounds using potassium hydroxides. *J. Clean. Prod.* **2017**, *147*, 254–262. [CrossRef]
41. Li, M.; Li, W.; Liu, S. Hydrothermal synthesis, characterization, and KOH activation of carbon spheres from glucose. *Carbohydr. Res.* **2011**, *346*, 999–1004. [CrossRef] [PubMed]
42. Vu, D.L.; Seo, J.S.; Lee, H.Y.; Lee, J.W. Activated carbon with hierarchical micro–mesoporous structure obtained from rice husk and its application for lithium–sulfur batteries. *RSC Adv.* **2017**, *7*, 4144–4151. [CrossRef]
43. Ng, S.W.L.; Yilmaz, G.; Ong, W.L.; Ho, G.W. One-step activation towards spontaneous etching of hollow and hierarchical porous carbon nanospheres for enhanced pollutant adsorption and energy storage. *Appl. Catal. B Environ.* **2018**, *220*, 533–541. [CrossRef]
44. Sun, X.; Wang, X.; Feng, N.; Qiao, L.; Li, X.; He, D. A new carbonaceous material derived from biomass source peels as an improved anode for lithium ion batteries. *J. Anal. Appl. Pyrolysis* **2013**, *100*, 181–185. [CrossRef]
45. Jiang, J.; Zhu, J.; Ai, W.; Fan, Z.; Shen, X.; Zou, C.; Liu, J.; Zhang, H.; Yu, T. Evolution of disposable bamboo chopsticks into uniform carbon fibers: A smart strategy to fabricate sustainable anodes for Li-ion batteries. *Energy Environ. Sci.* **2014**, *7*, 2670–2679. [CrossRef]
46. Zhang, D.; Wang, G.; Xu, L.; Lian, J.; Bao, J.; Zhao, Y.; Qiu, J.; Li, H. Defect-rich N-doped porous carbon derived from soybean for high rate lithium-ion batteries. *Appl. Surf. Sci.* **2018**, *451*, 298–305. [CrossRef]
47. Ou, J.; Yang, L.; Zhang, Z.; Xi, X. Nitrogen-doped porous carbon derived from horn as an advanced anode material for sodium ion batteries. *Microporous Mesoporous Mater.* **2017**, *237*, 23–30. [CrossRef]
48. Hernández-Rentero, C.; Marangon, V.; Olivares-Marín, M.; Gómez-Serrano, V.; Caballero, Á.; Morales, J.; Hassoun, J. Alternative lithium-ion battery using biomass-derived carbons as environmentally sustainable anode. *J. Colloid Interface Sci.* **2020**, *573*, 396–408. [CrossRef]
49. Zhang, Y.; Chen, L.; Meng, Y.; Xie, J.; Guo, Y.; Xiao, D. Lithium and sodium storage in highly ordered mesoporous nitrogen-doped carbons derived from honey. *J. Power Sources* **2016**, *335*, 20–30. [CrossRef]
50. Hong, K.L.; Qie, L.; Zeng, R.; Yi, Z.Q.; Zhang, W.; Wang, D.; Yin, W.; Wu, C.; Fan, Q.J.; Zhang, W.X.; et al. Biomass derived hard carbon used as a high performance anode material for sodium ion batteries. *J. Mater. Chem. A* **2014**, *2*, 12733–12738. [CrossRef]
51. Byon, H.R.; Gallant, B.M.; Lee, S.W.; Shao-Horn, Y. Role of oxygen functional groups in carbon nanotube/graphene freestanding electrodes for high performance lithium batteries. *Adv. Funct. Mater.* **2013**, *23*, 1037–1045. [CrossRef]

nanomaterials

MDPI

Review

A Review on the Effects of ZnO Nanowire Morphology on the Performance of Interpenetrating Bulk Heterojunction Quantum Dot Solar Cells

Meibo Xing, Longxiang Wang and Ruixiang Wang *

Beijing Engineering Research Centre of Sustainable Energy and Buildings, School of Environment and Energy Engineering, Beijing University of Civil Engineering and Architecture, Beijing 100044, China; xingmeibo@bucea.edu.cn (M.X.); wlx8611@163.com (L.W.)
* Correspondence: wangruixiang@bucea.edu.cn; Tel.: +86-29-82668738; Fax: +86-29-82668725

Abstract: Interpenetrating bulk heterojunction (IBHJ) quantum dot solar cells (QDSCs) offer a direct pathway for electrical contacts to overcome the trade-off between light absorption and carrier extraction. However, their complex three-dimensional structure creates higher requirements for the optimization of their design due to their more difficult interface defect states control, more complex light capture mechanism, and more advanced QD deposition technology. ZnO nanowire (NW) has been widely used as the electron transport layer (ETL) for this structure. Hence, the optimization of the ZnO NW morphology (such as density, length, and surface defects) is the key to improving the photoelectric performance of these SCs. In this study, the morphology control principles of ZnO NW for different synthetic methods are discussed. Furthermore, the effects of the density and length of the NW on the collection of photocarriers and their light capture effects are investigated. It is indicated that the NW spacing determines the transverse collection of electrons, while the length of the NW and the thickness of the SC often affect the longitudinal collection of holes. Finally, the optimization strategies for the geometrical morphology of and defect passivation in ZnO NWs are proposed to improve the efficiency of IBHJ QDSCs.

Keywords: interpenetrating bulk heterojunction; quantum dot solar cells; ZnO nanowire; synthetic method; geometric optimization; defect passivation

Citation: Xing, M.; Wang, L.; Wang, R. A Review on the Effects of ZnO Nanowire Morphology on the Performance of Interpenetrating Bulk Heterojunction Quantum Dot Solar Cells. *Nanomaterials* **2022**, *12*, 114. https://doi.org/10.3390/nano12010114

Academic Editor: Seok-In Na

Received: 23 November 2021
Accepted: 27 December 2021
Published: 30 December 2021

1. Introduction

The world environmental and energy crisis calls for the imminent development of renewable or nonconventional energies. As the most abundant source of clean energy on the planet, solar energy is an important approach to achieving the goal of carbon neutrality in the future [1]. To date, three generations of solar cells have been evolved to harvest solar energy as efficiently as possible [2], but they are still fundamentally limited in terms of solar cell efficiency, including thermalization losses from the absorption of high-energy photons, the non-absorption of low-energy photons, extraction losses due to unavoidable charge carrier recombination, and other mechanisms of energy loss [3].

Quantum dot solar cells offer the advantage of a zero-dimensional structure [4]. Due to their remarkable multiple exciton generation [5,6], hot carrier effect [7], possible intermediate band cell structure [8–10], and multi-junction cell structure [11,12], QDSCs offer the real possibility of boosting energy conversion efficiency beyond the Schockley and Queisser (SQ) limit of 32% for traditional silicon-based SCs [13]. In the past few decades, QDs have been widely researched and integrated in various kinds of SCs, such as Schottky junction colloidal quantum dot (CQD) SCs [14,15], depleted heterojunction CQDSCs [16–18], quantum junction CQDSCs [19–21], and quantum dot-sensitized solar cells (QDSSCs) [22–24]. However, the PbS QDSCs that have been widely studied have only reached a record efficiency of 13.3% [25], which is far from the theoretical efficiency of 45% for a single-junction

solar cell [26]. The main reason for this situation is that various sub-band gap trap states could be introduced in the synthesis and ligand exchange processes of CQD materials. CQDSCs are still limited by the trade-off between carrier extraction and light absorption. A typical planar n-p-p^+-type PbS QDSC usually features an absorption layer that is only about 300 nm thick, while a thickness of QD film of about 1 μm is required to achieve the full absorption of solar radiation. Generally, limited carrier diffusion length (L_D) and depletion width (W_D) are the main factors limiting the thickness of the absorption layer [27]. Thus, maximizing the recombination lifetimes of both charge carriers and their transport properties, which are related to L_D and W_D, is essential to achieve further advances in the thickness of the absorption layer. The IBHJ structure is considered to be another effective solution. IBHJ QDSCs feature a driving force to separate and transport the carriers with band bending and, at the same time, orthogonalize the direction of light absorption and electron–hole pair (EHP) separation, so that the absorber layer is thick enough to produce photocarriers that can be utilized [18]. Their n-type metal oxide acceptor is composed of 1D NWs (usually TiO_2 or ZnO; here, we mainly focus on ZnO, since it easily synthesizes various nanostructures and offers higher electron mobility than TiO_2). Simulation studies have shown that compared with planar solar cells, this type of cell structure is particularly advantageous when the optical absorption depth is comparable to the thickness of the device and the rate of carrier recombination in the depletion region is relatively large [28,29]. In addition, 3D structures have been shown to reduce surface optical reflection and enhance the absorption efficiency of SCs [30,31]. Moreover, the bending durability of ZnO NW arrays may offer promising prospects to meet the demands of flexible photovoltaic devices. Under bending conditions, interpenetrating structures can effectively release stress and thus resist the performance degradation caused by bending better than comparable planar devices [32]. Recently, a record short-circuit current density (JSC) of 33.2 mA cm^{-2} with a power conversion efficiency (PCE) of 10.62% was demonstrated for a PbS IBHJ QDSC employing the luminescence down-shifting method [33]. Further improvements of device performance require fine control of the morphology of NWs. For instance, in a piezoelectric strain sensor, inclined nanowires respond well to vertical contact forces, while vertically aligned nanowires are more sensitive to surface flow [34]. In IBHJ QDSCs, a better vertical arrangement of NWs can prevent the formation of large voids during the deposition of QDs [35]; the density, length, and surface defects of NWs directly affect the final performance of SCs. Besides, in real-world applications, different synthesis methods often feature different levels of morphology control precision, and the synthesis method must be considered to adapt to the application system of QDSC mass production. Therefore, it is necessary to review the preparation process of NW and analyze the morphology optimization mechanism of NWs.

In this study, several synthesis methods of ZnO NW are briefly introduced, ranging from vapor-phase methods and laser interference lithography to solution-based synthesis methods. The morphology control of hydrothermal-grown NW is mainly discussed, since hydrothermal (HT) method is simple, easy to operate, and suitable for large-scale application. Next, the effects of the geometrical morphology for the HT-grown ZnO NW on the performance of SCs is surveyed. Finally, the optimization strategies of NW morphology are discussed. Subsequently, the relationship between the process of photocarrier collection (electron transverse collection and hole longitudinal collection) and the morphology of NW is analyzed, and the control of the morphology of NW is proposed. In terms of interface optimization, the current strategies for the passivation of NW surface defects are summarized.

2. Preparation of ZnO Nanowires

Recently, ZnO NWs have gained considerable attention from the academic community for the fabrication of QD solar cells [36]. A variety of bottom-up approaches, including evaporation/chemical vapor deposition [37,38], solution-based synthesis methods (hydrothermal, electrodeposition) [39], and pulsed laser deposition (PLD) [40] has been exploited for the synthesis of ZnO NWs. Other growth methods, such as flame transport approach [41], electrospinning [42], molecular beam epitaxy (MBE) [43] etc., are also possible. Methods of controlling NW morphology by chemical vapor deposition and laser interference lithography are briefly introduced in the review, and then the hydrothermal method is mainly focused on, since it is simple and cheap.

2.1. Chemical Vapor Deposition

Typically, chemical vapor deposition (CVD) for the fabrication of ZnO NWs is carried out in a tubular furnace, as shown in Figure 1. The quartz boat with the Zn source and Si substrate were placed at the center of quartz tube, which was placed inside a tube furnace [44]. Generally, the formation of different diameters and lengths can be achieved by adjusting the flow rate of the carrier gas and the pressure during growth. In an experiment using argon as the carrier gas, the length and diameter of the NWs increase with the rise of oxygen supply. A further increase in the carrier gas flow rate triggers turbulent flow in the mixing process of the carrier gas and zinc vapor, and irregular results tend to occur [44]. Bhutto et al. [45] found that the final product was very short NWs, or even a layer of thin film at a low zinc vapor pressure, while the NWs grew with good orientation and uniform density at an appropriate vapor pressure. The condition of the substrate is another factor in the growth of aligned NW arrays. Well-aligned and uniform ZnO NW growth requires epitaxy, and the deposition of a c-oriented polycrystalline seed layer on a non-epitaxial substrate is an economical and versatile route [46]. Li et al. [47] found that the density of NWs increased and the degree of vertical arrangement improved with the increase in the seed layer thickness. Other studies have shown that the different deposition temperature and deposition methods of the ZnO seed layer also affect the orientation, morphology, and crystal quality of ZnO NWs grown by vapor deposition [47,48]. Furthermore, the metal catalysts in the vapor–solid–solid growth method are also important factors [49]. For example, neighboring metal catalysts may coalesce into larger-sized islands, leading to inferior control over the nanowire position and density when they are located at the semiconducting substrate during NW growth [50].

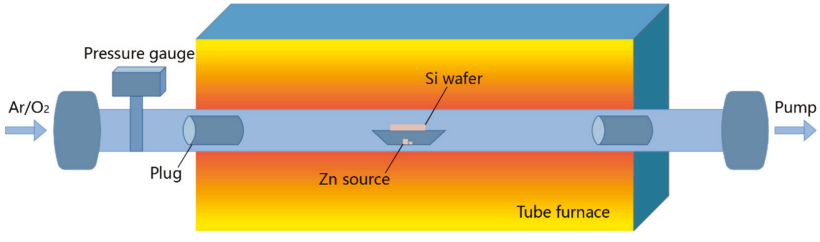

Figure 1. Schematic of CVD system used for the growth of ZnO NWs [44].

2.2. Laser Interference Lithography

The optical lithography and laser interference lithography (LIL) techniques, combining chemical and physical etching techniques to form patterned geometry, are more precisely designed and controllable methods used in the fabrication of ZnO nanostructures [51]. The LIL technique is based on the interference of two coherent light beams to form a horizontal standing wave pattern, which is applied to expose and record the patterns of periodic nanodot arrays (generally spin-coated onto a c-oriented ZnO seed layer) on the photoresist [52]. Wei et al. [53] demonstrated an approach to the patterned growth

of ZnO NW arrays by combining the LIL and hydrothermal (HT) growth methods. The epoxy-based negative photoresist SU-8 was spin-coated onto a 2-inch silicon or sapphire wafer with a (0001) surface-oriented ZnO layer above it. A uniform pattern of open-hole arrays was formed at the unexposed locations of the SU-8 layer after two consecutive laser exposures. Next, the substrate with a patterned SU-8 layer was placed facing downward into the growth solution for the growth of ZnO NWs, as shown in Figure 2 [53]. In this way, the diameter, spacing, and length of the NWs can be well controlled.

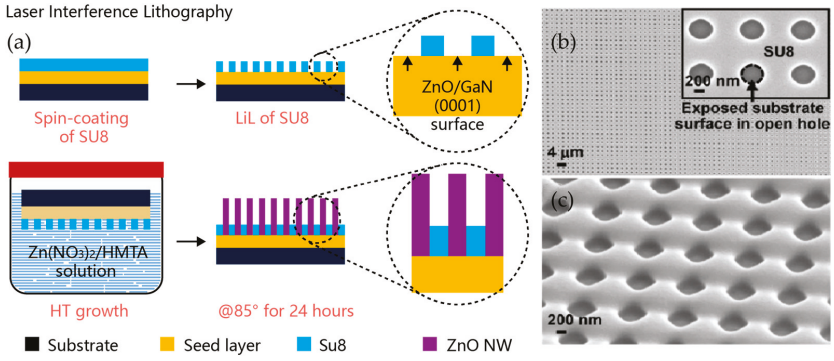

Figure 2. Schematics of the manufacturing process of ZnO NW arrays using laser interference techniques: (**a**) Fabrication process using the LIL approach for large-scale patterned ZnO NW arrays; (**b**) scanning electron microscope (SEM) image of patterned SU-8 film; (**c**) SEM image of patterned photoresist film [53].

2.3. Hydrothermal Method

Compared with other synthetic methods, the HT method has received widespread attention due to its advantages, including its low cost, low temperature, high yield, good expansibility, easy processing, and the flexibility it offers in the choice of both the synthesis pattern and the initial components (precursors and additives) [34,54,55]. The morphology and properties of ZnO NWs can be controlled by changing the growth parameters [56,57]. Generally, increasing the growth time causes the nanowires' aspect ratio to increase gradually, which is attributed to the fact that the axial growth rate is higher than the lateral growth rate [58,59]. Muchuweni et al. [60] observed improved crystallinity and poorly aligned NWs with increasing growth time. The length and diameter of the ZnO NWs vary with the concentration of growth solution; a higher concentration yields a larger length and diameter [61]. Amin et al. [57] observed the change from NWs to nanopillars and finally polycrystalline thin films upon changing from lower concentrations (<25 mM) to higher concentrations (>400 mM). In a similar study, Gerbreders et al. [62] concluded that the minimum concentration value is 25 mM; concentrations lower than this would lead to incomplete nanorod formation with chaotic orientations since the solutions would be depleted too quickly. Consistent with the effect of solution concentration, higher temperatures enhance the driving force of the chemical reaction, giving rise to high-aspect-ratio NWs [58]. The ZnO NW is homogeneous and well-arranged under 90 °C, which is considered to be the optimal temperature in many articles [62]. The PH value is another important factor. Redundant OH^- ions suppress the influence of the competition mechanism, hence the difference in growth rate in the different directions [62,63]. When the pH value of the solution is reduced, the acidic environment may etch the seed layer and thus reduce the density of the NWs, while on the other hand, abundant Zn^{2+} results in the growth of ZnO NWs with larger lengths and diameters [56,57]. However, the growth of NWs is not observed at a low pH value (pH < 4.6 in the research of Amin et al. [57]). This behavior is probably attributable to the absence of hydroxide complexes ($Zn(OH)_n$), which are essential for the growth of ZnO NWs [64].

As in the CVD method, substrate properties also play an important role. The effects of surface energy and seed layer annealing conditions on seed layer growth and HT-grown ZnO NWs were investigated by changing different conditions in the research of Park et al. [65], as shown in Figure 3a. Demes et al. [66] investigated the relationships between the characteristics of grown NWs and (i) the structural properties and morphologies of ZnO films (mean grain size (MGS), texture coefficient, and surface coverage rate) and (ii) growth duration time (t) in detail. The growth process of the NWs is shown in the Figure 3b. Specifically, the growth of the NWs starts from the nucleation site, with an initial diameter d0 at the seed layer surface, before proceeding along the lateral as well as the vertical direction at a rate of V_{lat} and V_{long}, respectively. According to the authors' observations, the main parameter influencing the NW aspect ratio and dimension appears to be the mean grain size of seed layers, while the texture coefficient of the seed layer can greatly influence the NW density [66]. In addition, the morphological properties of NWs grown using the HT method can also be optimized by postprocessing. Here, we briefly summarize the dominant factors affecting the morphology of hydrothermally grown NWs (see Table 1).

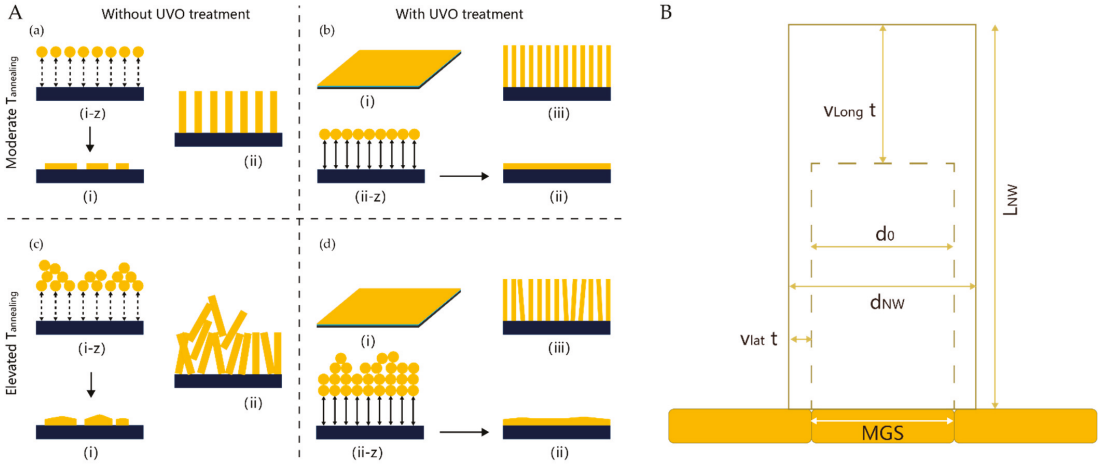

Figure 3. (**A**) Schematics of ZnO NW growth depending on substrate surface conditions and seed layer: (**a**) Without the ultraviolet ozone (UVO) treatment under a lower annealing temperature ($T_{annealing}$); (**b**) with UVO treatment; (**c**,**d**) with varied $T_{annealing}$ conditions [67]; (**B**) schematic representation of the NWs; growth [68].

Table 1. Factors influencing the morphology of hydrothermally grown NWs.

Conditions		Verticality	Density	Mean Length	Mean Diameter	Crystallinity
Seed layer properties	Thickness [67–69]	-	√	-	√	-
	Surface roughness [65,68,69]	√	√	-	√	-
	Texture coefficient [66]	-	√	-	-	-
	Mean grain size [66,70]	-	√	√	√	-

Table 1. *Cont.*

Conditions	Verticality	Density	Mean Length	Mean Diameter	Crystallinity
Nucleation site density [69,71]	-	√	-	-	-
Crystal orientation [67,72]	√	-	-	-	√
Growth time [57,60,62,73]	-	-	√	√	√
Concentration of solution [57,60,62,74]	-	√	√	√	√
Temperatures [57,60,62,73,75]	√	-	√	√	√
pH [57,62,75–77]	-	√	√	√	-
Post-annealing treatment [77,78]	√	-	-	-	√

3. Effect of ZnO Nanowire Morphology on the SCs

3.1. Basic Physical Characteristics for IBHJ Photovoltaic Device

The current density in typical silicon p–n junction SCs is given by the sum of the drift currents in an electric field and the diffusion currents [79,80],

$$J = qE(n\mu_e + p\mu_h) + q\left(D_e\frac{dn}{dx} + D_h\frac{dp}{dx}\right) \quad (1)$$

where n and p are the electron and hole concentration, respectively, $\mu_{e(h)}$ is the majority carrier mobility, E is the electric field in the device, and D_e and D_h are the electron and hole diffusion coefficients. Generally, the CQD absorption layer is treated as a bulk semiconductor to describe phenomena such as drift and diffusion, carrier generation and recombination, and transport and trapping in CQD films [81]. In a depleted heterojunction CQDSC, a planar heterojunction is formed between the QD film and a wider bandgap electrode, which establishes a depletion region. The effective carrier extraction length is defined as $W_{QD} + L_D$, where W_{QD} is the width of the depletion region residing in the QD absorption layer and L_D is the minority carrier diffusion length [82]. The depletion region width is determined by the doping concentration of the material, which features a trade-off with the open circuit voltage (V_{OC}). QD materials with low defect density and high carrier mobility enable the efficient extraction of photogenerated carriers in the quasineutral region through the diffusion process. Photocarriers generated in regions further away from the depletion region than their L_D recombine before they can be extracted. This limited extraction length results in a compromise between the extraction of carriers and the absorption of light. IBHJ structures can break this balance by decoupling the directions of photon absorption and charge collection. A typical IBHJ structure is shown in Figure 4a, where a three-dimensional depletion heterojunction is formed between the NW and the QD absorber layer. Due to the optimized collection of optical carriers and improved light trapping effect, QDSCs employing this structure usually feature enhanced short-circuit current density (J_{SC}) than their planar counterparts. The PV performances of the QDSCs incorporating ZnO NWs are gathered in Table 2.

Table 2. PV performances of the QDSCs integrating ZnO NW arrays.

Photoanode	QD Material	IBHJ QDSC Structure	J_{SC} (mA cm^{-2})	V_{OC} (mV)	FF	PCE (%)
ZnO NWs	PbSe [83]	ITO/ZnO/PbSe-EDT/α-NPD/Au	18.6	420	0.25	1.97
	PbS [84]	ITO/ZnO/PbS-BDT/MoO_3/Au	17.9	600	0.40	4.3
	PbS [85]	FTO/ZnO/PbS-CTAB/Au	34.47	361	0.488	6.074
	PbS [86] [a]	FTO/ZnO/PbS-CTAB/Au	30.7	420	0.478	6.16
	PbS [87]	FTO/ZnO/PbS-CTAB/Au	27.9	422	-	6.03
	PbS [88]	FTO/ZnO/PbS-CTAB/Au	28.8	419	0.47	5.7
	PbS [89] [b]	FTO/ZnO/PbS-TBAI/PbS-EDT/Au	21.51	520	0.450	5.04
	PbS [36]	ITO/ZnO/PbS-TBAI/PbS-EDT/Au	29.4	570	0.57	9.6
	PbS [32] [c]	ITO/ZnO/PbS-TBAI/PbS-EDT/Au	17.81	490	0.435	3.81
	PbS [90]	FTO/ZnO/PbS-TBAI/Au	27.6	351	0.486	4.70
	PbS [91] [d]	FTO/ZnO/PbS-TBAI/PbS-EDT/Au	26.0	497	0.56	7.2
	PbS [92] [e]	FTO/ZnO/PbS-CTAB/Au	23.2	603	0.56	7.78
	PbS [35] [f]	ITO/ZnO/PbS-TBAI/PbS-EDT/Au	27.5	540	0.64	9.52
	PbS [93] [g]	ITO/ZnO/PbS-TBAI/PbS-EDT/Au	31.1	610	0.57	10.8

[a,d] TiO_2-passivation. [b] $Mg(OH)_2$-passivation. [c] Flexible IBHJQDSC. [e] SnO_2-passivation. [f] ABA(4-aminobenzoic acid)-passivation. [g] H-plasma-passivation.

The depletion width of the CQD photovoltaic devices can be characterized by employing capacitance-voltage spectroscopy. The total depletion width (W_{DT}) of the device can be obtained as follows [94],

$$W_{DT} = \sqrt{\frac{qN_{QD}N_{ZnO}\varepsilon_{QD}\varepsilon_{ZnO}}{2(\varepsilon_{QD}N_{QD} + \varepsilon_{ZnO}N_{ZnO})}(V_{bi} - V)} \quad (2)$$

where N_i and ε_i (i = QD, ZnO) are the carrier density and permittivity of the n-type ZnO and p-type QDs, respectively. The value V_{bi} is the built-in potential and V is the applied bias. N_{ZnO} is usually the known parameter while, the carrier concentration of the CQD film is always obtained using Mott–Schottky analysis by fitting the linear region of $1/C^2$ (vicinity of V_{bi}). From W_{DT}, the corresponding depletion region into the CQD film can be obtained as

$$W_{QD} = W_{DT}\frac{\varepsilon_{ZnO}N_{ZnO}}{\varepsilon_{ZnO}N_{ZnO} + \varepsilon_{QD}N_{QD}} \quad (3)$$

With the lifetime and mobility known (mobility can be calculated from the SCLC regime), the diffusion length can easily be calculated according to the formula,

$$L_D = \sqrt{\frac{k_B T}{e}\mu\tau} \quad (4)$$

where k_B is the Boltzmann constant, T is the temperature, e is the elementary charge, μ is the electron mobility, and τ is the carrier lifetime. Other measurement methods of L_D can be seen in the study of Zhitomirsky et al. [95].

3.2. Density of Nanowires

Generally speaking, the density of NW arrays is an important factor affecting the performance of IBHJ SCs. Although NW arrays with high density can speed up the extraction of photocarriers, this leads to a lower volume filling fraction of the QD light-absorbing materials. More importantly, NW arrays with high density feature larger interface areas, which undoubtedly increase the carrier recombination at the interface and, hence, a dramatic V_{OC} loss. In addition, studies have shown that appropriate density control can enhance the capture ability of incident light. Therefore, it is of great practical significance to analyze the density regulation mechanism of NW arrays in detail. Progress in this area has generally been slow for two reasons. On the one hand, accurate and high-quality synthesis methods, such as photolithography and vapor deposition, often require expensive equipment, which runs counter to the goal of the large-scale application of QD photovoltaic devices. On the other hand, NWs grown by simple hydrothermal synthesis methods usually feature higher area density and more surface defects, and their morphology control is usually more complex.

A typical IBHJ SC prepared using hydrothermal NW array is shown in Figure 8a. Due to the high density of the NWs, the QD materials between NWs are usually completely exhausted. In this case, the surface recombination of NWs and the light harvesting efficiency (LHE) are the main considerations. Theoretically, the lower the nanowire density, the less constrained the surface recombination, provided that carriers can be collected efficiently. The usefulness of surface defect passivation is a clear indirect proof of this point. Ozu et al. [92] used SnO_2 layers to passivate the surface of ZnO NWs, and the PCE of the NW CQDSCs was improved from 5.6 to 7.8% (Figure 4). They attributed this to the reduced deep-level defect density and an optimized band-gap arrangement. For effective light management in the IBHJ structures, too large or too small an area density leads to higher light reflectance, as shown in Figure 5a, and an appropriate area density eventually leads to higher light absorption and higher J_{SC}. Recently, Tavakoli Dastjerdi et al. [93] obtained a champion device with a PCE of 10.1% by tuning the areal density of ZnO NWs ($\approx$150 per μm^2) by controlling the precursor concentration. In short, the density control of NWs requires a balance between the interface area and the light trapping effect of NWs. However, this is all based on satisfying the effective carrier collection, because spacing that is too large leads to poor carrier collection between NWs.

3.3. Length of Nanowires

The length of NWs is another important factor affecting device performance, and related studies have been widely reported. Studies have shown that both the total PCE and J_{SC} increase with the length of NWs under the condition of constant thickness of the QD absorption layer, as revealed in Figure 5b [83]. The PCE of the device increases with the thickness of the QD layer and eventually decreases due to bulk recombination and increasing series resistance under the condition that the length of NWs is constant as shown in Figure 5c [91]. In principle, long NW arrays allow the device to adopt a thicker QD absorption layer and can also enhance the light harvesting efficiency (LHE). However, increased device thickness eventually results in the deterioration of the carrier collection for a constant photocarrier diffusion length. Increasing the nanowire length causes poorer charge collection, since holes photoexcited near the front electrode must travel a long distance [88]. In addition, longer NWs mean a larger surface area, which leads to an increase in interfacial recombination events and, thus, a decreased V_{OC}.

Recently, Cheng et al. [91] fabricated devices with varied NW lengths to investigate the role of NWs in SCs. They found that the PCE reached its maximum under certain conditions and then gradually decreased, as shown in Figure 6. Through frequency domain time difference (FDTD) simulation, they found that internal light scattering and local light concentration caused by 3D structures may result in changes to carrier recombination dynamics. Increased internal scattering with longer NWs causes the light to concentrate in a certain region and, hence, an increased carrier recombination rate. Therefore, the

light trapping effect of NWs needs to be studied in detail to evaluate whether they are beneficial or harmful to a particular device. Notably, the QD absorber layer must slightly cover the NW arrays to avoid direct contact between the top ohmic contact and the ZnO. Jean et al. [84] found that the thermally evaporated MoO_3 interlayer, used to protect the QDs from damage during the destructive reverse contact deposition, could also act as a physical buffer layer to reduce the problem of short-circuit between the NWs and the back electrode.

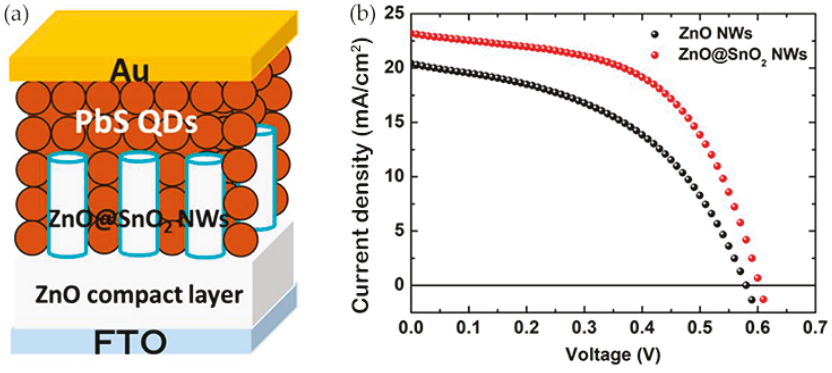

Figure 4. (**a**) Structural illustration of ZnO NW-based CQDSCs with SnO_2 passivation layers; (**b**) the J-V characteristics of ZnO NW CQDSCs with or without SnO_2 passivation [92].

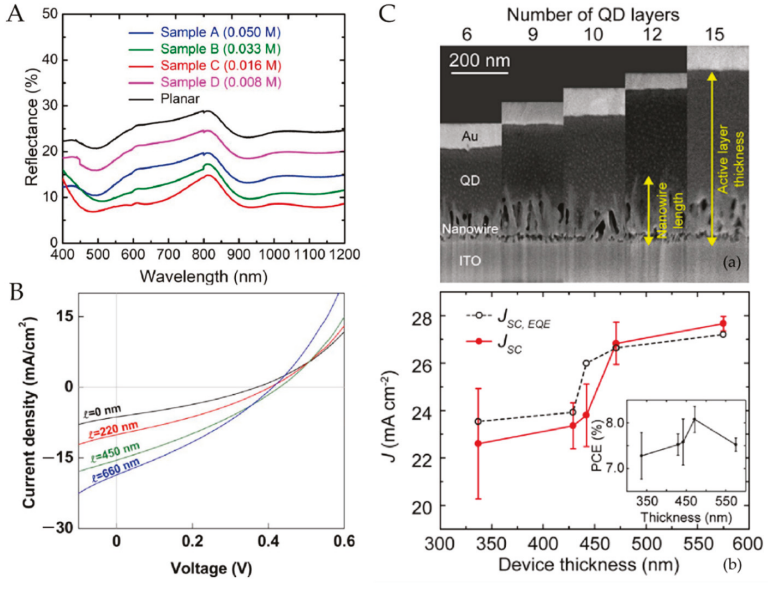

Figure 5. (**A**) Reflectance spectra of ZnO NWs with different areal densities grown on certain substrate [93]; (**B**) I-V curves of CQDSCs assembled with different length NWs [83]; (**C**) (**a**) SEM images of NW CQDSCs with different NW lengths, (**b**) corresponding device performance of different CQD layers [91].

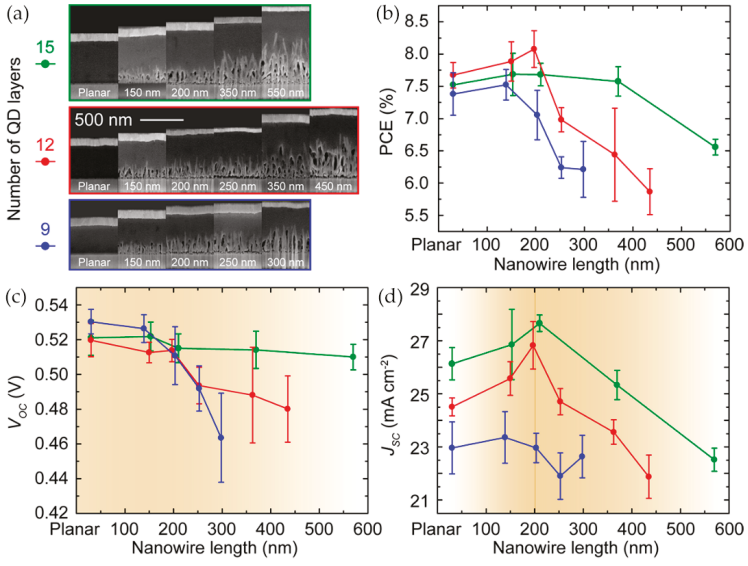

Figure 6. Performance variations of devices with different characteristics: (**a**) SEM images of devices with different NW lengths and CQD layers; (**b**) PCE, (**c**) V_{OC}, and (**d**) J_{SC} for sets of devices with different conditions [91].

4. Optimization Strategies of IBHJ QDSCs Based on ZnO NWs

4.1. Geometrical Morphology Optimization of Nanowires

The original intention to develop this bulk heterojunction structure was to increase the electrical contact area between the donor and the acceptor so that the photocarriers can be collected before they are captured by trap states. Moreover, NWs allow the light absorption and carrier extraction to be controlled independently [83]. Therefore, our core aim can be summarized as obtaining efficient carrier extraction and the increased thickness of light-absorbing materials. As early as 2012, Kramer et al. [96] proposed the spacing of nanopillars in their research on TiO_2 NWs QDSCs (Figure 7). However, longitudinal carrier collection is neglected, and this process often affects the overall thickness of the SCs.

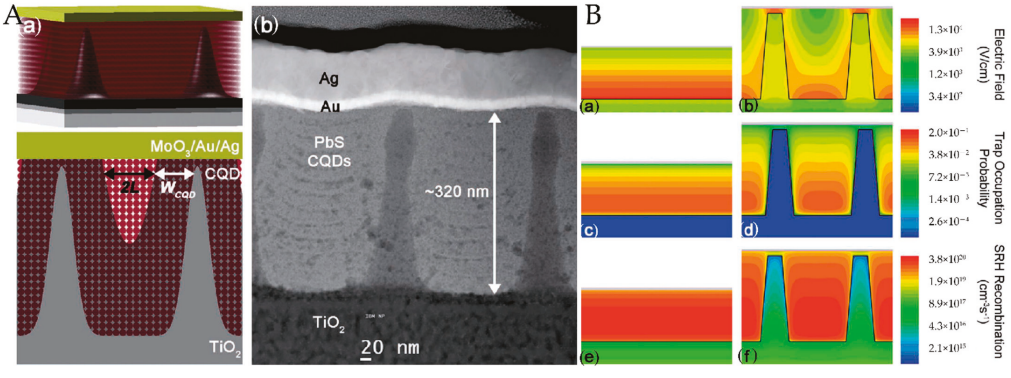

Figure 7. (**A**) (**a**) Schematic and (**b**) SEM images of CQDSCs; (**B**) electric field distributions, trap occupation, and SRH recombination of planar and nanopillar architectures [96].

Considering the efficient collection of photocarriers, it is necessary to distinguish between the electron and hole collection processes. To collect photogenerated electrons efficiently, the pitch size of the NWs should meet the following requirements (Figure 8),

$$d_{np-np} < 2 \times (W_{QD} + L_D) \quad (5)$$

$$d_{top} < W_{QD} + L_D \quad (6)$$

where d_{np-np} is the average spacing of NWs and d_{top} is the distance from the top of the NW to the back electrode. Notably, d_{top} is an upper bound on collection length. The depletion situation at the top of the nanowires is usually more complicated. Electrons are mainly collected horizontally, whereas holes often need to be transported vertically to the host electrode to form photocurrents. Therefore, the limited collection length of holes directly limits the length of the NWs and, thus, the thickness of the light-absorbing layer material,

$$D_{QD} < L + W_{QD} + L_D \quad (7)$$

where D_{QD} is the thickness of the QD absorption layer and L is the mean length of the NWs, which is limited to the hole collection length. Although studies have shown that holes in PbS QDs can diffuse a distance of over 1000 nm or longer under certain conditions [88], experimental and theoretical analysis is still needed to determine the optimal hole collection length. There are indications that even if IBHJ QDSCs with ultra-long NWs (1 μm to 2 μm) offer considerable efficiency, poor hole collection is likely to be the main factor limiting their efficiency. Experiments have shown that the external quantum efficiency decreases as the NWs grow in the short-wavelength regions, while the near-infrared band light increases as the NWs grow; this seems to be a good proof [91], since short-wavelength light is usually absorbed at the top of the cell and the holes usually feature a long collection distance. A QD absorption layer in the NW root area is likely to form a dead zone because holes are likely to quench or be captured in traps in the process of diffusion to the back electrode. Only near the NW top and the bottom of the SCs do the light absorption layer, NWs, and back electrode form an effective electrical pathway. A more detailed mechanism can be explored to a certain extent by using more sophisticated FDTD modeling to simulate the recombination of carriers in the QD region between the NWs. Furthermore, it is worth mentioning that the above parameters usually need to be determined according to the actual situation. For example, the width of the depletion region on the QD side usually depends on the doping concentration of the material. Here, we summarize some parameters of the bulk heterojunction formed between PbS quantum dots passivated by different ligands and ZnO in recent years (Table 3).

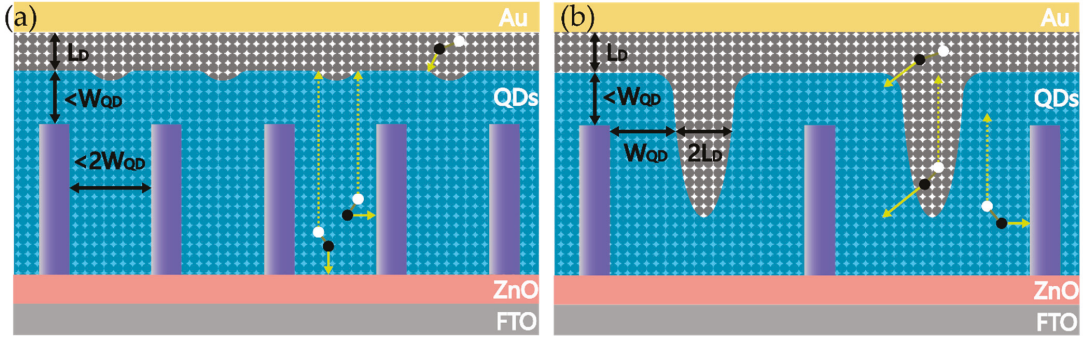

Figure 8. (**a**) IBHJ structure based on hydrothermal method; (**b**) ideal IBHJ structure.

Table 3. Characteristic parameters of several lead chalcogenide QD material layers.

Ligand	CQD Material	CQDSC Structure	Doping Density (cm^{-3})	Depletion Width (nm)	Diffusion Lengths (nm)	PCE (%)
Organic ligand	PbS-MPA [95]	-	-	-	30	-
	PbS-MPA [97]	-	-	-	70	-
Halide ligand	PbS-PbX_2 [98]	ITO/ZnO/PbS-PbX_2/PbS-EDT/Au	9.94×10^{16}	165	52	7.2
	PbO-PbS-TBAI [99]	ITO/ZnO/PbS-TBAI/PbS-EDT/Au	-	-	61	9.4
	PbAc-PbS-TBAI [99]	ITO/ZnO/PbS-TBAI/PbS-EDT/Au	-	-	95	10.8
	PbS-TBAI [95]	-	-	-	70	-
	PbS-TBAI [94]	ITO/ZnO/PbS-TBAI/PbS-EDT/Au	7.3×10^{16}	61.0 (at maximum PCE)	85	8.7
	PbS-I_2 + TBAI [94]	ITO/ZnO/PbS-I_2 + TBAI/PbS-EDT/Au	6.8×10^{16}	62.5 (at maximum PCE)	115	10.1
Hybrid ligand	PbS-MPA + $CdCl_2$ [100]	FTO/ZnO/PbS-MPA +$CdCl_2$/MoO_x/Au/Ag	1×10^{15}–1×10^{16}	-	80	7.6
	PbS-PbX_2 + MPE [98]	ITO/ZnO/PbS-PbX_2 + MPE/PbS-EDT/Au	1.96×10^{16}	288	94	9.6
	PbS-MPA/$CdCl_2$ [97]	-	-	-	230	-

As the main geometric parameter, the diameter of the nanowires has rarely been mentioned. Generally, the diameter of the NWs should not be too small, despite their high doping relative to QD materials. To achieve the maximum depletion width in the radial direction of the NWs, the diameter of the nanowire must be at least twice the depletion width of the ZnO NW [29]. Moreover, NWs that are too thin are easy to break during assembly due to their poor mechanical properties. In order to satisfy these conditions, the light trapping effect should receive sufficient attention. A high LHE can be achieved by adjusting the density and length of the NWs. This process, however, is often associated with the surface area of the nanowires. Striking a balance between low surface area and optimized light capture is also a critical issue. The final consideration is the surface passivation of the NWs, which is discussed in the next section.

4.2. Passivation of Defects in Nanowires

ZnO NWs prepared using the low-temperature HT procedure usually feature more defect states, including shallow-level trapping states originating in the vacancies or interstitials of zinc [101]; and deep level trapping states, which are formed by oxygen vacancy, hydroxyl groups, and excess oxygen [102]. Studies have shown that shallow defect states in ZnO can not only improve the electron mobility of ZnO, but also act as an additional path for electron injection from the QD layer to the NWs in some cases [103]. Instead, the deep-level trapping states are the critical target of defect passivation because they mainly serve as the recombination centers of photocarriers [104]. Generally, green and

yellow emissions in the PL spectra of ZnO are assigned to deep-level defects (red emissions are associated with either surface oxygen or surface OH groups), while violet and blue emissions are related to shallow defects [101]. A relevant description is presented in the article by Vempati et al., as shown in Figure 9a. Hence, we can estimate the defect density of ZnO NWs from these emissions.

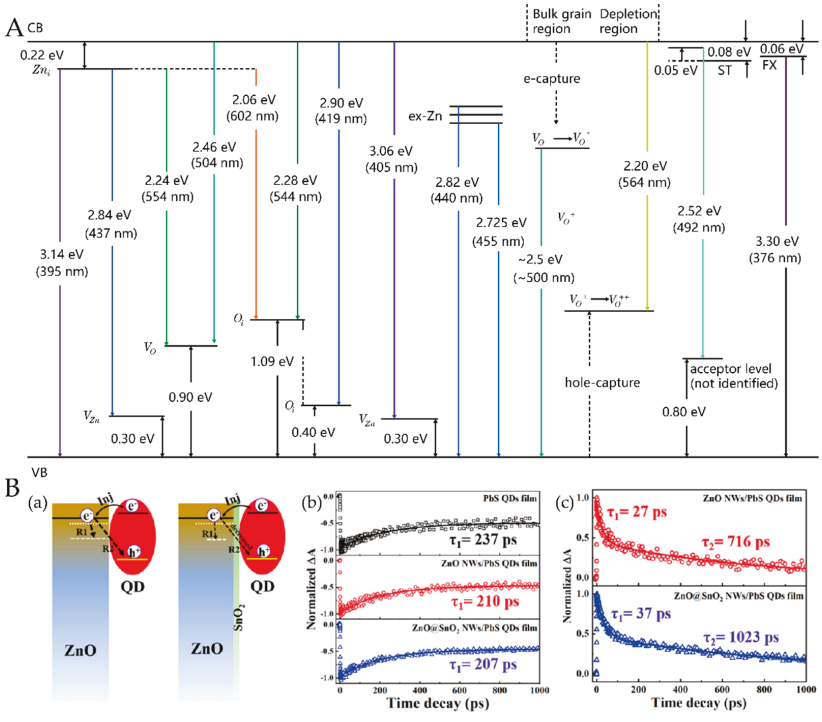

Figure 9. (**A**) Energy level diagram showing some of the principal defect levels in ZnO [101]; (**B**) (**a**) charge dynamic processes occurring at the ZnO NW/QD film interface. TA decay curves of the PbS QD film, ZnO NW/PbS QD film, and ZnO@SnO_2 NW/PbS QD film with a pump light of 470 nm and probe lights of (**b**) 960 and (**c**) 1500 nm [104].

The defect concentrations of HT-grown ZnO NWs can be significantly reduced by annealing [105]. Xu et al. [106] successfully eliminated or passivated the defect-related PL emissions of ZnO NWs by employing sealed post-annealing treatment. Concerning again the surface defects of NWs, Kim et al. [107] successfully reduced the number of excess-oxygen-related defects through thermal annealing in an H_2 ambient atmosphere above 300 °C. The excess-oxygen-related deep-level emissions were quenched completely, while the near band-edge emissions were greatly enhanced when H atoms were incorporated into ZnO NWs. These H atoms are most likely to exist in the form of shallow donors and may be removed after annealing at 400 °C [108–110]. Concerning the desorption of hydroxyl groups, Shi et al. [108] confirmed that annealing at 150 °C results in the removal of OH groups, but it may also introduce other hydrogen-related impurities. In a study of the overall performance of devices, Chang et al. [86] found that 350 °C might be the optimal annealing temperature, and the lowest defect emission and sufficient ZnO crystallinity were obtained at this temperature.

More recently, Tavakoli Dastjerdi et al. [93] passivated ZnO NW surface states using the hydrogen plasma treatment. Compared with the untreated NWs, the PL spectrum of the H-plasma-treated ZnO NWs showed a clear enhancement of near-band emissions and

a remarkable quenching of the visible emission peak. Through X-ray electron spectroscopy (XPS) analysis, the authors found an increase in the number of hydroxyl groups and attributed this to the passivated O-dangling bonds. Despite the increase in hydroxyl groups, reduced surface oxygen defects and possible H doping may lead to an improved overall performance [93,107]. Shi et al. [35] obtained a 9.3% PCE by introducing ABA-modified ZnO NW arrays in QDSCs. In addition to the passivation of ZnO surface defect states, ABA modification can change the interfacial dipole momentum between ZnO NWs and CQDs, thus effectively increasing the vacuum level.

Parallel to the class of passivation strategies for post-annealing and surface treatment, depositing organic/inorganic coatings to passivate the surface of ZnO NWs were also investigated [91,109]. Zhang et al. [104] clarified in detail the influence of surface SnO_2 passivation on the charge dynamic process in ZnO NWs by employing time-resolved photoluminescence (TRPL) and transient absorption (TA) spectroscopy techniques, as shown in Figure 9b. After SnO_2 passivation, the PL intensity of the deep-level defects related emission clearly decreased and the time constants of the two recombination pathways (R1 pathway, in which free electrons are trapped by defect states, and the R2 pathway, in which free electrons are recombined with the holes of PbS QDs) increased, which confirmed the positive effect of the surface passivation layer. Interestingly, Zang et al. [89] revealed the possibility of insulating interfacial modification with a $Mg(OH)_2$ interlayer; the performance of the IBHJ QDSCs improved, with a V_{OC} and PCE of 520 mV and 5.04%, respectively. Through the chemical reaction between ZnO and the TiO_2 precursor, Chang et al. [86] fabricated TiO_2-passivated ZnO NW CQDSCs. They provided direct proof of the reduced recombination in the surface-passivated cell by transient open-circuit photovoltage decay measurements. The results showed that the TiO_2-passivated cells exhibited much slower decay processes than those of the bare unpassivated cells. More recently, Cheng et al. [91] significantly minimized V_{OC} losses by passivating a ZnO nanowire surface with ALD TiO_2. Compared with unpassivated devices, the surface-passivated NW devices featured higher J_{sc} and V_{OC}, which was attributed to the passivated surface defects. The performance comparison before and after the passivation process can be seen intuitively in Table 4.

Table 4. Performance optimization of IBHJ QDSCs with passivation strategies.

Passivation Strategy	CQDSC Structure	-	J_{sc} (mA/cm^2)	V_{oc} (mV)	FF	PCE (%)
H-plasma-passivation [93]	ITO/ZnO NWs/PbS-TBAI/PbS-EDT/Au	non-treated	30.0	591	0.56	9.9
		H-plasma treated	31.1	610	0.57	10.8
ABA-passivation [35]	ITO/ZnO NWs/PbS-TBAI/PbS-EDT/Au	non-treated	27.4	510	0.60	8.41
		ABA-treated	27.5	540	0.64	9.52
$Mg(OH)_2$ [89]	FTO/ZnO NWs/PbS-TBAI/PbS-EDT/Au	without $Mg(OH)_2$	22.62	390	45.66	4.03
		with $Mg(OH)_2$	21.51	520	45.08	5.04
SnO_2 [92]	FTO/ZnO NWs/PbS-CTAB/Au	without SnO_2	20.4	580	0.47	5.55
		with SnO_2	23.2	603	0.56	7.78
CBD-TiO_2 [86]	FTO/ZnO NWs/PbS-CTAB/Au	without TiO_2	28.7	279	0.430	3.50
		with TiO_2	30.7	420	0.478	6.16
ALD-TiO_2 [91]	FTO/ZnO NWs/PbS-TBAI/PbS-EDT/Au	without TiO_2	25.3	505	0.54	6.9
		with TiO_2	26.0	497	0.56	7.2

4.3. Other Optimization Strategies

The effective infiltration of QDs in NW arrays is an important means of reducing interfacial defects. However, an important fact is that IBHJ QDSCs may feature a large number of voids, and these voids could cause a sharp decline in the performance of devices. Recently, more and more evidence has shown that the deposition method exerts an important effect on the morphology of thin films. Although the traditional spin-coating deposition method features advantages in small-scale fabrication due to its simplicity and practicability, it may be difficult to control the morphology due to the uneven shear stress distribution during the coating process [86]. In addition, it is still debatable whether mechanical fractures occur in the process of high-speed rotation of NW arrays, which aggravate the deterioration of the performance. A new deposition method based on the meniscus was proposed. "Meniscus-guided" means that the meniscus is shifted across the substrate by a coating head or viscous force to effectively guide and control film deposition [110]. Due to the inherent directivity of the coating process, the QDs can be effectively deposited by penetration. This method is appropriate for large-scale use. By simultaneously controlling the growth orientation of the NWs and introducing convective assembly as the CQD deposition technique, the dense packing and efficient infiltration of CQDs can be effectively improved. In this way, Shi et al. produced a finely interpenetrating OBHJ structure between ZnO NW arrays and PbS CQDs, and demonstrated a PCE of 9.92% in the devices [35].

QDSC design for stability is also an important subject for PV commercialization. Without considering the NW light aggregation effect and similar structural issues, IBHJ QDSCs are similar to planar QDSCs in that their device lifetime is mainly dependent on the QD material itself. Current synthesis and defect passivation techniques have been effective in reducing the oxidation sites associated with the stability of materials. PbS QDSCs can maintain their initial PCE in air with no encapsulation for 30 days [108]. In another study, ZnO NW-based CQDSCs exhibited excellent stable properties (the PCE was almost constant) after being stored in air for 250 days [92]. Further stability optimization strategies need to consider the mechanism of ambient factors (such as oxygen, water, and increased temperatures or high intensities of illumination) affecting the QDs. The intrinsic properties of the QDs themselves and their interplay with other materials are also factors to be considered [110].

5. Conclusions

IBHJ QDSCs form a 3D depletion region for the high-efficiency utilization of solar energy, which allows the incorporation of more QD material while maintaining efficient charge collection. As ETLs, ZnO NW structures should offer optimal electric continuity and need to be relatively transparent to visible light to avoid photon loss. In this study, an assessment was performed on the previous research into the preparation of ZnO NWs, and the effect of the ZnO NW morphology on performance and the optimization strategies of IBHJ QDSCs were summarized. The conclusions and outlooks are as follows:

(1) The HT method is more suitable for the large-scale application of IBHJ QDSCs due to its advantages of low temperature, high yield, and easy processing. The morphology of HT-grown NWs is influenced by the seed layer properties, growth time, concentration, temperatures, PH, and post-treatment conditions. However, it is necessary to investigate the mechanism of these influencing factors for the preparation of NWs with controllable morphologies. Furthermore, the optimization of surface defects and internal defects and the reliability of HT-doping elements also need to be studied further to improve the performance of the ETL and to tune the band-gap arrangement.

(2) The density of the NW affects the filling volume of QD materials. High-density NW arrays not only feature a large V_{OC} loss due to their large interface area, but also cause high reflectivity in the SCs, reducing the light absorption. The length of the nanowires determines the depth of the carrier collection and further affects the thickness of the SCs. However, long NWs often result in poor hole collection and increase the interface

area. In addition, the length of the nanowires affects the light trapping effect of the 3D structure, and may cause the aggregation of light absorption and ultimately affect the recombination of the carriers.

(3) The geometric morphology of the NW exerts a great influence on the transmission and collection of photocarriers. The optimization of NW spacing needs to take account of the transverse collection of electrons, while the length of the NW and the thickness of the SC absorption layer need to be determined after comprehensively analyzing the longitudinal aggregation of holes. In order to satisfy the carrier collection conditions as far as possible, reducing the NW density can increase the filling volume of QD light absorption material.

(4) In order to further optimize the 3D structure, more accurate carrier transport mechanism analysis needs to be carried out in combination with electrical simulation to determine the optimal electrical structure. The light-trapping effect caused by NWs also needs to be more accurately analyzed, since poor light scattering may lead to local light aggregation and thus affect the distribution and collection efficiency of photocarriers.

(5) The passivation of the NW surface is an important way to improve the V_{OC} of IBHJ QDSCs. Passivation strategies commonly include post-annealing, H-plasma treatment, and ABA surface treatment. Moreover, the addition of $Mg(OH)_2$, SnO_2, and TiO_2 buffer layers on the surface of NWs also effectively improves the performance of SCs. However, the effects of the passivation layer (including the passivation mechanism of the defects and the band arrangement of the battery) on the three-dimensional heterojunction remain to be explored. A comparative study of different passivation layers may be helpful in this regard.

Author Contributions: M.X. and R.W. designed and engineered the structure of the paper; M.X. helped analyze the cited papers; L.W. wrote the paper with support from M.X. and R.W. All authors have read and agreed to the published version of the manuscript.

Funding: This research was funded by National Natural Science Foundation of China (NSFC), grant number [No. 51906013] and the Pyramid Talent Training Project of Beijing University of Civil Engineering and Architecture, grant number [JDYC20200316].

Institutional Review Board Statement: Not applicable.

Conflicts of Interest: The authors declare no conflict of interest.

References

1. Gil, L.; Bernardo, J. An Approach to Energy and Climate Issues Aiming at Carbon Neutrality. *Renew. Energy Focus* **2020**, *33*, 37–42. [CrossRef]
2. Khalid, S.; Sultan, M.; Ahmed, E.; Ahmed, W. Chapter 1-Third-Generation Solar Cells. In *Emerging Nanotechnologies for Renewable Energy*; Ahmed, W., Booth, M., Nourafkan, E., Eds.; Micro and Nano Technologies; Elsevier: Amsterdam, The Netherlands, 2021. [CrossRef]
3. Green, M.; Emery, K.; Hishikawa, Y.; Warta, W.; Dunlop, E.; Barkhouse, D.; Gunawan, O.; Gokmen, T.; Todorov, T.; Mitzi, D. Solar cell efficiency tables (version 40). *IEEE Trans. Fuzzy Syst.* **2012**, *20*, 1114–1129. [CrossRef]
4. Weller, H. Colloidal Semiconductor Q-Particles: Chemistry in the Transition Region Between Solid State and Molecules. *Angew. Chemie Int. Ed. English* **1993**, *32*, 41–53. [CrossRef]
5. Schaller, R.D.; Klimov, V.I. High Efficiency Carrier Multiplication in PbSe Nanocrystals: Implications for Solar Energy Conversion. *Phys. Rev. Lett.* **2004**, *92*, 1–4. [CrossRef]
6. Goodwin, H.; Jellicoe, T.C.; Davis, N.J.L.K.; Böhm, M.L. Multiple Exciton Generation in Quantum Dot-Based Solar Cells. *Nanophotonics* **2018**, *7*, 111–126. [CrossRef]
7. Knig, D.; Casalenuovo, K.; Takeda, Y.; Conibeer, G.; Guillemoles, J.F.; Patterson, R.; Huang, L.M.; Green, M.A. Hot Carrier Solar Cells: Principles, Materials and Design. *Phys. E Low-Dimensional Syst. Nanostruct.* **2010**, *42*, 2862–2866. [CrossRef]
8. Marti, A.; Cuadra, L.; Luque, A. Quantum Dot Intermediate Band Solar Cell. *Conf. Rec. IEEE Photovolt. Spec. Conf.* **2000**, *2000*, 940–943. [CrossRef]
9. Luque, A.; Martí, A. The Intermediate Band Solar Cell: Progress toward the Realization of an Attractive Concept. *Adv. Mater.* **2010**, *22*, 160–174. [CrossRef] [PubMed]

10. Asahi, S.; Kaizu, T.; Kita, T. Adiabatic Two-Step Photoexcitation Effects in Intermediate-Band Solar Cells with Quantum Dot-in-Well Structure. *Sci. Rep.* **2019**, *9*, 1–8. [CrossRef]
11. McMeekin, D.P.; Mahesh, S.; Noel, N.K.; Klug, M.T.; Lim, J.C.; Warby, J.H.; Ball, J.M.; Herz, L.M.; Johnston, M.B.; Snaith, H.J. Solution-Processed All-Perovskite Multi-Junction Solar Cells. *Joule* **2019**, *3*, 387–401. [CrossRef]
12. Ikeri, H.I.; Onyia, A.I.; Vwavware, O.J. The Dependence of Confinement Energy on the Size of Quantum Dots. *Int. J. Sci. Res. Phys. Appl. Sci.* **2019**, *7*, 27–30. [CrossRef]
13. Shockley, W.; Queisser, H.J. Detailed Balance Limit of Efficiency of P-n Junction Solar Cells. *J. Appl. Phys.* **1961**, *32*, 510–519. [CrossRef]
14. Johnston, K.W.; Pattantyus-Abraham, A.G.; Clifford, J.P.; Myrskog, S.H.; MacNeil, D.D.; Levina, L.; Sargent, E.H. Schottky-Quantum Dot Photovoltaics for Efficient Infrared Power Conversion. *Appl. Phys. Lett.* **2008**, *92*, 1–4. [CrossRef]
15. Piliego, C.; Protesescu, L.; Bisri, S.Z.; Kovalenko, M.V.; Loi, M.A. 5.2% Efficient PbS Nanocrystal Schottky Solar Cells. *Energy Environ. Sci.* **2013**, *6*, 3054–3059. [CrossRef]
16. Zhang, Y.; Ding, C.; Wu, G.; Nakazawa, N.; Chang, J.; Ogomi, Y.; Toyoda, T.; Hayase, S.; Katayama, K.; Shen, Q. Air Stable PbSe Colloidal Quantum Dot Heterojunction Solar Cells: Ligand-Dependent Exciton Dissociation, Recombination, Photovoltaic Property, and Stability. *J. Phys. Chem. C* **2016**, *120*, 28509–28518. [CrossRef]
17. Spencer, B.F.; Leontiadou, M.A.; Clark, P.C.J.; Williamson, A.I.; Silly, M.G.; Sirotti, F.; Fairclough, S.M.; Tsang, S.C.E.; Neo, D.C.J.; Assender, H.E.; et al. Charge Dynamics at Heterojunctions for PbS/ZnO Colloidal Quantum Dot Solar Cells Probed with Time-Resolved Surface Photovoltage Spectroscopy. *Appl. Phys. Lett.* **2016**, *108*. [CrossRef]
18. Pattantyus-Abraham, A.G.; Kramer, I.J.; Barkhouse, A.R.; Wang, X.; Konstantatos, G.; Debnath, R.; Levina, L.; Raabe, I.; Nazeeruddin, M.K.; Gratzel, M. Depleted-Heterojunction Colloidal Quantum Dot Solar Cells. *ACS Nano* **2010**, *4*, 3374–3380. [CrossRef] [PubMed]
19. Rath, A.K.; Bernechea, M.; Martinez, L.; Pelayo Garcia De Arquer, F.; Osmond, J.; Konstantatos, G. Solution-Processed Inorganic Bulk Nano-Heterojunctions and Their Application to Solar Cells. *Nat. Photonics* **2012**, *6*, 529–534. [CrossRef]
20. Tang, J.; Liu, H.; Zhitomirsky, D.; Hoogland, S.; Wang, X.; Furukawa, M.; Levina, L.; Sargent, E.H. Quantum Junction Solar Cells. *Nano Lett.* **2012**, *12*, 4889–4894. [CrossRef] [PubMed]
21. Jia, Y.; Wang, H.; Wang, Y.; Shibayama, N.; Kubo, T.; Liu, Y.; Zhang, X.; Segawa, H. High-Performance Electron-Transport-Layer-Free Quantum Junction Solar Cells with Improved Efficiency Exceeding 10%. *ACS Energy Lett.* **2021**, 493–500. [CrossRef]
22. Chang, C.H.; Lee, Y.L. Chemical Bath Deposition of CdS Quantum Dots onto Mesoscopic TiO_2 Films for Application in Quantum-Dot-Sensitized Solar Cells. *Appl. Phys. Lett.* **2007**, *91*, 2–5. [CrossRef]
23. Kamat, P.V.; Bang, J.H. Quantum Dot Sensitized Solar Cells: Tale of Two Semiconductor Nanocrystals—CdSe and CdTe. *ACS Natl. Meet. B. Abstr.* **2009**, *3*, 1467–1476.
24. Sahu, A.; Garg, A.; Dixit, A. A Review on Quantum Dot Sensitized Solar Cells: Past, Present and Future towards Carrier Multiplication with a Possibility for Higher Efficiency. *Sol. Energy* **2020**, *203*, 210–239. [CrossRef]
25. Choi, M.J.; García de Arquer, F.P.; Proppe, A.H.; Seifitokaldani, A.; Choi, J.; Kim, J.; Baek, S.W.; Liu, M.; Sun, B.; Biondi, M.; et al. Cascade Surface Modification of Colloidal Quantum Dot Inks Enables Efficient Bulk Homojunction Photovoltaics. *Nat. Commun.* **2020**, *11*, 1–9. [CrossRef]
26. Beard, M.C.; Luther, J.M.; Semonin, O.E.; Nozik, A.J. Third Generation Photovoltaics Based on Multiple Exciton Generation in Quantum Confined Semiconductors. *Acc. Chem. Res.* **2013**, *46*, 1252–1260. [CrossRef]
27. Johnston, K.W.; Pattantyus-Abraham, A.G.; Clifford, J.P.; Myrskog, S.H.; Hoogland, S.; Shukla, H.; Klem, E.J.D.; Levina, L.; Sargent, E.H. Efficient Schottky-Quantum-Dot Photovoltaics: The Roles of Depletion, Drift, and Diffusion. *Appl. Phys. Lett.* **2008**, *92*, 1–4. [CrossRef]
28. Fan, Z.; Razavi, H.; Do, J.W.; Moriwaki, A.; Ergen, O.; Chueh, Y.L.; Leu, P.W.; Ho, J.C.; Takahashi, T.; Reichertz, L.A.; et al. Three-Dimensional Nanopillar-Array Photovoltaics on Low-Cost and Flexible Substrates. *Nat. Mater.* **2009**, *8*, 648–653. [CrossRef]
29. Kayes, B.M.; Atwater, H.A.; Lewis, N.S. Comparison of the Device Physics Principles of Planar and Radial P-n Junction Nanorod Solar Cells. *J. Appl. Phys.* **2005**, *97*, 114302. [CrossRef]
30. Garnett, E.; Yang, P. Light Trapping in Silicon Nanowire Solar Cells. *Nano Lett.* **2010**, *10*, 1082–1087. [CrossRef]
31. Krogstrup, P.; Jørgensen, H.I.; Heiss, M.; Demichel, O.; Holm, J.V.; Aagesen, M.; Nygard, J.; Fontcuberta i Morral, A. Single-Nanowire Solar Cells beyond the Shockley-Queisser Limit. *Nat. Photonics* **2013**, *7*, 306–310. [CrossRef]
32. Wang, Y.; Su, W.; Zang, S.; Li, M.; Zhang, X.; Liu, Y. Bending-Durable Colloidal Quantum Dot Solar Cell Using a ZnO Nanowire Array as a Three-Dimensional Electron Transport Layer. *Appl. Phys. Lett.* **2017**, *110*, 1–6. [CrossRef]
33. Tavakoli Dastjerdi, H.; Prochowic, D.; Yadav, P.; Tavakoli, M.M. Luminescence Down-Shifting Enables UV-Stable and Efficient ZnO Nanowire-Based PbS Quantum Dot Solar Cells with JSC Exceeding 33 MA Cm−2. *Sustain. Energy Fuels* **2019**, *3*, 3128–3134. [CrossRef]
34. Zhu, R.; Yang, R. Growth of Uniform Nanowires with Orientation Control. In *Synthesis and Characterization of Piezotronic Materials for Application in Strain/Stress Sensing*; Mechanical Engineering Series; Springer: Cham, Switzerland, 2018. [CrossRef]
35. Shi, G.; Kaewprajak, A.; Ling, X.; Hayakawa, A.; Zhou, S.; Song, B.; Kang, Y.W.; Hayashi, T.; Altun, M.E.; Nakaya, M.; et al. Finely Interpenetrating Bulk Heterojunction Structure for Lead Sulfide Colloidal Quantum Dot Solar Cells by Convective Assembly. *ACS Energy Lett.* **2019**, *4*, 960–967. [CrossRef]

36. Rekemeyer, P.H.; Chang, S.; Chuang, C.-H.M.; Hwang, G.W.; Bawendi, M.G.; Gradečak, S. Enhanced Photocurrent in PbS Quantum Dot Photovoltaics via ZnO Nanowires and Band Alignment Engineering. *Adv. Energy Mater.* **2016**, *6*, 1600848–1600854. [CrossRef]
37. Djuriić, A.B.; Ng, A.M.C.; Chen, X.Y. ZnO Nanostructures for Optoelectronics: Material Properties and Device Applications. *Prog. Quantum Electron.* **2010**, *34*, 191–259. [CrossRef]
38. Gomez, J.L.; Tigli, O. Zinc Oxide Nanostructures: From Growth to Application. *J. Mater. Sci.* **2013**, *48*, 612–624. [CrossRef]
39. Baruah, S.; Dutta, J. Hydrothermal Growth of ZnO Nanostructures. *Sci. Technol. Adv. Mater.* **2009**, *10*. [CrossRef] [PubMed]
40. Susner, M.A.; Carnevale, S.D.; Kent, T.F.; Gerber, L.M.; Phillips, P.J.; Sumption, M.D.; Myers, R.C. Catalyst-Free ZnO Nanowires on Silicon by Pulsed Laser Deposition with Tunable Density and Aspect Ratio. *Phys. E Low-Dimensional Syst. Nanostruct.* **2014**, *62*, 95–103. [CrossRef]
41. Kaps, S.; Bhowmick, S.; Gröttrup, J.; Hrkac, V.; Stauffer, D.; Guo, H.; Warren, O.L.; Adam, J.; Kienle, L.; Minor, A.M.; et al. Piezoresistive Response of Quasi-One-Dimensional ZnO Nanowires Using an in Situ Electromechanical Device. *ACS Omega* **2017**, *2*, 2985–2993. [CrossRef] [PubMed]
42. Zheng, Z.; Gan, L.; Zhang, J.B.; Zhuge, F.; Zhai, T.Y. An Enhanced UV-Vis-NIR an d Flexible Photodetector Based on Electrospun Zno Nanowire Array/PbS Quantum Dots Film Heterostructure. *Adv. Sci.* **2017**, *4*, 1–8. [CrossRef]
43. Isakov, I.; Panfilova, M.; Sourribes, M.J.L.; Warburton, P.A. Growth of ZnO and ZnMgO Nanowires by Au-Catalysed Molecular-Beam Epitaxy. *Phys. Status Solidi Curr. Top. Solid State Phys.* **2013**, *10*, 1308–1313. [CrossRef]
44. Bi, N.; Zhang, L.; Zheng, Q.; Zhuge, F.; Li, J.; Gao, X.P.A.; Du, J. Control of ZnO Nanowire Growth and Optical Properties in a Vapor Deposition Process. *J. Mater. Sci. Technol.* **2017**, *33*, 850–855. [CrossRef]
45. Bhutto, W.A.; Soomro, A.M.; Nizamani, A.H.; Saleem, H.; Khaskheli, M.A.; Sahito, A.G.; Das, R.; Khan, U.A.; Saleem, S. Controlled Growth of Zinc Oxide Nanowire Arrays by Chemical Vapor Deposition (CVD) Method. *Int. J. Comput. Sci. Netw. Secur.* **2019**, *19*, 135–141.
46. Greene, L.E.; Law, M.; Tan, D.H.; Montano, M.; Goldberger, J.; Somorjai, G.; Yang, P. General Route to Vertical ZnO Nanowire Arrays Using Textured ZnO Seeds. *Nano Lett.* **2005**, *5*, 1231–1236. [CrossRef] [PubMed]
47. Li, C.; Fang, G.; Li, J.; Ai, L.; Dong, B.; Zhao, X. Effect of Seed Layer on Structural Properties of ZnO Nanorod Arrays Grown by Vapor-Phase Transport. *J. Phys. Chem. C* **2008**, *112*, 990–995. [CrossRef]
48. Serrano, A.; Arana, A.; Galdámez, A.; Dutt, A.; Monroy, B.M.; Güell, F.; Santana, G. Effect of the Seed Layer on the Growth and Orientation of the ZnO Nanowires: Consequence on Structural and Optical Properties. *Vacuum* **2017**, *146*, 509–516. [CrossRef]
49. Yang, P.; Yan, H.; Mao, S.; Russo, R.; Johnson, J.; Saykally, R.; Morris, N.; Pham, J.; He, R.; Choi, H.J. Controlled Growth of ZnO Nanowires and Their Optical Properties. *Adv. Funct. Mater.* **2002**, *12*, 323–331. [CrossRef]
50. Shin, H.S.; Sohn, J.I.; Kim, D.C.; Huck, W.T.S.; Welland, M.E.; Choi, H.C.; Kang, D.J. Density Control of ZnO Nanowires Grown Using Au-PMMA Nanoparticles and Their Growth Behavior. *Nanotechnology* **2009**, *20*, 085601. [CrossRef] [PubMed]
51. Si, H.; Kang, Z.; Liao, Q.; Zhang, Z.; Zhang, X.; Wang, L.; Zhang, Y. Design and Tailoring of Patterned ZnO Nanostructures for Energy Conversion Applications. *Sci. China Mater.* **2017**, *60*, 793–810. [CrossRef]
52. Chong, T.C.; Hong, M.H.; Shi, L.P. Laser Precision Engineering: From Microfabrication to Nanoprocessing. *Laser Photonics Rev.* **2010**, *4*, 123–143. [CrossRef]
53. Wei, Y.; Wu, W.; Guo, R.; Yuan, D.; Das, S.; Wang, Z.L. Wafer-Scale High-Throughput Ordered Growth of Vertically Aligned ZnO Nanowire Arrays. *Nano Lett.* **2010**, *10*, 3414–3419. [CrossRef]
54. Hu, H.; Huang, X.; Deng, C.; Chen, X.; Qian, Y. Hydrothermal Synthesis of ZnO Nanowires and Nanobelts on a Large Scale. *Mater. Chem. Phys.* **2007**, *106*, 58–62. [CrossRef]
55. Podrezova, L.V.; Porro, S.; Cauda, V.; Fontana, M.; Cicero, G. Comparison between ZnO Nanowires Grown by Chemical Vapor Deposition and Hydrothermal Synthesis. *Appl. Phys. A Mater. Sci. Process.* **2013**, *113*, 623–632. [CrossRef]
56. Chevalier-César, C.; Capochichi-Gnambodoe, M.; Leprince-Wang, Y. Growth Mechanism Studies of ZnO Nanowire Arrays via Hydrothermal Method. *Appl. Phys. A Mater. Sci. Process.* **2014**, *115*, 953–960. [CrossRef]
57. Amin, G.; Asif, M.H.; Zainelabdin, A.; Zaman, S.; Nur, O.; Willander, M. Influence of PH, Precursor Concentration, Growth Time, and Temperature on the Morphology of ZnO Nanostructures Grown by the Hydrothermal Method. *J. Nanomater.* **2011**, *2011*. [CrossRef]
58. Akgun, M.C.; Kalay, Y.E.; Unalan, H.E. Hydrothermal Zinc Oxide Nanowire Growth Using Zinc Acetate Dihydrate Salt. *J. Mater. Res.* **2012**, *27*, 1445–1451. [CrossRef]
59. Yang, W.; Wang, Y.; Zhen, Q.; Shi, W. Effect of Growth Time on Morphology and Photovoltaic Properties of ZnO Nanowire Array Films. *Rare Met.* **2011**, *30*, 676–680. [CrossRef]
60. Muchuweni, E.; Sathiaraj, T.S.; Nyakotyo, H. Hydrothermal Synthesis of ZnO Nanowires on Rf Sputtered Ga and Al Co-Doped ZnO Thin Films for Solar Cell Application. *J. Alloys Compd.* **2017**, *721*, 45–54. [CrossRef]
61. Yu, J.; Yuan, Z.; Han, S.; Ma, Z. Size-Selected Growth of Transparent Well-Aligned ZnO Nanowire Arrays. *Nanoscale Res. Lett.* **2012**, *7*, 1–6. [CrossRef]
62. Gerbreders, V.; Krasovska, M.; Sledevskis, E.; Gerbreders, A.; Mihailova, I.; Tamanis, E.; Ogurcovs, A. Hydrothermal Synthesis of ZnO Nanostructures with Controllable Morphology Change. *CrystEngComm* **2020**, *22*, 1346–1358. [CrossRef]
63. Cao, B.; Cai, W. From ZnO Nanorods to Nanoplates: Chemical Bath Deposition Growth and Surface-Related Emissions. *J. Phys. Chem. C* **2008**, *112*, 680–685. [CrossRef]

64. Rakhsha, A.H.; Abdizadeh, H.; Pourshaban, E.; Golobostanfard, M.R.; Mastelaro, V.R.; Montazerian, M. Ag and Cu Doped ZnO Nanowires: A PH-Controlled Synthesis via Chemical Bath Deposition. *Materialia* **2019**, *5*, 100212. [CrossRef]
65. Park, J.S.; Mahmud, I.; Shin, H.J.; Park, M.K.; Ranjkesh, A.; Lee, D.K.; Kim, H.R. Effect of Surface Energy and Seed Layer Annealing Temperature on ZnO Seed Layer Formation and ZnO Nanowire Growth. *Appl. Surf. Sci.* **2016**, *362*, 132–139. [CrossRef]
66. Demes, T.; Ternon, C.; Riassetto, D.; Stambouli, V.; Langlet, M. Comprehensive Study of Hydrothermally Grown ZnO Nanowires. *J. Mater. Sci.* **2016**, *51*, 10652–10661. [CrossRef]
67. Song, J.; Lim, S. Effect of Seed Layer on the Growth of ZnO Nanorods. *J. Phys. Chem. C* **2007**, *111*, 596–600. [CrossRef]
68. Nirmal Peiris, T.A.; Alessa, H.; Sagu, J.S.; Ahmad Bhatti, I.; Isherwood, P.; Upul Wijayantha, K.G. Effect of ZnO Seed Layer Thickness on Hierarchical ZnO Nanorod Growth on Flexible Substrates for Application in Dye-Sensitised Solar Cells. *J. Nanoparticle Res.* **2013**, *15*. [CrossRef]
69. Nur, M.; Ghazali, I.; Ammar, M.; Nor, S.; Mustaffa, A.; Abubakar, S.; Husham, M.; Sagadevan, S.; Paiman, S. A Comparative Approach on One-Dimensional ZnO Nanowires for Morphological and Structural Properties. *J. Cryst. Growth* **2021**, *558*, 125997. [CrossRef]
70. Wu, W.Y.; Yeh, C.C.; Ting, J.M. Effects of Seed Layer Characteristics on the Synthesis of ZnO Nanowires. *J. Am. Ceram. Soc.* **2009**, *92*, 2718–2723. [CrossRef]
71. Cheng, J.J.; Nicaise, S.M.; Berggren, K.K.; Gradečak, S. Dimensional Tailoring of Hydrothermally Grown Zinc Oxide Nanowire Arrays. *Nano Lett.* **2016**, *16*, 753–759. [CrossRef]
72. Cossuet, T.; Roussel, H.; Chauveau, J.M.; Chaix-Pluchery, O.; Thomassin, J.L.; Appert, E.; Consonni, V. Well-Ordered ZnO Nanowires with Controllable Inclination on Semipolar ZnO Surfaces by Chemical Bath Deposition. *Nanotechnology* **2018**, *29*, 475601. [CrossRef]
73. Alshehri, N.A.; Lewis, A.R.; Pleydell-Pearce, C.; Maffeis, T.G.G. Investigation of the Growth Parameters of Hydrothermal ZnO Nanowires for Scale up Applications. *J. Saudi Chem. Soc.* **2018**, *22*, 538–545. [CrossRef]
74. Liu, Q.; Yasui, T.; Nagashima, K.; Yanagida, T.; Hara, M.; Horiuchi, M.; Zhu, Z.; Takahashi, H.; Shimada, T.; Arima, A.; et al. Ammonia-Induced Seed Layer Transformations in a Hydrothermal Growth Process of Zinc Oxide Nanowires. *J. Phys. Chem. C* **2020**, *124*, 20563–20568. [CrossRef]
75. Yi, Z.; Luo, J.; Ye, X.; Yi, Y.; Huang, J.; Yi, Y.; Duan, T.; Zhang, W.; Tang, Y. Effect of Synthesis Conditions on the Growth of Various ZnO Nanostructures and Corresponding Morphology-Dependent Photocatalytic Activities. *Superlattices Microstruct.* **2016**, *100*, 907–917. [CrossRef]
76. Abdulrahman, A.F.; Ahmed, S.M.; Hamad, S.M.; Almessiere, M.A.; Ahmed, N.M.; Sajadi, S.M. Effect of Different PH Values on Growth Solutions for the ZnO Nanostructures. *Chinese J. Phys.* **2021**, *71*, 175–189. [CrossRef]
77. Rayerfrancis, A.; Balaji Bhargav, P.; Ahmed, N.; Chandra, B.; Dhara, S. Effect of PH on the Morphology of ZnO Nanostructures and Its Influence on Structural and Optical Properties. *Phys. B Condens. Matter* **2015**, *457*, 96–102. [CrossRef]
78. Muchuweni, E.; Sathiaraj, T.S.; Nyakotyo, H. Effect of Annealing on the Microstructural, Optical and Electrical Properties of ZnO Nanowires by Hydrothermal Synthesis for Transparent Electrode Fabrication. *Mater. Sci. Eng. B Solid-State Mater. Adv. Technol.* **2018**, *227*, 68–73. [CrossRef]
79. Speirs, M.J.; Dirin, D.N.; Abdu-Aguye, M.; Balazs, D.M.; Kovalenko, M.V.; Loi, M.A. Temperature Dependent Behaviour of Lead Sulfide Quantum Dot Solar Cells and Films. *Energy Environ. Sci.* **2016**, *9*, 2916–2924. [CrossRef]
80. Nelson, J.A. *The Physics of Solar Cells*; World Scientific Publishing Company: Singapore, 2003; ISBN 1848168233.
81. Clifford, J.P.; Johnston, K.W.; Levina, L.; Sargent, E.H. Schottky Barriers to Colloidal Quantum Dot Films. *Appl. Phys. Lett.* **2007**, *91*, 253117. [CrossRef]
82. Kramer, I.J.; Sargent, E.H. The Architecture of Colloidal Quantum Dot Solar Cells: Materials to Devices. *Chem. Rev.* **2014**, *114*, 863–882. [CrossRef] [PubMed]
83. Leschkies, K.S.; Jacobs, A.G.; Norris, D.J.; Aydil, E.S. Nanowire-Quantum-Dot Solar Cells and the Influence of Nanowire Length on the Charge Collection Efficiency. *Appl. Phys. Lett.* **2009**, *95*, 1–4. [CrossRef]
84. Jean, J.; Chang, S.; Brown, P.R.; Cheng, J.J.; Rekemeyer, P.H.; Bawendi, M.G.; Gradecak, S.; Bulovic, V. ZnO Nanowire Arrays for Enhanced Photocurrent in PbS Quantum Dot Solar Cells. *Adv. Mater.* **2013**, *25*, 2790–2796. [CrossRef] [PubMed]
85. Wang, H.; Kubo, T.; Nakazaki, J.; Kinoshita, T.; Segawa, H. PbS-Quantum-Dot-Based Heterojunction Solar Cells Utilizing ZnO Nanowires for High External Quantum Efficiency in the near-Infrared Region. *J. Phys. Chem. Lett.* **2013**, *4*, 2455–2460. [CrossRef]
86. Chang, J.; Kuga, Y.; Mora-Seró, I.; Toyoda, T.; Ogomi, Y.; Hayase, S.; Bisquert, J.; Shen, Q. High Reduction of Interfacial Charge Recombination in Colloidal Quantum Dot Solar Cells by Metal Oxide Surface Passivation. *Nanoscale* **2015**, *7*, 5446–5456. [CrossRef]
87. Kawawaki, T.; Wang, H.; Kubo, T.; Saito, K.; Nakazaki, J.; Segawa, H.; Tatsuma, T. Efficiency Enhancement of PbS Quantum Dot/ZnO Nanowire Bulk-Heterojunction Solar Cells by Plasmonic Silver Nanocubes. *ACS Nano* **2015**, *9*, 4165–4172. [CrossRef]
88. Wang, H.; Gonzalez-Pedro, V.; Kubo, T.; Fabregat-Santiago, F.; Bisquert, J.; Sanehira, Y.; Nakazaki, J.; Segawa, H. Enhanced Carrier Transport Distance in Colloidal PbS Quantum-Dot-Based Solar Cells Using ZnO Nanowires. *J. Phys. Chem. C* **2015**, *119*, 27265–27274. [CrossRef]
89. Zang, S.; Wang, Y.; Su, W.; Zhu, H.; Li, G.; Zhang, X.; Liu, Y. Increased Open-Circuit Voltage of ZnO Nanowire/PbS Quantum Dot Bulk Heterojunction Solar Cells with Solution-Deposited $Mg(OH)_2$ Interlayer. *Phys. Status Solidi Rapid Res. Lett.* **2016**, *10*, 745–748. [CrossRef]

90. Wang, H.; Kubo, T.; Nakazaki, J.; Segawa, H. Solution-Processed Short-Wave Infrared PbS Colloidal Quantum Dot/ZnO Nanowire Solar Cells Giving High Open-Circuit Voltage. *ACS Energy Lett.* **2017**, *2*, 2110–2117. [CrossRef]
91. Cheng, J.J.; Chuang, C.H.M.; Hentz, O.; Rekemeyer, P.H.; Bawendi, M.G.; Gradečak, S. Dimension- and Surface-Tailored ZnO Nanowires Enhance Charge Collection in Quantum Dot Photovoltaic Devices. *ACS Appl. Energy Mater.* **2018**, *1*, 1815–1822. [CrossRef]
92. Ozu, S.; Zhang, Y.; Yasuda, H.; Kitabatake, Y.; Toyoda, T.; Hirata, M.; Yoshino, K.; Katayama, K.; Hayase, S.; Wang, R.; et al. Improving Photovoltaic Performance of ZnO Nanowires Based Colloidal Quantum Dot Solar Cells via SnO_2 Passivation Strategy. *Front. Energy Res.* **2019**, *7*, 11. [CrossRef]
93. Tavakoli Dastjerdi, H.; Prochowicz, D.; Yadav, P.; Tavakoli, M.M. Tuning Areal Density and Surface Passivation of ZnO Nanowire Array Enable Efficient PbS QDs Solar Cells with Enhanced Current Density. *Adv. Mater. Interfaces* **2020**, *7*, 1–9. [CrossRef]
94. Lan, X.; Voznyy, O.; Kiani, A.; García de Arquer, F.P.; Abbas, A.S.; Kim, G.; Liu, M.; Yang, Z.; Walters, G.; Xu, J. Passivation Using Molecular Halides Increases Quantum Dot Solar Cell Performance. *Adv. Mater.* **2016**, *28*, 299–304. [CrossRef]
95. Zhitomirsky, D.; Voznyy, O.; Hoogland, S.; Sargent, E.H. Measuring Charge Carrier Diffusion in Coupled Colloidal Quantum Dot Solids. *ACS Nano* **2013**, *7*, 5282–5290. [CrossRef]
96. Kramer, I.J.; Zhitomirsky, D.; Bass, J.D.; Rice, P.M.; Topuria, T.; Krupp, L.; Thon, S.M.; Ip, A.H.; Debnath, R.; Kim, H.C.; et al. Ordered Nanopillar Structured Electrodes for Depleted Bulk Heterojunction Colloidal Quantum Dot Solar Cells. *Adv. Mater.* **2012**, *24*, 2315–2319. [CrossRef]
97. Carey, G.H.; Levina, L.; Comin, R.; Voznyy, O.; Sargent, E.H. Record Charge Carrier Diffusion Length in Colloidal Quantum Dot Solids via Mutual Dot-to-Dot Surface Passivation. *Adv. Mater.* **2015**, *27*, 3325–3330. [CrossRef]
98. Sharma, A.; Mahajan, C.; Rath, A.K. Reduction of Trap and Polydispersity in Mutually Passivated Quantum Dot Solar Cells. *ACS Appl. Energy Mater.* **2020**, *3*, 8903–8911. [CrossRef]
99. Wang, Y.; Lu, K.; Han, L.; Liu, Z.; Shi, G.; Fang, H.; Chen, S.; Wu, T.; Yang, F.; Gu, M.; et al. In Situ Passivation for Efficient PbS Quantum Dot Solar Cells by Precursor Engineering. *Adv. Mater.* **2018**, *30*, 1–8. [CrossRef] [PubMed]
100. Ip, A.H.; Thon, S.M.; Hoogland, S.; Voznyy, O.; Zhitomirsky, D.; Debnath, R.; Levina, L.; Rollny, L.R.; Carey, G.H.; Fischer, A.; et al. Hybrid Passivated Colloidal Quantum Dot Solids. *Nat. Nanotechnol.* **2012**, *7*, 577–582. [CrossRef]
101. Vempati, S.; Mitra, J.; Dawson, P. One-Step Synthesis of ZnO Nanosheets: A Blue-White Fluorophore. *Nanoscale Res. Lett.* **2012**, *7*, 1–10. [CrossRef]
102. Zhang, X.; Qin, J.; Xue, Y.; Yu, P.; Zhang, B.; Wang, L.; Liu, R. Effect of Aspect Ratio and Surface Defects on the Photocatalytic Activity of ZnO Nanorods. *Sci. Rep.* **2014**, *4*, 4–11. [CrossRef]
103. Ding, C.; Zhang, Y.; Liu, F.; Kitabatake, Y.; Hayase, S.; Toyoda, T.; Wang, R.; Yoshino, K.; Minemoto, T.; Shen, Q. Understanding Charge Transfer and Recombination by Interface Engineering for Improving the Efficiency of PbS Quantum Dot Solar Cells. *Nanoscale Horizons* **2018**, *3*, 417–429. [CrossRef]
104. Zhang, Y.; Ozu, S.; Wu, G.; Ding, C.; Liu, F.; Liu, D.; Minemoto, T.; Masuda, T.; Hayase, S.; Toyoda, T.; et al. In-Depth Exploration of the Charge Dynamics in Surface-Passivated ZnO Nanowires. *J. Phys. Chem. C* **2020**, *124*, 15812–15817. [CrossRef]
105. Tam, K.H.; Cheung, C.K.; Leung, Y.H.; Djuris, A.B.; Fung, S.; Kwok, W.M.; Chan, W.K.; Phillips, D.L.; Ding, L.; Ge, W.K. Defects in ZnO Nanorods Prepared by a Hydrothermal Method. *J. Phys. Chem. B* **2006**, *110*, 20865–20871. [CrossRef]
106. Xu, S.; Cheng, C.; Guo, W.; He, Y.; Huang, R.; Du, S.; Wang, N. Tuning the Optical and Electrical Properties of Hydrothermally Grown ZnO Nanowires by Sealed Post Annealing Treatment. *Solid State Commun.* **2013**, *160*, 41–46. [CrossRef]
107. Kim, W.; Kwak, G.; Jung, M.; Jo, S.K.; Miller, J.B.; Gellman, A.J.; Yong, K. Surface and Internal Reactions of ZnO Nanowires: Etching and Bulk Defect Passivation by H Atoms. *J. Phys. Chem. C* **2012**, *116*, 16093–16097. [CrossRef]
108. Xing, M.; Wei, Y.; Wang, R.; Zhang, Z. Study on the Performance of ZMO/PbS Quantum Dot Heterojunction Solar Cells. *Sol. Energy* **2021**, *213*, 53–58. [CrossRef]
109. Chen, Q.; Ding, H.; Wu, Y.; Sui, M.; Lu, W.; Wang, B.; Su, W.; Cui, Z.; Chen, L. Passivation of Surface States in the ZnO Nanowire with Thermally Evaporated Copper Phthalocyanine for Hybrid Photodetectors. *Nanoscale* **2013**, *5*, 4162–4165. [CrossRef]
110. Albaladejo-Siguan, M.; Baird, E.C.; Becker-Koch, D.; Li, Y.; Rogach, A.L.; Vaynzof, Y. Stability of Quantum Dot Solar Cells: A Matter of (Life)Time. *Adv. Energy Mater.* **2021**, *11*, 2003457. [CrossRef]

nanomaterials

MDPI

Article

Encapsulating Metal-Organic-Framework Derived Nanocages into a Microcapsule for Shuttle Effect-Suppressive Lithium-Sulfur Batteries

Jinyun Liu [1,*,†], Yajun Zhu [1,†], Junfei Cai [2,†], Yan Zhong [1], Tianli Han [1], Zhonghua Chen [3,*] and Jinjin Li [2,*]

[1] Anhui Provincial Engineering Laboratory for New-Energy Vehicle Battery Energy-Storage Materials, College of Chemistry and Materials Science, Anhui Normal University, Wuhu 241002, China; yjzhu@ahnu.edu.cn (Y.Z.); yanzhong@ahnu.edu.cn (Y.Z.); hantianli@ahnu.edu.cn (T.H.)
[2] National Key Laboratory of Science and Technology on Micro/Nano Fabrication, Department of Micro/Nano-Electronics, Shanghai Jiao Tong University, Shanghai 200240, China; caijf001@sjtu.edu.cn
[3] Shenzhen FBTech Electronics Ltd., Shenzhen 518100, China
* Correspondence: jyliu@ahnu.edu.cn (J.L.); chenzhonghua@fbwtt.com (Z.C.); lijinjin@sjtu.edu.cn (J.L.)
† These authors contributed equally to this work.

Abstract: Long-term stable secondary batteries are highly required. Here, we report a unique microcapsule encapsulated with metal organic frameworks (MOFs)-derived Co_3O_4 nanocages for a Li-S battery, which displays good lithium-storage properties. ZIF-67 dodecahedra are prepared at room temperature then converted to porous Co_3O_4 nanocages, which are infilled into microcapsules through a microfluidic technique. After loading sulfur, the Co_3O_4/S-infilled microcapsules are obtained, which display a specific capacity of 935 mAh g^{-1} after 200 cycles at 0.5C in Li-S batteries. A Coulombic efficiency of about 100% is achieved. The constructed Li-S battery possesses a high rate-performance during three rounds of cycling. Moreover, stable performance is verified under both high and low temperatures of 50 °C and −10 °C. Density functional theory calculations show that the Co_3O_4 dodecahedra display large binding energies with polysulfides, which are able to suppress shuttle effect of polysulfides and enable a stable electrochemical performance.

Keywords: secondary battery; nanocomposite; microcapsule; capacity; stability

Citation: Liu, J.; Zhu, Y.; Cai, J.; Zhong, Y.; Han, T.; Chen, Z.; Li, J. Encapsulating Metal-Organic-Framework Derived Nanocages into a Microcapsule for Shuttle Effect-Suppressive Lithium-Sulfur Batteries. *Nanomaterials* **2022**, *12*, 236. https://doi.org/10.3390/nano12020236

Academic Editor: Christophe Detavernier

Received: 27 November 2021
Accepted: 10 January 2022
Published: 12 January 2022

1. Introduction

Recently, the demands for electric vehicles and portable electronics have been rapidly increasing. Considering this, investigations on secondary batteries are considered to be a significant direction. People are expecting higher capacity, longer cycling life, and faster charging of secondary batteries. As a promising next-generation secondary battery, the Li-S battery possesses a high theoretical energy density (2600 Wh kg^{-1}) and low cost of sulfur [1–4]. Recently, the research on Li-S batteries has been considered to be a significant field [5,6]. There are many problems for currently available Li-S batteries, such as the volumetric change of sulfur and shuttle effect reducing the electrochemical performance, which represent obstacles to commercialization [7].

In order to address those issues, many studies have been reported, in which the synthesis of yolk-shell structure hosts is considered to be a potential strategy [8–10]. Zhang et al. reported a yolk-shell ZnO by using a hydrothermal method, which provided a specific capacity of 1406 mAh g^{-1} at 0.1C [11]. Jiang et al. synthesized a yolk-shell nanomaterial consisting of SiO_2 core and carbon shell [12]. The cathode based on the yolk-shell SiO_2-carbon delivered 1200 mAh g^{-1} at a rate of 0.2C. Those achievements indicate that several yolk-shell structures exhibit enhanced adsorption towards polysulfides [13,14]. Reasonable engineering yolk-shell structure as sulfur host could promisingly improve the energy-storage properties [15,16]. However, general and simple preparation approaches for large-

scale yolk-shell materials are still highly required. In addition, several reports indicated that typical semiconductor Co_3O_4 is a promising sulfur host because of its strong interaction with sulfur and polysulfides [17–20]. With this in mind, developing creative Co_3O_4-based composite for Li-S batteries is attractive and would be of great significance [21–23].

Here, we present a microcapsule infilling by a metal–organic framework (MOF)-derived cobalt oxide nanocage as the sulfur host, which displays a high electrochemical performance. By using ZIF-67 as a precursor which was prepared through a hydrothermal approach, a porous dodecahedral Co_3O_4 nanocage was obtained (Figure 1). The experimental procedures are presented in the Supplementary Material. Then, Co_3O_4 nanocages were encapsulated into microcapsules through a microfluidic strategy. The real-time process of the cone and the formation of drops are displayed by Movie S1 and S2, respectively. The prepared microcapsules were carbonized for use as a sulfur host, which showed a long life of 200 cycles, along with a stable specific capacity of 935 mAh g^{-1} and a 100% Coulombic efficiency. After repeated tests, it displays a stable rate-performance, and the battery remains stable at −10 °C and 50 °C. Furthermore, density functional theory (DFT) calculations show that Co_3O_4 possesses large binding energies towards polysulfides, which are important for reducing the shuttle effect and enabling a stable electrochemical performance.

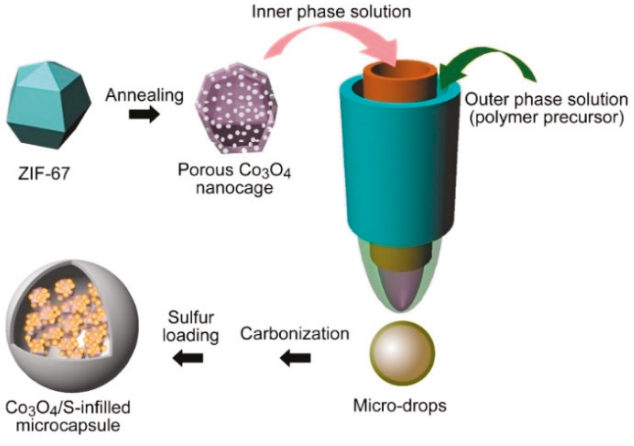

Figure 1. Microfluidic preparation of Co_3O_4/S-infilled microcapsules.

2. Results and Discussion

2.1. Structural and Microstructural Characterization

SEM image (Figure 2a) of ZIF-67 precursor shows a dodecahedron morphology with a size of 500 nm. Figure 2b shows the SEM image of porous dodecahedral Co_3O_4 obtained after annealing the precursor. The TEM image (Figure 2c) displays the porous Co_3O_4 nanocage clearly. The dodecahedral Co_3O_4 was encapsulated in microcapsule by using a coaxial focusing method. Figure 2d shows the SEM image of microcapsules with a size of about 50 μm. The microcapsule was observed by using an optical microscope (Figure 2e), and it is verified the Co_3O_4 uniformly distributes in the microcapsule. An SEM image of Co_3O_4-infilled microcapsules after annealing is shown in Figure 2f. A TEM image (Figure 2g) presents the edge of the microcapsule. It is observed that the shell of the microcapsule is very thin after calcination. After the microcapsules were broken manually, dodecahedral Co_3O_4 nanocages inside the microcapsule were observed clearly in Figure 2h,i. Figure 2j displays the microcapsules after loading sulfur, forming a Co_3O_4/S-infilled microcapsule structure. The surface become rough, which indicates that some of the sulfur was coated on microcapsules.

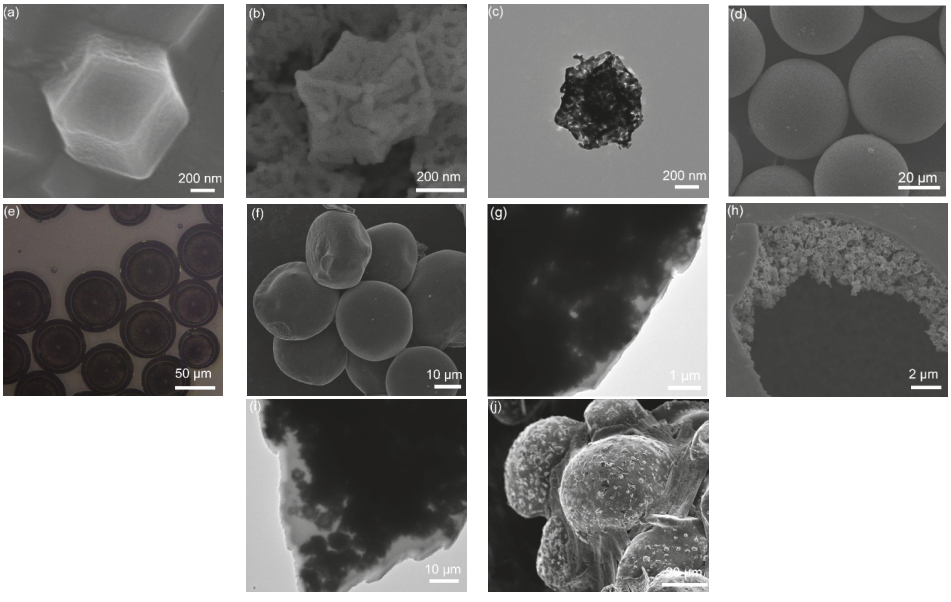

Figure 2. SEM photographs of (**a**) ZIF-67 and (**b**) dodecahedral Co_3O_4 nanocage. (**c**) TEM image of Co_3O_4. (**d**) SEM and (**e**) optical photographs of Co_3O_4-infilled microcapsules before carbonization. (**f**) SEM and (**g**) TEM images of carbonized microcapsules. (**h**) SEM and (**i**) TEM photographs of Co_3O_4-infilled microcapsule after breaking manually. (**j**) SEM image of microcapsules after loading sulfur.

The XRD pattern (Figure 3) is assigned to Co_3O_4 in terms of JCPDS card No. 42-1467, while the other peaks are attributed to sulfur (JCPDS card No. 99-0066). The signal of Co_3O_4 becomes unobvious after loading sulfur, which would be ascribed to the cover of sulfur signals. Figure S1 displays the HRTEM image of the porous Co_3O_4. The Co_3O_4 obtained after annealing ZIF-67 precursor exhibits a good crystallinity. The 0.28 nm lattice spacing matches the (220) crystalline plane, while the SAED pattern displays several diffraction rings, indicating a polycrystalline structure [24].

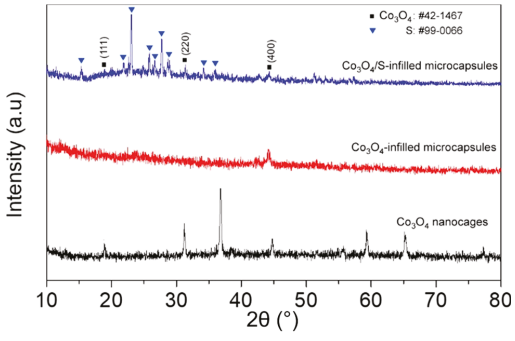

Figure 3. XRD patterns of the pristine Co_3O_4 nanocages and the capsules infilled with Co_3O_4 or Co_3O_4/S composite.

The composition and chemical states of the microcapsules are presented in the XPS spectra (Figure 4). The peak at 285 eV is from C1s, and the ones at 530 and 790 eV are ascribed to the O1s and Co2p, respectively, as shown in Figure 4a. The C 1s spectrum

(Figure 4b) shows two peaks, where the one at 284.6 eV is indexed to graphite carbon. Moreover, peak at 285.9 eV represents C=O [17]. O 1s spectrum (Figure 4c) exhibits three peaks at 530 eV, 532.2, and 533.5 eV, corresponding to lattice oxygen, -OH and H_2O molecules, respectively [25–27]. The Co 2P spectrum (Figure 4d) shows 781.0 and 799 eV of Co^{2+} [28], and 778.7 and 796.6 eV peaks are from Co^{3+} [29,30].

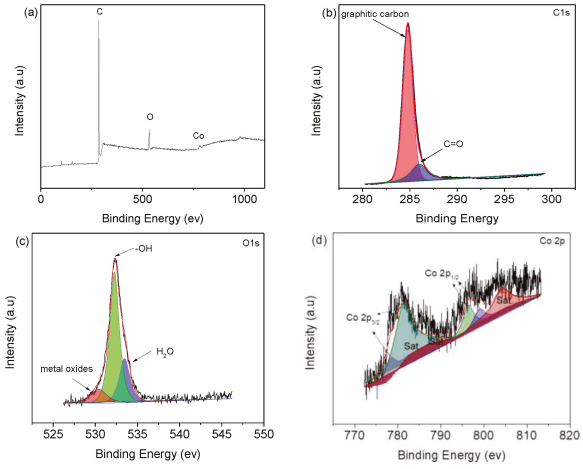

Figure 4. (**a**) XPS survey spectrum of Co_3O_4-infilled microcapsules. XPS spectra of (**b**) C 1s, (**c**) O 1s, and (**d**) Co 2p.

The elemental distribution of Co_3O_4-infilled microcapsules is shown in Figure 5. The elements C, Co, and O evenly distribute. In Figure 5e, the EDS spectrum shows that the composition of Co_3O_4 includes C, Co, and O [31], which has a high purity. Figure 6a presents the TGA curves of Co_3O_4-infilled microcapsules measured in air. The mass loss from 350 °C to 480 °C is caused by the decomposition of the carbon shell. The drop from 250 to 350 °C is attributed to sulfur evaporation [32,33]. The sulfur in the microcapsules is about 85 wt%, which is significant for a high-sulfur loading. Moreover, pure Co_3O_4-infilled microcapsules show that the content of Co_3O_4 nanocages is about 35 wt%. Figure 6b shows the Raman spectra of the Co_3O_4-infilled microcapsules with and without loading sulfur. The D- and G-bands of carbon locate at 1370 and 1670 cm^{-1}, respectively. In sulfur-loaded microcapsules, the peaks ranging from 150 to 475 cm^{-1} are assigned to sulfur.

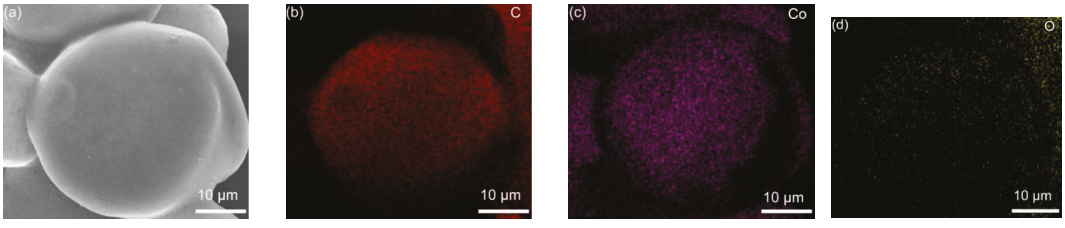

Figure 5. (**a**) SEM and (**b**–**d**) mapping images of the Co_3O_4-infilled microcapsules. (**e**) Related EDS spectrum.

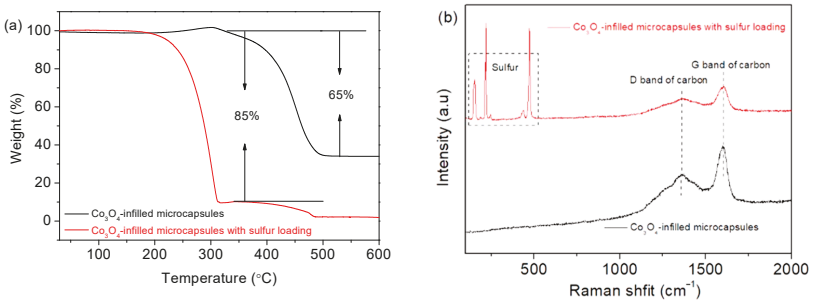

Figure 6. (**a**) TGA profiles and (**b**) Raman spectra of Co_3O_4-infilled microcapsules with and without loading sulfur.

2.2. Electrochemical Characterization

Figure 7a displays the CV curves. During the discharge, two reduction peaks at 2.25 and 1.95 V are attributed to the conversion of high-order polysulfide to Li_2S_4 and reduction of Li_2S_4 to Li_2S_2/Li_2S [34,35]. In the charging process, the oxidation at 2.4 V is ascribed to the conversion of Li_2S_2/Li_2S to Li_2S_n [36]. In Figure 7b, two discharge plateaus at 2.2 and 1.9 V are verified. The platform at 2.4 V in charge corresponds to oxidation peak [37]. It is noted that the overpotentials are observed, which may be attributed to the non-completed carbonization and the resulting limited conductivity. Figure 7c shows that the specific capacity remains 935 mAh g^{-1} after cycling 200 times at 0.5C (1C equates to fully charging or discharging the theoretical capacity in 1 h). The Coulombic efficiency is close to 100%. Compared to the performance of the Co_3O_4/S-infilled microcapsules, the capacity of pure sulfur powders is very low. In particular, the capacity decays rapidly after 150 cycles. In addition, the electrochemical performance of the microcapsules is also competitive compared to some other composites, as displayed in Table 1. Figure 7d shows the rate performance after repeated tests. In the second round, specific capacities are 1250, 1150, 860, and 500 mAh g^{-1} at rates of 0.1C, 0.2C, 0.5C, and 1C, respectively. It recovers to 1190 mAh g^{-1} once the rate is returned to 0.1C. Microcapsules exhibit a better reversibility and higher capacities than sulfur powders. It is attributed to the improved conductivity by the carbon shell and the reduced polysulfide loss by Co_3O_4 adsorption, which will be demonstrated by DFT calculations.

The Co_3O_4/S-infilled microcapsules-based Li-S battery also displays good cycling stability under different temperatures. Figure 8a shows that the capacity remains at 647 mAh g^{-1} after cycling 200 times under −10 °C. Besides cycling at a low temperature, the electrochemical performance at 50 °C is presented in Figure 8b, showing a specific capacity of 713 mAh g^{-1} after 200 cycles. Stable performance indicates that microcapsules can be used in different conditions, which are significant for practical applications.

Figure 9a displays CV curves of Co_3O_4/S-infilled microcapsules at 0.6 to 1 mV s^{-1}; Figure 9b displays a logarithmic relationship according to $i = av^b$, where i and v stand for the peak current and rate, respectively [49]. The b value of 0.5 represents a diffusive-controlled process, and b = 1 indicates a capacitive behavior. In this investigation, b values suggest mainly diffusion-controlled processes. Figure 9c shows the diffusion contribution ratios calculated on the basis of $i(v) = k_1v + k_2v^{1/2}$, where k_1v and $k_2v^{1/2}$ stand for capacitive and diffusion-controlled contributions, respectively. The results were fitted (Figure 9d) based on $I_P = 2.69 \times 10^5 \times n^{3/2}AD^{1/2}Cv^{1/2}$ [50], where I_p is the peak current; n is the number of electrons transferred during the reaction, which is 2 for Li-S batteries; A is the active electrode area (1.13 cm^2); D is the diffusion coefficient of lithium ion in unit of cm^2 s^{-1}; C is the concentration of Li ions in electrolyte in unit of mol mL^{-1} [51,52]; and n is the scanning rate in the unit of V s^{-1}. On the basis of the obtained slopes, the Li ion diffusion coefficients are calculated to be 3.8×10^{-9} and 1.8×10^{-9} cm^2 s^{-1}, which are close to some reports [53,54]. The good diffusion property is ascribed to the specific microcapsule

structure, which enables a good environment for contact with electrolytes; the porous scaffold of Co_3O_4 nanocages assembled by nanoparticles shortens the transfer pathway of ions.

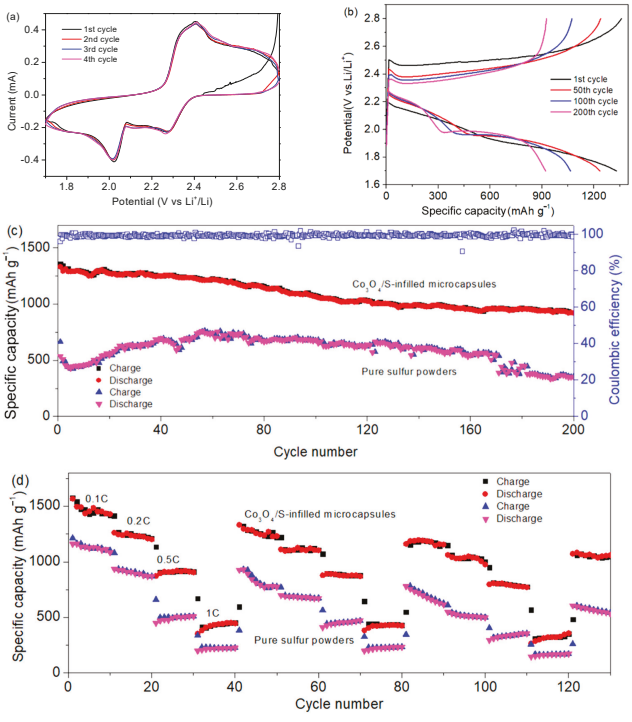

Figure 7. (**a**) CV curves of Co_3O_4/S-infilled microcapsules-based Li-S battery scanning at a rate of 0.1 mV s^{-1}. (**b**) Cycling curves at 0.5C. (**c**) Cycling performance at a rate of 0.5C. (**d**) Rate-performance of different samples.

Table 1. Comparison on the electrochemical performance of some composite-based cathodes.

Composite	Preparation Method	Cycling Rate	Cycle Number	Specific Capacity (mAh g^{-1})	Ref.
TiO_2@Co_3O_4/S nanospheres	Water bath	0.1C	100	817	[38]
Co_3O_4 powders/S	Hydrothermal method	0.1C	100	706	[39]
Co_3O_4 -CoN/CC	Hydrothermal method	3C	500	627	[40]
Co_3O_4/CoO/GNS/h-BN/S	Ball-milling	1C	250	356	[41]
S@Co_3O_4/C	Hydrothermal method	1C	500	520	[42]
Nano S/rGO	High pressure steam	5C	100	639	[43]
$NiCo_2S_4$@S	Hydrotherma method	0.5C	500	836	[44]
Yttria hollow spheres@C/S	Hydrothermal method	0.5C	200	842	[45]
Mo@N-G/S	Hydrothermal method	1C	500	615	[46]
S@N-Ta_2O_5/rGO	Co-precipitation	2C	600	825	[47]
S@MnO_2@SnO_2	Hydrothermal method	0.5C	500	566	[48]
Co_3O_4/S-infilled microcapsules	Microfluidic approach	0.5C	200	935	This work

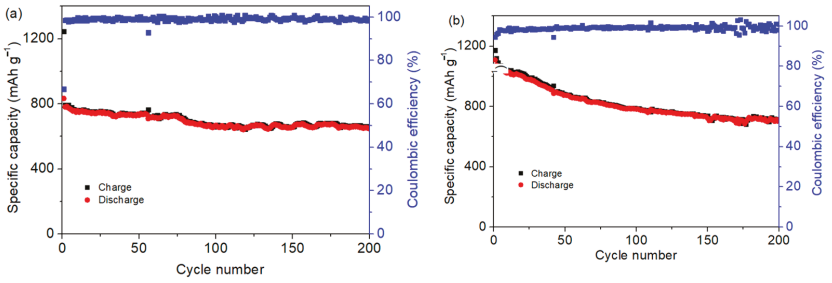

Figure 8. Specific capacities of Co_3O_4/S-infilled microcapsules when cycling at different temperatures of (**a**) −10 °C and (**b**) 50 °C at 0.5C.

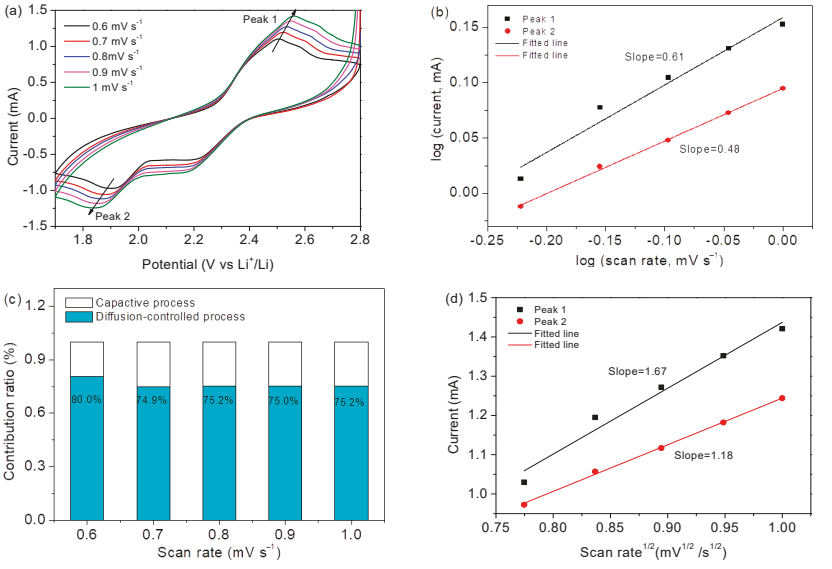

Figure 9. (**a**) CV profiles of the Co_3O_4/S-infilled microcapsules. (**b**) Relationship of log(*v*) vs log(*i*). (**c**) Contribution ratios. (**d**) Relationship of peak current vs. rate.

2.3. DFT Calculations

The binding of the Co_3O_4 with polysulfides was investigated by using DFT calculation on the adsorption energies. All calculations were conducted by using a Vienna Ab initio Simulation Package. In Figure 10, a series of surface adsorptions of Co_3O_4 towards the polysulfides (Li_2S, Li_2S_2, Li_2S_4, Li_2S_6, Li_2S_8) are presented. According to previous research [55–57], the (110) lattice plane in the Co_3O_4 is more prone to exposure due to the presence of Co^{3+} on the surface. Therefore, we focused on the adsorption energy of the polysulfides on the Co_3O_4 (110) surface. The side and top views of the geometric configurations of Co_3O_4 (110) surface are shown in Figure 10a. Then, the adsorption models were built up for the calculation of adsorption energy, which is shown in Figure 11. Figure 10b shows the surface adsorption energies toward the polysulfides, where the surface adsorption energies of the Co_3O_4 toward Li_2S, Li_2S_2, Li_2S_4, Li_2S_6, Li_2S_8 are 3.8, 4.0, 1.7, 3.1, and 3.5 eV, respectively, indicating a good adsorption capability of Co_3O_4 towards polysulfides. Figure 10c displays the charge density difference of the adsorption models. The distribution of the charge density connects polysulfides and Co_3O_4, indicating an electron transfer between

Co_3O_4 (110) surface and polysulfides. The charge density between polysulfides and Co_3O_4 illustrates the formation of bonds and further verifies the adsorption stability.

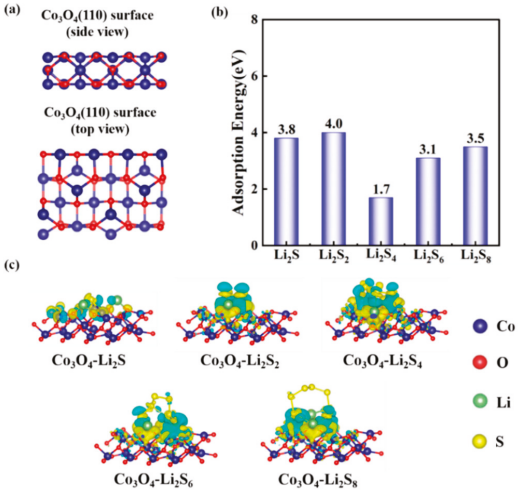

Figure 10. (**a**) Side and top views of the geometric configurations of Co_3O_4 (110) surface. (**b**) Surface adsorption energies towards polysulfides. (**c**) Electron density differences of the polysulfides (Li_2S, Li_2S_2, Li_2S_4, Li_2S_6, Li_2S_8).

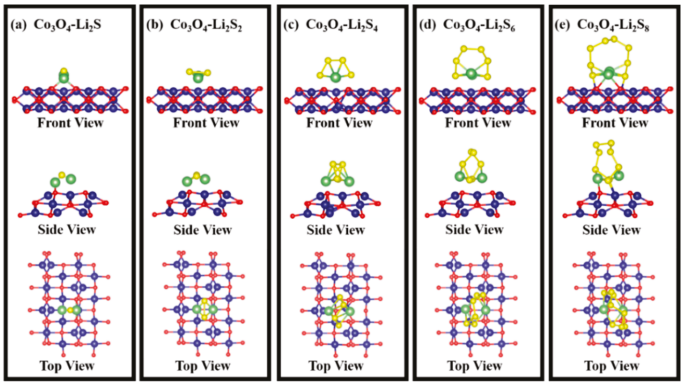

Figure 11. Adsorption models between polysulfides and Co_3O_4 (110) surface: (**a**) Co_3O_4-Li_2S; (**b**) Co_3O_4-Li_2S_2; (**c**) Co_3O_4-Li_2S_4; (**d**) Co_3O_4-Li_2S_6; (**e**) Co_3O_4-Li_2S_8.

3. Conclusions

In summary, a novel microcapsule system encapsulated with MOFs-derived Co_3O_4/S nanocages is developed, which displays a good electrochemical performance as a Li-S battery cathode. Dodecahedral ZIF-67 was synthesized, then it was converted to a porous Co_3O_4 nanocage which was infilled into a microcapsule through a microfluidic strategy. After 200 cycles at 0.5C, the specific capacity of Co_3O_4/S-infilled microcapsules remains 935 mAh g^{-1}. The Coulombic efficiency is about 100%. The constructed battery also shows a stable rate-performance, while good capacities are also achieved under both high and low temperatures of 50 °C and −10 °C. In addition, DFT calculations verify that the Co_3O_4 displays large binding energies towards all polysulfides including Li_2S, Li_2S_2, Li_2S_4, Li_2S_6, and Li_2S_8, reducing the loss of polysulfides. It is expected that the developed

microcapsule system and the high performance will be applicable for engineering other emerging Li-storage nanomaterials.

Supplementary Materials: The following supporting information can be downloaded at: https://www.mdpi.com/article/10.3390/nano12020236/s1, Figure S1: (a) HRTEM image and (b) selective area electron diffraction (SAED) pattern of the porous Co_3O_4. Movie S1: Real-time process of the cone. Movie S2: Formation of drops.

Author Contributions: Conceptualization, J.L. (Jinyun Liu); methodology, J.L. (Jinyun Liu); software, J.C. and J.L. (Jinjin Li); validation, Y.Z. (Yajun Zhu), Y.Z. (Yan Zhong) and T.H.; formal analysis, J.L. (Jinyun Liu), Y.Z. (Yan Zhong) and Z.C.; investigation, Y.Z. (Yajun Zhu); resources, J.C. and Z.C.; data curation, Y.Z. (Yan Zhong); writing—original draft preparation, J.L. (Jinyun Liu) and Y.Z. (Yajun Zhu); writing—review and editing, J.L. (Jinyun Liu), Z.C. and J.L. (Jinjin Li); visualization, Y.Z. (Yan Zhong); supervision, J.L. (Jinyun Liu) and J.L. (Jinjin Li); project administration, J.L. (Jinyun Liu); funding acquisition, J.L. (Jinyun Liu) and J.L. (Jinjin Li). All authors have read and agreed to the published version of the manuscript.

Funding: This research was funded by Key Research and Development Program of Wuhu, grant number 2019YF07; Natural Science Research Project for Universities in Anhui Province, grant numbers KJ2018ZD034 and KJ2019A0502; National Key R&D Program of China, grant number 2021YFC2100100, National Natural Science Foundation of China, grant number 21901157, Shanghai Science and Technology Project of China, grant number 21JC1403400, University Synergy Innovation Program of Anhui Province, grant number GXXT-2020-073; and Foundation of Anhui Laboratory of Molecule-Based Materials, grant number FZJ21012. The APC was funded by Natural Science Research Project for Universities in Anhui Province.

Institutional Review Board Statement: Not applicable.

Informed Consent Statement: Not applicable.

Data Availability Statement: Data sharing not applicable.

Conflicts of Interest: The authors declare no conflict of interest.

References

1. Yang, J.; Wang, J.; Dong, X.; Zhu, L.; Hou, D.; Zeng, W.; Wang, J. The potential application of VS_2 as an electrode material for Mg ion battery: A DFT study. *Appl. Surf. Sci.* **2021**, *544*, 148775. [CrossRef]
2. Bella, F.; De Luca, S.; Fagiolari, L.; Versaci, D.; Amici, J.; Francia, C.; Bodoardo, S. An overview on anodes for magnesium batteries: Challenges towards a promising storage solution for renewables. *Nanomaterials* **2021**, *11*, 810. [CrossRef]
3. Narumoto, N.; Okamoto, N.; Saito, T. Surface structure control and charge/discharge characteristics of bismuth anode materials by electrodeposition for magnesium-ion batteries. *J. Mater. Sci.* **2021**, *32*, 9990–9997.
4. Shah, R.; Mittal, V.; Matsil, E.; Rosenkranz, A. Magnesium-ion batteries for electric vehicles: Current trends and future perspectives. *Adv. Mech. Eng.* **2021**, *13*, 16878140211003398. [CrossRef]
5. Zhang, X.; Xie, H.; Kim, C.; Zaghib, K.; Mauger, A.; Julien, C. Advances in lithium-sulfur batteries. *Sci. Eng. R* **2017**, *121*, 1–29. [CrossRef]
6. Zhang, W.; Li, Y.; Lv, T.; Liu, W.; Luo, Y.; Guo, R.; Pei, H.; Lai, C.; Xie, J. Ti_3C_2/CNTs Macroporous conductive network boosts $Li_4Ti_5O_{12}$-TiO_2 anode performance for practical Li ion and Mg ion batteries. *J. Electrochem. Soc.* **2021**, *168*, 030505. [CrossRef]
7. Lin, X.; Liu, J.; Zhang, H.; Zhong, Y.; Zhu, M.; Zhou, T.; Qiao, X.; Zhang, H.; Han, T.; Li, J. General liquid-driven coaxial flow focusing preparation of novel microcapsules for rechargeable magnesium batteries. *Adv. Sci.* **2021**, *8*, 2002298. [CrossRef]
8. Zuo, C.; Tang, W.; Lan, B.; Xiong, F.; Tang, H.; Dong, S.; Zhang, W.; Tang, C.; Li, J.; Ruan, Y.; et al. Unexpected discovery of magnesium-vanadium spinel oxide containing extractable Mg^{2+} as a high-capacity cathode material for magnesium ion batteries. *Chem. Eng. J.* **2021**, *405*, 127005. [CrossRef]
9. Du, C.; Younas, W.; Wang, Z.; Yang, X.; Meng, E.; Wang, L.; Huang, J.; Ma, X.; Zhu, Y.; Cao, C. Constructing sheet-assembled hollow CuSe nanocubes to boost the rate capability of rechargeable magnesium batteries. *J. Mater. Chem. A* **2021**, *9*, 3648–3656. [CrossRef]
10. Xue, X.; Chen, R.; Song, X.; Tao, A.; Yan, W.; Kong, W.; Jin, Z. Electrochemical Mg^{2+} displacement driven reversible copper extrusion/intrusion reactions for high-rate rechargeable magnesium batteries. *Adv. Funct. Mater.* **2021**, *31*, 2009394. [CrossRef]
11. Shen, K.; Zhang, Z.; Wang, S.; Ru, Q.; Zhao, L.; Sun, L.; Hou, X.; Chen, F. Cucumber-shaped construction combining bismuth nanoparticles with carbon nanofiber networks as a binder-free and freestanding anode for Li-ion batteries. *Energy Fuels* **2020**, *34*, 8987–8992. [CrossRef]

12. Tao, X.; Zhang, J.; Xia, Y.; Huang, H.; Du, J.; Xiao, H.; Zhang, W.; Gan, Y. Bio-inspired fabrication of carbon nanotiles for high performance cathode of Li–S batteries. *J. Mater. Chem. A* **2014**, *2*, 2290–2296. [CrossRef]
13. Zuo, C.; Xiao, Y.; Pan, X.; Xiong, F.; Zhang, W.; Long, J.; Dong, S.; An, Q.; Luo, P. Organic-inorganic superlattices of vanadium oxide@polyaniline for high-performance magnesium-ion batteries. *ChemSusChem* **2021**, *14*, 2093–2099. [CrossRef]
14. Sopha, H.; Tesfaye, A.T.; Zazpe, R.; Michalicka, J.; Dvorak, F.; Hromadko, L.; Krbal, M.; Prikryl, J.; Djenizian, T.; Macak, J.M. ALD growth of MoS_2 nanosheets on TiO_2 nanotube supports. *FlatChem* **2019**, *17*, 100130. [CrossRef]
15. Panwar, V.; Jain, S.L. Ternary hybrid TiO_2-PANI-AuNPs for photocatalytic A3-coupling of aldehydes, amines and alkynes: First photochemical synthesis of propargyl amines. *Mater. Sci. Eng. C* **2019**, *99*, 191–201. [CrossRef] [PubMed]
16. Wang, S.; Liu, F.; Gao, C.; Wan, T.; Wang, L.; Wang, L.; Wang, L. Enhancement of the thermoelectric property of nanostructured polyaniline/carbon nanotube composites by introducing pyrrole unit onto polyaniline backbone via a sustainable method. *Chem. Eng. J.* **2019**, *370*, 322–329. [CrossRef]
17. Chen, Y.; Ji, X. Bamboo-like Co_3O_4 nanofiber as host materials for enhanced lithium-sulfur battery performance. *J. Alloys Compd.* **2019**, *777*, 688–692. [CrossRef]
18. Bosubabu, D.; Sivaraj, J.; Gurunathan, P.; Ramesha, K. Hollow Co_3O_4 microspheres grafted with nitrogen-doped carbon nanotubes as efficient sulfur host for high performing lithium-sulfur batteries. *Energy Fuels* **2020**, *34*, 16810–16818. [CrossRef]
19. Wang, P.; Zeng, R.; You, L.; Tang, H.; Zhong, J.; Wang, S.; Yang, T. Graphene-like matrix composites with Fe_2O_3 and Co_3O_4 as cathode materials for lithium-sulfur batteries. *ACS Appl. Nano Mater.* **2020**, *3*, 1382–1390. [CrossRef]
20. Saroha, R.; Oh, J.H.; Lee, J.S.; Kang, Y.C.; Jeong, S.M.; Kang, D.W.; Cho, C.; Cho, J.S. Hierarchically porous nanofibers comprising multiple core-shell Co_3O_4@graphitic carbon nanoparticles grafted within N-doped CNTs as functional interlayers for excellent Li-S batteries. *Chem. Eng. J.* **2021**, *426*, 130805. [CrossRef]
21. Wang, S.; Hou, X.; Zhong, Z.; Shen, K.; Zhang, G.; Yao, L.; Chen, F. Co_3O_4-NP embedded mesoporous carbon rod with enhanced electrocatalytic conversion in lithium-sulfur battery. *Sci. Rep.* **2018**, *8*, 16133. [CrossRef]
22. Xu, J.; Su, D.; Wang, G. Co_3O_4-carbon cloth free standing cathode for lithium sulfur battery. *IOP Conf. Ser. Mater. Sci. Eng.* **2017**, *222*, 012013. [CrossRef]
23. Cheng, H.; Wang, S.; Tao, D.; Wang, M. Sulfur/Co_3O_4 nanotube composite with high performances as cathode materials for lithium sulfur batteries. *Funct. Mater. Lett.* **2014**, *7*, 1450020. [CrossRef]
24. Zhang, K.; Xu, Y.; Lu, Y.; Zhu, Y.; Qian, Y.; Wang, D.; Zhou, J.; Lin, N.; Qian, Y. A graphene oxide-wrapped bipyramidal sulfur@polyaniline core–shell structure as a cathode for Li–S batteries with enhanced electrochemical performance. *J. Mater. Chem. A* **2016**, *4*, 6404–6410. [CrossRef]
25. Ali, M.; Guzman, R.C.; Cojocari, O.; Nellen, S.; Santamaría, G.; García-Munoz, L.E.; Segovia-Vargas, D.; Globisch, B.; Carpintero, G. Quasi-optic transmitter and receiver modules enabling next-Generation ultra-broadband wireless links at carrier-wave frequencies ranging from 60 to 180 GHz. *J. Infrared Millim. Terahertz Waves* **2019**, *40*, 688–695. [CrossRef]
26. Lv, C.; Li, S.; Che, Y.; Chen, H.; Shu, Y.; He, J.; Song, J. Study on the molybdenum electro-extraction from MoS_2 in the molten salt. *Sep. Purif. Technol.* **2021**, *258*, 118048. [CrossRef]
27. Tian, Y.; Zhou, M.; Pan, Y.; Du, X.; Wang, Q. MoS_2 as highly efficient co-catalyst enhancing the performance of Fe^0 based electro-fenton process in degradation of sulfamethazine: Approach and mechanism. *Chem. Eng. J.* **2021**, *403*, 126361. [CrossRef]
28. Wang, Z.; Zhang, J.; Wen, T.; Liu, X.; Wang, Y.; Yang, H.; Sun, J.; Feng, J.; Dong, S.; Sun, J. Highly effective remediation of Pb(II) and Hg(II) contaminated wastewater and soil by flower-like magnetic MoS_2 nanohybrid. *Sci. Total Environ.* **2020**, *699*, 134341. [CrossRef] [PubMed]
29. Wu, J.C.; Chen, S.S.; Yu, T.-C.; Wu, K.C.W.; Hou, C.H. Effective electrochemically controlled removal of fluoride ions using electrodeposited polyaniline-carbon nanotube composite electrodes. *Sep. Purif. Technol.* **2021**, *254*, 117561. [CrossRef]
30. Huang, Z.; Shi, L.; Muhammad, Y.; Li, L. Effect of ionic liquid assisted hydrothermal carbonization on the properties and gasification reactivity of hydrochar derived from eucalyptus. *J. Colloid Interface Sci.* **2021**, *586*, 423–432. [CrossRef]
31. Xu, K.; Liao, N.; Zhang, M.; Xue, W. Atomic-scale investigation of enhanced lithium, sodium and magnesium storage performance from defects in MoS_2/graphene heterostructures. *Nanoscale* **2020**, *12*, 7098–7108. [CrossRef] [PubMed]
32. Parra-Arciniega, S.M.; González-Juárez, E.; Hernández-Carrillo, R.A.; Briones-Martínez, R.; Jiménez-Barrera, R.M.; Garcia-Gómez, N.A.; Sánchez, E.M. A Mg^{2+}/Li^+ hybrid-ion battery based on MoS_2 prepared by solvothermal synthesis with ionic liquid assistance. *J. Mater. Sci. Mater. Electron.* **2020**, *31*, 14702–14713. [CrossRef]
33. Cui, L.; Zhou, L.; Kang, Y.M.; An, Q. Recent advances in the rational design and synthesis of two-dimensional materials for multivalent ion batteries. *ChemSusChem* **2020**, *13*, 1071–1092. [CrossRef] [PubMed]
34. Duan, D.H.; Zhao, W.W.; Chen, K.X.; Wang, Y.F.; Liu, S.B.; Zhou, X.X.; Chen, L.; Li, Y. MOF-71 derived layered Co-CoP/C for advanced Li-S batteries. *J. Alloy. Compd.* **2021**, *886*, 161203. [CrossRef]
35. Pu, X.; Song, T.; Tang, L.; Tao, Y.; Cao, T.; Xu, Q.; Liu, H.; Wang, Y.; Xia, Y. Rose-like vanadium disulfide coated by hydrophilic hydroxyvanadium oxide with improved electrochemical performance as cathode material for aqueous zinc-ion batteries. *J. Power Sources* **2019**, *437*, 226917. [CrossRef]
36. Sihag, A.; Xie, Z.L.; Thang, H.V.; Kuo, C.L.; Tseng, F.G.; Dyer, M.S.; Chen, H.Y.T. DFT Insights into Comparative Hydrogen Adsorption and Hydrogen Spillover Mechanisms of Pt4/Graphene and Pt4/Anatase (101) Surfaces. *J. Phys. Chem. C* **2019**, *123*, 25618–25627. [CrossRef]

37. Li, Y.; Xu, D.; Zhang, D.; Wei, Y.; Zhang, R.; Guo, Y. Study on MnO_2/MXene–Ti_3C_2 composite materials as cathode materials for magnesium batteries. *RSC Adv.* **2019**, *9*, 33572–33577. [CrossRef]
38. Liu, Z.; Liu, B.; Guo, P.; Shang, X.; Lv, M.; Liu, D.; He, D. Enhanced electrochemical kinetics in lithium-sulfur batteries by using carbon nanofibers/manganese dioxide composite as a bifunctional coating on sulfur cathode. *Electrochim. Acta* **2018**, *28*, 180–187. [CrossRef]
39. Li, X.; Ma, Y.; Tang, C. Advanced Co_3O_4 interlayer as an efficient polysulfide barrier for high-performance Li-S batteries. *Int. J. Electrochem. Sci.* **2019**, *14*, 3245–3252.
40. Wang, J.; Xiao, K.; Ouyang, B.; Zhang, L.; Yang, H. Simultaneous immobilization and conversion of polysulfides on Co_3O_4-CoN heterostructured mediators toward high-performance lithium–sulfur batteries. *ACS Appl. Energy Mater.* **2019**, *2*, 2570–2578. [CrossRef]
41. Mussa, Y.; Arsalan, M.; Alsharaeh, E. Cobalt oxide/graphene nanosheets/hexagonal boron nitride (Co_3O_4/CoO/GNS/h-BN) catalyst for high sulfur utilization in Li−S batteries at elevated temperatures. *Energy Fuels* **2021**, *35*, 8365–8377. [CrossRef]
42. Zhou, L.; Li, H.; Wu, X.; Zhang, Y.; Danilov, D.; Eichel, R.; Notten, P. Double-shelled Co_3O_4/C nanocages enabling polysulfides adsorption for high-performance lithium-sulfur batteries. *ACS Appl. Energy Mater.* **2019**, *2*, 8153–8162. [CrossRef]
43. Li, Y.; Yao, C.; Wang, C.; Yang, P.; Wu, R.; Fei, L.; Zhang, Y.; Jiang, Y. An approach through steam to form sulfur nanoparticles for lithium sulfur batteries. *Electorchem. Commun.* **2021**, *125*, 107010. [CrossRef]
44. Liu, B.; Huang, S.; Kong, D.; Hu, J.; Yang, H. Bifunctional $NiCo_2S_4$ catalysts supported on a carbon textile interlayer for ultra-stable Li-S battery. *J. Mater. Chem. A* **2019**, *7*, 7604. [CrossRef]
45. Zeng, P.; Chen, M.; Luo, J.; Liu, H.; Li, Y.; Peng, J.; Li, J.; Yu, H. Carbon-coated yttria hollow spheres as both sulfur immobilizer and catalyst of polysulfides conversion in lithium-sulfur batteries. *ACS Appl. Mater. Interfaces* **2019**, *11*, 42104–42113. [CrossRef]
46. Liu, Y.; Chatterjee, A.; Rusch, P.; Wu, C.; Nan, P.; Peng, M. Monodisperse Molybdenum Nanoparticles as Highly Efficient Electrocatalysts for Li-S Batteries. *ACS Nano* **2021**, *15*, 15047–15056. [CrossRef]
47. Sun, D.; Zhou, J.; Rao, D.; Zhu, L.; Niu, S.; Cai, J.; Fang, Y. Regulating the electron filling state of d orbitals in Ta-based compounds for tunable lithium-sulfur chemistry. *Sustain Mater. Technol.* **2021**, *28*, e00271. [CrossRef]
48. Zhou, P.; Han, T.; Gu, C.; Li, J.; Shen, Z.; Zhang, H.; Niu, J. A novel wheel-confined composite as cathode in Li-S batteries with high capacity retention. *J. Alloy Compd.* **2019**, *776*, 504–510. [CrossRef]
49. Du, C.; Zhu, Y.; Wang, Z.; Wang, L.; Younas, W.; Ma, X.; Cao, C. Cuprous self-doping regulated mesoporous CuS nanotube cathode materials for rechargeable magnesium batteries. *ACS Appl. Mater. Interfaces* **2020**, *12*, 35035–35042. [CrossRef] [PubMed]
50. Zhang, Y.; Liu, G.; Zhang, C.; Chi, Q.; Zhang, T.; Feng, Y.; Zhu, K.; Zhang, Y.; Chen, Q.; Cao, D. Low-cost $MgFe_xMn_{2-x}O_4$ cathode materials for high-performance aqueous rechargeable magnesium-ion batteries. *Chem. Eng. J.* **2020**, *392*, 123652. [CrossRef]
51. Tao, X.; Wang, J.; Liu, C.; Wang, H.; Yao, H.; Zheng, G.; Seh, Z.; Cai, Q.; Li, W.; Zhou, G.; et al. Balancing surface adsorption and diffusion of lithium polysulfides on nonconductive oxides for lithium-sulfur battery design. *Nat. Commun.* **2016**, *7*, 11203. [CrossRef]
52. Zhu, P.; Zhu, J.; Zang, J.; Chen, C.; Lu, Y.; Jiang, M.; Yan, C.; Dirican, M.; Selvan, R.; Zhang, X. A novel bi-functional double-layer rGO-PVDF/PVDF composite nanofiber membrane separator with enhanced thermal stability and effective polysulfide inhibition for high-performance lithium-sulfur batteries. *J. Mater. Chem. A* **2017**, *5*, 15096–15104. [CrossRef]
53. Gao, G.; Zheng, F.; Wang, L. Solid 3D Li−S battery design via stacking 2D conductive microporous coordination polymers and amorphous Li−S layers. *Chem. Mater.* **2020**, *32*, 1974–1982. [CrossRef]
54. Wang, K.; Guan, Y.; Jin, Z.; Wang, W.; Wang, A. $Te_{0.045}S_{0.955}$ PAN composite with high average discharge voltage for Li-S battery. *J. Energy Chem.* **2019**, *39*, 249–255. [CrossRef]
55. Zhang, H.; Cao, D.; Bai, X. Ni-Doped magnesium manganese oxide as a cathode and its application in aqueous magnesium-ion batteries with high rate performance. *Inorg. Chem. Front.* **2020**, *7*, 2168–2177. [CrossRef]
56. Harudin, N.; Osman, Z.; Majid, S.R.; Othman, L.; Hambali, D.; Silva, M.M. Improved electrochemical properties of $MgMn_2O_4$ cathode materials by Sr doping for Mg ion cells. *Ionics* **2020**, *26*, 3947–3958. [CrossRef]
57. Asif, M.; Rashad, M.; Shah, J.H.; Zaidi, S.D.A. Surface modification of tin oxide through reduced graphene oxide as a highly efficient cathode material for magnesium-ion batteries. *J. Colloid Interface Sci.* **2020**, *561*, 818–828. [CrossRef]

nanomaterials

MDPI

Article

Relation between Charging Times and Storage Properties of Nanoporous Supercapacitors

Timur Aslyamov [1,*,†], Konstantin Sinkov [2,†] and Iskander Akhatov [1]

[1] Skolkovo Institute of Science and Technology, Bolshoy Boulevard 30, Bld. 1, 121205 Moscow, Russia; I.Akhatov@skoltech.ru
[2] Schlumberger Moscow Research, Leningradskoe Shosse 16A/3, 125171 Moscow, Russia; sinkovk@gmail.com
* Correspondence: t.aslyamov@skoltech.ru
† These authors contributed equally to this work.

Abstract: An optimal combination of power and energy characteristics is beneficial for the further progress of supercapacitors-based technologies. We develop a nanoscale dynamic electrolyte model, which describes both static capacitance and the time-dependent charging process, including the initial square-root dependency and two subsequent exponential trends. The observed charging time corresponds to one of the relaxation times of the exponential regimes and significantly depends on the pore size. Additionally, we find analytical expressions providing relations of the time scales to the electrode's parameters, applied potential, and the final state of the confined electrolyte. Our numerical results for the charging regimes agree with published computer simulations, and estimations of the charging times coincide with the experimental values.

Keywords: supercapacitors; nanoporous electrodes; charging time

Citation: Aslyamov, T.; Sinkov, K.; Akhatov, I. Relation between Charging Times and Storage Properties of Nanoporous Supercapacitors. *Nanomaterials* **2022**, *12*, 587. https://doi.org/10.3390/nano12040587

Academic Editors: Marc Cretin, Sophie Tingry and Zhenghua Tang

Received: 17 January 2022
Accepted: 4 February 2022
Published: 9 February 2022

1. Introduction

Among all modern energy sources, supercapacitors demonstrate an extraordinary power density and an extremely long cycling life [1]. Such rapid charging and discharging occur due to fast adsorption-electrostatic processes, making supercapacitor technology environmentally friendly. These advantages open up a wide range of possible applications from small devices [2] to electric cars [3]. However, the widespread use of supercapacitor technology is limited by their relatively low energy density [4]. The implementation of nanoporous electrodes led to a severe increase in energy density through a significant increase in capacitance, first experimentally observed in sub-nanoporous carbon materials [5]. Moreover, subsequent experiments showed that the pore size giving the highest capacitance corresponds to the diameter of the electrolyte molecules [6]. The capacitance's oscillatory behavior as a function of pore size has been successfully described in terms of the classical density functional theory (c-DFT) [7], accounting for confined properties of the charged hard spheres at an applied electrostatic potential. The state of the art c-DFT approach [8] allows one to investigate how the supercapacitor parameters, namely electrodes' pore sizes [9,10] and electrolyte composition [11–13], affect energy storage performance.

In spite of the long history of [14–16] studies of porous electrode charging, the vast majority of existing dynamic models correspond to meso- and macropores (pore size $H \geq 2\,\text{nm}$), where the properties of confined dilute electrolytes are similar to the bulk ones. In this case, the charging time is often estimated using the transmission line model (TLM), first proposed and thoroughly studied in Refs. [14–16]. The TLM treats the electrolyte-filled pore as an equivalent circuit of resistors and capacitors. The corresponding total resistance R and capacitance C take into account the properties of the electrolyte in the bulk and double electric layer (EDL) states, respectively. More than half a century ago, de Levy proposed a diffusion equation for the electrostatic potential difference between the pore surface and the central plane, which leads to a time scale RC [14,15]. Significantly, the effective circuit

is used nowadays to investigate the various properties of the electrolyte charging [17–19]. Biesheuvel and Bazant extended transmission line approach considering pure capacitive process Ref. [20] and Faradaic reaction Refs. [21,22] in porous electrodes. For low applied potentials $U \ll 25\,\mathrm{mV}$ model [20] results in the TLM, which is the linearization of Poisson–Nernst–Planck (PNP) equations [23] at this limit. Because of the assumption of low applied potential, TLM misses some critical phenomena [24] at conditions corresponding to the majority of applications $U \sim 0.1$–$1\,\mathrm{V}$. For example, the nonlinear model [20] predicts the slower charging at higher potentials, which is crucial for the power performance. However, the PNP calculations [24] showed that this predicted charging slowdown is overestimated due to the unaccounted surface conductivity. Thus, an accurate description of the electrolyte–electrode interface is crucial for adequately modeling nanopore charging at moderate/high applied potentials.

Very recently, the TLM approach has been applied to nanoporous electrodes ($H \sim 2\,\mathrm{nm}$), and realistic scaling of the charging time has been obtained in terms of physically determined parameters [19]. The authors of ref. [19] have also shown that two comparable timescales exist at high applied potentials: the first one corresponds to the equivalent circuit model, and the second timescale is related to adsorption. A more detailed analysis of the charge dynamics in nanopores requires information on the packing properties of finite-sized ions, which goes beyond the [19] TLM models. The most realistic description of ion transport in nanopores was obtained using the molecular dynamics (MD) method. Molecular dynamics (MD) simulations [25,26] demonstrated that the charging of the electrolyte filled pores is described by three consecutive regimes (modes). More precisely, the charging starts with ions diffusion characterized by the slow squared-root dependence of the total charge on time. Further, ion transport corresponds to two exponential regimes at the intermediate and late times. The second exponential regime with a higher relaxation time becomes crucial in ultra-narrow pores, which results in a significant slowdown of the charging. The authors of ref. [27] demonstrated how to speed up the nanopores charging using time-dependent applied potential. Such control of the applied potential allows the ions to avoid the molecular clogging which causes the sluggish dynamics. Therefore, modeling the ions' transport inside nanopores is critical to designing the supercapacitors with the optimal relation between storage and power properties. In addition, an actual application of the ion transport models is capacitive deionization technologies which use an electrostatic field to remove salt ions and provide the water desalination during the filtration through porous electrodes [28]. Additionally, the recent experiments [29] demonstrated that the salt ions could be excluded from the confined water because of the steric effects of the nano-scale slit pores. Thus, it is crucial to combine the electrostatic and steric properties to model the ion transport inside the nanopores properly.

This paper describes the ion dynamics inside a nanopore as wide as a molecule. Such sub-nanoporous electrodes are necessary for further advances in supercapacitor-based technologies. However, the sub-nanopore size limitation causes a significant slowing down of ion motion and, consequently, the charge. We develop a theory based on the time-dependent version of the c-DFT approach (see refs. [30,31] for one of the first derivations, and ref. [32] for the comprehensive literature review). More precisely, we derive and numerically solve the transport equations for the charged ions in the three-dimensional narrow slit pores. Such pores exhibit negligibly small values of the width-to-length ratio, which allows us to derive an asymptotic model—a one-dimensional transport equation reflecting the properties of the ion dynamics inside 3D slit nanopores. The proposed theory describes three consecutive charging regimes: an initial root-square process and two exponential regimes with different time scales. The last exponential regime plays a crucial role in the ultra-narrow pores (pore width is around ion diameter) and results in the charging slowdown. Before the current work, the details of the charging inside ultra-narrow pores had been investigated using MD simulations only [25–27]. Indeed, since we use an accurate thermodynamic potential, our model accounts for the electric and packaging properties of finite-sized ions within the nanopores. It is an advantage over

recently published dynamic models [18,19], and allows us to relate charging times to the given characteristics of nanopore supercapacitors.

2. Model

We use the slit pore geometry shown in Figure 1, which describes the spatial structure of modern porous materials, such as graphene based electrodes [33,34] and graphene oxide (GO)/MXene fibers [35,36], exhibiting aligned slit-nanopores of width H comparable to electrolyte diameter d and length $L \gg H$. The considered materials are used in supercapacitor's technologies as the porous electrodes which accumulate charge through electric double layer formation without chemical reactions. More precisely, these materials show promising applications for wearable electronics and smart textiles devices due to outstanding energy density and high flexibility [37]. Moreover, our geometrical representation of the pore closely resembles recent molecular dynamic simulations of the supercapacitors [26,27], which allows us to make a comparison of our predictions with the MD-simulated electrolyte's behavior. The electrodes with inhomogeneous pore-network considered in refs. [21,38,39] are beyond the scope of our work. However, the developed model of individual slit nanopore charging can be implemented as a pore-network building block in the case of a non-trivial pore-size distribution [39]. A possible implementation follows from ref. [39], where our transport equations can replace the Navier–Stokes equation for the effective medium approximation—the porous reservoir is a uniform network of equal short pores.

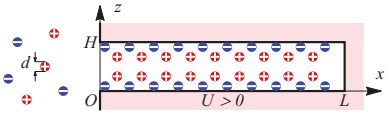

Figure 1. Slit pore connected to bulk volume of symmetric electrolyte, constant electric potential is applied to the pore walls.

In the case of slit pore geometry (Figure 1), the dynamic component density $\rho_i(t, x, z)$ for $i = 1, \ldots, n$ (where n is the number of components) depends on the coordinate x in lateral direction along the pore's surface and the normal distance to the surface z. Notice, that we assume the homogeneous distribution in the direction which is perpendicular to the x- and z-coordinates, see Figure 1. Therefore, to describe dynamics of the charging process, we apply the time-dependent version of c-DFT [40] in two spatial coordinates (x, z), defined in the general form as

$$\partial_t \rho_i - \beta D_i \nabla(\rho_i \nabla \mu_i) = 0, \tag{1}$$

where D_i is the diffusion coefficient of i-th component, $\beta = 1/k_B T$, k_B is the Boltzmann constant, T is the temperature, $\nabla = \{\partial_x, \partial_z\}$ is 2D gradient vector, and $\mu_i(t, x, z)$ is the local chemical potential of the i-th component.

To describe the confined electrolyte we use one of the most popular c-DFT approaches based on the confined hard sphere model [41] and an electrostatic extension [42] accounting for the contributions from Coulomb interaction and additional finite size residual correlations. The electrode's pores are considered as an open system connected with a bulk electrolyte. In accordance with Ref. [40], the chemical potentials $\mu_i(t, x, z)$ have the following form

$$\mu_i = k_B T \log\left(\rho_i \Lambda^3\right) + e Z_i \psi + \frac{\delta f_{\text{exc}}}{\delta \rho_i}, \tag{2}$$

where ψ is the electric potential, e is the proton charge, Z_i is the ion valency, Λ is the de Broglie wavelength. The electric potential $\psi(t, x, z)$ satisfies the Poisson equation

$$\beta e \Delta \psi = -4\pi l_B \sum_{i=1}^{n} Z_i \rho_i, \tag{3}$$

where $\Delta = \partial_{xx} + \partial_{zz}$ is the 2D Laplace operator and $l_B = \beta e^2/4\pi\epsilon\epsilon_0$ is the Bjerrum length. A detailed description of the used c-DFT approach including particular form of the excess term f_{exc} can be found in Appendix D. Additionally, see in Appendix D the static the capacitance's properties from implemented c-DFT which correspond to model [9] and show the realistic behavior.

Initially, no electrostatic potentials are applied, and the total charge of the symmetric electrolyte is zero. We consider a step charge when the potential changes abruptly from zero to some positive value $U > 0$. The applied potential causes the influx into the pores of oppositely charged ions called counter-ions (anions in the case of $U > 0$), while ions with a charge of the same sign as the applied potential (co-ions, cations for $U > 0$) are pushed out of the pore volume. Inside sub-nanopores, the local increase in the counter-ion density can strongly influence the co-ion desorption, hindering their release due to counter-ion clogging and thus leading to a notable slowdown of the charging process [26]. The main variables of interest are the charges associated with individual electrolyte components $Q_i(t) = -eZ_iL^{-1}\int_0^L\int_0^H dx\,dz\,\rho_i(t,x,z)$ and the surface total charge density $Q(t) = \sum_{i=1}^n Q_i(t)$. The final charge Q_∞ corresponds to the steady distributions $\rho_i^\infty(t,x,z) \equiv \rho_i^\infty(z)$, which are in equilibrium with the bulk electrolyte and depend on the applied potential U.

Considering Equations (1) and (3) in the slit-pore geometry (see (A5) and (A6)) with very small ratio $H/L \ll 1$, we seek the solutions of Equation (1) in the following forms:

$$\rho_i(t,x,z) = \rho_i^0(t,x,z) + \frac{H^2}{L^2}\rho_i^1(t,x,z) + \ldots, \tag{4}$$

$$\psi(t,x,z) = \psi^0(t,x,z) + \frac{H^2}{L^2}\psi^1(t,x,z) + \ldots. \tag{5}$$

where upper indices correspond to the $\mathcal{O}(1)$ and $\mathcal{O}(H^2/L^2)$ problems. As one can see in Appendix A, we use the $\mathcal{O}(1)$ equations to find that $\mu_i^0(t,x,z) \equiv \mu_i^0(t,x)$ do not depend on the z-coordinate; and electrostatic potential $\psi^0(t,x,z)$ can be found from the $\mathcal{O}(1)$-Poisson equation. Therefore, the $\mathcal{O}(1)$-problem allows us to describe the z-coordinate dependence, while $\mathcal{O}(H^2/L^2)$ provides information about dynamics and x-coordinate distribution. One of our most striking results is the demonstration that a complete solution to the problem $\mathcal{O}(H^2/L^2)$ is not required. Indeed, we derive an asymptotic model describing charging dynamics in terms of the pore cross-section averaged quantities for the $\mathcal{O}(1)$-variables $\rho_i^0(t,x,z)$ and $\mu_i^0(t,x,z)$, as follows (see details in Appendix A):

$$\partial_t\overline{\rho}_i^0(t,x) - \beta D_i\partial_x\left(\overline{\rho}_i^0(t,x)\partial_x\mu_i^0(\overline{\rho}_1^0,\ldots,\overline{\rho}_n^0)\right) = 0. \tag{6}$$

where, $\overline{\rho}_i^0(t,x) = \int_0^H dz\,\rho_i^0(t,x,z)/H$ are pore cross-section-averaged densities, and $\mu_i^0 = \overline{\mu}_i(\overline{\rho}_1,\ldots,\overline{\rho}_n)$ are functions of averaged densities only, see Appendix B. We close the 1D transport equation by the following initial and boundary conditions:

$$\overline{\rho}_i^0(t,0) = \overline{\rho}_i^\infty(U), \tag{7}$$

$$\partial_x\overline{\mu}_i^0(t,L) = 0, \tag{8}$$

$$\overline{\rho}_i^0(0,x) = \overline{\rho}_i|_{U=0} \tag{9}$$

where Equations (7) and (8) correspond to the open and closed boundaries, respectively; Equation (9) is the initial condition accounting for the confined electrolyte properties at $U = 0$. Such partial differential Equation (6) with (7)–(9) can be solved numerically using c-DFT as discussed in Appendix C.

Notice, that here and below we use $\rho_i \equiv \rho_i^0$, $\mu \equiv \mu^0$ and $\psi \equiv \psi^0$ the dominant terms in the expansions (4) and (5) over small parameter H/L. The chemical potentials μ_i are defined by the popular confined fluid c-DFT model, see Appendix D. It allows us to account for the realistic behavior of the electrolytes in confinement: alteration of over-screening/crowding interfaces [43]; the capacity oscillations in narrow nanopores [6]. Such subnanoscale properties are beyond the scope of the PNP equations [24], linear TLM models [23] or their very recent modifications [17,19]. Thus, since the derived transport equation correctly describes the ions-packing properties and the electrostatic fluctuations, we can extend the theoretical study to the ultra-narrow pores comparable to molecular size.

3. Results

Similar to some molecular simulations [25,26], we assume that electrolyte is a symmetric two component mixture consisting of the molecules with the diameters $d_1 = d_2 = d$ and the charge valences $Z_1 = -Z_2 = 1$. For the sake of simplicity, we set the diffusion coefficients of the components to be equal $D_1 = D_2 = D$. In the case of this symmetric electrolyte, it is also useful to introduce, following [9], the dimensionless variables $H^* = H/d$, $U^* = eU/k_BT$, $Q^* = Qd^2/e$, $\rho^* = \rho d^3$. It can be shown from dimensional arguments that the characteristic time for the considered problem is L^2/D and one can also introduce the scaled time $t^* = tD/L^2 = t/\tau$.

The charges of electrolyte components are conveniently defined in terms of average densities as $Q_i(t) = -eZ_iHL^{-1}\int_0^L dx\,\overline{\rho}_i(t,x)$. An example of the calculated time-dependent charges $Q(t)$ for subnanopore electrodes ($H^* = 1.5$ and $H^* = 2$) at sufficiently high potential $U^* = 10$ is shown in Figure 2a,b. A discussion of the used numerical methods can be found in Appendix C. As one can see from Figure 2a, the root-square law $Q \sim \sqrt{t}$ describes the notable part of the charging process at early times well. However, when the charge Q approaches the saturated value Q_∞, the trend changes to the exponential one. Figure 2b shows that in the case of larger pores with $H^* = 2$, the charging up to almost 95% is described by the following equation:

$$\frac{Q}{Q_\infty} = 1 - \frac{8}{\pi^2}e^{-t/\tau_1}. \tag{10}$$

Expression (10) is the leading term of the analytical solution of the TLM [24]. Despite that the pores sizes $H \sim d$ and potentials $U > k_BT/e$ are significantly beyond the ranges of TLM applicability, the published computer simulations [25,44] show the adequacy of exponential trend in Equation (10) for fitting of the charge dependency on time. We observed that at late times the calculated profiles $Q(t)$ in Figure 2b follow another exponential trend succeeding (10), which is notably slower and describes the charging until almost full saturation. The experimentally observed charging time for supercapacitors is around 10^3 s, while the published dynamic DFT models result in enormously underestimated values $\sim 10^{-9}$ s [19]. The proposed model provides both the realistic behavior of the capacitance's properties (Appendix D) and correct charging time scales. To provide numerical estimations we have used experimental parameters from refs. [19,45]: the pore length is $L = 0.5$ mm and confined diffusion coefficient $D = 2 \times 10^{-10}$ m^{2}s^{-1}. The full charging times estimations in the physical units for the pores $H^* = 1.5$ and $H^* = 2$ shown in Figure 2b correspond to around 700 s and 400 s, respectively, which agrees with the experimental characteristics.

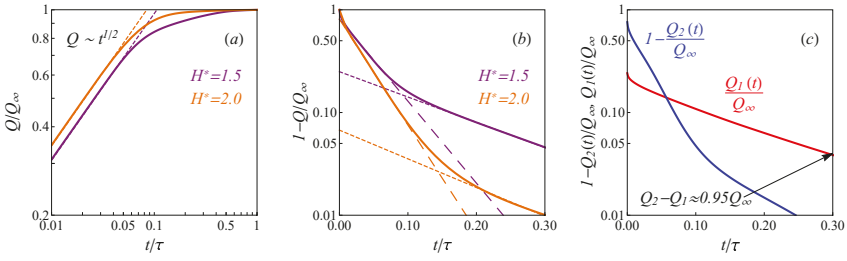

Figure 2. (**a**) The non-dimensional total charge (solid lines) profiles in the pores with different widths $H^* = 1.5$ and $H^* = 2.0$. The dashed lines indicate the square-root trends at early times. (**b**) The slit pore charging (solid lines) in the linear-log scale for $H^* = 1.5$ and $H^* = 2.0$. Long-dashed and short-dashed lines show two exponential trends (long-dashed and short-dashed lines) at intermediate and late times. (**c**) The separated total charge contributions from co-ions (red) counter-ions (blue) as function of time. In all plots $U^* = 10$ and $\tau = L^2/D$.

Calculations for a wide range of system parameters show that the full charging (say 95% for the sake of concreteness) in pores with $H^* \geq 2$ is described by the first exponential trend in Equation (10). For this reason, we use Equation (10) to fit the charging time τ_1^* from the calculated profiles $Q(t)$. Figure 3 demonstrates that the charging time for the electrodes of width $2 \leq H^* \leq 4$ and various electrolyte bulk densities ρ_0 and applied potentials $U^* \leq 4$ can be explicitly expressed in terms of macroscopic parameters as

$$\tau_1^* = \frac{4}{\pi^2} \frac{Q_\infty^*}{\overline{\rho}_\infty^* U^* H^*}. \tag{11}$$

Here, $\overline{\rho}_\infty^* = \overline{\rho}_{1,\infty}^* + \overline{\rho}_{2,\infty}^*$ is the total final density; the coefficient $4/\pi^2$ is obtained from the comparison with the TLM. The potentials considered here (up to 0.1 V in dimensional terms) correspond to the lower range of the values used in the modern experiments [45–47], but are significantly beyond the formal applicability range of the TLM [24]. To compare result Equation (11) with TLM relaxation time we consider the limit of large pores ($H^* \gg 1$) at extremely low potentials ($U^* \ll 1$). Unlike nano-confinement, in this limit, the total density is almost constant $\overline{\rho} \simeq 2\rho_0$, and the charge can be calculated from the linearization of the Gouy–Chapman theory $Q^* \simeq 4\rho_0^* U^* \lambda_D / d$, where λ_D is the Debye length. Inserting these approximations in Equation (11), we obtain $\tau_{\mathrm{TLM}}^* = 4\lambda_{\mathrm{D}}/(\pi^2 h_p)$, where h_p is the ratio of pore cross-sectional area to perimeter. Expression τ_{TLM}^* fits the TLM relaxation time from ref. [24]. Significantly, such assumptions are not relevant to nanopores charging due to the properties of the confined electrolyte. For example, the total charge Q becomes an oscillating function of H, average densities strongly depend on the ion sizes, and electrostatic correlations play a crucial role. Thus, our result Equation (11) generalizes the TLM predictions for the case of the charging in nanopores at moderate potentials. Thus, our approach is more general than standard TLM since it describes the charging at realistic nanopores conditions.

In addition, we have not met the derived expression (11) in the literature. However, we observed an interesting connection between expression (11) and the very recent result for the charging time published in ref. [44]. The authors of ref. [44] used the effective circuit to obtain RC-time of the charging inside nanoporous Metal Organic Frameworks electrodes. The application of this adopted TLM approach from ref. [44] to slit pores gives the following expression for relaxation time

$$\tau_{\mathrm{aTLM}} = \frac{4}{\pi^2} \frac{C_a L^2}{\sigma l}, \tag{12}$$

where using the notation adopted in ref. [44] the areal capacitance can be expressed as $C_a = Q_\infty / 2U$; the ionic conductivity inside the pore can be expressed in terms of the

electrical mobility of ions $m = eD/k_BT$ and ions density $\overline{\rho}_\infty$ as $\sigma = e\overline{\rho}_\infty m$. Inserting these electrolyte characteristics into Equation (A51) one can obtain that $\tau^*_{aTLM} = \tau^*_1$, see details in Appendix E. Therefore, Equation (11) is equivalent to one from the nanopores RC-circuit developed in ref. [44]. The advantage of our approach over the adopted TLM is self contained form provided by c-DFT's calculations without highly cost simulations.

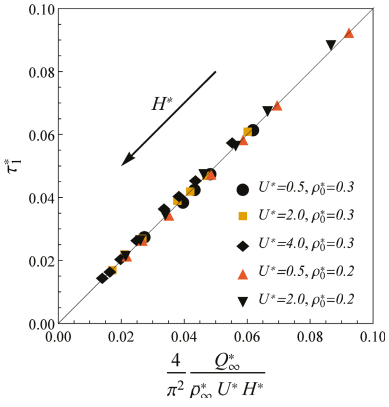

Figure 3. The calculated dimensionless charging time τ^*_1 for the electrodes with $H^* > 2$ at the external potentials $U^* \leq 4$ and the bulk electrolyte densities $\rho^*_0 = \{0.2, 0.3\}$ versus the scaling law (11). The arrow shows direction of the pores size increase.

The three consecutive dynamic regimes predicted in our work describe the results of molecular dynamics simulations published in refs. [25–27]. Similarly with ref. [25,26] we observed a stark contrast between the charging dynamics inside ultra-narrow $H^* = 1.5$ and wider $H^* = 2$ pores shown in Figure 2, for comparison, see Figures 2 and 3 in ref. [26] and ref. [25], respectively. In Figure 2b the first exponential regime (10) for $H^* = 1.5$ covers the charging up to only 75%. Therefore, the significant part of the full charging inside ultra-narrow pores ($H^* = 1.5$) is defined by the slower second exponential trend: the charge to 95% is ∼2 times slower than in the case of wider pores $H^* = 2$.

To investigate this effect numerically, we described the charge profiles near the saturation $Q(t) \sim 0.95Q_\infty$ in terms of another exponential trend $Q/Q_\infty = 1 - A_2 e^{-t/\tau_2}$, where $\tau_2 \geq \tau_1$ and A_2 are the fitting parameters. The results for the corresponding relaxation time τ^*_2 are shown in the inset of Figure 4. As one can see from this inset, expression (11) fits the charging time in larger pores ($H^* \geq 2$). However, we observed that in the case of the ultra-narrow pores $H^* \leq 1.7$, charging slow down becomes notable. We observed that the charging slowdown starts as the pore width becomes less than two molecular diameters ($H^* < 2$). In such confinement, the electrolyte behavior near the wall crucially influence on the ions distribution inside whole pore. Accordingly, it is reasonable to correlate the charging inside narrow pores not only with the average inner density $\overline{\rho}$ but the wall-contact density as well. As one can see from Figure 4, the charging time in ultra-narrow pores ($H^* \leq 1.7$) at high potential can be fitted to the following expression

$$\tau^*_2 = \frac{\overline{\rho}_\infty}{\rho_\infty(d/2)} + a_1 \frac{H^* - 1}{U^*} \tag{13}$$

where $\rho_\infty(d/2) = \rho_{\infty,1}(d/2) + \rho_{\infty,2}(d/2)$ is the wall-contact density at the final state of complete charging and $a_1 \simeq 0.6$ is the fitting parameter. The inverse dependence of charging time (13) on the potential U contributes as the pore's width increases. This behavior is consistent with the high potential limit ($H^*\overline{\rho}^*_\infty \simeq Q^*_\infty$) of expression (11), which fits the data well around $H^* = 2$.

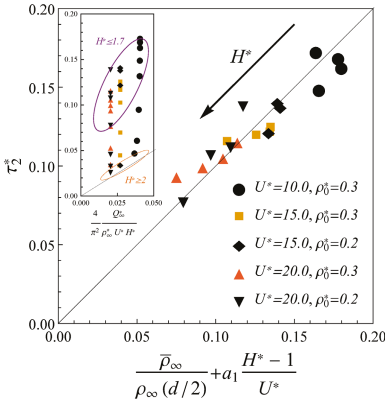

Figure 4. The dimensionless charging timescale τ_2^* for the electrodes with $1.3 \leq H^* \leq 1.7$ at the high external potentials $10 \leq U^* \leq 20$ versus the scaling law (13). The inset shows the same timescale versus the scaling law (11); the pores with $H^* \leq 1.7$ and $H^* \geq 2.0$ are marked with purple and orange ellipses.

To discuss the slowdown dynamics inside ultra-narrow pores we considered the dynamics of the co-ions/counter-ions separately. We observed that the contributions to total charge from the co-ions $Q_1(t)$ and counter-ions $Q_2(t)$ shown in Figure 2c exhibit significantly different relaxation times. More precisely, the counter-ions adsorption proceed more rapidly than slow outflux of the co-ions. Therefore, at the late times the counter-ions contribution is almost equal to the final charge $Q_2 \simeq Q_\infty$, while the co-ions' slow-release decrease the total charge $Q_\infty - Q_1$. The possible explanation of this phenomenon is that the co-ions are trapped in the crowded counter-ion phase. Such behavior of the ions in nanopores was observed in MD simulations of symmetric electrolyte [26,27]. To demonstrate that expression (13) is in agreement with this explanation, we consider the ultra-narrow pores $H \sim d$. Then, the second term in Equation (13) is negligible and the counter-ion density dominates $\overline{\rho}_{\infty,2} \gg \overline{\rho}_{\infty,1}$. Therefore, the relaxation time (13) can be written as $\tau_2 = L^2\overline{\rho}_{\infty,2}/D\rho_{\infty,2}(d/2)$. At the late times, such dynamics is equivalent to a diffusion process of co-ions with the effective diffusion coefficient $D_1 = \overline{\rho}_{\infty,2}D/\rho_{\infty,2}(d/2)$, while the counter ions component is already in equilibrium. This coefficient $D_1 < D$ is defined by the density and structure of the counter-ion component distribution, that confirms the idea that the the abrupt counter-ions adsorption induces slow diffusion of the co-ions.

This paper proved the concept of H/L-expansion in application to the nanoporous charging compared with the experiment and simulations results. This approach could be helpful in applications beyond the charging time calculations. For example, we recently became aware of paper [48], where the authors use the same asymptotic approach to calculate the impedance response in slit pores. In the future, the developed model could be perspective in the following research directions.

(I): We considered only the popular version of the Constant Potential Method (CPM)—the charging starts when the surface potential suddenly steps from zero to some value. However, the CPM mode does not cover charging at a constant electric current widely used in Galvanostatic Charge–Discharge (GCD) measurements. Additionally, recent MD simulations in ref. [27] show that the charging in nanopores can be accelerated applying time-dependent potential $U(t)$, which allows one to avoid ion clogging near the orifice. First of all, to describe the GCD- and $U(t)$-modes for the realistic supercapacitor's setup, one needs to account for the dynamics of the neutral electrolyte stored in the finite bulk volume between two oppositely charged porous electrodes. Therefore, the proposed model should be improved by accounting for the bulk electrolyte, as recently done for the TLM in ref. [17], and for PNP equations in ref. [49]. Then, the time-dependent potential

can be accounted for in boundary condition (8), assuming that $U(t)$ varies slowly then the diffusion time scale in z-direction H^2/D. Possible realization of GCD mode follows from very recent ref. [50]—one can use the boundary condition at $x = 0$ which indicates an applied current with the given period and amplitude (see Equation (7c) in [50]). (II): Our model is applied to the porous electrodes with flat smooth inner surface. Recently we developed model for the electrolytes structure near the electrodes with rough surfaces ref. [51]. Therefore, the proposed approach could be extended to the porous materials with rough surfaces accounting for the modified Poisson equation from ref. [51]. (III): We considered purely electrostatic supercapacitors, also known as electric double-layer capacitors. However, our approach can be extended to the pseudocapacitors' charging mechanism based on the Faradaic processes (redox reactions). For this case, the possible modifications are discussed in ref. [21], where the authors extended the porous electrode theory from [20], accounting for the Faradaic reaction rate. Notice that these fast reactions differ from the charging mechanism of Li-ion batteries, where the chemical reactions induce the changes in the electrode molecules making/breaking chemical bonds.

4. Conclusions

In conclusion, we developed a model of the charging dynamics in slit nanopores accounting for the confined properties of the electrolyte. We made significant simplification of the dynamic equations exploiting the slit-pore geometry but remaining the properties of the confined electrolytes. The developed model demands much lower computational resources than computer simulations and allows the investigation of a wide range of electrolyte and electrode parameters. Unlike the previous c-DFT applications to the ion dynamics, our results for the charging time coincide with experimental data well [19]. In addition, we described three consequent regimes of the supercapacitor's charging: the initial root-square diffusion and two exponential regimes with notably different time scales. These results agree with molecular dynamic simulations published in refs. [25–27]. We identified a threshold pore width below which the second exponential regime defines the full charging time. In this case, the charging inside ultra-narrow pores is notably slower and depends on the contact wall electrolytes density. These numerical estimations are crucial to avoid power density decrease using the ultra-narrow pores. Thus, the developed model will help investigate the relations between the supercapacitors' storage and dynamics properties.

Author Contributions: Conceptualization, T.A., K.S. and I.A.; methodology, T.A., K.S.; software, T.A., K.S.; validation, T.A., K.S. and I.A.; formal analysis, T.A., K.S. and I.A.; investigation, T.A., K.S. and I.A.; resources, T.A. and I.A.; data curation, T.A., K.S; writing—original draft preparation, T.A., K.S.; writing—review and editing, T.A., K.S. and I.A.; visualization, T.A., K.S.; supervision, I.A.; project administration, T.A.; funding acquisition, T.A. All authors have read and agreed to the published version of the manuscript.

Funding: T.A. acknowledges the financial support from the Russian Science Foundation (project number: 20-72-00183).

Institutional Review Board Statement: Not applicable.

Informed Consent Statement: Not applicable.

Data Availability Statement: Not applicable.

Acknowledgments: K.S. is grateful to Schlumberger management for the permission to publish this work. The authors are grateful to Mathijs Janssen and Mikhail Stukan for useful comments. T.A. and K.S. contributed equally to this work.

Conflicts of Interest: The authors declare no conflicts of interest.

Abbreviations

The following abbreviations are used in this manuscript:

c-DFT	Classical density functional theory
TLM	Transmission line model
MD	Molecular dynamics

Appendix A. Derivation of Pore Cross-Section Averaged Equations

Here we the describe derivation of the pore cross-section averaged equations

$$\partial_t \overline{\rho}_i - \beta D_i \partial_x (\overline{\rho}_i \partial_x \overline{\mu}_i) = 0 \tag{A1}$$

from the original three dimensional system

$$\partial_t \rho_i - \beta D_i \nabla (\rho_i \nabla \mu_i) = 0, \tag{A2}$$

$$\mu_i = k_B T \log\left(\rho_i \Lambda^3\right) + eZ_i\psi + \frac{\delta f_{\text{exc}}}{\delta \rho_i}, \tag{A3}$$

$$\beta e \Delta \psi = -4\pi l_B \sum_{i=1}^{n} Z_i \rho_i. \tag{A4}$$

Please refer to the main document for context and notation.

We consider transport along the slit pore aligned with the x-axis and perpendicular to z-axis. The aspect ratio of the pore is assumed to be large, and accordingly, we adopt classical thin-film / lubrication approximation scaling. The pore width H, length L, and applied voltage U are used as scales for z coordinate, x coordinate, and potentials μ_i, respectively. Additionally, for the sake of concreteness we scale D_i for different components with the value of the first component diffusion coefficient D at bulk conditions. Timescale of the problem is defined by $L^2/D\beta eU$ and characteristic density is $\beta eU/4\pi l_B H^2$.

After scaling, the dimensionless transport and Poisson equations are

$$\delta \partial_t \rho_i - \delta \partial_x (K_i \partial_x \mu_i) - \partial_z (K_i \partial_z \mu_i) = 0, \tag{A5}$$

$$\delta \partial_{xx} \psi + \partial_{zz} \psi - \sum_{i=1}^{n} Z_i \rho_i = 0. \tag{A6}$$

Here, $\delta = H^2/L^2 \ll 1$ and the additional definition $K_i = D_i \rho_i$ is introduced.

The system is supplied with boundary conditions enforcing zero fluxes

$$-K_i \partial_z \mu_i = 0, \quad z = 0, 1. \tag{A7}$$

and the value of electrostatic potential

$$\psi = 1, \quad z = 0, 1. \tag{A8}$$

at the channel walls.

We seek a formal asymptotic expansion of the densities ρ_i and the potential ψ in power series of $\delta \to 0$

$$\begin{aligned} \rho_i &= \rho_i^0 + \delta \rho_i^1 + \ldots, \\ \psi &= \psi^0 + \delta \psi^1 + \ldots. \end{aligned}$$

Substituting the latter expansion to (A5)–(A8) and collecting terms of the same order, one can obtain the $O(1)$ *problem*:

$$-\partial_z \left(K_i^0 \partial_z \mu_i^0\right) = 0, \tag{A9}$$

$$\partial_{zz}\psi^0 - \sum_{i=1}^{n} Z_i\rho_i^0 = 0, \tag{A10}$$

$$-K_i^0\partial_z\mu_i^0 = 0, \quad z = 0, 1. \tag{A11}$$

$$\psi^0 = 1, \quad z = 0, 1. \tag{A12}$$

Here, $K_i^0 = D_i\rho_i^0, \mu_i^0 = \mu_i\left[\rho_1^0, ..., \rho_n^0, \psi^0\right]$. Solution of the $O(1)$ problem will be discussed below. Here we only note that using (A9) and the boundary condition (A11), one can also promptly get

$$\partial_z\mu_i^0 = 0. \tag{A13}$$

Details of $O(1)$ problem are further considered in Appendix B.

$O(\delta)$ *problem*:

$$\partial_t\rho_i^0 - \partial_x\left(K_i^0\partial_x\mu_i^0\right) - \partial_z\left(K_i^0\partial_z\mu_i^1 + K_i^1\partial_z\mu_i^0\right) = 0, \tag{A14}$$

$$\partial_{xx}\psi^0 + \partial_{zz}\psi^1 - \sum_{i=1}^{n} Z_i\rho_i^1 = 0, \tag{A15}$$

$$-K_i^0\partial_z\mu_i^1 - K_i^1\partial_z\mu_i^0 = 0, \quad z = 0, 1. \tag{A16}$$

$$\psi^1 = 0, \quad z = 0, 1. \tag{A17}$$

Here $K_i^1 = D_i\rho_i^1$ and

$$\mu_i^1 = \sum_{j=1}^{n} \frac{\delta\mu_i}{\delta\rho_j}\left[\rho_1^0, ..., \rho_n^0, \psi^0\right]\rho_j^1 + \frac{\delta\mu_i}{\delta\psi}\left[\rho_1^0, ..., \rho_n^0, \psi^0\right]\psi^1.$$

The solution of the $O(\delta)$ problem is beyond the scope of the study. We limit ourselves to consideration of dynamical problem in the leading order of approximation and use $O(\delta)$ problem for rigorous derivation of the averaged equations only.

Integrating (A14) over the pore width and using boundary conditions (A16) and corollary (A13) one can get

$$\partial_t\overline{\rho}_i^0 - \partial_x\left(\overline{K}_i^0\partial_x\overline{\mu}_i^0\right) = 0. \tag{A18}$$

Here, $\overline{f} = \int_0^1 dz f$. The condition (A13) is used here while integrating the second term of (A14) by parts and to replace μ_i^0 by $\overline{\mu}_i^0$. The Equation (6) is essentially (A18) written in dimensional terms after dropping superscripts.

Appendix B. *O*(1) Problem

Casting the Equations (A10), (A12) and (A13) back to dimensional variables we get

$$\beta e\partial_{zz}\psi^0 = -4\pi l_B\sum_{i=1}^{n} Z_i\rho_i^0, \tag{A19}$$

$$\psi^0 = U, \quad z = 0, H, \tag{A20}$$

$$\partial_z\mu_i^0 = 0. \tag{A21}$$

The solution of (A19) with boundary conditions (A20) can be written in the integral form

$$\beta e\psi^0 = \beta eU + \frac{4\pi l_B z}{H}\int_0^H dz'(H - z')\sum_{i=1}^{n} Z_i\rho_i^0 - 4\pi l_B\int_0^z dz'(z - z')\sum_{i=1}^{n} Z_i\rho_i^0. \tag{A22}$$

It follows from (A21) that μ_i^0 does not depend on the z coordinate $\mu_i^0 = \overline{\mu}_i^0(t,x)$. Substituting the latter to (2) and rearranging terms, one can get the following equation for the density distribution across the pore

$$\rho_i^0 = \frac{1}{\Lambda^3}\exp\left(\beta\overline{\mu}_i^0\right)E_i^0. \tag{A23}$$

Here,

$$E_i^0 = \exp\left(-\beta e Z_i \psi^0 - \beta\frac{\delta f_{\text{exc}}}{\delta\rho_i}[\rho_1^0,...,\rho_n^0]\right)$$

and further details on f_{exc} can be found in Appendix D.

Formal integration of (A23) over $z \in [0,H]$ and the fact that $\overline{\mu}_i^0 = \overline{\mu}_i^0(t,x)$ allow to eliminate the chemical potential $\overline{\mu}_i^0$ and rewrite the equation in terms of average density $\overline{\rho}_i^0$ as

$$\rho_i^0 = \overline{\rho}_i^0\frac{E_i^0}{\overline{E}_i^0}. \tag{A24}$$

We look for effectively 1D equilibrium densities' distributions depending on t and x only parametrically via the average densities $\rho_i^0 = \rho_i^0(\overline{\rho}_i^0(t,x),z)$. Once the distributions are found from (A24) and (A22), one can evaluate (2) at any coordinate z, and thus, get the potentials as functions of average densities $\overline{\mu}_i^0 = \overline{\mu}_i^0(\overline{\rho}_i^0,...,\overline{\rho}_n^0)$.

Appendix C. Notes on Numerical Solution

Numerical solution of the transport Equation (6) involves two different tasks: solution of the dynamic equations given the potentials as function of densities and evaluation of potentials themselves.

For a given potential, spatial discretization of the system (6) is performed on a uniform staggered grid using finite volume method. The resulting system of nonlinear ODEs is solved by the built-in method of Wolfram Mathematica [52].

The potentials as functions of densities are defined by the solution of the $O(1)$ problem described in Appendix B. The system of Equation (A24) for $i = 1,\ldots,n$ comprises the fixed-point problem with the right-hand side defined by the dependency of excess energy variation on densities described in Appendix D and the solution (A22) of the Poisson Equations (A19) and (A20). Given $\overline{\rho}_i^0$, it is solved by the classical Picard iterations with underrelaxation involving intermediate step of (A19) and (A20) solution for current densities guess.

For the sake of computational efficiency, the potentials $\overline{\mu}_i^0$ are not evaluated "on the fly" during the solution of the dynamic Equation (6). Instead, the potentials are first calculated on a sufficiently fine grid in average densities space. Next, smooth interpolation is built based on the calculated values. Then, the interpolants are used while solving the dynamic problem.

Appendix D. Density Functional Theory

Here, we describe in detail the thermodynamic model of an electrolyte inside a nanopore, which is based on classical density functional theory (c-DFT). The version of this approach developed for neutral molecules is able to take into account the influence of nanoscale geometrical constraints [41]. The confined fluid model can be extended to electrolyte fluids accounting for electrostatic correlations and external Coulomb field [42]. We consider an open slit pore stored by neutral electrolyte mixture $\sum_{k=1}^n Z_k\rho_{k,b} = 0$ with known composition and chemical potentials $\{\mu\}_{k=1}^n$. Such confined system is described in terms of the Grand Canonical potential Ω and external field:

$$\Omega[\{\rho_i(\mathbf{r})\}] = F[\{\rho_i(\mathbf{r})\}] + \sum_{i=1}^n\int d\mathbf{r}\rho_i(\mathbf{r})(U_{\text{ext,i}}(\mathbf{r}) - \mu_i), \tag{A25}$$

where U_{ext} is the external field acting on a fluid molecule, μ is the chemical potential. In the case of charged molecules, the external fields contains not only wall potential, but also Coulomb field contribution:

$$U_{ext,i} = U_{w,i} + U_{C,i}. \tag{A26}$$

In our study, we use the hard sphere potential to described non-electrostatic fluid-solid interactions:

$$U_{w,i}(r) = \begin{cases} \infty & \text{if} \quad r < d_i/2 \\ 0 & \text{if} \quad r > d_i/2 \end{cases}. \tag{A27}$$

The slit pore geometry allows us to reduce the spatial density distribution $\rho_i(\mathbf{r})$ to the 1D function $\rho_i(z)$ of the normal distance to the solid surface. The Helmholtz energy of ionic liquids can be written as follows:

$$F = F_{id} + F_{hs} + F_C + F_{el}, \tag{A28}$$

where F_{id} is the ideal gas contribution; F_{hs} is the hard sphere term accounting for ionic excluded volume effects; F_C is the Coulomb interaction; F_{el} is the residual electric contribution. Here, only the ideal part is known exactly:

$$F_{id} = Ak_BT \sum_{i=1}^{n} \int dz \rho_i(z) \log\Big(\Big[\Lambda^3 \rho(z) \Big] - 1 \Big). \tag{A29}$$

The remaining terms define the excess part of the total Helmholtz free energy:

$$F_{exc} = F_{hs} + F_C + F_{el} \tag{A30}$$

In accordance with the DFT approach, the equilibrium density distributions are defined by the following system:

$$\frac{\delta \Omega}{\delta \rho_i} = 0, \quad i = 1, ..., n \tag{A31}$$

After substitution of expressions for the Helmholtz free energy (A28) and the external potential (A26), the conditions (A31) take a more explicit form:

$$\rho_i = \rho_i^0 \exp[-\beta U_{C,i} - \beta U_{w,i} - \lambda_i], \tag{A32}$$

where ρ_i^0 is the bulk component density, λ_i is the density derivative of the deviation of the excess terms from the bulk ones:

$$\lambda_i = \beta \frac{\delta(F_{exc} - F_{exc}^0)}{\delta \rho_i} \tag{A33}$$

where F_{exc}^0 is the bulk excess free energy corresponding to the homogeneous mixture $\{\rho_k^0\}_{k=1}^n$.

The functional derivative of the Coulomb contribution has the following form:

$$\beta \frac{\delta F_C}{\delta \rho_i} = Z_i l_B \sum_{j=1}^{n} Z_j \int d\mathbf{s} \frac{\rho_j(\mathbf{s})}{|\mathbf{s} - \mathbf{r}|}, \tag{A34}$$

where $l_B = \beta e^2 / 4\pi\epsilon\epsilon_0$ is the Bjerrum length. The right hand of expression (A34) can be rewritten in terms of external Coulomb field U_C and the mean electrostatic potential ψ:

$$Z_i e\psi - U_{C,i} = Z_i l_B \sum_{j=1}^{n} Z_j \int d\mathbf{s} \frac{\rho_j(\mathbf{s})}{|\mathbf{s} - \mathbf{r}|} \tag{A35}$$

Using expressions (A34) and (A35) Equation (A32) can be rewritten as follows:

$$\rho_i = \rho_i^{(0)} \exp\left[-\beta U_{\mathrm{w,i}} - \beta Z_i e\psi - \frac{\beta\delta}{A\delta\rho}(\Delta F_{\mathrm{hs}} + \Delta F_{\mathrm{el}})\right] \tag{A36}$$

where symbol Δ means the difference between confined and bulk energies.

The hard sphere contribution can be calculated using Fundamental Measure Theory [41] as:

$$\beta F_{\mathrm{hs}}[\rho_1(z), ..., \rho_n(z)] = A\int_0^H dz' \Phi(n_0, n_1, n_2, n_3, \mathbf{n}_{v1}, \mathbf{n}_{v2}) \tag{A37}$$

where the function Φ depends on the weighted densities n_α defined as:

$$\begin{aligned}
n_0 &= \sum_{k=1}^{n} \frac{1}{d_i}\int_{z-R}^{z+R} \rho_k(z')dz' \\
n_1 &= \frac{1}{2}\sum_{k=1}^{n} \int_{z-R}^{z+R} \rho_k(z')dz' \\
n_2 &= \sum_{k=1}^{n} \pi d_i \int_{z-R}^{z+R} \rho_k(z')dz' \\
n_3 &= \frac{1}{2}\sum_{k=1}^{n} \int_{z-R}^{z+R} \left[d_k^2 - (z-z')^2\right]\rho_k(z')dz' \\
\mathbf{n}_{v1} &= -\sum_{k=1}^{n} \frac{1}{d_k}\frac{\mathbf{z}}{z}\int_{z-R}^{z+R} dz'(z'-z)\rho(z') \\
\mathbf{n}_{v2} &= -2\pi\sum_{k=1}^{n} \frac{\mathbf{z}}{z}\int_{z-R}^{z+R} dz'(z'-z)\rho(z')
\end{aligned} \tag{A38}$$

We use one of the most popular version [9] of the Φ defined as:

$$\Phi = -n_0\log(1-n_3) + (n_1n_2 - \mathbf{n}_{v1}\mathbf{n}_{v2})/(1-n_3) + 1/(36\pi)(n_3\log(1-n_3) + n_3^2/(1-n_3)^2)(n_2^3 - 3n_2\mathbf{n}_{v2}^2)/n_3^3 \tag{A39}$$

Therefore, the functional derivative of the hard sphere contribution can be calculated by the following way:

$$\frac{\beta\delta F_{\mathrm{hs}}}{\delta_i\rho(z)} = A\int_0^H dz' \sum_\alpha \frac{\partial\Phi(n_\alpha)}{\partial n_\alpha}\frac{\delta n_\alpha}{\delta\rho_i} \tag{A40}$$

To calculate electrostatic term in Equation (A36), we use the approach described in ref. [42]:

$$\frac{\delta\Delta F_{\mathrm{el}}}{\delta\rho_i} = -\sum_{k=1}^{n}\int d\mathbf{s}\bar{c}_{ki}(\mathbf{r},\mathbf{s})\Delta\rho_k(\mathbf{s}) \tag{A41}$$

where the weighted correlation function defined as

$$\bar{c}_{ki}(\mathbf{r},\mathbf{s}) = \frac{\int c_{ki}(\mathbf{r}',\mathbf{s})f_{ki}(\mathbf{r}')}{\int d\mathbf{r}' f_{ki}(\mathbf{r}')} \tag{A42}$$

In our work, we use the FMT/WCA-k^2 approach, which corresponds to the following expression of f-function:

$$f_{ki}(\mathbf{r}') = \kappa^2(\mathbf{r}')\Theta(|\mathbf{r}-\mathbf{r}'| - d_{ki}) \tag{A43}$$

where $d_{ki} = (d_k + d_i)/2$ is the average diameter, and κ is the inverse Debye parameter given by

$$\kappa^2(\mathbf{r}') = 4\pi l_{\mathrm{B}}\sum_k^n \rho_k Z_k \tag{A44}$$

In accordance with work [42], here we use the approximated analytical expression for the weighted correlation function in terms of MSA solution:

$$\bar{c}_{ki}(\mathbf{r}', \mathbf{s}) \simeq c_{ki}^{MSA}(|\mathbf{r}' - \mathbf{s}|) = \beta U_{ki}(r) \left[1 - B_{ki}(\mathbf{r}') \frac{r}{d_{ki}}\right]^2 \Theta(d_{ki} - r) \tag{A45}$$

where $r = |\mathbf{r}' - \mathbf{s}|$ is the scalar distance, B_{ki} depends analytically on Debye parameter κ (A44) as

$$B_{ki} = \frac{1 + \kappa d_{ki} - \sqrt{1 + 2\kappa d_{ki}}}{\kappa d_{ki}} \tag{A46}$$

Therefore, the weighted correlation function (A42) in slit geometry $\rho(z)$ can be written as:

$$\bar{c}_{ki}(r) = \beta U_{ki}(r) \left[1 - 2B_{1,ki}(z) \frac{r}{d_{ki}} + B_{2,ki}\left(\frac{r}{d_{ki}}\right)\right] \Theta(d_{ij} - r) \tag{A47}$$

where

$$B_{m,ki}(z) = \frac{\int_{z-d_{ki}}^{z+d_{ki}} dz' B^m(z') \kappa^2(z') (d^2 - (z - z')^2)}{\int_{z-d_{ki}}^{z+d_{ki}} dz' \kappa^2(z') (d^2 - (z - z')^2)} \tag{A48}$$

In our work, we use the same system parameters as in ref. [9] corresponding to the dimensionless temperature $T^* = d/l_B = 0.15$. The characteristic dependence of the density distribution profiles on applied potential is shown in Figure A1. As shown in [9], such behavior of co- and counter-ions results in the oscillating capacity properties.

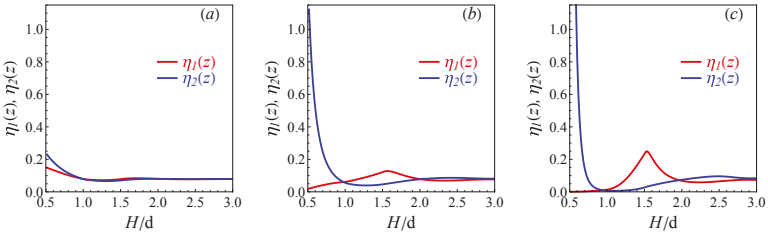

Figure A1. The dimensionless density distributions of positive $\eta_1(z) = v\rho_1(z)$ and negative $\eta_2(z) = v\rho_2(z)$ electrolyte's components inside pore $H^* = 6$ at various applied potentials $U^* = 0.5$ (**a**), $U^* = 5$ (**b**) and $U^* = 20$ (**c**). These calculations correspond to the bulk density $\rho_{0,1}^* = \rho_{0,2}^* = 0.15$ at the temperature $T^* = 0.15$.

Appendix E. Connection with Transition Line Model (TLM)

Here we supplement the analysis of the first exponential regime's time scale

$$\tau_1^* = \frac{4}{\pi^2} \frac{Q_\infty^*}{\overline{\rho}_\infty^* U^* H^*} \tag{A49}$$

by another connection with the result of TLM. In ref. [44] the TLM solution was used to describe the charging inside nanoporous metal organic frameworks (MOFs) electrodes. The following equation for the net pore charge after jump-wise application of constant potential was obtained:

$$\frac{Q(t)}{Q_\infty} = 1 - \frac{2}{\pi^2} \sum_{n=0}^{\infty} \frac{\exp\left[-\pi^2 (n + 1/2)^2 (l/L)^2 t/\tau\right]}{(n + 1/2)^2}. \tag{A50}$$

Here $\tau = C_a l/\sigma$ is the intrinsic relaxation time, C_a is the areal capacity of the pore, l is the pore volume divided by its surface area, σ is the ionic conductivity inside the pore. Please note that the exponent in (A50) differs from the given in the original paper by the factor of 4, because the symmetric pore connected to bulk electrolyte at both ends and effectively composed of two closed-end pores considered here was studied in [44].

The series in the right hand of expression (A50) can be approximated by the leading term $n = 0$, that result in the following time-scale of the TLM model:

$$\tau_{\mathrm{aTLM}} = \frac{4}{\pi^2}\frac{C_a L^2}{\sigma l}. \tag{A51}$$

For the slit pore geometry $l \approx H/2$. Using the notation adopted in this paper the areal capacitance can be expressed as $C_a = Q_\infty/2U$. Finally, the ionic conductivity inside the pore can be expressed in terms of the electrical mobility of ions $m = eD/k_\mathrm{B}T$ and ions density $\overline{\rho}_\infty$ as $\sigma = e\overline{\rho}_\infty m$. Substitution of these expressions to (A51) gives

$$\tau_{\mathrm{aTLM}} = \frac{4}{\pi^2}\frac{Q_\infty k_\mathrm{B}T}{e^2\overline{\rho}_\infty UH}\frac{L^2}{D}. \tag{A52}$$

Introducing dimensionless variables $H^* = H/d$, $U^* = eU/k_\mathrm{B}T$, $Q^* = Qd^2/e$, $\rho^* = \rho d^3$ and $t^* = tD/L^2$ used in the main document into the latter expression one can readily obtain that $\tau^*_{\mathrm{aTLM}} = \tau^*_1$, i.e. TLM time scale is equivalent to the time given by (A49).

References

1. Simon, P.; Gogotsi, Y. Materials for electrochemical capacitors. In *Nanoscience and Technology: A Collection of Reviews from Nature Journals*; World Scientific: Singapore, 2010; pp. 320–329.
2. Simon, P.; Gogotsi, Y. Perspectives for electrochemical capacitors and related devices. *Nat. Mater.* **2020**, *19*, 1151–1163. [CrossRef]
3. Horn, M.; MacLeod, J.; Liu, M.; Webb, J.; Motta, N. Supercapacitors: A new source of power for electric cars? *Econ. Anal. Policy* **2019**, *61*, 93–103. [CrossRef]
4. Shao, H.; Wu, Y.C.; Lin, Z.; Taberna, P.L.; Simon, P. Nanoporous carbon for electrochemical capacitive energy storage. *Chem. Soc. Rev.* **2020**, *49*, 3005–3039. [CrossRef] [PubMed]
5. Chmiola, J.; Yushin, G.; Gogotsi, Y.; Portet, C.; Simon, P.; Taberna, P.L. Anomalous increase in carbon capacitance at pore sizes less than 1 nanometer. *Science* **2006**, *313*, 1760–1763. [CrossRef]
6. Largeot, C.; Portet, C.; Chmiola, J.; Taberna, P.L.; Gogotsi, Y.; Simon, P. Relation between the ion size and pore size for an electric double-layer capacitor. *J. Am. Chem. Soc.* **2008**, *130*, 2730–2731. [CrossRef]
7. Jiang, D.e.; Jin, Z.; Wu, J. Oscillation of capacitance inside nanopores. *Nano Lett.* **2011**, *11*, 5373–5377. [CrossRef]
8. Härtel, A. Structure of electric double layers in capacitive systems and to what extent (classical) density functional theory describes it. *J. Phys. Condens. Matter* **2017**, *29*, 423002. [CrossRef]
9. Pizio, O.; Sokołowski, S.; Sokołowska, Z. Electric double layer capacitance of restricted primitive model for an ionic fluid in slit-like nanopores: A density functional approach. *J. Chem. Phys.* **2012**, *137*, 234705. [CrossRef]
10. Jiang, D.E.; Wu, J. Microscopic insights into the electrochemical behavior of nonaqueous electrolytes in electric double-layer capacitors. *J. Phys. Chem. Lett.* **2013**, *4*, 1260–1267. [CrossRef]
11. Lian, C.; Liu, K.; Van Aken, K.L.; Gogotsi, Y.; Wesolowski, D.J.; Liu, H.; Jiang, D.; Wu, J. Enhancing the capacitive performance of electric double-layer capacitors with ionic liquid mixtures. *ACS Energy Lett.* **2016**, *1*, 21–26. [CrossRef]
12. Neal, J.N.; Wesolowski, D.J.; Henderson, D.; Wu, J. Ion distribution and selectivity of ionic liquids in microporous electrodes. *J. Chem. Phys.* **2017**, *146*, 174701. [CrossRef] [PubMed]
13. Osti, N.C.; Gallegos, A.; Dyatkin, B.; Wu, J.; Gogotsi, Y.; Mamontov, E. Mixed ionic liquid improves electrolyte dynamics in supercapacitors. *J. Phys. Chem. C* **2018**, *122*, 10476–10481. [CrossRef]
14. De Levie, R. On porous electrodes in electrolyte solutions: I. Capacitance effects. *Electrochim. Acta* **1963**, *8*, 751–780. [CrossRef]
15. De Levie, R. On porous electrodes in electrolyte solutions—IV. *Electrochim. Acta* **1964**, *9*, 1231–1245. [CrossRef]
16. Posey, F.; Morozumi, T. Theory of potentiostatic and galvanostatic charging of the double layer in porous electrodes. *J. Electrochem. Soc.* **1966**, *113*, 176. [CrossRef]
17. Janssen, M. Transmission line circuit and equation for an electrolyte-filled pore of finite length. *Phys. Rev. Lett.* **2021**, *126*, 136002. [CrossRef] [PubMed]
18. Gupta, A.; Zuk, P.J.; Stone, H.A. Charging Dynamics of Overlapping Double Layers in a Cylindrical Nanopore. *Phys. Rev. Lett.* **2020**, *125*, 076001. [CrossRef]
19. Lian, C.; Janssen, M.; Liu, H.; van Roij, R. Blessing and Curse: How a Supercapacitor's Large Capacitance Causes its Slow Charging. *Phys. Rev. Lett.* **2020**, *124*, 076001. [CrossRef]
20. Biesheuvel, P.; Bazant, M. Nonlinear dynamics of capacitive charging and desalination by porous electrodes. *Phys. Rev. E* **2010**, *81*, 031502. [CrossRef] [PubMed]
21. Biesheuvel, P.; Fu, Y.; Bazant, M.Z. Diffuse charge and Faradaic reactions in porous electrodes. *Phys. Rev. E* **2011**, *83*, 061507. [CrossRef]

22. Biesheuvel, P.; Fu, Y.; Bazant, M. Electrochemistry and capacitive charging of porous electrodes in asymmetric multicomponent electrolytes. *Russ. J. Electrochem.* **2012**, *48*, 580–592. [CrossRef]
23. Bazant, M.Z.; Thornton, K.; Ajdari, A. Diffuse-charge dynamics in electrochemical systems. *Phys. Rev. E* **2004**, *70*, 021506. [CrossRef] [PubMed]
24. Mirzadeh, M.; Gibou, F.; Squires, T.M. Enhanced charging kinetics of porous electrodes: Surface conduction as a short-circuit mechanism. *Phys. Rev. Lett.* **2014**, *113*, 097701. [CrossRef] [PubMed]
25. Kondrat, S.; Wu, P.; Qiao, R.; Kornyshev, A.A. Accelerating charging dynamics in subnanometre pores. *Nat. Mater.* **2014**, *13*, 387–393. [CrossRef] [PubMed]
26. Breitsprecher, K.; Holm, C.; Kondrat, S. Charge me slowly, I am in a hurry: Optimizing charge–discharge cycles in nanoporous supercapacitors. *ACS Nano* **2018**, *12*, 9733–9741. [CrossRef] [PubMed]
27. Breitsprecher, K.; Janssen, M.; Srimuk, P.; Mehdi, B.L.; Presser, V.; Holm, C.; Kondrat, S. How to speed up ion transport in nanopores. *Nat. Commun.* **2020**, *11*, 1–10. [CrossRef] [PubMed]
28. Porada, S.; Zhao, R.; Van Der Wal, A.; Presser, V.; Biesheuvel, P. Review on the science and technology of water desalination by capacitive deionization. *Prog. Mater. Sci.* **2013**, *58*, 1388–1442. [CrossRef]
29. Gopinadhan, K.; Hu, S.; Esfandiar, A.; Lozada-Hidalgo, M.; Wang, F.; Yang, Q.; Tyurnina, A.; Keerthi, A.; Radha, B.; Geim, A. Complete steric exclusion of ions and proton transport through confined monolayer water. *Science* **2019**, *363*, 145–148. [CrossRef]
30. Dean, D.S. Langevin equation for the density of a system of interacting Langevin processes. *J. Phys. A Math. Gen.* **1996**, *29*, L613. [CrossRef]
31. Marconi, U.M.B.; Tarazona, P. Dynamic density functional theory of fluids. *J. Phys. Condens. Matter* **2000**, *12*, A413. [CrossRef]
32. te Vrugt, M.; Löwen, H.; Wittkowski, R. Classical dynamical density functional theory: From fundamentals to applications. *Adv. Phys.* **2020**, *69*, 121–247. [CrossRef]
33. Yoo, J.J.; Balakrishnan, K.; Huang, J.; Meunier, V.; Sumpter, B.G.; Srivastava, A.; Conway, M.; Mohana Reddy, A.L.; Yu, J.; Vajtai, R.; et al. Ultrathin planar graphene supercapacitors. *Nano Lett.* **2011**, *11*, 1423–1427. [CrossRef] [PubMed]
34. Yang, X.; Cheng, C.; Wang, Y.; Qiu, L.; Li, D. Liquid-mediated dense integration of graphene materials for compact capacitive energy storage. *Science* **2013**, *341*, 534–537. [CrossRef] [PubMed]
35. He, N.; Patil, S.; Qu, J.; Liao, J.; Zhao, F.; Gao, W. Effects of Electrolyte Mediation and MXene Size in Fiber-Shaped Supercapacitors. *ACS Appl. Energy Mater.* **2020**, *3*, 2949–2958. [CrossRef]
36. Li, S.; Fan, Z.; Wu, G.; Shao, Y.; Xia, Z.; Wei, C.; Shen, F.; Tong, X.; Yu, J.; Chen, K.; et al. Assembly of Nanofluidic MXene Fibers with Enhanced Ionic Transport and Capacitive Charge Storage by Flake Orientation. *ACS Nano* **2021**, *15*, 7821–7832. [CrossRef]
37. Yang, Q.; Xu, Z.; Fang, B.; Huang, T.; Cai, S.; Chen, H.; Liu, Y.; Gopalsamy, K.; Gao, W.; Gao, C. MXene/graphene hybrid fibers for high performance flexible supercapacitors. *J. Mater. Chem. A* **2017**, *5*, 22113–22119. [CrossRef]
38. Vasilyev, O.A.; Kornyshev, A.A.; Kondrat, S. Connections matter: On the importance of pore percolation for nanoporous supercapacitors. *ACS Appl. Energy Mater.* **2019**, *2*, 5386–5390. [CrossRef]
39. Lian, C.; Su, H.; Li, C.; Liu, H.; Wu, J. Non-negligible roles of pore size distribution on electroosmotic flow in nanoporous materials. *ACS Nano* **2019**, *13*, 8185–8192. [CrossRef]
40. Jiang, J.; Cao, D.; Jiang, D.e.; Wu, J. Time-dependent density functional theory for ion diffusion in electrochemical systems. *J. Phys. Condens. Matter* **2014**, *26*, 284102. [CrossRef]
41. Roth, R. Fundamental measure theory for hard-sphere mixtures: A review. *J. Phys. Condens. Matter* **2010**, *22*, 063102. [CrossRef]
42. Wang, Z.; Liu, L.; Neretnieks, I. The weighted correlation approach for density functional theory: A study on the structure of the electric double layer. *J. Phys. Condens. Matter* **2011**, *23*, 175002. [CrossRef] [PubMed]
43. Bazant, M.Z.; Storey, B.D.; Kornyshev, A.A. Double layer in ionic liquids: Overscreening versus crowding. *Phys. Rev. Lett.* **2011**, *106*, 046102. [CrossRef] [PubMed]
44. Bi, S.; Banda, H.; Chen, M.; Niu, L.; Chen, M.; Wu, T.; Wang, J.; Wang, R.; Feng, J.; Chen, T.; et al. Molecular understanding of charge storage and charging dynamics in supercapacitors with MOF electrodes and ionic liquid electrolytes. *Nat. Mater.* **2020**, *19*, 552–558. [CrossRef] [PubMed]
45. Janssen, M.; Griffioen, E.; Biesheuvel, P.; Van Roij, R.; Erné, B. Coulometry and calorimetry of electric double layer formation in porous electrodes. *Phys. Rev. Lett.* **2017**, *119*, 166002. [CrossRef] [PubMed]
46. Evlashin, S.; Fedorov, F.; Dyakonov, P.; Maksimov, Y.M.; Pilevsky, A.; Maslakov, K.; Kuzminova, Y.O.; Mankelevich, Y.A.; Voronina, E.; Dagesyan, S.; et al. Role of Nitrogen and Oxygen in Capacitance Formation of Carbon Nanowalls. *J. Phys. Chem. Lett.* **2020**, *11*, 4859–4865. [CrossRef] [PubMed]
47. Prehal, C.; Koczwara, C.; Amenitsch, H.; Presser, V.; Paris, O. Salt concentration and charging velocity determine ion charge storage mechanism in nanoporous supercapacitors. *Nat. Commun.* **2018**, *9*, 1–8. [CrossRef] [PubMed]
48. Tomlin, R.J.; Roy, T.; Kirk, T.L.; Marinescu, M.; Gillespie, D. Impedance response of ionic liquids in long slit pores. *arXiv* **2021**, arXiv:2110.07014.
49. Henrique, F.; Zuk, P.J.; Gupta, A. Charging dynamics of electrical double layers inside a cylindrical pore: Predicting the effects of arbitrary pore size. *Soft Matter* **2022**, *18*, 198–213. [CrossRef]
50. Zeng, L.; Wu, T.; Ye, T.; Mo, T.; Qiao, R.; Feng, G. Modeling galvanostatic charge-discharge of nanoporous supercapacitors. *Nat. Comput. Sci.* **2021**, *1*, 725–731. [CrossRef]

51. Aslyamov, T.; Sinkov, K.; Akhatov, I. Electrolyte structure near electrodes with molecular-size roughness. *Phys. Rev. E* **2021**, *103*, L060102. [CrossRef] [PubMed]
52. Wolfram Research, Inc. *Mathematica, Version 12.1*; Wolfram Research, Inc.: Champaign, IL, USA, 2020.

nanomaterials

MDPI

Article

An Array of Flag-Type Triboelectric Nanogenerators for Harvesting Wind Energy

Zhiqiang Zhao [1,2,3,†], Bin Wei [1,†], Yan Wang [4], Xili Huang [1], Bo Li [1], Fang Lin [1], Long Ma [1,2,3], Qianxi Zhang [1], Yongjiu Zou [4], Fang Yang [1,3], Hongchen Pang [1,3,*], Jin Xu [1,2,3,*] and Xinxiang Pan [1,2,3,*]

[1] Maritime College, School of Electronics and Information Technology, Guangdong Ocean University, Zhanjiang 524088, China; zhaozhiqiang929@gdou.edu.cn (Z.Z.); weibin2@stu.gdou.edu.cn (B.W.); 2112010010@stu.gdou.edu.cn (X.H.); boli@gdou.edu.cn (B.L.); linfang@gdou.edu.cn (F.L.); malong@gdou.edu.cn (L.M.); zhangqx@gdou.edu.cn (Q.Z.); neomailyf@gdou.edu.cn (F.Y.)
[2] Guangdong Provincial Shipping Intelligence and Safety Engineering Technology Research Center, Zhanjiang 524088, China
[3] Southern Marine Science and Engineering Guangdong Laboratory (Zhanjiang), Zhanjiang 524006, China
[4] Marine Engineering College, Dalian Maritime University, Dalian 116026, China; e0701746@u.nus.edu (Y.W.); zouyj0421@dlmu.edu.cn (Y.Z.)
* Correspondence: neomailphc@gdou.edu.cn (H.P.); jinxu@gdou.edu.cn (J.X.); panxx@gdou.edu.cn (X.P.)
† These authors contributed equally to this work.

Abstract: Harvesting wind energy from the ambient environment is a feasible method for powering wireless sensors and wireless transmission equipment. Triboelectric nanogenerators (TENGs) have proven to be a stable and promising technology for harvesting ambient wind energy. This study explores a new method for the performance enhancement and practical application of TENGs. An array of flag-type triboelectric nanogenerators (F-TENGs) for harvesting wind energy is proposed. An F-TENG consists of one piece of polytetrafluoroethylene (PTFE) membrane, which has two carbon-coated polyethylene terephthalate (PET) membranes on either side with their edges sealed. The PTFE was pre-ground to increase the initial charge on the surface and to enhance the effective contact area by improving the surface roughness, thus achieving a significant improvement in the output performance. The vertical and horizontal arrays of F-TENGs significantly improved the power output performance. The optimal power output performance was achieved when the vertical parallel distance was approximately $4D/15$ (see the main text for the meaning of D), and the horizontal parallel distance was approximately $2D$. We found that the peak output voltage and current of a single flag-type TENG of constant size were increased by 255% and 344%, respectively, reaching values of 64 V and 8 μA, respectively.

Keywords: flag-type; triboelectric nanogenerator; wind energy; array; network generation

Citation: Zhao, Z.; Wei, B.; Wang, Y.; Huang, X.; Li, B.; Lin, F.; Ma, L.; Zhang, Q.; Zou, Y.; Yang, F.; et al. An Array of Flag-Type Triboelectric Nanogenerators for Harvesting Wind Energy. *Nanomaterials* **2022**, *12*, 721. https://doi.org/10.3390/nano12040721

Academic Editor: Sophie Tingry

Received: 26 January 2022
Accepted: 17 February 2022
Published: 21 February 2022

1. Introduction

In the era of the Internet of Things (IoT), the widespread implementation of low-power wireless sensors, portable electronics, and wireless transmission devices is required. This requirement raised concerns regarding the associated increase in demand for energy supply, owing to the large number and dispersed locations of the required devices.

Wind power is a promising renewable energy source for wireless sensors and wireless transmission equipment because it is one of the cleanest sources of energy, with a wide distribution and high availability. Currently, wind power is mostly generated using large-scale equipment containing horizontal-axis propeller wind turbines with runners to drive generators for creating electricity [1,2]. A minority of wind power generation methods implement miniaturized equipment. Li et al. introduced a blade structure that uses the piezoelectric effect to collect wind energy. After changing the traditional arrangement of a flutter device parallel to the flow direction to a suspended cross-flow arrangement, the

vibration was amplified by an order of magnitude [3]. Perković et al. used the Gnus effect to generate electricity using high-altitude wind energy [4]. Ji et al. also used piezoelectric principles to fabricate a small wind energy collection device in a resonant cavity, which greatly improved the conversion efficiency compared to other small wind energy collection devices [5]. Perez et al. used a combination of the tremor effect and electret conversion to convert the flow-induced motion of a film into electrical energy [6]. To date, although the collection of wind energy is gradually becoming diversified, various problems remain concerning the implementation of miniaturized wind energy collection devices, such as their complex structure and low efficiency.

Triboelectric nanogenerators (TENGs) possess significant advantages over electromagnetic and piezoelectric power generators. Much work has been conducted on TENGs for wind energy harvesting. Various studies proposed a new type of power generation technology, which couples electrostatic induction with the triboelectric effect to efficiently convert mechanical energy into electrical energy [7–13]. In the field of wind energy collection, a substantial number of wind energy collection devices based on TENG were designed. For example, Yang et al. used a combination of fluorinated ethylene propylene (FEP) film and aluminum film in an acrylic tube to produce a self-powered sensor system that integrates wind energy collection and vector wind speed measurement [14]. Bae et al. used gold as a conductive material and used rigid plates coupled with flexible fabrics to generate electricity. This device could generate an instantaneous voltage of 220 V and a short-circuit current of 60 μA at a wind speed of 15 m/s, with an average power density of 0.86 mW [15]. Wang et al. reported on a systematic study of a combination of polyimide film and a TENG driven by elasto-aerodynamics, composed of copper electrodes, and fixed in an acrylic fluid channel, and derived a relationship between the output power density and the size of the fluid channel [16]. Zhao et al. proposed a flag-shaped TENG based on a weaving method, which collected high-altitude wind energy using power-sensing equipment to charge a lithium battery [17]. Wang et al. designed a sandwich flag-type triboelectric nanogenerator (F-TENG), which has a simpler structure and lower cost than other wind energy collection devices and maintained good output performance under conditions of high humidity. [18]. In addition, some scholars proposed the "all-in-one package" technology containing both TENG and PNG, which have great potential in harvesting energy from water waves (blue energy), airflow (wind energy), sound frequency (acoustic energy), vibrations/mechanical motions (such as body motions activities/sleeping), and in vivo body motions. These harvesting technologies are expected to dominate the future smart world [19–22].

Published research on wind energy harvesting based on TENGs precluded the full use of the characteristics of polytetrafluoroethylene (PTFE) electrets and aerodynamics, resulting in a low power output. This study explores a method for collecting wind energy based on a TENG providing direct power to low-power-consumption wireless terminals to solve the problems of energy needs, scattered arrangement, and environmental pollution. The optimal array structure of an F-TENG based on wind-induced fluid vortex-induced vibration is also discussed.

2. Materials and Methods

2.1. The Working Principle of a Single F-TENG

According to the power generation principle of an F-TENG, each contact surface of the triboelectric pair is regarded as a node and simplified to an equivalent capacitance model [23]. Based on the principle of the contact-mode freestanding TENG, the intrinsic output performance of the TENG can be deduced using electrodynamics. The formulas for calculating the open-circuit voltage V_{OC} and the short-circuit charge transfer Q_{SC} are as follows:

$$V_{OC} = \frac{2\sigma x(t)}{\varepsilon_0}; \quad (1)$$

$$Q_{SC} = \frac{2S\sigma x(t)}{d_0 + g}. \quad (2)$$

In these equations, the ratio of the thickness of the dielectric material between the two electrodes to the relative dielectric constant is defined as the effective thickness constant d_0, and the electrode gap g, whereas ε_0 is the relative dielectric constant of air, and $x(t)$ is the distance between the two triboelectric surfaces, which changes with time according to the external force-triggered condition. The quantity σ is the surface charge density of the PTFE and the conductive ink film, whereas S is the actual contact area between the PTFE and the conductive ink film. The relationship between the voltage (V), the amount of charge (Q), and the distance between the two triboelectric charges (x) of the F-TENG can be deduced using the electrodynamic theory [24]:

$$V = -\frac{Q}{C} + V_{OC} = -\left(\frac{d_0 + g}{\varepsilon_0 S}\right)Q + \frac{2\sigma x(t)}{\varepsilon_0}. \quad (3)$$

Based on Equation (1), an increase in the surface charge density of the PTFE effectively increases the output of the F-TENG charge. PTFE is an electret material [25] and its charge can be retained on its surface for a long time. Three F-TENGs of the same size were fabricated (length D = 150 mm, breadth B = 75 mm, thickness T = 80 μm). The PTFE films were treated with different grinding procedures.

The working principle of the F-TENG is shown in Figure 1a. Owing to the different stiffnesses, the bending degrees of the PTFE and the electrode are different, and flutter deformation occurs under the action of wind, resulting in alternating contact and separation between the PTFE and the electrode. In the F-TENG's original state, the electrode and PTFE are separated, and there is no charge transfer. When the F-TENG is bent upward, the PTFE comes into contact with the lower electrode. Owing to the difference in the electron affinity between the PTFE and electrode, the electrode and the surface of the PTFE carry positive and negative charges, respectively. As the electrodes are separated, a potential difference is created between the two electrodes, driving electrons through an external circuit from the upper electrode to the lower electrode and generating a current. When the F-TENG is bent downward, the PTFE is in contact with the upper electrode, which is positively charged. If the PTFE is separated from the upper electrode, the electrons flow in the opposite direction, and an opposite current will be generated in the external circuit. Therefore, owing to the alternating contact and separation between the PTFE and the conductive ink film electrode, a short-circuit alternating current is formed as the charge flows repeatedly between the two layers of the conductive ink film electrode.

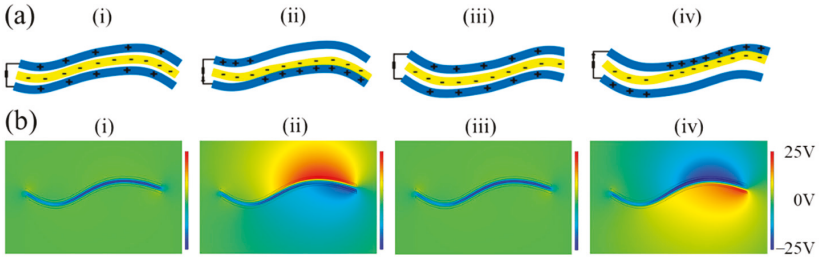

Figure 1. Working principle and simulation of the flag-type triboelectric nanogenerator (F-TENG): (**a**) power generation principle of F-TENG and (**b**) simulation graphic of COMSOL.

The COMSOL Multiphysics 5.6 software package was used to simulate the electrical distribution of the F-TENG during flutter deformation, as shown in Figure 1b. In the initial state, assuming that the surface of the PTFE carried a negative charge that was uniformly distributed, each of the two electrodes carried an equal amount of positive charge, and the total amount was equal to the negative charge mentioned above. As shown in Figure 1b(i), when the PTFE film is located at the center of the electrodes on both sides, the electric potential on the respective electrodes is equal, without any potential difference. When

the lower electrodes of the PTFE film are close to each other (as shown in Figure 1b(ii)), a potential difference is induced between the lower and upper electrodes. As shown in Figure 1b(iv), the PTFE then moves in the upward direction until it contacts the upper electrode, generating an electromotive force opposite to that in Figure 1b(ii).

2.2. The Fabrication and Pre-Grinding of an F-TENG

The structure of the designed TENG is illustrated in Figure 2a. A PTFE film with a thickness of 30 μm was chosen as the substrate material owing to its low weight, good workability, and electron affinity. Using screen-printing technology, conductive ink, as the flexible electrode, was coated onto a polyethylene terephthalate (PET) substrate with a thickness of 25 μm. The F-TENG adopted a "sandwich flexible structure" in the sequence electrode-PTFE-electrode, wherein an electrode was employed as both a triboelectric material and a conductive material. The surface microstructures of the PTFE films of the three respective types of F-TENGs we fabricated are shown in Figure 2b. The roughnesses of the three types of PTFE films obtained by grinding with different sandpapers (untreated group, ground by P10000 sandpaper, and ground by P400 sandpaper, the normal pressure/force is about 2 N and horizontal speed of grinding with the sandpaper is about 0.05 m/s) are obviously different.

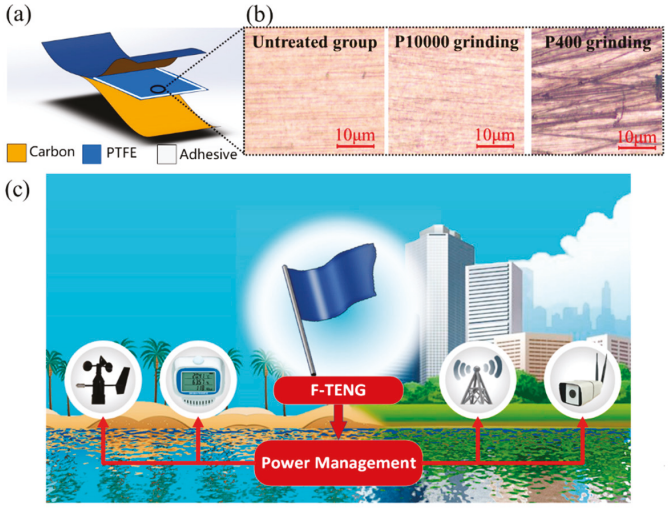

Figure 2. Structure and microstructure of F-TENGs: (**a**) structure and materials of each F-TENG; (**b**) microstructure of different types of polytetrafluoroethylene (PTFE) films after pre-grinding; and (**c**) schematic diagram of F-TENGs applied to wind harvesting and power supply.

2.3. Experimental Setup

The experimental setup for testing the F-TENGs' output performance in a low-speed wind tunnel is shown in Figure 3. The dimensions of the wind tunnel were 0.25 m (width) × 0.25 m (height) × 1 m (length), and the wind speed was varied between 2 m/s and 13 m/s using an inverter for speed control. A programmable electrometer (Keithley Model 6514, Cleveland, OH, USA) and Data Acquisition Board (NI DAQ, Shanghai Enai Instrument Co., Ltd., Shanghai, China) were used to realize the measurement and acquire the experimental data. A 3D printed structure was used to fix an F-TENG inside the wind tunnel. The position of the F-TENG could be changed in subsequent experiments.

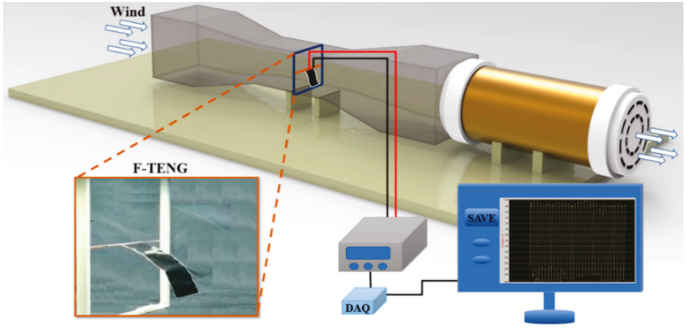

Figure 3. Schematic of the experimental apparatus for assessing F-TENG power generation performance in a wind tunnel.

2.4. Horizontal and Vertical Parallel Arrays of Double F-TENGs

The special membrane structure of an F-TENG allows for it to be stacked inside a small space to form power generation device arrays. Because of the effect of flow-induced vibration, interference occurs when two flags are positioned horizontally or vertically in parallel, resulting in changes in the vibration amplitude and frequency. With respect to the horizontal parallel arrays, Zhu [26] designed and performed a series of numerical simulations on the interaction of a pair of horizontal parallel flexible flags separated by a dimensionless distance ($0 \leq D_t \leq 5.5$) in a flowing, incompressible viscous fluid using the immersed boundary (IB) method at lower Reynolds numbers ($40 \leq Re \leq 220$). Based on the dimensionless IB formulation in component form, the elastic potential energy density E associated with the flags, and the Eulerian coordinates, X and Y (x and y components, respectively), of the flags, whose associated Lagrangian coordinate is α, are computed as follows:

$$E = \frac{1}{2}\hat{K}_s \int_\Gamma \left(\sqrt{\left(\frac{\partial X}{\partial \alpha}\right)^2 + \left(\frac{\partial Y}{\partial \alpha}\right)^2} - 1 \right)^2 \mathrm{d}\alpha + \frac{1}{2}\hat{K}_b \int_\Gamma \left(\left(\frac{\partial^2 X}{\partial \alpha^2}\right)^2 + \left(\frac{\partial^2 Y}{\partial \alpha^2}\right)^2 \right) \mathrm{d}\alpha; \quad (4)$$

$$\frac{\partial X}{\partial t}(\alpha, t) = \int_\Omega u\delta(x - X(\alpha, t))\delta(y - Y(\alpha, t))\mathrm{d}x\mathrm{d}y; \quad (5)$$

$$\frac{\partial Y}{\partial t}(\alpha, t) = \int_\Omega v\delta(x - X(\alpha, t))\delta(y - Y(\alpha, t))\mathrm{d}x\mathrm{d}y. \quad (6)$$

In the above equations, x and y are the Eulerian coordinates associated with the fixed computational domain, α is the Lagrangian coordinate associated with the moving flags, and t is the time. The quantities u and v are the components of the fluid velocity along the x and y axes, respectively. The symbol Γ represents the flags, and Ω represents the two-dimensional fluid domain (the rectangle with an aspect ratio of 2:1). The quantities $\hat{K}_s$ and $\hat{K}_b$ are the stretching/compression coefficient and bending modulus of the flags, respectively. The flag position (X, Y) is updated by applying Equations (5) and (6). Previous studies determined that the distance between the flags is the key factor in determining the energy received by the flag.

With respect to vertical parallel arrays, Wang [27] used the value of the dimensionless parameter St, which represents the vibration characteristics of objects, to describe the change in the swing of a single flag as a function of wind speed:

$$St = fA/U. \quad (7)$$

The peak value of the trailing edge displacement of the flag is represented by A, the swing frequency of the trailing edge by f, and the inflow velocity by U. Under different inlet wind speeds, the two flags may move in four different coupling modes: static, co-directional swing, reverse swing, and transition state. The experimental results laid the experimental foundation for our research on the vertical parallel mode. The four different coupling modes discussed to provide a reference for the optimal layout of the F-TENG in a vertical parallel array, which optimizes the output performance.

3. Results and Discussion

3.1. The Output Performance of a Single F-TENG with Different Pre-Grinding

As shown in Figure 4, the maximum output voltage (V_{max}) obtained experimentally for the untreated group is approximately 15–18 V at a wind speed of 7.2 m/s. The V_{max} of the F-TENG fabricated by grinding the PTFE with P10000 sandpaper is approximately 22 V. The roughness of the PTFE after grinding with P400 sandpaper is the greatest among the three samples, and the voltage output obtained with this sample of PTFE is also the largest. At a wind speed of 7.2 m/s, the output voltage and current of the F-TENG ground by P400 reaches 64 V and 8 μA, respectively, values that are approximately 255% and 344% higher, respectively, than those of the untreated group.

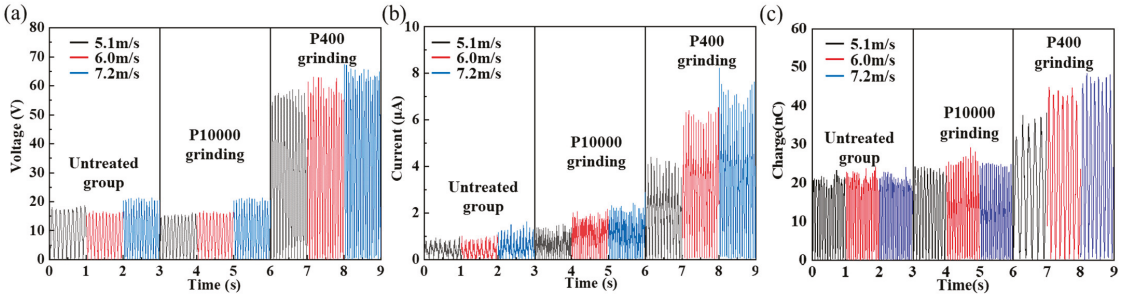

Figure 4. Output of F-TENG: (**a**) output of voltage with the degree of pre-grinding; (**b**) output of current with the degree of pre-grinding; (**c**) output of charge with the degree of pre-grinding.

Three F-TENGs were prepared using different pre-grinding methods. F-TENG #1 and #2 were ground using P10000 sandpaper, and F-TENG #3 was ground using P400 sandpaper. The voltages, currents, transferred charges, and power outputs ($P = I^2R$) obtained experimentally are displayed in Figure 5. The variations in the electrical properties of the three F-TENGs all show similar trends, but F-TENG #3 clearly delivered a superior level of performance. The analysis revealed that the electret characteristics of the PTFE film caused an increase in the surface charge density σ after the grinding treatment. According to Equation (1), in the process of alternating contact and separation between the PTFE film and the conductive ink film, the open-circuit voltage V_{OC} and the short-circuit charge transfer Q_{SC} increase in the same proportion, which leads to an increase in the current and power in the circuit. The micro-nano scratches that formed on the surface of the PTFE film after the pre-grinding treatment enhanced the degree of triboelectric contact between the PTFE and the conductive ink film, and further increased the amount of triboelectric charge. Therefore, the pre-grinding treatment is an important factor in improving the power generation performance of F-TENGs.

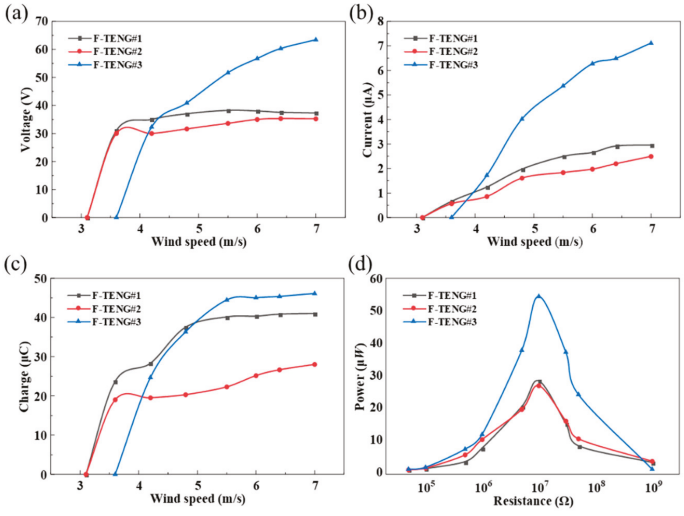

Figure 5. Variation of output of F-TENG#1, #2, and #3 with increasing wind speed: (**a**) voltage output of F-TENGs with different pre-grinding; (**b**) current output of F-TENGs with different pre-grinding; (**c**) charge output of F-TENGs with different pre-grinding; and (**d**) power output of F-TENGs with different pre-grinding.

3.2. Horizontal and Vertical Parallel Array Characterization of the Double F-TENGs

The interaction between the two flags in different modes of parallel motion can lead to different internal triboelectric states in an F-TENG. This characteristic can therefore be used to improve the power generation performance of F-TENGs. The use of an F-TENG to collect wind energy and increase the amplitude of vibration is beneficial for improving the output of electricity [18]. Two F-TENGs were arranged in horizontal parallel and vertical parallel modes, respectively, for interference experiments in a low-speed wind tunnel, with the results shown in Figure 6.

In the vertical parallel mode experiments, F-TENGs #1 and #2 with similar performance outputs were selected and placed in the vertical parallel mode. The vertical distance between the two flagpoles (e_P) was adjusted to $1D/15$, $2D/15$, $4D/15$, $6D/15$, and $8D/15$, owing to the limitation of the wind tunnel size, the maximum value that could be obtained for e_P was $8D/15$. The power output characteristics at different values of e_P were measured at a wind speed of 7.2 m/s. The contrast diagram of the maximum total output power when F-TENG #1 and #2 were connected to the circuit in series is shown in Figure 6a. When the interval $e_P = 1D/15$, the swing phases of the two flags were identical, and the total output power was low. When $e_P = 2D/15$, the swing phases of the two flags were chaotic, and the output was unstable, indicating that the configuration lay in the zone between phase coherence and anti-phase coherence. When $e_P \geq 4D/15$, the swing phases of the two flutter flags were opposite. When $e_P = 4D/15$, the maximum output power of the array with two F-TENGs was achieved at 67.8 μW, whereas the power density per unit area was 6.03 mW/m^2. The analysis indicated that the two flags fluttered in the opposite phase and were close to each other, which increased the triboelectric strength and contact area between the PTFE films and the electrodes, thus increasing the output of the F-TENGs. With an increase in the distance between the two flags, the contact area decreased, and the maximum output power decreased and tended to stabilize.

In the horizontal parallel mode experiments, as shown in Figure 6b, F-TENG # 3 was selected as the measurement unit, and an F-TENG of the same size was placed in front of it as the interference source. By changing the horizontal distance between the two flagpoles (e_T), the output characteristics of the rear flag (F-TENG #3) were analyzed to determine

the optimal distance for achieving the maximum power output. We assumed that the lengths of the F-TENG were D and assumed $0.5D$ as the moving distance. When $e_T = 2D$, the output power of F-TENG #3 reached its maximum and the maximum output power increased by approximately 17.9% compared to that of the single flag. With an increase in e_T, the interference gradually weakened, and the output power gradually decreased. When $e_T = 2.5D$, the output power was close to the output power of the single F-TENG. The reason for this phenomenon is that the front flag interfered with the airflow and formed a shedding vortex, which increased the vibration amplitude of the rear flag [26], thus increasing its output power.

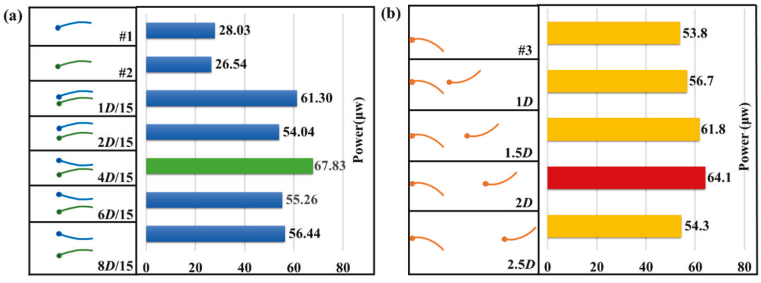

Figure 6. Contrast diagram of the maximum value of total power output of F-TENGs: (**a**) F-TENG #1 and #2 varying with e_P in vertical parallel mode and (**b**) F-TENG #3 varying with e_T in horizontal parallel mode.

3.3. Generation Performance of the F-TENGs Network

Based on the aforementioned results, we arranged twelve F-TENGs to form a power generation network, as shown in Figure 7a. In this array, the distance e_T was fixed at $1D$. By adjusting the vertical distance e_P in each group, the performance of the power generation network was measured; limited by the size of the wind tunnel, when three rows of F-TENGs were arranged in a vertically parallel mode, the maximum possible vertical distance e_P was $6D/15$. A circuit was designed for wind energy harvesting with an array of LEDs as the power output. The 2 electrodes of an F-TENG were sequentially connected to a rectifier to provide a direct current output, and 12 F-TENGs were connected in multiple modes to a power load composed of 100 LEDs. By setting the wind speed equal to 8.0 m/s in the wind tunnel, 100 LEDs are efficiently lit by the 12 F-TENGs arranged at separations of $4D/15$ in the vertical direction and at separations of $1D$ in the horizontal direction, as shown in Figure 7a,b.

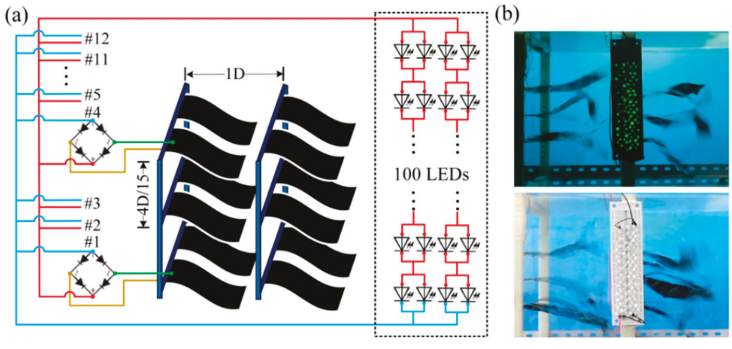

Figure 7. Network and output of F-TENGs: (**a**) schematic diagram of twelve F-TENGs combined for grid power and (**b**) photographs showing the array of twelve F-TENGs lighting up 100 LEDs.

4. Conclusions

The placement of a TENG device is challenging because of its aerodynamic and electrostatic characteristics. It is important to choose a reasonable distance between each F-TENG device to improve the output power. Therefore, a procedure for enhancing the performance of an F-TENG array and the associated networking design was proposed and investigated in the present paper. The designed F-TENG array effectively converted the flutter energy contained in wind into electrical energy by enhancing the triboelectric interaction between the PTFE membrane and a carbon-coated membrane, as well as increasing the charge on the PTFE membrane. In wind tunnel experiments, the maximum output voltage and current of the F-TENG array were enhanced by 255% and 344%, respectively, after pre-grinding the PTFE dielectric membranes. The F-TENG network was assembled in a configuration that enhanced its power generation performance. When the network contained two F-TENGs arranged in horizontal parallel mode at a separation of 1D, the peak output power of F-TENG #3 was increased by 17.9%. When F-TENG #1 and #2 were arranged in vertical parallel mode at a separation of 4D/15, the peak output power increased by 24.3%, and the power density per unit area reached 6.03 mW/m^2. When the network contained 12 F-TENGs separated by 1D in the horizontal direction and by 6D/15 in the vertical direction, under 8.0 m/s wind conditions, the array was able to light up 100 LEDs simultaneously. In this study, to efficiently place more energy harvesting elements in a small space, we selected an optimal F-TENG arrangement scheme. The arrangement was chosen in such a way that each F-TENG element can maximize the energy harvesting efficiency. The array of fabricated F-TENGs developed and tested in this study shows great potential for applications in wind energy harvesting and power supply for wireless sensors and devices.

5. Experimental Section

5.1. The Fabrication of the F-TENG Unit and Network

The construction process of the F-TENG is shown in Figure 2a. The F-TENG and the flagpole were connected using sticky tape. The size of the F-TENG was 150 mm (length) × 75 mm (width) × 80 μm (thickness). The PTFE and PET membranes were 30 μm and 25 μm in thickness, respectively. A conductive carbon ink electrode with a micrometer thickness was attached to the back side of the PET to serve as the flexible electrode. The F-TENG was composed of two flexible electrodes and one layer of PTFE membrane with their edges sealed up by 3M200C type dual adhesive tape whose width was 2 mm and thickness was 30 μm. The double surfaces of the PTFE membrane were pre-ground with sandpapers, such as P10000 and P400, before assembly.

The structure of the F-TENG network is shown in Figure 7a. The network in this experiment contained two frames made by a 3D printer with polylactic acid (PLA) material. Both frames were free to move to adjust their distance in the horizontal direction. The inner wall of the frame was provided with several equidistant grooves for inserting the flagpole and adjusting the distance of the flag in the vertical direction. Each frame was assembled with six F-TENGs with two flags arranged in the horizontal direction and three in the vertical direction.

5.2. Electrical Measurement of the TENG Unit and Network

A programmable electrometer was used to measure the electrical output of the unit and F-TENG. A wind tunnel with the dimensions of 0.25 m (width) × 0.25 m (height) × 1.0 m (length) simulated the wind conditions under which the experiments of the F-TENG unit and the network were performed. The wind speed varied from 2.0 m/s to 8.0 m/s, which was calibrated by a GM8903 type anemometer. At the right end of the wind tunnel, a blower was firmly installed, whose rotating speed was controlled by an inverter in order to adjust the wind speed.

Author Contributions: Z.Z. and B.W. contributed equally to this work. Conceptualization, methodology, Y.W., L.M. and J.X.; software, B.W.; validation, formal analysis, data curation, investigation, writing—review and editing, visualization, Z.Z., B.W. and X.H.; resources, supervision, project administration, funding acquisition, B.L., Q.Z., H.P. and X.P.; writing—original draft preparation, F.L., F.Y. and Y.Z. All authors have read and agreed to the published version of the manuscript.

Funding: This research was financially supported by the National Natural Science Foundation (Grant No. 51979045); the Project of Zhanjiang Science and Technology Research (Grant No. 2021B01075); and the Zhanjiang innovation and entrepreneurship team lead "pilot plan" project (Grant No. 2020LHJH003).

Institutional Review Board Statement: Not applicable.

Informed Consent Statement: Not applicable.

Data Availability Statement: Not applicable.

Conflicts of Interest: The authors declare no conflict of interest.

References

1. Wendler, R.; Calderón-Muñoz, W.R.; LeBoeuf, R. Energy-based iteration scheme of the double-multiple streamtube model in vertical-axis wind turbines. *Acta Mech.* **2016**, *227*, 3295–3303. [CrossRef]
2. Zhou, A.; Yu, D.; Wu, X.; Liu, J.; Li, R. Research on Intelligent Fault Diagnosis for Large-scale Wind Turbines Based on Ontology. *China Mech. Eng.* **2012**, *23*, 2075–2080.
3. Li, S.; Yuan, J.; Lipson, H. Ambient wind energy harvesting using cross-flow fluttering. *J. Appl. Phys.* **2011**, *109*, 026104. [CrossRef]
4. Perković, L.; Silva, P.; Ban, M.; Kranjčević, N.; Duić, N. Harvesting high altitude wind energy for power production: The concept based on Magnus' effect. *Appl. Energy* **2013**, *101*, 151–160. [CrossRef]
5. Ji, J.; Kong, F.; He, L.; Guan, Q.; Feng, Z. Piezoelectric Wind-Energy-Harvesting Device with Reed and Resonant Cavity. *Jpn. J. Appl. Phys.* **2010**, *49*, 311–333. [CrossRef]
6. Perez, M.; Boisseau, S.; Gasnier, P.; Willemin, J.; Reboud, J.L. An electret-based aeroelastic flutter energy harvester. *Smart Mater. Struct.* **2015**, *24*, 035004. [CrossRef]
7. Xu, M.Y.; Wang, P.H.; Wang, Y.C.; Zhang, S.; Wang, A.; Zhang, C.L.; Wang, Z.J.; Pan, X.X.; Wang, Z.L. A Soft and Robust Spring Based Triboelectric Nanogenerator for Harvesting Arbitrary Directional Vibration Energy and Self-Powered Vibration Sensing. *Adv. Energy Mater.* **2017**, *8*, 1702432. [CrossRef]
8. Liang, X.; Jiang, T.; Liu, G.; Feng, Y.; Zhang, C.; Wang, Z.L. Spherical triboelectric nanogenerator integrated with power management module for harvesting multidirectional water wave energy. *Energy Environ. Sci.* **2020**, *13*, 277–285. [CrossRef]
9. Gallardo-Vega, C.; Lopez-Lagunes, O.; Nava-Galindo, O.I.; De Leon, A.; Romero-Garcia, J.; Antonio Aguilera-Cortes, L.; Martinez-Castillo, J.; Herrera-May, A.L. Triboelectric Energy Harvester Based on Stainless Steel/MoS_2 and PET/ITO/PDMS for Potential Smart Healthcare Devices. *Nanomaterials* **2021**, *11*, 1533. [CrossRef]
10. Garofalo, E.; Cecchini, L.; Bevione, M.; Chiolerio, A. Triboelectric Characterization of Colloidal TiO_2 for Energy Harvesting Applications. *Nanomaterials* **2020**, *10*, 1181. [CrossRef]
11. Zhao, H.F.; Xiao, X.; Xu, P.; Zhao, T.C.; Song, L.G.; Pan, X.X.; Mi, J.C.; Xu, M.Y.; Wang, Z.L. Dual-Tube Helmholtz Resonator-Based Triboelectric Nanogenerator for Highly Efficient Harvesting of Acoustic Energy. *Adv. Energy Mater.* **2019**, *9*, 10. [CrossRef]
12. Shankaregowda, S.A.; Ahmed, R.; Liu, Y.; Nanjegowda, C.B.; Cheng, X.; Shivanna, S.; Ramakrishna, S.; Yu, Z.F.; Zhang, X.; Sannathammegowda, K. Dry-Coated Graphite onto Sandpaper for Triboelectric Nanogenerator as an Active Power Source for Portable Electronics. *Nanomaterials* **2019**, *9*, 12. [CrossRef] [PubMed]
13. Xu, M.Y.; Zhao, T.C.; Wang, C.; Zhang, S.L.; Li, Z.; Pan, X.X.; Wang, Z.L. High Power Density Tower-like Triboelectric Nanogenerator for Harvesting Arbitrary Directional Water Wave Energy. *ACS Nano* **2019**, *13*, 1932–1939. [CrossRef] [PubMed]
14. Yang, Y.; Zhu, G.; Zhang, H.L.; Chen, J.; Zhong, X.D.; Lin, Z.H.; Su, Y.J.; Bai, P.; Wen, X.N.; Wang, Z.L. Triboelectric Nanogenerator for Harvesting Wind Energy and as Self-Powered Wind Vector Sensor System. *ACS Nano* **2013**, *7*, 9461–9468. [CrossRef]
15. Bae, J.; Lee, J.; Kim, S.; Ha, J.; Lee, B.S.; Park, Y.; Choong, C.; Kim, J.B.; Wang, Z.L.; Kim, H.Y.; et al. Flutter-driven triboelectrification for harvesting wind energy. *Nat. Commun.* **2014**, *5*, 4929. [CrossRef]
16. Wang, S.H.; Mu, X.J.; Wang, X.; Gu, A.Y.; Wang, Z.L.; Yang, Y. Elasto-Aerodynamics-Driven Triboelectric Nanogenerator for Scavenging Air-Flow Energy. *ACS Nano* **2015**, *9*, 9554–9563. [CrossRef]
17. Zhao, Z.F.; Pu, X.; Du, C.H.; Li, L.X.; Jiang, C.Y.; Hu, W.G.; Wang, Z.L. Freestanding Flag-Type Triboelectric Nanogenerator for Harvesting High-Altitude Wind Energy from Arbitrary Directions. *ACS Nano* **2016**, *10*, 1780–1787. [CrossRef]
18. Wang, Y.; Yang, E.; Chen, T.Y.; Wang, J.Y.; Hu, Z.Y.; Mi, J.C.; Pan, X.X.; Xu, M.Y. A novel humidity resisting and wind direction adapting flag-type triboelectric nanogenerator for wind energy harvesting and speed sensing. *Nano Energy* **2020**, *78*, 105279. [CrossRef]
19. Bhunia, S.; Chandel, S.; Karan, S.K.; Dey, S.; Tiwari, A.; Das, S.; Kumar, N.; Chowdhury, R.; Mondal, S.; Ghosh, I.; et al. Autonomous self-repair in piezoelectric molecular crystals. *Science* **2021**, *373*, 321–327. [CrossRef]

20. You, Y.M.; Liao, W.Q.; Zhao, D.; Ye, H.Y.; Zhang, Y.; Zhou, Q.; Niu, X.; Wang, J.; Li, P.F.; Fu, D.W.; et al. An organic-inorganic perovskite ferroelectric with large piezoelectric response. *Science* **2017**, *357*, 306–309. [CrossRef]
21. Karan, S.K.; Maiti, S.; Lee, J.H.; Mishra, Y.K.; Khatua, B.B.; Kim, J.K. Recent Advances in Self-Powered Tribo-/Piezoelectric Energy Harvesters: All-In-One Package for Future Smart Technologies. *Adv. Funct. Mater.* **2020**, *30*, 52. [CrossRef]
22. Halder, L.; Maitra, A.; Das, A.K.; Bera, R.; Karan, S.K.; Paria, S.; Bera, A.; Si, S.K.; Khatua, B.B. Fabrication of an Advanced Asymmetric Supercapacitor Based on Three-Dimensional Copper–Nickel–Cerium–Cobalt Quaternary Oxide and GNP for Energy Storage Application. *ACS Appl. Electron. Mater.* **2019**, *1*, 189–197. [CrossRef]
23. Niu, S.M.; Wang, Z.L. Theoretical systems of triboelectric nanogenerators. *Nano Energy* **2015**, *14*, 161–192. [CrossRef]
24. Yang, E.; Wang, Y.; Wang, J.Y.; Wang, C.; Liu, C.X.; Wu, M.W.; Mi, J.C.; Xu, M.Y. Research on a film-flapping triboelectric nanogenerator for wind energy harvesting. *Sci. Sin. Technol.* **2021**, *51*, 684–698. [CrossRef]
25. Xu, W.H.; Zheng, H.X.; Liu, Y.; Zhou, X.F.; Zhang, C.; Song, Y.X.; Deng, X.; Leung, M.; Yang, Z.B.; Xu, R.X.; et al. A droplet-based electricity generator with high instantaneous power density. *Nature* **2020**, *578*, 392–396. [CrossRef]
26. Zhu, L. Interaction of two tandem deformable bodies in a viscous incompressible flow. *J. Fluid Mech.* **2009**, *635*, 455–475. [CrossRef]
27. Wang, S.; Sun, C.; Yin, X. Experiment of the Flapping Coupling Modes between Two Parallel Flags in a Aniform Flow. *J. Exp. Mech.* **2010**, *25*, 401–407.

nanomaterials

MDPI

Article

VO_2 as a Highly Efficient Electrocatalyst for the Oxygen Evolution Reaction

Yun-Hyuk Choi

School of Advanced Materials and Chemical Engineering, Daegu Catholic University, Gyeongsan 38430, Korea; yunhyukchoi@cu.ac.kr

Abstract: Herein, we report high electrocatalytic activity of monoclinic VO_2 (M1 phase) for the oxygen evolution reaction (OER) for the first time. The single-phase VO_2 (M1) nanoparticles are prepared in the form of uniformly covering the surface of individual carbon fibers constituting a carbon fiber paper (CFP). The VO_2 nanoparticles reveal the metal-insulator phase transition at *ca.* 65 °C (heating) and 62 °C (cooling) with low thermal hysteresis, indicating a high concentration of structural defect which is considered a grain boundary among VO_2 nanoparticles with some particle coalescence. Consequently, the VO_2/CFP shows a high electrocatalytic OER activity with the lowest η_{10} (350 mV) and Tafel slope (46 mV/dec) values in a 1 M aqueous solution of KOH as compared to those of the vacuum annealed V_2O_5 and the hydrothermally grown VO_2 (M1), α-V_2O_5, and γ'-V_2O_5. The catalytically active site is considered V^{4+} components and $V^{4+/5+}$ redox couples in VO_2. The oxidation state of V^{4+} is revealed to be more favorable to the OER catalysis compared to that of V^{5+} in vanadium oxide through comparative studies. Furthermore, the amount of V^{5+} component is found to be increased on the surface of VO_2 catalyst during the OER, giving rise to the performance degradation. This work suggests V^{4+} and its redox couple as a novel active component for the OER in metal-oxide electrocatalysts.

Keywords: electrocatalysis; oxygen evolution reaction; water splitting; vanadium oxide; nanoparticles

Citation: Choi, Y.-H. VO_2 as a Highly Efficient Electrocatalyst for the Oxygen Evolution Reaction. *Nanomaterials* **2022**, *12*, 939. https://doi.org/10.3390/nano12060939

Academic Editors: Marc Cretin, Sophie Tingry, Zhenghua Tang and Shiqiang (Rob) Hui

Received: 8 February 2022
Accepted: 9 March 2022
Published: 12 March 2022

1. Introduction

Renewable energy sources, such as wind and solar power, are providing an increasing share of the energy supply [1,2]. In particular, electrocatalytic water splitting is considered a promising strategy for the sustainable production of hydrogen from renewable energy sources [3–7]. However, overall water splitting suffers from the sluggish kinetics of anodic oxygen evolution reaction (OER) involving the four-electron oxidative half-reaction [8,9]. Therefore, an appropriate catalyst is necessary to accelerate the OER at low overpotentials (η) for enhanced energy conversion efficiencies [5]. The state-of-the-art OER catalysts are based on precious metals such as IrO_2 and RuO_2 with η close to 300 mV in a 1 M aqueous solution of KOH. However, the scarcity and high costs of those materials restrict their large-scale application [9]. In this regard, the earth-abundant transition-metal oxides based on Mn, Fe, Co, and Ni have been extensively investigated as alternative OER catalysts. In particular, Ni or Co-based layered double hydroxides (LDHs) exhibited high OER activities due to the oxidation or stabilization of Ni or Co ions forming the OER-active redox couples with the addition of Fe ion [8,10–12]. Also, spinel-type oxides such as Co_3O_4 and $NiCo_2O_4$ and amorphous Co-based oxides were proposed as promising OER catalysts [8,9,13,14]. Meanwhile, $Ba_{0.5}Sr_{0.5}Co_{0.8}Fe_{0.2}O_{3-\delta}$ (BSCF) perovskite was identified as the most promising OER catalyst based on orbital principles with the e_g occupation as a superior descriptor for oxygen evolution activity [15]. Other descriptor approaches of M-OH bond strength and ($\Delta G_O^* - \Delta G_{HO}^*$) were suggested to find superior catalysts [16,17]. However, application of such descriptors is limited to experimental work and finding novel catalysts based on other transition metals such as Nb, Ta, and V [9,18]. Among transition metal

oxides, OER activities of vanadium-based catalysts have seldom been explored although high OER activities for VOOH and Co-incorporated catalysts ($CoVO_x$, $Co_2V_2O_7$, $Co_3V_2O_8$, and $Co_3V_2O_8$) were recently highlighted [9,18–20]. However, we focused a spotlight on the fact that vanadium oxides (primarily, V_2O_5 and V_6O_{13}) exhibit excellent performance in various electrochemical devices such as Li-ion batteries and supercapacitors based on multiple vanadium oxidation states (V^{2+}, V^{3+}, V^{4+}, V^{5+}) and their redox couples [21–26]. Furthermore, the electrochemical reactivity and battery characteristics in VO_2 have often been reported [27–30]. Oxidative desulfurization of dibenzothiophene for monoclinic VO_2 was also reported [31]. V_2O_5 deposited on a high surface area oxide support (e.g., TiO_2 and Al_2O_3) is widely known as effective catalysts for selective oxidation of sulfur dioxide, naphthalene, *o*-xylene, alkyl pyridine, chlorinated hydrocarbon, and mercury in the chemical, petroleum, and environmental industries [32]. Despite such investigations, OER activities of binary VO_2 and V_2O_5 are rarely known.

In this work, we demonstrate a vacuum annealing approach for the direct integration of VO_2 nanoparticles onto conductive carbon finer paper (CFP), making the integration uniform and highly adhesive at the centimeter scale. The use of CFP is also intended to increase the exposure of catalytically active sites of VO_2 nanoparticles [33]. Since, in particular, VO_2 undergoes a phase transition between insulating monoclinic phase (M1) and metallic rutile phase (R) at *ca.* 67 °C in the bulk [34–37], the structural characterization of the VO_2/CFP involving the phase transition is carefully carried out. As a result, superior OER activity of VO_2 with low η and Tafel slope values is revealed as compared to that of V_2O_5. This result can be a cornerstone for understanding the V^{4+}-related active sites for OER and for the design of novel VO_2-based OER catalysts.

2. Experimental

Preparation of VO_2 (M1) nanoparticles by vacuum annealing: To prepare VO_2 nanoparticles coated on a carbon fiber paper (CFP), 0.1 g of V_2O_5 particles (Sigma-Aldrich, St. Louis, MI, USA) was dispersed in 10 mL of ethanol, followed by ultrasonication for 1 h. A solution loading of 100 μL/cm^2 using a micropipette was cast onto a bare CFP (Toray Paper 120) substrate with dimensions of 2 cm × 1 cm size, which was cleaned by ultrasonication in acetone, deionized water, and ethanol. The solution-coated CFP was allowed to dry in air overnight and placed within an alumina boat, which was placed at the center of a 1-inch-diameter horizontal cold-wall quartz tube furnace equipped with a rotary pump system. For annealing, the tube furnace was heated to 950 °C at a ramp rate of 20 °C/min under vacuum condition (~10 mTorr). After holding at 950 °C for 10 min, the furnace was allowed to cool naturally to room temperature. The annealed coat on CFP was then removed from the center of the furnace for characterization and electrocatalytic evaluation. To prepare V_2O_5 nanoparticles coated on CFP, the same V_2O_5-dispersion solution was cast onto a bare CFP substrate in the same way and allowed to dry in air overnight. Then, the solution-coated CFP was placed within the alumina boat placed at the furnace center, followed by annealing. The reactor was heated to a temperature of 950 °C at a ramp rate of 20 °C/min under an O_2 flow of 10 sccm and continuous vacuum pumping condition. After the temperature was held at 950 °C for 10 min, the furnace was then naturally cooled to room temperature.

Preparation of VO_2 (M1) nanoparticles for comparison: VO_2 (M1) nanoparticles were synthesized hydrothermally by adding 300 mg of V_2O_5 powder (Sigma-Aldrich) and 450 mg of oxalic acid (Fisher Scientific, Waltham, MA, USA) to 16 mL of deionized water (ρ = 18.2 MΩ/cm, purified using a Barnstead International NANOpure Diamond system) in a 23 mL polytetrafluoroethylene cup, as reported in previous work [38]. The reaction mixture was heated within an autoclave to 250 °C for 72 h. A matte-black powder was collected by vacuum filtration and washed with copious amounts of acetone and deionized water.

Preparation of α-V_2O_5 nanowires for comparison: α-V_2O_5 nanowires (with the average diameters of between 150–250 nm and lengths ranging from 1–100 μm) were synthesized according to a previously reported method [39]. In a typical reaction, 1.6 g of

V_2O_5 (Beantown Chemical, Hudson, NH, USA, 99.5%) were added to a 125 mL capacity Teflon-lined autoclave. Subsequently, 80 mL of deionized water (ρ = 18.2 MΩ/cm) and 8 mL of 2-propanol (ACS reagent grade) were added. The autoclave was heated at 210 °C for 48 h. Following the heating period, the autoclave was removed from the oven and allowed to cool autogenously. The resulting green to blue powder ($V_3O_7{\cdot}H_2O$) was separated by filtration and washed with copious amounts of water and 2-propanol and allowed to dry in air overnight. The dried paper-like product was placed in a ceramic crucible and heated in open air in a muffle furnace at 350 °C for 72 h with stirring every 24 h. The resulting yellow-orange paper-like product was lightly ground and used in further experiments without any subsequent modification.

Preparation of γ′-V_2O_5 microrods for comparison: The metastable γ′-V_2O_5 polymorph microrods (with average widths of 0.9–1.1 μm) were synthesized according to a previously reported synthesis [40]. In a typical reaction, about 1 g of α-V_2O_5 was added to 40 mL of acetonitrile (MilliporeSigma, Burlington, MA, USA, <50 ppm H_2O, 99.8%) under inert atmosphere. Subsequently, 1.25 molar equivalents (typically *ca.* 1 g) of LiI (Alfa Aesar, Haverhill, MA, USA, anhydrous, 98%) were added to the suspension. The reaction was allowed to proceed without stirring under inert atmosphere for 72 h. The dark green-blue γ-LiV_2O_5 product was separated by vacuum filtration and washed with copious amounts of acetonitrile and 2-propanol and allowed to dry in air overnight. The γ-LiV_2O_5 powder was then dispersed in 40 mL of acetonitrile under an inert atmosphere. Subsequently, 1.25 molar equivalents of $NOBF_4$ were added to the suspension, resulting in the complete topotactic deintercalation of lithium from the structure. The resulting orange/red powder was separated from the suspension by vacuum filtration, washed with copious amounts of acetonitrile and 2-propanol, and used without further modification.

Each 0.1 g of the prepared VO_2 (M1), α-V_2O_5, and γ′-V_2O_5 products was dispersed in 10 mL of ethanol, followed by ultrasonication for 1 h. Each solution loading of 100 μL/cm^2 using a micropipette was cast onto CFP and allowed to dry in air overnight.

Structural characterization: The morphology of the prepared materials was examined by field-emission scanning electron microscopy (FESEM) using a JEOL JSM-7500F instrument. Particles harvested from carbon fiber paper (CFP) substrate by ultrasonication in toluene and hydrothermally grown particles were examined by high-resolution transmission electron microscopy (HRTEM) using a JEOL JEM-2010 instrument operated at an accelerating voltage of 200 keV. Phase assignment was performed with the help of X-ray diffraction (XRD) using a Bruker D8-Advance instrument equipped with a Cu Kα source (λ = 1.5418 Å) as well as by Raman microprobe analysis using a Jobin-Yvon HORIBA LabRAM HR800 instrument coupled to an Olympus BX41 microscope. Raman spectra were collected with excitation from the 514.5 nm line of an Ar-ion laser; the laser power was kept below 10 mW to minimize photooxidation. Differential scanning calorimetry (DSC) analysis was performed using a TA Instruments Q2000 instrument. The temperature was scanned from 0 to 100 °C and back again to 0 °C at ramp rates ranging from 1 to 15 °C/min. For DSC experiments, the VO_2-deposited CFP was cut into small pieces and stacked in an aluminum T-Zero pan under a purge flow of Ar gas. A bare CFP was used as a reference. The chemical composition and oxidation states of the prepared materials were investigated by X-ray photoelectron spectroscopy (XPS, Omicron XPS) with Mg Kα radiation (1253.6 eV). Energy calibration was achieved by setting the C1s line from adventitious hydrocarbons to 284.8 eV. Vanadium K-edge X-ray absorption near-edge structure (XANES) spectra were collected at the Advanced Light Source (ALS) bending magnet beamline 10.3.2. V K-edge XANES spectra were recorded in fluorescence mode in the energy range 5450–5600 eV by continuously scanning a Si (111) monochromator (Quick XAS mode) from 20 eV below to 40 eV above the white line absorption. For XANES analysis, a suite of custom LabVIEW programs at the beamline was used to perform deadtime correction, energy calibration, glitch removal, pre-edge subtraction, and post-edge normalization. The Athena suite of programs in the IFEFFIT package was used to analyze the XANES spectra.

Electrochemical characterization: The oxygen evolution reaction (OER) performance of the prepared materials was evaluated using a three-electrode cell with the help of a Bio-Logic potentiostat (SP-200). All of the measurements were performed in a 1 M aqueous solution of KOH purged with N_2 gas. The vanadium oxides prepared on CFP were individually used as the working electrodes. A saturated calomel electrode (SCE) and a Pt foil were used as reference and counter electrodes, respectively. The potential versus SCE (E_{SCE}) was converted to the potential versus the reversible hydrogen electrode (RHE) (E_{RHE}) using the relation $E_{RHE} = E_{SCE} + 1.0464$ V [41]. Polarization curves for OER were measured using linear sweep voltammetry (LSV) in the range between 1.2 and 1.8 V versus RHE at a scan rate of 8 mV/s. The polarization curves were corrected for the ohmic potential drop (i*R*) losses, where *R* is the series resistance of the electrochemical cell as determined by electrochemical impedance spectroscopy (EIS) measurements. EIS measurements were performed in the range between 200 kHz and 50 mHz using an AC amplitude of 25 mV. The double-layer capacitance (C_{dl}) of the samples was determined by cyclic voltammetry (CV) at scan rates between 20–100 mV/s. Gas chromatography (GC) analysis of gaseous product was performed on the headspace of sealed electrocatalytic cells with the three-electrode configuration in a 1 M KOH electrolyte solution. The cells were sealed under an Ar ambient. After application of a constant voltage of 1.6 V versus RHE for 30 min, the headspace was sampled using a syringe. An Agilent Trace 1300 GC equipped with a thermal conductivity detector and a custom-made 120 cm stainless steel column packed with Carbosieve-II from Sigma-Aldrich was used for analysis. The carrier gas was Ar. Identification of O_2 produced from electrolysis were accomplished by withdrawing 200 μL of the headspace using a 0.5 mL Valco Precision Sampling Syringe, Series A-2 equipped with a Valco Precision Sampling syringe needle with a five-point side port.

3. Results and Discussion

The VO_2 nanoparticles have been prepared through the vacuum annealing of the V_2O_5 particles coated on a carbon fiber paper (CFP) at 950 °C, which is slightly higher than the melting point of V_2O_5 (690 °C at standard temperature and pressure). The field-emission scanning electron microscopy (FESEM) image in Figure 1a shows clearly that the produced VO_2 nanoparticles with the size of *ca.* 300 ± 76 nm in diameter uniformly cover the surface of individual carbon fibers (*ca*. 7 μm in diameter) constituting the CFP. The bare surface of CFP is comparatively shown with a smooth grain by FESEM images in Figure S1 of the Supplementary material. More specifically, the VO_2 nanoparticles have some particle coalescence, which results from solidifying after slightly melting down (see the high-magnification image in Figure 1b). The phase of VO_2 nanoparticles obtained should be defined since the VO_2 possesses three polymorphs, M1 monoclinic, M2 monoclinic, and R rutile phases, across the phase transition at *ca.* 67 °C in the bulk [34–37]. Each of them has distinctive Raman spectral signatures arising from the pronounced differences in local symmetry, where the space groups for the R and M1 phases are $P4_2/mnm$ ($D_{4h}{}^{14}$) and $P2_1/c$ ($C_{2h}{}^{3}$), respectively [36,37]. In particular, the most stable M1 phase at room temperature is characterized by 18 Raman-allowed modes, 9 each of A_g and B_g symmetry [36,37,42,43]. In Figure 1c, the Raman modes acquired for our VO_2 nanoparticles at room temperature are assigned to the M1 monoclinic phase of VO_2. The mode assignments denoted in Figure 1c are derived from group theory considerations and previously reported polarized Raman spectroscopy studies [42–44]. Furthermore, the XRD reflections acquired on CFP are indexed well to the M1 phase of VO_2 (Joint Committee on Powder Diffraction Standards (JCPDS) 43-1051), as shown in Figure S2. These results indicate that the VO_2 nanoparticles obtained here have a well-defined single M1 phase without any mixed phase.

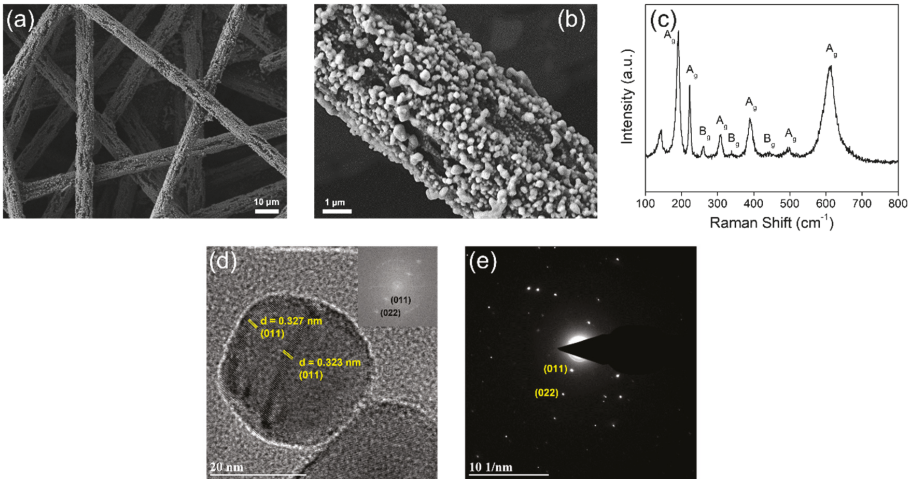

Figure 1. (**a**) a low-magnification and (**b**) high-magnification FESEM images and (**c**) room-temperature Raman spectrum acquired for the VO_2 (M1) nanoparticles formed on carbon fiber paper (514.5 nm laser excitation). (**d**) Lattice-resolved HRTEM image and (**e**) the indexed SAED pattern of the VO_2 (M1) nanoparticles harvested from the VO_2/CFP sample by ultrasonication for 1 h in toluene. An individual VO_2 (M1) nanoparticle shows an interplanar separation of 0.323–0.327 nm corresponding to the spacing between (200) lattice planes. The inset of (**d**) indicates its fast Fourier transform (FFT) image.

The structural characterization has been further performed using high-resolution transmission electron microscopy (HRTEM) and selected area electron diffraction (SAED). Figure 1d,e show the lattice-resolved HRTEM image and the indexed SAED pattern of an individual VO_2 (M1) nanoparticle harvested from the VO_2/CFP sample by ultrasonication for 1 h in toluene (low-magnification TEM image of VO_2 (M1) nanoparticles is shown in Figure S3a). The nanoparticle reveals the d-spacing of (011) lattice planes, which are the XRD main reflection of VO_2 M1 monoclinic phase. The (200) lattice planes of VO_2 M1 phase are also observed in another individual nanoparticle (Figure S3b). These results corroborate the single crystalline nature of the individual nanoparticles.

Meanwhile, it should be noticed that vanadium oxides have multiple vanadium oxidation states (V^{2+}, V^{3+}, V^{4+}, V^{5+}) [24,25]. Among them, VO_2 with the oxidation state of V^{4+} exhibits the characteristic phase transition phenomenon at near 67 °C as mentioned earlier, which is distinct from compounds with the other oxidation states. Such property can be used for characterizing the phase and defect of the prepared VO_2. In detail, the thermally and electrically induced metal-insulator phase transition in VO_2 is accompanied by a considerable consumption (M1 → R) or release (R → M1) of latent heat, given that it is a first-order transition [37,45]. The latent heat at the phase transition comprises an enthalpy component arising from the structural distortion of the lattice (which is compensated in part by a modulation of the phonon entropy) and conduction entropy of electrons [37,45–47]. Figure 2a shows differential scanning calorimetry (DSC) profiles acquired at various scan rates for the prepared VO_2 nanoparticles. The pronounced endothermic (M1 → R) and exothermic (R → M1) DSC traces centered at around 65 °C and 62 °C are observed upon heating and cooling, respectively; the temperatures are recognized at T_{max} which represents the temperature at the maximum height of the transition peak and is indicative of the maximum transformation rate [45]. Such DSC traces corroborate again that the prepared vanadium oxide is indeed VO_2 with the metal-insulator phase transition. Figure 2b shows the evolution of hysteresis, which is defined as the difference between T_{max} temperatures acquired upon heating and cooling across the scan rates. The T_{max} upon heating is slightly

altered between 65.2 °C and 65.7 °C across the measured scan rates, while the one upon cooling is almost constant with the values between 62.4 °C and 62.6 °C. As a result, it is found that the width of hysteresis in the prepared VO_2 nanoparticles here is relatively scan-rate-invariant compared to that of the hydrothermally prepared VO_2 nanoparticles previously [45]. The phase transitions in VO_2 upon heating and cooling are known to be mediated by defects such as oxygen vacancy, twin boundary, and grain boundary, which serve as phase nucleation sites [45,48]. The extent of supercooling of the high-temperature phase and superheating of the low-temperature phase (thermal hysteresis) can be decreased with increasing concentration of defects since the nucleation probability is increased with increasing defect density. Therefore, the low thermal hysteresis for the prepared VO_2 nanoparticles here indicates importantly that those nanoparticles possess a considerable number of structural defects.

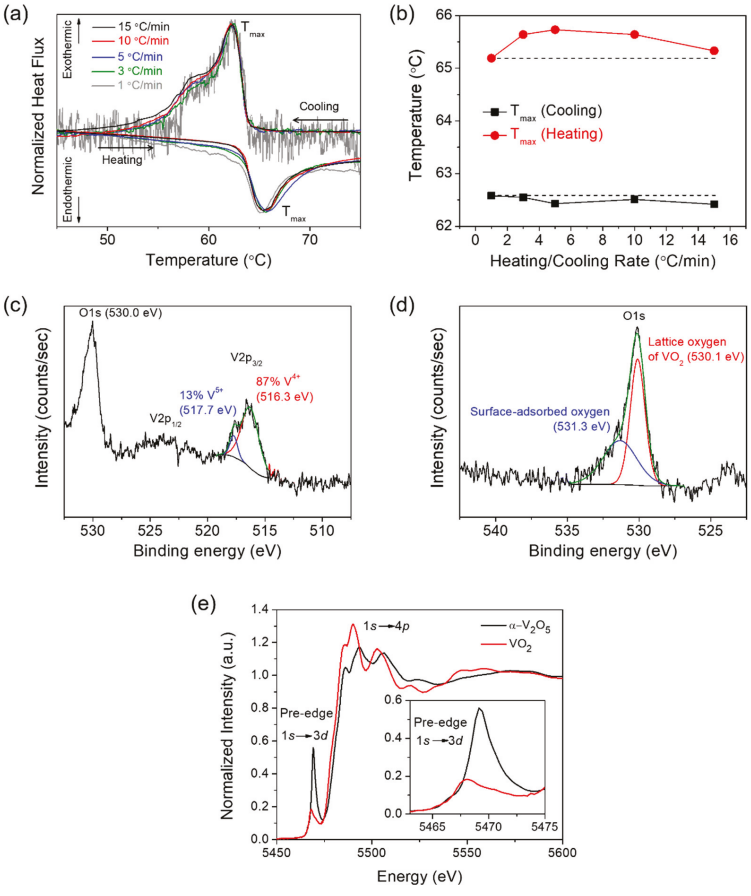

Figure 2. (**a**) Scan rate-dependent DSC results for the VO_2 (M1) nanoparticles formed on carbon fiber paper. Various scan rates with 15, 10, 5, 3, and 1 °C/min were applied. (**b**) Evolution of T_{max} for the VO_2 (M1) nanoparticles formed on carbon fiber paper, as a function of the heating/cooling rate. XPS spectra indicating (**c**) V 2p and (**d**) O 1s binding energies acquired for the VO_2 (M1) nanoparticles formed on carbon fiber paper. The V $2p_{3/2}$ peak in (**c**) and O 1s peak in (**d**) are deconvoluted into respective two sub-peaks. (**e**) Experimental V K-edge XANES spectra acquired for the VO_2 (M1) nanoparticles and α-V_2O_5 nanowires. The inset indicates the magnification of pre-edge peaks.

The oxidation state and stoichiometry of VO_2 have been characterized by X-ray photoelectron spectroscopy (XPS). Figure 2c,d show V 2p and O 1s spectra for the VO_2 nanoparticles, respectively. The V $2p_{3/2}$ spectrum can be deconvoluted into two sub-peaks arising from the V^{4+} (516.3 eV) and V^{5+} (517.7 eV) components in Figure 2c, where the binding energy values for the spectra correspond to the reported values [49–51]. Noticeably, it indicates that the prepared VO_2 consists primarily of V^{4+} component (87 at%) with the small amount of V^{5+} component (13 at%). The main peak for O 1s located at 530.1 eV is assigned to the lattice oxygen comprising the VO_2 in Figure 2d [49,52]. The additional oxygen component located at 531.3 eV can be assigned to the surface-adsorbed oxygen or the C-O and C=O bonds coming from it [52]. Figure 2e plots V K-edge X-ray absorption spectra of the prepared VO_2 and contrasting α-V_2O_5, acquired by X-ray absorption near-edge structure (XANES) spectroscopy. For comparison, α-V_2O_5 has been prepared in the form of nanowires by the hydrothermal method with the average diameters of between 150–250 nm and lengths ranging from 1–100 μm, according to a previously reported method [39]. The spectra consist of the pre-edge and white-line absorption features due to dipole-allowed transitions from V 1s to 3d states and from V 1s to 4p states, respectively. In Figure 2e, the VO_2 (composed of V^{4+} ions) exhibits the characteristic V K-edge absorption spectrum with obviously different line shape, intensity, and peak position from α-V_2O_5 (composed of V^{5+} ions), indicating the discrepancy in the local symmetry and oxidation state of vanadium atoms between two types of V-O systems [53]. Specifically, a broader pre-edge peak for VO_2 is observed at 5468.04 eV, shifting toward lower energy as compared to that of α-V_2O_5 (5469.13 eV) (see the inset of Figure 2e). On the other hand, a primary edge peak in the white-line absorption feature is more intensely observed at 5489.94 eV for VO_2. A distinctive pre-edge feature observed in V K-edge spectrum of α-V_2O_5 is essentially local in character and originates from the broken octahedral symmetry of the vanadium centers in V_2O_5 [53]. The asymmetric broadening and shift of the area-weighted centroid to lower energy in the pre-edge feature across two V-O systems is a result of the reduction of the V^{5+} sites to V^{4+} sites. Upon such a reduction of vanadium sites, the electron remains localized within V $3d_{xy}$ orbitals with stabilization of a small polaron and the excitation of core electrons requires less energy due to more screening charge at the excited atom, and thus the pre-edge feature is shifted to lower energy [21,22,53]. In addition to the red shift of the pre-edge peak position, the V^{4+} character contributes to the broadening of the pre-edge peak due to the increase of octahedral symmetry precluding V 4p-3d hybridization, as shown in the inset of Figure 2e. As a result, it is found that the prepared VO_2 is considerably stoichiometric and somewhat free from the point defect such as oxygen vacancy. Hence, the principal defect associated with the low thermal hysteresis across the phase transition for VO_2 nanoparticles is considered grain boundaries among VO_2 nanoparticles with some particle coalescence, as observed in FESEM image of Figure 1a.

To investigate the effect of vanadium oxidation state (V^{4+}/V^{5+}) on the electrocatalytic properties of vanadium oxide, we have further prepared V_2O_5 nanoparticles covering the carbon fibers through the annealing of the V_2O_5 particles coated on the CFP at 950 °C under an O_2 flow of 10 sccm and continuous vacuum pumping condition using a tube furnace. FESEM images in Figure S4a,b reveal the morphology of the V_2O_5 nanoparticles covering uniformly the surface of individual carbon fibers constituting the CFP, where the morphology and particle size are similar to those of the VO_2 nanoparticles. Only slightly faceted shape in the V_2O_5 nanoparticles is observed as compared with the VO_2 nanoparticles (Figure S4b). The Raman bands acquired for the prepared V_2O_5 nanoparticles in Figure S4c are well matched with the Raman-active modes of V_2O_5 reported in the literature [54,55]. XPS V 2p and O 1s spectra for the prepared V_2O_5 nanoparticles are shown in Figure S4a,b, respectively. The XPS result demonstrates that the prepared V_2O_5 nanoparticles are composed primarily of V^{5+} component (80 at%) with the small amount of V^{4+} component (20 at%). Besides, VO_2 (M1), α-V_2O_5, and γ'-V_2O_5 have been separately prepared by the hydrothermal methods for comparison, followed by drop-casting onto CFP. The agglomeration of the hydrothermally grown VO_2 (M1) nanoparticles in a few

nanometer size is shown by TEM in Figure S5a,b. The hydrothermally grown VO_2 (M1) nanoparticles are characterized to possess the same ratio of V^{4+} to V^{5+} by XPS (Figure S5c,d), which is a higher amount of V^{5+} component compared to the VO_2 nanoparticles prepared by the vacuum annealing. The α-V_2O_5 nanowires with the average diameters of between 150–250 nm and lengths ranging from 1–100 μm and the metastable γ′-V_2O_5 polymorph microrods with average widths of 0.9–1.1 μm were synthesized separately (their XRD patterns and FESEM images are shown in Figure S6).

The electrocatalytic OER characteristics of the vanadium oxides prepared on CFP have been investigated in a 1 M aqueous solution of KOH, using a conventional three-electrode setup. Figure 3a displays linear polarization curves, which have been corrected for ohmic potential drop (iR) losses. Bare CFP is contrasted as a control and is essentially catalytically inert toward OER. Remarkably high OER performance for the VO_2 (M1) nanoparticles prepared by the vacuum annealing on CFP is found with an overpotential of 350 mV, reaching a current density of 10 mA/cm^2 (η_{10}) and a Tafel slope of 46 mV/dec (Figure 3b). The hydrothermally grown VO_2 (M1) nanoparticles prepared by drop-casting on CFP exhibit the second-highest OER activity with a η_{10} value of 460 mV and a Tafel slope of 114 mV/dec. As compared to the VO_2 samples, V_2O_5 samples represent relatively low OER activities with higher η_{10} values more than 490 mV and higher Tafel slope values more than 130 mV/dec. Among the V_2O_5 samples, γ′-V_2O_5 shows the lowest η_{10} value of 490 mV, but its Tafel slope value (134 mV/dec) is roughly equal to that of α-V_2O_5 (131 mV/dec), indicating their same OER kinetics.

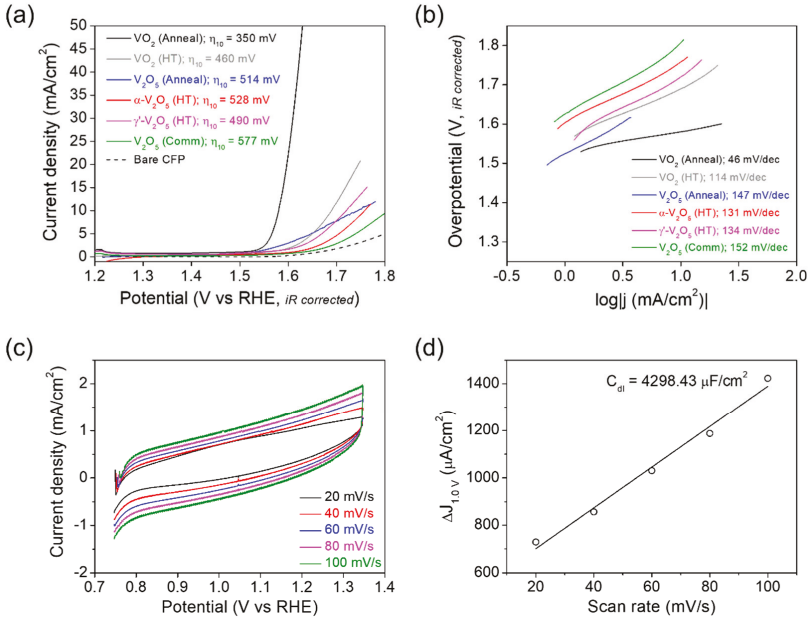

Figure 3. (**a**) Polarization curves and (**b**) Tafel plots measured for the vacuum-annealed VO_2 (M1) and V_2O_5, hydrothermally grown VO_2 (M1), α-V_2O_5, and γ′-V_2O_5, and commercial V_2O_5, prepared on carbon fiber paper, contrasted to data acquired for bare CFP. The data have been acquired in aqueous solutions of 1 M KOH using a three-electrode assembly. (**c**) Cyclic voltammograms acquired at various scan rates for the VO_2 (M1) nanoparticles formed on carbon fiber paper. (**d**) The differences in current density ($\Delta j = j_a - j_c$) at 1.0 V versus RHE are plotted as a function of the scan rate. The C_{dl} value is extrapolated from a linear fit to the plot.

We further measured the double layer capacitance (C_{dl}) for the samples using a cyclic voltammetry (CV) method to estimate the electrochemically active surface area (ECSA), which is directly proportional to C_{dl} [18,33]. The voltammograms for the VO_2 (M1) nanoparticles prepared by the vacuum annealing on CFP have been collected at various scan rates (20–100 mV/s) in the potential range of 0.75–1.35 V versus reversible hydrogen electrode (RHE) (a potential range with no Faradaic current), where the current is preponderantly due to the charging of the double layer (and not due to water oxidation), as shown in Figure 3c. The differences (Δj) of anodic and cathodic current densities at 1.0 V vs. RHE for the CV plot are shown as a function of the scan rate in Figure 3d. The slope of Δj vs. scan rate plot is equal to a value of $2C_{dl}$. The CV and Δj vs. scan rate plots acquired for the α-V_2O_5, γ'-V_2O_5, and commercial V_2O_5 samples prepared on CFP are shown in Figure S7 for comparison. As a result, the VO_2 (M1) nanoparticles prepared by the vacuum annealing, which have the lowest η_{10} (350 mV) and Tafel slope (46 mV/dec) values, are found to exhibit the highest C_{dl} value of 4298.43 $\mu F/cm^2$. By contrast, α-V_2O_5, γ'-V_2O_5, and commercial V_2O_5 show relatively low C_{dl} values of 742.54, 748.98, and 491.42 $\mu F/cm^2$, respectively (Figure S7). These experimental results definitely indicate that VO_2 shows higher OER activity than V_2O_5. In other words, it is concluded that V^{4+} in vanadium oxide composes a catalytically active site for the OER with high intrinsic activity. A much higher OER activity of the VO_2 (M1) nanoparticles prepared directly on CFP by the vacuum annealing compared to the hydrothermally grown and drop-casted ones can be explained by their improved coverage and adhesion on the carbon fibers (i.e., improved morphological factor by process innovation, facilitating charge transfer) as well as their higher V^{4+} content (87% for the former and 50% for the latter, according to the XPS result). For V_2O_5 catalysts, a slightly higher OER activity (lower η_{10}) of γ'-V_2O_5 than α-V_2O_5, despite their identical OER mechanism with the roughly same Tafel slope value, is regarded to result from a smaller particle size and concurrently higher ECSA (higher C_{dl} value) of γ'-V_2O_5 than α-V_2O_5 (Figure S6). Indeed, much bulkier commercial V_2O_5 particles with the lowest ECSA (lowest C_{dl}) show the lowest OER activity. However, it should be noted that these V^{5+}-constituted V_2O_5 catalysts reveal much lower OER activities compared to the V^{4+}-constituted VO_2 catalyst. According to the theoretically proposed mechanism, the OER proceeds in the four steps in a basic environment as per [8]:

$$4OH^- \rightarrow OH\,* + 3OH^- + e^- \quad (1)$$

$$OH\,* + 3OH^- \rightarrow O\,* + 2OH^- + H_2O + e^- \quad (2)$$

$$O\,* + 2OH^- + H_2O \rightarrow OOH\,* + OH^- + H_2O + e^- \quad (3)$$

$$OOH\,* + OH^- + H_2O \rightarrow O_2 + 2H_2O + e^- \quad (4)$$

where * denotes a surface adsorption site. The adsorption energies for intermediates of OH *, O *, and OOH *, formed in the reaction steps, determine the efficiency of the catalyst; i.e., the lowest overpotential is achieved when the energies of the OH * → O * (Equation (2)) and O * → OOH * (Equation (3)) steps are equalized. Thus, the lower energy disparity between two steps on the adsorption sites of the catalyst is, the higher efficiency of the catalyst is. Meanwhile, the entire water-splitting cycle can be divided into a metal oxidation step and metal reduction step with O_2 evolution, where the oxidation state and redox kinetics of the transition metal play important roles in determining the OER efficiency by affecting the adsorption energy [8]. When the kinetics of the metal reduction with O_2 evolution step is slow or rapid, the metal oxidation maintains a high-valent or low-valent state at the OER potential, respectively. Here, when the kinetics of the metal-reduction step is controlled to maintain the metal oxidation state with a high intrinsic OER activity at the OER potential, the OER activity of the catalyst is enhanced. Therefore, in this work, the high OER activity of VO_2 is attributed to the preservation of highly OER active V^{4+} components and $V^{4+/5+}$ redox couples in VO_2. Likewise, V^{3+}, Co^{3+}, Fe^{3+}, Ni^{3+}, and their redox couples are known to work as the OER-active species in certain crystal structures [8,18]. More

recently, the amorphous VO_x and $CoVO_x$ with V^{4+} were also reported to have high OER activities [9]. A high OER activity of the VO_2 (M1) with η_{10} of 350 mV and Tafel slope of 46 mV/dec is found to be comparable to those of various electrocatalysts reported in the literature (see Table S1): e.g., η_{10} of 390 mV for CoO_x, η_{10} of 465 mV for amorphous VO_x, η_{10} of 410 mV for V_2O_5, and 534 mV for Co_3O_4. In particular, the VO_2 (M1) shows a much lower level of Tafel slope value compared to the nickel-, cobalt-, and manganese-based catalysts as well as the other vanadium-based catalysts such as VOOH, amorphous VO_x, and V_6O_{13}. The η_{10} of VO_2 (M1) is even comparable to those of state-of-the-art OER catalysts, RuO_2 and IrO_2 with η_{10} of around 300 mV.

The oxygen evolution from the VO_2 (M1) nanoparticles prepared by the vacuum annealing on CFP has been corroborated by gas chromatography (GC) analysis. The resulting GC trance in Figure S8 shows the only peak eluting from the column at 2.29 min, corresponding to O_2. The long-term stability test of the VO_2 (M1) catalyst has been performed by 1000 repeated CV sweeps in a 1 M aqueous solution of KOH in the range between 0.75 and 1.60 V versus RHE at a scan rate of 100 mV/s. As sown in Figure 4a, the VO_2 (M1) catalyst exhibits stable performance with almost exactly superimposable polarization curves after 1000 sweeps. The FESEM image of the catalyst acquired after the long-term stability test is shown in Figure 4b. Compared with the morphology before 1000 sweeps in Figure 1b, there seemed to be no remarkable difference. To further investigate the surface state of the VO_2 (M1) catalyst after OER, XPS spectra were acquired for the catalyst after OER under a constant voltage of 1.6 V versus RHE for 30 min in a 1 M KOH electrolyte solution (Figure 4c,d). Noticeably, the V^{5+} component on the surface of the catalyst is found to be largely increased from 13% to 76% after OER, which is close to V_2O_5. Such an oxidation of vanadium during OER again corroborates a relatively poor OER activity of V^{5+} site in VO_2 (M1), although the overpotential and morphology for the catalyst did not change obviously until 1000 CV sweeps. Similarly, the metal oxidation behavior involving a performance degradation is found in the several literature reports. For example, the surface of VOOH catalyst is observed to oxidize from V^{3+} to V^{5+} after OER [18]. Also, Kim et al. reported the surface oxidation from Co^{2+} to Co^{3+} after OER in amorphous cobalt phyllosilicate catalyst [14].

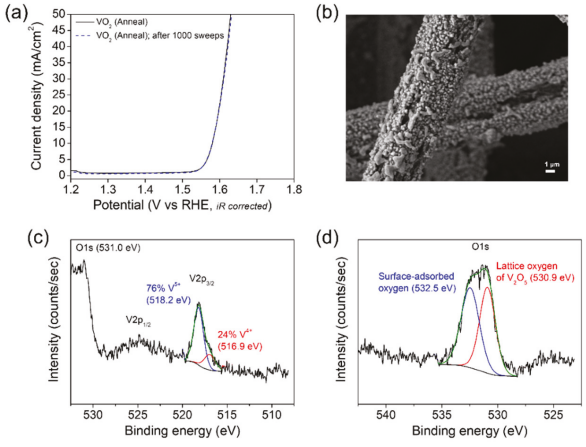

Figure 4. (**a**) Polarization curves of the VO_2 (M1) nanoparticles prepared by the vacuum annealing on CFP recorded before and after 1000 CV sweeps in a 1 M aqueous solution of KOH. (**b**) FESEM image acquired for the VO_2 (M1) nanoparticles after 1000 CV sweeps. XPS spectra of (**c**) V 2p and (**d**) O 1s acquired for the surface of the VO_2 (M1) catalyst after OER under a constant voltage of 1.6 V versus RHE for 30 min in a 1 M KOH electrolyte solution on the headspace of the electrocatalytic cell sealed under an Ar ambient with a three-electrode system.

The phase transition of VO_2 was investigated in this work only to identify an accurate preparation of the VO_2 (M1) nanoparticles. Since the phase transition temperature was found to be *ca.* 65 °C (heating) and 62 °C (cooling), the effect of phase transition on the OER in electrocatalytic systems operating at room temperature was ignored. Although the relationship between phase transition and electrocatalytic (including the OER) activity in VO_2 goes beyond the subject of this study, it can be another huge topic requiring further investigation.

4. Conclusions

In summary, in this work, the VO_2 (M1) is found to possess high electrocatalytic OER activity and stability for the first time. For this, the single-phase VO_2 (M1) nanoparticles, uniformly covering the surface of individual carbon fibers constituting the CFP, have been prepared through the vacuum annealing technique. The thermal analysis corroborates that the prepared VO_2 nanoparticles reveal the metal-insulator phase transition at *ca.* 65 °C (heating) and 62 °C (cooling) with the low thermal hysteresis, indicating a high concentration of structural defect which is considered grain boundaries among VO_2 nanoparticles with some particle coalescence. Consequently, the prepared VO_2 (M1) nanoparticles on CFP show a high electrocatalytic OER activity with the lowest η_{10} (350 mV) and Tafel slope (46 mV/dec) values in a 1 M aqueous solution of KOH as compared to those of the vacuum annealed V_2O_5 and the hydrothermally grown VO_2 (M1), α-V_2O_5, and γ′-V_2O_5. The catalytically active site is considered V^{4+} components and $V^{4+/5+}$ redox couples in VO_2. The oxidation state of V^{4+} is revealed to be more favorable to the OER catalysis compared to that of V^{5+} in vanadium oxide through comparative studies. Furthermore, the amount of V^{5+} component is found to be increased on the surface of VO_2 catalyst during OER, giving rise to the performance degradation. This work suggests V^{4+} and its redox couple as a novel active component for OER in metal-oxide electrocatalysts.

Supplementary Materials: The following supporting information can be downloaded at: https://www.mdpi.com/article/10.3390/nano12060939/s1, References [9,10,14,18–20,56–59] are cited in the Supplementary Materials. Figure S1. FESEM images of a bare carbon fiber paper (CFP). (b) illustrates the high-magnification image of a single carbon fiber. Figure S2. XRD pattern of VO_2 nanoparticles prepared on CFP. The reflections are indexed to VO_2 M1 phase. The reflections denoted by CFP arise from the graphitized CFP substrate. The vertical bars indicate the reflections of VO_2 M1 phase (Joint Committee on Powder Diffraction Standards (JCPDS) card# 43-1051). Figure S3. (a) Low-magnification TEM image of the VO_2 (M1) nanoparticles harvested from the VO_2/CFP sample by ultrasonication for 1 h in toluene. (b) Lattice-resolved HRTEM image of an individual VO_2 (M1) nanoparticle showing an interplanar separation of 0.242 nm corresponding to the spacing between (200) lattice planes. The inset indicates its fast Fourier transform (FFT) image. Figure S4. (a) Low- and (b) high-magnification FESEM images, (c) Raman spectrum (514.5 nm laser excitation), and XPS (d) V 2p and (e) O 1s spectra of the V_2O_5 nanoparticles prepared on CFP. Figure S5. (a) Low-magnification TEM and (b) HRTEM images of the VO_2 (M1) nanoparticles prepared by the hydrothermal method. XPS (c) V 2p and (d) O 1s spectra of the VO_2 (M1) nanoparticles. Figure S6. Indexed XRD patterns for (a) α- and (b) γ′-V_2O_5 polymorphs. FESEM images for (c) α- and (d) γ′-V_2O_5. The α- and γ′-V_2O_5 have been prepared by the hydrothermal methods. Figure S7. Cyclic voltammograms acquired at various scan rates for (a) α-V_2O_5, (c) γ′-V_2O_5, and (e) commercial V_2O_5 prepared on CFP. The differences in current density ($\Delta j = j_a - j_c$) at 0.9 or 1.0 V *versus* RHE are plotted as a function of the scan rate for (b) α-V_2O_5, (d) γ′-V_2O_5, and (f) commercial V_2O_5 prepared on CFP. The C_{dl} values are extrapolated from a linear fit to the plot. Figure S8. Gas chromatogram (GC) of the generated O_2 gas for the VO_2 (M1) nanoparticles prepared by the vacuum annealing on CFP. For GC analysis, the O_2 gas was captured after application of a constant voltage of 1.6 V *versus* RHE for 30 min in a 1 M KOH electrolyte solution on the headspace of the electrocatalytic cell sealed under an Ar ambient with a three-electrode system. Table S1. Comparison of the electrocatalytic OER activity for metal oxide catalysts.

Funding: This work was partly supported by the Technology development Program of the Korea government MSS (G21S318216201) and the National Research Foundation of Korea (NRF) grant of

the Korea government MSIT (2019R1G1A1006231). And the APC was funded by the Technology development Program of the Korea government MSS (G21S318216201).

Data Availability Statement: Not applicable.

Conflicts of Interest: The authors declare no conflict of interest.

References

1. She, Z.W.; Kibsgaard, J.; Dickens, C.F.; Chorkendorff, I.; Nørskov, J.K.; Jaramillo, T.F. Combining Theory and Experiment in Electrocatalysis: Insights into Materials Design. *Science* **2017**, *355*, eaad4998.
2. Fabbri, E.; Habereder, A.; Waltar, K.; Kötz, R.; Schmidt, T.J. Developments and Perspectives of Oxide-Based Catalysts for the Oxygen Evolution Reaction. *Catal. Sci. Technol.* **2014**, *4*, 3800–3821. [CrossRef]
3. Miao, C.; Zhang, T.; Li, F.; Zhang, L.; Sun, J.; Liu, D.; Wu, L.; Wang, H.; Chen, F.; He, L.; et al. Defect-Engineered Three-Dimensional Vanadium Diselenide Microflowers/Nanosheets on Carbon Cloth by Chemical Vapor Deposition for High-Performance Hydrogen Evolution Reaction. *Nanotechnology* **2021**, *32*, 265402. [CrossRef] [PubMed]
4. Dong, G.; Xie, F.; Kou, F.; Chen, T.; Wang, F.; Zhou, Y.; Wu, K.; Du, S.; Fang, M.; Ho, J.C. NiFe-Layered Double Hydroxide Arrays for Oxygen Evolution Reaction in Fresh Water and Seawater. *Mater. Today Energy* **2021**, *22*, 100883. [CrossRef]
5. Miao, C.; Zheng, X.; Sun, J.; Wang, H.; Qiao, J.; Han, N.; Wang, S.; Gao, W.; Liu, X.; Yang, Z.-X. Facile Electrodeposition of Amorphous Nickel/Nickel Sulfide Composite Films for High-Efficiency Hydrogen Evolution Reaction. *ACS Appl. Energy Mater.* **2021**, *4*, 927–933. [CrossRef]
6. Bian, L.; Gao, W.; Sun, J.; Han, M.; Li, F.; Gao, Z.; Shu, L.; Han, N.; Yang, Z.-X.; Song, A.; et al. Phosphorus-Doped MoS_2 Nanosheets Supported on Carbon Cloths as Efficient Hydrogen-Generation Electrocatalysts. *ChemCatChem* **2018**, *10*, 1571–1577. [CrossRef]
7. Wang, P.; Zhang, L.; Wang, Z.; Bu, D.; Zhan, K.; Yan, Y.; Yang, J.; Zhao, B. N and Mn Dual-Doped Cactus-Like Cobalt Oxide Nanoarchitecture Derived from Cobalt Carbonate Hydroxide as Efficient Electrocatalysts for Oxygen Evolution Reactions. *J. Colloid Interface Sci.* **2021**, *597*, 361–369. [CrossRef]
8. Kim, J.S.; Kim, B.; Kim, H.; Kang, K. Recent Progress on Multimetal Oxide Catalysts for the Oxygen Evolution Reaction. *Adv. Energy Mater.* **2018**, *8*, 1702774. [CrossRef]
9. Liardet, L.; Hu, X. Amorphous Cobalt Vanadium Oxide as a Highly Active Electrocatalyst for Oxygen Evolution. *ACS Catal.* **2018**, *8*, 644–650. [CrossRef]
10. Yu, L.; Yang, J.F.; Guan, B.Y.; Lu, Y.; Lou, X.W.D. Hierarchical Hollow Nanoprisms Based on Ultrathin Ni-Fe Layered Double Hydroxide Nanosheets with Enhanced Electrocatalytic Activity towards Oxygen Evolution. *Angew. Chem.* **2018**, *130*, 178–182. [CrossRef]
11. Bates, M.K.; Jia, Q.; Doan, H.; Liang, W.; Mukerjee, S. Charge-Transfer Effects in Ni-Fe and Ni-Fe-Co Mixed-Metal Oxides for the Alkaline Oxygen Evolution Reaction. *ACS Catal.* **2016**, *6*, 155–161. [CrossRef]
12. Qian, L.; Lu, Z.; Xu, T.; Wu, X.; Tian, Y.; Li, Y.; Huo, Z.; Sun, X.; Duan, X. Trinary Layered Double Hydroxides as High-Performance Bifunctional Materials for Oxygen Electrocatalysis. *Adv. Energy Mater.* **2015**, *5*, 1500245. [CrossRef]
13. Peng, Z.; Jia, D.; Al-Enizi, A.M.; Elzatahry, A.A.; Zheng, G. From Water Oxidation to Reduction: Homologous Ni-Co Based Nanowires as Complementary Water Splitting Electrocatalysts. *Adv. Energy Mater.* **2015**, *5*, 1402031. [CrossRef]
14. Kim, J.S.; Park, I.; Jeong, E.-S.; Jin, K.; Seong, W.M.; Yoon, G.; Kim, H.; Kim, B.; Nam, K.T.; Kang, K. Amorphous Cobalt Phyllosilicate with Layered Crystalline Motifs as Water Oxidation Catalyst. *Adv. Mater.* **2017**, *29*, 1606893. [CrossRef]
15. Suntivich, J.; May, K.J.; Gasteiger, H.A.; Goodenough, J.B.; Shao-Horn, Y. A Perovskite Oxide Optimized for Oxygen Evolution Catalysis from Molecular Orbital Principles. *Science* **2011**, *334*, 1383–1385. [CrossRef]
16. Bockris, J.O.M.; Otagawa, T. The Electrocatalysis of Oxygen Evolution on Perovskites. *J. Electrochem. Soc.* **1984**, *131*, 290–302. [CrossRef]
17. Man, I.C.; Su, H.-Y.; Calle-Vallejo, F.; Hansen, H.A.; Martínez, J.I.; Inoglu, N.G.; Kitchin, J.; Jaramillo, T.F.; Nørskov, J.K.; Rossmeisl, J. Universality in Oxygen Evolution Electrocatalysis on Oxide Surfaces. *ChemCatChem* **2011**, *3*, 1159–1165. [CrossRef]
18. Shi, H.; Liang, H.; Ming, F.; Wang, Z. Efficient Overall Water-Splitting Electrocatalysis Using Lepidocrocite VOOH Hollow Nanospheres. *Angew. Chem. Int. Ed.* **2017**, *56*, 573–577. [CrossRef]
19. Liu, J.; Ji, Y.; Nai, J.; Niu, X.; Luo, Y.; Guo, L.; Yang, S. Ultrathin Amorphous Cobalt-Vanadium Hydr(oxy)oxide Catalysts for the Oxygen Evolution Reaction. *Energy Environ. Sci.* **2018**, *11*, 1736–1741. [CrossRef]
20. Xing, M.; Kong, L.-B.; Liu, M.-C.; Liu, L.-Y.; Kang, L.; Luo, Y.-C. Cobalt Vanadate as Highly Active, Stable, Noble Metal-Free Oxygen Evolution Electrocatalyst. *J. Mater. Chem. A* **2014**, *2*, 18435–18443. [CrossRef]
21. Marley, P.M.; Horrocks, G.A.; Pelcher, K.E.; Banerjee, S. Transformers: The Changing Phases of Low-Dimensional Vanadium Oxide Bronzes. *Chem. Commun.* **2015**, *51*, 5181–5198. [CrossRef] [PubMed]
22. de Jesus, L.R.; Horrocks, G.A.; Liang, Y.; Parija, A.; Jaye, C.; Wangoh, L.; Wang, J.; Fischer, D.A.; Piper, L.F.J.; Prendergast, D.; et al. Mapping Polaronic States and Lithiation Gradients in Individual V_2O_5 Nanowires. *Nat. Commun.* **2016**, *7*, 12022. [CrossRef] [PubMed]
23. Chalker, C.J.; An, H.; Zavala, J.; Parija, A.; Banerjee, S.; Lutkenhaus, J.L.; Batteas, J.D. Fabrication and Electrochemical Performance of Structured Mesoscale Open Shell V_2O_5 Networks. *Langmuir* **2017**, *33*, 5975–5981. [CrossRef] [PubMed]

24. Ding, Y.-L.; Wen, Y.; Wu, C.; van Aken, P.A.; Maier, J.; Yu, Y. 3D V_6O_{13} Nanotextiles Assembled from Interconnected Nanogrooves as Cathode Materials for High-Energy Lithium Ion Batteries. *Nano Lett.* **2015**, *15*, 1388–1394. [CrossRef]
25. Zhai, T.; Lu, X.; Ling, Y.; Yu, M.; Wang, G.; Liu, T.; Liang, C.; Tong, Y.; Li, Y. A New Benchmark Capacitance for Supercapacitor Anodes by Mixed-Valence Sulfur-Doped V_6O_{13-x}. *Adv. Mater.* **2014**, *26*, 5869–5875. [CrossRef]
26. Sun, G.; Ren, H.; Shi, Z.; Zhang, L.; Wang, Z.; Zhan, K.; Yan, Y.; Yang, J.; Zhao, B. V_2O_5/Vertically-Aligned Carbon Nanotubes as Negative Electrode for Asymmetric Supercapacitor in Neutral Aqueous Electrolyte. *J. Colloid Interface Sci.* **2021**, *588*, 847–856. [CrossRef]
27. Singh, S.; Abtew, T.A.; Horrocks, G.; Kilcoyne, C.; Marley, P.M.; Stabile, A.A.; Banerjee, S.; Zhang, P.; Sambandamurthy, G. Selective Electrochemical Reactivity of Rutile VO_2 towards the Suppression of Metal-Insulator Transition. *Phys. Rev. B* **2016**, *93*, 125132. [CrossRef]
28. Khan, Z.; Senthilkumar, B.; Park, S.O.; Park, S.; Yang, J.; Lee, J.H.; Song, H.-K.; Kim, Y.; Kwak, S.K.; Ko, H. Carambola-Shaped VO_2 Nanostructures: A Binder-Free Air Electrode for an Aqueous Na-Air Battery. *J. Mater. Chem. A* **2017**, *5*, 2037–2044. [CrossRef]
29. Fleischmann, S.; Zeiger, M.; Jäckel, N.; Krüner, B.; Lemkova, V.; Widmaier, M.; Presser, V. Tuning Pseudocapacitive and Battery-Like Lithium Intercalation in Vanadium Dioxide/Carbon Onion Hybrids for Asymmetric Supercapacitor Anodes. *J. Mater. Chem. A* **2017**, *5*, 13039–13051. [CrossRef]
30. Khan, Z.; Singh, P.; Ansari, S.A.; Manippady, S.R.; Jaiswal, A.; Saxena, M. VO_2 Nanostructures for Batteries and Supercapacitors: A Review. *Small* **2021**, *17*, 2006651. [CrossRef]
31. Chen, K.; Liu, N.; Zhang, M.; Wang, D. Oxidative Desulfurization of Dibenzothiophene over Monoclinic VO_2 Phase-Transition Catalysts. *Appl. Catal. B* **2017**, *212*, 32–40. [CrossRef]
32. Wachs, I.E. Catalysis Science of Supported Vanadium Oxide Catalysts. *Dalton Trans.* **2013**, *42*, 11762–11769. [CrossRef] [PubMed]
33. Choi, Y.-H.; Lee, J.; Parija, A.; Cho, J.; Verkhoturov, S.T.; Al-Hashimi, M.; Fang, L.; Banerjee, S. An in Situ Sulfidation Approach for the Integration of MoS_2 Nanosheets on Carbon Fiber Paper and the Modulation of Its Electrocatalytic Activity by Interfacing with nC_{60}. *ACS Catal.* **2016**, *6*, 6246–6254. [CrossRef]
34. Whittaker, L.; Jaye, C.; Fu, Z.; Fischer, D.A.; Banerjee, S. Depressed Phase Transition in Solution-Grown VO_2 Nanostructures. *J. Am. Chem. Soc.* **2009**, *131*, 8884–8894. [CrossRef] [PubMed]
35. Whittaker, L.; Patridge, C.J.; Banerjee, S. Microscopic and Nanoscale Perspective of the Metal-Insulator Phase Transitions of VO_2: Some New Twists to an Old Tale. *J. Phys. Chem. Lett.* **2011**, *2*, 745–758. [CrossRef]
36. Whittaker, L.; Wu, T.-L.; Stabile, A.; Sambandamurthy, G.; Banerjee, S. Single-Nanowire Raman Microprobe Studies of Doping-, Temperature-, and Voltage-Induced Metal-Insulator Transitions of $W_xV_{1-x}O_2$ Nanowires. *ACS Nano* **2011**, *5*, 8861–8867. [CrossRef]
37. Horrocks, G.A.; Singh, S.; Likely, M.F.; Sambandamurthy, G.; Banerjee, S. Scalable Hydrothermal Synthesis of Free-Standing VO_2 Nanowires in the M1 Phase. *ACS Appl. Mater. Interfaces* **2014**, *6*, 15726–15732. [CrossRef]
38. Braham, E.J.; Andrews, J.L.; Alivio, T.E.G.; Fleer, N.A.; Banerjee, S. Stabilization of a Metastable Tunnel-Structured Orthorhombic Phase of VO_2 upon Iridium Doping. *Phys. Status Solidi A* **2018**, *215*, 1700884. [CrossRef]
39. Horrocks, G.A.; Likely, M.F.; Velazquez, J.M.; Banerjee, S. Finite Size Effects on the Structural Progression Induced by Lithiation of V_2O_5: A Combined Diffraction and Raman Spectroscopy Study. *J. Mater. Chem. A* **2013**, *1*, 15265–15277. [CrossRef]
40. Cocciantelli, J.M.; Gravereau, P.; Doumerc, J.P.; Pouchard, M.; Hagenmuller, P. On the Preparation and Characterization of a New Polymorph of V_2O_5. *J. Solid State Chem.* **1991**, *93*, 497–502. [CrossRef]
41. Liang, H.; Meng, F.; Cabán-Acevedo, M.; Li, L.; Forticaux, A.; Xiu, L.; Wang, Z.; Jin, S. Hydrothermal Continuous Flow Synthesis and Exfoliation of NiCo Layered Double Hydroxide Nanosheets for Enhanced Oxygen Evolution Catalysis. *Nano Lett.* **2015**, *15*, 1421–1427. [CrossRef] [PubMed]
42. Jones, A.C.; Berweger, S.; Wei, J.; Cobden, D.; Raschke, M.B. Nano-Optical Investigations of the Metal-Insulator Phase Behavior of Individual VO_2 Microcrystals. *Nano Lett.* **2010**, *10*, 1574–1581. [CrossRef] [PubMed]
43. Schilbe, P. Raman Scattering in VO_2. *Phys. B* **2002**, *316–317*, 600–602. [CrossRef]
44. Chou, J.Y.; Lensch-Falk, J.L.; Hemesath, E.R.; Lauhon, L.J. Vanadium Oxide Nanowire Phase and Orientation Analyzed by Raman Spectroscopy. *J. Appl. Phys.* **2009**, *105*, 034310. [CrossRef]
45. Braham, E.J.; Sellers, D.; Emmons, E.; Villarreal, R.; Asayesh-Ardakani, H.; Fleer, N.A.; Farley, K.E.; Shahbazian-Yassar, R.; Arròyave, R.; Shamberger, P.J.; et al. Modulating the Hysteresis of an Electronic Transition: Launching Alternative Transformation Pathways in the Metal-Insulator Transition of Vanadium (IV) Oxide. *Chem. Mater.* **2018**, *30*, 214–224. [CrossRef]
46. Salker, A.V.; Seshan, K.; Keer, H.V. Phase Transition Behaviour of VO_2. *Phys. Status Solidi* **1983**, *75*, K37–K40. [CrossRef]
47. Budai, J.D.; Hong, J.; Manley, M.E.; Specht, E.D.; Li, C.W.; Tischler, J.Z.; Abernathy, D.L.; Said, A.H.; Leu, B.M.; Boatner, L.A.; et al. Metallization of Vanadium Dioxide Driven by Large Phonon Entropy. *Nature* **2014**, *515*, 535–539. [CrossRef]
48. Fan, W.; Cao, J.; Seidel, J.; Gu, Y.; Yim, J.W.; Barrett, C.; Yu, K.M.; Ji, J.; Ramesh, R.; Chen, L.Q.; et al. Large Kinetic Asymmetry in the Metal-Insulator Transition Nucleated at Localized and Extended Defects. *Phys. Rev. B* **2011**, *83*, 235102. [CrossRef]
49. *NIST X-Ray Photoelectron Spectroscopy Database*; Version 4.1; National Institute of Standards and Technology: Gaithersburg, MD, USA, 2000. Available online: https://srdata.nist.gov/xps/ (accessed on 1 April 2018).
50. Miller, M.J.; Wang, J. Influence of Grain Size on Transition Temperature of Thermochromic VO_2. *J. Appl. Phys.* **2015**, *117*, 034307. [CrossRef]

51. Tangirala, M.; Zhang, K.; Nminibapiel, D.; Pallem, V.; Dussarrat, C.; Cao, W.; Adam, T.N.; Johnson, C.S.; Elsayed-Ali, H.E.; Baumgart, H. Physical Analysis of VO_2 Films Grown by Atomic Layer Deposition and RF Magnetron Sputtering. *ECS J. Solid State Sci. Technol.* **2014**, *3*, N89–N94. [CrossRef]
52. Zhang, P.; Li, M.; Deng, Q.; Zhang, J.; Wu, J.; Hu, Z.; Chu, J. Spectral Assignments in the Infrared Absorption Region and Anomalous Thermal Hysteresis in the Interband Electronic Transition of Vanadium Dioxide Films. *Phys. Chem. Chem. Phys.* **2016**, *18*, 6239–6246. [CrossRef] [PubMed]
53. Horrocks, G.A.; Braham, E.J.; Liang, Y.; de Jesus, L.R.; Jude, J.; Velázquez, J.M.; Prendergast, D.; Banerjee, S. Vanadium K-Edge X-ray Absorption Spectroscopy as a Probe of the Heterogeneous Lithiation of V_2O_5: First-Principles Modeling and Principal Component Analysis. *J. Phys. Chem. C* **2016**, *120*, 23922–23932. [CrossRef]
54. Abd-Alghafour, N.M.; Ahmed, N.M.; Hassan, Z. Fabrication and Characterization of V_2O_5 Nanorods Based Metal-Semiconductor-Metal Photodetector. *Sens. Actuators A* **2016**, *250*, 250–257. [CrossRef]
55. Chen, Y.; Yang, G.; Zhang, Z.; Yang, X.; Hou, W.; Zhu, J.-J. Polyaniline-Intercalated Layered Vanadium Oxide Nanocomposites—One-Pot Hydrothermal Synthesis and Application in Lithium Battery. *Nanoscale* **2010**, *2*, 2131–2138. [CrossRef]
56. McCrory, C.C.L.; Jung, S.; Peters, J.C.; Jaramillo, T.F. Bechmarking Heterogeneous Electrocatalysts for the Oxygen Evolution Reaction. *J. Am. Chem. Soc.* **2013**, *135*, 16977–16987. [CrossRef]
57. Walter, C.; Menezes, P.W.; Orthmann, S.; Schuch, J.; Cannor, P.; Kaiser, B.; Lerch, M.; Driess, M. A Molecular Approach to Manganese Nitride Acting as a High Performance Electrocatalyst in the Oxygen Evolution Reaction. *Angew. Chem.* **2018**, *130*, 706–710. [CrossRef]
58. Peng, X.; Wang, L.; Hu, L.; Li, Y.; Gao, B.; Song, H.; Huang, C.; Zhang, X.; Fu, J.; Huo, K.; et al. In Situ Segregation of Cobalt Nanoparticles on VN Nanosheets via Nitriding of $Co_2V_2O_7$ Nanosheets as Efficient Oxygen Evolution Reaction Electrocatalysts. *Nano Energy* **2017**, *34*, 1–7. [CrossRef]
59. Gao, T.; Jin, Z.; Liao, M.; Xiao, J.; Yuan, H.; Xiao, D. A Trimetallic V-Co-Fe Oxide Nanoparticles as an Efficient and Stable Electrocatalyst for Oxygen Evolution Reaction. *J. Mater. Chem. A* **2015**, *3*, 17763–17770. [CrossRef]

nanomaterials

MDPI

Article

Water Management for μDMFC with Foamed Stainless Steel Cathode Current Collector

Fan Zhang [1], Yanhui Zhang [1] and Zhengang Zhao [1,2,*]

[1] Faculty of Information Engineering and Automation, Kunming University of Science and Technology, Kunming 650500, China; zhangfan525025@163.com (F.Z.); yanhui_zhang01@163.com (Y.Z.)
[2] Yunnan Key Laboratory of Green Energy, Electric Power Measurement Digitalization, Control and Protection, Kunming 650000, China
* Correspondence: zhengang.zhao@kust.edu.cn

Abstract: For micro direct methanol fuel cell (μDMFC), water flooding on the cathode seriously affects the performance stability. Additionally, the effect of material and wettability of the cathode current collector (CCC) on the drainage capacity is studied to improve the μDMFC's performance. To this end, a CCC with foamed stainless steel was prepared to assemble the μDMFC due to its absorbency. Further, based on analyzing the gas–liquid two-phase flow characteristics of the μDMFC cathode, it was found that the gradient wettability CCC could accelerate the discharge of cathode water. Hence, the foam stainless steel CCC was partially immersed in a KOH solution to complete the gradient corrosion using its capillary force. Then, four different types of gradient wettability CCC were prepared by controlling the time of chemical corrosion. Finally, the performance of the μDMFC with different gradient wettability CCC was tested at room temperature using electrochemical impedance spectroscopy (EIS) and discharge voltage. The experimental results show that the gradient wettability CCC can improve the performance of the μDMFC by slowing down the rate of cathode flooding. The optimum corrosion time is 5 min at a concentration of 1 mol/L. Under these conditions, the CCC has the best gradient wettability, and the μDMFC has the lowest total impedance. The discharge voltage of the μDMFC with corroded CCC is increased by 33.33% compared to the uncorroded CCC μDMFC. The gradient wettability CCC designed in this study is economical, convenient, and practical for water management of the μDMFC.

Keywords: micro direct methanol fuel cell; water management; cathode current collector; foamed stainless steel; gradient wettability

Citation: Zhang, F.; Zhang, Y.; Zhao, Z. Water Management for μDMFC with Foamed Stainless Steel Cathode Current Collector. *Nanomaterials* **2022**, *12*, 948. https://doi.org/10.3390/nano12060948

Academic Editors: Marc Cretin, Sophie Tingry and Zhenghua Tang

Received: 12 February 2022
Accepted: 8 March 2022
Published: 14 March 2022

1. Introduction

With the rapid development of industry, the rate of consumption of fossil fuels has been dramatic. The micro direct methanol fuel cell (μDMFC), which relies on an internal redox reaction to generate electricity, provides a green route for environmental and energy concerns [1–3]. To effectively improve the performance of the μDMFC, in-depth research into cathode flooding should be implemented because excess water can severely block the gas channels and prevent O_2 from reaching the reaction sites uniformly [4–7]. Therefore, water management of the μDMFC is still a key technology [8–11].

To analyze the emergence of water flooding and the hazards it brings, scholars have developed different physical models for the gas–liquid two-phase flow in the cathode of fuel cells [12–16]. In 2020, Mehnatkesh et al. [17] used a deep neural network model to measure water coverage in fuel cells. The distribution of water in the flow field and the identification of areas of water accumulation in the gas channels were analyzed. In 2021, Rubio et al. [18] proposed a fuzzy model to determine the extent of fuel cells flooding or dehydration in real time. Salaberri et al. [19] used a pore grid model to analyze the relative effect of local water blockage on the gas diffusion layer and convection. Building the physical model of the gas–liquid two-phase flow in the fuel cell cathode is an important research direction [20,21].

However, experimental investigations are an essential part of scientific research, and other scholars have directly observed the water flooding phenomenon at the fuel cell cathode through experiments [22–24]. In 2020, Rahimi et al. [25] designed a transparent fuel cell stack and studied the effect of water flow state on voltage and pressure by visualization. In 2021, Chasen et al. [26] combined X-ray imaging and EIS to measure the water in the fuel cell flow field, which showed that the water content of the parallel flow field was much higher than that of the serpentine flow field. Based on theory and experimental investigations, scholars have designed different structures in the membrane electrode and cathode flow fields of fuel cells to mitigate water flooding [27,28]. In 2018, Fly et al. [29] analyzed the fluid distribution in the flow field of the metal foam fuel cell. The experimental results showed that the velocity of water covering the flow field was enhanced by 61% using the foam flow field. In 2019, Yuan et al. [30] used carbon aerogel to construct a water management layer in the membrane electrode of the fuel cell, and they found that the layer enhanced water recovery. In 2020, Karthikkyan et al. [31] placed porous inserts in the flow field to alleviate cathode flooding and showed that the insertion methods and insert specifications had significant effects on the performance of the fuel cell. Sun et al. [32] used foam metal instead of conventional current collectors and found that modifying the foam metal current collector with wettability could improve the performance of the fuel cell. Overall, the application of treated porous metals to μDMFC can effectively mitigate cathode flooding.

In this study, the cathode current collector (CCC) was prepared using foamed stainless steel, and the gas–liquid two-phase flow characteristics of the μDMFC cathode were analyzed. Then, the foam stainless steel CCC was partially immersed in a KOH solution to complete the gradient corrosion using its capillary force. The gradient wettability CCC can create a gradient force to accelerate the drainage in the cathode of the μDMFC. Compared to modified membrane electrode structures and flow field structures, the method of gradient wettability modification has the advantage of being economical, simple, and efficient. Those CCCs were classified according to the corrosion time: uncorroded CCC (N-CCC), 1 min corroded CCC (1-CCC), 5 min corroded CCC (5-CCC), and 9 min corroded CCC (9-CCC). Finally, the μDMFC with different gradient wettability CCC were tested at room temperature using EIS and discharge voltage.

2. Methods and Experiments

2.1. Gas–Liquid Two-Phase Flow in the Cathode of μDMFC

The μDMFC's structure is shown in Figure 1. The fabrication of the various parts of the μDMFC is the same as in the previous study [33]. The material of the CCC is foam stainless steel, and the flow field is of hole type, as shown in Figure 2. Then, the gas–liquid two-phase flow characteristics in the cathode of the μDMFC are analyzed to find a method that can enhance the performance.

The flow state of the liquid within the CCC is related to the permeability. According to Darcy's law:

$$\Delta P_{lp} = \frac{\mu_l \dot{m} \Delta L}{\rho_l K \pi r_{eff}^2} \tag{1}$$

where ΔP_{lp} is the pressure drop of the fluid, $\dot{m}$ is the flowing mass, ΔL is the distance, ρ_l is density, μ_l is kinetic viscosity, r_{eff} is the effective radius of the wick, and K is the permeability of the CCC. The capillary pressure of the CCC is calculated as follows:

$$\Delta P_{cp} = \frac{2\sigma \cos\theta}{r_{eff}} \tag{2}$$

where ΔP_{cp} is the capillary pressure provided by the CCC, σ is the surface tension of the H_2O, and θ is the contact angle. When the pressure drop of the liquid flow is equal to the capillary pressure, the maximum flow rate of water in the CCC is calculated as follows:

$$\dot{m}_{l,max} = \frac{2\rho_l K \pi r_{eff} \sigma \cos\theta}{\mu_l \Delta L} \tag{3}$$

where $\dot{m}_{l,max}$ is the maximum flow rate of water in the CCC. It can be seen from Equation (3) that reducing the contact angle can increase the flow rate of water and thus the timely discharge of water that accumulates in the flow field.

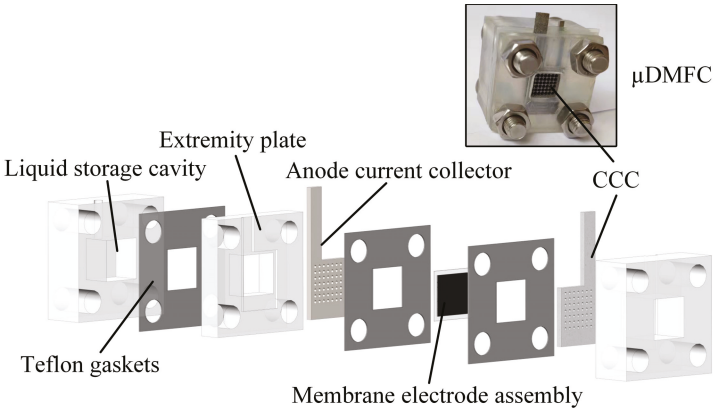

Figure 1. Schematic diagram of μDMFC.

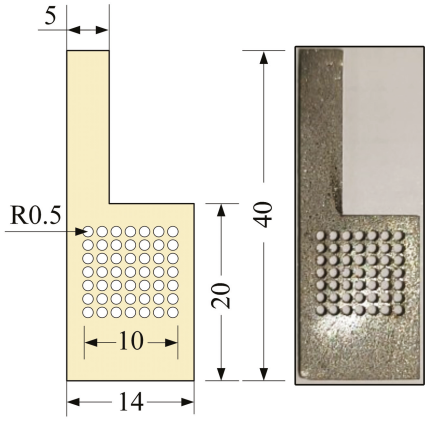

Figure 2. The CCC in mm.

Air flows mainly in a hole-type flow field, the flow state of which can be represented by the Hagen–Poiseuille equation:

$$\Delta P_{ap} = \frac{32\mu_a \overline{u}_a \Delta L}{D^2} \tag{4}$$

where ΔP_{ap} is the pressure drop of the air, μ_a is the viscosity of the air, $\overline{u}_a$ is the average flow rate of the air, and D is the effective diameter of the hole-type flow field. Further, the oxygen flow rate is calculated as follows:

$$\dot{m}_o = \frac{\Delta P_{ap} \rho_a \pi D^4}{128 \mu_a \Delta L} \times wt\% \tag{5}$$

where $\dot{m}_o$ is the flow rate of oxygen in the flow field, ρ_a is the density of air, and $wt\%$ is the mass fraction of oxygen. As can be seen from Equation (5), the flow rate of oxygen is proportional to the fourth power of the effective diameter of the flow field. If the CCC is not drained in time, the hole-type flow field will be blocked by excess water, resulting in the oxygen not reaching the cathode catalytic layer smoothly.

Overall, making a wettability modification to the foam stainless steel CCC can slow down cathode flooding and thus improve the performance of the μDMFC.

2.2. Gradient Wettability Modification for the CCC

For the gradient wettability modification of the CCC:

1. Using a laser cutting platform (Type 6060L-1000W), the CCC with the foamed stainless steel was machined, and then the surfaces of these CCC were polished smooth;
2. The CCC was cleaned with methanol, ethanol, and deionized water in turn, and then the dried CCC was immersed in the KOH solution of 1 mol/L to corrode. As shown in Figure 3a, the CCC was placed vertically with the bottom immersed to a depth of 2 mm;
3. Finally, the treated CCC was rinsed in deionized water and dried in a drying oven.

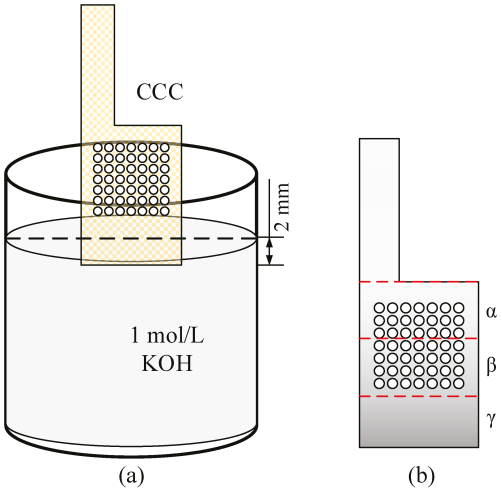

Figure 3. Wettability modification for the CCC. (**a**) The diagram of immersion; (**b**) Gradient partitioning.

During the treatment, the bottom of the CCC was immersed in the KOH solution, and then the solution climbed upwards under the capillary force. However, due to gravitational and viscous forces, the greater the height of the CCC, the smaller the mass of the climbed solution, resulting in a weaker corrosion strength. For ease of analysis, the CCC after modification was divided equally into three regions, α, β, and γ, as shown in Figure 3b.

The surface morphology of the CCC was analyzed. The selected equipment was TESCAN MIRA4, and an Oxford energy spectrometer was chosen. The scanning electron microscope (SEM) image shows that the surface of the CCC before the wettability modification has only a few tiny scratches, while the surface of the CCC after the wettability

modification has a layer of a nanostructure, as shown in Figure 4. This layer of nanostructure corroded by the KOH solution shows a uniform character and increases the surface roughness of the CCC. Compared to the prolonged hydroxide molten salt corrosion [34] and the electrochemical corrosion of the salt solution [35], the surface morphology of the CCC after the wettability modification is not substantially damaged. Therefore, the method does not significantly destroy the CCC's mechanical strength and electrical conductivity.

According to the Wenzel model:

$$cos\theta_w = R_{AF}cos\theta \tag{6}$$

where θ_w is the Wenzel contact angle and R_{AF} is the roughness of the wetted area. It can be seen that the nanostructure of the CCC surface can increase the surface roughness and reduce the contact angle.

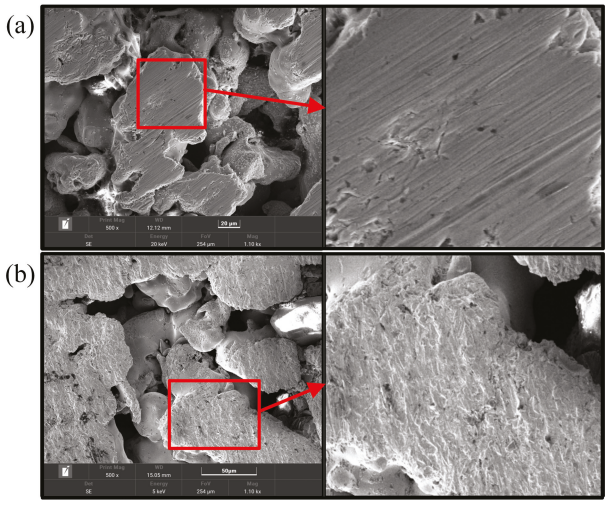

Figure 4. SEM of the CCC: (**a**) Before wettability modification; (**b**) After wettability modification.

The wettability modification can increase the capillary force and provide an additional capillary gradient force for the foamed stainless steel CCC. This increases the drainage capacity of the foam stainless steel CCC so that the μDMFC does not flood under high-intensity operating conditions.

2.3. Test System for μDMFC

The test system consists of a DC electronic load, an electrochemical workstation, and a thermostat, as shown in Figure 5. This test system can perform EIS, discharge, and polarisation curve tests for the μDMFC with different gradient wettability CCC. Before testing, the μDMFC was activated to bring the μDMFC into operation state [31,32]. Afterwards, the μDMFC was placed in a 25 °C thermostat and connected to the DC electronic load and the electrochemical workstation.

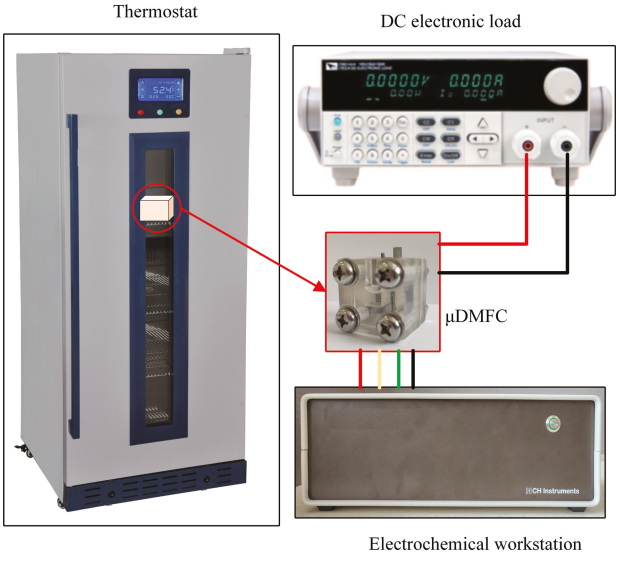

Figure 5. Test system of μDMFC.

3. Results and Discussion

3.1. Wettability Test

The contact angle for N-CCC is 120.905°, as shown in Figure 6. This is mainly caused by the air inside the foamed stainless steel reducing the surface energy, which results in a hydrophobic appearance, i.e., a contact angle greater than 90°. After the different wettability modifications, the α, β, and γ regions of the CCC all have a hydrophilic tendency, as shown in Figures 7–9.

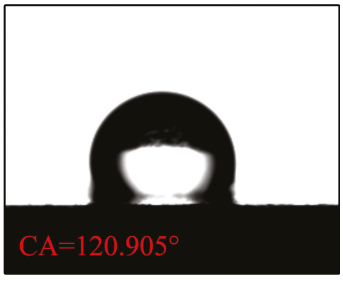

Figure 6. Wettability test of uncorroded CCC.

The droplet in the α region of the 1-CCC appears in suspension, and its contact angle is always 119.038°. The droplet in the β region of the 1-CCC appears to complete a slow penetration, and the contact angle drops to 103.00° at 20 s. In contrast, the droplet in the γ region took 20 s to penetrate completely. In the hydrophilic case, once the droplet comes into contact with the surface, it is drawn into the capillary pores by the driving force generated by the capillary effect [30,36]. From this, it is clear that the γ region of the 1-CCC is more hydrophilic than the β and α regions. Furthermore, it can be seen that the KOH solution can climb upwards along with the foamed stainless steel CCC by capillary forces to gradient-corrode the CCC. Additionally, the short immersion time results in a small mass of climbing KOH solution, and thus the β and α regions show hydrophobicity. For the 5-CCC, the droplet in the α region appears suspended, while the droplets in the

β and γ regions appear to conduct a complete penetration. The penetration time of the droplets in the β and γ regions are 15.2 s and 4.8 s, respectively. This result implies that with increasing immersion time of the CCC, the mass of the climbing KOH solution increases, and thus complete permeation occurs in the β region. For 9-CCC, the α, β, and γ regions all feature complete permeation. Their permeation times are 3.9 s, 2.3 s, and 1.7 s, respectively. This implies that the longer immersion time makes the KOH solution climb upwards in large quantities, which results in severe corrosion of the entire foamed stainless steel CCC. Therefore, the overall 9-CCC displays a hydrophilic state.

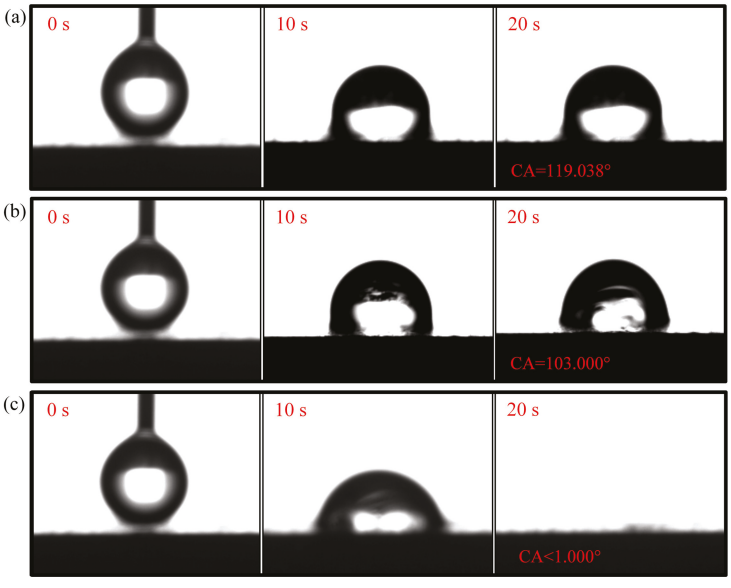

Figure 7. Wettability test of 1-CCC: (**a**) α region; (**b**) β region; (**c**) γ region.

The gradient behavior of the CCC after the wettability modification is shown in Table 1. According to the listed results, 119.038°–<1° for 1-CCC, 120.500°–<1° for 5-CCC, and $<$ 1°–<1° for 9-CCC. Furthermore, it can be seen that the hydrophilicity of the γ region of 5-CCC is superior to that of the γ region of 1-CCC because the droplet in the γ region of 5-CCC can penetrate more rapidly. Thus, the 9-CCC is almost without gradient wettability, and the 5-CCC has an optimal gradient wettability. Further, gradient wettability can generate gradient force to pull the liquid water to move directionally. The reason is that the more hydrophilic the wall, the stronger the adhesion between the droplet and the wall [3,37]. As the adhesion force increases, the contact area between the droplet and the wall increases, which causes the droplet to move towards higher hydrophilicity [38].

Table 1. Wettability of the CCC with different treatment times.

	1-CCC	**5-CCC**	**9-CCC**
α	119.038° (20 s)	120.500° (20 s)	<1° (3.9 s)
β	103.000° (20 s)	<1° (15.2 s)	<1° (2.3 s)
γ	<1° (20 s)	<1° (4.8 s)	<1° (1.7 s)

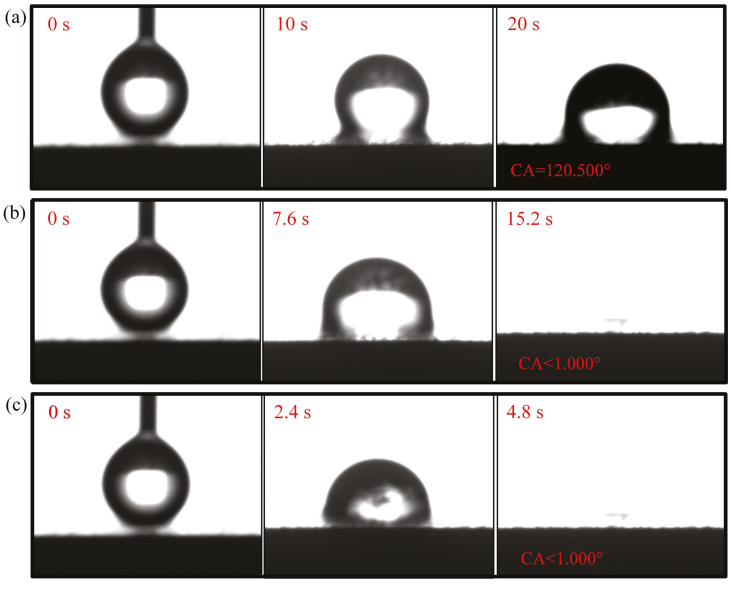

Figure 8. Wettability test of 5-CCC: (**a**) α region; (**b**) β region; (**c**) γ region.

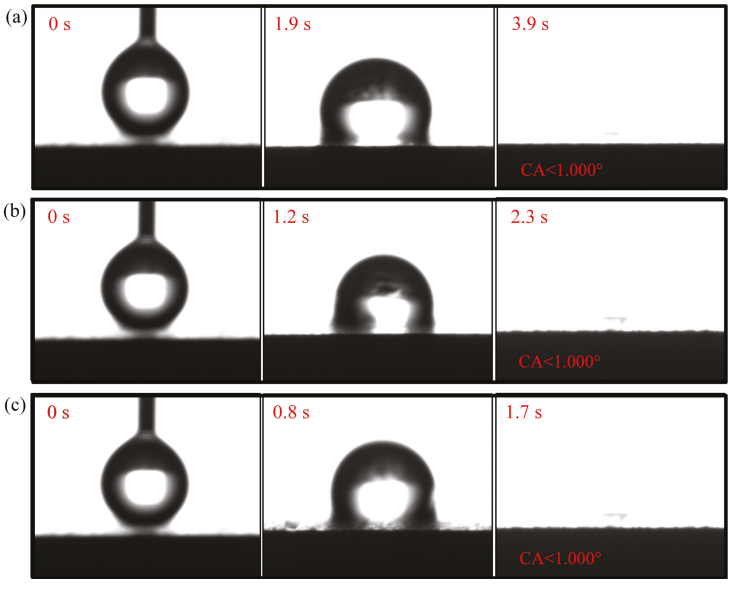

Figure 9. Wettability test of 9-CCC: (**a**) α region; (**b**) β region; (**c**) γ region.

3.2. Cathode Flooding

During the discharge process, water molecules are generated in the cathode of the μDMFC. The accumulation of these water molecules for a long time will form liquid water and affect the performance of the μDMFC. As shown in Figure 10, the μDMFC are discharged at 50 mA/cm^2 current to observe flooding of the hole-type flow field. It can be seen that most of the liquid water was in the cathode of the stainless steel μDMFC, while little of the liquid water was in the cathode of the foamed stainless steel μDMFC. This is because the liquid water of the foamed stainless steel μDMFC is absorbed into the

micropores by the capillary force. Moreover, this absorbing process does not change the water content inside the cathodic catalytic layer and does not affect the hydraulic pressure inside the membrane electrode assembly [30]. Therefore, the foamed stainless steel is suitable for water management studies with μDMFC.

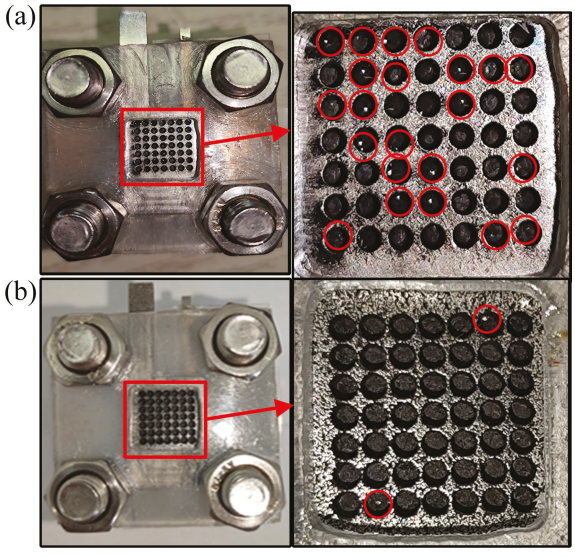

Figure 10. Flooding of the cathode. (**a**) μDMFC of stainless steel; (**b**) μDMFC of foamed stainless steel.

The polarization curves of the foamed stainless steel μDMFC were tested to find the optimum methanol solution concentration required for the discharge. As shown in Figure 11, the maximum power of the foam stainless steel μDMFC can reach 15.5 mW at a methanol solution concentration of 4 mol/L. Therefore, the methanol solution selection is 4 mol/L. Additionally, to perform a long and stable discharge of the μDMFC with different gradient wettability CCC, the current density selection is 80 mA/cm^2, and the discharge time selection is 150 min [32].

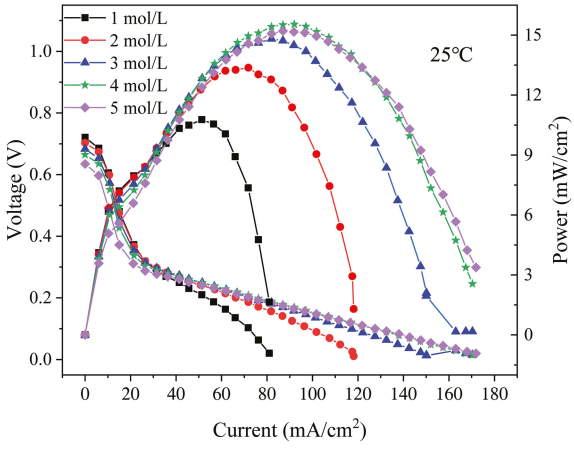

Figure 11. Polarization curves of foamed stainless steel μDMFC at 1 mol/L–5 mol/L methanol solution concentrations.

3.3. EIS

In this work, to investigate in depth the effect of the CCC with different gradient wettability on the performance of the μDMFC, AC impedance tests before and after discharge were carried out, as shown in Figures 12 and 13. Their contact impedance and total impedance are shown in Table 2. It can be seen that, before discharge, the contact impedance of the μDMFC with different gradient wettability CCC is 0.61 Ω [39]. However, the charge transfer impedance of N-CCC μDMFC is the smallest. This is because the surface of the gradient wettability CCC is corroded, which reduces its conductivity and leads to an increase in charge transfer impedance. After discharge, the EIS of the μDMFC with different gradient wettability CCC changed significantly. Their total and mass transfer impedance increased significantly, but the contact impedance decreased to 0.50 Ω [31,40]. This is because the water emerging in the cathode floods the catalytic layer, which increases the concentration loss and oxygen transfer resistance [1,26]. However, the water accumulated by prolonged discharge can raise the relative humidity of the reactant gas and further increase the water content in the membrane [7]. Increasing the level of membrane hydration can enhance the proton mobility and thus the electrical conductivity of the membrane [26,32].

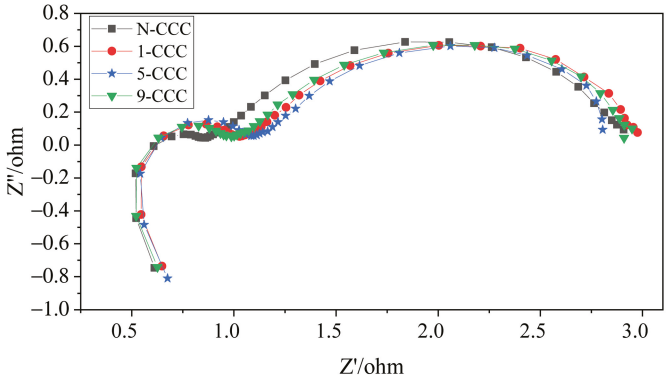

Figure 12. EIS of μDMFC with different gradient wettability CCC before discharge.

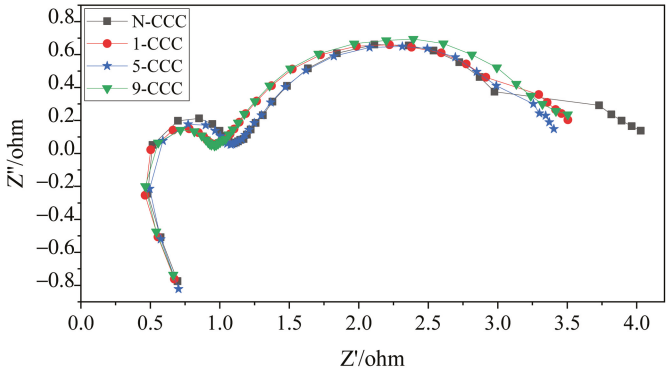

Figure 13. EIS of μDMFC with different gradient wettability CCC after discharge.

Table 2. Impedance of μDMFC with different gradient wettability CCC.

	N-CCC	1-CCC	5-CCC	9-CCC
Contact impedance (before discharge)	0.61 Ω	0.61 Ω	0.61 Ω	0.61 Ω
Contact impedance (after discharge)	0.50 Ω	0.50 Ω	0.50 Ω	0.50 Ω
Total impedance (before discharge)	2.91 Ω	2.95 Ω	2.81 Ω	2.91 Ω
Total impedance (after discharge)	4.03 Ω	3.51 Ω	3.40 Ω	3.50 Ω

In the low-frequency range, the μDMFC of 5-CCC has the smallest curve radius, while the μDMFC of N-CCC has the largest curve radius. Furthermore, the μDMFC of 1-CCC and 9-CCC have essentially the same curve radius, as shown in Figure 13. Thus, the total impedance of the μDMFC of 1-CCC and the μDMFC of 9-CCC are essentially the same. The μDMFC of 5-CCC has the lowest total impedance, while the μDMFC of N-CCC has the highest total impedance. This result implies that the cathode flooding of the μDMFC differs for the different gradient wettability CCC. The 5-CCC has the most suitable gradient wettability and can effectively direct water towards the end of the CCC. Hence, it can release the flow field channels and microporous channels of the CCC to provide more oxygen in the cathode of the μDMFC. The 1-CCC and the 9-CCC have relatively poor capillary gradient force and cannot effectively direct water towards the end of the CCC. Thus, it cannot effectively enhance the oxygen transfer rate on the cathode side. The N-CCC does not have capillary gradient force and cannot tract water from the CCC towards the end. Thus, it has a high resistance to oxygen transfer, which leads to increased cathodic polarization.

In general, after prolonged discharge, the total impedance of the μDMFC increases significantly, and the mass transfer impedance increases more than the charge transfer impedance. This implies that the effect of the mass transfer impedance on μDMFC performance is much greater than that of the charge transfer impedance under prolonged discharge. The use of wettability gradient force can increase oxygen transfer channels and improve mass transfer rate. Thus, it can effectively enhance the μDMFC's performance.

3.4. Discharge Voltage

Discharge voltage tests are carried out for different types of μDMFC with a methanol solution of 2 mL, as shown in Figure 14. At 1 h, the discharge voltage of the N-CCC μDMFC is 0.09 V. Compared to it, the discharge voltage of the 5-CCC μDMFC, 1-CCC μDMFC, and 9-CCC μDMFC increased by 33.33%, 27.28%, and 23.33%, respectively. This is because the large amount of liquid water produced by the cathode during the prolonged discharge blocks the microporous channels of the CCC, making the oxygen transport path less accessible. However, the gradient wettability CCC can effectively pull the water generated in the cathode towards the end of the CCC, and the particulate water in microporous channels evaporates more quickly, which can make the microporous channels of the CCC unobstructed and increase the drainage rate and oxygen transfer rate [41,42].

During the discharge process, the performance of the N-CCC μDMFC decreases the fastest while the performance of the 5-CCC μDMFC decreases the slowest. Additionally, the performance of the 1-CCC and 9-CCC μDMFC decreases at approximately the same rate. This implies that as the redox reaction progresses, more and more liquid water accumulates in the cathode of the μDMFC. The accumulation of liquid water reduces the transfer of oxygen to the membrane electrode assembly, which increases the polarization losses and makes the local current density distribution in the μDMFC very non-uniform. The μDMFC with suitable gradient wettability shows better performance stability.

The performance of the μDMFC is affected by the accumulation and distribution of liquid water [24]. If liquid water is not discharged from the cathode side in time, the diffusion efficiency of the gas is significantly reduced. Further, this can cause a rapid and unstable degradation in the performance of the μDMFC and affect the lifetime of the μDMFC [15].

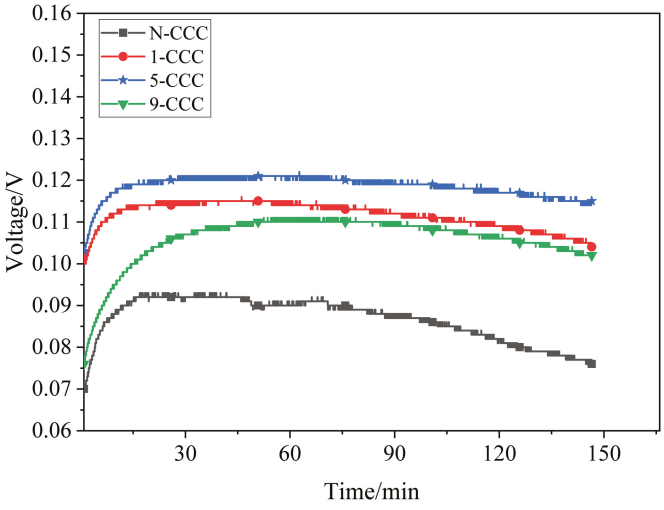

Figure 14. EIS of μDMFC with different gradient wettability CCC after discharge.

4. Conclusions

In this study, for the foamed stainless steel μDMFC, a gradient wettability CCC was prepared to avoid cathode flooding by analyzing the gas–liquid two-phase flow characteristics. Then, to find the suitable corrosion time, the wettability of four different types of CCC was tested. At room temperature, the μDMFC with different gradient wettability CCC were tested using EIS and discharge voltage. The main conclusions are as follows:

1. The foamed stainless steel is more suitable to prepare the gradient wettability CCC for water management of μDMFC cathode. The gradient of wettability of the 5-CCC is 120.500°–<1°. It is significantly better than the 1-CCC and 9-CCC. At 5 min treatment time conditions, the KOH solution of 1 mol/L can provide optimal gradient corrosion for the CCC;
2. After discharge of 150 min, the 5-CCC μDMFC has the lowest total impedance, whereas the N-CCC μDMFC has the highest total impedance. The 5-CCC has the most suitable gradient wettability and can effectively direct water towards the end of the CCC. Thus, it has more flow field channels and microporous channels and can provide more oxygen to the cathode of the μDMFC;
3. At 1 h, compared to the N-CCC μDMFC, the discharge voltage of the 1-CCC μDMFC, 5-CCC μDMFC, and 9-CCC μDMFC increased by 27.28%, 33.33%, and 23.33%, respectively. The μDMFC with gradient wettability CCC shows better stability and higher discharge voltage.

Author Contributions: Conceptualization, F.Z. and Z.Z.; methodology, F.Z. and Y.Z.; software, Y.Z. and F.Z.; validation, Z.Z., F.Z. and Y.Z.; formal analysis, F.Z.; investigation, F.Z.; resources, Z.Z.; data curation, F.Z.; writing—original draft preparation, F.Z. and Y.Z.; writing—review and editing, F.Z. and Z.Z.; visualization, Y.Z.; supervision, Z.Z.; project administration, Z.Z.; funding acquisition, Z.Z. All authors have read and agreed to the published version of the manuscript.

Funding: This work is partly supported by the National Natural Science Foundation of China (Grant No. 62162035) and the Applied Basic Foundation of Yunnan Province (Grant No. 202101AT070131, 202101AT070309).

Institutional Review Board Statement: Not applicable.

Informed Consent Statement: Not applicable.

Data Availability Statement: Not applicable.

Acknowledgments: The contributions of all my coauthors are gratefully acknowledged. Thanks are extended to the National Natural Science Foundation of China and the Applied Basic Foundation of Yunnan Province.

Conflicts of Interest: The authors declare no conflict of interest.

Abbreviations

The following abbreviations are used in this manuscript:

μDMFC	Micro direct methanol fuel cell
CCC	Cathode current collector
EIS	Electrochemical impedance spectroscopy
SEM	Scanning electron microscope
N-CCC	Uncorroded CCC
1-CCC	1 min corroded CCC
5-CCC	5 min corroded CCC
9-CCC	9 min corroded CCC
ΔP	Pressure drop, capillary pressure
$\dot{m}$	Flowing mass
ΔL	Distance
ρ	Density
μ	Kinetic viscosity
r_{eff}	Effective radius
K	Permeability
σ	Surface tension
θ	Contact angle
$\overline{u}$	Average flow rate
D	Effective diameter
$wt\%$	Mass fraction
Subscript l	Liquid
Subscript a	Air
Subscript o	Oxygen

References

1. Shanmugasundaram, S.; Rajaram, G.; Karthikeyan, P.; Vasanth, R.J. Comparison of perforated and serpentine flow fields on the performance of proton exchange membrane fuel cell. *J. Energy Inst.* **2017**, *90*, 363–371.
2. Liu, C.; Hu, S.; Yin, L.; Yang, W.; Yu, J.; Xu, Y.; Li, L.; Wang, G.; Wang, L. Micro Direct Methanol Fuel Cell Based on Reduced Graphene Oxide Composite Electrode. *Micromachines* **2021**, *12*, 72. [CrossRef]
3. Vijayakrishnan, M.K.; Palaniswamy, K.; Ramasamy, J.; Kumaresan, T.; Manoharan, K.; Rajagopal, T.K.R.; Maiyalagan, T.; Jothi, V.R.; Yi, S.-C. Numerical and experimental investigation on 25 cm^2 and 100 cm^2 PEMFC with novel sinuous flow field for effective water removal and enhanced performance. *Int. J. Hydrogen Energy* **2020**, *45*, 7848–7862. [CrossRef]
4. Hasheminasab, M.; Kermani, M.J.; Nourazar, S.S.; Khodsiani, M.H. A novel experimental based statistical study for water management in proton exchange membrane fuel cells. *Appl. Energy* **2020**, *264*, 114713. [CrossRef]
5. Yang, Z.; Du, Q.; Jia, Z.; Yang, C.; Jiao, K. Effects of operating conditions on water and heat management by a transient multi-dimensional PEMFC system model. *Energy* **2019**, *183*, 462–476. [CrossRef]
6. Flückiger, R.; Tiefenauer, A.; Ruge, M.; Aebi, C.; Büchi, F. Thermal analysis and optimization of a portable, edge-air-cooled PEFC stack. *J. Power Sources* **2007**, *172*, 324–333. [CrossRef]
7. Wu, J.; Galli, S.; Lagana, I.; Pozio, A.; Monteleone, G.; Xiao, Z.Y.; Martin, J.; Wang, H. An air-cooled proton exchange membrane fuel cell with combined oxidant and coolant flow. *J. Power Sources* **2009**, *188*, 199–204. [CrossRef]
8. Karthikeyan, P.; Velmurugan, P.; George, A.J.; Kumar, R.R.; Vasanth, R.J. Experimental investigation on scaling and stacking up of proton exchange membrane fuel cells. *Int. J. Hydrogen Energy* **2014**, *39*, 11186–11195. [CrossRef]
9. Bachman, J.; Charvet, M.; Santamaria, A.; Tang, H.Y.; Park, J.W.; Walker, R. Experimental investigation of the effect of channel length on performance and water accumulation in a PEMFC parallel flow field. *Int. J. Hydrogen Energy* **2012**, *37*, 17172–17179. [CrossRef]
10. Su, A.; Weng, F.B.; Hsu, C.Y.; Chen, Y.M. Studies on flooding in PEM fuel cell cathode channels. *Int. J. Hydrogen Energy* **2006**, *31*, 1031–1039. [CrossRef]

11. Koresawa, R.; Utaka, Y. Water control by employing microgrooves inside gas channel for performance improvement in polymer electrolyte fuel cells. *Int. J. Hydrogen Energy* **2015**, *40*, 8172–8181. [CrossRef]
12. Imbrioscia, G.M.; Fasoli, H.J. Simulation and study of proposed modifications over straight-parallel flow field design. *Int. J. Hydrogen Energy* **2014**, *39*, 8861–8867. [CrossRef]
13. Jaruwasupant, N.; Khunatorn, Y. Effects of difference flow channel designs on Proton Exchange Membrane Fuel Cell using 3-D Model. *Energy Procedia* **2011**, *9*, 326–337. [CrossRef]
14. Ashrafi, M.; Shams, M. The effects of flow-field orientation on water management in PEM fuel cells with serpentine channels. *Appl. Energy* **2017**, *208*, 1083–1096. [CrossRef]
15. Shimpalee, S.; Beuscher, U.; Van Zee, J.W. Analysis of GDL flooding effects on PEMFC performance. *Electrochim. Acta* **2007**, *52*, 6748–6754. [CrossRef]
16. Jiang, F.; Wang, C.Y. Numerical modeling of liquid water motion in a polymer electrolyte fuel cell. *Int. J. Hydrogen Energy* **2014**, *39*, 942–950. [CrossRef]
17. Mehnatkesh, H.; Alasty, A.; Boroushaki, M.; Khodsiani, M.H.; Kermani, M.J. Estimation of Water Coverage Ratio in Low Temperature PEM-Fuel Cell Using Deep Neural Network. *IEEE Sens. J.* **2020**, *20*, 10679–10686. [CrossRef]
18. Rubio, G.A.; Agila, W.E. A Fuzzy Model to Manage Water in Polymer Electrolyte Membrane Fuel Cells. *Processes* **2021**, *9*, 904. [CrossRef]
19. Garcia-Salaberri, P.A.; Zenyuk, I.V.; Weber, A.; Gostick, J.T. Modeling transport in gas diffusion layers using a composite continuum-pore network formulation. In Proceedings of the EChemCONSTORE I, Madrid, Spain, 28–29 January 2021.
20. Wang, Y.; Wang, S.; Wang, G.; Yue, L. Numerical study of a new cathode flow-field design with a sub-channel for a parallel flow-field polymer electrolyte membrane fuel cell. *Int. J. Hydrogen Energy* **2018**, *43*, 2359–2368. [CrossRef]
21. Birgersson, E.; Vynnycky, M. A quantitative study of the effect of flow-distributor geometry in the cathode of a PEM fuel cell. *J. Power Sources* **2006**, *153*, 76–88. [CrossRef]
22. Turhan, A.; Heller, K.; Brenizer, J.S. Quantification of liquid water accumulation and distribution in a polymer electrolyte fuel cell using neutron imaging. *J. Power Sources* **2006**, *160*, 1195–1203. [CrossRef]
23. Bozorgnezhad, A.; Shams, M.; Kanani, H.; Hasheminasab, M.; Ahmadi, G. The experimental study of water management in the cathode channel of single-serpentine transparent proton exchange membrane fuel cell by direct visualization. *Int. J. Hydrogen Energy* **2015**, *40*, 2808–2832. [CrossRef]
24. Iranzo, A.; Salva, A.; Boillat, P.; Biesdorf, J.; Tapia, E.; Rosa, F. Water build-up and evolution during the start-up of a PEMFC: Visualization by means of Neutron Imaging. *Int. J. Hydrogen Energy* **2016**, *42*, 13839–13849. [CrossRef]
25. Rahimi-Esbo, M.; Ranjbar, A.A.; Rahgoshay, S.M. Analysis of water management in PEM fuel cell stack at dead-end mode using direct visualization. *Renew. Energy* **2020**, *162*, 212–221. [CrossRef]
26. Tongsh, C.; Liang, Y.Q.; Xie, X.; Li, L.C.; Jiao, K. Experimental investigation of liquid water in flow field of proton exchange membrane fuel cell by combining X-ray with EIS technologies. *Sci. China Technol. Sci.* **2021**, *64*, 2153–2165. [CrossRef]
27. Song, K.Y.; Lee, H.K.; Kim, H.T. MEA design for low water crossover in air-breathing DMFC. *Electrochim. Acta* **2008**, *53*, 637–643. [CrossRef]
28. Zhu, X.; Li, J.; Qiang, L.; Xun, Z.; Ye, D. Effects of Ambient Conditions on the Cell Performance of a Passive Air-Breathing DMFC. *ASME Int. Conf. Fuel Cell Sci.* **2008**, *43181*, 751–756.
29. Fly, A.; Butcher, D.; Meyer, Q.; Whiteley, M.; Spencer, A.; Kim, C.; Shearing, P.R.; Brett, D.J.L.; Chen, R. Characterisation of the diffusion properties of metal foam hybrid flow-fields for fuel cells using optical flow visualisation and X-ray computed tomography. *J. Power Sources* **2018**, *395*, 171–178. [CrossRef]
30. Yuan, W.; Hou, C.; Zhang, X.; Zhong, S.; Liu, X. Constructing a Cathode Catalyst Layer of a Passive Direct Methanol Fuel Cell with Highly Hydrophilic Carbon Aerogel for Improved Water Management. *ACS Appl. Mater. Interfaces* **2019**, *11*, *41*, 37626–37634. [CrossRef]
31. Karthikeyan, M.; Karthikeyan, P.; Muthukumar, M.; Kannan, V.M.; Thanarajan, K.; Maiyalagan, T.; Hong, C.W.; Jothi, V.R.; Yi, S.C. Adoption of novel porous inserts in the flow channel of pern fuel cell for the mitigation of cathodic flooding. *Int. J. Hydrogen Energy* **2020**, *45*, 7863–7872. [CrossRef]
32. Sun, X.; Xie, X.; Wu, S.; Liu, Z.; Jiao, K. Investigation of metal foam porosity and wettability on fuel cell water management by Electrochemical Impedance Spectroscopy. *Int. J. Green Energy* **2021**, *18*, 708–719 . [CrossRef]
33. Zhang, F.; Zhang, Y.; Luo, C.; Zhang, D.; Zhao, Z. Performance study of μDMFC with foamed metal cathode current collector. *RSC Adv.* **2022**, *12*, 4145–4152. [CrossRef]
34. Pooja, M.; Ravishankar, K.; Madav, V. High temperature corrosion behaviour of stainless steels and Inconel 625 in hydroxide salt. *Mater. Today Proc.* **2021**, *46*, 2612–2615. [CrossRef]
35. Tan, L.; Wang, Z.; Ma, Y. Tribocorrosion Behavior and Degradation Mechanism of 316L Stainless Steel in Typical Corrosive Media. *Acta Metall. Sin.* **2021**, *34*, 813–824. [CrossRef]
36. Cho, J.; Neville, T.P.; Trogadas, P.; Meyer, Q.; Wu, Y.; Ziesche, R.; Boillat, P.; Cochet, M.; Manzi-Orezzoli, V.; Shearing, P. Visualization of liquid water in a lung-inspired flow-field based polymer electrolyte membrane fuel cell via neutron radiography. *Energy* **2019**, *170*, 14–21. [CrossRef]
37. Liu, S.; Zhang, L.; Wang, Z.; Li, R. Influence of the surface microstructure of the fuel cell gas diffusion layer on the removal of liquid water. *Int. J. Hydrogen Energy* **2021**, *46*, 31764–31777. [CrossRef]

38. Chen, Q.; Niu, Z.; Li, H.; Jiao, K.; Wang, Y. Recent progress of gas diffusion layer in proton exchange membrane fuel cell: Two-phase flow and material properties. *Int. J. Hydrogen Energy* **2021**, *46*, 8640–8671. [CrossRef]
39. Ahn, C.Y.; Lim, M.S.; Hwang, W.; Kim, S.; Park, J.E.; Lim, J.; Choi, I.; Cho, Y.H.; Sung, Y.E. Effect of Porous Metal Flow Field in Polymer Electrolyte Membrane Fuel Cell under Pressurized Condition. *Fuel Cells* **2017**, *17*, 652–661. [CrossRef]
40. Wang, X.; Chen, S.; Fan, Z.; Li, W.; Wang, S.; Li, X.; Zhao, Y.; Zhu, T.; Xie, X. Laser-perforated gas diffusion layer for promoting liquid water transport in a proton exchange membrane fuel cell. *Int. J. Hydrogen Energy* **2017**, *42*, 29995–30003. [CrossRef]
41. Hou, Y.; Zhang, G.; Qin, Y.; Du, Q.; Jiao, K. Numerical simulation of gas liquid two-phase flow in anode channel of low-temperature fuel cells. *Int. J. Hydrogen Energy* **2017**, *42*, 3250–3258. [CrossRef]
42. Karthikeyan, P.; Vasanth, R.J.; Muthukumar, M. Experimental investigation on uniform and zigzag positioned porous inserts on the rib surface of cathode flow channel for performance enhancement in PEMFC. *Int. J. Hydrogen Energy* **2015**, *40*, 4641–4648. [CrossRef]

nanomaterials

MDPI

Article

$NiFe_2O_4$/Ketjen Black Composites as Efficient Membrane Separators to Suppress the Shuttle Effect for Long-Life Lithium-Sulfur Batteries

Wen Jiang [1], Lingling Dong [1], Shuanghui Liu [1], Shuangshuang Zhao [2], Kairu Han [1], Weimin Zhang [1], Kefeng Pan [1,*] and Lipeng Zhang [2,*]

[1] School of Chemistry and Chemical Engineering, Shandong University of Technology, Zibo 255049, China; wengejang@126.com (W.J.); donglingling202107@163.com (L.D.); shuanghuiliu2020@163.com (S.L.); hankairu2022@126.com (K.H.); wmzhang@sdut.edu.cn (W.Z.)

[2] School of Materials and New Energy, South China Normal University, Shanwei 516600, China; 20219207@m.scnu.edu.cn

* Correspondence: xiaopandy@126.com (K.P.); zhanglipeng@sdut.edu.cn (L.Z.)

Abstract: Lithium-sulfur batteries exhibit great potential as one of the most promising energy storage devices due to their high theoretical energy density and specific capacity. However, the shuttle effect of the soluble polysulfide intermediates could lead to a severe self-discharge effect that hinders the development of lithium-sulfur batteries. In this paper, a battery separator has been prepared based on $NiFe_2O_4$/Ketjen Black (KB) modification by a simple method to solve the shuttle effect and improve the battery performance. The as-modified separator with the combination of small-size KB and $NiFe_2O_4$ nanoparticles can effectively use the physical and chemical double-layer adsorption to prevent polysulfide from the shuttle. Moreover, it can give full play to its catalytic effect to improve the conversion efficiency of polysulfide and activate the dead sulfur. The results show that the $NiFe_2O_4$/KB-modified separator battery still maintains a discharge capacity of 406.27 mAh/g after 1000 stable cycles at a high current density of 1 C. Furthermore, the coulombic efficiency remains at 99%, and the average capacity attenuation per cycle is only 0.051%. This simple and effective method can significantly improve the application capacity of lithium-sulfur batteries.

Keywords: lithium-sulfur battery; nano $NiFe_2O_4$; adsorption; separator modification

Citation: Jiang, W.; Dong, L.; Liu, S.; Zhao, S.; Han, K.; Zhang, W.; Pan, K.; Zhang, L. $NiFe_2O_4$/Ketjen Black Composites as Efficient Membrane Separators to Suppress the Shuttle Effect for Long-Life Lithium-Sulfur Batteries. *Nanomaterials* **2022**, *12*, 1347. https://doi.org/10.3390/nano12081347

Academic Editor: Sophie Tingry

Received: 10 March 2022
Accepted: 11 April 2022
Published: 14 April 2022

1. Introduction

The demand for a diverse and comprehensive transformation of the energy structure based on fossil energy for clean and renewable energy is becoming stronger and stronger in the energy field [1]. The electrochemical energy storage strategy based on the secondary batteries is considered the energy storage and conversion solution, with broad applicability in the new energy systems [2]. Investigations focus on developing new secondary battery systems with low cost, high energy density, and long cycle life. The lithium-sulfur (Li-S) secondary battery, which has a theoretical specific capacity of up to 1675 mAh/g and a theoretical energy density of 2600 kW/kg, is considered as one of the most promising next-generation secondary battery systems and has attracted extensive attention [3,4]. However, the shuttle effect of lithium polysulfides (LiPSs) between lithium metal anode and sulfur cathode results in serious problems such as the decrease of battery capacity, low coulombic efficiency, and the deterioration of cycle stability, which limit the practical application of Li-S batteries [5,6]. To overcome these issues, introducing a separator layer as a polysulfide shuttle barrier between anode and cathode is considered as an extremely effective strategy.

In recent years, researchers have proposed many approaches to optimize the construction of the separator layers to improve the battery's performance by enhancing the conductivity and boosting the adsorption of LiPSs. Manthiram et al. [7–10] proposed a

strategy of modifying the conductive layer on the cathode side of the electrode separator to improve the electrochemical reaction activity of the cathode active material, reducing the interface resistance and physically limiting the shuttle of polysulfides, thereby improving the battery rate performance and energy. Furthermore, Al_2O_3 [11,12], SnO_2 [13], MnO_2 [14], and other inorganic polar materials have been used to modify the conductive layer on the cathode side of the separator to improve the sulfur fixation effect of the separator. For example, N [15,16], P [17], O [18], B [19], and S [20,21] were also used to dope the carbon-based conductive layer on the cathode side of the separator to change the charge distribution state on the surface and improve the sulfur fixation. On this basis, the use of catalytic materials, which can capture and improve the conversion efficiency of LiPSs intermediates to functionalize the separator to improve the electrochemical performance of the battery, is an extremely effective strategy. Yi et al. [22] used Ir nanoparticles to modify KB to prepare the KB@Ir composite and used them as a catalytic layer on the separator to promote the redox reaction of lithium sulfide intermediates. The nanoparticles exhibited strong chemical adsorption on the polysulfide ions and effectively accelerated the kinetic process of polysulfide conversion. Giebeler et al. [23] embedded RuO_2 into mesoporous carbon and coated it on the separator as an electrochemically active polysulfide nest, which significantly improved the redox reaction efficiency of the polysulfide that migrated out of the cathode. This type of multifunctional separator could have three advantages: (1) improving the electronic conductivity of the battery and the utilization rate of the active materials, (2) limiting the shuttle effect and reducing the dissolution and diffusion of polysulfides, and (3) accelerating the reaction kinetic process of polysulfides and the thermodynamic process of the solvent interface. However, this catalytic layer is mainly made of precious metals such as Au, Pt, Ir, and Ru or their oxides, and the high cost of these materials could limit their broad applicability [24]. Therefore, an optimization strategy for the low-cost separator that also has conductive, adsorption, and catalytic functions could have a significant influence on promoting the application of Li-S batteries.

Ketjen Black(KB) is a common commercial porous carbonaceous material with excellent conductivity, often used as the sulfur host [25,26] or the separator sulfur fixation body [27–29] of Li-S batteries to improve their conductivity. The fluffy accumulation of particles retains many pores, providing pathways for ion transfer. Moreover, its soft texture can alleviate the volume expansion of the cathode and separator. Meanwhile, in previous studies, $NiFe_2O_4$ mainly was used as a lithium storage material as the negative electrode material for lithium-ion batteries [30–37]. Recent studies have shown that nano $NiFe_2O_4$, which is mainly used as a lithium storage material for lithium-ion batteries, has a strong adsorption effect on polysulfides and capture-soluble polysulfides. Some researchers used it as a sulfur host and successfully inhibited the shuttle effect of polysulfides [38,39]. It is worth mentioning that $NiFe_2O_4$ has also been proven to accelerate the reaction kinetic process of polysulfides, which indicates that it has a relatively good catalytic effect on the redox reaction of polysulfides on the cathode [40–42]. Moreover, the modification of the positive electrode material is an efficient method to improve the electrochemical performance of Li-S batteries. Transferring the conductive carbonaceous material introduced into the cathode and the adsorptive catalytic material to the battery separator could be a promising strategy to enhance the development of Li-S batteries [43–46].

In this work, we innovatively loaded nano-$NiFe_2O_4$ on the membrane as a separator layer. The $NiFe_2O_4$/KB modified battery separator not only enhanced the conductivity of the separator but also improved its adsorption of polysulfides, accelerated the kinetic processes of oxidation and reduction of sulfides, and added the function of the secondary current collector to the separator. The results showed that the Li-S battery with the $NiFe_2O_4$/KB-modified separator had excellent rate performance and long-cycle stability. It maintained a discharge capacity of 406.27 mAh/g after 1000 stable cycles at a high current density of 1 C, with an average capacity attenuation of only 0.051% per cycle. This simple and effective method significantly improved the application capacity of Li-S batteries.

2. Materials and Methods

2.1. Preparation of $NiFe_2O_4$ Nanoparticles

$NiFe_2O_4$ nanoparticles were prepared by the improved hydrothermal method. Weigh 8 g of iron nitrate ($Fe(NO_3)_3 \cdot 9H_2O$ (Aladdin Inc., Shanghai, China)), 2.9 g of nickel nitrate ($Ni(NO_3)_2 \cdot 6H_2O$ (Aladdin Inc., Shanghai, China)), and 0.9 g of urea (CN_2H_4O (Aladdin Inc., Shanghai, China)) in 100 mL of deionized water and stir well, transfer to a hydrothermal autoclave and keep reacting at 180 °C for 24 h, then cool naturally to room temperature. After centrifugal collection of the precipitate, the precipitate was washed with water and ethanol, respectively, and the precipitation was dried at 60 °C for 12 h to obtain a reddish-brown powder. The dried powder was put into a tube furnace for heat treatment at 400 °C for 3 h and then ground uniformly to obtain $NiFe_2O_4$ nanoparticles.

2.2. Preparation of $NiFe_2O_4$/KB-Modified Separator

The ratio of the slurry and the orientation of the coating were determined based on the preliminary study in S1. The prepared $NiFe_2O_4$ nanoparticles, commercial KB, and binder PVDF were mixed to prepare a coating slurry with a mass ratio of 9:27:4. Firstly, the PVDF was dissolved into the 1-Methyl-2-pyrrolidinone (NMP) to obtain the mixed solution, and then the $NiFe_2O_4$ nanoparticles were added to the mixed solution by grinding and mixing the $NiFe_2O_4$ nanoparticles with the KB particles, which was stirred for 8 h at room temperature to obtain the coating slurry. A 50 μm spatula was used to coat the mixed slurry on the PP separator. After drying at 40 °C for 12 h, it was cut and stored in a glove box. The same method was used to prepare the KB-coated separator. Figure S1c shows a schematic diagram of the preparation process of the $NiFe_2O_4$/KB-modified separator.

2.3. Characterization of Materials

A Cu-Kα radiation X-ray diffractometer (Rigaku Inc., Tokyo, Japan) was used for X-ray powder diffractometry (XRD) to verify the formation of the products. A Raman spectrometer (Horiba Inc., Paris, France) was used to analyze the crystal structure of the prepared samples. An X-ray photoelectron spectroscope (Thermo Inc., Waltham, MA, USA) recorded the samples' X-ray photoelectron spectrum (XPS). A Fourier Infrared Spectrometer (Thermo Inc., Waltham, MA, USA) was used to record the Fourier Transform Infrared (FT-IR) spectrum (S2) of the samples. The SEM micrographs were collected using a field emission environmental scanning electron microscope (FEI Inc., Hillsboro, OR, USA) equipped with an EDX microanalyzer. A field emission high-resolution projection electron microscope (FEI Inc., Hillsboro, OR, USA) was used to characterize the morphology of the prepared samples (S3).

2.4. Electrochemical Characterization

The assembled battery (S4) was left for 12 h to ensure that the electrolyte thoroughly wetted the inside of the battery. A Xinwei tester was used to conduct the constant current charge, and discharge tests of the battery were conducted at 1.7–2.8 V. An electrochemical workstation (Chenhua Inc., Shanghai, China) was used for cyclic voltammetry (CV) and electrochemical AC impedance (EIS) tests. The CV test voltage range was 1.5–3.0 V, and the sweep speed was 0.1 mV/s. The AC impedance scanning frequency was from the high frequency of 100 kHz to the low frequency of 0.01 Hz, with an amplitude of 5 mV.

2.5. Theoretical Calculation

The Vienna Ab initio Simulation Package (VASP) software was used for density functional theory (DFT) in the simulation calculations [47,48]. A 3×3 super-monolithic flat plate model containing two layers of atoms totaling 252 atoms was built to simulate the surface of $NiFe_2O_4$(1 0 0). The height of the vacuum layer was set to 15 Å. The cut-off energy was set to 500 eV. The sampling of the Brillouin zone was geometrically optimized using the Monkhorst–Pack format of a ($1 \times 1 \times 1$) k-point grid. The generalized gradient

approximation (GGA) and the Perdew, Burke, and Ernzerhof (PBE) functional were used to optimize the structures [49,50]. The binding energy (E_b) of the adsorbate was defined as

$$E_b = E_{total} - E_{slab} - E_s \quad (1)$$

where E_{total} represents the total energy of the adsorbent model, and E_{slab} and E_s are the energy of the corresponding bare board and free adsorbent, respectively.

3. Results

3.1. Characterization of Nano $NiFe_2O_4$ Materials

Figure 1a shows the XRD pattern of the prepared $NiFe_2O_4$ sample. The characteristic peaks are assigned to (111), (220), (311), (222), (400), (422), (511), and (440) crystal planes. All the peak values correspond to the standard pattern of $NiFe_2O_4$ crystal (PDF 74-2801) [51]. There are no pronounced impurity peaks in the XRD pattern, and the peak shapes of all characteristic peaks are sharp, indicating that the crystallinity of the as-prepared $NiFe_2O_4$ material is high. The grain size of $NiFe_2O_4$ calculated based on the XRD pattern (S5) is 17–26 nm, with an average grain size of 20 nm. The $NiFe_2O_4$ nanoparticles can shorten the diffusion path of Li^+ and expand the specific surface area to form more reaction sites.

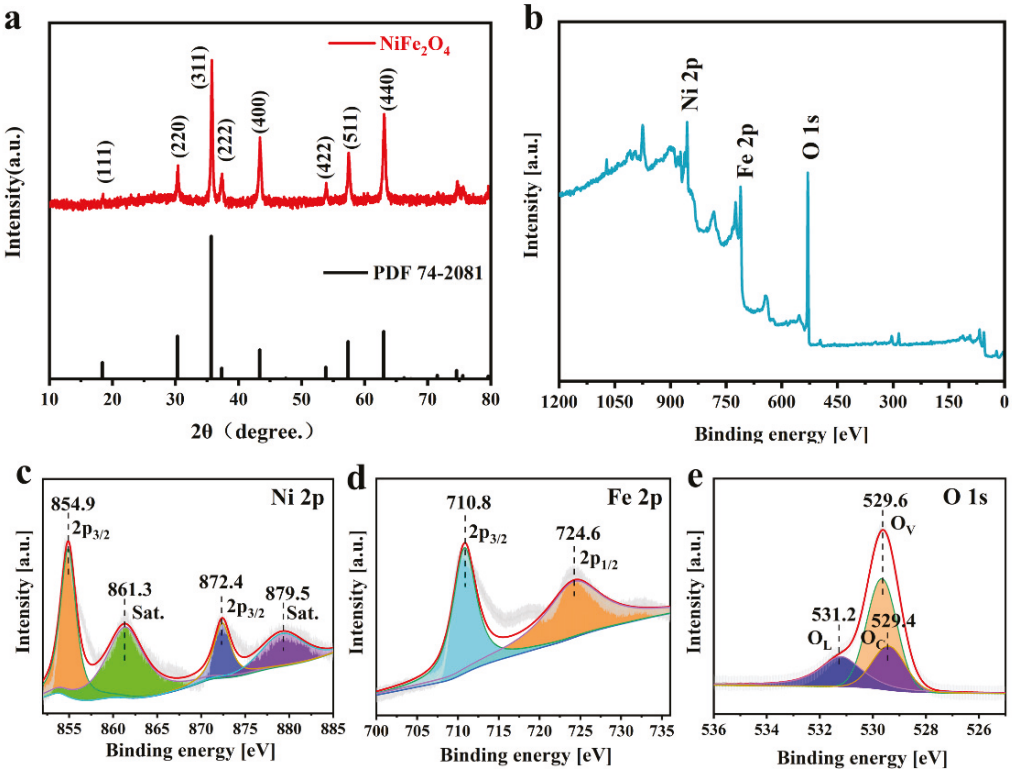

Figure 1. (**a**) The X-ray diffraction pattern of $NiFe_2O_4$, and the XPS spectra of $NiFe_2O_4$ nanoparticles: (**b**) survey spectra, (**c**) Ni 2p, (**d**) Fe 2p, and (**e**) O 1s.

XPS was used to obtain the detailed elemental composition and oxidation state characterization of the samples. Figure 1b shows the presence of three elements—Ni, Fe, and O—in the synthesized materials. The two prominent peaks in Figure 1c are located at 854.9 eV and 872.4 eV, corresponding to Ni $2p_{3/2}$ and Ni $2p_{1/2}$, respectively. In addition,

the two satellite peaks of Ni^{2+} are located at 861.36 eV and 879.5 eV. The two main peaks at 710.85 eV and 724.65 eV in Figure 1d represent Fe $2p_{3/2}$ and Fe $2p_{1/2}$ of Fe^{3+}. Figure 1e shows three peaks in the O 1s region, representing O_L (531.2 eV), O_C (529.4 eV), and O_V (529.65 eV), respectively [52].

The Raman spectrum (Figure S2a) shows that the $NiFe_2O_4$ nanoparticles have stable ferromagnetism, as the peaks at 219.12 cm^{-1}, 285.88 cm^{-1}, 479.68 cm^{-1}, 572.4 $cm^{-1,}$ and 689.93 cm^{-1} correspond to the spinel structure $T_{2g}(1)$, E_g, $T_{2g}(2)$, $T_{2g}(3)$, and $A1_g$ vibration, respectively [53,54]. No other impurity peaks are found on the Raman spectrum, implying that the crystal form of $NiFe_2O_4$ nanoparticles was uniform and consistent with the XRD results.

The FT-IR spectrum (Figure S2b) of the samples shows that there are two main absorption bands at 599.75 cm^{-1} and 472.47 cm^{-1}, which correspond to the vibration of the tetrahedron and octahedron crystal structure of the $NiFe_2O_4$. The normal vibration mode of the tetrahedral cluster (599.75 cm^{-1}) is higher than the vibration mode of octahedral clusters (472.47 cm^{-1}). This is because the bond length of tetrahedral clusters is shorter than that of octahedral clusters, consistent with the previous reports [55]. The Raman spectrometer and infrared spectroscopy results are consistent with the XPS investigations, further confirming the synthesis of nano-$NiFe_2O_4$ with spinel structure.

Figure 2a shows the SEM micrograph of the $NiFe_2O_4$ nanoparticles. It can be observed the particles have a very rough surface and a fluffy structure formed by cross-linking between particles. Figure S3a shows the N_2 adsorption-desorption isotherms of $NiFe_2O_4$ nanoparticles. The Brunauer–Emmett–Teller method (BET) surface area of the $NiFe_2O_4$ nanocomposite was calculated to be 49.4 m^2g^{-1}. Figure S3a shows a typical type IV curve and type H3 hysteresis loop, indicating a majority of mesopores [56]. The rough surface can provide a larger specific surface area to provide sufficient active sites for the adsorption and conversion of lithium polysulfides on the separator. TEM further disclosed the detailed morphology of the samples (Figure 2b Figure S3b,c). The grain distribution of $NiFe_2O_4$ was relatively uniform, with a particle size within 20–30 nm, consistent with the XRD results. The EDS mapping results of O, Fe, and Ni elements (Figure 2c–e) reveal that the atomic ratio Ni content is 19% and Fe content is 40%. Their ratio is 1:2.1, which follows the ratio setting during the material preparation, and all of these are evenly distributed.

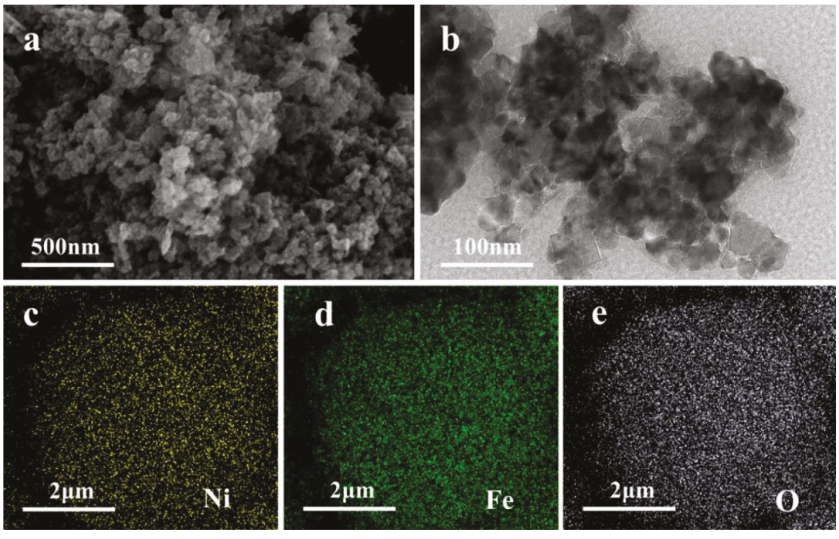

Figure 2. (**a**) The SEM and (**b**) TEM micrographs of $NiFe_2O_4$, and the element mapping of Ni (**c**), Fe (**d**), and O (**e**).

3.2. Morphology Analysis of $NiFe_2O_4$/KB-Modified Separator

Figure 3a shows the SEM image of the pristine PP separator. The typical sub-micron long needle-like pores formed by the dry stretching process can be observed. These pores provide channels for the electrolyte penetration and lithium-ion transfer. However, the long-chain soluble LiPSs could easily pass through these large pores of the separator to the other side of the electrode, causing irreversible capacity loss.

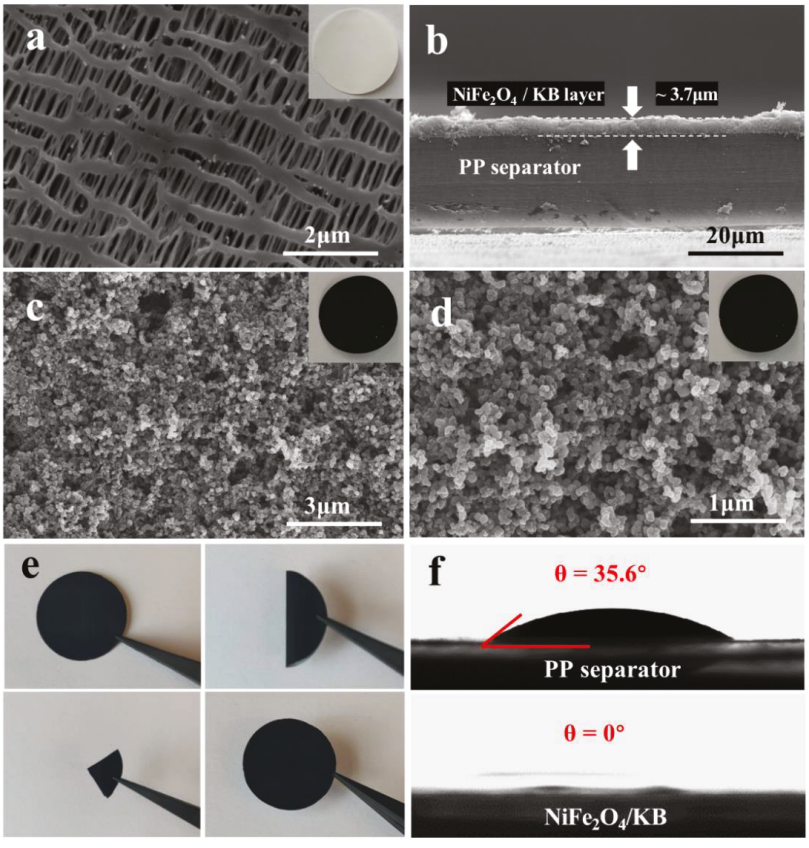

Figure 3. The SEM images of (**a**) the pristine PP separator and (**b**) the $NiFe_2O_4$/KB-modified separator in cross-sectional view, and (**c**,**d**) with different magnifications; (**e**) a digital photo of the $NiFe_2O_4$/KB-modified separator under mechanical stability tests; (**f**) the electrolyte contact angles of pristine PP and the $NiFe_2O_4$/KB-modified separator.

In order to solve the shortcomings of the pristine PP separator without affecting the ion transmission, a modified layer with $NiFe_2O_4$/KB was coated on one side of the separator. Figure 3b shows a cross-sectional view of the $NiFe_2O_4$/KB-modified separator. The pristine separator of the coating layer was in close contact with the surface and adhered well. An appropriate thickness of about 3.7 μm was chosen to avoid the impact on the lithium-ion transmission and battery internal resistance from an overly thick coating. Figure 3c,d present the surface morphology of the $NiFe_2O_4$/KB-modified separator, and the upper right corner of Figure 3c shows the digital camera image of the as-coated modified separator. The SEM images show that the accumulated KB particles on the coating surface have a porous structure filled with liquid electrolytes, and convenient ion diffusion. $NiFe_2O_4$ nanoparticles are uniformly dispersed in the 3D porous structure formed by the accumu-

lation of KB particles, which could anchor the polysulfide diffused from the cathode to the anode side. The accumulation formed the 3D structure, providing sufficient reaction space for the catalytic conversion. In addition, the functional carbon coating could act as a conductive secondary current collector, promoting electron transport and increasing the sulfur utilization rate. The two cooperate to firmly block the polysulfide on one side of the separator and prevent its shuttle effect on both sides of the separator, which becomes a powerful barrier to block the shuttle of polysulfide.

Figure 3e shows the folding/unfolding test of the modified separator. After repeated folding and deep bending, the modified material still adhered to the surface of the PP separator without any peeling. The results show that $NiFe_2O_4$/KB has good adhesion to the PP separator, and the modified separator has excellent mechanical stability and flexibility.

The wettability of the battery separator surface is an essential factor in improving interface compatibility, shortening the electrolyte filling time, and promoting lithium ions' migration. The contact angle test was used to evaluate the wettability of these membranes. Figure 3f shows the contact angle of the electrolyte drop on the surface of the separator, and the contact angle between the electrolyte and the PP separator was 35.6°. When the electrolyte drop reached the surface of the $NiFe_2O_4$/KB separator, it immediately wet the $NiFe_2O_4$/KB separator. These results indicate that the $NiFe_2O_4$/KB coating could be beneficial to accelerate the penetration of the electrolyte, promoting the transmission of lithium ions and improving the electrochemical performance during the discharge/charge process.

3.3. Electrochemical Analysis of $NiFe_2O_4$/KB-Modified Separator

Figure 4 shows the electrochemical performance of the assembled Li-S batteries. The cyclic voltammetry (CV) curves of pristine PP separator (Figure S4a), KB modified separator (Figure S4b), and $NiFe_2O_4$/KB-modified separator batteries were taken in a voltage range of 1.5–3.0 V and a sweep rate of 0.1 mV/s. Figure 4a presents the CV curves of the first three circles of the $NiFe_2O_4$/KB-modified separator. The CV curves show two reduction peaks and a broad oxidation peak. The two reduction peaks at 2.29 V and 1.96 V are attributed to the reduction of S_8 to lithium polysulfide (Li_2S_x, $x \geq 4$) and further reduction to solid Li_2S_2 and Li_2S. The broad oxidation peak near 2.52 V was attributed to the coupling conversion of Li_2S_2/Li_2S to LiS_8/S [10,57–59]. The peak voltage in the CV curves does not change significantly, indicating that the $NiFe_2O_4$/KB-modified separator has good redox reversibility. Figure 4b shows the EIS of the $NiFe_2O_4$/KB-modified separator. The semicircular high-frequency area of the EIS diagram represents the charge transfer resistance (R_{ct}) of the electrochemical reaction at the electrode interface, and the oblique line low-frequency area presents the Warburg impedance related to the ion diffusion in the electrolyte [60–62]. The EIS diagram shows that the charge transfer resistance of the $NiFe_2O_4$/KB-modified separator (R_{ct} = 80.39 Ω) is lower than that of the PP (R_{ct} = 184.2 Ω) and KB (R_{ct} = 110.3 Ω) separators. Table S1 shows the ionic conductivity data calculated from the EIS for different separators. There was no increase in the battery's internal resistance due to the addition of the coating layer, revealing that the introduction of the coating layer increases the interface conductivity and enhances the transfer of interface charges. The $NiFe_2O_4$ on the separator provides the active site, which strongly interacts with the soluble polysulfide and greatly accelerates the kinetics of the redox reaction, which is consistent with the better rate performance of the battery [63].

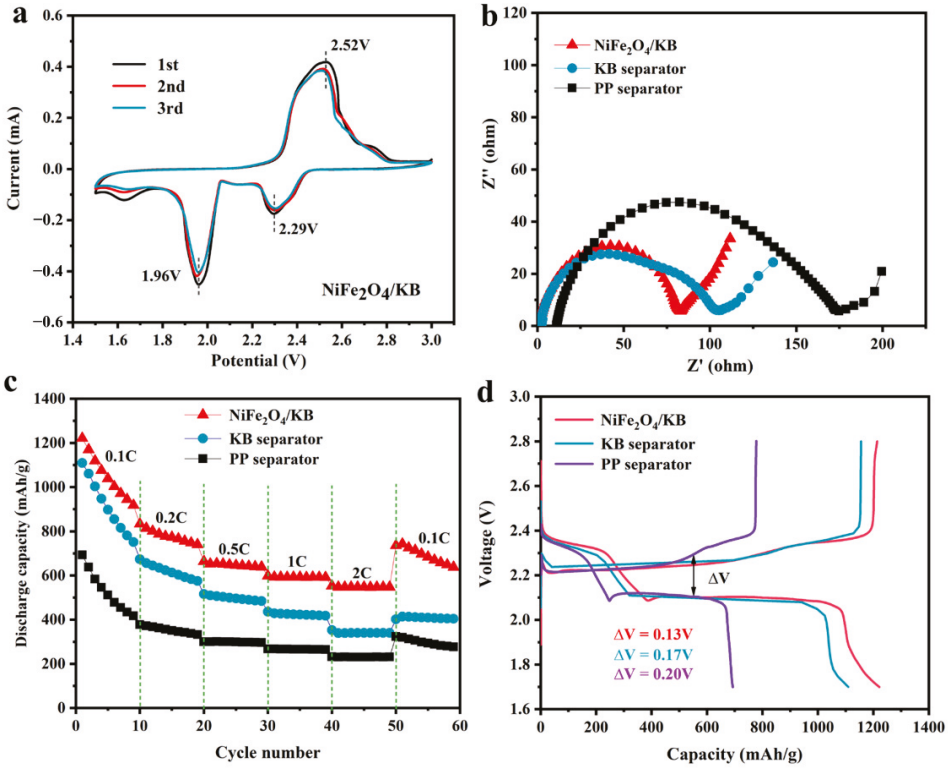

Figure 4. (**a**) The CV curves of the Li-S battery with the $NiFe_2O_4$/KB-modified separator; (**b**) the EIS of $NiFe_2O_4$/KB, KB, and the pristine PP separator; (**c**) the rate performance of the batteries with different separators between 0.1 C and 2 C; and (**d**) the charge/discharge curves of different separators at 0.1 C.

Figure 4c shows the rate performance of these batteries with different separators. It can be observed that the rate performance of the $NiFe_2O_4$/KB-modified separator assembled battery is significantly better compared to other batteries. At rates of 0.1, 0.2, 0.5, 1, and 2 C, the discharge capacities of the $NiFe_2O_4$/KB-modified separator assembled battery are 1221.4, 833.1, 663.6, 598.1, and 553.2 mAh/g, respectively. When the rate is restored to 0.1 C, the battery capacity is 735.8 mAh/g. When the KB separator is used, the capacities are 1109.7, 673.6, 516.3, 435.7, and 352.8 mAh/g, respectively. Furthermore, when the rate is restored to 0.1 C, the battery capacity is 401.5 mAh/g. The battery capacities of the pristine separator are 692.8, 377.6, 300.2, 267.2, and 232.2 mAh/g, respectively, and when the rate is restored to 0.1 C, it is 323.1 mAh/g. Figure S5 shows the charge/discharge profiles of the corresponding separators at different rates. Figure 4d shows the charge/discharge profiles of three batteries at 0.1 C, and two distinctive discharge platforms of Li-S batteries are observed. The short discharge platform at a high potential of 2.3 V corresponds to converting elemental S_8 into soluble long-chain polysulfide LiPSs, and the low potential at 2.1 V corresponds to the process of converting LiPSs into insoluble discharge end products Li_2S_2/Li_2S [64]. For the pristine PP separator, KB-modified separator, and $NiFe_2O_4$/KB-modified separator, the potential intervals between the charge and discharge platforms were 0.13, 0.17, and 0.20 mV, respectively. Compared with the PP and KB-modified separators, the $NiFe_2O_4$/KB-modified separator has the smallest potential interval, indicating that the $NiFe_2O_4$/KB-modified separator battery has better dynamic characteristics.

Figure 5 shows the cycling performance of batteries with different separators. The batteries assembled with different separators were subjected to the long-cycle tests at 0.5 C and 1 C, respectively. Figure 5a shows the cycling performance graph of batteries equipped with different separators at 0.5 C. The initial discharge capacity of the battery with the pristine separator is 802.6 mAh/g and decreases to 394.6 mAh/g after 100 cycles, and the retention rate is only 49.1%. However, when the separator is modified with a pure KB coating layer, the capacity retention rate is 52.3%, a significant improvement compared with the pristine separator (the initial capacity of this battery is 917.6 mAh/g and decays to 479.9 mAh/g after 100 cycles). It can be observed that the improvement of the stability is limiting when only carbon layer is added. However, the first capacity reaches as high as 1079.6 mAh/g and remains at 753.1 mAh/g after 100 cycles (with a capacity retention rate of 69.7%) with the $NiFe_2O_4$/KB-modified separator. It can be observed that the battery capacity retention rate of the $NiFe_2O_4$/KB-modified separator is about 1.5 times that of the pristine separator, which exhibits good cycling performance. This may be attributed to the improved conductivity due to the introducing of KB nanoparticles. Furthermore, the chemical adsorption of $NiFe_2O_4$ particles relieves the shuttle effect of polysulfides, improves the dynamic conversion rate of polysulfides, and increases the utilization rate of active materials. Moreover, the coating layer has good hydrophilicity and liquid retention to store more electrolytes and improved ion conductivity.

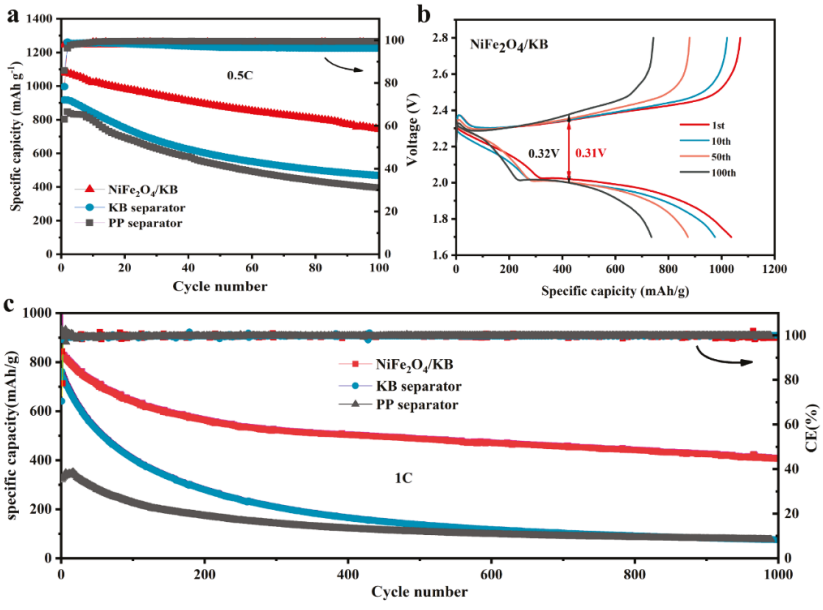

Figure 5. (**a**) The cycling performance of different separators at 0.5 C (the first two circles at 0.1 C), (**b**) the charge/discharge curves with different cycles of $NiFe_2O_4$/KB-modified separator battery at a current density of 0.5 C, and (**c**) the long-term cycling stability of separators at 1 C.

Figure 5b shows the charge/discharge curves using the $NiFe_2O_4$/KB-modified separator at a current density of 0.5 C with different cycling numbers. The average overpotential of the battery with the original PP separator increases from 0.18 V to 0.37 V (Figure S6a) after 100 cycles. In comparison, the average overpotential of the KB-modified separator battery rises from 0.20 V to 0.34 V (Figure S6b). On the other hand, the overpotential of the battery with $NiFe_2O_4$/KB-modified separator has no noticeable change, and the capacity decay rate is slower. Studies have proved that pure KB has a particular effect on the modification of the separator [26,29]. However, the effect is more evident after adding

$NiFe_2O_4$, indicating that the addition of $NiFe_2O_4$ plays a crucial role in improving the electrochemical performance of Li-S batteries.

Figure 5c shows the cycling performance graph of $NiFe_2O_4$/KB-modified separator at a high rate. The corresponding charge/discharge platform (Figure S7) shows that the $NiFe_2O_4$/KB-modified separator battery has the smallest overpotential (0.29 V) at a high rate. Furthermore, the $NiFe_2O_4$/KB-modified separator battery still has a relatively high initial discharge capacity at a high current density of 1 C. At the high current density, its decay rate is faster than that of the low density. After 100 cycles, the battery capacity decreases to 641.2 mAh/g. The battery still has a specific discharge capacity of 406.27 mAh/g after 1000 cycles, with an average capacity attenuation of only 0.051% per cycle. This stable cycling performance is better compared with previous results (Table S2). The accelerated decay rate can occur when the current density is high; the formation rate of lithium polysulfide is fast; and the output is large, that is, higher than the adsorption capacity of $NiFe_2O_4$ particles. It can be seen that compared to the battery with the $NiFe_2O_4$/KB-modified separator, the batteries with the pristine separator and the KB-coated separator have a very rapid capacity decay during the long 1000 cycles. Therefore, it can be concluded that using $NiFe_2O_4$/KB to coat the separator can significantly improve the battery's cycle life and make the battery cycle stable for a long time.

Figure 6a shows the working principle diagram of a Li-S battery with a $NiFe_2O_4$/KB-modified separator. The soluble polysulfide ions from the desulfurized cathode could form S_8, and the short-chain insoluble Li_2S_2 and Li_2S were deposited on the separator through the disproportionation reaction. Since the separator is an electronic insulator, the "dead sulfur" deposited on the separator can no longer participate in the electrochemical reaction, resulting in the decrease of the battery's energy density. Under the premise of ensuring the electronic insulation between the positive and negative electrodes, KB was introduced as a conductive layer between the separator and the cathode, and the fluffy KB particles were piled together. On the one hand, it could buffer the shuttle of polysulfide ions in the cathode and has a certain physical inhibitory effect on the migration of polysulfides, slowing down the attenuation of battery capacity. On the other hand, the KB conductive layer could be used as a "second current collector", providing a place for the electrochemical reaction of polysulfide ions. It could activate the "dead sulfur" to avoid the capacity loss caused by the deactivation of active materials.

The adsorption and catalytic effects of $NiFe_2O_4$ were the keys to achieving long-term stable cycling of Li-S batteries, which could be further verified by the polysulfide adsorption experiments (S13). It can be seen from Figure 6b that the Li_2S_6 solution became colorless after $NiFe_2O_4$ was added, while the color of the sample with KB remained nearly unchanged. This shows that $NiFe_2O_4$ has an excellent adsorption capacity for polysulfides. Further UV-Vis measurements showed that the intensity corresponding to the S_6^{2-} peak at 280 nm for the sample with KB decreases slightly [65]. On the other hand, after the addition of $NiFe_2O_4$, the absorption intensity of the S_6^{2-} peak decreases significantly, further verifying the excellent adsorption capacity of $NiFe_2O_4$ for polysulfides, which plays a key role in the long-term stable cycling of the battery.

According to density functional theory (DFT) calculations, the interactions between $NiFe_2O_4$ and polysulfides are deeply investigated, and the binding energy of Li_2S_x (x = 1, 2, 4, 6) with $NiFe_2O_4$ is calculated. Figure 6c and Figure S8a show the adsorption configuration of Li_2S_x (x = 1, 2, 4, 6) with the $NiFe_2O_4$ (1 0 0) surface in side and top view. DFT calculations show that the adsorption energy of $NiFe_2O_4$ for Li_2S_6 is −1.83 eV. In addition, calculations show that $NiFe_2O_4$ has strong adsorption for Li_2S_6, Li_2S_2, and Li_2S_4 (Figure S8b). The high binding energy between polysulfide molecules and $NiFe_2O_4$ indicates that $NiFe_2O_4$ has a strong polysulfide limiting ability, which is also consistent with the results of the polysulfide adsorption tests. $NiFe_2O_4$ could form a strong adsorption effect for polysulfides by the formation of Li-O and S-O bonds. The strong adsorption between polysulfides and $NiFe_2O_4$ could eliminate the shuttle effect of polysulfides and contribute to the excellent cycling stability. Moreover, nano- $NiFe_2O_4$ could act as a catalyst for the conversion of

polysulfides. The $NiFe_2O_4$/KB layer coating does not block the original separator's pores, and the tiny $NiFe_2O_4$ nanoparticles have a larger specific surface area to form more reaction sites. The modified separator that combines $NiFe_2O_4$ and KB, on the one hand, could use the physical adsorption and barrier of KB and the chemical adsorption capacity of nickel ferrite to block polysulfides on the side of the cathode to prevent the shuttle of polysulfides. On the other hand, $NiFe_2O_4$ can give full play to its catalytic effect on the "second current collector" formed by the KB conductive layer and improve polysulfides' conversion efficiency. The synergy significantly reduces the shuttle effect of polysulfides, which is important for reducing the corrosion loss of lithium, enhances the rate electrochemical performance; and promotes the long-term stability of the Li-S battery.

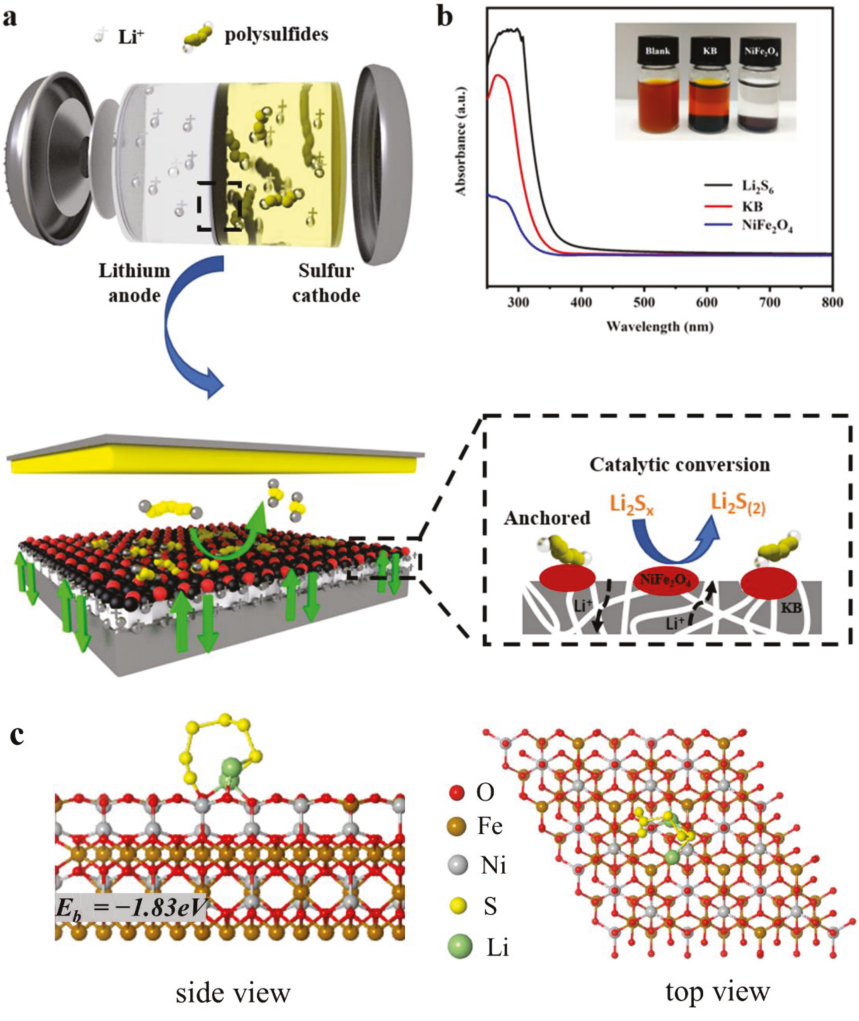

Figure 6. (**a**) The working principle of the $NiFe_2O_4$/KB-modified separator Li-S battery; (**b**) the UV-Visible spectrum of the Li_2S_6 solution containing KB and $NiFe_2O_4$ (the inset is a photo of sealed vials of Li_2S_6/DOL/DME solutions after contact with KB and $NiFe_2O_4$ 1 h later), and (**c**) the side view of and top view of the adsorption configuration of Li_2S_6 on the $NiFe_2O_4$ (1 0 0) surface.

4. Conclusions

This section is not mandatory but can be added to the manuscript if the discussion is unusually long or complex. We prepared $NiFe_2O_4$ nanoparticles by a simple hydrothermal method and improved the wettability of the separator to the electrolyte using the good hydrophilicity of $NiFe_2O_4$. $NiFe_2O_4$ used its binding force toward polysulfides and chemical adsorption to hinder the shuttle effect. In order to avoid the introduced $NiFe_2O_4$ particles hindering the lithium-ion transmission channel, porous carbon KB was introduced to resolve this situation. The introduced carbon layer could construct a porous transmission channel, improve the interface conductivity of the separator and the cathode, increase the electron conductivity, restrict the polysulfide diffusion, and improve the transfer of lithium ions without avoid increasing the internal resistance of the battery. The $NiFe_2O_4$/KB-modified separator battery could reach a capacity of 1079.6 mAh/g at 0.5 C. After 100 cycles, the capacity remained at 753.1 mAh/g, and the capacity retention rate was 69.7%. After 1000 cycles at a high rate of 1 C, the battery still had a specific discharge capacity of 406.27 mAh/g, and the average capacity attenuation per cycle was only 0.051%. The experiments have proved that using the $NiFe_2O_4$/KB-surface-coating-modified separator is a simple and effective method to improve the performance of the Li-S battery.

Supplementary Materials: The following supporting information can be downloaded at: https://www.mdpi.com/article/10.3390/nano12081347/s1, Figure S1: schematic illustration of coated $NiFe_2O_4$/KB separator; Figure S2:(a) Raman spectra of $NiFe_2O_4$ nanocomposite;(b) FT-IR spectra of $NiFe_2O_4$ nanoparticles. Figure S3: N_2 adsorption–desorption isotherms of $NiFe_2O_4$ nanoparticles; Figure S4: (a) cyclic voltammetry curves of the battery with PP separator; (b) cyclic voltammetry curves of the battery with KB separator. Figure S5: (a) charging and discharging curves of PP separator at different rates; (b) charging and discharging curves of KB separator at different rates; (c) charging and discharging curves of $NiFe_2O_4$/KB separator at different rates. Figure S6: charge/discharge voltage profiles with PP (a) and KB (b) separator at 0.5 C with different cycles. Figure S7: (a) charge/discharge voltage profiles with different separator at 1C for the first cycle; charge/discharge curves of cells with PP (b), KB (c), and $NiFe_2O_4$/KB separator (d) at 1C for different cycles. Figure S8: (a) side view of and top view of the adsorption configuration of Li_2S_x (x = 1,2,4) on the $NiFe_2O_4$ (1 0 0) surface; (b) the adsorption energy of Li_2S_x (x = 1,2,4,6) on the $NiFe_2O_4$ (1 0 0) surface. Table S1: summary of the electrochemical performance of the Li−S batteries configured with different modified separators and interlayers. References [66–83] are mentioned in Supplementary Materials.

Author Contributions: Conceptualization, L.Z. and K.P.; methodology, W.Z., L.Z. and W.J.; software, S.L.; validation, L.D., S.Z. and K.H.; formal analysis, K.H.; investigation, L.D.; resources, K.P.; data curation, W.J.; writing—original draft preparation, W.J. and K.H.; writing—review and editing, W.J.; visualization, W.J. and L.D.; supervision, L.Z. and K.P. All authors have read and agreed to the published version of the manuscript.

Funding: This research was funded by the National Natural Science Foundation of China (51574160; 21776175), the National Key Research and Development Program of China (2017YFB0102004), the Shandong Province National Natural Science Foundation (ZR2014EEM049), the Key Research and Development Program of Shandong Province (2017CSGC0502; 2017GGX40102), and the State Key Laboratory of Pressure Hydrometallurgical Technology of Associated Nonferrous Metal Resources (yy20160010).

Data Availability Statement: Data presented in this article are available on request from the corresponding author.

Acknowledgments: We thank the anonymous referee for the helpful comments and constructive remarks on this manuscript.

Conflicts of Interest: The authors declare no conflict of interest.

References

1. Goodenough, J.B. Energy Storage Materials: A Perspective. *Energy Storage Mater.* **2015**, *1*, 158–161. [CrossRef]
2. Bao, W.; Liu, L.; Wang, C.; Choi, S.; Wang, D.; Wang, G. Facile Synthesis of Crumpled Nitrogen-Doped MXene Nanosheets as a New Sulfur Host for Lithium-Sulfur Batteries. *Adv. Energy Mater.* **2018**, *8*, 1702485. [CrossRef]

3. Dunn, B.; Kamath, H.; Tarascon, J.-M. Electrical Energy Storage for the Grid: A Battery of Choices. *Science* **2011**, *334*, 928–935. [CrossRef] [PubMed]
4. Yang, Y.; Zheng, G.; Cui, Y. Nanostructured Sulfur Cathodes. *Chem. Soc. Rev.* **2013**, *42*, 3018–3032. [CrossRef] [PubMed]
5. Peng, H.-J.; Huang, J.-Q.; Cheng, X.-B.; Zhang, Q. Review on High-Loading and High-Energy Lithium-Sulfur Batteries. *Adv. Energy Mater.* **2017**, *7*, 1700260. [CrossRef]
6. Larcher, D.; Tarascon, J.M. Towards Greener and More Sustainable Batteries for Electrical Energy Storage. *Nat. Chem.* **2015**, *7*, 19–29. [CrossRef]
7. Kim, H.M.; Hwang, J.Y.; Manthiram, A.; Sun, Y.K. High-Performance Lithium-Sulfur Batteries with a Self-Assembled Multiwall Carbon Nanotube Interlayer and a Robust Electrode-Electrolyte Interface. *ACS Appl. Mater. Interfaces* **2016**, *8*, 983–987. [CrossRef] [PubMed]
8. Chung, S.H.; Han, P.; Manthiram, A. A Polysulfide-Trapping Interface for Electrochemically Stable Sulfur Cathode Development. *ACS Appl. Mater. Interfaces* **2016**, *8*, 4709–4717. [CrossRef] [PubMed]
9. Chung, S.H.; Manthiram, A. High-Performance Li-S Batteries with an Ultra-lightweight MWCNT-Coated Separator. *J. Phys. Chem. Lett.* **2014**, *5*, 1978–1983. [CrossRef]
10. Chung, S.H.; Manthiram, A. A Polyethylene Glycol-Supported Microporous Carbon Coating as a Polysulfide Trap for Utilizing Pure Sulfur Cathodes in Lithium-Sulfur Batteries. *Adv. Mater.* **2014**, *26*, 7352–7357. [CrossRef] [PubMed]
11. Xu, Q.; Hu, G.C.; Bi, H.L.; Xiang, H.F. A Trilayer Carbon Nanotube/AL_2O_3/Polypropylene Separator for Lithium-Sulfur Batteries. *Ionics* **2014**, *21*, 981–986. [CrossRef]
12. Zhang, Z.; Lai, Y.; Zhang, Z.; Zhang, K.; Li, J. Al_2O_3-Coated Porous Separator for Enhanced Electrochemical Performance of Lithium Sulfur Batter-Ies. *Electrochim. Acta* **2014**, *129*, 55–61. [CrossRef]
13. Wei, W.; Li, J.; Wang, Q.; Liu, D.; Niu, J.; Liu, P. Hierarchically Porous SnO_2 Nanoparticle-Anchored Polypyrrole Nanotubes as a High-Efficient Sulfur/Polysulfide Trap for High-Performance Lithium-Sulfur Batteries. *ACS Appl. Mater. Interfaces* **2020**, *12*, 6362–6370. [CrossRef] [PubMed]
14. Sun, W.; Ou, X.; Yue, X.; Yang, Y.; Wang, Z.; Rooney, D.; Sun, K. A Simply Effective Double-Coating Cathode with MnO_2 Nanosheets/Graphene as Functionalized Interlayer for High Performance Lithium-Sulfur Batteries. *Electrochim. Acta* **2016**, *207*, 198–206. [CrossRef]
15. Wu, F.; Qian, J.; Chen, R.; Ye, Y.; Sun, Z.; Xing, Y.; Li, L. Light-Weight Functional Layer on a Separator as a Polysulfide Immobilizer to Enhance Cycling Stability for Lithium–Sulfur Batteries. *J. Mater. Chem. A* **2016**, *4*, 17033–17041. [CrossRef]
16. Zhang, Z.; Wang, G.; Lai, Y.; Li, J.; Zhang, Z.; Chen, W. Nitrogen-Doped Porous Hollow Carbon Sphere-Decorated Separators for Advanced Lithium–Sulfur Batteries. *J. Power Sources* **2015**, *300*, 157–163. [CrossRef]
17. Wu, Z.Z.; Wang, S.Y.; Wang, R.Y.; Liu, J.; Ye, S.H. Carbon Nanotubes as Effective Interlayer for High Performance Li-I_2 Batteries: Long Cycle Life and Superior Rate Performance. *J. Electrochem. Soc.* **2018**, *165*, A1156–A1159. [CrossRef]
18. Zhou, X.; Wang, P.; Zhang, Y.; Wang, L.; Zhang, L.; Zhang, L.; Xu, L.; Liu, L. Biomass Based Nitrogen-Doped Structure-Tunable Versatile Porous Carbon Materials. *J. Mater. Chem. A* **2017**, *5*, 12958–12968. [CrossRef]
19. Zhang, S.S. Heteroatom-Doped Carbons: Synthesis, Chemistry and Application in Lithium/Sulphur Batteries. *Inorg. Chem. Front.* **2015**, *2*, 1059–1069. [CrossRef]
20. Zhang, J.; Shi, Y.; Ding, Y.; Peng, L.; Zhang, W.; Yu, G. A Conductive Molecular Framework Derived Li_2S/N,P-Codoped Carbon Cathode for Advanced Lithium-Sulfur Batteries. *Adv. Energy Mater.* **2017**, *7*, 1602876. [CrossRef]
21. Ramakrishnan, P.; Baek, S.-H.; Park, Y.; Kim, J.H. Nitrogen and Sulfur Co-doped Metal Monochalcogen Encapsulated Honeycomb Like Carbon Nanostructure as a High Performance Lithium-Ion Battery Anode Material. *Carbon* **2017**, *115*, 249–260. [CrossRef]
22. Zuo, P.; Hua, J.; He, M.; Zhang, H.; Qian, Z.; Ma, Y.; Du, C.; Cheng, X.; Gao, Y.; Yin, G. Facilitating the Redox Reaction of Polysulfides by an Electrocatalytic Layer-Modified Separator for Lithium–Sulfur Batteries. *J. Mater. Chem. A* **2017**, *5*, 10936–10945. [CrossRef]
23. Balach, J.; Jaumann, T.; Muhlenhoff, S.; Eckert, J.; Giebeler, L. Enhanced Polysulphide Redox Reaction Using a RuO_2 Nanoparticle-Decorated Mesoporous Carbon as Functional Separator Coating for Advanced Lithium-Sulphur Batteries. *Chem. Commun.* **2016**, *52*, 8134–8137. [CrossRef] [PubMed]
24. Ren, Y.X.; Zhao, T.S.; Liu, M.; Zeng, Y.K.; Jiang, H.R. A Self-Cleaning Li-S Battery Enabled by a Bifunctional Redox Mediator. *J. Power Sources* **2017**, *361*, 203–210. [CrossRef]
25. Tashima, D.; Kishita, T.; Maeno, S.; Nagasawa, Y. Mesoporous Graphitized Ketjenblack as Conductive Nanofiller for Supercapacitors. *Mater. Lett.* **2013**, *110*, 105–107. [CrossRef]
26. Tang, H.; Yao, S.; Shen, X.; Xi, X.; Xiao, K. Lithium-Sulfur Batteries with High Rate and Cycle Performance by using Multilayered Separators Coated with Ketjen Black. *Energy Technol.* **2017**, *5*, 623–628. [CrossRef]
27. Rana, M.; Li, M.; Huang, X.; Luo, B.; Gentle, I.; Knibbe, R. Recent Advances in Separators to Mitigate Technical Challenges Associated with Re-Chargeable Lithium Sulfur Batteries. *J. Mater. Chem. A* **2019**, *7*, 6596–6615. [CrossRef]
28. Park, C.K.; Park, S.B.; Lee, S.Y.; Lee, H.; Jang, H.; Cho, W.I. Electrochemical Performances of Lithium-air Cell with Carbon Materials. *Bull. Korean Chem. Soc.* **2010**, *31*, 3221–3224. [CrossRef]
29. Zhao, D.; Qian, X.; Jin, L.; Yang, X.; Wang, S.; Shen, X.; Yao, S.; Rao, D.; Zhou, Y.; Xi, X. Separator Modified by Ketjen Black for Enhanced Electrochemical Performance of Lithium–Sulfur Batteries. *RSC Adv.* **2016**, *6*, 13680–13685. [CrossRef]

30. Chen, X.; Huang, Y.; Zhang, K.; Feng, X.; Li, S. Self-Assembled Flower-like $NiFe_2O_4$ Decorated on 2D Graphene Nanosheets Composite and Their Excellent Electrochemical Performance as Anode Materials for LIBs. *J. Alloy. Compd.* **2016**, *686*, 905–913. [CrossRef]
31. Cherian, C.T.; Sundaramurthy, J.; Reddy, M.V.; Suresh Kumar, P.; Mani, K.; Pliszka, D.; Sow, C.H.; Ramakrishna, S.; Chowdari, B.V. Morphologically Robust $NiFe_2O_4$ Nanofibers as High Capacity LI-Ion Battery Anode Material. *ACS Appl. Mater. Interfaces* **2013**, *5*, 9957–9963. [CrossRef] [PubMed]
32. Kumar, P.R.; Mitra, S. Nickel Ferrite as a Stable, High Capacity and High Rate Anode for Li-Ion Battery Applications. *RSC Adv.* **2013**, *3*, 25058–25064. [CrossRef]
33. Li, C.; Wang, X.; Li, S.; Li, Q.; Xu, J.; Liu, X.; Liu, C.; Xu, Y.; Liu, J.; Li, H.; et al. Optimization of $NiFe_2O_4$/rGO Composite Electrode for Lithium-Ion Batteries. *Appl. Surf. Sci.* **2017**, *416*, 308–317. [CrossRef]
34. Qin, G.; Wu, X.; Wen, J.; Li, J.; Zeng, M. A Core-Shell $NiFe_2O_4$@SiO_2 Structure as a High-Performance Anode Material for Lithium-Ion Batteries. *Chem. Electro. Chem.* **2019**, *6*, 911–916.
35. Qu, L.; Hou, X.; Huang, X.; Liang, Q.; Ru, Q.; Wu, B.; Lam, K.-H. Self-Assembled Porous $NiFe_2O_4$ Floral Microspheres Inlaid on Ultrathin Flake Graphite as Anode Materials for Lithium Ion Batteries. *ChemElectroChem* **2017**, *4*, 3148–3155.
36. Yu, H.; Fan, H.; Yadian, B.; Tan, H.; Liu, W.; Hng, H.H.; Huang, Y.; Yan, Q. General Approach for MOF-Derived Porous Spinel AFe_2O_4 Hollow Structures and Their Superior Lithium Storage Properties. *ACS Appl. Mater. Interfaces* **2015**, *7*, 26751–26757. [CrossRef] [PubMed]
37. Yue, H.; Ren, C.; Wang, G.; Li, G.; Jin, R. Oxygen-Vacancy-Abundant Ferrites on N-Doped Carbon Nanosheets as High-Performance Li-Ion Battery Anodes. *Chemistry* **2020**, *26*, 10575–10584. [CrossRef]
38. Fan, Q.; Liu, W.; Weng, Z.; Sun, Y.; Wang, H. Ternary Hybrid Material for High-Performance Lithium-Sulfur Battery. *J. Am. Chem. Soc.* **2015**, *137*, 12946–12953. [CrossRef]
39. Zhang, Z.; Wu, D.-H.; Zhou, Z.; Li, G.-R.; Liu, S.; Gao, X.-P. Sulfur/Nickel Ferrite Composite as Cathode with High-Volumetric-Capacity for Lithium-Sulfur Battery. *Sci. China Mater.* **2018**, *62*, 74–86. [CrossRef]
40. Wei, K.; Zhao, Y.; Cui, Y.; Wang, J.; Cui, Y.; Zhu, R.; Zhuang, Q.; Xue, M. Lithium Phosphorous Oxynitride (LiPON) Coated $NiFe_2O_4$ Anode Material with Enhanced Electrochemical Performance for Lithium Ion Batteries. *J. Alloy. Compd.* **2018**, *769*, 110–119. [CrossRef]
41. Zhang, Z.; Basu, S.; Zhu, P.; Zhang, H.; Shao, A.; Koratkar, N.; Yang, Z. Highly Sulfiphilic Ni-Fe Bimetallic Oxide Nanoparticles Anchored on Carbon Nanotubes Enable Effective Immobilization and Conversion of Polysulfides for Stable Lithium-Sulfur Batteries. *Carbon* **2019**, *142*, 32–39. [CrossRef]
42. Wang, H.; Zhang, N.; Li, Y.; Zhang, P.; Chen, Z.; Zhang, C.; Qiao, X.; Dai, Y.; Wang, Q.; Liu, S. Unique Flexible $NiFe_2O_4$@S/rGO-CNT Electrode via the Synergistic Adsorption/Electrocatalysis Effect toward High-Performance Lithium-Sulfur Batteries. *J. Phys. Chem. Lett.* **2019**, *10*, 6518–6524. [CrossRef] [PubMed]
43. Jin, L.; Fu, Z.; Qian, X.; Huang, B.; Li, F.; Wang, Y.; Shen, X. Catalytic Co-N-C Hollow Nanocages as Separator Coating Layer for Lithium Sulfur Batterys. *Microporous Mesoporous Mater.* **2021**, *316*, 110927. [CrossRef]
44. Ramasubramanian, B.; Reddy, M.V.; Zaghib, K.; Armand, M.; Ramakrishna, S. Growth Mechanism of Micro/Nano Metal Dendrites and Cumulative Strategies for Countering Its Impacts in Metal Ion Batteries: A Review. *Nanomaterials* **2021**, *11*, 2476. [CrossRef]
45. Xue, W.; Shi, Z.; Suo, L.; Wang, C.; Wang, Z.; Wang, H.; So, K.P.; Maurano, A.; Yu, D.; Chen, Y.; et al. Intercalation-Conversion Hybrid Cathodes Enabling Li–S Full-Cell Architectures with Jointly Superior Gravimetric and Volumetric Energy Densities. *Nat. Energy* **2019**, *4*, 374–382. [CrossRef]
46. Yao, W.; Zheng, W.; Xu, J.; Tian, C.; Han, K.; Sun, W.; Xiao, S. ZnS-SnS@NC Heterostructure as Robust Lithiophilicity and Sulfiphilicity Mediator toward High-Rate and Long-Life Lithium-Sulfur Batteries. *ACS Nano.* **2021**, *15*, 7114–7130. [CrossRef]
47. Kresse, G.; Furthmüller, J. Efficient Iterative Schemes for Ab Initio Total-Energy Calculations Using a Plane-Wave Basis Set. *Phys. Rev. B* **1996**, *54*, 11169–11186. [CrossRef]
48. Kresse, G.; Furthmüller, J. Efficiency of Ab-Initio Total Energy Calculations for Metals and Semiconductors Using a Plane-Wave Basis Set. *Comput. Mater. Sci.* **1996**, *6*, 15–50. [CrossRef]
49. Kresse, G.; Joubert, D. From Ultrasoft Pseudopotentials to the Projector Augmented-Wave Method. *Phys. Rev. B* **1999**, *59*, 1758–1775. [CrossRef]
50. Perdew, J.P.; Burke, K.; Ernzerhof, M. Generalized Gradient Approximation Made Simple. *Phys. Rev. Lett.* **1996**, *77*, 3865–3868. [CrossRef]
51. Zhou, D.; Permien, S.; Rana, J.; Krengel, M.; Sun, F.; Schumacher, G.; Bensch, W.; Banhart, J. MNFO Investigation of Electronic and Local Structural Changes during Lithium Uptake and Release of Nano-Crystalline $NiFe_2O_4$ by X-ray Absorption Spectroscopy. *J. Power Sources* **2017**, *342*, 56–63. [CrossRef]
52. Lima, D.R.; Jiang, N.; Liu, X.; Wang, J.; Vulcani, V.A.S.; Martins, A.; Machado, D.S.; Landers, R.; Camargo, P.H.C.; Pancotti, A. Employing Calcination as a Facile Strategy to Reduce the Cytotoxicity in $CoFe_2O_4$ and $NiFe_2O_4$ Nanoparticles. *ACS Appl. Mater. Interfaces* **2017**, *9*, 39830–39838. [CrossRef] [PubMed]
53. Duraia, E.-S.M.; Adebiyi, B.M.; Beall, G.W. An Approach to Nickel Ferrite Synthesis. *J. Mater. Sci. Mater. Electron.* **2019**, *30*, 8286–8290. [CrossRef]

54. Athika, M.; Devi, V.S.; Elumalai, P. Cauliflower-Like Hierarchical Porous Nickel/Nickel Ferrite/Carbon Composite as Superior Bifunctional Catalyst for Lithium-Air Battery. *ChemistrySelect* **2020**, *5*, 3529–3538. [CrossRef]
55. Salah, L.M. Spectroscopic Studies of the Effect of Addition of Y3+on Structural Characteristics of Ni-Zn Ferrites. *Phys. Status Solidi* **2006**, *203*, 271–281. [CrossRef]
56. Soam, A.; Kumar, R.; Sahoo, P.K.; Mahender, C.; Kumar, B.; Arya, N.; Singh, M.; Parida, S.; Dusane, R.O. Synthesis of Nickel Ferrite Nanoparticles Supported on Graphene Nanosheets as Composite Electrodes for High Performance Supercapacitor. *ChemistrySelect* **2019**, *4*, 9952–9958. [CrossRef]
57. Xiao, Z.; Yang, Z.; Wang, L.; Nie, H.; Zhong, M.; Lai, Q.; Xu, X.; Zhang, L.; Huang, S. A Lightweight TiO_2/Graphene Interlayer, Applied as a Highly Effective Polysulfide Absorbent for Fast, Long-Life Lithium-Sulfur Batteries. *Adv. Mater.* **2015**, *27*, 2891–2898. [CrossRef]
58. Seh, Z.W.; Sun, Y.; Zhang, Q.; Cui, Y. Designing High-Energy Lithium-Sulfur Batteries. *Chem. Soc. Rev.* **2016**, *45*, 5605–5634. [CrossRef]
59. Park, G.D.; Lee, J.; Piao, Y.; Kang, Y.C. Mesoporous Graphitic Carbon-TiO_2 Composite Microspheres Produced by a Pilot-Scale Spray-Drying Process as an Efficient Sulfur Host Material for Li-S Batteries. *Chem. Eng. J.* **2018**, *335*, 600–611. [CrossRef]
60. Zeng, P.; Huang, L.; Zhang, X.; Zhang, R.; Wu, L.; Chen, Y. Long-Life and High-Areal-Capacity Lithium-Sulfur Batteries Realized by a Honeycomb-like N, P Dual-Doped Carbon Modified Separator. *Chem. Eng. J.* **2018**, *349*, 327–337. [CrossRef]
61. Ghazi, Z.A.; He, X.; Khattak, A.M.; Khan, N.A.; Liang, B.; Iqbal, A.; Wang, J.; Sin, H.; Li, L.; Tang, Z. MoS_2 /Celgard Separator as Efficient Polysulfide Barrier for Long-Life Lithium-Sulfur Batteries. *Adv. Mater.* **2017**, *29*, 1606817. [CrossRef] [PubMed]
62. Lee, J.Y.; Park, G.D.; Choi, J.H.; Kang, Y.C. Structural Combination of Polar Hollow Microspheres and Hierarchical N-Doped Carbon Nanotubes for High-Performance Li-S Batteries. *Nanoscale* **2020**, *12*, 2142–2153. [CrossRef] [PubMed]
63. Wang, Y.; Guo, X.; Chen, C.; Wang, Y.; Li, Q.; Wu, Z.; Zhong, B.; Chen, Y. Alleviating the Shuttle Effect via Bifunctional $MnFe_2O_4$/AB Modified Separator for High Performance Lithium Sulfur Battery. *Electrochim. Acta* **2020**, *354*, 136704. [CrossRef]
64. Zhang, S. Improved Cyclability of Liquid Electrolyte Lithium/Sulfur Batteries by Optimizing Electrolyte/Sulfur Ratio. *Energies* **2012**, *5*, 5190–5197. [CrossRef]
65. Li, C.; Zhao, Y.; Zhang, Y.; Luo, D.; Liu, J.; Wang, T.; Gao, W.; Li, H.; Wang, X. A New Defect-Rich and Ultrathin ZnCo Layered Double Hydroxide/Carbon Nanotubes Architecture to Facilitate Catalytic Conversion of Polysulfides for High-Performance Li-S Batteries. *Chem. Eng. J.* **2021**, *417*, 129248. [CrossRef]
66. Gu, X.; Tong, C.-J.; Lai, C.; Qiu, J.; Huang, X.; Yang, W.; Wen, B.; Liu, L.-M.; Hou, Y.; Zhang, S. A porous nitrogen and phosphorous dual doped graphene blocking layer for high performance Li–S batteries. *J. Mater. Chem. A* **2015**, *3*, 16670–16678. [CrossRef]
67. Raja, M.; Suriyakumar, S.; Angulakshmi, N.; Manuel Stephan, A. High performance multi-functional trilayer membranes as permselective separators for lithium–sulfur batteries. *Inorg. Chem. Front.* **2017**, *4*, 1013–1021. [CrossRef]
68. Yang, L.; Li, G.; Jiang, X.; Zhang, T.; Lin, H.; Lee, J.Y. Balancing the chemisorption and charge transport properties of the interlayer in lithium–sulfur batteries. *J. Mater. Chem. A* **2017**, *5*, 12506–12512. [CrossRef]
69. Li, H.; Sun, L.; Zhao, Y.; Tan, T.; Zhang, Y. A novel CuS/graphene-coated separator for suppressing the shuttle effect of lithium/sulfur batteries. *Appl. Surf. Sci.* **2019**, *466*, 309–319. [CrossRef]
70. Shan, L.; Yurong, C.; Jing, Y.; Feixia, R.; Jun, W.; Babu, S.; Xin, Y.; Junkuo, G.; Juming, Y. Entrapment of polysulfides by a Ketjen Black & mesoporous TiO_2 modified glass fiber separator for high performance lithium-sulfur batteries. *J. Alloy. Compd.* **2019**, *779*, 412–419.
71. Zhu, F.; Liu, J.; Zhao, H.; Li, J.; Li, Q.; Xi, Y.; Liu, M.; Wang, C. Preparation and Performance of Porous Polyetherimide/Al2O3 Separator for Enhanced Lithium-Sulfur Batteries. *ChemElectroChem* **2019**, *6*, 2883–2890. [CrossRef]
72. Liu, Y.; Qin, X.; Zhang, S.; Liang, G.; Kang, F.; Chen, G.; Li, B. Fe_3O_4-Decorated Porous Graphene Interlayer for High-Performance Lithium-Sulfur Batteries. *ACS Appl. Mater. Interfaces* **2018**, *10*, 26264–26273. [CrossRef]
73. Li, Q.; Liu, M.; Qin, X.; Wu, J.; Han, W.; Liang, G.; Zhou, D.; He, Y.-B.; Li, B.; Kang, F. Cyclized-polyacrylonitrile modified carbon nanofiber interlayers enabling strong trapping of polysulfides in lithium–sulfur batteries. *J. Mater. Chem. A* **2016**, *4*, 12973–12980. [CrossRef]
74. Fan, C.-Y.; Liu, S.-Y.; Li, H.-H.; Shi, Y.-H.; Wang, H.-C.; Wang, H.-F.; Sun, H.-Z.; Wu, X.-L.; Zhang, J.-P. Synergistic mediation of sulfur conversion in lithium–sulfur batteries by a Gerber tree-like interlayer with multiple components. *J. Mater. Chem. A* **2017**, *5*, 11255–11262. [CrossRef]
75. Lai, Y.; Wang, P.; Qin, F.; Xu, M.; Li, J.; Zhang, K.; Zhang, Z. A carbon nanofiber@mesoporous δ-MnO_2 nanosheet-coated separator for high-performance lithium-sulfur batteries. *Energy Storage Mater.* **2017**, *9*, 179–187. [CrossRef]
76. Bizuneh, G.G.; Fan, J.; Sun, C.; Xiangfei, Y.; Xue, F.; Deng, D.; Lei, J.; Lin, X.; Jia, Y.; Yang, J.; et al. $LaLiO_2$-Based Multi-Functional Interlayer for Enhanced Performance of Li-S Batteries. *J. Electrochem. Soc.* **2019**, *166*, A68–A73. [CrossRef]
77. Ali, S.; Waqas, M.; Jing, X.; Chen, N.; Chen, D.; Xiong, J.; He, W. Carbon-Tungsten Disulfide Composite Bilayer Separator for High-Performance Lithium-Sulfur Batteries. *ACS Appl. Mater. Interfaces* **2018**, *10*, 39417–39421. [CrossRef]
78. Yang, Y.; Wang, S.; Zhang, L.; Deng, Y.; Xu, H.; Qin, X.; Chen, G. CoS-interposed and Ketjen black-embedded carbon nanofiber framework as a separator modulation for high performance Li-S batteries. *Chem. Eng. J.* **2019**, *369*, 77–86. [CrossRef]
79. Tan, L.; Li, X.; Wang, Z.; Guo, H.; Wang, J. Lightweight Reduced Graphene Oxide@MoS_2 Interlayer as Polysulfide Barrier for High-Performance Lithium-Sulfur Batteries. *ACS Appl. Mater. Interfaces* **2018**, *10*, 3707–3713. [CrossRef]

80. Chung, S.-H.; Han, P.; Singhal, R.; Kalra, V.; Manthiram, A. Electrochemically Stable Rechargeable Lithium-Sulfur Batteries with a Microporous Carbon Nanofiber Filter for Polysulfide. *Adv. Energy Mater.* **2015**, *5*, 1500738. [CrossRef]
81. Yin, F.; Ren, J.; Zhang, Y.; Tan, T.; Chen, Z. A PPy/ZnO functional interlayer to enhance electrochemical performance of lithium/sulfur batteries. *Nanoscale Res. Lett.* **2018**, *13*, 307. [CrossRef] [PubMed]
82. An, D.; Shen, L.; Lei, D.; Wang, L.; Ye, H.; Li, B.; Kang, F.; He, Y.-B. An ultrathin and continuous $Li_4Ti_5O_{12}$ coated carbon nanofiber interlayer for high rate lithium sulfur battery. *J. Energy Chem.* **2019**, *31*, 19–26. [CrossRef]
83. Shi, N.; Xi, B.; Feng, Z.; Wu, F.; Wei, D.; Liu, J.; Xiong, S. Insight into different-microstructured ZnO/graphene-functionalized separators affecting the performance of lithium–sulfur batteries. *J. Mater. Chem. A* **2019**, *7*, 4009–4018. [CrossRef]

nanomaterials

MDPI

Article

Improving the Stability of Lithium Aluminum Germanium Phosphate with Lithium Metal by Interface Engineering

Yue Zhang [1], Hanshuo Liu [2,*], Zhong Xie [2], Wei Qu [2] and Jian Liu [1,*]

[1] School of Engineering, Faculty of Applied Science, University of British Columbia, 3333 University Way, Kelowna, BC V1V 1V7, Canada; yue.zhang@ubc.ca
[2] Energy, Mining and Environment Research Center, National Research Council Canada, 4250 Wesbrook Mall, Vancouver, BC V6T 1W5, Canada; zhong.xie@nrc-cnrc.gc.ca (Z.X.); wei.qu@nrc-cnrc.gc.ca (W.Q.)
* Correspondence: hanshuo.liu@nrc-cnrc.gc.ca (H.L.); jian.liu@ubc.ca (J.L.)

Abstract: Lithium aluminum germanium phosphate (LAGP) solid electrolyte is receiving increasing attention due to its high ionic conductivity and low air sensitivity. However, the poor interface compatibility between lithium (Li) metal and LAGP remains the main challenge in developing all-solid-state lithium batteries (ASSLB) with a long cycle life. Herein, this work introduces a thin aluminum oxide (Al_2O_3) film on the surface of the LAGP pellet as a physical barrier to Li/LAGP interface by the atomic layer deposition technique. It is found that this layer induces the formation of stable solid electrolyte interphase, which significantly improves the structural and electrochemical stability of LAGP toward metallic Li. As a result, the optimized symmetrical cell exhibits a long lifetime of 360 h with an areal capacity of 0.2 mAh cm^{-2} and a current density of 0.2 mA cm^{-2}. This strategy provides new insights into the stabilization of the solid electrolyte/Li interface to boost the development of ASSLB.

Keywords: lithium aluminum germanium phosphate; lithium metal anode; interface modification; atomic layer deposition

Citation: Zhang, Y.; Liu, H.; Xie, Z.; Qu, W.; Liu, J. Improving the Stability of Lithium Aluminum Germanium Phosphate with Lithium Metal by Interface Engineering. *Nanomaterials* **2022**, *12*, 1912. https://doi.org/10.3390/nano12111912

Academic Editors: Marc Cretin, Sophie Tingry and Zhenghua Tang

Received: 7 May 2022
Accepted: 30 May 2022
Published: 3 June 2022

Publisher's Note: MDPI stays neutral with regard to jurisdictional claims in published maps and institutional affiliations.

1. Introduction

Lithium metal is a promising anode candidate for constructing high-energy-density lithium batteries due to its high specific capacity (3860 mAh g^{-1}) and low redox potential (−3.05 V vs. standard hydrogen electrode) [1,2]. Currently, its development is plagued by the intrinsic safety issues of liquid electrolytes because of the flammability of organic solvents used [3,4]. Replacing organic liquid electrolytes with non-flammable and highly conductive solid electrolytes (SEs) is an effective approach to improving battery safety [5,6]. With respect to this, there is growing research interest in the development of all-solid-state lithium-ion batteries (ASSLBs), and significant progress has been made over the past few years [7–9]. Critical characteristics of SEs include high lithium-ion conductivity, excellent chemical stability, and good mechanical properties [10]. Various SEs have been well developed, such as polymer-based SEs, garnet-type $Li_7La_3Zr_2O_{12}$ [11], sulfide [12], and NASICON-type $LiM_2(PO_4)_3$ (M = Ti, Ge, Hf, Zr, Sn) [13], as well as composite SEs [14–16]. Aluminum (Al) -doped NASICON-type $Li_{1+x}Al_xGe_{2-x}(PO_4)_3$ (LAGP) oxides have received tremendous attention due to their high chemical and electrochemical stability in the air, high ionic conductivity (>10^{-4} S cm^{-1}), and good mechanical strength [10]. The fast Li-ion conduction in the LAGP system benefits from the main Li-ion diffusion pathway along 36*f* and M_2 interstitial sites resulting from Al^{3+} to Ge^{4+} substitution [17]. LAGP SEs have been synthesized by various routes, from melt-quenching [18], sintering [19], sol-gel [20], to hot-press [21], etc. Controlling key parameters such as crystallization and sintering temperature or pressure is critical in tailoring desirable highly-conductive LAGP pellets [21–23].

Li/LAGP interfacial incompatibility remains the main challenge for the further development of ASSLBs. Due to the high Fermi energy level of Li metal, germanium (Ge) in

LAGP would be irreversibly degraded upon being contacted with Li metal at the Li/LAGP interface, resulting in an increased impedance versus time [24]. When an electrical current is applied to the Li metal anode, part of Li ions can be reduced at the LAGP side, leading to a local volume expansion which triggers cracks in the LAGP SE [25]. These cracks could cause the pulverization of SEs, mechanical deterioration, or even cell failure (short circuit) [26]. Consequently, the unstable Li/LAGP interface causes inferior cell capacity and lifetime, which need to be mitigated using effective interfacial stabilization strategies.

Li et al. [27] introduced a succinonitrile-based plastic interlayer between Li metal and LAGP by in situ solidification. This interlayer isolated the direct contact between Li and LAGP and regulated uniform Li-ion distribution, which enabled a 240-h cycle life in symmetrical Li cells. Zhou et al. [28] sputtered an amorphous Ge thin film on the LAGP surface, which ensured intimate Li/LAGP contact and suppressed the unexpected Ge reduction, thus contributing to a superior symmetrical cell over 100 cycles at 0.1 mA cm^{-2}. Xiong et al. [29] created a quasi-solid-state paste interlayer composed of LAGP nanoparticles and ionic liquid, which enabled fast Li-ion conduction and improved chemical stability toward metallic Li, and suppressed thermal runaway. Sun et al. [30] adopted the atomic layer deposition (ALD) technique to coat ultrathin aluminum oxide (Al_2O_3) on the surface of $Li_{1.3}Al_{0.3}Ti_{1.7}(PO_4)_3$ (LATP), and the Li/LATP interface was significantly stabilized at 0.01 mA cm^{-2}. Currently, most Li/LAGP/Li symmetrical cells show a long cycle time at a low current density of 0.1 mA cm^{-2} [1,3,25,26,28,31–37], making it hard to meet the demand for practical applications. Improving the electrochemical stability of LAGP at higher current densities is an urgent task in the development of high-energy-density ASSLBs [38].

In this work, the effect of sintering temperature on the structure and ionic conductivity of LAGP is investigated, and 850 °C is found as the optimal sintering temperature to reach an ionic conductivity of 2.4×10^{-4} S cm^{-1} at room temperature. Furthermore, an ultrathin Al_2O_3 coating layer is deposited in the LAGP pellet surface via the ALD technique, which physically isolates the contact between Li metal and LAGP SE and enhances the electrochemical stability of LAGP toward metallic Li. The Li symmetrical cell with Al_2O_3-coated LAGP SE showed an excellent lifetime of 360 h at a current density of 0.2 mA cm^{-2} and capacity density of 0.2 mAh cm^{-2}, which is higher than most previously reported Li/LAGP/Li cells with interlayer modification.

2. Materials and Methods

2.1. Materials

LAGP powders with a stoichiometric formula of $Li_{1.5}Al_{0.5}Ge_{1.5}(PO_4)_3$ were purchased from the Shanghai Institute of Ceramics (Shanghai, China). The precursors for ALD were trimethylaluminium (TMA) and deionized water (H_2O). Lithium hexafluorophosphate ($LiPF_6$, Gotion, CAS: 21324-40-3), ethylene carbonate (EC, Gotion, CAS: 96-49-1), and diethyl carbonate (DEC, Gotion, CAS: 105-58-8) were used as received for coin cell assembly.

2.2. Preparation of LAGP Pellets

LAGP pellets were made by a conventional dry-pressing method (15T Compact Hydraulic Pellet Press, MTI Corporation, Richmond, CA, USA). To begin, 0.2 g LAGP of powder was placed into a stainless-steel die with 12 mm diameter and pressed at 200 MPa uniaxial pressure at room temperature for 2 min. The obtained pellets were then transferred into a ceramic crucible. The sintering process was conducted at 800–900 °C in the air for 6 h at a heating rate of 2° min^{-1} in a tube furnace. The thickness of the as-prepared LAGP pellets was about 0.8 mm.

2.3. Atomic Layer Deposition of Al_2O_3 on LAGP

The Al_2O_3 layer was coated on LAGP in a commercial ALD reactor (GEMStar™ XT Atomic Layer Deposition Systems, Singapore). The coating process was carried out at 100 °C by following a TMA pulse/TMA purge/H_2O pulse/H_2O purge sequence in each cycle. After 50 cycles, Al_2O_3 films were deposited on LAGP noted as LAGP@$Al_2O_3$50.

2.4. Materials Characterizations

The morphologies and microstructures of LAGP powder and pallets were observed and analyzed by scanning electron microscopy (SEM) and energy dispersive spectroscopy (EDS). X-ray diffraction (XRD) was used to analyze the crystal structure of LAGP. Surface elemental analysis was investigated by X-ray photoelectron spectroscopy (XPS).

Electrochemical impedance spectroscopy EIS measurements were carried out at 25 °C and elevated temperatures (30–60 °C). The LAGP pellets were Au-coated on both sides as electrodes and clamped for conduction. The ionic conductivity (σ) of LAGP was measured by Equation (1):

$$\sigma = \frac{L}{RA} \quad (1)$$

where L and A are the thickness and effective area of LAGP, respectively, and R is the resistance obtained by EIS) testing within a frequency range of 0.01–10^6 Hz with an AC amplitude of 5 mV.

2.5. Electrochemical Measurements

CR2032 cells were assembled in an argon-filled glovebox workstation with H_2O and O_2 less than 0.1 ppm. First, 10 µL electrolyte (1 M $LiPF_6$ in EC: DEC) were added to each Li/LAGP/Li cell. Symmetrical Li/LAGP/Li cells were tested in NEWARE battery cycler (CT-4008T-5V50mA-164, Shenzhen, China) at room temperature and 40 °C with current densities ranging from 0.02 to 0.2 mA cm^{-2} with a plating-striping time of 1 h. The cycled Li/LAGP batteries were disassembled in the argon-filled glove box and then characterized by SEM and XPS to collect surface composition information.

3. Results and Discussion

Figure 1 presents the SEM images of LAGP pellets sintered at 800, 850, and 900 °C, respectively. Most LAGP particles have small sizes of less than 1 µm, as shown in Figure S1. After being pressed and sintered at high temperatures (800–900 °C), LAGP particles were closely stacked to form a dense surface, and no pores were found in higher-magnification images, ensuring continuous Li-ion pathways to achieve high ionic conductivity. The ionic conductivity of LAGP solid electrolyte relies on the Li-ion conduction in both bulk (σ_{bulk}) and along the grain boundary (σ_{gb}). With the sintering temperature increasing, unit cell volumes would grow to form wider Li-ion migration channels, thus leading to higher bulk conductivity σ_{bulk} [23,39]. The Li-ion conduction along the grain boundary (σ_{gb}) mainly depends on grain-grain ceramics contact and density. High sintering temperatures above 850 °C would possibly induce cracks due to grain strain, decrease ceramics density, and slow down Li-ion transport at the grain boundary [23,40,41]. Consequently, LAGP sintered at 850 °C showed the highest ionic conductivity.

XRD patterns of LAGP pellets sintered at 800–900 °C are shown in Figure 2a. All the characteristic peaks of LAGP pellets match well with the LAGP powders and can be indexed as $LiGe_2(PO_4)_3$ (JCPDS PDF No. 80-1924). Figure 2b gives the Nyquist plot of LAGP pellets sintered at 800–900 °C measured in a frequency range of 0.01–1 × 10^6 Hz at room temperature. LAGP T850 possesses a smaller electrochemical impedance (283 Ω) than LAGP T800 (390 Ω) and T900 (392 Ω), thus leading to higher ionic conductivity of 2.4 × 10^{-4} S cm^{-1} (vs. 2.0 × 10^{-4} and 1.8 × 10^{-4} S cm^{-1} for T800 and T900, respectively) as illustrated in Figure 2c. Further, the relationship between impedance and temperature for LAGP T850 is plotted in Figure 2d. It could be found that the impedance markedly decreases from 260 to 92 Ω with temperature increasing from 30 to 60 °C, corresponding to the ionic conductivity from 2.6 × 10^{-4} to 7.3 × 10^{-4} S cm^{-1}. LAGP T850 will be selected as a reference for further electrochemical stability tests with Li metal due to its highest ionic conductivity.

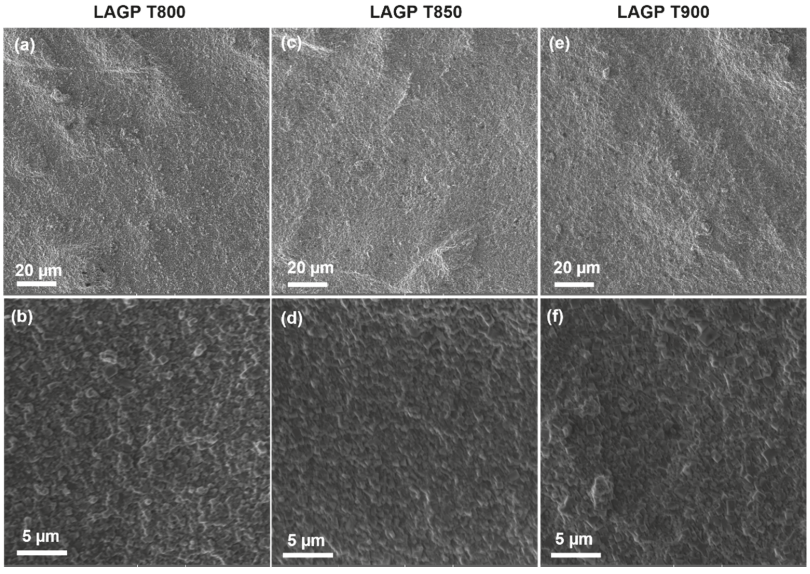

Figure 1. SEM images of LAGP pellets sintered at (**a**,**b**) 800 °C, (**c**,**d**) 850 °C, and (**e**,**f**) 900 °C.

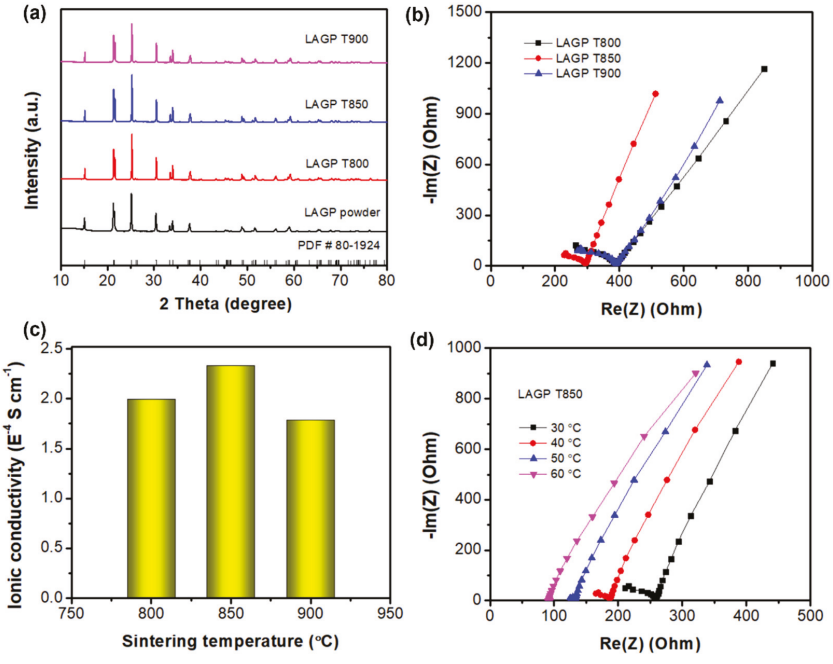

Figure 2. (**a**) XRD patterns, (**b**) Nyquist plots, (**c**) ionic conductivities of LAGP T800, LAGP T850, and LAGP T900 pellets, (**d**) Nyquist plots of LAGP T850 at 30–60 °C.

Figure S2 shows a voltage-time profile of Li/LAGP/Li symmetrical cell at room temperature. It could be found that the voltage hysteresis is gradually increasing at a low current density of 0.02 mA cm^{-2} and rapidly rises to 3 V at only 0.04 mA cm^{-2}. The

large overpotential can be attributed to the unstable Li/LAGP interface and Li dendric deposition [26]. Herein, the Al_2O_3 layer is deposited on the surface of LAGP, as illustrated in Figure 3a, which can separate LAGP from the Li metal to prevent side reactions. The thickness of the Al_2O_3 layer is controlled at 5 nm based on our previous study on the P2-$Na_{0.66}(Mn_{0.54}Co_{0.13}Ni_{0.13})O_2$ cathode [42]. Figure 3b–g displays the SEM images of LAGP and LAGP@$Al_2O_3$50 from the top view and cross-section. Both demonstrate a compact and flat surface without pores. There is no noticeable change found in the surface and cross-section morphology.

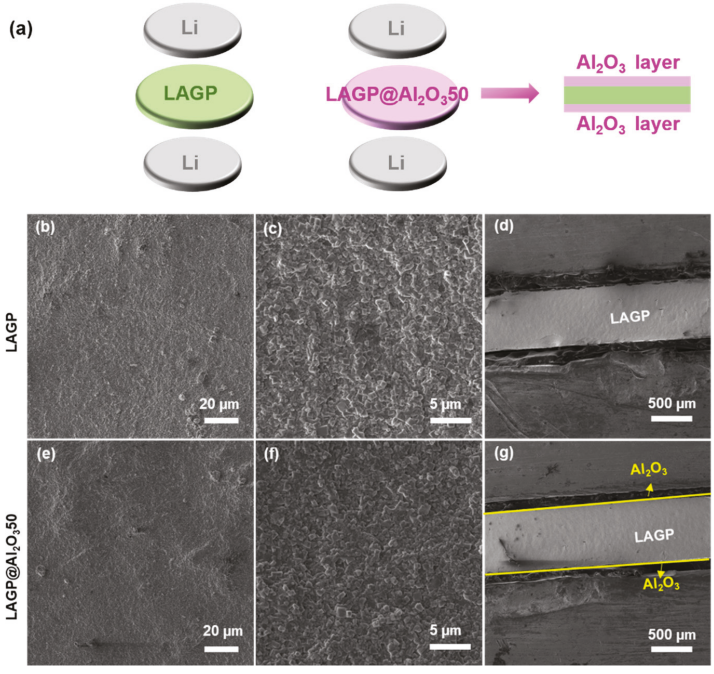

Figure 3. (**a**) Schematic illustration of Li/LAGP/Li and Li/LAGP@Al_2O_3/Li cell configurations, top-view and cross-sectional SEM images of (**b**–**d**) LAGP and (**e**–**g**) LAGP@$Al_2O_3$50.

XPS characterization was carried out to investigate the surface chemistry of LAGP with and without the Al_2O_3 layer. As shown in Figure S3 and Table S1, Ge, P, and Li elements are only detected on bare LAGP surface and absent for LAGP@$Al_2O_3$50, suggesting the successful deposition of Al_2O_3 film on the LAGP surface. The prominent peak in Li 1s XPS spectra (Figure 4a) is assigned to Li oxide of LAGP [43], while it is not detectable in LAGP@$Al_2O_3$50 (Figure 4b). Al 2p peaks can be resolved into $2p_{1/2}$ and $2p_{3/2}$ peaks corresponding to the existence of Al in LAGP and ALD-Al_2O_3 (Figure 4c,d). Similarly, P is only observed in bare LAGP (Figure 4e) and is absent for Al_2O_3-coated LAGP (Figure 4f). Therefore, it can be concluded that the thin Al_2O_3 layer by ALD is successfully deposited on the surface of LAGP without significant morphology change. The Al_2O_3 layer is expected to induce a stable interface between Li and LAGP, suppress side reactions, and enhance the electrochemical stability of LAGP toward metallic Li.

Figure 5a shows voltage profiles of symmetrical Li cells with bare and Al_2O_3-coated LAGP SEs at 0.02–0.2 mA cm^{-2} at 40 °C. Li/LAGP/Li cell has a lower overpotential at the initial current density of 0.02 mA cm^{-2}, which becomes larger with the increase in current density and finally fails at 0.12 mA cm^{-2}. In comparison, the Li/LAGP@$Al_2O_3$50/Li cell exhibits a stable voltage hysteresis after initial cycles and undergoes a repeated Li

plating/stripping process at a much higher current density of 0.2 mA cm^{-2}. The steady voltage profiles of LAGP@$Al_2O_3$50 (Figure 5b,c) indicate the formation of a stable solid electrolyte interphase (SEI) between Li and LAGP. Long-term cycling performance is evaluated for the Li/LAGP@$Al_2O_3$50/Li cell, which exhibits a long lifetime of 320 h at the areal capacity of 0.2 mAh cm^{-2} and current density of 0.2 mA cm^{-2} (Figure 5d). The voltage hysteresis is mostly stabilized at 0.3 V until 250 h and then shows a slight increase, as illustrated in Figure 5e. It should be noted that the rate test is performed following the cycling test from the same Li/LAGP@$Al_2O_3$50/Li cell. Consequently, this cell has a 360-h Li plating/stripping duration at 0.2 mAh cm^{-2}.

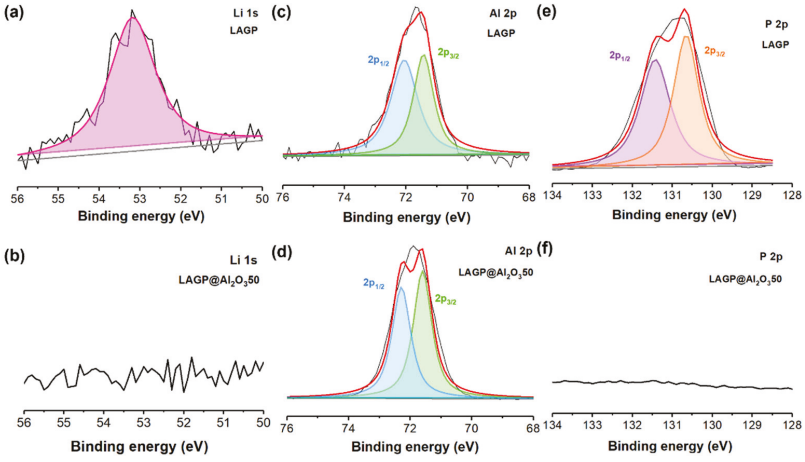

Figure 4. XPS spectra of (**a**,**b**) Li 1s, (**c**,**d**) Al 2p, and (**e**,**f**) P 2p of LAGP and LAGP@$Al_2O_3$50.

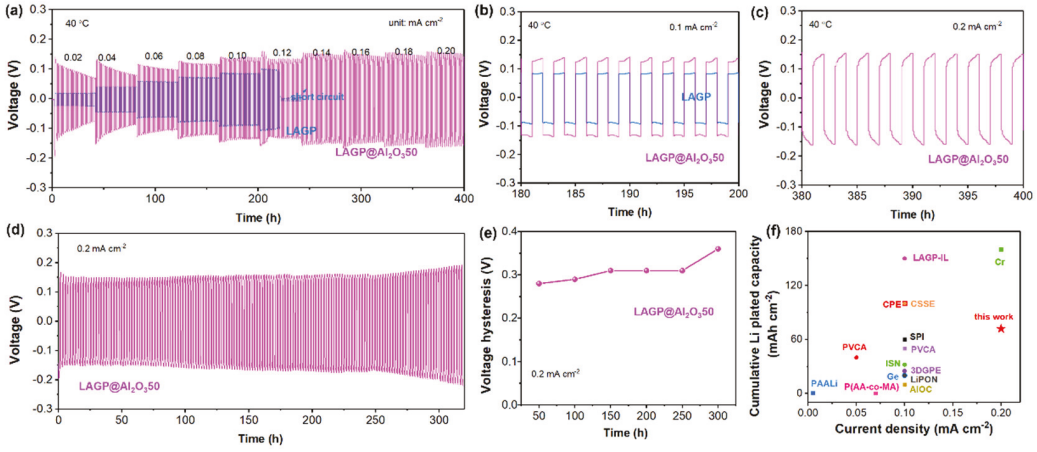

Figure 5. (**a**) Rate performance of symmetrical Li cells with bare and Al_2O_3-coated LAGPs as SEs at 0.02–0.2 mA cm^{-2} at 40 °C, voltage profiles at (**b**) 0.1 and (**c**) 0.2 mA cm^{-2}, (**d**) long-term cycling performance of the Li/LAGP@$Al_2O_3$50/Li cell at 0.2 mA cm^{-2} (areal capacity: 0.2 mAh cm^{-2}) and (**e**) corresponding voltage hysteresis, (**f**) comparison of cumulative Li plated capacity from this work and literatures.

Moreover, Table 1 and Figure 5f compare cumulative Li plated capacity of previous Li/LAGP/Li cells and this work in the cycling test. It can be seen that most of the previous studies proposed polymer interlayer to modify Li/LAGP interface and assessed the cycling performance at 0.1 mA cm^{-2}, which demonstrated smaller cumulative Li plated capacity below 60 mAh cm^{-2}. Although the Li/Cr-LAGP-Cr/Li [3] cell showed a high Li plated capacity of 160 mAh cm^{-2}, the overpotential is as large as 1.2 V upon Li plating/stripping behaviors. In comparison, this work employs an inorganic Al_2O_3 layer to stabilize Li/LAGP interface, and the cell possesses a much smaller overpotential of 0.3 V at 0.2 mA cm^{-2}.

Table 1. Comparison of Li/LAGP/Li cells with interface modification.

Cell Configuration	Interface Modification Layer	Cycling Performance	Cumulative Li Plated Capacity ($mAh\ cm^{-2}$)	References
Li/PP-LAGP-PP/Li *	PP	500s @0.25 mA	-	[31]
Li/SPI-LAGP-SPI/Li *	SPI, by in situ solidification, 10 μm	600 h @0.1 mA cm^{-2}	60	[1]
PAALi/LAGP/PAALi *	PAALi + LAGP	100 h @0.005 mA cm^{-2}	0.5	[32]
Li/P(AA-co-MA)-LAGP-P(AA-co-MA)/Li	P(AA-co-MA), by spray-coating, 1.5 μm	20,000 s @0.07 mA cm^{-2}	0.39	[25]
Li/PVCA-LAGP-PVCA/Li *	LiTFSI/PVCA,	500 h @0.1 mA cm^{-2}	50	[33]
Li/AIOC-LAGP-AIOC/Li	AIOC, by spin coating, 11 μm	100 h @0.1 mA cm^{-2}	10	[34]
Li/CPE-LAGP-CPE/Li	CPE, by spin coating	1000 h @0.1 mA cm^{-2}	100	[36]
Li/lSN-LAGP-lSN/Li *	SN + LLZAO + FEC + LiTFSI, by in situ solidification	320 h @0.1 mA cm^{-2}	32	[27]
Li/Ge-LAGP-Ge/Li	Ge, by puttering, 60 nm	200 h @0.1 mA cm^{-2}	20	[28]
Li/Cr-LAGP-Cr/Li	Cr, by sputtering, 30 nm	800 h @0.2 mA cm^{-2}	160 (overpotential: 1.2 V)	[3]
Li/LAGP-IL-LAGP-LAGP-IL/Li	LAGP-IL	1500 h @0.1 mA cm^{-2}	150	[29]
Li/3DGPE-LAGP-3DGPE/Li *	PVDF-HFP + PEGDE + DPPO, 100 μm	250 h @0.1 mA cm^{-2}	25	[44]
Li/CSSE-LAGP-CSSE/Li	PVC + TPU + LiTFSI, 50 μm	1000 h @0.1 mA cm^{-2}	100	[45]
Li/PVCA-LAGP-PVCA/Li	PVCA + FEC	800 h @0.05 mA cm^{-2}	40	[37]
Li/LiPON-LAGP-LiPON/Li	LiPON, by sputtering, 3 μm	200 h @0.1 mA cm^{-2}	20	[26]
Li/Al_2O_3-LAGP- Al_2O_3/Li *	Al_2O_3, by ALD, 5 nm	360 h @0.2 mA cm^{-2}	72 (overpotential: 0.3 V)	This work

*: 10 μL liquid electrolyte was used, or the interlayer was immersed in liquid electrolyte.

To reveal the internal structural change after repeated cycles, the cycled Li/LAGP/Li and Li/LAGP@$Al_2O_3$50/Li were disassembled for further analysis. Figure 6 shows the SEM images and digital photos of cycled LAGP and LAGP@$Al_2O_3$50. Abundant pores and cracks are observed in cycled-bare LAGP at different magnifications, and the cycled LAGP surface turns yellow, implying possible Ge^{4+} reduction after being in contact with Li metal [25]. The pores and cracks may originate from continuous Li dendrite deposition at the unstable Li/LAGP interface and ultimately cause a short circuit failure [25,26]. On the contrary, Al_2O_3-coated LAGP illustrates a flat and dense surface after cycling, indicating the generation of stable SEI. This Al_2O_3-induced SEI regulates Li dendrites and induces a reliable symmetrical Li cell. Therefore, the deposited thin Al_2O_3 film is beneficial for stabilizing the Li/LAGP interface and regulating Li dendrites.

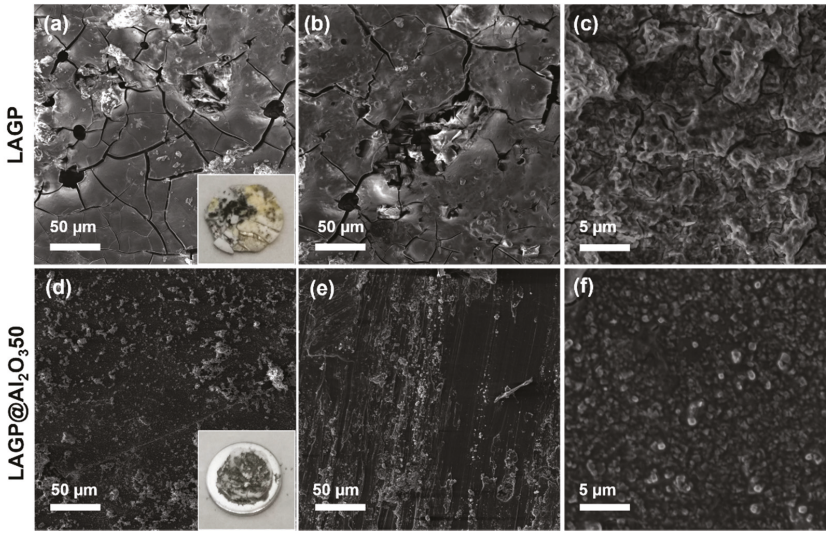

Figure 6. Top-view SEM images of cycled (**a**–**c**) LAGP and (**d**–**f**) LAGP@$Al_2O_3$50. The insets of (**a**,**d**) show the photos of cycled LAGP and LAGP@$Al_2O_3$50.

Meanwhile, a XPS test was performed to collect surface elemental information of cycled LAGP and LAGP@$Al_2O_3$50. As shown in Figures S4 and 7a, and Table S2, the Al signal is absent in bare LAGP, implying the formation of an Al-deficient SEI layer. Al 2p spectra in Figure 7b can be assigned to two peaks at 72.2 and 71.5 eV, respectively, which slightly shift to 72.7 and 72.0 eV with 1060 s etching (corresponding to about 8.8 nm depth from the top of the surface). Since the SEI layers are usually ~70 nm or thicker [46,47], both the 0 s and 1060 s etching spectra should come from the SEI layer instead of the LAGP SE. Meanwhile, the absence of Al signal from the cycled bare LAGP sample also indicates that the 1060 s etching does not reach the bulk LAGP SE. The peak shift of Al 2p spectra reveals the compositional variation in the SEI layer along the vertical direction of cycled LAGP@$Al_2O_3$50. The surface Li 1s spectrum (0 s etching) of cycled bare LAGP (Figure 7c) can be decomposed into two peaks located at 53.1 and 52.3 eV, respectively, corresponding to LiF and Li_2O_2 in the SEI layer. The surface Li 1s spectrum (0 s etching) obtained from LAGP@$Al_2O_3$50 shows higher binding energies of 53.5 and 53.0 eV for LiF and Li_2O_2 (Figure 7d). It should be noted that the Li 1s spectrum from cycled LAGP@$Al_2O_3$50 surface has a smaller LiF/Li_2O_2 ratio than cycled bare LAGP, suggesting the different SEI compositions from the coated and uncoated LAGPs. A higher LiF/Li_2O_2 ratio is observed in the Li 1s spectrum of cycled LAGP@$Al_2O_3$50 after 1060 s etching, implying a gradient distribution of LiF/Li_2O_2 in the SEI layer. F 1s spectra in Figure 7e,f originate from Li_xPF_y and LiF, which could be ascribed to the decomposition of the small addition of liquid electrolyte ($LiPF_6$ in EC:DEC) [37]. The LiF/Li_xPF_y ratio becomes larger for the LAGP@$Al_2O_3$50 after 1060s etching, which also indicates the compositional variation in the SEI layer along with the depth. The XPS results suggest that the SEI layers formed on the bared LAGP and Al_2O_3 coated LAGP possess different compositions. The Al_2O_3 coating induces an Al-containing SEI layer [48,49], formed on the surface of LAGP after repeated Li plating/stripping cycles. This unique SEI layer enhances the electrochemical stability of LAGP SE and extends the lifetime of Li/LAGP/Li symmetrical cells.

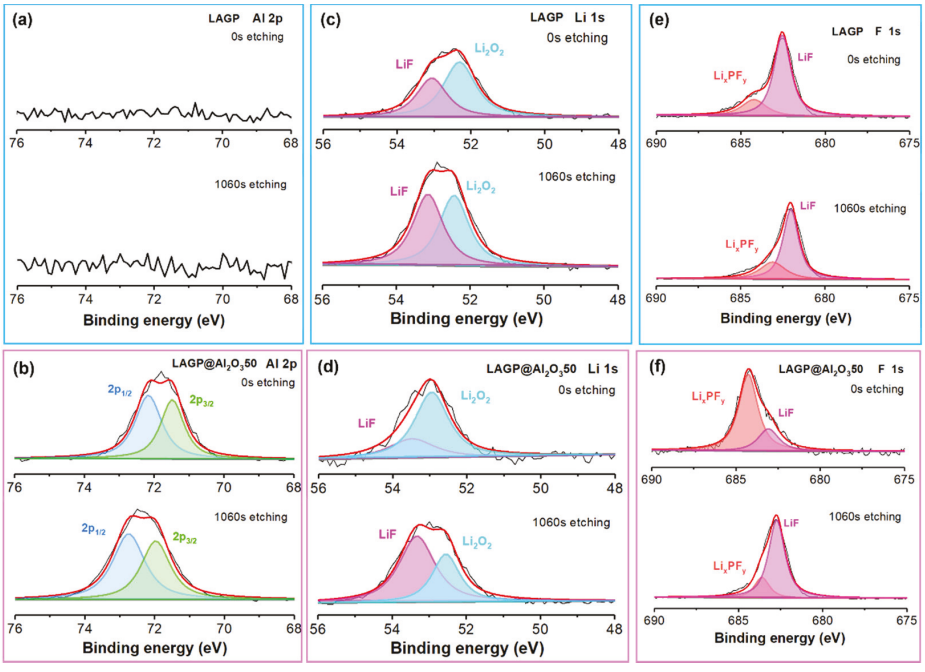

Figure 7. XPS spectra of (**a**,**b**) Al 2p, (**c**,**d**) Li 1s, (**e**,**f**) F 1s of the surface of LAGP and LAGP@$Al_2O_3$50 after cycling test.

4. Conclusions

In summary, a thin Al_2O_3 film was deposited on the surface of LAGP pellet by the ALD method to address the issue of Li/LAGP interface incompatibility. The optimized Li/LAGP@$Al_2O_3$50/Li cell maintained a stable voltage profile up to 0.2 mA cm^{-2} and exhibited a 360-h cycling duration at the capacity density of 0.2 mAh cm^{-2}. Remarkably, this cell showed a superior cumulative Li plated capacity of 72 mAh cm^{-2} at 0.2 mA cm^{-2} current density. SEM and XPS characterizations suggest that Al_2O_3 film induced the formation of an Al-rich SEI layer to regulate Li dendrite deposition and contributes to a uniform and dense interface after long Li plating/stripping cycles.

Supplementary Materials: The following supporting information can be downloaded at: https://www.mdpi.com/article/10.3390/nano12111912/s1. Figure S1: SEM image of LAGP powder, Figure S2: Voltage-time profile of the Li/LAGP/Li cell tested at 25 °C, Figure S3: XPS survey spectra of LAGP and LAGP@Al_2O_3 before the cycling test, Figure S4: XPS survey spectra of LAGP and LAGP@Al_2O_3 after the cycling test, Table S1: Elemental composition of LAGP and LAGP@$Al_2O_3$50 from XPS before battery tests, Table S2: Elemental composition of LAGP and LAGP@$Al_2O_3$50 from XPS after cycling tests.

Author Contributions: Conceptualization, J.L. and H.L.; methodology, Y.Z. and J.L.; validation, Y.Z.; investigation, Y.Z. and H.L.; resources, J.L.; writing—original draft preparation, Y.Z.; writing—review and editing, Z.X., W.Q. and J.L.; visualization, Y.Z.; supervision, J.L.; funding acquisition, H.L. and J.L. All authors have read and agreed to the published version of the manuscript.

Funding: This research was funded by Mitacs Accelerate Program, Natural Sciences and Engineering Research Council of Canada (NSERC), Canada Foundation for Innovation (CFI), BC Knowledge Development Fund (BCKDF), the University of British Columbia (UBC), and National Research Council Canada (NRC) Ideation Fund through New Beginnings Initiative (INB-000654-1).

Institutional Review Board Statement: Not applicable.

Informed Consent Statement: Not applicable.

Data Availability Statement: Data is contained within the article or supplementary material.

Conflicts of Interest: The authors declare no conflict of interest.

References

1. Cheng, Z.; Pan, H.; Li, C.; Mu, X.; Du, Y.; Zhang, F.; Zhang, X.; He, P.; Zhou, H. An in situ solidifying strategy enabling high-voltage all-solid-state Li-metal batteries operating at room temperature. *J. Mater. Chem. A* **2020**, *8*, 25217–25225. [CrossRef]
2. Han, X.; Chen, J.; Chen, M.; Zhou, W.; Zhou, X.; Wang, G.; Wong, C.P.; Liu, B.; Luo, L.; Chen, S.; et al. Induction of planar Li growth with designed interphases for dendrite-free Li metal anodes. *Energy Storage Mater.* **2021**, *39*, 250–258. [CrossRef]
3. Cortes, F.J.Q.; Lewis, J.A.; Tippens, J.; Marchese, T.S.; McDowell, M.T. How Metallic Protection Layers Extend the Lifetime of NASICON-Based Solid-State Lithium Batteries. *J. Electrochem. Soc.* **2019**, *167*, 050502. [CrossRef]
4. Gao, Z.; Sun, H.; Fu, L.; Ye, F.; Zhang, Y.; Luo, W.; Huang, Y. Promises, Challenges, and Recent Progress of Inorganic Solid-State Electrolytes for All-Solid-State Lithium Batteries. *Adv. Mater.* **2018**, *30*, e1705702. [CrossRef]
5. Manthiram, A.; Yu, X.; Wang, S. Lithium battery chemistries enabled by solid-state electrolytes. *Nat. Rev. Mater.* **2017**, *2*, 16103. [CrossRef]
6. Sun, C.; Liu, J.; Gong, Y.; Wilkinson, D.P.; Zhang, J. Recent advances in all-solid-state rechargeable lithium batteries. *Nano Energy* **2017**, *33*, 363–386. [CrossRef]
7. Zheng, F.; Kotobuki, M.; Song, S.; Lai, M.O.; Lu, L. Review on solid electrolytes for all-solid-state lithium-ion batteries. *J. Power Sources* **2018**, *389*, 198–213. [CrossRef]
8. Wang, Q.; Jiang, L.; Yu, Y.; Sun, J. Progress of enhancing the safety of lithium ion battery from the electrolyte aspect. *Nano Energy* **2019**, *55*, 93–114. [CrossRef]
9. Chen, J.; Wu, J.; Wang, X.; Zhou, A.A.; Yang, Z. Research progress and application prospect of solid-state electrolytes in commercial lithium-ion power batteries. *Energy Storage Mater.* **2021**, *35*, 70–87. [CrossRef]
10. Ye, T.; Li, L.; Zhang, Y. Recent Progress in Solid Electrolytes for Energy Storage Devices. *Adv. Funct. Mater.* **2020**, *30*, 2000077. [CrossRef]
11. Lu, W.; Xue, M.; Zhang, C. Modified $Li_7La_3Zr_2O_{12}$ (LLZO) and LLZO-polymer composites for solid-state lithium batteries. *Energy Storage Mater.* **2021**, *39*, 108–129. [CrossRef]
12. Chen, S.; Xie, D.; Liu, G.; Mwizerwa, J.P.; Zhang, Q.; Zhao, Y.; Xu, X.; Yao, X. Sulfide solid electrolytes for all-solid-state lithium batteries: Structure, conductivity, stability and application. *Energy Storage Mater.* **2018**, *14*, 58–74. [CrossRef]
13. Hou, M.; Liang, F.; Chen, K.; Dai, Y.; Xue, D. Challenges and perspectives of NASICON-type solid electrolytes for all-solid-state lithium batteries. *Nanotechnology* **2020**, *31*, 132003. [CrossRef] [PubMed]
14. Liu, Y.; He, P.; Zhou, H. Rechargeable Solid-State Li-Air and Li-S Batteries: Materials, Construction, and Challenges. *Adv. Energy Mater.* **2018**, *8*, 1701602. [CrossRef]
15. Li, L.; Deng, Y.; Chen, G. Status and prospect of garnet/polymer solid composite electrolytes for all-solid-state lithium batteries. *J. Energy Chem.* **2020**, *50*, 154–177. [CrossRef]
16. Li, S.; Zhang, S.-Q.; Shen, L.; Liu, Q.; Ma, J.-B.; Lv, W.; He, Y.-B.; Yang, Q.-H. Progress and Perspective of Ceramic/Polymer Composite Solid Electrolytes for Lithium Batteries. *Adv. Sci.* **2020**, *7*, 1903088. [CrossRef]
17. Kuo, P.H.; Du, J. Lithium Ion Diffusion Mechanism and Associated Defect Behaviors in Crystalline $Li_{1+x}Al_xGe_{2-x}(PO_4)_3$ Solid-State Electrolytes. *J. Phys. Chem. C* **2019**, *123*, 27385–27398. [CrossRef]
18. Yan, B.; Zhu, Y.; Pan, F.; Liu, J.; Lu, L. $Li_{1.5}Al_{0.5}Ge_{1.5}(PO_4)_3$ Li-ion conductor prepared by melt-quench and low temperature pressing. *Solid State Ion.* **2015**, *278*, 65–68. [CrossRef]
19. Yang, G.; Safanama, D.; Phuah, K.C.; Adams, S. Enhanced $Li_{1+x}Al_xGe_{2-x}(PO_4)_3$ Anode-Protecting Membranes for Hybrid Lithium-Air Batteries by Spark Plasma Sintering. *ACS Omega* **2020**, *5*, 18205–18212. [CrossRef]
20. Zhang, M.; Takahashi, K.; Imanishi, N.; Takeda, Y.; Yamamoto, O.; Chi, B.; Pu, J.; Li, J. Preparation and Electrochemical Properties of $Li_{1+x}Al_xGe_{2-x}(PO_4)$ Synthesized by a Sol-Gel Method. *J. Electrochem. Soc.* **2012**, *159*, A1114–A1119. [CrossRef]
21. Paolella, A.; Zhu, W.; Bertoni, G.; Perea, A.; Demers, H.; Savoie, S.; Girard, G.; Delaporte, N.; Guerfi, A.; Rumpel, M.; et al. Toward an All-Ceramic Cathode–Electrolyte Interface with Low-Temperature Pressed NASICON $Li_{1.5}Al_{0.5}Ge_{1.5}(PO_4)_3$ Electrolyte. *Adv. Mater. Inter.* **2020**, *7*, 2000164. [CrossRef]
22. Thokchom, J.S.; Kumar, B. The effects of crystallization parameters on the ionic conductivity of a lithium aluminum germanium phosphate glass–ceramic. *J. Power Sources* **2010**, *195*, 2870–2876. [CrossRef]
23. Pershina, S.V.; Pankratov, A.A.; Vovkotrub, E.G.; Antonov, B.D. Promising high-conductivity $Li_{1.5}Al_{0.5}Ge_{1.5}(PO_4)_3$ solid electrolytes: The effect of crystallization temperature on the microstructure and transport properties. *Ionics* **2019**, *25*, 4713–4725. [CrossRef]
24. Chung, H.; Kang, B. Mechanical and Thermal Failure Induced by Contact between a $Li_{1.5}Al_{0.5}Ge_{1.5}(PO_4)_3$ Solid Electrolyte and Li Metal in an All Solid-State Li Cell. *Chem. Mater.* **2017**, *29*, 8611–8619. [CrossRef]

25. He, L.; Sun, Q.; Chen, C.; Oh, J.A.S.; Sun, J.; Li, M.; Tu, W.; Zhou, H.; Zeng, K.; Lu, L. Failure Mechanism and Interface Engineering for NASICON-Structured All-Solid-State Lithium Metal Batteries. *ACS Appl. Mater. Interfaces* **2019**, *11*, 20895–20904. [CrossRef] [PubMed]
26. Zhang, Z.; Chen, S.; Yang, J.; Liu, G.; Yao, X.; Cui, P.; Xu, X. Stable cycling of all-solid-state lithium battery with surface amorphized $Li_{1.5}Al_{0.5}Ge_{1.5}(PO_4)_3$ electrolyte and lithium anode. *Electrochim. Acta* **2019**, *297*, 281–287. [CrossRef]
27. Liu, Q.; Yu, Q.; Li, S.; Wang, S.; Zhang, L.; Cai, B.; Zhou, D.; Li, B. Safe LAGP-based all solid-state Li metal batteries with plastic super-conductive interlayer enabled by in-situ solidification. *Energy Storage Mater.* **2020**, *25*, 613–620. [CrossRef]
28. Liu, Y.; Li, C.; Li, B.; Song, H.; Cheng, Z.; Chen, M.; He, P.; Zhou, H. Germanium Thin Film Protected Lithium Aluminum Germanium Phosphate for Solid-State Li Batteries. *Adv. Energy Mater.* **2018**, *8*, 1702374. [CrossRef]
29. Xiong, S.; Liu, Y.; Jankowski, P.; Liu, Q.; Nitze, F.; Xie, K.; Song, J.; Matic, A. Design of a Multifunctional Interlayer for NASCION-Based Solid-State Li Metal Batteries. *Adv. Funct. Mater.* **2020**, *30*, 2001444. [CrossRef]
30. Liu, Y.; Sun, Q.; Zhao, Y.; Wang, B.; Kaghazchi, P.; Adair, K.R.; Li, R.; Zhang, C.; Liu, J.; Kuo, L.-Y.; et al. Stabilizing the Interface of NASICON Solid Electrolyte against Li Metal with Atomic Layer Deposition. *ACS Appl. Mater. Interfaces* **2018**, *10*, 31240–31248. [CrossRef]
31. Bosubabu, D.; Sivaraj, J.; Sampathkumar, R.; Ramesha, K. LAGP | Li Interface Modification through a Wetted Polypropylene Interlayer for Solid State Li-Ion and Li–S batteries. *ACS Appl. Energy Mater.* **2019**, *2*, 4118–4125. [CrossRef]
32. He, L.; Chen, C.; Kotobuki, M.; Zheng, F.; Zhou, H.; Lu, L. A new approach for synthesizing bulk-type all-solid-state lithium-ion batteries. *J. Mater. Chem. A* **2019**, *7*, 9748–9760. [CrossRef]
33. Hu, Y.; Zhong, Y.; Qi, L.; Wang, H. Inorganic/polymer hybrid layer stabilizing anode/electrolyte interfaces in solid-state Li metal batteries. *Nano Res.* **2020**, *13*, 3230–3234. [CrossRef]
34. Li, C.; Chen, Y.; Li, Z.; Zhang, Y.; Fang, Z.; Xu, J.; Sun, Y.; Bao, H.; Cheng, H. Construction of sticky ionic conductive buffer layer for inorganic electrolyte toward stable all-solid-state lithium metal batteries. *J. Power Sources* **2021**, *495*, 229765. [CrossRef]
35. Li, L.; Zhang, Z.; Luo, L.; You, R.; Jiao, J.; Huang, W.; Wang, J.; Li, C.; Han, X.; Chen, S. Enhancing the interface stability of $Li_{1.3}Al_{0.3}Ti_{1.7}(PO_4)_3$ and lithium metal by amorphous $Li_{1.5}Al_{0.5}Ge_{1.5}(PO_4)_3$ modification. *Ionics* **2020**, *26*, 3815–3821. [CrossRef]
36. Li, W.; Wang, Q.; Jin, J.; Li, Y.; Wu, M.; Wen, Z. Constructing dual interfacial modification by synergetic electronic and ionic conductors: Toward high-performance LAGP-Based Li-S batteries. *Energy Storage Mater.* **2019**, *23*, 299–305. [CrossRef]
37. Zhang, S.; Zeng, Z.; Zhai, W.; Hou, G.; Chen, L.; Ci, L. Bifunctional In Situ Polymerized Interface for Stable LAGP-Based Lithium Metal Batteries. *Adv. Mater. Inter.* **2021**, *8*, 2100072. [CrossRef]
38. Kerman, K.; Luntz, A.; Viswanathan, V.; Chiang, Y.-M.; Chen, Z. Review—Practical Challenges Hindering the Development of Solid State Li Ion Batteries. *J. Electrochem. Soc.* **2017**, *164*, A1731–A1744. [CrossRef]
39. Zhu, Y.; Zhang, Y.; Lu, L. Influence of crystallization temperature on ionic conductivity of lithium aluminum germanium phosphate glass-ceramic. *J. Power Sources* **2015**, *290*, 123–129. [CrossRef]
40. DeWees, R.; Wang, H. Synthesis and Properties of NaSICON-type LATP and LAGP Solid Electrolytes. *ChemSusChem* **2019**, *12*, 3713–3725. [CrossRef]
41. Mariappan, C.R.; Yada, C.; Rosciano, F.; Roling, B. Correlation between micro-structural properties and ionic conductivity of $Li_{1.5}Al_{0.5}Ge_{1.5}(PO_4)_3$ ceramics. *J. Power Sources* **2011**, *196*, 6456–6464. [CrossRef]
42. Kaliyappan, K.; Liu, J.; Xiao, B.; Lushington, A.; Li, R.; Sham, T.-K.; Sun, X. Enhanced Performance of P2-$Na_{0.66}(Mn_{0.54}Co_{0.13}Ni_{0.13})O_2$ Cathode for Sodium-Ion Batteries by Ultrathin Metal Oxide Coatings via Atomic Layer Deposition. *Adv. Funct. Mater.* **2017**, *27*, 1701870. [CrossRef]
43. Oswald, S.; Thoss, F.; Zier, M.; Hoffmann, M.; Jaumann, T.; Herklotz, M.; Nikolowski, K.; Scheiba, F.; Kohl, M.; Giebeler, L.; et al. Binding Energy Referencing for XPS in Alkali Metal-Based Battery Materials Research (II): Application to Complex Composite Electrodes. *Batteries* **2018**, *4*, 36. [CrossRef]
44. Yu, Q.; Han, D.; Lu, Q.; He, Y.-B.; Li, S.; Liu, Q.; Han, C.; Kang, F.; Li, B. Constructing Effective Interfaces for $Li_{1.5}Al_{0.5}Ge_{1.5}(PO_4)_3$ Pellets To Achieve Room-Temperature Hybrid Solid-State Lithium Metal Batteries. *ACS Appl. Mater. Interfaces* **2019**, *11*, 9911–9918. [CrossRef]
45. Zhai, P.; Fu, L.; Yuan, S.; Shi, L.; Zhu, J.; Zhao, Y.; Wang, Z. Ionic Conductive Thermoplastic Polymer Welding Layer for Low Electrode/Solid Electrolyte Interface Resistance. *ACS Appl. Energy Mater.* **2020**, *3*, 7011–7019. [CrossRef]
46. Wang, M.; Huai, L.; Hu, G.; Yang, S.; Ren, F.; Wang, S.; Zhang, Z.; Chen, Z.; Peng, Z.; Shen, C.; et al. Effect of LiFSI Concentrations To Form Thickness- and Modulus-Controlled SEI Layers on Lithium Metal Anodes. *J. Phys. Chem. C* **2018**, *122*, 9825–9834. [CrossRef]
47. Nojabaee, M.; Kuster, K.; Starke, U.; Popovic, J.; Maier, J. Solid Electrolyte Interphase Evolution on Lithium Metal in Contact with Glyme-Based Electrolytes. *Small* **2020**, *16*, e2000756. [CrossRef]
48. Jung, S.C.; Han, Y.-K. How Do Li Atoms Pass through the Al_2O_3 Coating Layer during Lithiation in Li-ion Batteries? *J. Phys. Chem. Lett.* **2013**, *4*, 2681–2685. [CrossRef]
49. Zhang, B.; Zhong, J.; Pan, F.; Lin, Z. Potential Solid-State Electrolytes with Good Balance between Ionic Conductivity and Electrochemical Stability: $Li_{5-x}M_{1-x}M_x'O_4$ (M = Al and Ga and M′ = Si and Ge). *ACS Appl. Mater. Interfaces* **2021**, *13*, 61296–61304. [CrossRef]

nanomaterials

MDPI

Review

Development and Applications of Embedded Passives and Interconnects Employing Nanomaterials

Shanggui Deng [1,†], Sharad Bhatnagar [2], Shan He [1,3,*,†], Nabeel Ahmad [4,*], Abdul Rahaman [5], Jingrong Gao [5], Jagriti Narang [6], Ibrahim Khalifa [7] and Anindya Nag [8,9]

1 Department of Food Science and Pharmaceutics, Zhejiang Ocean University, Zhoushan 316022, China
2 Faculty of Life and Environmental Sciences, University of Tsukuba, 1-1-1, Tennodai, Tsukuba 305-8572, Ibaraki, Japan
3 Institute for NanoScale Science and Technology, College of Science and Engineering, Flinders University, Bedford Park 5042, Australia
4 Department of Biotechnology, School of Allied Sciences, Dev Bhoomi Uttarakhand University, Naugaon 248007, India
5 School of Food Science and Engineering, South China University of Technology, Guangzhou 510641, China
6 Department of Biotechnology, School of Chemical and Life Sciences, New Delhi 110062, India
7 Food Technology Department, Faculty of Agriculture, Benha University, Moshtohor 13736, Egypt
8 Faculty of Electrical and Computer Engineering, Technische Universität Dresden, 01062 Dresden, Germany
9 Centre for Tactile Internet with Human-in-the-Loop (CeTI), Technische Universität Dresden, 01069 Dresden, Germany
* Correspondence: shan.he@flinders.edu.au (S.H.); nabeel.biotech@gmail.com (N.A.)
† These authors contributed equally to this work.

Abstract: The advent of nanotechnology has initiated a profound revolution in almost all spheres of technology. The electronics industry is concerned with the ongoing miniaturization of devices and as such requires packaging technologies that will make the devices more compact and resilient. 3D packaging, system in package, and system on chip are the various packaging techniques that utilize nanoscale components for their implementation. The active components of the ICs have kept pace with Moore's law, but the passive components have proven an impediment in the race for miniaturization. Moreover, the toxic effects and nano-scale problems associated with conventional soldering techniques have entailed the active involvement of nanotechnology in the search for answers. Recent advances in these fields and the diverse nanomaterials which are being employed to resolve these issues have been discussed in detail.

Keywords: embedded components; resistors; capacitors; inductors; interconnects; nanomaterials

Citation: Deng, S.; Bhatnagar, S.; He, S.; Ahmad, N.; Rahaman, A.; Gao, J.; Narang, J.; Khalifa, I.; Nag, A. Development and Applications of Embedded Passives and Interconnects Employing Nanomaterials. *Nanomaterials* **2022**, *12*, 3284. https://doi.org/10.3390/nano12193284

Academic Editor: Patrick Fiorenza

Received: 10 April 2022
Accepted: 13 September 2022
Published: 21 September 2022

Publisher's Note: MDPI stays neutral with regard to jurisdictional claims in published maps and institutional affiliations.

1. Introduction

The era of nanotechnology is slowly but surely making its way across the threshold of conventional technologies. The creation and manipulation of a structure at a range of 1 nm to 100 nm refer to nanotechnology [1]. The field of electronics has already entered the nano zone since the size of integrated circuits reached below 100 nm [2]. With the 22 nm complementary metal-oxide semiconductor (CMOS) in development, nanotechnology has established itself well in the field of electronics [3]. However, apart from integrated circuits (ICs), the bulk of the components (about 80%) are discrete passive components (capacitors, resistors, inductors) and these components occupy a majority of the space on the surface of a printed circuit board (PCB) [4]. The consistently increasing demand for miniaturization and high performance at a low cost for microelectronics has considerably shifted the attention towards packaging technologies: system on chip (SOC) and system in package (SiP) being the premier among them [5]. 3D system packaging is the only way to further reduce the volume and bulk of the microelectronics products available today and this is where nanotechnology comes into the picture. The aim of nano-packaging is to develop

nanoscale passives, interfaces, and interconnections, which can be compressed into highly miniaturized systems. The standard definition of nano-packaging, according to IEEE can be considered as follows: "Nano-packaging can be defined as the process of interconnecting, powering, cooling, and protecting the nanocomponents made of nanomaterials to form electronic and bioelectronic systems for greatly improved functionality and cost [6]."

Over the last sixty years, there has been exceptional improvement in the speed and reliability of the microprocessor. According to Moore's law, the number of transistors in semiconductor devices or ICs would double approximately every two years [7]. This has more or less held true for the active components of ICs, but the passive components have been unable to follow the miniaturization trend completely because of issues with material development and fabrication technologies. To overcome the size and space demanded by the discrete passive components, an alternative technology called embedded passives is being researched for the past decades. This technique involves embedding the passives directly at the substrate level and thereby reducing the need for bulky discrete components. These passives can be used in conjunction with the latest packaging technologies to further scale down the size of electronic equipment. Even though the technology has been in the making for quite a few years, it has not yet been made for commercial applications largely due to materials and process issues [7]. Therefore, it is quite necessary to develop some materials that will permit suitable fabrication processes and will also perform well enough on electrical and mechanical criteria.

2. Embedded Capacitors

The capacitor is a component used to store electrical energy in an electric field. It usually stores energy in the form of electrostatic fields in between the plates. The removal of discrete capacitors from the surface and the embedding of them directly into the substrate board can lead to a reduction in size and weight as well as an increase in reliability, performance, and reduced cost. Requirements for the development of materials to fabricate embedded capacitors include a high dielectric constant (k), high breakdown, low dielectric loss, low leakage current, and good stability [8].

High k Nanomaterials for Embedded Capacitors

Early attempts at the fabrication of high k dielectric materials yielded results in the form of ferroelectric ceramic materials, ferroelectric ceramic–polymer composites, conductive filler–polymer composites, and all organic polymer composites. Each of these had a disadvantage associated with them, each distinct in every case. In the case of ferroelectric ceramic materials, the high sintering temperature for fabrication was an issue. Examples of this category include Barium titanate ($BaTiO_3$), lead zirconatetitanate ($PbZrTiO_3$), etc. [9,10]. Ferroelectric ceramic–polymer composites suffered from some fabrication issues like poor dispersion of filler within the matrix and a lack of adhesion between other components in PCB. Notable examples of such composites include poly(vinylidenefluoride-co-trifluoroethylene) (P(VDF-TrFE)), magnesium niobate–lead titanate (PMN-PT) + ($BaTiO_3$) [11,12]. Conductive filler—polymer composites such as Ni/PVDF composite, and LNO/PVDF (Li-Doped NiO/polyvinylidene fluoride) were reported to have very high k values but they also had the drawback of high dielectric loss and conductivity. Even then, these materials have a distinct advantage over ceramic/polymer composites. Organic polymer composites have been fabricated by using an organic filler material having a high dielectric constant with a polymer matrix also exhibiting the same. Examples include CuPc (copper–phthalocyanine) dispersed in P(VDF-TrFE) (poly (vinylidenefluoride-co-trifluoroethylene) [13]. These composites showed a high dielectric constant but suffered from high dielectric loss too. These composites are being further researched for embedded capacitors application.

The fabrication of high k dielectric constant materials has made considerable progress owing to advances in nanotechnology. Due to the unique physical and chemical properties of materials at the nanoscale, these materials may provide the solution to the issues plaguing the current technology and will point toward the future direction of electronic packaging.

To understand the dielectric properties of the polymers, a multi-core model has been proposed. According to their theory, the interface of a spherical inorganic filler particle embedded in a polymer environment consists of three discrete layers: a bonded layer, a bound layer, and a loose layer, with an electric double layer overlapping the three layers [14]. The bonded layer is the one that comes in direct contact with the filler surface, the bound layer is the one present in the interfacial region, and the electric double layer is the one where the prevailing atmosphere is similar to that of the bulk polymer. The second layer unsettles the motion of the dipoles from polar groups, consequently reducing the permittivity. The electric double layer is indirectly responsible for the reduction in dielectric constant too. Therefore, the bound layer and electric double layer properties must be controlled if the dielectric properties are to be modified. Attaching the specific organic groups to the surface of the particle can lead to the modification of the properties and interfacial area. The choice of the surface organic assembly and its various properties such as size, polarity, polarizability, and mobility could have a foremost bearing on the dielectric properties of the polymer nanocomposites [15].

Nanoparticles dispersed polymer is an excellent alternative due to its low-temperature processing and nano-sized particles allowing the formation of thinner dielectrics that are able to achieve high capacitance density [16]. The affordable processing and mechanical properties of polymers, combined with the distinct magnetic and electrical properties of nanoparticles, make polymer-nanoparticles composite a great idea. There are two types of fillers that have been researched extensively for the fabrication of nanocomposite materials: ferroelectric ceramic fillers and conductive fillers [17].

3. Ferroelectric Ceramic–Polymer Composites

The dielectric constant of these polymers is dependent upon the concentration of the filler used or the filler loading volume. As the filler loading volume increases, so does the dielectric constant. However, a very large loading volume also results in uneven dispersion and a lack of adhesion. The ambient processing conditions for the ceramic and unique properties of nanoparticles can lead to the fabrication of high-k materials. Barium titanate ($BaTiO_3$) has been the most researched material for this category along with epoxy composites due to its high dielectric value. *k* values more than 150 to about 200 have been generated by using this ceramic-polymer composite. Cho et al. fabricated a $BaTiO_3$-epoxy thin film with a thickness of 7 μm exhibiting a dielectric value of 100, 10 nF/cm^2 capacitance, with low leakage current values of 10^{-8} A/cm^2 [10]. A modified hydrothermal reaction method was used by Suibin et al. to synthesize $BaTiO_3$ powder and the nanocomposite had a dielectric value of 19.4 at 10 kHz, and a loss factor of 0.02, with a 50% loading volume. The high dielectric value and low loss were attributed to the tetragonal crystal phase and uniform dispersion [18]. Das et al. developed a $BaTiO_3$–epoxy flexible nanocomposite having a thickness from 2 microns to 25 microns exhibiting high capacitance (10–100 nF/inch^2) and low loss (0.02–0.04) at 1 MHz. The capacitance of these films could be increased up to 500 nF/inch^2 by the modification of composites with nanomaterials such as lead zirconatetitanate (PZT), lead lanthanum (PLZT), Zinc oxides (ZnO), Lead magnesium niobate (PMN) and PMN-PT (Lead magnesium niobate-lead titanate) [19,20]. Thermally treated $BaTiO_3$ was used by Hanemann to increase the composite permittivity by inducing the phase change into tetragonal one and crystal lattice relaxation. Composites with a solid load of around 78% with a bimodal particle size distribution showed *k* values around 50 and a loss factor around 5% [21].

Xu et al. have optimized the $BaTiO_3$–epoxy nanocomposite based on loading capacity and dielectric constant. The loading capacity above 50% has several physical and mechanical disadvantages in real applications, so the loading capacity was maintained at 50%, whereas the dielectric value was maintained at around 50. The optimized rubberized nanocomposite showed a high dielectric constant above 50, a high breakdown voltage of 89 MV/m, and low leakage current values of 1.9×10^{-11} A/cm^2 [22]. Perovskite ($Ca_{2-x}Sr_xNb_3O_{10}$) nanosheets have been fabricated by Osada and Sasaki using the

Langmuir–Blodgett method. These nanofilms exhibited a high dielectric of greater than 200 and quite a low leakage current of 10^{-7} A/cm^2 in films having a thickness of around 5 nm [23].

3.1. Conductive/Metallic Nanoparticles-Polymer Composites

The high loading volume of ceramic fillers in the polymer composite not only leads to an increase in k values but also drastically reduces adhesion and mechanical capabilities, making it less adaptable for usage on the circuit board. Another alternative is to fabricate conductive filler systems that exhibit a drastic increase in dielectric constant in the percolation systems as it nears the percolation threshold [24]. The k value of such composites can be given by:

$$\frac{k}{k_m} = [f_c - f]^{-s} \quad (1)$$

where, k_m = dielectric constant of the matrix,
f = volume fraction of the filler,
f_c = volume fraction at percolation threshold,
and s = exponent of about 1.

The filler of metallic nanoparticles brings about unique properties in the composite. These materials have been marked as good candidates for embedded capacitor applications because of their high k, although the dielectric loss in these materials is very difficult to control because the conductive/metallic particles can easily form a conductive pathway in the composite as the percolation threshold is achieved. Since these composites usually require a lesser loading capacity volume as compared to polymer composites, they provide balanced mechanical properties with better adhesion. Different metallic/conductive fillers that are being used for these composites are silver (Ag), aluminum (Al), carbon black, etc. [25–27]. The major bottleneck for these composites is the narrow processing window between achieving a high k and a low dielectric loss. A wide variety of approaches have been used to improve the quality and overcome the shortcomings of these nano-composites.

Initial approaches to developing conductive filler–polymer composites utilized an epoxy–silver-based composite by using silver as a conductive filler. The dielectric constant was reported to be around 1000 and was achieved around the percolation threshold with low dielectric loss (<0.02) and good adhesion [28,29]. Lu et al. synthesized novel carbon black–polymer composites containing in situ formed silver nanoparticles. The high dielectric constant was attributed to the filing of charges at the extended interface of the interfacial polarization-based composites. The decrease in dielectric loss was credited to the Coulomb blockade effect of the Ag nanoparticles exhibiting the quantum effect of metal nanoparticles. The major effect on the properties was due to the size, size distribution, and loading level of the metal nanoparticles [30]. The different categories of conductive filler nanocomposites are discussed below. The differentiation has been performed based on the methodology that has been employed by various researchers for improving the dielectric value and reducing the dielectric loss tangent value.

3.2. Three Phase Nanocomposites

Three-phase percolative silver–$BaTiO_3$–epoxy nanocomposite was synthesized by Qi et al. The incorporation of silver into epoxy resin led to a significant increase in the dielectric properties of the resin and $BaTiO_3$ was further mixed to create a high dielectric constant polymer composite. These composites demonstrated a high dielectric constant of approximately 450 which was 110 times higher than that of the epoxy matrix, with a dielectric strength of 5 kV/mm at room temperature [31]. George and Sebastian synthesized a similar $Ca[(Li_{1/3}Nb_{2/3})_{0.8}Ti_{0.2}]\ O_{3-\delta}$(CLNT)–epoxy–silver, three-phase composite by a two-step mixing and thermosetting technique. The addition of a 0.28 volume fraction of silver increased the relative permittivity of the composite from 8 to 142 at 1 MHz [32].

3.2.1. Use of High *k* Polymer Matrix

The *k* values of the composite can also be increased by using a high *k* polymer matrix for the conductive filler. The high *k* polymer matrix is further reinforced by a high *k* polymer conductive filler. Lu et al. utilized this approach to generate uniformly dispersed Ag particles of around 10 nm into the polymer matrix using photochemical reduction. The number of nanoparticles in the polymer matrix was estimated at around 10% by weight. Self-passivated Al particles were then incorporated into the Ag–epoxy matrix to further improve the dielectric constant. The presence of an oxide layer on Al particles leads to the lower loss of dielectric. The composite showed a 50% increase in dielectric values as compared to Al-filled epoxy composites and the dielectric loss tangent was below 0.1 [33]. Recently, a similar approach was used by Li et al. to fabricate a Copper (Cu)–Epoxy matrix using a thermal reduction method which generated Cu nanoparticles around 100 nm with uniform dispersion. $BaTiO_3$ ceramic particles with a high dielectric constant were incorporated into this Cu–epoxy matrix which enhanced the dielectric constant while maintaining the low dielectric loss compared with the $BaTiO_3$/epoxy composite. Nanocomposites obtained by ex-situ techniques exhibited a comparable dielectric constant with much lower dielectric loss compared to in-situ BT/Cu–epoxy composites. The improved dielectric performance of nanocomposites was attributed to the excellent dispersion of Cu nanoparticles as well as the strong interfacial interaction between Cu nanoparticles and epoxy matrix in the in-situ Cu–epoxy matrices [34].

3.2.2. Use of Surface Modification

Surface modification of metallic fillers via the introduction of surfactant coating can lead to a reduction in the dielectric loss of the nanocomposites. Qi et al. reported an epoxy-based composite containing silver nanoparticles having an average size of 40 nm coated with a layer of mercaptosuccinic acid (MSA) to promote the formation of Ag–epoxy while retaining the flexibility of the matrix. The dielectric constant and loss increased with the increasing filler concentration up to 22%. At the Ag concentration of 22% by volume, the dielectric constant was found to be 308 and the dielectric electric loss was quite low at 0.05 when measured at 1 kHz. The decrease in the dielectric constant after 22% was attributed to the porosity, which may have been caused by the adsorbed surfactant layer which leaves space between the Ag particles and the creation of voids that are not occupied by the polymer. Since no rapid increase in the dielectric loss was evident, it was concluded that the formation of the conducting filler network was prevented by the surfactant coating layer [28]. The dependence of dielectric value and dielectric loss on silver volume and frequency is demonstrated in Figure 1.

Ren et al. have synthesized polymer-coated silver nanoparticles by the reduction of Tollen's reagent by means of mercaptosuccinic acid/polyethylene glycol (MSA/PEG) copolymers as reducing agents and stabilizers concurrently. The average size of Ag particles was between 10 to 120 nm, which could be controlled by changing the MSA/PEG ratio. The surface-coated Ag particles were then incorporated into the epoxy matrix leading to the formation of Ag–epoxy nanocomposites. The nanocomposites with a 25% filler volume loading exhibited a dielectric constant of 237 while the dielectric loss was below 0.08 at 1 kHz. The dielectric properties were found to be dependent upon the volume fraction of silver nanoparticles in epoxy resin [35] as shown in Figure 2. A novel idea for surface modification has been researched by Luo et al. In this method, the surface modification of $BaTiO_3$ nanoparticles was performed using Ag nanoparticles, effectively making it a metal–ceramic filler. Nano Ag particles of 20 nm dimension were grown over 100 nm $BaTiO_3$, which effectively prevented the Ag nanoparticle contact within the PVDF membrane, inhibiting the formation of a conducting path. The filler loading of 43.4% by volume, the *k* value of the composite was 94.3 and a dielectric loss of 0.06 was exhibited by the composite. On increasing the filler volume further, the *k* value increased to 160 at the same frequency and the loss tangent remained low at 0.11 [36].

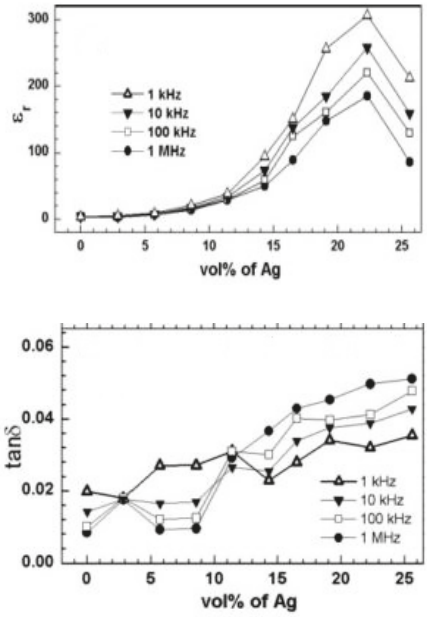

Figure 1. The dependence of dielectric value and dielectric loss on silver volume and frequency. Reprinted with permission from [29]; Copyright 2005, John Wiley and Sons.

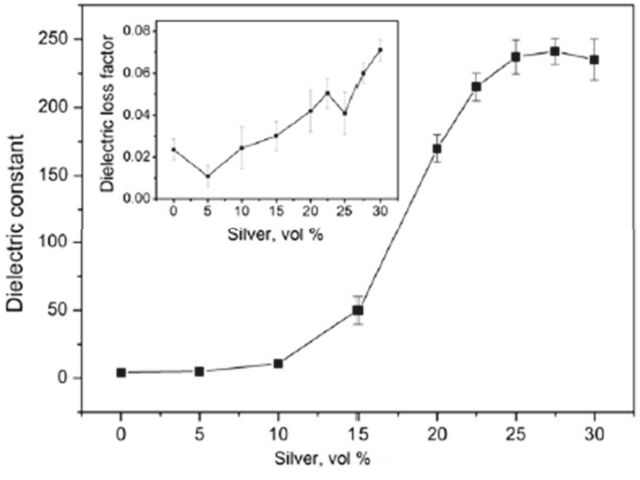

Figure 2. The dependence of dielectric constant and dielectric loss factor with volume fraction of silver. Reprinted with permission from [35]; Copyright 2012, Elsevier.

3.2.3. Use of Core-Shell Structured Fillers

The direct contact of conductive metal fillers leads to the formation of a conductive path that will direct to a higher dielectric loss at or above the percolation threshold. Core-shell structured fillers were projected as an alternative to this problem as the nonconductive shells can act as a barrier between the conductive metal fillers, thereby reducing the dielectric loss and increasing the *k* values. Xu et al. developed a high *k* polymer based on self-passivating Al as filler. The size of the Al nanoparticles was found to be around 100 nm, with an oxide thickness of about 2.8 nm as shown in Figure 3a. The layer of aluminum

oxide acted as an electric barrier and significantly affected the dielectric properties of the Al-epoxy composite. A dielectric constant of 109 and dielectric loss of 0.02 at 10 kHz was observed at an 80% loading of Al by weight [37] as in Figure 3b.

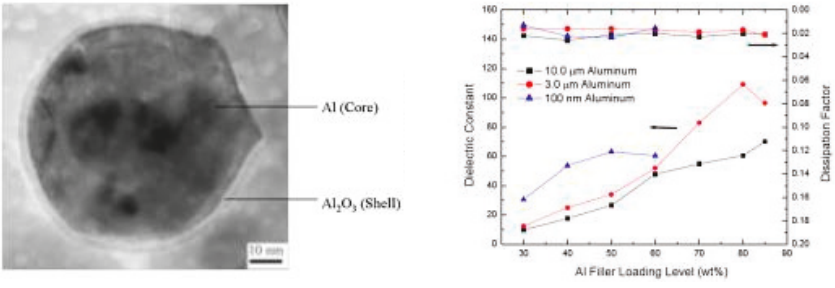

(**a**) (**b**)

Figure 3. (**a**) TEM image of Al nanoparticle with Al oxide coating (**b**) dependence of dielectric constant on filler loading volume. Reprinted with permission from [37]; Copyright 2005, AIP Publishing.

Copper nanowires have been used in conjunction with PVDF polymer to formulate a nanocomposite with a high dielectric constant. The dielectric properties of these nanocomposites were compared to that of a multiwalled carbon nanotube (MWCNT) filler with PVDF polymer. It was surmised that as compared to the MWCNT-filled PVDF, this novel Cu nanowire–PVDF polymer exhibited better dielectric permittivity values with lower loss at room temperature in the frequency range of 10^{-1} to 10^{-6} Hz. The higher conductivity was attributed to the Cu core providing a high number of mobile carriers impacting the interfacial polarization whereas the lower loss was attributed to the formation of an oxide layer over the nanowires leading to suppression of the formation of the conductive path. Because of the presence of the oxide layer over the wire, this process can be classified among the core-shell structured fillers [38].

Shen et al. fabricated a polymer composite using Ag cores coated with organic dielectric shells as fillers. This dielectric shell acts as an interparticle barrier and prevents the Ag particles from coming into direct contact. It also encourages the uniform dispersion of the filler in the polymer matrix leading to k values of more than 300 and a low dielectric loss of 0.05 [39].

Recent examples of this category include gold nanoparticles of 15 nm homogenously coated with a 10 nm layer of SnO_2 having high capacitance by Oldfield et al., carbonaceous shell coating on Ag cores by Shen et al., synthesis of TiO_2 (Titanium oxide) nanoparticles coated with a paraffin layer by Balasubramanian et al., gold nanoparticles coated with polystyrene; and gold, silver, and titanium coated with silica shell core by Badi et al., amongst others [40–43].

Other examples of core-shell hybrid fillers other than metallic fillers are discussed below. Wang et al. have synthesized core-shell structured $BaTiO_3$–polystyrene nanoparticles (BT–PS) with varying PS shell thickness and studied the influence of shell thickness on the dielectric properties. Two types of BT–PS were synthesized: with the shell thickness of 3 nm and 12 nm by controlling the polymerization time. Composites comprising core-shell nanoparticles exhibited higher dielectric constant, higher breakdown strength, and lower breakdown voltage as compared to the PS matrix. Composites filled with BT–PS with a 3 nm shell exhibited better dielectric properties as compared to BT–PS with a 12 nm shell. A maximum energy density of 4.24 J/cm^3 obtained in BT–PS/PS films [44] was demonstrated.

Guo et al. have reported the fabrication of Novel core/shell structured multi-walled carbon nanotube/amorphous carbon (MWCNT@AC) nanohybrids which were used as fillers to improve the dielectric properties of poly (vinylidene fluoride) (PVDF)-based composites. The MWCNTs served as the core and amorphous carbon served as the shell.

The composites exhibited a high possible *k* value of 5910 and dielectric loss of around 2, which is considerably better than that of MWCNT/PVDF composites [45].

Core-shell structured hyperbranched aromatic polyamide grafted barium titanate (BT-HBP) hybrid was used as a filler for a Poly (vinylidene fluoride-trifluoroethylene-chlorofluoroethylene) (PVDF-TrFE-CFE) matrix by Xie et al. to obtain a high dielectric constant value of 1485.5 at 1 kHz at a 40% loading volume. Enhanced interfacial polarization between the BT–HBP and polymer matrix was the reason for the observed high dielectric constant [46].

3.3. Embedded Resistors

The second group of passive components that are routinely studied to shrink the size of printed circuit boards and printed wiring boards (PCB/PWB) is the resistor [47]. Embedded resistors will also be able to increase the reliability and electrical performance of the circuit [48]. The integration of resistors also reduces the area requirement on the PCB/PWB, thereby potentially increasing the device functionality by placing more active components which provide gain to the system. In embedded systems, resistors are generally sheets of a material that are sized appropriately to achieve a certain resistance and whose ends are used for interconnection to other components. The resistive materials in embedded applications should have high electrical resistivity, low-temperature coefficient of resistance (TCR), and should be easy to process [48–50]. Apart from this, nanoparticle-based embedded resistors have another set of factors that limit their use in mainstream electronics. Yield, reliability, and a range of resistance are needed to be researched for nanoparticle-based resistors. The resistance of the material depends upon the dimension and the property of the materials.

Another factor that is important in the fabrication of the resistors is the temperature coefficient of resistance (TCR). The rate of change of resistance with temperature is termed the TCR of the material. It is measured in units of ppm/°C and can be determined using the resistance change from some reference temperature and the change in temperature [51]. A positive value of TCR means that the resistance increases with the temperature, for example, in pure metals, whereas negative TCR means that the resistance is decreasing with the increase in temperature, such as in the case of carbon, silicon, etc. For some metal alloys, the TCR values are close to zero, meaning that the resistance does not vary with the temperature, a property that can be utilized for the formation of a high-precision resistor [52].

Traditionally, metal pastes consisting of metal particles and organic resin have been used for the fabrication of resistors. This paste is applied on the surface of the substrate and after the application of a high temperature; metal particles melt and fuse to form a film [53]. The natural properties of nanoparticles can be harnessed to fabricate low-cost resistors at low temperatures. The nanoparticle-based resistors can be classified into the following major categories: cermets, metal alloys, and carbon-filled polymers. Cermets are a mixture of ceramics and metals which can be fabricated by a number of methods such as evaporation, sputtering, co-evaporation, co-sputtering, plasma polymerization, and the mixing of metal ions in polymers [54]. Some examples of cermet resistors are discussed below.

3.4. Cermets

Lim et al. fabricated a SiO_2-Pt nano-composite ceramic metal by the co-sputtering method. Cermet was fabricated by uniformly dispersing Pt particles into the SiO_2 matrix. Resistivity values of 880 to 193,820 μΩ·cm were obtained at 3–20 mTorr, and the temperature coefficient of resistance was in the range of 383.189 to −3229.14 ppm/K [55].

Park et al. demonstrated the fabrication of Ta_3N_5–Ag nanocomposite thin films with near-zero temperature coefficients of resistance (TCR) fabricated by a reactive co-sputtering method which can be used as thin-film embedded resistors. The TCR value of the film was found to be near zero due to the balancing of the positive TCR value of Ag and negative TCR value of Ta–N at a resistivity higher than 0.005 Ω·cm. The co-sputtering

was performed at the nitrogen partial pressure of 55% and the fabricated thin film had a resistivity of 0.0059 Ω·cm and power density of 0.94 W/cm^2. The TCR value was found to be +34 ppm/K [56] as shown in Figure 4. Thin cermet films of thickness from 2 to 40 nm were fabricated by sputter deposition from $CrSi_2$–Cr–SiC targets by a dual cathode dc S-gun magnetron by Felmetsger. The atomic ratio of Si to Cr was found to be about 2:1. At a film thickness below 2.5 nm, the temperature coefficient of resistance (TCR) was significantly increased. Cermet films with thicknesses in the range of 2.5–4 nm had sheet resistances ranging from 1800 to1200 Ω/□ and TCR values from −50 ppm/°C to near zero, respectively [57].

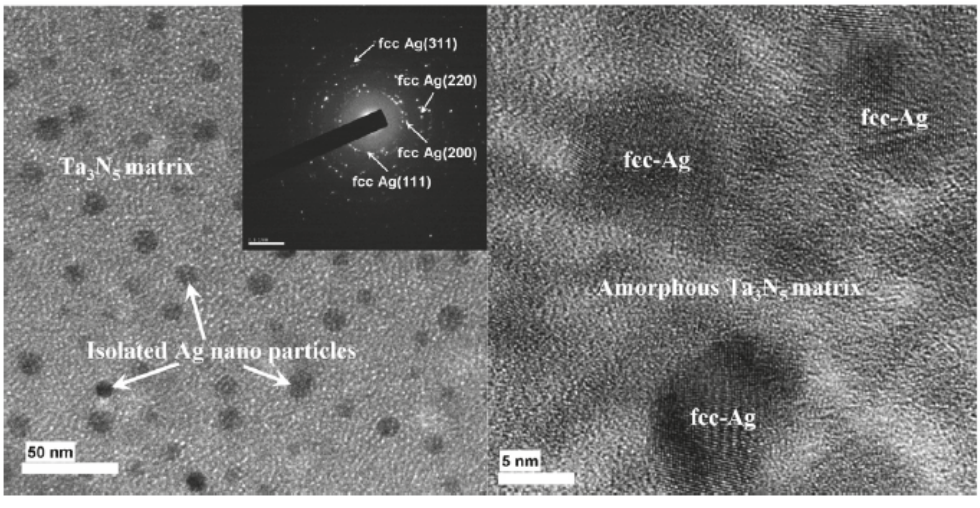

Figure 4. Ag nanocomposite thin film deposited at 55% N_2 partial pressure. Reprinted with permission from [56]; Copyright 2008, Elsevier.

Liu et al. fabricated Al–$Zr_2(WO_4)$ $(PO_4)_2$ (Al-ZWP) nano-cermets with the aim of controlling the coefficient of thermal expansion (CTE). SEM imaging and elemental mapping showed that the cermets consisted of uniform nanoparticles with sizes around 100 nm and Al and ZWP were found to be homogeneously dispersed in the cermets. The CTEs of the cermets were found in the range from -2.74×10^{-6} K^{-1} to $\sim 25.68 \times 10^{-6}$ K^{-1}. Depending on Al:ZWP mass ratio, the cermet could act as a capacitor or a resistor [58].

Nash et al. fabricated a series of amorphous chromium oxide (CrOx) films by dc sputtering and the sheet resistance of CrOx could be modified by increasing the level of oxygen doping. By varying the level of oxygen doping, the room temperature sheet resistance could be controlled from 28 Ω/□ to 32.6 k Ω/□. The film thicknesses were found to be in the range of 179 nm for growth in pure argon to 246 nm for growth with an oxygen partial pressure of 0.7 mTorr. Among the two contacts studied, the gold layer was found to be more favorable as compared to the silicon-niobium contact, the specific contact resistivity of chromium oxide to gold interfaces being 0.14 mΩ·cm^2. These chromium oxide films can be used as high-Value resistors nanoscale circuits [59] in Figure 5.

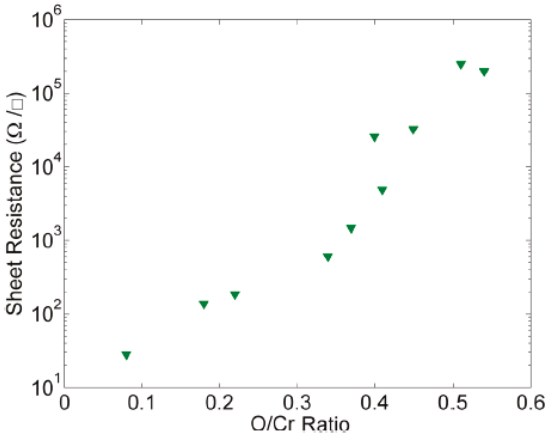

Figure 5. Dependence of sheet resistance of chromium oxide films with the oxygen-to-chromium mass ratio at room temperature. Reprinted with permission from [59]; Copyright 2014, AIP Publishing.

3.5. Metal Alloys

Other classes of nanoparticle-based resistors can be termed metal alloys which can be fabricated by the deposition of thin metal films by either sputtering or electroless plating. These materials are also termed resistive alloys. Among these alloys, the most prominently used alloys are NiCr, NiCrAlSi, CrSi, TiN_xO_y, and TaN_x. These resistors have also been made commercially available by some companies such as Gould and Ohmega. Nichrome (NiCr) resistors have been widely studied in terms of power handling, thermal performance, adhesion, and etching resolution. NiCr can be alloyed with Al and Si to improve thermal stability and reduce TCR, hence forming NiCrAlSi. A thin film of NiCr and NiCrAlSi can be deposited on the copper films to make an embedded resistor. Sheet resistance values of 25 to 250 Ω/sq can be obtained by varying the sheet thickness [60].

Andziulis et al. have fabricated nano-multilayer resistive films consisting of Cr–Ni–Si material. This multilayer structure consisted of 3–8 nm resistive layers with 1–2 nm sliced barrier insulator layers spaced in between to prevent the vertical coalescence of metal grains. Magnetron sputtering was used to deposit the thin films, and plasma oxidation was used to create the barrier insulator from segregated silicon. The composition of the alloy was 54% Cr, 06% Ni and 40% Si by weight so that enough silicon is present for the formation of the barrier as well as the matrix. The sheet resistance was found to be 300–550 ohm/sq. and the TCR value was in the range from ±2 ppm/K to −60 ppm/K [61].

TaN_x has been widely used as a resistive alloy for embedded resistor applications. The formation of this alloy typically consists of the reactive sputtering of Ta in a nitrogen atmosphere. These alloys can achieve stable resistivities equipped with 250 μΩ·cm with TCR of around −75 ppm/°C [62]. Sputtered TiN_xO_y has been shown to offer comparatively higher resistivity up to 5 kΩ/sq with TCR of ±100 ppm/°C [63].

3.6. Carbon-Based Composites

Carbon-filled polymers are the latest entrants into resistor technology. The advent of nanotechnology has made these materials a possibility. Carbon nanotubes, nano-fibers, carbon black, etc. can be used as fillers in composite materials to manufacture composite resistors. For example, multiwall carbon nanotubes made by chemical vapor deposition were dispersed in an epoxy polymer by 0.01 wt.% to achieve a resistivity in the range of 10^6–10^9 Ω·cm range [64]. Similarly, carbon nanofibres mixed (1% by weight) with epoxy resin which were aligned using the AC field have been reported to show resistivity in the range of 10^6–10^7 [65]. The use of carbon black as a filler (0.12 wt.%) epoxy resin and the application of a static electricity field by metal electrodes resulted in the growth of dendrites

from the anode. The resistance values of the composite ranged from 2×10^3 to 10^{11} Ω·cm and could be controlled by varying the applied voltage and curing temperature [66].

3.7. Embedded Inductors

An inductor is a passive component present in a circuit that is used to store energy in the form of a magnetic field. Inductors form an integral part of the circuitry used in various spheres such as wireless communication (for radio frequency applications), computers, automotives, peripherals, etc. (for power supply). As such, they cover a plethora of functions from acting as amplifiers, filters, regulators to converters, and oscillators, etc. Embedded inductors require a lot of research and development on the performance front before they can be properly incorporated into packaging systems. The major hindrances in the development of embedded inductors include their low-quality factor (Q-factor), high losses, and limitations of proper miniature fabrication techniques [67,68].

Where these losses are of significant concern, air core inductors are used. To achieve high inductance though, magnetic cores exhibiting high permeability are required. Other important factors include high resistance to reduce eddy losses, operation at high frequencies, and low coercivity. Improvement in these factors can result in high inductance, which will in turn lead to a decrease in the number of windings, which could probably lead to miniaturization of the system. The change in properties at the nanoscale could lead to high resistance and high permeability and as such are desirable candidates as a material for fabrication.

The design of the inductor also affects the inductance capacity. Electrical, mechanical properties, and reliability issues are dependent upon the design of the inductor. There is a number of designs available for inductors that have been widely researched. The most important and thoroughly studied of these are spiral inductors because of their simple designs and high efficiency. Solenoid inductors are important for discrete components because of their high inductance and high-quality factor but they suffer from the drawbacks of inefficient packaging and high leakage. Toroidal inductors are used where low leakage currents, high inductance, and low electromagnetic interference are required. Some novel designs have been studied to overcome the traditional drawbacks of inductors; these include inductors with micro slits and surface planarization [69].

Apart from the material issues, the problems plaguing the use of nanomaterials in embedded inductors are the fabrication techniques. The growth of thin films can be achieved using techniques such as sputtering, plasma enhanced deposition, electroplating, chemical vapor deposition, etc. The patterning techniques, though, such as photolithography, micromachining, and ion milling need refining. The frequency characteristics, DC resistance, and inductance can be controlled by patterning. Some recent techniques have been developed for thin film deposition such as spin coating, spin sprayed thin films, etc. [70,71].

New classes of nanomaterials with high permeability are being researched for the fabrication of thin-film-embedded inductors. The reduction in the size might lead to a reduction in losses and stray capacitance. The materials which can operate at high frequencies with lower losses, hence increasing the inductance are the need of the hour. The various classes of magnetic nanomaterials for inductor cores are discussed below.

4. Alloy-Based Nanomaterials for Inductor Cores

4.1. Iron-Based Alloys

Iron-based alloys have been used in low-frequency and high-power inductors owing to lower losses. Nickel–iron-based alloys termed perm alloys can achieve a high range of permeability. Perm alloy is a nickel–iron magnetic alloy, containing 80% nickel and 20% iron. Molybdenum, copper, etc. are added to perm alloy to increase the permeability and reduce coercive losses. Perm alloy has low magneto crystalline anisotropy and magnetostriction which helps it to achieve high permeability. Yang et al. have developed on-chip planar inductors using nickel–ion permalloy ($Ni_{80}Fe_{17}Mo_3$) of sub-100 nm in diameter to increase the inductance while maintaining the magnetic performance for high-frequency

circuitry [72]. Zhao et al. have developed permalloy–SiO_2 granular films with induced anisotropy using multilayer alternate sputtering with different power. The films were synthesized with different metallic volume fractions and exhibited excellent soft magnetic properties with high resistivity. Soft magnetic properties were directly dependent upon the metallic volume fraction whereas resistivity was inversely dependent upon it [72].

4.2. Cobalt-Based Cores

Magnetostriction can be reduced to a much higher extent by using cobalt-based alloys. Soft magnetic Co-based granular films possess properties such as high saturation magnetization, high anisotropy, and high resistivity. Soft magnetic properties of the sputtered films are only found in limited composition ranges and require low sputter pressure. Co–Al–O and Cr–Zr–O are the only oxide alloys that are suitable for inductor applications. Co–Al–O films exhibited a resistivity of 500–1000 μΩ·cm, a magnetic flux of about 80 Oe, and B_s of about 10 kG. With the addition of palladium, Co–Al–Pd–O, the soft magnetic properties and H_k value of the film were significantly improved, with H_k more than 180 Oe [73]. Nanogranular Co–Al–O films with a maximum resistivity of 110 mΩ·cm were fabricated by Amiri et al. These films were deposited by using pulsed dc reactive sputtering of a $Co_{72}Al_{28}$ target in an oxygen/argon ambient. The average grain size was found to be 80 nm. The effect of deposition power on resistivity and permeability of films showed that resistivity increase is associated with a decrease in coercivity but is only achievable at lower permeability and higher relaxation losses [74].

Co–Zr–O alloys exhibit preferable properties on water-cooled substrates which makes them suitable for embedded inductor applications. Ohnuma et al. reported the fabrication of Co–Zr–O nanogranular films using rf reactive sputtering in argon and oxygen ambiance. The least amount of coercivity was obtained at 55% and 70% of cobalt. The films near $Co_{60}Zr_{10}O_{30}$ were reported to have a value of anisotropy at 150 Oe, saturation magnetization (H_k) values of 9 kG, coercivities lesser than 3 Oe, and resistivity more than 1000 μΩ·cm. These films exhibited an excellent response of permeability to high frequency. The ferromagnetic resonance frequency values were exceeded 3 GHz [75].

Lu et al. have developed a 30 MHz power inductor utilizing nanogranular material soft magnetic material Co–Zr–O by sputtering on a polyimide substrate. The inductor was able to achieve an inductance of 470 nH and Q of 67, which was professed to double using process improvements [76]. Multilayer Co–Zr–O/ZrO_2 thin films have been used by Yao et al. to improve the performance of the magnetic core and reduce the eddy current loss. V groove inductors were fabricated on Si substrate using sputtering techniques. The inductors exhibited an inductance of 3.4 nH in a range of 10 to 100 MHz, a dc resistance of 3.83 mΩ, a quality factor of up to at least 50, and can be applied in the manufacturing of high-power-density high-efficiency dc-dc converter devices [77].

Nitrides of Co alloys offer much wider compositional ranges for anisotropy but usually exhibit higher coercivities and lower permeabilities. Co–Al–N films were prepared by the rf-sputtering method to obtain soft magnetic properties at high frequencies by Kijima et al. The films were composed of Co nanogranules of 3–5 nm dispersed in the AlN matrix. Ferromagnetic properties were obtained in the range of compositions with cobalt content from 47–80 at.%. The films exhibited high coercivity in the range of 20–50 Oe and showed perpendicular magnetic anisotropy. The permeability of $Co_{80}Al_{14}N_6$ film was constant up to 1 GHz and ferromagnetic resonance frequency (FMR) was at around 1.2 GHz [78].

Cao et al. fabricated Co–HfN nanogranular films with varying Co content exhibiting anisotropy over a wide composition range. The films were composed of crystallized Co nanogranules dispersed in an amorphous HfN matrix. The coercivity was in the range of 15–75 Oe. $Co_{58}Hf_{14}N_{28}$ films displayed a permeability of 40 and a ferromagnetic resonance frequency (FMR) of 2 GHz [79].

4.3. Iron-Cobalt-Based Cores

In accordance with the Pauling—Slater curve, Fe–Co alloys have the highest magnetization compared to all the other iron alloys. These alloys exhibit a high magnetization saturation value of more than 20 kG. CoFeN films with high saturation magnetization of 24 kG, anisotropy of about 20 Oe, and low coercivity of about 1 Oe have been prepared by Sun et al. [80]. CoFeN native oxide films prepared using rf reactive magnetic sputtering in argon and nitrogen ambiances were demonstrated by Ha et.al. These films exhibited low coercivity below 1 Oe and magnetization of almost 22 kG. The anisotropy field was found to be as high as 67 Oe and consequently, the FMR value increased to 3 GHz [81]. This decrease in coercitivity was due to the addition of nitrogen. Similarly, the addition of Si or Ni can also lead to a decrease in coercivity. (CoFe)–Si–O/Si–O multilayer nanogranular magnetic thin films were produced on SiO_2/Si substrates using inductively coupled rf sputtering by Ikeda et al. The ratio of the optimized multilayer structure in terms of the CoFe monolayer to the Si-O layer was found to be 6:1 nm. This film exhibited excellent soft magnetism performance in high-frequency regions. The permeability was found to be 200, the resistivity was found to be 2.2 mΩ·cm and FMR was about 2.86 GHz [82]. Ge at al. fabricated $(Fe_{65}Co_{35})_x(SiO_2)_{1-x}$ granular films by magnetron sputtering. The films were composed of $Fe_{65}Co_{35}$ particles uniformly dispersed in an amorphous SiO_2 matrix. When the range of the x value was from 0.7 to 0.5, the films exhibited a small coercivity value of less than 4 Oe and resistivity up to 5.48×10^3 μΩ·cm. The minimum coercivity value was found to be 1.7 Oe with a resistivity of 2.86×10^3 μΩ·cm at x equaling 0.57. The real permeability of the sample was found to be 170 and the FMR frequency was about 2.4 GHz [83].

Kim et al. have studied the effect of the addition of boron on the magnetic properties and high-frequency characteristics Fe-Co alloys. Boron was added to Fe_7Co_3-based thin films and it was found that the addition of boron resulted in an increase in anisotropy, resistivity, and a decrease in coercivity without any loss of saturation magnetization. This increase was found to be dependent upon grain size, grain morphology, and orientation. $Fe_{55}Co_{28}B_{17}$ displayed a ferromagnetic resonance frequency of 3.3 GHz and a linear effective permeability of 350 up to 2 GHz [84].

Fe–Co–Zr–O alloys have been found to possess high magnetic fluxes and as such can be used for inductor cores. Fe–Co–Zr–O films have been designed by Ohnuma et al. using reactive sputtering under oxygen–argon ambiance, utilizing Fe-Co-Zr alloy. The films consisted of base-centered cubic Fe-Co nanoparticles with nanoparticles of ZrO dispersed in between. These films exhibit a high magnetic flux density of 23 kG and low coercivity which was attributed to ZrO nanoparticles mediated inhibition of growth of Fe–Co. The process parameters of the fabrication process must be controlled strictly in order to maintain the high magnetic saturation since the increase in the value of oxides could prove unfavorable [85].

(Co–Fe)–Al–O nanogranular thin films have been found to have a large resistivity, a high saturation magnetization, and excellent high-frequency properties making them an attractive option for inductor cores. Sohn et al. reported Co-Fe-Al-O nanogranular thin film fabrication using rf magnetron sputtering in an argon-oxygen atmosphere to produce base-centered cubic Co-Fe particles lesser than 5 nm in the Al-O matrix. These films consistently produced high resistivity up to 400 μΩ·cm, a saturation magnetization of 16 kG, and an anisotropy field of 45 Oe. The high-frequency magnetic properties were found to be excellent which can be gauged by a high FMR value of 2.3 GHz and a real permeability value of 315 [86]. Ha et al. have studied the effect of thickness in the range of 50 to 1200 nm upon the high-frequency characteristics of (Co–Fe)–Al–O soft magnetic thin films. The coercivity and anisotropy fields of these films are dependent upon the film composition and the roughness of the surface. The resistivity of these films increased with the decrease in the grain size and increase in the oxide volume. The films were composed of a multi-phase structure consisting of α-CoFe (1 1 0), and α-CoFe (2 1 1) with minor phase CoFe–oxides and Al_2O_3 as the matrix. The effective permeability of this film was more than

1000 and was found unvarying up to 700 MHz while the film thickness remained under 1000 nm. The film exhibited excellent high-frequency properties owing to high resistivity and high anisotropy [87].

4.4. Ferrite Nanomaterials for Inductor Cores

The condition of high resistivity requirement for fabrication of inductors can be easily sated using ferrite materials. Ferrites are the compounds of transition metals with oxygen that are ferromagnetic but nonconductive [88]. Soft ferrites having low coercivity are used for inductor cores. Ferrite materials possess high ferromagnetic resonance frequency, and low imaginary permeability and can increase the Q factor in inductors in the high-frequency range. Ferrite-based polymer composites are being researched since the traditional ceramic-based substrates require a very high temperature for processing. At the nanoscale dimensions, the transport, mechanical and electrical properties are dependent on the nanograin boundaries rather than the material and exhibit themselves differently as compared to the bulk material. The major use of ferrites is in radio frequency circuits for receiving and transmission [88].

Ni–Zn–Cu and Co_2Z (spinal and magnetoplumbite, respectively) nano-powders prepared using the sol-gel method have been used for integration with a single layer and multilayer on-chip conductor. The maximum inductance gain value was found to be 21% for Co_2Z and 35% for Ni–Zn–Cu in the 10 GHz range in a single layer on-chip inductor integrated with ferrite nanomaterial whereas, for multilayer plus ferrite, the maximum inductance gain was 20 and 25%. The increase in Q factor corresponding to the single layer was 100 and 160% for Co_2Z and Ni–Zn–Cu, respectively, in the 3 GHz whereas the Q factor increase for the multilayer inductor was 40 and 50% for the same. Integration of a solenoid inductor with nanomaterial led to an increase in inductance by 63 and 168% by Co_2Z and Ni–Zn–Cu, respectively, at frequency ranges more than 20 GHz. At high frequencies, the Q factor decreases but at lower frequencies, the gain is 71 and 157% with Co_2Z and Ni–Zn–Cu at 100 MHz [88]. Inductance and Quality factors for various layers of an inductor with ferrite nanomaterial are shown in Figure 6.

Ni–Zn–Cu ferrite nanoparticles-magnetic-core has also been used by Ni et al. in RF ICs. Vertical magnetic cores with multiple-layer stacked-spiral structures were designed to realize compact inductive devices in RF ICs. This design obtained a high L-density of over 700 nH/mm^2 as well as an 80% chip size reduction with reference to planar inductors. The high performance of the inductor was dependent on both the material and the design [89].

Nano-granular $Zn_xFe_{3-x}O_4$ ferrite films have been fabricated on an Ag-coated glass substrate using dimethylamine borane complex -DMAB-Fe $(NO_3)_3$-Zn $(NO_3)_2$ solution. The composition of this film was dependent upon the x value ranging from 0 to 0.99. As the x changes, the microstructure of the film varies from non-uniform nanogranules to fine and uniform nanogranules of 50–60 nm in size. The saturation magnetization was found to be increasing from 75 emu/g to108 emu/g when the x varied from 0 to 0.33. From 0.33, it decreased constantly till reaching 5 emu/g at the x value of 0.99. The coercivity decreased steadily from 116 to 13 Oe [90].

4.5. Novel Nanomaterials for Inductor Cores

Recently, carbon nanotubes, nanofibers, nanowires, etc. have been used to create composite polymers for high Q nano inductor applications. Carbon nanotubes (CNT) are preferable for such applications due to their unique interconnecting properties which exhibit lower skin effects as compared to copper interconnects and the resistance of CNT interconnects remains the same even at a high frequency. The inductors made of CNT have several theoretical merits. The magnetic field induced in CNT is 1000 times larger as compared to copper wire and therefore the inductance is quite large. The inductors fabricated from CNTs are smaller as compared to traditional inductors in ICs since they can be bent [91]. Multiwalled carbon nanotube (MWCNT) inductors or single-walled carbon nanotube (SWCNT) bundles have been fabricated and researched by several researchers.

The interconnect properties, and electrical and magnetic properties of MWCNTs have been found to be quite high as compared to copper wires. All the research points towards higher inductance, higher Q factor, and lower losses as compared to conventional copper wires [92–97].

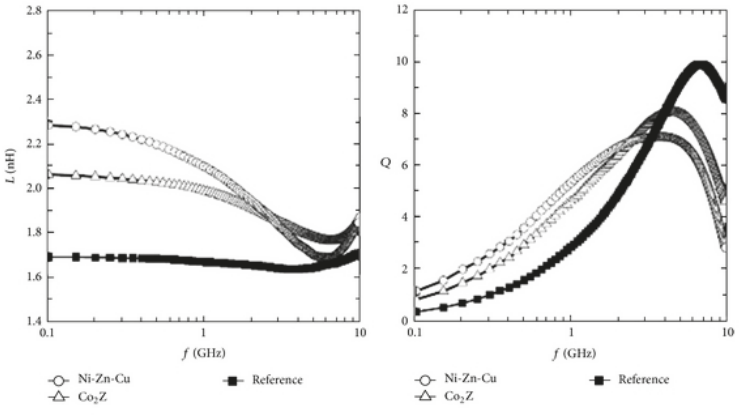

(**a**)

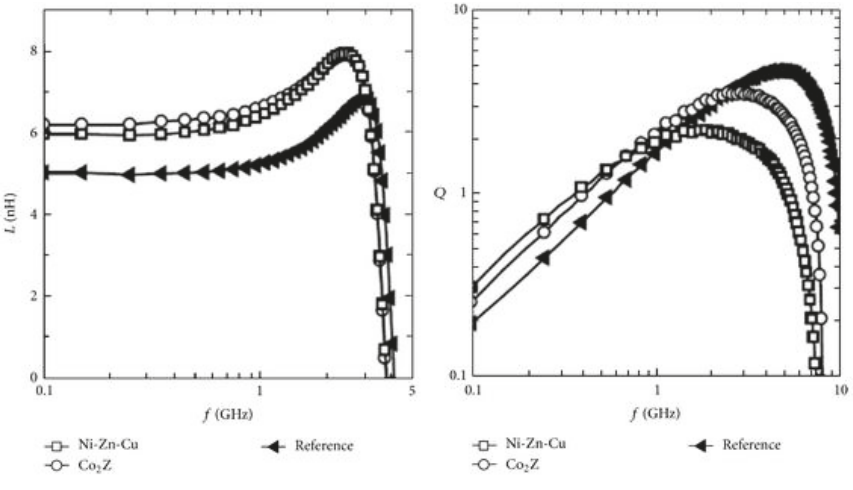

(**b**)

Figure 6. *Cont.*

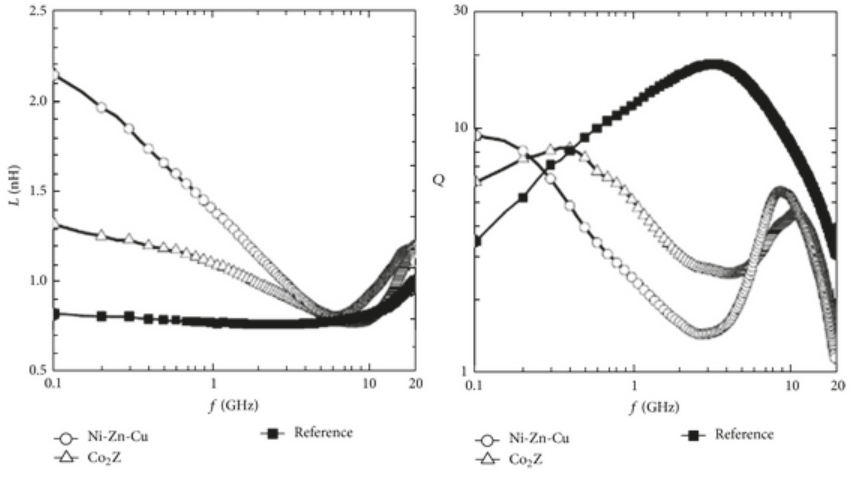

(**c**)

Figure 6. Inductance and Quality factor for (**a**) single layer, (**b**) multilayer, and (**c**) solenoid inductor with ferrite nanomaterial. Reprinted with permission from [88].

A novel design of MWCNT-based stacked inductors has been described by Bruce C. Kim. The MWCNT-based embedded rf inductors were fabricated on silicon and ceramic substrate which will provide high inductance and quality factors [93]. A high Q nanoinductor based on MWCNT and an introductory layer of nano composite film ($Cu/CoFe_2O_4$) exhibited an inductance of 6.25 nH, with a Q factor of 186 at 2.4 GHz. The maximum inductance and maximum Q factor were found to be 6.6 nH and 440, respectively, and the chip area was reduced by 25% as compared to conventional microscale inductors [97]. Figure 7 shows the inductance and Q factor of the MWCNT inductor with respect to frequency. Wiselin et al. have fabricated a spiral inductor made of carbon nanofibres exhibiting an inductance of 4 nH at 1.2 GHz and a Q factor of 40.5. The self-resonant frequency of the designed inductor is predicted to be in the range of 20 GHz to 30 GHz and since the energy loss is low, the inductor can be used in high-frequency applications [98].

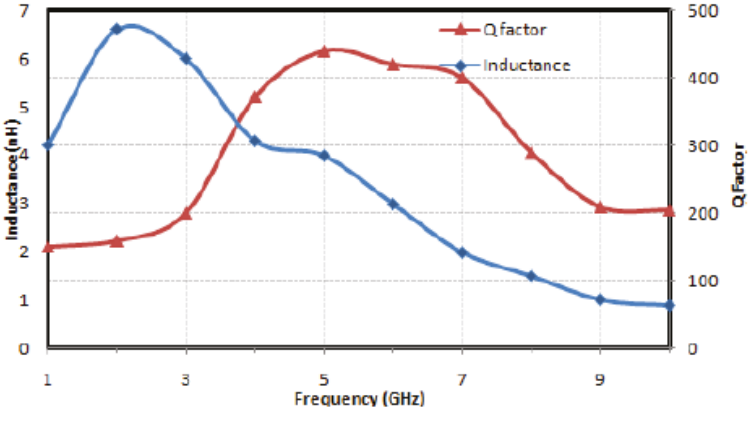

Figure 7. Inductance and Q factor of MWCNT inductor with respect to frequency. Reprinted with permission from [97].

Inductors based on nanowires using nanoporous anodic alumina as substrates have been researched by Spiegel et al. and Hamoir et al. [99,100]. Both have used ferromagnetic Ni nanowires to increase the inductance and quality factor of the inductors. Hamoir et al. have shown a 30% increase in the inductance value and a 23% increase in the quality factor compared to other such ferromagnetic inductors [100]. Spiegel et al. have contrasted the quality factor to that of the inductor built on non-magnetic Si and found the anodic alumina substrate-nanowire-based inductor to be far superior under the FMR frequency. Tunability to magnetic field increases the frequency range and also increases the permeability in the lower frequency ranges [99].

Magnetic nanocomposite pastes have also been used for high-frequency properties. Silica-coated cobalt– benzo–cyclo–butane (BCB) and Ni–Zn ferrite epoxy composites have been used to fabricate inductors. These nanocomposites were screen printed onto FR4 substrates and were then patterned using an etch-back process to fabricate inductors. Co–silica–BCB nanocomposite paste was found to have high permittivity and permeability in the range of 5–10 which makes it a candidate for miniaturized antenna fabrication. Inductors made up of Ni–Zn ferrite–epoxy composites exhibited high permeability in the range of 5–15 at low MHz frequencies and 2.5–3 at higher GHz frequencies. The quality factor, Q, was found to be more than 100 for ferrite-epoxy composite samples [101].

5. Nanomaterials for Interconnect Technology

The role of interconnect in the electrical industry is to connect the active and passive components to the substrate and to facilitate the power supply, and signal transmission among each other, etc. [102]. Traditionally, lead-containing solders most importantly, eutectic tin/lead (Sn/Pb), have been used for electronic packaging owing to their low melting temperatures and good wetting characteristics on a variety of substrates. Chip scale packages, flip chip technologies, etc. are being currently used for interconnections. Apart from the inherent toxicity of lead-based solders, other problems such as incompatibility with miniaturization due to issues of fabrication techniques are making the use of traditional solders difficult. Therefore, there is a need for the development of novel materials which can serve as interconnect in the new upcoming packaging technologies to further increase the miniaturization of the devices. The two major alternatives that have been fueled by the advent of nanotechnology are lead-free solders and polymer-based-electrically-conductive adhesives (ECA) [103,104].

5.1. Nanoparticle-Based Lead-Free Solder

The major difficulty with lead-free solders is the higher melting temperature required for such solders. This high processing/melting temperature leads to high reflow temperature which in turn builds up the stress and promotes other defects. Nanoparticles provide an alternative to overcome this problem since the particle size in the nanometer range potentially offers a chance for decreased temperature coupled with increased mechanical strength. The addition of nanoparticles to conventional solders may improve their properties. A number of alloys have been considered for the development of lead-free solders mainly involving Sn–Cu, Sn–Ni, and Sn–Ag [105].

Sn–Ag–Cu alloys have been researched extensively for this application. Several researchers are working on reducing the temperature of these alloys either by tinkering with the composition or by developing different fabrication techniques which affect the size dependency of the melting point. Gao et al. have developed a Sn–Ag–Cu lead-free solder alloy having an equivalent melting temperature to that of the Sn–Pb alloy. The nanoparticles in this study were prepared using the consumable direct arc current technique and the nanoparticles developed were in the range of 15–60 nm with an average being 30 nm. This alloy exhibited a melting onset temperature of the nanoparticles of the Sn–Ag–Cu solder as low as 179 °C which is comparable to eutectic Sn–Pb alloys which have melting temperatures in the range of 180–190 °C. Although some nanoparticles did not melt at low

temperatures and could potentially be detrimental to this approach, the work nonetheless presents a novel way of reducing the melting temperature [106].

Similarly, Zou et al. have studied melting point depression in lead-free Sn–3.0Ag–0.5Cu (wt.%) solder alloy by reducing the size of the particles produced by the direct arc current technique. The melting temperature of both bulk and nanoparticles was examined and the melting point of nanoparticles having an average size of 30 nm showed a depression in the value by 10 °C as compared to bulk alloy [107].

The addition of cobalt (Co) and nickel (Ni) to Sn–Ag–Cu increases the growth of Cu_6Sn_5 but reduces the growth of Cu_3Sn. The addition of both the particles results in the reduction of the interdiffusion coefficient in Cu_3Sn but had no effect on the melting point of the alloy. These particles did not increase the intermetallic compound thickness and reduced Kirkendall voids, consequently increasing the solder strength and drop test performance. The addition of platinum (Pt) has also been associated with increased drop test performance [108,109].

Jiang et al. have studied the size dependency of the melting point in 96.5Sn–3.5Ag alloys. They used a low-temperature chemical reduction method to synthesize variously sized Sn–Ag alloys. Surface stabilizing agents were used to avert the oxidation of the synthesized particles since oxidation does not allow a reduction in temperature. A melting point as low as 194 °C was achieved when the diameter of nanoparticles was around 10 nm. The solder paste composed of synthesized Sn–Ag nanoalloy was used for the wetting test on the Cu substrate and it exhibited a characteristic Cu_6Sn_5 intermetallic compound formation. This demonstrated the possibility of Sn–Ag alloy being used as a low-temperature lead-free solder [110] as shown in Figure 8.

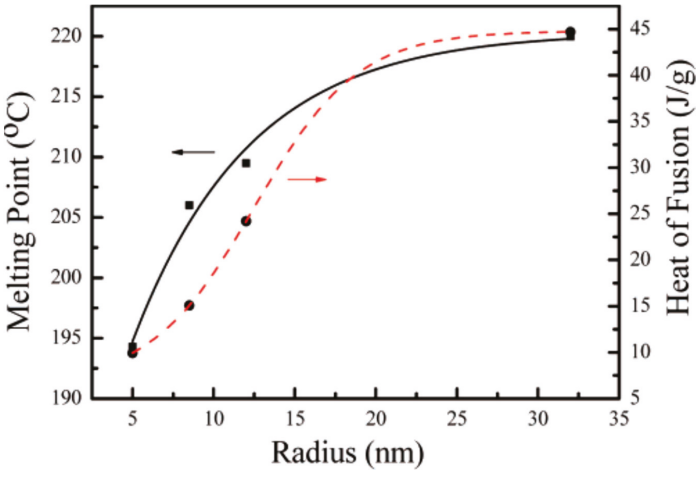

Figure 8. Melting point: heat of fusion dependence on the radius of the synthesized Sn–Ag nanoparticles. Reprinted with permission from [110]; Copyright 2007, American Chemical Society.

Sn–Co–Cu alloy has been developed to overcome the cost of the Sn–Ag–Cu/Sn–Ag alloys. It is being perceived as a cost-effective alternative to the Sn–Ag–Cu alloys. It also suffers from the problem of a high melting point. Sn–0.4Co–0.7Cu (wt.%) lead-free solder alloy was studied by Zou et al. with the aim of decreasing the melting point of the alloy by using nanosized particles. On using the nanoparticle-sized grains from 10 to 50 nm in the alloy, the melting temperature of the alloy was reduced by 5 °C as compared to the bulk alloy. The depression in the melting point was attributed to the increase in the particles' free energy caused by the reduction in particle size [111].

Although a lot of research has been performed on nanoparticles-based lead-free solder materials, their mechanical properties, reliability studies, and processability in packaging

technologies still need further elucidation and as such, still, a lot of research is required before this solder replaces the conventional alloys and becomes a reality in the miniaturized digital world.

5.2. Electrically Conductive Adhesives

Another class of interconnects that is being researched widely is called electrically conductive adhesives (ECA) [112]. These consist of organic or polymeric matrices which bind metal fillers and form nanocomposites. The metal fillers conduct the electricity and are responsible for the electrical properties, whereas, the matrix is responsible for the mechanical properties. Therefore, ECA provides easy access to controlling the properties of the final product. These adhesives have several advantages over conventional solders such as low processing temperature, lesser fabrication steps, and hence less cost, and fine pitch capacity owing to the presence of conductive fillers. However, they also suffer from a number of drawbacks such as limited electrical and thermal conductivity, a lack of reliability, and poor mechanical strength, comparatively [112,113]. On the basis of the filler loading volume, ECAs are segregated into three parts, isotropically conductive adhesives (ICA): those which provide electrical conductivity in all the three coordinates (x,y,z) due to very high filler content near their percolation threshold, anisotropically conductive adhesives (ACA): those which provide conductivity in just one direction (z-axis) owing to low filler loading and, nonconductive adhesives (NCA): those which provide conductivity in one direction (z-axis) owing to the lack of filler material [114] as shown in Figure 9.

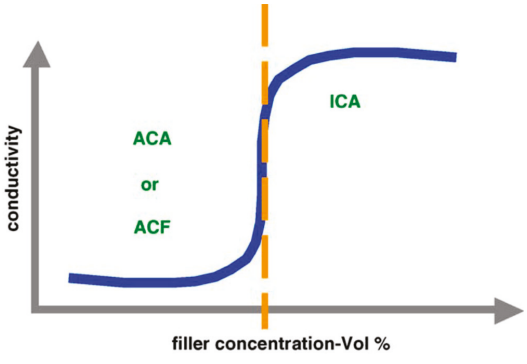

Figure 9. Curve representing the relationship conductivity and filler concentration with respect to percolation threshold. Reprinted with permission from [115]; Copyright 2006, Elsevier.

6. Isotropically Conductive Adhesives (ICA)

6.1. ICAs with Silver Nanowires

ICAs are composed of polymer matrix and conductive filler. Thermosetting and thermoplastic materials are generally used as a polymer. Thermoset epoxies are the most common matrices due to their physical and mechanical properties and thermoplastics are added where strengthening is required for the matrix. The conductive fillers include metals like silver, gold, nickel, etc., and carbon-based materials in different morphologies [116,117].

Wu et al. have studied ICA using Ag nanowires as the conductive filler and its properties were compared with conventional ICAs using 1 µm Ag particles and 100 nm Ag particles as the filler. At low filler volumes of Ag nanowires, ICA exhibited lower bulk resistivity and similar shear strength as compared to ICA filled with micrometer and nanometer-sized particles but the shear strength of ICA with particles decreased while trying to match the conductivity of ICA with nanowires. The increase in the conductivity of nanowires was attributed to lower contact resistance, stable network, and tunneling effects [118].

6.2. ICAs with Silver Nanoparticles

Jiang et al. have prepared ICAs filled with silver nanoparticles. To increase the conductivity of the ICA, Ag nanoparticles were treated with various surfactants. The resistivity of the ICA was reduced to 2.4×10^{-4} Ω·cm. The low resistivity was attributed to the sintering of the nanoparticles. In another approach, nanoparticles were surface functionalized using diacids and were then mixed with silver flakes before use as a conductive filler. The use of diacids for surface modification reduced the resistivity to 5×10^{-6} Ω·cm. The decreased resistivity was a consequence of the sintering of silver nanoparticles which was confirmed using morphological analysis [119,120].

6.3. ICAs with Carbon Nanotubes (CNTs)

Multiwalled-carbon-nanotubes (MWCNT) have been used with epoxy resin to formulate ICA. The epoxy-MWCNT composite has a significantly lower percolation threshold as compared to a metal-filled epoxy composite, although, the conductivity of epoxy-MWCNT was of lower magnitude as compared to a metal-filled epoxy composite. The electrical conductivity of the composite is governed by the inherent conductivity and contact resistance of MWCNTs. The shear strength and strength-to-weight ratio of the composite were found to be greater than the metal-filled ICA [121].

Silver-coated carbon nanotubes (SCCNT) have been used as a filler to prepare isotropic conductive adhesives (ICA). The properties of this composite and ICA filled with multiwalled-carbon-nanotubes were compared with 1 μm Ag-filled ICAs. The resistivity value for ICA filled with MWCNTs was found to be 2.4×10^{-4} Ω·cm at 31% loading and at filler content of 28%, SCCNT exhibited the lowest conductive resistivity of 2.2×10^{-4} Ω·cm. ICAs filled with both MWCNT and SCCNT exhibited a high shear strength value of 19.9 MPa on the Al substrate and 18.2 MPa on the Cu substrate [122]. The relationship between bulk resistivity and shear strength of the ICA with the volume content of CNT is shown in Figure 10.

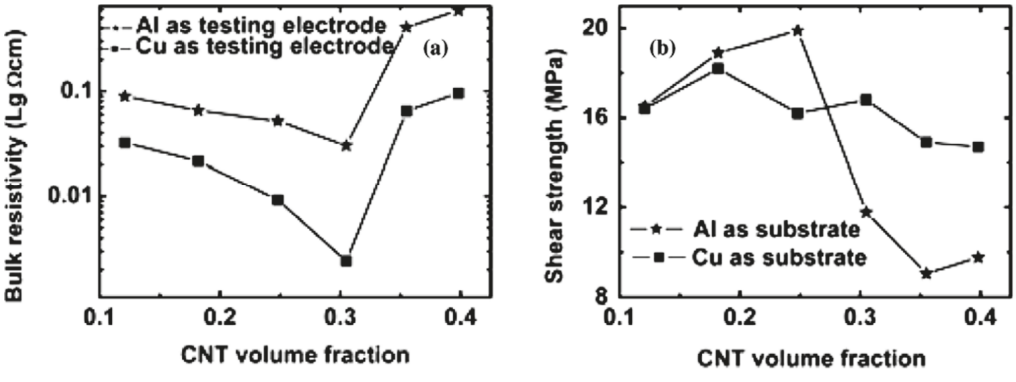

Figure 10. (**a**,**b**) The relationship between bulk resistivity, shear strength of ICA with the volume content of CNT. Reprinted with permission from [122]; Copyright 2007, Elsevier.

7. Anisotropic Conductive Adhesives/Anisotropic Conductive Films (ACA/ACF)

ACA/ACF is generally used to achieve an ultra-high pitch interconnection. These have been used widely for packaging in liquid crystal displays (LCDs). ACA filled with nano-Ag particles has been studied to understand the effect of nano-sized Ag particles on its capacity. ACA filled with nano-Ag, exhibits reduced joint resistance and increased current carrying capacity. This feature was attributed to the sintering of Ag particles well below their melting temperature and consequently increased the interfacial contact area between the Ag particles and bond pads. Treatment of the nano-Ag particles with self-assembled

monolayers of different types helped in further increasing the conductivity by increasing the interfacial contact area to a great extent [123].

Li et al. have used a similar treatment of Ag-nano filler by two SAMs, namely dicarboxylic acid, and dithiol. The treatment increased the conductivity of ACAs significantly and the resistance value was decreased from 10^{-3} Ω to 10^{-5} Ω with SAMs-coated silver fillers. This increase in electrical properties was attributed to the bonding between SAM and Ag-nano fillers, consequently increasing the contact interfacial area [124].

Nonconductive Adhesives (NCA)

Electrically interactive interconnects can be formed by using organic adhesives without any filler. In this method, two contacts are connected using NCA under a moderate value of temperature and pressure. The contact formation depends upon the roughness of the surfaces in contact. Few contact spots are created which allow the current to flow. During the sealing process, pressure is applied, and contacts increase in accordance with the elasticity or flexibility of components. The application of pressure leads to an increase in the interfacial contact area and hence leads to better conductivity. NCA has shown better electrical conductivity than ACA but also suffers from a contact-resistant problem since no metallurgical joints are formed. The nano-sized particles are able to increase the interfacial contact area and reduce the pressure required for fabrication, further increasing the conductivity [115].

8. Conclusions

The miniaturization of digital devices using nano-packaging techniques has been hampered by the challenges of the fabrication of nano-sized passive components and interconnect technology. Recent advances in nanotechnology have made it possible to reduce the size of passives to nano-scale by utilizing unique methodologies and materials, thereby increasing the odds of the development of embedded passives, consequently leading to compact and high-quality devices. The denigration of conventional lead-based soldering technology in aspects of health and electrical properties has led to the development of alternate interconnect technology. Nanotechnology has proven its worth in this sector also via the development of nanomaterials-based interconnects having similar or superior properties compared to traditional techniques. In summary, nanotechnology has started to emerge over and above the limitation of books and labs and thus is influencing our lives.

Author Contributions: Conceptualization, S.D., S.B. and N.A.; methodology, S.B., N.A. and J.G.; software, S.H.; validation, I.K. and A.N.; investigation, S.D., N.A. and S.B.; resources, J.N. and A.R.; data curation, A.N. and S.B.; writing—original draft preparation, S.D., S.B., J.N. and N.A.; writing—review and editing, A.R., I.K., S.H. and A.N.; visualization, J.N. and I.K.; supervision, S.H. and N.A.; project administration, S.H.; funding acquisition, S.H. All authors have read and agreed to the published version of the manuscript.

Funding: The study was funded by the National Natural Science Foundation of China (32150410363), S&T projects of Guangzhou City (project No.: 202102020731), Guangzhou City University Alliance Fundamental Research Fund (Fund No.: 20210210486), and the S&T projects of China's Ministry (QN2021163001L). The authors are also thankful for the funding provided by the German Research Foundation (DFG, Deutsche Forschungsgemeinschaft) as part of Germany's Excellence Strategy—EXC 2050/1—Project ID 390696704—Cluster of Excellence, Centre for Tactile Internet with Human-in-the Loop (CeTI) of Technische University Dresden.

Data Availability Statement: The raw data supporting the conclusions of this article will be made available by the authors, without undue reservation.

Conflicts of Interest: The authors declare that there is no potential conflict of interest.

References

1. Ahmad, N.; Bhatnagar, S.; Ali, S.S.; Dutta, R. Phytofabrication of bioinduced silver nanoparticles for biomedical applications. *Int. J. Nanomed.* **2015**, *10*, 7019.

2. Rogers, J.A.; Someya, T.; Huang, Y. Materials and mechanics for stretchable electronics. *Science* **2010**, *327*, 1603–1607. [CrossRef]
3. Wang, G.L.; Moeen, M.; Abedin, A.; Kolahdouz, M.; Luo, J.; Qin, C.L.; Zhu, H.L.; Yan, J.; Yin, H.Z.; Li, J.F.; et al. Optimization of SiGe selective epitaxy for source/drain engineering in 22 nm node complementary metal-oxide semiconductor (CMOS). *J. Appl. Phys.* **2013**, *114*, 123511. [CrossRef]
4. Woodgate, J.M. 5—Conductors and Insulators, Passive Components, Printed Circuit Boards. In *TV and Video Engineer's Reference Book*; Jackson, K.G., Townsend, G.B., Eds.; Butterworth-Heinemann: Oxford, UK, 1991; pp. 5/1–5/11.
5. Yan, L.; Lopez, C.M.; Shrestha, R.P.; Irene, E.A.; Suvorova, A.A.; Saunders, M. Magnesium oxide as a candidate high-κ gate dielectric. *Appl. Phys. Lett.* **2006**, *88*, 142901. [CrossRef]
6. Ranjan, S.; Dasgupta, N.; Lichtfouse, E. *Nanoscience in Food and Agriculture*; Springer: Cham, Switzerland, 2016.
7. Waldrop, M.M. The chips are down for Moore's law. *Nat. News* **2016**, *530*, 144. [CrossRef] [PubMed]
8. Morris, J.E. Nanopackaging: Nanotechnologies and electronics packaging. In *Nanopackaging*; Springer: Cham, Switzerland, 2018; pp. 1–44.
9. Gregorio, R.; Cestari, M.; Bernardino, F. Dielectric behaviour of thin films of β-PVDF/PZT and β-PVDF/$BaTiO_3$ composites. *J. Mater. Sci.* **1996**, *31*, 2925–2930. [CrossRef]
10. Tohge, N.; Takahashi, S.; Minami, T. Preparation of $PbZrO_3$–$PbTiO_3$ ferroelectric thin films by the sol–gel process. *J. Am. Ceram. Soc.* **1991**, *74*, 67–71. [CrossRef]
11. Cho, S.-D.; Lee, J.-Y.; Hyun, J.-G.; Paik, K.-W. Study on epoxy/$BaTiO_3$ composite embedded capacitor films (ECFs) for organic substrate applications. *Mater. Sci. Eng. B* **2004**, *110*, 233–239. [CrossRef]
12. Rao, Y.; Wong, C. Material characterization of a high-dielectric-constant polymer–ceramic composite for embedded capacitor for RF applications. *J. Appl. Polym. Sci.* **2004**, *92*, 2228–2231. [CrossRef]
13. Dang, Z.-M.; Nan, C.-W.; Xie, D.; Zhang, Y.-H.; Tjong, S. Dielectric behavior and dependence of percolation threshold on the conductivity of fillers in polymer-semiconductor composites. *Appl. Phys. Lett.* **2004**, *85*, 97–99. [CrossRef]
14. Pleşa, I.; Noţingher, P.V.; Schlögl, S.; Sumereder, C.; Muhr, M. Properties of Polymer Composites Used in High-Voltage Applications. *Polymers* **2016**, *8*, 173. [CrossRef] [PubMed]
15. Tanaka, T.; Kozako, M.; Fuse, N.; Ohki, Y. Proposal of a multi-core model for polymer nanocomposite dielectrics. *IEEE Trans. Dielectr. Electr. Insul.* **2005**, *12*, 669–681. [CrossRef]
16. Wurm, F.R.; Weiss, C.K. Nanoparticles from renewable polymers. *Front. Chem.* **2014**, *2*, 49. [CrossRef] [PubMed]
17. Song, K.; Liu, C.; Guo, J.Z. *Polymer-Based Multifunctional Nanocomposites and Their Applications*, 1st ed.; Elsevier: Amsterdam, The Netherlands, 2018.
18. Luo, S.; Sun, R.; Zhang, J.; Yu, S.; Du, R.; Zhang, Z. Synthesis and characterization of Nano $BaTiO_3$/epoxy composites for embedded capacitors. In Proceedings of the 2009 International Conference on Electronic Packaging Technology & High Density Packaging, Beijing, China, 10–13 August 2009; pp. 856–859.
19. Das, R.N.; Lauffer, J.M.; Markovich, V.R. Fabrication, integration and reliability of nanocomposite based embedded capacitors in microelectronics packaging. *J. Mater. Chem.* **2008**, *18*, 537–544. [CrossRef]
20. Das, R.N.; Egitto, F.D.; Lauffer, J.M.; Markovich, V.R. Laser micromachining of nanocomposite-based flexible embedded capacitors. In Proceedings of the 2007 Proceedings 57th Electronic Components and Technology Conference, Sparks, NV, USA, 29 May–1 June 2007; pp. 435–441.
21. Hanemann, T.; Gesswein, H.; Schumacher, B. Development of new polymer–$BaTiO_3$-composites with improved permittivity for embedded capacitors. *Microsyst. Technol.* **2011**, *17*, 195–201. [CrossRef]
22. Xu, J.; Moon, K.-S.; Pramanik, P.; Bhattacharya, S.; Wong, C. Optimization of epoxy-barium titanate nanocomposites for high performance embedded capacitor components. *IEEE Trans. Compon. Packag. Technol.* **2007**, *30*, 248–253. [CrossRef]
23. Osada, M.; Sasaki, T. New dielectric nanomaterials fabricated from nanosheet technique. *ECS Trans.* **2012**, *45*, 3. [CrossRef]
24. Hu, H.; Zhang, F.; Luo, S.; Chang, W.; Yue, J.; Wang, C.-H. Recent advances in rational design of polymer nanocomposite dielectrics for energy storage. *Nano Energy* **2020**, *74*, 104844. [CrossRef]
25. Huang, Y.; Kormakov, S.; He, X.; Gao, X.; Zheng, X.; Liu, Y.; Sun, J.; Wu, D. Conductive polymer composites from renewable resources: An overview of preparation, properties, and applications. *Polymers* **2019**, *11*, 187. [CrossRef] [PubMed]
26. Alemour, B.; Badran, O.; Hassan, M.R. A Review of using conductive composite materials in solving lightening strike and ice accumulation problems in aviation. *J. Aerosp. Technol. Manag.* **2019**, *11*, e1919. [CrossRef]
27. Friedrich, K. Polymer composites for tribological applications. *Adv. Ind. Eng. Polym. Res.* **2018**, *1*, 3–39. [CrossRef]
28. Rao, Y.; Wong, C. A novel ultra high dielectric constant epoxy silver composite for embedded capacitor application. In Proceedings of the 8th International Advanced Packaging Materials Symposium (Cat. No. 02TH8617), Stone Mountain, GA, USA, 3–6 March 2002; pp. 243–248.
29. Qi, L.; Lee, B.I.; Chen, S.; Samuels, W.D.; Exarhos, G.J. High-dielectric-constant silver–epoxy composites as embedded dielectrics. *Adv. Mater.* **2005**, *17*, 1777–1781. [CrossRef]
30. Lu, J.; Moon, K.-S.; Xu, J.; Wong, C. Synthesis and dielectric properties of novel high-K polymer composites containing in-situ formed silver nanoparticles for embedded capacitor applications. *J. Mater. Chem.* **2006**, *16*, 1543–1548. [CrossRef]
31. Qi, L.; Lee, B.I.; Samuels, W.D.; Exarhos, G.J.; Parler, S.G., Jr. Three-phase percolative silver–$BaTiO_3$–epoxy nanocomposites with high dielectric constants. *J. Appl. Polym. Sci.* **2006**, *102*, 967–971. [CrossRef]

32. George, S.; Sebastian, M.T. Three-phase polymer–ceramic–metal composite for embedded capacitor applications. *Compos. Sci. Technol.* **2009**, *69*, 1298–1302. [CrossRef]
33. Lu, J.; Moon, K.-S.; Wong, C. Silver/polymer nanocomposite as a high-k polymer matrix for dielectric composites with improved dielectric performance. *J. Mater. Chem.* **2008**, *18*, 4821–4826. [CrossRef]
34. Li, G.; Yu, S.; Sun, R.; Lu, D. Clean and in-situ synthesis of copper–epoxy nanocomposite as a matrix for dielectric composites with improved dielectric performance. *Compos. Sci. Technol.* **2015**, *110*, 95–102. [CrossRef]
35. Ren, H.; Tang, S.; Syed, J.A.; Meng, X. Incorporation of silver nanoparticles coated with mercaptosuccinic acid/poly (ethylene glycol) copolymer into epoxy for enhancement of dielectric properties. *Mater. Chem. Phys.* **2012**, *137*, 673–680. [CrossRef]
36. Luo, S.; Yu, S.; Sun, R.; Wong, C.-P. Nano Ag-deposited $BaTiO_3$ hybrid particles as fillers for polymeric dielectric composites: Toward high dielectric constant and suppressed loss. *ACS Appl. Mater. Interfaces* **2014**, *6*, 176–182. [CrossRef]
37. Xu, J.; Wong, C. Low-loss percolative dielectric composite. *Appl. Phys. Lett.* **2005**, *87*, 082907. [CrossRef]
38. da Silva, A.B.; Arjmand, M.; Sundararaj, U.; Bretas, R.E.S. Novel composites of copper nanowire/PVDF with superior dielectric properties. *Polymer* **2014**, *55*, 226–234. [CrossRef]
39. Shen, Y.; Lin, Y.; Li, M.; Nan, C.W. High dielectric performance of polymer composite films induced by a percolating interparticle barrier layer. *Adv. Mater.* **2007**, *19*, 1418–1422. [CrossRef]
40. Oldfield, G.; Ung, T.; Mulvaney, P. Au@ SnO2 core–shell nanocapacitors. *Adv. Mater.* **2000**, *12*, 1519–1522. [CrossRef]
41. Shen, Y.; Lin, Y.; Nan, C.W. Interfacial effect on dielectric properties of polymer nanocomposites filled with core/shell-structured particles. *Adv. Funct. Mater.* **2007**, *17*, 2405–2410. [CrossRef]
42. Balasubramanian, B.; Kraemer, K.L.; Reding, N.A.; Skomski, R.; Ducharme, S.; Sellmyer, D.J. Synthesis of monodisperse TiO_2− paraffin core− shell nanoparticles for improved dielectric properties. *ACS Nano* **2010**, *4*, 1893–1900. [CrossRef]
43. Ekanath, D.M.; Badi, N.; Bensaoula, A. Modeling and Simulation of Artificial Core-Shell Based Nanodielectrics for Electrostatic Capacitors Applications. In Proceedings of the Boston COMSOL Multiphysics Conference 2011, Boston, MA, USA, 13–15 October 2011.
44. Wang, D.; Huang, M.; Zha, J.-W.; Zhao, J.; Dang, Z.-M.; Cheng, Z. Dielectric properties of polystyrene based composites filled with core-shell $BaTiO_3$/polystyrene hybrid nanoparticles. *IEEE Trans. Dielectr. Electr. Insul.* **2014**, *21*, 1438–1445. [CrossRef]
45. Guo, Q.; Xue, Q.; Sun, J.; Dong, M.; Xia, F.; Zhang, Z. Gigantic enhancement in the dielectric properties of polymer-based composites using core/shell MWCNT/amorphous carbon nanohybrids. *Nanoscale* **2015**, *7*, 3660–3667. [CrossRef]
46. Xie, L.; Huang, X.; Huang, Y.; Yang, K.; Jiang, P. Core-shell structured hyperbranched aromatic polyamide/$BaTiO_3$ hybrid filler for poly (vinylidene fluoride-trifluoroethylene-chlorofluoroethylene) nanocomposites with the dielectric constant comparable to that of percolative composites. *ACS Appl. Mater. Interfaces* **2013**, *5*, 1747–1756. [CrossRef] [PubMed]
47. Sandborn, P.; Etienne, B.; Subramanian, G. Application-specific economic analysis of integral passives in printed circuit boards. *Electron. Packag. Manuf. IEEE Trans.* **2001**, *24*, 203–213. [CrossRef]
48. Ju, C.-W.; Lee, S.-P.; Lee, Y.-M.; Hyun, S.-B.; Park, S.; Song, M.-K. *Embedded Passive Components in MCM-D for RF Applications*; IEEE: Piscataway, NJ, USA, 2000; pp. 211–214.
49. Codreanu, N.; Ionescu, C.; Svasta, P.; Golumbeanu, V. Advanced methods for electromagnetic investigation of PCB/PWB layouts. In *Advanced Topics in Optoelectronics, Microelectronics, and Nanotechnologies III*; SPIE: Bellingham, WA, USA, 2007; p. 663513.
50. Bhattacharya, S.K.; Tummala, R.R. Next generation integral passives: Materials, processes, and integration of resistors and capacitors on PWB substrates. *J. Mater. Sci. Mater. Electron.* **2000**, *11*, 253–268. [CrossRef]
51. Zandman, F.; Szwarc, J. Non-Linearity of Resistance/Temperature Characteristic: Its Influence on Performance of Precision Resistors. *Vishay Precis. Group Tech. Rep* **2013**, *108*, 1–10.
52. Marin, B.C.; Root, S.E.; Urbina, A.D.; Aklile, E.; Miller, R.; Zaretski, A.V.; Lipomi, D.J. Graphene–metal composite sensors with near-zero temperature coefficient of resistance. *ACS Omega* **2017**, *2*, 626–630. [CrossRef] [PubMed]
53. Maxfield, C.M. Chapter 18—Printed Circuit Boards (PCBs). In *Bebop to the Boolean Boogie (Third Edition)*; Maxfield, C.M., Ed.; Newnes: Boston, MA, USA, 2009; pp. 251–276.
54. Zhao, G.; Huang, X.; Tang, Z.; Huang, Q.; Niu, F.; Wang, X. Polymer-based nanocomposites for heavy metal ions removal from aqueous solution: A review. *Polym. Chem.* **2018**, *9*, 3562–3582. [CrossRef]
55. Lim, S.-K.; Na, S.-H.; Park, E.-M.; Kim, J.-S.; Suh, S.-J. Electrical and structural properties of a Co-sputtered SiO_2-Pt composite thin film for an embedded resistor. *J. Korean Phys. Soc.* **2012**, *61*, 1056–1059. [CrossRef]
56. Park, I.-S.; Park, S.-Y.; Jeong, G.-H.; Na, S.-M.; Suh, S.-J. Fabrication of Ta_3N_5–Ag nanocomposite thin films with high resistivity and near-zero temperature coefficient of resistance. *Thin Solid Film.* **2008**, *516*, 5409–5413. [CrossRef]
57. Felmetsger, V.V. Microstructure and temperature coefficient of resistance of thin cermet resistor films deposited from $CrSi_2$–Cr–SiC targets by S-gun magnetron. *J. Vac. Sci. Technol. A* **2010**, *28*, 33–40. [CrossRef]
58. Liu, X.-S.; Cheng, F.-X.; Wang, J.-Q.; Song, W.-B.; Yuan, B.-H.; Liang, E.-J. The control of thermal expansion and impedance of Al–Zr_2 $(WO_4)(PO_4)_2$ nano-cermets for near-zero-strain Al alloy and fine electrical components. *J. Alloys Compd.* **2013**, *553*, 1–7. [CrossRef]
59. Nash, C.; Fenton, J.; Constantino, N.; Warburton, P. Compact chromium oxide thin film resistors for use in nanoscale quantum circuits. *J. Appl. Phys.* **2014**, *116*, 224501. [CrossRef]
60. Wang, J.; Clouser, S. Thin film embedded resistors. In Proceedings of the IPC Expo 2001, Anaheim, CA, USA, 1–5 April 2001; p. S08-01.

61. Andziulis, A.; Andziuliene, B.; Vaupsas, J.; Zadvydas, M. High stability nano-multilayer resistive films. *Surf. Coat. Technol.* **2006**, *200*, 6212–6217. [CrossRef]
62. Coates, K.; Chien, C.-P.; Hsiao, Y.-Y.; Kovach, D.; Tang, C.-H.; Tanielian, M. Development of thin film resistors for use in multichip modules. In Proceedings of the 1998 International Conference on Multichip Modules and High Density Packaging (Cat. No. 98EX154), Denver, CO, USA, 15–17 April 1998; pp. 490–495.
63. Shibuya, A.; Matsui, K.; Takahashi, K.; Kawatani, A. Embedded TiNxOy thin-film resistors in a build-up CSP for 10 Gbps optical transmitter and receiver modules. In Proceedings of the 51st Electronic Components and Technology Conference (Cat. No. 01CH37220), Orlando, FL, USA, 29 May–1 June 2001; pp. 847–851.
64. Martin, C.; Sandler, J.; Windle, A.; Schwarz, M.-K.; Bauhofer, W.; Schulte, K.; Shaffer, M. Electric field-induced aligned multi-wall carbon nanotube networks in epoxy composites. *Polymer* **2005**, *46*, 877–886. [CrossRef]
65. Prasse, T.; Cavaille, J.-Y.; Bauhofer, W. Electric anisotropy of carbon nanofibre/epoxy resin composites due to electric field induced alignment. *Compos. Sci. Technol.* **2003**, *63*, 1835–1841. [CrossRef]
66. Prasse, T.; Flandin, L.; Schulte, K.; Bauhofer, W. In situ observation of electric field induced agglomeration of carbon black in epoxy resin. *Appl. Phys. Lett.* **1998**, *72*, 2903–2905. [CrossRef]
67. Bajwa, R.; Yapici, M.K. Integrated On-Chip Transformers: Recent Progress in the Design, Layout, Modeling and Fabrication. *Sensors* **2019**, *19*, 3535. [CrossRef]
68. Kobe, O.; Chuma, J.; Jamisola, R.; Chose, M. A review on quality factor enhanced on-chip microwave planar resonators. *Eng. Sci. Technol. Int. J.* **2016**, *20*. [CrossRef]
69. Yamaguchi, M.; Baba, M.; Suezawa, K.; Moizumi, T.; Arai, K.; Haga, A.; Shimada, Y.; Tanabe, S.; Itoh, K. Improved RF integrated magnetic thin-film inductors by means of micro slits and surface planarization techniques. *IEEE Trans. Magn.* **2000**, *36*, 3495–3498. [CrossRef]
70. Bräuer, G. 4.03—Magnetron Sputtering. In *Comprehensive Materials Processing*; Hashmi, S., Batalha, G.F., Van Tyne, C.J., Yilbas, B., Eds.; Elsevier: Oxford, UK, 2014; pp. 57–73.
71. Li, P.H.; Chu, P.K. 1—Thin film deposition technologies and processing of biomaterials. In *Thin Film Coatings for Biomaterials and Biomedical Applications*; Griesser, H.J., Ed.; Woodhead Publishing: Sawston, UK, 2016; pp. 3–28.
72. Yang, C.; Koh, K.; Zhu, X.; Lin, L. On-chip RF inductors with magnetic nano particles medium. In Proceedings of the 2011 16th International Solid-State Sensors, Actuators and Microsystems Conference, Beijing, China, 5–9 June 2011; pp. 2801–2804.
73. Ohnuma, S.; Fujimori, H.; Mitani, S.; Masumoto, T. High-frequency magnetic properties in metal–nonmetal granular films. *J. Appl. Phys.* **1996**, *79*, 5130–5135. [CrossRef]
74. Khalili Amiri, P.; Zhuang, Y.; Schellevis, H.; Rejaei, B.; Vroubel, M.; Ma, Y.; Burghartz, J.N. High-resistivity nanogranular Co–Al–O films for high-frequency applications. *J. Appl. Phys.* **2007**, *101*, 09M508. [CrossRef]
75. Ohnuma, S.; Lee, H.; Kobayashi, N.; Fujimori, H.; Masumoto, T. Co-Zr-O nano-granular thin films with improved high frequency soft magnetic properties. *IEEE Trans. Magn.* **2001**, *37*, 2251–2254. [CrossRef]
76. Lu, S.; Sun, Y.; Goldbeck, M.; Zimmanck, D.R.; Sullivan, C.R. 30-MHz power inductor using nano-granular magnetic material. In Proceedings of the 2007 IEEE Power Electronics Specialists Conference, Orlando, FL, USA, 17–21 June 2007; pp. 1773–1776.
77. Yao, D.; Levey, C.G.; Tian, R.; Sullivan, C.R. Microfabricated V-groove power inductors using multilayer Co–Zr–O thin films for very-high-frequency DC–DC converters. *IEEE Trans. Power Electron.* **2012**, *28*, 4384–4394. [CrossRef]
78. Kijima, H.; Ohnuma, S.; Masumoto, H. High-frequency soft magnetic properties of isotropic Co-Al-N Films. *IEEE Trans. Magn.* **2011**, *47*, 3928–3931. [CrossRef]
79. Sun, N.; Wang, S. Anisotropy dispersion effects on the high frequency behavior of soft magnetic Fe–Co–N thin films. *J. Appl. Phys.* **2003**, *93*, 6468–6470. [CrossRef]
80. Cao, Y.; Zhang, Y.; Ohnuma, S.; Kobayashi, N.; Masumoto, H. Structure and high-frequency magnetic properties of Co-HfN nanogranular films. In Proceedings of the 2015 IEEE International Magnetics Conference (INTERMAG), Beijing, China, 11–15 May 2015; p. 1.
81. Ha, N.; Park, B.; Kim, H.; Kim, C.; Kim, C. High frequency characteristics and magnetic properties of CoFeN/native-oxide multilayer films. *J. Magn. Magn. Mater.* **2005**, *286*, 267–270. [CrossRef]
82. Ikeda, K.; Kobayashi, K.; Fujimoto, M. Multilayer nanogranular magnetic thin films for GHz applications. *J. Appl. Phys.* **2002**, *92*, 5395–5400. [CrossRef]
83. Ge, S.; Yao, D.; Yamaguchi, M.; Yang, X.; Zuo, H.; Ishii, T.; Zhou, D.; Li, F. Microstructure and magnetism of FeCo–SiO_2 nano-granular films for high frequency application. *J. Phys. D Appl. Phys.* **2007**, *40*, 3660. [CrossRef]
84. Kim, I.; Kim, J.; Kim, K.H.; Yamaguchi, M. Effects of boron contents on magnetic properties of Fe-Co-B thin films. *IEEE Trans. Magn.* **2004**, *40*, 2706–2708. [CrossRef]
85. Ohnuma, S.; Fujimori, H.; Masumoto, T.; Xiong, X.Y.; Ping, D.; Hono, K. FeCo–Zr–O nanogranular soft-magnetic thin films with a high magnetic flux density. *Appl. Phys. Lett.* **2003**, *82*, 946–948. [CrossRef]
86. Sohn, J.; Byun, D.J.; Lim, S.H. Nanogranular Co–Fe–Al–O sputtered thin films for magnetoelastic device applications in the GHz frequency range. *J. Magn. Magn. Mater.* **2004**, *272*, 1500–1502. [CrossRef]
87. Ha, N.; Yoon, T.; Kim, H.; Lim, J.; Kim, C.; Kim, C. High frequency permeability of soft magnetic CoFeAlO films with high resistivity. *J. Magn. Magn. Mater.* **2005**, *290*, 1571–1575. [CrossRef]

88. Cai, H.-L.; Zhan, J.; Yang, C.; Chen, X.; Yang, Y.; Chi, B.-Y.; Wang, A.; Ren, T.-L. Application of Ferrite Nanomaterial in RF On-Chip Inductors. *J. Nanomater.* **2013**, *2013*, 832401. [CrossRef]
89. Ni, Z.; Zhan, J.; Fang, Q.; Wang, X.; Shi, Z.; Yang, Y.; Ren, T.-L.; Wang, A.; Cheng, Y.; Gao, J. Design and analysis of vertical nanoparticles-magnetic-cored inductors for RF ICs. *IEEE Trans. Electron Devices* **2013**, *60*, 1427–1435. [CrossRef]
90. Tian, Q.; Wang, Q.; Xie, Q.; Li, J. Aqueous Solution Preparation, Structure, and Magnetic Properties of Nano-Granular $Zn_xFe_{3-x}O_4$ Ferrite Films. *Nanoscale Res. Lett.* **2010**, *5*, 1518. [CrossRef]
91. Tsubaki, K.; Nakajima, Y.; Hanajiri, T.; Yamaguchi, H. Proposal of carbon nanotube inductors. *Proc. J. Phys. Conf. Ser.* **2006**, *38*, 49. [CrossRef]
92. Kim, B.C. Novel design of carbon nanotube based RF inductors. *J. Nanotechnol. Eng. Med.* **2010**, *1*, 011003. [CrossRef]
93. Kim, B.C. Development of CNT-based inductors for integrated biosensors. In Proceedings of the 2009 Annual International Conference of the IEEE Engineering in Medicine and Biology Society, Minneapolis, MN, USA, 2–6 September 2009; pp. 4116–4119.
94. Watts, P.; Hsu, W.; Randall, D.; Kotzeva, V.; Chen, G. Fe-filled carbon nanotubes: Nano-electromagnetic inductors. *Chem. Mater.* **2002**, *14*, 4505–4508. [CrossRef]
95. Nieuwoudt, A.; Massoud, Y. Predicting the performance of low-loss on-chip inductors realized using carbon nanotube bundles. *IEEE Trans. Electron Devices* **2007**, *55*, 298–312. [CrossRef]
96. Plombon, J.; O'Brien, K.P.; Gstrein, F.; Dubin, V.M.; Jiao, Y. High-frequency electrical properties of individual and bundled carbon nanotubes. *Appl. Phys. Lett.* **2007**, *90*, 063106. [CrossRef]
97. Sreeja, B.; Radha, S. Fabrication and characterization of high-q nano-inductor for power electronics. *Bonfring Int. J. Power Syst. Integr. Circuits* **2011**, *1*, 43–47.
98. Wiselin, J.; Suseela, S.B.; Jalaja, B.V.; Ramani, S.D.S.P.; Prasad, R.; Devaraj, S.; Shahul, S.; Swaminathan, S. A Low cost carbon nanofiber based spiral inductor: Inference and implementation. *Adv. Mater. Sci. Eng.* **2014**, *2014*, 384917. [CrossRef]
99. Spiegel, J.; Renaux, C.; Darques, M.; De La Torre, J.; Piraux, L.; Simon, P.; Raskin, J.-P.; Huynen, I. Ferromagnetic inductors on commercial nanoporous anodic alumina. In Proceedings of the 2009 European Microwave Conference (EuMC), Rome, Italy, 29 September–1 October 2009; pp. 582–585.
100. Hamoir, G.; Piraux, L.; Huynen, I. Q-factor improvement of integrated inductors using high aspect ratio ferromagnetic nanowires. *Microw. Opt. Technol. Lett.* **2012**, *54*, 1633–1637. [CrossRef]
101. Xiao, T.; Ma, X.; Zhang, H.; Reisner, D.; Raj, P.; Wan, L.; Tummala, R. Magnetic nanocomposite paste: An ideal high-μ, k and q nanomaterial for embedded inductors in high frequency electronic applications. In Proceedings of the 9th World Multiconference Systemics, Cyberntics Informatics, Orlando, FL, USA, 10–13 July 2005; pp. 10–13.
102. Li, H.; Xu, C.; Banerjee, K. Carbon Nanomaterials: The Ideal Interconnect Technology for Next-Generation ICs. *IEEE Des. Test Comput.* **2010**, *27*, 20–31.
103. Zhao, M.; Zhang, L.; Liu, Z.-Q.; Xiong, M.-Y.; Sun, L. Structure and properties of Sn-Cu lead-free solders in electronics packaging. *Sci. Technol. Adv. Mater.* **2019**, *20*, 421–444. [CrossRef] [PubMed]
104. Shen, J.; Chan, Y.C. Research advances in nano-composite solders. *Microelectron. Reliab.* **2009**, *49*, 223–234. [CrossRef]
105. Amagai, M. A study of nanoparticles in Sn–Ag based lead free solders. *Microelectron. Reliab.* **2008**, *48*, 1–16. [CrossRef]
106. Gao, Y.; Zou, C.; Yang, B.; Zhai, Q.; Liu, J.; Zhuravlev, E.; Schick, C. Nanoparticles of SnAgCu lead-free solder alloy with an equivalent melting temperature of SnPb solder alloy. *J. Alloys Compd.* **2009**, *484*, 777–781. [CrossRef]
107. Zou, C.D.; Gao, Y.L.; Yang, B.; Xia, X.Z.; Zhai, Q.J.; Andersson, C.; Liu, J. Nanoparticles of the lead-free solder alloy Sn-3.0Ag-0.5Cu with large melting temperature depression. *J. Electron. Mater.* **2009**, *38*, 351–355. [CrossRef]
108. Haseeb, A.; Leng, T.S. Effects of Co nanoparticle addition to Sn–3.8Ag–0.7Cu solder on interfacial structure after reflow and ageing. *Intermetallics* **2011**, *19*, 707–712. [CrossRef]
109. Amagai, M. A study of nanoparticles in SnAg-based lead free solders for intermetallic compounds and drop test performance. In Proceedings of the 56th Electronic Components and Technology Conference 2006, San Diego, CA, USA, 30 May–2 June 2006; p. 21.
110. Jiang, H.; Moon, K.-S.; Hua, F.; Wong, C. Synthesis and thermal and wetting properties of tin/silver alloy nanoparticles for low melting point lead-free solders. *Chem. Mater.* **2007**, *19*, 4482–4485. [CrossRef]
111. Liu, J.; Lu, D.; Andersson, C.; Zou, C.; Gao, Y.; Yang, B.; Zhai, Q.; Andersson, C.; Liu, J. Melting temperature depression of Sn-0.4Co-0.7Cu lead-free solder nanoparticles. *Solder. Surf. Mt. Technol.* **2009**, *21*, 9–13. [CrossRef]
112. Aradhana, R.; Mohanty, S.; Nayak, S.K. A review on epoxy-based electrically conductive adhesives. *Int. J. Adhes. Adhes.* **2020**, *99*, 102596. [CrossRef]
113. Kausar, A. 9—Application of Polymer-Based Composites: Conductive Pastes Based on Polymeric Composite/Nanocomposite. In *Electrical Conductivity in Polymer-Based Composites*; Taherian, R., Kausar, A., Eds.; William Andrew Publishing: Norwich, NY, USA, 2019; pp. 255–274.
114. Lu, D.; Wong, C. Electrically Conductive Adhesives (ECAs). In *Materials for Advanced Packaging*; Lu, D., Wong, C., Eds.; Springer: Boston, MA, USA, 2017; pp. 421–468.
115. Li, Y.; Wong, C. Recent advances of conductive adhesives as a lead-free alternative in electronic packaging: Materials, processing, reliability and applications. *Mater. Sci. Eng. R Rep.* **2006**, *51*, 1–35. [CrossRef]
116. Post, W.; Susa, A.; Blaauw, R.; Molenveld, K.; Knoop, R.J.I. A Review on the Potential and Limitations of Recyclable Thermosets for Structural Applications. *Polym. Rev.* **2020**, *60*, 359–388. [CrossRef]

117. Li, Y.; Lu, D.; Wong, C. Isotropically conductive adhesives (ICAs). In *Electrical Conductive Adhesives with Nanotechnologies*; Springer: New York, NY, USA, 2010; pp. 121–225.
118. Wu, H.; Liu, J.; Wu, X.; Ge, M.; Wang, Y.; Zhang, G.; Jiang, J. High conductivity of isotropic conductive adhesives filled with silver nanowires. *Int. J. Adhes. Adhes.* **2006**, *26*, 617–621. [CrossRef]
119. Jiang, H.; Moon, K.-s.; Li, Y.; Wong, C. Surface functionalized silver nanoparticles for ultrahigh conductive polymer composites. *Chem. Mater.* **2006**, *18*, 2969–2973. [CrossRef]
120. Jiang, H.; Moon, K.-S.; Lu, J.; Wong, C. Conductivity enhancement of nano silver-filled conductive adhesives by particle surface functionalization. *J. Electron. Mater.* **2005**, *34*, 1432–1439. [CrossRef]
121. Li, J.; Lumpp, J.K. Electrical and mechanical characterization of carbon nanotube filled conductive adhesive. In Proceedings of the 2006 IEEE Aerospace Conference, Big Sky, MT, USA, 4–11 May 2006; p. 6.
122. Wu, H.; Wu, X.; Ge, M.; Zhang, G.; Wang, Y.; Jiang, J. Properties investigation on isotropical conductive adhesives filled with silver coated carbon nanotubes. *Compos. Sci. Technol.* **2007**, *67*, 1182–1186. [CrossRef]
123. Li, G.Y.; Wong, C. Nano-Ag filled anisotropic conductive adhesives (ACA) with self-assembled monolayer and sintering behavior for high. In Proceedings of theElectronic Components and Technology, Lake Buena Vista, FL, USA, 31 May–3 June 2005; pp. 1147–1154.
124. Li, Y.; Moon, K.-S.; Wong, C. Monolayer-protected silver nano-particle-based anisotropic conductive adhesives: Enhancement of electrical and thermal properties. *J. Electron. Mater.* **2005**, *34*, 1573–1578. [CrossRef]

nanomaterials

MDPI

Review

Comparative Review on the Aqueous Zinc-Ion Batteries (AZIBs) and Flexible Zinc-Ion Batteries (FZIBs)

Md. Al-Amin [1], Saiful Islam [2,*], Sayed Ul Alam Shibly [3] and Samia Iffat [4]

[1] Department of Chemistry, University of Louisville, Louisville, KY 40292, USA
[2] Natural Science (Chemistry), American International University Bangladesh, Dhaka 1229, Bangladesh
[3] Basic Science Department, Primeasia University, Dhaka 1213, Bangladesh
[4] Telephone Shilpa Sangstha Ltd., Gazipur, Dhaka 1710, Bangladesh
* Correspondence: saiful@aiub.edu; Tel.: +880-163-391-4241

Abstract: Lithium-ion batteries (LIBs) have been considered an easily accessible battery technology because of their low weight, cheapness, etc. Unfortunately, they have significant drawbacks, such as flammability and scarcity of lithium. Since the components of zinc-ion batteries are nonflammable, nontoxic, and cheap, AZIBs could be a suitable replacement for LIBs. In this article, the advantages and drawbacks of AZIBs over other energy storage devices are briefly discussed. This review focused on the cathode materials and electrolytes for AZIBs. In addition, we discussed the approaches to improve the electrochemical performance of zinc batteries. Here, we also discussed the polymer gel electrolytes and the electrodes for flexible zinc-ion batteries (FZIBs). Moreover, we have outlined the importance of temperature and additives in a flexible zinc-ion battery. Finally, we have discussed anode materials for both AZIBs and FZIBs. This review has summarized the advantages and disadvantages of AZIBs and FZIBs for future applications in commercial battery technology.

Keywords: aqueous zinc-ion battery; flexible zinc-ion battery; anode and cathode materials

Citation: Al-Amin, M.; Islam, S.; Shibly, S.U.A.; Iffat, S. Comparative Review on the Aqueous Zinc-Ion Batteries (AZIBs) and Flexible Zinc-Ion Batteries (FZIBs). *Nanomaterials* **2022**, *12*, 3997. https://doi.org/10.3390/nano12223997

Academic Editor: Carlos Miguel Costa

Received: 24 September 2022
Accepted: 7 November 2022
Published: 13 November 2022

Publisher's Note: MDPI stays neutral with regard to jurisdictional claims in published maps and institutional affiliations.

1. Introduction

Lithium-ion batteries (LIBs) have attracted much attention to battery technology due to their low weight, high energy densities, and specific power. Unfortunately, LIBs have major drawbacks, such as energy density limits, high cost, toxic nature, and safety issues [1,2]. Therefore, large-scale applications of LIBs are still challenging because of these limitations. However, lead-acid- and nickel-cadmium-based batteries are currently dominant in the present battery energy storage market due to their low cost and durability [1,3–5]. They have limitations such as poor energy densities and environmental problems due to toxic electrodes. Moreover, various alkali metal cations (such as Na^+ and K^+) and multivalent charge carriers (such as Mg^{2+}, Al^{3+}, and Zn^{2+}) have been investigated in aqueous electrolyte-based batteries. For example, aqueous zinc-ion batteries are particularly appealing since Zn has a large natural abundance, a low redox potential, a high theoretical capacity, intrinsic safety, and low toxicity [1,2,5–9].

Aqueous zinc-ion batteries (AZIBs) are facing challenges due to the deteriorating effect of cathode and anode materials [10–15]. Hence, these effects are responsible for lowering the coulombic efficiency and the specific capacity of AZIBs. Scientists are still working to overcome these issues regarding AZIBs [1–3,5–8,15–20]. Additionally, they are giving more attention to modifying cathodes, which can enhance the electrochemical performance. Materials with a spinel or layer structure, such as Mn-based, vanadium-based, and Prussian blue analogous, are attracting attention for modifying electrode materials for AZIBs [11,21–28]. Among them, Mn-based materials have gained a lot of interest in the cathode materials because of their diverse crystal structures, different valence states, and high-voltage platforms [26,29–32]. First, alkaline electrolytes acting as primary electrolytes were used in Mn-based materials in the 1860s. Unfortunately, several challenges appeared in

the alkaline electrolyte system in ZIBs, such as the dendrite and byproducts of the Zn anode resulting in low coulombic efficiency and poor cycle performance. In 1988, Yamamoto et al. used a mild acid $ZnSO_4$ electrolyte in α-MnO_2 to enhance the electrochemical performance, although this approach did not attract much scientific attention [33]. Similarly, Wang et al. have shown exceptional results when they used a moderate acid $ZnSO_4$ electrolyte in α-MnO_2, and it has shown good reversibility and cyclability [34]. However, aqueous zinc-ion batteries (AZIBs) are still under investigation, and the complexity arising from aqueous electrolytes is hindering the creation of highly cyclic stable ZIBs. Scientists are looking for suitable electrolytes in place of aqueous electrolytes to reduce these issues, such as dendrite formation, cathode dissolution, etc. They are considering that electrolytes that have a lesser water content might reduce the parasitic reaction and could improve cyclic stability as well as electrochemical performance.

Flexible zinc-ion batteries (FZIBs) are now being considered a sustainable selection to power portable electronics thanks to the development of aqueous rechargeable zinc-ion batteries (AZIBs) [35–37]. FZIBs with polymeric matrix electrolytes not only have better huge pile capabilities but also have better electrochemical behavior, as they eliminate dendrite formation and cathode dissolution [37–42]. As illustrated in Figure 1, flexible ZIBs have considerable potential for wearable applications due to their qualities such as exceptional flexibility, tolerance to deformation, and compatibility with the traditional textile industry. Several strategies for the fabrication of flexible ZIBs with both energy storage performance and mechanical robustness have been recently developed. However, the development of the strategy of ZIBs is still in its infancy. In this review, we provide recent updates on AZIBs and FZIBs.

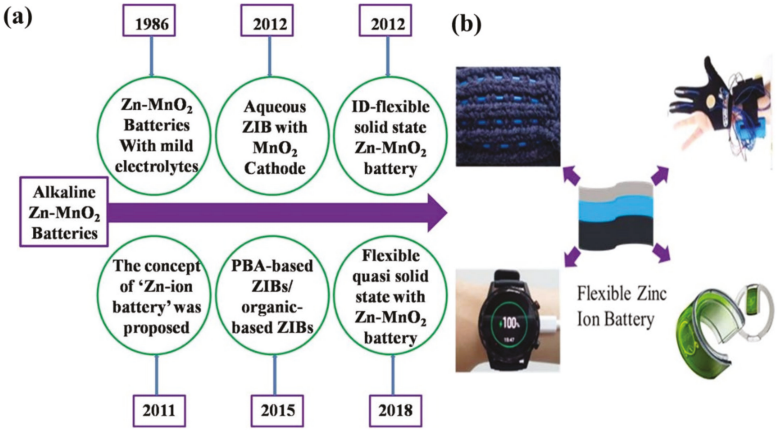

Figure 1. (**a**) A brief history of the development of ZIBs and FZIBs. (**b**) Exciting applications of flexible zinc-ion batteries.

2. Zinc-Ion Batteries (ZIBs)

Zinc-ion batteries consist of Zn metal as an anode and metal oxides as cathodes. Basically, Zn salt is used as an electrolyte for transporting Zn^{2+} ions during charge–discharge [34]. As illustrated in Figure 2a, MnO_2 was used as a cathode, Zn foil was used as an anode, and mild aqueous $ZnSO_4$ solution was utilized as an electrolyte. The reaction mechanism of Zn/MnO_2 is as follows (Figure 2b):

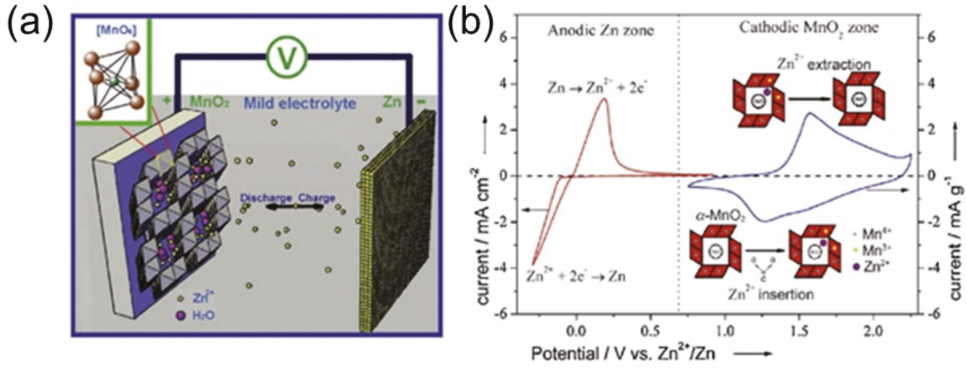

Figure 2. (**a**) A schematic illustration of aqueous ZIBs. (**b**) Zn storage mechanism of Zn/MnO_2 system at anode and cathode sides. Reprinted with permission from Ref. [34]. Copyright 2011 Wiley.

Anode:

$$Zn \leftrightarrow Zn^{2+} + 2e^{-} \quad (1)$$

Cathode:

$$Zn^{2+} + 2e^{-} \leftrightarrow ZnMn_2O_4 \quad (2)$$

Here, Zn stripping and deposition happened at the anode and Zn insertion/extraction occurred at the cathode during the discharge–charge. Wei Sun et al. [43] and Buke Wu et al. [44] have proposed a new reaction mechanism and confirmed the Zn^{2+} and H+ co-insertion mechanism during discharge.

2.1. Advantages of ZIBs over Other Energy Storage Devices

ZIBs have attracted much attention because of their lower cost, high storage capacity, etc. In addition, ZIBs are less flammable than lithium-ion batteries (LIBs). Although sodium-ion and potassium-ion are cheaper than LIBs, they also have flammability issues, like LIBs [1–5]. Above all, ZIBs are a suitable candidate for future-generation battery technology. Unfortunately, several barriers exist in the way of further implementations involving side products (hydrogen production, dissolution, and contact resistance) and zinc dendrite growth at the anode. These issues are hindering the creation of sustainable ZIBs. Hence, developing strategies of anodes and electrolytes and the reaction mechanisms are crucial. These developments could reduce cathode erosion, zinc dendrites' formation, hydrogen evolution, and other issues [7–10]. It is assumed from the literature review of ZIBs that electrolytes and durable cathodes and anodic materials could play a pivotal role in making sustainable ZIBs. As a result, considerably more attention should be directed to electrolyte development technologies to produce greatly extended durability and consistency. As illustrated in Figure 3, the possibility of ZIB over other energy storage systems is because of the high energy density of the Zn batteries. In this section of the review, we will provide a more recent update on ZIBs.

2.2. Zinc-Ion Batteries (ZIBs)—The Electrolytes and the Anode Materials

Zinc anode has issues such as HER (hydrogen evolution reaction), dendrite formation, and shape abnormalities, which could play a significant role in degrading the cyclic stability and performance of ZIBs. These issues lead to a smaller coulombic efficiency. However, the cyclic stability and performance vary depending on the anode materials. Therefore, its performance is still poorer. One of the most popular and successful methods to mitigate adverse reactions and the growth of zinc dendrites is to add additives to electrolytes [11,18,24–26,29,30,46,47]. Two types of additives are generally employed in aqueous ZIBs, organic and inorganic. For

example, organic additives, including polyethyleneimine (PEI), polyethylene glycol (PEG), poly(vinyl alcohol) (PVA), and diethyl ether, can bind on the tips of zinc patches to reduce local current density. Other organic additives such as benzotriazole (BTA), tetrabutylammonium bromide (TBAB), potassium persulfate (KPS), dimethyl sulfoxide (DMSO), benzotriazole (BTA), and ethanol can mostly adsorb on the anode surface, which can considerably reduce species diffusion and strong corrosion resistance. Additionally, some organic additives, such as ethylene glycol (EG), glucose, and DMSO, could impact the solvent evaporation process of solvated Zn^{2+} ions [42,48–54]. For example, the use of vanillin as a bifunctional additive in an aqueous electrolyte to stabilize Zn electrochemistry was reported by Cheng et al. [55]. The Zn anode, which was dipped in 5 mM of vanillin modified with a 2 M $ZnSO_4$ electrolyte, has demonstrated the storage capacity (10 mAh cm^{-2} at 1 mA cm^{-2}), cycling stability (1 mAh cm^{-2} for 1000 h), and coulombic efficiency (99.8%). In Figure 4, a clear effect of vanillin on Zn appeared.

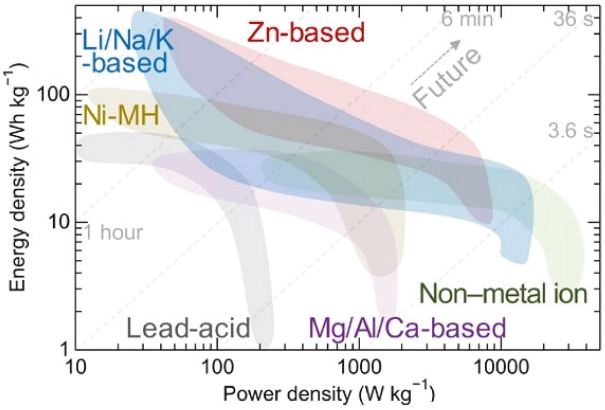

Figure 3. A comparative energy density curve for ZIBs and other energy storage systems. Reprinted with the permission from Ref. [45]. Copyright 2022 Science.

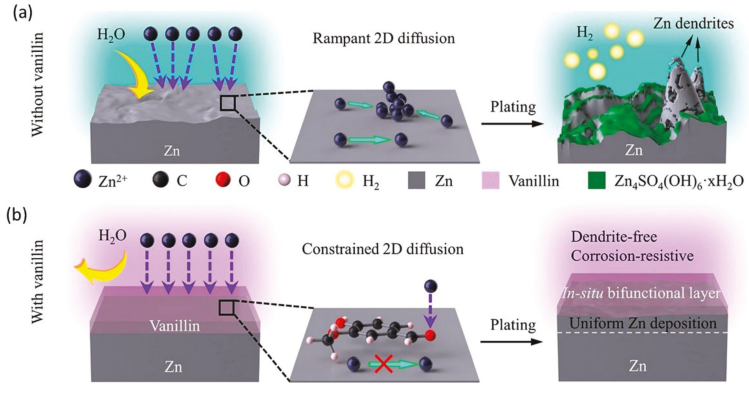

Figure 4. Schematics and bifunctional mechanism of vanillin sustaining Zn electrochemistry: Zn^{2+} diffusion/adsorption and Zn plating characteristics in (**a**) vanillin-free and (**b**) vanillin-containing aqueous $ZnSO_4$ electrolytes are depicted schematically. Reprinted with permission from Ref. [55]. Copyright 2021 American Chemical Society.

Without the vanillin additive in $ZnSO_4$ electrolytes (Figure 4a), the apparent reaction between the aqueous solution and the thermodynamically unstable Zn anode incites parasitic reactions responsible for HER corrosion and a $Zn_4SO_4(OH)_6$ xH_2O byproduct. In addition, the horizontal movement of Zn^{2+} ions can invoke deposition on sporadically

scattered prominent nuclei, which can limit surface energy and surface area, heterogeneous Zn plating/stripping, and promote dendritic development. The vanillin surface could not only cover active Zn from a free water attack through two-dimensional (2D) adsorption, but could also promote perpendicular Zn^{2+} migration and severely curb overgrown 2D diffusion, climaxing homogeneous and dendrite-free Zn building. Similarly, Qin et al. showed a hybrid electrolyte containing graphene oxide as a supplement that boosts consistent electric field distribution and eliminates Zn^{2+} nucleation over-potential, the smooth zinc electrodeposition layer, and reaction kinetics [56]. The symmetric zinc battery with graphene oxide addition consisted of a solid zinc anode that extended around 650 h at 1 mA cm^{-2} and kept a cycle life of 140 h at 10 mA cm^{-2}. A 3D laser microscope was used to study the surface morphology of zinc anodes. In the initial condition, the electric field on the velvety surface of pure zinc foil was disseminated uniformly in the same order, as shown in Figure 5a–i.

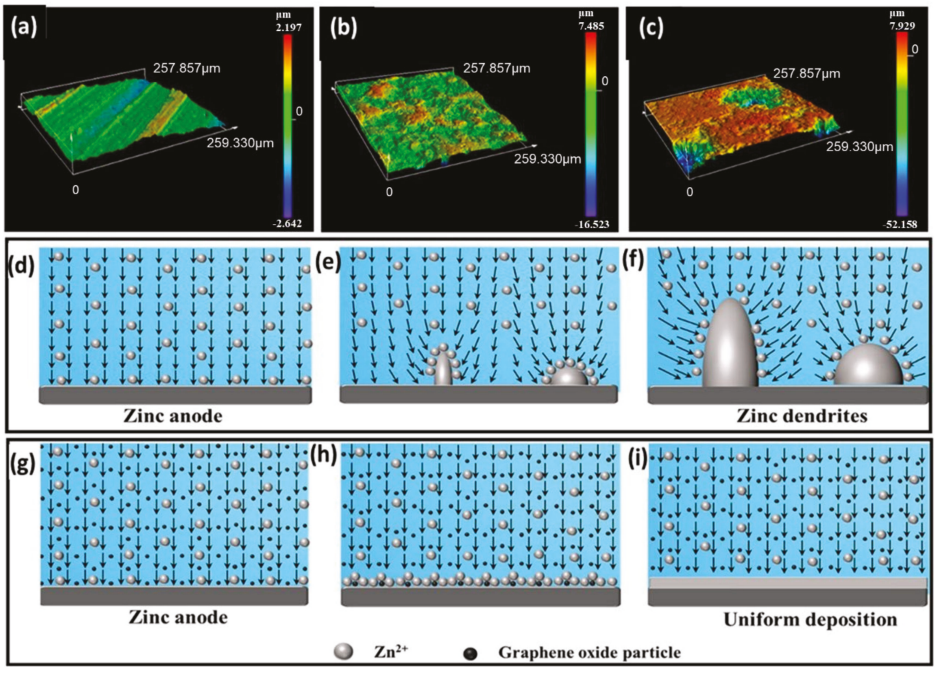

Figure 5. 3D laser images of (**a**) the untouched zinc anode, (**b**) the zinc anode without GO additive, and (**c**) the zinc anode with GO additive after cycling. The electric field dispersal on the zinc anode (**d**–**f**) surface without GO electrolyte additive and (**g**–**i**) with GO electrolyte additive. The vectorial field describes the direction of the electric field. Reprinted with permission from Ref. [56]. Copyright 2021 American Chemical Society.

When Zn^{2+} began to build up from a selected vicinity of the zinc floor, a distinguishable electric-powered subject turned established, and numerous outcomes confirmed that the neighborhood electric-powered subject after the dendrite tip turned into as much as two times that of a starting electrodeposit in the long run, mainly due to the formation of zinc ions within the dendrite tip (Figure 5e). Those indentations or dendrites popped up as purple regions within the 3D laser image (Figure 5b). Besides that, because the electrodeposit has become more potent and has been cut down the center into thinner dendrites (Figure 5f), the depth of the electrical subject ought to attain three instances or more than the preliminary electric-powered subject, indicating that the end effect enhanced until the battery demonstrated excessive impedance. Additionally, because of the inclination to

lessen the floor power and decrease transmission paths, the presently exposed zinc coating has become the ultimate electrodeposition location. Using GO as an electrolyte addition, on the other hand, may completely repair the dendrite problem (Figure 5c). The bonding among GO debris in addition to Zn could not prevent distinguishable electric-powered fields from forming (Figure 5h) and could perhaps simply show the dissemination of the electrical subject; however, it may additionally confirm that charged Zn^{2+} operates right away to the anode floor (Figure 5i), resulting in a steady zinc deposition layer. Additionally, Mantia et al. tested the morphology and kinetics of zinc electrodeposition in a 0.5 M $ZnSO_4$ solution with the use of branched polyethyleneimine (BPEI) as an electrolyte additive [53]. When BPEI is present, the electrodeposited layers undergo modifications from laminated hexagonal huge crystals to a compact layer, not using an essential boom form. Furthermore, it was discovered that deposition of BPEI at the substrate's floor influences the kinetics of zinc electrodeposition and slows grain expansion, favoring nucleation overgrowth. As a result, BPEI guarantees that conductivity is calmly dispersed and that the deposited layer is uniform. Figure 6 illustrates the effectiveness of zinc electrodeposition with 30 and 300 ppm of BPEI, compared to the absence of BPEI. When no additive is introduced, the preliminary electrodeposition performance drops to much less than 75%, then steadily climbs to 88%.

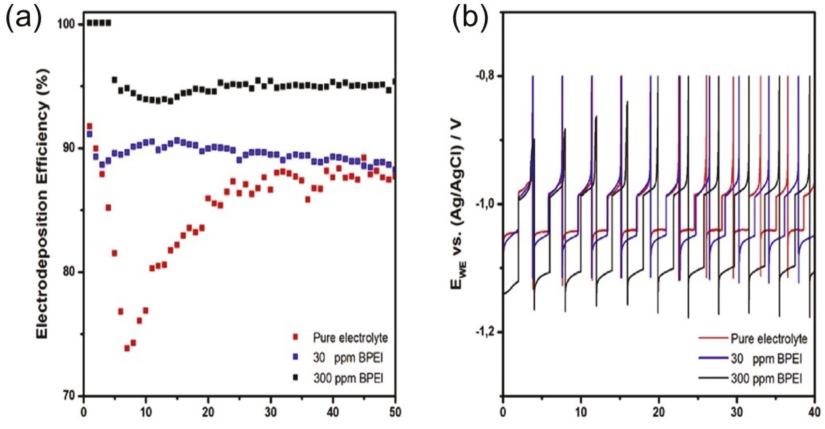

Figure 6. (**a**) Zinc electrodeposition efficiency upon 50 cycles without BPEI, and with 30 and 300 ppm of BPEI as an additive in 0.5 M of $ZnSO_4$. (**b**) Potential variation of the working electrode during zinc deposition and dissolution in different solutions. Reprinted with permission from Ref. [53]. Copyright 2017 Elsevier.

The partial overlaying of zinc by zinc hydroxide or zinc oxide in the seventh cycle is noted to be the cause of this phenomenon. This prevents extra zinc from being electrodeposited, resulting in a vast preliminary over-potential that favors hydrogen formation. The minimum overall performance is observed when 30 ppm BPEI is added, whereby the overall performance is 88%. For the 4 primary cycles, the electrodeposition overall performance is 100% with the presence of 300 ppm BPEI. Following this, the performance is decreased to 95% and remains constant for the trial (Figure 6a). As a result, raising the additive from 30 to 300 ppm can increase the zinc electrodeposition overall performance from 88% to 95%. Furthermore, as proven in Figure 6b, BPEI adsorption does not affect the oxidation over-potential, however it does affect the cathodic over-potential, which might be 10 mV more with the presence of 30 ppm BPEI than with the natural electrolyte. The upward thrust in cathodic over-potential reaches 60 mV in the presence of 300 ppm BPEI.

2.3. Aqueous Zinc-Ion Batteries (AZIBs)—Cathode Materials

Sustainable cathodic materials of ZIBs require the following characteristics, such as a proper structure, excellent structural consistency, ideal working voltage, electrochemical

stability, high energy storage density, and reduced cost and environmental consequences [1–5]. However, there are still several obstacles suppressing the advancement of this field. The most common issues are cathode dissolution byproducts. Scientists are trying to reduce these issues to make sustainable AZIBs. There are several cathode materials, such as manganese-based, vanadium-based, other materials-based, etc. Manganese-based material is a promising cathode material due to its lower cost, low toxicity, low combustible, high abundance, high storage capacity, and high ionic conductivity. Furthermore, the structural properties of MnO_2 (α, β, γ, δ, λ) provide some adequate pathways and surfaces for the transport and accumulation of other metal ions, including Zn ions (Table 1). Chain-type, tunnel-type, and layered-type structures are interconnected to form MnO_6 octahedra as the fundamental structural component by connecting vertices or edges [30,57–60]. These structural versatilities of MnO_2 usually lead to making excellent cathode materials.

Table 1. The recent updates of Mn-based cathode materials.

Cathode Materials	Electrolyte	Cyclability (mAh g^{-1})	Ref.
α-MnO_2	1 M $ZnSO_4$	100 after 100 cycles at 6C (*n*C = a full discharge in 1/*n* h)	[34]
α-MnO_2	1 M $ZnSO_4$	140 after 30 cycles at 10.5 mA g^{-1}	[58]
α-MnO_2–CNT	2 M $ZnSO_4$	100 after 500 cycles at 5000 mA g^{-1}	[61]
α-MnO_2	1 M $ZnSO_4$	130 after 30 cycles at 42 mA g^{-1}	[62]
α-MnO_2	1 M $ZnSO_4$	147 after 50 cycles at 83 mA g^{-1}	[29]
γ-MnO_2	1 M $ZnSO_4$	158 after 40 cycles at 0.5 mA cm^{-2}	[11]
α-MnO_2	1 M $ZnSO_4$	104 after 75 cycles at 83 mA g^{-1}	[26]
V-doped α-MnO_2	1 M $ZnSO_4$	131 after 100 cycles at 66 mA g^{-1}	[63]
α-MnO_2@C	1 M $ZnSO_4$	189 after 50 cycles at 66 mA g^{-1}	[27]
β-MnO_2	1 M $ZnSO_4$	135 after 200 cycles at 200 mA g^{-1}	[12]
β-MnO_2	3 M	135 after 2000 cycles at 6.5C (*n*C = a full discharge of 308 mA g^{-1} in 1/n h)	[64]
PANI-δ-MnO_2	2 M $ZnSO_4$	280 after 200 cycles at 200 mA g^{-1}	[65]
MnO_2	1 M $ZnSO_4$	1.67 mAh cm^{-2} after 1800 cycles at 60 mA cm^{-2}	[66]
δ-MnO_2	1 M $ZnSO_4$	175 after 1000 cycles at 3096 mA g^{-1}	[59]
Mn-deficient $ZnMn_2O_4$	2 M $ZnSO_4$ + 0.2 M $MnSO_4$	100% capacity retention after 1000 cycles at 3 A g^{-1}	[67]

The electrochemical execution shifted concurring with the different gem shapes. These tracts make the MnO_2 reasonable for economical application in super-capacitors and lithium-ion batteries. For example, Yuan et al. showed that a manganese-based metal-organic system (MOF) can be utilized as a moved forward cathode for ZIBs [68]. The oxygen atoms of two neighboring -COO– are utilized to implement coordination unsaturation of Mn. Its moderately high reactivity and quick electrochemical response energy are upheld by its ideal unsaturated coordination degree, which offers prevalent Zn^{2+} transport and electron trade all through repetitive charging/discharging cycles. Due to the aforementioned characteristics, this MOF-based anode incorporates a huge capacity of 138 mAh g^{-1} at 100 mA g^{-1} and a long lifespan (93.5% capacity holding after 1000 cycles at 3000 mA g^{-1}).

Figure 7a illustrates that as the current density increases from 100 to 3000 mA g^{-1}, the distinctive volume of $MnH_3BTCMOF_4$ expands from 98 to 138 mAh g^{-1}. This current density implies that it has higher capacity retention than $MnH_3BTCMOF_2$ and $MnH_3BTCMOF_6$. Cycle implementation of diverse cathode materials has been extensively studied (Figure 7b). The $MnH_3BTCMOF_4$ cathode shows remarkable specific volume retention of 96.4% after 100 cycles and 100% coulombic efficiency at 100 mA g^{-1}. When built as a full battery, the device also shows a very long cycle stability with a Zn anode at 2 M Zn (CF_3SO_3), with

93.5% of the installed power after 1000 cycles at 3000 mA g^{-1} (Figure 7c). In addition, Liang et al. have reported that the potassium-ion stabilization and oxygen deficiency of K0.8Mn8O16 make it a high-energy and robust cathode for neutral aqueous ZIB [69]. They identified a strong energy output of 398 Wh kg^{-1} (depending on the mass of the cathode) and high stability over 1000 cycles, with no significant capacity loss. At 100 mA g^{-1}, the initial capacitance of the KMO electrode was 216 mAh g^{-1}, but it increased to 320 mAh g^{-1} by the tenth cycle (Figure 8a). This effect may be due to the initial activation of the highly crystalline KMO. After 50 cycles, the KMO capacity will be 278 mAh g^{-1}, and the MnO_2 capacity will be 136 mA h g^{-1} (only 60% of the initial capacity) (Figure 8b).

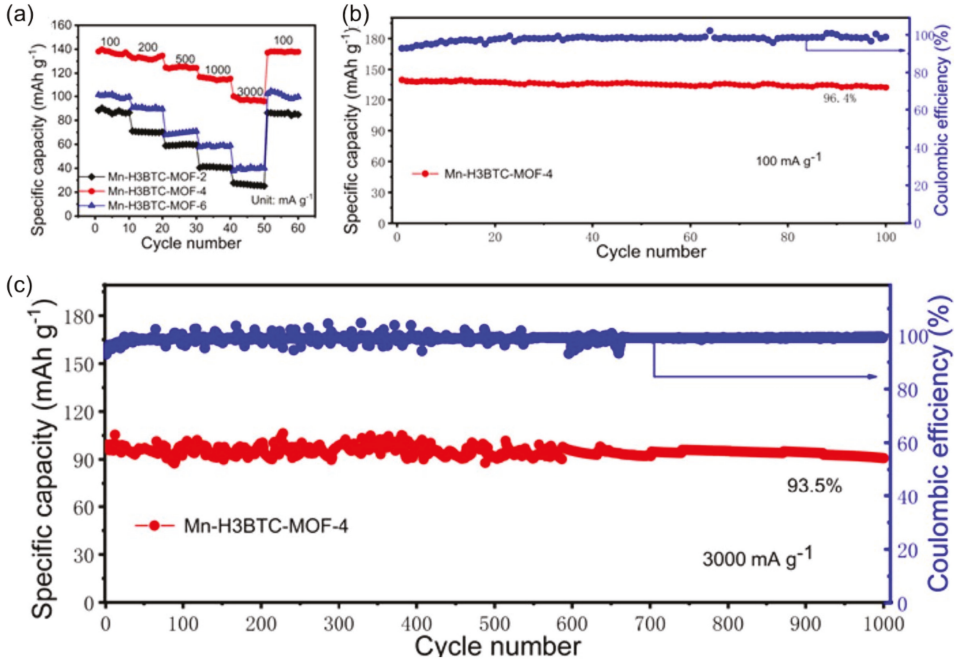

Figure 7. (**a**) The rate capability (from 100 to 3000 mA g^{-1}) and (**b**,**c**) cycling performance of Mn-H_3BTC-MOF-4 at 100 and at 3000 mA g^{-1}, respectively. Reprinted with permission from Ref. [68]. Copyright 2021 American Chemical Society.

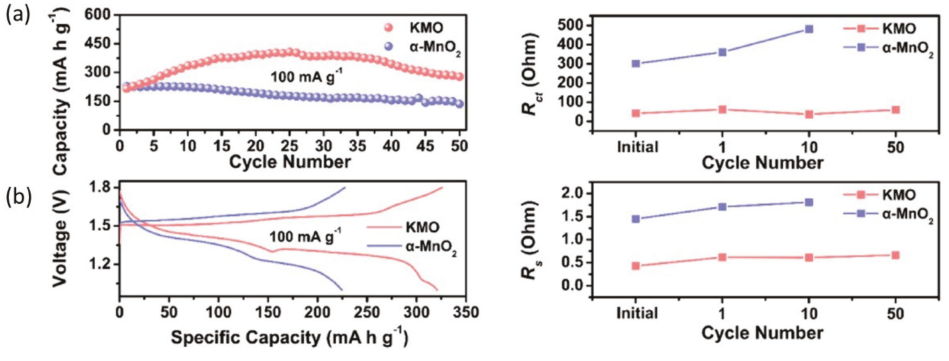

Figure 8. (**a**) Cycling performance at 100 mA g^{-1} and corresponding galvanostatic charge/discharge curves at the tenth cycle. (**b**) Plots of electrolyte resistance, Rs, and charge-transfer resistance, Rct. Reprinted with permission from Ref. [69]. Copyright 2019 Elsevier.

The Rs of KMO cathodes does not change particularly during cycling, but it significantly increases for α-MnO_2 cathodes, firmly fused with the capacity decrease. Islam et al. also improved the electrochemical performance of MnO_2 by carbon coating [27]. Other than manganese-based cathodes, vanadium oxide (V_2O_5) has been studied extensively as a cathode material for lithium-, sodium-, and zinc-ion batteries. The researchers found some issues such as poor ionic conductivity, low capacity, and structural instability of the V_2O_5. Several attempts have been made to solve these problems. Yan et al. [70] improved Li insertion capability into V_2O_5 by adding Na ions. It is not only effective for lithium-ion batteries, but this technique is also applicable for other metal-ion batteries. The addition of metal ions (Na^+, K^+, Li^+) act as pillars and enhance the structural stability of V_2O_5 in AZIBs [46,47,71–73]. Though vanadium-based cathodes offer high capacity, they fail to reach high voltage. In this situation, hybrid ion batteries can reach high potential [74].

3. Flexible Zinc-Ion Battery

Zinc has been recognized as one of the most promising anode materials because of its high theoretical capacity, large abundance, low cost, high corrosion resistance in aqueous electrolytes, non-toxicity, low oxidation/reduction potential, environmental friendliness, and good reversibility. However, aqueous zinc-ion batteries (AZIBs) confront some unexpected issues, including water-mediated parasitic reactions that speed up zinc dendrite formation, the dissolution of cathode materials, and the construction of byproducts on the cathode. Hence, these issues arise from the parasitic response, hampering an aqueous zinc battery's capacity and cyclic stability. Scientists around the globe are working on resolving these issues. They have employed several strategic solutions, such as changing electrolytes, surface engineering, and structural/hierarchical design. Moreover, electrical vehicles and portable devices have been transformed by smart energy storage. The rate of penetration into flexible electronic markets by the present smart energy storage technologies is remarkable. Largely flexible devices require additional requirements, such as bendable, twistable, stretchy, and ultrathin batteries, to adjust mechanical deformation under working conditions. Flexible batteries are essential power sources for these devices. Currently, flexible zinc-ion batteries have attracted more attention for their low cost and considerable energy density [75–78].

Polymer/hydrogel electrolytes such as poly(vinyl alcohol) (PVA) and polyacrylamide (PAM) can play a significant role in resolving these issues because of the lower content of water in polymer/hydrogel electrolytes. In addition, solid–solid contact between electrodes and the electrolyte rather than a solid–liquid interface can create a significant barrier for preventing the formation of dendrites and the dissolution of cathode materials. Meanwhile, the stable solid–solid interface has unexpected capabilities such as self-healing, elasticity, anti-freezing, and thermal sensitivity [69,75,76,79,80].

Although polymer/hydrogel electrolytes in flexible zinc-ion batteries have achieved tremendous advancements in battery technology, they have some drawbacks, such as ionic activities, length of time effects of polymer/hydrogel electrolytes, ubiquitous charge-transfer mechanisms at the solid–solid interface are unclear, etc. Understanding the mechanisms of polymer gel electrolytes in electrochemical performance is still vague [69,75,76,79,80]. In this section, we will provide recent updates on flexible zinc-ion batteries. To design flexible zinc-ion batteries, it is required to study the basic components of the system, such as the flexible electrodes (cathode and anode), current collector, electrolyte, and separator. Moreover, some important parameters, such as bending properties (geometry), mechanical stability, and energy density, etc., are considered for practical applications. Comprising all the above issues discussed in this section, recent updates on flexible zinc-ion batteries are summarized in Table 2.

Table 2. The recent updates of the flexible zinc-ion battery.

Cathode Materials	Electrolyte	Capacity	Energy Density	Cycling Stability	Ref.
Co(III) rich-Co_3O_4@CC	$ZnSO_4$/$CoSO_4$/ PAM gel	52 (8 A g^{-1})	360.8 Wh kg^{-1} (0.5 A g^{-1})	94.6% capacity retention 2000 cycles (2 A g^{-1})	[81]
ZOV@graphene foam	$ZnSO_4$/fumed Silica	204 (0.5 C)	115 Wh kg^{-1}	89% capacity retention 2000 cycles (20 C)	[82]
MnO_2@PEDOT@CC	$ZnCl_2$/$MnSO_4$/ PVA gel	282.4 (0.7 A g^{-1})	504.9 Wh kg^{-1}	77.7% capacity retention after 300 cycles	[83]
Expanded MoS_2@CC	$ZnSO_4$/starch-g-PAM gel	202.6 (0.1 A g^{-1})	148.2 Wh kg^{-1}	98.6% capacity retention after 600 cycles	[84]
$NaV_3O_8{\cdot}1.5H_2O$@the steel meshes	Na_2SO_4/$ZnSO_4$/ gelatin gel	160 (0.5 A g^{-1})	144 Wh kg^{-1}	77% capacity retention after 100 cycles (0.5 A g^{-1})	[85]
MnO_2@the CNT paper	$ZnSO_4$/$MnSO_4$/ gelatin-g-PAM gel	306	6.18 mW h cm^{-2}	97% capacity retention after 1000 cycles (2772 mA g^{-1})	[86]
MnO_2@CC	$ZnSO_4$/$MnSO_4$/ gelatin gel	265 (1 C)	-	76.9% capacity retention after 1000 cycles	[87]
MnO_2@nitrogen-doped CC	$ZnCl_2$/$MnSO_4$/ PVA gel	353 (0.5 A g^{-1})	440 Wh kg^{-1}	86.7% capacity retention after 1000 cycles	[7]
MnO_2/rGO@CC	$ZnSO_4$/$MnSO_4$	332.2 (0.3 A g_{-1})	456.2 Wh kg^{-1}	96% capacity retention after 500 cycles (6 A g^{-1})	[88]
Freestanding graphene/ VO_2 composite films	$Zn(CF_3SO_3)_2$	194 (8 A g^{-1})	65 Wh kg^{-1}	99% capacity retention after 1000 cycles	[89]
MnO_2@CNT film	$ZnSO_4$/$MnSO_4$/ xanthan gel	260 (1 C)	364 Wh kg^{-1}	90% capacity retention after 330 cycles (1 C)	[90]
Polyaniline@carbon Felts	$Zn(CF_3SO_3)_2$/ PVA gel	109 (0.5 A g^{-1})	-	91.7% capacity retentions after 200 cycles	[91]
MnO_2@CNT fiber	$Zn(CF_3SO_3)_2$/ PVA gel	290 (0.1 A g^{-1})	360 Wh kg^{-1}	75% capacity retention after 300 cycles	[92]
MnO_2@PPy@ stainless Steel	$ZnSO_4$/$MnSO_4$/ gelatin–borax gel	135.2 (1 C)	-	87% capacity retention after 500 cycles, 60% capacity retention after 1000 cycles	[93]
MnO_2@CNT yarn	$ZnSO_4$/$MnSO_4$/ PAM gel	302.1	53.8 mWh cm^{-3}	98.5% capacity retention after 500 cycles	[94]
ZnHCF@MnO_2@Ni foil	$ZnSO_4$/PVA gel	89 (100 mA g^{-1})	149 Wh kg^{-1}	71% capacity retention after 500 cycles (400 mA g^{-1})	[95]
Husk-like α-MnO_2	1 M $ZnSO_4$ + 0.1M $MnSO_4$ Gel	321 (0.33mAg^{-1})		100 mAh g^{-1} after 100 cycles (333 mA g^{-1})	[96]
Ce-MnO_2@CC	polyacrylamide–$ZnSO_4$–$MnSO_4$(PAM/$ZnSO_4$-$MnSO_4$) gel	311 mAh g^{-1} at (100 mA g^{-1})	370 Wh kg^{-1}	106 mAh g^{-1} (2000 mA g^{-1})	[97]
Nanocellulose-Based Hybrid Hydrogels	3 M ZnCI/2M NH_4CI/1 M $ZnSO_4$ Solid electrolyte	149.4 mAh/g (0.5 A/g)	113.2 mWh/g	96% capacity retention after 1000 cycles	[98]

Polymer/Gel Electrolytes

Polymer electrolytes for ZIBs are classified into solid polymer electrolytes, new hydrogel electrolytes, and hybrid polymer electrolytes. In this context, polymer electrolytes surpass aqueous electrolytes to prevent zinc dendrite development and reduce cathode dissolution. In addition, the polymer electrolytes' additional functionalities lessen parasitic weight invasion in the separator and enhance mechanical performance. Solid polymer electrolytes have more mechanical strength than hybrid polymer electrolytes, although hydrogel electrolytes have a competitive ionic conductivity compared to aqueous electrolytes. Due to their stable structure, solid polymer electrolytes are expected to limit zinc dendrite formation the most. In contrast, hydrogel electrolytes are projected to have a weaker ability to prevent dendrite formation due to the water content in the hydrogel. Combining these benefits, hybrid polymer electrolytes that offer the optimal balance between these viewpoints are critical for further commercialization. They provide high ionic conductivities and multi-competitive functionalities and mechanical behaviors. A three-dimensional, double-cross-linked gelatin and sodium alginate hydrogel imbibed with $ZnSO_4$ aqueous solution was used as an electrolyte membrane for flexible Zn-ion batteries, according to Huang et al. [79]. They discovered that the three-dimensional, double-cross-linked gelatin and sodium alginate hydrogel had better electrochemical behavior, easy fabrication, electrochemical stability, and Zn anode suitability [78,99].

The polymer membrane was well-staged between the V_2O_5/CNT cathode and the Zn/graphite paper anode (Figure 9a) [79]. Figure 9b shows the cycle life of a flexible battery at 2.0 Ag^{-1}. The battery capacity is 251 mAh g^{-1} after the first cycle and 188 mAh g^{-1} after 200 cycles, with a coulombic efficiency of over 99.8%. Figure 9b,c further show that after 400 bending cycles, the battery can be bent differently with bending diameters of 30 and 10 mm, retaining 89% and 86% of the original capacity, respectively. As shown in Figure 9d, the cell can fold 55 cycles under a load of 1470 times the device's weight, maintaining 74% of its original capacity. Similarly, poly (3,4-ethylene dioxythiophene) polystyrene sulfonic acid (PEDOT: PSS) is incorporated into polyaniline (PANI) on carbon nanotubes (CNTs) for electrochemical behavior and cycle stability [75]. It shows excellent activity in improving electrochemical behavior. Although the discharge capacity has been shown to gradually decrease with increasing current density, the high conductivity of the tCNTs-PA-PE cathode describes a large capacity of 145 $mAhg^{-1}$ (Figure 10a) even at a sharp current density of 10 Ag^{-1} (Figure 10b) and exemplary cycle stability (Figure 10c), with the reversible capacitance of 113 mAh g^{-1} over 1500 cycles, and remarkable 100% coulombic efficiency (Figure 10d).

The Zn powder carbon film coated on the Zn anode was expected to prevent the abnormal growth of dendrites and promote the performance of Zn. Zhi et al. have shown a stretchable zinc-ion battery (ZIB) with double-helix electrodes and a cross-linked polyacrylamide (PAM) electrolyte [76]. It exhibits a high specific volume, volumetric energy density (302.1 mAh g^{-1} and 53.8 $mWhcm^{-3}$, respectively), and excellent cycle stability (98.5% capacity retention after 500 cycles). In addition, the semisolid-state yarn ZIB showed excellent stretchability (up to 300% elongation) and excellent water tightness (high-capacity retention of 96.5% after 12 h of underwater operation). In Figure 11a, the yarn battery showed high discharge capacities of 260.4, 211.5, 168.7, and 117.7 mAh g^{-1}, respectively, at current densities of 0.2, 0.5, 1, and 1.5 Ag^{-1}. Most notably, even with a current density of 0.2 Ag^{-1}, the average discharge capacity of 235.8 mAh g^{-1} is restored. This corresponds to 96.5% of the initial average capacity (244.3 mAh g^{-1}).

Higher efficiency may be due to the consistency of the electrodes and the high ionic conductivity of the PAM-based electrolyte. The deformability test was very sustainable (Figure 11b). The load was evaluated after the trigger. This was almost 97.2% under normal conditions, and it was found that 93.6% of the capacity was stable even after discharge

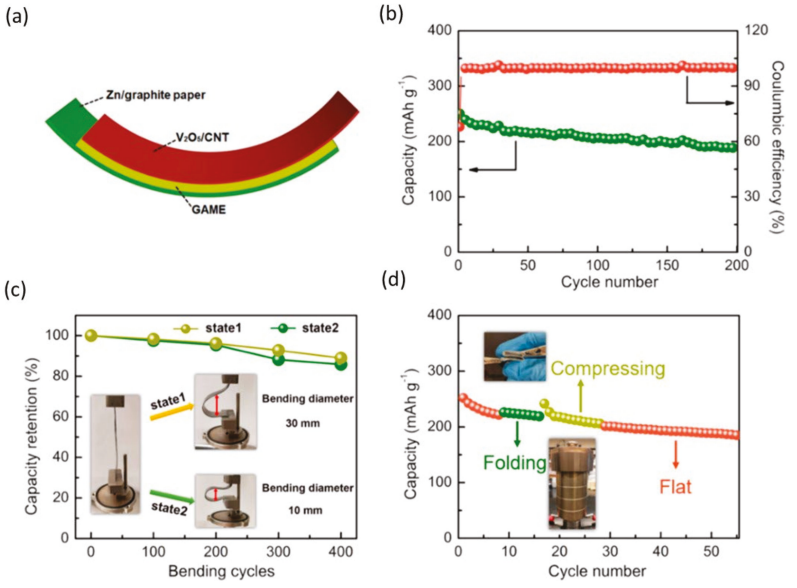

Figure 9. Configuration and performance of a flexible semisolid Zn/V_2O_5 battery. (**a**) Schematic diagram of a flexible semisolid Zn/V_2O_5 battery. (**b**) Cyclic performance at 2.0 Ag^{-1}. (**c**) Capacity retention vs. bending cycle at 2.0 Ag^{-1}. The insets show photographs of the battery under two bending states. (**d**) Cyclic performance under various mechanical stimuli at 2.0 Ag^{-1}. Reprinted with permission from Ref. [79]. Copyright 2019 American Chemical Society.

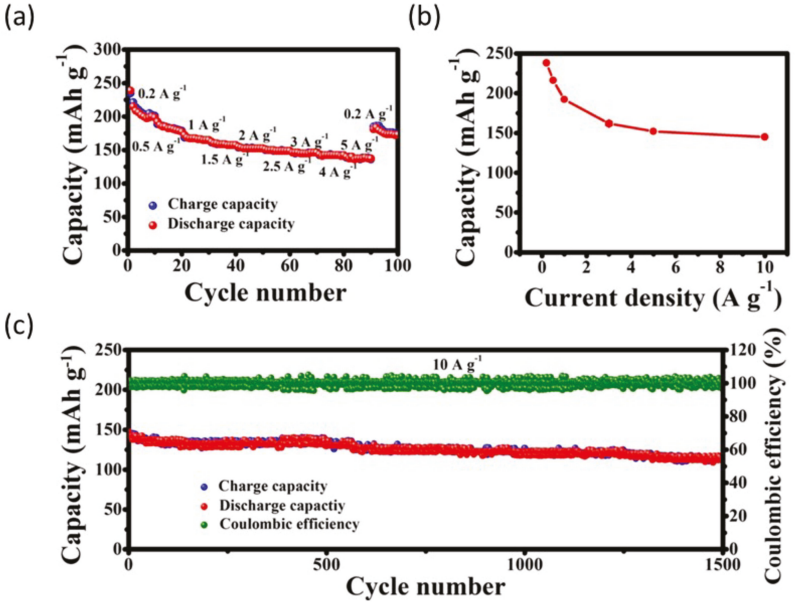

Figure 10. Electrochemical performance of the t-CNTs–PA–PE cathode in ZIBs. (**a**,**b**) Rate performance, and (**c**) cyclic performance at 10 Ag^{-1}. Reprinted with permission from Ref. [75]. Copyright 2019 American Chemical Society.

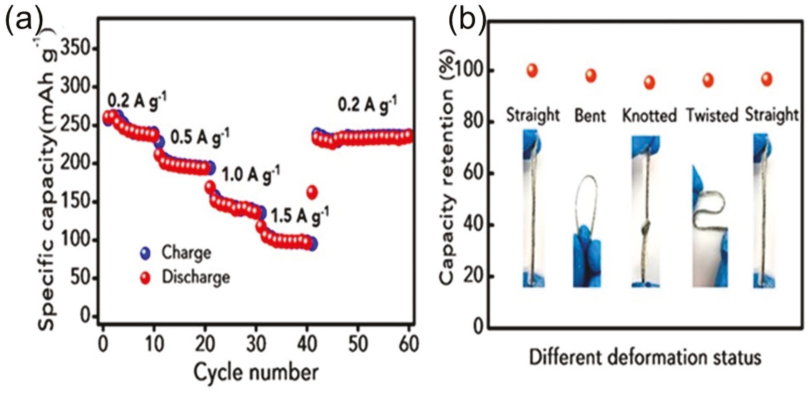

Figure 11. Electrochemical performance of the rechargeable yarn ZIB. (**a**) Rate capabilities at various current densities. (**b**) The capacity retention of the yarn ZIB under various deformation statuses. Reprinted with permission from Ref. [76]. Copyright 2018 American Chemical Society.

The hybrid polymer electrolyte was found to have a coulombic efficiency of over 99% and capacity retention of 96% after 1000 cycles at 2 Ag^{-1} according to Parkin et al. [80]. As the sampling rate increased from 0.1 to 1 mVs^{-1}, the electrochemical response under capacitive control became much more sensitive, as shown in Figure 12a. As shown in Figure 12b, the charge/discharge rates of SAPAM, SA, and AZIB were studied with gradual current densities ranging from 0.1 to 5 Ag^{-1} over 5 cycles for each current density. As a result, the SAPAM battery achieved an amazing 305 mAh g^{-1} at 0.1 Ag^{-1}, and the coulombic efficiency (CE) was 96.2%, while the CE of the original SA battery was 91.6% at 258 $mAhg^{-1}$. In addition, Niederberger et al. used a polydimethylsiloxane (PDMS) substrate and a polyacrylamide (PAM) hydrogel electrolyte, and a capacity of 176.5 mAh g^{-1} was achieved after 120 cycles at various stress levels of up to 50% [100].

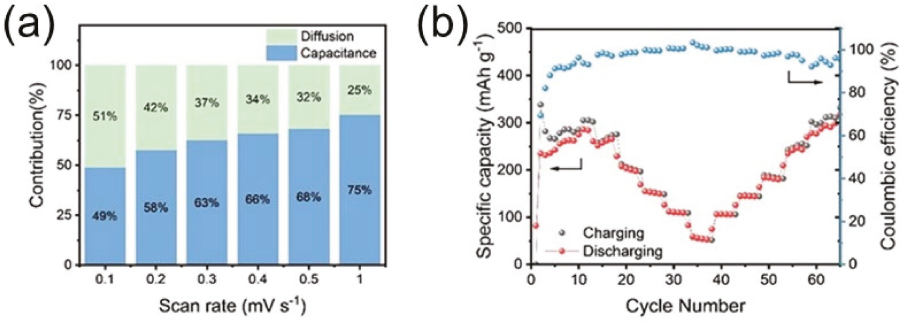

Figure 12. SAPAM electrolyte under the full-cell test: (**a**) diffusion-capacitive control contribution is presented in the bar chart, and (**b**) charge/discharge rate performance of current densities from 0.1 to 5 Ag^{-1}. Reprinted with permission from Ref. [80]. Copyright 2021 American Chemical Society.

Figure 13a shows the GCD profile obtained at 1 C (= 308 mA g^{-1}). In the 1st, 10th, 100th, and 120th cycles, the transparent zinc-ion battery becomes 64.5, 74.4, 151.2, and 144.9 $mAhg^{-1}$. At a current density of 1 C, Figure 13b shows the no-load cycle performance of the transparent cell. According to Madan et al., Figure 12a shows the cycle life of a cell determined by a low-voltage GCD test with a current density of 0.5 Ag^{-1} over 300 cycles [101]. A maximum average specific volume of 248.5 mAh g^{-1} was reported, after which the capacitance value sharply dropped. However, the capacity loss rate after 60 cycles was relatively small, and

the average capacity after 300 cycles reached 175 mAhg^{-1}. The average capacity has reached 175 mAh g^{-1}. The achieved 96.5% coulombic efficiency is also shown in Figure 14a. There was a dramatic decline in the first 15 cycles alone, steadily fluctuating. In addition, Figure 14b shows the discharge curves for cycles 1 and 100 at 0.5 Ag^{-1}. Figure 14c shows that the discharge curves at different bending radii align with the original flat state. This shows that the cell works well even when deformed, with a minor loss of capacity.

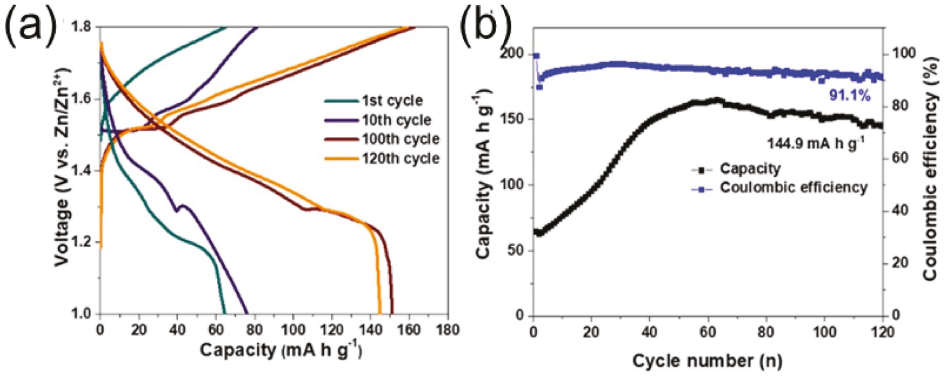

Figure 13. (**a**) Cycling performance of the transparent unstrained battery at a current density of 1 C. (**b**) GCD profiles of the transparent unstrained battery at the 1st, 10th, 100th, and 120th cycles at a current density of 1 C (=308 mA h g^{-1}). Reprinted with permission from Ref. [100]. Copyright 2021 American Chemical Society.

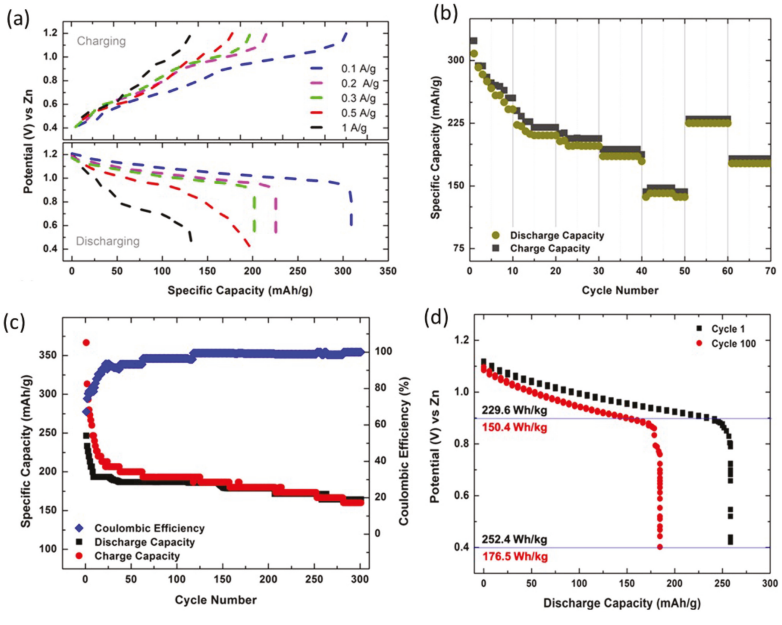

Figure 14. (**a**) Charge–discharge profiles of the assembled cells run at different current densities. (**b**) Rate capability of the Zn-EMD cell with the novel chitosan-alkaline electrolyte cycled between 0.4 and 0.2 V. (**c**) Cycling performance at 0.5 Ag^{-1}. (**d**) Discharge curves for cycles 1 and 100 until 0.4 V at 0.5 Ag^{-1} with energy density. Reprinted with permission from Ref. [101]. Copyright 2021 American Chemical Society.

This shows that the performance stability of the cell is good even under physical bending. In addition, Figure 14d shows the discharge curves for cycles 1 and 100 at 0.5 Ag^{-1}. Wang and his group have used the graft copolymer xanthan gum polyacrylamide (XGPAM) and cotton cellulose nanofiber (CNF) combined [102]. They have high ionic conductivity (28.8 mS cm^{-1}), better adhesion, specific strength, large and strong ion adsorption, solid specific capacity (237 mAh g^{-1}), and excellent cycle stability (86.2% capacity registered at 1000 cycles). The XGPAM/CNF-based ZIB has low bulk and resistivity, indicating a strong electrode–electrolyte interface. This speeds up the electrochemical reaction. As shown in Figure 15a, the rated capacity of the flexible ZIB was also evaluated using three different hydrogel electrolytes. At 1, 2, 3, and 5 C rate, the enhanced specific discharge capacities of 237, 220, 195, and 147 mAh g^{-1}, respectively exhibits by the XGPAM/CNF-based ZIB were. Figure 15b shows matching charge/discharge graphs at different rates, whose two plateau functions match the two pairs of redox peaks on the CV curve. In addition, the long-cycle stability of the flexible ZIB based on XGPAM/CNF was remarkable, with a capacity retention of 86.2% after 1000 cycles at 4 C and a coulombic accuracy of almost 100% (Figure 15c).

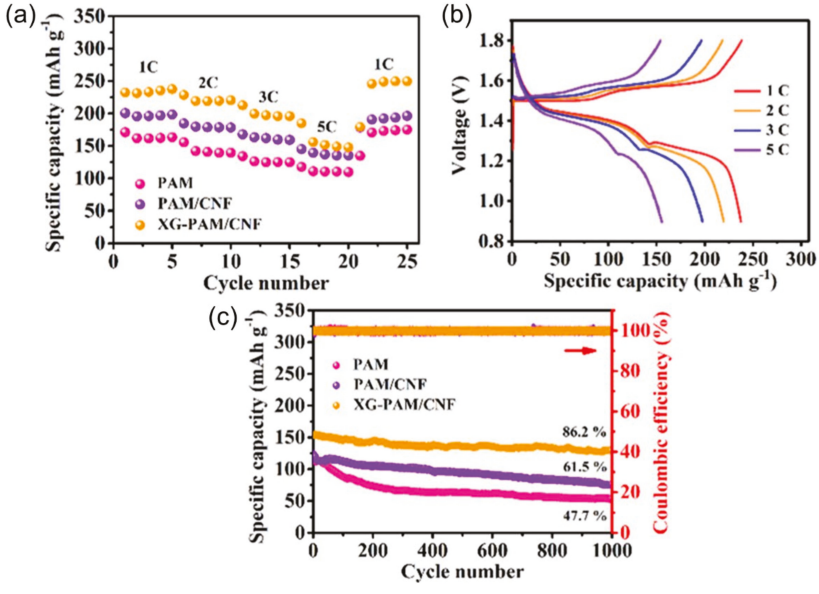

Figure 15. (**a**) Rate capacity of the flexible ZIBs at different rates and (**b**) corresponding charge–discharge curves of the XGPAM/CNF hydrogel. (**c**) Long-term cycle behavior and the corresponding coulombic efficiency of the flexible ZIBs at 4 C. Reprinted with permission from Ref. [102]. Copyright 2020 American Chemical Society.

4. Anodes for AZIBs and AFZIBs

As previously stated, complications arising from undesired Zn dendrites would lead to prolonged stripping/plating treatments, resulting in water consumption and irreversible negative effects, which could be responsible for degrading the coulombic efficiency (CE) accompanied by an inferior operation life [1–5]. When the Zn dendrite grows at a steady rate, the separator may develop short circuits, posing a security issue. Due to the usage of excessive Zn metal, the discharge rate and consumption proportion of Zn metal anodes are usually poor and do not represent the full energy density. Published studies presently suggest that Zn dendrites may be prevented by modifying the surface of the Zn anode, electrodepositing Zn on 3D nanostructures, adjusting the separator composition, and changing the electrolyte [6–10]. Although such solutions can generally help stabilize cells,

the problem of establishing Zn dendrites remains unsolved. Nonetheless, these anode materials have low capacitance, have irreversible phase shifts, and their capacitance drops rapidly during Zn^{2+} insertion/extraction, which severely limits their use. As a result, the creation of an improved insertion anode material for ZIB with a strong structure, high capacitance, and higher power density was very attractive. Hur et al. has used a simple spin-coating process to protect the Zn anode using a protective thin layer of highly polar poly (vinylidene difluoride) (β-PVDF) [103]. The β-PVDF layer is robust and has adjusted the Zn stripping/plating process while withstanding erosion. In the asymmetric cell test, the resulting β-PVDF-coated Zn anode (β-PVDF@Zn) outperformed both bare Zn metal and α-PVDF@Zn at a low overvoltage of 40 mV at 2000 h of operation. In addition, PVDF has extended the life of the entire cell to 4000 cycles while maintaining excellent cycle stability. Two redox peaks of 0.59 and 0.78 were clearly visible in the first cycle (Figure 16a), after which a slightly dark pair of reduction/oxidation peaks in the range 0.9 to 1.1 diverged in each cell. However, after 3 cycles, all peaks in these profiles were integrated into 0.59/0.78 and 0.89/1.14, respectively, according to the Zn^{2+} two-step intercalation/deintercalation process (Figure 16b). The discharge capacities of the batteries using the β-PVDF@Zn anode were 276, 267, 253, 220, and 154 mAh g^{-1} at a high current density of 0.1, 1, 2, 4, and 8 Ag^{-1}, respectively, as shown in Figure 16c.

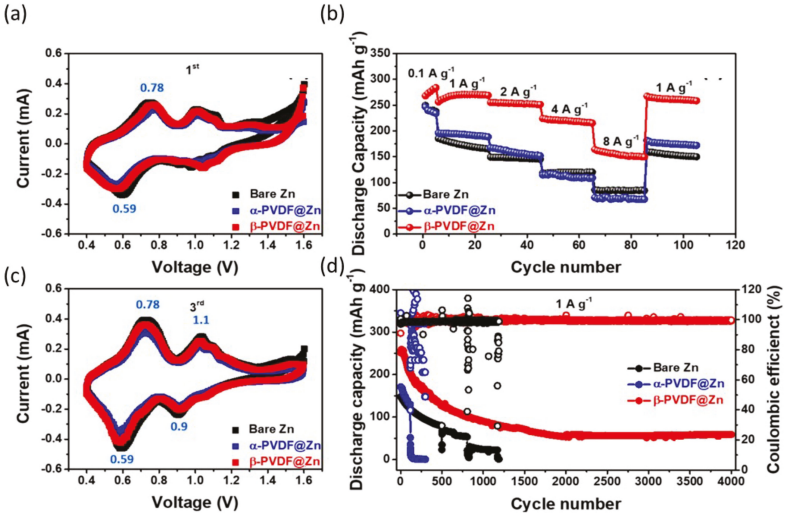

Figure 16. Electrochemical performance of β-PVDF@Zn (red), α-PVDF@Zn (blue), and bare Zn (black) full cells with V_2O_5/C cathode: first (**a**) and third (**b**) CV curves at 0.2 mV s^{-1} from 0.4 to 1.6 V. Rate performance (**c**) at various current densities of 0.1, 1, 2, 4, 8, and 1 Ag^{-1}, and long-term cycling performance (**d**) at a current density of 1 Ag^{-1}. Reprinted with permission from Ref. [103]. Copyright 2021 American Chemical Society.

Even after 20 cycles for each period of growing the current rate, the capacity bounced back to 265 mAh g^{-1} when the current density unexpectedly plummeted to 1 Ag^{-1}. The β-PVDF cell outperformed the others in terms of rate and cycling, completely overtaking their uninteresting traits. Finally, at a rate of 1 Ag^{-1}, the long-term cycle life was assessed (Figure 16d). A cathode material (MnO_2) ultrathin layer is first coated upon the surface of the carbon cloth as active sites for in situ nucleation and guided nucleation and growth of metal Zn, according to Shao et al. [104]. Consequently, the CC@MnO_2-UTF@Zn anode can be cycled in an aqueous electrolyte and keep its cycling performance consistent during repeated Zn deposition/stripping procedures. After 100 cycles, the complete cell with the Zn plate anode shows a more extensive capacity loss, with 157 mAh g^{-1} (41.8% capacity

retention). Long-term cycling performance was also assessed at 1 Ag^{-1}. The complete cell with the CC@MnO_2-UTF@Zn anode still has a high coulombic efficiency of almost 100% and a specific capacity of 186 mAh g^{-1} after 300 cycles (81.0% of capacity retention). The creation of freestanding, super versatile, and conductive carbon nanotube (CNT)/paper scaffolds to maintain zinc metal anodes has been described by Wang et al. [104]. The scaffold-stabilized zinc anodes had low polarization strengths, a long cycling life of over 1800 h, and superior charging–discharging capabilities.

Zinc-ion batteries/hybrid capacitors with ultralong cycle lifetimes were also successfully produced, due to the scaffold-stabilized zinc anodes' robust electrochemical stability and reversibility [105]. The V_2O_5 | $Zn(CF_3SO_3)_2$ | Zn@CNTS ZICs have been charged/discharged at 3 Ag^{-1} for 2000 cycles and the activated carbon | $Zn(CF_3SO_3)_2$ | Zn@CNTS ZIBs have been charged/discharged at 2 Ag^{-1} for 7000 cycles (Figure 17a–d). Both have an excessive degree of cyclical balance. A unique 2D ultrathin-layered zinc orthovanadate array cathode, a Zn array anode supported with the aid of conductive porous graphene foam, and a gel electrolyte were used by Fan et al. to develop a high-end, ultra-strong, flexible, quasi-solid-country zinc-ion battery [82]. Each electrode has a nanoarray construction that ensures high-fee functionality and prevents dendrite formation.

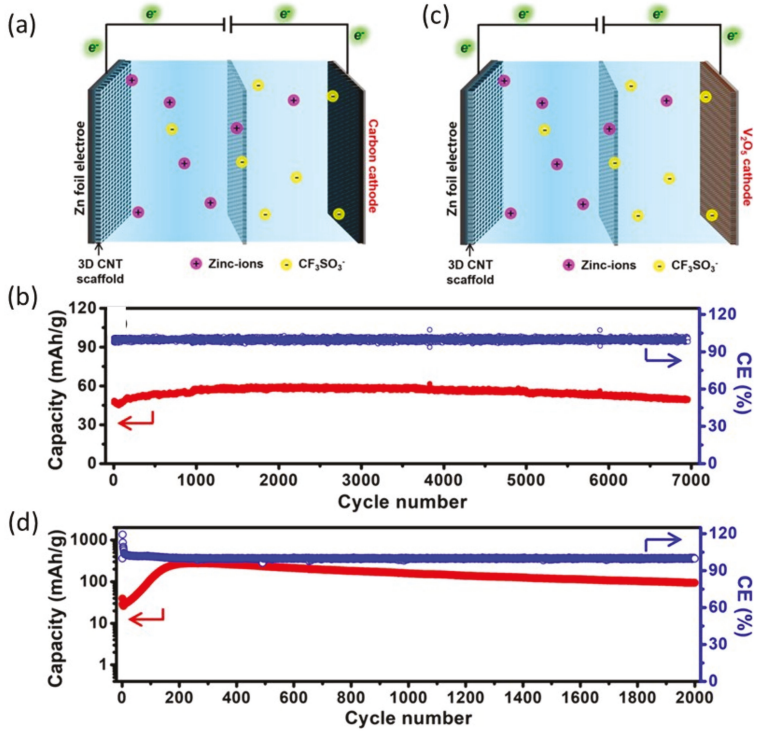

Figure 17. (**a**) Schematics, (**b**) cycling performance of activated carbon | $Zn(CF_3SO_3)_2$ | Zn@CNTS ZICs, (**c**) schematics, and (**d**) cycling performance of Zn@CNTS | $Zn(CF_3SO_3)_2$ | V_2O_5 ZIBs. Reprinted with permission from Ref. [105]. Copyright 2020 Elsevier.

The porous, thin, ZOV nanoarray shape with uncovered 2D ion channels is vital in this regard to enable ions to gain entry to and velocity-fee switch at the electrode/electrolyte interface with a short Zn^{2+} and electronic transport direction. Figure 18 demonstrates the excessive price of the overall performance. At 10 C, the release abilities are greater than 160 mAh g^{-1}, and 101 mAh g^{-1} at 50 C. Subsequently, even at high fees, our QSS-ZIB demonstrates correct cycling sustainability. After 800 cycles, the capability stays flat, and

after 2000 cycles (89% of the preliminary value), a selected capability of 125 mAh g^{-1} may nevertheless be maintained at 20 C.

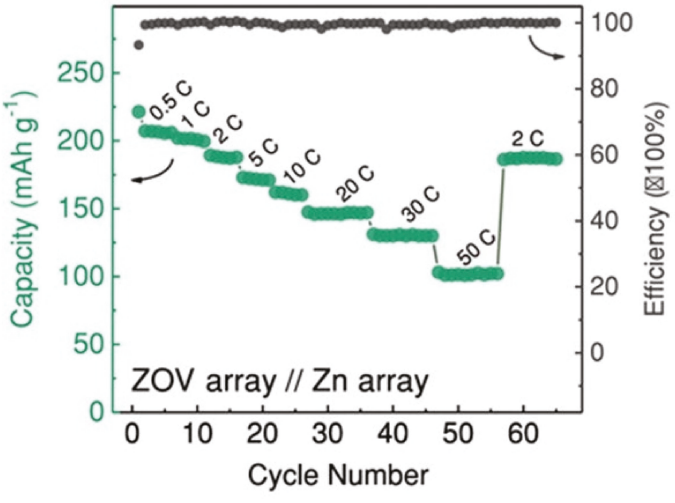

Figure 18. Quasi-solid-state ZIB performance with ZOV array as a cathode and Zn array as an anode. The rate capability of the cell at varied current densities, from 0.5 to 50 C. Reprinted with permission from Ref. [82]. Copyright 2018 Wiley.

From the above discussion, it can be concluded that similar types anode can be used for both AZIBs and AFZIBs. However, special designated flexible anodes are required for AFZIBs, whereas Zn foil can be used for AZIBs. No supporting current collector is needed while using Zn foil as an anode. In contrast, Zn-containing carbonaceous compounds such as Zn@Graphene, Zn@CNT, etc., are directly used as anode materials, and carbon materials can act as current collectors. This kind of anode is more effective in AFZIBs.

5. Challenges of Flexible Zinc-Ion Battery

Due to its outstanding performance and stretching/bending characteristics, the flexible zinc-ion battery is a promising invention for future commercial battery technology [37]. However, appropriate electrolytes and suitable compatible electrodes are the critical issues for the sustainable development of FIBs. Although extensive research has been carried out in these areas, it is still in its infancy. Therefore, we have discussed some recent updates about electrolytes and electrodes for AFZIBs. Electrolytic engineering is a promising way to make sustainable FIBs. Even though flexible zinc-based batteries work well in the lab, they are unable to find real-world applications, partly due to the substandard performance of the hydrogel electrolytes under dire circumstances. For example, hydrogels, which have high ionic conductivity and good flexibility, are one of the most promising flexible electrolytes for flexible zinc-based batteries. Their innate water-saturated polymeric networks facilitate diffusion of ions, resulting in greater ionic conductivity, hydrogel interfaces ensure strong interaction with electrodes, and their dimensionally stable properties enable flexible zinc-based batteries to be used in a wide range of applications. Nevertheless, the ramifications of harsh operational conditions on the battery's quality and longevity, which are crucial for implementing flexible zinc-based batteries, are still to be studied. Furthermore, the hydrogel electrolyte is more sensitive to the environment than electrodes in the flexible zinc-based battery system due to its fragile nature and water-saturated body. For loose zinc-based batteries, the revocation of hydrogel electrolytes at severe temperature changes and diverse anomalies are still a concern. Liu et al., for instance, discovered that at ambient temperature, organohydrogel electrolytes (OHEs) have superior performance

(122.1 mAh g^{-1}, 5 Ag^{-1}) and sturdy cycle stability (81.5%, 4000 cycles) [82]. This is attributed to the high-performance change examined from 0.2 to 5 Ag^{-1} via editing the contemporary density (Figure 19a). The primarily OHE-based Zn||PANI battery has desirable excessive-fee-cycling overall performance, as may be validated [106]. The specific capacity of the OHE-based total battery is 207.7 mA h g^{-1} at a 0.2 Ag^{-1} contemporary density. After 4000 cycles at a high cutting-edge density of 5 Ag^{-1}, the particular capability of the OHE-based Zn||PANI battery remains at 108.4 mA h g^{-1}, displaying a potential retention charge of more than 80%. In the cycle technique, the coulombic performance is almost 100% (Figure 19b), confirming that the primarily OHE-based Zn||PANI battery is electrochemically solid within the voltage range of 0.6–1.6 V, and that no unfavorable reactions take place. The security of OHE-based batteries as flexible strength storage systems was then tested by subjecting the OHE-based Zn||PANI batteries to rigorous operational situations. The primarily OHE-based battery keeps a consistent price and discharge conduct, as illustrated in Figure 19c,d, and a similar charge–discharge profile, observed even in adverse situations. Although the cell is bent at different angles (90°, 180°, etc.) and is placed in different conditions (compressed, hammered, soaked), it can deliver similar capacity at 90° and 180° bending angles.

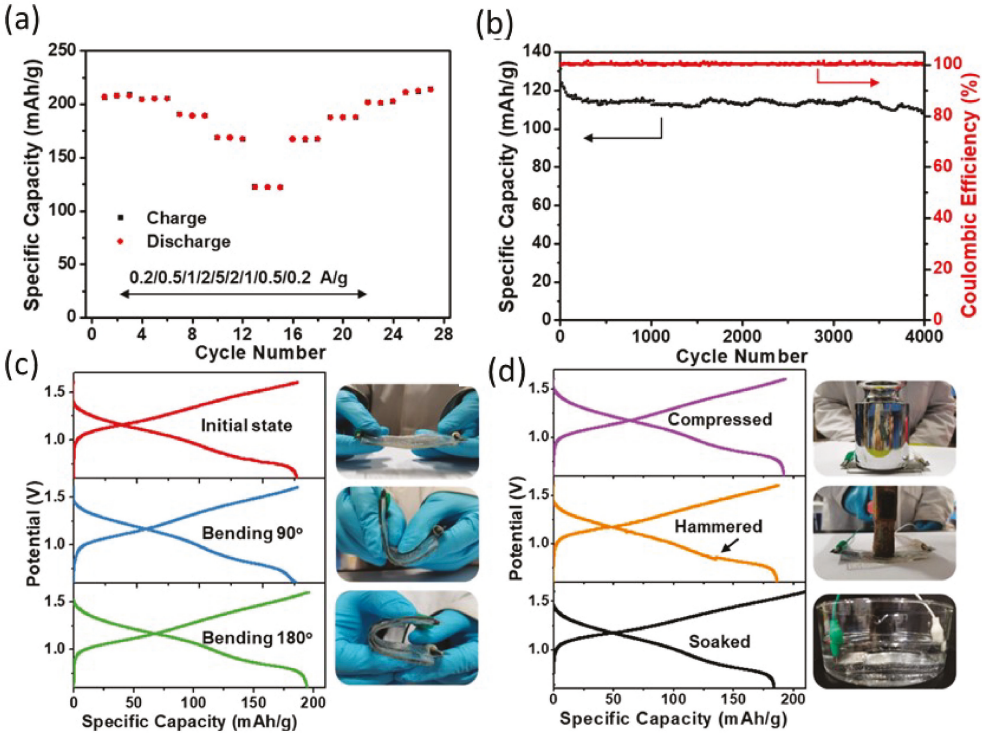

Figure 19. Electrochemical performance of OHE-based Zn||PANI battery at room temperature. (**a**) Cycling performance at various current densities. (**b**) Long-term cycling performance at 5.0 Ag^{-1} for 4000 cycles. (**c**,**d**) Charging and discharging stability of the OHE-based battery under a series of harsh working conditions. Reprinted with permission from Ref. [106]. Copyright 2021 American Chemical Society.

However, within the flexible zinc-based battery system, the hydrogel electrolyte seems more environmentally sensitive than the electrode fracture toughness and water-saturated body. Hence, two things occur if the temperature goes below 20 °C, and then the ionic

conductivity of the hydrogel electrolyte dramatically reduces. Dehydration occurs if the temperature goes above 50 °C. Structure deformation, salt crystallization, and decreased ionic conductivity result from the simple dehydration of the hydrogel at extremely high temperatures (50 °C). Chen et al. have shown a flexible zinc-ion battery consisting of an optimized concentrated hydrogel electrolyte sandwiched between an ultrathin zinc anode and an $NH_4V_3O_8 \cdot 1.9H_2O$ cathode for enhanced performance at a subzero temperature [107]. The resultant flexible battery performs perfectly when a concentrated hydrogel electrolyte is synthesized using 1.2 g of xanthan gum saturated in 4 m of $ZnCl_2$ solution, having an extremely high capacity of 201 and 83 mAh g^{-1} under 0.2 Ag^{-1} at −20 and −40 °C, respectively. Figure 20 illustrates the electrochemical behavior of batteries relying on these condensed hydrogel electrolytes at 20 and −20 °C. Under 0.5 mVs^{-1} at 20 °C, Figure 20a shows the CV curves of the batteries incorporating hydrogel electrolytes synthesized with 1.2 g of gum and 3, 4, or 5 m of salt solution, respectively, while Figure 20b shows the CV curves of the two batteries. The battery with the hydrogel electrolyte prepared with 4 m of salt solution generates a CV curve with wider regions and sharper peaks. The proportion of zinc ions intercalated into the electrode measures the scale of the CV curve, with a greater area showing more significant zinc ions intercalated into the electrode. The width of peaks is determined by the restricting phase of mechanisms (mass or electron transfer velocity); consequently, sharper peaks indicate faster transport kinetics during this scenario. At −20 °C, the variation between the CV curves of the two batteries is even greater, indicating better electrochemical performance and quicker and more efficient transport kinetics from the 4 m hydrogel electrolyte, especially.

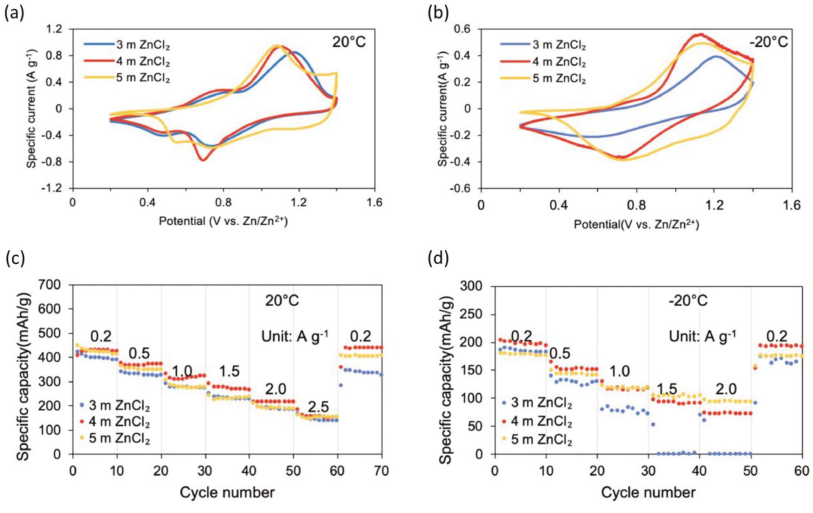

Figure 20. Under 0.5 mV s^{-1}, the CV curves of the batteries based on the hydrogel electrolytes prepared using 3/4/5 m $ZnCl_2$ combined with 1.2 g of xanthan gum at (**a**) 20 °C and (**b**) −20 °C. Rate performances of the batteries based on the electrolytes prepared using 1.2 g of xanthan gum combined with 3/4/5 m $ZnCl_2$ solution at (**c**) 20 °C and (**d**) −20 °C. Reprinted with permission from Ref. [107]. Copyright 2021 Elsevier.

At −20 °C, the variation between the CV curves of the two batteries is even greater, indicating better electrochemical performance and quicker and more efficient transport kinetics from the 4 m hydrogel electrolyte, especially at subzero temperatures, plausibly due to greater ionic conductivity due to the elevated salt concentration. The operations of the batteries incorporating hydrogel electrolytes made with 1.2 g of gum and 3, 4, or 5 m of salt solution, correspondingly, at 20 °C are shown in Figure 20c, whereas the c-rate performance of these three batteries at −20 °C are shown in Figure 20d. Chen et al. reported breaking

the initial hydrogen-bond network in $ZnCl_2$ solution by altering the electrolyte structure, inhibiting water freezing, and lowering the aqueous electrolyte's solid–liquid temperature within the range from 0 to −114 °C [68]. This $ZnCl_2$-based low-temperature electrolyte enables polyaniline||Zn batteries to function in an exceeding temperature range of −90 to 60 °C, which covers the complete planet's surface temperature range. These polyaniline||Zn batteries are durable at −70 °C (84.9 mA h g^{-1}) and have capacity retention of 100% after 2000 cycles. The ionic conductivities of the several C_{ZnCl2} electrolytes (1, 5, 7.5, 10, and 30 m) and also the standard electrolyte (2 m $ZnSO_4$ and a few m $Zn(CF_3SO_3)_2$ electrolyte) were investigated within the temperature range of −100–60 °C to enhance and choose the optimum LTE with optimum ionic conduction at cold temperatures (Figure 21a). Regardless of the fact that the 1 and 5 m $ZnCl_2$ electrolytes block at −12.6 and −46.0 °C, correspondingly, they need a robust ionic conductivity at cold temperatures, due to ionic conduction facilitated by the concentrated electrolyte below their major Tt. Conversely, solid ice obstructs ionic conduction and reduces ionic conductivities by a tenth compared to the frozen-solid 7.5 m $ZnCl_2$ electrolyte at −80 °C. Although the T_t of the 10 m $ZnCl_2$ electrolyte is low below −100 °C, it also features a quicker ionic conductivity reduction than the 7.5 m $ZnCl_2$ electrolyte. The 7.5 m $ZnCl_2$ electrolyte showed a high ionic conductivity of 1.79 mS cm^{-1} at −60 °C and 0.02 mS cm^{-1} at −100 °C thanks to the extended liquid-phase temperature range and relatively low concentration. The activation energies of ionic conduction in electrolytes were computed using the Arrhenius equation to quantitatively display the change of ionic conductivity with temperature. As illustrated in Figure 21b, there are two stages, one at high temperatures and the other at cold temperatures, both with various activation energies.

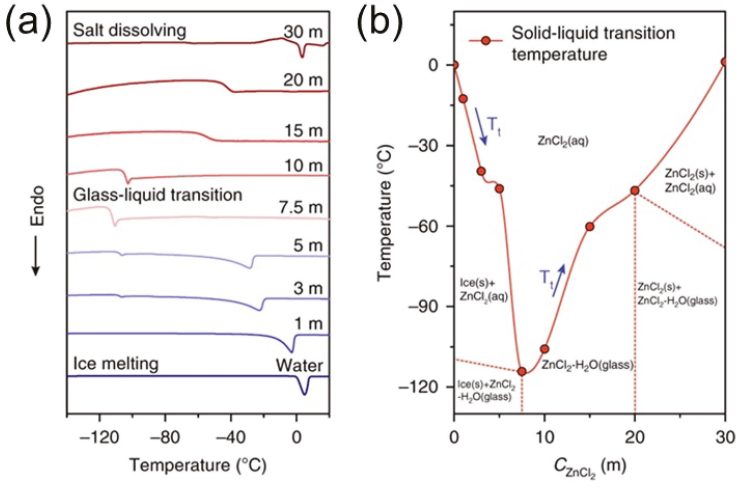

Figure 21. The properties of solid–liquid transitions and the mechanism of vitrification. Thermodynamic change and transition of different C_{ZnCl2} electrolytes at low temperatures. (**a**) DSC test from −150 to 20 °C at a heating rate of 5 °C min^{-1}. (**b**) The major Tt vs. C_{ZnCl2} and the phase composition of $ZnCl_2$ solution at different temperatures and concentrations. Reprinted with permission from Ref. [108]. Copyright 2020 Nature.

The mechanical stability of the electrode during lengthy displacement and the unexpected dendrite expansion during cycling are the most important issues encountered by zinc metal anodes, which tend to end in poor cycle performance and coulombic efficiency of the battery, restricting the lifetime of flexible zinc-ion batteries. Zinc may be a better electrode material than lithium because it is less costly, features a high percentage within the crust, and features a smaller redox equilibrium potential. Furthermore, because zinc is not sensitive to the environment, it is cheaper to fabricate and package zinc-based batteries than lithium-based batteries. Traditional zinc-based batteries, such as Zn-MnO_2, Zn-Ni,

and Zn-Air, currently exist on the market, however, they are mostly hard and applied in non-flexible electronic devices. Several studies have been conducted to make these batteries more adjustable. Furthermore, ZIBs have a bright future in wearable electronics thanks to their increased energy density, relatively low costs, environmentally friendly nature, reliability, and other advantages. ZIBs have received a lot of interest as a possible alternative to lithium-ion batteries. Besides that, the difficulties encountered by zinc metal anodes are the electrode's reliability value during lengthy displacement and unrestrained dendrite growth throughout cycling, leading to poor cycle effectiveness and battery coulombic efficiency, limiting the expected lifespan of flexible zinc-ion batteries, and negatively impacting their useful application.

6. Conclusions

Cathodes' dissolution and dendrite formation from aqueous electrolytes in an aqueous zinc-ion battery can negatively affect the storage capacity and cyclic stability. However, several approaches have been applied to form sustainable AZIBs, but they are still in their infancy. A flexible zinc-based battery is a promising technology because of gel electrolytes. Since they behave as electrolytic conductors and electrode separators, gel electrolytes are an important part of the flexible zinc-based battery. The influences of severe working conditions (i.e., cold and hot temperatures, physical deflections) on gel electrolytes and zinc-based batteries were systematically reviewed in this paper. Likewise, we introduced possible approaches and summarized their existing issues. It is proving to be useful to ascertain the battery function in quite a broad temperature range for an extended length of time without having to sacrifice other electrochemical behavior, which is completely essential for real implementation.

Author Contributions: Conceptualization and supervision, S.I. (Saiful Islam); writing—original draft preparation, M.A.-A.; Revision and English, S.U.A.S.; Revision, S.I. (Samia Iffat). All authors have read and agreed to the published version of the manuscript.

Funding: This research received no external funding.

Institutional Review Board Statement: Not applicable.

Informed Consent Statement: Not applicable.

Conflicts of Interest: Authors declare no conflict of interest.

References

1. Zhang, H.; Lu, W.; Li, X. Progress and Perspectives of Flow Battery Technologies. *Electrochem. Energy Rev.* **2019**, *2*, 492–506. [CrossRef]
2. Lu, W.; Li, X.; Zhang, H. The next Generation Vanadium Flow Batteries with High Power Density—A Perspective. *Phys. Chem. Chem. Phys.* **2018**, *20*, 23–35. [CrossRef] [PubMed]
3. Leung, P.; Shah, A.A.; Sanz, L.; Flox, C.; Morante, J.R.; Xu, Q.; Mohamed, M.R.; Ponce de León, C.; Walsh, F.C. Recent Developments in Organic Redox Flow Batteries: A Critical Review. *J. Power Sources* **2017**, *360*, 243–283. [CrossRef]
4. Winsberg, J.; Hagemann, T.; Janoschka, T.; Hager, M.D.; Schubert, U.S. Redox-Flow Batteries: From Metals to Organic Redox-Active Materials. *Angew. Chem. Int. Ed.* **2017**, *56*, 686–711. [CrossRef] [PubMed]
5. Wang, L.-P.; Li, N.-W.; Wang, T.-S.; Yin, Y.-X.; Guo, Y.-G.; Wang, C.-R. Conductive Graphite Fiber as a Stable Host for Zinc Metal Anodes. *Electrochim. Acta* **2017**, *244*, 172–177. [CrossRef]
6. Wang, X.; Wang, F.; Wang, L.; Li, M.; Wang, Y.; Chen, B.; Zhu, Y.; Fu, L.; Zha, L.; Zhang, L.; et al. An Aqueous Rechargeable $Zn//Co_3O_4$ Battery with High Energy Density and Good Cycling Behavior. *Adv. Mater.* **2016**, *28*, 4904–4911. [CrossRef]
7. Qiu, W.; Li, Y.; You, A.; Zhang, Z.; Li, G.; Lu, X.; Tong, Y. High-Performance Flexible Quasi-Solid-State Zn–MnO_2 Battery Based on MnO_2 Nanorod Arrays Coated 3D Porous Nitrogen-Doped Carbon Cloth. *J. Mater. Chem. A* **2017**, *5*, 14838–14846. [CrossRef]
8. Kang, Z.; Wu, C.; Dong, L.; Liu, W.; Mou, J.; Zhang, J.; Chang, Z.; Jiang, B.; Wang, G.; Kang, F.; et al. 3D Porous Copper Skeleton Supported Zinc Anode toward High Capacity and Long Cycle Life Zinc Ion Batteries. *ACS Sustain. Chem. Eng.* **2019**, *7*, 3364–3371. [CrossRef]
9. Liang, Y.; Dong, H.; Aurbach, D.; Yao, Y. Current Status and Future Directions of Multivalent Metal-Ion Batteries. *Nat. Energy* **2020**, *5*, 646–656. [CrossRef]
10. Liu, W.; Lu, W.; Zhang, H.; Li, X. Aqueous Flow Batteries: Research and Development. *Chem. A Eur. J.* **2019**, *25*, 1649–1664. [CrossRef]

11. Alfaruqi, M.H.; Mathew, V.; Gim, J.; Kim, S.; Song, J.; Baboo, J.P.; Choi, S.H.; Kim, J. Electrochemically Induced Structural Transformation in a γ-MnO_2 Cathode of a High Capacity Zinc-Ion Battery System. *Chem. Mater.* **2015**, *27*, 3609–3620. [CrossRef]
12. Islam, S.; Alfaruqi, M.H.; Mathew, V.; Song, J.; Kim, S.; Kim, S.; Jo, J.; Baboo, J.P.; Pham, D.T.; Putro, D.Y.; et al. Facile Synthesis and the Exploration of the Zinc Storage Mechanism of β-MnO_2nanorods with Exposed (101) Planes as a Novel Cathode Material for High Performance Eco-Friendly Zinc-Ion Batteries. *J. Mater. Chem. A* **2017**, *5*, 23299–23309. [CrossRef]
13. Zeng, Y.; Zhang, X.; Qin, R.; Liu, X.; Fang, P.; Zheng, D.; Tong, Y.; Lu, X. Dendrite-Free Zinc Deposition Induced by Multifunctional CNT Frameworks for Stable Flexible Zn-Ion Batteries. *Adv. Mater.* **2019**, *31*, 1903675. [CrossRef] [PubMed]
14. Li, C.; Shi, X.; Liang, S.; Ma, X.; Han, M.; Wu, X.; Zhou, J. Spatially Homogeneous Copper Foam as Surface Dendrite-Free Host for Zinc Metal Anode. *Chem. Eng. J.* **2020**, *379*, 122248. [CrossRef]
15. Wang, Z.; Huang, J.; Guo, Z.; Dong, X.; Liu, Y.; Wang, Y.; Xia, Y. A Metal-Organic Framework Host for Highly Reversible Dendrite-Free Zinc Metal Anodes. *Joule* **2019**, *3*, 1289–1300. [CrossRef]
16. Wang, S.-B.; Ran, Q.; Yao, R.-Q.; Shi, H.; Wen, Z.; Zhao, M.; Lang, X.-Y.; Jiang, Q. Lamella-Nanostructured Eutectic Zinc–Aluminum Alloys as Reversible and Dendrite-Free Anodes for Aqueous Rechargeable Batteries. *Nat. Commun.* **2020**, *11*, 1634. [CrossRef]
17. Han, C.; Li, W.; Liu, H.K.; Dou, S.; Wang, J. Principals and Strategies for Constructing a Highly Reversible Zinc Metal Anode in Aqueous Batteries. *Nano Energy* **2020**, *74*, 104880. [CrossRef]
18. Hu, P.; Zhu, T.; Wang, X.; Wei, X.; Yan, M.; Li, J.; Luo, W.; Yang, W.; Zhang, W.; Zhou, L.; et al. Highly Durable $Na_2V_6O_{16}{\cdot}1.63H_2O$ Nanowire Cathode for Aqueous Zinc-Ion Battery. *Nano Lett.* **2018**, *18*, 1758–1763. [CrossRef]
19. Tian, Y.; An, Y.; Wei, C.; Xi, B.; Xiong, S.; Feng, J.; Qian, Y. Flexible and Free-Standing Ti_3C_2Tx MXene@Zn Paper for Dendrite-Free Aqueous Zinc Metal Batteries and Nonaqueous Lithium Metal Batteries. *ACS Nano* **2019**, *13*, 11676–11685. [CrossRef] [PubMed]
20. Liu, B.; Wang, S.; Wang, Z.; Lei, H.; Chen, Z.; Mai, W. Novel 3D Nanoporous Zn–Cu Alloy as Long-Life Anode toward High-Voltage Double Electrolyte Aqueous Zinc-Ion Batteries. *Small* **2020**, *16*, 2001323. [CrossRef]
21. Li, H.; Soc, J.E.; Li, H.; Xu, C.; Han, C.; Chen, Y.; Wei, C. Enhancement on Cycle Performance of Zn Anodes by Activated Carbon Modification for Neutral Rechargeable Zinc Ion Batteries. *J. Electrochem. Soc.* **2015**, *162*, A1439. [CrossRef]
22. Sawada, Y. Transition of Growth Form from Dendrite to Aggregate. *Phys. A Stat. Mech. Appl.* **1986**, *140*, 134–141. [CrossRef]
23. Gomes, A.; da Silva Pereira, M.I. Pulsed Electrodeposition of Zn in the Presence of Surfactants. *Electrochim. Acta* **2006**, *51*, 1342–1350. [CrossRef]
24. Nayana, K.O.; Venkatesha, T. V Bright Zinc Electrodeposition and Study of Influence of Synergistic Interaction of Additives on Coating Properties. *J. Ind. Eng. Chem.* **2015**, *26*, 107–115. [CrossRef]
25. Yan, L.; Zeng, X.; Li, Z.; Meng, X.; Wei, D.; Liu, T.; Ling, M.; Lin, Z.; Liang, C. An Innovation: Dendrite Free Quinone Paired with $ZnMn_2O_4$ for Zinc Ion Storage. *Mater. Today Energy* **2019**, *13*, 323–330. [CrossRef]
26. Alfaruqi, M.H.; Islam, S.; Gim, J.; Song, J.; Kim, S.; Pham, D.T.; Jo, J.; Xiu, Z.; Mathew, V.; Kim, J. A High Surface Area Tunnel-Type α-MnO_2 Nanorod Cathode by a Simple Solvent-Free Synthesis for Rechargeable Aqueous Zinc-Ion Batteries. *Chem. Phys. Lett.* **2016**, *650*, 64–68. [CrossRef]
27. Islam, S.; Alfaruqi, M.H.; Song, J.; Kim, S.; Pham, D.T.; Jo, J.; Kim, S.; Mathew, V.; Baboo, J.P.; Xiu, Z.; et al. Carbon-Coated Manganese Dioxide Nanoparticles and Their Enhanced Electrochemical Properties for Zinc-Ion Battery Applications. *J. Energy Chem.* **2017**, *26*, 815–819. [CrossRef]
28. Ren, H.-Z.; Zhang, J.; Wang, B.; Luo, H.; Jin, F.; Zhang, T.-R.; Ding, A.; Cong, B.-W.; Wang, D.-L. A V_2O_3@N–C Cathode Material for Aqueous Zinc-Ion Batteries with Boosted Zinc-Ion Storage Performance. *Rare Met.* **2022**, *41*, 1605–1615. [CrossRef]
29. Alfaruqi, M.H.; Gim, J.; Kim, S.; Song, J.; Jo, J.; Kim, S.; Mathew, V.; Kim, J. Enhanced Reversible Divalent Zinc Storage in a Structurally Stable α-MnO_2 nanorod Electrode. *J. Power Sources* **2015**, *288*, 320–327. [CrossRef]
30. Alfaruqi, M.H.; Gim, J.; Kim, S.; Song, J.; Pham, D.T.; Jo, J.; Xiu, Z.; Mathew, V.; Kim, J. A Layered δ-MnO_2 Nanoflake Cathode with High Zinc-Storage Capacities for Eco-Friendly Battery Applications. *Electrochem. Commun.* **2015**, *60*, 121–125. [CrossRef]
31. Wei, C.; Xu, C.; Li, B.; Du, H.; Kang, F. Preparation and Characterization of Manganese Dioxides with Nano-Sized Tunnel Structures for Zinc Ion Storage. *J. Phys. Chem. Solids* **2012**, *73*, 1487–1491. [CrossRef]
32. Yuan, C.; Zhang, Y.; Pan, Y.; Liu, X.; Wang, G.; Cao, D. Investigation of the Intercalation of Polyvalent Cations (Mg^{2+}, Zn^{2+}) into λ-MnO_2 for Rechargeable Aqueous Battery. *Electrochim. Acta* **2014**, *116*, 404–412. [CrossRef]
33. Shoji, T.; Hishinuma, M.; Yamamoto, T. Zinc-Manganese Dioxide Galvanic Cell Using Zinc Sulphate as Electrolyte. Rechargeability of the Cell. *J. Appl. Electrochem.* **1988**, *18*, 521–526. [CrossRef]
34. Xu, C.; Li, B.; Du, H.; Kang, F. Energetic Zinc Ion Chemistry: The Rechargeable Zinc Ion Battery. *Angew. Chem. Int. Ed.* **2012**, *51*, 933–935. [CrossRef] [PubMed]
35. Lu, X.; Yu, M.; Wang, G.; Tong, Y.; Li, Y. Flexible Solid-State Supercapacitors: Design, Fabrication and Applications. *Energy Environ. Sci.* **2014**, *7*, 2160–2181. [CrossRef]
36. Wu, K.; Huang, J.; Yi, J.; Liu, X.; Liu, Y.; Wang, Y.; Zhang, J.; Xia, Y. Recent Advances in Polymer Electrolytes for Zinc Ion Batteries: Mechanisms, Properties, and Perspectives. *Adv. Energy Mater.* **2020**, *10*, 1903977. [CrossRef]
37. Cai, X.; Peng, M.; Yu, X.; Fu, Y.; Zou, D. Flexible Planar/Fiber-Architectured Supercapacitors for Wearable Energy Storage. *J. Mater. Chem. C* **2014**, *2*, 1184–1200. [CrossRef]
38. Sumboja, A.; Liu, J.; Zheng, W.G.; Zong, Y.; Zhang, H.; Liu, Z. Electrochemical Energy Storage Devices for Wearable Technology: A Rationale for Materials Selection and Cell Design. *Chem. Soc. Rev.* **2018**, *47*, 5919–5945. [CrossRef]

39. Yu, M.; Lin, D.; Feng, H.; Zeng, Y.; Tong, Y.; Lu, X. Boosting the Energy Density of Carbon-Based Aqueous Supercapacitors by Optimizing the Surface Charge. *Angew. Chem. Int. Ed.* **2017**, *56*, 5454–5459. [CrossRef]
40. Gaikwad, A.M.; Whiting, G.L.; Steingart, D.A.; Arias, A.C. Highly Flexible, Printed Alkaline Batteries Based on Mesh-Embedded Electrodes. *Adv. Mater.* **2011**, *23*, 3251–3255. [CrossRef]
41. Yu, P.; Zeng, Y.; Zhang, H.; Yu, M.; Tong, Y.; Lu, X. Flexible Zn-Ion Batteries: Recent Progresses and Challenges. *Small* **2019**, *15*, 1804760. [CrossRef]
42. Sepúlveda, A.; Speulmanns, J.; Vereecken, P.M. Bending Impact on the Performance of a Flexible $Li_4Ti_5O_{12}$-Based All-Solid-State Thin-Film Battery. *Sci. Technol. Adv. Mater.* **2018**, *19*, 454–464. [CrossRef] [PubMed]
43. Sun, W.; Wang, F.; Hou, S.; Yang, C.; Fan, X.; Ma, Z.; Gao, T.; Han, F.; Hu, R.; Zhu, M.; et al. Zn/MnO_2 Battery Chemistry With H^+ and Zn^{2+} Coinsertion. *J. Am. Chem. Soc.* **2017**, *139*, 9775–9778. [CrossRef] [PubMed]
44. Wu, B.; Zhang, G.; Yan, M.; Xiong, T.; He, P.; He, L.; Xu, X.; Mai, L. Graphene Scroll-Coated α-MnO_2 Nanowires as High-Performance Cathode Materials for Aqueous Zn-Ion Battery. *Small* **2018**, *14*, 1–8. [CrossRef] [PubMed]
45. Chao, D.; Zhou, W.; Xie, F.; Ye, C.; Li, H.; Jaroniec, M.; Qiao, S.-Z. Roadmap for Advanced Aqueous Batteries: From Design of Materials to Applications. *Sci. Adv.* **2022**, *6*, eaba4098. [CrossRef]
46. Islam, S.; Lee, S.; Lee, S.; Hilmy Alfaruqi, M.; Sambandam, B.; Mathew, V.; Hwang, J.-Y.; Kim, J. Triggering the Theoretical Capacity of $Na_{1.1}V_3O_{7.9}$ Nanorod Cathode by Polypyrrole Coating for High-Energy Zinc-Ion Batteries. *Chem. Eng. J.* **2022**, *446*, 137069. [CrossRef]
47. Islam, S.; Alfaruqi, M.H.; Putro, D.Y.; Soundharrajan, V.; Sambandam, B.; Jo, J.; Park, S.; Lee, S.; Mathew, V.; Kim, J. K+ Intercalated V_2O_5 Nanorods with Exposed Facets as Advanced Cathodes for High Energy and High Rate Zinc-Ion Batteries. *J. Mater. Chem. A* **2019**, *7*, 20335–20347. [CrossRef]
48. Wang, J.; Qiu, H.; Zhao, Z.; Zhang, Y.; Zhao, J.; Ma, Y.; Li, J.; Xing, M.; Li, G.; Cui, G. Anti-Corrosive Hybrid Electrolytes for Rechargeable Aqueous Zinc Batteries. *Chem. Res. Chinese Univ.* **2021**, *37*, 328–334. [CrossRef]
49. Trudgeon, D.P.; Li, X. The Effect of Electrolyte and Additive Concentration on Zinc–Nickel Flow Cell Performance. *Electrochim. Acta* **2021**, *367*, 137479. [CrossRef]
50. Bayaguud, A.; Luo, X.; Fu, Y.; Zhu, C. Cationic Surfactant-Type Electrolyte Additive Enables Three-Dimensional Dendrite-Free Zinc Anode for Stable Zinc-Ion Batteries. *ACS Energy Lett.* **2020**, *5*, 3012–3020. [CrossRef]
51. Liu, X.; Bolton, O.; Akolkar, R. Experimental and Modeling Studies of the Hysteresis Behavior and Dendrite Suppression Efficacy of an Electrolyte Additive in Zinc Electrodeposition. *J. Electrochem. Soc.* **2019**, *166*, D583–D588. [CrossRef]
52. Hosseini, S.; Abbasi, A.; Uginet, L.-O.; Haustraete, N.; Praserthdam, S.; Yonezawa, T.; Kheawhom, S. The Influence of Dimethyl Sulfoxide as Electrolyte Additive on Anodic Dissolution of Alkaline Zinc-Air Flow Battery. *Sci. Rep.* **2019**, *9*, 14958. [CrossRef] [PubMed]
53. Bani Hashemi, A.; Kasiri, G.; La Mantia, F. The Effect of Polyethyleneimine as an Electrolyte Additive on Zinc Electrodeposition Mechanism in Aqueous Zinc-Ion Batteries. *Electrochim. Acta* **2017**, *258*, 703–708. [CrossRef]
54. Xu, W.; Zhao, K.; Huo, W.; Wang, Y.; Yao, G.; Gu, X.; Cheng, H.; Mai, L.; Hu, C.; Wang, X. Diethyl Ether as Self-Healing Electrolyte Additive Enabled Long-Life Rechargeable Aqueous Zinc Ion Batteries. *Nano Energy* **2019**, *62*, 275–281. [CrossRef]
55. Zhao, K.; Liu, F.; Fan, G.; Liu, J.; Yu, M.; Yan, Z.; Zhang, N.; Cheng, F. Stabilizing Zinc Electrodes with a Vanillin Additive in Mild Aqueous Electrolytes. *ACS Appl. Mater. Interfaces* **2021**, *13*, 47650–47658. [CrossRef]
56. Abdulla, J.; Cao, J.; Zhang, D.; Zhang, X.; Sriprachuabwong, C.; Kheawhom, S.; Wangyao, P.; Qin, J. Elimination of Zinc Dendrites by Graphene Oxide Electrolyte Additive for Zinc-Ion Batteries. *ACS Appl. Energy Mater.* **2021**, *4*, 4602–4609. [CrossRef]
57. Lee, J.; Ju, J.B.; Cho, W.I.; Cho, B.W.; Oh, S.H. Todorokite-Type MnO_2 as a Zinc-Ion Intercalating Material. *Electrochim. Acta* **2013**, *112*, 138–143. [CrossRef]
58. Lee, B.; Yoon, C.S.; Lee, H.R.; Chung, K.Y.; Cho, B.W.; Oh, S.H. Electrochemically-Induced Reversible Transition from the Tunneled to Layered Polymorphs of Manganese Dioxide. *Sci. Rep.* **2014**, *4*, 6066. [CrossRef]
59. Li, Y.; Wang, S.; Salvador, J.R.; Wu, J.; Liu, B.; Yang, W.; Yang, J.; Zhang, W.; Liu, J.; Yang, J. Reaction Mechanisms for Long-Life Rechargeable Zn/MnO_2 Batteries. *Chem. Mater.* **2019**, *31*, 2036–2047. [CrossRef]
60. Qiu, N.; Chen, H.; Yang, Z.; Sun, S.; Wang, Y. Low-Cost Birnessite as a Promising Cathode for High-Performance Aqueous Rechargeable Batteries. *Electrochim. Acta* **2018**, *272*, 154–160. [CrossRef]
61. Xu, D.; Li, B.; Wei, C.; He, Y.-B.; Du, H.; Chu, X.; Qin, X.; Yang, Q.-H.; Kang, F. Preparation and Characterization of MnO_2/Acid-Treated CNT Nanocomposites for Energy Storage with Zinc Ions. *Electrochim. Acta* **2014**, *133*, 254–261. [CrossRef]
62. Lee, B.; Lee, H.R.; Kim, H.; Chung, K.Y.; Cho, B.W.; Oh, S.H. Elucidating the Intercalation Mechanism of Zinc Ions into α-MnO_2 for Rechargeable Zinc Batteries. *Chem. Commun.* **2015**, *51*, 9265–9268. [CrossRef] [PubMed]
63. Alfaruqi, M.H.; Islam, S.; Mathew, V.; Song, J.; Kim, S.; Tung, D.P.; Jo, J.; Kim, S.; Baboo, J.P.; Xiu, Z.; et al. Ambient Redox Synthesis of Vanadium-Doped Manganese Dioxide Nanoparticles and Their Enhanced Zinc Storage Properties. *Appl. Surf. Sci.* **2017**, *404*, 435–442. [CrossRef]
64. Zhang, N.; Cheng, F.; Liu, J.; Wang, L.; Long, X.; Liu, X.; Li, F.; Chen, J. Rechargeable Aqueous Zinc-Manganese Dioxide Batteries with High Energy and Power Densities. *Nat. Commun.* **2017**, *8*, 405. [CrossRef] [PubMed]
65. Huang, J.; Wang, Z.; Hou, M.; Dong, X.; Liu, Y.; Wang, Y.; Xia, Y. Polyaniline-Intercalated Manganese Dioxide Nanolayers as a High-Performance Cathode Material for an Aqueous Zinc-Ion Battery. *Nat. Commun.* **2018**, *9*, 2906. [CrossRef]
66. Chao, D.; Zhou, W.; Ye, C.; Zhang, Q.; Chen, Y.; Gu, L.; Davey, K.; Qiao, S.-Z. An Electrolytic Zn–MnO_2 Battery for High-Voltage and Scalable Energy Storage. *Angew. Chem. Int. Ed.* **2019**, *58*, 7823–7828. [CrossRef]

67. Islam, S.; Alfaruqi, M.H.; Putro, D.Y.; Park, S.; Kim, S.; Lee, S.; Ahmed, M.S.; Mathew, V.; Sun, Y.-K.; Hwang, J.-Y.; et al. In Situ Oriented Mn Deficient $ZnMn_2O_4$@C Nanoarchitecture for Durable Rechargeable Aqueous Zinc-Ion Batteries. *Adv. Sci.* **2021**, 2002636. [CrossRef]
68. Yin, C.; Pan, C.; Liao, X.; Pan, Y.; Yuan, L. Coordinately Unsaturated Manganese-Based Metal–Organic Frameworks as a High-Performance Cathode for Aqueous Zinc-Ion Batteries. *ACS Appl. Mater. Interfaces* **2021**, *13*, 35837–35847. [CrossRef]
69. Fang, G.; Zhu, C.; Chen, M.; Zhou, J.; Tang, B.; Cao, X.; Zheng, X.; Pan, A.; Liang, S. Suppressing Manganese Dissolution in Potassium Manganate with Rich Oxygen Defects Engaged High-Energy-Density and Durable Aqueous Zinc-Ion Battery. *Adv. Funct. Mater.* **2019**, *29*, 1808375. [CrossRef]
70. Yan, M.; Zhao, L.; Zhao, K.; Wei, Q.; An, Q.; Zhang, G.; Wei, X.; Ren, W.; Mai, L. The Capturing of Ionized Oxygen in Sodium Vanadium Oxide Nanorods Cathodes under Operando Conditions. *Adv. Funct. Mater.* **2016**, *26*, 6555–6562. [CrossRef]
71. He, P.; Zhang, G.; Liao, X.; Yan, M.; Xu, X.; An, Q.; Liu, J.; Mai, L. Sodium Ion Stabilized Vanadium Oxide Nanowire Cathode for High-Performance Zinc-Ion Batteries. *Adv. Energy Mater.* **2018**, *8*, 1–6. [CrossRef]
72. Islam, S.; Alfaruqi, M.H.; Sambandam, B.; Putro, D.Y.; Kim, S.; Jo, J.; Kim, S.; Mathew, V.; Kim, J. A New Rechargeable Battery Based on a Zinc Anode and a NaV_6O_{15} Nanorod Cathode. *Chem. Commun.* **2019**, *55*, 3793–3796. [CrossRef] [PubMed]
73. Alfaruqi, M.H.; Mathew, V.; Song, J.; Kim, S.; Islam, S.; Pham, D.T.; Jo, J.; Kim, S.; Baboo, J.P.; Xiu, Z.; et al. Electrochemical Zinc Intercalation in Lithium Vanadium Oxide: A High-Capacity Zinc-Ion Battery Cathode. *Chem. Mater.* **2017**, *29*, 1684–1694. [CrossRef]
74. Islam, S.; Alfaruqi, M.H.; Putro, D.Y.; Mathew, V.; Kim, S.; Jo, J.; Kim, S.; Sun, Y.K.; Kim, K.; Kim, J. Pyrosynthesis of $Na_3v_2(Po_4)3$@c Cathodes for Safe and Low-Cost Aqueous Hybrid Batteries. *ChemSusChem* **2018**, *11*, 2239–2247. [CrossRef] [PubMed]
75. Liu, Y.; Xie, L.; Zhang, W.; Dai, Z.; Wei, W.; Luo, S.; Chen, X.; Chen, W.; Rao, F.; Wang, L.; et al. Conjugated System of PEDOT:PSS-Induced Self-Doped PANI for Flexible Zinc-Ion Batteries with Enhanced Capacity and Cyclability. *ACS Appl. Mater. Interfaces* **2019**, *11*, 30943–30952. [CrossRef]
76. Li, H.; Liu, Z.; Liang, G.; Huang, Y.; Huang, Y.; Zhu, M.; Pei, Z.; Xue, Q.; Tang, Z.; Wang, Y.; et al. Waterproof and Tailorable Elastic Rechargeable Yarn Zinc Ion Batteries by a Cross-Linked Polyacrylamide Electrolyte. *ACS Nano* **2018**, *12*, 3140–3148. [CrossRef]
77. Xu, Y.; Xu, X.; Guo, M.; Zhang, G.; Wang, Y. Research Progresses and Challenges of Flexible Zinc Battery. *Front. Chem.* **2022**, *10*. [CrossRef]
78. Dong, H.; Li, J.; Guo, J.; Lai, F.; Zhao, F.; Jiao, Y.; Brett, D.J.L.; Liu, T.; He, G.; Parkin, I.P. Insights on Flexible Zinc-Ion Batteries from Lab Research to Commercialization. *Adv. Mater.* **2021**, *33*, 2007548. [CrossRef]
79. Lu, Y.; Zhu, T.; Xu, N.; Huang, K. A Semisolid Electrolyte for Flexible Zn-Ion Batteries. *ACS Appl. Energy Mater.* **2019**, *2*, 6904–6910. [CrossRef]
80. Dong, H.; Li, J.; Zhao, S.; Jiao, Y.; Chen, J.; Tan, Y.; Brett, D.J.L.; He, G.; Parkin, I.P. Investigation of a Biomass Hydrogel Electrolyte Naturally Stabilizing Cathodes for Zinc-Ion Batteries. *ACS Appl. Mater. Interfaces* **2021**, *13*, 745–754. [CrossRef]
81. Ma, L.; Chen, S.; Li, H.; Ruan, Z.; Tang, Z.; Liu, Z.; Wang, Z.; Huang, Y.; Pei, Z.; Zapien, J.A.; et al. Initiating a Mild Aqueous Electrolyte Co_3O_4/Zn Battery with 2.2 V-High Voltage and 5000-Cycle Lifespan by a Co(Iii) Rich-Electrode. *Energy Environ. Sci.* **2018**, *11*, 2521–2530. [CrossRef]
82. Chao, D.; Zhu, C.; Song, M.; Liang, P.; Zhang, X.; Tiep, N.H.; Zhao, H.; Wang, J.; Wang, R.; Zhang, H.; et al. A High-Rate and Stable Quasi-Solid-State Zinc-Ion Battery with Novel 2D Layered Zinc Orthovanadate Array. *Adv. Mater.* **2018**, *30*, 1803181. [CrossRef] [PubMed]
83. Zeng, Y.; Zhang, X.; Meng, Y.; Yu, M.; Yi, J.; Wu, Y.; Lu, X.; Tong, Y. Achieving Ultrahigh Energy Density and Long Durability in a Flexible Rechargeable Quasi-Solid-State Zn–MnO2 Battery. *Adv. Mater.* **2017**, *29*, 1700274. [CrossRef] [PubMed]
84. Li, H.; Yang, Q.; Mo, F.; Liang, G.; Liu, Z.; Tang, Z.; Ma, L.; Liu, J.; Shi, Z.; Zhi, C. MoS_2 Nanosheets with Expanded Interlayer Spacing for Rechargeable Aqueous Zn-Ion Batteries. *Energy Storage Mater.* **2019**, *19*, 94–101. [CrossRef]
85. Wan, F.; Zhang, L.; Dai, X.; Wang, X.; Niu, Z.; Chen, J. Aqueous Rechargeable Zinc/Sodium Vanadate Batteries with Enhanced Performance from Simultaneous Insertion of Dual Carriers. *Nat. Commun.* **2018**, *9*, 1656. [CrossRef] [PubMed]
86. Li, H.; Han, C.; Huang, Y.; Huang, Y.; Zhu, M.; Pei, Z.; Xue, Q.; Wang, Z.; Liu, Z.; Tang, Z.; et al. An Extremely Safe and Wearable Solid-State Zinc Ion Battery Based on a Hierarchical Structured Polymer Electrolyte. *Energy Environ. Sci.* **2018**, *11*, 941–951. [CrossRef]
87. Liu, Z.; Mo, F.; Li, H.; Zhu, M.; Wang, Z.; Liang, G.; Zhi, C. Advances in Flexible and Wearable Energy-Storage Textiles. *Small Methods* **2018**, *2*, 1800124. [CrossRef]
88. Huang, Y.; Liu, J.; Huang, Q.; Zheng, Z.; Hiralal, P.; Zheng, F.; Ozgit, D.; Su, S.; Chen, S.; Tan, P.-H.; et al. Flexible High Energy Density Zinc-Ion Batteries Enabled by Binder-Free MnO_2/Reduced Graphene Oxide Electrode. *npj Flex. Electron.* **2018**, *2*, 21. [CrossRef]
89. Dai, X.; Wan, F.; Zhang, L.; Cao, H.; Niu, Z. Freestanding Graphene/VO_2 Composite Films for Highly Stable Aqueous Zn-Ion Batteries with Superior Rate Performance. *Energy Storage Mater.* **2019**, *17*, 143–150. [CrossRef]
90. Zhang, S.; Yu, N.; Zeng, S.; Zhou, S.; Chen, M.; Di, J.; Li, Q. An Adaptive and Stable Bio-Electrolyte for Rechargeable Zn-Ion Batteries. *J. Mater. Chem. A* **2018**, *6*, 12237–12243. [CrossRef]
91. Wan, F.; Zhang, L.; Wang, X.; Bi, S.; Niu, Z.; Chen, J. An Aqueous Rechargeable Zinc-Organic Battery with Hybrid Mechanism. *Adv. Funct. Mater.* **2018**, *28*, 1804975. [CrossRef]

92. Wang, K.; Zhang, X.; Han, J.; Zhang, X.; Sun, X.; Li, C.; Liu, W.; Li, Q.; Ma, Y. High-Performance Cable-Type Flexible Rechargeable Zn Battery Based on MnO2@CNT Fiber Microelectrode. *ACS Appl. Mater. Interfaces* **2018**, *10*, 24573–24582. [CrossRef] [PubMed]
93. Wang, Z.; Ruan, Z.; Liu, Z.; Wang, Y.; Tang, Z.; Li, H.; Zhu, M.; Hung, T.F.; Liu, J.; Shi, Z.; et al. A Flexible Rechargeable Zinc-Ion Wire-Shaped Battery with Shape Memory Function. *J. Mater. Chem. A* **2018**, *6*, 8549–8557. [CrossRef]
94. Ma, L.; Chen, S.; Pei, Z.; Li, H.; Wang, Z.; Liu, Z.; Tang, Z.; Zapien, J.A.; Zhi, C. Flexible Waterproof Rechargeable Hybrid Zinc Batteries Initiated by Multifunctional Oxygen Vacancies-Rich Cobalt Oxide. *ACS Nano* **2018**, *12*, 8597–8605. [CrossRef]
95. Lu, K.; Song, B.; Zhang, Y.; Ma, H.; Zhang, J. Encapsulation of Zinc Hexacyanoferrate Nanocubes with Manganese Oxide Nanosheets for High-Performance Rechargeable Zinc Ion Batteries. *J. Mater. Chem. A* **2017**, *5*, 23628–23633. [CrossRef]
96. Putro, D.Y.; Alfaruqi, M.H.; Islam, S.; Kim, S.; Park, S.; Lee, S.; Hwang, J.-Y.; Sun, Y.-K.; Kim, J. Quasi-Solid-State Zinc-Ion Battery Based on α-MnO_2 Cathode with Husk-like Morphology. *Electrochim. Acta* **2020**, *345*, 136189. [CrossRef]
97. Song, Y.; Li, J.; Qiao, R.; Dai, X.; Jing, W.; Song, J.; Chen, Y.; Guo, S.; Sun, J.; Tan, Q.; et al. Binder-Free Flexible Zinc-Ion Batteries: One-Step Potentiostatic Electrodeposition Strategy Derived Ce Doped-MnO_2 Cathode. *Chem. Eng. J.* **2022**, *431*, 133387. [CrossRef]
98. Liu, J.; Lai, J.; Huang, X.; Liu, H. Nanocellulose-Based Hybrid Hydrogels as Flexible Cathodes of Aqueous Zn-Ion Batteries. *Nano* **2019**, *14*, 1950047. [CrossRef]
99. Liu, C.; Xie, X.; Lu, B.; Zhou, J.; Liang, S. Electrolyte Strategies toward Better Zinc-Ion Batteries. *ACS Energy Lett.* **2021**, *6*, 1015–1033. [CrossRef]
100. Liu, T.; Chen, X.; Tervoort, E.; Kraus, T.; Niederberger, M. Design and Fabrication of Transparent and Stretchable Zinc Ion Batteries. *ACS Appl. Energy Mater.* **2021**, *4*, 6166–6179. [CrossRef]
101. Poosapati, A.; Vadnala, S.; Negrete, K.; Lan, Y.; Hutchison, J.; Zupan, M.; Madan, D. Rechargeable Zinc-Electrolytic Manganese Dioxide (EMD) Battery with a Flexible Chitosan-Alkaline Electrolyte. *ACS Appl. Energy Mater.* **2021**, *4*, 4248–4258. [CrossRef]
102. Wang, B.; Li, J.; Hou, C.; Zhang, Q.; Li, Y.; Wang, H. Stable Hydrogel Electrolytes for Flexible and Submarine-Use Zn-Ion Batteries. *ACS Appl. Mater. Interfaces* **2020**, *12*, 46005–46014. [CrossRef] [PubMed]
103. Hieu, L.T.; So, S.; Kim, I.T.; Hur, J. Zn Anode with Flexible β-PVDF Coating for Aqueous Zn-Ion Batteries with Long Cycle Life. *Chem. Eng. J.* **2021**, *411*, 128584. [CrossRef]
104. Chen, Y.; Li, J.; Zhang, S.; Cui, J.; Shao, M. Highly Reversible Zinc Anode Enhanced by Ultrathin MnO_2 Cathode Material Film for High-Performance Zinc-Ion Batteries. *Adv. Mater. Interfaces* **2020**, *7*, 2000510. [CrossRef]
105. Dong, L.; Yang, W.; Yang, W.; Tian, H.; Huang, Y.; Wang, X.; Xu, C.; Wang, C.; Kang, F.; Wang, G. Flexible and Conductive Scaffold-Stabilized Zinc Metal Anodes for Ultralong-Life Zinc-Ion Batteries and Zinc-Ion Hybrid Capacitors. *Chem. Eng. J.* **2020**, *384*, 123355. [CrossRef]
106. Li, X.; Wang, H.; Sun, X.; Li, J.; Liu, Y.-N. Flexible Wide-Temperature Zinc-Ion Battery Enabled by an Ethylene Glycol-Based Organohydrogel Electrolyte. *ACS Appl. Energy Mater.* **2021**, *4*, 12718–12727. [CrossRef]
107. Wang, Y.; Chen, Y. A Flexible Zinc-Ion Battery Based on the Optimized Concentrated Hydrogel Electrolyte for Enhanced Performance at Subzero Temperature. *Electrochim. Acta* **2021**, *395*, 139178. [CrossRef]
108. Zhang, Q.; Ma, Y.; Lu, Y.; Li, L.; Wan, F.; Zhang, K.; Chen, J. Modulating Electrolyte Structure for Ultralow Temperature Aqueous Zinc Batteries. *Nat. Commun.* **2020**, *11*, 4463. [CrossRef]

catalysts

MDPI

Article

The Study on the Active Site Regulated $RuO_x/Sn_{0.2}Ti_{0.8}O_2$ Catalysts with Different Ru Precursors for the Catalytic Oxidation of Dichloromethane

Yang Yang [1,*], Zhong Zheng [1], Mengyue Kong [2], Zhesheng Hua [1], Zhengda Yang [3], Ye Jiang [3], Shaojun Liu [1], Xinhuan Yan [2,*] and Xiang Gao [1]

[1] Institute for Thermal Power Engineering, Zhejiang University, Hangzhou 310027, China; 21927034@zju.edu.cn (Z.Z.); 21927085@zju.edu.cn (Z.H.); phoenix205@zju.edu.cn (S.L.); xgao1@zju.edu.cn (X.G.)
[2] College of Chemical Engineering, Zhejiang University of Technology, Hangzhou 310014, China; mykong2015@126.com
[3] College of New Energy, China University of Petroleum (East China), Qingdao 266580, China; yzd019@upc.edu.cn (Z.Y.); jiangye@upc.edu.cn (Y.J.)
* Correspondence: 11527077@zju.edu.cn (Y.Y.); xhyan@zjut.edu.cn (X.Y.)

Abstract: Chlorine-containing volatile organic compounds (CVOCs) present in industrial exhaust gas can cause great harm to the human body and the environment. In order to further study the catalytic oxidation of CVOCs, an active site regulated $RuO_x/Sn_{0.2}Ti_{0.8}O_2$ catalyst with different Ru precursors was developed. With Dichloromethane as the model molecule, the activity test results showed that the optimization of Ru precursor using Ru colloid significantly increased the activity of the catalyst (T_{90} was reduced by about 90 °C when the Ru loading was 1 wt%). The analysis of characterization results showed that the improvement of the catalytic performance was mainly due to the improvement of the active species dispersion (the size of Ru cluster was reduced from 3–4 nm to about 1.3 nm) and the enhancement of the interaction between the active species and the support. The utilization efficiency of the active components was improved by nearly doubling TOF value, and the overall oxidation performance of the catalyst was also enhanced. The relationship between the Ru loading and the catalytic activity of the catalyst was also studied to better determine the optimal Ru loading. It could be found that with the increase in Ru loading, the dispersibility of RuO_x species on the catalyst surface gradually decreased, despite the increase in their total amount. The combined influence of these two effects led to little change in the catalytic activity of the catalyst at first, and then a significant increase. Therefore, this research is meaningful for the efficient treatment of CVOCs and further reducing the content of active components in the catalysts.

Keywords: air pollution; dichloromethane; catalytic oxidation; Ru; colloid

Citation: Yang, Y.; Zheng, Z.; Kong, M.; Hua, Z.; Yang, Z.; Jiang, Y.; Liu, S.; Yan, X.; Gao, X. The Study on the Active Site Regulated $RuO_x/Sn_{0.2}Ti_{0.8}O_2$ Catalysts with Different Ru Precursors for the Catalytic Oxidation of Dichloromethane. *Catalysts* **2021**, *11*, 1306. https://doi.org/10.3390/catal11111306

Academic Editors: Zhenghua Tang, Marc Cretin and Sophie Tingry

Received: 27 September 2021
Accepted: 25 October 2021
Published: 28 October 2021

1. Introduction

Chlorine-containing volatile organic compounds (CVOCs) are widely present in waste gas emitted by industries such as dry cleaning, medicine, organic synthesis, and metal processing [1–4]. CVOCs is listed as one of the culprits of the atmospheric ozone hole and promotes the generation of haze and photochemical smog. Due to its strong toxicity and bioaccumulation, CVOCs will cause great harm to the human body as well. Therefore, many CVOCs have been listed as priority pollutants by the United States, China and many other countries [5–8]. The catalytic combustion method is considered to be an advanced technology that can effectively eliminate CVOCs due to its advantages of low ignition temperature, low energy consumption, high removal efficiency, and small secondary pollution [9,10]. Because the existing catalysts generally face problems such as low catalytic activity and poor chlorine poisoning resistance, the development of efficient and stable catalysts is at the core of catalytic combustion process research [11].

The important reason of chlorine poisoning deactivation of the catalyst is that the Cl species adsorbed on the surface of the catalyst is difficult to remove in a sufficient time-frame, thus blocking the active sites of the catalyst [9,12]. Ru-based catalysts are widely used in heterogeneous catalysis, including the decomposition of various organic compounds [13,14] and the oxidation of carbon monoxide [15,16], due to their excellent redox performance. At the same time, because of the unique promotion of Ru species to Deacon reaction ($4HCl + O_2 = 2Cl_2 + 2H_2O$) [17], Ru-based catalyst possess great stability under HCl/Cl_2 conditions. Therefore, the introduction of Ru species is expected to significantly improve the chlorine poisoning resistance and oxidation performance of the catalyst. In addition, the acidic sites on the surface of the catalyst can effectively adsorb and activate the C-Cl bonds of the CVOC molecules, thereby improving the low-temperature catalytic activity of the catalyst [10,18,19]. Our previous study found that $Sn_{0.2}Ti_{0.8}O_2$ support could not only provide sufficient Lewis acid sites, but also effectively solve the problem of Ru species aggregation by contributing to the epitaxy growth of Ru species on its surface due to its rutile crystal form [20]. With further in-depth research, how to further improve the catalytic activity of the catalyst, reduce the active component Ru loading, and reduce the cost of catalyst preparation has become a major problem that needs to be overcome.

Many methods aimed at increasing the catalytic activity of catalysts essentially increase the total number of active sites on the catalyst surface. The total number of active sites on the catalyst surface is related to many factors. First, increasing the content of active components on the catalyst can increase the total number of active sites to a certain extent [21]. However, not all the loaded active components are highly active, if the active components are aggregated on the catalyst surface, the total number of active sites may be far less than the active component loading [22], so the dispersibility of the active components should also be considered. The optimization of the catalyst preparation method can significantly improve the physical and chemical properties of the catalyst [23]. Studies have shown that pre-preparing precious metals such as Ag, Au, Pt and Pd into nanoparticles before loading them can significantly improve the dispersion of active components and improve the utilization efficiency of active components [21,24–28]. In addition, the improvement of support crystal types [20] and the addition of specific anchor sites [29,30] can effectively promote the dispersion of active components and prevent their agglomeration.

In this paper, we optimized the Ru precursor and used $Sn_{0.2}Ti_{0.8}O_2$ as support to prepare efficient and stable CVOCs catalysts. Using DCM (dichloromethane) as the model molecule, differences in catalytic activity between the catalysts using different Ru precursors under the same RuO_x loading condition was compared, and the physical and chemical properties of the catalyst were analysed by a variety of characterization analysis methods. In addition, in order to select the optimal RuO_x loading more scientifically and efficiently, we adjusted the RuO_x loading to study the specific relationship between the catalytic performance of the catalyst and the RuO_x content.

2. Experimental Section

2.1. Catalyst Preparation

$Sn_{0.2}Ti_{0.8}O_2$ support was prepared by using the co-precipitation method. A certain amount of $SnCl_4$ and tetrabutyl titanate (TBT) was added into deionized water. After full stirring, 25% ammonia solution was added to adjust the pH to 10. After 12 h of aging, the precipitate was dried, ground, and calcined at 500 °C for 5 h to obtain the final support (which was named as ST).

The o-1-RuST sample was obtained by loading Ru through the traditional impregnation method. The support powder was added after mixing an appropriate amount of $RuCl_3$ precursor solution and quantificational 15% hydrogen peroxide solution under the condition of 95 °C water bath. The catalyst with 1 wt% Ru loading was evaporated, dried, ground, and calcined at 500 °C for 5 h. In order to further confirm the significant

improvement in the catalytic performance by the optimization of Ru precursor, we also prepared the o-5-RuST sample with a Ru loading of 5 wt% for catalytic activity comparison.

Three samples with Ru mass fractions of 0.1 wt%, 0.5 wt% and 1 wt% were obtained by loading Ru through Ru colloid solution, which was named c-0.1-RuST, c-0.5-RuST and c-1-RuST, respectively. The preparation method of Ru colloidal solution is as follows: The precursor $RuCl_3$ was dissolved in propylene carbonate solution at a concentration of 0.3 mg/mL. Then, PVP (Polyvinylpyrrolidone) with a molar ratio of 20:1 to $RuCl_3$ and Triethylamine with a molar ratio of 10:1 to $RuCl_3$ were added. After fully stirring, transferred the solution to the autoclave, passed hydrogen to 8 MPa, heated to 30 °C and reacted for 2 h to obtain the desired colloid solution. The Ru colloid solution was then taken with different content and fully mixed with the support powder, evaporated, dried, ground, and calcined at 500 °C for 5 h to obtain the three samples with different Ru contents.

The chemical reagents used in the preparation of the catalyst are shown in Table S1.

2.2. Catalyst Characterization

XRF characterization using Bruker D8 Advance (Bruker, Berlin, Germany) was performed to measure the actual content of Ti and Ru in the catalyst. The D2 PHASER (Bruker, Berlin, Germany) crystal diffractometer was used for XRD characterization to quantitatively and qualitatively analyse the phase parameters of the catalyst. XPS technique with the equipment of Thermo ESCALAB 250XI (Waltham, MA, America) was used to determine the valence distribution of Ru and O elements on the surface of the catalyst, and the binding energy of all elements was calibrated with C 1 s at 284.8 eV as the standard. TEM-mapping was used to characterize and observe the catalyst particle size and surface element dispersion, and the instrument model was JEOL 2100F TEM/STEM (Tokyo, Japan). The size of Ru clusters in each sample was further observed using a spherical aberration-corrected transmission electron microscope, the model of which was Titan ChemiSTEM (Thermo fisher, Waltham, MA, America). An AutoChem II 2920 (Micromeritics, GA, America) model of automatic temperature programmed chemical adsorption instrument was used performed H2-TPR characterization to determine the oxidation-reduction performance and the metal dispersion of the catalysts. After pre-treatment and purging, H2-TPR was performed from 100 °C to 800 °C. The CO pulse adsorption experiment was pre-treated at 300 °C for 2 h, and then pulsed with helium to 50 °C. The experiment was carried out in the CO pulse system.

2.3. Catalytic Oxidation Performance Evaluation

Next, 200 mg of the grinded catalyst sample with particle sizes of 40–60 mesh was weighed and put on the quartz cotton catalytic bed, which was inside the quartz tube reactor with the inner diameter of 6 mm, and the pipeline pressure was maintained at 0.2 Mpa. The weight hourly space velocity (WHSV) was set to 45,000 $mL{\cdot}g^{-1}{\cdot}h^{-1}$, and the total intake gas flow rate was set to 150 mL/min. The concentration of DCM was 1000 ppm, the concentration of O_2 was 20%, and the balance gas was N_2. Gasmet (model Dx-4000 (GASMET, Vantaa, Finland)) was used to measure the concentration of DCM and other carbon-containing products in the outlet gas. On the basis of the following reaction Equation: $CH_2Cl_2 + O_2 \rightarrow CO_2 + CO + H_2O + HCl + Cl_2 + CH_xCl_yO_z$, the DCM conversion and the CO_2 selectivity (S_{CO_2}) were calculated according to the following Equation:

$$DCM = \frac{c_{in} - c_{out}}{c_{out}} \times 100\% \quad (1)$$

$$S_{CO_2} = \frac{c_{CO_2}}{c_{in} - c_{out}} \times 100\% \quad (2)$$

where c_{in} and c_{out}, respectively, represent the intake concentration and outlet concentration of *DCM*.

In addition, the WHSV when measuring the turnover frequency (*TOF*) value of *DCM* oxidation was set to 112,500 mL·g^{-1} h^{-1} (80 mg catalyst sample was taken, other conditions were the same as the activity test). The calculation formula of *TOF* value is as follows:

$$TOF = \frac{X_{DCM} \times F_{DCM} \times M_{Ru}}{m_{cat} \times X_{Ru} \times D_{Ru}} \quad (3)$$

where X_{DCM} and X_{Ru}, respectively, represent the concentration of *DCM* and *Ru*, respectively, F_{DCM} represents the flow rate of *DCM* (mol·s^{-1}), M_{Ru} represents the molar mass of *Ru*, D_{Ru} is the dispersion of *Ru* and m_{cat} is the mass of catalyst.

3. Results and Discussion

3.1. DCM Catalytic Oxidation Performance Test Results

Figure 1 illustrates the DCM catalytic oxidation performance test results for each sample. Based on the carbon balance, the higher the proportion of CO_2 in the product, the smaller the amount of other toxic organic by-products produced. From the obtained results shown in Figure 1a, we could find that the loading of Ru can significantly improve the catalytic activity of the catalysts for DCM. It could also be found that the T_{90} of the c-1-RuST sample was about 90 °C lower than that of the o-1-RuST sample, which was 290 °C and 380 °C, respectively. This indicated that using Ru colloid instead of the original RuO_2 as precursor to load active components could improve the catalytic activity of the catalyst to a large extent. By further comparing the catalytic activity of the c-1-RuST and the o-5-RuST sample (as shown in Figure S1), it could be seen that the catalytic activity of the c-1-RuST was also significantly higher than that of the o-5-RuST (T_{90} was about 290 °C and 340 °C, respectively). Therefore, the optimization of Ru precursor could effectively reduce the loading of active components, and thus reduce the production cost of the catalyst. At the same time, it also can be found that when Ru colloid loading amount was gradually increased, the catalytic activity of the samples did not change much at first (even slightly decreased), and then showed an upward trend. Among them, the c-1-RuST sample had the best catalytic performance for DCM. As for the results showed in Figure 1b, we could find that the loading of Ru could significantly improve the CO_2 selectivity of the catalysts in the catalytic oxidation of DCM and there was a certain improvement of the CO_2 selectivity after using Ru colloid as precursor instead of RuO_2. We also could find that, when increasing the loading of RuO_x, the CO_2 selectivity of the catalysts also got a gradual improvement. The CO_2 selectivity of c-1-RuST sample remained higher than 80% after the temperature was higher than 300 °C, and stabilized at around 95% after the temperature reached 350 °C.

The stability test result of the c-1-RuST sample is shown in Figure 2. According to the experimental results, the c-1-RuST sample could maintain high catalytic activity (the conversion rate was always higher than 90%) and high product CO_2 selectivity (always above 80%) for DCM at 300 °C for more than 24 h. Therefore, it can be seen that the c-1-RuST catalyst could degrade DCM molecules stably and efficiently for a long time. At the same time, we can find that the conversion % during the stability test had increased to a certain extent. The reason might be that the surface characteristics of the catalysts had changed during the reaction, which in turn led to changes in the catalytic activity and CO_2 selectivity of the catalysts for the oxidation of DCM. From the point of view of the results, this change was favourable.

In order to further study the specific reasons why the optimization of Ru precursor using Ru colloid could improve the performance of the catalyst, and systematically explain the effect of RuO_x loading on the performance of the catalyst, relevant characterizations on the physico-chemical properties of the catalysts were conducted.

3.2. The Analysis of Physico-Chemical Properties of the Catalyst

XRD characterization was conducted on each sample to further study the effect of RuO_x loading on the crystal structure under different Ru precursors and different RuO_x loading conditions, the results are shown in Figure 3. Based on the information of ICSD

PDF # 76-0332, we found that all samples showed a rutile structure, showing that the loading of RuO_x did not significantly affect the crystal structure of the support for the four samples tested. The characteristic peaks of ruthenium oxide crystals were not detected for two reasons. First, the RuO_x species on the surface of the catalyst were highly dispersed in amorphous or crystalline form. Second, the crystal morphology of rutile RuO_x and $Sn_{0.2}Ti_{0.8}O_2$ was similar to each other, with the characteristic peak positions at 27.19°, 35.69° and 56.08°, which were close to the peak positions of the support and were difficult to distinguish.

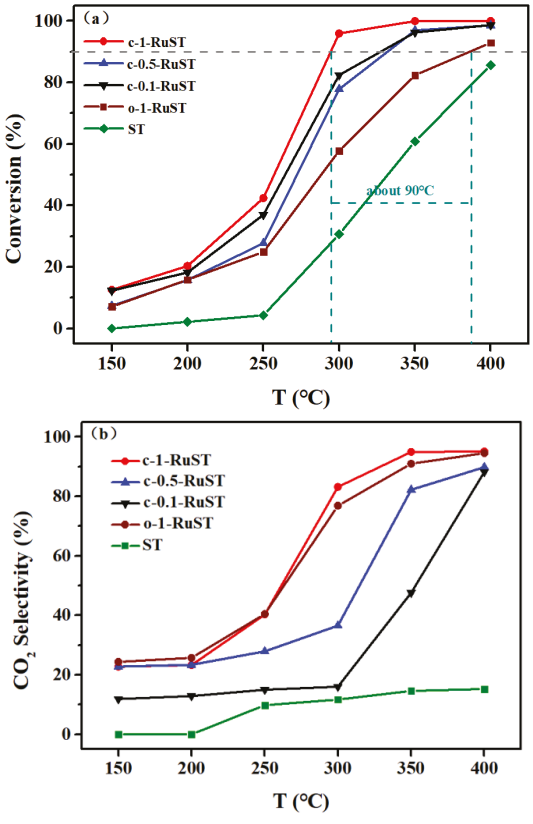

Figure 1. DCM catalytic oxidation performance test results for each sample: (**a**) DCM conversion and (**b**) CO_2 selectivity. Test conditions: (DCM) = 1000 ppm, GHSV = 45,000 $mL \cdot g^{-1} \cdot h^{-1}$.

From the results of TEM-Mapping showed in Figure S2, we can see that for all samples, RuO_x species were highly dispersed on the surface of the catalyst support. The research results showed that RuO_x species could grow epitaxially on the support with the same crystal structure [31], this also explained the good dispersion of RuO_x on $Sn_{0.2}Ti_{0.8}O_2$. The spherical aberration correction transmission electron microscope was further used to observe the size of the Ru clusters of each sample, and the experimental results are shown in Figure 4. It can be inferred from the figure that the surface of the catalyst loaded by the Ru colloid had smaller Ru clusters. Most of the Ru clusters on the surface of o-1-RuST samples were about 3–4 nm in diameter, while the Ru clusters on the surface of c-1-RuST samples were about 1.3 nm in diameter. Therefore, the optimization of Ru precursor using Ru colloid can improve the dispersity of RuO_x species, significantly improve the utilization rate of active components, and then increase the total number of active sites on the catalyst

surface. In addition, we could also find that with the increase in RuO_x loading, the size of Ru clusters on the catalyst surface gradually increased. The size of Ru clusters in the c-1-RuST sample was extremely small, and it was hard to see obvious Ru clusters, as for the c-0.5-RuST sample, there were many small Ru clusters with a diameter of about 1 nm, and the diameter of the Ru clusters on the surface of the c-1-RuST sample was about 1.3 nm. Therefore, we could see that when increasing the loading of RuO_x, the dispersibility of RuO_x species decreased by degrees, thereby reducing the utilization of active components.

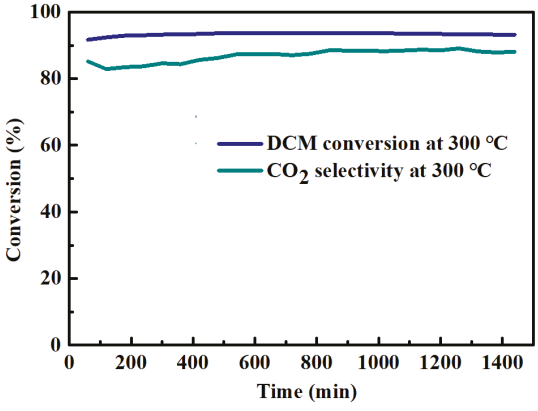

Figure 2. Stability evaluation test results of the c-1-RuST sample.

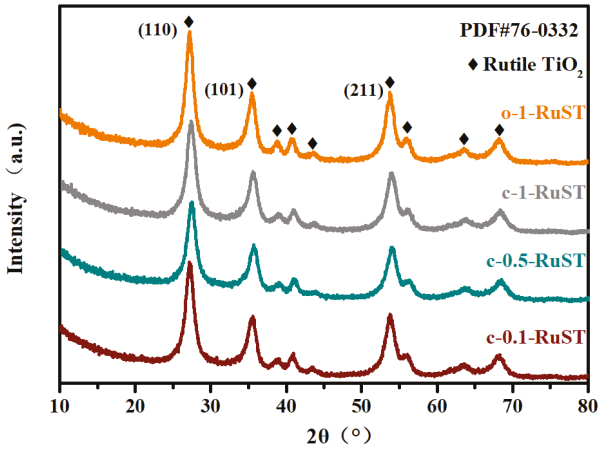

Figure 3. XRD patterns of the samples. Peak information for crystal plane acquired from the ICSD Powder Diffraction File card of Rutile TiO_2 (card No. 76-0332) is also marked in the figure.

We carried out a CO pulse adsorption experiment to further verify the rule between RuO_x species dispersibility and RuO_x loading, and the results are shown in Table 1. The metal dispersion and metallic surface area of Ru in the c-0.1-RuST sample were significantly higher than those in the c-0.5-RuST sample, and the values in the c-0.5-RuST sample were also higher than those in the c-1-RuST sample. This can also explain why when increasing the loading of RuO_x, the catalytic activity of the samples did not change significantly at first and then increased. At first, as the RuO_x loading increased, the total number of RuO_x species increased but the dispersibility decreased. The effects of the two offset each other, resulting in little change in the total number of active sites of the catalyst and little

change in catalyst performance; subsequently, with the further increase in RuO_x loading, the increase in the total number of RuO_x species gradually played a dominant role, and the total number of active sites of the catalyst increased, leading to the improvement of the catalytic performance of the catalyst.

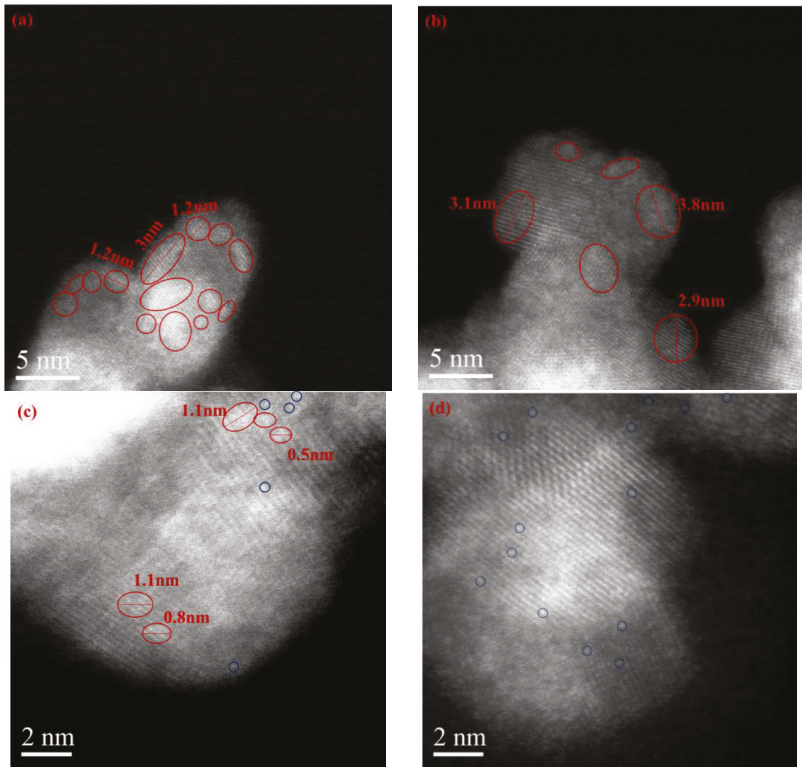

Figure 4. HAADF-STEM images of (**a**) the c-1-RuST sample, (**b**) the o-1-RuST sample, (**c**) the c-0.5-RuST sample and (**d**) the c-0.1-RuST sample. Representative Ru clusters and single-atom Ru in each sample and the diameters of some of the Ru clusters are also marked in the figure.

Table 1. CO pulse adsorption experiment results of samples with different RuO_x loadings.

Samples	Metal Dispersion (%)	Metallic Surface Area (m^2/g)
c-0.1-RuST	15.86	75.59
c-0.5-RuST	7.18	34.20
c-1-RuST	2.35	11.19

We further studied the physico-chemical properties of each sample, and some results are shown in Table 2. The molar ratio of tin to titanium (Sn_{mol}:Ti_{mol}) of each sample was between 0.246 and 0.250, basically the same as our pre-set value (0.25), and the actual loading of Ru species also met the expectation. The deviation of the actual Ru content of some samples from the expected Ru content might because we loaded Ru species through impregnation method, which might inevitably lead to some errors. For example, for the c-1-RuST sample, quantitative support powder and colloid solution were fully stirred in a beaker, then transferred to a flask for rotary evaporation. During this process, some Ru species might not be loaded on the surface of the catalysts. For instance, there might be

some colloidal solution containing Ru species remaining on the inner wall of the container that cannot be completely transferred. These factors inevitably caused the difference between the final loading of Ru species and the originally intended loading of Ru species, but from the XRF test results, this deviation was not very large. At the same time, the actual Ru content in the c-1-RuST sample was slightly less than that of the o-1-RuST, but its catalytic performance was much better than the latter, which also showed the superiority of the modification of the active component precursor. In addition, the BET surface area of the c-1-RuST sample was significantly larger than that of the o-1-RuST sample. At the same time, the pore size of the c-1-RuST sample was also significantly smaller than that of the o-1-RuST sample. This might be due to the fact that the particle size of Ru in Ru colloid was smaller than that in precursor of RuO_2. The RuO_x species in Ru colloid could distribute more evenly on the catalyst surface, and efficiently reduce the adverse effect of blocking the pore of the support on the specific surface area of the catalyst. This result is consistent with the HAADF-STEM test results. It could be seen that the optimization of Ru precursor using Ru colloid was beneficial to improve the dispersion of RuO_x species, thereby increasing the total number of active sites on the catalyst surface. However, with the increase in RuO_x loading, the BET surface area of the catalyst decreased slightly, indicating that the above adverse effect could not be completely eliminated.

Table 2. Characterization results of some physico-chemical properties of RuST series samples.

Samples	Sn_{mol}:Ti_{mol} [a]	Ru (wt%) [a]	BET (m^2/g)	Pore Size (nm)
o-1-RuST	0.250	1.13	64.87	13.44
c-1-RuST	0.248	0.857	80.61	11.88
c-0.5-RuST	0.246	0.415	83.51	10.66
c-0.1-RuST	0.250	0.141	85.31	10.45

[a] Calculated from XRF measurement.

In order to explore the influence of the Ru precursor optimization on the valence state of Ru species, we performed XPS characterization. The specific data is shown in Figure 5. The binding energy of Ru^{4+} species could be identified as 280.4 eV, and the binding energy of Ru^{6+} species could be identified as 282.5 eV [32,33]. It can be seen from the Figure that both samples contained Ru^{4+}, which corresponded to the crystalline RuO_2 or RuO_2 thin films on the catalyst surface. Meanwhile, Ru^{n+} ($4 < n < 6$) with valence states between +4 and +6 were found in both samples. The difference was that Ru^{n+} accounted for only 14.2% of Ru species in the o-1-RuST sample, while for c-1-RuST sample, Ru^{n+} accounts for as much as 60.4%. Previous studies have shown that the interface charge transfer between the Ru species and the support will affect the charge density of the Ru species, and the strength of electronic interaction of strong metal-support interactions (SMSI) will directly affect the valence state of Ru on the catalyst surface [34]. Therefore, we can infer that the formation of Ru^{n+} species was due to the close interaction between Ru and support, Ru gave electrons through the Ru–O–M (Sn, Ti) bond and thus exhibited a higher valence state than +4. The Ru clusters on the surface of the c-1-RuST sample were smaller than that in the o-1-RuST sample, and the Ru species of the c-1-RuST sample could better diffuse and distribute on the surface of catalyst, which was more conducive to the formation of bonds between Ru and other surrounding elements to form SMSI. More than half of the Ru in the c-1-RuST sample was bound to the support, which indicated that loading Ru in colloidal form greatly improved the utilization efficiency of active components, so more active sites could be formed on the catalyst surface. The specific effects of Ru^{n+} species on the catalytic activity will be further discussed in detail in combination with the XPS results of O 1s.

The oxygen species distribution and oxygen vacancy concentration of the catalyst usually have a great impact on the catalyst oxidation performance, so we measured the valence distribution of oxygen element on the surface of each sample, and the results are shown in Figure 6. The peak value near 529.6 eV could be assigned to lattice oxygen species (O_{Lat}), that at around 530.3 eV could be assigned to oxygen vacancy species (O_V), and

that at around 531.3 eV could be classified as surface adsorbed oxygen species (O_{ad}). O_{ad} can quickly participate in the reaction with the adsorbed DCM molecules and oxidize the reactants, thus improving the catalytic performance of the samples [35]. The oxygen vacancy concentration is very important for the adsorption and dissociation of oxygen during the reaction. Increasing the oxygen vacancy concentration can increase the oxygen transmission rate on the catalyst surface, so that the oxygen consumed by the reaction can be quickly replenished, thereby promoting the deep oxidation of DCM molecules. The oxygen vacancy concentration on the surface of each sample could be evaluated by calculating the ratio of O_V/O_{Lat} [36]. The oxygen vacancy concentration value of the o-1-RuST, the c-1-RuST, the c-0.5-RuST and the c-0.1-RuST sample was 1.44, 1.53, 1.47 and 1.50, respectively. Comparing the O1s spectra of the o-1-RuST and the c-1-RuST samples, we could find that the c-1-RuST sample had more O_{ad} and a higher oxygen vacancy concentration on the surface, which was consistent with the catalytic activity and CO_2 selectivity test results of the two samples. The distribution of RuO_x species on the surface of the c-1-RuST sample was more uniform, which helped to adsorb more oxygen; at the same time, the c-1-RuST sample had a higher proportion of Ru^{n+}, the forming of Ru–O–M (Sn, Ti) bonds could significantly increase the oxygen vacancy concentration [37,38]; the above two points encouraged the catalyst toward a better redox performance, and thus had better low-temperature catalytic activity and CO_2 selectivity [39]. Therefore, we can infer that the optimization of the Ru precursor was beneficial to increase the number of active oxidation sites of the catalyst, thus helping to improve the overall catalytic performance of the catalyst.

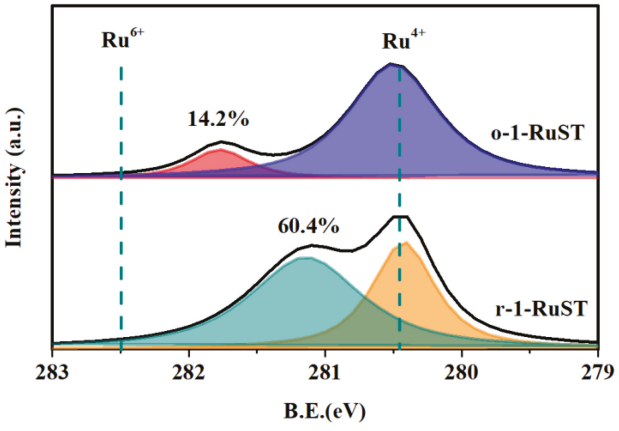

Figure 5. XPS data of Ru 3d for the c-1-RuST sample and o-1-RuST sample. The peak positions of Ru^{4+} and Ru^{6+} binding energy and the ratio of Ru^{n+} ($4 < n < 6$) to the total number of Ru species in the two samples are also marked in the Figure.

Comparing the O1s spectra of the three samples of the c-1-RuST, the c-0.5-RuST, and the c-0.1-RuST, it could be concluded that when the Ru loading was increased, the O_{ad} content of the catalyst gradually increased, which showed that the RuO_x species on the catalyst surface was the key sites for the adsorption of environmental oxygen. Furthermore, the oxygen vacancy concentration of each sample followed the c-1-RuST > the c-0.1-RuST > the c-0.5-RuST, this might because the c-0.1-RuST sample had the smallest size of Ru clusters and the smaller size of Ru clusters could show stronger electron interaction with the support [36]. At the same time, this result was consistent with the test results of the catalytic performance of each sample for DCM, suggesting that the c-0.1-RuST sample with better RuO_x species dispersibility had a higher utilization efficiency of active components and had a larger total number of active sites of the catalyst than the c-0.5-RuST sample.

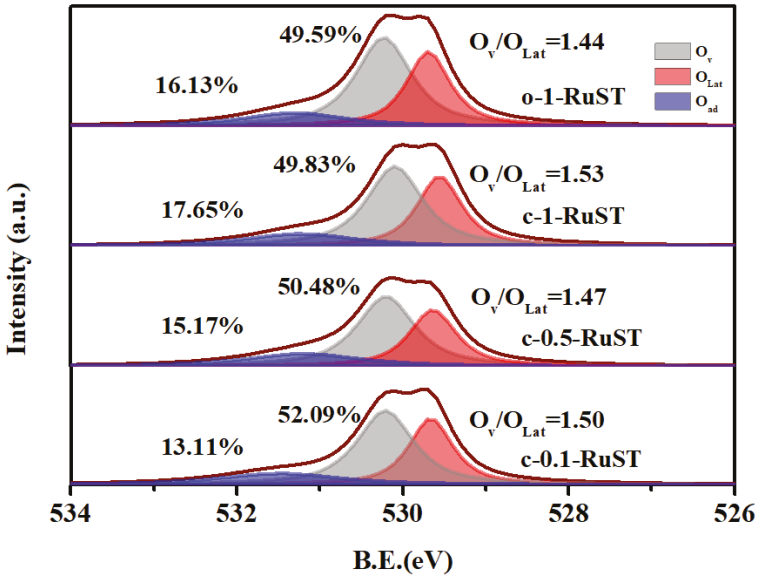

Figure 6. XPS data of O 1s for the samples. The proportion of O_{ad} and O_V in the total number of oxygen species in each sample and the oxygen vacancy concentration (O_V/O_{Lat}) of each sample are also marked in the Figure.

The slight shift of the binding energy peak value of oxygen species in each sample showed that there were differences in the electronic environment of oxygen atoms in different samples. The difference in strength of the interaction between the Ru species and the support in different samples might be the reason for this phenomenon. The binding energy of oxygen species in the c-1-RuST sample was lower than that in the o-1-RuST sample, which was consistent with the results of HAADF-STEM images and XPS data of Ru 3d. In c-1-RuST sample; there was a stronger interaction between Ru species and the support, forming more Ru-O-M bonds, resulting in more electron transfer from Ru to O and a decrease in the binding energy of oxygen species. The order of binding energy of oxygen species in the c-1-RuST, the c-0.5-RuST, and the c-0.1-RuST sample was the same as the order of oxygen vacancy concentration. This could be explained by the fact that the c-0.1-RuST sample had the smallest size of Ru clusters, which had a stronger interaction with the support, but the Ru content of the c-1-RuST sample was much greater than that of the c-0.1-RuST sample.

In order to further explore the redox performance of the catalysts, we performed H_2-TPR characterization on the samples, and the results are shown in Figure 7. Observing the image, we could find that the four samples all had a reduction peak at 250 °C to 400 °C and this can be attributed to the reduction of Sn^{4+} [20]. The reduction peak from 450 °C to 750 °C can be attributed to the reduction of bulk oxygen in the support [40]. It can be found that the reduction peak of this part was basically the same for each sample. The reduction peak located near 240 °C was caused by the reduction of oxygen on the catalyst surface [40], which varied greatly among different samples. The reduction peak area of the c-1-RuST sample near 240 °C was significantly larger than that of the o-1-RuST sample, indicating that the c-1-RuST sample had more surface oxygen, which was consistent with the results of CO_2 selectivity and XPS data of O 1 s. This showed that the smaller and more uniformly distributed RuO_x in the c-1-RuST sample could form more oxidation active sites and absorb more environmental oxygen, thus improving the oxidation-reduction performance of the catalyst. At the same time, comparing the samples of the c-1-RuST, the c-0.5-RuST and the c-0.1-RuST, it could be seen that with the increase in RuO_x species

loading, the oxygen content on the catalyst surface gradually increased, showing that the total amount of oxygen increased with the increase in RuO_x loading, which is also coincide to the CO_2 selectivity results of each sample. It was difficult to observe obvious RuO_x species reduction peaks in the image, because the content of RuO_x species in the samples was too low, and the reduction peak of Ru species was close to the reduction peak of surface oxygen.

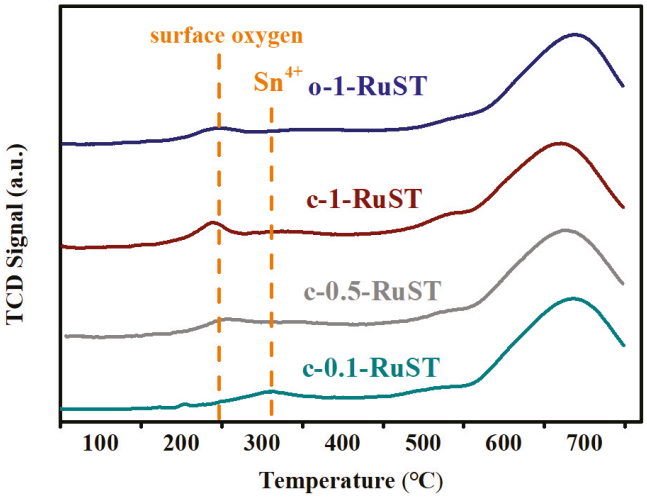

Figure 7. H_2-TPR profiles of the catalysts. The reduction peak positions of Sn^{4+} and oxygen species on the catalyst surface are also marked in the figure.

In order to verify the effect of optimization of Ru precursor on the utilization efficiency of active sites and the overall catalytic performance of the catalyst, we calculated the TOF values of the c-1-RuST sample and the o-1-RuST sample at 230–280 °C, and the results are shown in the Figure 8. The experimental WHSV was maintained at 112,500 $mL \cdot g^{-1} \cdot h^{-1}$, and the DCM conversion rate was controlled to be less than 20%, so that the reaction rate was not affected by diffusion, and only depended on the number of active sites. It can be seen from the experimental calculation results that the TOF value of the c-1-RuST sample for DCM was always significantly higher than that of the o-1-RuST sample, even up to about twice the value (for example, at 270 °C, the TOF value of the c-1-RuST sample was 0.20, and which of the o-1-RuST sample was 0.12). In conclusion, loading Ru species in the form of Ru colloid could improve the catalytic performance of a single active site, and then improve the overall catalytic activity of the samples. Based on the results of the previous characterization analysis, the reason may be that the optimization of Ru precursor could help to improve the dispersion of RuO_x species on the catalyst surface, thus promoting a larger proportion of Ru species to form Ru–O–M bonds with the support, generating more $Ru^{n+}(4 < N < 6)$. This change significantly increased the adsorbed oxygen content and oxygen vacancy concentration on the catalyst surface, thus leading to the improvement of the catalyst oxidation performance. Therefore, under the condition of similar RuO_x loading, the c-1-RuST sample with higher RuO_x species utilization rate could catalyse and oxidize more DCM molecules in the same experimental conditions.

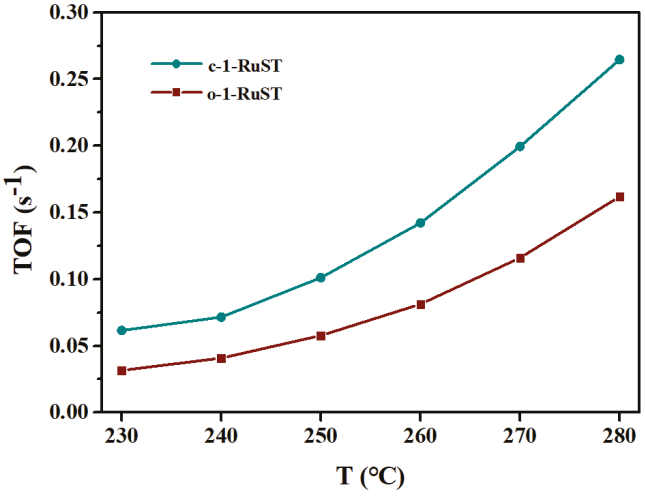

Figure 8. TOF for DCM oxidation on the c-1-RuST and the o-1-RuST sample. Test conditions: [DCM] = 1000 ppm, WHSV = 112,500 mL·g^{-1}·h^{-1}.

4. Conclusions

In this article, the Ru precursor was optimized using Ru colloid and a unique catalyst preparation method was developed. The Ru species was loaded on the $Sn_{0.2}Ti_{0.8}O_2$ support in colloidal form, which improved the utilization efficiency of active components, and effectively improved the catalytic activity (T_{90} was reduced by about 90 °C from 380 °C to 290 °C) and the CO_2 selectivity. Through the activity test and various characterization analyses, it could be concluded that the optimization of Ru precursor could significantly increase the dispersion of RuO_x species (the size of Ru clusters was reduced from 3–4 nm to about 1.3 nm), improve the utilization of active components (nearly doubled the TOF value at each temperature measured), and increase the interaction between the active components and the support. This improvement effectively increased the total number of active sites of the catalyst, thus improving the catalyst oxidation capability.

In addition, for the sake of better determining the optimal Ru loading, the relationship between the Ru loading and the catalytic activity of the catalyst was further studied. The experimental results reflected that with the increase in Ru loading, the total amount of RuO_x species on the catalyst surface increased, while the dispersibility of that gradually decreased. This resulted in little change in the total number of active sites of the catalyst, and little change in the catalytic activity of the samples (T_{90} of the c-0.1-RuST and the c-0.5-RuST for DCM was about 330 °C and 335 °C respectively) when the content of Ru was low (less than 0.5 wt%). When the content of Ru was high (above than 0.5 wt%), the positive effect caused by the increase in the total active component amount gradually played a leading role, and the catalytic performance of the catalyst was significantly improved.

In conclusion, the study is conducive to the efficient treatment of CVOCs and can provide theoretical guidance for further reducing the content of active components (the Ru loading could be reduced from about 5% to less than 1%) and production cost, thus having broad industrial application prospects.

Supplementary Materials: The following are available online at https://www.mdpi.com/article/10.3390/catal11111306/s1, Figure S1 Results of catalytic performance evaluation for DCM oxidation over the c-1-RuST and the o-1-RuST sample. Test conditions: (DCM) = 1000 ppm; WHSV = 45,000 mL·g^{-1}·h^{-1}, Figure S2 EDS-Mapping characterization results of (a) the c-1-RuST sample, (b) the o-1-RuST sample, (c) the c-0.5-RuST sample and (d) the c-0.1-RuST sample, Table S1 Chemical reagents used in catalyst preparation.

Author Contributions: Conceptualization, Y.Y. and X.Y.; methodology, Z.Z.; software, M.K.; validation, S.L.; formal analysis, Z.Z.; investigation, Z.Z.; resources, X.Y.; data curation, Z.H.; writing—original draft preparation, Z.Z.; writing—review and editing, Y.Y.; visualization, Z.Y.; supervision, Y.J.; project administration, X.G.; funding acquisition, X.G. All authors have read and agreed to the published version of the manuscript.

Funding: This research was founded by the [National Natural Science Foundation of China] grant number [No.51836006] and [No.52006192] and [Qingdao Science and Technology Demonstration and Guidance Project] grant number [21-1-4-sf-8-nsh].

Conflicts of Interest: The authors declare no conflict of interest.

References

1. Geng, C.; Yang, W.; Sun, X.; Wang, X.; Bai, Z.; Zhang, X. Emission factors, ozone and secondary organic aerosol formation potential of volatile organic compounds emitted from industrial biomass boilers. *J. Environ. Sci.* **2019**, *83*, 64–72. [CrossRef] [PubMed]
2. Amnuaylojaroen, T.; Macatangay, R.C.; Khodmanee, S. Modeling the effect of VOCs from biomass burning emissions on ozone pollution in upper Southeast Asia. *Heliyon* **2019**, *5*, e02661. [CrossRef]
3. Liu, Y.; Song, M.; Liu, X.; Zhang, Y.; Hui, L.; Kong, L.; Zhang, Y.; Zhang, C.; Qu, Y.; An, J.; et al. Characterization and sources of volatile organic compounds (VOCs) and their related changes during ozone pollution days in 2016 in Beijing, China. *Environ. Pollut.* **2019**, *257*, 113599. [CrossRef] [PubMed]
4. Doucette, W.J.; Wetzel, T.A.; Dettenmaier, E.; Gorder, K. Emission rates of chlorinated volatile organics from new and used consumer products found during vapor intrusion investigations: Impact on indoor air concentrations. *Environ. Forensics* **2018**, *19*, 185–190. [CrossRef]
5. Hossaini, R.; Chipperfield, M.; Montzka, S.A.; Leeson, A.; Dhomse, S.S.; Pyle, J.A. The increasing threat to stratospheric ozone from dichloromethane. *Nat. Commun.* **2017**, *8*, 15962. [CrossRef]
6. Blanch-Raga, N.; Palomares, A.E.; Triguero, J.M.; Puche, M.; Fetter, G.; Bosch, P. The oxidation of trichloroethylene over different mixed oxides derived from hydrotalcites. *Appl. Catal. B Environ.* **2014**, *160–161*, 129–134. [CrossRef]
7. Dobrzyńska, E.; Pośniak, M.; Szewczynska, M.; Buszewski, B. Chlorinated Volatile Organic Compounds—Old, However, Actual Analytical and Toxicological Problem. *Crit. Rev. Anal. Chem.* **2010**, *40*, 41–57. [CrossRef]
8. Krol, M.C.; Lelieveld, J.; Oram, D.E.; Sturrock, G.A.; Penkett, S.A.; Brenninkmeijer, C.A.M.; Gros, V.; Williams, J.; Scheeren, H.A. Continuing emissions of methyl chloroform from Europe. *Nature* **2003**, *421*, 131–135. [CrossRef]
9. Li, C.; Zhao, Y.; Song, H.; Li, H. A review on recent advances in catalytic combustion of chlorinated volatile organic compounds. *J. Chem. Technol. Biotechnol.* **2019**, *95*, 2069–2082. [CrossRef]
10. Zheng, Z.; Yang, Y.; Li, H.; Xin, Q.; Zhang, S.; Liu, Y.; Liu, S.; Zheng, C.; Song, H.; Gao, X. Effect of multi-pollutant on the catalytic oxidation of dichloromethane over RuO_2-WO_3/$Sn_{0.2}Ti_{0.8}O_2$ catalyst. *Fuel* **2020**, *278*, 118207. [CrossRef]
11. Yang, Y.; Liu, S.; Zhao, H.; Li, H.; Qu, R.; Zhang, S.; Zhu, X.; Zheng, C.; Gao, X. Promotional effect of doping Cu into cerium-titanium binary oxides catalyst for deep oxidation of gaseous dichloromethane. *Chemosphere* **2018**, *214*, 553–562. [CrossRef] [PubMed]
12. Tian, M.; Guo, X.; Dong, R.; Guo, Z.; Shi, J.; Yu, Y.; Cheng, M.; Albilali, R.; He, C. Insight into the boosted catalytic performance and chlorine resistance of nanosphere-like meso-macroporous CrO_x/$MnCo_3O_x$ for 1,2-dichloroethane destruction. *Appl. Catal. B Environ.* **2019**, *259*, 118018. [CrossRef]
13. Aouad, S.; Abi-Aad, E.; Aboukaïs, A. Simultaneous oxidation of carbon black and volatile organic compounds over Ru/CeO_2 catalysts. *Appl. Catal. B Environ.* **2009**, *88*, 249–256. [CrossRef]
14. Okal, J.; Zawadzki, M. Influence of Catalyst Pretreatments on Propane Oxidation Over Ru/gamma-Al_2O_3. *Catal. Lett.* **2009**, *132*, 225–234. [CrossRef]
15. Joo, S.H.; Park, J.Y.; Renzas, J.; Butcher, D.R.; Huang, W.; Somorjai, G.A. Size Effect of Ruthenium Nanoparticles in Catalytic Carbon Monoxide Oxidation. *Nano Lett.* **2010**, *10*, 2709–2713. [CrossRef] [PubMed]
16. Chen, H.-T. First-Principles Study of CO Adsorption and Oxidation on Ru-Doped CeO_2(111) Surface. *J. Phys. Chem. C* **2012**, *116*, 6239–6246. [CrossRef]
17. Hevia, M.A.; Amrute, A.P.; Schmidt, T.; Pérez-Ramírez, J. Transient mechanistic study of the gas-phase HCl oxidation to Cl_2 on bulk and supported RuO_2 catalysts. *J. Catal.* **2010**, *276*, 141–151. [CrossRef]
18. Sun, W.; Gong, B.; Pan, J.; Wang, Y.; Xia, H.; Zhang, H.; Dai, Q.; Wang, L.; Wang, X. Catalyticcombustion of CVOCs over Cr_xTi_{1-x} oxide catalysts. *J. Catal.* **2020**, *391*, 132–144. [CrossRef]
19. Lv, X.; Cai, S.; Chen, J.; Yan, D.; Jiang, M.; Jia, H. Tuning the degradation activity and pathways of chlorinated organic pollutants over CeO_2 catalyst with acid sites: Synergistic effect of Lewis and Brønsted acid sites. *Catal. Sci. Technol.* **2021**. [CrossRef]
20. Yang, Y.; Li, H.; Zhao, H.; Qu, R.; Zhang, S.; Hu, W.; Yu, X.; Zhu, X.; Liu, S.; Zheng, C.; et al. Structure and crystal phase transition effect of Sn doping on anatase TiO_2 for dichloromethane decomposition. *J. Hazard. Mater.* **2019**, *371*, 156–164. [CrossRef]
21. Chen, X.; Zhao, Z.; Zhou, Y.; Zhu, Q.; Pan, Z.; Lu, H. A facile route for spraying preparation of Pt/TiO_2 monolithic catalysts toward VOCs combustion. *Appl. Catal. A Gen.* **2018**, *566*, 190–199. [CrossRef]

22. Todorova, S.; Blin, J.; Naydenov, A.; Lebeau, B.; Kolev, H.; Gaudin, P.; Dotzeva, A.; Velinova, R.; Filkova, D.; Ivanova, I.; et al. Co_3O_4-MnO_x oxides supported on SBA-15 for CO and VOCs oxidation. *Catal. Today* **2019**, *357*, 602–612. [CrossRef]
23. Topka, P.; Dvořáková, M.; Kšírová, P.; Perekrestov, R.; Čada, M.; Balabánová, J.; Koštejn, M.; Jirátová, K.; Kovanda, F. Structured cobalt oxide catalysts for VOC abatement: The effect of preparation method. *Environ. Sci. Pollut. Res.* **2019**, *27*, 7608–7617. [CrossRef]
24. Wang, F.; Li, Z.; Wang, H.; Chen, M.; Zhang, C.; Ning, P.; He, H. Nano-sized Ag rather than single-atom Ag determines CO oxidation activity and stability. *Nano Res.* **2021**, 1–5. [CrossRef]
25. Veisi, H.; Azizi, S.; Mohammadi, P. Green synthesis of the silver nanoparticles mediated by Thymbra spicata extract and its application as a heterogeneous and recyclable nanocatalyst for catalytic reduction of a variety of dyes in water. *J. Clean. Prod.* **2018**, *170*, 1536–1543. [CrossRef]
26. Xu, L.; Chen, D.; Qu, J.; Wang, L.; Tang, J.; Liu, H.; Yang, J. Replacement reaction-based synthesis of supported palladium catalysts with atomic dispersion for catalytic removal of benzene. *J. Mater. Chem. A* **2018**, *6*, 17032–17039. [CrossRef]
27. Agarwal, N.; Freakley, S.J.; McVicker, R.U.; Althahban, S.M.; Dimitratos, N.; He, Q.; Morgan, D.J.; Jenkins, R.L.; Willock, D.J.; Taylor, S.H.; et al. Aqueous Au-Pd colloids catalyze selective CH_4 oxidation to CH_3OH with O_2 under mild conditions. *Science* **2017**, *358*, 223–227. [CrossRef] [PubMed]
28. Zhao, Y.; Jia, L.; Medrano, J.A.; Ross, J.R.H.; Lefferts, L. Supported Pd Catalysts Prepared via Colloidal Method: The Effect of Acids. *ACS Catal.* **2013**, *3*, 2341–2352. [CrossRef]
29. Zhao, Y.; Chen, D.; Liu, J.; He, D.; Cao, X.; Han, C.; Lu, J.; Luo, Y. Tuning the metal-support interaction on chromium-based catalysts for catalytically eliminate methyl mercaptan: Anchored active chromium species through surface hydroxyl groups. *Chem. Eng. J.* **2020**, *389*, 124384. [CrossRef]
30. Li, H.; Wang, G.; Zhang, F.; Zou, L.; Zou, Z.; Yang, H. An Atomically Dispersed Pt Catalyst Anchored on an Fe/N/C Support for Enhanced Hydrogen Evolution Reaction. *J. Phys. Chem. C* **2020**, *124*, 11760–11766. [CrossRef]
31. Seitsonen, A.P.; Over, H. Oxidation of HCl over TiO_2-Supported RuO_2: A Density Functional Theory Study. *J. Phys. Chem. C* **2010**, *114*, 22624–22629. [CrossRef]
32. Nong, S.; Dong, W.; Yin, J.; Dong, B.; Lu, Y.; Yuan, X.; Wang, X.; Bu, K.; Chen, M.; Jiang, S.; et al. Well-Dispersed Ruthenium in Mesoporous Crystal TiO_2 as an Advanced Electrocatalyst for Hydrogen Evolution Reaction. *J. Am. Chem. Soc.* **2018**, *140*, 5719–5727. [CrossRef] [PubMed]
33. National Institute of Standards and Technology. *NIST X-ray Photoelectron Spectroscopy Database, Version 4.1*; National Institute of Standards and Technology: Gaithersburg, MD, USA, 2012. Available online: http://srdata.nist.gov/xps/ (accessed on 20 April 2020).
34. Guo, Y.; Mei, S.; Yuan, K.; Wang, D.J.; Liu, H.C.; Yan, C.H.; Zhang, Y.W. Low-Temperature CO_2 Methanation over CeO_2-Supported Ru Single Atoms, Nanoclusters, and Nanoparticles Competitively Tuned by Strong Metal–Support Interactions and H-Spillover Effect. *ACS Catal.* **2018**, *8*, 6203–6215. [CrossRef]
35. Yang, Y.; Li, H.; Zhang, S.; Yu, X.; Liu, S.; Qu, R.; Zheng, C.; Gao, X. Different reactive behaviours of dichloromethane over anatase TiO_2 supported RuO_2 and V_2O_5. *Catal. Today* **2019**, *355*, 349–357. [CrossRef]
36. Li, J.; Liu, Z.; Cullen, D.A.; Hu, W.; Huang, J.; Yao, L.; Peng, Z.; Liao, P.; Wang, R. Distribution and Valence State of Ru Species on CeO_2 Supports: Support Shape Effect and Its Influence on CO Oxidation. *ACS Catal.* **2019**, *9*, 11088–11103. [CrossRef]
37. Liotta, L.; Ousmane, M.; Di Carlo, G.; Pantaleo, G.; Deganello, G.; Marcì, G.; Retailleau, L.; Giroir-Fendler, A. Total oxidation of propene at low temperature over Co_3O_4–CeO_2 mixed oxides: Role of surface oxygen vacancies and bulk oxygen mobility in the catalytic activity. *Appl. Catal. A Gen.* **2008**, *347*, 81–88. [CrossRef]
38. Pu, Z.-Y.; Liu, X.-S.; Jia, A.-P.; Xie, Y.-L.; Lu, J.-Q.; Luo, M.-F. Enhanced Activity for CO Oxidation over Pr- and Cu-Doped CeO_2 Catalysts: Effect of Oxygen Vacancies. *J. Phys. Chem. C* **2008**, *112*, 15045–15051. [CrossRef]
39. Dai, Q.; Wu, J.; Deng, W.; Hu, J.; Wu, Q.; Guo, L.; Sun, W.; Zhan, W.; Wang, X. Comparative studies of P/CeO_2 and Ru/CeO_2 catalysts for catalytic combustion of dichloromethane: From effects of H_2O to distribution of chlorinated by-products. *Appl. Catal. B Environ.* **2019**, *249*, 9–18. [CrossRef]
40. Li, J.; Liu, Z.; Wang, R. Support structure and reduction treatment effects on CO oxidation of SiO_2 nanospheres and CeO_2 nanorods supported ruthenium catalysts. *J. Colloid Interface Sci.* **2018**, *531*, 204–215. [CrossRef]

catalysts

MDPI

Article

Water Splitting on Multifaceted $SrTiO_3$ Nanocrystals: Computational Study

Maksim Sokolov [1,*], Yuri A. Mastrikov [1,*], Guntars Zvejnieks [1], Dmitry Bocharov [1] and Eugene A. Kotomin [1] and Veera Krasnenko [2]

[1] Institute of Solid State Physics, University of Latvia, Kengaraga 8, LV1063 Riga, Latvia; guntars.zvejnieks@cfi.lu.lv (G.Z.); Dmitrijs.Bocarovs@cfi.lu.lv (D.B.); jevgenijs.kotomins@cfi.lu.lv (E.A.K.)
[2] Institute of Physics, University of Tartu, W.Ostwaldi 1, 50411 Tartu, Estonia; veera.krasnenko@ut.ee
* maksims.sokolovs@cfi.lu.lv (M.S.); yuri.mastrikov@cfi.lu.lv (Y.A.M.)

Abstract: Recent experimental findings suggest that strontium titanate $SrTiO_3$ (STO) photocatalytic activity for water splitting could be improved by creating multifaceted nanoparticles. To understand the underlying mechanisms and energetics, the model for faceted nanoparticles was created. The multifaceted nanoparticles' surface is considered by us as a combination of flat and "stepped" facets. Ab initio calculations of the adsorption of water and oxygen evolution reaction (OER) intermediates were performed. Our findings suggest that the "slope" part of the step showed a natural similarity to the flat surface, whereas the "ridge" part exhibited significantly different adsorption configurations. On the "slope" region, both molecular and dissociative adsorption modes were possible, whereas on the "ridge", only dissociative adsorption was observed. Water adsorption energies on the "ridge" (−1.50 eV) were significantly higher than on the "slope" (−0.76 eV molecular; −0.83 eV dissociative) or flat surface (−0.79 eV molecular; −1.09 eV dissociative).

Keywords: STO; OER; DFT; stepped surface; water splitting

Citation: Sokolov, M.; Mastrikov, Y.A.; Zvejnieks, G.; Bocharov, D.; Kotomin, E.A.; Krasnenko, K. Water Splitting on Multifaceted $SrTiO_3$ Nanocrystals: A Computational Study. *Catalysts* **2021**, *11*, 1326. https://doi.org/10.3390/catal11111326

Academic Editors: Zhenghua Tang, Marc Cretin and Sophie Tingry

Received: 12 October 2021
Accepted: 30 October 2021
Published: 31 October 2021

1. Introduction

Strontium titanate $SrTiO_3$ (STO) is a well-known material for water splitting [1–12]. The process of water adsorption and dissociation was studied in detail [13–15]. The effects of doping are investigated in [16]. Recent developments in nanocrystal synthesis offered materials with enhanced charge separation achieved by heterojunction [17,18], mesocrystallinity [19], or the exposed anisotropic facets [20,21]. Nanoparticles synthesized by Takata et al. [20] were made from STO doped by aluminium and photodeposited cocatalysts Rh/Cr_2O_3 and CoOOH, and demonstrated a quantum efficiency of up to 96% in the range of 350 to 360 nm. Synthesized six and eighteen-facet STO nanocrystals, as described in [21], demonstrated high catalytic activity in water splitting. When doped by Pt and Co_3O_4 on particular facets, these nanoparticles exhibited even higher performance. Such an improvement is attributed to the unique properties of anisotropic facets of the particles.

One of the key properties of a high-performance water splitting material is a low charge recombination rate. Adsorption of water and oxygen evolution reaction (OER) intermediates on stepped surfaces is expected to be qualitatively different than that on flat surfaces. Featuring surfaces of different orientations, the 18-facet nanoparticle provides a natural platform for efficient charge separation. The six-facet nanoparticle is essentially a cube with the {0 0 1} faces. Its edges, however, can be considered as a different reaction area from the {0 0 1} flat parts. Currently, to the best of our knowledge, the structure of the surface of these nanoparticles is described only at the nanoscale. To reveal the properties of different reaction areas of multi-faceted nanoparticles, an atomistic model has to be designed and tested.

In 18-facet STO nanoparticle, the {0 0 1} facets are combined with the facets parallel to the {1 1 0} crystallographic plane. Although for the real material, the surfaces {0 0 1}

and $\{1\,0\,0\}$ are not equivalent [22], for the present study, the distortion of the perovskite structure is irrelevant and the orientation of the surfaces are given relative to the cubic phase. As it was shown in [23], the ideal polar $\{1\,1\,0\}$ surface is unstable. Its stabilization can be achieved by forming steps of the more stable $\{0\,0\,1\}$ orientation [24].

In the present study, we propose an atomistic model of the $\{0\,0\,1\}$ stepped surface, which is relevant to both six as well as eighteen-facet STO nanoparticles. On this surface, we simulate OER, as suggested by Nørskov [25]. The four-step reaction includes adsorption of H_2O, HO^*, O^*, and HOO^* species. The results will be used to perform thermodynamic simulations of the OER to obtain over-potential η^{OER} values.

An extensive investigation of OER on the flat STO surface was performed by Cui et al. [14]. For the flat $\{0\,0\,1\}$, the STO surface of the over-potential value of 0.66 V was obtained.

2. Methods and Computational Details

We performed density functional theory (DFT) calculations using the Vienna Ab initio Simulation Package (VASP) [26–29]. Computational details are listed in Table 1. Relaxed rhombohedral $SrTiO_3$ phase ($R\bar{3}c$) with the optimized lattice constant a_0 of 3.92 Å was used. We compared flat surface and stepped surface, as shown in Figures 1 and 2, respectively. Adsorbate was placed on both terminations of the slab to neutralize the electric dipole moment.

Adsorption energy $E_{ads,\,x}$ for the configuration x was calculated by Equation (1), where E_x is the total energy of the configuration with the adsorbate, E_{surf} is the total energy of the corresponding surface without the adsorbate, E_{H_2O} is the total energy of water, E_{H_2} is the total energy of molecular hydrogen, and coefficients c_1 and c_2 are determined so that the total number of particles on the left hand side of the equation is zero. Factor $\frac{1}{2}$ is a result of the adsorbate being placed on both terminations of the slab. Lower adsorption energy corresponds to the stronger binding.

All figures were created in the VESTA visualization system [30].

$$E_{ads,\,x} = \frac{1}{2}(E_x - (E_{surf} + c_1 E_{H_2O} + c_2 E_{H_2})) \quad (1)$$

Table 1. Computational details.

Software	VASP 6 [27–29]
Exchange-correlation functional	GGA-PBE [31]
Pseudopotentials	Ultra Soft [32,33] potentials using the Projector Augmented Wave (PAW) method [34,35]
Smearing	Gaussian smearing
Ti-valence configuration	$3p^6 3d^2 4s^2$, valence 10, energy cutoff 222 eV, generated 07.09.2000
Sr-valence configuration	$4s^2 4p^6 5s^2$, valence 10, energy cutoff 229 eV, generated 07.09.2000
O-valence configuration	$2s^2 2p^4$, valence 6, energy cutoff 400 eV, generated 08.04.2002
H-valence configuration	$1s^1$, valence 1, energy cutoff 250 eV, generated 15.06.2001
Spin polarization	Non-spin polarized calculation
Plane wave basis set cut-off	520 eV
Flat surface geometry (Figure 1)	$2a_0 \times 4a_0$ surface cell, seven layers-thick, 20 Å vacuum gap, 144 atoms
Stepped surface geometry (Figure 2)	$2(2a_0 \times 2a_0)$, $2\sqrt{2}a_0$ thickness, 10 Å vacuum gap, 104 atoms
Flat surface k-point mesh	$4 \times 2 \times 2$ Monkhorst-Pack [36]
Stepped surface k-point mesh	$4 \times 4 \times 2$ Monkhorst-Pack [36]

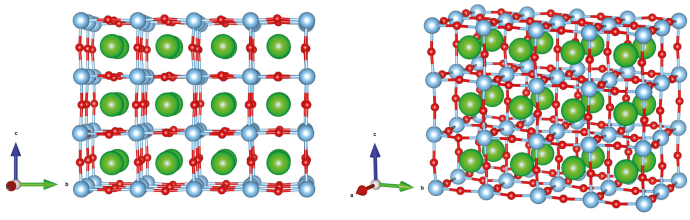

(**a**) (**b**)

Figure 1. Flat surface cell. (**a**) Front view. (**b**) Isometric view.

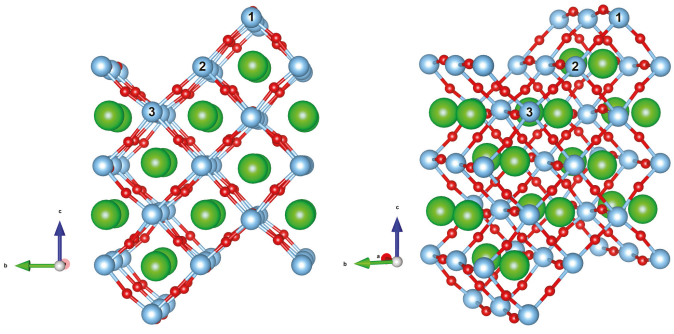

(**a**) (**b**)

Figure 2. Stepped surface cell. The one-ridge adsorption area; two-slope adsorption area; and three-gully adsorption area. (**a**) Front view. (**b**) Isometric view.

3. Results and Discussion

3.1. Water Adsorption

It is important to understand how water adsorption on stepped surfaces distinguishes from that on flat surfaces. On flat surfaces, the most preferable water adsorption site is atop titanium. The stepped model of faceted surfaces features three regions: the ridge, slope, and gully, marked on Figure 2.

On flat surfaces, two adsorption modes are possible: molecular (Figure 3a; $E_{ads} = -0.79$ eV) and dissociative (Figure 3b; $E_{ads} = -1.09$ eV), with dissociative being more energetically favorable, which is in agreement with Reference [13]. In [13], it was demonstrated that there is no significant transition barrier (0.09 eV) between the two adsorption modes. On the stepped surface, the situation is more complex and each adsorption region should be discussed separately.

On the *Slope* region, there are several possible adsorption configurations. The most energetically favorable one is dissociative adsorption along Slope (Figure 4d; $E_{ads} = -0.83$ eV), followed closely by molecular adsorption (Figure 4b,c with E_{ads} of -0.76 eV and -0.71 eV, respectively). Molecular adsorption energy on the slope was loosely dependent on the orientation of water molecules. Dissociation towards the gully or ridge was less favorable (Figure 4e,f with E_{ads} of -0.62 eV and -0.41 eV, respectively). Although, similarly to flat surfaces, one of the possible dissociative configurations on the slope was more favorable than molecular ones, the difference between energies was not as large, thus it cannot be unequivocally concluded, wherein the adsorption mode dominates.

On the *Ridge* region, only one configuration was observed: water dissociation accompanied by spontaneous oxygen vacancy formation (Figure 4a). It also had the lowest adsorption energy (strongest adsorption) of −1.50 eV among all the tested configurations. The investigation of the question regarding whether the ridge breaks down irreversibly or whether the vacancy is healed during subsequent water adsorption is out of scope of this paper.

On the *Gully* region, only one dissociative configuration was found, but only hydrogen was adsorbed, while oxygen was on the slope. Moreover, this configuration had a relatively weak binding (Figure 4g, $E_{ads} = -0.49$ eV), hence we did not investigate it further.

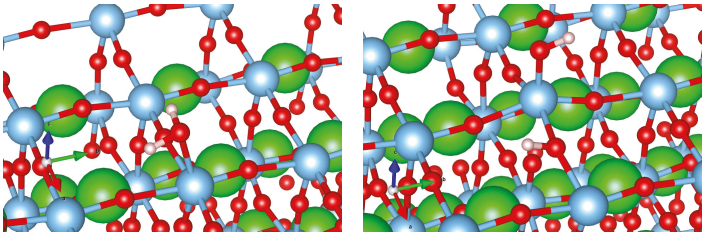

(**a**) (**b**)

Figure 3. Water adsorption configuration on the stepped surface. (**a**) Molecular adsorption on the flat surface: $E_{ads} = -0.79$ eV. (**b**) Dissociative adsorption on the flat surface: $E_{ads} = -1.09$ eV.

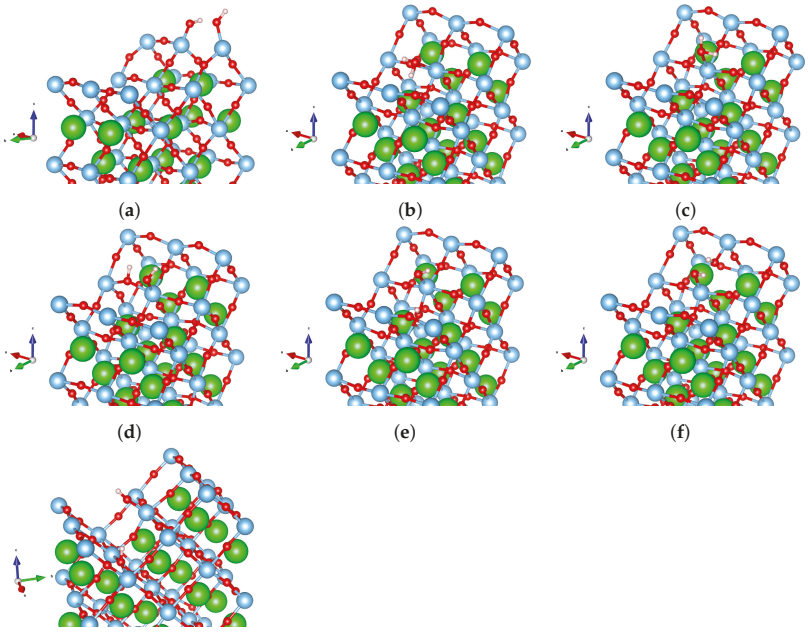

(**a**) (**b**) (**c**)

(**d**) (**e**) (**f**)

(**g**)

Figure 4. Water adsorption configurations on the stepped surface. (**a**) Adsorption on the ridge region. $E_{ads} = -1.50$ eV. (**b**) Molecular adsorption on the slope region with water oriented towards the gully. $E_{ads} = -0.76$ eV. (**c**) Molecular adsorption on the slope region with water oriented towards the ridge. $E_{ads} = -0.71$ eV. (**d**) Dissociative adsorption on the slope region with hydrogen migrated along the slope. $E_{ads} = -0.83$ eV. (**e**) Dissociative adsorption on the slope region with hydrogen migrated towards the gully. $E_{ads} = -0.62$ eV. (**f**) Dissociative adsorption on the slope region with hydrogen migrated towards the ridge. $E_{ads} = -0.41$ eV. (**g**) Dissociative adsorption on the gully region. $E_{ads} = -0.49$ eV.

3.2. Oxygen Evolution Reaction (OER) Intermediates

To perform thermodynamic simulations to estimate STO photo-catalytic activity, it is necessary to compute adsorption energies for oxygen evolution reaction (OER) intermediates: HO^*, O^*, and HOO^*, where the star * denotes the active adsorption site. All energies are compiled in Table 2.

Results for the flat surface are shown in Figure 5. HO^* had only one possible configuration, as shown in Figure 5a. There were two possible configurations for O^*: where oxygen from the adsorbate bonded to surface oxygen, denoted as $O^*_{(O_{surf})}$ (Figure 5b), and where oxygen was atop titanium, denoted as O^* (Figure 5c). The $O^*_{(O_{surf})}$ adsorption energy was much lower (2.87 eV versus 3.52 eV), thus it was more energetically favorable. The HOO^* adsorbate also had two configurations: one where hydrogen bonded to surface oxygen (Figure 5d), denoted as $H_{(O_{surf})}OO^*$, and the other where hydrogen bonded to the adsorbate's oxygen (Figure 5e), denoted as HOO^*. In [14], only the second configuration was mentioned, although its adsorption energy was significantly higher than that of the $H_{(O_{surf})}OO^*$ configuration: 4.24 eV versus 3.64 eV.

The adsorption of intermediates on the slope (Figure 6) was similar to that of the flat surface: only one HO^* configuration (Figure 6a), $O^*_{(O_{surf})}$ (Figure 6b), and O^* (Figure 6c), and two HOO^* configurations, namely $H_{(O_{surf})}OO^*$ (Figure 6d) and HOO^* (Figure 6e) were observed. $O^*_{(O_{surf})}$ was more energetically favorable than O^* (2.93 eV versus 4.11 eV) and $H_{(O_{surf})}OO^*$ was more favorable than HOO^* (3.48 eV versus 4.52 eV), analogous to the flat surface. HO^* on the slope had higher adsorption energy than HO^* on the flat surface (1.35 eV versus 0.77 eV).

Results for the intermediates on the ridge region are shown in Figure 7. For each intermediate, only one adsorption configuration was observed. HO^* (Figure 7a) and HOO^* (Figure 7c), similarly to the water adsorption, were accompanied by spontaneous oxygen vacancy formation, while O^* bonded between surface oxygen and titanium (Figure 7b).

Table 2. Adsorption energies of oxygen evolution reaction (OER) intermediates on different types of surfaces.

Surface Type	HO^*, eV	O^*, eV	HOO^*, eV
Flat surface	0.77 (Figure 5a)	2.87 (Figure 5b)/3.52 (Figure 5c)	3.64 (Figure 5d)/4.24 (Figure 5e)
Slope	1.35 (Figure 6a)	2.93 (Figure 6b)/4.11 (Figure 6c)	3.48 (Figure 6d)/4.52 (Figure 6e)
Ridge	1.24 (Figure 7a)	2.40 (Figure 7b)	3.13 (Figure 7c)

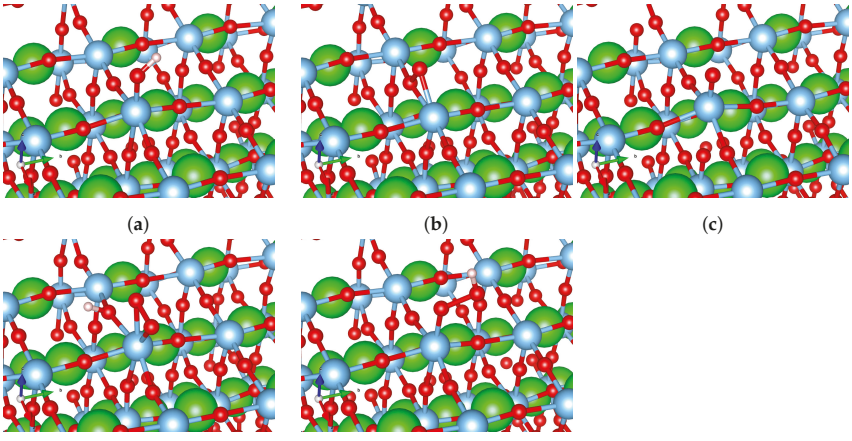

Figure 5. OER intermediates on the flat surface. (**a**) HO^* adsorbate on the flat surface: $E_{ads} = 0.77$ eV. (**b**) $O^*_{(O_{surf})}$ adsorbate on the flat surface: $E_{ads} = 2.87$ eV. (**c**) O^* adsorbate on the flat surface: $E_{ads} = 3.52$ eV. (**d**) $H_{(O_{surf})}OO^*$ adsorbate on the flat surface: $E_{ads} = 3.64$ eV. (**e**) HOO^* adsorbate on the flat surface, standard configuration:
$E_{ads} = 4.24$ eV.

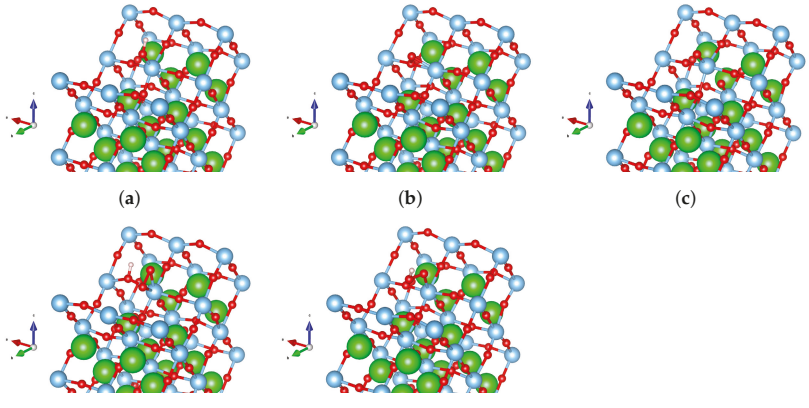

Figure 6. OER intermediates on the slope of the stepped surface. (**a**) HO^* adsorbate on the slope region: $E_{ads} = 1.35$ eV. (**b**) $O^*_{(O_{surf})}$ adsorbate on the slope region: $E_{ads} = 2.93$ eV. (**c**) O^* adsorbate on the slope region: $E_{ads} = 4.11$ eV. (**d**) $H_{(O_{surf})}OO^*$ adsorbate on the slope region: $E_{ads} = 3.48$ eV. (**e**) HOO^* adsorbate on the slope region: $E_{ads} = 4.52$ eV.

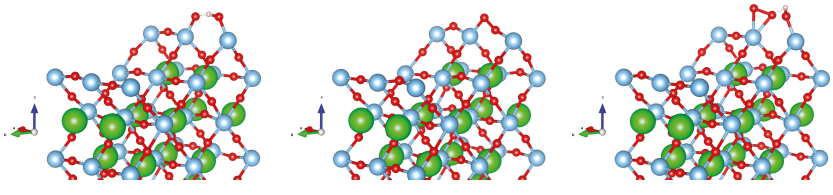

Figure 7. OER intermediates on the ridge of the stepped surface. (**a**) HO^* adsorbate on the ridge region: $E_{ads} = 1.24$ eV. (**b**) O^* adsorbate on the ridge region: $E_{ads} = 2.40$ eV. (**c**) HOO^* adsorbate on the ridge region: $E_{ads} = 3.13$ eV.

4. Conclusions

We have performed a detailed investigation of water adsorption and oxygen evolution reaction (OER) intermediate adsorption on strontium titanate $SrTiO_3$ flat and stepped surfaces. In contrast to the flat surface, the stepped surface, a significant part of which comprises the ridge region, demonstrated high adsorption energies as well as pronounced structural transformations caused by the adsorbate. Our findings suggest that:

- The ridge region permits dissociative water adsorption only, accompanied by spontaneous formation of oxygen vacancy;
- Results for the flat surface are in agreement with other computational studies [13];
- On the slope region, both molecular and dissociative adsorption modes are possible;
- Adsorption of both water and its intermediates on the slope region is similar to that on flat surfaces;
- Except for atomic hydrogen, no adsorption was observed on the gully region; and
- There are different adsorption configurations of OER intermediates possible on flat surfaces and slope regions.

Author Contributions: Conceptualization, Y.A.M. and E.A.K.; data curation, M.S. and V.K.; formal analysis, M.S.; funding acquisition, D.B. and E.A.K.; investigation, M.S., Y.A.M., G.Z. and V.K.; methodology, Y.A.M., D.B. and E.A.K.; project administration, D.B. and E.A.K.; resources, Y.A.M. and E.A.K.; software, M.S.; supervision, Y.A.M., D.B. and E.A.K.; validation, M.S., Y.A.M., G.Z. and V.K.; visualization, M.S.; writing—original draft, M.S.; writing—review and editing, Y.A.M., D.B. and E.A.K. All authors have read and agreed to the published version of the manuscript.

Funding: The financial support of M-ERA.NET2 Sun2Chem project is greatly acknowledged by E.K. Authors thank Marjeta Maček Kržmanc and Chi-Sheng Wu, for the fruitful discussions. The financial support of FLAG-ERA JTC project To2Dox is acknowledged by Y.A.M. This paper is based upon the work from COST Action 18234, supported by COST (European Cooperation in Science and Technology). The support is greatly acknowledged by Y.A.M. and V.K. The grant No. 1.1.1.2/VIAA/1/16/147 (1.1.1.2/16/I/001) under the activity of Post-doctoral research aid is greatly acknowledged by M.S. and D.B.

Acknowledgments: The Institute of Solid State Physics, University of Latvia (Latvia) as the Centre of Excellence has received funding from the European Union's Horizon 2020 Frame-work Programme H2020-WIDESPREAD-01-2016-2017-Teaming Phase2 under grant agreement No. 739508, project CAMART^2. The computer resources were provided by the Stuttgart Supercomputing Center (project DEFTD 12939) and Latvian Super Cluster (LASC).

Conflicts of Interest: The authors declare no conflict of interest.

References

1. Kato, H.; Kudo, A. Visible-Light-Response and Photocatalytic Activities of TiO_2 and $SrTiO_3$ Photocatalysts Codoped with Antimony and Chromium. *J. Phys. Chem. B* **2002**, *106*, 5029–5034. [CrossRef]
2. Miyauchi, M.; Nakajima, A.; Watanabe, T.; Hashimoto, K. Photocatalysis and Photoinduced Hydrophilicity of Various Metal Oxide Thin Films. *Chem. Mater.* **2002**, *14*, 2812–2816. [CrossRef]
3. Konta, R.; Ishii, T.; Kato, H.; Kudo, A. Photocatalytic Activities of Noble Metal Ion Doped $SrTiO_3$ under Visible Light Irradiation. *J. Phys. Chem. B* **2004**, *108*, 8992–8995. [CrossRef]
4. Yu, S.C.; Huang, C.W.; Liao, C.H.; Wu, J.C.; Chang, S.T.; Chen, K.H. A novel membrane reactor for separating hydrogen and oxygen in photocatalytic water splitting. *J. Membr. Sci.* **2011**, *382*, 291–299. [CrossRef]
5. Kato, H.; Kobayashi, M.; Hara, M.; Kakihana, M. Fabrication of $SrTiO_3$ exposing characteristic facets using molten salt flux and improvement of photocatalytic activity for water splitting. *Catal. Sci. Technol.* **2013**, *3*, 1733. [CrossRef]
6. Wang, B.; Shen, S.; Guo, L. $SrTiO_3$ single crystals enclosed with high-indexed 023 facets and 001 facets for photocatalytic hydrogen and oxygen evolution. *Appl. Catal. B Environ.* **2015**, *166–167*, 320–326. [CrossRef]
7. Ham, Y.; Hisatomi, T.; Goto, Y.; Moriya, Y.; Sakata, Y.; Yamakata, A.; Kubota, J.; Domen, K. Flux-mediated doping of $SrTiO_3$ photocatalysts for efficient overall water splitting. *J. Mater. Chem. A* **2016**, *4*, 3027–3033. [CrossRef]
8. Foo, G.S.; Hood, Z.D.; Wu, Z. Shape Effect Undermined by Surface Reconstruction: Ethanol Dehydrogenation over Shape-Controlled $SrTiO_3$ Nanocrystals. *ACS Catal.* **2018**, *8*, 555–565. [CrossRef]
9. Li, D.; Yu, J.C.C.; Nguyen, V.H.; Wu, J.C.; Wang, X. A dual-function photocatalytic system for simultaneous separating hydrogen from water splitting and photocatalytic degradation of phenol in a twin-reactor. *Appl. Catal. B Environ.* **2018**, *239*, 268–279. [CrossRef]
10. Kampouri, S.; Stylianou, K.C. Dual-Functional Photocatalysis for Simultaneous Hydrogen Production and Oxidation of Organic Substances. *ACS Catal.* **2019**, *9*, 4247–4270. [CrossRef]
11. Kanazawa, T.; Nozawa, S.; Lu, D.; Maeda, K. Structure and Photocatalytic Activity of PdCrOx Cocatalyst on $SrTiO_3$ for Overall Water Splitting. *Catalysts* **2019**, *9*, 59. [CrossRef]
12. Saleem, Z.; Pervaiz, E.; Yousaf, M.U.; Niazi, M.B.K. Two-dimensional materials and composites as potential water splitting photocatalysts: A review. *Catalysts* **2020**, *10*, 464. [CrossRef]
13. Guhl, H.; Miller, W.; Reuter, K. Water adsorption and dissociation on $SrTiO_3$ (001) revisited: A density functional theory study. *Phys. Rev. B Condens. Matter Mater. Phys.* **2010**, *81*, 155455. [CrossRef]
14. Cui, M.; Liu, T.; Li, Q.; Yang, J.; Jia, Y. Oxygen Evolution Reaction (OER) on Clean and Oxygen Deficient Low-Index $SrTiO_3$ Surfaces: A Theoretical Systematic Study. *ACS Sustain. Chem. Eng.* **2019**, *7*, 15346–15353. [CrossRef]
15. Holmström, E.; Spijker, P.; Foster, A.S. The interface of $SrTiO_3$ and H_2O from density functional theory molecular dynamics. *Proc. R. Soc. A Math. Phys. Eng. Sci.* **2016**, *472*. [CrossRef]
16. Chen, H.C.; Huang, C.W.; Wu, J.C.S.; Lin, S.T. Theoretical Investigation of the Metal-Doped $SrTiO_3$ Photocatalysts for Water Splitting. *J. Phys. Chem. C* **2012**, *116*, 7897–7903. [CrossRef]
17. Afroz, K.; Moniruddin, M.; Bakranov, N.; Kudaibergenov, S.; Nuraje, N. A heterojunction strategy to improve the visible light sensitive water splitting performance of photocatalytic materials. *J. Mater. Chem. A* **2018**, *6*, 21696–21718. [CrossRef]
18. Maček Kržmanc, M.; Daneu, N.; Čontala, A.; Santra, S.; Kamal, K.M.; Likozar, B.; Spreitzer, M. $SrTiO_3/Bi_4Ti_3O_{12}$Nanohetero structural Platelets Synthesized by Topotactic Epitaxy as Effective Noble-Metal-Free Photocatalysts for pH-Neutral Hydrogen Evolution. *ACS Appl. Mater. Interfaces* **2021**, *13*, 370–381. [CrossRef] [PubMed]
19. Li, X.; Yu, J.; Jaroniec, M. Hierarchical photocatalysts. *Chem. Soc. Rev.* **2016**, *45*, 2603–2636. [CrossRef]
20. Takata, T.; Jiang, J.; Sakata, Y.; Nakabayashi, M.; Shibata, N.; Nandal, V.; Seki, K.; Hisatomi, T.; Domen, K. Photocatalytic water splitting with a quantum efficiency of almost unity. *Nature* **2020**, *581*, 411–414. [CrossRef]

21. Mu, L.; Zhao, Y.; Li, A.; Wang, S.; Wang, Z.; Yang, J.; Wang, Y.; Liu, T.; Chen, R.; Zhu, J.; et al. Enhancing charge separation on high symmetry $SrTiO_3$ exposed with anisotropic facets for photocatalytic water splitting. *Energy Environ. Sci.* **2016**, *9*, 2463–2469. [CrossRef]
22. Tomio, T.; Miki, H.; Tabata, H.; Kawai, T.; Kawai, S. Control of electrical conductivity in laser deposited $SrTiO_3$ thin films with Nb doping. *J. Appl. Phys.* **1994**, *76*, 5886–5890. [CrossRef]
23. Noguera, C. Polar oxide surfaces. *J. Phys. Condens. Matter* **2000**, *12*, R367–R410. [CrossRef]
24. Bachelet, R.; Valle, F.; Infante, I.C.; Sánchez, F.; Fontcuberta, J. Step formation, faceting, and bunching in atomically flat $SrTiO_3$ (110) surfaces. *Appl. Phys. Lett.* **2007**, *91*, 251904. [CrossRef]
25. Man, I.C.; Su, H.Y.; Calle-Vallejo, F.; Hansen, H.A.; Martínez, J.I.; Inoglu, N.G.; Kitchin, J.; Jaramillo, T.F.; Nørskov, J.K.; Rossmeisl, J. Universality in Oxygen Evolution Electrocatalysis on Oxide Surfaces. *ChemCatChem* **2011**, *3*, 1159–1165. [CrossRef]
26. Kresse, G.; Hafner, J. Ab initio molecular dynamics for liquid metals. *Phys. Rev. B* **1993**, *47*, 558–561. [CrossRef]
27. Kresse, G.; Hafner, J. Ab initio molecular-dynamics simulation of the liquid-metal–amorphous-semiconductor transition in germanium. *Phys. Rev. B* **1994**, *49*, 14251–14269. [CrossRef] [PubMed]
28. Kresse, G.; Furthmüller, J. Efficiency of ab-initio total energy calculations for metals and semiconductors using a plane-wave basis set. *Comput. Mater. Sci.* **1996**, *6*, 15–50. [CrossRef]
29. Kresse, G.; Furthmüller, J. Efficient iterative schemes for ab initio total-energy calculations using a plane-wave basis set. *Phys. Rev. B* **1996**, *54*, 11169–11186. [CrossRef]
30. Momma, K.; Izumi, F. VESTA 3 for three-dimensional visualization of crystal, volumetric and morphology data. *J. Appl. Crystallogr.* **2011**, *44*, 1272–1276. [CrossRef]
31. Perdew, J.P.; Burke, K.; Ernzerhof, M. Generalized Gradient Approximation Made Simple. *Phys. Rev. Lett.* **1996**, *77*, 3865–3868. [CrossRef] [PubMed]
32. Vanderbilt, D. Soft self-consistent pseudopotentials in a generalized eigenvalue formalism. *Phys. Rev. B* **1990**, *41*, 7892–7895. [CrossRef]
33. Kresse, G.; Hafner, J. Norm-conserving and ultrasoft pseudopotentials for first-row and transition elements. *J. Phys. Condens. Matter* **1994**, *6*, 8245–8257. [CrossRef]
34. Blöchl, P.E. Projector augmented-wave method. *Phys. Rev. B* **1994**, *50*, 17953–17979. [CrossRef]
35. Kresse, G.; Joubert, D. From ultrasoft pseudopotentials to the projector augmented-wave method. *Phys. Rev. B* **1999**, *59*, 1758–1775. [CrossRef]
36. Monkhorst, H.J.; Pack, J.D. Special points for Brillouin-zone integrations. *Phys. Rev. B* **1976**, *13*, 5188–5192. [CrossRef]

catalysts

MDPI

Article

Palladium-Nickel Electrocatalysts on Nitrogen-Doped Reduced Graphene Oxide Nanosheets for Direct Hydrazine/Hydrogen Peroxide Fuel Cells

Mir Ghasem Hosseini [1,2,*], Vahid Daneshvari-Esfahlan [1,3], Hossein Aghajani [4], Sigrid Wolf [3] and Viktor Hacker [3,*]

[1] Electrochemistry Research Laboratory, Department of Physical Chemistry, Faculty of Chemistry, University of Tabriz, Tabriz 51666-16471, Iran; v.daneshvari@tabrizu.ac.ir
[2] Department of Materials Science and Nanotechnology, Engineering Faculty, Near East University, Nicosia 99318, Turkey
[3] Institute of Chemical Engineering and Environmental Technology, Graz University of Technology, Inffeldgasse 25/C, 8010 Graz, Austria; sigrid.wolf@tugraz.at
[4] Faculty of Materials & Metallurgy Engineering, Iran University of Science and Technology, Tehran 13114-16846, Iran; haghajani@iust.ac.ir
* Correspondence: mg-hosseini@tabrizu.ac.ir (M.G.H.); viktor.hacker@tugraz.at (V.H.)

Abstract: In the present work, nitrogen-doped reduced graphene oxide-supported (NrGO) bimetallic Pd–Ni nanoparticles (NPs), fabricated by means of the electrochemical reduction method, are investigated as an anode electrocatalyst in direct hydrazine–hydrogen peroxide fuel cells (DHzHPFCs). The surface and structural characterization of the synthesized catalyst affirm the uniform deposition of NPs on the distorted NrGO. The electrochemical studies indicate that the hydrazine oxidation current density on Pd–Ni/NrGO is 1.81 times higher than that of Pd/NrGO. The onset potential of hydrazine oxidation on the bimetallic catalyst is also slightly more negative, i.e., the catalyst activity and stability are improved by Ni incorporation into the Pd network. Moreover, the Pd–Ni/NrGO catalyst has a large electrochemical surface area, a low activation energy value and a low resistance of charge transfer. Finally, a systematic investigation of DHzHPFC with Pd–Ni/NrGO as an anode and Pt/C as a cathode is performed; the open circuit voltage of 1.80 V and a supreme power density of 216.71 mW cm^{-2} is obtained for the synthesized catalyst at 60 °C. These results show that the Pd–Ni/NrGO nanocatalyst has great potential to serve as an effective and stable catalyst with low Pd content for application in DHzHPFCs.

Keywords: hydrazine electrooxidation; anode; Pd–Ni nanoparticles; nitrogen-doped reduced graphene oxide; direct hydrazine fuel cell

Citation: Hosseini, M.G.; Daneshvari-Esfahlan, V.; Aghajani, H.; Wolf, S.; Hacker, V. Palladium-Nickel Electrocatalysts on Nitrogen-Doped Reduced Graphene Oxide Nanosheets for Direct Hydrazine/Hydrogen Peroxide Fuel Cells. *Catalysts* **2021**, *11*, 1372. https://doi.org/10.3390/catal11111372

Academic Editors: Marc Cretin, Sophie Tingry and Zhenghua Tang

Received: 29 October 2021
Accepted: 12 November 2021
Published: 14 November 2021

1. Introduction

Direct hydrazine–hydrogen peroxide fuel cells (DHzHPFCs) are known as unique power sources for air-independent applications in space and underwater. The use of hydrazine (N_2H_4) as a high-energy fuel in FCs has been investigated since the 1970s [1,2], specifically as an alternative fuel in portable power sources [3–5]. N_2H_4 is considered a promising liquid fuel for the following reasons: (1) its handling is safer; (2) its electrooxidation occurs without the generation of carbon dioxide, which leads to a reduction of greenhouse gas emissions; (3) catalysts are not poisoned during the N_2H_4 oxidation reaction due to lack of the carbonaceous intermediates production, as reported by Mohammed et al., who investigated the sensitive electrochemical detection of hydrazine based on SnO_2/CeO_2 nanostructured oxide and reported the high stability, sensitivity and repeatability of hydrazine oxidation on the synthesized nanomaterial [6]; and (4) because of the high theoretical electromotive force of 1.56 V [7] and power density (PD) of 5.4 KWh L^{-1} observed for DHzHPFCs. On the other hand, a simple internal structure of fuel cells is obtained

with an oxidant of hydrogen peroxide (H_2O_2) [8–10]. Compared to the oxygen reduction reaction (ORR) with a theoretical electrode potential of 1.23 V, the theoretical electrode potential of the H_2O_2 reduction reaction (HRR, 1.77 V) and the corresponding kinetics is higher. Thus, the ideal open circuit voltage (OCV) of the single FC and its PW is increased using H_2O_2 as an alternative fuel to oxygen. The anode, cathode, and overall cell reactions in the DHzHPFC are:

$$\text{Anode}: N_2H_4 + OH^- \rightarrow N_2 + 4H_2O + 4e^- \quad E^\circ = -1.21 \text{ V vs. SHE} \tag{1}$$

$$\text{Cathode}: 2H_2O_2 + 4H^+ \rightarrow +4e^- + 4H_2O \quad E^\circ = 0.92 \text{ V vs. SHE} \tag{2}$$

$$\text{Overall}: N_2H_4 + 2H_2O_2 \rightarrow N_2 + 4H_2O \quad E^\circ = 2.13 \text{ V vs. SHE} \tag{3}$$

In DHzHPFC, a Nafion membrane is used, electrons transferring from anode to cathode and Na^+ migration occurring in the opposite direction. According to Equation (3), H_2O and N_2 are products of this type of DFC [10,11]. Various chemicals have been designed recently and their performances as catalysts examined in the DHzHPFC [3,5,9,12–18]. For example, the accumulation of gas bubbles on the electrode surface is effectively solved by using a nano-hill morphology of vertical graphene, by means of which a superoleophobic electrode was obtained that could accelerate the elimination process of bubbles generated on the anodic electrode surface. Yin et al. report on a DHzHPFC that yields a high-power density of 84 mW cm^{-2} using a Zr/Ni alloy as the anode and Pt/C as the cathode [19]. In another report on DHzHPFC, with a Pt-based anode (10.0 mg cm^{-2}) and an Au/C cathode (10.0 mg cm^{-2}), a high PD of 1.02 W cm^{-2} and an OCV of 1.75 V at 80 °C is reported [20]. In the course of this work, Yan et al. [21] fabricated dealloyed nanoporous gold leaves and found that these catalysts present high performances for both N_2H_4 oxidation (HzOR) and HRR. One method to improve the electrocatalytic activity of anode electrocatalysts is by preparing core–shell nanoparticles, in which the core and shell are composed of different elements. Preparation of different core–shell nanoparticles, including Ni–Pt, Ni–Pd, and Ni–Ru, on reduced graphene oxide (rGO) have been recently reported by Hossieni et al., [13]. The reported single fuel cell results show that Ni–Pd/rGO resulted in an improvement in power density (204.79 mW cm^{-2}) equal to 10.03% and 47.32% with respect to Ni–Pt/rGO (186.12 mW cm^{-2}) and Ni–Ru/rGO (139.01 mW cm^{-2}), respectively, which was attributed to the synergistic effects between Pd and Ni metals.

Such observations allowed the implementation of a DHzHPFC based on these porous membrane catalysts with an OCV of 1.2 V and a maximum power density (MPD) of 195.0 mW cm^{-2} at 80 °C with a total loading of 0.1 mg cm^{-2} Au on each side. Although high power densities and OCVs are obtained, the critical impediment to the commercialization of DHzHPFC technology is still linked to high-cost catalysts prepared from resource-limited noble metals. Additionally, the current nanoelectrodes have further disadvantages, including structural irregularity, irregular distribution, and agglomeration during operation. These disadvantages mean that it is necessary to prepare low-cost, highly active, and more stable catalysts. To achieve this goal, ideal nanoelectrocatalysts should be highly conducive to facilitating the transfer of electrons/ions and possess a high active surface to increase the catalytic efficiency of desired nanocatalysts in the DHzHPFC community [22,23]. Alloying noble metals with cheap transition metals is well-known as one way to decrease the content of noble metals. Among non-precious transition metals, Ni is a low-cost and co-catalyst active metal, and its alloying with Pd refreshes the active sites of Pd; it thus improves the corresponding activity/stability of the bimetallic catalyst as a result of Pd–Ni synergistic influences [24,25]. The selection of a suitable catalyst support is another important parameter that improves fuel cell performance, in addition to reducing the price of catalysts. In this respect, graphene and its derivatives, as an allotrope of single-layer carbon atoms arranged in a two-dimensional honeycomb lattice, have received more attention in scientific communications due to their unique properties, including strong electrical conductivity (6500 S m^{-1}) [26,27], a high theoretical specific surface area, high thermal and chemical stability, and an adjustable bandgap. These characteristics

led to graphene being engaged as a carbon support in several applications, especially for Energy Generation [28–30]. Although graphene possesses unique properties, the path of its commercialization remains a challenge for researchers. For graphene to be transferred from the laboratory to consumer-utilized products, it is necessary to produce large-scale graphene which is practical and competitive. For this reason, better understanding of graphene and its derivatives as a step to introducing this material into industrial-scale production has a high importance. Different methods for preparation of graphene and its derivates along with their sustainability have been reviewed recently by Umar et al., [29] helping the researchers investigating the high-quality production of these nanomaterials. Furthermore, graphene oxide (GO) has various functional groups, i.e., −COOH and −OH, for immobilization of different active species. Recently, the incorporation of heteroatoms and especially nitrogen [31–34] into the carbon plane has attracted great attention.

In fact, by doping the carbon plane with nitrogen atoms, the electronic density of the neighboring carbon atoms is redistributed, inducing an electrophilic center in the adjacency of nitrogen atoms, and modifies the geometry and the electron donor character of the resultant nitrogen-doped GO. [35] The uniform dispersion with a narrow small metal particle size is also obtained by the incorporation of nitrogen atoms into the GO skeleton [36]. Based on the literature [37,38], the nitrogen atoms in the NrGO support are effective in changing the oxidation state of Pd and its NPs' size, suggesting deposition of Pd^{2+} on NrGO as oxo/hydroxo clusters of Pd. Following clustering, the metal oxide species are reduced, leading to the formation of Pd NPs. Charge localization occurs on the catalyst support and is attacked by activated hydrogen atoms from the Pd NPs at the quaternary nitrogen sites, resulting in uniform growth of the Pd metal NPs.

This work reports the preparation of NrGO-supported bimetallic Pd–Ni alloy NPs by polyol method and its use as an anode catalyst towards the production of HzOR in DHzHPFCs. In this respect, the phase, elemental composition, and surface morphology of the fabricated nanostructure were qualified by employing X-ray diffraction (XRD), field emission scanning electron microscopy (FE-SEM), energy-dispersive X-ray spectroscopy (EDX), Fourier-transform infrared spectroscopy (FT-IR), and transmission electron microscopy (TEM). Cyclic voltammetry (CV), chronoamperometry (CA), and electrochemical impedance spectroscopy (EIS) methods were utilized to study hydrazine oxidation on the synthesized nanocatalyst and these results were compared with the results for the Pd/NrGO electrocatalyst. Finally, the cell performance of DHzHPFC was investigated by considering different operation conditions on cell potential and its MPD. In the DHzHPFCs experiments, the membrane electrode assembly (MEA) was obtained using the catalyst-coated membrane (CCM) method.

2. Results and Discussion

2.1. Physical Characterization of Nanocatalysts

The functional groups of the catalyst support can simplify the incorporation of metal nanoparticles on surfaces. According to recent work [39], FT-IR was conducted to qualify the GO functional groups and their changes in NrGO support after simultaneous nitrogen atom doping of the GO skeleton and reduction of oxygenated species, as shown in Figure 1a. In both spectra (in the range of 400–4000 cm^{-1}), the band at 3400 cm^{-1} demonstrates the O–H stretch of the –OH group. During oxidation or functionalization of GO, the carboxyl groups have fluctuated, which leads to a clear peak at 3400 cm^{-1}. Four characteristic bands can be observed in the spectrum of GO, with one at 1728 cm^{-1} arising from stretching vibrations of C=O in carbonyl and carboxyl groups and the other three at 1624 cm^{-1}, 1220 cm^{-1}, and 1085 cm^{-1}, devoted to the C=C, C–OH, and C–O stretching vibrations, respectively. In the case of NrGO, the bands at 1624 and 1220 cm^{-1} are not observed and the intensity peaks of other oxygenated functional groups decrease. Additionally, the superposition of C=C and C=N vibrations leads to shifts in the in-plane vibration of C=C from 1624 to 1556 cm^{-1}. Moreover, a new peak appears at 1187 cm^{-1} which can be related to the C-N bonds. These observations provide valuable information in regard to

the existence of nitrogen-containing groups in the synthesized catalyst support in close agreement with reports in the literature [39–41].

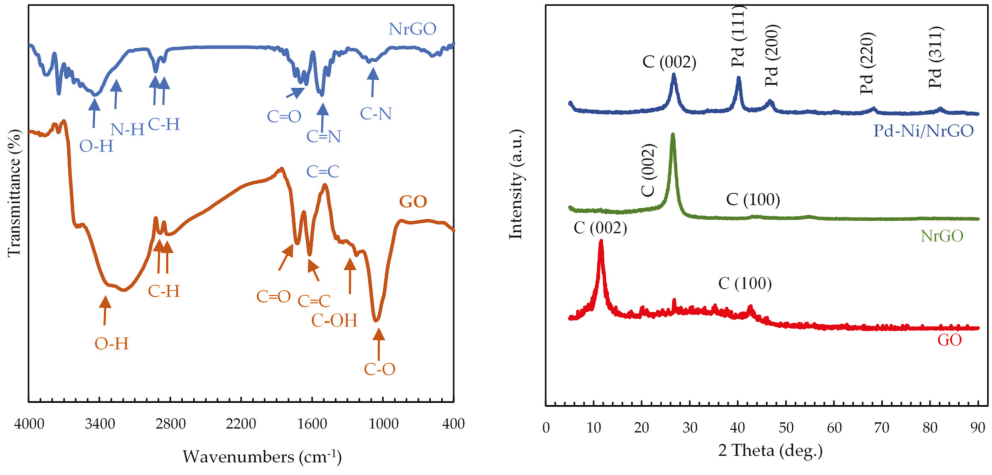

(**a**) (b)

Figure 1. (**a**) FT-IR spectra of GO and NrGO [1]. (**b**) XRD patterns of GO and NrGO, and Pd–Ni/NrGO. Reprinted with permission from ref. [1]. Copyright 2021 American Chemical Society.

Figure 1b presents XRD patterns of GO, NrGO, and Pd–Ni/NrGO samples; the existence of sharp peaks in these XRD patterns characterize a crystalline structure for the synthesized materials. The strong sharp peak of a basal plane in the graphitic structure (002) is seen at a 2θ value of 11.49° with d-spacing of 0.77 nm in the XRD pattern of GO [42]. Such a peak is also observed in the XRD spectra of NrGO and Pd–Ni/NrGO but moving to a higher 2θ value of 26.45° than that of GO [43,44]. The interlayer spacing of NrGO samples was about 0.340 nm, which is a somewhat smaller than that in the bare rGO (0.37 nm), which is ascribed to the more compact graphitic structure created after nitrogen doping [39,45,46].

The four strong, sharp peaks at 40.15°, 46.80°, 68.29°, and 82.28° are observed for the Pd–Ni/NrGO catalyst with the miller indices (111), (200), (220), and (311), respectively, for the face-centered-cubic (fcc) lattice crystal structure facets of the Pd (JCPDS No. 01-087-0641) [47,48]. Pd (111) presents the strongest sharp peak for oxidation of an active facet of small organic molecules. As seen in Figure 1b, the deposition of Pd–Ni metal Nps on the NrGO support has no influence on the support structure; the peaks for NrGO are maintained with a decrease in intensity. By comparing the XRD pattern of Pd–Ni/NrGO with the standard powder diffraction file of Pd (JCPDS No. 01-087-0641) and Ni (JCPDS No. 00-04-0850), it is concluded that all the peaks for synthesized catalysts are placed between the peaks of Pd and Ni metal NPs. These results reveal the successful preparation of the Pd–Ni/NrGO nanostructure in good accordance with those reported in the literature [39,47–50].

Figure 2a,b presents the FE-SEM image of NrGO planner sheets with wrinkled and folded features, indicating that the generic morphology of GO is preserved after nitrogen doping [51]. As displayed in Figure 2c, the FE-SEM micrograph of the Pd–Ni/NrGO sample displays the Pd–Ni metallic NPs dispersed uniformly on the surface of NrGO, and the compact exfoliated multilayers of NrGO features is restricted after the incorporation of metal NPs. This means that the Pd–Ni NPs form independently on the rough and planar nanosheets provided by NrGO without any aggregation. It is found that the particle size of Pd–Ni is around 11–13 nm.

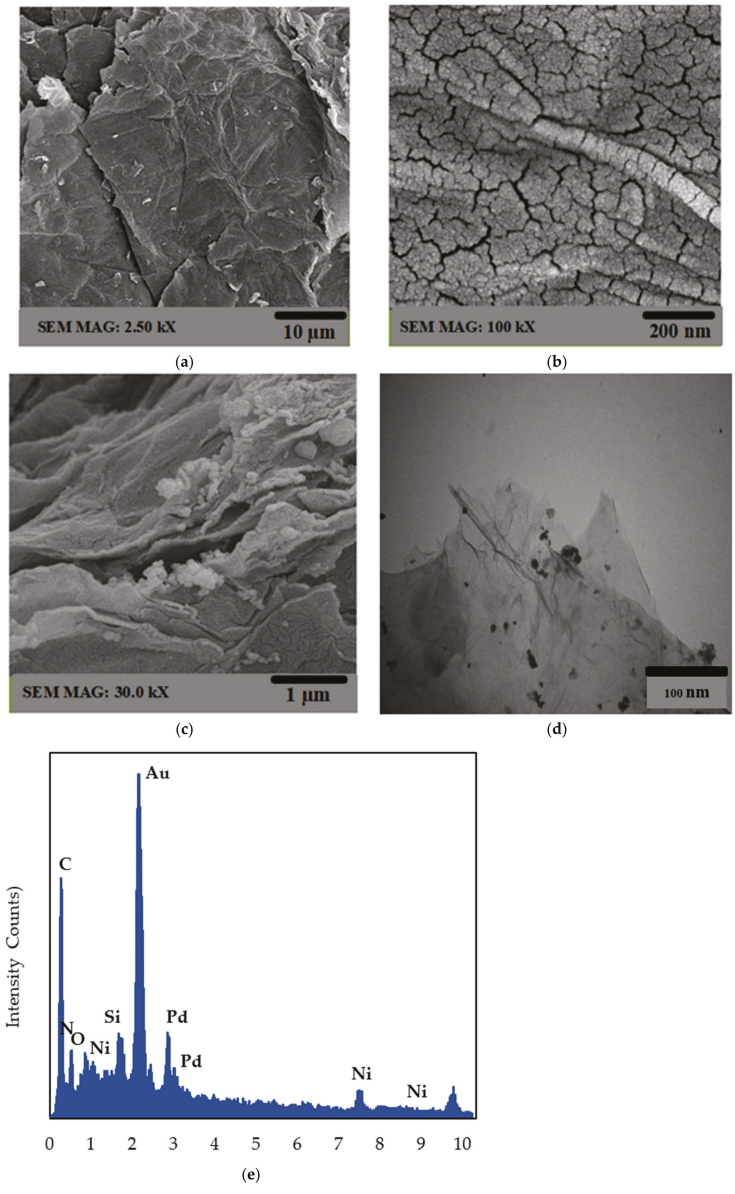

Figure 2. (**a**–**c**) FESEM images of (**a**,**b**) NrGO and (**c**) Pd–Ni/NrGO. (**d**) TEM image and (**e**) EDX image of Pd–Ni/NrGO.

To determine the distribution of each element on the synthesized catalyst, a back scattered electron (BSE) image was captured, and the result is displayed in Figure S1 in the Supplementary Material. As seen in this figure, there are white and gray zones which are associated with the presence of higher and lower average atomic numbers, respectively. White-colored aggregates are mainly made up of a metallic phase (Pd and Ni) whereas darker aggregates are richer in oxygen, nitrogen, and carbon. These images are corroborated by SEM images performed on the synthesized catalyst along with the

uniform distribution of metal nanoparticles on the catalyst support (Figure 2c) and the EDX map (Figure S2).

To further observe the morphology of Pd–Ni/NrGO, TEM images were recorded, as seen in Figure 2d. It can be seen that the bimetallic nanoparticles are scattered homogeneously on the NrGO sheet with a narrow size range. The uniform dispersion of Pd–Ni NPs on catalyst support may be attributed to the shifting of the d-band centers of supported Pd atoms to the Fermi level by the incorporation of nitrogen into graphene [52,53]. The obtained results from EDX analysis (as seen in Figure 2e) indicated the existence of C (42.19 wt%), N (16.23 wt%), O (21.16 wt%), Pd (11.08 wt%), and Ni (9.34 wt%) in the synthesized catalyst. This means that the total metal content of the electrocatalyst is around 20 wt% with a weight ratio of 1:1 for Pd to Ni metals. Figure S2 presents the elemental mapping images of the synthesized catalyst which confirm the uniform deposition of bimetallic NPs on the active sites of N-rGO.

2.2. Half-Cell Measurements

CV is employed for the determination of the catalytic activity of Pd–Ni/NrGO against HzOR. In this respect, the CVs of the NrGO in the presence and absence of N_2H_4 0.02 mol L^{-1} are recorded at a sweep rate of 100 mV s^{-1} and presented in Figure 3a. No obvious peak is seen in each solution, confirming a capacitive current background without any perceptible faradaic processes and inactivity of NrGO against HzOR.

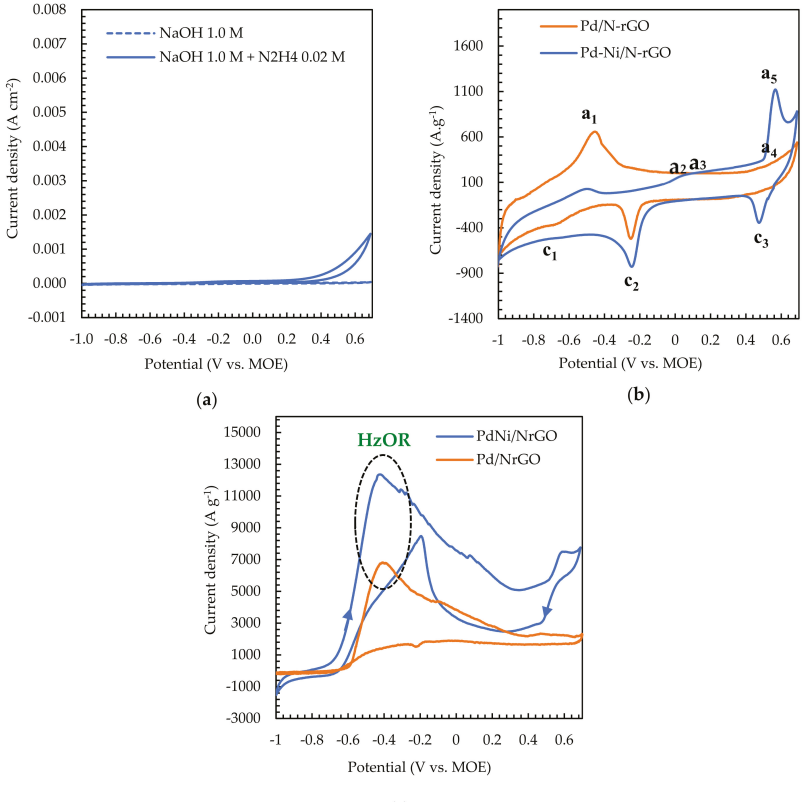

Figure 3. The CVs in the NaOH 1.0 mol L^{-1} under a sweep rate of 100 mVs^{-1} (**a**) for NrGO in the presence and absence of N_2H_4 0.02 mol L^{-1}, (**b**) for Pd/NrGO and Pd–Ni/NrGO in the absence of N_2H_4, (**c**) for Pd–Ni/NrGO in the presence of N_2H_4 0.02 mol L^{-1}.

The CV method has been used recently for the investigation of borohydride oxidation reaction kinetics that occurred on the bimetallic Pd-based nanocatalysts and also for the calculation of their electrochemical active surface area (ECSA), which determines the electrode kinetics for various redox reactions taking place at the electrode surface. Following on from previous work [39], we decided here to record again the CVs of the Pd–Ni/NrGO and Pd/NrGO in NaOH 1.0 mol L^{-1} with a sweep rate of 100 mV s^{-1}, as seen in Figure 3b. In both plots, hydrogen desorption and adsorption peaks (a_1 and C_1) are observed from the −0.75 to −0.3 V potential range in the forward and backward sweeps, respectively. The peaks shown in the potentials above 0.35 V (a_4) are related to the palladium oxide formation peak, while the palladium oxide reduction peak is seen at the potential window of −0.2 to −0.4 V in the backward scan.

The first peak in the anodic scan (a_2) is observed at a potential of 0.03 V which can be assigned to the reaction: $Ni + 2OH^- \rightarrow \alpha - Ni(OH)_2 + 2e^-$, followed then by an irreversible transformation of α-$Ni(OH)_2$ to β-$Ni(OH)_2$ (a_3) by moving to the more positive potentials. The same behavior has been recently reported in the literature [54]. Once the β phase is produced, it cannot be electrochemically removed/reduced from the surface of the electrode because of its high electrochemical stability [54]. By increasing potential, the next increase in the anodic current density (a_5) is seen at a potential of (0.4–0.6) V; this may be attributed to the electrochemical conversion of Ni^{+3}/Ni^{+2}, where β-$Ni(OH)_2$ is oxidized to β-NiOOH. In the cathodic region, at the potential +0.4 to +0.6 V, the β-NiOOH is reduced to β-$Ni(OH)_2$ (c_3). These reduction and oxidation peaks (a_5 and c_3) correspond to the reversible conversion of Ni^{+3}/Ni^{+2}, as described with Equations (4)–(6) [54,55]:

$$Ni(OH)_2 + OH^- \rightarrow NiOOH + H_2O + e^- \quad (4)$$

$$NiO + OH^- \rightarrow NiOOH + e^- \quad (5)$$

$$Ni + 3OH^- \rightarrow NiOOH + 3e^- \quad (6)$$

The area of the PdO reduction region in the CVs plotted in Figure 3b is utilized to compute the electrochemical active surface area (ECSA) of Pd/NrGO and Pd–Ni/NrGO catalysts. As is known, a high value of ECSA for each electrocatalyst reveals a high number of electrocatalytic active sites and vice versa. Thereby, the HzOR kinetics at various Pd-based electrodes is controlled with the ECSA [56]. The ECSA of Pd-based catalysts is computed with Equation (7) [33].

$$ECSA = \frac{Q_{PdO}}{(0.405 \times [Pd])} \quad (7)$$

Q_{PdO} denotes the coulombic charge (mC) and it is computed by integrating of the palladium oxide reduction peak; the value of 0.405 is the conversion factor (mC cm^{-2}) that corresponds to palladium oxide reduction; [Pd] is related to the loading amount of the Pd-based catalyst. The calculated ECSA for two synthesized catalysts is given in Table 1. It is noticed that the ECSA for Pd–Ni/NrGO is 2.61 times higher than that of Pd/NrGO; thus, the existence of Ni atoms in bimetallic catalysts significantly alters the electronic structure of Pd and its electrochemical activity.

Table 1. The electrochemically active surface area (ECSA), hydrazine oxidation current density (i_p), and onset potential of HzOR on the Pd–Ni/NrGO and Pd/NrGO catalysts.

Catalyst Type	ECSA (m^2 g^{-1})	i_p (A g^{-1})	Onset Potential (V vs. MOE)
Pd/NrGO	63.67	6821.22	−0.40
Pd–Ni/NrGO	166.38	12,360.50	−0.45

Cyclic voltammograms of Pd–Ni/NrGO and Pd/NrGO catalysts in NaOH 1.0 mol L^{-1} containing N_2H_4 0.02 mol L^{-1} at the sweep rate of 100 mV s^{-1} are presented in Figure 3c.

A dramatic change can be seen in comparison to the CVs recorded in the absence of N_2H_4. The peak of HzOR for the Pd–Ni/NrGO and Pd/NrGO electrocatalysts is seen at a potential window of −0.6 to −0.4 V. The following reaction describes the peak of HzOR for the synthesized catalysts.

$$N_2H_4 + 4OH^- \rightarrow N_2 + 4H_2O + 4e^- \quad (8)$$

As reported in Table 1, the current density of HzOR on the Pd–Ni/NrGO (12,360.50 A g^{-1}) is 1.81 times higher than that of Pd/NrGO (6821.22 A g^{-1}). In addition, the reported onset hydrazine oxidation potentials in Table 1 show a more negative value for the Pd–Ni/NrGO (−0.45 V) than the Pd/NrGO (−0.40 V). It can be concluded that embedding Ni atoms into the Pd network not only reduced the preparation cost but also enhanced the catalytic performance due to the synergistic effects between Pd and Ni along with an increment in the effective surface area of this electrode.

To obtain more information regarding the electrochemical kinetic parameters of the Pd–Ni/NrGO electrode, CVs were recorded at several scan rates. Figure 4a presents the CV curves in an aqueous solution of NaOH 1.0 mol L^{-1} containing N_2H_4 0.02 mol L^{-1} at various sweep rates. According to this Figure, the anodic current (i_p) increases by increasing the scan rates. At the same time, the peak potential is moved to more positive values, suggesting an irreversible electrochemical process [57]. Equation (9) describes the relationship between peak potential, E_p (V), and sweep rate, v (V s^{-1}), for an irreversible electrochemical process [58]:

$$E_p = E^0 + \left[\frac{RT}{(1-\alpha)nF}\right]\left\{0.78 + \ln\frac{D_0}{k_s} + \ln\left[\frac{(1-\alpha)nFv}{RT}\right]^{\frac{1}{2}}\right\} \quad (9)$$

where E_0, R, T, α, F, and D_0, are the standard potential (V), gas constant (8.314 J K^{-1} mol^{-1}), temperature (K), charge transfer coefficient, Faraday constant (96,485 C mol^{-1}), and diffusion coefficient of N_2H_4 (cm^2 s^{-1}), respectively. n corresponds to the number of transferred electrons in the rate-determination step. k_s denotes the standard heterogeneous rate constant (cm s^{-1}). When the IP values are established in terms of the square root of the scan rate ($v^{\frac{1}{2}}$), a linear relation is observed (as detailed in Figure 4b), suggesting a diffusion-controlled process for the electrooxidation of N_2H_4. By increasing scan rates, the number of electrochemically active species and the length of the diffusion path through penetration of the reaction zone from the electrode surface into the inner parts are increased [59]. The relation between i_p and the sweep rate along with the other influencing parameters on the IP values can be represented with Equation (10) [59]:

$$i_p = 2.99 \times 10^5 n(\alpha n)^{\frac{1}{2}} A D_0^{\frac{1}{2}} v^{\frac{1}{2}} c_0^* \quad (10)$$

$$n\alpha = \frac{1.857RT}{\left(F\left(E_p - E_{\frac{p}{2}}\right)\right)} \quad (11)$$

In this relation, A and $E_{p/2}$ are the electrode surface area (cm^2) and half-peak potential (V), respectively. c_0^* refers to the bulk concentration of electroactive species [60].

The concentration of N_2H_4 was optimized during the electrooxidation of N_2H_4 on the Pd–NrGO catalyst. The recorded CV curves in a solution of NaOH 1.0 mol L^{-1} and various concentrations of N_2H_4 at a sweep rate of 100 mV s^{-1} are represented in Figure 5a. The HzOR peak potential is shifted slightly towards positive values by increasing N_2H_4 concentration and the highest i_p value is obtained at N_2H_4 0.1 mol L^{-1}. This observation may be explained by the existence of a large number of electroactive species in solution. According to Equation (10), it is expected that the anodic current density will increase with increasing N_2H_4 concentration, as observed in Figure 5a [61]. By plotting log i_p values in terms of log[N_2H_4], a straight linear relationship is obtained (Figure 5b). The order of the

N_2H_4 oxidation reaction on the Pd–Ni/NrGO catalyst is calculated from the slope of the log i_p vs. log[N_2H_4] plot (Figure 5b) according to Equations (12) and (13):

$$\text{Rate} = i_p = k[N_2H_4]^{\beta} \quad (12)$$

$$\log i_p = \log k + \beta \log[N_2H_4] \quad (13)$$

where k, [N_2H_4], and β are the reaction rate constant and the bulk concentration of N_2H_4, and reaction order, respectively. The value of 0.92 on Pd–Ni/NrGO, which is close to a typical value of 1 reveals a first-order reaction for HzOR with this catalyst and is consistent with the values reported in other works [62].

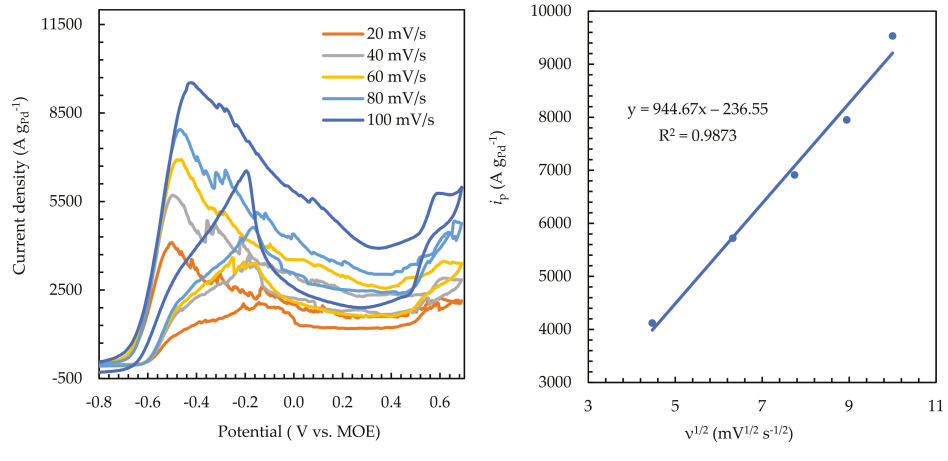

Figure 4. (**a**) The effects of sweep rate on the CVs of Pd–Ni/NrGO in NaOH 1.0 mol L^{-1} + N_2H_4 0.02 mol L^{-1}. (**b**) The plot of HzOR peak current vs. $v^{1/2}$ for Pd–Ni/NrGO.

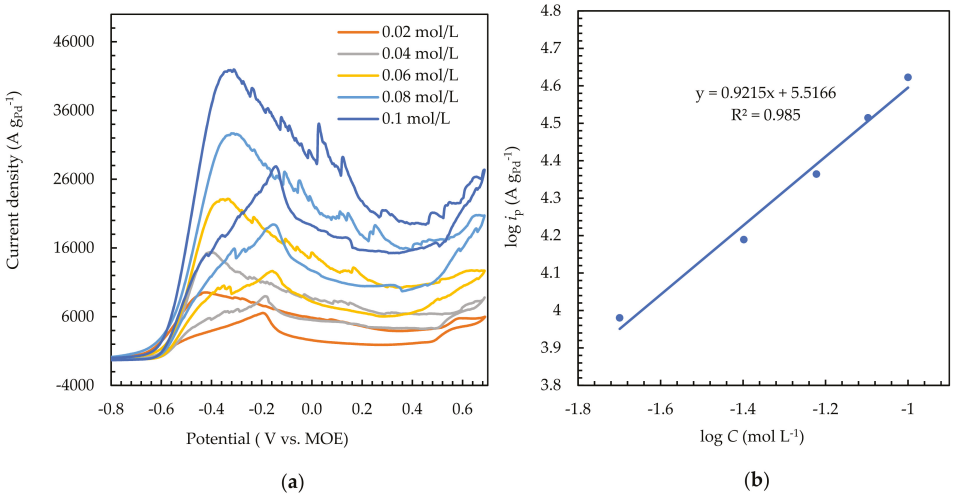

Figure 5. (**a**) The effects of N_2H_4 concentration on the CVs of Pd–Ni/NrGO in NaOH 1.0 mol L^{-1} at a constant sweep rate of 100 mV s^{-1}. (**b**) The plot of log C_{N2H4}-log i_p for Pd–Ni/NrGO.

Electrolyte temperature also influences the performance of electrodes with the effect that it has on the rate of the charge transfer process in the electrode/electrolyte interface and mass diffusion in electrolyte solutions. Figure 6a reveals the CV curves of Pd–Ni/NrGO at different temperatures in an aqueous solution of 1.0 mol L^{-1} NaOH containing 0.1 mol L^{-1} N_2H_4. All CV curves have similar shapes, which suggests the same reaction mechanisms at the investigated temperatures. The current density of the Pd–Ni/NrGO catalyst increases by raising the temperature from 25 to 35, 45, and 55 °C. This is due to the endothermic reaction that takes place at the Pd–Ni/NrGO electrode surface. The activation energy (E_a, J mol^{-1}) can be calculated by the Arrhenius equation (Equation (14)) [63]:

$$-\frac{E_a}{RT^2} = \frac{\partial(\ln i_p)}{\partial T} \quad (14)$$

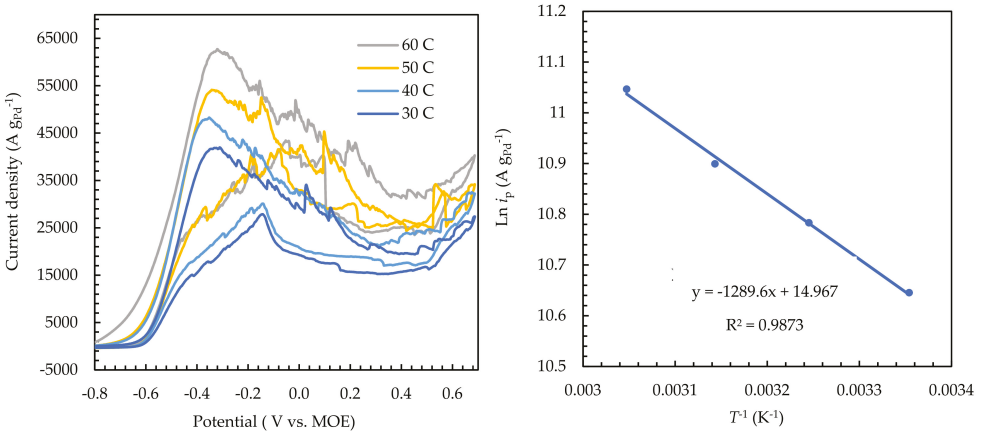

Figure 6. (**a**) The effects of temperature on the CVs of Pd–Ni/NrGO in NaOH 1.0 mol L^{-1} + N_2H_4 0.1 mol L^{-1} at a constant sweep rate of 100 mV s^{-1}. (**b**) The Plot of ln i_p vs. $1/T$ for Pd–Ni/NrGO.

Arrhenius plots of the Pd–Ni/NrGO catalyst are plotted in Figure 6b. The E_a value for this catalyst is obtained as 10.72 kJ mol^{-1}. The low value of E_a for the Pd–Ni/NrGO catalyst reveals that the electrooxidation of hydrazine occurs easily for this catalyst, which may be ascribed to its large specific surface area and massive catalytic active sites offered due to the unbeatable morphology of NrGO supported Pd–Ni nanoparticles.

CA is a powerful electrochemical technique for surveying the stability and catalytic performance of electrodes. Figure 7 presents the CA curves for hydrazine electrooxidation in a NaOH 1.0 mol L^{-1} + N_2H_4 0.1 mol L^{-1} solution under a potential of −0.5 V vs. MOE. In the beginning, a sharp oxidation current is seen for each electrode, which relates to the free active sites of these electrodes from adsorbed molecules. After a few seconds, the oxidation current is reduced, which may be related to the occupation of the active sites. According to Figure 7a, the current density of Pd–Ni/NrGO (~11,100 A g^{-1}) is higher than that of Pd/NrGO (~5770 A g^{-1}) after stabilization for 3000 s. Furthermore, the resulting current density percentage decrease for Pd–Ni/NrGO (54.31%) is lower than that of Pd/NrGO (67.80%) (as seen in Figure 7b), suggesting the better durability of Pd–Ni/NrGO compared to Pd/NrGO. The results obtained from the CA analysis are consistent with the CV results.

EIS is utilized to explore the electron transfer kinetics of Pd–Ni/NrGO towards HzOR. Nyquist plots were recorded in NaOH 1.0 mol L^{-1} containing N_2H_4 x mol L^{-1} (x: 0.02, 0.06, and 0.1) at different potentials (−0.5 and −0.9 V) and various temperatures (25 and 45 °C), and the results are displayed in Figure 8.

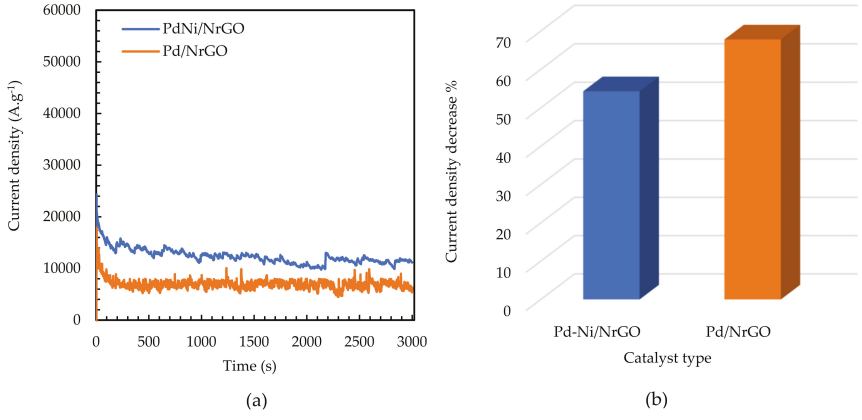

Figure 7. (**a**) CA curves of Pd–Ni/NrGO and Pd/NrGO in NaOH 1.0 mol L^{-1} + N_2H_4 0.1 mol L^{-1} at −0.5 V. (**b**) The resulting current density percentage decrease for Pd–Ni/NrGO and Pd/NrGO at a potential of −0.5 vs. MOE and 25 °C for 3000 s.

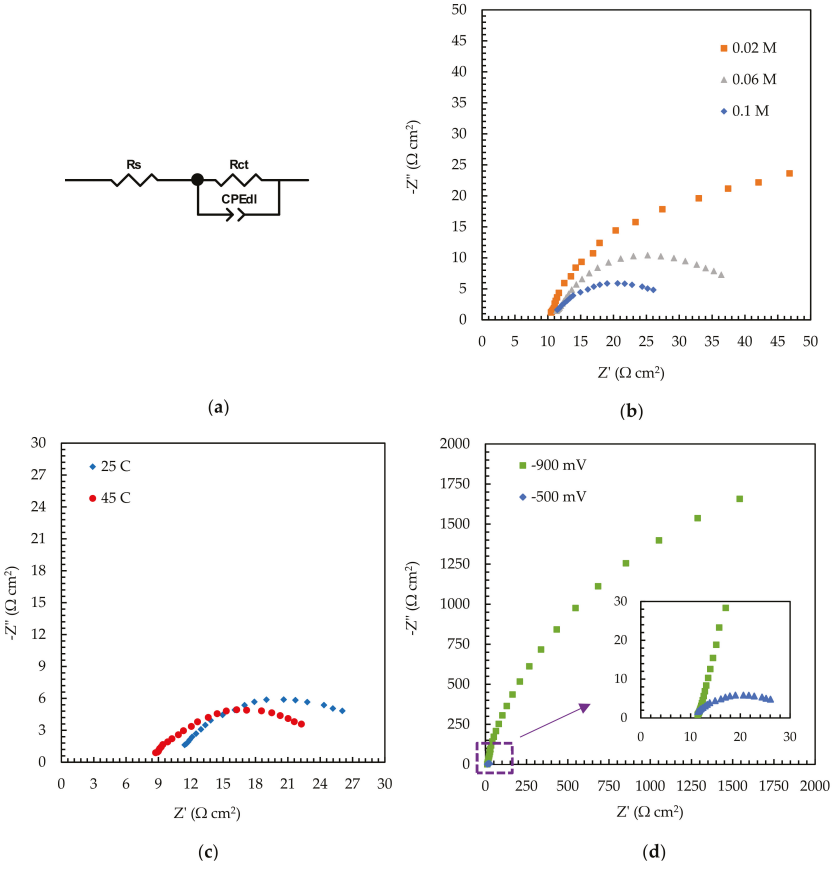

Figure 8. (**a**) The equivalent circuit utilized for fitting of the EIS information; the influence of (**b**) concentration of N_2H_4, (**c**) temperature, and (**d**) potential on the EIS spectra of Pd–Ni/N-rGO.

The EIS data obtained are fitted by an equivalent circuit depicted in Figure 8a. The elements of R_s, R_{ct}, and CPE_{dl} in the equivalent circuit depict electrolyte solution resistance, charge transfer resistance, and the constant phase element of the electrical double layer, respectively. The intersection of impedance spectra (Figure 8b–d) with the x-axis at high frequencies is the electrolyte solution resistance, and it corresponds to the ohmic resistance of the electrolyte between the anode and the reference electrode, the anode ohmic resistance, and the contact resistance. The high-frequency semicircle relates to the charge transfer of the HzOR that has taken place on the anode electrode. Table 2 summarizes the obtained charge transfer resistances of the Pd–Ni/NrGO catalyst towards HzOR.

Table 2. The values of R_{ct} for HzOR on the Pd–Ni/NrGO catalyst at different concentrations of hydrazine, temperatures, and voltages.

N_2H_4 Concentration (mol L^{-1})	Potential (V vs. MOE)	Temperature (°C)	R_{ct} (Ω cm^2)
0.02	−0.5	25	92.76
0.06	−0.5	25	31.27
0.1	−0.5	25	22.03
0.1	−0.5	45	17.12
0.1	−0.9	25	4422

In accordance with Figure 8b–d, a low circle diameter is observed for the synthesized catalyst, indicating a low R_{ct} value and thereby a fast charge transfer on the Pd–Ni/NrGO. By increasing the N_2H_4 concentration (Figure 8b), at T = 25 °C and a potential of −0.5 V, the R_{ct} values are reduced, which may be attributed to the increment reaction kinetics by raising the sorption of N_2H_4 on the electrode surface. A decrease in R_{ct} is seen in Figure 8c with increasing temperature at a potential of −0.5 V and N_2H_4 0.1 mol L^{-1}, and this suggests that the charge transfer rate is promoted at the electrode/electrolyte interface at high temperatures. As presented by the fitting results in Figure 8d, under T = 25 °C and N_2H_4 0.1 M, the R_{ct} is reduced from 44.22 to 22.03 with an enhancement of the polarization potential from −0.9 to −0.5 V. The reason for this observation could be the faradaic reactions that occurred at the potential of −0.5 V. No faradaic reaction occurs, however, at the potential of −0.9 V. All results obtained from EIS measurements are consistent with the CV results.

2.3. Single-Cell Tests

The performance of Pd–Ni/NrGO in a DHzHPFC using H_2SO_4 0.5 mol L^{-1}, with several oxidant concentrations, and NaOH 2.0 mol L^{-1}, with various fuel concentrations at three temperatures, was evaluated by monitoring the power density curves (I–P curves) and polarization curves (I–V curves). Figure 9 depicts the I–P and I–V curves of DHzHPFC assembled with Pd–Ni/NrGO (1.0 mg cm^{-2}) as an anode and Pt/C (0.5 mg cm^{-2}) as a cathode under several operating conditions. Taking the electrode reaction and the Nernst equation (Equation (15)) into account, the OCP is enhanced with the increment of H_2O_2 concentrations (Figure 9a). Thus, the maximum power density (MPD) is enhanced from 101.93 mW cm^{-2} to 120.50 and 152.74 mW cm^{-2} by increasing the concentration of H_2O_2 from 0.5 M to 1.0 and 2.0 mol L^{-1}, respectively. The MPD is reduced to 130.25 mW cm^{-2}, however, by a further increase in the H_2O_2 concentration to 3.0 mol L^{-1}. This may be due to the fast chemical decomposition of H_2O_2 and its crossover from the membrane and also the poisoning of the electrode surface by the attachment of gas bubbles produced from H_2O_2 decomposition [4,11,64] at a high H_2O_2 concentration (i.e., above 3.0 mol L^{-1}). H_2O_2 2.0 mol L^{-1} is thus chosen as the optimum concentration at which the cell performance reaches its maximum.

$$E = E^0 + \frac{RT}{nF} \ln \frac{[N_2H_4][H_2O_2]^2}{[N_2][H_2O]^4} \quad (15)$$

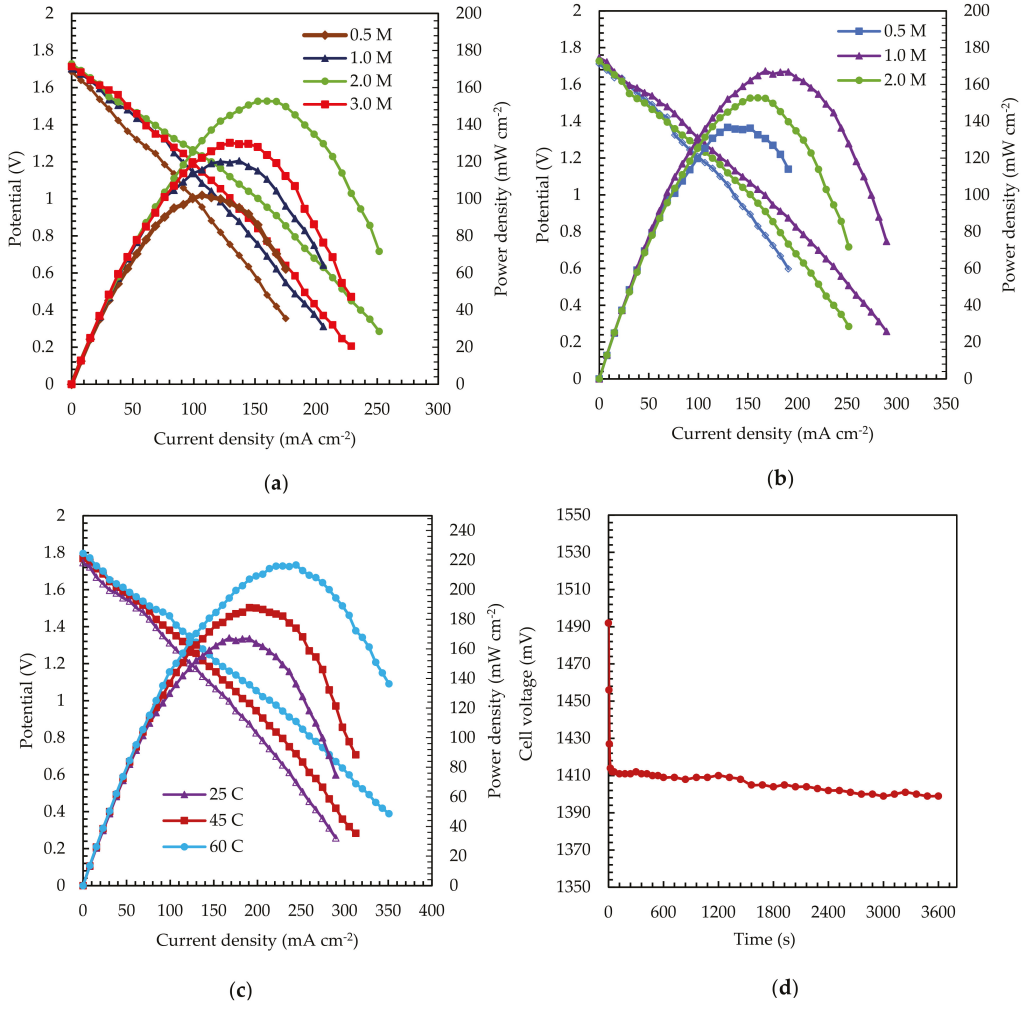

Figure 9. The effects of operation conditions on the performance of DHzHPFC designed with Pd–Ni/NrGO (1.0 mg cm^{-2}) as an anode and Pt/C (0.5 mg cm^{-2}) as a cathode: (**a**) H_2O_2 concentration, (**b**) N_2H_4 concentration, and (**c**) temperature; (**d**) stability test for Pd–Ni/NrGO at a discharging current of 90 mA cm^{-2}.

To optimize the concentration of N_2H_4, three concentrations of 0.5, 1.0, and 2.0 mol L^{-1} were tested and the results are presented in Figure 9b. It can be perceived that the MPDs increased from 136.72 to 167.38 mW cm^{-2} by incremental N_2H_4 concentrations from 0.5 mol L^{-1} to 1.0 mol L^{-1}. Additionally, the anode potential and cell OCP are enhanced with raising N_2H_4 concentrations, which may be explained based on the electrode reaction and Nernst equation. The fuel diffusion and the oxidation kinetics of N_2H_4 are promoted with an increased N_2H_4 concentration. However, the MPD is reduced to 152.74 mW cm^{-2}, at which the N_2H_4 concentration is 2.0 mol L^{-1} as a consequence of increasing hydrolysis of N_2H_4 and its crossover [4,65,66].

As presented in the electrochemical tests, the performance of the Pd–Ni/NrGO catalyst is very sensitive to temperature. In this context, the DHzHPFC performance at different temperatures was also examined and the obtained results are presented in Figure 9c. Varying the temperature from 25 to 45 and 60 °C, DHzHPFC presents an enhanced peak power

density from 167.38 to 187.87 and 216.71 mW cm^{-2}, respectively. The high values of OCV and MPD reveal that the kinetics of N_2H_4 oxidation and H_2O_2 reduction is promoted with an enhanced temperature [24]. The achieved MPDs for the Pd–Ni/NrGO electrocatalyst at various N_2H_4 concentrations, H_2O_2 concentrations, and temperatures are reported in Table 3. A comparison of DHzHPFC performances for different reported anode catalysts in the literature is provided in Table 4. As seen in this Table, the Pd–Ni/NrGO electrocatalyst exhibits an equal or greater catalytic performance, suggesting that Pd–Ni/NrGO is an excellent anode electrocatalyst in DHzHPFC applications.

Table 3. The MPDs value for DHzHPFC with the Pd–Ni/NrGO electrocatalyst as an anode at various experimental FC conditions.

FC Condition			MPD/(mW cm^{-2})
$[N_2H_4]$/(mol L^{-1})	$[H_2O_2]$/(mol L^{-1})	T/(°C)	
2.0	0.5	25	101.93
2.0	1.0	25	120.50
2.0	2.0	25	152.74
2.0	3.0	25	130.25
0.5	2.0	25	136.72
1.0	2.0	25	167.38
1.0	2.0	45	187.87
1.0	2.0	60	216.71

Table 4. The comparison of DHzHPFC performances under different experimental FC conditions.

Anode	Cathode	Membrane	Anolyte	Catholyte	Temperature (°C)	Maximum Power Density (mW cm^{-2})	Ref.
$Pt_{53}Cu_{47}$/C (0.5 mg cm^{-2})	Pt/C (20 wt.%) (1.0 mg cm^{-2})	Tokuyama	KOH 1.0 M + N_2H_4 1.0 M	O_2 flow rate: 30 SCCM	80	56.1	[67]
$Ni_{0.6}Co_{0.4}$ nanosheets (1.4 mg cm^{-2})	Pt/C (40.0 wt.%)	Nafion 115	KOH 4.0 M + N_2H_4 20.0 wt%	H_2O_2 20.0% + H_2SO_4 0.5 M	80	107.1	[68]
Pd/CNT (1.0 mg cm^{-2})	Pt/C (0.25 mg cm^{-2})	Nafion 117	NaOH 1.0 M + N_2H_4 2.0 M	O_2 flow rate: 150.0 mL min^{-1}	60	110	[69]
Co–Au/C (1.0 mg cm^{-2})	Au/C (1.0 mg cm^{-2})	Nafion 117	NaOH 2.0 M + N_2H_4 2.0 M	H_2O_2 2.0 M + H_2SO_4 0.5 M	60	122.8	[4]
MoC_x–NC (1.0 mg cm^{-2})	Pt/C (1.0 mg cm^{-2})	KOH-doped PBI	KOH 6.0 M + N_2H_4 0.5 M	O_2 Flux: 0.2 slpm	80	158.26	[70]
Ni–Pd/rGO (1.0 mg cm^{-2})	Pt/C (0.5 mg cm^{-2})	Nafion 117	NaOH 2.0 M + N_2H_4 1.0 M	H_2O_2 2.0 M + H_2SO_4 0.5 M	60	204.8	[13]
Pd–Ni/NrGO (1.0 mg cm^{-2})	Pt/C (0.5 mg cm^{-2})	Nafion 117	N_2H_4 1.0 M + NaOH 2.0 M	H_2O_2 2.0 M + H_2SO_4 0.5 M	25 60	187.87 216.71	This work

Stability is a vital parameter in the determination of DHzHPFC performance. In Figure 9d, stability tests were adopted for a single cell with the Pd–Ni/NrGO as an anode, Pt/C as a cathode, NaOH 2.0 mol L^{-1} + N_2H_4 1.0 mol L^{-1} as an anolyte, and H_2SO_4 0.5 mol L^{-1} + H_2O_2 2.0 mol L^{-1} as a catholyte at a constant current of 90 mA cm^{-2} and 25 °C. It can be noticed that after a potential decay in the first seconds, it maintained a relatively stable value during the test. The observed oscillation in the cell voltage may be related to the addition of new fuel solution, restarting the measurements, possible minor changes in cell temperature, the oxygen produced from H_2O_2 decomposition at the cathode, or the hydrogen produced from the hydrolysis of N_2H_4 at the anode. It is evident that the produced gas bubbles cumulate on the electrode and so block the transfer of N_2H_4 or H_2O_2 solution, leading to instant loss of cell performance. As a result, the Pd–Ni/NrGO anode assembled DHzHPFC presents a relatively stable performance.

3. Experimental

3.1. Materials

The purity of the materials used for the synthesis of Pd–Ni/NrGO is given in Table S1. In all the experiments, double-distilled deionized water (0.055 μS cm^{-1}) was used to prepare solutions and all materials were of analytical grade.

3.2. Methods

Production of a Pd–Ni/NrGO electrocatalyst. Firstly, the GO was synthesized using a modified Hummers method [71]. More details of GO preparation are provided in the Supplementary Information. NrGO was produced by the addition of 1.5 g urea to 200 mL GO suspension (2.5 mg mL^{-1} in H_2O) and stirred for 120 min. After the elimination of the solvent with a rotary evaporator, the resultant solid was conveyed into a tubular furnace and treated at 800 °C under an N_2 atmosphere for 45 min. The obtained powder was cooled to ambient temperature under constant N_2 flow and designated as NrGO. After that, appropriate amounts of $NiCl_2.6H_2O$ (35.0 mM) and $PdCl_2$ (32.0 mM) were put into 160.0 mL of NrGO suspension (0.5 mg mL^{-1} isopropanol and distilled water (*v*/*v*: 4/1)) under ultrasonication. The pH was adjusted to 10.0 by gradually adding 20.0 mL of NaOH solution containing 150.0 mg of $NaBH_4$ to the suspension at 90 °C. The mixture was then refluxed at 99 °C for 240 min. The Pd–Ni/NrGO precipitate was filtered using Whatman filter paper, rinsed with water, and then dried.

3.3. Physical and Electrochemical Characterization

FTIR (PerkinElmer, Waltham, MA, USA, (300–4300 cm^{-1})) was used to analyze the nature of chemical bonds in terms of functional groups of the GO and NrGO samples. SEM (MIRA3FEG-SEM, Tescan, Brno, Czech Republic) and TEM (PHILIPS, Amsterdam, The Netherland, CM 120) were utilized to determine the surface morphology of the Pd–Ni/NrGO catalyst, along with the characterization of elemental distribution on the surface of synthesized materials, using EDX. The crystallographic structure of the synthesized catalyst was investigated by XRD (PHILIPS, PW1730, Netherland).

All electrochemical tests were performed using a Gamry Potentiostat/Galvanostat/ZRA (Reference 600™, Warminster, PA, USA) in a three-electrode cell consisting of a platinized titanium rod as a counter electrode and Hg/HgO (MOE) electrode as a reference electrode. The working electrode was constructed by dropping a specific quantity of catalyst ink on a glassy carbon electrode (GCE, 0.196 cm^2). The catalyst ink was provided by dispersing synthesized powders (5.0 mg) into isopropanol: water solution (*v*/*v*: 2/1) containing Nafion solution under ultrasonication for 120 min.

The electrochemical behavior of the samples was studied by CV, CA, and EIS techniques. CV tests were performed in NaOH 1.0 mol L^{-1} and N_2H_4 × mol L^{-1} (x: 0–0.1 mol L^{-1}) at sweep rates of 20 to 100 mV s^{-1} and various temperatures (298.15–328.15) K. The CA tests were conducted in aqueous solutions of NaOH 1.0 mol L^{-1} + N_2H_4 0.1 mol L^{-1} at −0.5 V vs. MOE. All EIS tests were carried out in a frequency range of 10^5 to 10^{-1} Hz with an r.m.s amplitude of modulation potential of ±10 mV.

3.4. DHzHPFC Measurements

The MEA used for the DHzHPFCs performance test was produced using the CCM technique [72]. Before the compression process of the MEA, the Nafion®117 membrane surface was hydrothermally treated according to the procedure described in the literature [24]. The commercial Pt/C (0.5 mg_{metal} cm^{-2}), as a cathode ink, and Pd–Ni/NrGO (1.0 mg_{Pd} cm^{-2}), as an anode ink, were sprinkled directly on both sides of the treated membrane. The catalyst inks were supplied by ultrasonically mixing specific quantities of anodic catalyst, 2-propanol, H_2O, and Nafion solution for 30 min. The as-manufactured catalyst-coated Nafion membrane was hot-pressed at 100 °C for 1.0 min, followed by heating at 80 °C for 15 min. Subsequently, the membrane was immersed in 2.0 mol L^{-1} NaOH for 3 days. Finally, the catalyst-coated membrane was assembled, together with the

produced gas diffusion electrodes (GDE), and placed between two graphite blocks as flow plates (Scheme 1). An alkaline hydrazine solution was employed as the fuel on the anode side by using homemade pumps. On the cathode side, an acidic solution of H_2O_2 was used as the oxidizing agent. DHzHPFC performance experiments were carried out after cell activation and current density–potential (I–V) and current density–power density (I–P) curves were recorded at various cell conditions. The procedure used for the cell activation is explained in the supporting information.

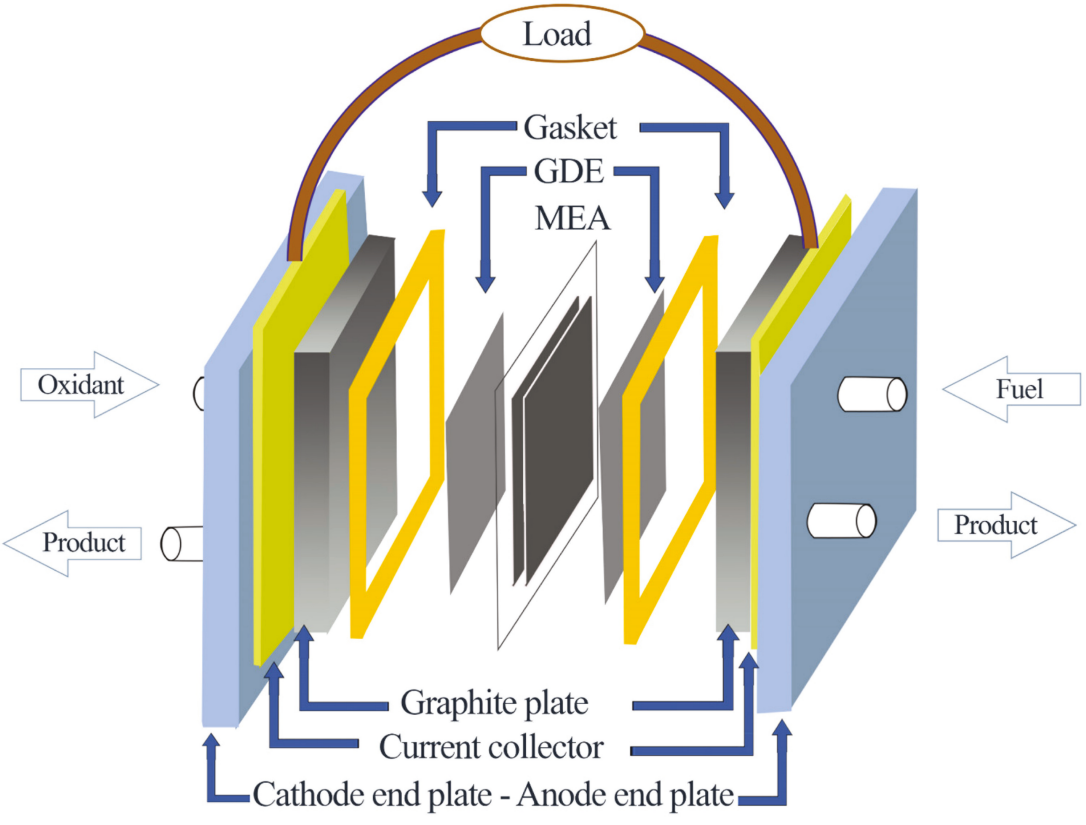

Scheme 1. The components of DHzHPFCs.

4. Conclusions

The Pd–Ni alloy nanoparticles were successfully deposited onto the NrGO support using the electrochemical reduction method. FTIR and XRD spectroscopic studies successfully demonstrated nitrogen doping in GO. SEM, EDX, and TEM images also confirmed uniform dispersion of Pd–Ni nanoparticles with a narrow crystalline size in the range of 11–13 nm. The electrochemical properties of the Pd–Ni/NrGO and Pd/NrGO catalysts were investigated by employing CV, CA, CP, and EIS techniques, and the results proved that Pd–Ni/NrGO has a higher catalytic activity and a longer lifetime in comparison with Pd/NrGO. The results also indicated that the Pd–Ni/NrGO has a higher ECSA (166.38 m2 g^{-1}) than that of Pd/NrGO (63.67 m2 g^{-1}). Furthermore, the Pd–Ni/NrGO showed a higher catalytic activity toward hydrazine electrooxidation compared with Pd/NrGO; thus, the hydrazine oxidation current density on the Pd–Ni/NrGO (12,360.50 A g^{-1}) was higher than that of Pd/NrGO (6821.22 A g^{-1}). The low activation energy for the electrooxidation of hydrazine

on the Pd–Ni/NrGO catalyst (10.72 kJ mol^{-1}) revealed that the electrooxidation of hydrazine occurs readily on this catalyst. The results of the DHzHPFC setup showed a high maximum power density in the range of 216.71 mW cm^{-2} under optimal conditions. In summary, this work has demonstrated that the unique Pd–Ni/NrGO catalyst has promise as a potential anode electrocatalyst for DHzHPFC applications.

Supplementary Materials: The following are available online at https://www.mdpi.com/article/10.3390/catal11111372/s1: Table S1: A summary of the purity of the used materials; Figure S1: The BSE image of the Pd–Ni/NrGO catalyst; Figure S2: The elemental mapping images of each element in Pd–Ni/N-rGO, and more details regarding synthesizing of GO.

Author Contributions: Conceptualization, M.G.H. and V.D.-E.; validation, M.G.H. and H.A.; formal analysis, V.D.-E.; investigation and writing—original draft preparation, V.D.-E.; writing—review and editing, M.G.H., V.D.-E., S.W. and V.H.; supervision, M.G.H. and V.H.; project administration, M.G.H. and V.H.; funding acquisition, M.G.H. and V.H. All authors have read and agreed to the published version of the manuscript.

Funding: This research was supported by the Office of the Vice Rector for Research of the University of Tabriz, and the Austrian Science Fund (FWF) under grant number I 3871-N37, and Open Access Funding by the Graz University of Technology.

Acknowledgments: The authors gratefully acknowledge financial support from the Office of the Vice-Rector for Research of the University of Tabriz, the Austrian Science Fund (FWF) under grant number I 3871-N37, and Open Access Funding by the Graz University of Technology.

Conflicts of Interest: There are no conflict to declare.

References

1. Andrew, M.R.; Gressler, W.J.; Johnson, J.K.; Short, R.T.; Williams, K.R. Engineering aspects of hydrazine-air fuel-cell power systems. *J. Appl. Electrochem.* **1972**, *2*, 327–336. [CrossRef]
2. Tamura, K.; Kahara, T. Exhaust Gas Compositions and Fuel Efficiencies of Hydrazine–Air Fuel Cells. *J. Electrochem. Soc.* **1976**, *123*, 776–780. [CrossRef]
3. Akbar, K.; Kim, J.H.; Lee, Z.; Kim, M.; Yi, Y.; Chun, S.-H. Superaerophobic graphene nano-hills for direct hydrazine fuel cells. *NPG Asia Mater.* **2017**, *9*, e378. [CrossRef]
4. Abdolmaleki, M.; Ahadzadeh, I.; Goudarziafshar, H. Direct hydrazine-hydrogen peroxide fuel cell using carbon supported Co@Au core-shell nanocatalyst. *Int. J. Hydrog. Energ.* **2017**, *42*, 15623–15631. [CrossRef]
5. Silva, T.L.; Cazetta, A.L.; Zhang, T.; Koh, K.; Silva, R.; Asefa, T.; Almeida, V.C. Nanoporous Heteroatom-Doped Carbons Derived from Cotton Waste: Efficient Hydrazine Oxidation Electrocatalysts. *ACS Appl. Energ. Mater.* **2019**, *2*, 2313–2323. [CrossRef]
6. Mohammad, A.; Ehtisham Khan, M.; Alarifi, I.M.; Cho, M.H.; Yoon, T. A sensitive electrochemical detection of hydrazine based on SnO_2/CeO_2 nanostructured oxide. *Microchem. J.* **2021**, *171*, 106784. [CrossRef]
7. Blomen, L.J.M.J.; Mugerwa, M.N. *Fuel Cell Systems*; Springer: Boston, MA, USA, 1993; ISBN 0-306-44158-6.
8. Amirfakhri, S.J.; Meunier, J.-L.; Berk, D. A comprehensive study of the kinetics of hydrogen peroxide reduction reaction by rotating disk electrode. *Electrochim. Acta* **2013**, *114*, 551–559. [CrossRef]
9. Zhang, X.-Y.; Shi, S.; Yin, H.-M. CuPd Alloy Oxide Nanobelts as Electrocatalyst towards Hydrazine Oxidation. *ChemElectroChem* **2019**, *6*, 1514–1519. [CrossRef]
10. Wei, J.; Wang, X.; Wang, Y.; Guo, J.; He, P.; Yang, S.; Li, N.; Pei, F.; Wang, Y. Carbon-Supported Au Hollow Nanospheres as Anode Catalysts for Direct Borohydride−Hydrogen Peroxide Fuel Cells. *Energ. Fuels* **2009**, *23*, 4037–4041. [CrossRef]
11. Cao, D.; Chen, D.; Lan, J.; Wang, G. An alkaline direct $NaBH_4$–H_2O_2 fuel cell with high power density. *J. Power Sources* **2009**, *190*, 346–350. [CrossRef]
12. Khilari, S.; Pradhan, D. MnFe2O4@nitrogen-doped reduced graphene oxide nanohybrid: An efficient bifunctional electrocatalyst for anodic hydrazine oxidation and cathodic oxygen reduction. *Catal. Sci. Technol.* **2017**, *7*, 5920–5931. [CrossRef]
13. Hosseini, M.G.; Mahmoodi, R.; Abdolmaleki, M. High performance direct hydrazine-hydrogen peroxide fuel cell using reduced graphene oxide supported Ni@M (M = Pt, Pd, Ru) nanoparticles as novel anodic electrocatalysts. *New J. Chem.* **2018**, *42*, 12222–12233. [CrossRef]
14. Sapner, V.S.; Chavan, P.P.; Munde, A.V.; Sayyad, U.S.; Sathe, B.R. Heteroatom (N, O, and S)-Based Biomolecule-Functionalized Graphene Oxide: A Bifunctional Electrocatalyst for Enhancing Hydrazine Oxidation and Oxygen Reduction Reactions. *Energ. Fuels* **2021**, *35*, 6823–6834. [CrossRef]
15. Zabielaitė, A.; Balčiūnaitė, A.; Šimkūnaitė, D.; Lichušina, S.; Stalnionienė, I.; Šimkūnaitė-Stanynienė, B.; Naruškevičius, L.; Tamašauskaitė-Tamašiūnaitė, L.; Norkus, E.; Selskis, A.; et al. High Performance Direct N_2H_4-H_2O_2 Fuel Cell Using Fiber-Shaped Co Decorated with Pt Crystallites as Anode Electrocatalysts. *J. Electrochem. Soc.* **2019**, *167*, 054502. [CrossRef]

16. Nagai, T.; Kojima, T.; Takeichi, N.; Asahi, M.; Yamazaki, S.-i.; Siroma, Z.; Fujiwara, N.; Ioroi, T. Performance of Perovskite-Type Oxides for Oxygen Reduction Reaction in Direct Hydrazine Fuel Cell. *J. Electrochem. Soc.* **2020**, *167*, 164506. [CrossRef]
17. Milikić, J.; Oliveira, R.C.P.; Tapia, A.; Santos, D.M.F.; Zdolšek, N.; Trtić-Petrović, T.; Vraneš, M.; Šljukić, B. Ionic Liquid-Derived Carbon-Supported Metal Electrocatalysts as Anodes in Direct Borohydride-Peroxide Fuel Cells. *Catalysts* **2021**, *11*, 632. [CrossRef]
18. Bortoloti, F.; Angelo, A.C.D. Ordered PtSn/C Electrocatalyst: A High Performance Material for the Borohydride Electrooxidation Reaction. *Catalysts* **2017**, *7*, 198. [CrossRef]
19. Yin, W.X.; Li, Z.P.; Zhu, J.K.; Qin, H.Y. Effects of NaOH addition on performance of the direct hydrazine fuel cell. *J. Power Sources* **2008**, *182*, 520–523. [CrossRef]
20. Lao, S.J.; Qin, H.Y.; Ye, L.Q.; Liu, B.H.; Li, Z.P. A development of direct hydrazine/hydrogen peroxide fuel cell. *J. Power Sources* **2010**, *195*, 4135–4138. [CrossRef]
21. Yan, X.; Meng, F.; Xie, Y.; Liu, J.; Ding, Y. Direct N2H4/H2O2 Fuel Cells Powered by Nanoporous Gold Leaves. *Sci. Rep.* **2012**, *2*, 941. [CrossRef]
22. Huang, R.; Wen, Y.-H.; Shao, G.-F.; Sun, S.-G. Insight into the Melting Behavior of Au–Pt Core–Shell Nanoparticles from Atomistic Simulations. *J. Phys. Chem. C* **2013**, *117*, 4278–4286. [CrossRef]
23. Gholinejad, M.; Khosravi, F.; Afrasi, M.; Sansano, J.M.; Nájera, C. Applications of bimetallic PdCu catalysts. *Catal. Sci. Technol.* **2021**, *11*, 2652–2702. [CrossRef]
24. Ma, J.; Sahai, Y.; Buchheit, R.G. Direct borohydride fuel cell using Ni-based composite anodes. *J. Power Sources* **2010**, *195*, 4709–4713. [CrossRef]
25. Hosseini, M.G.; Mahmoodi, R. Ni@M (M = Pt, Pd and Ru) core@shell nanoparticles on a Vulcan XC-72R support with superior catalytic activity toward borohydride oxidation: Electrochemical and fuel cell studies. *New J. Chem.* **2017**, *41*, 13408–13417. [CrossRef]
26. Smith, A.T.; LaChance, A.M.; Zeng, S.; Liu, B.; Sun, L. Synthesis, properties, and applications of graphene oxide/reduced graphene oxide and their nanocomposites. *Nano Mater. Sci.* **2019**, *1*, 31–47. [CrossRef]
27. Chen, Y.; Tian, Y.; Qiu, Y.; Liu, Z.; He, H.; Li, B.; Cao, H. Synthesis and superior cathode performance of sandwiched LiMn2O4@rGO nanocomposites for lithium-ion batteries. *Mater. Today Adv.* **2019**, *1*, 100001. [CrossRef]
28. Lei, Y.; Lu, J.; Luo, X.; Wu, T.; Du, P.; Zhang, X.; Ren, Y.; Wen, J.; Miller, D.J.; Miller, J.T.; et al. Synthesis of porous carbon supported palladium nanoparticle catalysts by atomic layer deposition: Application for rechargeable lithium-O2 battery. *Nano Lett.* **2013**, *13*, 4182–4189. [CrossRef]
29. Taqi-uddeen Safian, M.; Umar, K.; Mohamad Ibrahim, M.N. Synthesis and scalability of graphene and its derivatives: A journey towards sustainable and commercial material. *J. Clean. Prod.* **2021**, *318*, 128603. [CrossRef]
30. Yaqoob, A.A.; Mohamad Ibrahim, M.N.; Umar, K.; Bhawani, S.A.; Khan, A.; Asiri, A.M.; Rizwan Khan, M.; Azam, M.; Al Ammari, A.M. Cellulose Derived Graphene/Polyaniline Nanocomposite Anode for Energy Generation and Bioremediation of Toxic Metals via Benthic Microbial Fuel Cells. *Polymers* **2021**, *13*, 135. [CrossRef]
31. Lu, Z.-J.; Bao, S.-J.; Gou, Y.-T.; Cai, C.-J.; Ji, C.-C.; Xu, M.-W.; Song, J.; Wang, R. Nitrogen-doped reduced-graphene oxide as an efficient metal-free electrocatalyst for oxygen reduction in fuel cells. *RSC Adv.* **2013**, *3*, 3990–3995. [CrossRef]
32. Ren, J.; Zhang, J.; Yang, C.; Yang, Y.; Zhang, Y.; Yang, F.; Ma, R.; Yang, L.; He, H.; Huang, H. Pd nanocrystals anchored on 3D hybrid architectures constructed from nitrogen-doped graphene and low-defect carbon nanotube as high-performance multifunctional electrocatalysts for formic acid and methanol oxidation. *Mater. Today Energ.* **2020**, *16*, 100409. [CrossRef]
33. Yang, H.; Ko, Y.; Lee, W.; Züttel, A.; Kim, W. Nitrogen-doped carbon black supported Pt–M (M = Pd, Fe, Ni) alloy catalysts for oxygen reduction reaction in proton exchange membrane fuel cell. *Mater. Today Energ.* **2019**, *13*, 374–381. [CrossRef]
34. Guo, R.; An, N.; An, S.; Zhang, J.; Chou, K.; Guan, L.; Tian, X. One-Step Preparation of Nitrogen-Doped Platinum-Based Catalysts for Electrocatalytic Oxidation of Ethanol. *Catalysts* **2021**, *11*, 1264. [CrossRef]
35. Wu, G.; Santandreu, A.; Kellogg, W.; Gupta, S.; Ogoke, O.; Zhang, H.; Wang, H.-L.; Dai, L. Carbon nanocomposite catalysts for oxygen reduction and evolution reactions: From nitrogen doping to transition-metal addition. *Nano Energ.* **2016**, *29*, 83–110. [CrossRef]
36. Zhou, Y.; Neyerlin, K.; Olson, T.S.; Pylypenko, S.; Bult, J.; Dinh, H.N.; Gennett, T.; Shao, Z.; O'Hayre, R. Enhancement of Pt and Pt-alloy fuel cell catalyst activity and durability via nitrogen-modified carbon supports. *Energ. Environ. Sci.* **2010**, *3*, 1437–1446. [CrossRef]
37. Schauermann, S.; Nilius, N.; Shaikhutdinov, S.; Freund, H.-J. Nanoparticles for Heterogeneous Catalysis: New Mechanistic Insights. *Acc. Chem. Res.* **2013**, *46*, 1673–1681. [CrossRef]
38. Wilde, M.; Fukutani, K.; Naschitzki, M.; Freund, H.J. Hydrogen absorption in oxide-supported palladium nanocrystals. *Phys. Rev. B* **2008**, *77*, 113412. [CrossRef]
39. Hosseini, M.G.; Daneshvari-Esfahlan, V.; Wolf, S.; Hacker, V. Novel Bimetallic Pd–X (X = Ni, Co) Nanoparticles Assembled on N-Doped Reduced Graphene Oxide as an Anode Catalyst for Highly Efficient Direct Sodium Borohydride–Hydrogen Peroxide Fuel Cells. *ACS Appl. Energ. Mater.* **2021**, *4*, 6025–6039. [CrossRef]
40. Kumar, N.A.; Choi, H.-J.; Shin, Y.R.; Chang, D.W.; Dai, L.; Baek, J.-B. Polyaniline-Grafted Reduced Graphene Oxide for Efficient Electrochemical Supercapacitors. *ACS Nano* **2012**, *6*, 1715–1723. [CrossRef]

41. Xue, Y.; Liu, J.; Chen, H.; Wang, R.; Li, D.; Qu, J.; Dai, L. Nitrogen-Doped Graphene Foams as Metal-Free Counter Electrodes in High-Performance Dye-Sensitized Solar Cells. *Angew. Chem. Int. Ed.* **2012**, *51*, 12124–12127. [CrossRef]
42. Mu, X.; Yuan, B.; Feng, X.; Qiu, S.; Song, L.; Hu, Y. The effect of doped heteroatoms (nitrogen, boron, phosphorus) on inhibition thermal oxidation of reduced graphene oxide. *RSC Adv.* **2016**, *6*, 105021–105029. [CrossRef]
43. Kumar, M.P.; Raju, M.M.; Arunchander, A.; Selvaraj, S.; Kalita, G.; Narayanan, T.N.; Sahu, A.K.; Pattanayak, D.K. Nitrogen Doped Graphene as Metal Free Electrocatalyst for Efficient Oxygen Reduction Reaction in Alkaline Media and Its Application in Anion Exchange Membrane Fuel Cells. *J. Electrochem. Soc.* **2016**, *163*, F848–F855. [CrossRef]
44. Soo, L.T.; Loh, K.S.; Mohamad, A.B.; Daud, W.R.W.; Wong, W.Y. Effect of nitrogen precursors on the electrochemical performance of nitrogen-doped reduced graphene oxide towards oxygen reduction reaction. *J. Alloy. Compd.* **2016**, *677*, 112–120. [CrossRef]
45. Fuge, G.M.; Rennick, C.J.; Pearce, S.R.J.; May, P.W.; Ashfold, M.N.R. Structural characterisation of CNx thin films deposited by pulsed laser ablation. *Diam. Relat. Mater.* **2003**, *12*, 1049–1054. [CrossRef]
46. Jang, J.W.; Lee, C.E.; Lyu, S.C.; Lee, T.J.; Lee, C.J. Structural study of nitrogen-doping effects in bamboo-shaped multiwalled carbon nanotubes. *Appl. Phys. Lett.* **2004**, *84*, 2877–2879. [CrossRef]
47. Gopalsamy, K.; Balamurugan, J.; Thanh, T.D.; Kim, N.H.; Hui, D.; Lee, J.H. Surfactant-free synthesis of NiPd nanoalloy/graphene bifunctional nanocomposite for fuel cell. *Compos. Part B Eng.* **2017**, *114*, 319–327. [CrossRef]
48. Zhang, J.-W.; Zhang, B.; Zhang, X. Enhanced catalytic activity of ternary NiCoPd nanocatalyst dispersed on carbon nanotubes toward methanol oxidation reaction in alkaline media. *J. Solid State Electrochem.* **2017**, *21*, 447–453. [CrossRef]
49. Wang, J.; Bao, J.; Zhou, Y.; Zhang, Y.; Sun, B.; Wang, M.; Sheng, X.; Liu, W.; Luo, C.; Xue, Y.; et al. Dopamine-assisted synthesis of rGO@NiPd@NC sandwich structure for highly efficient hydrogen evolution reaction. *J. Solid State Electrochem.* **2020**, *24*, 137–144. [CrossRef]
50. Shviro, M.; Polani, S.; Dunin-Borkowski, R.E.; Zitoun, D. Bifunctional Electrocatalysis on Pd-Ni Core-Shell Nanoparticles for Hydrogen Oxidation Reaction in Alkaline Medium. *Adv. Mater. Interfaces* **2018**, *5*, 1701666. [CrossRef]
51. Mageed, A.K.; Radiah, D.; Salmiaton, A.; Izhar, S.; Razak, M.A.; Yusoff, H.M.; Yasin, F.; Kamarudin, S. Preparation and Characterization of Nitrogen Doped Reduced Graphene Oxide Sheet. *Int. J. Appl. Chem.* **2016**, *12*, 104–108.
52. Liu, S.; Huang, S. Theoretical insights into the activation of O2 by Pt single atom and Pt4 nanocluster on functionalized graphene support: Critical role of Pt positive polarized charges. *Carbon* **2017**, *115*, 11–17. [CrossRef]
53. Esrafili, M.D.; Asadollahi, S. Exploring different reaction mechanisms for oxidation of CO over a single Pd atom incorporated nitrogen-doped graphene: A DFT study. *Appl. Surf. Sci.* **2019**, *463*, 526–534. [CrossRef]
54. Trafela, S.; Zavasnik, J.; Sturm, S.; Rozman, K.Z. Formation of a $Ni(OH)_2$/NiOOH active redox couple on nickel nanowires for formaldehyde detection in alkaline media. *Electrochim. Acta* **2019**, *309*, 346–353. [CrossRef]
55. Medway, S.L.; Lucas, C.A.; Kowal, A.; Nichols, R.J.; Johnson, D. In situ studies of the oxidation of nickel electrodes in alkaline solution. *J. Electroanal. Chem.* **2006**, *587*, 172–181. [CrossRef]
56. El-Shafei, A.A. Electrocatalytic oxidation of methanol at a nickel hydroxide/glassy carbon modified electrode in alkaline medium. *J. Electroanal. Chem.* **1999**, *471*, 89–95. [CrossRef]
57. Dong, H.; Feng, R.; Ai, X.; Cao, Y.; Yang, H.; Cha, C. Electrooxidation Mechanisms and Discharge Characteristics of Borohydride on Different Catalytic Metal Surfaces. *J. Phys. Chem. B* **2005**, *109*, 10896–10901. [CrossRef]
58. Santos, D.M.F.; Sequeira, C.A.C. Cyclic voltammetry investigation of borohydride oxidation at a gold electrode. *Electrochim. Acta* **2010**, *55*, 6775–6781. [CrossRef]
59. Bard, A.J.; Faulkner, R.L. *Electrochemical Methods: Fundamentals and Applications*; Wiley: New York, NY, USA, 1980.
60. Denuault, G.; Mirkin, M.V.; Bard, A.J. Direct determination of diffusion coefficients by chronoamperometry at microdisk electrodes. *J. Electroanal. Chem. Interfacial Electrochem.* **1991**, *308*, 27–38. [CrossRef]
61. Ding, W.; Wu, M.; Liang, M.; Ni, H.; Li, Y. Sensitive Hydrazine Electrochemical Biosensor Based on a Porous Chitosan–Carbon Nanofiber Nanocomposite Modified Electrode. *Anal. Lett.* **2015**, *48*, 1551–1569. [CrossRef]
62. Vats, T.; Dutt, S.; Kumar, R.; Siril, P.F. Facile synthesis of pristine graphene-palladium nanocomposites with extraordinary catalytic activities using swollen liquid crystals. *Sci. Rep.* **2016**, *6*, 33053. [CrossRef]
63. Hosseini, M.G.; Momeni, M.M.; Faraji, M. Highly Active Nickel Nanoparticles Supported on TiO_2 Nanotube Electrodes for Methanol Electrooxidation. *Electroanalysis* **2010**, *22*, 2620–2625. [CrossRef]
64. Wu, H.J.; Wang, C.; Liu, Z.X.; Mao, Z.Q. Influence of operation conditions on direct $NaBH_4/H_2O_2$ fuel cell performance. *Int. J. Hydrog. Energ.* **2010**, *35*, 2648–2651. [CrossRef]
65. Liu, B.H.; Li, Z.P.; Arai, K.; Suda, S. Performance improvement of a micro borohydride fuel cell operating at ambient conditions. *Electrochim. Acta* **2005**, *50*, 3719–3725. [CrossRef]
66. Duteanu, N.; Vlachogiannopoulos, G.; Shivhare, M.R.; Yu, E.H.; Scott, K. A parametric study of a platinum ruthenium anode in a direct borohydride fuel cell. *J. Appl. Electrochem.* **2007**, *37*, 1085–1091. [CrossRef]
67. Crisafulli, R.; De Barros, V.V.S.; Rodrigues De Oliveira, F.E.; De Araújo Rocha, T.; Zignani, S.; Spadaro, L.; Palella, A.; Dias, J.A.; Linares, J.J. On the promotional effect of Cu on Pt for hydrazine electrooxidation in alkaline medium. *Appl. Catal. B Environ.* **2018**, *236*, 36–44. [CrossRef]

68. Feng, G.; Kuang, Y.; Li, P.; Han, N.; Sun, M.; Zhang, G.; Sun, X. Single Crystalline Ultrathin Nickel–Cobalt Alloy Nanosheets Array for Direct Hydrazine Fuel Cells. *Adv. Sci.* **2017**, *4*, 1600179. [CrossRef]
69. Paganin, V.A.; Ticianelli, E.A.; Gonzalez, E.R. Development and electrochemical studies of gas diffusion electrodes for polymer electrolyte fuel cells. *J. Appl. Electrochem.* **1996**, *26*, 297–304. [CrossRef]
70. Deng, J.; Li, X.; Imhanria, S.; Chen, K.; Deng, X.; Wang, W. Molybdenum carbide-nitrogen doped carbon composites as effective non-precious electrocatalyst for direct hydrazine fuel cell. *Electrochim. Acta* **2021**, *384*, 138417. [CrossRef]
71. Hummers, W.S.; Offeman, R.E. Preparation of Graphitic Oxide. *J. Am. Chem. Soc.* **1958**, *80*, 1339. [CrossRef]
72. Prasanna, M.; Cho, E.A.; Lim, T.H.; Oh, I.H. Effects of MEA fabrication method on durability of polymer electrolyte membrane fuel cells. *Electrochim. Acta* **2008**, *53*, 5434–5441. [CrossRef]

catalysts

MDPI

Article

N, S, P-Codoped Graphene-Supported Ag-$MnFe_2O_4$ Heterojunction Nanoparticles as Bifunctional Oxygen Electrocatalyst with High Efficiency

Hongzhou Dong [1], Yingjie Chen [1,*], Chong Gong [1], Lina Sui [1], Qiong Sun [1], Kangle Lv [2,*] and Lifeng Dong [1,3,*]

[1] College of Materials Science and Engineering, Qingdao University of Science and Technology, Qingdao 266042, China; dhz1001@qust.edu.cn (H.D.); gcshd97427@126.com (C.G.); linasui@qust.edu.cn (L.S.); sunqiong@qust.edu.cn (Q.S.)
[2] College of Resources and Environmental Science, South-Central University for Nationalities, Wuhan 430074, China
[3] Department of Physics, Hamline University, St. Paul, MN 55104, USA
* Correspondence: chenyingjie@qust.edu.cn (Y.C.); lvkangle@mail.scuec.edu.cn (K.L.); dongLifeng@qust.edu.cn (L.D.)

Abstract: Due to slow kinetics of oxygen reduction reaction (ORR) and oxygen evolution reaction (OER) during discharging and charging processes, it is essential to rationally design and synthesize non-precious metal bifunctional electrocatalysts with good performance for metal-air batteries. Herein, Ag-$MnFe_2O_4$ heterojunction nanoparticles supported on N, S, P-codoped graphene (NSPG) are developed with enhanced ORR and OER bifunctional electrocatalytic activities and stability. In contrast, S, P-doped graphene (SPG) and N, P-doped graphene (NPG) show less stabilization for the heterojunction particles. For example, under alkaline conditions, the ORR half-wave potential of Ag-$MnFe_2O_4$/NSPG can reach 0.831 V, and the over potential for OER is 0.56 V at the current density 10 $mA \cdot cm^{-2}$. Furthermore, Ag-$MnFe_2O_4$/NSPG shows better methanol resistance and durability than Pt/C catalysts.

Keywords: bifunctional; graphene; electrocatalyst; $MnFe_2O_4$

Citation: Dong, H.; Chen, Y.; Gong, C.; Sui, L.; Sun, Q.; Lv, K.; Dong, L. N, S, P-Codoped Graphene-Supported Ag-$MnFe_2O_4$ Heterojunction Nanoparticles as Bifunctional Oxygen Electrocatalyst with High Efficiency. *Catalysts* **2021**, *11*, 1550. https://doi.org/10.3390/catal11121550

Academic Editors: Marc Cretin, Sophie Tingry and Zhenghua Tang

Received: 24 November 2021
Accepted: 10 December 2021
Published: 19 December 2021

1. Introduction

Design and synthesis of efficient bifunctional oxygen electrocatalysts are of critical importance but challenging for large-scale implementations of Zn-air batteries [1]. Recently, silver and metal oxides were reported as potential alternative candidates for Pt-based catalysts [2,3]. After loading onto carbon supports, these relatively inexpensive candidates can promote both oxygen reduction reaction (ORR) and oxygen evolution reaction (OER). The combination of silver and metal oxide nanocrystals can improve their electrical conductivity and bifunctional activity due to direct or indirect coupling and electron transfer between them. For example, the combination of Mn-oxides with Fe, N-codoped carbon can scavenge hydrogen peroxide for ORR [4]. Different methods have been established to synthesize N-doped carbon materials from CO_2 [5] and biomass materials [6]. An increased surface nitrogen content was identified as one of the reasons for excellent activity [7]. However, the volume-specific activity and electronic conductivity of these candidates still need to be improved.

Graphene (G) has been explored as non-metal catalyst and support for electrochemical reactions. Pristine graphene has no catalytic activity [8], but chemical doping of heteroatoms into graphene lattices could transfer nearby carbon atoms into "active sites". Additionally, defects including single C atom vacancy, Stone-Wales defects, and grain boundaries can modify electronic structures [9]. For example, sole-doped carbons, dual-doped carbons (N/S [10,11], N/B [12], and N/P [13,14]), and triple-doped carbon materials (N/P/S [15]) demonstrated improved electrochemical properties. The introduction of N

and/or S atoms could increase spin polarization and charge density of adjacent carbon atoms to enhance electrocatalytic activities [16,17]. P-doped graphene could provide active sites to facilitate the formation and dissociation of OOH, the rate-limiting step of ORR [18]. Furthermore, duel-doped and tri-doped graphene demonstrates even better performances as an electrocatalyst than single-doped graphene due to synergetic effects among different heteroatoms [9,19]. However, catalytic activities of doped graphene are still not comparable to Pt/C.

In addition, these dopped graphene can also be utilized to support and stabilize metal-containing catalysts. According to the hard-soft-acid-base theory, the binding ability of hard base decreases along with its reducing electro-negativity [20]. Generally, silver is a soft acid [21], while sulfur is a soft base. The affinity interaction between silver and sulfur helps stabilize the heterostructure of catalysts. Similarly, the affinity interaction between iron and nitrogen in carbon materials improves the performance of oxygen electrocatalysts [22,23]. There are various bifunctional catalysts, including Co_3O_4 @ graphene [24], Co_3O_4/N-doped graphene [25], and $CoFe_2O_4$/graphene aerogel [26]. Graphene supports are believed to promote electron transfer and facilitate mass transport of reactants to electrocatalysts. It is possible to boost the performances of metal heterojunction particle electrocatalysts by the supporting of multi-doped graphene.

Herein, S, P-co-doped graphene (SPG), N, P-co-doped graphene (NPG), and N, S, P-multi-doped graphene (NSPG) are synthesized and utilized as supports for Ag-$MnFe_2O_4$ heterojunction nanoparticles. Compared with SPG and NPG, NSPG shows better stabilization for the heterojunction structure. As a result, Ag-$MnFe_2O_4$/NSPG demonstrates better electrocatalytic performance and higher catalytic activity for ORR and OER.

2. Results and Discussion

XRD analyses were conducted to identify crystallographic structures of carbon-based materials and transition metal oxide NPs. As shown in Figure 1a, there is a typical diffraction peak around 26°, corresponding to the (002) plane of graphene. It indicates that various oxygen-containing functional groups on graphene oxide disappear to form graphene after calcination [27], and NPG, SPG, and NSPG have good structures. The XRD patterns of Ag-$MnFe_2O_4$/NPG, Ag-$MnFe_2O_4$/SPG, and Ag-$MnFe_2O_4$/NSPG (Figure 1b) display diffraction features of Ag (JCPDS 65-2871) and $MnFe_2O_4$ (JCPDS 10-0319). The peaks at 38.1°, 44.3°, and 64.5° correspond to the (111), (200) and (220) planes of Ag, respectively [28].

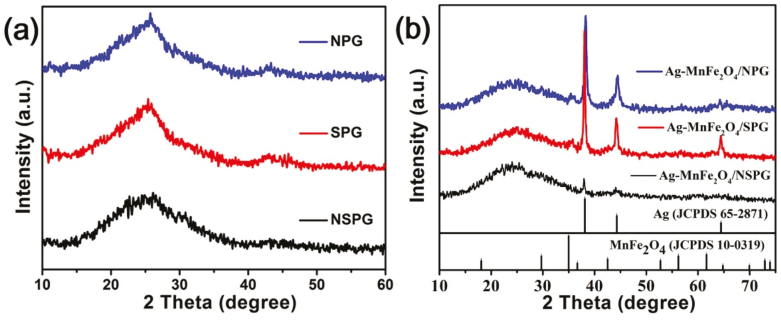

Figure 1. (**a**) XRD patterns of NPG, SPG and NSPG. (**b**) XRD patterns of Ag-$MnFe_2O_4$/NPG, Ag-$MnFe_2O_4$/SPG and Ag-$MnFe_2O_4$/NSPG.

Raman spectra of Ag-$MnFe_2O_4$/NPG, Ag-$MnFe_2O_4$/SPG, and Ag-$MnFe_2O_4$/NSPG are shown in Figure 2. The D bands around 1350 cm^{-1} are associated with the sp^3 defect sites, while the G bands near 1600 cm^{-1} represent the bond stretching of sp^2-bonded pairs [10]. The I_D/I_G ratios for Ag-$MnFe_2O_4$/NPG, Ag-$MnFe_2O_4$/SPG, and Ag-

$MnFe_2O_4$/NSPG are 0.99, 0.99, 1.01, respectively. It indicates similar defect features for NPG, SPG, and NSPG.

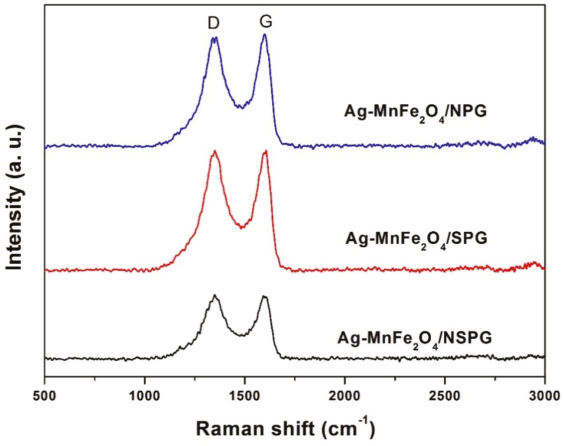

Figure 2. Raman spectra of Ag-$MnFe_2O_4$/NPG, Ag-$MnFe_2O_4$/SPG, and Ag-$MnFe_2O_4$/NSPG.

The elemental mapping images of NSPG exhibit the stacking of curved graphene layers (Figure 3) and C (red), N (green), P (bright yellow), O (orange), and S (blue) elements are uniformly distributed on the NSPG surface. Thus, N, S, and P elements are successfully doped into graphene.

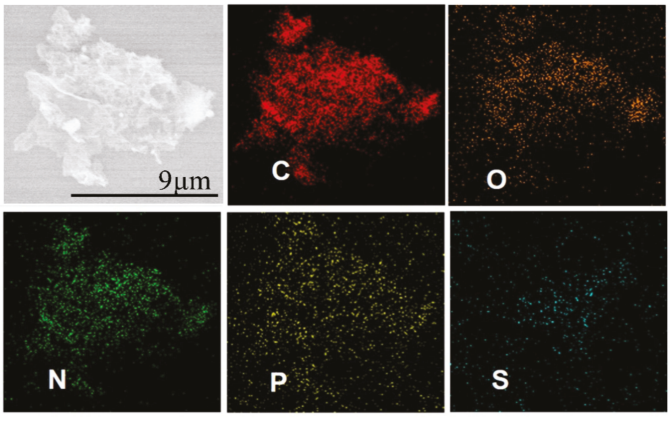

Figure 3. EDS elemental mapping images of NSPG.

TEM images in Figure 4 exhibit that heterogeneous nanoparticles are uniformly dispersed on the doped graphene sheets, which can facilitate electron transport during catalytic processes and more exposure of active sites, thereby enhancing catalytic performances of the catalyst. There is no obvious aggregation of Ag-$MnFe_2O_4$ nanoparticles on the supports, indicating successful loading of nanoparticles on doped graphene. Interestingly, the size of Ag nanocomposites on different supports showed small differences. The average size of Ag nanocrystals in Ag-$MnFe_2O_4$/NSPG is near 8 nm, while those for Ag-$MnFe_2O_4$/NPG and Ag-$MnFe_2O_4$/SPG are near 11 nm. It is proved that various doping elements have different effects on metal particles.

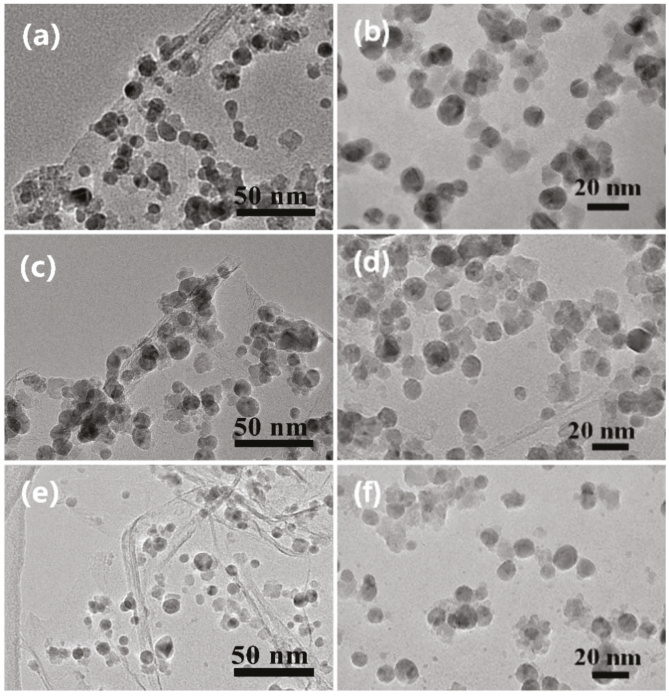

Figure 4. TEM images for (**a**,**b**) Ag-$MnFe_2O_4$/NPG, (**c**,**d**) Ag-$MnFe_2O_4$/SPG, and (**e**,**f**) Ag-$MnFe_2O_4$/NSPG.

XPS survey spectra in Figure 5a show the presence of doping elements and loading nanoparticles. As given in Figure 5b,c the bonds of N 1s (Pyridinic N: 398.32 eV) and S 2p (S $2P_{1/2}$: 165.23 eV) of Ag-$MnFe_2O_4$/NSPG have slightly negative shift than N 1s (Pyridinic N: 398.58 eV) of Ag-$MnFe_2O_4$/NPG and S 2p (S $2P_{1/2}$: 165.31 eV) of Ag-$MnFe_2O_4$/SPG, and the sharpness of the peak shape slightly decreases. From Table 1, the contents of N 1s and S 2p in Ag-$MnFe_2O_4$/NSPG are lower than N 1s in Ag-$MnFe_2O_4$/NPG and S 2p in Ag-$MnFe_2O_4$/SPG, respectively. Doping elements and metal nanoparticles can provide defect locations, and electron transfer between them can offer large number of ORR catalytically active sites to easily adsorb oxygen and greatly improve catalytic activity [29]. In addition, the combination of N and Fe and the effect of doping P on C and N have been shown to improve the ORR activity. Therefore, Ag-$MnFe_2O_4$/NSPG can have higher catalytic activities than other samples.

Table 1. Elemental contents determined by XPS.

Samples	Content (at. %)						
	N 1s	**S 2p**	**P 2p**	**C 1s**	**Ag 3d**	**Mn 2p**	**Fe 2p**
Ag-$MnFe_2O_4$/NPG	2.65	/	0.89	91.38	1.59	1.25	2.24
Ag-$MnFe_2O_4$/SPG	/	2.55	0.86	91.85	1.53	1.28	1.93
Ag-$MnFe_2O_4$/NSPG	1.65	1.72	0.93	90.92	1.48	1.22	2.08

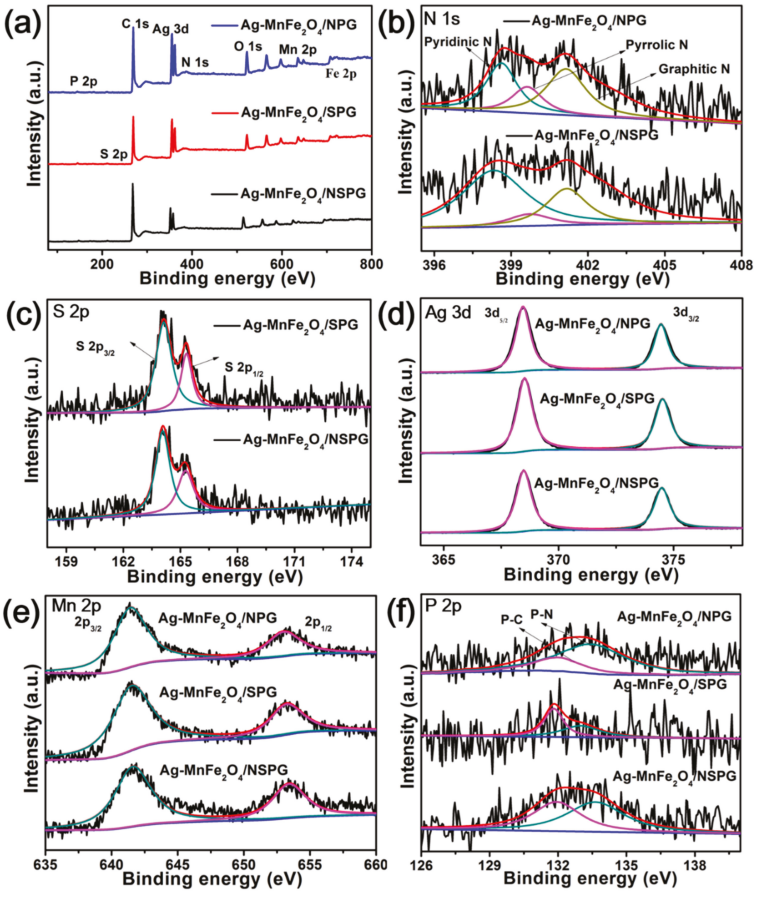

Figure 5. (**a**) XPS survey spectra and corresponding high-resolution spectra of (**b**) N 1s, (**c**) S 2p, (**d**) Ag 3d, (**e**) Mn 2p, and (**f**) P 2p.

For the determination of the bulk content of Ag, Mn, and Fe in the synthesized catalysts, ICP-OES was used. Elemental concentrations are given in Table 2. The atom ratios of Ag: Mn: Fe were, respectively, 1:1.01:1.83, 1:1.11:1.79, and 1:1.09:1.79 in Ag-$MnFe_2O_4$/NPG, Ag-$MnFe_2O_4$/SPG, and Ag-$MnFe_2O_4$/NSPG, and the loading contents of Ag-$MnFe_2O_4$ were 22.02 wt.%, 21.61 wt.%, 22.13 wt.%, respectively.

Table 2. Concentrations of Ag, Mn, and Fe determined by ICP-OES.

	Elemental Concentration (ppm)		
	Ag	**Mn**	**Fe**
Ag-$MnFe_2O_4$/NPG	183.5	94.3	173.6
Ag-$MnFe_2O_4$/SPG	177.9	100.4	164.8
Ag-$MnFe_2O_4$/NSPG	182.8	101.6	169.4

To evaluate ORR catalytic performances of obtained composites, cyclic voltammetry (CV), and linear sweep voltammetry (LSV) measurements were performed in O_2- or N_2-saturated 0.1 M KOH solution using a rotating disk electrode (RDE). Some important data of ORR catalytic performances are shown in Table 3. Figure 6a shows CVs of the three

samples to explore their ORR catalytic activities. There are obvious reduction peaks appear for catalysts in O_2-saturated electrolyte. The reduction peaks between 0.80 V and 1.10 V correspond to the reduction of AgO to Ag, while the peaks in the range of 0.60 V to 0.80 V are assigned to ORR catalytic activities. The ORR peak potentials of Ag-$MnFe_2O_4$/NSPG (0.775 V) is more positive than that of Ag-$MnFe_2O_4$/SPG (0.733 V) and Ag-$MnFe_2O_4$/NPG (0.723 V). The results show that Ag-$MnFe_2O_4$/NSPG and Ag-$MnFe_2O_4$/SPG have good electrocatalytic properties. To get further insight into ORR activities, LSVs of the samples with the same scan rate (5 mV s^{-1}) and rotating speed (1600 rpm) are shown in Figure 6b. Onset potential of Ag-$MnFe_2O_4$/NSPG (0.887 V) is better than those of Ag-$MnFe_2O_4$/SPG (0.871 V), Ag-$MnFe_2O_4$/NPG (0.869 V), and commercial Pt/C (0.879 V). A similar trend is observed in half-wave potentials. Ag-$MnFe_2O_4$/NSPG presents as of 0.831 V, more positive than Ag-$MnFe_2O_4$/SPG (0.769 V), Ag-$MnFe_2O_4$/NPG (0.741 V) and Pt/C (0.827 V), indicating that Ag-$MnFe_2O_4$/NSPG has superior ORR activities. As reported, Ag-$MnFe_2O_4$ nanoparticles supported on N, S-co-doped graphene was detected to be 0.824 V of half-wave potential in LSV [30]. This clearly shows that the doping of graphene with N, S, and P can significantly improve electrocatalytic activities of Ag-$MnFe_2O_4$ toward ORR. Co-doping of NS, NP, SP, or NSP in graphene can produce asymmetric spin or charge density, resulting in more active sites and higher catalytic activity than single doping catalysts [31]. The results also show that NSPG can significantly improve electrocatalytic performances of Ag-$MnFe_2O_4$. The electrocatalytic performances of different catalysts are shown in Figure 7.

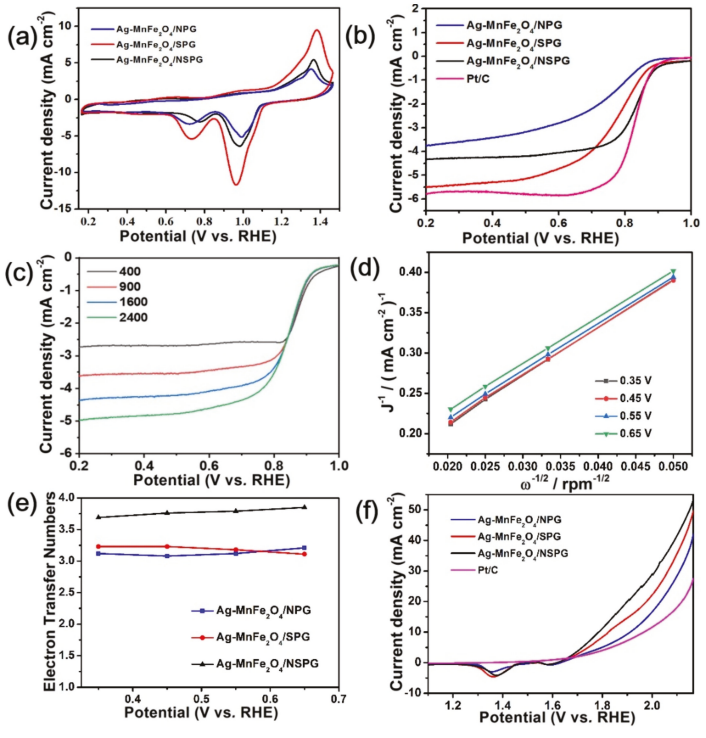

Figure 6. (**a**) CV and (**b**) LSV curves of the three samples. (**c**) ORR polarization curves of Ag-$MnFe_2O_4$/NSPG at different rotation rates and their corresponding (**d**) K-L plots and (**e**) n values in comparison to two other samples. (**f**) OER LSV curves of the three samples and Pt/C.

Table 3. ORR catalytic performances of the three samples.

	Peak Potentials(V) in CV	Onset Potential(V) in LSV	Half-Wave Potential(V) in LSV
Ag-$MnFe_2O_4$/NPG	0.723	0.869	0.741
Ag-$MnFe_2O_4$/SPG	0.733	0.871	0.769
Ag-$MnFe_2O_4$/NSPG	0.775	0.887	0.831
Pt/C	/	0.879	0.827

In order to clarify redox kinetic characteristics and catalytic pathway of Ag-$MnFe_2O_4$/NSPG, LSV measurements were conducted (Figure 6c). Limit current density rises with increasing electrode rotation rate, enabling more sufficient O_2 arrive on the surface of electrodes, which means higher conversion and faster diffusion kinetics for the catalyst. The corresponding K-L plots (Figure 6d) show an approximate linear relationship at different potentials, indicating the first-order reaction kinetics for ORR. The numbers of electron transfer for different samples during the ORR pathway are given in Figure 6e. The n values of Ag-$MnFe_2O_4$/NPG, Ag-$MnFe_2O_4$/SPG, and Ag-$MnFe_2O_4$/NSPG are calculated to be 3.08~3.21, 3.11~3.23, and 3.69~3.85, respectively. Thus, it indicates an available four electron pathway for Ag-$MnFe_2O_4$/NSPG.

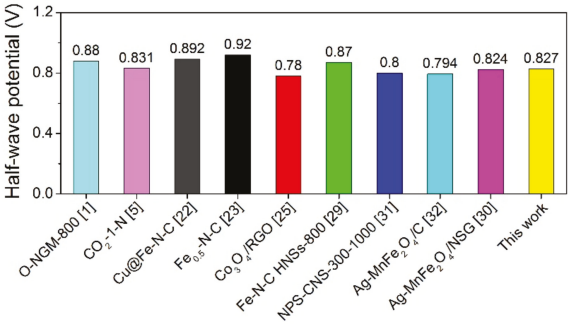

Figure 7. The half-wave potential (vs. RHE) for ORR of different catalysts reported in references.

In addition, the OER performances of Ag-$MnFe_2O_4$/NPG, Ag-$MnFe_2O_4$/SPG, Ag-$MnFe_2O_4$/NSPG and Pt/C were studied in O_2-saturated 0.1 M KOH electrolyte with a scanning rate of 1600 rpm (Figure 6f). Prior to the onset of OER, Ag-$MnFe_2O_4$ nanoparticles have a redox peak in the region of 1.3~1.6 V (vs. RHE). The potential of Ag-$MnFe_2O_4$/NSPG at the current density of 10 $mA \cdot cm^{-2}$ (Ej = 10) is 1.79 V, which is better than Ag-$MnFe_2O_4$/NPG (1.91 V), Ag-$MnFe_2O_4$/SPG (1.82 V) and Pt/C (1.97 V). Thus, the corresponding overpotential of Ag-$MnFe_2O_4$/NSPG is 560 mV, much smaller than Pt/C (740 mV). Ag-$MnFe_2O_4$/NSPG also demonstrates good OER catalytic performances.

To investigate the durability and methanol crossover effect of Ag-$MnFe_2O_4$/NSPG and Pt/C, chronoamperometric tests were carried out in O_2-saturated 0.1 M KOH. As shown in Figure 8a, Ag-$MnFe_2O_4$/NSPG catalyst displays 13.2% decay after 15,000 s, while Pt/C shows 29.1% decay. Current versus time (I-t) plots along with methanol addition are shown in Figure 8b. As 5 mL methanol is added into electrolyte at 400 s, the ORR current of Ag-$MnFe_2O_4$/NSPG has no significant change, indicating that Ag-$MnFe_2O_4$/NSPG catalyst has high catalytic selectivity for methanol. In comparison, Pt/C shows sharp current change due to the oxidation of methanol. It demonstrates the better methanol tolerance of Ag-$MnFe_2O_4$/NSPG.

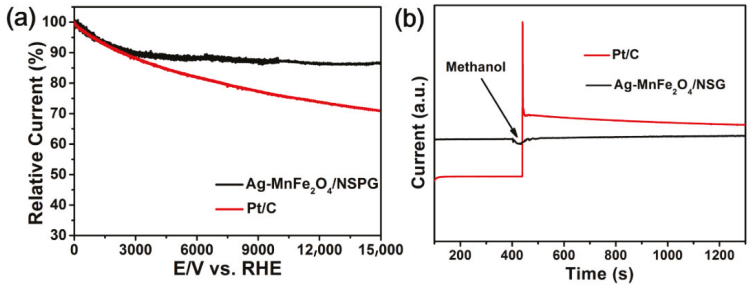

Figure 8. (**a**) Chronoamperometric response and (**b**) durability assessment of Ag-$MnFe_2O_4$/NSPG.

3. Experimental Section

3.1. Chemical Reagents and Materials

Nafion (5%), ferric acetylacetonate (99%), manganic acetylacetonate (99%), silver acetate (99%), melamine (99%), and 1-dodecanol (98%) were purchased from Sigma-Aldrich. Oleic acid (90%) and oleylamine (80%) were obtained from Aladdin. Phytic acid (50% in water) was obtained from Macklin. Dibenzyl disulfide (98%) was purchased from Beantown Chemical. 20 wt.% Pt/C was purchased from Hesen.

3.2. Material Synthesis

Synthesis of Ag-$MnFe_2O_4$ NPs. Ag-$MnFe_2O_4$ nanoparticles (NPs) were synthesized as reported [32]. Then, 1.0 mL oleic acid, 1.0 mL oleylamine, and 10 mL 1-dodecanol were mixed with stirring and heated to 220 °C. Then, 120 mg silver acetate was added and reacted for 1 h. The mixture was then cooled down to 200 °C. Next, 120 mg ferric acetylacetonate and 60 mg manganic acetylacetonate were subsequently added and reacted for another 1 h. The mixture was heated up to 220 °C and reacted 2 h. Finally, the mixture was cooled to room temperature. Products were collected and washed three times with ethanol.

Synthesis of NPG/SPG/NSPG. NPG, SPG, and NSPG were synthesized by similar route to NG [30]. Graphene oxide (GO) was synthesized by the Hummers' method [33]. Then, 100 mg GO was dispersed in 100 mL deionized water with ultra-sonication for 4 h to achieve a uniform solution. Then, 50 mg melamine and 50 mL phytic acid were slowly added into the dispersion. After 1 h ultra-sonication, the suspension was maintained under stirring at 90 °C for 2 h. After centrifugation with water, the precipitate was freeze-dried under vacuum. Finally, the powder was calcinated at 700 °C for 4 h at a heating rate of 5 °C min^{-1} with a flow of Ar gas, denoted as NPG. SPG and NSPG were also synthesized with similar routes except for the replacement of melamine with 50 mg dibenzyl disulfide for SPG, 25 mg melamine and 25 mg dibenzyl disulfide for NSPG, respectively.

Synthesis of Ag-$MnFe_2O_4$/NPG, Ag-$MnFe_2O_4$/SPG and Ag-$MnFe_2O_4$/NSPG. Ag-$MnFe_2O_4$ NPs (8 mg) and doped graphene (16 mg) were dispersed in 24 mL toluene with stirring. After 16 h, solid materials were collected and washed with water for three times. The obtained materials were dried at room temperature and labeled as Ag-$MnFe_2O_4$/NPG, Ag-$MnFe_2O_4$/SPG and Ag-$MnFe_2O_4$/NSPG nanocomposites.

3.3. Material Characterizations

Transmission electron microscopy (TEM), X-ray diffraction (XRD), X-ray photoelectron spectroscopic (XPS), and Raman analyses of the samples were carried out as reported [30]. The content of nanoparticles in Ag-$MnFe_2O_4$/NSPG was determined by dissolving 0.25 g nanocomposite in 20 mL 5.0% HNO_3 solution for 2 h at room temperature and another 6 min at 80 °C, and then diluted to 100 mL with ultrapure water. Finally, elemental concentrations were measured by PerkinElmer Avio 200 ICP-OES.

3.4. Electrochemical Measurements

Ink of catalyst sample including 4.0 mg catalyst powder, 1.0 mg carbon black, 800 μL water, 200 μL isopropanol, and 20 μL Nafion (5%) was ultrasonicated for 1 h. Then, 3 μL ink was pipetted onto a glassy carbon disk. The ORR and OER performances were then studied with the rotating disk electrode (RDE) technique using the ALS RRDE-3A and CHI 760D system as reported [30].

4. Conclusions

In summary, heterojunction Ag-$MnFe_2O_4$ nanoparticles have been synthesized and supported on various doped graphenes, including NPG, SPG, and NSPG. Among these composites, Ag-$MnFe_2O_4$/NSPG demonstrate superior ORR and OER electrocatalytic performances, excellent durability and methanol resistance. ORR half-wave potential of Ag-$MnFe_2O_4$/NSPG reaches 0.831 V, which exceeds that of commercial Pt/C (0.827 V). When the OER current density is 10 $mA{\cdot}cm^{-2}$, the potential of Ag-$MnFe_2O_4$/NSPG is 1.79 V, which also exceeds that of Pt/C (1.97 V). The multi-doping also stabilizes the loading of metal particles, so that Ag-$MnFe_2O_4$/NSPG shows good methanol resistance and excellent durability. After 14,000 s, the current loss is only reduced by 13.2%, much lower than that of Pt/C (29.1%). This indicates that metal particles/doped graphene composites have great application potentials and good prospects in metal-air batteries.

Author Contributions: H.D. and Y.C. designed the experiments and wrote the article; C.G., L.S. and Q.S. performed the experiments and analyzed the data; K.L. and L.D. designed the experiments. All authors have read and agreed to the published version of the manuscript.

Funding: This work was supported by the National Natural Science Foundation of China (21905153). Additionally, L. F. Dong thanks financial support from the Malmstrom Endowed Fund at Hamline University.

Conflicts of Interest: The authors declare no conflict of interest.

References

1. Wang, M.; Wang, W.; Qian, T.; Liu, S.; Li, Y.; Hou, Z.; Goodenough, J.B.; Ajayan, P.M.; Yan, C. Oxidizing vacancies in nitrogen-doped carbon enhance air-cathode activity. *Adv. Mater.* **2019**, *31*, 1803339. [CrossRef] [PubMed]
2. Shi, F.; He, J.; Zhang, B.; Peng, J.; Ma, Y.; Chen, W.; Li, F.; Qin, Y.; Liu, Y.; Shang, W.; et al. Plasmonic-enhanced oxygen reduction reaction of silver/graphene electrocatalysts. *Nano Lett.* **2019**, *19*, 1371–1378. [CrossRef] [PubMed]
3. Thaheem, I.; Kim, K.J.; Lee, J.J.; Joh, D.W.; Jeong, I.; Lee, K.T. High performance $Mn_{1.3}Co_{1.3}Cu_{0.4}O_4$ spinel based composite cathodes for intermediate temperature solid oxide fuel cells. *J. Mater. Chem. A* **2019**, *7*, 19696–19703. [CrossRef]
4. Santori, P.G.; Speck, F.D.; Cherevko, S.; Firouzjaie, H.A.; Peng, X.; Mustain, W.E.; Jaouen, F. High performance FeNC and Mn-oxide/FeNC layers for AEMFC cathodes. *J. Electr. Soc.* **2020**, *167*, 134505. [CrossRef]
5. Ratso, S.; Walke, P.R.; Mikli, V.; Ločs, J.; Šmits, K.; Vītola, V.; Šutka, A.; Kruusenberg, I. CO_2 turned into a nitrogen doped carbon catalyst for fuel cells and metal–air battery applications. *Green Chem.* **2021**, *23*, 4435–4445. [CrossRef]
6. Kaare, K.; Yu, E.; Käämbre, T.; Volperts, A.; Dobele, G.; Zhurinsh, A.; Niaura, G.; Tamasauskaite Tamasiunaite, L.; Norkus, E.; Kruusenberg, I. Biomass-derived Graphene-like Catalyst Material for Oxygen Reduction Reactio. *ChemNanoMat* **2021**, *7*, 307–313. [CrossRef]
7. Ratso, S.; Zitolo, A.; Käärik, M.; Merisalu, M.; Kikas, A.; Kisand, V.; Rähn, M.; Paiste, P.; Leis, J.; Sammelselg, V.; et al. Non-precious metal cathodes for anion exchange membrane fuel cells from ball-milled iron and nitrogen doped carbide-derived carbons. *Renew. Energy* **2021**, *167*, 800–810. [CrossRef]
8. Qu, L.; Liu, Y.; Baek, J.B.; Dai, L. Nitrogen-doped graphene as efficient metal-free electrocatalyst for oxygen reduction in fuel cells. *ACS Nano.* **2011**, *4*, 1321–1326. [CrossRef]
9. Liang, J.; Jiao, Y.; Jaroniec, M.; Qiao, S.Z. Sulfur and nitrogen dual-doped mesoporous graphene electrocatalyst for oxygen reduction with synergistically enhanced performance. *Angew. Chem. Int. Edit.* **2012**, *51*, 11496–11500. [CrossRef]
10. Wang, X.; Wang, J.; Wang, D.; Dou, S.; Ma, Z.; Wu, J.; Tao, L.; Shen, A.; Ouyang, C.; Liu, Q.; et al. One-pot synthesis of nitrogen and sulfur co-doped graphene as efficient metal-free electrocatalysts for the oxygen reduction reaction. *Chem. Commun.* **2014**, *50*, 4839–4842. [CrossRef]
11. Liu, Z.; Nie, H.; Yang, Z.; Zhang, J.; Jin, Z.; Lu, Y.; Xiao, Z.; Huang, S. Sulfur-nitrogen co-doped three-dimensional carbon foams with hierarchical pore structures as efficient metal-free electrocatalysts for oxygen reduction reactions. *Nanoscale* **2013**, *5*, 3283–3288. [CrossRef]
12. Wang, S.; Zhang, L.; Xia, Z.; Roy, A.; Chang, D.W.; Baek, J.B.; Dai, L. BCN graphene as efficient metal-free electrocatalyst for the oxygen reduction reaction. *Angew. Chem. Int. Edit.* **2012**, *51*, 4209–4212. [CrossRef]

13. Kumatani, A.; Miura, C.; Kuramochi, H.; Ohto, T.; Wakisaka, M.; Nagata, Y.; Ida, H.; Takahashi, Y.; Hu, K.; Jeong, S.; et al. Chemical dopants on edge of holey graphene accelerate electrochemical hydrogen evolution reaction. *Adv. Sci.* **2019**, *6*, 1900119. [CrossRef]
14. Zhang, N.; Liu, F.; Xu, S.; Wang, F.; Yu, Q.; Liu, L. Nitrogen-phosphorus co-doped hollow carbon microspheres with hierarchical micro-meso-macroporous shells as efficient electrodes for supercapacitors. *J. Mater. Chem. A* **2017**, *5*, 22631–22640. [CrossRef]
15. Yang, S.; Peng, L.; Huang, P.; Wang, X.; Sun, Y.; Cao, C.; Song, W. Nitrogen, phosphorus, and sulfur co-doped hollow carbon shell as superior metal-free catalyst for selective oxidation of aromatic alkanes. *Angew. Chem. Int. Edit.* **2016**, *55*, 4016–4020. [CrossRef]
16. Zhang, X.; Lu, Z.; Xu, G.; Wang, T.; Ma, D.; Yang, Z.; Yang, L. Single Pt atom stabilized on nitrogen doped graphene: Co oxidation readily occurs via the tri-molecular Eley-Rideal mechanism. *Chem. Phys.* **2015**, *17*, 20006–20013. [CrossRef]
17. Zhang, Y.; Fugane, K.; Mori, T.; Niu, L.; Ye, J. Wet chemical synthesis of nitrogen-doped graphene towards oxygen reduction electrocatalysts without high-temperature pyrolysis. *J. Mater. Chem.* **2012**, *22*, 6575. [CrossRef]
18. Zhang, X.; Lu, Z.; Fu, Z.; Tang, Y.; Ma, D.; Yang, Z. The mechanisms of oxygen reduction reaction on phosphorus doped grapheme. *J. Power Sour.* **2015**, *276*, 222–229. [CrossRef]
19. Razmjooei, F.; Singh, K.P.; Song, M.; Yu, J. Enhanced Electrocatalytic activity due to additional phosphorous doping in nitrogen and sulfur-doped graphene: A comprehensive study. *Carbon* **2014**, *78*, 257–267. [CrossRef]
20. Riel, A.M.S.; Jessop, M.J.; Decato, D.A.; Massena, C.J.; Nascimento, V.R.; Berryman, O.B. Experimental investigation of halogen-bond hard-soft acid-base complementarity. *Acta Crystallogr.* **2017**, *73*, 203–209. [CrossRef]
21. Talluri, B.; Thomas, T. Indications of hard-soft-acid-base interactions governing formation of ultra-small (r < 3 nm) digestively ripened copper oxide quantum-dots. *Chem. Phys. Lett.* **2017**, *685*, 84–88. [CrossRef]
22. Wang, Z.; Jin, H.; Meng, T.; Liao, K.; Meng, W.; Yang, J.; He, D.; Xiong, Y.; Mu, S. Fe, Cu-coordinated ZIF-derived carbon framework for efficient oxygen reduction reaction and zinc-air batteries. *Adv. Funct. Mater.* **2018**, *28*, 1802596. [CrossRef]
23. Lee, S.H.; Kim, J.; Chung, D.Y.; Yoo, J.M.; Lee, H.S.; Kim, M.J.; Mun, B.S.; Kwon, S.G.; Sung, Y.E.; Hyeon, T. Design principle of Fe-N-C electrocatalysts: How to optimize multimodal porous structures. *J. Am. Chem. Soc.* **2019**, *141*, 2035–2045. [CrossRef]
24. Geng, H.; Guo, Y.; Ding, X.; Wang, H.; Zhang, Y.; Wu, X.; Jiang, J.; Zheng, J.; Yang, Y.; Gu, H. Porous cubes constructed by cobalt oxide nanocrystals with graphene sheet coatings for enhanced lithium storage properties. *Nanoscale* **2016**, *8*, 7688–7694. [CrossRef]
25. Kumar, K.; Canaff, C.; Rousseau, J.; Clacens, S.A.; Kokoh, B. Effect of the oxide-carbon heterointerface on the activity of Co_3O_4/NRGO nanocomposites toward ORR and OER. *J. Phys. Chem.* **2016**, *120*, 7949–7958. [CrossRef]
26. Qiu, B.; Deng, Y.; Du, M.; Xing, Y.; Zhang, J. Ultradispersed cobalt ferrite nanoparticles assembled in graphene aerogel for continuous photo-Fenton reaction and enhanced lithium storage performance. *Sci. Rep.* **2016**, *6*, 29099. [CrossRef]
27. Zou, J.; Kim, F. Diffusion driven layer-by-layer assembly of graphene oxide nanosheets into porous three-dimensional macrostructures. *Nat. Commun.* **2014**, *5*, 5254. [CrossRef]
28. Yu, S.; Webster, R.D.; Zhou, Y.; Yan, X. Novel carboxylated graphene oxide-CuS-Ag nanocomposite glass coating for organic degradation under solar light. *J. Chem. Technol. Biotechnol.* **2017**, *92*, 2626–2634. [CrossRef]
29. Chen, Y.; Li, Z.; Zhu, Y.; Sun, D.; Liu, X.; Xu, L.; Tang, Y. Atomic Fe dispersed on N-doped carbon hollow nanospheres for high-efficiency electrocatalytic oxygen reduction. *Adv. Mater.* **2019**, *31*, 1806312. [CrossRef]
30. Chen, Y.; Shi, Z.; Li, S.; Feng, J.; Pang, B.; Yu, L.; Zhang, W.; Dong, L. N, S-codoped graphene supports for Ag-$MnFe_2O_4$ nanoparticles with improved performance for oxygen reduction and oxygen evolution reactions. *J. Electroanal. Chem.* **2020**, *860*, 113930. [CrossRef]
31. Zhu, Y.; Cao, C.; Jiang, W.; Yang, S.; Hu, J.; Song, W.; Wan, L. Nitrogen, phosphorus and sulfur co-doped ultrathin carbon nanosheets as a metal-free catalyst for selective oxidation of aromatic alkanes and the oxygen reduction reaction. *J. Mater. Chem.* **2016**, *4*, 18470–18477. [CrossRef]
32. Chen, Y.; Liu, S.; Shi, Z.; Yu, J.; Dong, H.; Qin, Y.; Yu, L.; Dong, L. Effect of electronic coupling on the electrocatalytic performance of Ag-MFe_2O_4 (M = Co, Mn) nanocomposites. *J. Electrochem. Soc.* **2017**, *164*, F1483–F1488. [CrossRef]
33. Hummers, W.S., Jr.; Offeman, R.E. Preparation of graphitic oxide. *J. Am. Chem. Soc.* **1958**, *80*, 1339. [CrossRef]

catalysts

MDPI

Article

Fabrication of Polyaniline Ni-Complex Catalytic Electrode by Plasma Deposition for Electrochemical Detection of Phosphate through Glucose Redox Reaction as Mediator

Hyun-Woong Lee [1], Jae-Ni Yoo [2], In-Keun Yu [3,*] and Seong-Ho Choi [1,2,*]

[1] Department of Cosmetic Science, Hannam University, Daejeon 34054, Korea; hw8000@naver.com
[2] Department of Chemistry, Hannam University, Daejeon 34054, Korea; wosl159@naver.com
[3] Plasma Technology Research Institute, Korea Institute of Fusion Energy (KFE), Gunsan 54004, Korea
* Correspondence: ikyu@kfe.re.kr (I.-K.Y.); shchoi@hnu.kr (S.-H.C.)

Abstract: We report here the preparation and characterization of polyaniline Ni-complex catalytic electrode by one-pot plasma deposition for the electrochemical detection of phosphate via the redox reaction of glucose. We first prepared a precursory solution by combining $NiCl_2$ and 3-aminobenzoic acid in a mixed solution of methanol (MeOH) and water, and adding aniline as a conductive polymeric precursor for increasing the electron transfer potential. We then synthesized the catalytic electrode in a one-step cold plasma process by preparing the precursors on ITO glass. We characterized the obtained Ni-coordinate catalytic electrode via X-ray photoelectron spectroscopy (XPS), field emission scanning electron microscopy (SEM), and electrochemical methods. Electrochemical characterization produced stable redox properties of Ni^{3+}/Ni^{2+} couples in a 0.1 M NaOH solution. Cyclic voltametric experiments have drastically increased electrocatalytic oxidation and reduction of glucose by increasing the concentration of phosphate (PO_4^{3-}) ions using the prepared Ni-modified catalytic electrodes. From these results, the prepared catalytic electrode could be used as the electrochemical sensor for phosphate in actual water.

Keywords: plasma deposition; polyaniline Ni-complex catalytic electrode; electrochemical detection; phosphate ion; glucose; redox behavior of Ni^{3+}/Ni^{2+} couples

Citation: Lee, H.-W.; Yoo, J.-N.; Yu, I.-K.; Choi, S.-H. Fabrication of Polyaniline Ni-Complex Catalytic Electrode by Plasma Deposition for Electrochemical Detection of Phosphate through Glucose Redox Reaction as Mediator. *Catalysts* **2022**, *12*, 128. https://doi.org/10.3390/catal12020128

Academic Editors: Marc Cretin, Sophie Tingry, Zhenghua Tang and Morris D. Argyle

Received: 4 December 2021
Accepted: 18 January 2022
Published: 21 January 2022

1. Introduction

Quantitative evaluation of phosphates, both of inorganic compounds and organic compounds, is important in biomedical research, biological diagnosis, and environmental monitoring [1–3]. The sensing range of phosphorus is between 0.2 in 10 mg/L in natural and waste waters and between 0.2 and 50 mg/kg in soil. A maximum permissible concentration of phosphate in river water is 0.32 μM and ranges between 0.0143 and 0.143 mM in wastewater [4]. As a diagnostic fluid, the concentration of phosphate ions in human saliva is variable, ranging from between 5 and 14 mM [5]. Adult human serum with a range of 0.81 to 1.45 mM PO_4^{3-} was used [6]. Many researchers have developed various detection methods for phosphate such as phosphate ion selective electrodes [7], chromatography [8], spectroscopy [9], and the development of sensors exploiting enzymatic reactions [10,11]. However, little has been reported about electrochemical detection, which is known as a simpler method then those described above.

On the other hand, there are many studies published about the nonenzymatic electrochemical detection of glucose based on metallic nanoparticle electrodes, which contain Ni, Pd, Au, Co, and nanoparticles, etc. [12,13]. Furthermore, metal-complex electrodes were also reported such as Cu-complex, Ni-complex, and Zn-complex electrode, etc., for the detection of glucose [14,15]. In a previous paper, we also prepared the Ni-complex electrode by a plasma process for the detection of methanol [16]. In the study, we used polyacrylic acid as ligands to immobilize the metal Ni. However, though polyacrylic acid

was a good ligand for immobilizing Ni ions, the vinyl polymers and polyacrylic acid were not good electron transfer materials because of their low conductivity.

Conducting polymers are important functional materials which have been widely applied to prepare electrochemical biosensors, due to their interesting and tunable chemical, electrical, and structural properties [17–20]. Therefore, conducting polymers have been widely applied in the fields of bioanalytical and biomedical science [21], drug delivery [22,23], tissue engineering [24], and cell culture [25] because of their essential properties and biocompatibility [26,27]. In addition, conducting polymers express an attractive sensitive material for biosensors because of electrical properties that allow them to transmit biochemical information onto electrical signals. Furthermore, conducting polymers can be easily grafted by modifying their functional groups, which offers the possibility of improving their ability to sense and quantify bioanalytes or to maximize the interactions between biomolecules and functional polymers [28,29]. Therefore, after a short explanation of the electrochemical processes used in conducting polymer-based biosensors, the biosensors will be described to enhance the recently advanced research into conducting polymer-based electrochemical biosensors.

Low temperature plasmas can be prepared for polymers in laboratories and in industrial applications. Low temperature plasma is the electric glow discharge made by using power sources such as AC, DC, and microwave [30–32]. Alternatively, high temperature plasmas are not used for making organic materials due to their heat labile characteristics. Plasma polymerization is not limited to preparing organic materials, and the plasma synthesis of inorganic materials should be included in plasma polymerization. However, little has been reported about the plasma polymerization of aniline as a conducting polymer precursor because it was difficult to make conjugation bonds from the main chains in polyaniline by plasma polymerization until now.

In this study, we first fabricated polyaniline Ni-coordinate catalytic electrode by applying a one-step plasma polymerization process and investigated the electrochemical redox of glucose as a mediator to measure the phosphate ion for the electrochemical sensor of phosphate in actual water. We found that a polyaniline Ni-complex catalytic electrode can be applied as an electrochemical oxidation for glucose in the presence of high concentrations of phosphate.

2. Results

2.1. Contact Angle Analysis

The No. 1, 2, 3, and 4 electrodes used were: an indium tin oxide (ITO) electrode; a polyaniline-grafted ITO electrode; the benzoic acid-modified polyaniline electrode; and a polyaniline Ni-complex catalytic electrode, respectively. Figure 1 shows the contact angles of the prepared polyaniline Ni-coordinate catalytic electrodes found by applying the plasma process. The contact angle is important wherever the intensity of the phase contact between liquid and solid substances needs to be checked or assessed. By examining the water contact angles, we determined that the contact angle of the bare ITO electrode, No. 1 was 77° and the contact angles of the polyaniline Ni-coordinated catalytic electrodes, No. 2, No. 3, and No. 4 were 60°, 53°, and 51°, respectively, at room temperature. As a result, the base ITO glass had nearly hydrophobic characteristics and a high contact angle. Compared to base ITO glass, the contact angles of the prepared polyaniline Ni-coordinated electrodes were remarkably low, due to the presence of a large amount of the functionalized COOH groups from 3-aminobenzoic acid, which had hydrophilic properties. The existence of hydrophilic metallic coordination materials on each electrode also converted hydrophobic ITO to hydrophilic characteristics. From these results, we concluded that the polymeric metallic (Ni)-complex surface has hydrophilic properties. It is shown that the polyaniline Ni-complex catalytic electrode was successfully coated onto ITO surfaces by the one-pot plasma process easily and simply.

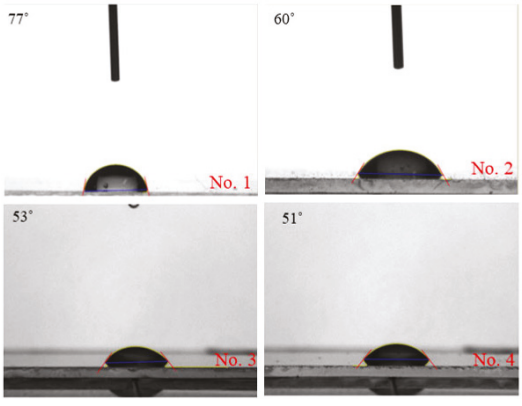

Figure 1. Contact angles of the prepared catalytic electrode by plasma deposition (see Table 1).

2.2. SEM Data Analysis

The surface morphologies of the original ITO electrode (No. 1) and the polyaniline Ni-complex catalytic electrodes (No. 2, 3, and 4 in Table 1), were exhibited by scanning them with electron microscopy (SEM) (Figure 2). The polyaniline Ni-complex catalytic electrode surface appears amorphous, morphology that was suggested by the clear deposition of polyaniline Ni-complex onto the ITO substrate. When we used a cross-linker of 3-aminobenzoic acid (No. 3 and 4), the polyaniline was aggregated because the main chains of polyaniline connected with each other.

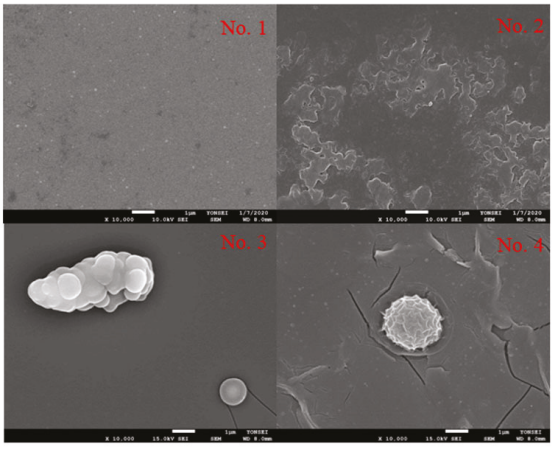

Figure 2. SEM images of the prepared catalytic electrode surface by plasma deposition (see Table 1).

2.3. AFM Data Analysis

Figure 3 exhibits the AFM data of the prepared polyaniline Ni-complex catalytic electrode surfaces by the one-pot plasma process (see Table 1). In No. 1, the ITO surface roughness is lower than that of the polyaniline-grafted ITO electrode (No. 2), the benzoic acid-modified polyaniline electrode (No. 3), and the polyaniline Ni-complex catalytic electrode (No. 4). These results mean that the polyaniline Ni-complex catalytic electrodes were successfully coated by one-pot cold plasma deposition.

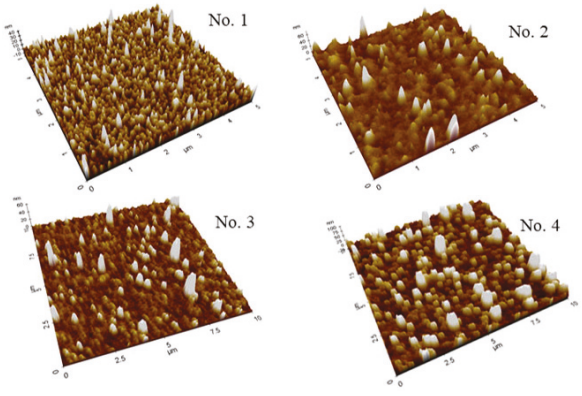

Figure 3. AFM images of the prepared catalytic electrode surface by plasma deposition (see Table 1).

2.4. EDS Data Analysis

Figure 4 demonstrates SEM-EDAX analysis of the prepared polyaniline Ni-complex catalytic electrode surfaces by cold plasma deposition (No. 4 in Table 1). The EDAX images of the prepared Ni-complex catalytic electrodes exhibit significant spots of carbon, oxygen, and Ni on their surfaces. This means that the surface deposition of polyaniline Ni-complex on the ITO electrodes via the one-step cold plasma process was successful.

Element	Wt%	Wt% Sigma	Atomic %
N	4.39	0.69	10.81
O	23.07	0.28	49.75
Na	1.58	0.06	2.36
Mg	0.53	0.04	0.75
Al	0.84	0.04	1.07
Si	12.79	0.14	15.71
P	0.92	0.05	1.03
K	1.07	0.16	0.95
Ca	2.13	0.08	1.83
Ni	0.36	0.12	0.21
In	47.24	0.45	14.20
Sn	3.62	0.30	1.05
W	1.46	0.22	0.27
Total:	100.00		100.00

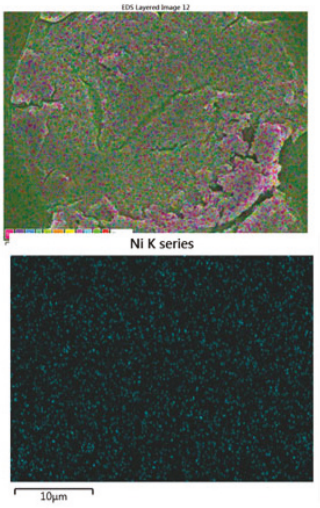

Figure 4. EDAX analysis of the prepared Ni-modified catalytic electrode surface by plasma deposition (No. 4 in Table 1).

2.5. XPS Data Analysis

Figure 5 shows the XPS survey scan spectra data of the amino benzoic acid-modified polyaniline (No. 3) and the polyaniline Ni-complex catalytic electrodes (No. 4) fabricated via cold plasma deposition. In No. 3, there are no Ni peaks at 853 eV, while in No. 4, the two peaks at 853.3 eV and 834.9 eV, included binding to the energies of NiO $2p^{3/2}$ and NiO $2p^{1/2}$, designating the presence of Ni in the electrode. Additionally, the peaks at 400 eV suggest that the N is in the form of cross-linked chemicals of amino benzoic acid, acting as ligands. The O1s peak is roughly 531.8 eV, which indicates the presence of a carboxylic acid (amino benzoic acid) in the electrode.

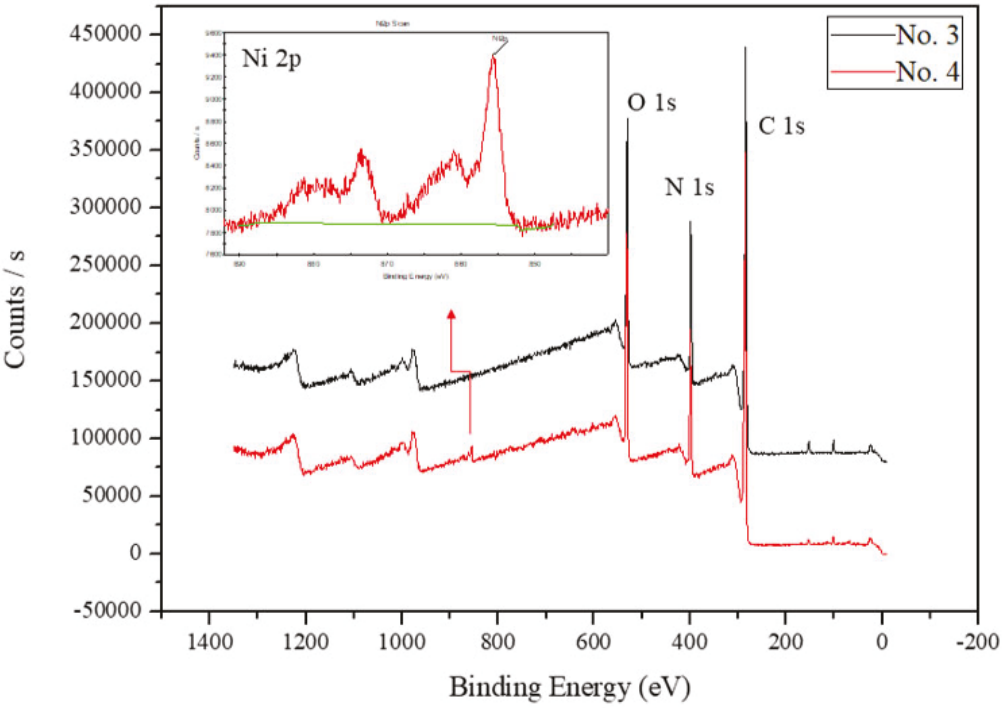

Figure 5. XPS survey scan spectra of the prepared catalytic electrode surface by plasma deposition (see Table 1).

2.6. Electrochemical Data Analysis

We performed cyclic voltammetry to determine the electrochemical performance of the prepared polyaniline Ni-complex catalytic electrodes. Figure 6 exhibits the cyclic voltammetry (CV) of these electrodes in 0.1 M NaOH electrolyte with a scan rate of 100 mV/min. The cyclic voltammogram of the synthesized Ni-complex catalytic electrodes facilitated the oxidation-reduction peak, which was indicated by the oxidation and reduction of the Ni^{2+}/Ni^{3+} couple in the NaOH electrolyte on the left side. From these results, we suggest that the Ni-complex catalytic electrode could be used as an electrochemical catalyst sensor for the detection of organic molecules. Therefore, we selected glucose as the mediator molecule to obtain its redox peak. When we added the glucose to NaOH electrolytes, the redox peaks of Ni^{2+}/Ni^{3+} couples of the polyaniline Ni-complex catalytic electrode were shifted as shown by the red line of cyclic voltammogram on the right side in Figure 6. Furthermore, the current values and electrochemical potential windows were increased by adding glucose. These results mean the glucose is also oxidized and reduced on the Ni-complex catalytic electrode. To determine phosphate ion molecules, we added sodium phosphate in NaOH electrolytes with glucose and Ni-complex catalytic electrodes to obtain the shifted redox peaks of cyclic voltammograms, as shown by the blue line on the right side in Figure 6. These results strongly indicate that the prepared Ni-complex catalytic electrode could be used as an electrochemical catalytic sensor for the detection of phosphate.

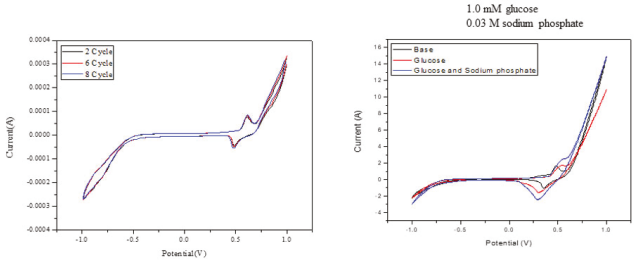

Figure 6. Cyclic voltammograms of the prepared catalytic electrode (No. 4) in 0.1 M NaOH with scan rate 100 mV/min.

2.7. Electrochemical Detection of Phosphate

Figure 7 shows cyclic voltammograms of 1.0 mM glucose by the prepared Ni-complex catalytic electrode (No. 4) in 0.1 M NaOH electrolytes with different sodium phosphate levels and a scan rate of 100 mV/min. The redox peaks of glucose rose by increasing the concentration of sodium phosphate to 0.006 M. This electrochemical detection indicated that the prepared Ni-complex catalytic electrode could be used as an electrocatalytic biosensor for sensing phosphate ions. The catalytic efficiency, presented as a current density value of the fabricated Ni-complex catalytic electrodes for detection of glucose oxidation without sodium phosphate, was calculated to be 11.5 mAM^{-1} cm^{-2}. We also examined that the stability of the fabricated polyaniline Ni-complex catalytic electrode via cyclic voltammetry. The current value of the fabricated Ni-complex catalytic electrode decreased to about 21.3% from its maximum peak after 120 cycles, which suggests an acceptable stability was achieved.

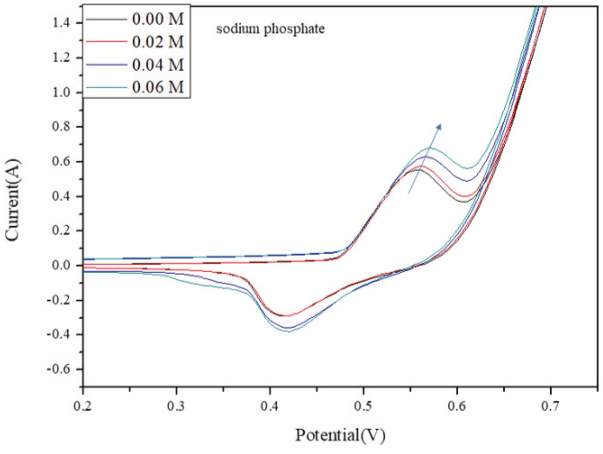

Figure 7. Cyclic voltammograms of 1.0 mM glucose by the prepared catalytic electrode (No. 4).with different sodium phosphate in 0.1 M NaOH with scan rate 100 mV/min.

3. Discussion

The polymeric metal coordination of chemicals with Ni^{2+}/Ni^{3+} redox couples have received considerable interest in recent years due to their properties of alkalinizing electrolytes. There are many common applications for using redox mediators between target compounds and the prepared electrodes in many electrochemical redox processes. Furthermore, the fabrication process is usually simple and easy and the characteristics of the coatings that result can be carefully controlled [33]. In a previous paper [16,34], polymeric metal complex chemicals with Ni, Cu, and Fe were synthesized via an alternate current

(AC) plasma deposition process to detect H_2O_2 and methanol, respectively. The exhibited method of polymeric fabrication, specifically, conducting a polymer metallic coordinator with a glucose redox reaction as a catalytic mediator, was effective. Therefore, we examined the plasma polymerization of the precursors as shown in Figure 8. Figure 8 exhibits the schematic preparation of polyaniline Ni-complex catalytic electrode by plasma process for detection of phosphate. If we begin with aniline as an electron transfer material, metal salts as catalytic mediators can be synthesized by coordinating metal ions with the carboxyl groups of 3-aminobenzoic acid.

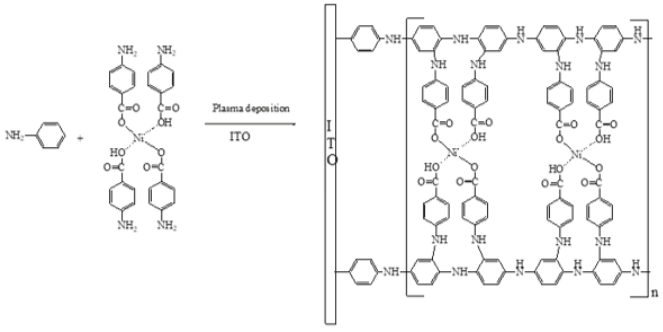

Figure 8. Schematic preparation of polyaniline Ni-complex catalytic electrode by plasma process for detection of phosphate.

On the other hand, linear polyaniline can be synthesized in two ways: by chemical oxidation of aniline monomers in an acid solution [35]; or by electrochemical oxidation [36]. Cross-linked polyaniline exhibits characteristics similar to that of linear polyaniline but with lower values of conductivity and solubility in solvents and a higher mechanical strength [37]. Plasma polymerization is a more easy and simple process than conventional polymerization, which involves casting film from a solution because the fewer fabrication steps are needed in the former. It is a free solvent, room temperature process that does not require the use of chemical oxidants. The ultra-thin film with controllable thicknesses in the nanometer range can easily be formed on the surfaces of substrates by plasma polymerization [38]. Plasma polymerization mechanisms are a major source of free radicals and negative ions attributed to the collisions of the monomer molecules with electrons generated by electric discharges [39]. The polymers from plasma polymerization do not contain regularly repeating units; while the chains are branched and randomly terminated with a high degree of cross-linking. The free radicals are trapped, and this results in changes to the plasma polymer network over time [40]. Polyaniline formations on film structures by plasma polymerization have been reported earlier. There is not much detailed information available about polyaniline structure by plasma polymerization.

In our case, plasma is a partially ionized gas with radicals, ions, electrons, photons, and molecules that are excited during the plasma process. It is a highly reactive mixture of species, which are different from conventional gaseous mixtures. The resulting catalysts under the influence of plasma, can include very different species from those prepared by conventional thermal preparation. Plasma has been extensively applied for catalyst preparation because of this [16]. In this experiment, the precursors with metallic coordination were vaporized as plasma. Polymeric-Ni coordinated chemicals with special morphology were controlled through a fast-collision process using a quenched gas, as shown in Figure 9. Figure 9 shows the possible polymerization mechanism of the functional polyaniline during the cold plasma process. During the plasma process, precursor radicals were generated as shown in Figure 9 (1), and then the generated aniline radicals were polymerized as shown by the schematic in Figure 9 (2) and (3). Finally, we obtained the carboxylic acid-modified polyaniline as shown in Figure 9 (4).

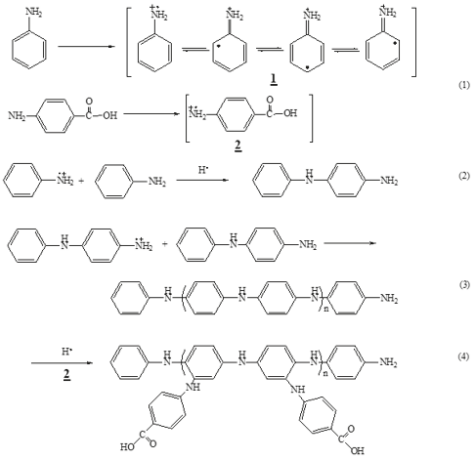

Figure 9. Possible polymerization mechanism of the funetional polyaniline during cold plasma process.

Figure 10 exhibits the electrocatalytic mechanism of a glucose redox reaction on the surface of a Ni-complex polymeric catalytic electrode. The Ni^{2+} was first electrochemically oxidized to Ni^{3+}, which then reacted electrochemically with glucose and resulted in the glucose converting to products such as lactone and in the regeneration of the catalyst.

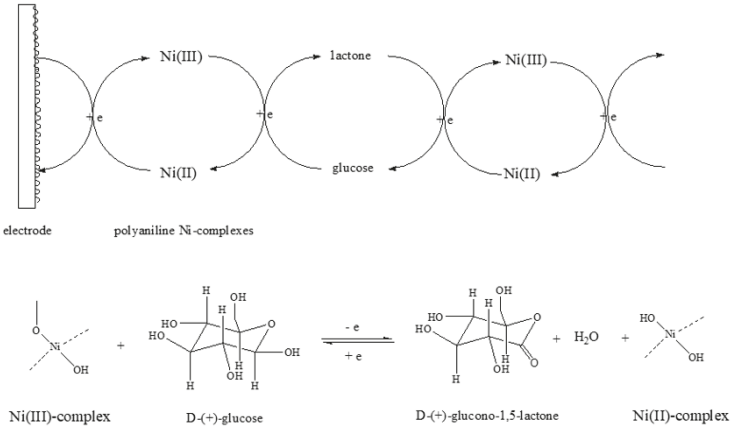

Figure 10. Catalytic redox mechanism of glucose on polyaniline Ni-complex electrode prepared by plasma process for detection of phosphate.

Figure 11 exhibits the formation of D-(+)-glucos-6-phosphate during the electrochemical process of alkaline electrolytes with the presence of a phosphate ion. The prepared D-glucose-6-phosphate compounds show the shifted redox peaks as shown in Figure 11.

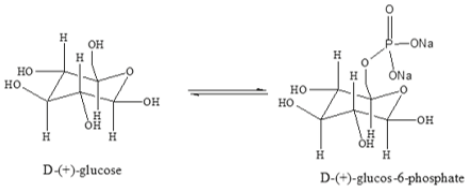

Figure 11. Formation of D-(+)-glucos-6-phosphate during electrochemical process.

4. Materials and Methods

4.1. Reagents

Aniline, indium tin oxide (ITO) plate as the working electrode (30–60 Ω/sq, 25 mm × 25 mm × 1.1 mm, Sigma Aldrich Co.), 3-Aminobenzocic Acid (Tokyo Kasei), nickel chloride (NiCl2, Oriental Chemical Industry, Osaka, Japan), potassium chloride (KCl, Ducsan Pharmaceutical Co., Ltd., Seoul, Korea), methyl alcohol (MeOH, Samchun, Pyeongtaek-si, Korea), and sodium hydroxide (NaCl, Samchun) were purchased, respectively, and used during treatments.

Phosphate buffer solution (PBS) was synthesized by mixing 0.1 M NaH_2PO_4 and 0.1 M Na_2HPO_4 and the pH was controlled to a value of 7.4. For this, we obtained a water purification experiment solution by Milli Q plus water purification systems (Millipore, Co., Ltd., Toronto, ON, Canada), and the final resistance of water was 18.2 MΩ cm^{-1}).

4.2. Research Instruments

We determined the surface characteristics and contact angle (PHOENIX 300, Surface Electro Optics Co., Ltd., Seoul, Korea), using scanning electron microscopy (FE-SEM, S 4800, Hitachi, Tokyo, Japan) and X-ray photoelectron spectroscopy (MultiLab. ESCA 2000, Thermo Fisher Scientific, Inc., MA, USA). We performed cyclic voltammetry (CV) using a VersaSTAT 3 potentiostat/galvanostat (AMETEK, Pennsylvania, USA) and a conventional 3 electrode system with an ITO plate as the working electrode, a platinum wire as the counter electrode, and Ag/AgCl as a reference electrode.

We used a plasma device with power restricted to the range of 200 to 250 W. Most of the experiments were performed in the region of 200 W. The torch used in this experiment was conical and the diameter of the torch tip was 2.0 mm. Nitrogen was supplied as the working gas in a tank connected to the plasma generator, with a flow controller inside. The plasma generator was applied to hold the pressure at a constant level. The percussor solution was injected into the plasma device jet by a syringe pump in the downstream region. The ITO plate was placed under a plasma jet at a distance of 1 cm and manually moved during the plasma deposition process.

4.3. Preparation of Polyaniline Ni-Complex Catalytic Electrode

Table 1 exhibits the preparation condition of precursors for AC plasma process. We prepared the precursor solutions for the experiment as follows. First, a precise amount of a nickel chloride salt was dissolved in the mixture of a water and methanol solution, and then added the 3-aminobenzoic acid as ligands and aniline as the electron transfer material. This detailed the precursor solution for the preparation of polyaniline Ni-complex catalytic electrode as shown in Table 1. Subsequently, the ITO plate was pre-washed in ethanol and ultrasonicated for ten minutes before plasma deposition. The ITO substrate was slowly moved in the x and y directions during the deposition process and the deposition time was 5 min. The precursors were injected into the AC plasma jet using a syringe pump at a flow rate of 0.3 mL/min, and the nitrogen gas pressure was kept constant at 0.018 MPa. After the deposition process was completed, the prepared electrode was washed in a MeOH/H_2O mixture to remove nonreactive precursors, then dried and stored at 4 °C before application.

Table 1. Preparation condition of precursors for AC plasma process.

	Aniline (mmol)	3-Aminobenzocic Acid (mmol)	Nickel Chloride (mmol)	Water (mL)	MeOH (mL)
No. 1	-	-	-	-	-
No. 2	54.8	-	-	-	-
No. 3	54.8	0.2	-	0.5	0.08
No. 4	54.8	0.2	0.2	0.5	0.04

5. Conclusions

The polyaniline Ni-coordinate catalytic electrode for glucose oxidation could be successfully prepared by a one-pot plasma process of synthesized precursor solutions. We successfully fixed the fabricated Ni-complex catalytic electrode with Ni coordination chemicals on the surface of an ITO substrate by adjusting SEM, contact angle, XPS, cyclic voltammetry, and SEM-EDS, and evaluated the catalytic efficiency of glucose in an alkaline solution. From the results, we have arrived the following conclusions:

(1) A polyaniline Ni-coordinated catalytic electrode can be fabricated easily and simply by one-pot plasma deposition without further treatment.
(2) The catalytic activity and anodic peak potential of glucose were 11.5 $mAM^{-1}cm^{-2}$ and 0.54 V, respectively. Therefore, the polyaniline Ni-complex catalytic electrode shows higher catalytic activity for glucose oxidation.
(3) By adding phosphate, the currents of anodic peak potential rose as phosphate ion concentration increased.
(4) The stability of the polymeric Ni coordination electrode seems to be acceptable for practical applications.
(5) The fabricated polyaniline Ni-complex catalytic electrode could be used as phosphate sensors.

Author Contributions: Conceptualization, S.-H.C.; methodology, I.-K.Y.; software, formal analysis, H.-W.L.; investigation, J.-N.Y.; data curation, S.-H.C.; writing—original draft preparation, H.-W.L.; writing—review and editing, S.-H.C.; visualization, J.-N.Y.; supervision, S.-H.C.; funding acquisition, I.-K.Y. All authors have read and agreed to the published version of the manuscript.

Funding: This research was supported by the R&D Program of "Plasma Convergence & Fundamental Research (code No. 1711124796)" through the Korea Institute of Fusion Energy (KFE) and funded by the Government funds, Republic of Korea.

Conflicts of Interest: The authors declare no conflict of interest.

References

1. Min, J.-K.; Yoo, H.-S.; Lee, E.-Y.; Lee, W.-J.; Lee, Y.-M. Simultaneous Quantitative Analysis of Sphingoid Base 1-Phosphates in Biological Samples by o-Phthalaldehyde Precolumn Derivatization after Dephosphorylation with Alkaline Phosphatase. *Anal. Biochem.* **2002**, *303*, 167–175. [CrossRef]
2. Bian, X.; Li, X.; Qi, P.; Chi, Z.; Ye, R.; Lu, S.; Cai, Y. Quantitative design and analysis of marine environmental monitoring networks in coastal waters of China. *Mar. Pollut. Bull.* **2019**, *143*, 144–151. [CrossRef]
3. Rouser, G.; Siakotos, A.N.; Fleischer, S. Quantitative analysis of phospholipids by thin-layer chromatography and phosphorus analysis of spots. *Lipids* **1966**, *1*, 85–86. [CrossRef] [PubMed]
4. Litke, D.W. Review of Phosphorus Control Measures in the United States and Their Effects on Water Quality. In *Water-Investigations Report, USGS*; US Department of the Interior: Washington, DC, USA, 1999; Volume 99.
5. Poureslami, H.; Hoseinifar, R.; Khazaeli, P.; Hoseinifar, R.; Sharifi, H.; Poureslami, P. Changes in the Concentration of Ions in Saliva and Dental Plaque after Application of CPP-ACP with and without Fluoride among 6–9 Year Old Children. *J. Dent. Biomater.* **2017**, *4*, 361–366.
6. Bansal, V.K. Chapter 198Serum Inorganic Phosphorus. In *Clinical Methods: The History, Physical, and Laboratory Examinations*, 3rd ed.; Butterworths: Boston, MA, USA, 1990.
7. Khaleda, E.; Hassana, H.N.A.; Girgis, A.; Metelka, R. Construction of novel simple phosphate screen-printed and carbon paste ion-selective electrodes. *Talanta* **2008**, *77*, 737–743. [CrossRef]

8. Kelani, K.M.; Badran, O.M.; Rezk, M.R.; Elghobashy, M.R.; Eid, S.M. Widening the applications of the Just-Dip-It approach: A solid contact screen-printed ion-selective electrode for the real-time assessment of pharmaceutical dissolution testing in comparison to off-line HPLC analysis. *RSC Adv.* **2021**, *11*, 31855–31864. [CrossRef]
9. Altura, B.M.; Altura, B.T. Role of Magnesium and Calcium in Alcohol-Induced Hypertension and Strokes as Probed by In Vivo Television Microscopy, Digital Image Microscopy, Optical Spectroscopy, 31P-NMR, Spectroscopy and a Unique Magnesium Ion-Selective Electrode. *Alcohol. Clin. Exp. Res.* **1994**, *18*, 1057–1068. [CrossRef]
10. Law, A.T.; Adeloju, S.B. Progress and recent advances in phosphate sensors: A review. *Talanta* **2013**, *114*, 191–203. [CrossRef] [PubMed]
11. Zeitoun, R.; Biswas, A. Potentiometric Determination of Phosphate Using Cobalt: A Review. *J. Electrochem. Soc.* **2020**, *167*, 127507. [CrossRef]
12. Nie, H.; Yao, Z.; Zhou, X.; Yang, Z.; Huang, S. Nonenzymatic electrochemical detection of glucose using well-distributed nickel nanoparticles on straight multi-walled carbon nanotubes. *Biosens. Bioelectron.* **2011**, *30*, 28–34. [CrossRef] [PubMed]
13. Meng, L.; Jin, J.; Yang, G.; Lu, T.; Zhang, H.; Cai, C. Nonenzymatic Electrochemical Detection of Glucose Based on Palladium−Single-Walled Carbon Nanotube Hybrid Nanostructures. *Anal. Chem.* **2009**, *81*, 7271–7280. [CrossRef]
14. Benjamin, M.; Manoj, D.; Thenmozhi, K.; Bhagat, P.R.; Saravanakumar, D.; Senthilkumar, S. A bioinspired ionic liquid tagged cobalt-salophen complex for nonenzymatic detection of glucose. *Biosens. Bioelectron.* **2017**, *91*, 380–387. [CrossRef]
15. Yhobu, Z.; Brinda, K.N.; Achar, G.; Małecki, J.G.; Keri, R.S.; Nagaraju, D.H.; Budagumpi, S. Glucose electrocatalysts derived from mono- or dicarbene coordinated nickel(II) complexes and their mesoporous carbon composites. *Appl. Organomet. Chem.* **2021**, *35*, e6446. [CrossRef]
16. Jeon, J.S.; Yu, I.K.; Kim, W.; Choi, S.-H. Electrocatalytic Oxidation of Methanol by a Polymeric Ni Complex-modified Electrode Prepared by a One-step Cold-Plasma Process. *Front. Chem.* **2020**, *8*, 595616. [CrossRef] [PubMed]
17. Naseri, M.; Fotouhi, L.; Ehsani, A. Recent Progress in the Development of Conducting Polymer-Based Nanocomposites for Electrochemical Biosensors Applications: A Mini-Review. *Chem. Rec.* **2018**, *18*, 599–618. [CrossRef] [PubMed]
18. El-Said, W.A.; Abdelshakour, A.; Choi, J.-H.; Choi, J.-W. Application of Conducting Polymer Nanostructures to Electrochemical Biosensors. *Molecules* **2020**, *25*, 307. [CrossRef] [PubMed]
19. Das, T.K.; Prusty, S. Review on Conducting Polymers and Their Applications. *Polym. Plast. Technol. Eng.* **2012**, *51*, 1487–1500. [CrossRef]
20. Stenger-Smith, J.D. Intrinsically electrically conducting polymers. Synthesis, characterization, and their applications. *Prog. Polym. Sci.* **1998**, *23*, 57–79. [CrossRef]
21. Epstein, A.J. Electrically Conducting Polymers: Science and Technology. *MRS Bull.* **1997**, *22*, 16–23. [CrossRef]
22. Svirskis, D.; Travas-Sejdic, J.; Rodgers, A.; Garg, S. Electrochemically controlled drug delivery based on intrinsically conducting polymers. *J. Control. Release* **2010**, *146*, 6–15. [CrossRef]
23. Otero, T.F.; Martinez, V.; Arias-Pardilla, J. Biomimetic electrochemistry from conducting polymers. A review Artificial muscles, smart membranes, smart drug delivery and computer/neuron interfaces. *Electrochim. Acta* **2012**, *84*, 112–128. [CrossRef]
24. Guo, B.; Ma, P.X. Conducting Polymers for Tissue Engineering. *Biomacromolecules* **2018**, *19*, 1764–1782. [CrossRef] [PubMed]
25. Wong, J.Y.; Langer, R.; Ingverg, D.E. Electrically conducting polymers can noninvasively control the shape and growth of mammalian cells. *Proc. Natl. Acad. Sci. USA* **1994**, *91*, 3201–3204. [CrossRef] [PubMed]
26. Adeloju, S.B.; Wallace, G.G. Conducting Polymers and the Bioanalytical Sciences: New Tools for Biomolecular Communications-A Review. *Analyst* **1996**, *121*, 699–703. [CrossRef]
27. Park, Y.; Jung, J.; Chang, M. Research Progress on Conducting Polymer-Based Biomedical Applications. *Appl. Sci.* **2019**, *9*, 1070. [CrossRef]
28. Hackett, A.J.; Malmström, J.; Travas-Sejdic, J. Functionalization of conducting polymers for biointerface applications. *Prog. Polym. Sci.* **2017**, *70*, 18–33. [CrossRef]
29. Bhattacharyaa, A.; Misra, B.N. Grafting: A versatile means to modify polymers Techniques, factors and applications. *Prog. Polym. Sci.* **2004**, *29*, 767–814. [CrossRef]
30. Czerwiec, T.; Renevier, N.; Michel, H. Low-temperature plasma-assisted nitriding. *Surf. Coat. Technol.* **2000**, *131*, 267–277. [CrossRef]
31. Foest, R.; Schmidt, M.; Becker, K. Microplasmas, an emerging field of low-temperature plasma science and technology. *Int. J. Mass Spectrom.* **2006**, *248*, 87–102. [CrossRef]
32. Fu, W.; Zhang, C.; Nie, C.; Li, X.; Yan, Y. A high efficiency low-temperature microwave-driven atmospheric pressure plasma jet. *Appl. Phys. Lett.* **2019**, *114*, 254106. [CrossRef]
33. Zeghioud, H.; Assadi, A.A.; Khellaf, N.; Djelal, H.; Amrane, A.; Rtimi, S. Photocatalytic Performance of CuxO/TiO_2 Deposited by HiPIMS on Polyester under Visible Light LEDs:Oxidants, Ions Effect, and Reactive Oxygen Species Investigation. *Materials* **2019**, *12*, 412. [CrossRef]
34. Bui, Q.T.; Yu, I.-K.; Gopalan, A.I.; Gopalan, S.A.; Gopalan, S.; Kim, W.; Choi, S.-H. Facile Fabrication of Metal Oxide Catalytic Electrodes by AC Plasma Deposition and Electrochemical Detection of Hydrogen Peroxide. *Catalysts* **2019**, *9*, 888. [CrossRef]
35. Tran, H.D.; D'Arcy, J.M.; Wang, Y.; Beltramo, P.J.; Strong, V.A.; Kaner, R.B. The oxidation of aniline to produce "polyaniline": A process yielding many different nanoscale structures. *J. Mater. Chem.* **2011**, *21*, 3534–3550. [CrossRef]

36. Lapkowski, M.; Berrada, K.; Quillard, S.; Louarn, G.; Lefrant, S.; Pron, A. Electrochemical Oxidation of Polyaniline in Nonaqueous Electrolytes: "In Situ" Raman Spectroscopic Studies. *Macromolecules* **1995**, *28*, 1233–1238. [CrossRef]
37. Zeghioud, H.; Lamouri, S.; Safidine, Z.; Belbachir, M. Chemical synthesis and characterization of highly soluble conducting polyaniline in mixtures of common solvents. *J. Serb. Chem. Soc.* **2015**, *80*, 917–931. [CrossRef]
38. Jiang, Z.; Jiang, Z.; Yu, X.; Meng, Y. Preparation of Proton Exchange Membranes by a Plasma Polymerization Method and Application in Direct Methanol Fuel Cells (DMFCs). *Plasma Processes Polym.* **2010**, *7*, 382–389. [CrossRef]
39. Choukourov, A.; Biederman, H.; Slavinska, D.; Hanley, L.; Grinevich, A.; Boldyryeva, H.; Mackova, A. Mechanistic Studies of Plasma Polymerization of Allylamine. *J. Phys. Chem. B* **2005**, *109*, 23086–23095. [CrossRef] [PubMed]
40. Cech, V.; Studynka, J.; Janos, F.; Perina, V. Influence of Oxygen on the ChemicalStructure of Plasma Polymer Films Deposited from a Mixture of Tetravinylsilane and Oxygen Gas. *Plasma Processes Polym.* **2007**, *4*, S776–S780. [CrossRef]

catalysts

MDPI

Article

Iron Phosphide Precatalyst for Electrocatalytic Degradation of Rhodamine B Dye and Removal of *Escherichia coli* from Simulated Wastewater

Takwa Chouki [1], Manel Machreki [1], Jelena Topić [2], Lorena Butinar [3], Plamen Stefanov [4], Erika Jez [3], Jack S. Summers [5], Matjaz Valant [1], Aaron Fait [6] and Saim Emin [1,*]

[1] Materials Research Laboratory, University of Nova Gorica, 5270 Ajdovscina, Slovenia; takwa.chouki@student.ung.si (T.C.); manel.machreki@student.ung.si (M.M.); matjaz.valant@ung.si (M.V.)
[2] Laboratory for Environmental and Life Sciences, University of Nova Gorica, 5000 Nova Gorica, Slovenia; jelena.topic@ung.si
[3] Wine Research Centre, University of Nova Gorica, Glavni Trg 8, 5271 Vipava, Slovenia; lorena.butinar@ung.si (L.B.); erika.jez@ung.si (E.J.)
[4] Institute of General and Inorganic Chemistry, Bulgarian Academy of Sciences, 1113 Sofia, Bulgaria; stefanov@svr.igic.bas.bg
[5] Department of Chemistry and Physics, Western Carolina University, Cullowhee, NC 28723, USA; summers@email.wcu.edu
[6] The Jacob Blaustein Institutes for Desert Research, Ben-Gurion University of the Negev, Midreshet Ben-Gurion 84990, Israel; aaron.fait@gmail.com
* Correspondence: saim.emin@ung.si; Tel.: +386-5-365-35-38

Citation: Chouki, T.; Machreki, M.; Topić, J.; Butinar, L.; Stefanov, P.; Jez, E.; Summers, J.S.; Valant, M.; Fait, A.; Emin, S. Iron Phosphide Precatalyst for Electrocatalytic Degradation of Rhodamine B Dye and Removal of *Escherichia coli* from Simulated Wastewater. *Catalysts* **2022**, *12*, 269. https://doi.org/10.3390/catal12030269

Academic Editors: Marc Cretin, Sophie Tingry and Zhenghua Tang

Received: 19 January 2022
Accepted: 21 February 2022
Published: 28 February 2022

Publisher's Note: MDPI stays neutral with regard to jurisdictional claims in published maps and institutional affiliations.

Abstract: Electrocatalysis using low-cost materials is a promising, economical strategy for remediation of water contaminated with organic chemicals and microorganisms. Here, we report the use of iron phosphide (Fe_2P) precatalyst for electrocatalytic water oxidation; degradation of a representative aromatic hydrocarbon, the dye rhodamine B (RhB); and inactivation of *Escherichia coli* (*E. coli*) bacteria. It was found that during anodic oxidation, the Fe_2P phase was converted to iron phosphate phase (Fe_2P-iron phosphate). This is the first report that Fe_2P precatalyst can efficiently catalyze electrooxidation of an organic molecule and inactivate microorganisms in aqueous media. Using a thin film of Fe_2P precatalyst, we achieved 98% RhB degradation efficiency and 100% *E. coli* inactivation under an applied bias of 2.0 V vs. reversible hydrogen electrode in the presence of in situ generated reactive chlorine species. Recycling test revealed that Fe_2P precatalyst exhibits excellent activity and reproducibility during degradation of RhB. High-performance liquid chromatography with UV-Vis detection further confirmed the electrocatalytic (EC) degradation of the dye. Finally, in tests using *Lepidium sativum* L., EC-treated RhB solutions showed significantly diminished phytotoxicity when compared to untreated RhB. These findings suggest that Fe_2P-iron phosphate electrocatalyst could be an effective water remediation agent.

Keywords: Fe_2P-iron phosphate; electrocatalysis; rhodamine B; *Escherichia coli*; reactive chlorine species

1. Introduction

Electrochemical oxidation has emerged as a promising means of eliminating contaminants from water [1]. The growing presence in wastewaters of organic pollutants such as pharmaceuticals, pesticides and dyes has become a major concern, as has the presence of heavy metals and pathogenic microorganisms. Removal of these substances is complex and energy-inefficient [2–7]. Anodic oxidation of organics at electrode surfaces is one set of methods for removing these contaminants [8,9]. Direct oxidation occurs by electron transfer between the substrate molecule and the electrode surface [9,10], whereas indirect oxidation involves the generation of reactive oxygen species (ROS) or reactive chlorine species (RCS).

ROS include hydroxyl radicals (•OH), hydrogen peroxide (H_2O_2) and ozone (O_3). RCS include chlorine (Cl_2), hypochlorous acid (HClO), chlorate (ClO^-) and chlorine radicals (Cl• or $Cl_2^{\bullet -}$) [11–13]. RCS such as Cl_2 and HClO have been shown to be effective in the degradation of alcohols [11], carboxylic acids [14], dyes [15], pharmaceuticals [16] and tannery effluents [17] and for inactivation of microorganisms [18]. During the process of RCS generation, oxidation of Cl^- ions yields Cl_2, which is stable in acidic medium (pH < 3.3) or hydrolyzes to HClO (3.3 < pH < 7.5) and ClO^- ion (pH > 7.5) [11]. The standard potential for the Cl_2 evolution (Cl^-/Cl_2 1.36 V vs. normal hydrogen electrode (NHE)) is relatively low, making it an attractive option for efficient electrochemical wastewater treatment [19].

Electrochemical oxidation of organics usually allows the oxidation of pollutants to H_2O and CO_2. This approach is often used for remediation of organics, including dye molecules such as methylene blue [20], rhodamine B (RhB) [21] and methyl orange [20]. RhB removal from wastewater is particularly important due to its toxicity and carcinogenic effects [21].

The application of the electrocatalytic (EC) process for water disinfection has been investigated as well [22,23]. In water recycling, water disinfection constitutes the final crucial step, which represents the last barrier against harmful microorganisms [23,24]. Disinfection is necessary to remove harmful bacteria present in wastewater. These bacteria include *Salmonella* [25], *Escherichia coli* (*E. coli*) [26], *Pseudomonas aeruginosa* [18] and *Enterococcus faecalis* [27]. *E. coli* is the preferred indicator for fecal contamination in drinking water [28].

Materials such as platinum (Pt) [26,29], iridium oxide (IrO_2) [30], titanium dioxide (TiO_2) [31,32], tin dioxide (SnO_2) [15,21,32], boron-doped diamond (BDD) [21,33] and dimensionally stable anodes (Ti/TiO_2-RuO_2, Ti/RuO_2-IrO_2) [15,34] have already been employed as electrocatalysts for RhB dye degradation and *E. coli* inactivation. Available evidence indicates that Pt and IrO_2 are efficient catalysts for oxidation of Cl^- ions that exhibit low-onset potential (~1.42 V) for Cl_2 evolution [35]. However, their widespread application is unfeasible since these materials are scarce and costly [36]. Other, less expensive materials, such as TiO_2, SnO_2 and BDD, are inefficient electrocatalysts since they require high overpotential for Cl_2 evolution [19].

Transition metal phosphides (TMPs) such as iron phosphide, copper phosphide, cobalt phosphide and nickel phosphide [37,38] and transition metal phosphates (TMPHs) made of cobalt phosphate, nickel phosphate, manganese phosphate, iron phosphate, etc., have emerged as promising alternatives to the noble metal catalysts (e.g., Pt) for electrochemical water splitting [38,39]. TMPs and TMPHs show great promise as catalysts since they are made of abundant elements and offer high catalytic activity [38]. For example, Fe_2P was demonstrated to deliver 10 mA cm^{-2} at an overpotential of 290 mV vs. RHE to drive O_2 evolution reaction (OER) in 1 M KOH [40]. On the other side, TMPH made of nickel-iron hydroxylphosphate (NiFe-OH-PO_4) was shown to deliver a current density of 20 mA cm^{-2} at an overpotential of 249 mV for OER [41]. In addition to OER studies, TMP made of ternary NiCoFe phosphide was demonstrated as a suitable catalyst for oxidation of Cl^- ions to Cl_2 gas [42]. The latter ability of TMPs can be used as an effective strategy in wastewater treatment where Cl^- ions are present. Although TMPs are studied extensively, there are still unclear points associated with their stabilities observed during the water electrolysis experiments. The majority of the published articles on the use of TMPs in OER studies demonstrate the formation of a thin metal phosphate or metal oxide/hydroxide layer after the water electrolysis tests [38,43,44]. Often, the conclusion about the state of catalyst is drawn using techniques such as energy-dispersive X-ray spectroscopy or surface sensitive techniques such as X-ray photoelectron spectroscopy. However, to properly address possible phase conversions, the use of X-ray diffraction is also needed in addition to the above-mentioned techniques.

In the present study, Fe_2P transformed into iron phosphate during electrocatalytic degradation of RhB dye and inactivation of *E. coli* bacteria. Since the phase is not well defined, it is abbreviated as Fe_2P-iron phosphate. To our knowledge, Fe_2P-iron phosphate

electrocatalysts have never been applied for the degradation of organics and disinfection of water. First, we synthesized colloidal Fe_2P nanoparticles (NPs) using a solvothermal approach, followed by spin-coating titanium (Ti) substrates with Fe_2P. To activate the Fe_2P catalyst, a short heat treatment at 450 °C was carried out. The role of heat treatment is two-fold: first, to activate the catalyst by removal of organic capping molecules; second, to improve the adhesion of the catalyst onto the substrate [45]. The degradation of RhB was monitored using UV-Vis spectroscopy and high-performance liquid chromatography (HPLC) with spectroscopic monitoring. The inactivation of *E. coli* was monitored by plating bacteria suspension onto a medium after the treatment. Bacterial regrowth experiments and enumeration confirmed the rapid and complete inactivation of *E. coli*. Recycling test and linear sweep voltammetry revealed that Fe_2P-iron phosphate electrode exhibits excellent reproducibility. The catalysts were characterized using scanning electron microscopy (SEM), transmission electron microscopy (TEM), X-ray photoemission spectroscopy (XPS) and X-ray diffraction (XRD), along with other suitable electrochemical techniques.

2. Results and Discussion

2.1. Characterization of Fe_2P Thin Films

XRD diffractogram of the sample taken before heat treatment revealed that Fe_2P is its sole constituent (Figure 1a). The intense diffraction peaks at 40.37, 44.30 and 52.91° correspond to (111), (201) and (002) crystallographic planes of the hexagonal Fe_2P ($P\bar{6}2m$, PDF # 1008826). The calculated crystal lattice parameters are in good agreement with the literature data for hexagonal Fe_2P ($a = b = 5.851 \pm 0.0034$ Å, and $c = 3.507 \pm 0.0026$ Å) [46]. The crystallite size and the intrinsic strain calculated using the Williamson−Hall (W−H) method yielded an average size of 18 ± 0.0010 nm and $4.5 \times 10^{-3} \pm 0.0007$ a.u., respectively (Text S1, Figure S1). The reliability of the refined fit was assessed by the weighted profile (R_{wp}) and Bragg (R_b) factor values that, at $R_{wp} = 4.23\%$ and $R_b = 4.11\%$, met the established criteria ($R_{wp} < 20\%$) for good refinement [47]. The XRD pattern of the Fe_2P catalyst (Figure S2) after the heating procedure (450 °C) was almost identical to that recorded for the initially synthesized Fe_2P NPs. This result confirms that the stoichiometry and crystal structure were unchanged by the procedure.

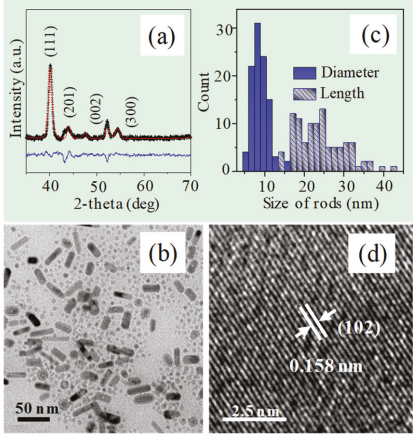

Figure 1. (**a**) XRD pattern of Fe_2P with a Rietveld refinement fit. (**b**) TEM image of Fe_2P NPs. (**c**) Size distribution plots of Fe_2P NRs taken from (**b**). (**d**) HR-TEM image taken from an individual Fe_2P NP.

TEM studies revealed that the obtained Fe_2P sample contained two morphologies: nanospheres (NSs) and nanorods (NRs) (Figure 1b). The nanosphere Fe_2P had a uniform diameter (about 5 ± 0.1 nm on average, as shown in Figure S3), while Fe_2P NRs varied in size (reaching 8.79 ± 0.03 nm in diameter and 23 ± 0.98 nm in length on average, as shown

in Figure 1c). HR-TEM studies indicated that the lattice spacing of 0.158 nm corresponds to the (102) crystal plane of hexagonal Fe_2P (Figure 1d).

We studied the morphology of the obtained Fe_2P thin film using SEM. As seen in Figure 2a,b, the morphology of Fe_2P thin film contains large aggregates and densely packed NPs. An SEM image taken at high magnification shows that the diameter of Fe_2P particles is on the order of 200 nm (Figure 2c). The thickness of the resulting Fe_2P film, as determined from the cross-section SEM image, is about ~2 µm (Figure 2d). EDS analysis combined with elemental maps for Fe and P confirmed that these agglomerates were made of iron phosphide and that the stoichiometric ratio of Fe:P elements is 2:1 (Figure 2e−i).

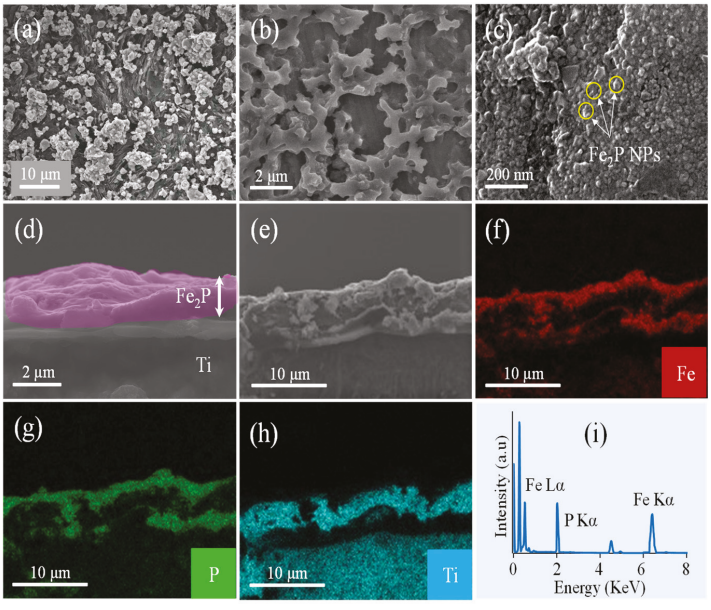

Figure 2. SEM images of Fe_2P thin film at different magnifications in (**a**–**c**) top views and in (**d**) cross-sectional view. (**f**–**h**) Images with elemental maps are given for Fe, P and Ti, taken from the Fe_2P sample shown in (**e**). (**i**) EDS spectrum recorded from the image in (**e**).

2.2. Electrochemical Studies

The catalytic activity of Fe_2P films was studied using linear sweep voltammetry (LSV). Figure 3a shows liner sweep voltammograms of Fe_2P film recorded in four electrolytes (0.06 M), namely NaCl, NH_4Cl, Na_2SO_4 and NaOH. In each case, the recorded onset potential for Faradaic processes is close to ~1.7 V vs. RHE. The current in Na_2SO_4 and NaOH electrolytes is lower due to the dominating O_2 evolution reaction [48]. However, in the presence of NaCl and NH_4Cl electrolytes, O_2 evolution at the anode competes with oxidation of Cl^- ions leading to Cl_2. We also performed an LSV study with the Fe_2P catalyst in 10^{-5} M RhB solution (0.06 M NaCl) before the heat treatment experiment (Figure S4). We found that the current density is insufficiently low (0.05 mA cm^{-2} at 2 V vs. RHE) compared to that after the heating procedure at 450 °C. The goal behind this heat treatment was to remove the organics that act as an insulating layer between the iron phosphide catalyst and the electrolyte [45]. The slopes of Tafel plots (plots of potential versus logarithm of current) are useful for interpreting polarization curves [45]. We found that the Tafel slopes obtained for Fe_2P depended on the electrolyte. In solutions containing 0.06 M electrolyte, the Tafel slopes were 144 (NaCl), 218 (NH_4Cl), 227 (NaOH) and 245 (Na_2SO_4) mV dec^{-1} (Figure S5a). Since lower Tafel slope correlates with higher catalyst activity, this result is consistent with oxidation occurring fastest in NaCl solution (Text S2). Interfacial charge-transfer kinetics on

Fe_2P were analyzed using EIS measurements. This analysis showed that the charge transfer resistance (R_{ct}) was low at high bias voltages, indicating fast charge-transfer kinetics during water oxidation reaction (R_{ct} < 40 ohm cm^2) [49]. A Nyquist plot and a discussion of the relevant circuit and its analysis are presented in the supplemental section (Figure S5c). The electrochemically active surface area (ECSA) of the initial Fe_2P film was determined from the CVs obtained in 1 M KOH (pH 14) (Figure S6) [50]. The calculated ECSA value of 0.6 cm^2 exceeded the 0.3 cm^2 geometric area (assuming a flat surface). The details of the calculation are described in Text S3.

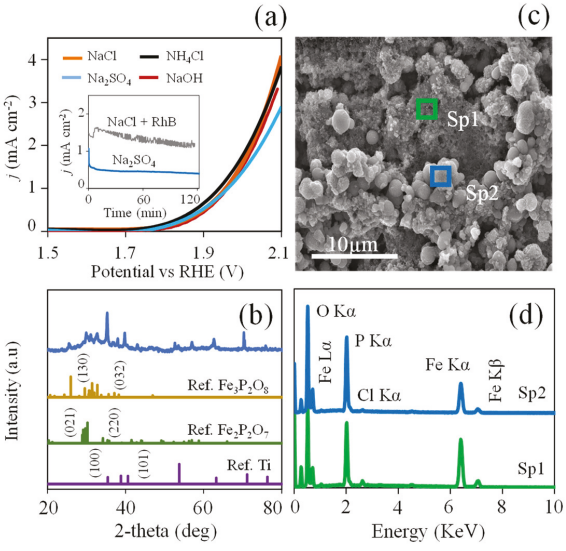

Figure 3. (**a**) LSV of Fe_2P catalyst in 0.06 M NaCl, NH_4Cl, NaOH and Na_2SO_4 at pH 5. The inset in (**a**) is the *I-t* plot obtained for different electrolytes with and without 1×10^{-5} M RhB at 2.0 V vs. RHE. (**b**) XRD pattern of Fe_2P film after the electrolysis. References are given with labels. (**c**) SEM image of Fe_2P after electolysis (Cl^- system). (**d**) EDS spectra recorded from the image in (**c**).

Chronoamperometric (*I-t*) experiments demonstrated that the Fe_2P precatalyst satisfactorily retained the initial current level during the 2 h test time. These tests were conducted in 0.06 M Na_2SO_4 and in 0.06 M NaCl with 10^{-5} M RhB at an applied bias of 2.0 V vs. RHE (inset in Figure 3a). In 10^{-5} M RhB solution, we observed a slight decrease in current level from 1.5 to 1.3 mA cm^{-2} during the initial 40 min. However, the current level stabilized later. After the electrolysis, the film was studied using XRD (Figure 3b). Although there is an insignificant change in the current level during electrolysis, the XRD shows clearly the transformation of Fe_2P phase into iron phosphate phase (mixture of $Fe_2P_2O_7$ (PDF # 2300034) and $Fe_3P_2O_8$ (PDF # 2300033)). The obtained iron phosphate phase is composed of two phosphate phases, but we believe that a uniform single phase may occur after a sufficiently long electrolysis time. In addition to the XRD study, we also performed point EDS measurements from the image given in Figure 3c after the EC degradation of RhB in 0.06 M NaCl (Figure 3d). EDS analysis confirmed that the atomic ratio of Fe:P is equal to 1.8:1 (Sp1). However, when we recorded spectrum 2 (Sp2), we noticed that the atomic ratio of Fe:P is equal to 1.4:1. In both spectra, we observed some additional peaks such as oxygen and Cl^- ions. Images with elemental maps for Fe, P, Cl, O and C taken from the Fe_2P sample (after electrolysis) are provided in Figure S7. The low-intensity peak of Cl^- ions indicates that these are adsorbed on the Fe_2P surface in minor quantities (0.6 at.% $\geq$). The intense peak of oxygen confirms the formation of iron phosphate phase. From the obtained data, we concluded that a large amount of Fe_2P film was converted to iron phosphate. The

amount of metal phosphate obtained exceeds that reported in other systems where it was claimed that phase conversion occurs only on a few atomic surface layers [38,51].

2.3. RhB Dye Degradation Studies

The activity of the Fe_2P-iron phosphate thin film as an anode material for organic molecule degradation was studied by monitoring its effect on the absorbance spectra of a solution of RhB dye. As shown in Figure 4a, the 550 nm absorption peak of RhB was completely degraded to baseline in 40 min in 0.06 M NH_4Cl (pH 5). The degradation is much faster in 0.06 M NaCl, being complete in under 2 min (a magnified region of RhB degradation in 0.06 M NaCl is shown in Figure S8). The slower degradation rate in NH_4Cl electrolyte is attributed to ammonium cation (NH_4^+) oxidation which competes with Cl^- oxidation [52]. Pérez et al. (2012) showed that NH_4^+ degrades to N_2 and nitrate (NO_3^-) in reactions with oxidizing chlorine species [52] (Equations (1) and (2)):

$$2/3\ NH_4^+ + HClO \rightarrow 1/3\ N_2 + H_2O + 5/3\ H^+ + Cl^- \quad (1)$$

$$NH_4^+ + 4\ HClO \rightarrow NO_3^- + H_2O + 6H^+ + 4\ Cl^- \quad (2)$$

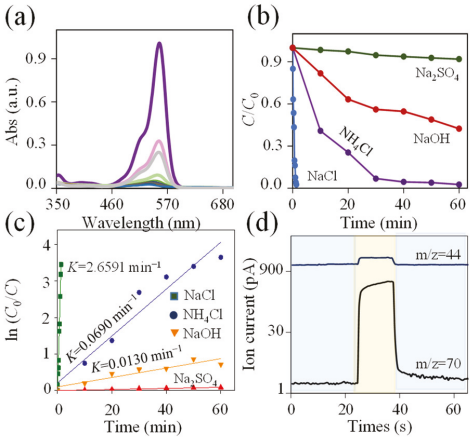

Figure 4. (**a**) Time-dependent absorption spectra of RhB in 0.06 M NH_4Cl. (**b**) C/C_0 vs. time in different electrolytes at 2.0 V vs. RHE. (**c**) Pseudo-first-order degradation kinetics of RhB in different electrolytes at 2.0 V vs. RHE. (**d**) Ionic current vs. time detected using mass spectrometry.

When Na_2SO_4 and NaOH (pH 5) were used as electrolytes, RhB dye degradation was negligible (Figure 4b). What degradation does occur is ascribed to the formation of $SO_4^{\bullet-}$ and •OH species. However, it is well known that in an acidic environment $SO_4^{\bullet-}$ radicals are less effective than •OH radicals which favorably form in alkaline solutions [53]. In acidic media at pH 5, the generation of •OH is assumed to occur unfavorably. AlHamedi et al. (2009) demonstrated that •OH reacts with SO_4^{2-} ions, as shown in the following reaction:

$$SO_4^{2-} + \bullet OH \rightarrow SO_4^{\bullet-} + OH^- \quad (3)$$

As a control experiment, we assessed the catalytic activity of pure Ti substrate in 0.06 M NaCl. In the absence of Fe_2P-iron phosphate, the bare Ti produced indistinct RhB dye degradation (Figure S8). We also investigated the kinetics of Fe_2P-iron phosphate catalyzed RhB oxidation. The RhB dye decomposition rate, presented in the form of degradation efficiency (D), was calculated using the following equation: $D\ (\%) = ((C_0 - C_t)/C_0) \times 100$, where C_0 is the initial concentration (t = 0 min) and C_t is the concentration at a defined reaction time point [54]. The highest D value (equivalent to 98%) was achieved in 0.06 M

NaCl within 1.3 min (Figure S9). The change in RhB dye concentration was assessed by a pseudo-first-order kinetic model: $\ln(C_0/C) = k_1 t$, where C and C_0 are the RhB dye concentrations at time t and time zero, respectively, and k_1 is the pseudo-first-order rate constant calculated from the slope of the straight line (Text S4, Table S1) [55]. Our results are in good agreement with other published studies of electrochemical RhB degradation [15]. As shown in Figure 4c, the highest $k_1 = 2.6591\ \text{min}^{-1}$ was obtained with NaCl electrolyte. This larger k value indicates that RhB dye degraded about 1772 times faster than in Na_2SO_4 ($k_1 = 0.0015\ \text{min}^{-1}$) and 204 times faster than in NaOH electrolyte ($k_1 = 0.0130\ \text{min}^{-1}$). Here, the obtained k_1 constants in Cl^--containing electrolytes using Fe_2P-iron phosphate are higher than on other anode materials reported in earlier electrochemical studies. For example, using Ti/RuO_2–IrO_2 catalyst during RhB dye degradation under EC condition yielded $k_1 = 0.079\ \text{min}^{-1}$ [15].

Coumarin was used as a probe molecule to determine whether •OH radicals participate in RhB degradation in chloride solutions (Text S5). This molecule reacts with •OH radicals to form a highly fluorescent product called 7-HC which has a peak at ~456 nm [56]. The absence of a 7-HC emission peak suggests that •OH radicals are suppressed in NaCl electrolyte (Figure S10) [11]. Results of the experiments described above suggest that EC degradation of RhB occurs via an indirect oxidation mechanism in which RCS, but not ROS, play a crucial role [57]. To further test this hypothesis, we measured the evolution of in situ generated Cl_2 using the DPD colorimetric method [58]. In the presence of Cl_2, DPD is oxidized to a radical cation ($DPD^{\bullet+}$) with an absorption peak at 515 nm [59]. In these experiments, we observed the growth of the 515 nm peak, further supporting the proposal that RCS participate in RhB degradation (Figure S11). The results are consistent with the EC-chlorine system where HClO plays an essential role during the degradation of RhB [30,60]. In a similar way, Baddouh et al. (2018) have previously demonstrated the electrooxidation of Cl^- to HClO at Ti/RuO_2–IrO_2 anode. At pH 5, HClO is expected to be the dominant form of RCS [58].

To further confirm RCS participation in the electrochemical degradation of RhB, we monitored the evolution of Cl_2 using mass spectrometry (MS) (Figure 4d). The sudden rise in ionic current at 25 s indicates the presence of fragment ions with the mass-to-charge ratio (m/z) for Cl_2 and CO_2 equal to 70 and 44, respectively. Here, CO_2 is produced from RhB degradation during the electrocatalytic oxidation process. On the counter electrode, the H_2 gas is evolved (Figure S12).

Further support for our hypothesis that HClO participates in RhB degradation comes from chemical oxidation studies with NaOCl (Figure 5). We found that complete dye decolorization was achieved using ~0.4 mM NaOCl. This result further supports the hypothesis that RhB decolorization in EC mode is mainly conducted by the generated HClO species (the RhB degradation mechanism is discussed in detail in Text S6). Under potentiostatic conditions (at 2.0 V vs. RHE) during the 4 min reaction process in 0.06 M NaCl, the amount of measured HClO is estimated as 2.5 mg L^{-1} (Figure S11), which corresponds to a current to HClO conversion efficiency of 73.7% (Text S7).

As indicated in studies of EC-mediated azo dye degradation, applied potential can significantly influence the degradation efficiency [5]. Herein, we studied RhB degradation in 0.06 M NaCl at three bias potentials (1.8, 1.9 and 2.0 V vs. RHE, Figure 6a). In this experiment, > 97% degradation was observed in 1.3 min at 2.0 V and in 20 min at 1.9 V (voltage vs. RHE). In contrast, at an applied potential of 1.8 V, 56% efficiency was achieved in 20 min (Figure S9b). Thus, higher potentials give rise to fast oxidation of Cl^- to RCS, leading to rapid dye degradation.

We evaluated the stability of the Fe_2P-iron phosphate film against corrosion under conditions of the EC reaction by performing an experiment where a single Fe_2P-iron phosphate film was used to degrade multiple samples of RhB. Figure 6b shows the result of this recycling test for RhB degradation at 1.9 V vs. RHE bias potential in 0.06 M NaCl. The data in Figure 6b reveal over 97% RhB degradation efficiency for each of the four runs,

confirming the stability of Fe_2P-iron phosphate thin film against corrosion and the potential for its reuse in EC studies.

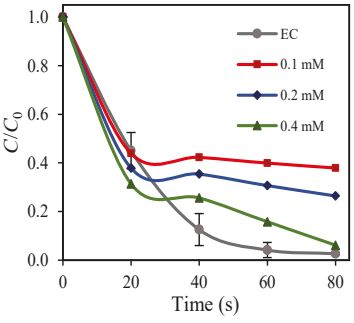

Figure 5. Comparison of RhB degradation in the EC system under 0.06 M NaCl vs. chemical oxidation at different NaOCl concentrations.

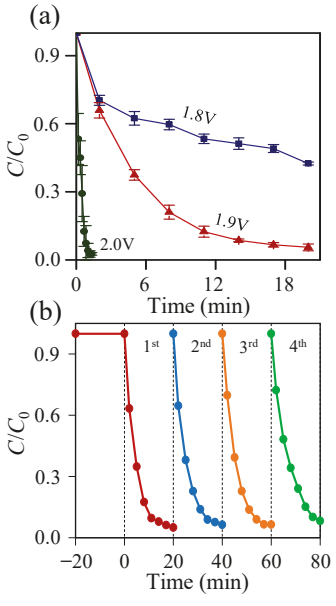

Figure 6. (**a**) C/C_0 vs. time during EC degradation of RhB over Fe_2P-iron phosphate at different applied potentials in 0.06 M NaCl. (**b**) Recycling test for EC degradation of RhB over Fe_2P-iron phosphate in 0.06 M NaCl at 1.9 V vs. RHE.

The stability of the Fe_2P-iron phosphate films was further validated by LSV characterization of films before and after the reusability tests. We characterized the electrochemical activity of the film by LSV and the surface morphology by SEM (Figure S13). The LSV measurements revealed a slight increase in current after the stability test. The SEM measurements showed that film morphology was unaltered by the EC process. Both these results confirm the adequacy and compatibility of this electrode in EC wastewater treatment.

The composition and chemical state of Fe_2P thin film were characterized by XPS. As with the characterization studies described above, we measured XPS data before and after exposing the Fe_2P film to EC conditions. The spectrum of the Fe_2P electrode before RhB degradation is shown in Figure 7a. Selected regions of the XPS spectra recorded before and

after RhB degradation are shown in Figure 7b–d. The photoelectron Fe 2p peaks exhibit a doublet at 711.0 eV (Fe $2p_{3/2}$) and 724.0 eV (Fe $2p_{1/2}$) due to spin–orbit splitting. A less intense peak is also observed at 713.5 eV. These peaks can be attributed to the formation of iron(III) phosphate on the Fe_2P surface [61]. The P 2p spectrum displays two peaks with 133.0 and 134.0 eV binding energies, which are attributed to P $2p_{3/2}$ and P $2p_{1/2}$ levels of P in the Fe_2P [61]. The peak at 133 eV can be assigned to P-C binding [62]. Because the surface oxidation of the Fe_2P particles is unavoidable, the peak at 134.0 eV has been observed for phosphorus in a high oxidation state and refers to surface-oxidized P species [61]. These findings suggest that these species can also be assigned to the formation of a thin iron phosphate layer. To gain a better understanding of Fe_2P catalyst stability, we also recorded XPS spectra after the EC degradation of RhB dye (Figure 7). The intensities of the XPS core-level spectra of Fe 2p and P 2p greatly decreased after the test. Moreover, an intense peak formed at 201.5 eV and was attributed to the Cl 2p core-level emission (Figure 7d). These results confirm that, during EC degradation, Cl^- ions are strongly adsorbed on the Fe_2P surface. Moreover, the large amount of chloride ions adsorbed on the surface attenuates the signal from Fe_2P, thus markedly decreasing the intensity of the Fe 2p and P 2p peaks. These results are in good agreement with the EDS analysis.

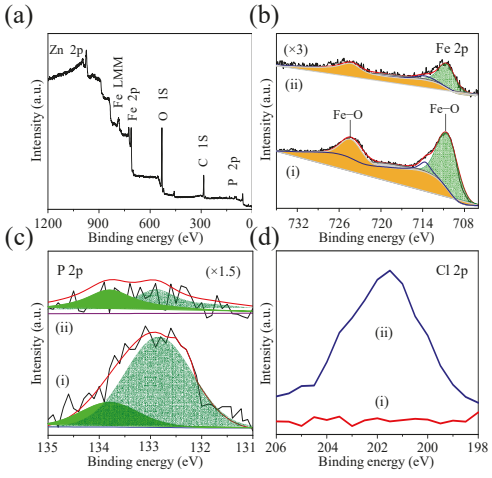

Figure 7. (**a**) XPS survey spectrum of Fe_2P. (**b**–**d**) XPS core-level spectra of Fe 2p, P 2p and Cl 2p recorded (i) before and (ii) after the test.

We employed HPLC to monitor RhB dye degradation. The reference sample of RhB dye produced an apparent peak at 15.0 min elution time (Figure 8). We monitored the disappearance of the RhB absorbance peak (λ = 550 nm) in NaCl, NH_4Cl and Na_2SO_4. As shown in Figure S14, complete degradation was accomplished within 2 min in 0.06 M NaCl and 60 min in 0.06 M NH_4Cl while degradation in 0.06 M Na_2SO_4 remained incomplete after 180 min. Monitoring degradation at multiple detection wavelengths failed to show the appearance of additional peaks in the HPLC chromatograms. This indicates that no degradation by-products with strong absorption in the UV-Vis are formed. From this, we conclude that complete degradation occurs in Cl^--containing electrolytes (Figure 8). The use of HPLC was also motivated by the fact it overcomes the interference of Cl^- ions seen as a bottleneck in other methods such as the total organic carbon and the chemical oxygen demand.

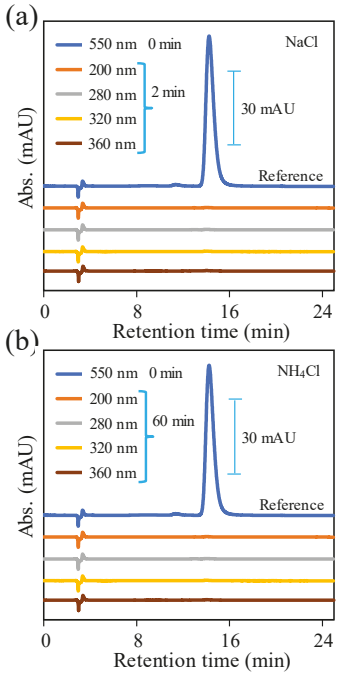

Figure 8. HPLC chromatograms of RhB measured after the EC treatment in (**a**) 0.06 M NaCl after 2 min test with different λ_{det} and (**b**) 0.06 M NH_4Cl measured after 60 min at different λ_{det}, using 1×10^{-5} M RhB aqueous solution as the reference.

In earlier studies related to EC wastewater treatment, chlorate or perchlorate ions were identified as by-products [63]. We note that these by-products were observed when the applied current densities were in the 5–30 mA cm^{-2} range [64]. Consequently, we believe that chlorate formation is less likely under the conditions adopted in our study since the current densities do not exceed 2 mA cm^{-2}. Further, the detection at shorter wavelengths (200 nm) in HPLC demonstrates that intermediates with lower molecular weight (phthalic acid, benzoic acid, α-hydroxyglutaric acid, etc.) which might form during RhB degradation [65] are absent from our reaction medium after the EC treatment process.

2.4. Phytotoxicity Test of RhB and Electrochemical Inactivation of E. coli Bacteria

2.4.1. Phytotoxicity Test of RhB

To assess the quality of EC-treated RhB water solutions, phytotoxicity test was performed using *L. sativum* whereby seed germination index and root growth of *L. sativum* were used to evaluate the phytotoxic effect of RhB in 0.06 M NaCl at pH 5 (Figure S15). Before electrochemical treatment, the germination index for *L. sativum* in RhB solution, 0.06 M NaCl, pH 5 was 75.9%. After electrochemical treatment of this solution, the germination index rose to 84%. Similarly, the average root length increased from 17.7 to 18.9 mm after treatment (Figure 9a). These results show electrochemically treated solutions have little to no phytotoxicity [66] (further details about our phytotoxicity study are provided in Text S8).

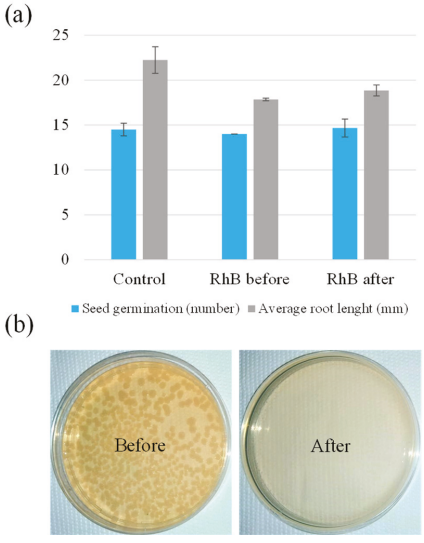

Figure 9. (**a**) Seed germination test for toxicity analysis of RhB solutions. (**b**) Growth of *E. coli* on agar plate before the EC treatment and after 40 min of exposure of *E. coli* to EC treatment.

2.4.2. Electrochemical Inactivation of *E. coli* Bacteria

Inactivation of *E. coli* using the Fe_2P-iron phosphate thin film electrode was investigated in NaCl electrolyte. The catalytic activity of Fe_2P-iron phosphate films was determined using the LSV method. Figure S16a shows LSV characteristics of Fe_2P-iron phosphate film recorded in 0.06 M NaCl (pH 5), with the initial *E. coli* concentration, determined with plating, being 1.1×10^8 CFU/mL. The recorded onset potential is close to 1.7 V vs. RHE. Figure S16b shows the chronoamperometric experiment of Fe_2P-iron phosphate catalyst conducted in 0.06 M NaCl with 1.1×10^8 CFU/mL of *E. coli* at an applied bias of 2.0 V vs. RHE. We observed a decrease in current density during the first 90 min, starting from 0.9 mA cm^{-2}. However, the current density later stabilized and reached a plateau at 0.46 mA cm^{-2}. The activity of the Fe_2P-iron phosphate electrode was further validated by LSV after the stability test (inset in Figure S16a). The LSV measurement revealed a slight decrease in current after the 120 min stability test, which confirms the suitability of this electrode in EC water disinfection. After 40 min of EC exposure at 0.9 mA cm^{-2}, no viable bacteria were detected, indicating 100% disinfecting efficiency in NaCl electrolyte (Figure 9b). However, in comparison to the initial *E. coli* concentration, we observed a 26.7% decline in the control bacterial solution after 160 min incubation in 0.06 M NaCl (pH 5) without EC treatment.

One of the major concerns of electrodisinfection involving active chlorine is the formation of chlorination by-products (ClO_2^- and ClO_3^-). However, it is known that chlorate formation occurs at higher current densities and is less likely to evolve under the conditions (0.9 mA cm^{-2}) adopted in our study [64].

All these results indicate that the EC treatment with Fe_2P-iron phosphate electrodes is a promising alternative procedure compared with other known materials considering the high-efficiency processes for dye degradation (Table S2) and water disinfection (Table S3).

3. Materials and Methods

3.1. Chemicals

The following chemicals were used in this study: oleylamine (70%, OLA), iron pentacarbonyl (99.9%, $Fe(CO)_5$), acetone (95%), ethanol (98%) and potassium hydroxide (97%, KOH), obtained from Sigma-Aldrich; triphenylphosphine (99%, TPP), RhB (≥95%), squa-

lene (98%, SQ), chloroform (99.5%, $CHCl_3$), sodium sulfate (99%, Na_2SO_4), sodium chloride (99%, NaCl), coumarin and sodium hypochlorite (NaOCl), purchased from Alfa Aesar; ammonium chloride (≥99%, NH_4Cl) and 7-hydroxycoumarin (7-HC), acquired from Acros Organics; and a titanium block (99.9%) obtained from Baoji Quanjin Industry & Trade Co., Ltd. (Baoji, China).

3.2. Preparation of Fe_2P Thin Films

Fe_2P was synthesized using TPP precursor adopting the method described by Chouki et al. (2020) [45]. The synthesis procedure and the experimental measurements are described in detail in Text S9 and S10 in Supporting Information (SI).

3.3. E. coli Preparation and Evaluation of Removal Efficiency

One colony from a 2-day-old culture of *E. coli* DSM 489, grown on tryptic soy agar (Fluka), was inoculated into 50 mL liquid tryptone medium (Fluka) in 250 mL Erlenmeyer flask and incubated for 16 h at 37 °C (150 rpm). The culture was centrifuged at 4000 rpm for 10 min, and bacterial cells were washed with filter-sterilized 0.06 M NaCl (pH 5) solution. Bacterial solution was adjusted to O.D. (600 nm) 0.15 and used for electrochemical removal of 1.1×10^8 CFU/mL *E. coli* bacteria in 0.06 M NaCl at an applied bias of 2.0 V vs. RHE.

To evaluate *E. coli* removal efficiency, samples were withdrawn at four different time points with 40 min increment during the EC experiment. The control bacterial suspension without any treatment was also plated at the beginning and at the end of the experiment. Serial dilutions (10-fold) of samples were spread onto plates with the tryptic soy agar (Fluka). Plates were counted after 24 h incubation at 37 °C and bacterial counts were expressed as CFU/mL.

3.4. Phytotoxicity Test Using Lepidium sativum L.

Lepidium sativum L. (L. sativum) was used to assess the acute toxicity of RhB before and after treatment in 0.06 M NaCl at pH 5. The test is described in the SI.

4. Conclusions

In this work, we report for the first time the transformation of Fe_2P into iron phosphate during EC degradation of RhB dye (98%) and inactivation of *E. coli* bacteria (100%). We demonstrated that, under the experimental conditions, Cl^- ions are oxidized to HClO, which plays an essential role in the water treatment process. The recycling test (degradation test) of RhB dye over Fe_2P-iron phosphate film at 1.9 V vs. RHE revealed excellent reproducibility. Phytotoxicity tests revealed that EC treatment of RhB solutions decreased the inhibition of *L. sativum* germination, which serves as an indicator for reduced toxicity. Hence, this work demonstrates the tremendous potential of Fe_2P-iron phosphate as an efficient electrocatalyst in water cleaning studies. We propose that EC degradation of organics and inactivation of pathogenic bacteria could be also extended to other TMPHs.

Supplementary Materials: The following supporting information can be downloaded at: https://www.mdpi.com/article/10.3390/catal12030269/s1. Text S1: Rietveld refinement analysis and Williamson–Hall method. Figure S1: Williamson–Hall plot. Figure S2: XRD pattern of Fe_2P after heat treatment. Figure S3: Size distribution of Fe_2P NSs. Figure S4: LSV characteristic of Fe_2P particles recorded in 10^{-5} M RhB + 0.06 M NaCl conducted before heat treatment. Text S2: Tafel plots and EIS. Figure S5: (a) Tafel plots of different electrolytes; (b) Nyquist plot of Fe_2P thin film in 0.06 M Na_2SO_4; (c) Charge transfer resistance vs. applied voltages; (d) A circuit element used to fit the data. Text S3: Calculation of electrocatalytic active surface area. Figure S6: CVs of Fe_2P at different scan rates in 1 M KOH; (b) Current vs. scan rate taken from (a). Figure S7: Images with elemental maps are given for Fe, P, Cl, O and C taken from the Fe_2P sample (after electrolysis). Figure S8: Time profiles of RhB degradation in NaCl conducted with Ti and Fe_2P-iron phosphate electrodes. Figure S9: Degradation efficiency of RhB. Text S4: Kinetic models. Table S1: Pseudo-first-order and pseudo-second-order rate constants and correlation coefficients of RhB dye on Fe_2P-iron phosphate film. Text S5: Fluorescence spectra of Fe_2P-iron phosphate catalyst in 20 μM coumarin. Figure S10: Fluorescence spectra of Fe_2P

catalyst in 20 μM coumarin before and after the test. Figure S11: Detection of HClO by DPD method. Figure S12: MS measurement of H_2 and O_2 gas during the RhB degradation. Text S6: Degradation mechanism of RhB dye. Text S7: Calculation of the current generation efficiency of HClO. Figure S13: LSV plots and SEM images of Fe_2P-iron phosphate electrode recorded before and after the recycling test. Figure S14: HPLC of 1×10^{-5} M RhB solution in the presence of NaCl, NH_4Cl and Na_2SO_4. Text S8: Phytotoxicity test using *Lepidium sativum L.* Figure S15: Images of *Lepidium sativum* L. incubated in Petri dishes with RhB before and after EC treatment. Figure S16: LSV of Fe_2P-iron phosphate catalyst in NaCl seeded with 1.1×10^8 CFU/mL of *E. coli* bacteria and *I-t* plot obtained in 0.06 M NaCl + 1.1×10^8 CFU/mL of *E. coli* at 2.0 V vs. RHE. Table S2: Selected materials used in EC degradation of different dye molecules. Table S3: Selected materials used in EC inactivation of *E.coli* bacteria. Text S9: Synthesis and characterization of Fe_2P thin film. Text S10: Catalyst evaluation. Figure S17: Photograph of the cappuccino cell and EC cell used in the dye degradation studies. Table S4: Characteristics of RhB dye. [67–92] are cited in the Supplementary Materials.

Author Contributions: T.C. designed and conducted the experiments, analyzed the data and wrote the manuscript. M.M. contributed to DPD measurements. J.T. carried out the HPLC measurements. L.B. contributed to phytotoxicity tests, inactivation of *E. coli* bacteria and fundraising. P.S. carried out the XPS measurements. E.J. contributed to phytotoxicity tests. J.S.S. contributed to manuscript editing. M.V. contributed to manuscript editing. A.F. contributed to manuscript editing. S.E. supervised the work and contributed to data analysis, manuscript writing, editing, fundraising and project administration. All authors have read and agreed to the published version of the manuscript.

Funding: This research was funded by the Slovenian Research Agency under the bilateral project for scientific cooperation between Slovenia and the State of Israel (NI-0002). Scholarships were provided by the Public Scholarship, Development, Disability and Maintenance Fund of Slovenia for PhD studies at the University of Nova Gorica. Financial support was provided by the Slovenian Research Agency (research core funding: P2-0412).

Data Availability Statement: Data are contained within the article or Supplementary Materials.

Acknowledgments: This work was financially supported by the Slovenian Research Agency under the bilateral project for scientific cooperation between Slovenia and the State of Israel (NI-0002). T. Chouki and M. Machreki acknowledge the scholarships provided by the Public Scholarship, Development, Disability and Maintenance Fund of Slovenia (Ad futura program) for PhD studies at the University of Nova Gorica. S. Emin and M. Valant acknowledge the financial support from the Slovenian Research Agency (research core funding: P2-0412).

Conflicts of Interest: The authors declare that they have no known competing financial interests or personal relationships that could have influenced the work reported in this paper.

References

1. Oturan, M.A. Electrochemical advanced oxidation technologies for removal of organic pollutants from water. *Environ. Sci. Pollut. Res.* **2014**, *21*, 8333–8335. [CrossRef] [PubMed]
2. Faouzi Elahmadi, M.; Bensalah, N.; Gadri, A. Treatment of aqueous wastes contaminated with Congo Red dye by electrochemical oxidation and ozonation processes. *J. Hazard. Mater.* **2009**, *168*, 1163–1169. [CrossRef] [PubMed]
3. Anas, M.; Han, D.S.; Mahmoud, K.; Park, H.; Abdel-Wahab, A. Photocatalytic degradation of organic dye using titanium dioxide modified with metal and non-metal deposition. *Mater. Sci. Semicond. Process.* **2015**, *41*, 209–218. [CrossRef]
4. Raza, N.; Raza, W.; Gul, H.; Kim, K.H. ZnO–ZnTe hierarchical superstructures as solar-light-activated photocatalysts for azo dye removal. *Environ. Res.* **2021**, *194*, 110499. [CrossRef] [PubMed]
5. Fan, L.; Zhou, Y.; Yang, W.; Chen, G.; Yang, F. Electrochemical degradation of aqueous solution of Amaranth azo dye on ACF under potentiostatic model. *Dye. Pigment.* **2008**, *76*, 440–446. [CrossRef]
6. Zhao, S.; Li, S.; Zhao, Z.; Su, Y.; Long, Y.; Zheng, Z.; Cui, D.; Liu, Y.; Wang, C.; Zhang, X.; et al. Microwave-assisted hydrothermal assembly of 2D copper-porphyrin metal-organic frameworks for the removal of dyes and antibiotics from water. *Environ. Sci. Pollut. Res.* **2020**, *27*, 39186–39197. [CrossRef]
7. Hashim, K.S.; Kot, P.; Zubaidi, S.L.; Alwash, R.; Al Khaddar, R.; Shaw, A.; Al-Jumeily, D.; Aljefery, M.H. Energy efficient electrocoagulation using baffle-plates electrodes for efficient *Escherichia coli* removal from wastewater. *J. Water Process Eng.* **2020**, *33*, 101079. [CrossRef]
8. Bensalah, N.; Louhichi, B.; Abdel-Wahab, A. Electrochemical oxidation of succinic acid in aqueous solutions using boron doped diamond anodes. *Int. J. Environ. Sci. Technol.* **2012**, *9*, 135–143. [CrossRef]

9. Ammar, H.B.; Brahim, M.B.; Abdelhédi, R.; Samet, Y. Green electrochemical process for metronidazole degradation at BDD anode in aqueous solutions via direct and indirect oxidation. *Sep. Purif. Technol.* **2016**, *157*, 9–16. [CrossRef]
10. Patil, S.A.; Hägerhäll, C.; Gorton, L. Electron transfer mechanisms between microorganisms and electrodes in bioelectrochemical systems. *Bioanal. Rev.* **2014**, *1*, 71–129. [CrossRef]
11. Koo, M.S.; Chen, X.; Cho, K.; An, T.; Choi, W.; Chen, X.; Cho, K.; An, T.; Choi, W. In situ photoelectrochemical chloride activation using a WO_3 electrode for oxidative treatment with simultaneous H_2 evolution under visible light. *Environ. Sci. Technol.* **2019**, *53*, 9926–9936. [CrossRef] [PubMed]
12. Moreira, F.C.; Boaventura, R.A.R.; Brillas, E.; Vilar, V.J.P. Electrochemical advanced oxidation processes: A review on their application to synthetic and real wastewaters. *Appl. Catal. B Environ.* **2017**, *202*, 217–261. [CrossRef]
13. Wacławek, S.; Lutze, H.V.; Grübel, K.; Padil, V.V.T.; Černík, M.; Dionysiou, D.D. Chemistry of persulfates in water and wastewater treatment: A review. *Chem. Eng. J.* **2017**, *330*, 44–62. [CrossRef]
14. Lemeyonouin, P.; Guillaume, A.; Honoré, K.K.; Albert, T. Influence of chlorides on the electrochemical oxidation of formic acid on thermally prepared platinum electrodes. *Int. J. Pure Appl. Sci. Technol.* **2013**, *14*, 33–43.
15. Baddouh, A.; Bessegato, G.G.; Rguiti, M.M.; El Ibrahimi, B.; Bazzi, L.; Hilali, M.; Zanoni, M.V.B. Electrochemical decolorization of Rhodamine B dye: Influence of anode material, chloride concentration and current density. *J. Environ. Chem. Eng.* **2018**, *6*, 2041–2047. [CrossRef]
16. Babu, B.R.; Venkatesan, P.; Kanimozhi, R.; Basha, C.A. Removal of pharmaceuticals from wastewater by electrochemical oxidation using cylindrical flow reactor and optimization of treatment conditions. *J. Environ. Sci. Health-Part A Toxic/Hazard. Subst. Environ. Eng.* **2009**, *44*, 985–994. [CrossRef]
17. Martínez-Huitle, C.A.; Ferro, S. Electrochemical oxidation of organic pollutants for the wastewater treatment: Direct and indirect processes. *Chem. Soc. Rev.* **2006**, *35*, 1324–1340. [CrossRef]
18. Ganizadeh, F.; Rezaee, A.; Godini, H. Elimination of pathogenic bacteria using electrochemical process containing steel mesh electrode. *J. Adv. Environ. Health Res.* **2017**, *5*, 23–28. [CrossRef]
19. Yang, Y. Recent advances in the electrochemical oxidation water treatment: Spotlight on byproduct control. *Front. Environ. Sci. Eng.* **2020**, *14*, 1264–1267. [CrossRef]
20. Duan, T.; Chen, Y.; Wen, Q.; Duan, Y. Novel composition graded Ti/Ru-Sb-SnO_2 electrode synthesized by selective electrodeposition and its application for electrocatalytic decolorization of dyes. *J. Phys. Chem. C* **2015**, *119*, 7780–7790. [CrossRef]
21. Maharana, D.; Niu, J.; Gao, D.; Xu, Z.; Shi, J. Electrochemical degradation of Rhodamine B over Ti/SnO_2-Sb electrode. *Water Environ. Res.* **2015**, *87*, 304–311. [CrossRef] [PubMed]
22. Bergmann, M.E.H.; Koparal, A.S. Studies on electrochemical disinfectant production using anodes containing RuO_2. *J. Appl. Electrochem.* **2005**, *35*, 1321–1329. [CrossRef]
23. Martínez-Huitle, C.A.; Brillas, E. Electrochemical alternatives for drinking water disinfection. *Angew. Chem.-Int. Ed.* **2008**, *47*, 1998–2005. [CrossRef] [PubMed]
24. Bensalah, N.; Abdel-Wahab, A. Electrochemical inactivation of *P. Aeruginosa*, *A. hydrophila*, *L. pneumophila* using boron doped diamond anodes. *J. Adv. Oxid. Technol.* **2013**, *16*, 9–15. [CrossRef]
25. Barashkov, N.N.; Eisenberg, D.; Eisenberg, S.; Shegebaeva, G.S.; Irgibaeva, I.S.; Barashkova, I.I. Electrochemical chlorine-free AC disinfection of water contaminated with *Salmonella typhimurium* bacteria. *Russ. J. Electrochem.* **2010**, *46*, 306–311. [CrossRef]
26. Jeong, J.; Kim, J.Y.; Cho, M.; Choi, W.; Yoon, J. Inactivation of *Escherichia coli* in the electrochemical disinfection process using a Pt anode. *Chemosphere* **2007**, *67*, 652–659. [CrossRef]
27. Ghasemian, S.; Asadishad, B.; Omanovic, S.; Tufenkji, N. Electrochemical disinfection of bacteria-laden water using antimony-doped tin-tungsten-oxide electrodes. *Water Res.* **2017**, *126*, 299–307. [CrossRef]
28. Ajiboye, T.O.; Babalola, S.O.; Onwudiwe, D.C. Photocatalytic inactivation as a method of elimination of *E. coli* from drinking water. *Appl. Sci.* **2021**, *11*, 1313. [CrossRef]
29. Jain, R.; Sharma, N.; Bhargava, M. Electrochemical degradation of Rhodamine B dye in textile and paper industries effluent. *J. Sci. Ind. Res.* **2003**, *62*, 1138–1144.
30. Kothari, M.S.; Shah, K.A. Electrochemical oxidation for decolorization of Rhodamine-B dye using mixed metal oxide electrode: Modeling and optimization. *Water Sci. Technol.* **2020**, *81*, 720–731. [CrossRef]
31. Ahmadi, A.; Wu, T. Inactivation of *E. coli* using a novel TiO_2 nanotube electrode. *Environ. Sci. Water Res. Technol.* **2017**, *3*, 534–545. [CrossRef]
32. Yang, M.; Liu, X.; Chen, J.; Meng, F.; Zhang, Y.; Brandl, H.; Lippert, T.; Chen, N. Photocatalytic and electrochemical degradation of methylene blue by titanium dioxide. *Chin. Sci. Bull.* **2014**, *59*, 1964–1967. [CrossRef]
33. Li, H.; Zhu, X.; Ni, J. Inactivation of *Escherichia coli* in Na_2SO_4 electrolyte using boron-doped diamond anode. *Electrochim. Acta* **2010**, *56*, 448–453. [CrossRef]
34. Li, X.Y.; Diao, H.F.; Fan, F.X.J.; Gu, J.D.; Ding, F.; Tong, A.S.F. Electrochemical wastewater disinfection: Identification of its principal germicidal actions. *J. Environ. Eng.* **2004**, *130*, 1217–1221. [CrossRef]
35. Vos, J.G.; Koper, M.T.M. Measurement of competition between oxygen evolution and chlorine evolution using rotating ring-disk electrode voltammetry. *J. Electroanal. Chem.* **2018**, *819*, 260–268. [CrossRef]
36. Wang, L.; Qin, M.; Yang, W.; Gao, Y.; Li, Y.Y. Efficient electrochemical water oxidation and oxidative degradation of Rhodamine B: A comparative study using high-purity birnessites containing Li^+, Na^+ or K^+ ions. *ChemistrySelect* **2017**, *2*, 5587–5594. [CrossRef]

37. Chouki, T.; Lazarević, D.; Donkova, B.V.; Emin, S. Synthesis of efficient iron phosphide catalyst for electrocatalytic hydrogen generation. *Bulg. Chem. Commun.* **2021**, *53*, 72–77. [CrossRef]
38. Yao, Y.; Mahmood, N.; Pan, L.; Shen, G.; Zhang, R.; Gao, R.; Aleem, F.E.; Yuan, X.; Zhang, X.; Zou, J.J. Iron phosphide encapsulated in P-doped graphitic carbon as efficient and stable electrocatalyst for hydrogen and oxygen evolution reactions. *Nanoscale* **2018**, *10*, 21327–21334. [CrossRef]
39. Guo, R.; Lai, X.; Huang, J.; Du, X.; Yan, Y.; Sun, Y.; Zou, G.; Xiong, J. Phosphate-based electrocatalysts for water splitting: Recent Progress. *ChemElectroChem* **2018**, *5*, 3822–3834. [CrossRef]
40. Tang, K.; Wang, X.; Wang, M.; Xie, Y.; Zhou, J.; Yan, C. Highly sensitive activity on Ni/Fe ratio of monodispersed ternary nickel iron phosphide for efficient water oxidation. *ChemElectroChem* **2017**, *4*, 2150–2157. [CrossRef]
41. Lei, Z.; Bai, J.; Li, Y.; Wang, Z.; Zhao, C. Fabrication of nanoporous nickel-iron hydroxylphosphate composite as bifunctional and reversible catalyst for highly efficient intermittent water splitting. *ACS Appl. Mater. Interfaces* **2017**, *9*, 35837–35846. [CrossRef]
42. Li, P.; Wang, S.; Samo, I.A.; Zhang, X.; Wang, Z.; Wang, C.; Li, Y.; Du, Y.; Zhong, Y.; Cheng, C.; et al. Common-ion effect triggered highly sustained seawater electrolysis with additional NaCl production. *Research* **2020**, *2020*, 2872141. [CrossRef] [PubMed]
43. Li, P.; Zeng, H.C. Promoting electrocatalytic oxygen evolution over transition-metal phosphide-based nanocomposites via architectural and electronic engineering. *ACS Appl. Mater. Interfaces* **2019**, *11*, 46825–46838. [CrossRef] [PubMed]
44. Li, P.; Zeng, H.C. Bimetallic Ni-Fe phosphide nanocomposites with a controlled architecture and composition enabling highly efficient electrochemical water oxidation. *J. Mater. Chem. A* **2018**, *6*, 2231–2238. [CrossRef]
45. Chouki, T.; Machreki, M.; Emin, S. Solvothermal synthesis of iron phosphides and their application for efficient electrocatalytic hydrogen evolution. *Int. J. Hydrogen Energy* **2020**, *45*, 21473–21482. [CrossRef]
46. Park, J.; Koo, B.; Hwang, Y.; Bae, C.; An, K.; Park, J.G.; Park, H.M.; Hyeon, T. Novel synthesis of magnetic Fe_2P nanorods from thermal decomposition of continuously delivered precursors using a syringe pump. *Angew. Chem.-Int. Ed.* **2004**, *43*, 2282–2285. [CrossRef] [PubMed]
47. Rasras, A.; Hamdi, R.; Mansour, S.; Samara, A.; Haik, Y. Study of the magnetocaloric effect in single-phase antiferromagnetic $GdMnO_3$. *J. Phys. Chem. Solids* **2021**, *149*, 109798. [CrossRef]
48. Sharif, F.; Roberts, E.P.L. Electrochemical oxidation of an organic dye adsorbed on tin oxide and antimony doped tin oxide graphene composites. *Catalysts* **2020**, *10*, 263. [CrossRef]
49. Lu, C.; Jothi, P.R.; Thersleff, T.; Budnyak, T.M.; Rokicinska, A.; Yubuta, K.; Dronskowski, R.; Kuśtrowski, P.; Fokwa, B.P.T.; Slabon, A. Nanostructured core-shell metal borides-oxides as highly efficient electrocatalysts for photoelectrochemical water oxidation. *Nanoscale* **2020**, *12*, 3121–3128. [CrossRef]
50. Chouki, T.; Donkova, B.; Aktarla, B.; Stefanov, P.; Emin, S. Growth of $MoSe_2$ electrocatalyst from metallic molybdenum nanoparticles for efficient hydrogen evolution. *Mater. Today Commun.* **2021**, *26*, 101976. [CrossRef]
51. Li, P.; Li, W.; Chen, R.; Lin, Y. Boosting the oxygen evolution electrocatalysis performance of iron phosphide via architectural design and electronic modulation. *ACS Sustain. Chem. Eng.* **2020**, *8*, 9206–9216. [CrossRef]
52. Gendel, Y.; Lahav, O. Revealing the mechanism of indirect ammonia electrooxidation. *Electrochim. Acta* **2012**, *63*, 209–219. [CrossRef]
53. Wang, H.; Zhang, X.; Su, Y.; Yu, H.; Chen, S.; Quan, X.; Yang, F. Photoelectrocatalytic oxidation of aqueous ammonia using TiO_2 nanotube arrays. *Appl. Surf. Sci.* **2014**, *311*, 851–857. [CrossRef]
54. Baddouh, A.; El Ibrahimi, B.; Amaterz, E.; Rguiti, M.M.; Bazzi, L.; Hilali, M. Removal of the Rhodamine B dye at $Ti/Ru_{0.3}Ti_{0.7}O_2$ anode using flow cell system. *J. Chem.* **2019**, *2019*, 1424797. [CrossRef]
55. Zhang, Y.; Ji, Y.; Li, J.; Bai, J.; Chen, S.; Li, L.; Wang, J.; Zhou, T.; Jiang, P.; Guan, X.; et al. Efficient ammonia removal and toxic chlorate control by using $BiVO_4/WO_3$ heterojunction photoanode in a self-driven PEC-chlorine system. *J. Hazard. Mater.* **2021**, *402*, 123725. [CrossRef] [PubMed]
56. Xiang, Q.; Yu, J.; Wong, P.K. Quantitative characterization of hydroxyl radicals produced by various photocatalysts. *J. Colloid Interface Sci.* **2011**, *357*, 163–167. [CrossRef] [PubMed]
57. Bru, R.; Van Duijne, A.K.; Braakhuis, L.; Saha, P.; Jeremiasse, A.W.; Mei, B.; Mul, G. Comparative analysis of photocatalytic and electrochemical degradation of 4-Ethylphenol in saline conditions. *Environ. Sci. Technol.* **2019**, *53*, 8725–8735. [CrossRef]
58. Ji, Y.; Bai, J.; Li, J.; Luo, T.; Qiao, L.; Zeng, Q.; Zhou, B. Highly selective transformation of ammonia nitrogen to N_2 based on a novel solar-driven photoelectrocatalytic-chlorine radical reactions system. *Water Res.* **2017**, *125*, 512–519. [CrossRef]
59. Iguchi, S.; Miseki, Y.; Sayama, K. Efficient hypochlorous acid (HClO) production: Via photoelectrochemical solar energy conversion using a $BiVO_4$ -based photoanode. *Sustain. Energy Fuels* **2018**, *2*, 155–162. [CrossRef]
60. Benvenuti, T.; Gabriel, A.P.; Heberle, A.N.A.; Lucena, M.P.P.; Petter, P.M.H.; Meneguzzi, Á.; Bernardes, A.M. Evaluation of direct photolysis, electrooxidation and photoelectrooxidation for Rhodamine-B degradation. *Braz. J. Chem. Eng.* **2018**, *35*, 957–968. [CrossRef]
61. Norouzi, N.; Choudhury, F.A.; El-Kaderi, H.M. Iron phosphide doped, porous carbon as an efficient electrocatalyst for oxygen reduction reaction. *ACS Appl. Energy Mater.* **2020**, *3*, 2537–2546. [CrossRef]
62. Zhang, Y.; Wang, Y.; Luo, R.; Yang, Y.; Lu, Y.; Guo, Y.; Liu, X.; Cao, S.; Kim, J.K.; Luo, Y. A 3D porous FeP/rGO modulated separator as a dual-function polysulfide barrier for high-performance lithium sulfur batteries. *Nanoscale Horiz.* **2020**, *5*, 530–540. [CrossRef] [PubMed]

63. Yuan, R.; Ramjaun, S.N.; Wang, Z.; Liu, J. Effects of chloride ion on degradation of Acid Orange 7 by sulfate radical-based advanced oxidation process: Implications for formation of chlorinated aromatic compounds. *J. Hazard. Mater.* **2011**, *196*, 173–179. [CrossRef]
64. Radjenovic, J.; Sedlak, D.L. Challenges and opportunities for electrochemical processes as next-generation technologies for the treatment of contaminated water. *Environ. Sci. Technol.* **2015**, *49*, 11292–11302. [CrossRef] [PubMed]
65. de Araújo, D.M.; Sáez, C.; Martínez-Huitle, C.A.; Cañizares, P.; Rodrigo, M.A. Influence of mediated processes on the removal of Rhodamine with conductive-diamond electrochemical oxidation. *Appl. Catal. B Environ.* **2015**, *166–167*, 454–459. [CrossRef]
66. Machreki, M.; Chouki, T.; Martelanc, M.; Butinar, L.; Vodopivec, B.M.; Emin, S. Preparation of porous α-Fe_2O_3 thin films for efficient photoelectrocatalytic degradation of Basic blue 41 dye. *J. Environ. Chem. Eng.* **2021**, *9*, 105495. [CrossRef]
67. Zhou, X.; Liu, D.; Bu, H.; Deng, L.; Liu, H.; Yuan, P.; Du, P.; Song, H. XRD-based quantitative analysis of clay minerals using reference intensity ratios, mineral intensity factors, Rietveld, and full pattern summation methods: A critical review. *Solid Earth Sci.* **2018**, *3*, 16–29. [CrossRef]
68. Von Dreele, R.B. Protein crystal structure analysis from high-resolution X-Ray powder-diffraction data. *Methods Enzymol.* **2003**, *368*, 254–267. [CrossRef] [PubMed]
69. Nath, D.; Singh, F.; Das, R. X-ray diffraction analysis by Williamson-Hall, Halder-Wagner and size-strain plot methods of CdSe nanoparticles- a comparative study. *Mater. Chem. Phys.* **2020**, *239*, 122021. [CrossRef]
70. Zhu, K.; Ren, X.; Sun, X.; Zhu, L.; Sun, Z. Effect of supporting electrolyte on the surface corrosion and anodic oxidation performance of graphite electrode. *Electrocatalysis* **2019**, *10*, 549–559. [CrossRef]
71. Society, T.E. Water electrolysis using diamond thin film electrodes. *J. Electrochem. Soc.* **1998**, *145*, 2358.
72. Kuo, D.Y.; Paik, H.; Nelson, J.N.; Shen, K.M.; Schlom, D.G.; Suntivich, J. Chlorine evolution reaction electrocatalysis on RuO_2(110) and IrO_2(110) grown using molecular-beam epitaxy. *J. Chem. Phys.* **2019**, *150*, 041726. [CrossRef] [PubMed]
73. McCrory, C.C.L.; Jung, S.; Peters, J.C.; Jaramillo, T.F. Benchmarking heterogeneous electrocatalysts for the oxygen evolution reaction. *J. Am. Chem. Soc.* **2013**, *135*, 16977–16987. [CrossRef] [PubMed]
74. Sivarajasekar, N.; Srileka, S.; Samson Arun Prasath, S.; Robinson, S.; Saravanan, K. Kinetic modeling for biosorption of Metylene Blue onto H_3PO_4 activated acacia arabica. *Carbon Lett.* **2008**, *9*, 181–187. [CrossRef]
75. Mehta, A.; Mishra, A.; Kainth, S.; Basu, S. Carbon quantum dots/TiO_2 nanocomposite for sensing of toxic metals and photodetoxification of dyes with kill waste by waste concept. *Mater. Des.* **2018**, *155*, 485–493. [CrossRef]
76. Oliveira, F.H.; Osugi, M.E.; Paschoal, F.M.M.; Profeti, D.; Olivi, P.; Zanoni, M.V.B. Electrochemical oxidation of an acid dye by active chlorine generated using Ti/$Sn_{(1-x)}Ir_xO_2$ electrodes. *J. Appl. Electrochem.* **2007**, *37*, 583–592. [CrossRef]
77. Cho, K.; Hoffmann, M.R. Urea degradation by electrochemically generated reactive chlorine species: Products and reaction pathways. *Environ. Sci. Technol.* **2014**, *48*, 11504–11511. [CrossRef] [PubMed]
78. Kusmierek, E. Semiconductor electrode materials applied in photoelectrocatalytic wastewater treatment—An overview. *Catalysts* **2020**, *10*, 439. [CrossRef]
79. Mañas, P.; De las Heras, J. Phytotoxicity test applied to sewage sludge using Lactuca sativa L. and Lepidium sativum L. seeds. *Int. J. Environ. Sci. Technol.* **2018**, *15*, 273–280. [CrossRef]
80. Andrade, L.S.; Ruotolo, L.A.M.; Rocha-Filho, R.C.; Bocchi, N.; Biaggio, S.R.; Iniesta, J.; García-Garcia, V.; Montiel, V. On the performance of Fe and Fe,F doped Ti-Pt/PbO_2 electrodes in the electrooxidation of the Blue Reactive 19 dye in simulated textile wastewater. *Chemosphere* **2007**, *66*, 2035–2043. [CrossRef]
81. Chen, X.; Chen, G.; Gao, F.; Yue, P.L. High-performance Ti/BDD electrodes for pollutant oxidation. *Environ. Sci. Technol.* **2003**, *37*, 5021–5026. [CrossRef]
82. Fan, L.; Zhou, Y.; Yang, W.; Chen, G.; Yang, F. Electrochemical degradation of Amaranth aqueous solution on ACF. *J. Hazard. Mater.* **2006**, *137*, 1182–1188. [CrossRef] [PubMed]
83. Cameselle, C.; Pazos, M.; Sanromán, M.A. Selection of an electrolyte to enhance the electrochemical decolourisation of indigo. Optimisation and scale-up. *Chemosphere* **2005**, *60*, 1080–1086. [CrossRef] [PubMed]
84. Lopes, A.; Martins, S.; Morão, A.; Magrinho, M.; Gonçalves, I. Degradation of a textile dye C. I. Direct Red 80 by electrochemical processes. *Port. Electrochim. Acta* **2004**, *22*, 279–294. [CrossRef]
85. Salazar, R.; Ureta-Zañartu, M.S.; González-Vargas, C.; Brito, C.d.N.; Martinez-Huitle, C.A. Electrochemical degradation of industrial textile dye disperse yellow 3: Role of electrocatalytic material and experimental conditions on the catalytic production of oxidants and oxidation pathway. *Chemosphere* **2018**, *198*, 21–29. [CrossRef] [PubMed]
86. Chen, X.; Gao, F.; Chen, G. Comparison of Ti/BDD and Ti/SnO_2-Sb_2O_5 electrodes for pollutant oxidation. *J. Appl. Electrochem.* **2005**, *35*, 185–191. [CrossRef]
87. Chang, J.H.; Wang, Y.L.; Dong, C.D.; Shen, S.Y. Electrocatalytic degradation of azo dye by vanadium-doped TiO_2 nanocatalyst. *Catalysts* **2020**, *10*, 482. [CrossRef]
88. Ozturk, D.; Yilmaz, A.E. Investigation of electrochemical degradation of Basic Red 13 dye in aqueous solutions based on COD removal: Numerical optimization approach. *Int. J. Environ. Sci. Technol.* **2020**, *17*, 3099–3110. [CrossRef]
89. Hamad, H.; Bassyouni, D.; El-Ashtoukhy, E.S.; Amin, N.; Abd El-Latif, M. Electrocatalytic degradation and minimization of specific energy consumption of synthetic azo dye from wastewater by anodic oxidation process with an emphasis on enhancing economic efficiency and reaction mechanism. *Ecotoxicol. Environ. Saf.* **2018**, *148*, 501–512. [CrossRef] [PubMed]

90. Teng, X.; Li, J.; Wang, Z.; Wei, Z.; Chen, C.; Du, K.; Zhao, C.; Yang, G.; Li, Y. Performance and mechanism of methylene blue degradation by an electrochemical process. *RSC Adv.* **2020**, *10*, 24712–24720. [CrossRef]
91. Jeong, J.; Kim, J.Y.; Yoon, J. The role of reactive oxygen species in the electrochemical inactivation of microorganisms. *Environ. Sci. Technol.* **2006**, *40*, 6117–6122. [CrossRef] [PubMed]
92. Gusmão, I.C.C.P.; Moraes, P.B.; Bidoia, E.D. Studies on the electrochemical disinfection of water containing Escherichia coli using a dimensionally stable anode. *Brazilian Arch. Biol. Technol.* **2010**, *53*, 1235–1244. [CrossRef]

catalysts

MDPI

Article

Silver-Carbonaceous Microsphere Precursor-Derived Nano-Coral Ag Catalyst for Electrochemical Carbon Dioxide Reduction

Xiangxiang Li, Shuling Chang, Yanting Wang and Lihong Zhang *

Department of Catalysis Science and Technology and Tianjin Key Laboratory of Applied Catalysis Science & Technology, School of Chemical Engineering and Technology, Tianjin University, Tianjin 300350, China; lixx347@163.com (X.L.); cslq0818@163.com (S.C.); w2016016061@163.com (Y.W.)
* Correspondence: zlh_224@tju.edu.cn; Tel.: +86-150-2225-5828

Abstract: The selective and effective conversion of CO_2 into available chemicals by electrochemical methods was applied as a promising way to mitigate the environment and energy crisis. Metal silver is regarded as an efficient electrocatalyst that can selectively convert CO_2 into CO at room temperature. In this paper, a series of coral-like porous Ag (CD-Ag) catalysts were fabricated by calcining silver-carbonaceous microsphere (Ag/CM) precursors with different Ag content and the formation mechanism of CD-Ag catalysts was proposed involving the Ag precursor reduction and CM oxidation. In the selective electrocatalytic reduction of CO_2 to CO, the catalyst 15 CD-Ag showed a stable current density at -6.3 mA/cm^2 with a Faraday efficiency (FE) of ca. 90% for CO production over 5 h in -0.95 V vs. RHE. The excellent performance of the 15 CD-Ag catalysts is ascribed to the special surface chemical state and the particular nano-coral porous structure with uniformly distributed Ag particles and pore structure, which can enhance the electrochemical active surface areas (ECSA) and provide more active sites and porosity compared with other CD-Ag catalysts and even Ag foil.

Keywords: carbon dioxide reduction; silver; carbonaceous microsphere; carbon monoxide; electrochemical

Citation: Li, X.; Chang, S.; Wang, Y.; Zhang, L. Silver-Carbonaceous Microsphere Precursor-Derived Nano-Coral Ag Catalyst for Electrochemical Carbon Dioxide Reduction. *Catalysts* **2022**, *12*, 479. https://doi.org/10.3390/catal12050479

Academic Editors: Marc Cretin, Sophie Tingry and Zhenghua Tang

Received: 24 March 2022
Accepted: 21 April 2022
Published: 23 April 2022

1. Introduction

Electrocatalytic conversion of CO_2 into other available chemicals is considered an effective strategy to carry out carbon neutrality [1]. In the past few decades, researchers have found that it is possible to convert CO_2 into useful chemicals, such as CO, HCOOH, CH_4, C_2H_6O, C_2H_4, and so on [2–6], using ambient electrochemical methods. Therefore, electrochemical CO_2 reduction reaction (CO_2RR) has received wide attention as a promising strategy for carbon cycle and sustainable energy conversion [7]. In order to achieve this goal, an important way is to develop an efficient electrocatalyst with high activity, selectivity, and stability.

In recent decades, researchers have evaluated the selective electrochemical CO_2RR over a variety of transition metal materials in CO_2-saturated aqueous solutions. Among them, Au [8–11], Ag [12–15], and Zn [16–19] are considered to be effective in the system of electrochemical CO_2RR to CO. Although metallic Au usually has the best CO selectivity among these metals, its relatively high cost and low abundance have limited its wide utilization, while the utilization prospect of metallic Zn is also inadequate due to its low CO selectivity [20]. Metallic Ag has drawn extensive attention on account of its moderate cost and high CO selectivity. In order to further enhance the electrocatalytic performance of CO_2RR over Ag-based catalysts, various strategies were applied to modify them, including adjusting the size and shape, constructing surface defects, inducing growth of specific crystal planes, and introducing other elements [21,22].

Lu et al. [23] prepared a porous nano-Ag electrocatalyst by dealloying a precursor of Ag–Al alloy and evaluating it in the process of electrochemical CO_2RR to CO under moderate overpotentials of <0.50 V. The reason for the high selectivity of ca. 92% over the porous nano-Ag electrocatalyst was attributed to the large ECSA and high intrinsic activity in contrast to polycrystalline Ag. In addition, a series of Ag-based electrocatalysts with excellent performance were also synthesized by treating Ag electrodes via different oxidation-reduction processes. For example, Ma et al. [24] pretreated an Ag electrode by potential anodization in an alkaline solution to obtain a Ag_2O layer, and the fabricated Ag_2O layer was electrically reduced in situ to an oxide-derived nanostructured Ag (OD-Ag) electrocatalyst at the initial stage of electrolysis. The OD-Ag electrocatalyst showed approximately 80% catalytic selectivity of CO_2 electroreduction to CO at 0.49 V. Furthermore, an Ag nano-coral catalyst obtained via oxidation-reduction of chloride precursor [25], and sulfide-derived porous Ag microrods using a facile plasma vulcanization treatment [26], were studied in the CO_2 electroreduction process and obtained a magnificent activity for CO production with low overpotential. The nano-Ag electrocatalysts can also be obtained by in situ electrochemical reductions of Ag_2CO_3, which is formed by anodic-etching of polycrystalline Ag foil and displayed excellent catalytic performance of electrochemical CO_2RR to CO [27]. These previous studies illustrate that the Ag-based precursors derived porous nano-Ag electrocatalysts can provide abundant active centers, which is beneficial to achieve excellent electrocatalytic performance.

Herein, we used glucose as the carbon source to form carbonaceous microspheres by hydrothermal synthesis, then prepared several kinds of Ag/CM precursors with different Ag content by the incipient wetness impregnation method, and finally obtained coral-like porous Ag catalyst by calcination. This study provides a new way to prepare silver catalysts with a three-dimensional structure by Ag/C precursor derivatization. Compared with Ag foil, the CD-Ag catalysts can obtain higher current density and FE_{CO} at the same potential. Among them, the 15 CD-Ag catalyst has the best catalytic activity and selectivity in the process of electrochemical CO_2RR to CO, and it exhibited a stable current density at -6.3 mA/cm^2 and a high FE of ca. 90% for CO production over 5 h in -0.95 V vs. RHE. The characterization results indicated that the improved catalytic performance was related to the special surface chemical state, crystal phase composition, and high ECSA which arose from the uniform distribution of Ag particles and porous structure depending on the Ag content in the precursors. Therefore, the nano-Ag-based catalysts prepared by calcining Ag/CM precursors could provide a new design idea for the electrochemical CO_2RR to CO.

2. Results and Discussion

2.1. Characterization of the Electrocatalysts

2.1.1. Phase Structure

A variety of physical and chemical characterizations were carried out to explore the properties of catalysts. To analyze the crystal structure of the prepared CD-Ag, the X-ray diffraction (XRD) patterns of three different CD-Ag samples and Ag foil are shown in Figure 1. It shows that the diffraction peaks at angle 2θ equal to 38.1°, 44.3°, 64.4°, 77.4°, and 81.5° correspond to the (111), (200), (220), (311), and (222) crystal planes of Ag [JCPDS file No. 04-0783], respectively, and no other diffraction peaks appear. It can be seen that with the increase in Ag content in the Ag/CM precursor, the relative intensities of the diffraction peak of prepared CD-Ag materials gradually increase. The relatively sharp Ag diffraction peak reflects an enhancement in crystallinity of the Ag phase [28]. This is likely because of the growth of Ag microcrystalline along the (111) and (200) directions with the increasing amount of Ag precursor on CM support during the preparation stage. These results indicated that CD-Ag has a good metallic Ag crystal structure.

As shown in Figure S1, the transmission electron microscopy (TEM) image of all CD-Ag samples was performed. The TEM image of 15 CD-Ag shows the uniformly distributed round Ag nanoparticles with a particle size distribution in the range of 18–78 nm centered at 40 nm, while 10 CD-Ag shows a particle size distribution in the range of

12–82 nm centered at 25 nm, and 20 CD-Ag shows a particle size distribution in the range of 24–86 nm centered at 50 nm. It is worth noting that the particles of the 10 CD-Ag and 20 CD-Ag samples have relatively tight cross-linking, especially the 20 CD-Ag stacking to form irregular bulk. Obviously, with the increase in Ag content in the precursor, the particle size of the as-synthesized CD-Ag catalysts also increases. However, the particles of the 15 CD-Ag samples showed a relatively uniform distribution, while others show different agglomeration and cross-linking states. Furthermore, two clear adjacent lattice spacings of 0.208 nm and 0.234 nm can be found in all high-resolution TEM (HR-TEM) images, which correspond to Ag (200) and Ag (111) crystal planes, respectively. This further confirms the successful preparation of Ag nanoparticles.

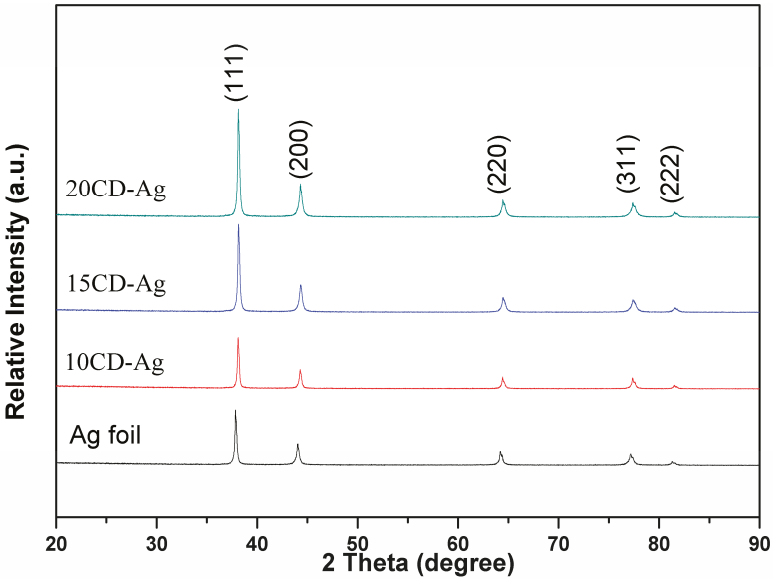

Figure 1. XRD patterns of the prepared CD-Ag materials and Ag foil.

2.1.2. Surface Morphology and Composition

Furthermore, the surface morphology of Ag foil and the prepared CD-Ag materials are characterized by a scanning electron microscope (SEM), and the details are shown in Figure 2. It can be easily recognized that the Ag foil has a relatively flat surface, while the CD-Ag materials demonstrate an obvious three-dimensional coral-like porous structure. Among the three different CD-Ag catalysts, the coral-like porous structure of the 15 CD-Ag is constructed by the uniform and tiny Ag particles together with uniform pore size. On the other hand, a non-uniform Ag particle and pore size distribution can be found for 10 CD-Ag and 20 CD-Ag. Especially, the smaller Ag particles of the 10 CD-Ag are closely combined with each other and some larger Ag particles are dotted among them, while 20 CD-Ag is mainly composed of more large Ag particles along with fewer small Ag particles among them. The burning of carbonaceous microspheres contributes to the formation of abundant pores on the surface of CD-Ag electrode materials [29]. The difference in morphology of three CD-Ag materials should be related to the different loading amounts of Ag on CM, which affects the burning off of CM and the reduction of $AgNO_3$ particles in the calcination process, which then results in different pore structures and Ag particle sizes. The representative SEM image (Figure S2) shows the CM are covered by a uniform shell of $AgNO_3$ particles. The shell thickness is predicted to increase with the increase in Ag content. During the calcination process, the reduction of $AgNO_3$ and oxidation behavior of

CM can be described by thermogravimetric analysis (TG), as shown in Figure S3, and the possible reduction reaction is given in Formula (1).

$$AgNO_3 + C = Ag + NO_2 + CO \quad (1)$$

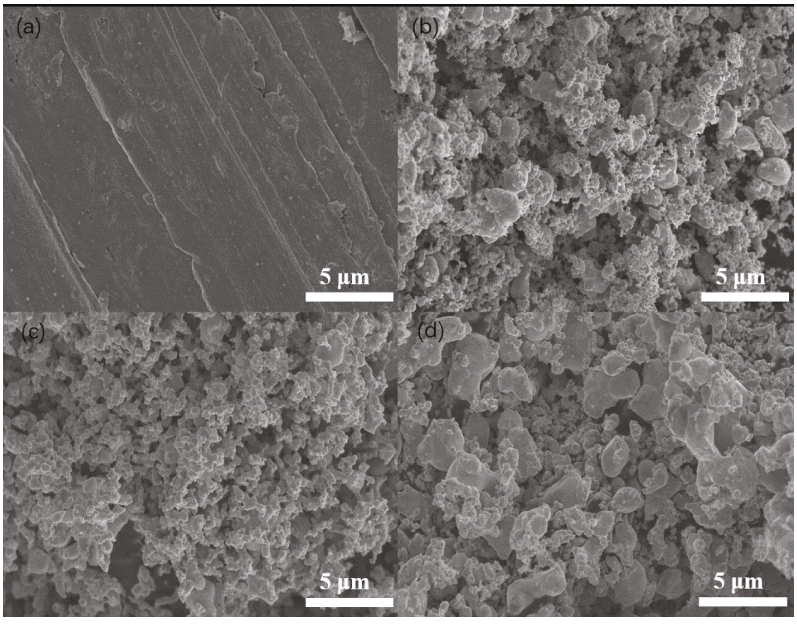

Figure 2. SEM images of Ag materials: (**a**) Ag foil; (**b**) 10 CD-Ag; (**c**) 15 CD-Ag; (**d**) 20 CD-Ag.

According to the loading amount of Ag and Formula (1), the theoretical mass losses of 10 Ag/CM, 15 Ag/CM, and 20 Ag/CM due to the reduction of $AgNO_3$ by CM are 6.5%, 9.3%, and 12.3%, respectively. Except for 20 Ag/CM, the theoretical mass losses of 10 Ag/CM and 15 Ag/CM are consistent with experimental data at the first step below 250 °C. Therefore, the first mass loss step can be assigned to the reduction of $AgNO_3$ particles by CM, while the second one above 250 °C should be related to the burn-off of CM. For 20 Ag/CM, the difference between the theoretical and experimental values indicates that the $AgNO_3$ particles cannot be fully reduced in the first step arising from the thick $AgNO_3$ shell, weakening the reduction effectiveness of CM. This also means the reduction of residual $AgNO_3$ particles could take place together with the burning-off of CM in the second mass loss step. At high temperatures, many factors, such as the rapid reduction of residual $AgNO_3$ particles, the disappearing confinement of CM, and the heat released from combustion, could result in the metallic Ag particles sintering and their growth in different degrees, along with different pore formations. As for 15 Ag/CM, the $AgNO_3$ particles can be fully reduced at low temperatures. The confinement of pores and surface functional groups of CM is in favor of dispersing and stabilizing the reduced Ag particles. In the second stage, the combustion temperature of CM increases in accordance with the order of 15 Ag/CM, 20 Ag/CM, and 10 Ag/CM, depending on the different activity of Ag species for CM combustion. In any case, the low-temperature combustion of CM can inhibit the growth of Ag particles and damage pore channels easier. These functions result in the formation of small Ag particles and uniform pore size on 15 CD-Ag. The existence of a small amount of big Ag particles and pores on 10 CD-Ag is mainly attributed to the high-temperature removal of CM. For 20 CD-Ag, the formation of a large amount of big Ag particles and pores should be related to the rapid reduction of residual $AgNO_3$ particles along with the high-temperature removal of CM, which accelerates agglomeration, the

growth of Ag particles, and the pore collapse of CM. In a word, only the appropriate Ag content in 15 Ag/CM precursors can balance the $AgNO_3$ reduction and carbonaceous microspheres oxidation and obtain the well-dispersed small Ag particles and uniformly distributed pore structure.

Furthermore, we added the SEM images of these CD-Ag catalysts after stability tests in Figure S4 and found that these catalysts exhibited particle agglomeration on the surface after the reaction, especially the 10 CD-Ag electrode had more particle agglomeration than other electrodes. Interestingly, the 20 CD-Ag material is composed of more large particles, but in the SEM images after the reaction, we observed that some large particles peeled off the surface of the 20 CD-Ag electrodes, meanwhile some small particles were exposed.

In addition, the elemental compositions of three CD-Ag samples are analyzed by energy-dispersive X-ray spectroscopy (EDS), and the details are listed in Table S1. It is observed that only elements Ag, C, and O can be detected by EDS and the percentage of the Ag is more than 96.00% and even displays a slight increase trend from 20 CD-Ag to 15 CD-Ag and to 10 CD-Ag. The existence of the O element indicates that the formation of Ag^+ is possible on the surface of CD-Ag.

2.1.3. Surface Chemical States of Elements

The surface composition and chemical states of Ag foil and three kinds of CD-Ag materials were investigated by X-ray photoelectron spectroscopy (XPS). As expected by the EDS result, the Ag 3d, C 1s, and O 1s signals appear in the wide scan XPS spectra for all samples (Figure 3a). Figure 3b displays the XPS peak of the Ag 3d region. The bands at the binding energy (BE) of 368.2 eV and 374.2 eV can be attributed to the Ag $3d_{5/2}$ and Ag $3d_{3/2}$ of the Ag foil, respectively. Compared with the Ag foil, the Ag $3d_{5/2}$ and Ag $3d_{3/2}$ peaks for the synthesized CD-Ag materials slightly shift to the lower BE value of 367.8 eV and 373.8 eV, respectively. This means the surface electron density of CD-Ag is higher than that of the Ag foil due to the existence of the O species with high electronegativity. The negative shift of BE value also proves that there is a trace amount of Ag^+ on the surface of the synthesized CD-Ag materials [30,31]. For the cause of further exploring the chemical state of Ag and O on the surface of the prepared CD-Ag materials, the deconvoluted XPS profiles are shown in Figure 3c,d for 15 CD-Ag and Figure S5 for the others. As for the Ag 3d peak of 15 CD-Ag, two fitting peaks located at the BE values of 367.6 eV and 373.6 eV are ascribed to Ag^+, while the other two fitting peaks with BE values of 367.9 eV and 373.9 eV can be attributed to Ag^0 [32]. This is because in the air atmosphere of 300 °C, even though the oxidation of CM and the reduction of $AgNO_3$ are dominant, some reduced Ag^0 will inevitably be further reoxidized to Ag^+ [33]. This discrepancy between XPS and XRD characterization of CD-Ag materials can be attributed to the fact that XPS is a more surface-sensitive technique while XRD is a more bulk-sensitive technique [34]. Moreover, the O 1s spectrum of the 15 CD-Ag material is shown in Figure 3d, which can be deconvoluted into three peaks centered at around 529.1 eV, 530.8 eV, and 531.8 eV, corresponding to the chemically bonded O−Ag specie (O_I), the surface absorbed atomic O species (O_{II}) and the residual O−H of H_2O (O_{III}) that possibly existed in the absorbed moisture, respectively [30,35]. As shown in Figure S5, the peak-splitting of Ag 3d and O 1s of the other two CD-Ag materials are similar to the 15 CD-Ag material.

2.2. Electrocatalytic Performance

In order to study the electrocatalytic performance of CO_2RR over CD-Ag electrodes with different Ag content in the precursors, the comparison of electrochemical CO_2RR activity of Ag foil and CD-Ag electrodes was presented in Figure 4a. By comparing these with the linear sweep voltammetry (LSV) curves for CO_2RR over Ag foil and three CD-Ag electrodes it can be observed that the current density displays an increasing trend with the increase in applied potential in the range from −0.35 to −1.35 V vs. RHE for these CD-Ag electrodes, but there is no significant increase for the current density of Ag foil at the low applied potential until the applied potential is higher than −0.65 V vs. RHE, indicating

CD-Ag electrodes possess the higher catalytic activity than that of Ag foil. Considering the results of EDS and XPS analysis, the difference in catalytic activity between CD-Ag and Ag foil could be ascribed to the presence of oxygen species on the CD-Ag surface. Related literature by Jee et al. [36] has demonstrated the surface O of Ag electrodes modifies the electronic state of Ag and causes it to have a stronger interaction with *COOH and *CO intermediates, which can decrease the onset potential for CO_2RR to CO production. Furthermore, the CD-Ag electrodes have a similar current density growth trend but the current density of the 15 CD-Ag electrode is larger than the other two electrodes at the same applied potential. It can be deduced that the different Ag contents in Ag/CM precursors play an important role in electrochemical CO_2RR over these three CD-Ag electrodes.

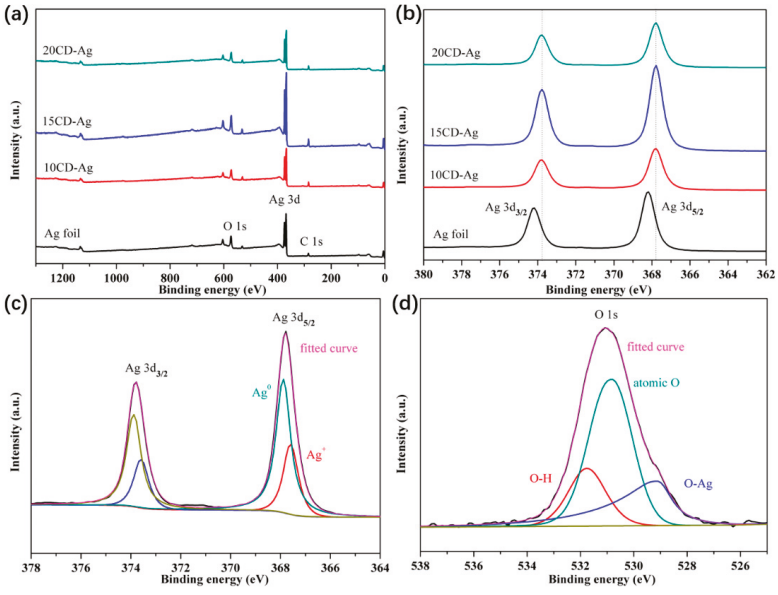

Figure 3. XPS spectra of (**a**) wide scan region and (**b**) Ag 3d of Ag foil and three different CD-Ag materials; the deconvoluted peak of (**c**) Ag 3d and (**d**) O 1s of 15 CD-Ag material.

To better evaluate the enhanced CO_2RR performance of CD-Ag electrodes derived from Ag/CM precursors with different Ag content, the controlled potential electrolysis experiments were carried out on Ag foil and CD-Ag electrodes at different applied potentials to plot the FE curves for the main product CO and H_2 of CO_2RR (Figure 4b,c). As shown in Figure 4b, the FE for CO (FE_{CO}) of Ag foil and CD-Ag electrodes gradually increases with enhancing applied potential, all CD-Ag electrodes show higher FE_{CO} than Ag foil during a substantial applied potential range, while the 15 CD-Ag electrodes exhibit the best CO_2 reduction activity. The FE_{CO} of the 15 CD-Ag electrode is close to 90% at −0.95 V vs. RHE and exceeded 90% in the range of −1.05 to −1.25 V vs. RHE. In contrast, the FE_{CO} of Ag foil remained below 90% throughout the whole applied potential range. When the FE_{CO} of 15 CD-Ag is 89.7% at −0.95 V vs. RHE, the FE_{CO} of Ag foil is only 64.3%. Although all CD-Ag electrodes show better electrocatalytic performance than the Ag foil, there are still some differences among them. It can be determined that the 15 CD-Ag electrode has the best selectivity of CO_2RR to CO compared to the 10 CD-Ag and 20 CD-Ag, and the 15 CD-Ag electrode can obtain excellent performance of CO_2RR to CO in a wide applied potential range. Moreover, the maximum FE_{CO} of 15 CD-Ag is 94.9% at −1.15 V vs. RHE, while at the same applied potential, the maximum FE_{CO} of 10 CD-Ag and 20 CD-Ag is 90.4% and 87.7%, respectively. Furthermore, as seen in Figure S6, CO partial current density and mass activity of different Ag electrodes at various potentials exhibited a similar trend.

The calculated CO partial current density of 15 CD-Ag is higher than those of Ag foil and other CD-Ag in the whole applied potential range. The CO mass activity of 15 CD-Ag is calculated to be 11.7 mA/mg at −0.95 V vs. RHE, while for 10 CD-Ag and 20 CD-Ag catalysts, these values are 7.3 and 7.0 mA/mg, respectively. Indeed, these results further confirm that the 15 CD-Ag sample has the optimal catalytic performance. In the system of electrochemical CO_2RR, the H_2 evolution reaction (HER) is considered the main side reaction, therefore the increase in the FE for H_2 always corresponds to the decrease in FE_{CO} (Figure 4c). As expected, the FE for H_2 of the four Ag electrodes decreases gradually with the increase in applied potential from −0.65 to −1.15 V vs. RHE and falls from Ag foil to 20 CD-Ag to 10 CD-Ag and to 15 CD-Ag at the same applied potential. These contrasts indicate that CD-Ag electrodes can effectively enhance the electrocatalytic activity and selectivity of CO_2RR to CO and significantly inhibit H_2 evolution compared with traditional Ag foil material.

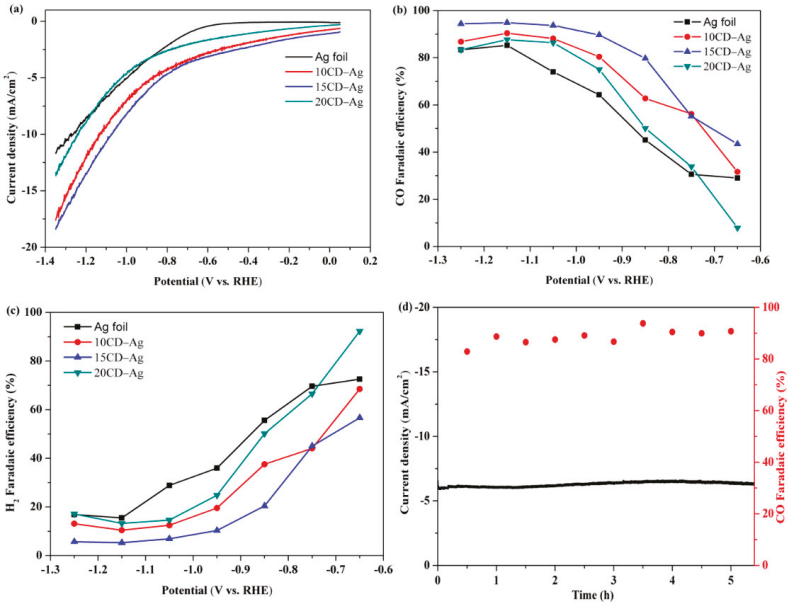

Figure 4. Electrochemical CO_2RR performance of: (**a**) LSV curves; (**b**) FE of CO; and (**c**) FE of H_2 over different electrodes at various applied potentials and (**d**) Current density and FE of CO vs. reaction time over 15 CD-Ag electrode during 5 h of long-time operation at −0.95 V vs. RHE.

The enhancement of the performance should be related to the crystal structure and the special microstructure of CD-Ag electrodes derived from Ag/CM precursors. As indicated by previous studies [13,37], the production efficiency of CO was greatly affected by the crystal structure, and the catalytic activity of electroreduction of CO_2 to CO by single-crystal Ag with different crystal faces decreases in the order of Ag (110) > Ag (111) > Ag (100). However, the diffraction peak of Ag (110) was not observed in the XRD pattern because the (110) reflection in a face-centered cubic structure is forbidden. Ham et al. [38] have estimated the relative number of surface (220) by using the intensity ratio of (220) and (111) peaks as a new descriptor, thus reflecting the ratio of (110) structure in Ag catalyst. We compared the (220)/(111) strength ratio by this method and found that from 10 CD-Ag to 15 CD-Ag and to 20 CD-Ag, the (220)/(111) strength ratio of the sample became smaller, suggesting that the highly active Ag (110) structure in CD-Ag decreased as the Ag content in the precursor increased. On the other hand, it is worth noting that in all the HR-TEM images of the CD-Ag catalysts, only the Ag (111) and (200) crystal planes on the catalyst surface can

be distinguished, which indicates that the surface of the CD-Ag catalyst is dominated by these two crystal planes, especially Ag (111) planes. These results indicated that in addition to the crystal structure, other factors are also involved in CO production efficiency. Many studies have investigated the role of the surface morphology of catalysts in CO_2RR and developed high-performance catalysts by optimizing the surface morphology [39]. The SEM characterization results indicated that Ag materials show different surface morphology (Figure 2). The difference in morphology of three CD-Ag materials should be related to the different loading amounts of Ag on CM, and the details were discussed above. According to the relatively high current density on the 15 CD-Ag electrode, shown in Figure 4, it can be confirmed that the well-dispersed small Ag particles and uniformly distributed pore structure on the 15 CD-Ag electrode provides more active sites to promote CO production than the other electrodes.

Furthermore, it is necessary to evaluate the electrocatalytic stability of the 15 CD-Ag electrode. Therefore, a long-term chronoamperometry experiment of CO_2RR was performed on 15 CD-Ag at a moderate applied potential of −0.95 V vs. RHE. As shown in Figure 4d, 15 CD-Ag displays a relatively stable current density of -6.3 mA/cm^2 with a FE_{CO} of ca. 90% over 5 h. The stability of other electrodes under the same conditions was also tested and the details are shown in Figure S7. The Ag foil also shows a stable current density at -2.2 mA/cm^2, but the corresponding FE_{CO} presents a severe fluctuation between 40% and 60%. At the same time, the FE_{CO} of the 10 CD-Ag quickly decreases from 85% to 60% along with a slight increasing current density from 4.7 to 5.5 mA/cm^2 during the reaction time. As for the 20 CD-Ag electrode, shown in Figure S7c, the FE_{CO} remains a small fluctuation at about 80% within 5 h, but the current density fluctuates greatly with the reaction time compared to the other electrodes. In order to study the stability of these CD-Ag catalysts, we added the SEM images of these CD-Ag catalysts after stability tests in Figure S3. As shown in Figure S3, excessive particle aggregation on the surface of the 10 CD-Ag electrode reduced the active site of electrochemical CO_2RR to CO, which in turn was conducive to the production of H_2, thus it was likely the main reason for the decrease in FE_{CO} in the 10 CD-Ag electrode. Interestingly, the fresh 20 CD-Ag material has larger Ag particles, so agglomeration is probably not the main reason for its stability change. In fact, a large amount of Ag particles, especially large particles, peeled off from the carbon paper after a reaction of 5 h, as shown in the SEM image of 20 CD-Ag. This phenomenon can explain that the current density of 20 CD-Ag fluctuates in the stability test. Notably, it can be found that the Ag particles on the used 15 CD-Ag electrode are still kept in uniform small corals, which is the same as the fresh one. This indicates that the superior stability of the 15 CD-Ag electrode is mainly related to the stable Ag particle size and porosity. These experimental results show that the 15 CD-Ag electrode demonstrates excellent stability within 5 h.

The comparison of ECSA is another important way to explore the difference in the electrochemical CO_2RR performance of Ag foil and CD-Ag electrodes. The ECSA of Ag foil and CD-Ag electrodes were estimated by measuring the double-layer capacitance (C_{dl}) in 0.1 M $KHCO_3$ electrolyte saturated with CO_2. The details are shown in Figure S8, and the C_{dl} data of these different Ag electrodes are calculated from these results. The linear regression of the C_{dl} diagram is shown in Figure 5, and the C_{dl} values corresponding to each sample are summarized in parentheses, which show that the C_{dl} value of the 15 CD-Ag electrode (5.25 mF/cm^2) is more than 40 times larger than that of the Ag foil (0.12 mF/cm^2), while the C_{dl} value of the 10 CD-Ag and 20 CD-Ag electrode correspond to (1.85 mF/cm^2) and (1.04 mF/cm^2), respectively. Obviously, the 15 CD-Ag electrode exhibits the largest ECSA among these four materials. The increased ECSA represents the exposure of more Ag-active sites [26]. The highest ECSA of the 15 CD-Ag electrode can be attributed to the absence of agglomerates and uniform microstructure, which was proven by SEM. It can be inferred that this is the dominant reason for the excellent electrochemical performance of the 15 CD-Ag electrode.

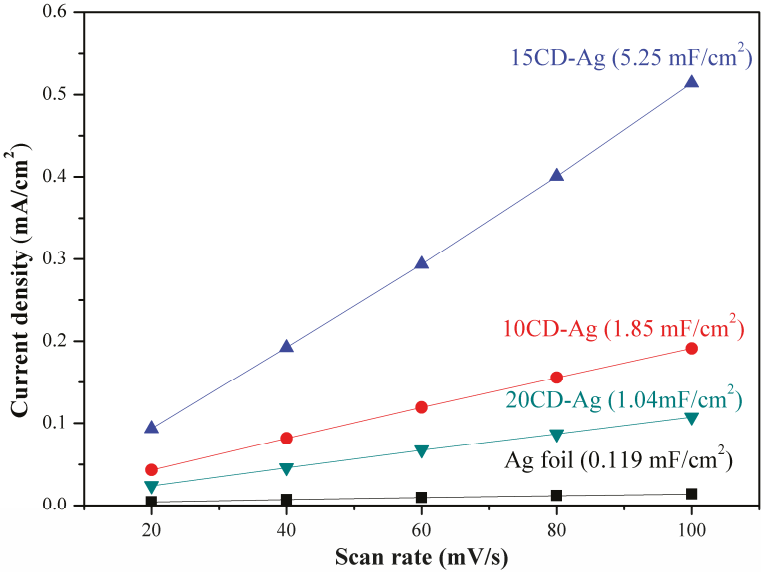

Figure 5. The linear regression of the C_{dl} of Ag foil and three different CD-Ag electrodes and the C_{dl} values listed in parentheses.

According to previous literature [13,40–42], there are three elementary reaction steps on the Ag electrode for CO_2RR to CO:

$$CO_2(g) + H^+(aq) + e^- + * = {}^*COOH \quad (2)$$

$${}^*COOH + H^+(aq) + e^- = {}^*CO + H_2O \quad (3)$$

$${}^*CO = CO(g) + * \quad (4)$$

where * denotes an active site. In the first step of the electrochemical reduction of CO_2, the adsorbed *COOH was formed through a proton-coupled electron transfer. Subsequent reactions included the *COOH intermediate gaining a proton and an electron and then reducing *CO and H_2O. Finally, the *CO was desorbed from the Ag catalyst surface to form CO. To gain insight into the reaction mechanism for CO_2RR to CO, Tafel analysis as an important electrokinetic study to elucidate the CO_2 reduction pathway was performed. As shown in Figure S9, the Tafel slope of Ag foil is 150 mV/dec which implies that the rate-determining step (RDS) is described in Equation (3). The Tafel slope on the 15 CD-Ag is 114 mV/dec, which is very close to a theoretical Tafel value of 118 mV/dec, so it can be inferred that the proton-coupled electron transfer step is likely the RDS for the 15 CD-Ag. The 10 CD-Ag and 20 CD-Ag electrodes have a higher Tafel slope of 121 mV/dec and 135 mV/dec, suggesting similar reaction kinetics and rate-limiting steps on all CD-Ag. These results indicated that the CD-Ag might provide more moderate binding energy for the key intermediates of *COOH and *CO than Ag foil, thus decreasing the onset potential and increasing catalytic activity for CO_2RR to CO production.

Based on the discussions above, we conclude that the excellent catalytic performance of 15 CD-Ag in the electrochemical reduction of CO_2 to CO can be attributed to the following reasons: (1) The characterization results of SEM and TEM proved that the coral-like porous Ag catalyst possesses well-dispersed small Ag particles and uniformly distributed pore structure, which provides a larger ECSA and more accessible active sites to promote CO production, and the catalyst maintains morphological stability after 5 h of electrolysis; (2) The small amount of O on the Ag catalyst surface revealed by the EDS and XPS results could modify the electronic state of Ag and make it have stronger interaction with *COOH

and *CO intermediates, which can decrease the onset potential; (3) The XRD results illustrate that the Ag catalyst has a good crystal structure, and the relatively abundant high-activity Ag (110) crystal face exposed on the surface of the catalyst particles enhances the catalytic activity. Moreover, as shown in Table S2, such electrochemical CO_2RR catalytic performance of the coral-like porous Ag is comparable to previously reported Ag-based electrocatalysts. These results indicate that the coral-like porous Ag prepared in this study can be used as a highly selective electrocatalyst for electrochemical CO_2RR to CO.

3. Materials and Methods

3.1. Materials

Ag foil (purity 99.998%, thickness 0.025 mm) and silver nitrate ($AgNO_3$, 99.995%) were purchased from Alfa Aesar (Shanghai, China). Glucose ($C_6H_{12}O_6$) and ethanol (C_2H_6O) were purchased from Macklin (Shanghai, China). Nafion® perfluorinated resin solution (5 wt% water solution) was purchased from DuPont (Wilmington, DE, USA), carbon paper (CP, TGP-H-60) was purchased from Toray (Tokyo, Japan). Potassium bicarbonate ($KHCO_3$, 99.9%, Aladdin, Shanghai, China) was used to prepare the electrolytes. All solutions were prepared with deionized water.

3.2. Sample Preparation

Carbonaceous microspheres (CM) were synthesized according to the previously reported method [43]. In a typical procedure, 8 g of glucose was dissolved in 70 mL of deionized water to obtain a clear solution, the solution was then transferred and sealed in 80 mL Teflon-sealed autoclave. The Teflon-sealed autoclave was cooled to room temperature under natural conditions after being kept at 180 °C for 4 h. The products were treated by multiple cycles of centrifugation, washing, and re-dispersion in deionized water and further in ethanol until the rinsing solution became neutral and finally dried at 80 °C for 4 h to obtain CM.

The CM-supported Ag samples with different Ag content were obtained by incipient wetness impregnation method. Briefly, the as-synthesized CMs were impregnated with aqueous solution containing $AgNO_3$, and the wet solids were dispersed by ultrasound for 30 min and then placed at room temperature for 12 h, and finally dried at 120 °C for 12 h. The solid products are named 10 Ag/CM, 15 Ag/CM, and 20 Ag/CM, respectively, and the numbers are the mass percentage of Ag calculated by $M_{Ag} \times 100\%/(M_{Ag} + M_{CM})$. The final Ag catalysts were prepared by calcining the precursors at 300 °C for 6 h in air and marked as 10 CD-Ag, 15 CD-Ag, and 20 CD-Ag, respectively. The Ag foil and CP were cleaned by immersion and sonication sequentially in ethanol and deionized water for 30 min.

3.3. Electrode Preparation

Catalyst inks were prepared by mixing deionized water (460 μL), catalyst (10 mg), nafion solution (40 μL), and ethanol (500 μL). The inks were then sonicated for 30 min until obtained a uniform slurry and then painted on the CP with 100 μL ink. After the catalyst ink was loaded on the CP and dried at room temperature, the electrode used in this experiment had a 0.5 mg/cm^2 catalyst loading.

3.4. Electrochemical Methods

All electrochemical tests were carried out using an electrochemical workstation (CHI instrument 660E, Chenhua, Shanghai, China) and a three-electrode system was used throughout the process. The counter electrode and reference electrode were gauze platinum electrode and saturated calomel electrode (SCE), respectively. All potentials in this paper are converted to the reversible hydrogen electrode (RHE) reference scale by the following Equation:

$$E(\text{vs. RHE}) = E(\text{vs. SCE}) + 0.0591 \times \text{pH} + 0.241 \quad (5)$$

Under the experimental conditions, Nafion 117 cation-exchange membrane (Dupont, Wilmington, DE, USA) was devoted to separating the working electrode compartment from the counter electrode compartment in a gas-tight two-component H-type electrochemical cell, and preventing the products produced by the working electrode from diffusing into the counter electrode compartment. An aqueous solution of 0.1 M $KHCO_3$ was used as electrolyte at ambient temperature and pressure, and CO_2 was used for purification at a rate of 20 mL/min for at least 30 min prior to measurement. Throughout the test, the electrolyte was stirred at a constant rate using a magnetic stirring device. A gas chromatograph (GC, SP2100) (Shanghai, China) equipped with a TDX-01 column was used to detect the gas-phase products. CO and H_2 were quantified by a flame ionization detector (FID, Shanghai, China) equipped with methanizer and thermal conductivity detector (TCD, Shanghai, China), respectively. The FE value of product was calculated by the following Equation:

$$FE\% = \frac{z \times n \times F}{Q} \times 100\% \quad (6)$$

where z represents the number of electrons exchanged (z = 2 for CO_2RR to CO or H_2), n is the mole number of an identified product, F is the Faraday constant (96,485 C/mol), and Q is the total quantity of electric charge passed.

3.5. Electrochemical Active Surface Area

The ECSA was estimated by the C_{dl} which is measured by the cyclic voltammetry (CV). The CV was tested in the electrolytic cell within the non-Faradaic range (0.65 to 0.45 V vs. RHE) in 0.1 M $KHCO_3$ electrolyte. The C_{dl} values were calculated by plotting the scan rate versus $\Delta j/2$ (where Δj is the difference between cathodic and anodic current densities) at 0.55 V vs. RHE.

3.6. Physical Characterization

XRD tests were performed on a D8-Foucas diffractometer instrument (Bruker AXS GmbH, Karlsruhe, Germany) equipped with Cu-Kα radiation (λ = 0.15418 nm). Scan steps were performed at 8°/min between 2θ values from 10–70°. The SEM (JEOL Regulus 8100, Tokyo, Japan) and TEM (JEOL JEM2100-F, Tokyo, Japan) were used to characterize the morphology and nanostructure of these materials. The EDS coupled to the SEM was carried out with an Oxford Instruments Ultim-max detector (Oxford, England) based on Silicon drift technology with a 100 mm^2 active area. The TG (HITACHI STA7300, Tokyo, Japan) with a heating rate of 2 °C/min from room temperature to 300 °C in air was used to analysis the calcination process of the Ag/CM precursors. The surface composition of these materials was investigated by XPS (Thermo Fisher Scientific K-Alpha+, Waltham, MA, USA) with an X-ray source of a monochromatized Al Kα radiation (1486.6 eV). The BE scale was calibrated according to the C 1s peak (284.8 eV).

4. Conclusions

In summary, we prepared CM using glucose as the raw material by the hydrothermal method and obtained a series of Ag/CM precursors with different Ag content by the incipient wetness impregnation method. Subsequently, a series of CD-Ag catalysts were prepared by calcination. Compared to Ag foil, CD-Ag electrodes display better CO_2RR performance in a wide potential range, and 15 CD-Ag had the best activity and selectivity. A high FE of 89.7% for CO was achieved on 15 CD-Ag at a potential of −0.95 V vs. RHE, while the FE_{CO} of Ag foil was only 64%. The current density and FE of CO for 15 CD-Ag were almost unchanged over 5 h at −0.95 V vs. RHE. Furthermore, the maximum FE_{CO} of 15 CD-Ag was 95% at −1.15 V vs. RHE. The significant improvement in catalytic activity and selectivity of CO reduction by CO_2 is related to the surface composition and microstructure of the catalyst, among which 15 CD-Ag has the most uniform coral-like porous structure. The uniform pore channel can increase the ECSA, and larger ECSA provides more active sites, thus promoting CO production. The surface O on the catalyst

modulated the interaction between Ag and key intermediates *COOH and *CO, thus changing RDS. In addition, the ratio of Ag (110) facets on the catalyst surface also affects the performance of electrochemical CO_2RR to CO. This work provides a new catalyst and synthesis method for electrochemical CO_2RR, which is a prospective way to solve the challenge of low activity and low selectivity of electrochemical CO_2RR.

Supplementary Materials: The following supporting information can be downloaded at: https://www.mdpi.com/article/10.3390/catal12050479/s1, Figure S1: TEM image and the statistics of particle size distribution in inset (a, b, c) and HR-TEM (a', b', c') of different sample 10 CD-Ag, 15 CD-Ag and 20 CD-Ag, respectively; Figure S2: SEM image of the representative sample 15 Ag/CM precursor; Figure S3: Thermogravimetric analysis (TG) profiles for the Ag/CM precursors during the calcination process; Figure S4: SEM images of different CD-Ag electrodes after 5 h electrolysis: (a) 10 CD-Ag; (b) 15 CD-Ag and 20 CD-Ag, respectively; Figure S5: The deconvoluted peak of (a) Ag 3d and (b) O 1s of 10 CD-Ag material and (c) Ag 3d and (d) O 1s of 20 CD-Ag material; Figure S6: CO partial current density depending on applied potential, and (b) mass activity depending on applied potential; Figure S7: Current density and FE of CO during 5 h of long-time operation at −0.95 V vs. RHE for (a) Ag foil; (b) 10 CD-Ag; (c) 20 CD-Ag electrode, respectively; Figure S8: CV curves on (a) Ag foil; (b) 10 CD-Ag; (c) 15 CD-Ag; (d) 20 CD-Ag electrode with a potential range from 0.65 to 0.45 V vs. RHE in a CO_2 bubbled 0.1 M $KHCO_3$ electrolyte; Figure S9: Tafel plots of the CO partial current density for Ag foil and CD-Ag. Table S1: The elemental compositions of three CD-Ag samples obtained from EDS; Table S2: Comparison of catalytic performances of our catalyst with different Ag-based electrocatalysts producing CO in the literature. References [44,45] are cited in the supplementary materials.

Author Contributions: Conceptualization, X.L.; methodology, X.L. and S.C.; formal analysis, Y.W.; investigation, X.L.; resources, Y.W.; data curation, S.C.; writing—original draft preparation, X.L.; writing—review and editing, L.Z. All authors have read and agreed to the published version of the manuscript.

Funding: This research was funded by the National Natural Science Foundation of China (21776214).

Data Availability Statement: Data are contained within the article or Supplementary Materials.

Acknowledgments: The authors gratefully thank the State Key Laboratory of Chemical Resource Engineering, Tianjin University, China.

Conflicts of Interest: The authors declare no conflict of interest.

References

1. Zhang, W.; Hu, Y.; Ma, L.; Zhu, G.; Wang, Y.; Xue, X.; Chen, R.; Yang, S.; Jin, Z. Progress and Perspective of Electrocatalytic CO_2 Reduction for Renewable Carbonaceous Fuels and Chemicals. *Adv. Sci.* **2018**, *5*, 1700275. [CrossRef] [PubMed]
2. Rosen, B.A.; Salehi-Khojin, A.; Thorson, M.R.; Zhu, W.; Whipple, D.T.; Kenis, P.J.; Masel, R.I. Ionic liquid-mediated selective conversion of CO_2 to CO at low overpotentials. *Science* **2011**, *334*, 643–644. [CrossRef]
3. Benson, E.E.; Kubiak, C.P.; Sathrum, A.J.; Smieja, J.M. Electrocatalytic and homogeneous approaches to conversion of CO_2 to liquid fuels. *Chem. Soc. Rev.* **2009**, *38*, 89–99. [CrossRef]
4. Peterson, A.A.; Norskov, J.K. Activity Descriptors for CO_2 Electroreduction to Methane on Transition-Metal Catalysts. *J. Phys.Chem. Lett.* **2012**, *3*, 251–258. [CrossRef]
5. Kuhl, K.P.; Hatsukade, T.; Cave, E.R.; Abram, D.N.; Kibsgaard, J.; Jaramillo, T.F. Electrocatalytic Conversion of Carbon Dioxide to Methane and Methanol on Transition Metal Surfaces. *J. Am. Chem. Soc.* **2014**, *136*, 14107–14113. [CrossRef]
6. Chen, Z.; Wang, T.; Liu, B.; Cheng, D.; Hu, C.; Zhang, G.; Zhu, W.; Wang, H.; Zhao, Z.J.; Gong, J. Grain-Boundary-Rich Copper for Efficient Solar-Driven Electrochemical CO_2 Reduction to Ethylene and Ethanol. *J. Am. Chem. Soc.* **2020**, *142*, 6878–6883. [CrossRef]
7. Song, R.B.; Zhu, W.; Fu, J.; Chen, Y.; Liu, L.; Zhang, J.R.; Lin, Y.; Zhu, J.J. Electrode Materials Engineering in Electrocatalytic CO_2 Reduction: Energy Input and Conversion Efficiency. *Adv. Mater.* **2019**, *32*, 1903796. [CrossRef] [PubMed]
8. Ham, Y.S.; Kim, M.J.; Choi, J.; Choe, S.; Lim, T.; Kim, S.-K.; Kim, J.J. Fabrication of Au Catalysts for Electrochemical Reduction of CO_2 to Syngas. *J. Nanosci. Nanotechnol.* **2016**, *16*, 10846–10852. [CrossRef]
9. Kim, K.-S.; Kim, W.J.; Lim, H.-K.; Lee, E.K.; Kim, H. Tuned Chemical Bonding Ability of Au at Grain Boundaries for Enhanced Electrochemical CO_2 Reduction. *ACS Catal.* **2016**, *6*, 4443–4448. [CrossRef]
10. Cave, E.R.; Montoya, J.H.; Kuhl, K.P.; Abram, D.N.; Hatsukade, T.; Shi, C.; Hahn, C.; Norskov, J.K.; Jaramillo, T.F. Electrochemical CO_2 reduction on Au surfaces: Mechanistic aspects regarding the formation of major and minor products. *Phys. Chem. Chem. Phys.* **2017**, *19*, 15856–15863. [CrossRef] [PubMed]

11. Zhu, W.; Michalsky, R.; Metin, O.; Lv, H.; Guo, S.; Wright, C.; Sun, X.; Peterson, A.A.; Sun, S. Monodisperse Au Nanoparticles for Selective Electrocatalytic Reduction of CO_2 to CO. *J. Am. Chem. Soc.* **2017**, *139*, 9408. [CrossRef] [PubMed]
12. Salehi-Khojin, A.; Jhong, H.-R.M.; Rosen, B.A.; Zhu, W.; Ma, S.; Kenis, P.J.A.; Masel, R.I. Nanoparticle Silver Catalysts That Show Enhanced Activity for Carbon Dioxide Electrolysis. *J. Phys. Chem. C* **2013**, *117*, 1627–1632. [CrossRef]
13. Rosen, J.; Hutchings, G.S.; Lu, Q.; Rivera, S.; Zhou, Y.; Vlachos, D.G.; Jiao, F. Mechanistic Insights into the Electrochemical Reduction of CO_2 to CO on Nanostructured Ag Surfaces. *ACS Catal.* **2015**, *5*, 4293–4299. [CrossRef]
14. Kim, C.; Eom, T.; Jee, M.S.; Jung, H.; Kim, H.; Min, B.K.; Hwang, Y.J. Insight into Electrochemical CO_2 Reduction on Surface-Molecule-Mediated Ag Nanoparticles. *ACS Catal.* **2016**, *7*, 779–785. [CrossRef]
15. Qi, K.; Zhang, Y.; Li, J.; Charmette, C.; Ramonda, M.; Cui, X.; Wang, Y.; Zhang, Y.; Wu, H.; Wang, W.; et al. Enhancing the CO_2-to-CO Conversion from 2D Silver Nanoprisms via Superstructure Assembly. *ACS Nano* **2021**, *15*, 7682–7693. [CrossRef]
16. Won, D.H.; Shin, H.; Koh, J.; Chung, J.; Lee, H.S.; Kim, H.; Woo, S.I. Highly Efficient, Selective, and Stable CO_2 Electroreduction on a Hexagonal Zn Catalyst. *Angew. Chem. Int. Ed.* **2016**, *55*, 9297–9300. [CrossRef]
17. Zhang, T.; Zhong, H.; Qiu, Y.; Li, X.; Zhang, H. Zn electrode with a layer of nanoparticles for selective electroreduction of CO_2 to formate in aqueous solutions. *J. Mater. Chem. A* **2016**, *4*, 16670–16676. [CrossRef]
18. Nguyen, D.L.T.; Jee, M.S.; Won, D.H.; Jung, H.; Oh, H.-S.; Min, B.K.; Hwang, Y.J. Selective CO_2 Reduction on Zinc Electrocatalyst: The Effect of Zinc Oxidation State Induced by Pretreatment Environment. *ACS Sustain. Chem. Eng.* **2017**, *5*, 11377–11386. [CrossRef]
19. Guo, M.; Li, X.; Huang, Y.; Li, L.; Li, J.; Lu, Y.; Xu, Y.; Zhang, L. CO_2-Induced Fibrous Zn Catalyst Promotes Electrochemical Reduction of CO_2 to CO. *Catalysts* **2021**, *11*, 477. [CrossRef]
20. Yu, Q.; Meng, X.; Shi, L.; Liu, H.; Ye, J. Superfine Ag nanoparticle decorated Zn nanoplates for the active and selective electrocatalytic reduction of CO_2 to CO. *Chem. Commun.* **2016**, *52*, 14105–14108. [CrossRef] [PubMed]
21. Sun, D.; Xu, X.; Qin, Y.; Jiang, S.P.; Shao, Z. Rational Design of Ag-Based Catalysts for the Electrochemical CO_2 Reduction to CO: A Review. *ChemSusChem* **2020**, *13*, 39–58. [CrossRef] [PubMed]
22. Mahyoub, S.A.; Qaraah, F.A.; Chen, C.; Zhang, F.; Yan, S.; Cheng, Z. An overview on the recent developments of Ag-based electrodes in the electrochemical reduction of CO_2 to CO. *Sustain. Energy Fuels* **2020**, *4*, 50–67. [CrossRef]
23. Lu, Q.; Rosen, J.; Zhou, Y.; Hutchings, G.S.; Kimmel, Y.C.; Chen, J.G.; Jiao, F. A selective and efficient electrocatalyst for carbon dioxide reduction. *Nat. Commun.* **2014**, *5*, 3242. [CrossRef] [PubMed]
24. Ma, M.; Trzesniewski, B.J.; Xie, J.; Smith, W.A. Selective and Efficient Reduction of Carbon Dioxide to Carbon Monoxide on Oxide-Derived Nanostructured Silver Electrocatalysts. *Angew. Chem. Int. Ed.* **2016**, *55*, 9748–9752. [CrossRef] [PubMed]
25. Hsieh, Y.-C.; Senanayake, S.D.; Zhang, Y.; Xu, W.; Polyansky, D.E. Effect of Chloride Anions on the Synthesis and Enhanced Catalytic Activity of Silver Nanocoral Electrodes for CO_2 Electroreduction. *ACS Catal.* **2015**, *5*, 5349–5356. [CrossRef]
26. Yang, J.M.; Du, H.S.; Yu, Q.; Zhang, W.; Zhang, Y.; Ge, J.Y.; Li, H.; Liu, J.Y.; Li, H.M.; Xu, H. Porous silver microrods by plasma vulcanization activation for enhanced electrocatalytic carbon dioxide reduction. *J. Colloid Interface Sci.* **2022**, *606*, 793–799. [CrossRef] [PubMed]
27. Ma, M.; Liu, K.; Shen, J.; Kas, R.; Smith, W.A. In Situ Fabrication and Reactivation of Highly Selective and Stable Ag Catalysts for Electrochemical CO_2 Conversion. *ACS Energy Lett.* **2018**, *3*, 1301–1306. [CrossRef]
28. Yu, Y.; Zhong, N.; Fang, J.H.; Tang, S.S.; Ye, X.C.; He, Z.Q.; Song, S. Comparative Study between Pristine Ag and Ag Foam for Electrochemical Synthesis of Syngas with Carbon Dioxide and Water. *Catalysts* **2019**, *9*, 57. [CrossRef]
29. Yang, G.; Zhang, J.; Wang, P.; Sun, Q.; Zheng, J.; Zhu, Y. Light scattering enhanced photoanodes for dye-sensitized solar cells prepared by carbon spheres/TiO_2 nanoparticle composites. *Curr. Appl. Phys.* **2011**, *11*, 376–381. [CrossRef]
30. Zhang, S.; Mo, Z.Z.; Wang, J.; Liu, H.L.; Liu, P.; Hu, D.; Tan, T.X.; Wang, C. Ultra-stable oxygen species in Ag nanoparticles anchored on g-C3N4 for enhanced electrochemical reduction of CO_2. *Electrochim. Acta* **2021**, *390*, 138831. [CrossRef]
31. Costa, R.S.; Aranha, B.S.R.; Ghosh, A.; Lobo, A.O.; da Silva, E.T.S.G.; Alves, D.C.B.; Viana, B.C. Production of oxalic acid by electrochemical reduction of CO_2 using silver-carbon material from babassu coconut mesocarp. *J. Phys. Chem. Solids* **2020**, *147*, 109678. [CrossRef]
32. Rocha, T.C.; Oestereich, A.; Demidov, D.V.; Havecker, M.; Zafeiratos, S.; Weinberg, G.; Bukhtiyarov, V.I.; Knop-Gericke, A.; Schlogl, R. The silver-oxygen system in catalysis: New insights by near ambient pressure X-ray photoelectron spectroscopy. *Phys. Chem. Chem. Phys.* **2012**, *14*, 4554–4564. [CrossRef] [PubMed]
33. Jiang, K.; Kharel, P.; Peng, Y.; Gangishetty, M.K.; Lin, H.-Y.G.; Stavitski, E.; Attenkofer, K.; Wang, H. Silver Nanoparticles with Surface-Bonded Oxygen for Highly Selective CO_2 Reduction. *ACS Sustain. Chem. Eng.* **2017**, *5*, 8529–8534. [CrossRef]
34. Jalil, P.A.; Faiz, M.; Tabet, N.; Hamdan, N.M.; Hussain, Z. A study of the stability of tungstophosphoric acid, $H_3PW_{12}O_{40}$, using synchrotron XPS, XANES, hexane cracking, XRD, and IR spectroscopy. *J. Catal.* **2003**, *217*, 292–297. [CrossRef]
35. Prieto, P.; Nistor, V.; Nouneh, K.; Oyama, M.; Abd-Lefdil, M.; Díaz, R. XPS study of silver, nickel and bimetallic silver–nickel nanoparticles prepared by seed-mediated growth. *Appl. Surf. Sci.* **2012**, *258*, 8807–8813. [CrossRef]
36. Jee, M.S.; Kim, H.; Jeon, H.S.; Chae, K.H.; Cho, J.; Min, B.K.; Hwang, Y.J. Stable surface oxygen on nanostructured silver for efficient CO_2 electroreduction. *Catal. Today* **2017**, *288*, 48–53. [CrossRef]
37. Hoshi, N.; Kato, M.; Hori, Y. Electrochemical reduction of CO, on single crystal electrodes of silver Ag(111), Ag(100) and Agi(110). *J. Electroan. Chem.* **1997**, *440*, 283–286. [CrossRef]

38. Ham, Y.S.; Choe, S.; Kim, M.J.; Lim, T.; Kim, S.-K.; Kim, J.J. Electrodeposited Ag catalysts for the electrochemical reduction of CO_2 to CO. *Appl. Catal. B Environ.* **2017**, *208*, 35–43. [CrossRef]
39. Pan, F.P.; Yang, Y. Designing CO_2 reduction electrode materials by morphology and interface engineering. *Energy Environ. Sci.* **2020**, *13*, 2275–2309. [CrossRef]
40. Liu, S.-Q.; Wu, S.-W.; Gao, M.-R.; Li, M.-S.; Fu, X.-Z.; Luo, J.-L. Hollow Porous Ag Spherical Catalysts for Highly Efficient and Selective Electrocatalytic Reduction of CO_2 to CO. *ACS Sustain. Chem. Eng.* **2019**, *7*, 14443–14450. [CrossRef]
41. He, Z.; Liu, T.; Tang, J.; Zhou, C.; Wen, L.; Chen, J.; Song, S. Highly active, selective and stable electroreduction of carbon dioxide to carbon monoxide on a silver catalyst with truncated hexagonal bipyramidal shape. *Electrochim. Acta* **2016**, *222*, 1234–1242. [CrossRef]
42. Qiu, J.P.; Tang, J.T.; Shen, J.; Wu, C.W.; Qian, M.Q.; He, Z.Q.; Chen, J.M.; Song, S. Preparation of a silver electrode with a three-dimensional surface and its performance in the electrochemical reduction of carbon dioxide. *Electrochim. Acta* **2016**, *203*, 99–108.
43. Sun, X.M.; Li, Y.D. Colloidal carbon spheres and their core/shell structures with noble-metal nanoparticles. *Angew. Chem. Int. Ed.* **2004**, *43*, 597–601. [CrossRef] [PubMed]
44. Xi, W.; Ma, R.; Wang, H.; Gao, Z.; Zhang, W.; Zhao, Y. Ultrathin Ag Nanowires Electrode for Electrochemical Syngas Pro-duction from Carbon Dioxide. *ACS Sustain. Chem. Eng.* **2018**, *6*, 7687–7694. [CrossRef]
45. Liu, S.; Tao, H.; Zeng, L.; Liu, Q.; Xu, Z.; Liu, Q.; Luo, J.L. Shape-Dependent Electrocatalytic Reduction of CO_2 to CO on Triangular Silver Nanoplates. *J. Am. Chem. Soc.* **2017**, *139*, 2160–2163. [CrossRef] [PubMed]

catalysts

MDPI

Article

Coupling $LaNiO_3$ Nanorods with FeOOH Nanosheets for Oxygen Evolution Reaction

Minghong Sun [1], Qicheng Zhang [1], Qiming Chen [1], Xiaohan Hou [1], Wenchao Peng [1], Yang Li [1], Fengbao Zhang [1], Qing Xia [1] and Xiaobin Fan [1,2,3,*]

[1] State Key Laboratory of Chemical Engineering, School of Chemical Engineering and Technology, Tianjin University, Tianjin 300072, China; minghongsun@tju.edu.cn (M.S.); zhangqicheng@tju.edu.cn (Q.Z.); qimingchen@tju.edu.cn (Q.C.); xiaohanhou@tju.edu.cn (X.H.); wenchao.peng@tju.edu.cn (W.P.); liyang1895@tju.edu.cn (Y.L.); fbzhang@tju.edu.cn (F.Z.); xiaqing@tju.edu.cn (Q.X.)
[2] Haihe Laboratory of Sustainable Chemical Transformations, Tianjin 300192, China
[3] Institute of Shaoxing, Tianjin University, Shaoxing 312300, China
* Correspondence: xiaobinfan@tju.edu.cn

Abstract: Perovskite-based electrocatalysts with compositional flexibility and tunable electronic structures have emerged as one of the promising non-noble metal candidates for oxygen evolution reaction (OER). Here, we propose a heterostructure comprising perovskite oxide ($LaNiO_3$) nanorods and iron oxide hydroxide (FeOOH) nanosheets as an effective electrochemical catalyst for OER. The optimized 0.25Fe-LNO catalyst with an interesting 1D-2D hierarchical structure shows a low overpotential of 284 mV at 10 mA cm^{-2} and a small Tafel slope of 69 mV dec^{-1}. The enhanced performance can be explained by the synergistic effect between $LaNiO_3$ and FeOOH, resulting in an improved electrochemically active surface area, facilitated charge transfer and the optimized adsorption of OH intermediates.

Keywords: perovskite oxide; oxygen evolution; FeOOH; electrocatalyst

Citation: Sun, M.; Zhang, Q.; Chen, Q.; Hou, X.; Peng, W.; Li, Y.; Zhang, F.; Xia, Q.; Fan, X. Coupling $LaNiO_3$ Nanorods with FeOOH Nanosheets for Oxygen Evolution Reaction. *Catalysts* **2022**, *12*, 594. https://10.3390/catal12060594

Academic Editors: Yongjun Feng, Zhenghua Tang, Marc Cretin and Sophie Tingry

Received: 10 April 2022
Accepted: 24 May 2022
Published: 30 May 2022

1. Introduction

Faced with the growing energy crisis and environmental issues, it is imperative to exploit effective and green devices for energy storage and conversion [1–3]. The rational design of oxygen evolution reaction (OER) electrocatalysts is of great significance to the applications of water electrolyzers [4,5]. However, the sluggish kinetics and high overpotential of OER caused by the complex multiple electron transfer process are obstacles to its large-scale application [6]. Although Ir- and Ru-based oxide are recognized as the benchmark OER catalysts with high electrochemical activity, their high cost and low abundance have compelled the development of earth-abundant and efficient non-noble metal OER catalysts [7,8]. In recent years, tremendous efforts have been devoted to research on transition metal-based catalysts, such as transition metal oxides, [9] sulfides [10] and oxyhydroxides [11].

As the promising candidates, perovskite oxides with a general formula of ABO_3 have attracted increasing attention owing to their compositional flexibility, tunable electronic structures and chemical stability [12,13]. To guide the design of ABO_3 catalysts for OER, ($\Delta G_{O^*} - \Delta G_{OH^*}$) [14] and e_g orbital filling [15] have been proposed as catalytic activity descriptors. According to the volcano maps obtained by describing OER activity with the descriptors, $LaNiO_3$ (LNO) shows better performance in the family of ABO_3 and is considered a prospective candidate for optimization [14–16]. Nonetheless, the electrocatalytic performance of the LNO remains unsatisfactory due to its limited active sites and poor electrical conductivity [13,17]. On the one hand, the perovskite oxides synthesized by traditional solid-state and sol-gel methods generally have a large size and low surface area, resulting in poor catalytic activity. Previous studies have demonstrated that morphology

engineering is an effective method to enhance the activity of perovskite-based electrocatalysts by increasing the surface area, such as nanorods [18], nanofibers [19] nanotubes [20] and porous structure [21]. On the other hand, intrinsic catalytic activity is also an important consideration in perovskite-based catalyst design [22]. The adsorption and desorption of OH are key steps in the alkaline OER process, and optimizing the adsorption energy of intermediates can boost OER intrinsic catalytic activity [23,24]. Constructing heterogeneous structures is a general method which can not only modulate the electronic structure but also generate synergistically active sites [13,19,25]. Among the various perovskite-based composites, perovskite/transition metal-based composites exhibit excellent performance, such as $CoS_2/LaCo_{0.2}Fe_{0.8}O_3$, [12] $MoSe_2/La_{0.5}Sr_{0.5}CoO_{3-\delta}$ [26] and $Fe_2O_3/LaNiO_3$ [27]. Meanwhile, FeOOH is considered a promising catalyst for OER, with high OH adsorption capacity [28,29] that can be introduced into perovskite-based composites to accelerate OER kinetics.

Here, we propose the 1D-2D $LaNiO_3$ nanorods-FeOOH nanosheets heterostructure as an effective catalyst for oxygen evolution reaction. The optimized 0.25Fe-LNO catalyst displays a lower overpotential and a smaller Tafel slope when compared with the other counterparts. The experimental results demonstrate that the excellent OER catalytic performance of $LaNiO_3$/FeOOH could be attributed to the synergistic effect between LNO and FeOOH as well as the morphology engineering of LNO, encouraging the strong electron interaction, the facilitated charge transfer and the improved active sites.

2. Results and Discussion

Scheme 1 schematically illustrates the synthesis process for hierarchical $LaNiO_3$/FeOOH composites by two steps. Briefly, the perovskite LNO nanorods were synthesized by the hydrothermal method and then immersed in alkaline solutions of K_2FeO_4 with different concentrations to obtain the hierarchical LNO-FeOOH composites, denoted as xFe-LNO, x = 0.125, 0.25, 0.5, 0.75. The more experimental details are shown in the experimental section.

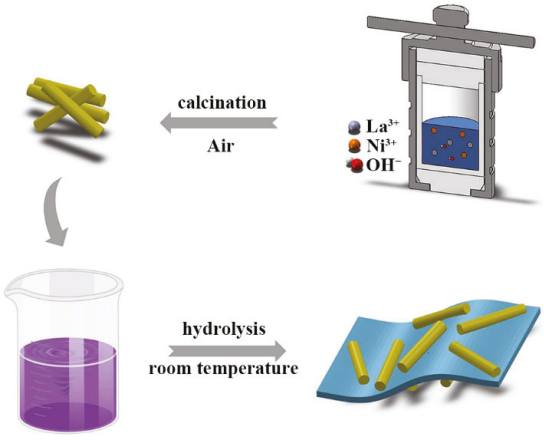

Scheme 1. Schematic illustration for the synthesis of Fe-LNO.

The powder X-ray diffraction (XRD) patterns of LNO, FeOOH and xFe-LNO are shown in Figure 1a. The diffraction peaks of the obtained LNO match well with the standard peaks of $LaNiO_3$ (JCPDS No. 33-0711), whereas FeOOH shows no diffraction peak. Generally, FeOOH prepared by hydrolysis at low temperatures has poor crystallinity without obvious diffraction peaks in the XRD spectrum [30–32]. Although the diffraction peaks of FeOOH appear in some cases, the peak intensity is also very weak due to the room temperature synthesis [33]. In addition, experimental conditions such as concentration and whether or not to stir could also affect the crystallinity. According to the XRD spectrum, the

FeOOH prepared in this work has a lower crystallinity and presents an amorphous form. It is worth noting that the diffraction peaks' position corresponding to $LaNiO_3$ (JCPDS No. 33-0711) remains unchanged in the xFe-LNO samples, but the corresponding peak intensity gradually decreases with the increase in x value. This phenomenon is inconsistent with Fe doping, which will cause a shift in the diffraction peaks corresponding to $LaNiO_3$ to lower angles in the XRD spectrum [34,35], but it is consistent with the formation of amorphous substances on the surface of LNO [20]. Furthermore, new diffraction peaks corresponding to $La(OH)_3$ (JCPDS No. 36-1481) appear, owing to the presence of NaOH in the K_2FeO_4 solution, but the perovskite structure remains. To identify the FeOOH phase, Raman spectra were performed (Figure 1b). For the hydrolysis products of K_2FeO_4, the six characteristic peaks (214, 283, 310, 377, 517 and 674 cm^{-1}) are well-indexed to the layered γ-FeOOH structure. The peak at 377 cm^{-1} is the characteristic of γ-FeOOH, and the peaks at 310 and 517 cm^{-1} are ascribed to the Fe–OH stretching modes. The broad peak located at 674 cm^{-1} can be attributed to the stretching of Fe–O, [33,36,37] while the weak peak at 1310 cm^{-1} corresponds to the H_2O intercalated in the layered FeOOH [37–39]. Note that the LNO sample has no vibrational modes of Raman response, and the 0.25Fe-LNO exhibits weaker vibrational bands at 310, 377, 517 and 674 cm^{-1} compared with the LNO nanorods counterpart. The peaks at 214 cm^{-1} and 283 cm^{-1} correspond to the layer structure, which mainly depends on the degree of disorder (stacking fault) and/or grain size [40]. The disappearance of the peaks only indicates that the LNO stacking on the FeOOH surface weakens the mode of the layer structure. These results suggest the successful formation of the FeOOH-LNO composite.

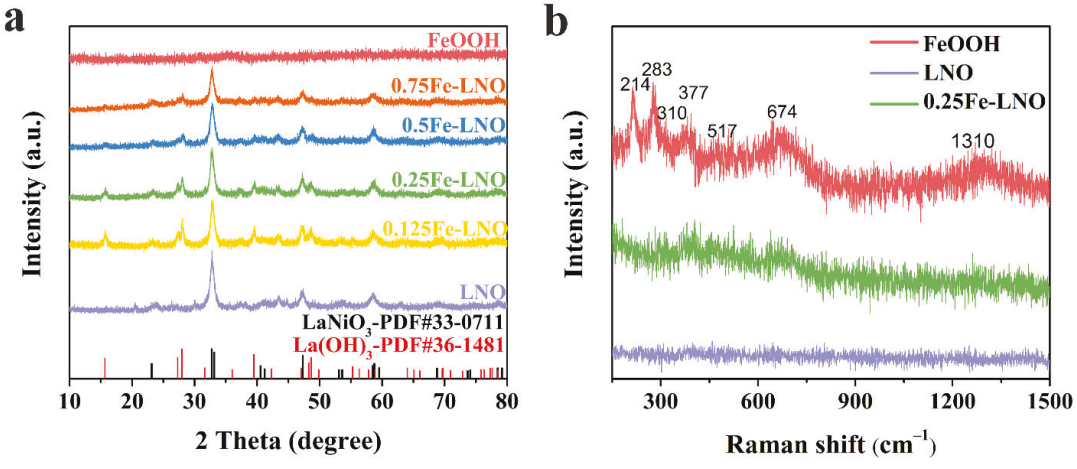

Figure 1. (**a**) XRD pattern of LNO, FeOOH and Fe-LNO samples (**b**) Raman spectrum of LNO, FeOOH and 0.25Fe-LNO.

Scanning electron microscopy (SEM) reveals that the hydrothermal synthesized LNO exhibits a nanorod structure with lengths of 30–100 nm and diameters of 10–20 nm (Figure 2a), while the FeOOH, as the hydrolysates of K_2FeO_4, is composed of aggregated nanosheets (Figure S1, Supplementary Materials). The drying process in the preparation leads to agglomeration, which makes the SEM image of 0.25Fe-LNO unable to fully display the morphology of the sample. Nonetheless, the nanosheets can still be identified in the marked regions of Figure 2b, demonstrating the successful introduction of FeOOH and forming the composites. Note that this hierarchical structure results in an increase in the specific surface area (SSA). The Brunauer–Emmett–Teller (BET) analysis actually shows that the SSA of the obtained 0.25Fe-LNO is 40.4 $m^2\ g^{-1}$, which is almost twice that of the LNO nanorods (22.8 $m^2\ g^{-1}$) (Figure S2, Supplementary Materials). Transmission

electron microscopy (TEM) was carried out to further unveil the morphology and structure of LNO and 0.25Fe-LNO. TEM images at different magnifications of 0.25Fe-LNO (Figures 2d and S3, Supplementary Materials) demonstrate that the morphology of the LNO nanorods with the diameters of 10–20 nm remained basically unchanged, which is consistent with the SEM and TEM image of the LNO (Figure 2a,c). More importantly, it can be clearly seen that the nanorods attach randomly to the thin nanosheets, indicating the existence of 1D-2D heterostructures that are consistent with the synthesis results of Scheme 1. The composition of this heterostructure was further determined by the high-resolution TEM (HRTEM) images. The lattice fringes of the LNO nanorods are measured to be 0.273 and 0.384 nm, corresponding to the (110) and (101) facets of $LaNiO_3$ (JCPDS No. 33-0711), respectively (Figure S4, Supplementary Materials). As shown in Figure 2e,f, the HRTEM images of 0.25Fe-LNO reflects the intact contact between the LNO nanorods and the FeOOH nanosheets, and the FeOOH has no regular interplanar spacing due to poor crystallinity, which is consistent with the results of the XRD. To further identify the composition of the nanosheets, the HAADF-TEM image of 0.25Fe-LNO and the corresponding elemental mapping images are shown in Figure S5 (Supplementary Materials), which can further prove the existence of FeOOH nanosheets and the formation of a 1D-2D $LaNiO_3$ nanorods-FeOOH nanosheets heterostructure. The clear and coherent interface between the LNO and FeOOH displayed in the TEM image of 0.25Fe-LNO can favor the electronic transfer and the biphasic synergy catalysis, as verified by subsequent X-ray photoelectron spectroscopy (XPS) and electrochemical measurements [19].

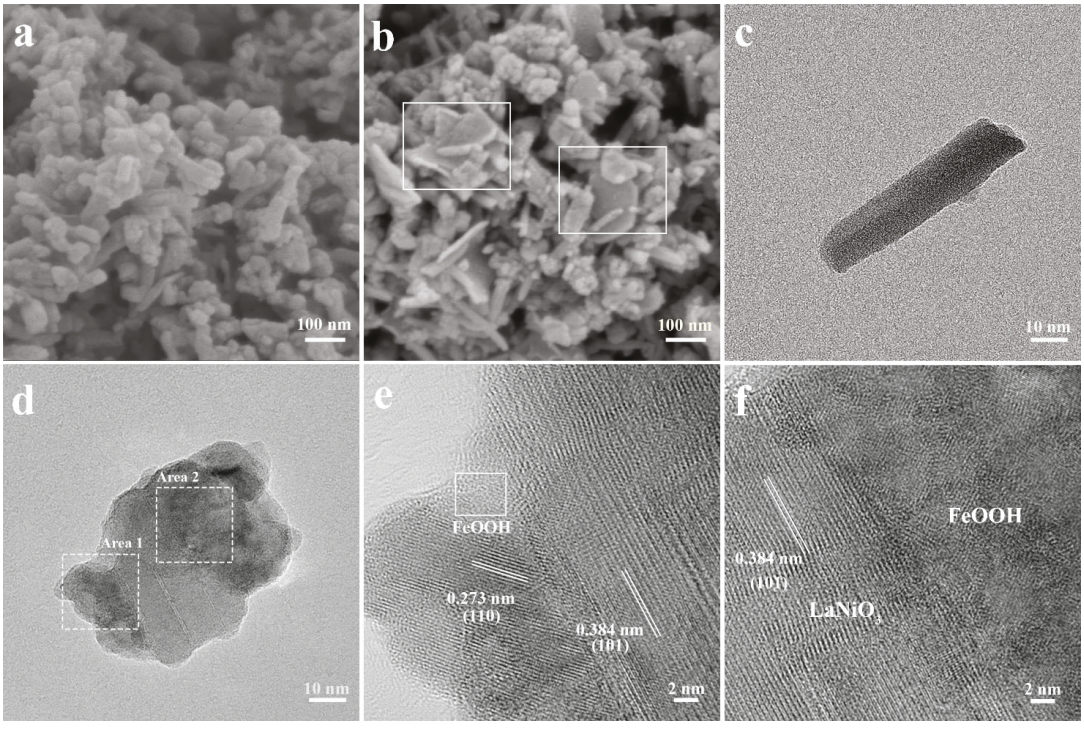

Figure 2. SEM images of (**a**) LNO and (**b**) 0.25Fe-LNO. TEM images of (**c**) LNO and (**d**) 0.25Fe-LNO. HRTEM image of 0.25Fe-LNO corresponding to the (**e**) Area 1 and (**f**) Area 2, as marked in (**d**).

The elemental compositions and electronic structure of the LNO, FeOOH and 0.25Fe-LNO were investigated by XPS. The survey spectra (Figure S6, Supplementary Materials) confirm that La, Ni, Fe and O are the main elements in the 0.25Fe-LNO. The XPS spectra of the La 3d

and Ni 2p of LNO and 0.25Fe-LNO are shown in Figure 3a,b. Considering that the binding energy region of La $3d_{3/2}$ and Ni $2p_{3/2}$ partially overlap, [41,42] the peak position and intensity of La $3d_{3/2}$ and Ni $2p_{3/2}$ are distinguished by those of La $3d_{5/2}$ and Ni $2p_{1/2}$ [43]. Moreover, it is noted that the peaks of La $3d_{3/2}$ and $3d_{5/2}$ are multiplet-split owing to the charge transfer from the bonded oxygen to the empty La 4f [44]. The La $3d_{5/2}$ and $3d_{3/2}$ of LNO are located at 834.37/837.80 and 850.79/853.43, whereas those of 0.25Fe-LNO are positioned at 834.87/838.35 and 851.34/853.98, respectively. It demonstrates a binding energy upshift of 0.55 eV in the 0.25Fe-LNO compared to the LNO nanorods [44,45]. Similarly, the Ni 2p spectra of 0.25Fe-LNO consist of Ni $2p_{3/2}$ (855.65 eV) and Ni $2p_{1/2}$ (872.95 eV), with two satellites whose binding energy is 0.20 eV higher than those of LNO, implying an increased oxidation state of Ni [46]. These shifts in the peak positions indicate a shift in the Fermi level with respect to the core levels rather than the charging effects. First, the charge compensation and energy calibration were used to remove the charge effect. Further, the charging effect caused by a significant net positive charge accumulates at the surface of insulators and will lead to a positive shift in the binding energy of the sample. Given that the conductivity of LNO is worse than that of 0.25Fe-LNO, the charging effect of LNO should be more obvious than that of 0.25Fe-LNO. However, the binding energy of 0.25Fe-LNO is positively shifted compared to that of LNO in the Ni 2p and La 3d XPS spectrum. High-spin Fe^{3+} and Fe^{2+} cause complex multiplet-split in the Fe 2p spectrum [47]. Since the multiple splitting of Fe^{2+} and Fe^{3+} is too complicated to distinguish, and dividing Fe 2p into different oxidation states could also identify the shift in the peak positions well, it is not necessary to distinguish multiple peaks for each oxidation state [33,48]. As demonstrated in Figure 3c, the Fe 2p spectra consist of two spin–orbit doublets with satellites, and the Fe species could be deconvoluted into Fe^{2+} and Fe^{3+}. The peaks of 0.25Fe-LNO at 712.16/725.42 and 710.19/723.45 eV correspond to Fe^{3+} $2p_{3/2}/2p_{1/2}$ and Fe^{2+} $2p_{3/2}/2p_{1/2}$, respectively [49]. Further, the peak at around 706 eV is assigned to the Ni Auger peak in the 0.25Fe-LNO. Compared with those of pure FeOOH, the Fe 2p peaks of 0.25Fe-LNO downshift 0.29 eV. The chemical shifts strongly confirm the electron transfer from the LNO nanorods to the FeOOH in 0.25Fe-LNO, which can lead to a synergetic effect to improve the OER electrocatalytic activity. [50] In addition, Figure 3d displays the O 1 s spectra of LNO and 0.25Fe-LNO, which can be deconvoluted into four peaks corresponding to the lattice oxygen species (O^{2-}, 528.32 eV), superoxidative oxygen ($O2^{2-}/O^{-}$, 529.44 eV), hydroxyl groups (–OH, 531.12 eV) and adsorbed water (H_2O, 532.18 eV) [51]. The content of adsorbed water oxygen mainly depends on the atmospheric conditions rather than the material properties [48]. When calculating the proportion of oxygen species, the content of adsorbed water should be removed. It is noted that the proportion of hydroxyl groups in the oxygen species of 0.25Fe-LNO (76.3%) is significantly higher than that of LNO (62.5%), indicating the higher surface coverage (θ) of the OH species in the 0.25Fe-LNO sample [52]. A high θ value is beneficial for OH adsorption on the catalyst surface, which can enhance OER intrinsic activity [26,52].

The OER catalytic performance of as-prepared catalysts was measured in a 1 M KOH electrolyte. As shown in Figure 4a, the linear sweep voltammetry (LSV) polarization curves demonstrate that the OER activity of the xFe-LNO catalysts significantly exceeds that of the LNO or FeOOH alone. Among them, the 0.25Fe-LNO catalyst displays the best performance, with the lowest overpotential of 284 mV at the current density of 10 mA cm^{-2}—even better than commercial RuO_2 and IrO_2 (Figure S7, Supplementary Materials). The LNO and FeOOH exhibit poor performance, with overpotentials of 363 and 330 mV, generating the same density current of 10 mA cm^{-2}, respectively. The Tafel slopes of xFe-LNO, FeOOH and LNO are shown in Figure 4b, which are used to reflect the OER kinetics reaction rate and the charge transfer ability [7,53]. As expected, the 0.25Fe-LNO sample displays the lowest Tafel slope of 69 mV·dec^{-1}, which is significantly smaller than those of the LNO nanorods (120 mV·dec^{-1}), FeOOH nanosheets (92 mV·dec^{-1}) and RuO_2 (84 mV·dec^{-1}). Note that all the Tafel slopes of the other xFe-LNOs catalysts are smaller than those of the individual components. For the four-electron transfer oxygen

evolution reaction, the Tafel slope is closely related to the reaction mechanism and can even predict the rate-determining step. Furthermore, the rate-determining step moves closer to the beginning part of the multiple-electron transfer reaction as the Tafel slope increases. As the first electron transfer reaction, when the adsorption of the OH groups is the rate-determining step, the corresponding Tafel slope is 120 mV dec^{-1} [54]. This suggests that the adsorption of OH groups is the OER rate-limiting step of LNO. These low Tafel slopes of the xFe-LNO could be attributed to the high coverage of the hydroxyl group and the obvious charge transfer between FeOOH and LNO, as discussed above. During the electrochemical test of perovskite-based catalysts, conductive agents are usually added to the ink in a certain mass ratio to remove the electrode conductivity limit. To further demonstrate the catalyst-specific results, the LSV polarization curves and corresponding Tafel plots of these samples without Ketjenblack carbon were added in the Supplementary Materials (Figure S8). The catalyst-specific activity of 0.25Fe-LNO significantly surpasses that of LNO and FeOOH. The addition of Ketjenblack carbon can improve the performance of these catalysts to varying degrees, and the positive influence on LNO and FeOOH is greater than that on 0.25Fe-LNO, indicating that the heterostructure enhances the conductivity of LNO and FeOOH. The resistivities of 0.25Fe-LNO are almost twice those of LNO, as tested by a four-probe resistance tester, which further confirmed the above conclusion (Supplementary Materials).

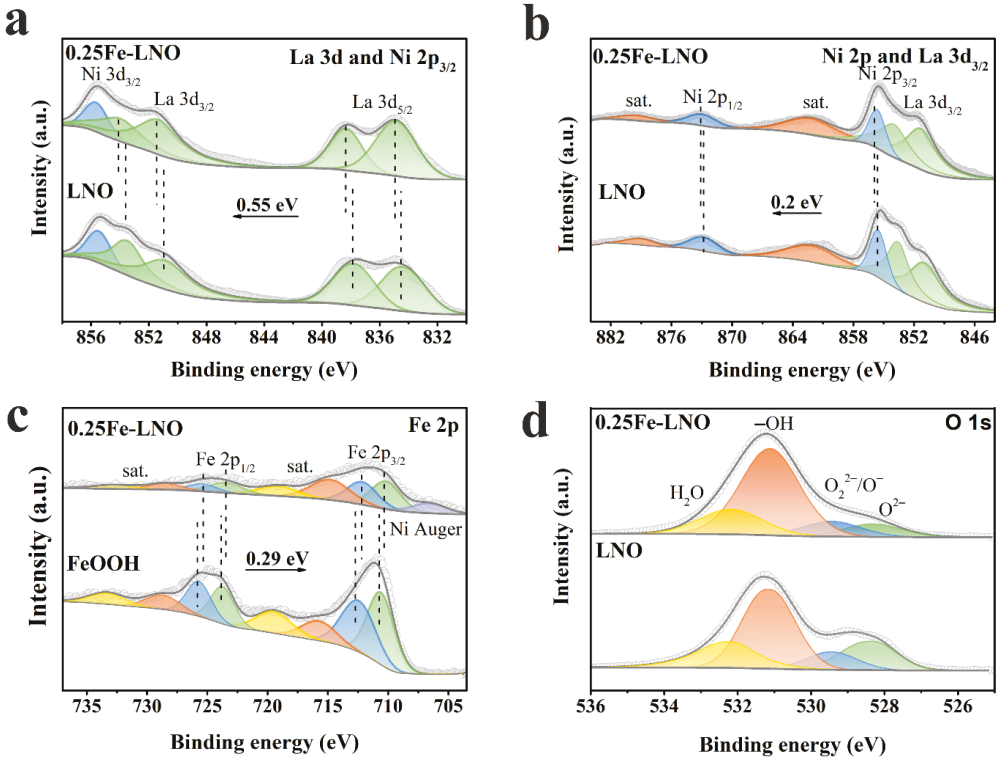

Figure 3. XPS spectra of (**a**) La 3d, (**b**) Ni 2p, (**c**) Fe 2p and (**d**) O 1s.

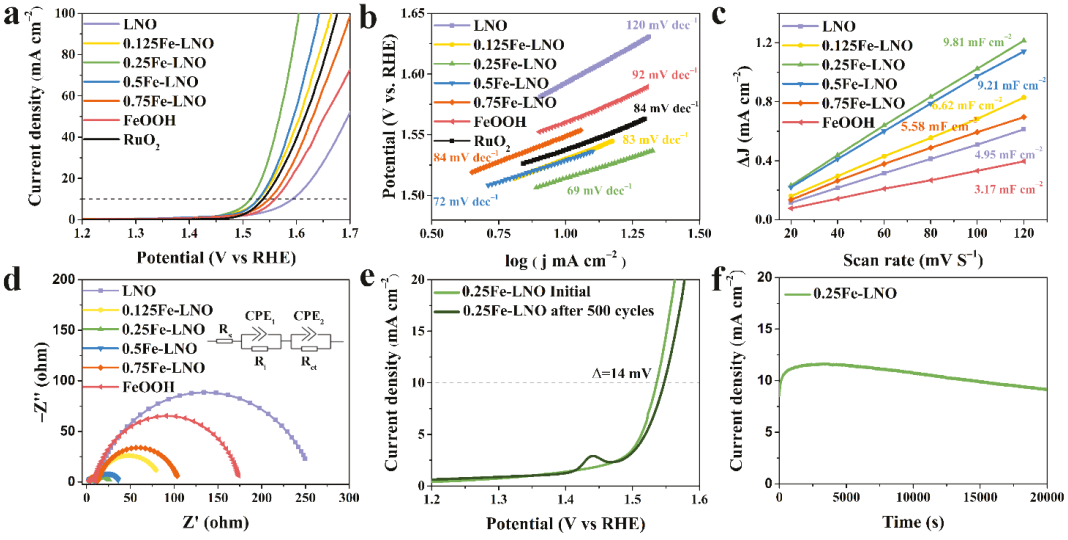

Figure 4. (**a**) LSV of LNO, FeOOH and Fe-LNO samples. (**b**) The corresponding Tafel plots. (**c**) Linear fits of half capacitive currents versus scan rates for the extraction of the double-layer capacitances. (**d**) Nyquist plots. The inset of (**d**) is the equivalent circuit diagram. (**e**) The initial polarization curves and the 500th cycles of 0.25Fe-LNO. (**f**) The chronoamperometric curves of 0.25Fe-LNO.

To further elucidate the enhanced electrochemical performance of 0.25Fe-LNO, cyclic voltammetry (CV) and EIS measurements were carried out. The CV curves measured from 20 mV S^{-1} to 120 mV S^{-1} of the LNO, xFe-LNO and FeOOH samples are displayed in Figure S9 (Supplementary Materials). The electrochemically active surface area (ECSA) is in direct proportion to the double-layer capacity (C_{dl}) [10,55,56]. The C_{dl} value of the 0.25Fe-LNO (9.81 mF cm^{-2}) is approximately 3.1 and 2.0 times higher than that of the FeOOH nanosheets (3.17 mF cm^{-2}) and LNO nanorods (4.95 mF cm^{-2}), indicating that the composite holds more electrocatalytically active sites than the single component (Figure 4c). The increased ECSA should be the reason, at least in part, for the enhanced OER activity of the 0.25Fe-LNO catalyst, which is highly consistent with the results of SSA discussed above. The LSV curves normalized by the ECSA of LNO, xFe-LNO, FeOOH and RuO_2 are presented to probe the intrinsic activity of the active sites in Figure S10 (Supplementary Materials). Among them, 0.25Fe-LNO has the highest intrinsic activity, indicating that the composite can not only increase the ECSA but also enhance the intrinsic activity. In Figure 4d, the Nyquist plots of each catalyst are manifested as two semi-circles, and the semicircles at the lower and higher frequency ranges represent the interface resistance and charge transfer resistance, respectively [57]. The corresponding equivalent circuit, which consists of the solution resistance (R_s), the interface resistance (R_i), the charge-transfer resistance (R_{ct}) and two constant phase elements (CPE), is shown in the inset of Figure 4d. We found that the R_{ct} of 0.25Fe-LNO (19.1 Ω) was significantly reduced in comparison with those of LNO (250.6 Ω) and FeOOH (166.4 Ω), suggesting that the composite catalyst possesses rapid charge-transfer kinetics [58,59]. The more fitting parameters of the Nyquist plots are listed in Table S1 (Supplementary Materials), and the trend of R_{ct} is line with the results of the Tafel slopes. To demonstrate the positive effect of the close contact between LNO and FeOOH, the electrochemical performance of the $LaNiO_3$/FeOOH composite prepared by physical mixing (0.25Fe/LNO) was measured as a comparison (Figure S11, Supplementary Materials). 0.25Fe/LNO displays increased OER activity when compared with LNO and FeOOH. However, the OER performance of 0.25Fe/LNO is far inferior to that of 0.25Fe-LNO due to the smaller active surface area

and the larger charge-transfer resistance. Compared with 0.25Fe/LNO, 0.25Fe-LNO exhibits enhanced synergy and charge transfer between LNO and FeOOH. In addition, the turnover frequency (TOF) of the LNO, xFe-LNO and FeOOH catalysts at 1.60 V vs. RHE was calculated and is listed in Table S2 (Supplementary Materials). 0.25Fe-LNO exhibits a TOF value of 0.243 S^{-1}, an order of magnitude higher than those of LNO (0.031 S^{-1}) and FeOOH (0.022 S^{-1}), proving that 0.25Fe-LNO possesses superior intrinsic activity [7]. The durability test shows that the overpotential of the 0.25Fe-LNO composite catalyst only increased by 14 mV at the current density of 10 mA cm^{-2} after 500 CV cycles (Figure 4e). The peak at 1.45 V vs. RHE after 500 CV cycles is the oxidation peak of the Ni species, because the Ni based electrocatalyst $LaNiO_3$ experiences the self-surface reconstruction during the electrochemical activation process, forming the amorphous active phase. [53,60]. A clear activation process is also observed during the first as-shown 20,000 s (Figure 4f). For the Chronoamperometry test, the Ni foam was covered by the catalyst as the working electrode, and the interaction and the interface effect between the catalyst and the Ni foam are usually negligible [22,59]. On the one hand, the activity of the Ni foam is far inferior to that of the prepared catalyst (Figure S12, Supplementary Materials); on the other hand, the catalyst dropped on the Ni foam is on a microscale and has less effect than that growing on it.

3. Materials and Methods

3.1. Material Synthesis

3.1.1. Synthesis of LNO Nanorods

The LNO nanorods were synthesized by the hydrothermal method. A stoichiometric amount of $La(NO_3)_3{\cdot}6H_2O$ (0.125 mmol, 54.2 mg) and $Ni(HCO_2)_2{\cdot}2H_2O$ (0.125 mmol, 24.1 mg) were dissolved in 22.5 mL of deionized (DI) water followed by strong stirring to form a clear solution. Then, 2.5 mL 1 M KOH solution was slowly dropped into it to form a light green suspension and was continuously stirred for 15 min. Thereafter, the suspension was transferred into a 50 mL Teflon-lined stainless-steel autoclave and heated at 180 °C for 10 h in an oven. The resulting product was washed by DI after cooling to room temperature naturally and then dried. The light green powders were calcined at 250 °C for 2 h and then calcined at 650 °C for 5 h in air, with the heating rate at 5 °C min^{-1}. The obtained black powders were stirred in 12.5 mL 0.01 M HNO_3 solution for 15 min to remove the impurities. The LNO nanorods were obtained after being dried.

3.1.2. Synthesis of xFe-LNO (x = 0.125, 0.25, 0.5, 0.75)

Different amounts of the substance K_2FeO_4 were dissolved in 50 mL 6 M NaOH solution by sonication for 10 min to obtain the K_2FeO_4 solution with different concentrations. The role of NaOH is to regulate the hydrolysis rate of K_2FeO_4, which can promote uniform distribution of the composites. Next, the as-prepared $LaNiO_3$ nanorods (0.375 mmol) were added into the solution and sonicated for another 10 min to disperse uniformly. In addition, x stands for the molar ratios of K_2FeO_4:($LaNiO_3$ + K_2FeO_4) in the xFe-LNO samples. For example, the 0.25Fe-LNO sample with the best OER catalytic performance corresponds to 0.125 mmol K_2FeO_4. Subsequently, the above suspension was stirred for 24 h. Finally, the xFe-LNO samples were obtained after being washed several times with DI water.

3.2. Material Characterizations

The phase structures were determined by X-ray diffraction (XRD, D8-Focus with Cu Kα radiation, BRUKER, Karlsruhe, Germany). The Raman spectra were scanned with an excitation wavelength of 532 nm on a Horiba LabRAM HR Evolution instrument (HORIBA Scientific, Paris, France). The morphology and microstructure of the samples were characterized by scanning electron microscopy (SEM, S4800, HITACHI, Tokyo, Japan) and transmission electron microscopy (TEM, JEM-F200, JEOL, Tokyo, Japan). The Brunauer–Emmett–Teller (BET) specific surface area of the samples was obtained via N_2 desorption-adsorption isotherms (SSA-7000, BJBulider, Beijing, China). The surface chemical states

were analyzed by X-ray photoelectron spectroscopy (XPS, Thermo Scientific K-Alpha+, ThermoFisher Scientific, Waltham, MA, USA). For XPS, the pass energy is 50.00 eV, and the photoemission angle is 45°. To remove the charging effect leading to the peak positions' shift towards high binding energy, charge compensation was used during the testing, and the energy was calibrated by C 1s = 284.8 eV for all samples.

3.3. Electrochemical Measurements

All of the electrochemical measurements were performed in a 1 M KOH electrolyte in a standard three-electrode system on a CHI 760E (Shanghai Chenhua Instrument, Shanghai, China) electrochemical station at room temperature, in which a graphite rod and Ag/AgCl (3.5 M KCl) were respectively applied as the counter and reference electrodes. A glassy carbon (GC) electrode with a diameter of 3 mm, which was covered by a thin catalyst film, was used as the working electrode (except for special instructions). All the catalysts were mixed with conductive carbon (Ketjenblack carbon) at a mass ratio of 7:3 to remove the electrode conductivity limitation. Typically, 3.5 mg of the as-prepared catalyst and 1.5 mg of Ketjenblack carbon were dispersed in a 1 mL solution containing 0.45 mL deionized water, 0.5 mL ethanol and 50 μL 0.5 wt% Nafion solution, followed by ultrasonication for at least 1 h to form a homogeneous ink. Then, 5 μL of ink was dropped on the GC electrode with a catalyst loading density of 0.352 mg_{total} cm^{-2} (0.246 mg_{cat} cm^{-2}) and dried at room temperature. The measured potentials were calibrated to the standard reversible hydrogen electrode (RHE) according to the Nernst equation ($E_{RHE} = E_{Ag/AgCl} + 0.059\ pH + 0.196$).

The linear sweeping voltammograms (LSVs) were obtained at a scan rate of 5 mV s^{-1} with iR compensation (E_{iR} corrected = $E - IR_s$, where R_s is the Ohmic resistance of 1 M KOH and i is the current). The electrochemical double-layer capacitance (C_{dl}) was calculated by cyclic voltammogram (CV) measurements, with different scan rates of 20, 40, 60, 80, 100 and 120 mV S^{-1} in a non-Faradaic current region. Electrochemical impedance spectra (EIS) measurements were recorded at 1.56 V versus the RHE in a frequency range of 10^6–10^{-1} Hz under an AC voltage of 5 mV. The ECSA of a catalyst sample was calculated by the formula: $ECSA = C_{dl}/C_s$, where C_s is the specific capacitance and was generally around 0.04 mF cm^{-2} in the alkaline solution [61,62]. The turnover frequency (TOF) was calculated by the formula: $TOF = (j \times A)/(4 \times F \times n)$, where j (A cm^{-2}) is the current density obtained by the LSV measurement, A is the geometric area of the GC with catalysts (0.07065 cm^{-2}), F is the Faraday constant (96485.3 C mol^{-1}) and n is the number of active sites of the catalysts coated on the electrode. The stability test of the 0.25Fe-LNO by CV cycling was conducted in a potential range of 1.0–1.58 V versus the RHE at a scan rate of 100 mV s^{-1}, and a chronoamperometry test was conduct at 1.56 V versus the RHE with Ni foam covered by the catalyst (0.375 mg_{total} cm^{-2}) as the working electrode.

4. Conclusions

In summary, we proposed a two-step strategy for the synthesis of perovskite oxides and FeOOH heterostructures with an interesting 1D-2D hierarchical structure. By adjusting the different ratio of the two components, a variety of xFe-LNO composites were prepared. The catalytic performance test shows that the optimized 0.25Fe-LNO catalyst displays a significantly enhanced the OER performance in alkaline electrolytes in comparison to the pristine $LaNiO_3$ nanorods and FeOOH nanosheets, even outperforming the RuO_2. We found that the enhanced performance could be explained by the morphology engineering of LNO and the synergistic effect of the perovskite oxides and FeOOH. The introduction of this hierarchical structure not only increases the electrochemically active surface area but also results in an abundant contact area between LNO and FeOOH. Therefore, an accelerated charge transfer and synergistic effect are observed. This strategy also provides a new way to obtain perovskite oxides OER catalysts with better performance.

Supplementary Materials: The following supporting information can be downloaded at: https://www.mdpi.com/article/10.3390/catal12060594/s1, Figure S1: SEM image of FeOOH nanosheets;

Figure S2: N_2 adsorption–desorption isotherms of LNO and 0.25Fe-LNO; Figure S3: TEM image of 0.25Fe-LNO; Figure S4: HRTEM image of LNO; Figure S5: HAADF-TEM image of 0.25Fe-LNO and the corresponding elemental mapping images; Figure S6: XPS survey spectra of LNO and 0.25Fe-LNO; Figure S7: (a) LSV of LNO, FeOOH, Fe-LNO and IrO_2 samples. (b) The corresponding Tafel plots; Figure S8: (a) LSV of LNO, FeOOH and 0.25Fe-LNO samples without Ketjenblack carbon. (b) The corresponding Tafel plots; Figure S9: CV curves measured from 20 mV S^{-1} to 120 mV S^{-1} of (a) LNO, (b) 0.125Fe-LNO, (c) 0.25Fe-LNO, (d) 0.5Fe-LNO, (e) 0.75Fe-LNO and (f) FeOOH; Figure S10: ECSA-normalized LSV of LNO, xFe-LNO, FeOOH and RuO_2; Figure S11: (a) LSV of LNO, FeOOH, 0.25Fe-LNO and 0.25Fe/LNO samples. (b) The corresponding Tafel plots. (c) Linear fits of half capacitive currents versus scan rates for the extraction of the double-layer capacitances. (d) Nyquist plots; Figure S12: The LSV of Ni foam; Table S1: The fitting parameters of Nyquist plots; Table S2: TOF @ 1.60 V vs. RHE (S^{-1}) of the LNO, xFe-LNO and FeOOH samples. Table S3: Atomic ratios of xFe-LNO from the SEM-EDS results.

Author Contributions: Conceptualization, X.F.; methodology, M.S.; software, M.S.; validation, W.P., Y.L., F.Z., Q.X. and X.F.; formal analysis, M.S.; investigation, M.S.; resources, X.F.; data curation, M.S.; writing—original draft preparation, M.S.; writing—review and editing, Q.Z., Q.C. and X.H.; visualization, M.S.; supervision, X.F., W.P., Y.L., F.Z. and Q.X.; project administration, X.F.; funding acquisition, X.F., W.P., Y.L., F.Z. and Q.X. All authors have read and agreed to the published version of the manuscript.

Funding: This research was funded by the National Natural Science Funds of China (grant number 21878226), the Innovative Research Group Project of the National Natural Science Foundation of China (grant number 22121004) and the Haihe Laboratory of Sustainable Chemical Transformations for financial support (grant number CYZC202107).

Data Availability Statement: Not applicable.

Conflicts of Interest: The authors declare no conflict of interest.

References

1. Liu, W.; Zheng, D.; Deng, T.; Chen, Q.; Zhu, C.; Pei, C.; Li, H.; Wu, F.; Shi, W.; Yang, S.W.; et al. Boosting Electrocatalytic Activity of 3d-Block Metal (Hydro)oxides by Ligand-Induced Conversion. *Angew. Chem. Int. Edit.* **2021**, *60*, 10614–10619. [CrossRef] [PubMed]
2. Wang, H.F.; Tang, C.; Zhang, Q. A Review of Precious-Metal-Free Bifunctional Oxygen Electrocatalysts: Rational Design and Applications in Zn-Air Batteries. *Adv. Funct. Mater.* **2018**, *28*, 1803329. [CrossRef]
3. Chu, S.; Majumdar, A. Opportunities and challenges for a sustainable energy future. *Nature* **2012**, *488*, 294–303. [CrossRef]
4. Zhou, J.; Zhang, L.; Huang, Y.C.; Dong, C.L.; Lin, H.J.; Chen, C.T.; Tjeng, L.H.; Hu, Z. Voltage- and time-dependent valence state transition in cobalt oxide catalysts during the oxygen evolution reaction. *Nat. Commun.* **2020**, *11*, 1984. [CrossRef] [PubMed]
5. Huang, Z.F.; Song, J.J.; Du, Y.H.; Xi, S.B.; Dou, S.; Nsanzimana, J.M.V.; Wang, C.; Xu, Z.C.J.; Wang, X. Chemical and structural origin of lattice oxygen oxidation in Co-Zn oxyhydroxide oxygen evolution electrocatalysts. *Nat. Energy.* **2019**, *4*, 329–338. [CrossRef]
6. Yu, M.; Budiyanto, E.; Tuysuz, H. Principles of Water Electrolysis and Recent Progress in Cobalt-, Nickel-, and Iron-Based Oxides for the Oxygen Evolution Reaction. *Angew. Chem. Int. Ed. Engl.* **2022**, *61*, e202103824. [CrossRef]
7. Yao, Y.H.; Zhang, Z.Y.; Jiao, L.F. Development Strategies in Transition Metal Borides for Electrochemical Water Splitting. *Energy Environ. Mater.* **2022**, *5*, 470–485. [CrossRef]
8. Chen, Q.; Zhang, Q.; Liu, H.; Liang, J.; Peng, W.; Li, Y.; Zhang, F.; Fan, X. Preparation of Hollow Cobalt-Iron Phosphides Nanospheres by Controllable Atom Migration for Enhanced Water Oxidation and Splitting. *Small* **2021**, *17*, e2007858. [CrossRef]
9. Song, F.; Bai, L.; Moysiadou, A.; Lee, S.; Hu, C.; Liardet, L.; Hu, X. Transition Metal Oxides as Electrocatalysts for the Oxygen Evolution Reaction in Alkaline Solutions: An Application-Inspired Renaissance. *J. Am. Chem. Soc.* **2018**, *140*, 7748–7759. [CrossRef]
10. Zhai, P.; Zhang, Y.; Wu, Y.; Gao, J.; Zhang, B.; Cao, S.; Zhang, Y.; Li, Z.; Sun, L.; Hou, J. Engineering active sites on hierarchical transition bimetal oxides/sulfides heterostructure array enabling robust overall water splitting. *Nat. Commun.* **2020**, *11*, 5462. [CrossRef]
11. Yu, J.; Wang, J.; Long, X.; Chen, L.; Cao, Q.; Wang, J.; Qiu, C.; Lim, J.; Yang, S.H. Formation of FeOOH Nanosheets Induces Substitutional Doping of CeO_{2-x} with High-Valence Ni for Efficient Water Oxidation. *Adv. Energy. Mater.* **2021**, *11*, 2002731. [CrossRef]
12. Tang, L.; Chen, Z.; Zuo, F.; Hua, B.; Zhou, H.; Li, M.; Li, J.H.; Sun, Y.F. Enhancing perovskite electrocatalysis through synergistic functionalization of B-site cation for efficient water splitting. *Chem. Eng. J.* **2020**, *401*, 126082. [CrossRef]

13. Liu, D.; Zhou, P.; Bai, H.; Ai, H.; Du, X.; Chen, M.; Liu, D.; Ip, W.F.; Lo, K.H.; Kwok, C.T.; et al. Development of Perovskite Oxide-Based Electrocatalysts for Oxygen Evolution Reaction. *Small* **2021**, *17*, e2101605. [CrossRef]
14. Man, I.C.; Su, H.Y.; Calle-Vallejo, F.; Hansen, H.A.; Martínez, J.I.; Inoglu, N.G.; Kitchin, J.; Jaramillo, T.F.; Nørskov, J.K.; Rossmeisl, J. Universality in Oxygen Evolution Electrocatalysis on Oxide Surfaces. *ChemCatChem* **2011**, *3*, 1159–1165. [CrossRef]
15. Suntivich, J.; May, K.J.; Gasteiger, H.A.; Goodenough, J.B.; Shao-Horn, Y. A perovskite oxide optimized for oxygen evolution catalysis from molecular orbital principles. *Science* **2011**, *334*, 1383–1385. [CrossRef] [PubMed]
16. Yan, S.; Xue, Y.; Li, S.; Shao, G.; Liu, Z. Enhanced Bifunctional Catalytic Activity of Manganese Oxide/Perovskite Hierarchical Core-Shell Materials by Adjusting the Interface for Metal-Air Batteries. *ACS Appl. Mater. Inter.* **2019**, *11*, 25870–25881. [CrossRef] [PubMed]
17. Zhu, Y.L.; Zhou, W.; Zhong, Y.J.; Bu, Y.F.; Chen, X.Y.; Zhong, Q.; Liu, M.L.; Shao, Z.P. A Perovskite Nanorod as Bifunctional Electrocatalyst for Overall Water Splitting. *Adv. Energy. Mater.* **2017**, *7*, 1602122. [CrossRef]
18. Zhao, T.W.; Wang, Y.; Chen, X.J.; Li, Y.B.; Su, Z.; Zhao, C. Vertical Growth of Porous Perovskite Nanoarrays on Nickel Foam for Efficient Oxygen Evolution Reaction. *ACS Sustain. Chem. Eng.* **2020**, *8*, 4863–4870. [CrossRef]
19. He, B.; Tan, K.; Gong, Y.; Wang, R.; Wang, H.; Zhao, L. Coupling amorphous cobalt hydroxide nanoflakes on $Sr_2Fe_{1.5}Mo_{0.5}O_{5+delta}$ perovskite nanofibers to induce bifunctionality for water splitting. *Nanoscale* **2020**, *12*, 9048–9057. [CrossRef]
20. Zhao, C.; Li, N.; Zhang, R.; Zhu, Z.; Lin, J.; Zhang, K.; Zhao, C. Surface Reconstruction of $La_{0.8}Sr_{0.2}Co_{0.8}Fe_{0.2O3-delta}$ for Superimposed OER Performance. *ACS Appl. Mater. Inter.* **2019**, *11*, 47858–47867. [CrossRef]
21. Dai, J.; Zhu, Y.; Zhong, Y.; Miao, J.; Lin, B.; Zhou, W.; Shao, Z. Enabling High and Stable Electrocatalytic Activity of Iron-Based Perovskite Oxides for Water Splitting by Combined Bulk Doping and Morphology Designing. *Adv. Mater. Interfaces* **2018**, *6*, 1801317. [CrossRef]
22. Chen, G.; Zhu, Y.; Chen, H.M.; Hu, Z.; Hung, S.-F.; Ma, N.; Dai, J.; Lin, H.-J.; Chen, C.-T.; Zhou, W.; et al. An Amorphous Nickel-Iron-Based Electrocatalyst with Unusual Local Structures for Ultrafast Oxygen Evolution Reaction. *Adv. Mater.* **2019**, *31*, e1900883. [CrossRef] [PubMed]
23. Sun, J.; Du, L.; Sun, B.; Han, G.; Ma, Y.; Wang, J.; Huo, H.; Du, C.; Yin, G. Bifunctional $LaMn_{0.3}Co_{0.7}O_3$ Perovskite Oxide Catalyst for Oxygen Reduction and Evolution Reactions: The Optimized e_g Electronic Structures by Manganese Dopant. *ACS Appl. Mater. Inter.* **2020**, *12*, 24717–24725. [CrossRef] [PubMed]
24. Medford, A.J.; Vojvodic, A.; Hummelshoj, J.S.; Voss, J.; Abild-Pedersen, F.; Studt, F.; Bligaard, T.; Nilsson, A.; Norskov, J.K. From the Sabatier principle to a predictive theory of transition-metal heterogeneous catalysis. *J. Catal.* **2015**, *328*, 36–42. [CrossRef]
25. Li, Y.X.; Zhang, X.Y.; Wu, Z.J.; Sheng, H.B.; Li, C.; Li, H.Y.; Cao, L.X.; Dong, B.H. Coupling porous Ni doped $LaFeO_3$ nanoparticles with amorphous FeOOH nanosheets yields an interfacial electrocatalyst for electrocatalytic oxygen evolution. *J. Mater. Chem. A.* **2021**, *9*, 23545–23554. [CrossRef]
26. Oh, N.K.; Kim, C.; Lee, J.; Kwon, O.; Choi, Y.; Jung, G.Y.; Lim, H.Y.; Kwak, S.K.; Kim, G.; Park, H. In-situ local phase-transitioned $MoSe_2$ in $La_{0.5}Sr_{0.5}CoO_{3-delta}$ heterostructure and stable overall water electrolysis over 1000 hours. *Nat. Commun.* **2019**, *10*, 1723. [CrossRef]
27. Gong, C.; Zhao, L.; Li, S.; Wang, H.W.; Gong, Y.S.; Wang, R.; He, B.B. Atomic layered deposition iron oxide on perovskite $LaNiO_3$ as an efficient and robust bi-functional catalyst for lithium oxygen batteries. *Electrochim. Acta* **2018**, *281*, 338–347. [CrossRef]
28. Subbaraman, R.; Tripkovic, D.; Chang, K.C.; Strmcnik, D.; Paulikas, A.P.; Hirunsit, P.; Chan, M.; Greeley, J.; Stamenkovic, V.; Markovic, N.M. Trends in activity for the water electrolyser reactions on 3d M(Ni,Co,Fe,Mn) hydr(oxy)oxide catalysts. *Nat. Mater.* **2012**, *11*, 550–557. [CrossRef]
29. Zhang, Z.; He, B.; Chen, L.; Wang, H.; Wang, R.; Zhao, L.; Gong, Y. Boosting Overall Water Splitting via FeOOH Nanoflake-Decorated $PrBa_{0.5}Sr_{0.5}Co_2O_{5+delta}$ Nanorods. *ACS Appl. Mater. Inter.* **2018**, *10*, 38032–38041. [CrossRef]
30. Liu, J.; Qian, G.; Zhang, H.; Chen, J.; Wang, Y.; He, H.; Luo, L.; Yin, S. Amorphous FeOOH coating stabilizes WO_2-Na_xWO_3 for accelerating oxygen evolution reaction. *Chem. Eng. J.* **2021**, *426*, 131253. [CrossRef]
31. Zhao, J.W.; Li, C.F.; Shi, Z.X.; Guan, J.L.; Li, G.R. Boosting Lattice Oxygen Oxidation of Perovskite to Efficiently Catalyze Oxygen Evolution Reaction by FeOOH Decoration. *Research* **2020**, *2020*, 6961578. [CrossRef] [PubMed]
32. Zhang, X.; Liu, Y.; Dong, S.; Ye, Z.; Wei, Y. Low-temperature synthesized nanocomposites with amorphous FeOOH on Ti3C2Tx for supercapacitors. *J. Alloys Compd.* **2018**, *744*, 507–515. [CrossRef]
33. Wang, K.; Du, H.; He, S.; Liu, L.; Yang, K.; Sun, J.; Liu, Y.; Du, Z.; Xie, L.; Ai, W.; et al. Kinetically Controlled, Scalable Synthesis of gamma-FeOOH Nanosheet Arrays on Nickel Foam toward Efficient Oxygen Evolution: The Key Role of In-Situ-Generated gamma-NiOOH. *Adv. Mater.* **2021**, *33*, e2005587. [CrossRef] [PubMed]
34. Wang, H.; Wang, J.; Pi, Y.; Shao, Q.; Tan, Y.; Huang, X. Double Perovskite LaFex Ni1-x O3 Nanorods Enable Efficient Oxygen Evolution Electrocatalysis. *Angew. Chem. Int. Ed. Engl.* **2019**, *58*, 2316–2320. [CrossRef] [PubMed]
35. Zhang, D.; Song, Y.; Du, Z.; Wang, L.; Li, Y.; Goodenough, J.B. Active LaNi1-xFexO_3 bifunctional catalysts for air cathodes in alkaline media. *J. Mater. Chem. A* **2015**, *3*, 9421–9426. [CrossRef]
36. Li, Z.; Lv, L.; Ao, X.; Li, J.-G.; Sun, H.; An, P.; Xue, X.; Li, Y.; Liu, M.; Wang, C.; et al. An effective method for enhancing oxygen evolution kinetics of $LaMO_3$ (M = Ni, Co, Mn) perovskite catalysts and its application to a rechargeable zinc–air battery. *Appl. Catal. B Environ.* **2020**, *262*, 118291. [CrossRef]
37. Nguyen, T.; Montemor, M.F. γ-FeOOH and amorphous Ni-Mn hydroxide on carbon nanofoam paper electrodes for hybrid supercapacitors. *J. Mater. Chem. A* **2018**, *6*, 2612–2624. [CrossRef]

38. Nieuwoudt, M.K.; Comins, J.D.; Cukrowski, I. The growth of the passive film on iron in 0.05 M NaOH studied in situ by Raman micro-spectroscopy and electrochemical polarisation. Part I: Near-resonance enhancement of the Raman spectra of iron oxide and oxyhydroxide compounds. *J. Raman. Spectrosc.* **2011**, *42*, 1335–1339. [CrossRef]
39. Chemelewski, W.D.; Lee, H.C.; Lin, J.F.; Bard, A.J.; Mullins, C.B. Amorphous FeOOH oxygen evolution reaction catalyst for photoelectrochemical water splitting. *J. Am. Chem. Soc.* **2014**, *136*, 2843–2850. [CrossRef]
40. Colomban, P.; Cherifi, S.; Despert, G. Raman identification of corrosion products on automotive galvanized steel sheets. *J. Raman. Spectrosc.* **2008**, *39*, 881–886. [CrossRef]
41. Wang, J.; Gao, Y.; Ciucci, F. Mechanochemical Coupling of MoS_2 and Perovskites for Hydrogen Generation. *Acs Appl. Energ. Mater.* **2018**, *1*, 6409–6416. [CrossRef]
42. Thanh, T.D.; Chuong, N.D.; Balamurugan, J.; Van Hien, H.; Kim, N.H.; Lee, J.H. Porous Hollow-Structured $LaNiO_3$ Stabilized N,S-Codoped Graphene as an Active Electrocatalyst for Oxygen Reduction Reaction. *Small* **2017**, *13*, 1701884. [CrossRef] [PubMed]
43. Choi, M.J.; Kim, T.L.; Kim, J.K.; Lee, T.H.; Lee, S.A.; Kim, C.; Hong, K.; Bark, C.W.; Ko, K.T.; Jang, H.W. Enhanced Oxygen Evolution Electrocatalysis in Strained A-Site Cation Deficient $LaNiO_3$ Perovskite Thin Films. *Nano Lett.* **2020**, *20*, 8040–8045. [CrossRef]
44. Si, C.H.; Zhang, C.; Sunarso, J.; Zhang, Z.H. Transforming bulk alloys into nanoporous lanthanum-based perovskite oxides with high specific surface areas and enhanced electrocatalytic activities. *J. Mater. Chem. A* **2018**, *6*, 19979–19988. [CrossRef]
45. Mickevicius, S.; Grebinskij, S.; Bondarenka, V.; Vengalis, B.; Sliuziene, K.; Orlowski, B.A.; Osinniy, V.; Drube, W. Investigation of epitaxial $LaNiO_{3-x}$ thin films by high-energy XPS. *J. Alloys Compd.* **2006**, *423*, 107–111. [CrossRef]
46. Lima, S.M.; Assaf, J.M.; Pena, M.A.; Fierro, J.L.G. Structural features of La1-xCexNiO3 mixed oxides and performance for the dry reforming of methane. *Appl. Catal. A Gen.* **2006**, *311*, 94–104. [CrossRef]
47. Biesinger, M.C.; Payne, B.P.; Grosvenor, A.P.; Lau, L.W.M.; Gerson, A.R.; Smart, R.S.C. Resolving surface chemical states in XPS analysis of first row transition metals, oxides and hydroxides: Cr, Mn, Fe, Co and Ni. *Appl. Surf. Sci.* **2011**, *257*, 2717–2730. [CrossRef]
48. Feng, J.-X.; Xu, H.; Dong, Y.-T.; Ye, S.-H.; Tong, Y.-X.; Li, G.-R. FeOOH/Co/FeOOH Hybrid Nanotube Arrays as High-Performance Electrocatalysts for the Oxygen Evolution Reaction. *Angew. Chem. Int. Ed.* **2016**, *55*, 3694–3698. [CrossRef]
49. Li, K.L.; Liu, X.Y.; Zheng, T.X.; Jiang, D.B.; Zhou, Z.; Liu, C.Q.; Zhang, X.M.; Zhang, Y.X.; Losic, D. Tuning MnO_2 to FeOOH replicas with bio-template 3D morphology as electrodes for high performance asymmetric supercapacitors. *Chem. Eng. J.* **2019**, *370*, 136–147. [CrossRef]
50. Feng, J.X.; Ye, S.H.; Xu, H.; Tong, Y.X.; Li, G.R. Design and Synthesis of FeOOH/CeO_2 Heterolayered Nanotube Electrocatalysts for the Oxygen Evolution Reaction. *Adv. Mater.* **2016**, *28*, 4698–4703. [CrossRef]
51. Pan, Y.; Xu, X.; Zhong, Y.; Ge, L.; Chen, Y.; Veder, J.M.; Guan, D.; O'Hayre, R.; Li, M.; Wang, G.; et al. Direct evidence of boosted oxygen evolution over perovskite by enhanced lattice oxygen participation. *Nat. Commun.* **2020**, *11*, 2002. [CrossRef] [PubMed]
52. Jung, K.N.; Jung, J.H.; Im, W.B.; Yoon, S.; Shin, K.H.; Lee, J.W. Doped lanthanum nickelates with a layered perovskite structure as bifunctional cathode catalysts for rechargeable metal-air batteries. *ACS Appl. Mater. Interfaces* **2013**, *5*, 9902–9907. [CrossRef] [PubMed]
53. Kwon, J.; Han, H.; Jo, S.; Choi, S.; Chung, K.Y.; Ali, G.; Park, K.; Paik, U.; Song, T. Amorphous Nickel-Iron Borophosphate for a Robust and Efficient Oxygen Evolution Reaction. *Adv. Energy Mater.* **2021**, *11*, 2100624. [CrossRef]
54. Suen, N.T.; Hung, S.F.; Quan, Q.; Zhang, N.; Xu, Y.J.; Chen, H.M. Electrocatalysis for the oxygen evolution reaction: Recent development and future perspectives. *Chem. Soc. Rev.* **2017**, *46*, 337–365. [CrossRef]
55. Khodabakhshi, M.; Chen, S.; Ye, T.; Wu, H.; Yang, L.; Zhang, W.; Chang, H. Hierarchical Highly Wrinkled Trimetallic NiFeCu Phosphide Nanosheets on Nanodendrite Ni_3S_2/Ni Foam as an Efficient Electrocatalyst for the Oxygen Evolution Reaction. *ACS Appl. Mater. Interfaces* **2020**, *12*, 36268–36276. [CrossRef]
56. Chang, C.; Zhu, S.; Liu, X.; Chen, Y.; Sun, Y.; Tang, Y.; Wan, P.; Pan, J. One-Step Electrodeposition Synthesis of Bimetal Fe- and Co-Doped NiPi/P for Highly Efficient Overall Water Splitting. *Ind. Eng. Chem. Res.* **2021**, *60*, 2070–2078. [CrossRef]
57. Wang, X.; Zhang, Y.; Si, H.; Zhang, Q.; Wu, J.; Gao, L.; Wei, X.; Sun, Y.; Liao, Q.; Zhang, Z.; et al. Single-Atom Vacancy Defect to Trigger High-Efficiency Hydrogen Evolution of MoS_2. *J. Am. Chem. Soc.* **2020**, *142*, 4298–4308. [CrossRef]
58. Li, Z.; Xue, K.H.; Wang, J.; Li, J.G.; Ao, X.; Sun, H.; Song, X.; Lei, W.; Cao, Y.; Wang, C. Cation and Anion Co-doped Perovskite Nanofibers for Highly Efficient Electrocatalytic Oxygen Evolution. *ACS Appl. Mater. Interfaces* **2020**, *12*, 41259–41268. [CrossRef]
59. Chen, Q.; Gong, N.; Zhu, T.; Yang, C.; Peng, W.; Li, Y.; Zhang, F.; Fan, X. Surface Phase Engineering Modulated Iron-Nickel Nitrides/Alloy Nanospheres with Tailored d-Band Center for Efficient Oxygen Evolution Reaction. *Small* **2022**, *18*, e2105696. [CrossRef]
60. Li, Y.; Du, X.; Huang, J.; Wu, C.; Sun, Y.; Zou, G.; Yang, C.; Xiong, J. Recent Progress on Surface Reconstruction of Earth-Abundant Electrocatalysts for Water Oxidation. *Small* **2019**, *15*, 1901980. [CrossRef]
61. McCrory, C.C.L.; Jung, S.H.; Peters, J.C.; Jaramillo, T.F. Benchmarking Heterogeneous Electrocatalysts for the Oxygen Evolution Reaction. *J. Am. Chem. Soc.* **2013**, *135*, 16977–16987. [CrossRef] [PubMed]
62. Morales, D.M.; Risch, M. Seven steps to reliable cyclic voltammetry measurements for the determination of double layer capacitance. *J. Phys. Energy* **2021**, *3*, 034013. [CrossRef]

catalysts

MDPI

Article

Versatile Bifunctional and Supported IrNi Oxide Catalyst for Photoelectrochemical Water Splitting

Sifani Zavahir [1], Umme Hafsa [1,2], Hyunwoong Park [3] and Dong Suk Han [1,2,*]

[1] Center for Advanced Materials, Qatar University, Doha P.O. Box 2713, Qatar
[2] Department of Chemical Engineering, Qatar University, Doha P.O. Box 2713, Qatar
[3] School of Energy Engineering, Kyungpook National University, Daegu 702-701, Korea
* Correspondence: dhan@qu.edu.qa

Abstract: Designing a high-performance electrocatalyst that operates with photon-level energy is of the utmost importance in order to address the world's urgent energy concerns. Herein, we report IrNi nanoparticles uniformly distributed on cost-effective activated carbon support with a low mass loading of 3% by weight to drive the overall water splitting reaction under light illumination over a wide pH range. The prepared IrNi nanomaterials were extensively characterized by SEM/EDX, TEM, XRD, Raman, and UV-visible absorption spectroscopy. The experimental results demonstrate that when the Ir:Ni ratio is 4:1, the water splitting rate is high at 32 and 25 mA cm^{-2} for hydrogen (at −1.16 V) and oxygen evolution reactions (at 1.8 V) in alkaline electrolyte, respectively, upon the light irradiation (100 mW cm^{-2}). The physical and electrochemical characterization of metal and alloy combinations show that the cumulative effect of relatively high crystallinity (among the materials used in this study), reduced charge recombination rate, and improved oxygen vacancies observed with the 4Ir1Ni@AC electrode is the reason for the superior activity obtained. A high level of durability for hydrogen and oxygen evolution under light illumination is seen in the chronoamperometric study over 15 h of operation. Overall water splitting examined in 0.1 M of NaOH medium at a 50 mV s^{-1} scan rate showed a cell voltage of 1.94 V at a 10 mA cm^{-2} current density.

Keywords: IrNi; photoelectrochemical; water splitting; HER; OER

Citation: Zavahir, S.; Hafsa, U.; Park, H.; Han, D.S. Versatile Bifunctional and Supported IrNi Oxide Catalyst for Photoelectrochemical Water Splitting. *Catalysts* **2022**, *12*, 1056. https://doi.org/10.3390/catal12091056

Academic Editor: Marc Cretin

Received: 16 August 2022
Accepted: 12 September 2022
Published: 16 September 2022

1. Introduction

Out of all forms of renewable energy and their respective production procedures, hydrogen produced by photoelectrochemical means employing water as the input (source of hydrogen) is regarded as the most cost-effective and sustainable [1–3]. The world is transitioning toward a hydrogen economy, with it having a projected 12% market share in the energy sector by the year 2050 [4]. The shift from fossil fuels to hydrogen is expedited by the undeniable urgency of the climate situation and the commitment of every country to achieve net-zero emissions, which are valued at USD 174 billion [5]. Regardless of the understanding of its importance, industrial hydrogen production is dominated by methane reforming [6,7].

Electrochemical means of hydrogen production have achieved a good performance in alkaline medium [8–10]. However, it has been noticed that catalysts encounter a higher ohmic resistance when performing the dual role of HER and OER at a single site [11]. This leads to a higher polarization loss in addition to sluggish reaction kinetics [7,12,13]. In the search for novel materials for commercial-scale electrolyzer systems, bifunctional catalysts with a low internal ohmic resistance and improved mass transport yielding high current densities are in high demand [14,15]. These catalysts can be created by introducing defect sites [16,17], focusing on a certain morphology [18,19], sticking to a certain crystal facet [20], or using core-shell nanoparticles [21]. However, the most viable method for an electrochemical system driven by photon energy is to create a heterojunction

by incorporating two compatible metal/metal or metal/nonmetal materials to achieve a favorable band bending [22,23].

The overall water splitting process involves two half-reactions taking place at the boundary line of a triple-phase, namely, a solid-phase electrocatalyst; a liquid electrolyte; and the gaseous products formed during the progression of the reaction [24]. Lately, several iridium (Ir) and nickel (Ni) based electrocatalysts of different modes, namely core-shell nanostructured [21] and dislocation-strained Ir and Ni nanoparticles [25], have been studied with regard to the hydrogen evolution reaction. IrO_2 has a strong light absorbance in the UV–visible region in addition to its intrinsic oxygen evolution activity [26,27]. NiO, on the other hand, has been studied in relation to the hydrogen evolution reaction for many years [28,29]. NiO is also a well-known visible-light catalyst used in degradation reactions [30,31].

In light of this, here, we report the facile synthesis of an IrNi oxide alloy with improved light absorption properties for visible light-driven electrochemical water splitting. The total metal weight was maintained at 3% of the total catalyst weight, and the support used was a cost-effective porous activated carbon. For comparison, 3% by weight (in feed) of individual mono metallic nickel supported on AC (3%Ni@AC) and 3% by weight (in feed) of iridium supported on AC (3%Ir@AC) were also prepared. Of the three different Ir to Ni weight compositions (1:4, 1:1, and 4:1) evaluated, the 4:1 Ir:Ni on AC matrix was found to deliver superior hydrogen and oxygen photocurrents in alkaline, acidic, and neutral media. We believe that the results of this study will contribute to new insights into photoelectrochemical water splitting by IrNi oxide alloy. The simultaneous redox capability shown here will encourage the experimental adoption of IrNi-based materials in explore other chemical reactions of industrial importance under visible light conditions.

2. Results and Discussion

Metal and alloys of Ir and Ni on the AC prepared in this study were initially evaluated to determine their hydrogen (HER) and oxygen (OER) evolution reaction, as shown in Figure 1. Working pH has more impact on electrocatalysis than other types of catalysis. Hence, activity was tested in alkaline, neutral, and acidic media under a light intensity of 100 mW cm^{-2} (Figure 1a–f). The dark counterparts of the light-mediated electrolysis showed a far lower current density for each respective catalyst for any given potential value (Figure 2a–f). Hence, to improve clarity and assist in easy interpretation, only the current density values of the light-assisted system are shown in Figure 1a–f. It is evident from Figure 1a–c that, regardless of the nature of the electrolyte, Ir@AC showed the least activity towards hydrogen evolution, with it not exceeding -1 mA cm^{-2} at -1.16 V (vs. RHE). In the NaOH medium, the HER activity was significantly higher with the use of alloy combinations compared to that obtained with single metals (Figure 1a). The highest values obtained among the studied materials were recorded with the 4Ir1Ni@AC catalyst with a current density of -32 mA cm^{-2} at -1.16 V. This value was more than eight-fold higher than that obtained for the 1Ir4Ni@AC catalyst (-3.7 mA cm^{-2} at -1.16 V). This observation is worth further exploration. Ni catalysts are known for their intrinsic activity in hydrogen evolution [28]. Introducing a low percentage of Ir into Ni to form 1Ir4Ni (20% of Ir and 80% of Ni) improved the hydrogen evolution of Ni by 3%. Conversely, a low level of addition of Ni to the Ir led to a marginal increase in hydrogen reduction compared to that of Ir. Equal weight percentages of Ir and Ni in the AC matrix resulted in a cathodic current density of -9.5 mA cm^{-2} at -1.16 V, which was higher than that of the 1Ir1Ni@AC mixture (1Ir1Ni@AC-p, -4.9 mA cm^{-2} at -1.16 V) prepared by mixing equal amounts by mass of monometallic Ir@AC and Ni@AC. Alloying has been demonstrated to play an indispensable role in the rational regulation of the band structure of parent metal oxides by modifying the electron distribution in addition to modulating the surface and interface of the electrode and electrolyte, respectively [32,33]. The incorporation of Ni has recently been shown to reduce the hydrogen binding energy of Ir by up to 2.5 times the inherent activity of the metal [33]. This is apparent in the present system in alkaline

media, where the hydrogen reduction is visualized in terms of activity enhancement by alloying Ir with Ni. In line with this observation, in the present system, tremendously high improvements were achieved after alloying Ir with Ni, with Ir being the major phase of the oxide alloy. Alkaline electrolyzers are more sought after for hydrogen generation at large scales due to the high purity of the hydrogen gas produced and their impressive long-term stability [34–36]. However, it is no secret that alkaline electrolyzers suffer from sluggish reaction kinetics, with electrolyzers' activity in acid being 2–3-fold higher compared to that in alkaline environments.

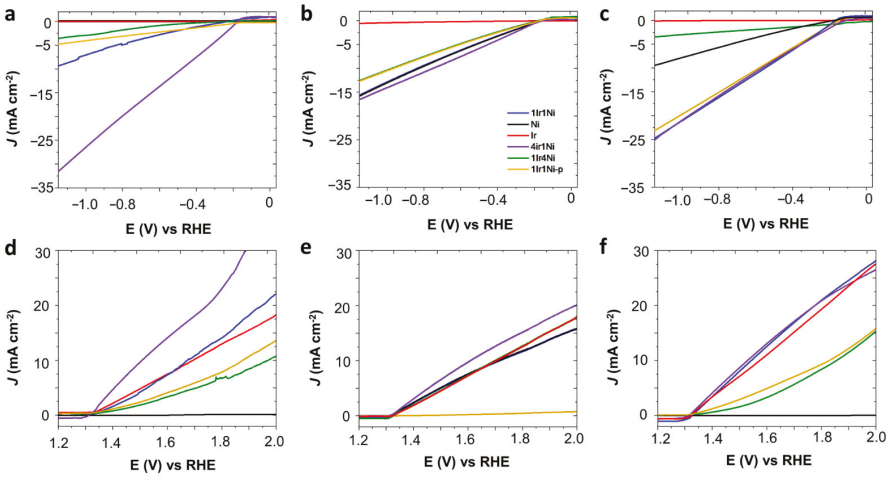

Figure 1. Linear sweep voltammetry (LSV) curves of Ir and Ni metals and alloys on activated carbon matrix; the test was performed at a 50 mV s^{-1} scan rate in (**a**,**d**) 0.1 M NaOH, (**b**,**e**) 0.1 M Na_2SO_4, and (**c**,**f**) 0.1 M H_2SO_4 electrolyte at room temperature in the presence of 1 sunlight illumination (1.5 G AM, 100 mW cm^{-2}). The material code was similar in all graphs; refer to (**b**) for the labeling.

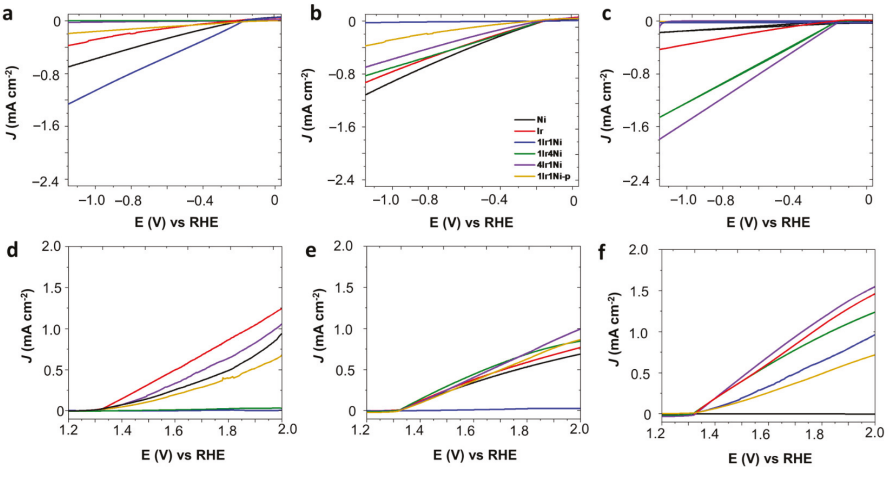

Figure 2. Linear sweep voltammetry (LSV) curves of Ir and Ni metal and alloys on activated carbon matrix, test performed at 50 mV s^{-1} scan rate in the dark (light off) condition in (**a**,**d**) 0.1 M NaOH, (**b**,**e**) 0.1 M Na_2SO_4 and (**c**,**f**) 0.1 M H_2SO_4 electrolyte at room temperature. Material code is similar in all graphs and refers to (**b**) for the labeling (blue: 1Ir1Ni@AC, violet: 4Ir1Ni@AC, red: Ir@AC, black: Ni@AC, green: 1Ir4Ni@AC and brown: 1Ir1Ni@AC-p).

Critically comparing the activity of catalysts in acidic media (0.1 M H_2SO_4, Figure 1c) with that in alkaline (Figure 1a), it is noted that, except for 4Ir1Ni, lowering the medium pH increased the hydrogen production. In acidic media, Ni metal shows a characteristic catalytic activity of −9.5 mA cm^{-2} at −1.16 V, while an ultra-low current density was witnessed in the alkaline electrolyte. The 1Ir4Ni@AC catalyst had similar activity in both acidic (−3.7 mA cm^{-2}) and alkaline media (−3.6 mA cm^{-2}). In the acidic media, 1Ir1Ni@AC, 1Ir1Ni@AC-p, and 4Ir1Ni@AC (−23 to −25 mA cm^{-2}) yielded similar current densities, despite the difference of Ir and Ni in mass ratios and the distribution of the elements across the matrix. It is necessary to evaluate the HER performance of the catalysts on different electrolyte media in order to discover the descriptors that govern the HER activity [37]. In the neutral electrolyte, Ni@AC and 1Ir4Ni@AC demonstrated higher HER current densities than those seen in acidic and alkaline media. In the case of 1Ir4Ni@AC, its activity was similar in acid and alkali environments, while it was four-fold higher in Na_2SO_4. For Ni, its current density at −1.16 V was improved from near-zero to −9.5 to −15.9 mA cm^{-2} by switching the electrolyte from NaOH to H_2SO_4 to Na_2SO_4. Regardless of the electrolyte used, 4Ir1Ni@AC demonstrated the highest activity, as measured by the current density, among the metal and alloy combinations studied. Nevertheless, 4Ir1Ni@AC showed higher activity in alkaline media (−32 mA cm^{-2}) than in acidic (−24.8 mA cm^{-2}) or neutral (−16.7 mA cm^{-2}) media. Hence, 4Ir1Ni can be described as being active in a wide pH range for HER under the illumination of light. Irrespective of the recent observations made regarding the importance of surface-adsorbed hydroxyl during the water dissociation step, it has been proven that H_{ads} plays a key role [38]. It is anticipated that different trends will be observed in different electrolytes. For example, in photoelectrocatalysis, the first step involves generating a photovoltage upon absorbing the light and electrocatalyst and then employing this voltage to drive the respective HER reaction. In addition to alloy molar ratio modulation and the corresponding electronic structure, the photovoltage generated in each scenario varies as the electrolyte is switched, contributing to the different electrolyte/electrode interface interaction effects.

In the broader context, oxygen evolution (OER) under light illumination takes place in a few steps. Initially, solar absorption by the metal (Ir or Ni) or alloy (IrNi) oxide center of the catalyst generates holes, which are transferred to the bulk electrolyte in the femto-second scale and dissociate water to form hydroxyl ions. Oxygen molecules are finally generated at the triple-phase (which is the boundary line between the solid electrode, liquid electrolyte, and gaseous product) as a result of a series of bond-making and breaking processes.

IrO_2 is known for its inherent OER activity, particularly in acidic media [39]. In this study, we utilized the catalyst in a low loading with an AC matrix and driven by solar absorption under a light intensity of 1 sun. In line with the literature precedent, we achieved a result of 20.04 mA cm^{-2} for Ir@AC in 0.1 M H_2SO_4 at 1.8 V (vs. RHE) (Figure 1f), while the result was lower yet similar in NaOH (13.5 mA cm^{-2}) and Na_2SO_4 (13 mA cm^{-2}) electrolytes. In acidic electrolyte, the incorporation of Ni in Ir enhanced the intrinsic activity of Ir by 7.8% when Ir was a major phase. Conversely, the activity of Ir was reduced by 55.8% when the major component was Ni (8.84 mA cm^{-2} with 1Ir4Ni@AC). Ir and Ni in equal weight ratios demonstrated a higher current density, similar to that obtained for 4Ir1Ni@AC (21.6 mA cm^{-2} at 1.8 V), while in the case of a chemical mix, the well-combined physical mixture gave a much lower current density of 9.7 mA cm^{-2} at 1.8 V. In the alkaline media (Figure 1d), Ir@AC and 1Ir1Ni@AC demonstrated similar activity (~13.5 mA cm^{-2}), while 4Ir1Ni@AC yielded a superior activity of 24.38 mA cm^{-2}. It is noteworthy that in both acidic and alkaline media, Ni@AC exhibited the least performance of <1 mA cm^{-2} at 1.8 V, while in neutral media, it was the physical mixture of 1Ir1Ni@AC that achieved the least activity. A detailed evaluation of the different metal and alloy combinations that can be used for HER and OER in different electrolyte media provided important information on the supreme photoelectrocatalytic activity of 4Ir1Ni@AC for overall water splitting. Thus, it is important to analyze the characteristics of 4Ir1Ni@AC compared to those of other

metals and alloys. Observations showed evidence that the d band center of 4Ir1Ni was in a favorable position to drive the HER and OER at high rates.

In order to understand the outstanding photoelectrocatalytic behavior of the 4Ir1Ni@AC catalyst, the characteristics of the materials were evaluated by several different means. Morphological analysis by SEM revealed a similar appearance of all samples under the same magnification, highlighting only the porous activated carbon matrix (Figure 3a and Figure S1). Activated carbon is known to be amorphous, with a large internal surface area and pore volume. Higher magnification under TEM, however, showed nanoparticles that were uniformly distributed across an AC matrix (Figure 3b and Figure S2). The selected area electron diffraction (SAED) patterns observed in the diffraction rings of TEM indicate the partial crystallinity of 4Ir1Ni (Figure 3c). Apart from 4Ir1Ni@AC, Ni was shown to be crystalline (Figure S3). The analysis of the elemental composition by EDX affirmed the relative weight ratios of Ir and Ni in the alloy combinations to be within reasonable limits of the feed mass ratios (Table S1, Figure S4), whereas the Ir to Ni relative weight ratios were 1.2 ± 0.1:1 in 1Ir1Ni@AC, 1:3.5 ± 0.2 in 1Ir4Ni@AC, and 4.2 ± 0.1:1 in 4Ir1Ni@AC. Powder X-ray diffraction patterns of the Ir and Ni metal and alloy @AC samples showed the apparent camouflaging of the Ir- and Ni-related peaks by a broad peak spanning an angle range of approximately 40 to 47° 2θ related to the AC moiety (Figure 3d). However, in the Ir-Ni alloys, there were three peaks in the 20–30° range, specifically at 21.79°, 25.70°, and 27.92°, which were attributed to diffractions arising from the IrNi alloy particles [25,33]. It is noteworthy that alloy diffractions were more pronounced in 4Ir1Ni@AC than in other combinations. In addition, with 4Ir1Ni@AC, two additional peaks located at an angle of 43.29° for the (200) plane of NiO and 51.86° for the (200) plane of Ni can be seen. The 1:1 mixture of Ir and Ni prepared with a well-combined physical mixture exhibited the weakest diffraction pattern. In the Ir@AC (211) plane, the diffraction of IrO_2 was visible at 54.77°. Hence, it is understood that 4Ir1Ni@AC possesses a higher level of crystallinity compared to other materials used in this study.

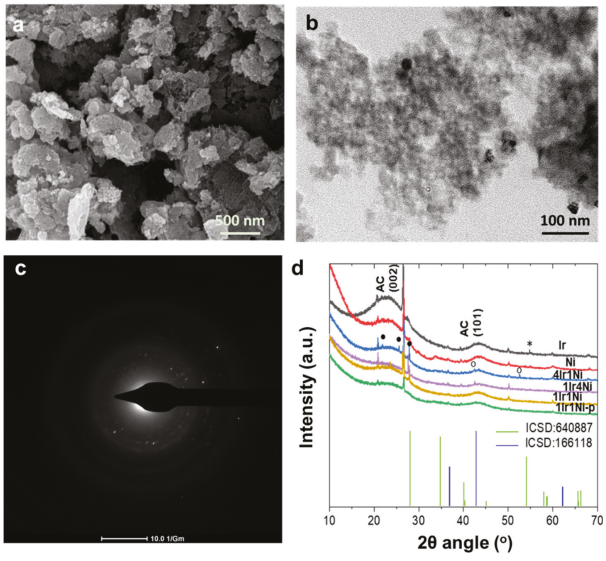

Figure 3. (**a**) SEM and (**b**) TEM representation of 4Ir1Ni@AC; the scalar bar is specified in the image. (**c**) SAED diffraction pattern of 4Ir1Ni@AC and (**d**) powder X-ray diffraction pattern in the 10–70° 2θ angle range, with peak tips marked with (*) for IrO_2, (•) for alloy, and (°) for Ni, peaks of AC are indexed with 'AC' prefix. ICSD 640,887 and ICSD 166,118 refer to the standard diffraction peak patterns of IrO_2 and NiO, respectively.

It is apparent from the outstanding edge observed with the 4Ir1Ni@AC catalyst that the light absorption and the resultant bandgap of the passive layer play definite roles in its superior activity. In this aspect, Figure 4a demonstrates the diffuse reflectance light absorption spectra of each metal and alloy combination. The presence of oxygen vacancies is known to enhance the light absorbance in the visible region. This is expected in 4Ir1Ni@AC, whose convincing sub band excitation can be seen in the visible region of the UV–visible spectra. Two resolved peaks can be seen: one at the UV–visible boundary and the second being an intense peak in the visible region. The UV-visible spectrum of Ir@AC was broad with an ambiguous peak at 330–380 nm range, and Ni@AC showed a wide, well-defined curved peak at 455 nm [40]. The enhanced light absorption in the visible region plays an undeniable role in photovoltage generation in the visible region upon irradiance with simulated solar light with a 100-mW cm^{-2} intensity. Additionally, Raman tests was performed on the materials, and the intense Raman signals arising from the activated carbon support (Figure S5a) limit the recognition of Raman signals of Ni center (460 cm^{-1}, 530 cm^{-1} for Ni-O bond) and Ir center (360 cm^{-1}, Ir-O bend). However, the Raman signals of the 4Ir1Ni@AC material shift to a lower frequency region compared to the singular systems as shown in Figure S5b, suggesting the existence of oxygen vacancies in the material. Since 4Ir1Ni@AC and 1Ir1Ni@AC demonstrated the best and second-best photoelectrochemical water splitting properties, respectively, these two materials were evaluated carefully to identify the origin of the activity. According to the Tauc plot of 4Ir1Ni@AC and 1Ir1Ni@AC given in Figure 4b, the band gaps were calculated to be 2.70 and 4.19 eV, respectively. Bandgap narrowing was thus witnessed with 4Ir1Ni@AC compared to 1Ir1Ni@AC. A Mott–Schottky analysis was then performed to elucidate the electronic band potentials of the two (Figure 4c). The resultant flat band potentials were found to be −0.92 V for 4Ir1Ni@AC and −0.70 V for 1Ir1Ni@AC (vs. NHE). Additionally, it is worth mentioning that both the 4Ir1Ni@AC and 1Ir1Ni@AC electrodes exhibited positive slopes indicative of n-type semiconductor behavior. The conduction band minimum is usually in 0~0.2 V, higher than that of the flat band potential for n-type semiconductor materials [41–43] and, in this regard, it can be set to 0.1 V considering the effective mass (electron) and charge carrier concentration. The conduction band minimum was thereby calculated to be −1.02 V and −0.80 V for 4Ir1Ni@AC and 1Ir1Ni@AC, respectively. The conduction band edge of 1Ir1Ni@AC was relatively more downshifted than 4Ir1Ni@AC. However, the valance band maximums were found to be 1.7 V (4Ir1Ni@AC) and 3.5 V (1Ir1Ni@AC) in the assessment of the band gap values obtained from the Tauc plot (Figure 4b), and the conduction band minimum values obtained from the Mott–Schottky plots (Figure 4c). Therefore, it can be concluded that the valance band edge of 4Ir1Ni@AC is relatively rising compared to 1Ir1Ni@AC. Comparing the Mott–Schottky slopes, 1Ir1Ni@AC was slightly steeper than that of 4Ir1Ni@AC. This lower Mott–Schottky slope reveals a higher donor density in the 4Ir1Ni@AC material, which may be more ascribed to oxygen vacancies [44,45]. A higher donor density improves the charge carrier separation and transport, which directly causes an increase in charge collection efficiency and a drop in charge recombination. Light-induced photoelectrochemical activity analysis is not complete without identifying the influence of charge recombination, which plays a crucial role in the transient photocurrent response. Regardless of the higher absorbance of light by NiO@AC (Figure 4a), it had a lower activity, indicative of a possible impact of charge recombination. Photoluminescence (PL) spectra were measured for metal and alloy materials upon excitation with 350 nm light at room temperature. From the general trend, the luminescent spectra had two emissions in the visible region, one centered at 557 nm and the other at 601 nm, at varying intensities (Figure 4d). The first emission at 557 nm (equivalent to a 2.22 eV photon energy) can be attributed to the near band edge (NBE) emission caused by the room-temperature free excitations in the region [46]. A higher luminescence intensity is indicative of a higher radiative charge recombination rate, which has a detrimental effect on the photo-induced reaction. The 4Ir1Ni@AC showed less intense PL peaks compared to the pattern of 1Ir1Ni@AC, which further confirms the

enhanced interfacial interaction in the case of the 4:1 Ir to Ni ratio. The improvement in interfacial interaction at the heterojunction promoted the photogenerated charge carrier separation of electrons and holes and sequentially suppressed the charge recombination. The weak photoelectrochemical behavior of NiO was apparent, with significantly more intense PL emissions (Figure S6).

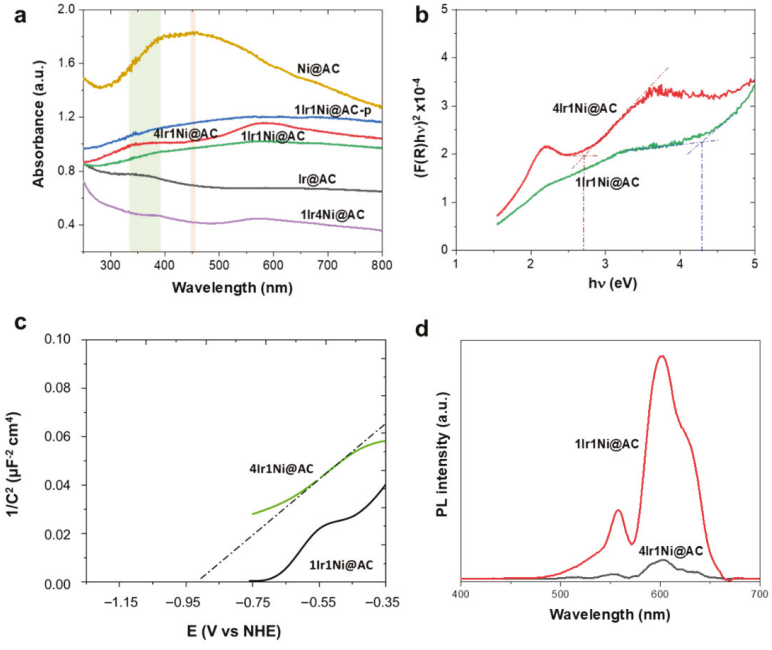

Figure 4. (**a**) UV–visible absorbance spectra of all metal and alloy combinations used in this study: shaded area at 330–380 nm reflects characteristic peak position for IrO_2 and shade at 455 nm is for NiO, (**b**) Tauc plot, (**c**) Mott–Schottky plot, and (**d**) PL emission spectra obtained upon excitation with light in the 350 nm range.

The hydrogen evolution activity of 4Ir1Ni@AC was compared between electrolytes with different pHs. As shown in Figure 1a–c and the chronoamperometry tests in Figure 5a, the photo-assisted electrochemical hydrogen evolution of 4Ir1Ni@AC was further confirmed by chronoamperometry in NaOH and H_2SO_4. Regardless of the extent, finding a light-absorbing electrocatalyst material that can perform HER over a wide pH range is very important with respect to water electrolysis. This variation in activity is evident in Figure 5b, where the potential is displayed when the system delivers a current density of -10 mA cm^{-2}. The corresponding Tafel plot for 4Ir1Ni@AC, given in Figure S7, shows a Tafel slope of 43.2 mV dec^{-1} for NaOH, 45.4 mV dec^{-1} for Na_2SO_4, and 49.7 mV dec^{-1} for H_2SO_4, respectively. The values are higher than the 28.1 mV dec^{-1} reported for MOF-supported IrNi in another study on HER in 0.5 M H_2SO_4 [47]. Considering the industrial favor of alkaline electrolyzes, the long-term stability of the system was assessed in 0.1 M NaOH electrolyte for a duration of 5 h using chronoamperometry at -1.16 V over a 3-day period, accounting for 15 h of operation altogether. The cathodic current density did not decrease over the period of the test, indicating persistent hydrogen evolution activity over time as shown in Figure 5c. A current density range of -34.5 mA cm^{-2} to -33 mA cm^{-2} was seen throughout the test. The profilometry assessment of the 4Ir1Ni@AC coating after the stability test revealed the good adhesion of the coating to the FTO substrate, with the roughness parameter changing from 22.31 μm for the fresh coating to 24.51 μm for the

coating after 15 h of operation (Figure 6). Between the test runs, the electrode was rinsed clean with running DI and dried in a vacuum oven at 40 °C.

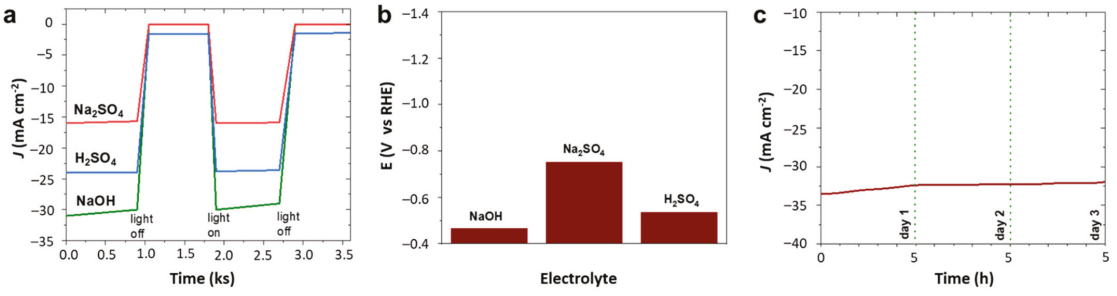

Figure 5. (**a**) Chopped chronoamperometry at −1.16 V (RHE). (**b**) Potential at −10 mA cm^{-2} current density. (**c**) Chronoamperometry in 0.1 M NaOH at −1.16 V (vs. RHE) for 4Ir1Ni@ AC catalyst.

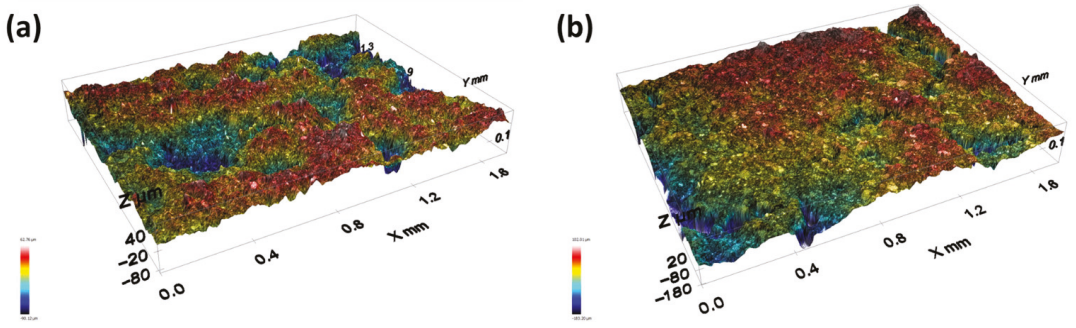

Figure 6. Surface topography curves obtained from Profilometer at ×10 objective lens. (**a**) 4Ir1Ni@AC—freshly made, R_a (roughness parameter) 22.31 µm; (**b**) 4Ir1Ni@AC—after 15 h chronoamperometry testing at −1.16 V in 0.1 M NaOH electrolyte, R_a (roughness parameter) 24.51 µm.

Similar to chronoamperometry in Figure 5a for hydrogen evolution, oxygen evolution assessed with intermittent light exposure given in Figure 7a clearly demonstrated the oxygen evolution potential of 4Ir1Ni@AC in alkaline and acidic media in particular with assured light-induced electrochemical activity. Electrochemical impedance (EIS) analysis showed a wider arc radius for the light-off reaction and a depressed semicircle for the light induced reaction in 0.1 M Na_2SO_4 solution. The lower arc radius shown in Figure S8 for light on reaction is due to the efficient interfacial charge transfer facilitated by lower interfacial layer resistance resulting in improved reaction dynamics. However, the oxygen evolution potential measured at current density of 10 mA cm^{-2} (Figure 7b) for 4Ir1Ni@AC exhibited a pattern similar to that observed for HER. The 4Ir1Ni@AC required a higher potential to reach the same current density when it was in the Na_2SO_4 electrolyte, while the difference between NaOH and H_2SO_4 was negligible. Despite the slight variation, the overpotential of OER with 4Ir1Ni@AC catalyst seen in this study was visibly lower than that observed by Lv et al. [33] with IrNi nano flowers in another study. The related Tafel slopes were found to be lower than those reported for IrNi nanocluster catalyst in KOH electrolyte media [48]. As shown in the Tafel plot in Figure S9, the 4Ir1Ni@AC exhibits an OER Tafel slope of 21.75 mV dec^{-1} in NaOH, 32.75 mV dec^{-1} in Na_2SO_4, and 25.04 mV dec^{-1} in H_2SO_4, respectively. The chronoamperometric curve of 4Ir1Ni@AC was very stable in NaOH, with a drop in current density of only 2 mA cm^{-2} seen after 15 h of durability evaluation carried out at 1.8 V by 5 h operations over three days (Figure 7c).

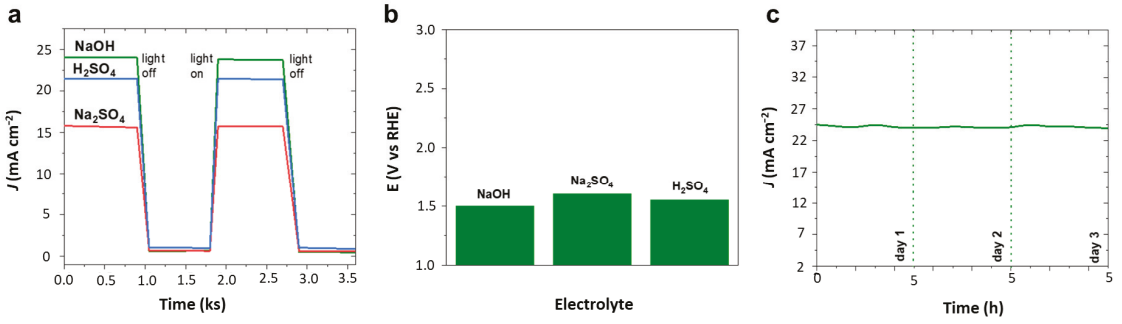

Figure 7. (**a**) Chopped chronoamperometry at 1.8 V (vs. RHE). (**b**) Potential at 10 mA cm^{-2} current density. (**c**) Chronoamperometry in 0.1 M NaOH at 1.8 V (vs. RHE) for 4Ir1Ni@ AC catalyst.

To assess the overall water splitting ability of the 4Ir1Ni@AC electrocatalyst under one sunlight irradiation of 100 mW cm^{-2} intensity, a water-splitting experiment was carried out with two 4Ir1Ni@AC film electrodes as the cathode and anode materials, respectively. Figure 8a represents the overall cell function measured by linear sweep voltammetry in positive and negative potential, with the mechanism (Figure 8b). It is observed that at a current density of 10 mA cm^{-2}, hydrogen evolution overpotential was observed to be −0.43 V and oxygen evolution overpotential was 0.25 V, resulting in an overall cell voltage of 1.94 V. The HER overpotential is high compared to other Ir-based materials for overall water splitting, as given in Table S2. However, the OER overpotential achieved by 4Ir1Ni@AC is much lower than the values reported for Ir-based electrocatalysts. The charge transfer processes occurring on IrNi nanoparticle is further illustrated in Figure 8b with respect to oxidation and reduction sites upon solar illumination. The reported HER overpotential is as low as 23 mV at a current density of 10 mA cm^{-2} using commercial 20% Pt/C and Ru/C catalysts [49,50], but considering the low mass loading of the active material (Ir and Ni) in the studied catalysts, the performance is promising. In fact, the overall cell voltage is comparable to the 1.56 V reported for non-precious metal-based $CoNiO_2$@rGO supported on Ni foam [51]. Hence, the potential of using IrNi alloys in a cost-effective activated carbon support with an appropriate Ir-to- Ni ratio for use in an electrolyte (not primarily limited to alkaline media) was demonstrated.

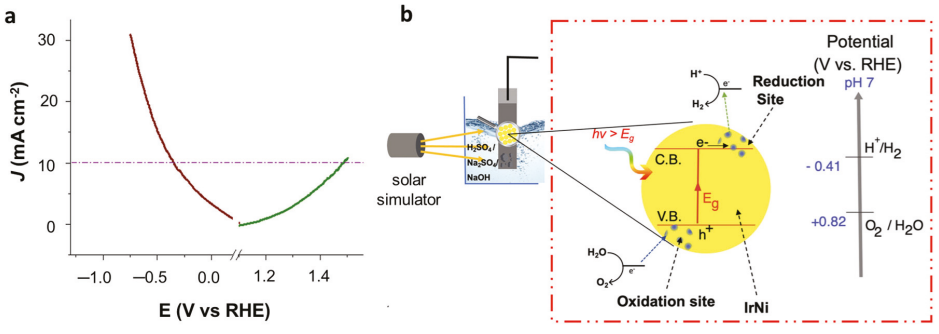

Figure 8. (**a**) Overall water splitting performance of 4Ir1Ni@AC catalyst in 0.1 M NaOH electrolyte in a two-electrode setup under illumination of 1 sunlight. (**b**) Schematic diagram of the photoelectrochemical process occurring on IrNi particle irradiated with light.

3. Materials and Methods

3.1. Materials

$Ni(NO_3)_2{\cdot}6H_2O$ (99.9%), $IrCl_3{\cdot}xH_2O$ (reagent grade), activated carbon (AC), poly(vinylidene fluoride) (PVDF, M_w ~534 k), $NaBH_4$ (98%) and *N*-methyl-2-pyrrolidone (NMP, 99%), NaOH (98%), and Na_2SO_4 (99%, anhydrous) were purchased from Sigma-Aldrich and used in the experiments without additional purification. Acetylene carbon (MTI company, St. Richmond, CA, USA), H_2SO_4 (98%, BDH), ethanol (99%, ISOLAB), and acetone (ISOLAB) were used. For all experiments requiring water, deionized water (DI) from a Mill1 Q-type water purification system was utilized, and the resistivity of the deionized water was $\geq$18.2 MΩ cm.

3.2. Synthesis of Metal and Alloys Supported on Activated Carbon

Ni@AC: A total of 500 mg of AC powder was dispersed in 100 mL of DI water in a clean, dry 250 mL beaker. The solution was kept under stirring for 20 min. Then, the desired amount of Ni salt (e.g.: 74 mg for 3% of Ni@AC) was weighed according to the weight percentage of Ni expected in the finally prepared Ni@AC catalyst powder and introduced into the AC dispersion. Meanwhile, 20 mL of freshly prepared 0.01 M $NaBH_4$ solution was introduced dropwise into the solution under vigorous stirring. Stirring was continued for another 30 min, and the mixture was aged at room temperature for 24 h. Catalyst powders were then separated and washed with DI 3 times and finally with ethanol under centrifugation. Catalyst samples were dried in a vacuum oven at 60 °C for 24 h, followed by annealing at 150 °C for 4 h in a muffle furnace.

Ir@AC: A total of 500 mg of AC powder was dispersed in 100 mL of DI in a dry clean 250 mL beaker. The solution was kept under stirring for 20 min. A total of 0.01 M of an aqueous solution of $IrCl_3{\cdot}xH_2O$ was prepared in a 250 mL volumetric flask. Then, the desired volume of Ir salt (7.5 mL $IrCl_3{\cdot}xH_2O$ solution for 3% of Ir@AC) solution was introduced according to the weight percentage of Ir expected in the finally prepared Ir@AC catalyst powder. Meanwhile, 20 mL of 0.1 M $NaBH_4$ solution was freshly prepared and added dropwise into the solution under vigorous stirring. The stirring was continued for another 30 min, and the solution was aged at room temperature for 24 h. Aged catalyst powders were washed with DI 3 times and finally with ethanol. Catalyst samples were dried in a vacuum oven at 60 °C for 24 h, followed by annealing at 150 °C for 4 h in a muffle furnace.

IrNi@AC: The alloy catalysts of Ir and Ni were fabricated in three different elemental ratios, namely, 4:1, 1:1, and 1:4, respectively. The percentage was stated based on Ir and Ni centers in the feed composition. The synthesis procedure used was similar to that of mono metal@AC, except for the addition of desired amounts of both $Ni(NO_3)_2$ salt in powder form and Ir^{3+} solution at the same time before the introduction of $NaBH_4$. The salt composition in the feed used to fabricate a 1:1 ratio of Ir:Ni was 12.5 mL of 0.01 M of $IrCl_3{\cdot}xH_2O$ (5 mL for 1:4 and 20 mL for 4:1) solution and 124 mg of $Ni(NO_3)_2$ (198.4 mg for 1:4 and 49.6 mg for 4:1). The total IrNi composition was maintained at 3% of the weight of the AC support at the beginning, with the relative ratio between Ir:Ni being 4:1 (4Ir1Ni@AC), 1:1 (1Ir1Ni@AC), and 1:4 (1Ir4Ni@AC).

Another 1:1 (1Ir1Ni@AC-p) physical mixture of Ir@AC and Ni@AC was prepared by blending annealed Ir@AC (50 mg) and annealed Ni@AC (50 mg) together in an agate mortar until they were well combined to obtain 100 mg of 1Ir1Ni@AC-p.

3.3. Electrode Preparation

Fluorine-doped tin oxide glass (FTO ~500 nm thick, 8 ohms/square, NSG Group, Ottawa, ON, Canada) was used as the substrate for the electrode. An electrode with dimensions of 3 × 1 cm^2 with intended coating dimensions of 2 × 1 cm^2 was used. The substrate was cleaned extensively prior to coating by sequential ultrasonic cleaning with acetone, ethanol, and DI for 5 min each, followed by drying under a stream of nitrogen gas.

Coating ink solution preparation: A finely ground mixture of catalyst powder, acetylene carbon, and PVDF powder at an 80:10:10 weight ratio was made into a casting ink of the desired consistency with the use of NMP solvent. The ink was ultrasonically mixed for 1 min to improve the homogeneity and stirred at 800 rpm for 2 h before casting it on FTO glass. The surface of the FTO glass was ensured to be conductive by testing the resistance of each side with a handheld multimeter.

Catalyst-coated FTO glass preparation: A portable vacuum-free spin-coating machine (Ossila, Sheffield, UK) was used to coat the ink on the FTO substrate. One short end of the FTO glass was taped and placed onto a dice with a fitting well size. Spin coating was performed in two steps: firstly, with rotation at 400 rpm for 1 min, followed by rotation at 1200 rpm for 2 min. The FTO electrode with a uniform coating was then dried in a vacuum oven for 3 h at 120 °C and employed in electrochemical experiments.

3.4. Characterization

Scanning electron microscopy with energy-dispersive X-ray spectroscopy (SEM/EDX, Nova NanoSEM 450 (FEI, Hillsboro, OR, USA) with a tungsten filament operating at 200 kV and a back-scattered electron detector was used for the visualization of the catalyst powders prepared at the micro- and nanometer scale. X-ray diffraction (XRD, Empyrean (Malvern Panalytical, Kassel, Germany)) with Cu Kα radiation at 60 kV was employed in the Bragg angle range from 5° to 40° in order to understand the crystallographic plane and the existence of each metal oxide/hydroxide phase along with the crystallinity. UV–visible spectra were recorded using a Cary 5000 instrument (Agilent, Santa Clara, CA, USA) in the 200–800 nm range, after background and blank correction in diffuse reflectance light absorption mode. Surface roughness evaluation of the photoelectroactive film was performed by surface topography imaging using a Leica DCMB instrument equipped with a 10× EPI objective lens over an area of 1.75 × 1.32 mm^2. The luminescent behavior of the prepared catalyst powders was evaluated on the PL density spectrum of the catalyst in the 365 to 800 nm range after exciting the material at 330 nm with the Fluoromax 4 device from Horiba, Japan. Raman analysis was performed on a DXR3 Raman Microscope (Thermo Fisher Scientific, Waltham, MA, USA) with a wavelength of 532 nm, a 40× scan, and a laser power of 10 using 50× microscope objectives.

3.5. Photoelectrochemical Testing

Photoelectrochemical tests were performed in alkaline, acidic, and neutral media with 0.1 M NaOH, 0.1 M H_2SO_4, and 0.1 M Na_2SO_4 as the electrolyte solutions, respectively. The electrochemical test reactor consisted of a quartz window, and the tests were carried out in a three-electrode configuration. The potentiostat1010 (Gamry, Warminster, PA, USA) workstation was employed in all the electrochemical tests. The catalyst coated on the FTO glass substrate was the working electrode. A Pt wire was used as the counter electrode, and a saturated calomel electrode (SCE) was used as the reference electrode under a 1 sun AM 1.5 G intensity (100 mW cm^{-2}). The light illumination was sourced from a Sunlight Solar Simulator (ABET Tech., Inc., Milford, CT, USA).

The cyclic voltammetry (CV) test was performed from +2.0 V to −1.2 V vs. RHE at a scan rate of 50 mV s^{-1} in the absence and presence of light in order to assess the HER and OER activity in this potential range. LSV tests were conducted from 0 to 2.0 V (OER) and 0 to −1.2 V (HER) vs. RHE. Furthermore, Mott–Schottky graphs were attained at a frequency of 10 kHz and an AC voltage of 10 mV rms while sweeping the potential in the −1.16 to 1.24 V (vs. RHE) range. Stability tests were carried out using chronoamperometry in the presence of light at 1.64 V (vs. RHE) for 15 h and at −1.16 V (vs. RHE) for 15 h. Electrochemical impedance spectroscopy (EIS) study was performed on 0.1 M Na_2SO_4 electrolyte using a 4Ir1Ni@AC electrode in a potential range from 10 mHz to 100 kHz frequency range and 5 mV AC amplitude.

4. Conclusions

In conclusion, IrNi oxide alloy nanoparticles with an appropriate Ir to Ni weight ratio (4Ir1Ni@AC) were demonstrated to drive improved hydrogen and oxygen evolution reactions over a wide pH range at light illumination of one sunlight (100 mW cm^{-2} intensity) compared to individual Ir@Ac and Ni@AC. An overall water splitting assessment affirmed 1.94 V cell voltage at 10 mA cm^{-2} current density for 4Ir1Ni@AC catalyst under 1.5 G AM light illumination of 100 mW cm^{-2} in alkaline media. The HER overpotential was 0.43 V, and the OER was 0.25 V under the same conditions. The detailed assessment of the light absorption behavior using Mott–Schottky graphs, Tauc plots, PL emission spectra, and Raman studies affirmed the favorable d-band center and oxygen vacancies in 4Ir1Ni@AC catalyst, which are responsible for its superior catalytic performance and minimal charge recombination effect. The electrodes were demonstrated to have significantly high durability, as evidenced by the highly consistent cathodic current and less than 2 mA cm^{-2} drop in anodic current over 15 h of cell operation in alkaline electrolyte.

Supplementary Materials: The following are available online at https://www.mdpi.com/article/10.3390/catal12091056/s1, Figure S1. SEM images of (a) Ni@AC, (b) 1Ir4Ni@AC, (c) 1Ir1Ni@AC, (d) 4Ir1Ni@AC and (e) Ir@AC, scaler bar in the images refer to 1 µm; Figure S2. TEM images of (a) Ni@AC, (b) 1Ir4Ni@AC, (c) 1Ir1Ni@AC, and (d) Ir@AC, scaler bar is given in each image; Figure S3. SAED ring pattern of Ni@AC; Figure S4. SEM-EDX spectra of (a) Ir@AC (b) Ni@AC and (c) 4Ir1Ni@AC showing the elements present in each catalyst material; Figure S5. Raman spectra of Ir@AC, Ni@AC and 4Ir1Ni@AC (a) 300 3500 cm^{-1} and (b) 200-800 cm^{-1} frequency range; Figure S6. PL emission spectra of metal and alloy nanoparticles of Ir and Ni, after excitation at 350 nm; Figure S7. Tafel slope for HER reaction under 1.5 G AM light illumination in a. NaOH, b. Na_2SO_4 and c. H_2SO_4 electrolyte solutions; Figure S8. EIS spectra of 4Ir1Ni@AC electrode in 0.1 M Na_2SO_4 electrolyte measured from 10 mHz to 100 kHz frequency range at 5 mV AC amplitude; Figure S9. Tafel slope for OER reaction under 1.5 G AM light illumination in a. NaOH, b. Na_2SO_4 and c. H_2SO_4 electrolyte solutions; Table S1. Relative mass ration between Ir and Ni; Table S2. Summary of recently reported Ir based electrocatalysts for water splitting performance. References [52–57] are cited in the supplementary materials.

Author Contributions: Conceptualization, D.S.H.; methodology, D.S.H. and S.Z.; validation, H.P., D.S.H. and S.Z.; formal analysis, S.Z. and U.H.; investigation, U.H.; resources, D.S.H. and H.P.; data curation, S.Z. and H.P.; writing—original draft preparation, S.Z.; writing—review and editing, all authors; supervision, D.S.H.; project administration, D.S.H.; funding acquisition, D.S.H. and S.Z. All authors have read and agreed to the published version of the manuscript.

Funding: This publication was made possible by NPRP grant # NPRP13S-0202-200228 from the Qatar National Research Fund (a member of Qatar Foundation). The statements made herein are solely the responsibility of the authors.

Data Availability Statement: Not applicable.

Acknowledgments: The authors thank the Centre for Advanced Materials, Qatar University, for the facility support. The Raman, TEM and SEM imaging was supported by the Central Laboratories Unit, Qatar University.

Conflicts of Interest: The authors declare no conflict of interest.

References

1. Sun, H.; Tian, C.; Fan, G.; Qi, J.; Liu, Z.; Yan, Z.; Cheng, F.; Chen, J.; Li, C.P.; Du, M. Boosting activity on Co_4N porous nanosheet by coupling CeO_2 for efficient electrochemical overall water splitting at high current densities. *Adv. Funct. Mater.* **2020**, *30*, 1910596. [CrossRef]
2. Chen, J.; Xiao, R.; Fu, K.; Wu, Y.; Guo, Y.; Yang, S.; Li, H.; Zheng, J.; Li, X. Metal hydride mediated water splitting: Electrical energy saving and decoupled H_2/O_2 generation. *Mater. Today* **2021**, *47*, 16–24. [CrossRef]
3. Hui, L.; Xue, Y.; Huang, B.; Yu, H.; Zhang, C.; Zhang, D.; Jia, D.; Zhao, Y.; Li, Y.; Liu, H. Overall water splitting by graphdiyne-exfoliated and-sandwiched layered double-hydroxide nanosheet arrays. *Nat. Commun.* **2018**, *9*, 5309. [CrossRef]
4. Yusaf, T.; Laimon, M.; Alrefae, W.; Kadirgama, K.; Dhahad, H.A.; Ramasamy, D.; Kamarulzaman, M.K.; Yousif, B. Hydrogen Energy Demand Growth Prediction and Assessment (2021–2050) Using a System Thinking and System Dynamics Approach. *Appl. Sci.* **2022**, *12*, 781. [CrossRef]

5. Zhongming, Z.; Wei, L. Hydrogen Economy Hints at New Global Power Dynamics. Available online: http://resp.llas.ac.cn/C666/handle/2XK7JSWQ/344685 (accessed on 4 May 2022).
6. Iulianelli, A.; Ribeirinha, P.; Mendes, A.; Basile, A. Methanol steam reforming for hydrogen generation via conventional and membrane reactors: A review. *Renew. Sustain. Energy Rev.* **2014**, *29*, 355–368. [CrossRef]
7. Ranjekar, A.M.; Yadav, G.D. Steam reforming of methanol for hydrogen production: A critical analysis of catalysis, processes, and scope. *Ind. Eng. Chem. Res.* **2021**, *60*, 89–113. [CrossRef]
8. Soni, R.; Miyanishi, S.; Kuroki, H.; Yamaguchi, T. Pure water solid alkaline water electrolyzer using fully aromatic and high-molecular-weight poly (fluorene-alt-tetrafluorophenylene)-trimethyl ammonium anion exchange membranes and ionomers. *ACS Appl. Energy Mater.* **2020**, *4*, 1053–1058. [CrossRef]
9. Nakajima, Y.; Fujimoto, N.; Hasegawa, S.; Usui, T. Advanced Alkaline Water Electrolyzer for Renewable Hydrogen Production. *ECS Trans.* **2017**, *80*, 835. [CrossRef]
10. Andrade, A.M.; Liu, Z.; Grewal, S.; Nelson, A.J.; Nasef, Z.; Diaz, G.; Lee, M.H. MOF-derived Co/Cu-embedded N-doped carbon for trifunctional ORR/OER/HER catalysis in alkaline media. *Dalton Trans.* **2021**, *50*, 5473–5482. [CrossRef]
11. Ursua, A.; Gandia, L.M.; Sanchis, P. Hydrogen production from water electrolysis: Current status and future trends. *Proc. IEEE* **2011**, *100*, 410–426. [CrossRef]
12. Lin, Y.; Gao, Y.; Fan, Z. Printable Fabrication of Nanocoral-Structured Electrodes for High-Performance Flexible and Planar Supercapacitor with Artistic Design. *Adv. Mater.* **2017**, *29*, 1701736. [CrossRef] [PubMed]
13. Li, D.; Park, E.J.; Zhu, W.; Shi, Q.; Zhou, Y.; Tian, H.; Lin, Y.; Serov, A.; Zulevi, B.; Baca, E.D. Highly quaternized polystyrene ionomers for high performance anion exchange membrane water electrolysers. *Nat. Energy* **2020**, *5*, 378–385. [CrossRef]
14. Liu, Z.-X.; Wang, X.-L.; Hu, A.-P.; Tang, Q.-L.; Xu, Y.-L.; Chen, X.-H. 3D Se-doped NiCoP nanoarrays on carbon cloth for efficient alkaline hydrogen evolution. *J. Cent. South Univ.* **2021**, *28*, 2345–2359. [CrossRef]
15. Yan, X.; Biemolt, J.; Zhao, K.; Zhao, Y.; Cao, X.; Yang, Y.; Wu, X.; Rothenberg, G.; Yan, N. A membrane-free flow electrolyzer operating at high current density using earth-abundant catalysts for water splitting. *Nat. Commun.* **2021**, *12*, 4143. [CrossRef] [PubMed]
16. Zhu, Y.; Liu, X.; Jin, S.; Chen, H.; Lee, W.; Liu, M.; Chen, Y. Anionic defect engineering of transition metal oxides for oxygen reduction and evolution reactions. *J. Mater. Chem. A* **2019**, *7*, 5875–5897. [CrossRef]
17. Zhang, H.; Lv, R. Defect engineering of two-dimensional materials for efficient electrocatalysis. *J. Mater.* **2018**, *4*, 95–107. [CrossRef]
18. Yu, H.; Yu, X.; Chen, Y.; Zhang, S.; Gao, P.; Li, C. A strategy to synergistically increase the number of active edge sites and the conductivity of MoS_2 nanosheets for hydrogen evolution. *Nanoscale* **2015**, *7*, 8731–8738. [CrossRef]
19. Miao, J.; Xiao, F.-X.; Yang, H.B.; Khoo, S.Y.; Chen, J.; Fan, Z.; Hsu, Y.-Y.; Chen, H.M.; Zhang, H.; Liu, B. Hierarchical Ni-Mo-S nanosheets on carbon fiber cloth: A flexible electrode for efficient hydrogen generation in neutral electrolyte. *Sci. Adv.* **2015**, *1*, e1500259. [CrossRef]
20. Fang, L.; Jiang, Z.; Xu, H.; Liu, L.; Gu, X.; Wang, Y. Crystal-plane engineering of $NiCo_2O_4$ electrocatalysts towards efficient overall water splitting. *J. Catal.* **2018**, *357*, 238–246. [CrossRef]
21. Kuttiyiel, K.A.; Sasaki, K.; Chen, W.-F.; Su, D.; Adzic, R.R. Core–shell, hollow-structured iridium–nickel nitride nanoparticles for the hydrogen evolution reaction. *J. Mater. Chem. A* **2014**, *2*, 591–594. [CrossRef]
22. Zhu, C.; Wang, A.L.; Xiao, W.; Chao, D.; Zhang, X.; Tiep, N.H.; Chen, S.; Kang, J.; Wang, X.; Ding, J. In situ grown epitaxial heterojunction exhibits high-performance electrocatalytic water splitting. *Adv. Mater.* **2018**, *30*, 1705516. [CrossRef] [PubMed]
23. Yu, H.; Xue, Y.; Hui, L.; Zhang, C.; Li, Y.; Zuo, Z.; Zhao, Y.; Li, Z.; Li, Y. Efficient hydrogen production on a 3D flexible heterojunction material. *Adv. Mater.* **2018**, *30*, 1707082. [CrossRef] [PubMed]
24. Hemmerling, J.R.; Mathur, A.; Linic, S. Design principles for efficient and stable water splitting photoelectrocatalysts. *Acc. Chem. Res.* **2021**, *54*, 1992–2002. [CrossRef] [PubMed]
25. Liu, S.; Hu, Z.; Wu, Y.; Zhang, J.; Zhang, Y.; Cui, B.; Liu, C.; Hu, S.; Zhao, N.; Han, X. Dislocation-Strained IrNi Alloy Nanoparticles Driven by Thermal Shock for the Hydrogen Evolution Reaction. *Adv. Mater.* **2020**, *32*, 2006034. [CrossRef]
26. Ramadan, W.; Feldhoff, A.; Bahnemann, D. Assessing the photocatalytic oxygen evolution reaction of $BiFeO_3$ loaded with IrO_2 nanoparticles as cocatalyst. *Sol. Energy Mater. Sol. Cells* **2021**, *232*, 111349. [CrossRef]
27. Frame, F.A.; Townsend, T.K.; Chamousis, R.L.; Sabio, E.M.; Dittrich, T.; Browning, N.D.; Osterloh, F.E. Photocatalytic water oxidation with nonsensitized IrO_2 nanocrystals under visible and UV light. *J. Am. Chem. Soc.* **2011**, *133*, 7264–7267. [CrossRef]
28. Faid, A.Y.; Barnett, A.O.; Seland, F.; Sunde, S. Ni/NiO nanosheets for alkaline hydrogen evolution reaction: In situ electrochemical-Raman study. *Electrochim. Acta* **2020**, *361*, 137040. [CrossRef]
29. Kou, T.; Chen, M.; Wu, F.; Smart, T.J.; Wang, S.; Wu, Y.; Zhang, Y.; Li, S.; Lall, S.; Zhang, Z. Carbon doping switching on the hydrogen adsorption activity of NiO for hydrogen evolution reaction. *Nat. Commun.* **2020**, *11*, 590. [CrossRef]
30. Soofivand, F.; Salavati-Niasari, M. Step synthesis and photocatalytic activity of NiO/graphene nanocomposite under UV and visible light as an effective photocatalyst. *J. Photochem. Photobiol. A Chem.* **2017**, *337*, 44–53. [CrossRef]
31. Torki, F.; Faghihian, H. Photocatalytic activity of NiS, NiO and coupled NiS–NiO for degradation of pharmaceutical pollutant cephalexin under visible light. *RSC Adv.* **2017**, *7*, 54651–54661. [CrossRef]
32. Wang, P.; Wang, B. Designing Self-Supported Electrocatalysts for Electrochemical Water Splitting: Surface/Interface Engineering toward Enhanced Electrocatalytic Performance. *ACS Appl. Mater. Interfaces* **2021**, *13*, 59593–59617. [CrossRef] [PubMed]

33. Lv, F.; Zhang, W.; Yang, W.; Feng, J.; Wang, K.; Zhou, J.; Zhou, P.; Guo, S. Ir-based alloy nanoflowers with optimized hydrogen binding energy as bifunctional electrocatalysts for overall water splitting. *Small Methods* **2020**, *4*, 1900129. [CrossRef]
34. Gandía, L.M.; Oroz, R.; Ursúa, A.; Sanchis, P.; Diéguez, P.M. Renewable hydrogen production: Performance of an alkaline water electrolyzer working under emulated wind conditions. *Energy Fuels* **2007**, *21*, 1699–1706. [CrossRef]
35. Subbaraman, R.; Tripkovic, D.; Strmcnik, D.; Chang, K.-C.; Uchimura, M.; Paulikas, A.P.; Stamenkovic, V.; Markovic, N.M. Enhancing hydrogen evolution activity in water splitting by tailoring Li^+-Ni(OH) $_2$-Pt interfaces. *Science* **2011**, *334*, 1256–1260. [CrossRef] [PubMed]
36. Mahmood, N.; Yao, Y.; Zhang, J.W.; Pan, L.; Zhang, X.; Zou, J.J. Electrocatalysts for hydrogen evolution in alkaline electrolytes: Mechanisms, challenges, and prospective solutions. *Adv. Sci.* **2018**, *5*, 1700464. [CrossRef]
37. Wei, C.; Sun, Y.; Scherer, G.n.G.; Fisher, A.C.; Sherburne, M.; Ager, J.W.; Xu, Z. Surface composition dependent ligand effect in tuning the activity of nickel–copper bimetallic electrocatalysts toward hydrogen evolution in alkaline. *J. Am. Chem. Soc.* **2020**, *142*, 7765–7775. [CrossRef]
38. Danilovic, N.; Subbaraman, R.; Strmcnik, D.; Chang, K.C.; Paulikas, A.; Stamenkovic, V.; Markovic, N.M. Enhancing the alkaline hydrogen evolution reaction activity through the bifunctionality of $Ni(OH)_2$/metal catalysts. *Angew. Chem.* **2012**, *124*, 12663–12666. [CrossRef]
39. Lee, W.H.; Ko, Y.-J.; Kim, J.H.; Choi, C.H.; Chae, K.H.; Kim, H.; Hwang, Y.J.; Min, B.K.; Strasser, P.; Oh, H.-S. High crystallinity design of Ir-based catalysts drives catalytic reversibility for water electrolysis and fuel cells. *Nat. Commun.* **2021**, *12*, 4271. [CrossRef]
40. Mohan, S.C.; Bhattacharjee, D.; Deka, R.C.; Jothivenkatachalam, K. Combined experimental and theoretical investigations on the encapsulation of nickel (II) tet-a complex in zeolite Y and its photocatalytic activity. *RSC Adv.* **2016**, *6*, 71214–71222. [CrossRef]
41. Wu, X.; Ng, Y.H.; Wang, L.; Du, Y.; Dou, S.X.; Amal, R.; Scott, J. Improving the photo-oxidative capability of BiOBr via crystal facet engineering. *J. Mater. Chem. A* **2017**, *5*, 8117–8124. [CrossRef]
42. Tu, X.; Qian, S.; Chen, L.; Qu, L. The influence of Sn (II) doping on the photoinduced charge and photocatalytic properties of BiOBr microspheres. *J. Mater. Sci.* **2015**, *50*, 4312–4323. [CrossRef]
43. Wang, S.; Wang, L.; Huang, W. Bismuth-based photocatalysts for solar energy conversion. *J. Mater. Chem. A* **2020**, *8*, 24307–24352.
44. Su, T.; Yang, Y.; Na, Y.; Fan, R.; Li, L.; Wei, L.; Yang, B.; Cao, W. An insight into the role of oxygen vacancy in hydrogenated TiO2 nanocrystals in the performance of dye-sensitized solar cells. *ACS Appl. Mater. Interfaces* **2015**, *7*, 3754–3763. [CrossRef]
45. Kong, X.Y.; Ng, B.-J.; Tan, K.H.; Chen, X.; Wang, H.; Mohamed, A.R.; Chai, S.-P. Simultaneous generation of oxygen vacancies on ultrathin BiOBr nanosheets during visible-light-driven CO_2 photoreduction evoked superior activity and long-term stability. *Catal. Today* **2018**, *314*, 20–27. [CrossRef]
46. Cai, H.; You, Q.; Hu, Z.; Duan, Z.; Cui, Y.; Sun, J.; Xu, N.; Wu, J. Fabrication and correlation between photoluminescence and photoelectrochemical properties of vertically aligned ZnO coated TiO_2 nanotube arrays. *Sol. Energy Mater. Sol. Cells* **2014**, *123*, 233–238. [CrossRef]
47. Paul, S.C.; Dey, S.C.; Molla, M.A.I.; Islam, M.S.; Debnath, S.; Miah, M.Y.; Ashaduzzaman, M.; Sarker, M. Nanomaterials as electrocatalyst for hydrogen and oxygen evolution reaction: Exploitation of challenges and current progressions. *Polyhedron* **2021**, *193*, 114871. [CrossRef]
48. Pi, Y.; Shao, Q.; Wang, P.; Guo, J.; Huang, X. General formation of monodisperse IrM (M = Ni, Co, Fe) bimetallic nanoclusters as bifunctional electrocatalysts for acidic overall water splitting. *Adv. Funct. Mater.* **2017**, *27*, 1700886. [CrossRef]
49. Zhang, J.; Wang, G.; Liao, Z.; Zhang, P.; Wang, F.; Zhuang, X.; Zschech, E.; Feng, X. Iridium nanoparticles anchored on 3D graphite foam as a bifunctional electrocatalyst for excellent overall water splitting in acidic solution. *Nano Energy* **2017**, *40*, 27–33. [CrossRef]
50. Lv, F.; Feng, J.; Wang, K.; Dou, Z.; Zhang, W.; Zhou, J.; Yang, C.; Luo, M.; Yang, Y.; Li, Y. Iridium–tungsten alloy nanodendrites as pH-universal water-splitting electrocatalysts. *ACS Cent. Sci.* **2018**, *4*, 1244–1252. [CrossRef]
51. Pan, Z.-Y.; Tang, Z.; Zhan, Y.-Z.; Sun, D. Three-dimensional porous $CoNiO_2$@reduced graphene oxide nanosheet arrays/nickel foam as a highly efficient bifunctional electrocatalyst for overall water splitting. *Tungsten* **2020**, *2*, 390–402. [CrossRef]
52. Karfa, P.; Majhi, K.C.; Madhuri, R. Shape-dependent electrocatalytic activity of iridium oxide decorated erbium pyrosilicate toward the hydrogen evolution reaction over the entire pH range. *ACS Catal.* **2018**, *9*, 8830–8843.
53. Kumar, S.S.; Himabindu, V. Hydrogen production by PEM water electrolysis—A review. *Mater. Sci. Energy Technol.* **2019**, *2*, 442–454.
54. McCrory, C.C.; Jung, S.; Ferrer, I.M.; Chatman, S.M.; Peters, J.C.; Jaramillo, T.F. Benchmarking hydrogen evolving reaction and oxygen evolving reaction electrocatalysts for solar water splitting devices. *J. Am. Chem. Soc.* **2015**, *137*, 4347–4357.
55. McCrory, C.C.; Jung, S.; Peters, J.C.; Jaramillo, T.F. Benchmarking heterogeneous electrocatalysts for the oxygen evolution reaction. *J. Am. Chem. Soc.* **2013**, *135*, 16977–16987.
56. Nakagawa, T.; Beasley, C.A.; Murray, R.W. Efficient electro-oxidation of water near its reversible potential by a mesoporous IrOx nanoparticle film. *J. Phys. Chem. C* **2009**, *113*, 12958–12961.
57. Reier, T.; Pawolek, Z.; Cherevko, S.; Bruns, M.; Jones, T.; Teschner, D.; Selve, S.; Bergmann, A.; Nong, H.N.; Schlögl, R.; et al. Molecular insight in structure and activity of highly efficient, low-Ir Ir–Ni oxide catalysts for electrochemical water splitting (OER). *J. Am. Chem. Soc.* **2015**, *137*, 13031–13040.

MDPI
St. Alban-Anlage 66
4052 Basel
Switzerland
Tel. +41 61 683 77 34
Fax +41 61 302 89 18
www.mdpi.com

MDPI Books Editorial Office
E-mail: books@mdpi.com
www.mdpi.com/books

MDPI
St. Alban-Anlage 66
4052 Basel
Switzerland

Tel: +41 61 683 77 34

www.mdpi.com

ISBN 978-3-0365-6911-6